COBEM-97

Vol. 2

Vol 2

Tema 32

Escoamentos Compressíveis e Incompressíveis

XIV Brazilian Congress of Mechanical Engineering
Obeid Plaza Hotel Convention Center - Bauru - SP/Brazil
December 08-12th 1997

PAPER CODE: COB1227

ESTUDO ANALÍTICO DOS FENÔMENOS TRANSITÓRIOS OCASIONADOS POR GRANDES BOLSAS DE AR CONFINADAS NOS SISTEMAS HIDRÁULICOS

Carlos Augusto de Carvalho Magalhães, Rodrigo de Melo Porto & Hans George Arens
Departamento de Hidráulica e Saneamento, Escola de Engenharia de São Carlos - EESC - USP
CEP: 13.560-250 - Caixa Postal 539 - São Carlos, Brasil - E-mail: cacmagal@sc.usp.br

Abstract

The flow in a hydraulic installation can be affected by various conditions such as starting or stopping the pumps or turbines and the changes in the valve setting. During such conditions, there arise situations in wich pressures and velocities in pipes can be determined by mathematical models in order to verify if their extreme values are within the admissible range. One of the reasons for the transient behavior is the presence of air confined during these alterations. When the pipes are not properly designed or if it is not completely full or air bleeding, large amounts of air may be confined in the system. Pockets of air can cause severe transient behavior if such pockets deslocate from one place to the other giving rise to local acceleration and consequently large velocities and pressures. The higher pressure may be of the order of 15 times the static pressure in the system. Thus, this paper considers pratical and safe procedure (rigid or elastic models) that permit calculation of transient pressures given that there is no analytical solution available. This study also conducts a sensitivity analysis on the various factors involved in the problem.

Keywords

air pockets; hydraulic transients; waterhammer; bolsas de ar; transientes hidráulicos.

1. INTRODUÇÃO

O transiente hidráulico é governado pelas equações da quantidade de movimento (momentum) e da continuidade. A solução dessas equações permite a determinação de pressões e velocidades em função do tempo e, daí, a interpretação física do fenômeno relaciona a causa (manobra) ao efeito (transiente hidráulico) fornecendo subsídios para otimização do projeto. Uma das causas da potencialização do transiente pode ser devido a presença de ar aprisionado durante o fenômeno.

O conceito *golpe de ariete* é usado como sinônimo do transiente hidráulico quando se considera, no equacionamento do fenômeno, a elasticidade da tubulação e a compressibilidade do líquido (modelo elástico). Se tais fatores são desprezados diz-se que a situação transitória corresponde a uma *oscilação de massa* (modelo rígido).

Se uma tubulação não estiver satisfatoriamente projetada ou não for adequadamente cheia e purgada, grandes quantidades de ar poderão ficar aprisionadas. Contrariamente aos efeitos benéficos de pequenas quantidades de ar disperso, grandes bolsões podem ser a fonte de transientes severos, caso estes bolsões se desloquem de um local para outro, haja visto que o ar age como uma mola, proporcionando acelerações locais que resultam em altas velocidades e, subseqüentemente, em altas pressões transientes.

Particularmente, nestes sistemas que contêm ar confinado, as sobrepressões podem ocorrer devido ao rápido enchimento da tubulação, ou à partida de uma bomba. As sobrepressões geradas, conforme comprovado teoricamente, podem ser até 15 vezes maiores que as pressões estáticas do sistema.

Em conseqüência, há a necessidade do estabelecimento de metodologias de aplicação prática e segura (modelos rígido e elástico) que permitam estimar a magnitude das pressões transitórias, pois não há solução analítica para este problema.

2. OBJETIVOS

O propósito do presente trabalho é de efetuar um estudo analítico dos fenômenos transitórios ocasionados por bolsas de ar confinadas em condutos forçados, com o intuito de comparar os modelos elástico, rígido de coluna líquida variável e rígido de coluna líquida constante, visto que não há solução analítica para esta situação física. Dentro deste estudo será realizada uma análise de sensibilidade com relação aos fatores intervenientes no sistema hidráulico (coeficiente politrópico, tempo de abertura da válvula, fator de atrito, carga hidráulica disponível, comprimento inicial da bolsa de ar, diâmetro do conduto e o ângulo entre o eixo da tubulação com o nível de referência horizontal).

3. MODELOS MATEMÁTICOS

Este item tem como intuito apresentar os modelos matemáticos a serem empregados no sistema hidráulico da figura 01 que é semelhante ao proposto por Martin (1976), e realizar um estudo comparativo analítico entre estes modelos. No lugar do reservatório para proporcionar carga hidráulica poderia ser perfeitamente usado um conjunto motor-bomba.

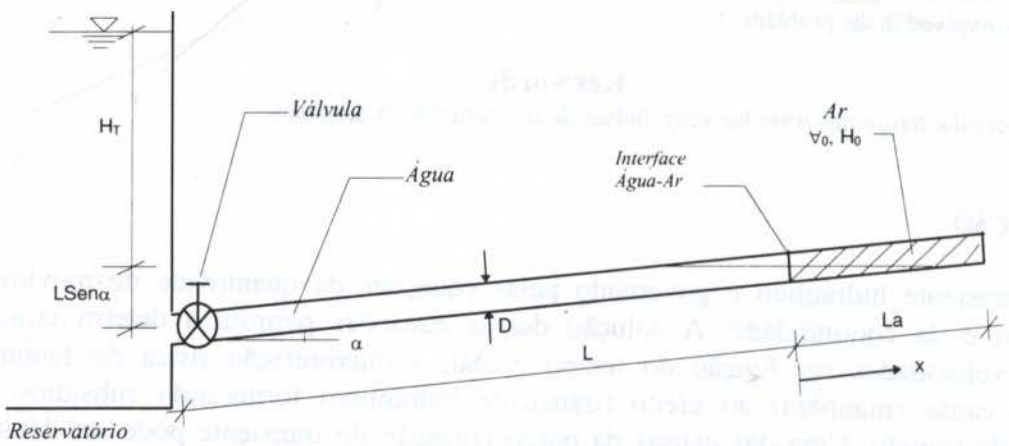

Figura 01 - Esquema idealizado para o estudo analítico do efeito do ar aprisionado

Por limitações do número de páginas no presente artigo, não será realizada a dedução de algumas equações. No entanto, tais deduções podem ser encontradas na bibliografia citada.

Para simular as condições transitórias devido à abertura da válvula do esquema da figura 01, as seguintes hipóteses básicas são feitas:

a) A massa de ar na bolsa permanece constante durante o fenômeno.
b) No comportamento da bolsa de ar é assumido que a expansão e contração da bolsa de ar seguem a equação politrópica para um gás ideal.
c) A interface Ar / Água ocupa toda a seção transversal do tubo e é suave e normal ao eixo do conduto.

Admitindo que x seja a variação do comprimento da coluna líquida, e V a velocidade da interface, as hipóteses a) e c) permitem estabelecer a seguinte expressão como sendo a equação da continuidade:

$$\frac{dx}{dt} = V \qquad (01)$$

A seguir serão apresentados os modelos rígido de coluna líquida variável (MCLV), rígido de coluna líquida constante (MCLC) e o elástico.

3.1. Modelo Rígido

Quando há pequenas variações na carga do transitório hidráulico, é possível considerar o conduto como indeformável e o líquido como incompressível, caracterizando assim a oscilação de massa. Desta forma, a equação fundamental para o modelo rígido é:

$$\frac{dV}{dt} = \frac{g}{(L+x)}\cdot\left[H_T^* - H_0^*\cdot\left(\frac{\forall_0}{\forall}\right)^n\right] - \frac{x}{(L+x)}\cdot g\cdot \operatorname{sen}\alpha - \left[\frac{K}{2\cdot(L+x)} + \frac{f}{2\cdot D}\right]\cdot V.|V| - \frac{V^2}{2\cdot(L+x)} \qquad (02)$$

onde:
D : diâmetro do conduto (m);
H_T^* : carga de pressão absoluta do reservatório com relação à interface ar / água (m);
K : coeficiente de perda de carga localizada da válvula (adim.);
f : fator de atrito de Darcy-Weisbach (adim.);
$\forall$: volume da bolsa de ar (m^3);
x : comprimento de variação da coluna líquida (m);
$H^* = H + H_a$: carga de pressão absoluta da bolsa de ar (m);
n : coeficiente politrópico que varia de 1,0 (lento processo isotérmico) a 1,4 (rápido processo adiabático) (adim.);
$\forall_0$: volume inicial da bolsa de ar (m^3);
H_0 : carga de pressão inicial relativa da bolsa de ar (m).

É escrito $V.|V|$ ao invés de V^2, para que se tenha o sentido real do escoamento durante o transitório. Na eq.(02) verifica-se claramente que a diferença de carga nos extremos do conduto é utilizada para acelerar o líquido no seu interior e vencer as perdas.

As condições iniciais (t = 0) são:

$H^*(0) = H_0^*$; $V(0) = 0$; $\forall(0) = \forall_0$; $x(0) = 0$.

A eq.(02) juntamente com as condições de contorno representam um sistema de equações diferenciais ordinárias (EDOs) não lineares cuja solução analítica é impossível, sendo necessária, para resolver o problema transitório, a aplicação de um esquema numérico

que possibilite a obtenção da solução aproximada. Assim, o sistema de equações foi integrado numericamente pelo método de Runge-Kutta de 4ª ordem. Este sistema de oscilação de massa em que é considerado a variação do comprimento da coluna líquida com o tempo, é denominado de *modelo rígido de coluna líquida variável* (MCLV). Tal modelo também foi estudado por Guarga et al. (1994), Abreu et al. (1991) e Chaudhry (1989).

No *modelo rígido de coluna líquida constante* (MCLC) para a abertura instantânea da válvula (K = 0), proposto por Martin (1976), não é considerada a variação da coluna líquida (x =0) na equação do momentum, assim como a carga cinética é desprezada em face aos outros termos da equação ($V^2/2g \approx 0$). Portanto, o MCLC é um caso particular do MCLV.

3.1.1. Forma Adimensional do Modelo Rígido

Para tornar adimensional as equações para o modelo rígido é necessário definir valores numéricos de referência para cada uma das variáveis que aparecem nas equações. A situação da condição inicial é sempre uma boa indicação para a definição dos valores de referência, pois embora estes possam ser escolhidos arbitrariamente, deverão ser bem definidos para cada problema específico que se está analisando.

Assim, na adimensionalização das variáveis x, t, V, $\forall$ e H^* efetuou-se as seguintes mudanças de variáveis:

$$x = \hat{x} \cdot L \; ; \; t = \hat{t} \cdot t_R \; ; \; V = \hat{V} \cdot V_R \; ; \; \forall = \hat{\forall} \cdot \forall_0 \; ; \; H^* = \hat{H}^* \cdot H_T^*$$

em que t_R e V_R são um tempo e uma velocidade de referência cuja determinação surge da própria análise dimensional efetuada. As variáveis com ^ correspondem aos seus valores adimensionalizados. Portanto, t_R e V_R são respectivamente:

$$t_R = \left(\frac{L \cdot \forall_0}{g \cdot H_T^* \cdot D^2} \right)^{1/2} \; ; \; V_R = \left(\frac{g \cdot H_T^* \cdot \forall_0}{D^2 \cdot L} \right)^{1/2}$$

Desta forma, a equação do momentum do modelo de oscilação de massa adimensionalizado é:

$$\frac{d\hat{V}}{d\hat{t}} = \frac{1}{(1+\hat{x})} \cdot \left(1 - \frac{1}{\pi_1 \cdot \hat{\forall}^{\pi_3}} \right) - \pi_4 \cdot \frac{\hat{x}}{(1+\hat{x})} - \left[\frac{\pi_6 \cdot \pi_5}{2.(1+\hat{x})} + \frac{\pi_2}{2} \right] \cdot \hat{V} \cdot |\hat{V}| - \frac{\pi_5}{2.(1+\hat{x})} \cdot V^2 \qquad (03)$$

onde:

π_i : número adimensional independente ($1 \le i \le 7$).

$$\pi_1 = \frac{H_T^*}{H_0^*} \; ; \; \pi_2 = f \cdot \frac{\forall_0}{D^3} \; ; \; \pi_3 = n \; ; \; \pi_4 = \frac{L \operatorname{sen} \alpha}{H_T^*} \; ; \; \pi_5 = \frac{\forall_0}{D^2 L} \; ; \; \pi_6 = K \; ; \; \pi_7 = \frac{a}{\sqrt{g \cdot H_T^*}}$$

a : celeridade (m/s^2).

Com isto, duas situações do fenômeno físico que está sendo estudado através do modelo rígido, serão semelhantes se as condições de contorno forem similares e os adimensionais, π_i, forem respectivamente iguais para as duas situações. Tal condição de semelhança governa a extrapolação dos resultados de ensaios em modelo para o protótipo.

3.2. Modelo Elástico

O modelo elástico corresponde à situação física do escoamento transiente na qual são consideradas conjuntamente, sob a ação das variações de pressão, os efeitos de deformação da tubulação no regime elástico e do líquido que se comprime e se dilata segundo uma condição isotérmica definida a cada instante pelo seu módulo de elasticidade volumétrico. Geralmente, esse regime elástico ocorre quando há grandes variações de carga, caracterizando assim o golpe de aríete.

Na análise do golpe de aríete deverão ser verificadas as equações diferenciais parciais da conservação da massa e da quantidade de movimento (momentum) para a determinação das pressões (ou cargas) e velocidades (ou vazões) em função da posição e do tempo.

Para representar a fase transitória do líquido na tubulação com o comprimento da coluna variável, as equações do momentum e da conservação da massa, são escritas, respectivamente, a seguir:

$$L_1: \quad \frac{1}{A}\cdot\frac{\partial Q}{\partial t}+\frac{Q}{A^2}\cdot\frac{\partial Q}{\partial x}+g\frac{\partial H}{\partial x}+\frac{f\cdot Q.|Q|}{2\cdot D.A^2}+g\cdot \operatorname{sen}\alpha = 0 \qquad (04)$$

$$L_2: \quad \frac{\partial H}{\partial t}+\frac{Q}{A}\cdot\frac{\partial H}{\partial x}+\frac{a^2}{gA}\cdot\frac{\partial Q}{\partial x}=0 \qquad (05)$$

onde:
Q é vazão em m^3/s, e A a área da seção transversal do conduto em m^2.

Sabe-se que devido à presença de termos não lineares, uma solução explícita para essas equações não é disponível. Portanto, um método numérico é recomendado para resolver essas equações, no caso o método das características.

No método das características as equações diferenciais parciais (EDPs) são antes convertidas em equações diferenciais ordinárias (EDOs), as quais são então resolvidas por um método de diferenças finitas. Uma vez que as características representam o curso de ondas ou perturbações que se deslocam, esse é o método mais apropriado para analisar sistemas descritos por equações do tipo hiperbólicos.

Assim, ao aplicar o método das características e em seguida o método de diferenças finitas nas eqs.(04) e (05), para finalmente adimensionalizar as equações resultantes, obtém-se:

$$C^+: \quad \hat{H}_P = \hat{C}_R - \hat{B}\cdot\hat{Q}_P \qquad (06)$$

$$C^-: \quad \hat{H}_P = \hat{C}_S + \hat{B}\cdot\hat{Q}_P \qquad (07)$$

onde:

$$\hat{C}_S = \hat{H}_S - \left(\hat{B}-\hat{R}\cdot|\hat{Q}_S|\right)\cdot\hat{Q}_S + \pi_4.\hat{B}\cdot\Delta\hat{t}\;;\; \hat{C}_R = \hat{H}_R + \left(\hat{B}-\hat{R}\cdot|\hat{Q}_R|\right)\cdot\hat{Q}_R - \pi_4.\hat{B}\cdot\Delta\hat{t}$$

$$\hat{B} = \pi_7\cdot\sqrt{\pi_5}\;;\; \hat{R} = \frac{\hat{B}.\pi_2.\Delta\hat{t}}{2}$$

Desta forma, a eq.(06) é válida ao longo da linha de características positivas RP e a eq.(07) é válida ao longo da linha de características negativas SP. Os índices R e S indicam os valores das variáveis conhecidos à montante e à jusante, respectivamente, do ponto P, no intervalo de tempo anterior. O contorno de montante é uma simples válvula, e o de jusante é tratado como uma bolsa de ar de massa única.

4. ANÁLISE DE SENSIBILIDADE

Na maior parte dos projetos de engenharia em que a análise dos transientes deve ser estudada, a ocorrência da sobrepressão é de fundamental importância. Desta forma, uma análise de sensibilidade dos diferentes parâmetros que podem afetar a sobrepressão é muito importante de ser realizada.

Observando os modelos matemáticos, nota-se que a sobrepressão depende dos seguintes parâmetros fundamentais: relação de H_T^*/H_0^* ou π_1; coeficiente politrópico n ou π_3; inclinação do tubo α ou π_4; tempo de abertura da válvula e fator de atrito f ou π_2.

O coeficiente politrópico n varia de 1,0 (processo lentamente isotérmico) a 1,4 (processo rapidamente adiabático). A variação da relação da carga máxima (H^*_{MAX} / H^*_T) em função do coeficiente politrópico ou π_3 é mostrada na figura 02:

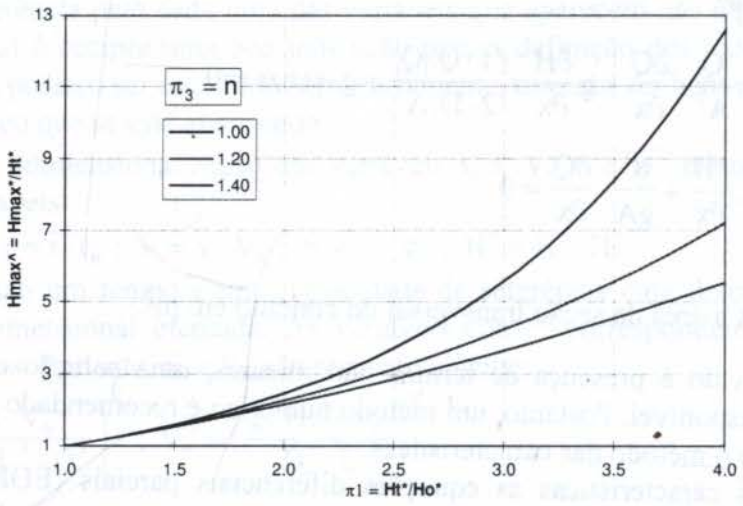

Figura 02 - Influência do coeficiente politrópico n ou π_3 com relação à sobrepressão máxima
($\pi_2 = 0{,}00$; $\pi_4 = 0{,}0$; $\pi_5 = 1{,}00$; $\pi_6 = 0{,}0$)

Neste gráfico verifica-se que valores de π_3 maiores proporcionam menores sobrepressões. Observa-se também, é claro, que a medida que π_1 é maior, a sobrepressão aumenta. Com relação à inclinação do tubo (α) é mostrado na figura 03, que conforme a inclinação do conduto aumenta com a horizontal, a sobrepressão eleva-se.

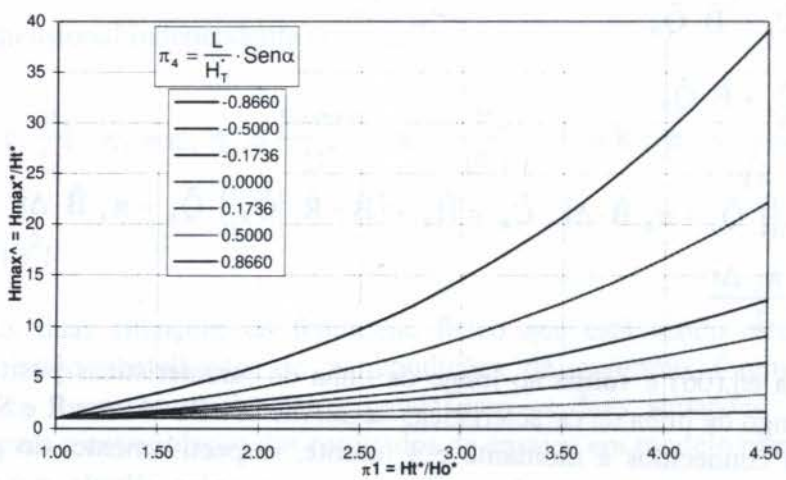

Figura 03 - Influência da inclinação do conduto α ou π_4 com relação à sobrepressão máxima
($\pi_2 = 0{,}00$; $\pi_3 = 1{,}2$; $\pi_5 = 1{,}00$; $\pi_6 = 0{,}0$)

Um caminho para atenuar as altas pressões transitórias no sistema hidráulico analisado é uma manobra lenta de abertura da válvula. Em geral a magnitude da sobrepressão depende do tipo de lei de fechamento do registro.

A figura 04 mostra um gráfico adimensional da sobrepressão com relação ao fator de atrito, usando parâmetro π_1. E o fator de atrito é representado pelo parâmetro adimensional π_2.

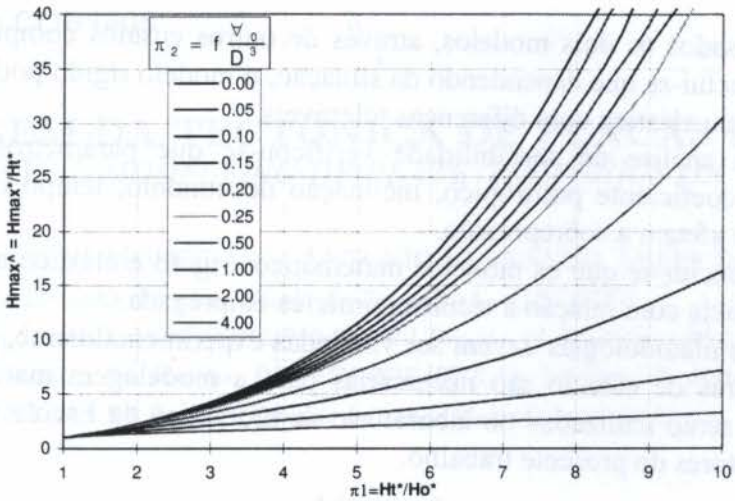

Figura 04 - Influência da inclinação do fator de atrito f ou π_2 com relação à sobrepressão máxima ($\pi_3 = 1{,}20$; $\pi_4 = 0{,}0$; $\pi_5 = 1{,}00$; $\pi_6 = 0{,}0$)

Como nota-se na figura acima, quanto menor o fator de atrito, maior a sobrepressão.

5. ESTUDO DE CASO

Com a finalidade de validação do modelo elástico e rígido os mesmos foram aplicados numericamente ao exemplo de Guarga et al. (1994). Para isto, as soluções obtidas neste trabalho são comparadas com as de Guarga et al. (1994).

Seja a instalação indicada na figura 01 com os seguintes dados: L = 100 m; D = 200 mm; $H_T^* = 31{,}10$ m; $H_0^* = 10{,}40$ m; f = 0,020; n = 1,20; $\forall_0 = 4{,}00$ m^3; a = 1000 m/s; $\alpha = 0^o$ (tubulação horizontal) e K = 0 (abertura instantânea da válvula).

Os modelos elástico e rígido são gerados na figura 05, na qual são apresentados os valores das cargas de pressão absoluta e velocidade de escoamento variando com o tempo, devido à oscilação de massa provocada pela abertura instantânea da válvula de montante.

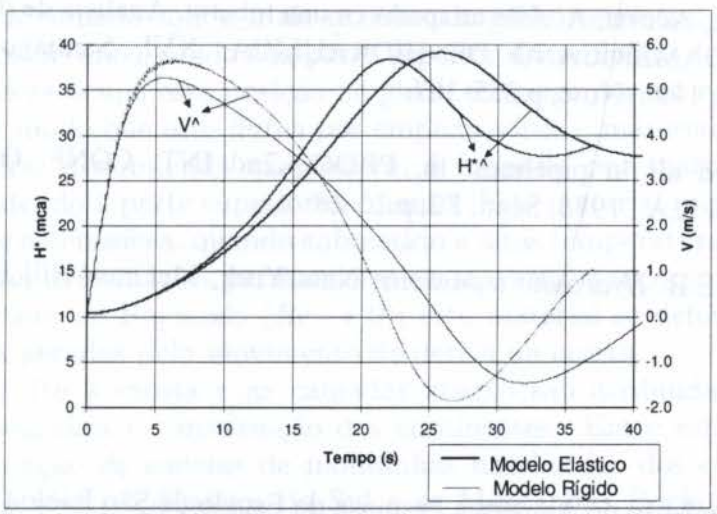

Figura 05 - Modelos Rígido e Elástico aplicados ao sistema hidráulico da figura 01

6. CONCLUSÕES

O estudo de caso, como relatado anteriormente, também foi estudado por GUARGA et al. (1994) e, o seu resultado apresentado no referido artigo, ao ser comparado com a figura 05, verificou-se que a solução é idêntica ao modelo rígido, haja visto que foi empregada esta modelagem.

Ao serem analisados os dois modelos, através de outros ensaios computacionais por ora não publicados, conclui-se que dependendo da situação, o modelo rígido pode ser aplicado perfeitamente no lugar do elástico com diferenças toleráveis.

Com relação à análise de sensibilidade verificou-se que parâmetros como carga hidráulica disponível, coeficiente politrópico, inclinação do conduto, tempo de abertura da válvula e fator de atrito afetam a sobrepressão.

Desta forma, conclui-se que os modelos matemáticos rígido e elástico aqui estudados possuem uma boa acurácia com relação a técnica numérica empregada.

No entanto, tais metodologias devem ser validadas experimentalmente, haja visto que hipóteses simplificadoras de cálculo são necessárias para a modelagem matemática. Estes ensaios experimentais serão realizados no laboratório de hidráulica da Escola de Engenharia de São Carlos pelos autores do presente trabalho.

7. REFERÊNCIAS BIBLIOGRÁFICAS

Abreu, J.; Cabrera, E.; García-Serra, J.; Izquierdo, J. Boundary between elastic and inelastic models in hydraulic transients analysis with entrapped air pockets. In: INT. CONF. ON HYDR. TRANSIENTS WITH WATER COLUMN SEPARATION, Valencia, Spain, 1991. Anais. Valencia, IAHR, 1991. Sept., p.159-181.

Cabrera, E.; Abreu, J.; Pérez, R.; Vela, A. Influence of liquid length variation in hydraulic transients. *Journal of Hidraulic Engineering*, ASCE, v.118, n.12, p.1639-1650, Dec., 1992.

Chaudhry, M.H. Application of lumped and distributed approaches for hydraulic transients analysis. In: INTERNATIONAL CONGRESS ON CASES AND ACCIDENTS IN FLUID SYSTEMS, São Paulo, Brasil, 1989. Anais I. São Paulo, 1989. Mar., p.72-79.

Guarga, R.; Lorenzo, E.; Acosta, A. Aire atrapado en una tuberia. Analisis de dos modelos. In: CONGRESO LATINOAMERICANO DE HIDRÁULICA, XVI, Santiago, Chile, 1994. Anais. Santiago, IAHR, 1994. Nov., p.355-367.

Martin, C.S. Entrapped air in pipelines. In: PROC., 2nd INT. CONF. ON PRESSURE SURGES, London, B.H.R.A., 1976. Sept., F2, p.15-28.

Streeter, V.L.; Wylie, E.B. *Hydraulic transients*. New York, McGraw-Hill Book Company, 1967. p.209-217.

8. AGRADECIMENTOS

Ao apoio da Fundação de Amparo à Pesquisa do Estado de São Paulo (FAPESP).

XIV Brazilian Congress of Mechanical Engineering
Obeid Plaza Hotel Convention Center - Bauru - SP/Brazil
December 08-12th 1997

PAPER CODE: COB1405

MODELAGEM DA TECTÔNICA DE PLACAS NA CROSTA TERRESTRE / *MODELLING OF PLATE TECTONICS ON EARTH'S CRUST*

ROGER MATSUMOTO MOREIRA† & ANTONIO FERNANDO TELES DA SILVA ‡
† *Departamento de Desenho Técnico, Escola de Engenharia, CTC/UFF*
R.Paço da Pátria,156,bl.D,sl.505 CEP24210-240 RJ Brasil - E-mail: roger@labmf1.com.ufrj.br
‡*Laboratório de Mecânica dos Fluidos, PEM/COPPE/UFRJ & Instituto de Matemática/UFRJ*
CP68503 CEP21945-970 RJ Brasil - E-mail: fernando@labmf1.com.ufrj.br

Abstract

A simplified modelling of the interaction between the continental lithosphere and the asthenosphere underneath it is proposed; in this model the lithosphere is considered as a rigid slab moving over and onto a viscous layer, that represents the asthenosphere. The asthenosphere, laying underneath the lithosphere, is represented as a fluid of very high viscosity; also the thinner lithospheric layer forming the ocean floor layer has been supressed, leaving in its place a free surface. The transient Stokes flow resulting from the translation of the rigid slab is modelled and solved by a Boundary Integral equation based on Lorentz reciprocal theorem.

Keywords

Movimento de placas tectônicas / Plate tectonics, escoamento de Stokes / Stokes flow, Método da Integral de Contorno / Boundary Integral Method.

1. INTRODUÇÃO

A litosfera é a camada sólida mais externa do globo terrestre, formando os continentes e o solo dos oceanos, sendo sua parte superior denominada de crosta. O material que forma a litosfera ocupa esta posição no globo terrestre por ser constituída de material mais leve, de modo que este *flutua* por empuxo sobre o material abaixo. A camada abaixo da litosfera, denominada astenosfera, é formada por material mais pesado e dúctil, correspondendo à parte superior do manto. Este material rochoso, que compõe a base da litosfera e astenosfera, quando submetido a altas temperaturas e tensões, tende a longo prazo a sofrer deformações permanentes e a se comportar como um fluido escoando a baixíssimo número de Reynolds ($Re \rightarrow 0$); este material se deforma continuamente devido às tensões geradas pelo movimento de deriva da crosta.

À interação entre a crosta e as camadas abaixo são atribuídas certas feições na conformação topográfica e constituição dos continentes. Entre estas feições podemos mencionar a formação de cadeias de montanhas nas bordas dos continentes, como a Cordilheira dos Andes na América do Sul e as Montanhas Rochosas na América do Norte, e ainda, possivelmente, a formação de bacias sedimentares, como as que ocorrem

na costa leste e nordeste do Brasil. Existe ainda o transporte de materiais entre a crosta e as camadas adjacentes que ocorre, principalmente, através do fenômeno de subducção de placas da crosta, onde placas oceânicas se introduzem sob outras placas e afundam na astenosfera. Existem ainda possivelmente outros fenômenos que levam ao transporte no sentido inverso.

O interesse no presente trabalho é investigar o quanto uma modelagem simples para a interação entre a base da litosfera e a astenosfera pode ajudar na compreensão de fenômenos tectônicos. A modelagem proposta supõe que a crosta, localizada no topo da litosfera continental, é rígida e tem uma fronteira bem definida com a base da litosfera, composta de material mais dúctil. A base da litosfera e a astenosfera são supostas como sendo constuidas por fluidos com viscosidade extremamente elevada. A crosta oceânica é fina o suficiente a ponto de não resistir às tensões da base da litosfera e astenosfera e não será considerada. Vamos estudar, em resumo, o problema esquematizado na figura abaixo, em que a placa sólida com reentrâncias representa a crosta, na parte superior da litosfera continental, que avança ou recua sobre um fluido abaixo e à frente desta, que representa a base da litosfera e a astenosfera, com solo oceânico ausente. Note ainda que a curvatura do planeta é desprezada.

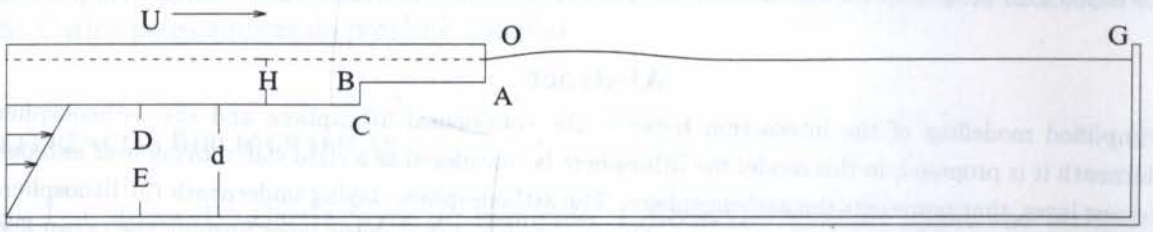

Figura 1. Geometria do problema em estudo.

2. MODELAGEM MATEMÁTICA

O problema esboçado na figura 1 representa o escoamento produzido pelo movimento impulsivo de uma placa sólida com uma dada espessura, movendo-se com velocidade constante U, de cerca de 5 cm/ano, sobre uma camada espessa de fluido; a placa afunda no fluido até uma profundidade H, de 40 km aproximadamente, que é menor que sua espessura como mostrado na figura 1. O fluido, abaixo e à frente da placa, tem viscosidade μ de aproximadamente 4×10^{19} kg/m/s e densidade ρ de 3.2 kg/m^3, cujas magnitudes variam tão amplamente a ponto de impedir resultados precisos de cálculos computacionais. Para resolver este problema, vamos introduzir medidas de comprimento, massa e tempo mais adequadas para uma melhor compreensão do fenômeno em estudo. Desta forma, definimos a espessura de submersão da placa H, a velocidade da placa U e a densidade do fluido ρ como sendo, respectivamente, as unidades de comprimento, velocidade e densidade do problema em estudo. Neste sistema, o tempo é medido em unidades de $\frac{H}{U}$ ($\simeq 0.8$ milhão de anos), as acelerações em unidades de $\frac{\mu U}{\rho H^2}$ ($\simeq 12.4$ m/s^2) e as pressões em unidades de $\frac{\mu U}{H}$ ($\simeq 1.6$ MPa). O número de Reynolds, com base nestes valores, é igual a:

$$Re = \frac{\rho H U}{\mu} \simeq 10^{-24}. \qquad (1)$$

Um número de Reynolds tão baixo permite que a hipótese de escoamento de Stokes seja válida em uma escala de milhares de quilômetros. Sendo o escoamento bidimensional, limitamos o escoamento à direita da placa e abaixo desta por uma superfície

rígida, permitindo a obtenção de uma solução válida em toda a região fluida. Em particular, estamos interessados em casos em que a profundidade d é muito grande, com a superfície livre se extendendo, na horizontal, por várias profundidades d.

Em um escoamento de Stokes, o campo de velocidades $\mathbf{u}$ e a pressão p satisfazem às seguintes equações adimensionais em toda a região fluida:

$$\nabla.\mathbf{u} = 0, \qquad -\nabla p + \mathbf{g} + \nabla^2\mathbf{u} = 0. \tag{2}$$

As condições de contorno nas fronteiras do escoamento são dadas em termos de velocidades $\mathbf{u}$ e tensões $\mathbf{f}$ onde, em notação indicial:

$$f_i = \left[-p\delta_{ij} + \mu\left(\frac{\partial u_i}{\partial x_j} + \frac{\partial u_j}{\partial x_i}\right)\right]n_j. \tag{3}$$

Desta forma, os contornos da região em estudo podem ser divididos em quatro partes descritas abaixo, de acordo com a figura 1:

i) O trecho entre os pontos G e O representa a superfície livre, onde a componente tangencial da tensão é nula e a componente normal assume o valor da pressão exercida por material acima desta superfície. Supondo que esta pressão tem valor uniforme p_0 neste trecho, vamos sem perda de generalidade considerar $p_0 = 0$ e daí obter a condição para a tensão na superfície livre, $\mathbf{f} = (0, 0)$. Neste trecho, as incógnitas são as componentes da velocidade $\mathbf{u}$.

ii) O trecho entre os pontos O e D corresponde ao contorno da placa rígida em contato com o fluido, onde devem valer as condições de impenetrabilidade e de não-escorregamento, $\mathbf{u} = (U, 0)$. Neste trecho, as incógnitas são as componentes da tensão $\mathbf{f}$.

iii) O trecho entre os pontos D e E representa uma região longe o suficiente da porção frontal da placa, de forma que o escoamento possa ser suposto como o que ocorre entre duas placas infinitas e paralelas, a superior movendo-se com velocidade U e a inferior em repouso. A velocidade no espaço entre as placas apresenta então um perfil linear, $\mathbf{u} = (U(1+\frac{H+y}{d}), 0)$, onde $-(d+H) \leq y \leq -H$. A tensão na placa superior, na superfície fluida vertical e no fundo pode ser determinada utilizando-se a equação 3 em conjunto com a condição de velocidade linear dada acima, neste mesmo item iii); esta tensão é então $f_i = (\mu U/d)\omega_{ij}n_j$, onde:

$$\omega = \begin{pmatrix} 0 & 1 \\ 1 & 0 \end{pmatrix}.$$

iv) O trecho entre os pontos E e G se compõe de um fundo rígido horizontal e de uma parede vertical. Nesta região valem a condição de não-escorregamento e impenetrabilidade, $\mathbf{u} = (0, 0)$, e a tensão é calculada como uma incógnita do problema.

O problema de valor de contorno formulado pelo sistema de equações 2 e pelas condições de contorno descritas nos ítens i), ii), iii) e iv) desta seção será referido como problema principal e estudaremos sua solução na secção 4. Note que o problema em estudo não contém derivadas temporais, embora seja um problema de evolução e as velocidades sejam derivadas materiais das posições das partículas fluidas. O escoamento fica inteiramente determinado, em qualquer instante, pela geometria dos contornos da região fluida e pelas condições impostas ao campo de velocidades e tensões sobre estes contornos, caracterizando um problema de regime quase-estático. A evolução do escoamento pode então ser calculada a partir de um esquema Euleriano:

$$\mathbf{x}(\xi, t + \Delta t) = \mathbf{x}(\xi, t) + \mathbf{u}(\xi, t)\Delta t + \mathcal{O}(\Delta t^2), \tag{4}$$

onde ξ é o parâmetro que descreve o contorno da superfície livre.

3. REFORMULAÇÃO DO PROBLEMA PRINCIPAL

Nos escoamentos de Stokes em que a aceleração da gravidade desempenha um papel expressivo, no presente caso devido à superfície livre, o problema é reformulado de acordo com Pozrikidis (1988), de modo que a gravidade seja transferida das equações governantes do fenômeno para as condições de contorno. Embora no presente caso esta transferência não seja indispensável, este procedimento simplificará a aplicação da condição de contorno dinâmica na superfície livre e permite a reversibilidade do escoamento.

Esta reformulação do problema principal se baseia na decomposição do escoamento como a superposição de dois componentes: um básico e um perturbado, representados, respectivamente, por ˜ e ¯ . Isto é permitido pois o problema principal, constituído pelas equações governantes e suas condições de contorno, é linear. Tem-se portanto para todo o domínio fluido que:

$$\mathbf{u} = \tilde{\mathbf{u}} + \bar{\mathbf{u}}, \qquad \mathbf{f} = \tilde{\mathbf{f}} + \bar{\mathbf{f}}. \tag{5}$$

O escoamento básico é suposto em repouso em todo o domínio fluido, $\tilde{\mathbf{u}} = 0$, e com tensão *hidrostática* em todas as fronteiras, $\tilde{\mathbf{f}} = -(\mathbf{g}.\mathbf{x})\ \mathbf{n}$, satisfazendo trivialmente o sistema de equações 2.

O escoamento perturbado, com solução $\bar{\mathbf{u}}$ e $\bar{\mathbf{f}}$, deve satisfazer:

$$\nabla \cdot \bar{\mathbf{u}} = 0, \qquad -\nabla \bar{p} + \nabla^2 \bar{\mathbf{u}} = 0, \tag{6}$$

com condições de contorno para a velocidade de perturbação $\bar{\mathbf{u}}$ idênticas àquelas do problema principal, expressas nos ítens ii), iii) e iv), já que $\tilde{\mathbf{u}} = 0$ e, por consequência de 5, $\bar{\mathbf{u}} = \mathbf{u}$. As condições de contorno para a tensão de perturbação $\bar{\mathbf{f}}$ diferem das do problema principal devido à ausência da componente *hidrostática* na pressão. Assim, substituindo as devidas expressões de $\mathbf{f}$ e $\tilde{\mathbf{f}}$ em 5, produz-se a condição de contorno para $\bar{\mathbf{f}}$ na superfície livre: $\bar{\mathbf{f}} = (\mathbf{g}.\mathbf{x})\ \mathbf{n}$. É desta maneira que a aceleração da gravidade $\mathbf{g}$ entra no problema, através da condição de tensão $\mathbf{f}$ nula na superfície livre para o escoamento principal. A condição de contorno para a tensão no trecho DE também é alterada, tornando-se, $\bar{f}_i = \frac{\mu U}{d}\omega_{ij} n_j$. Portanto, devemos determinar os valores de $\bar{\mathbf{u}}$ e $\bar{\mathbf{f}}$ que satisfaçam o sistema de equações 6, com condições de contorno nas fronteiras rígidas descritas pelas expressões de velocidade e tensão resumidas acima nesta seção.

4. SOLUÇÃO DO PROBLEMA DE VALOR DE CONTORNO

O escoamento perturbado pode ser resolvido em forma adimensional através da seguinte equação integral, (ver Higdon (1985)):

$$\bar{u}_i(\mathbf{x_m}) = \frac{1}{2\pi}\left\{\int_S \left[ln(r)\bar{f}_i(\mathbf{x_n}) - \frac{r_i r_j}{r^2}\bar{f}_j(\mathbf{x_n}) - 4\frac{r_i r_j r_k}{r^4}\bar{u}_j(\mathbf{x_n})n_k\right]dS\right\}, \tag{7}$$

onde $i, j, k = 1, 2$; $\bar{\mathbf{u}}$ e $\bar{\mathbf{f}}$ são a velocidade e a tensão de perturbação no contorno; $\mathbf{n}$ é o vetor normal unitário; $\mathbf{x_m}$ e $\mathbf{x_n}$ são os vetores posição; $r_i = \mathbf{x} - \mathbf{x_m}$; $r = |r_i|$.

Uma aproximação da solução é obtida a partir da definição de uma malha de pontos nodais em todos os contornos da região fluida, mostrada na figura 1. O contorno da região fluida $\mathbf{x}$, a velocidade $\bar{\mathbf{u}}$ e a tensão $\bar{\mathbf{f}}$ são então parametrizados por meio de *splines* cúbicos naturais passando pelos pontos nodais (ver Liggett & Salmon (1981) e Riess & Johnson (1982)). Desta forma, a equação integral 7 pode ser aproximada por um sistema de equações lineares para os valores das incógnitas na malha de pontos nodais;

estas incógnitas são as tensões $\bar{\mathbf{f}}$ nas superfícies rígidas e as velocidades $\bar{\mathbf{u}}$ na superfície livre. Resolvendo-se o sistema de equações lineares obtém-se uma aproximação para o campo de velocidades e tensões em todo o contorno da superfície fluida. A partir do conhecimento do campo de velocidades e tensões nos contornos, podemos obter o campo de velocidades $\bar{\mathbf{u}}$ no interior da região fluida, bastando para isto substituirmos na equação 7 o fator $\frac{1}{2\pi}$ por $\frac{1}{4\pi}$.

A solução do problema principal, exposta na seção 2, será obtida aplicando-se as soluções do escoamento perturbado às expressões 5. A evolução temporal do problema é obtida a partir da equação 4.

5. IMPLEMENTAÇÃO COMPUTACIONAL

Soluções numéricas preliminares mostram que a solução do sistema de equações 2 exige uma malha bastante refinada, e exige ainda que o ponto D da figura 1 esteja bastante longe (a vários comprimentos H) do ponto O; estas condições restringem o uso de máquinas de pequeno porte para a obtenção de resultados confiáveis. Além disto os resultados parecem ser sensíveis a uma razão entre as extensões horizontal e vertical do contorno, sendo melhores para razões maiores, ou seja, a região mostrada na figura 1 deve ter, idealmente, o aspecto de uma faixa longa, na direção horizontal, e estreita, na direção vertical. Os resultados apresentados são obtidos no Cray J90 do Núcleo de Computação Avançada da Coppe/UFRJ.

Duas simulações são calculadas com a geometria descrita na figura 1; na primeira a placa avança para a direita com velocidade U, dada na sec cão 2 do presente trabalho, enquanto que na segunda há um recuo com velocidade $-U$. Note que a placa possui duas superfícies horizontais, a mais curta com um comprimento de $10H$ e a segunda semi-infinita; as duas faces verticais em contato com o fluido têm comprimento de $0.5H$. A limitação de recursos computacionais força a colocação de um fundo plano a uma profundidade de $9H$ e a parede vertical inicialmente, no tempo $t = 0$, a uma distância de $100H$; idealmente estes valores deveriam ser maiores, especialmente o segundo. Como este é um problema de evolução, soluções do problema de valor de contorno devem ser obtidas a cada passo de tempo; deste modo o número de passos de tempo que podem ser computados está limitada pelos recursos computacionais; o tempo de CPU disponível permite computar satisfatoriamente 12 passos de tempo; o tempo de máquina é de cerca de 9000 seg CPU para cada caso. As simulações são realizadas por um período de aproximadamente de 5.2 milhões de anos, embora idealmente devêssemos obter resultados para um tempo total que fosse pelo menos 10 vezes maior.

6. ANÁLISE DOS RESULTADOS

As figuras 2 e 3 mostram, respectivamente, a deformação sofrida pela superfície livre devido ao movimento de avanço e recuo da placa rígida a velocidades U e $-U$. Podemos observar na figura 2 que a placa avança horizontalmente $6.5H$ sobre a camada fluida que emerge, causando uma elevação considerável de no máximo $0.843H$ (37.2 km) para o intervalo de tempo considerado (6.5 u.t.). Este resultado revela que o confinamento do escoamento de Stokes através do fundo e da parede propicia uma forte elevação da superfície livre. Esta afirmação é ratificada pela elevação observável na região próxima à parede. Desta forma, pode-se assumir que a perturbação gerada pela placa rígida irá se propagar por uma extensão muitas vezes maior que o domínio em estudo.

Analogamente, na figura 3 observamos a formação de uma depressão na superfície livre, revelando profundidades de até $0.809H$ ($\cong$ 32.36 km). Este resultado é inferior

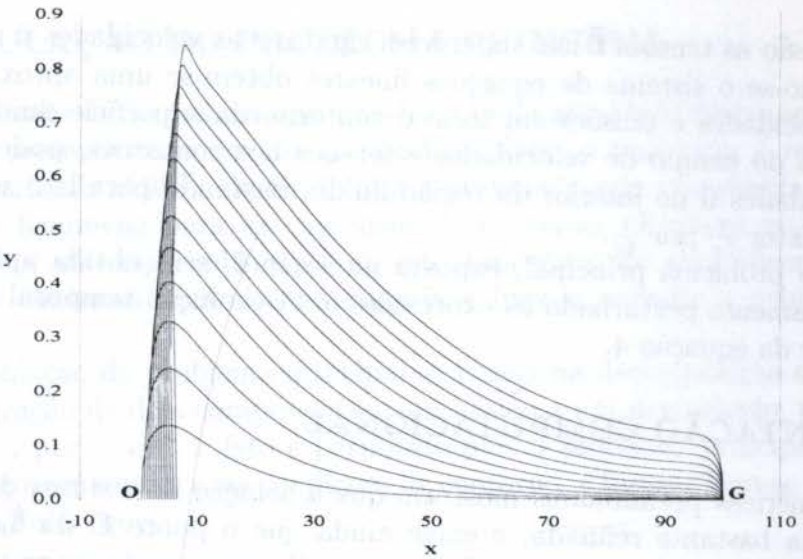

Figura 2. Evolução da superfície livre ocorrida com o avanço da placa rígida; foram realizados 13 incrementos temporais de 0.5 u.t., totalizando 5200000 anos.

em módulo quando comparado à máxima altura atingida quando a placa se desloca com uma velocidade positiva. Investigando-se mais detalhadamente esta ocorrência, verificou-se que a diferença entre os picos dos casos de velocidade positiva e negativa (para um mesmo intervalo de tempo) aumenta a medida que fazemos o avanço no tempo. Esta diferença mostra que, decorridos 1.0 u.t., o pico com a placa avançando é 0.9 % maior que o respectivo valor com a placa recuando, sendo este valor de 4.2 % quando passados 6.5 u.t. Diante destas evidências podemos afirmar que a parede exerce uma considerável influência sobre a solução do problema proposto, pois ela representa um obstáculo para o movimento do fluido que se desloca a montante da placa quando esta está avançando, ao mesmo tempo que ela atua sobre o escoamento reverso (placa recuando), promovendo uma espécie de sucção na região fluida, o que justificaria o aparecimento de profundidades inferiores, em módulo, às alturas encontradas para o caso de velocidade positiva.

Os resultados apresentados são obtidos sem considerar uma redefinição da distribuição de pontos nas superfícies do contorno a cada passo no tempo. No entanto, até este ponto na evolução temporal verificamos que a massa total variou de menos de 0.1%. A partir de 7.0 u.t. os resultados obtidos são menos confiáveis, com a presença de pequenas oscilações no perfil da superfície livre próxima à placa. Outra característica observável no gráfico 2 é o avanço de fluido sobre a placa, visível a partir de 2.5 u.t., onde temos o 1^o ponto nodal da superfície livre ultrapassando o ponto O em termos da coordenada x.

Ainda para o caso da placa avançando, nota-se que a crista da ondulação formada vai assumindo um aspecto pontudo que não se observa para a velocidade negativa; não está descartada a hipótese de que esta seja apenas um efeito da relativa proximidade da parede vertical. Naturalmente a aceleração da gravidade contribui para que os perfis tenham formatos diferentes. A gravidade e o movimento da placa são os agentes da deformação na superfície e aqui ocorrem algumas questões. Uma destas questões é a possibilidade de existência de estado estacionário para a placa recuando; neste estado, o cavado produzido a jusante da placa, que recua, manteria um perfil estacionário devido ao escoamento, por gravidade, de fluido à jusante do cavado. Uma outra questão relaciona-se com o resultado de variações na velocidade da placa, avançando

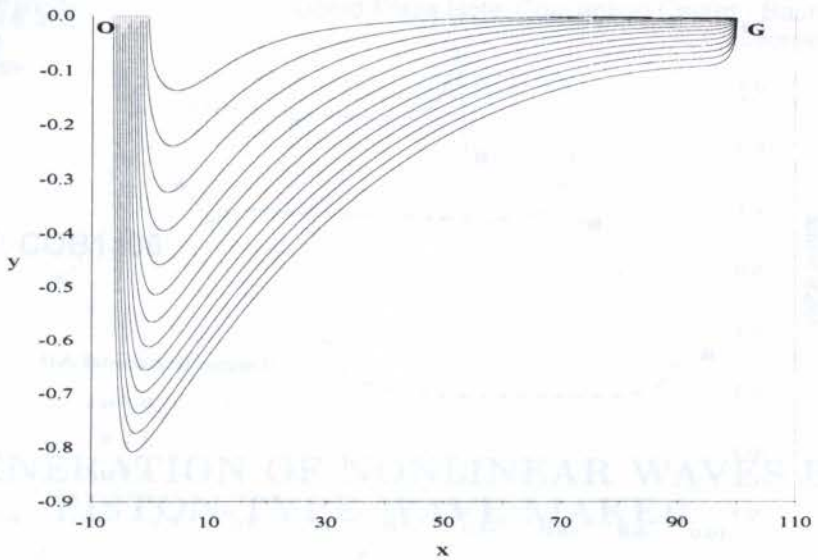

Figura 3. Evolução da superfície livre ocorrida com o recuo da placa rígida; foram realizados 13 incrementos temporais de 0.5 u.t., totalizando 5200000 anos.

ou recuando. O efeito combinado destas variações com a ação da gravidade, onde fluido em porções mais altas da superfície se derrama em direção às depressões, poderia possívelmente produzir ondulações na superfície livre. Para os movimentos de avanço da placa a crista sobe continuamente, de acordo com a figura 2, uma questão é avaliar em quanto tempo o efeito de alçamento da superfície livre, produzido pelo movimento da placa, vai se equilibrar com o escoamento para baixo governado pela gravidade.

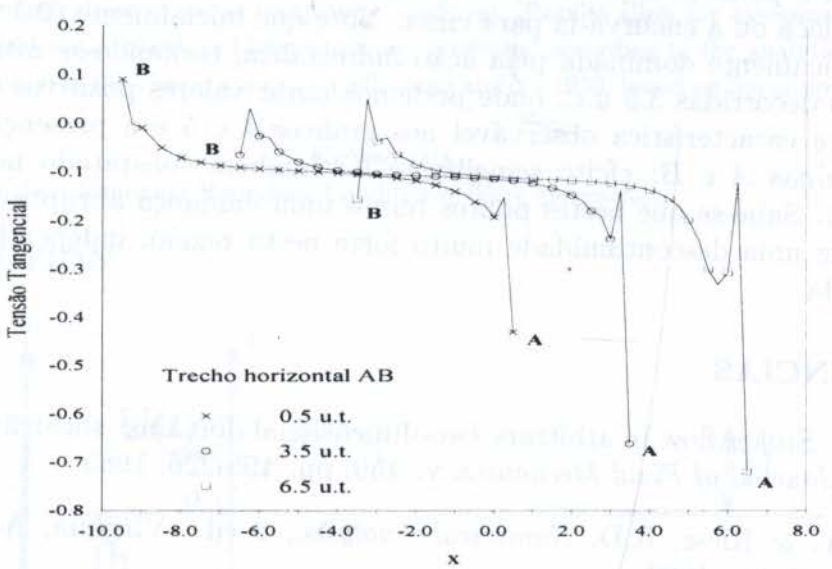

Figura 4. Distribuição da tensão tangencial no trecho horizontal AB considerando-se $U > 0$; a malha utilizada é de $0.25H$.

As figuras 4 e 5 mostram as distribuições das tensões tangencial e normal no trecho horizontal AB da placa que avança sobre o fluido; é perceptível na figura 4 a inversão de sinal da tensão tangencial, denotando a reversão do escoamento e indicando a presença de uma célula de recirculação. Moffatt (1964) mostra que em um escoamento de Stokes podemos obter sucessões infinitas de vórtices lentos, podendo este fenômeno ocorrer até mesmo junto a uma superfície livre. No presente caso poderíamos afirmar

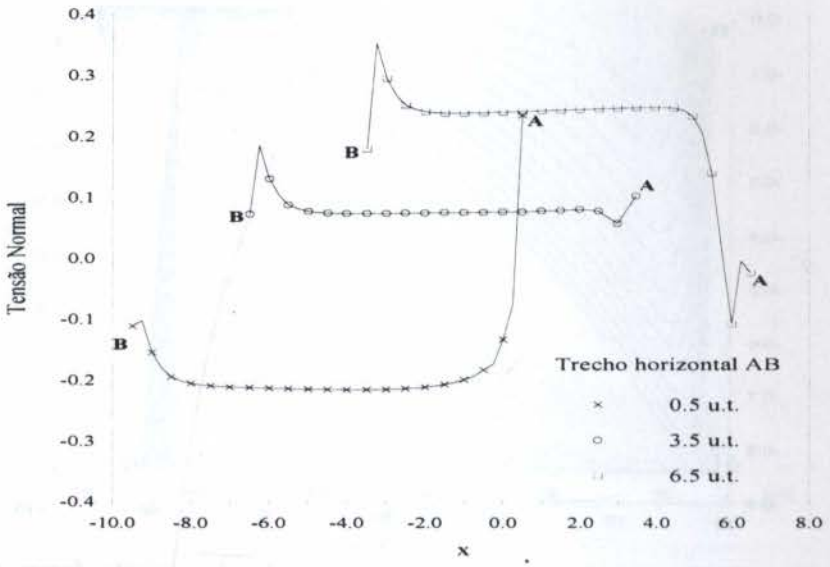

Figura 5. Distribuição da tensão normal no trecho horizontal AB considerando-se $U > 0$; a malha utilizada é de $0.25H$.

que se encontra junto à reentrância do ponto B uma sucessão de vórtices lentos que podem ter um importante papel no transporte de material entre diferentes camadas da litosfera e astenosfera. Isto é bastante interessante, já que tais vórtices podem produzir a recirculação de material entre diferentes camadas do manto, de especial interesse em nosso estudo.

Outra característica notada na figura 5 é o aumento da tensão normal, com valores positivos, para a placa avançando sobre o fluido; esta tensão tende a levantar a parte da frente da placa ou a encurvá-la para cima. Note que inicialmente (0.5 u.t.) a tensão normal é praticamente dominada pela ação *hidrostática*, tornando-se nítida a ação da massa quando decorridas 3.5 u.t., onde podemos notar valores positivos para a tensão normal. Outra característica observável nos gráficos 4 e 5 é a presença de picos de tensão nas quinas A e B; efeito semelhante foi também constatado no trabalho de Higdon (1985). Sabe-se que nestes pontos temos uma mudança abrupta na inclinação, o que introduz uma descontinuidade muito forte nesta região, independentemente da malha utilizada.

7. REFERÊNCIAS

Higdon, J.J.L. Stokes flow in arbitrary two-dimensional domains: shear flow over ridges and cavities, *Journal of Fluid Mechanics*, v. 159, pp. 195-226, 1985.

Johnson, L.W. & Riess, R.D. *Numerical Analysis.*, 2 ed. Virginia, Addison-Wesley Publishing Company, 1982.

Liggett, J.A. & Salmon, J.R. Cubic Spline Boundary Elements, *International Journal for Numerical Methods in Engineering*, v. 17, pp. 543-556, 1981.

Moffatt, H.K. Viscous and resistive eddies near a sharp corner, *Journal of Fluid Mechanics*, v. 18, pp. 1-18, 1964.

Pozrikidis, C. The flow of a liquid film along a periodic wall, *Journal of Fluid Mechanics*, v. 188, pp. 275-300, 1988.

XIV Brazilian Congress of Mechanical Engineering
Obeid Plaza Hotel Convention Center - Bauru - SP/Brazil
December 08-12th 1997

PAPER CODE: COB1406

THE GENERATION OF NONLINEAR WAVES BY A PISTON-TYPE WAVE MAKER

JULIO TOMAS AQUIJE CHACALTANA† & ANTONIO FERNANDO TELES DA SILVA‡
†*Dpto. Mecânica Computacional, CNPq/ Laboratorio Nacional de Computação Científica*
CEP 22220-160 R. Lauro Müller, 455, RJ.-Brazil: juliotac@alpha.lncc.br
‡*Lab. Mec. Fluidos, PEM/Coppe/ UFRJ & Inst. de Matemática/UFRJ,*
CP 68503 CEP 21945-970, Rio de Janeiro, RJ.-Brazil: fernando@labmf1.com.ufrj.br

Abstract

The generation of large amplitude waves by a wave-maker in a canal is simulated with a Boundary Integral numerical code. The code is based on Potential Theory and the free surface boundary conditions, dynamical and kinematical are taken as completely nonlinear. Results allow for assessments of experimental and theoretical work. Short and long waves are generated according to the analytic motions, for the wave-maker, derived in the classic work of Ursell, Dean and Yu 1959, based on linear approximations.

Keywords

Piston-type Wave-maker, Nonlinear Boundary Conditions, Wave generation.

1. INTRODUCTION

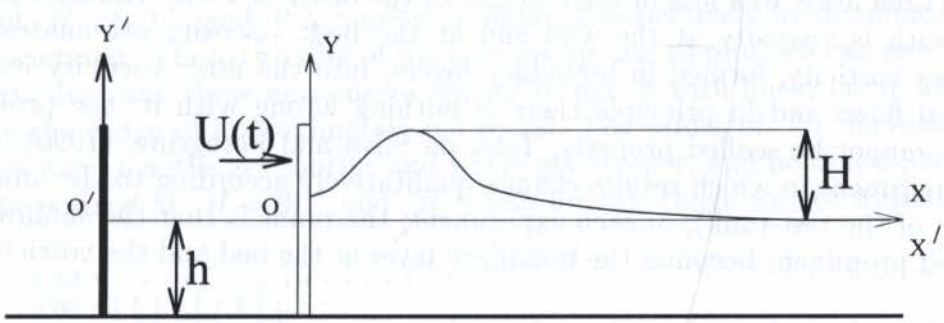

Fig. 1. Schematic representation of wave generation by piston type wavemaker. The non-inertial system XY move with velocity $U(t)$ and $X'Y'$ is the inertial system.

A precise and efficient numerical code simulating a canal equiped with a piston type wave maker has been developed, see J.T.A. Chacaltana & A. F. Teles da Silva (1997).

On an ideally long and wide canal, see figure 1 above, we work with a velocity potential ϕ such that: $\frac{\partial \phi}{\partial x} = u$, $\frac{\partial \phi}{\partial y} = v$; ϕ is the solution of the following initial and boundary value problem :

$$\nabla^2 \phi = 0 \qquad (1)$$

which is the governing equation valid on the whole fluid region;

$$\frac{\partial \phi}{\partial t} + \frac{1}{2}(u^2 + v^2) + gY = 0 \tag{2}$$

$$\frac{D\mathbf{R}}{Dt} = \nabla \phi = \mathbf{u} \tag{3}$$

which are respectively the nonlinear dynamic and kinematic condition valid on the free surface; note that $\mathbf{u} = (u, v)$ and $\mathbf{R} = (X, Y)$ are respectively the velocity at the free surface and a parametrization of the free surface. The conditions for ϕ at the wavemaker, the bed and the far end of the canal are, respectively:

$$\frac{\partial \phi}{\partial x} = U(t), \qquad \frac{\partial \phi}{\partial y} = 0, \qquad \phi = 0 \tag{4}$$

The motions start from rest and hence the initial conditions for $\mathbf{R}$ and ϕ at the free surface are:

$$\mathbf{R} = (X, 0), \qquad \phi = 0 \tag{5}$$

The solution for the transient problem stated above corresponds to a run of the wavemaker-canal system. Results are presented in nondimensional form; we use a system of units in which the acceleration of gravity, g, is the unity of acceleration; the undisturbed depth h of the canal is the unity of length. Consequently the units of time and linear velocity are respectively $\sqrt{h/g}$ and $\sqrt{hg}$.

In such an experiment, several undesireable characteristics of real test-tanks are absent. One the main problems with experimental test-tanks is that reflections from the beach at the far end of the canal are unavoidable for most test-tanks in use; test-tank beaches should ideally absorb the entire wave energy but there is always some reflection, which contaminates the wave field. Another common problem is that it is difficult to seal the space between the moving piston and the walls of the canal; it is repported, Madsen, (1970), that leakage of water through the gap may lead to a significant loss in wave-height; according to Madsen an unsealed area of 0.29% of the wetted board area leads to a loss of wave height of the order of 2.8%. Another problem to be dealt with is viscosity at the wall and at the bed; viscosity attenuates waves and introduces vorticity, formed in boundary layers, into the flow; vorticity is always present in real flows and in principle there is nothing wrong with it; the problem is that the flow cannot be scalled properly, Teles da Silva and Peregrine, (1990), discuss a classical experiment in which results change qualitatively according to the amount of water, (depth of the test-tank), in each experiment; the point is that the shallower the water the most prominent becomes the boundary layer at the bed and the vorticity shed

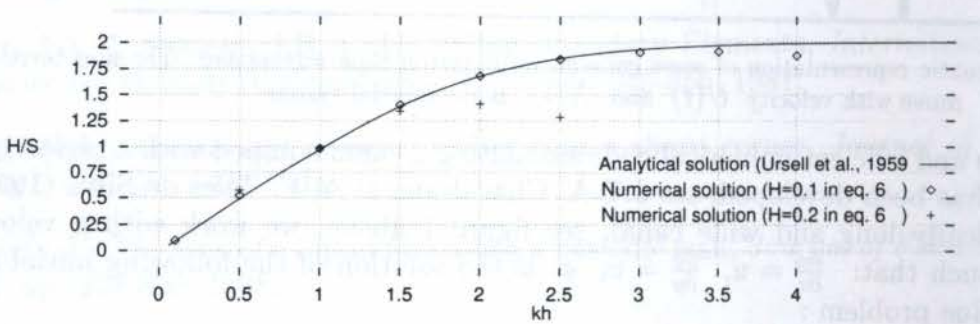

Fig. 2. Numerical results compared with the analytical solution of Ursell et al. (1959) for simple harmonic motion by piston wavemaker. This numerical results were obtained in order to reproduce the wave–height given by equation (6). In this picture k is the wavenumber, h is the depth, H is the predicted wave height and S is the stroke of the piston type wavemaker.

from it. A not less important problem to be dealt in real test-tanks is 3-dimensional effects which appear in the form of transverse waves; these cross waves may be excited in different manners and an important one is the leakage through the space between piston board and wall, already mentioned.

Despite the features outlined above, test-tanks are far more versatile and in a way easier to handle than computations; nevertheless numerical simulations are an important tool in the design of experiment in test-tanks and in the assessment of accuracy in results. In the present work we look at the generation of wave trains, in a test-tank, as described in the classical work of Ursell, Dean an Yu, (1959).

2. RESULTS

In this paper computed solutions of the transient problem stated above are used in the assessment of the linear theory, for wave-generation by wave-makers, as presented in the classic work of Ursell, Dean and Yu (1959); in this work the authors present a relationship between the stroke S of the wavemaker, that is the full length of the periodic excursion of the wave-maker, and the wave height H of waves to be generated; for a piston-type wave-maker this is:

$$\frac{H}{S} = \frac{2(\cosh(2kh) - 1)}{\sinh(2kh) + 2kh} \tag{6}$$

where k is the wave number and h is the depth. The wave-maker motion is governed by

$$U(t) = \frac{1}{2} S\sigma \sin(\sigma t) \tag{7}$$

σ is the frequency associated with the wave number k through the dispersion relationship. Figure 2 reproduces the curve of kh against $\frac{H}{S}$; waves obeying the linearised version of the boundary value problem stated above appear as points on this curve. Numerical experiments have been conducted for a range of values of kh; namely $kh = 0.1, 0.5, 1.0, 1.5, 2.0, 2.5, 3.0, 3.5, 4.0$, for each of these values two wave-trains, with wave-height H of 0.1 and 0.2, marked in figure 2 respectively by diamonds and plus signs are generated. These two sets of wave-trains appear to produce two new curves on the $\frac{H}{S} \times kh$ diagram; these new curves appear to match with linear curve for kh frequencies in the range of approximately 0.5 to 1.5. For values of kh increasing above these values wave-lengths get shorter and waves get steeper, and nonlinear, because the wave-height is fixed at $H = 0.1$ and $H = 0.2$; for this range we get waves which are

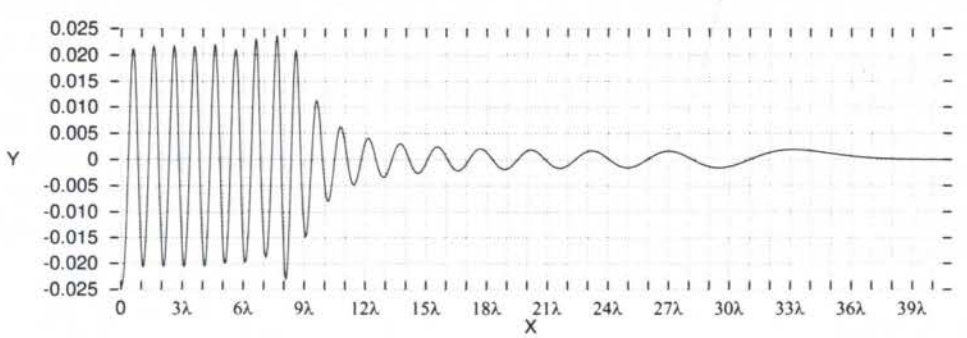

Fig. 3.a Schematic representation of the free surface at $t = 63.9044$ units of non–dimensional time. In this numerical experiment we take the case E experimental data of Chaplin (1984). These experimental data in non–dimensional units are: $H = 0.0424$ and $kh = 3.43$, so that we have $\lambda = 1.8318$ and $T = 3.3962$.

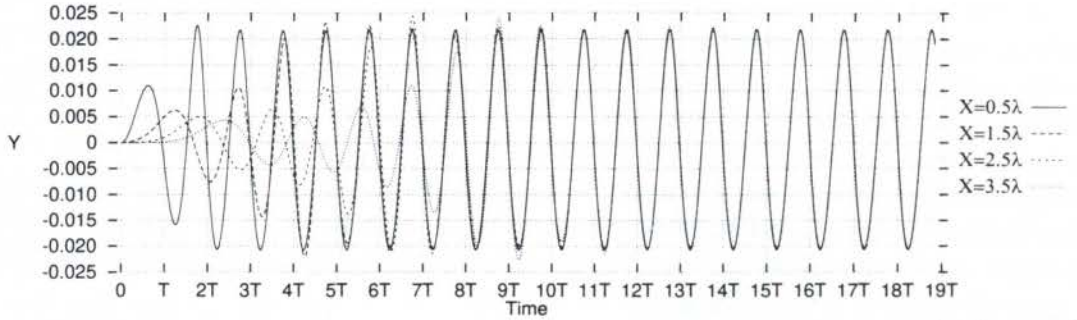

Fig. 3. b Time history of the free surface registered by four stations at locations 0.5λ, 1.5λ, 2.5λ and 3.5λ from the piston wavemaker. A remarkable convergence in the harmonic oscillation of the wave height is observed after 10 periods for the piston movement. In this numerical experiment we consider $H = 0.0424$ and $kh = 3.43$, so that we have $\lambda = 1.8318$ and $T = 3.3962$.

lower in the diagram. For values with a value of kh below 0.5 waves become longer and in this way some nonlinearity appears; these waves can be better approximated by cnoidal wave theory. The nonlinearity on this side, lower values of kh, is weaker than the nonlinearity for higher values of this parameter; the reason is that slopes are gentler. This explains why the departure from the linear curve in figure 2 is less pronounced for lower values of kh.

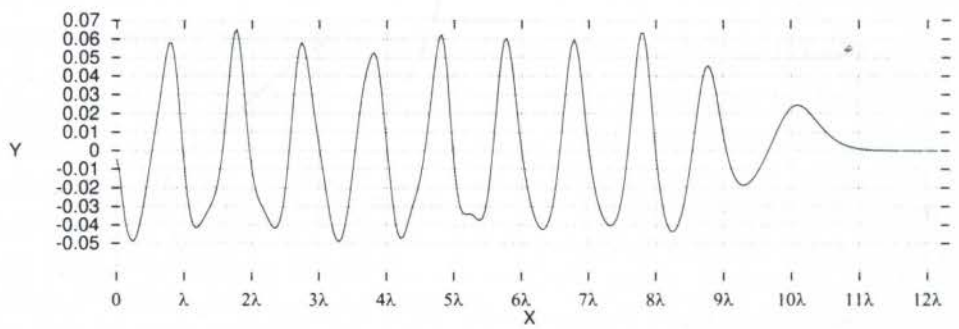

Fig. 4. a Schematic representation of the free surface at $t = 130.713 = 10T$ units of non-dimensional time. In this numerical experiment we consider $H = 0.1$ and $kh = 0.5$, so that we have $\lambda = 12.5664$ and $T = 13.0713$.

2.1 Wave gage readings

In order to get the value of H for each wave train, numerical wave gages have been placed at different positions along the canal. A typically linear wave produced in a test-tank experiment, Chaplin, 1984, with a wave height of 0.0424 and a kh value of 3.43. Figure 3a shows at time $t = 63.9044$ time units a profile which is typical, of this type of experiment, with bore like little long waves at the front followed by the wave train; the wave train shows, typically, a first and last wave that are larger than the ones in between. Wave gage readings at positions at distances 0.5, 1.5, 2.5 and 3.5 wavelengths measured from the mean position of the wave-maker are shown in figure 3b; all the readings agree after 15 wave periods and we get a very steady wave train with a wave-height over stroke ratio that produce a point right over the linear curve in figure 2.

2.2 Steeper waves

The linear theory overpredicts the ratio $\frac{H}{S}$ for the shorter waves; figures 4a and 4b shows profile and wave-gage readings for the wave with $H = 0.1$ and $kh = 3.5$; this wave appears as a point below the linear curve. For $H = 0.2$ the wave with $kh = 3.0$ breaks; it is important to remark that the highest possible nonlinear wave for this value

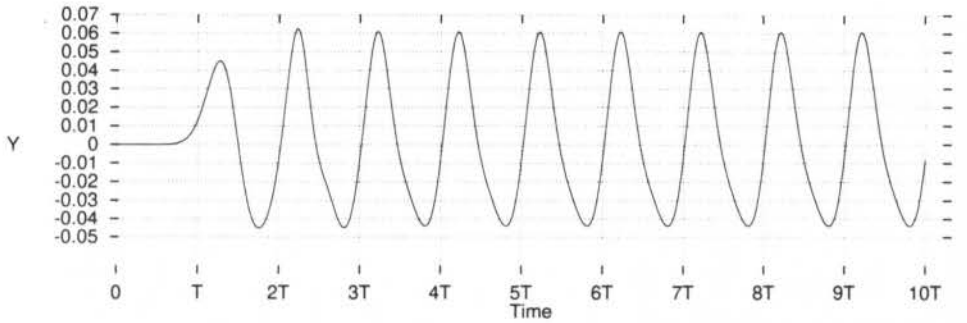

Fig. 4.b Time history of the free surface registered by the station located at λ from the piston wavemaker. In this numerical experiment we consider $H = 0.1$ and $kh = 0.5$, so that we have $\lambda = 12.5664$ and $T = 13.0713$.

of kh is of about $H = 0.2935$, computed as in Teles da Silva and Peregrine 1988, which is unstable; and a steady wave with this value of kh and $H = 0.2$ is certainly stable, as it is just of about two thirds of the highest wave for this value of kh; so it can certainly be generated by a more appropriate, higher order, wave-maker motion.

2.3 Longer waves

As apparent in figure 2, for lower values of kh the departure from the linear prediction is slighter, as compared with higher values of kh, unless we get too close to $kh = 0$. Figures 4a and 4b show the wave profile and wave-gage readings for waves of $kh = 0.5$, taken from a distance of one wave-length from the mean position of the wave-maker; the presence of higher order free harmonics is just discernible from figure 5a, these higher harmonics appear in readings of wave-gages set further down the canal. Computing the evolution of a higher wave, $kh = 0.5$, $H = 0.2$ we get more higher order free harmonics as shown in figures 5a and 5b, notice that these harmonics are discernible from the wave-gage readings at a distance of one wave length from the mean position of the wave-maker. If instead of increasing the wave-height we keep it fixed and increase the wave length considering a wave-train with $kh = 0.1$ and $H = 0.1$; we get after some time a free surface profile infested with high order free harmonics as shown in figure 6a; figure 6b shows the readings for wave-gages at points placed at a distance of 1, 2, 3 and 4 wave-lengths from the mean position of the wave-maker; the readings for the first wave-gage show a regular wave-train the amplitude of which is used to place the point $kh = 0.1$ and $H = 0.1$ in the diagram of figure 2. Readings for the wave-gages placed further downstream show the wave-train breaking apart in high order harmonic components. Figure 7 is a space time-diagram of the generation of a small amplitude

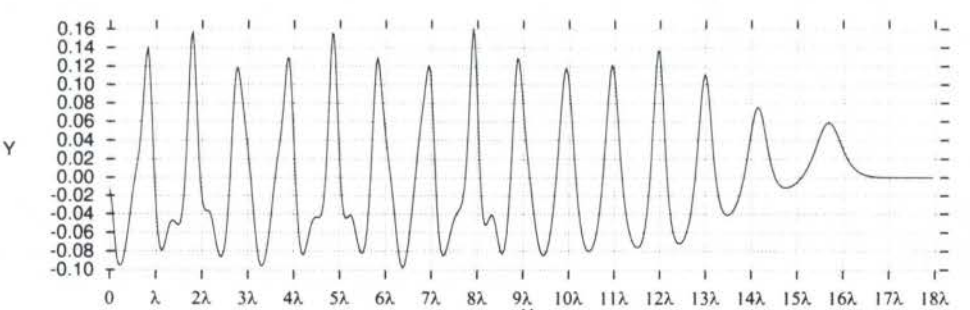

Fig. 5. a Schematic representation of the free surface at $t = 196.065 = 15T$ units of non-dimensional time. In this numerical experiment we consider $H = 0.2$ and $kh = 0.5$, so that we have $\lambda = 12.5664$ and $T = 13.0713$.

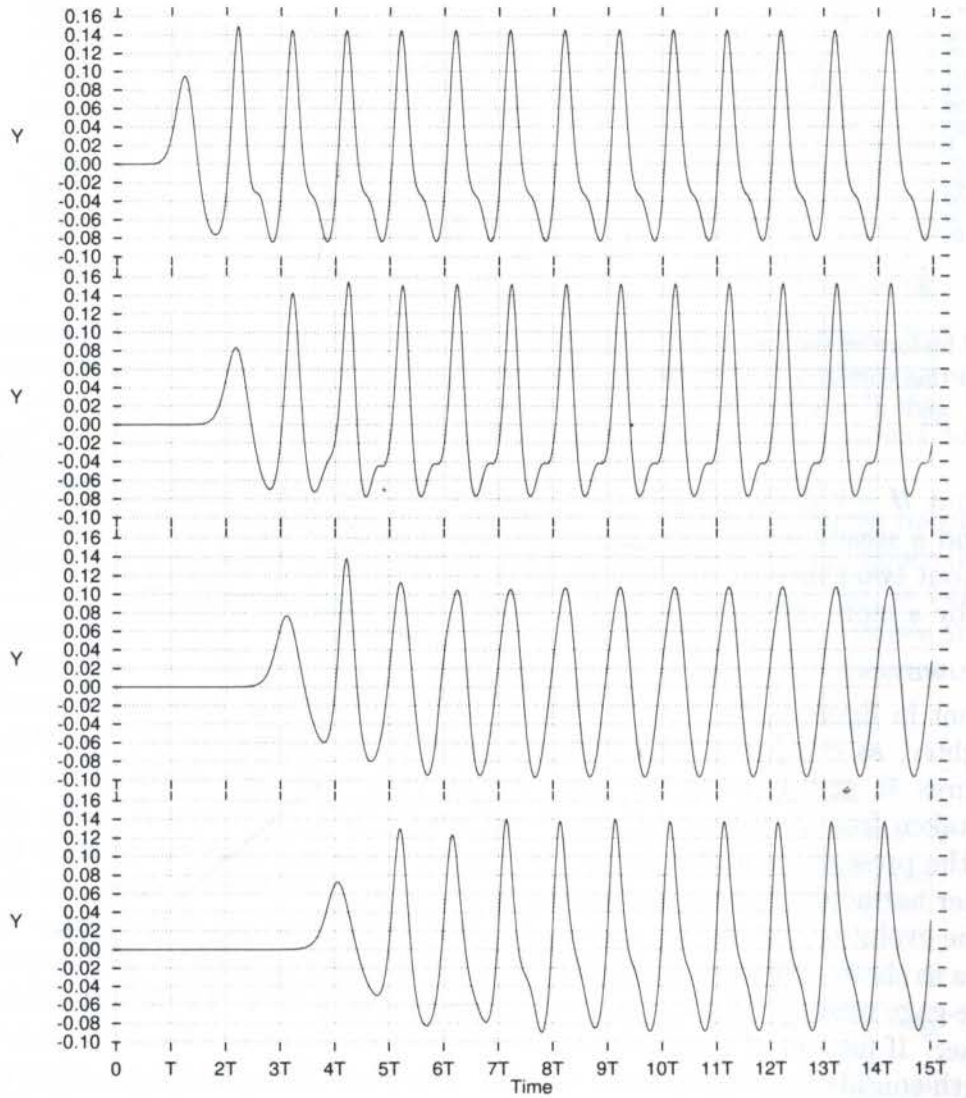

Fig. 5.b Time history of the free surface registered by four station at locations λ, 2λ, 3λ and 4λ from the piston wavemaker. In this numerical experiment we consider $H = 0.2$ and $kh = 0.5$, so that we have $\lambda = 12.5664$ and $T = 13.0713$.

solitary wave; this is obtained through a wave-maker motion obeying:

$$U'(t) = H' sech^2(\sqrt{\frac{3H'}{4h'^3}}(x' - U't')$$

$$\eta' = H' sech^2 \sqrt{\frac{3H'}{4h'^3}}(x' - U't')$$

$$U' = (1 + \frac{1}{2}\frac{H'}{h'})\sqrt{gh'}$$

3. DISCUSSION

Results of experiments in the numerical wave-tank in a first place validate the code as results for typically linear wave trains accurately agree with the predictions of the

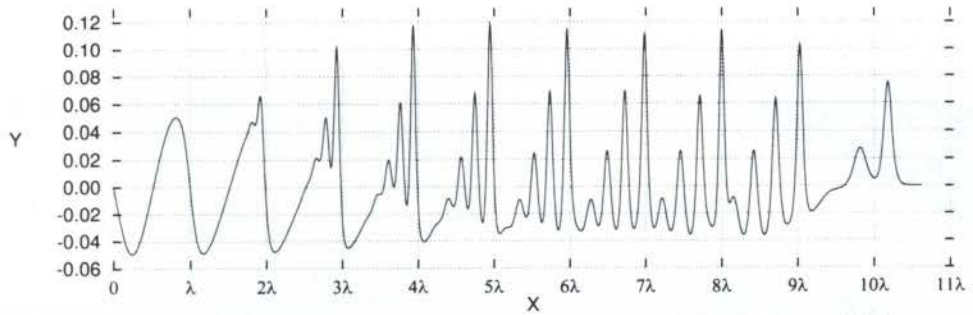

Fig. 6. a Schematic representation of the free surface at $t = 629.3642 = 10T$ units of non–dimensional time. In this numerical experiment we consider $H = 0.1$ and $kh = 0.1$, so that we have $\lambda = 62.8319$ and $T = 62.9364$.

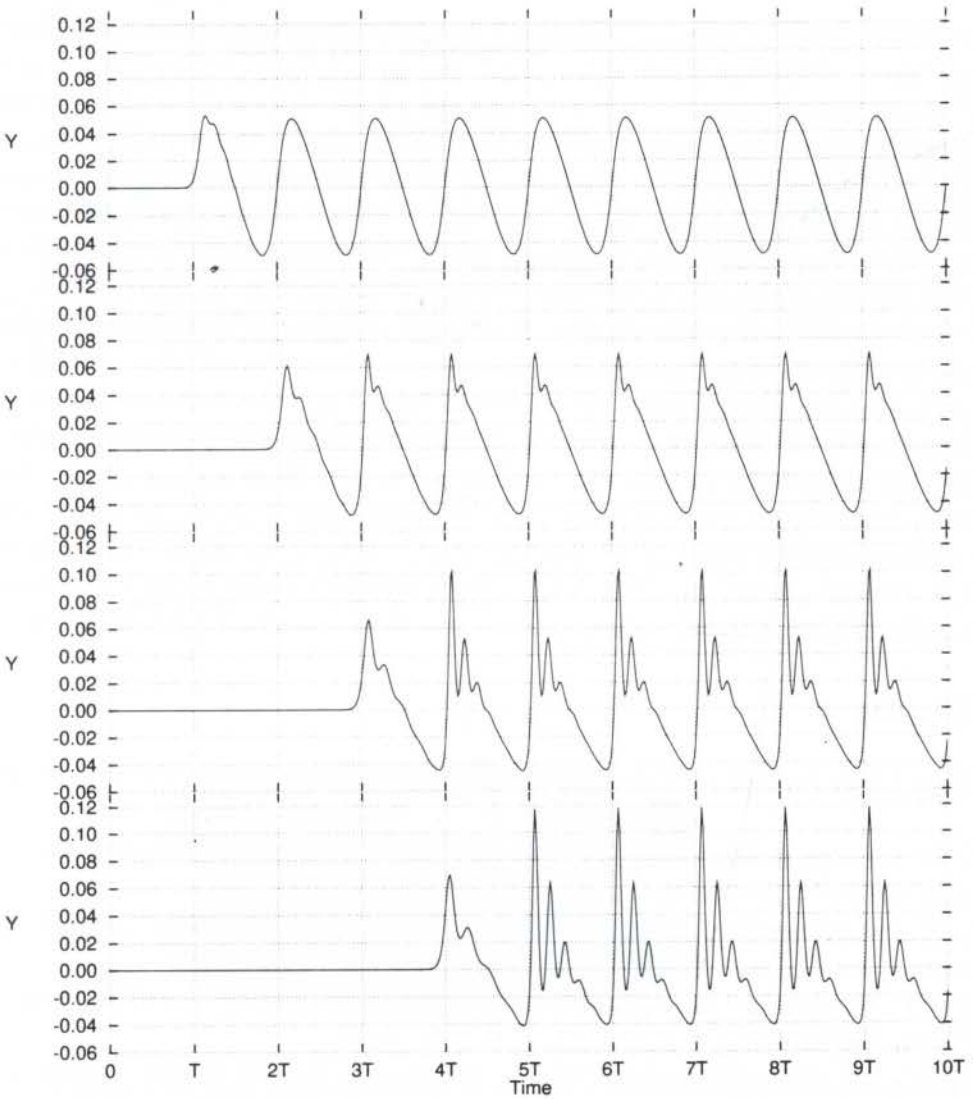

Fig. 6.b Time history of the free surface registered by four stations at locations λ, 2λ, 3λ and 4λ from the piston wavemaker. In this numerical experiment we consider $H = 0.1$ and $kh = 0.1$, so that we have $\lambda = 62.8319$ and $T = 62.9364$.

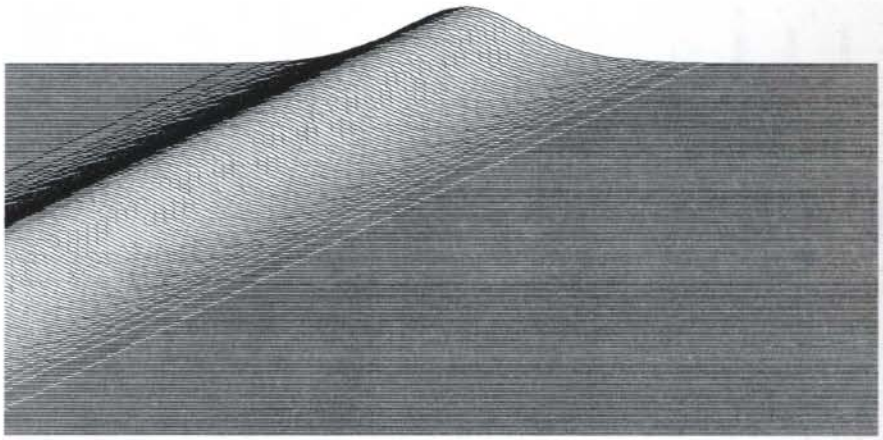

Fig. 7. Generation of solitary wave by piston type wavemaker.

theory; such accuracy cannot easily be obtained in real experiments because of intrinsic difficulties associated with real fluid flows, such as the setup of experiments and the calibration of measuring devices. And in a second place the numerical experiments tell about bounds for the application of the linear theory for potential flows in the programming of wave-maker motions. Results in figure 2 show that higher waves can behave linearly for moderate values of kh. For higher values of kh the departure from linear behaviour is quite conspicuous; waves go under the linear curve as they are quite steep. For lower values of kh the departure from the linear curve, figure 2, is slight, waves appear to get a little over the curve. Although things, for these lower values of kh are a bit elusive; the wave in figure 6, for instance, with values of $kh = 0.1$, $H = 0.1$, produces a point almost exactly over the curve of figure 2, (the wave-height is taken from measurements at a distance of one wave-length from the mean position of the wave board), although no wave-train of this wave-height is produced, as seen in figures 6a and 6b. Even though, certainly, a linear steady wave with this value of kh, $kh = 0.1$, can be produced for a small enough value of H; and naturally longer waves in shallower water can be better generated piston motions based on solutions of the K de V equation as shown in Synolakis (1990); the wave in figure ?? has been generated by such motions.

4. REFERENCES

CHACALTANA, J.T.A & TELES DA SILVA, A.F. A Numerical Wave-Maker, in preparation, 1997.

CHAPLIN, J. R. Nonlinear Forces on a Horizontal Cylinder beneath Waves, *Journal of Fluid Mechanics*, vol.147, pp.449-464, 1984.

MADSEN, O. Waves Generated by a Piston-Type Wavemaker *Proc. of the 12th International Conference on Coastal Engineering*, 1970.

SYNOLAKIS, C.E. Generation of Long Waves in Laboratory, *Journal of Waterway, Port, Coastal and Ocean Engineering*, vol.116, n2, 252-266, 1990.

TELES DA SILVA, A. F. & PEREGRINE, D. H., Steep, Steady Finite Depth Const. Vort. Water Waves, *Journal Fluid Mechanics*, vol. 195, 281-302,1988.

TELES DA SILVA, A. F. & PEREGRINE, D. H., Nonlinear Evolution of Undular and Breaking Bores, *Proc. of the 22nd International Conference on Coastal Engineering*, 1990.

URSELL, F., DEAN, R.G. & YU, Y. S. i Forced Small Amplitude Waves: a Comparison with Theory and Experiment, *Journal of Fluid Mechanics*, vol.7, pp.33-52, 1959.

XIV Brazilian Congress of Mechanical Engineering
Obeid Plaza Hotel Convention Center - Bauru - SP/Brazil
December 08-12th 1997

PAPER CODE: COB335

PRESSURE-BASED SOLUTION FOR THE RADIAL STOKES FLOWS: VALIDATION AND PROPERTIES

Jáuber C. Oliveira and Cristina H. Amon
Mechanical Engineering Department
Carnegie Mellon University, Pittsburgh, PA 15213
E-mails: jo2p+@andrew.cmu.edu and camon+@andrew.cmu.edu

Abstract

A novel pressure-based methodology is proposed and implemented to approximate the solution of the partial differential equations that model radial Stokes flows between two parallel disks. Eigenfunction expansions and Green's function representations are combined to obtain directly the pressure distribution for a variety of inflow boundary conditions. The velocity field is accurately recovered from the pressure distribution. This methodology was implemented numerically and validated with both exact solutions and numerical spectral element results. By exploring the analytical characteristics of the method, we extract additional information on the behavior of the solution in terms of the inflow functions and we prove rigorously the existence and uniqueness of solutions.

Keywords

pressure-based, radial Stokes flow, Green's functions, eigenfunctions

1. INTRODUCTION

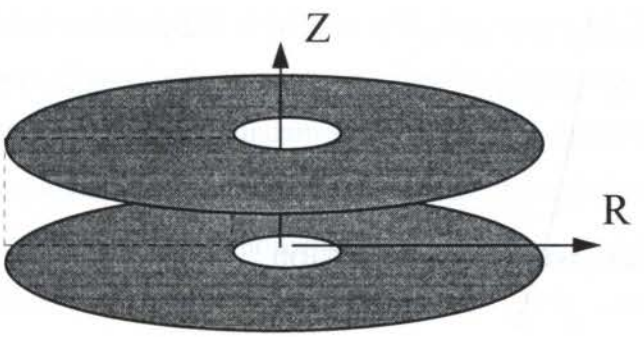

Figure 1: Radial source flow between two stationary parallel disks.

In this paper, we present the validation and additional results of a novel methodology, proposed in Oliveira (1997), to approximate the solutions of partial differential equations that model the Stokes flow between two parallel disks (Fig. 1). This investigation addresses a more fundamental view of radial flows and the fact that the associated geometry renders a mathematical problem tractable with semi-analytical approaches.

Previous semi-analytical approaches in radial flows are mainly based on analytical techniques with the objective of predicting the pressure distribution and boundary layer separation. Series expansions were utilized to include inertial effects in the analytical models. The region near to the inlet radius was the main source of discrepancy between analytical models and experiments (e.g., Jackson and Symmons, 1965). Ishizawa (1966) combined series expansions to represent the inlet region with the integral method to represent the rest of the domain in order to construct a very elaborate method to account for inertia. However, Ishizawa's approach was not able to predict correctly flow separation and two-dimensional vortical structures (Raal, 1978). This disagreement is probably due to the inherent inaccuracy of the integral method. Chatterjee (1986) used classical integral transforms to solve the Stokes flow problem for the idealized case of the radial Stokes flow between two infinite parallel disks with axial inflow from a pipe.

Our initial goal was to provide a semi-analytical solution to the two-dimensional axisymmetric Stokes flow problem for a variety of physically meaningful inflow boundary conditions. From such initial motivation, this pressure-based methodology has evolved, which is the central issue of this paper. This formulation was first implemented in a symbolic software (Oliveira and Amon, 1996) so as to take advantage of the symbolic manipulations and simpler programming. However, more complex inflow boundary conditions and the interest in extending the method required a fully numerical implementation.

This paper describes briefly this method in section 2 and presents results to validate its numerical implementation in section 3 as well as additional results regarding solution properties in section 4.

2 General Description: Pressure-Based Method

This paper describes a novel semi-analytical pressure-based method which we developed to solve the radial Stokes flow for a variety of inflow boundary conditions. As a preliminar step, we present in this section the main ideas of the method as well as our motivation for

proposing it. We refer to Oliveira (1997) for more details (governing equations, boundary conditions, etc.), which are not included due to space constraints. Nevertheless, the governing equations are the non-dimensional incompressible Navier-Stokes equations written in cylindrical coordinates. The Reynolds number, Re, is defined as Ve R_1/ν, where Ve is the mean velocity at the inlet, R_1 is the dimensional inner radius and ν is the kinematic viscosity. Ve and s, the distance between the two parallel disks, are used to obtain the non-dimensional equations. Arbitrary non-dimensional inflow functions f(x) and g(x) are prescribed at the entrance of the domain $\Omega := (r_1, r_2) \times (0, 1)$. We assume axisymmetry and also that the flow leaves the domain with zero axial velocity under atmospheric pressure. Then, the governing equations can be re-written by changing variables so as to make the boundary conditions homogeneous. By assuming initially that $f, g \in \{w(x) \in C^2(0.\ 1)$: $w(0)=0, w(1)=0\}$ and $\int_0^1 g\, dx = 1$, we conclude the formulation of the problem, which is solved by the pressure-based method.

This pressure-based method focuses on the pressure field as the important variable of the problem, as it is the case in most of the applications in lubrication. Therefore, instead of following traditional mathematical and numerical approaches (see e.g., Girault and Raviart, 1986) where emphasis is given to the velocity field (or to streamfunctions and/or vorticity), we formulate the problem having the pressure as the important variable to solve for. There are a couple other reasons for such a choice. The first comes from the fact that this alternative approach has not been investigated previously and, therefore, we lack knowledge about its potential for providing additional insight. The mathematical problem associated with this method is simpler than the one related to other approaches, since we avoid working with multiple (divergence-free) function spaces. The pressure-based method requires basically the theory of L^2 spaces, from Functional Analysis, and the theory of integral equations and eigenfunction expansions. These ideas amount for a simpler framework, since the troublesome continuity requirement becomes the fundamental governing equation, which is satisfied 'weakly' and the linear momentum equations are 'inverted' through Green's function integral representations. In addition, the well-known problem of compatibility between spaces of velocity and pressure (see detailed discussion in Oliveira, 1997), which is present in most numerical schemes, does not exist in the proposed pressure-based method.

In a summarized view of the method, we invert the linear momentum equations by means of Green's function integral representations for both components of the velocity field.

Then, we use an eigenfunction expansion to approximate the pressure distribution. Finally, to satisfy the incompressibility constraint, we enforce mass conservation in a weak sense. Thus, if $\mathbf{v} = \mathbf{G}(p)$ denotes the vector form of the Green's function integral equations, and if "$\nabla \cdot \mathbf{v} = 0$" represents the weak form of the mass conservation equation, then we obtain a weak form in terms of the pressure field and input data: "$\nabla \cdot \mathbf{G}(p) = 0$". This weak form completely describes the pressure field and can be seen as an integral equation of the form $K(p) = h$, where h is a function of the Green's functions and input data. By substituting the eigenfunction expansion for the pressure, we obtain a linear system of equations for the pressure coefficients. Then, the matrices of coefficients and right-hand side vector are formed. This system is solved by LU-decomposition. All integrations involved are solved either symbolically or numerically by Gauss-Legendre integration. To speed-up calculations, all functions evaluations are performed only at the collocation points used in the numerical integration. Then, after solving the system, we obtain an approximation for the pressure distribution. This approximation allows us to recover the velocity field, since $\mathbf{v} = \mathbf{G}(p)$. It turns out that the most efficient way to recover the velocity field is to calculate the axial component from the Green's function representation and obtain the radial component of the velocity from the integral transformed momentum equations in the radial direction (Oliveira, 1997).

3. VALIDATION

To evaluate the performance and robustness of the proposed pressure-based approach, we choose inflow conditions that generate flow separation and recirculation zones at the entrance of the flow domain. This extreme case is chosen to test our accuracy in predicting the flow field at the 'stiff' region close to the geometric singularities. We impose complex inflow functions corresponding to a two-dimensional flow given by the functions: $f(x) = -2x^3 + 2x^2$ and $g(x) = -110x^9(x - 1)$. This flow condition induces an adverse pressure field at the entrance region, which rapidly readjusts to a one-dimensional field. Figure 2 shows a comparison between the pressure isolines obtained with the pressure-based semi-analytical approach and a spectral element numerical solver (see Patera, 1984; Amon, 1993). The pressure-based approximate solution was obtained with 20 x 30 modes and 139 x 289 collocation points for integrations. The spectral element Stokes solution utilizes 48 macro-elements with 7 x 7 internal collocation points per element. In the spectral-element case, we utilized a refined mesh at the inlet of the computational domain so as to confine any effects

due to the geometric singularity at the entrance of the domain. The comparison is fair, except close to the singularities at (0, 0.5) and (1, 0.5), where extremely steep gradients are present.

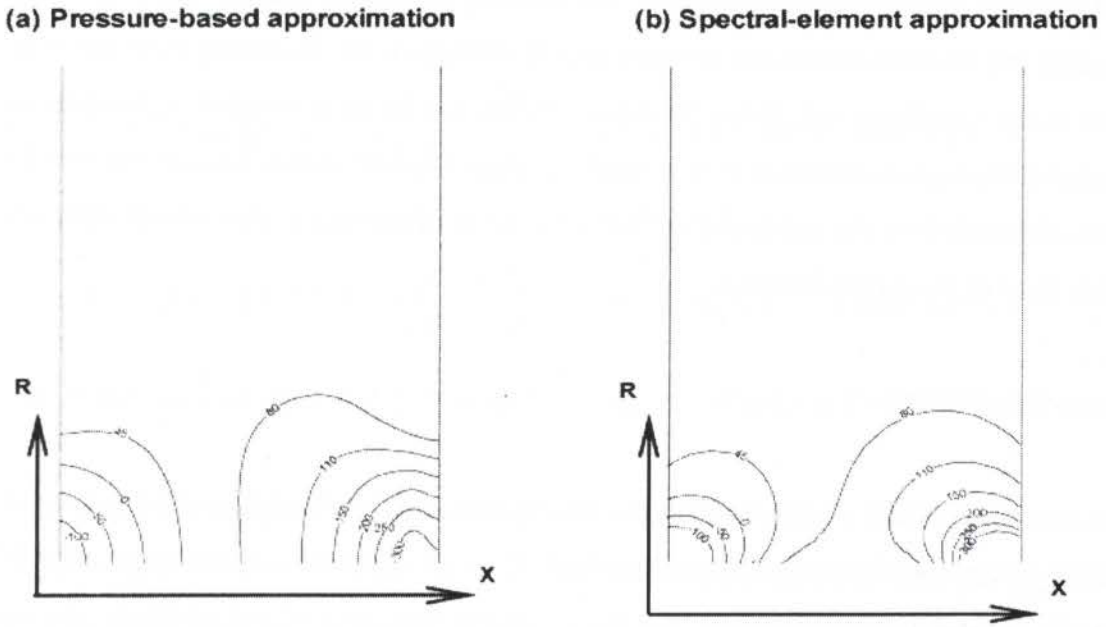

Figure 2- Comparison of isobars: pressure-based method versus spectral-element method.

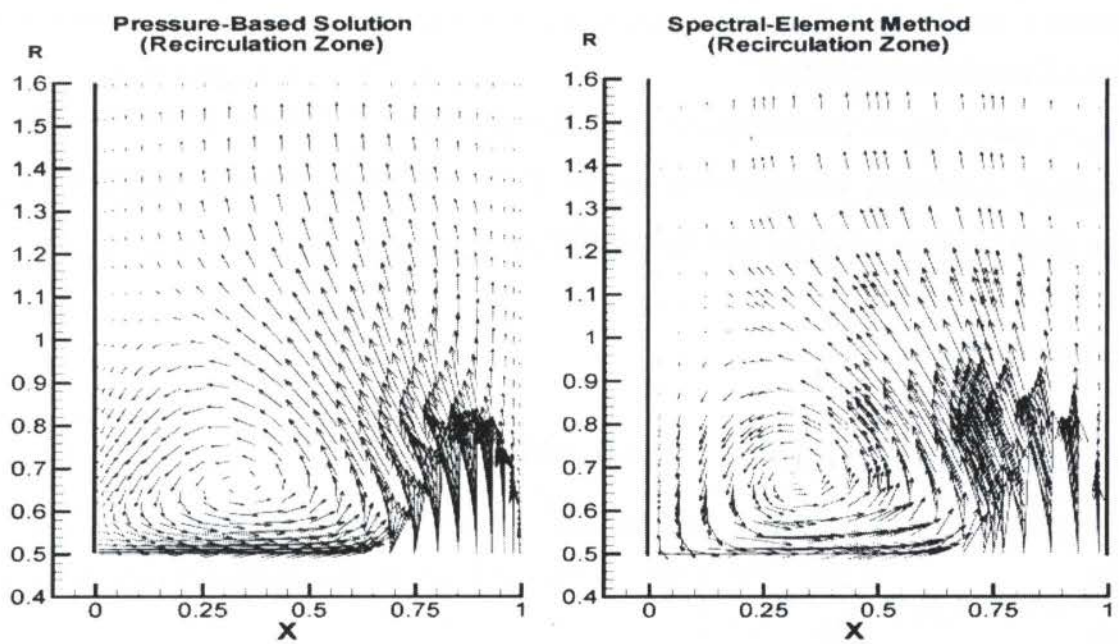

Figure 3- Comparison of velocity vectors: pressure-based versus spectral element method.

Lastly, we show in Fig. 3 the velocity vectors obtained by the pressure-based semi-analytical method (left figure) and through the spectral-element solver (right figure). The recirculation zone is properly captured by the pressure-based solution and there is good agreement with the spectral-element solution. The velocity components in the pressure-based approximation are calculated from the pressure approximation in the following way: the axial component of the velocity is calculated by means of Green's function integral representation and the radial component is obtained by a normalized eigenfunction expansion and the Fourier coefficients obtained from the integral transformed version of the linear momentum equation for creeping flow in the radial direction.

4. SOLUTION PROPERTIES

This section contains results which are consequences of the formulation of the radial Stokes flow problem and the pressure-based method. They are obtained with the motivation of extracting the most information out of the mathematical structure of the problem and its solution. The main issues are the establishment of the well-posedness of the problem (existence, uniqueness and continuous dependence of the solution with the input data) and additional information on the behavior of the solution in terms of the input data. We refer to Oliveira (1997) for details on the assumptions involved as well as the mathematical proofs.

Fact 1: (Exact Closed Form Solution)

Let u_s, v_s and p_s denote the solution of the Stokes problem. Let f(x) and g(x) denote the inflow boundary conditions corresponding to the axial and radial velocity components, respectively. If $f(x) = 0\ \forall x \in [0,1]$ then it follows that:

(i) $g(x) = 6(x - x^2)$;

(ii) $v_s(x,r) = \dfrac{6r}{r_1}\left(x - x^2\right)$ *and* $u_s(x,r) = 0$; and

(iii) $\dfrac{\partial p_s}{\partial x} = 0$ *and* $p_s = \dfrac{12 r_1^2}{\mathrm{Re}} \ln\left(\dfrac{r_2}{r}\right)$.

FACT 2: (Pressure Approximation ⇒ Velocity Approximation)

Let u, v and p be the solution to the Stokes problem. If the pressure approximation (p_{ap}) converges in $\mathbf{H}^1(\Omega)$, then the following estimates hold for the approximations of the axial (u_{ap}) and radial (v_{ap}) velocity components :

$$\left|u(x,r)-u_{ap}(x,r)\right| \le M_u \,\mathrm{Re}\left\|\frac{\partial p}{\partial x}-\frac{\partial p_{ap}}{\partial x}\right\|_2 \text{, where } M_u \in (0,\infty) \text{ and } (x,r) \in \Omega$$

$$\left|v(x,r)-v_{ap}(x,r)\right| \le M_v \,\mathrm{Re}\left\|\frac{\partial p}{\partial r}-\frac{\partial p_{ap}}{\partial r}\right\|_2 \text{, where } M_v \in (0,\infty) \text{ and } (x,r) \in \Omega$$

where Re is Reynolds number and $\|\ \|_2$ is the $\mathbf{L}^2$-norm with respect to Ω.

Fact 3: (Exponential Decay of the Axial Component of the Velocity)

Suppose $p \in \{w(x, r) \in \mathbf{H}^1(\Omega) \mid w(x, r_2) = 0\}$. Then the axial component of the velocity decays exponentially to zero as the radial coordinate is increased, after a few radii from the inflow region.

Fact 4: (Decay of the Radial Component of the Velocity to the Exact Solution)

Suppose that p belongs to the set $\Phi:=\{w(x, r) \in \mathbf{H}^1(\Omega) \mid w(x, r_2) = 0\}$. Then the radial component of the velocity decays to the exact solution as the radial coordinate is increased, after a couple radii from the inflow region.

Fact 5: (Existence and Uniqueness)

If $\mathbf{v}$, $p \in \mathbf{H}^2(\Omega) \times \mathbf{H}^2(\Omega) \times \mathbf{H}^1(\Omega)$, then there exists a unique solution of the Stokes problem.

5. REFERENCES

AMON, C. H., Spectral Element-Fourier Method for Transitional Flows in Complex Geometries, *AIAA Journal*, vol. 31, no. 1, pp. 42-48, 1993.

CHATTERJEE, A., *Radial Flow Plasma Reactors: Fluid Dynamics and Transport Studies*, Ph.D. Thesis, Pennsylvania State University, 1986.

FRIEDMAN, B., *Principles and Techniques of Applied Mathematics*, Dover Publications, Inc., 1990.

GIRAULT, V., RAVIART, P.-A., *Finite Element Approximation of the Navier-Stokes Equations*, Springer-Verlag, 1979.

ISHIZAWA, S., The Axi-Symmetric Laminar Flow in an Arbitrary Shaped Narrow Gap, 2nd Report, *Bull. Jap. Soc. Mech. Engrs.*, vol. 9, no. 33, pp. 86-103, 1966.

JACKSON, J. D., SYMMONS, G. R., An Investigation of Laminar Radial Flow between Two Parallel Discs, *Appl. Sci. Res.*, vol. 15, pp. 59-75, 1965.

OLIVEIRA, J. C., *Evolution of Nonlinear Instabilities and Mathematical Analysis of Radial Flows*. Ph. D. Thesis, Carnegie Mellon University, 1997.

OLIVEIRA, J. C., AMON, C. H., Semi-Analytical Solution for the Radial Stokes Flow between Two Parallel Disks, *ENCIT 96/LATCYM 96*, Federal University of Santa Catarina, Florianopolis-SC-Brazil, vol. 1, pp. 61-66, 1996.

PATERA, A. T., Spectral Element Method for Fluid Dynamics, *Journal of Computational Physics*, vol. 54, no. 3, pp. 468-488, 1984.

RAAL, J. D., Radial Source Flow Between Parallel Disks , *J. Fluid Mech.*, vol. 85, part 3, pp. 401-416, 1978.

XIV Brazilian Congress of Mechanical Engineering
Obeid Plaza Hotel Convention Center - Bauru - SP/Brazil
December 08-12th 1997

PAPER CODE: COB693

NUMERICAL SIMULATION OF TWO-DIMENSIONAL BOUNDARY LAYER SEPARATION CONTROL /

SIMULAÇÃO NUMÉRICA DO CONTROLE DA SEPARAÇÃO DE UMA CAMADA LIMITE BIDIMENSIONAL

Norberto Mangiavacchi*, Gregory Hernandez, Thilo Schoenfeld, Franck Nicoud
CERFACS, 42 avenue Gustave Coriolis, F-31057 Toulouse, France
** Currently at NACAD-COPPE/UFRJ, Caixa Postal 68516, CEP 21945-970, Rio de Janeiro, RJ, Brazil. E-mail: norberto@coc.ufrj.br*

Abstract

The control of the separation on two-dimensional boundary layers at low Mach numbers is analyzed by time-accurate numerical solutions of the compressible Navier-Stokes equations. The control strategy is based on the application of a variable suction/blowing in the proximity of the separation. Open-loop unsteady suction/blowing actuations show the sensitivity of the flow to the control strategy. A simple closed-loop proportional control has been implemented, that uses a tangential shear stress sensor for the feedback control, and that controls the normal velocity at the actuator position. Parallel numerical simulations were performed with the AVBP library on a 32-processor Meiko CS-2, and on a 4-processor IBM SP2. Results show the effectiveness of the control approach in stabilizing the flow and suppressing the periodic shedding of vortices.

Keywords

Active control, boundary layer separation, numerical simulation.
Controle ativo, separação de camada limite, simulação numérica.

1. INTRODUCTION

The control of boundary layer separation is a problem encountered in many important practical applications, such as airplane wings, car airfoils, diffusers, etc. Prevention of separation often improves the performance of such devices by increasing pressure recovery, enhancing lift and reducing total drag. Both experimental and numerical simulations have been applied for study of the active control of laminar boundary-layer flows. Joslin *et al* (1994) provide an overview of such techniques as they apply to the control of instabilities in laminar boundary-layers. Experimental investigations using controlled suction in two-dimensional airfoil models have shown (Alrefai & Acharya, 1995) the feasibility of the application of leading-edge suction for flow control in pitching airfoils.

Our interest is to numerically simulate the control of the separation on model problems that are geometrically simple, but contain most of the physical features and difficulties associated with separated flows in real applications. Two basic geometric configurations that have these qualifications have been presented in a previous work (Hernandez *et al.*

1996). The first configuration is the flow of a two-dimensional boundary layer which separates due to an imposed adverse pressure gradient. The second is the separation of a two-dimensional boundary layer over a corner. In both cases the flow is laminar upstream of the detachment point, and the flow becomes unsteady in the proximity of the detachment point. Comparisons between the two model problems allow to distinguish the effects due to the adverse pressure gradient in the flat plate on the first case from the geometrical effects due to the corner on the second case. In this work we will show results on the numerical simulations of the two-dimensional boundary layer separation control on the first case. Results for the second case are available in Hernandez (1996). The plan of the paper is as follows. In the next section, details are given concerning the computational problem and algorithms that are used in the numerical simulation. In section 3.1 we provide results for the uncontrolled problem, and we show the effect of a suction/blowing forcing in the stable boundary layer without pressure gradient. In section 3.2 we show the results of the use of a proportional control.

2. NUMERICAL METHODS

The simulations are performed using the AVBP software library, which has been developed at CERFACS. The program has been validated previously for the two and three dimensional laminar Navier-Stokes equations. The flow solver used for the discretization of the governing equations is based on a finite-volume method, and has the ability to handle unstructured grids of arbitrary cell type.

The underlying numerical approximation is a second order centered differences cell-vertex scheme with the conservative flow variables associated with the vertices of the cells. The discretized equations are solved using a standard explicit four stage Runge-Kutta scheme. As well as being optimized for scalar and vector architectures, the flow solver has been fully parallelized, ported and tested on a wide range of distributed memory machines. For the parallel implementation we adopt a master-slave paradigm with message passing based on standard libraries such as PVM and PARMACS. For the application the global computational domain is sub-divided using a Recursive Inertia Bisection algorithm. The resulting set of non-overlapping domains contains a well-balanced number of elements in order to achieve an acceptable parallel efficiency.

The computational grid consists of 200 x 100 nodes, the free-stream Mach number is $M_\infty = 0.2$ and the Reynolds number is $Re_\Theta = 230$, based on the momentum thickness Θ at the detachment point and the outer velocity. The boundary condition at the upper boundary is imposed using a soft "non-reflecting" condition (Rudy and Strikwerda, 1980). When the pressure gradient is established, it imposes a suction at the upper boundary, such that a mass fraction S (typically, $S = 0.22$) of the inflow leaves the domain through a small region in the upper boundary.

Two parameters are used to define the bondary conditions at the upper boundary. One corresponds to the suction parameter, S defined as the fraction of the entering flow removed through the upper boundary. This parameter defines the total difference of pressure encountered between the inflow and the outflow. A second scale parameter, L_p, defines the lenght over which the pressure changes from the inflow condition to the outflow condition. A smooth hyperbolic tangent pressure profile is used, given by:

$$p(x) = p_0 + \frac{1}{4\rho}(1 - (1 - S)^2)(1 + \tanh((x - x_p)/L_p)) \qquad (1)$$

For the current computations, the values $L_p = 0.25$, and $x_p = 3.5$ where chosen. The pressure profile is applied at $t = 0$ to the top boundary. To decrease the effect of reflections at the outlet boundary, an "exit zone" approach has also been applied, together with a fully non reflecting boundary condition. The grid is progressively stretched in the buffer region, and viscosity dumps considerably the vortical structures before they leave the domain. Figure 1 shows schematically the domain of computation.

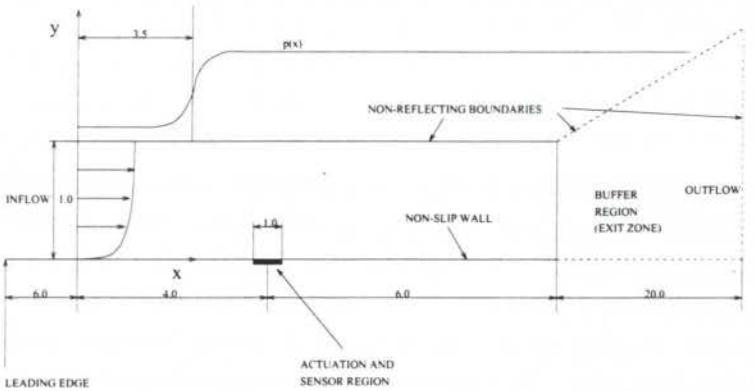

Figure 1: Schematic of the domain of computation.

A polynomial fitting to the Blasius flat plate boundary layer in the absence of pressure gradient is used for both initialization of the flow field and as the inflow velocity boundary condition at the left boundary. The left boundary of the domain is located at a distance $\Delta x_0 = 6.0$, downstream from the leading edge of the flat plate. The figure also shows the location of the actuation and sensor region used to control the flow.

3. RESULTS

For low values of the pressure gradient the flow separates forming a closed and steady separated bubble. However, as the pressure gradient is increased, the flow becomes unsteady, with periodic shedding of vortices. Figure 2 shows the vorticity, x-velocity, and pressure fields for the boundary layer with pressure gradient for the case $S = 0.22$.

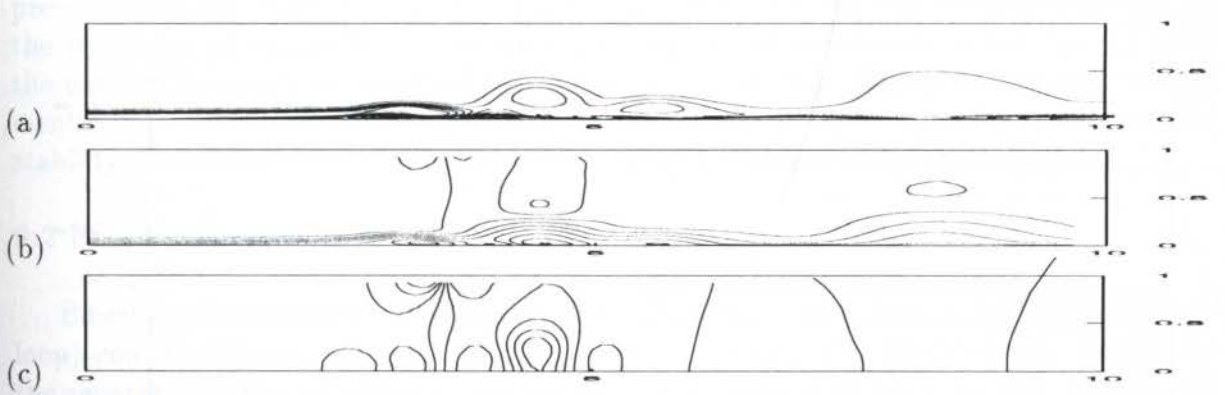

Figure 2: (a) Vorticity, (b)x-velocity and (c)pressure fields, for limit-cycle shedding on a boundary layer with adverse pressure gradient. $S = 0.22$.

Vortices are visible as regions of high vorticity (vorticity blobs), and as regions of low pressure. In figure 3, the time evolution of the near wall velocity and pressure at a downstream location shows the periodic separation of the flow as vortical structures pass by the specified location. The impulsive application of the pressure profile at $t = 0$ results in a transient regime that lasts until about $t = 5$. After that time, the flow continues to evolve more smoothly until it reaches either a steady state or a quasi-periodic behavior. Since vortical structures cause both a local reduction in the wall shear stress and a local pressure drop, there is a strong correlation between the two that can be explored in order to control the separation.

3.1 Active Control

The behavior of the boundary layer is affected by the presence of perturbations in the flow. Periodic disturbances are typical in many applications. Also, since the behavior of the basic flow is almost periodic, it is important to include in the study the behavior of the flow under the influence of periodic disturbances. Two types of perturbations are of interest: perturbations coming from upstream, and perturbations originating at the wall close to the detachment point. The perturbations originating at the wall seem more easily applicable to real cases, and more adequate for close-loop control. In this work, perturbations originating at the wall close to the detachment point were introduced by means of suction and blowing in a region of the wall centered at $x = 4$ and of unit length.

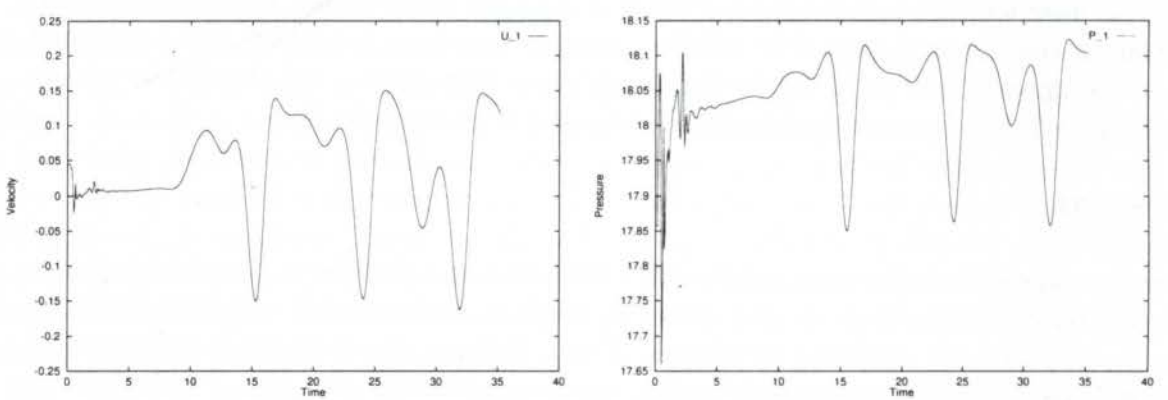

Figure 3: The time evolution of the near wall velocity and pressure at a downstream location ($x = 5.0$).

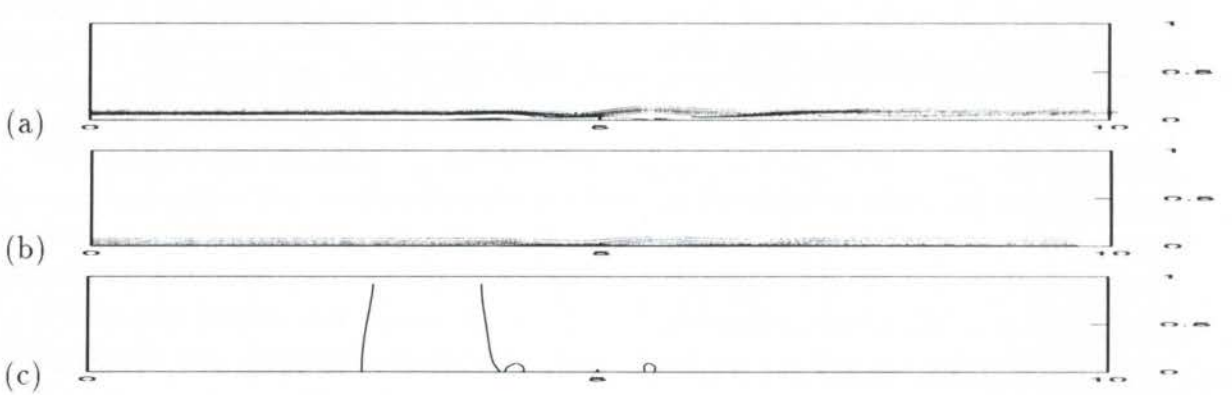

Figure 4: (a) Vorticity, (b) x-velocity, and (c) pressure field $S = 0.0$, with sinusoidal perturbation $S_n = 0.022, f = 0.25$.

The suction normal velocity at the actuator v_n is given by

$$v_n(x,t) = s(x) * \sin(2\pi f t) \tag{2}$$

The function $s(x)$ is chosen to be a parabolic profile that produces a total mass flux of $S_n = 0.022$, and $f = 0.25$. When this periodic perturbation was applied to the boundary layer over the flat plate with no pressure gradient ($S = 0$, see figure 4), it was found that Tollmien-Schlichting (TS) waves could be observed downstream of the excitation point. Figure 5 shows the time evolution of the actuation velocity v_n, and the pressure and tangential velocity at a point located downstream and close to the wall ($x = 5, y = 4 \times 10^{-3}$) It can be seen that when the actuation velocity is negative (suction), the tangential velocity increases (and so does the wall shear stress, τ_w), and conversely, when v_n is positive, τ_w decreases, with a time lag due to the distance from the point where the perturbation is introduced to the monitored point.

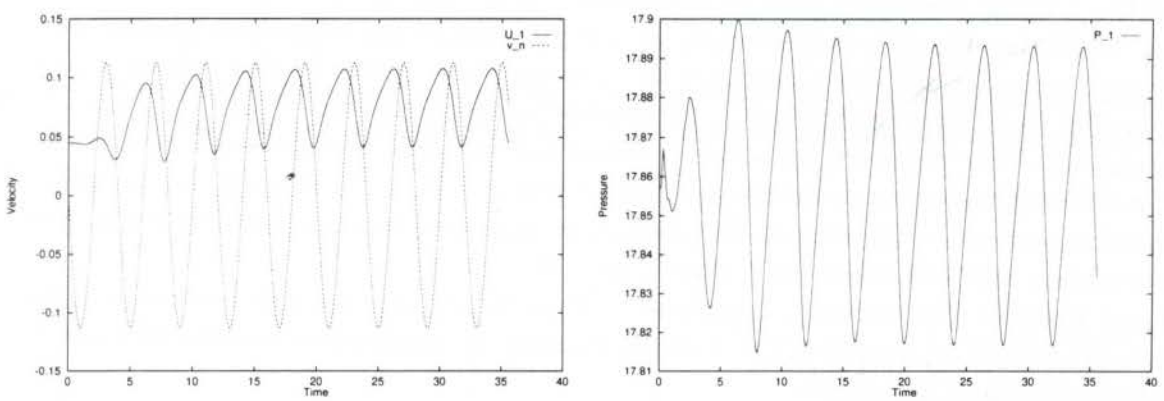

Figure 5: The evolution in time of (a)the actuator normal velocity and the tangential velocity at a downstream location,(b) wall pressure at $x = 5$. Periodic suction and blowing in a Blasius boundary layer without imposed pressure gradient ($S = 0.$)

However, an important feature is that, in spite that the mean injection/suction is zero, there is an average increase in τ_w. Applying the same perturbation in the adverse pressure gradient case ($S = 0.22$) results in the locking of the shedding frequency with the frequency of excitation, as long as the frequncy of excitation is not too far from the natural frequency as observed in the non-perturbed case. Applying a steady suction results in a reduction of the thickness of the boundary layer, therefore increases the stability of the flow.

3.2 Proportional Control

Based on the observations made on the excited separated flow, a feed-back (closed-loop) control scheme, has been implemented to simulate the effect of this control on the separation. The objective of the control in this case is to keep the flow steady and attached, reducing the size of the separation bubble, and avoiding the periodic shedding of vortices. The type of feedback law used is based on the observation that the removal of low momentum and/or reverse-flow fluid in the separation region can prevent lift-up

of the shear layer and prevent vortex formation, as observed in boundary layers over pitching airfoils (Alrefai *et al.* 1995).

The position of the sensor and actuator region for the proportional control implemented are schematically represented in figure 1. The control region has a unit lenght, and is centered at $x = 4$. It can be noted that sensor and actuator are located at the same point. The control law , which prescribes the wall-normal velocity boundary conditions at the control region, is given by:

$$v_n(x,t) = -\frac{\tau_w(x) - \tau_0}{\tau_0}|s(x)| \tag{3}$$

The function $s(x)$ is a parabolic profile. The magnitude of $s(x)$ was chosen based on the results of the sensitivity of the flow to perturbations, to have the same amplitude ($S_n = 0.022$) as the case $S = 0$ shown in figure 4. The set-point of the controller is given by τ_0, which is the desired shear stress at the sensor/actuator location, and is chosen to be approximately the value found at the location of the sensor/actuator in the case of the laminar boundary layer in the absence of adverse pressure gradient (Blasius profile). Since the actuation is exerted by suction/blowing at the wall, the actuation does not perturb substantially the sensor, which measures shear stress at the suction point. Additionally, since sensor and actuator are located at the same point, there is no need to compensate for time delay effects between sensor and actuator signals in the controller.

Two different test were performed with the controller. In the first case, the controller is turned on since the beginning of the simulation, and therefore prevents the formation of the shedding vortices before they grow (case CA).

Figure 6 shows the vorticity, x-velocity, and pressure fields for the controlled case, using eq (3). It can be seen that the separated region is considerably small, and there is no periodic shedding of vortices.

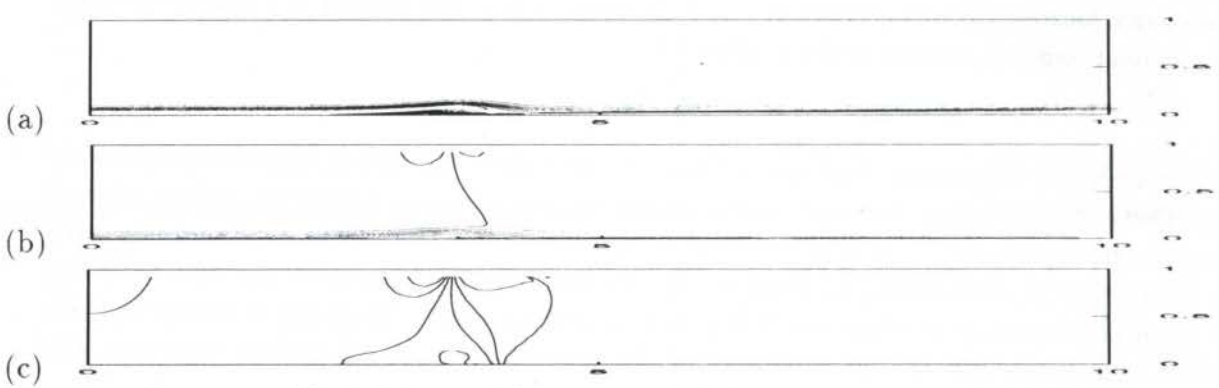

Figure 6: (a) Vorticity, (b) x-velocity, and (c) pressure fields for steady state controlled flow $S = 0.22$ (cases CA and CB).

Figure 7 shows the time history of the suction at the center of the actuator location ($x = 4$), and the velocity at a point close to the wall at a downstream location ($x = 5$). In the second case (CB), the controller is turned on after the flow has reached a quasi-periodic state, with strong shedding of vortices.

In the figure 8 it can be seen that, shortly after the time at which the control is switched on ($t = 20$), the flow becomes more steady and the backflow is eliminated at the

downstream location. The steady state solution for case CB is essentially the same that in the case CA. The final suction velocity required for the control in both cases is quite small, as compared to the far-field velocity. However the second case requires a much higher initial suction velocity than the first case (about three times larger). The most relevant fact is that the controller is able to re-establish the steady controlled regime even after the oscillatory regime has been reached.

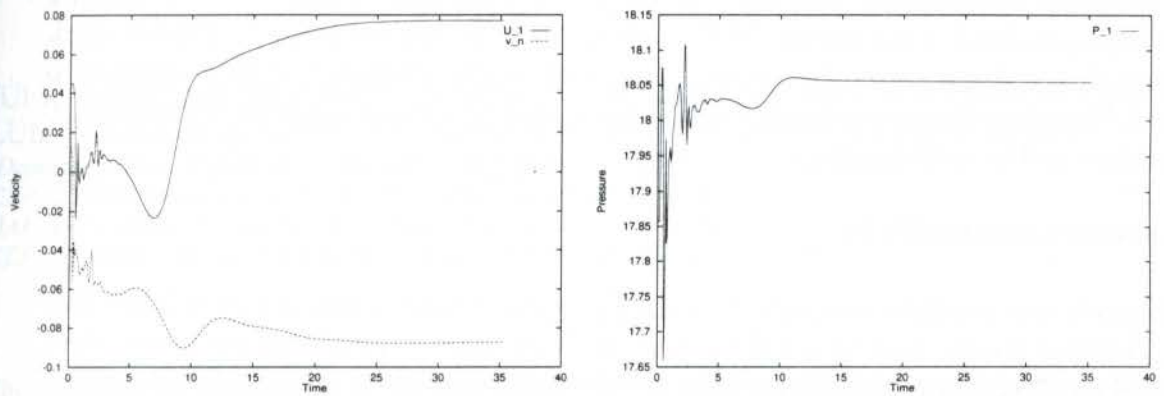

Figure 7: The evolution in time of (a) the actuator normal velocity (v_n) and the tangential velocity (U_1) at ($x = 5$), and (b) the wall pressure at ($x = 5$). Case CA: proportional controller started at $t = 0$.

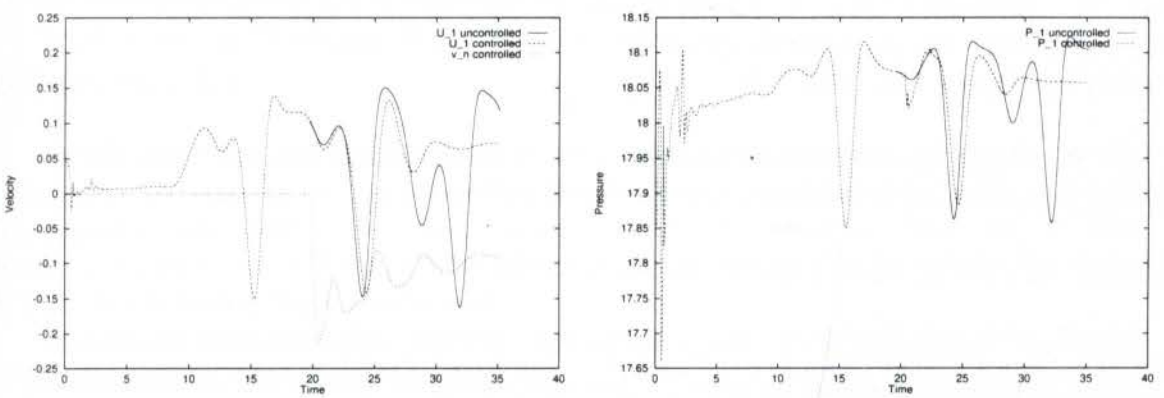

Figure 8: The evolution in time of (a) the actuator normal velocity (v_n controlled) and the tangential velocity (U_1 controlled) for the controlled case together with the tangential velocity for the uncontrolled case (U_1 uncontrolled) at $x = 5$, and (b) the wall pressure for the controlled and uncontrolled cases (P_1 controlled and uncontrolled) at $x = 5$. Case CB: proportional controller started at $t = 20$.

It is possible that a feed-back control scheme actuating by means of a variable (unsteady) suction/blowing may result in a improvement in the efficiency of the actuation, therefore requiring less actuation energy to keep the flow under control. Also, it is possible to use the pressure as the sensor signal, as long as sensor and actuator are placed at a certain distance. These experiments are currently in progress.

4. CONCLUSIONS

The numerical simulation of the control of separation on a two dimensional boundary layer which separates due to an imposed adverse pressure gradient has been performed. Results of the simulations show that by adopting a simple scheme of shear sensor and injection/suction actuator and a simple feedback law, it is possible to stabilize the separation bubble, and reduce its size considerably. The simulated flow shows that there is no vortex shedding in the controlled case, and the flow is essentially steady. Very promising results were obtained, even though the adopted law was not optimized. Future work will focus on the design of better control laws, and on the extension of this analysis to turbulent boundary layer separation. The application of neural network techniques to this problem will be addressed.

5. ACKNOWLEDGEMENTS

This work was partially supported by the European Commission, under a TMR Research Training Grant, and by a CNPq post-doctoral grant. Initial computations were performed on the 32-processor Meiko CS2 parallel computer at CERFACS in the framework of the GPMIMD2 european project. Later computations were performed on the 4-node IBM SP2 at NACAD/COPPE/UFRJ. All computation were performed using the AVBP library (Version 2.5).

6. REFERENCES

ALREFAI, M., ACHARYA, M., Controlled leading-edge suction for the management of unsteady separation over pitching airfoils, 26th AIAA Fluid Dynamics Conference, June 19-22, 1995/San Diego, CA. AIAA 95-2188.

HENK, R. W., 1990, An experimental study of the mechanics of an unsteady, three-dimensional separation. Ph.D. thesis, Stanford University.

HERNANDEZ, G., Ph.D. Thesis, I.N.P., Toulouse, 1996.

HERNANDEZ, G., SCHONFELD, T. MANGIAVACCHI, N., NICOUD, F. 1996, Numerical active control of two-dimensional boundary layer separation, 1st AIAA Theoretical Fluid Mechanics Conference, New Orleans, June 17-20.

JOSLIN, R. D, ERLEBACHER, G., AND HUSSAINI, M. Y., Active control of instabilities in laminar boundary-layer flow. An overview. ICASE Rept. 94-97, Hampton, VA, Dec. 1994.

PAULEY, L. L., MOIN, P., AND REYNOLDS, W. C. 1990, The structure of two-dimensional separation, *J. Fluid Mech.* **220**, 397-411.

RUDY, D. H., AND STRIKWERDA, J. C. 1980, A nonreflecting outflow boundary condition for subsonic Navier-Stokes calculations, *J. Comput. Phys.* **36**, 55-70.

XIV Brazilian Congress of Mechanical Engineering
Obeid Plaza Hotel Convention Center - Bauru - SP/Brazil
December 08-12th 1997

PAPER CODE: COB716

OBTENÇÃO DE MODELO DE PERDAS DE PRESSÃO TOTAL EM COMPRESSORES AXIAIS / *MODELLING OF TOTAL PRESSURE LOSS IN AXIALS COMPRESSORS*

JÚLIO SANTANA ANTUNES[1] , MARIA DE FÁTIMA CASTRO LACAZ SANTOS[1], JOÃO LUIZ FILGUEIRAS AZEVEDO[2], JOÃO ROBERTO BARBOSA[2] E EDSON BASSO[2]
[1]*Departamento de Matemática - Faculdade de Engenharia - UNESP - Guaratinguetá*
CEP 12500-000 Guaratinguetá, Brasil - E-mail: santana@feg.unesp.br.
[2]*IAE-ASE - Centro Tecnológico de Aeronáutica - São José dos Campos*
CEP 12228-900 São José dos Campos, Brasil - E-mail: azevedo@ase2.cta.br.

Abstract

The paper presents simulations of cascade flows using the two-dimensional Navier-Stokes equations. An implicit, approximate factorization method which allows the simulation of flows regardless of the speed regime is adopted. Spatial discretization of the governing equations uses a central difference algorithm. Boundary conditions are implemented based on one-dimensional characteristic relations for the Euler equations. Numerical tests are performed for flows in axial compressors with DCA profiles.

Keywords

Navier-Stokes, Compressores Axiais, Simulação Numérica, Escoamento Compressível, Diferenças Finitas
Navier-Stokes, Axials Compressors, Numerical Simulation, Compressivel Flow, Finites Differences

1. INTRODUÇÃO

O presente trabalho descreve parte dos esforços no sentido de se desenvolver a capacidade de simular as equações de Navier-Stokes bidimensionais com aplicações a escoamentos em grades de compressores axiais. O objetivo final do esforço de desenvolvimento é obter ferramentas numéricas que permitam estudar correlações de perdas de pressão total em compressores axiais.

A solução numérica das equações governantes será realizada por uma técnica de diferenças finitas baseada no algoritmo desenvolvido por Martins(1994). Este método é um aprimoramento do algoritmo original de Beam & Warming (1976,1978) no sentido de permitir a simulaçâo de escoamento em uma faixa mais ampla de velocidades. Para escoamento com alto número de Reynolds, usa-se a aproximação da camada fina com objetivo de simplificar a implementação do método numérico e diminuir o tempo de computação.

As derivadas espaciais das equações são aproximadas por operadores de diferenças finitas centradas e, para marcha no tempo é utilizado o esquema de Euler implícito. Para discretização dos termos viscosos são usados diferenças centradas de ponto médio. A implementação das condições de contorno é baseada no conceito das relações características das equações não viscosas da gasdinâmica em uma dimensão. O estudo descrito neste trabalho consiste em

aplicar a metodologia Martins(1994) para escoamentos em grades do tipo DCA (Double Circular Arc) de compressores axiais com escoamento subsônico.

2. DESENVOLVIMENTO

O método utilizado neste trabalho, faz-se uma mudança das variáveis dependentes, em que a pressão substitui a densidade como variável principal. Este artifício é usado pois a variação de pressão é relevante em todas as faixas de números de Mach.

Assim, depois de substituir densidade por pressão e temperatura, usando a equação de estado, pode-se reescrever as equações na forma de lei de conservação, num sistema de coordenadas curvílineas, como segue:

$$\frac{\partial Q(q)}{\partial \tau}+\frac{\partial F(q)}{\partial \xi}+\frac{\partial G(q)}{\partial \eta}=\mathrm{Re}^{-1}\frac{\partial S}{\partial \eta} \tag{1}$$

O vetor de variáveis primitivas é dado por,

$$q=\begin{Bmatrix} p \\ u \\ v \\ T \end{Bmatrix} \tag{2}$$

O vetor de variáveis conservadas pode, então, ser escrito como

$$Q=J^{-1}\begin{Bmatrix} \frac{p}{T} \\ \frac{pu}{T} \\ \frac{pv}{T} \\ \frac{p}{(\gamma-1)}+\frac{p}{2RT}(u^2+v^2) \end{Bmatrix} \tag{3}$$

e os vetores de fluxo são escritos como

$$F=J^{-1}\begin{Bmatrix} \frac{pU}{T} \\ \frac{puU}{T}+Rp\xi_x \\ \frac{pvU}{T}+Rp\xi_y \\ \left[\frac{\gamma\, p}{(\gamma-1)}+\frac{p}{2RT}(u^2+v^2)\right]U-p\xi_t \end{Bmatrix} \tag{4}$$

$$G = J^{-1}\begin{Bmatrix} \dfrac{pV}{T} \\ \dfrac{puV}{T} + Rp\eta_x \\ \dfrac{pvV}{T} + Rp\eta_y \\ \left[\dfrac{\gamma\, p}{(\gamma-1)} + \dfrac{p}{2RT}(u^2+v^2)\right]V - p\eta_t \end{Bmatrix} \tag{5}$$

O vetor de fluxo viscoso pode ser escrito como:

$$S = J^{-1}\begin{bmatrix} 0 \\ \mu\left(\eta_x^2+\eta_y^2\right)u_\eta + (\mu/3)\left(\eta_x u_\eta + \eta_y v_\eta\right)\eta_x \\ \mu\left(\eta_x^2+\eta_y^2\right)v_\eta + (\mu/3)\left(\eta_x u_\eta + \eta_y v_\eta\right)\eta_y \\ \left(\eta_x^2+\eta_y^2\right)\left[0.5\,\mu\left(u^2+v^2\right)_\eta + \mu\left(a^2\right)_\eta / (\gamma-1)\Pr\right] \\ +(\mu/3)\left(\eta_x u_\eta + \eta_y v_\eta\right)\left(\eta_x u + \eta_y v\right) \end{bmatrix} \tag{6}$$

A nomenclatura é a usualmente utilizada em mecânica dos fluidos computacional (CFD), como ρ para densidade, u e v componentes da velocidade cartesiana, Re é o número de Reynolds, Pr é o número de Prandtl, P é a pressão, T é a temperatura, a é a velocidade do som, μ coeficiente de viscosidade, γ calor específico do ar, R constante do gás e U,V componentes contravariantes de velocidade.

3 - IMPLEMENTAÇÃO NUMÉRICA

As equações governantes foram discretizadas utilizando um método de diferenças finitas implícito, com um esquema de fatoração aproximada em forma de delta. O método de Euler implícito é usado para marcha no tempo, e diferenças centradas são usadas para aproximação das derivadas espaciais. O resultado do esquema é de segunda ordem de precisão no espaço, mas somente de primeira ordem de precisão no tempo. O algoritmo pode ser escrito na forma de operador como

$$L_\xi L_\eta \Delta q^n = (D^n)^{-1}(R_\xi + R_\eta) \tag{7}$$

onde os operadores são definidos como

$$\begin{aligned} L_\xi &= I + \Delta t (D^n)^{-1}\delta_\xi A^n - \varepsilon_I \Delta t \nabla_\xi \Delta_\xi \\ L_\eta &= I + \Delta t (D^n)^{-1}\delta_\xi B^n - \Delta t\, \mathrm{Re}^{-1}\bar{\delta}_\eta M^n - \varepsilon_I \Delta t \nabla_\eta \Delta_\eta \end{aligned}$$

$$\begin{aligned} R_\xi &= -\Delta t \delta_\xi F^n + H_\xi \\ R_\eta &= -\Delta t \delta_\eta G^n + H_\eta + \Delta t\, \mathrm{Re}^{-1}\bar{\delta}_\eta S_\eta \end{aligned} \tag{8}$$

$$H_{\xi} = -\Delta t \varepsilon_E J^{-1} \left(\nabla_{\xi} \Delta_{\xi}\right)^2 J\overline{Q}^n$$

$$H_{\eta} = -\Delta t \varepsilon_E J^{-1} \left(\nabla_{\eta} \Delta \eta\right)^2 J\overline{Q}^n$$

Nas equações acima, δ_{ξ} e δ_{η} são operadores de diferenças centradas, ∇_{ξ}, ∇_{η} e Δ_{ξ}, Δ_{η} são operadores de diferenças "backward" e "forward", respectivamente, $\overline{\delta}_{\eta}$ é um operador de diferenças centradas de ponto médio, A, B e D são matrizes jacobianas de fluxo não viscoso e M é a matriz jacobiana de fluxo que contém os termos viscosos. Na definição dos operadores utilizados no algoritmo, já foram incluídos os termos de dissipação artificial necessários à estabilidade numérica. Foi empregado o modelo de dissipação não linear, pois mostrou ser mais adequado. A adição de termos de dissipação artificial modifica o sistema de equações original; do lado direito do algoritmo, esses termos são uma combinação de termos de segunda e quarta ordem, com o objetivo de manter a tridiagonalidade das matrizes a serem invertidas.

4 - CONDIÇÕES DE CONTORNO

A implementação das condições de contorno foram baseadas nas relações características em uma dimensão das equações da gasdinâmica. As condições de contorno utilizadas para a superfície sólida para escoamentos permanentes, é assumido gradiente de pressão nulo na direção normal a superfície e escoamento considerado tangente na parede. A velocidade é extrapolada impondo-se condição de escoamento normal nulo sobre a superfície, com isso obtém-se as componentes cartesianas de velocidade fazendo V = 0 e extrapolando U por

$$\begin{Bmatrix} u \\ v \end{Bmatrix} = J^{-1} \begin{bmatrix} \eta_y & -\xi_y \\ -\eta_x & \xi_x \end{bmatrix} \begin{Bmatrix} U \\ V \end{Bmatrix} \tag{9}$$

A temperatura foi calculada assumindo-se gradiente nulo normal a parede (parede adiabática). Para as fronteiras externas foram utilizadas condições de contorno não reflexivas, baseadas nas relações características unidimensionais (Azevedo et al., 1992). Elas originam-se das equações de Euler bidimensionais, em coordenadas cartesianas, e assumem uma "operação" em x, e são dadas por:

$$\frac{\partial \rho}{\partial t} - \frac{1}{a^2}\frac{\partial p}{\partial t} = -u\left(\frac{\partial p}{\partial x} - \frac{1}{a^2}\frac{\partial p}{\partial x}\right)$$

$$\frac{\partial v}{\partial t} = -u\frac{\partial v}{\partial x}$$

$$\frac{\partial p}{\partial t} + \rho a \frac{\partial u}{\partial t} = -(u+a)\left(\frac{\partial p}{\partial x} + \rho a \frac{\partial u}{\partial x}\right) \tag{10}$$

$$\frac{\partial p}{\partial t} - \rho a \frac{\partial u}{\partial t} = -(u+a)\left(\frac{\partial p}{\partial x} - \rho a \frac{\partial u}{\partial x}\right)$$

onde a é a velocidade do som.

Assim, para fronteira de entrada subsônica, três condições podem ser fixadas(pressão, ângulo de escoamento e temperatura) e uma extrapolada(velocidade). Para uma fronteira de saída subsônica, uma condição deve ser fixada(pressão) e três extrapoladas(velocidades e densidade). Para a condição de periodicidade foi utilizada da seguinte maneira: o vetor das variáveis conservadas para j=1 antes e depois do bordo de ataque é igual ao vetor das variáveis conservadas em j= jmax antes e depois do bordo de fuga.

5. RESULTADOS E COMENTÁRIOS

A solução numérica apresentada refere-se a escoamento em grades de perfis do tipo DCA (Double Circular Arc) sem arredondamento dos bordos de ataque e fuga para compressores axiais com entrada e saída subsônica. Uma das malhas típicas utilizada apresenta 69 pontos na direção ξ e 19 pontos na direção η (malha "grossa") e a outra apresenta 193 pontos na direção ξ e 43 pontos na direção η (malha "fina") . Para os casos testados o ângulo de escoamento é de 47,5° e ângulo de ataque de zero graus, ângulo de montagem da grade 47,5° e razão de espaçamento 0,45, como pode ser visto pela fig. 1.

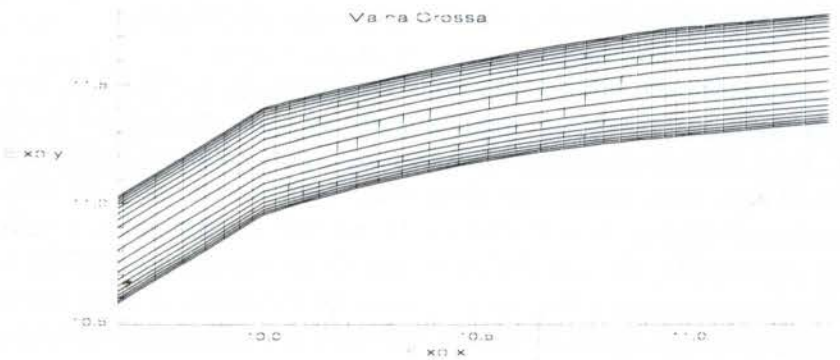

Figura 1 - Malha Grossa

A fig. 2 mostra os vetores velocidades na região entre as grades do perfil DCA utilizando uma malha grossa. Pela figura nota-se que existe uma formação de vórtices na parte superior do perfil. Estes vórtices parecem estar associados a se ter um aerofólio com bordo de ataque afilado e com ângulo de ataque diferente de zero.

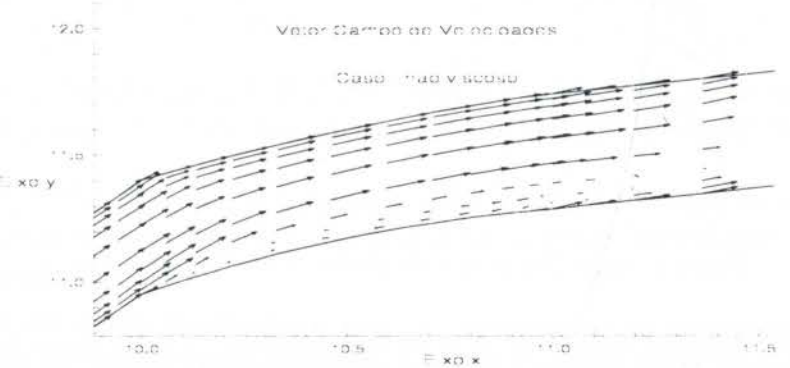

Figura 2 - Vetor Campo de velocidades - Caso: não viscoso

A fig. 3 mostra o campo de velocidades, ou seja, o número de Mach em toda a região entre as pás. O número de Mach para este caso foi considerado 0,8. Pela fig. 3 percebe a

existência de uma região de baixa velocidade(região em azul), onde ocorre a separação do escoamento.

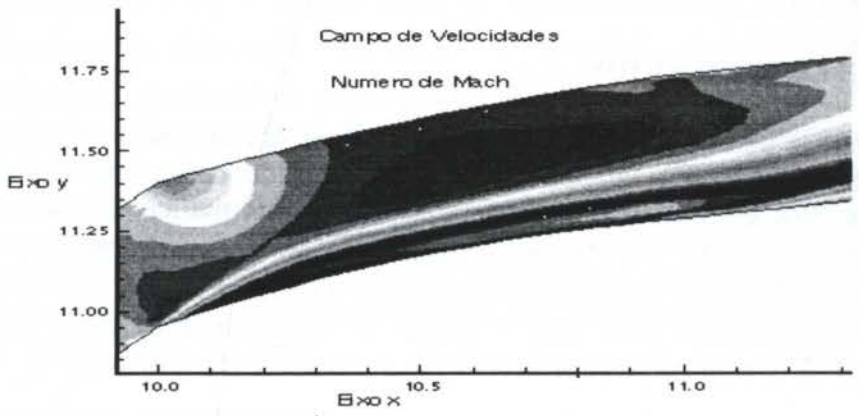

Figura 3 - Distribuição do Número de Mach - caso não viscoso

A fig. 4 mostra os vetores de velocidades entre as grades do perfil DCA, considerando escoamento viscoso laminar, utilizando-se uma malha grossa com um número de Reynolds da ordem de 5,0 x 10^5. Este número de Reynolds é possível, pois estamos trabalhando com as equações de Navier-Stokes com média de Reynolds, onde os termos de flutuação são desprezados, bem como os efeitos de turbulência. O número de Reynolds é utilizado para termos uma idéia da velocidade, ele não define o tipo de escoamento.(não diz respeito as características físicas do escoamento). Para este número de Reynolds, o qual pertence a uma zona de transição, não esta sendo aplicado nenhum modelo de turbulência. Do mesmo modo, nota-se a presença de formação de vórtices.

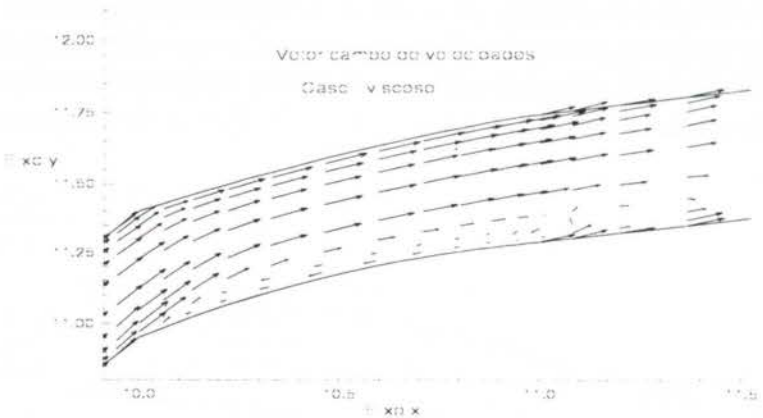

Figura 4 - Vetor Campo de velocidades - Caso: viscoso

A fig. 5 mostra o campo de velocidades, ou seja, o número de Mach em toda a região entre as pás. O número de Mach para este caso foi considerado novamente de 0,8. Pela fig. 5 percebe a existência de uma região de baixa velocidade(região em azul), onde ocorre a separação do escoamento.

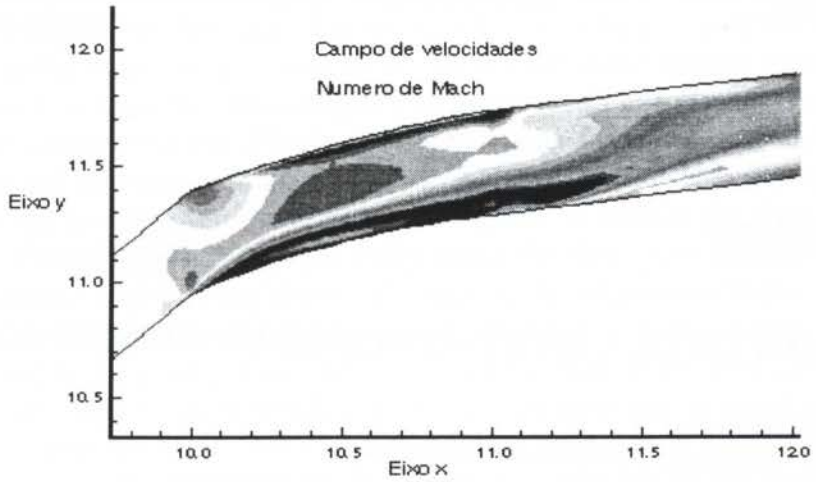

Figura 5 - Distribuição do Número de Mach - Caso viscoso

A perda de pressão total definida neste trabalho é dada pela relação entre as diferençsa de pressão total na entrada e saída pela diferença de pressão total na entrada pela pressão estática na entrada. A pressão total encontrada para o caso não viscoso foi de 0,027 enquanto para o caso viscoso foi de 0,068. O resultado obtido experimentalmente encontrado para o caso viscoso com turbulência em AGARD-AR-275 foi de 0,046. Como pode ser visto os resultados são da mesma ordem de grandeza, levando-se em conta que no método utilizado neste trabalho não foi implementado o modelo de turbulência.

6. REFERÊNCIAS

AZEVEDO, J. L. F., FICO, N. G. C. R., JR., ORTEGA, M. A., AND LUNA, G. C., Nozzle Flow Computations Using the Euler Equations, ICAS Paper No. 92-4.1.2, *Proceedings of the 18th Congress of the International Council of the Aeronautical Sciences*, Vol. I, pp. 97 - 107, Beijing, P. R. of China, Sept, 1992.

AZEVEDO, J. L. F., Euler Solutions of Transonic Nozzle Flows, *Anais do III Encontro de Ciências Térmicas, Vol. I,* pp. 243-248, Itapema, SC, Dez., 1990.

BEAM, R. M. AND WARMING, R. F., "An Implicit Finite-Difference Algorithm for Hyperbolic Systems in Conservation-Law Form", *Journal of Computational Physics*, Vol. 22, pp. 87-110, Sept., 1976.

BEAM, R. M., AND WARMING, R. F., " An Implicit Factored Scheme or the Compressible Navier-Stokes Equations", *AIAA Journal,* Vol. 18, No. 4, pp. 393 - 402, April, 1978.

MARTINS, R. J., " Um Método de Diferenças Finitas para Simulação de Escoamentos em Qualquer Regime de Velocidade", Tese de Mestrado. Instituto Tecnológico de Aeronautica, São José dos Campos, SP, 1994.

Tests Cases for Computation of Internal Flows in Aero Engine Components. AGARD-AR-275, July 1990.

XIV Brazilian Congress of Mechanical Engineering
Obeid Plaza Hotel Convention Center - Bauru - SP/Brazil
December 08-12th 1997

PAPER CODE: COB236

SUPERSONIC FLOW OVER A SPIKE-NOSED BODY OF REVOLUTION

ALGACYR MORGENSTERN JR.
Divisão de Sistemas Espaciais - CTA/Instituto de Aeronáutica e Espaço
CEP 12228-904 São José dos Campos, SP, Brasil - E-mail: algacyr@ase-n2.iae.cta.br

Abstract

The unsteady, viscous, supersonic flow over a spike-nosed body of revolution was numerically investigated by solving the Navier-Stokes equations. The time-accurate computations were performed employing an implicit algorithm based on the second-order time accurate LU-SGS scheme with the incorporation of a subiteration procedure to maintain time accuracy. Self-sustained oscillations for a Mach number of 3.0 and Reynolds number of 7.87 x 10^6/m were observed in the numerical computations, for a spike length to shoulder height ratio of 1.74, confirming the experimental result. The numerical result predicted correctly the discrete frequency range as well as the sound pressure intensities. The flow structure is also presented and discussed.

Keywords

unsteady flow; supersonic flow; spike-nosed body; time-accurate computations; Newton-like subiterations.

1. INTRODUCTION

Spike-nosed configurations have been studied for application on a variety of practical configurations. A fixed spike placed on the nose of blunt bodies to reduce drag, on ablating reentry vehicles to alleviate heating on the body surface, in projectile configurations as a standoff distance, etc. The flow field around such configurations was observed to exhibit the phenomenon of self-excited shock oscillations, causing some harmful effects to vehicles by excessive noise levels and structural loadings. This phenomenon is highly unstable, and the necessary conditions for it to occur are the presence of a shear layer with an inflection point in the velocity profile, a reflecting surface, and the appropriate spike length to permit in phase reflections of pressure waves. If these conditions are met, highly organized oscillations of the impinging flow are sustained by feedback of upstream pressure propagation through the subsonic separated region to the shear layer origin, and by amplification of the disturbances until a limit cycle is reached.

An experimental investigation performed by Calarese and Hankey(1985) revealed the unstable shock structure as consisting of a strong detached bow shock at the spike's tip which then collapses into a conical shock that intersects a quasi normal shock near the body's shoulder. It was also given evidence that the shock oscillates axially in a symmetric fashion with respect to the spike as well as in an asymmetric fashion for certain configurations and flow conditions.

The experiments showed that the onset of shock oscillations only occur for a certain range of the protruded spike length at fixed values of the spike and forebody diameter. It was also observed that once the shock oscillations are induced by the spike outward motion, they

sustain themselves even when the spike reaches a length which would require the onset of a stable shock configuration. The same occurring when the spike is retracted, i.e., the existing stable shock configuration tends to remain unchanged for spike lengths which would require the onset of shock oscillations. This indicates that a hysteresis phenomenon occurs.

Numerical solutions of the Navier-Stokes equations for flows over spike-nosed bodies have been obtained by many authors. Shang, et. al.(1980), investigated the longitudinal mode of oscillations, the pressure amplitude of the disturbance as well as the shear layer and shock wave systems. Mikhail(1991 and 1996) investigated the flow over projectiles with a spike-nosed configuration and tripping rings. Although these efforts succeeded in simulate this complex unsteady flow, it was used an explicit algorithm in these works. Due to stability requirements, explicit algorithms impose a very severe limit in the time step to advance the numerical solution which can be much smaller than the time step required by the physics of the problem. To overcome this difficulty, an implicit time-accurate algorithm is employed in the present work and the time step is dictated by the physics of the problem. Computed spectral power estimates of pressure time history results are compared with experimental data for validation purposes. Instantaneous pressure and Mach contours are presented to describe the unsteady oscillatory shock motion.

2. MATHEMATICAL FORMULATION

2.1 Governing Equations

The compressible laminar flow over a spike-nosed body is governed by the Navier-Stokes equations. These equations for axisymmetric and two-dimensional flow can be expressed in the following strong conservation form, where the dependent variables ρ, u, v, and Et, are density, components of velocity in the x and y coordinate directions, and total energy, respectively, p being pressure, T being temperature, and t denoting time:

$$\frac{\partial Q}{\partial t} + \frac{\partial (F - F_v)}{\partial x} + \frac{\partial (G - G_v)}{\partial y} + \left(\frac{(G - G_v)}{y} + \frac{(H - H_v)}{y} \right) \beta = 0 \qquad (1)$$

where

$$Q = \begin{pmatrix} \rho \\ \rho u \\ \rho v \\ Et \end{pmatrix}, \quad F = \begin{pmatrix} \rho u \\ \rho u u + p \\ \rho u v \\ u (Et + p) \end{pmatrix}, \quad F_v = \begin{pmatrix} 0 \\ \tau_{xx} \\ \tau_{xy} \\ u \tau_{xx} + v \tau_{xy} - q_x \end{pmatrix},$$

$$G = \begin{pmatrix} \rho v \\ \rho v u \\ \rho v v + p \\ v (Et + p) \end{pmatrix}, \quad G_v = \begin{pmatrix} 0 \\ \tau_{xy} \\ \tau_{yy} \\ u \tau_{xy} + v \tau_{yy} - q_y \end{pmatrix},$$

$$H = \begin{pmatrix} 0 \\ 0 \\ - p \\ 0 \end{pmatrix}, \quad H_v = \begin{pmatrix} 0 \\ 0 \\ - \tau_{\theta\theta} \\ 0 \end{pmatrix}$$

$$\tau_{xx} = -\frac{2}{3}\mu \nabla . V + 2\mu \frac{\partial u}{\partial x}, \qquad \tau_{xy} = \mu\left(\frac{\partial u}{\partial y} + \frac{\partial v}{\partial x}\right), \qquad \tau_{xy} = -\frac{2}{3}\mu \nabla . V + 2\mu \frac{\partial v}{\partial y}$$

$$\tau_{\theta\theta} = -\frac{2}{3}\mu \nabla . V + 2\mu \frac{v}{y}, \qquad \nabla . V = \frac{\partial u}{\partial x} + \frac{\partial v}{\partial y} + \left(\frac{v}{y}\right)\beta$$

$$q_x = -Cp \frac{\mu}{Pr}\frac{\partial T}{\partial x}, \qquad q_y = -Cp \frac{\mu}{Pr}\frac{\partial T}{\partial y}$$

where μ is molecular viscosity, and $\beta = 1$ or 0 for axisymmetric and two-dimensional flow, respectively.

The equation of state for a perfect gas, $p = \rho R T$ is used for closure, and the dependence of molecular viscosity on temperature is given by Suhterland's law.

Equation (1) is then transformed to the ξ-η computational plane in conservation law form.

2.2 Numerical Algorithm

The present time-accurate numerical method is based on the observation that a δ-form of the governing unsteady equations may be constructed with various combinations of the flux formulae and their Jacobeans. Furthermore a suitable choice of the factorization procedure yields a scheme with fast convergence and low computational time per iteration.

Eq. (1) can be written in difference form as

$$\left[\frac{3}{2} I + \Delta t \left(D_\xi \hat{A} \bullet + D_\eta \hat{B} \bullet\right)\right] \delta \hat{Q}^n$$

$$= \frac{1}{2}\delta \hat{Q}^{n-1} - \Delta t \left\{D_\xi \left(\hat{F}^n - \hat{F}_v^n\right) + D_\eta \left(\hat{G}^n - \hat{G}_v^n\right) + \frac{\beta}{y}\left[\left(\hat{G}^n - \hat{G}_v^n\right) + \left(\hat{H}^n - \hat{H}_v^n\right)\right]\right\} \qquad (2)$$

where a second order accurate Euler three-point backward time discretization is used. The inviscid and viscous fluxes are linearized by:

$$\hat{F}^{n+1} = \hat{F}^n + \hat{A}\,\Delta\hat{Q}^n, \qquad \hat{F}_v^{n+1} = \hat{F}_v^n,$$

and the inviscid flux Jacobean matrix defined as

$$\hat{A} = \frac{\partial \hat{F}}{\partial \hat{Q}}$$

similarly for $\hat{G}$, $\hat{G}_v$, and $\hat{B}$.

A finite volume approach is used in the treatment of the spatial discretization of the fluxes. Second order central differences are used in the left hand side. A fourth order artificial dissipation is added to the right hand side to control the undesired effect of odd and even point decoupling characteristic of central differences.

In the present two-dimensional algorithm, the lower-upper symmetric-Gauss-Seidel factorization scheme proposed by (Yoon, S. and Kwak, D., 1992) is used. The advantage of this factorization is that the construction of the diagonal of the L and U matrices permits a scalar inversion, leading to a very efficient and vectorizable algorithm. The Jacobean matrix $\hat{A} = \hat{A}^+ + \hat{A}^-$ is approximated by

$$\hat{A}^{\pm} = \frac{1}{2}\left[\hat{A} \pm r\left(\hat{A}\right)\right]$$

where

$$r(\hat{A}) = \max[\,|\lambda(\hat{A})|\,]$$

and $\lambda(\hat{A})$ is the eigenvalue of the Jacobean matrix $\hat{A}$. A similar procedure is applied to the Jacobean matrix $\hat{B}$.

With these approximations the factorization matrices are given by

$$L = (\frac{3}{2} + \Delta t\, r)\, \mathrm{I} - \Delta t\, (\hat{A}^{+}_{i-1,j} + \hat{B}^{+}_{i,j-1})$$

$$D = (\frac{3}{2} + \Delta t\, r)\, \mathrm{I}$$

$$U = (\frac{3}{2} + \Delta t\, r)\, \mathrm{I} + \Delta t\, (\hat{A}^{-}_{i+1,j} + \hat{B}^{-}_{i,j+1})$$

where

$$r = r(\hat{A}) + r(\hat{B})$$

Equation (2) can thus be written as

$$\mathrm{L\,D^{-1}U}\,\delta\hat{Q}^{n} = \mathrm{RHS[Eq.(2)]} \qquad (3)$$

The solution is then obtained in three steps as follows

$$\delta\hat{Q}^{*} = \mathrm{L^{-1}\,RHS}$$

$$\delta\hat{Q}^{**} = \mathrm{D}\,\delta\hat{Q}^{*} \qquad (4)$$

$$\delta\hat{Q}^{n} = \mathrm{U^{-1}}\,\delta\hat{Q}^{**}$$

This scheme has given good results for steady flow calculations (Yoon and Kwak, 1992). However, for unsteady flow calculations the approximation of the flux Jacobean matrices and the linearization procedure reduce the accuracy of the time discretization. To overcome this difficulty a procedure presented in Matsuno (1989) is introduced. At each time step a Newton-like sub-iteration procedure is performed until convergence is achieved for each time step, while maintaining the unsteady form of the governing equations in the RHS of the algorithm. The idea of sub-iterations is that the governing equations may be iterated in pseudo time for each physical time-step; at convergence of the pseudo time iterations (sub-iterations), the linearization and factorization errors go to zero, and the full temporal accuracy of the numerical discretization is recovered. This can be obtained by adding a pseudo time derivative of the dependent variable vector to Eq.(1) and using a backward first-order accurate time difference formula to discretize the pseudo time derivative. Applying an Euler implicit scheme at the (n+1) time level, it may be written in difference form as

$$\mathrm{L\,D^{-1}U}\,\delta\hat{Q}^{n,\nu} = -\frac{3}{2}(\hat{Q}^{n,\nu} - \hat{Q}^{n}) + \mathrm{RHS\ of\ Eq.\ (2)},$$

$$\nu = 0, 1, 2, 3, \ldots$$

where

$$\delta\hat{Q}^{n,\nu} = \hat{Q}^{n,\nu+1} - \hat{Q}^{n,\nu}$$

here ν denotes the pseudo time level. For $\nu = 0$, $\hat{Q}^{n,\nu} = \hat{Q}^{n}$, and the algorithm reduces to the steady state formulation of Yoon and Kwak (1992). At convergence of the sub-iteration

procedure $\delta\hat{Q}^{n,\nu} \rightarrow 0$ and the accuracy of the solution at each time step is the accuracy of the discretized unsteady governing equations. The solution is obtained in three steps, given by

$$\delta\hat{Q}^{*} = L^{-1}\ RHS$$

$$\delta\hat{Q}^{**} = D\ \delta\hat{Q}^{*}$$

$$\delta\hat{Q}^{\nu} = U^{-1}\ \delta\hat{Q}^{**}$$

For the steady flow problem only a single time-level sequence is used. As discussed above, the iterations for the unsteady problem are conducted in both physical time and pseudotime using the same numerical method.

3. RESULTS

The geometry of the spike-nosed body is formed by a truncated cone with nine degree half-angle and a 0.0381 m hemisphere-cylinder nose. The flow conditions for these computations are free stream Mach number of 3.0, stagnation temperature of 310.8 K, and unit Reynolds number of 7.87×10^6/m. The numerical grid, shown in Fig. 1, is formed by 121x81 grid points in the stream-wise, and radial directions respectively, with clustering in the regions of large flow gradients and close to the body surfaces. The computed results are compared with experimental data (Calarese and Hankey, 1983) in the form of power spectral densities of pressure time history sampled at the body's frustrum. In Figs. 2 and 3 the computed pressure and Mach contours for four instants in time are presented to illustrate the oscillatory behavior of the flow. At the first instant, time t_1, a strong bow conical shock convects downstream towards the body's shoulder. As this shock structure convects downstream it intersects a quasi normal shock near the body's shoulder , instant t_2. It then eventually interacts with the body's

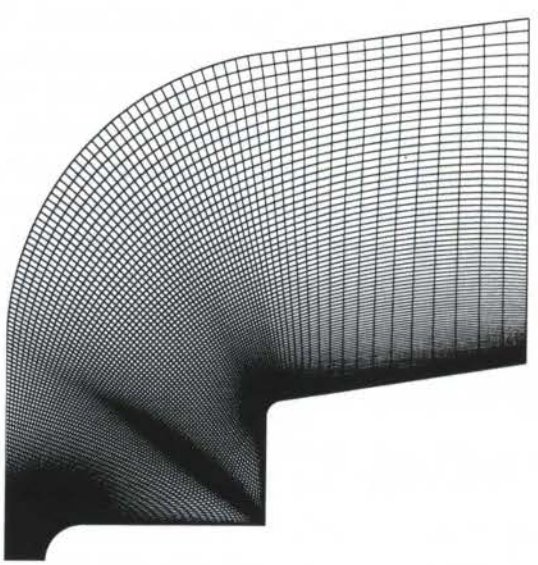

Figure 1. Numerical grid, 121x81 grid points.

shoulder and causes a pressure wave to be reflected upstream. This reflected pressure wave causes the shock structure to move upstream, instant t_3, and with its movement a pressure relieving effect originates in the shoulder region, instant t_4. The reduction in pressure in the region between the body and the shock structure induces the downstream movement of the

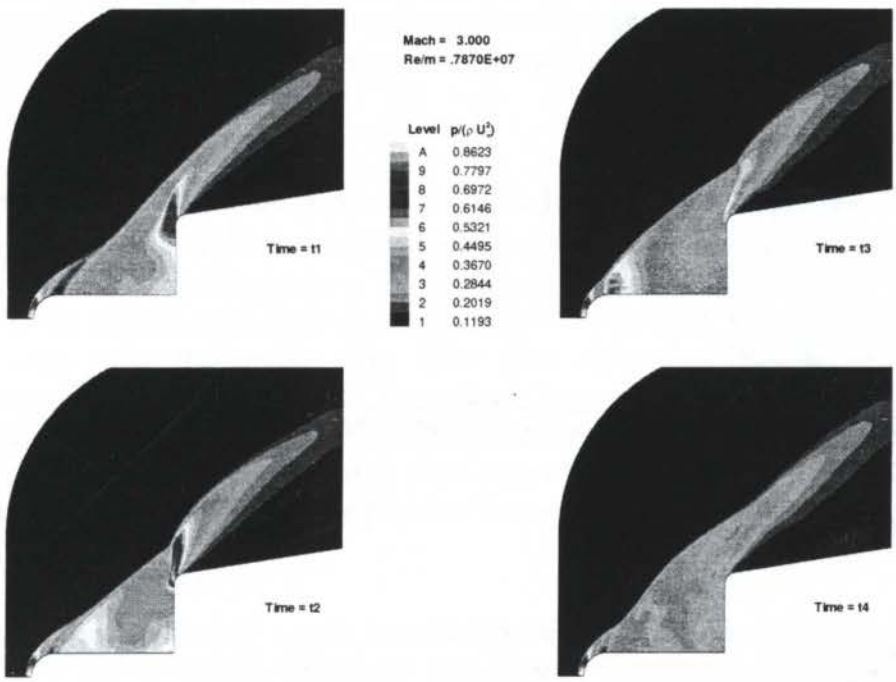

Figure 2. Instantaneous pressure contours for Spike-Nosed body solution.

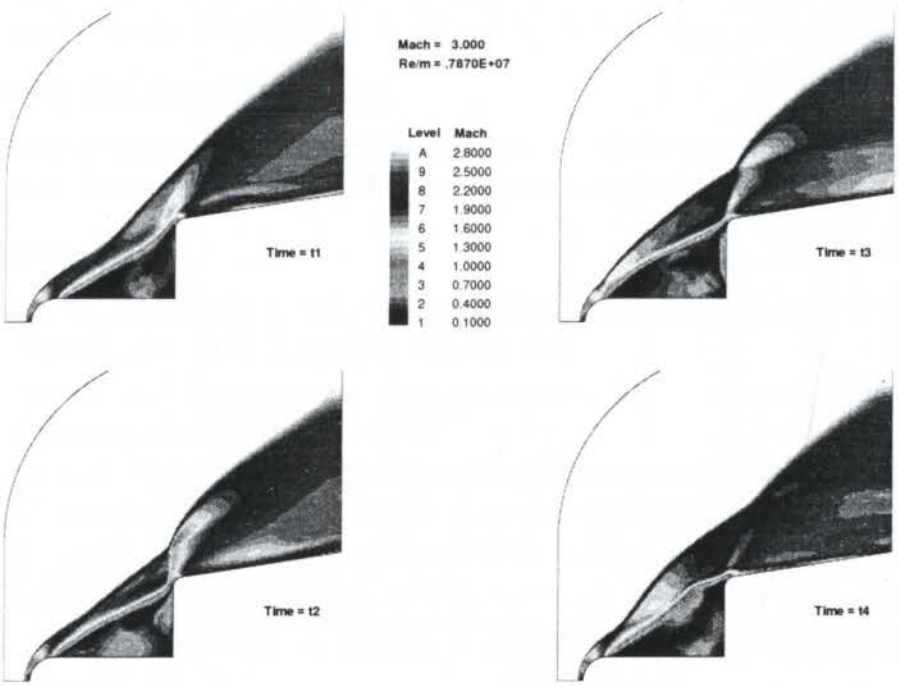

Figure 3. Instantaneous Mach contours for Spike-Nosed body solution

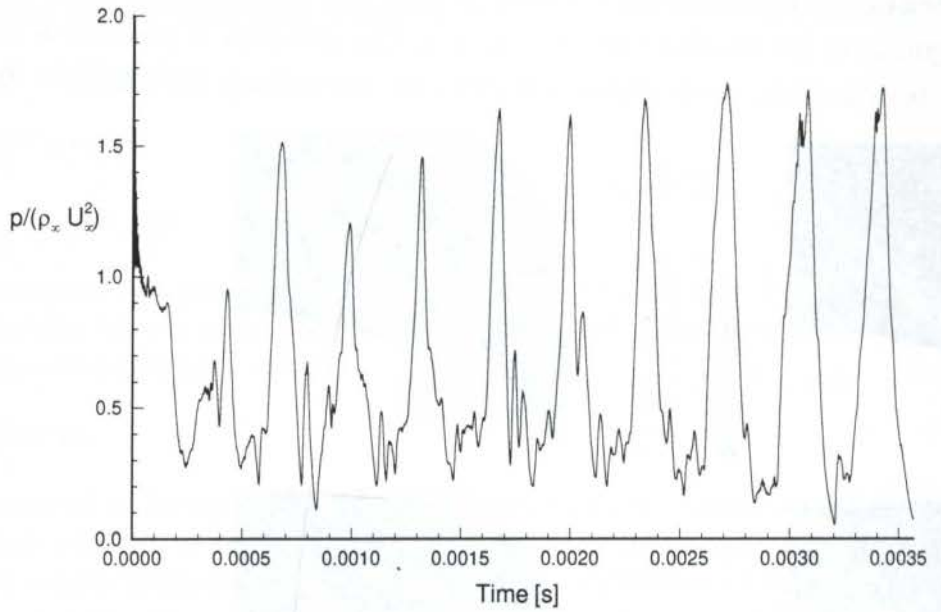

Figure 4. Pressure time history.

shock structure, and the cycle is repeated in a periodic fashion.

Figure 4. displays the pressure time history sampled at the body's frustrum close to its shoulder. It can be observed that the periodic variation emerges roughly after about 0.0022 seconds time lapse. The oscillatory behavior persisted thereafter and maintained its amplitude

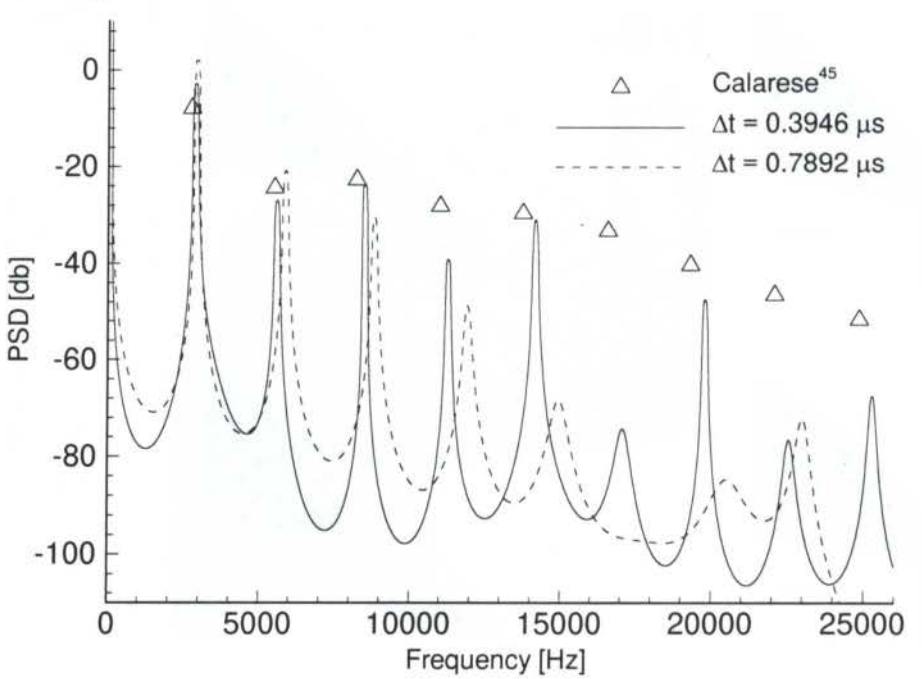

Figure 5. Spike-nosed body spectral power estimate.

and wave form without a dramatic damping or decaying being recognized. after the transients of the solution initialization are surpassed

Computed spectral power estimates of pressure time history, obtained by applying the MEM, are compared with experimental data for two time intervals, Δt = 0.3946 and 0.7892 μ sec in Fig. 5. The results of computations with the small time step predict the first nine frequency modes in very good agreement with the experimental data. The amplitudes of the first five modes, where the power spectral density is defined as:

$$PSD = 20 \log_{10}\left(\frac{power}{p0}\right) \tag{5}$$

where p_0 is the stagnation pressure behind a normal shock, are in good agreement with the experimental data. The computed amplitudes for the sixth, eighth, and ninth, modes do not show the same good agreement. Nevertheless, the experimental trend where the even-odd amplitudes exhibit different levels of decay is well captured. The computations with the larger time step, twice the smaller one, show good agreement only for the first three modes. However, as the frequency level increases it loses accuracy or does not resolve the modes. This illustrates that although the code is robust enough to solve the problem with a large time step, the physics of the problem is what dictates the size of the time step, and care must be taken in the determination of the physical time step.

4. CONCLUSIONS

The flow field over a spike-nosed body was numerically simulated by solving the time dependent Navier-Stokes equations. The implicit algorithm employed resulted very robust, allowing the time step to advance the solution be dictated by the physics of the problem. Self-sustained oscillations were observed in the numerical simulation reproducing the oscillatory motion observed in the experiments. The numerical solution predicted accurately the frequency of oscillations and amplitudes of the fundamental modes of oscillation. The present work demonstrated the ability of the present numerical algorithm to study unsteady flows.

5. ACKNOWLEDGMENTS

The Centro Nacional de Supercomputação - UFRGS provided time on the Cray Y-MP computer. The author gratefully acknowledge this support.

6. REFERENCES

Calarese, W., and Hankey, W.L. Modes of Shock-Wave Oscillations on Spike Tipped Bodies, *AIAA Journal*, vol. 32, n. 2, pp.185-192, Feb. 1985.

Matsuno, K., A Time-Accurate Iterative Scheme For Solving the Unsteady Compressible Flow Equations, *AIAA Paper 89*-1992CP, 1989.

Mikhail, A.G. Spike-Nosed Projectiles: Computations and Dual Flow Modes in Supersonic Flight, *Journal of Spacecraft*, vol 28, n. 4, pp. 418-424, July-Aug. 1991.

Mikhail, A.G. Spike-Nosed Projectiles With Vortex Rings: Steady and Nonsteady Flow Simulations, *Journal of Spacecraft and Rockets*, vol. 33, n. 1, pp. 8-14, Jan.-Feb. 1996.

Shang, J.S., Hankey, W.L., and Smith, R.E. Flow Oscillations of Spike-Tipped Bodies, *AIAA Paper 80-0062*, Jan. 1980.

Yoon, S. and Kwak, D., Implicit Navier-Stokes Solver For Three-Dimensional Compressible Flow, *AIAA* Journal, vol. 30, pp. 2653-2659, November 1992.

XIV Brazilian Congress of Mechanical Engineering
Obeid Plaza Hotel Convention Center - Bauru - SP/Brazil
December 08-12th 1997

PAPER CODE: COB545

DIRECTED-ENERGY AIR SPIKE INLET AT MACH 10 WITH 15-25 kW ARC POWER

P.G.P. Toro, H.T. Nagamatsu, L.N. Myrabo
Department of Mechanical Engineering, Aeronautical Engineering and Mechanics
Rensselaer Polytechnic Institute, Troy, NY 12180-3590 - USA
torop@rpi.edu, nagamh@rpi.edu, myrabl@rpi.edu

Abstract

The use of thermal energy as a means of enhancing flight performance of blunt bodies at hypersonic speeds is investigated. The "Directed-Energy Air Spike" (DEAS) inlet concept proposes the beamed transmission of concentrated energy forward of a moving vehicle in order to change the bow shock configuration from a detached normal (strong) shock wave to an oblique, parabolic-shaped (weak) shock wave. This new approach provides low aerodynamic drag and heating, or also deflects the oncoming air into an annular hypersonic inlet. The compressed inlet air can either be accelerated to produce thrust or decelerated to extract onboard electric power. A 6-in. diameter blunt body model was fabricated and pressure transducers are installed at its surface and equipped with 6-in. long slender plasma torch at the stagnation point. This model has been installed in the RPI 24-in. diameter Hypersonic Shock Tunnel and used to test the Directed-Energy Air Spike concept. Pitot pressures have been measured at the maximum diameter annular region of the blunt body. Surface pressure and pitot rake pressure surveys as well as the Schlieren photographs will be presented for Mach number 10 with 15-25 kW power at the tip of the spike

Keywords

Directed-Energy Air Spike (DEAS), Hypersonic Flows, Hypersonic vehicle

1. INTRODUCTION

In an attempt to travel at ever increasing velocities in an efficient manner, Myrabo and Raizer (1994) have recently proposed the "Directed-Energy Air Spike" (DEAS). The DEAS inlet concept enables active control of external aerothermodynamics for an advanced hypersonic transatmospheric vehicle by replacing directed energy for mass, conventionally in the form of a sharp nosed structure.

One major advantage of the directed-energy air spike over a solid mass spike is that it has no weight. In addition, the propulsion system design of a transatmospheric vehicle using the DEAS inlet presents two more advantages: 1) employs a detached parabolic bow shock wave to contain a rarefied, "hot air pocket" that substantially reduces the flow Mach number impacting the vehicle forebody; and 2) directs the incident hypersonic air flow toward the periphery of the craft where the annular inlet of the magnetohydrodynamic (MHD) slipstream accelerator is located.

The directed-energy air spike in front of a craft may be created by a shock wave propagating from a weak laser-supported detonation (LSD) wave. The pressure at the LSD wave front, being higher than atmospheric pressure, deflects the incident air flow from the axial direction and forces it to flow over the spike to the periphery of the craft (Figure 1).

The feasibility of transatmospheric flight is limited by phenomena such as aerodynamic drag and heating, as well as related thermal management problems. Traditional blunt nosed hypersonic vehicles generate a strong detached, normal shock wave in the nose region, which produces a high aerodynamic drag and low aerodynamic heating. On the other hand, a traditional slender body with a sharp leading edge produces a conical, weak attached shock wave (with low drag), but significant heating is created at the tip of this forebody .

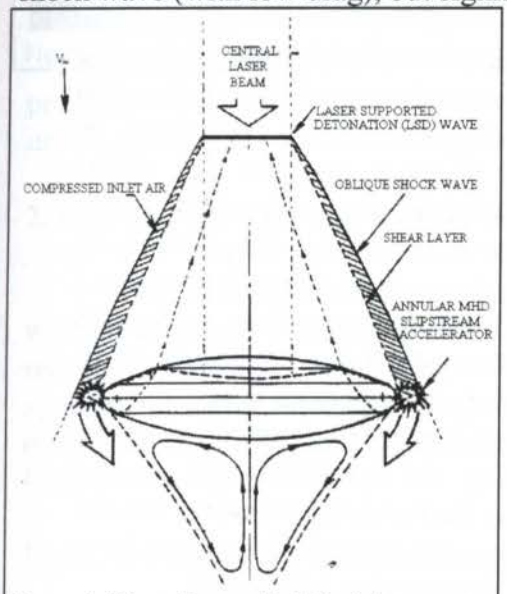

Figure 1. Direct-Energy Air Spike inlet concept.

To resolve these difficulties, an efficient transatmospheric hypersonic vehicle design has to combine a low drag coefficient (to maximize the net propulsive thrust) with low heat transfer rates (to minimize thermal protection system mass).

One lightweight alternative to carrying structural mass to induce oblique shocks that reduce aerodynamic drag and heating, was proposed by several authors in the late 50's and early 60's: i.e., slender protruding spikes (Bogdonoff and Vas, 1959 and Crawford, 1959).

The new approach of the "directed-energy air spike" inlet (Myrabo and Raizer, 1994) proposes the use of beamed eletromagnetic power to accomplish the same functions. The DEAS concept eliminates the need to carry the structural mass associated with a physical solid spike while at the same time enjoying the advantages of having one. The directed-energy air spike inlet creates a detached oblique (parabolic-shaped) shock wave that provides three basic functions: a) decrease in the aerodynamic drag; b) decrease in heat transfer rates, and; c) deflection of the oncoming air into an annular hypersonic inlet. This inlet air can either be subsequently accelerated by an MHD slipstream accelerator to produce thrust, or decelerated to extract onboard electric power.

The vehicle geometry in Figure 1, consists of a 'double Apollo disc', wherein the upper and lower contours are identical and are scaled directly from the Apollo command module's lower heat shield. A physical spike is used in the present investigation to inject the power necessary for running the "directed-energy air spike". This simplifies the experimental apparatus. A 6-in. diameter model of the vehicle was constructed, equipped with a 6-in. long slender plasma torch to heat the incident Mach number flow in the RPI 24-in. diameter hypersonic shock tunnel (Minucci and Nagamastu, 1993).

Without the plasma torch, the model is a simple blunt body in hypersonic flow. Note that the experimental model apparatus used herein to investigate the DEAS concept, is simply a spiked blunt body in hypersonic flow, when plasma torch is not supplied with either electric power as cooling gas. Bogdonoff and Vas (1959) experimentally studied the such flowfields around flat-faced and hemispherical-nosed axisymmetric bodies at a Mach number of about 14 in helium flow. They found that forebody pressure levels decreased by an order of magnitude and the heat transfer fell to a fraction of what it was without the spike.

Crawford (1959) has confirmed the above observations. He also concluded that the physical spike reduces the drag-to-heat transfer ratio, thus compromising the use of such an artifact for reentry flight where a high drag-to-heat ratio is necessary.

Computational investigations have simulated flow phenomena over spiked hemispheres at Mach 7 and Mach 6.8 by the use of a TVD scheme (Kubota et al., 1994, and Fujita and Kubota, 1992). The pressure results agree very well with the experimental data. Recently, Yamauchi et al. (1995) numerically simulated the supersonic flow over a spiked blunt body and found that the drag was reduced when compared to the blunt body with no spike. These researchers characterize the flowfield by a conical shock wave from the tip of the spike, a separated region in front of the blunt body, and the resulting reattachment shock wave, as shown in the Figure 2.

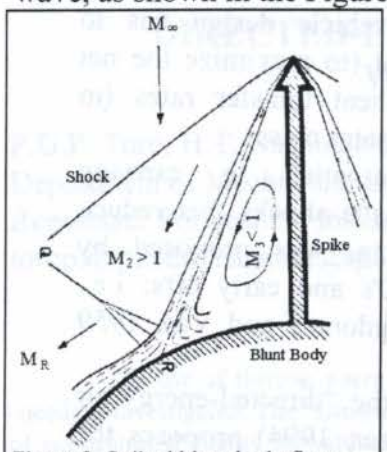

Figure 2. Spiked blunt body flow.

The present model of the plasma torch with gas flowing inside the spike but no power at the tip of the spike, will produce a flowfield which is formed by exhausting an underexpanded sonic jet in a direction opposite that of the hypersonic mainstream. This flowfield, was studied by Moraes (1985).. The pressure distribution indicates that the jet works as an *aerodynamic* spike (in analogy to a *solid* spike). It produces a reduction of the static pressure on the body front surface by inducing a flow separation, and so reduces the drag of the body, due to reduced dynamic pressure in the separated flow.

When the plasma torch on the DEAS model is operating, the arc at its tip is simulating the breakdown of air and subsequent blast wave caused by the focused microwave or laser energy. By comparing the two flowfields (i.e., resulting from the unpowered spiked blunt body, and the powered blunt body), the effect of the heat addition may be determined.

A theoretical approach to optimizing DEAS/vehicle integration is reported by Myrabo et al. (1994). The analysis determined the flow conditions inside the directed-energy air spike and enabled a heat transfer analysis to be performed.

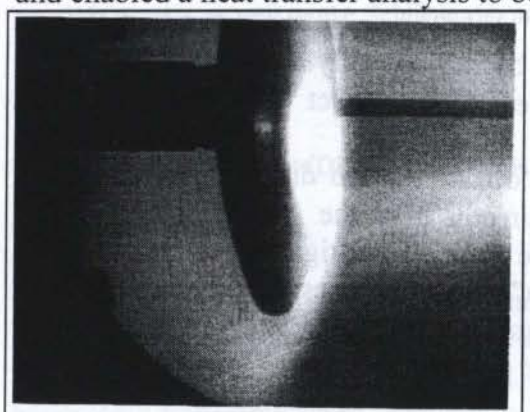
Figure 3. Schlieren photo with powered torch.

An experiment (Marsh et al. 1996) was conducted in the RPI 24-in diameter hypersonic shock tunnel with an axisymmetric 6-in. diameter blunt-bodied model, equipped with a 6-in. long electrically-heated plasma torch to verify the theoretical directed-energy air spike concept (Myrabo and Raizer, 1994), at Mach 10 flow with a stagnation temperature of 800 K. The Schlieren photo in Figure 3 proves that the bow shock wave is substantially deflected from a conical into a parabolic shape, when heat is added.

Next, the 6-in. diameter blunt body model was equipped with pressure transducers and re-installed in the hypersonic shock tunnel, Figure 4. The flow field and the pressure distributions over the model were determined for Mach number 10 flow and a stagnation temperature of about 1000 K, with and without the arc discharge. Schlieren photographs revealed the shock wave and separated shear layer, as created by the Air Spike (Diaz et al. 1996). Toro et al. (1997) extended the previous work to higher Mach numbers (Mach numbers of 10-20).

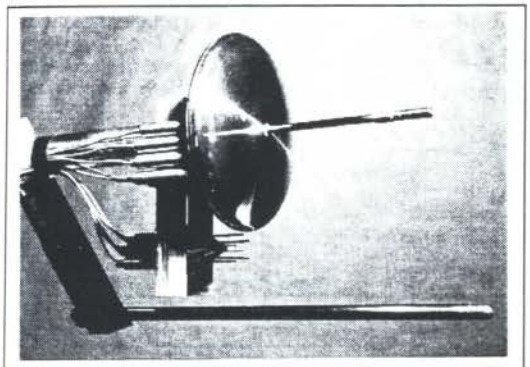

Figure 4. Photo of the model with the plasma torch.

The surface and the pitot pressure experimental data for Mach number flow 10 are presented using 15 kW and 25 kW at the tip of the spike. The purpose of this experimental investigation is to show the change of oblique weak shock to parabolic shape weaker shock.

2. EXPERIMENTAL APPARATUS

The test apparatus was designed to simulate the effects of a directed-energy air spike with an electrically-heated plasma torch, and to enable the measurement of pressure drag reductions across a blunt Lightcraft forebody at hypersonic speeds. This pressure data was simultaneously obtained in two regions: across the Lightcraft forebody surface, and within the outer annular slipstream region (which comprises the external compression air inlet for the Lightcraft's engine).

Lightcraft Model and Electrically-heated plasma

The same Lightcraft model used in the earlier works (Marsh et al. 1996, Diaz et al. 1996 and Toro et al. 1997) was employed for this investigation. Piezoelectric pressure transducers were installed into the above mentioned regions, in order to quantify the aerothermodynamic effects of the Air Spike phenomena.

The first region comprises the Lightcraft forebody (i.e., stagnation surface) where static and stagnation pressure data were first measured for the torchless Lightcraft model. Next static pressure data was obtained for the Lightcraft model fitted with the plasma torch (Figure 5).

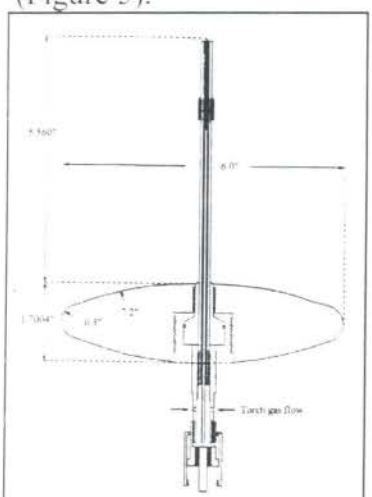

Fig. 5. Model with torch installed.

When the model was tested as a blunt body with no spike, eight piezoelectric pressure gauges were used to measure the static pressure along the frontal surface. The pressure gauge at the central stagnation point was installed only when the model was not fitted with the torch. Therefore, when the Lightcraft model was tested under the Air Spike configuration, seven pressure gauges were used. Additional pitot pressures are taken within the annular air inlet region of the Lightcraft. As mentioned above this slipstream annulus region is located just outside the Lightcraft model's perimeter.

The stagnation point of the Lightcraft model was fitted with an electrically-heated plasma torch measuring 6-in. long and 0.25-in. external diameter. The torch is fitted with an axial tungsten cathode and a cylindrical copper anode; both are insulated by a short annulus made of Macor (Figure 5). The plasma torch is designed for a choked airflow existing at the tip, in order to prevent 'arc blow-back' during the hypersonic test.

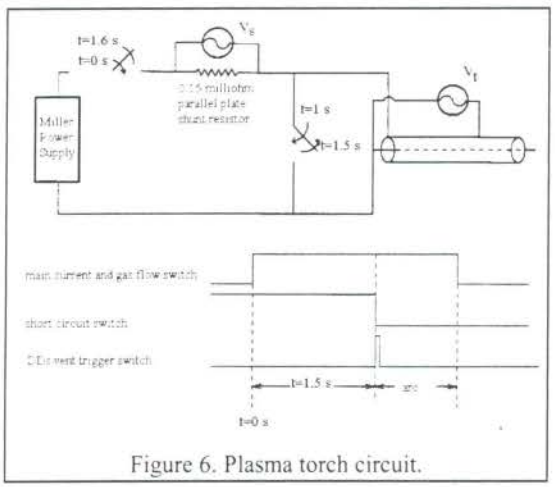

Figure 6. Plasma torch circuit.

The high current discharge across the torch anode/cathode gap is generated by a Miller model SRH-333 portable, direct-current welding unit. This unit uses magnetic relays and rheostats that yield noticeable start-up transient behavior, at time scales long compared with the hypersonic flow run time. Therefore, it was necessary to momentarily short-circuit the current before energizing the plasma torch. Figure 6 shows the plasma torch circuit, a brief description of it can be found in the previous proof-of-concept work (Marsh et al. 1996).

RPI 24-in. Hypersonic Shock Tunnel

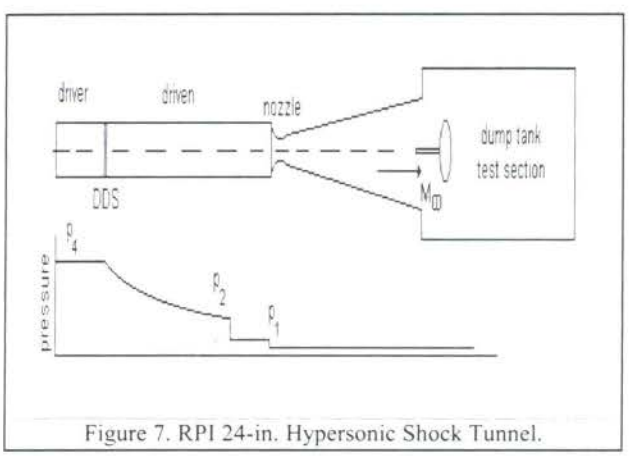

Figure 7. RPI 24-in. Hypersonic Shock Tunnel.

The RPI 24-in. diameter Hypersonic Shock Tunnel, Figure 7, was used to obtain the Mach number 10 flow for the present experiment. It was designed, built and used at the General Electric Research and Development Center and was subsequently donated to RPI. Minucci (1993) describes in detail the five components of this facility: the driver tube section, the DDS (Double Diaphragm Section), the driven tube section, the nozzle, and the dump tank. The facility is capable of generating reservoir enthalpies up to 6.5 MJ/kg when operating in the equilibrium interface mode with helium in the driver section. The driver tube contain the high pressure expanding gas, p_4. Air or Helium was used for the present experiment.

The driver and driven tubes are separated by a double diaphragm section (DDS). This section houses one diaphragm at either end. The DDS section controls the rupture of the diaphragms that initiate the shock wave. Stainless steel diaphragms are used to separate the driver and driven gases.

For the present investigation, the driven tube was pressurized to about 14.6 psia (p_2) for low Mach number 10. In addition, this section contains the ports for the instrumentation used to analyze the flow, as well as a clamping section that holds a third diaphragm which separates the driven tube from the nozzle and dump tank section. This diaphragm allows the dump tank to have a pressure several orders of magnitude lower than the pressure in the driven tube (p_1), facilitating flow establishment in the hypersonic nozzle. Aluminum diaphragms were used in the clamping section.

A 15-degree half angle conical nozzle is attached at the end of the driven tube and protrudes inside the dump tank. By using different nozzle throats located in the clamping section, the nozzle area ratio can be varied, to produce nominal Mach numbers from 8 to 25.

The 5-ft. diameter, 200-cubic foot dump tank serves as a large vacuum tank which houses the test section with the model. Two windows in the test section allow flow field visualization via a single pass, spark gap light source Schlieren system located adjacent to the exterior of the dump tank.

Several shock tube conditions are monitored in order to determine free stream conditions of the nominal flow Mach number. This data is subsequently transmitted to two RPI-developed flow programs: one to determine reservoir conditions in the reflected region of the driven tube; a second program to use these reflected conditions, and the measured free stream pitot pressure, in order to determine free stream flow parameters. These programs were developed for the RPI Hypersonic Shock Tunnel by Minucci (1991).

The shock tube parameters that are measured are: 1) the elapsed response time between two heat gauges; 2) reservoir pressure P5 located at the position of the nozzle entrance at the end of the driven tube; 3) reservoir/reflected pressure transducer P2P5 located upstream from the aluminum diaphragm; and 4) the free stream pitot probe in the test section located at the same planar position as the stagnation point of the Lightcraft plasma torch.

Shock tube and free stream data as well as Lightcraft and pitot rake pressure data is collected with an 18 channel Tektronix Testlab 2520 Data Acquisition System. Data to determine the arc power is collected with a separate Nicolet digital oscilloscope, in order to avoid electromagnetic interference between the high noise arc welding supply current and the pressure transducer signals.

3. Results

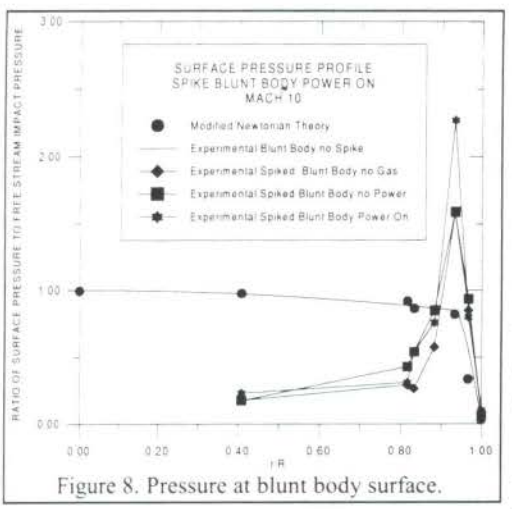

Figure 8. Pressure at blunt body surface.

The present experiment was conducted at free stream Mach number 10 for the following configurations: a) blunt body with no spike; b) spiked blunt body with no gas (inside de spike), c) spiked blunt body with cooling gas flowing in a direction opposite that of the hypersonic flow, and d) spiked blunt body with cooling gas and heat at the tip by arc. In 'b' and 'c' cases no power is supplied at the plasma torch. The arc power ranged from 15 to 25 kW, with mass flow rates of air through the torch tip between 0.15 and 0.20 g/s for Mach number 10 flow.

1) When the bare 6-in. diameter model (i.e., with no spike) is tested in the 24-in. diameter hypersonic shock tunnel, the experimental results were found to agree very well with the analytical results from modified Newtonian theory. Also, the Schlieren photo for Mach number 10 flow shows that the shock is symmetrical, and the stand-off distance of 0.8 cm agrees with theoretical calculation, (Figure 9);

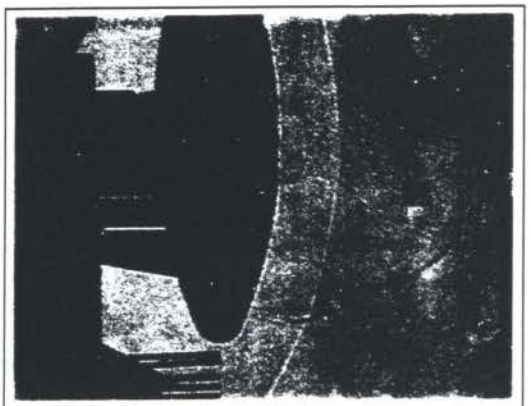

Figure 9. Blunt body Schlieren photograph.

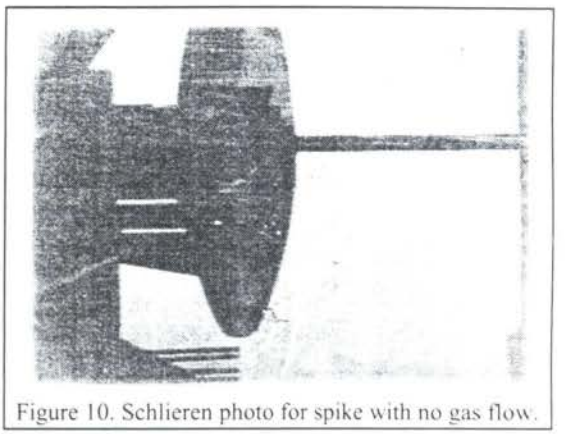

Figure 10. Schlieren photo for spike with no gas flow.

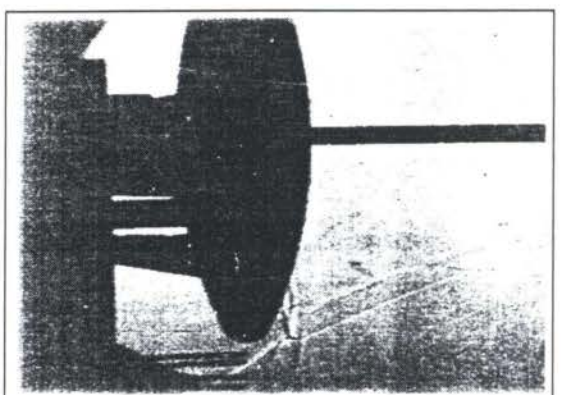

Figure 11. Schlieren photo for spike with gas flow.

2) When the model is fitted with the powerless torch, the flow field is very similar to the well known spiked blunt-body experiments in which a conical shock structure is attached to the tip of the torch. The Schlieren photo in Figure 10, reveals the location of the reattachment point, and the oblique shape of the shock wave;

3) When mass (cooling gas flowing in a direction opposite that of the hypersonic flow) is injected through the powerless torch at Mach number 10 flow, note from the Schlieren photo in Figure 11 that the shear layer becomes turbulent, but the position of the bow shock wave is not substantially changed.

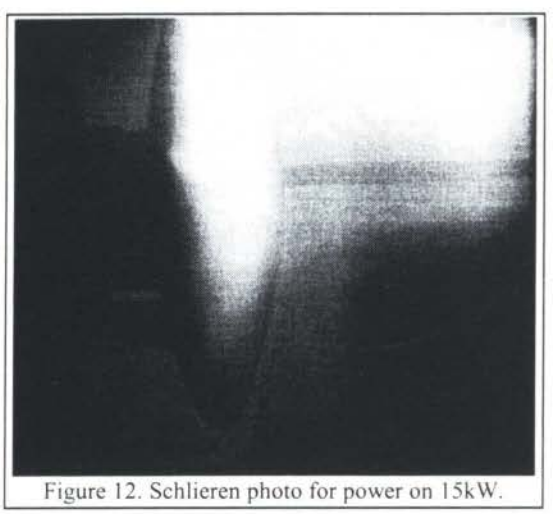

Figure 12. Schlieren photo for power on 15kW.

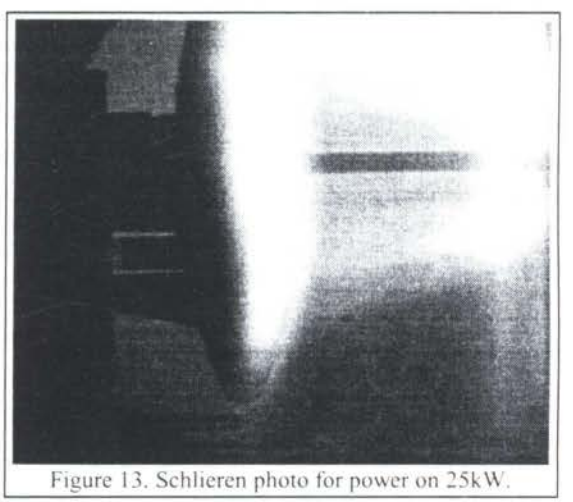

Figure 13. Schlieren photo for power on 25kW.

4) Adding heat, 15 kW power, at the torch tip deflects the incident shock wave away from the periphery of the lightcraft but it remains turbulent as the spiked blunt body with gas flow, Figure 11. Increasing the heat to 25 kW deflects the incident shock wave away from the rim of the blunt body more but the flow becomes more stable than 15 kW. When arc power is limited to between 15 kW and 25 kW (Figure 12 and 13 respectively), with mass flow rates of air through the torch tip between 0.15 to 0.20 g/s the shock wave remains oblique. This increases the static pressure, Figure 8, at the same lightcraft surface position (r/R=0.93) where the surface pressure is maximum for the unpowered torch configurations, and finally.

5) When 34 kW is added (Marsh et al. 1996) to the flow by powering-up the torch, the attached shock wave becomes parabolic in shape and the flow becomes completely stable

Minucci, M.A.S., and Nagamatsu, H.T., "Hypersonic Shock Tunnel Testing at an Equilibrium Interface condition of 4100K," Journal of Thermophysics and Heat Transfer, vol. 7, 1993, pp. 251-260.

Moraes Jr., P. and Ganzer, U., "The Flowfield of a Sonic Jet Exhausting against a Supersonic Flow," VIII COBEM, pp. 113- 115, Brazil, Dec. 1985.

Myrabo, L. and Raizer, Yu. P., "Laser Induced Air Spike for Advanced Transatmospheric Vehicles," AIAA-94-2451, June, 1994.

Myrabo, L., Seo, J., Head, D., March, J. and Cassenti, B., "Thermal Management System for an Ultralight Microwave Propelled Transatmospheric Vehicle," AIAA 94-2924, Jun. 1994.

Toro, P.G.P.; Myrabo, L.N. and Nagamatsu, H.T., "Experimental Investigation of Hypersonic Directed-Energy Air Spike Inlet at Mach 10-20," AIAA 97-0795, Jan. 97.

Yamauchi, M., Fujii, K., and Higashino, F., "Numerical Investigation of Supersonic Flows Around a Spiked Blunt Body," J. of Spacecraft and Rockets, vol. 32, no. 1, Jan./Feb. 1955.

Tema 33

Escoamentos em Meios Porosos

XIV Brazilian Congress of Mechanical Engineering
Obeid Plaza Hotel Convention Center - Bauru - SP/Brazil
December 08-12th 1997

PAPER CODE: COB1093

RECONSTRUCTION OF 3-D PORE STRUCTURE BY THE TRUNCATED GAUSSIAN METHOD USING FOURIER TRANSFORM

LIANG ZHIRONG, CELSO PERES FERNANDES, FÁBIO SANTANA MAGNANI & PAULO CESAR PHILIPPI
Laboratório de Meios Porosos e Propriedades Termofisicas de Materiais
Departamento de Engenharia Mecânica, Universidade Federal de Santa Catarina
88040 - 900 Florianópolis, SC, Brasil - E-mail: liang@lmpt.ufsc.br

Abstract

The purpose of reconstructed porous medium is to simulate invasion processes of fluids and determine important petrophysical and reservoir engineering properties such as permeability, capillary pressure and relative permeability curves. In this paper, we improve the truncated Gaussian method for reconstruction of porous media using Fourier transform. The method is based on the idea that an arbitrary complex pore structure can be described by the values of a phase function at each point in the porous media. If the pore structure is statistically homogeneous, it can be described by the porosity and correlation function, which are measured from 2-D binarized image of thin section of the sample. If correlation function of Gauss field is positive-definite, corresponding Gauss field can be found. Since Fourier transform of correlation function is power spectrum of the field and the phase angle does not affect the correlation structures, then the Gauss field can be generated by using Fourier transform. An algorithm, which is a nice split-radix, n-dimensional and fast-Fourier transform is used. At last, the 3-D porous media are generated using the truncated Gaussian method. The result for Fontainebleau sandstone shows that the porosity and correlation functions reproduce well.

Keywords

Porous media; reconstruction; 3-D pore structure; image analysis; Fourier transform

1. INTRODUCTION

The general objective of reconstructed porous media is to mimic more closely the geometry of real media. This reconstruction process is attractive for a number of reasons. The most important is the versatility of the process since it allows the combination of many different structures. The other advantage is that the method enables us to create numerical samples with the desired properties. This method has been applied to previously the prediction of important petrophysical and reservoir engineering properties, such as permeability (Adler *et al.*, 1990) and formation factor (Ioannidis *et al.*, 1995) with reasonable success. The information on the porous medium is obtained from the optical analysis of the structure. This method has been applied mostly to geological macroporous media (sandstones) with a characteristic length scale ranging from 0.1 to 10 mm, but can also be applied to macroporosity of packed columns, and in principle to microporous materials. Joshi (1974), Quiblier (1984), Adler *et al.* (1990) and Fernandes (1994) have extensively studied this operation. A random and discrete binary field $Z(\mathbf{x})$ can be devised from a independent Gaussian field $X(\mathbf{x})$, which passed through a linear filter to yield a field $Y(\mathbf{x})$ from $X(\mathbf{x})$ and then a nonlinear filter to generate $Z(\mathbf{x})$. By assuming homogeneity and isotropy, 3-D pore

structure can thus be constructed from 2-D porous sections, conserving the first and second moments, i.e., porosity and correlation function. Another way to carry out linear filter is to generate $Y(\mathbf{x})$ from $X(\mathbf{x})$ using Fourier transform (Adler, 1992). From a computational point of view, the use of the fast Fourier transform algorithm, instead of laborious solution of nonlinear equation, makes the Fourier transform superior to linear filter method. Application of the Fourier transform method in 3-D is, however, restricted by resident memory requirements. Ioannidis et al. (1995) combined the two methods to generate porous media of the larger sizes. Yao *et al.* (1993) compared the moments of order larger than two of the phase function for real and reconstructed porous media. For a particular 3-D sample it is shown that the so-called reconstructed medium lies very close to the real material as regards its spatial porosity distribution up to and including four-point correlation functions of phase function representing the distribution.

To overcome above problems, existence theorem (Papoulis, 1965) provides an alternative of generating normal field. The truncated Gaussian method by using Fourier transform is proposed in this paper. The difference between this method and the previous one is that we directly generate the $Y(\mathbf{x})$ from its correlation function $R_Y(\mathbf{u})$. This method does not need the linear filter and so avoids solving the nonlinear equations. Using the fast Fourier transform makes this algorithm more efficient. On the other side, the independent Gaussian field $X(\mathbf{x})$ is not needed. It reduces the resident memory requirements of computer. Therefore, both operating time and computer memory requirements are improved. This is the advantage of the truncated Gaussian method by using Fourier transform. When the reconstructed porous medium is generated, the transport process such as invasion process of fluids can be simulated and macroscopic properties such as permeability, capillary pressure and relative permeability curves can be determined (Adler, 1992; Fernandes, 1994; Magnani, 1996; Liang, 1997).

2. THE TRUNCATED GAUSSIAN METHOD BY USING FOURIER TRANSFORM

2.1. Basic Concepts

According to the existence theorem of the stochastic process (Papoulis, 1965), given a positive-definite function R(u), i.e., its Fourier transform is positive, we can find a stochastic process having R(u) as its correlation function. This theorem is usually established by constructing a normal process with R(u). In order to generate 3-D discrete pore structure, we need some definitions. The pore space of a porous media can be characterized by the phase function $Z(\mathbf{x})$ as follows:

$$Z(\mathbf{x}) = \begin{cases} 1 \text{ when } \mathbf{x} \text{ belongs to the pore space} \\ 0 \text{ otherwise} \end{cases} \tag{1}$$

The porosity ε, the correlation function $C(\mathbf{u})$ and the normalized correlation function $R_Z(\mathbf{u})$ can be defined by the statistical average (which will be denoted by an overbar):

$$\varepsilon = \overline{Z(\mathbf{x})}, \tag{2}$$

$$C(\mathbf{u}) = \overline{Z(\mathbf{x})\ Z(\mathbf{x}+\mathbf{u})}\ , \tag{3}$$

$$R_Z(\mathbf{u}) = \frac{\overline{[Z(\mathbf{x})-\varepsilon]\cdot[Z(\mathbf{x}+\mathbf{u})-\varepsilon]}}{(\varepsilon-\varepsilon^2)}. \tag{4}$$

The purpose of the present work is to generate a three-dimensional random porous medium with a given porosity and correlation function. Equivalently, the idea is to generate a random function $Z(\mathbf{x})$ that is equal to zero in the solid phase and to one in the pore phase. $Z(\mathbf{x})$ must verify the two average properties. Porosity is a given positive number smaller than 1. $R_Z(\mathbf{u})$ is a given function of $\mathbf{u}$ that verifies the general properties of a correlation function but is otherwise arbitrary.

The subsequent analysis is restricted to homogeneous media, where the statistical characteristics are assumed to be independent of position **x** in space. Because of homogeneity, the porosity is a constant and $R_Z(\mathbf{u})$ only depends upon the vector **u**; that is, each is independent of position **x**. Moreover, when the porous medium is isotropic, R_Z is a function only of $u=|\mathbf{u}|$, and not of the direction of **u**; i.e., $R_Z(\mathbf{u})= R_Z(u)$.

Several methods exist to generate discrete random variables that verify Eq. (2) - (4). Here truncated Gaussian method by using Fourier transform is proposed and discussed in the next sections.

2.2. Generation of Gaussian field

Adler *et al.* (1990) and Fernandes (1994) generated the isotropic media by a simplified version of an algorithm presented by Quiblier (1984) for general 3-D porous media. This algorithm was itself an extension of a 2-D scheme devised by Joshi (1974). A random and discrete field $Z(\mathbf{x})$ can be devised from a independent Gaussian fields $X(\mathbf{x})$ when the latter is successively passed through a linear and nonlinear filter. The random variables $X(\mathbf{x})$ are assumed to be normally distributed with a mean equal to zero and a variance equal to one. The variables are independent. A linear operator can be defined by an array of coefficients $a(\mathbf{u})$, where **u** belongs to a finite cube $[0, Lc]^3$ in Z^3. Outside this cube, $a(\mathbf{u})$ is equal to zero. A new random field $Y(\mathbf{x})$ can be expressed as a linear combination of the random variable $X(\mathbf{x})$:

$$Y(\mathbf{x}) = \sum_{\mathbf{u}\in[0,Lc]^3} a(\mathbf{u})\ X(\mathbf{x}_t), \tag{5}$$

where the translated vector $\mathbf{x}_t$ is defined modulo N for each of its component and N is the side size of reconstructed porous medium. The correlation function $R_Y(u)$ of $Y(\mathbf{x})$ is seen to be

$$R_Y(u) = \sum_{r,s,t\in[0,Lc]} a_{r,s,t}\ a_{u+r,s,t}, \tag{6}$$

where u+r is determined mod N. The difficult of above linear filter is to get $a(\mathbf{u})$ by solving the Eq. (6), that is a nonlinear equation system. For Lc larger than 32, it was long, difficult and sometimes impossible (Adler, 1992). Adler (1992) proposed a version using Fourier transform. From a computational point of view, the use of the fast Fourier transform algorithm, instead of laborious solution of nonlinear equation, makes the Fourier transform superior to the above method. Application of Fourier transform to the Eq. (5) is, however, restricted by resident memory requirements because there are three variables and Fourier transform of each variable needs complex variable. To overcome above problems, existence theorem provides an alternative of generating normal field. For a normal field, the correlation function is equal to the normalized correlation function. So we will not distinguish them in this paper. Given a positive-definite function $R_Y(u)$, we can find a stochastic process $Y(\mathbf{x})$ having $R_Y(u)$ as its correlation function. By definition of Fourier transform (Gonzalez and Wood, 1992) and the Wiener-Khinchin theorem, the Fourier transform of the correlation function of a field also is its power spectrum, which is the square of Fourier transform of the field. Therefore, if the correlation function of an arbitrary field is known, one can use Fourier transform to generate this field $Y(\mathbf{x})$ with the same correlation function (Pardo-Igúzquiza and Chica-Olmo, 1993). These relations can be shown in Figure 1.

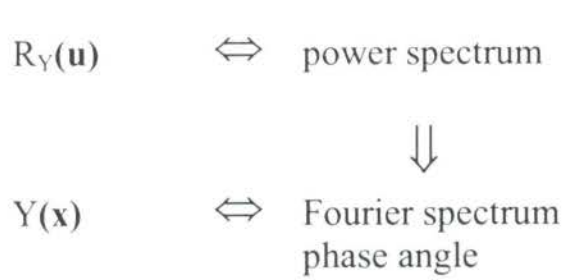

Figure 1: Basic relations among stochastic process, correlation function, power spectrum and Fourier spectrum.

In this way, we first generate the Gauss field $Y(\mathbf{x})$ directly from its correlation function, then use the truncated method to generate $Z(\mathbf{x})$, which is the same with nonlinear filter.

To generate $Y(\mathbf{x})$, the Fourier spectrum cannot be random but it can be related to the spectral density which depends on the correlation model $R_Y(u)$ that we wish to impose on realization and can be calculated from $R_Z(u)$ of the sample. The phase angle does not affect the correlation structures, then it can be taken at random from a uniform distribution between 0 and 2π. In this way we construct the complex Fourier spectrum. The Fourier transform of a real function is Hermitian function. Then, the complex coefficients F(u,v,w) must be Hermitian, this is even real part and odd imaginary part. By calculating the inverse Fourier transform of the complex coefficients, the Gauss field $Y(\mathbf{x})$ is obtained with the specified correlation model.

Since the random variable $Y(\mathbf{x})$ has a standard normal distribution (with a zero mean and a variance equal to one), its normalized correlation function is the same with its correlation function and its distribution function P(y) is given by the following:

$$P(y) = \frac{1}{\sqrt{2\pi}} \int_{-\infty}^{y} \exp(-y^2/2)\, dy, \tag{7}$$

2.3. Generation of binary field

To extract $Z(\mathbf{x})$ from $Y(\mathbf{x})$, one applies a nonlinear filter G, that is, the random variable Z is a deterministic function of Y (Adler *et al.*, 1990):

$$Z = G(Y). \tag{8}$$

When G is known, the statistical properties of the random field Z can be derived from the properties of Y.

The deterministic function G is defined by the following condition. When the random variable Y is equal to y, Z takes the value z:

$$z = \begin{cases} 1 & \text{if } P(y) \le \varepsilon \\ 0 & \text{otherwise} \end{cases}. \tag{9}$$

$R_Z(u)$ can be expressed as a series in terms of $R_Y(u)$:

$$R_Z(u) = \sum_{m=0}^{\infty} a_m^2 \, R_Y^m(u). \tag{10}$$

where the coefficients a_m are given by

$$a_m = \frac{1}{\sqrt{2\,\pi\,m!}} \int_{-\infty}^{+\infty} a(y)\, e^{-y^2/2}\, H_m(y)\, dy, \tag{11}$$

together with

$$a(y) = \frac{\varepsilon - 1}{\sqrt{\varepsilon\,(1-\varepsilon)}} \qquad \text{if } P(y) \le \varepsilon, \tag{12}$$

$$a(y) = \frac{\varepsilon}{\sqrt{\varepsilon\,(1-\varepsilon)}} \qquad \text{if } P(y) > \varepsilon. \tag{13}$$

The Hermite polynomials $H_m(y)$ is defined as follows:

$$H_m(y) = (-1)^m\, e^{y^2/2}\, \frac{d^m}{dy^m} e^{-y^2/2}. \tag{14}$$

When one wants to simulate a given porous media, the first problem is the determination of the correlation function $R_Y(u)$. When the porosity is given, the correlation function $R_Y(u)$ can be derived from $R_Z(u)$. Once $R_Y(u)$ is calculated, porous media can be simulated by directly using the Fourier transform and nonlinear filter, and their general properties can be examined critically. Arbitrary samples of porous media can be reconstructed possessing the same porosity and correlation function.

2.4. Reconstruction process of 3-D porous media

If we want to generate a $N_x \times N_y \times N_z$ cube from known porosity and correlation function, the reconstruction process of 3-D porous media by using Fourier transform method (Liang, 1997) can be concluded as follows:

(1) Measurement of porosity ε and normalized correlation function $R_Z(u)$:

The porosity ε and normalized correlation function $R_Z(u)$ is obtained from the image of thin section of the sample using Fourier transform.

(2) Calculation of $R_Y(u)$ from the measured $R_Z(u)$:

$R_Y(u)$ is determined numerically as follows (Adler *et al.*, 1990): The series in Eq. (10) is limited to a maximum value m=M. Our data were obtained with M=30 for $R_Y \leq 0.9$. For $R_Y > 0.9$, the following approximate equation is used in order to get good precision of R_Y.

$$R_Z = 1 - \beta (1 - R_Y)^{1/2}. \qquad (15)$$

where β is the coefficient which is calculated from $R_Y=0.9$. The integral in Eq. (11) is evaluated for y ranging from -10 to +10.

(3) For the 3-D case, $R_Y(i,j,k)$ is obtained from $R_Y(u)$ as follows:

For $0 \leq i \leq \frac{N_x}{2}, 0 \leq j \leq \frac{N_y}{2}, 0 \leq k \leq \frac{N_z}{2}$, $R_Y(i,j,k) = R_Y(u)$ if $\sqrt{i^2 + j^2 + k^2} = u$. Otherwise the symmetric properties of correlation function is used due to the isotropic property.

(2) Power spectrum:

By definition, the power spectrum is the Fourier transform of the correlation function. In order to get the power spectrum, an algorithm, which is a nice split-radix, n-dimensional and fast Fourier transform by Singleton (1969), is used to calculate the Fourier transform of $R_Y(i,j,k)$.

(3) Fourier spectrum:

The Fourier spectrum can be obtained from the power spectrum, which is the square root of power spectrum.

(4) Phase angle:

The generation of phase angle is taken at random from a uniform distribution between 0 and 2π. We first generate random variables uniformly distributed between 0 and 1 by a random generator (Press *et al.*, 1986). Then phase angle is equal to product of them and 2π.

(5) Complex Fourier coefficients:

The Fourier transform of a real function is Hermitian function. Then complex coefficients F(u,v,w) must be Hermitian, this is even real part and odd imaginary part. This property has to be used to generate the complex Fourier coefficients.

(6) Inverse Fourier transform:

By calculating the inverse Fourier transform of F(u,v,w), the discrete Gaussian field $Y(\mathbf{x})$ is obtained with the specified correlation function $R_Y(u)$. The inverse discrete Fourier transform can be rapidly and efficiently computed with the mentioned algorithm of the fast Fourier transform.

(7) Nonlinear filter:

Nonlinear filter operation is the same with one used by Adler *et al.* (1990) and Fernandes (1994). $Z(\mathbf{x})$ is obtained using Eq. (9).

3. RESULTS AND DISCUSSIONS

We selected a thin section of Fontainebleau sandstone GF2, which was used by Alder et al. (1990). Figure 2 shows its photograph. Each pixel corresponds to 3.8 μm. The porosity is 0.25 and the normalized correlation function is shown in Figure 3. We have used the method proposed in section 2 to generate 3-D porous medium for GF2 sample. One reconstructed porous medium is shown in Figure 4. The results of statistical properties of reconstructed

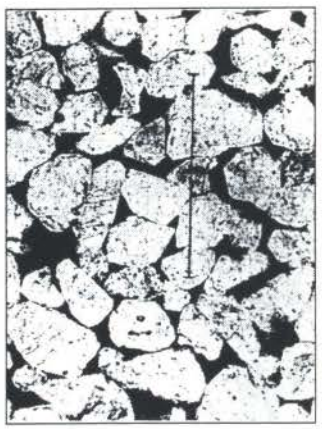

Figure 2: A thin section of the Fontainebleau Sandstone GF2 (Adler *et al.*, 1990). The pore pace appears black.

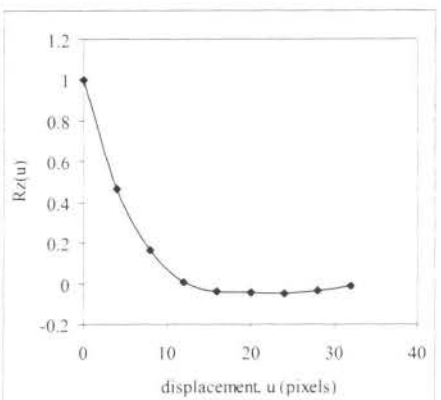

Figure 3: The normalized correlation function of sample.

porous media are compared with the ones of sample and obtained by Adler *et al.* (1990). These are shown in Figure 5. Figure 6 and Figure 7 show the slice display of a reconstructed porous medium of Figure 4 by any direction and three orthogonal directions, respectively. Figure 8 shows two cross sections generated by different phase angle distributions. These images possess the similar patterns. It looks like the same feature as the thin section of real sample (see Figure 2).

For a given image of the sample, the correlation length λ and length per pixel α are fixed. When one uses the original normalized correlation function $R_Y(u)$, it is useless to take into account every point of R_Y. Usually one point is selected every n points. Let ζ be the number of points where correlation is to be calculated in reconstructing the porous structure, i.e.

$$\zeta = \frac{\lambda}{n\alpha}$$

Usually a cube is generated i.e., the size of cube is $N_x=N_y=N_z=N$, when one reconstructs the porous media. Because the correlation function is even, to prevent any overlap between the negative and positive values of the displacement distance u through the spatial periodicity, N should be larger than 2ζ, i.e.:

$$\zeta << N/2$$

The other condition is natural to require that the correlation length λ contains many points, i.e.:

$$1 << \zeta$$

The above two conditions can be summarized up by the following inequalities:

$$1 << \zeta << N/2$$

The stronger these inequalities are, the better. But the increases in N require large computer memory and more running time.

This method was also used to generate 3-D pore structure for the other porous materials such as Berea sandstone (Liang, 1997) and lime mortar. The porosity and correlation function reproduce well.

4. CONCLUSIONS

1. The truncated Gaussian method by using Fourier transform is proposed to generate 3-D pore structure from 2-D image of the sample in this paper. The Gauss field $Y(\mathbf{x})$ is generated directly from its correlation function, then the truncated method is used to generate the phase function $Z(\mathbf{x})$. The porosity and correlation functions of the reconstructed porous media are in good agreement with the ones of real sample.

2. The advantage of the new method is that it does not need the linear filter and so avoids solving the nonlinear equations. Using the fast Fourier transform makes this algorithm more efficient. Both operating time and computer memory requirements are improved.

3. Phase angle distributions are taken at random. They do not affect the correlation function. Therefore, different phase angle distributions generate similar patterns of the pore structure.

4. When the reconstructed porous medium is generated, the transport process such as invasion process of fluids can be simulated and macroscopic properties such as permeability, capillary pressure and relative permeability curves can be determined.

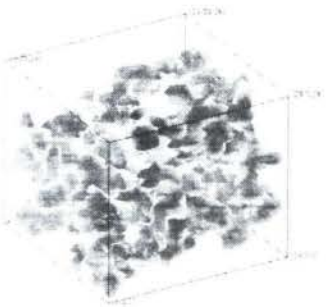

Figure 4: A reconstructed porous medium for sample GF2. (Sizes=30^3).

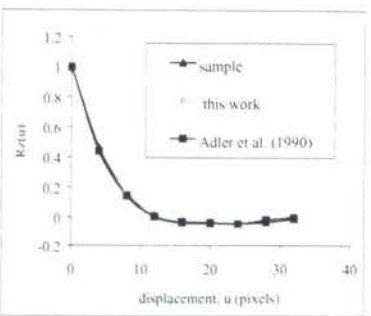

Figure 5: Comparison of $R_Z(u)$ of reconstructed porous media with sample between this work and Adler *et al.* (1990).

Figure 6: The oblique slice display of a reconstructed porous medium in Figure 4 by any direction.

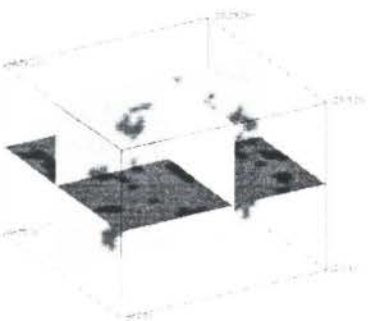

Figure 7: The slice display of a reconstructed porous medium in Figure 4 by three orthogonal direction.

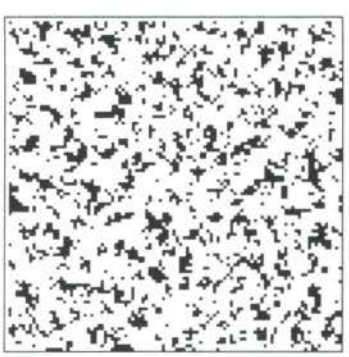

(a)

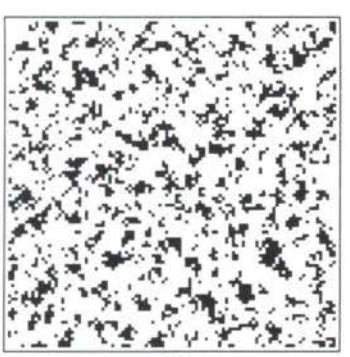

(b)

Figure 8: Two cross sections generated by different phase angle distributions (a) seed=-100 (b) seed=-200. (Sizes 100×100).

References

Adler, P.M. *Porous Media: Geometry and Transports*, Butterworth-Heinemann, New York, 1992.

Adler, P.M., Jacquin C.G. & Quiblier J.A. Flow in Simulated Porous Media, *Int. J. Multiphase Flow*, vol.16, pp.691-712, 1990.

Fernandes, C.P. *Caracterização Morfotopológica de Espaços Porosos: Reconstituição Multiescala e Simulação de Processos de Invasão de Fluidos Não-Molhantes*, Ph. D. thesis, Federal University of Santa Catarina, Florianópolis, 1994.

Gonzalez, R.C. & Wood R.E. *Digital Image Processing*, Addison-Wesley Publishing Company, 1992.

Ioannidis, M.A., Kwiecien M. & Chatzis I. Computer Generation and Application of 3-D Model Porous Media: From Pore-Level Geostatistics to the Estimation of Formation Factor, Paper *SPE 30201* presented at the Petroleum Computer Conference, Houston, TX, 1995.

Joshi, M.Y. *A Class of Stochastic Models for Porous Media*, Ph D thesis, University of Kansas, 1974.

Liang, Z.R. *Computer Generation and Application of 3-D Reconstructed Porous Structure: From 2-D Images to the Prediction of Permeability*, Ph.D. thesis, Federal University of Santa Catarina, Florianópolis, 1997.

Magnani, F.S. *Determinaçao das Configurações de Equilíbrio em Meios Porosos Indeformáveis*, Ph. D. thesis, Federal University of Santa Catarina, Florianópolis, 1996.

Papoulis, A. *Probability, Random Variables, and Stochastic Processes*, McGraw-Hill, Inc., New York, 1965.

Pardo-Igúzquiza, E. & Chica-Olmo M. The Fourier Integral Method: An Efficient Spectral Method for Simulation of Random Fields, *Mathematical Geology*, vol.25, pp.177-217, 1993.

Philippi P.C., Yunes P.R., Fernandes C.P. & Magnani F.S. The Microstructure of Porous Building Materials: Study of A Cement and Lime Mortar, *Transport in Porous Media*, vol.14, pp.219-245, 1994.

Press, W.H., Flannery, B.P., Teukolsky, S.A. & Vetterling, W.T. *Numerical Recipes – The Art of Scientific Computing*, University of Cambridge Press, Cambridge, pp.818, 1986.

Quiblier, J.A. A New Three-Dimensional Modeling Technique for Studying Porous Media, *Journal of Colloid and Interface Science*, vol.98, pp.84-102, 1984.

Singleton, R.C. An Algorithm for Computing the Mixed Radix Fast Fourier Transform, *IEEE Transactions on Audio and Electroacoustics*, vol.AU-17, pp.93-103, 1969.

Yao, J., Frykman, P., Kalaydjian, F., Thovert, J.F. & Adler, P.M. High-Order Moments of the Phase Function for Real and Reconstructed Model Porous Media: A Comparison, *Journal of Colloid and Interface Science*, vol.156, pp.478-490, 1993.

XIV Brazilian Congress of Mechanical Engineering
Obeid Plaza Hotel Convention Center - Bauru - SP/Brazil
December 08-12th 1997

PAPER CODE: COB1094

EXTRACTION OF 3-D PORE NETWORK AND PREDICTION OF PERMEABILITY FOR RESERVOIR ROCKS

LIANG ZHIRONG, PAULO CESAR PHILIPPI, CELSO PERES FERNANDES & FÁBIO SANTANA MAGNANI
Laboratório de Meios Porosos e Propriedades Termofisicas de Materiais
Departamento de Engenharia Mecânica, Universidade Federal de Santa Catarina
88040 - 900 Florianópolis, SC, Brasil - E-mail: liang@lmpt.ufsc.br

Abstract

The main purpose of the present work is to determine the 3-D pore structure network by using image analysis techniques and predict the permeability of the porous rock. The skeleton of a 3-D pore structure provides a way of visualizing the graph of the pore network. It is extracted using a thinning algorithm, which preserves connectivity, i.e., the network and original pore structure have the same topology. It gives both visual and quantitative information about the connectivity of the pore space, the coordination number for every node and local hydraulic radius. Once the network of pore structure is obtained, the macroscopic transport properties of the rock such as permeability can be calculated. In this paper, the reconstructed porous media for Berea sandstone is used to extract 3-D pore network. The predicted permeability for 500mD Berea sandstone rock is in good agreement with the experimental value and empirical correlations.

Keywords

Porous media; skeleton; 3-D pore structure; permeability

1. INTRODUCTION

The prediction of equilibrium and transport properties of porous media is a long-standing problem of great theoretical and practical interest, particularly in petroleum reservoir engineering (Dullien, 1992). The permeability is the most important physical property of a porous medium in the same way as the porosity is its most important geometrical property. Past theoretical attempts to derive macroscopic transport coefficients from the microstructure of porous media entailed a simplified representation of the pore space, often as a bundle of capillary tubes. These models have been widely applied because of their convenience and familiarity to the engineers. But they do have some limitations. For example, they are not well suited for describing effect of the pore space inter-connectivity and long range correlation in the system. Network models have been advanced to describe phenomena at the microscopic level and have been extended in the last few years to describe various phenomena at the macroscopic level. These models are mostly based on a network representation of the porous media in which larger pores (pore bodies) are connected by narrower pores (pore throats). Network models represent the most important and widely used class of geometric models for porous media (Hilfer, 1996). They are not only used in theoretical calculations but also in the form of micromodels in experimental observations. Dullien (1992) reviewed the details of various pore-scale processes, including detailed descriptions of many aspects of network models. The most important features of pore network geometry and topology that affect fluid

distribution and flow in reservoir rocks are the pore throat and pore body size distributions, and the pore body-to-pore throat size aspect ratio and the pore body coordination number (Ioannids and Chatzis, 1993). These data have been tentatively assumed in the previous works. The extension of these techniques to real porous media has been complicated by the difficulty in describing the complex 3-D pore structure of real reservoir rocks.

Information about the pore structure of reservoir rocks is often obtained from mercury intrusion and sorption isotherm. Mercury intrusion and sorption isotherm data provide statistical information about the pore throat size distribution. Advanced techniques such as micro-computed tomography and serial sectioning do provide a detailed description of the 3-D pore structures of rocks. These techniques are, however, expensive and not readily available. Recently, image analysis methods used over pictures of highly polished surfaces of porous materials (e.g., Adler *et al.*, 1990 and Philippi *et al.*, 1994), taken with an electron scanning microscope have been used to describe the porous structure. One of the most interesting results of image analysis in the study of porous structure is the reconstruction of porous media. This method has been applied previously to the prediction of important petrophysical and reservoir engineering properties such as permeability (Adler *et al.*, 1990) with reasonable success. Thovert *et al.* (1993) used the reconstructed porous medium and developed thinning algorithms to obtain the graph of the 3-D pore structure. The topological characteristics, such as the number of loops were derived. Bakke and Øren (1996) generated 3-D pore networks based on numerical modeling of the main sandstone-forming geological processes. The 3-D pore space network of the modeled sandstone was extracted from its complementary mineral matrix network using 3-D image analysis techniques. It was used as input to a two-phase network flow simulator. Absolute and relative permeabilities were computed for a Bentheimer sandstone. However, although their algorithms worked well on their models, the proof for a 3-D thinning algorithm to preserve connectivity is much more difficult. Recently, Ma (1994) proposed sufficient conditions for providing a 3-D thinning algorithm to preserve connectivity, i.e., an object and its skeleton have the same topology. It enables the network to preserve the same connectivity with pore space.

In the present work, the 3-D reconstructed pore structure is used to extract the graph of 3-D pore space (skeleton) by using a thinning algorithm, which preserves connectivity. Using a thinning algorithm, the main flow path for a single flow is obtained, which is classified into nodes and links. The local cross-sectional area and perimeter normal to the flow path in each link is recorded to compute the local hydraulic radius. Resistance to flow is calculated by assigning hydraulic resistance to each link. A fluid pressure is calculated at each node, and total volumetric flux through the network is computed. Then the absolute permeability is predicted from the corresponding network for the sample.

2. THE GRAPH OF 3-D PORE STRUCTURE

The real or reconstructed porous media are three-dimensional and possess a very complex geometry, which is difficult to grasp either qualitatively or quantitatively. When flow problems are considered, connectivity is important. For instance, dead ends play an important role in diffusional processes, while being irrelevant for permeability on physical grounds. Serra (1982) and Adler (1992) define the skeleton of the pore space as the set of points (voxels) at equal distance from two or more points of the solid wall. The skeleton may thus be thought as a spatial representation of the median line of pore space. This spatial median line will contain points where two or more lines meet. These meeting points are the network nodes, which are connected to other nodes by links.

2.1. Extraction of skeleton

The skeleton of an object is often obtained by a thinning algorithm. Thinning is a preprocessing operation of pattern recognition since a thinned object is easier to trace and hence is easier to recognize. Generally, thinning is a layer-by-layer erosion of an object until only a unit-width skeleton is left. In 2-D image analysis, skeleton extraction from binary images is carried out by means of various algorithms. Pieritz (1994) used median line graph technique to characterize 2-D porous materials. This is not the case for the 3-D case. One possible reason is that the proof for a 3-D thinning algorithm to preserve connectivity is much more difficult than in the 2-D case. Thovert et al (1993) succeeded in developing a 3-D thinning algorithm that worked well on their models. However, as discussed by Bakke and Øren (1996), visual examination showed that in some complex voxel junctions, the algorithm introduced artificial holes in the pore network skeleton. This can, for fluid flow purposes, be quite catastrophic because it may result in the definition of artificial hydraulic circuits and wrong coordination numbers for pore bodies.

A thinning algorithm should preserve connectivity, i.e., an object and its skeleton should maintain the same connectivity structure. Ma (1994) proposed sufficient conditions for providing a 3-D thinning algorithm to preserve connectivity. We state Ma's results as follows:

Theorem 1 A 3-D thinning algorithm preserves connectivity if all of the following conditions hold:

Only simple points can be deleted.

If two black corners, p and q, of a unit lattice square are deleted, then {p, q} is simple.

If three black corners, p, q and r, of a unit lattice square are deleted, then {p, q, r} is simple.

If four black corners, p, q, r, and s, of a unit lattice square are deleted, then {p, q, r, s} is simple.

No black components contained in a unit lattice cube can be deleted completely.

Ma (1995) further proposed a 3-D fully parallel thinning algorithm for generating medial faces. In this work, the above 3-D thinning algorithms are used to extract the skeleton of the pore space, which preserves connectivity.

The skeleton gives us a simplified graph of 3-D pore structure. If one knows the 3-D pore structure of a real or reconstructed porous medium, the real network of the medium can be obtained. So, when using this skeleton it is not necessary to make any assumption concerning coordination number and site and/or bond sizes, to characterize the structure, as it is usual when working with classical percolation networks.

2.2. "Pore sizes"-hydraulic radius

For general porous microstructures, it is difficult to define "pores" or "pore bodies". The reason for using the hydraulic radius r_H is that r_H is a useful measure of "size" in the case of irregularly shaped cross sections. Dullien[1] showed that the values of reciprocal hydraulic radius ($1/r_H$) and twice the reciprocal mean radius of curvature ($2/r_m$) in a capillary tube are very approximate. Here $2/r_m$ is related to the capillary pressure P_c; i.e., the pressure difference across the fluid/fluid interface of mean radius of curvature r_m, in mechanical equilibrium. Laplace's equation gives:

$$P_C = \frac{2\sigma}{r_m}, \qquad (1)$$

where σ is the interfacial tension. For the case of nonzero contact angle θ, r_m must be replaced by R, according to the relation

$$R = r_m \cos\theta. \qquad (2)$$

The definition of hydraulic radius r_H of a capillary is as follows:

$$r_H = \frac{\text{area of cross section}}{\text{length of perimeter of cross section}}. \quad (3)$$

For the general case of irregular capillaries, the minimum value of the ratio given by above equation must be found by varying the orientation of the sectioning plane about the same fixed point inside the capillary. The minimum value of this ratio is the hydraulic radius r_H of irregular capillary at the fixed point. Both radii r_m and r_H are best suited to the case of pore throats that control both capillary penetration by a non-wetting fluid into the porous medium and the flow rate of fluids through the porous medium.

3. SIMULATION OF PERMEABILITY IN 3-D POROUS MEDIA

Permeability measures quantitatively the ability of a porous medium to conduct fluid flow. The permeability is defined by Darcy's law:

$$Q = \frac{K\ A}{\mu}\ \frac{\Delta P}{L}. \quad (4)$$

where Q is the volumetric flow rate, A is the normal cross-sectional area of the sample, L is the length of the sample in the macroscopic flow direction, $\Delta P \equiv P_1 - P_2$ is hydrostatic pressure drop, and μ is the viscosity of the fluid. Darcy's law is limited to viscous (or creeping) flow, Newtonian fluids, absence of physical or chemical changes due to the fluid, no slip, and isotropic media. Q and P in Eq. (4) are macroscopic averages, measured over several pore lengths or more. If this average is taken over a length larger than any correlation length in the pore structure of the medium (i. e., we measure Q in a statistically homogeneous sample), then the permeability K is a well-defined, intensive property of the rock, which characterizes its flow resistance.

Measurement of permeability in the case of isotropic media is usually performed on linear, mostly cylindrically shaped, "core" samples. The experiment can be arranged so as to have either horizontal or vertical flow through the sample. Great care must be taken in every case to prevent bypassing of the sample by the fluid. In principle, measurement at a single steady flow rate permits calculation of the permeability from Darcy's law.

3.1. Permeability models

Because of the laborious experimentation, it is not surprising that much effort has been made to theoretically predict the permeability. Dullien (1992) divided permeability models into the following types: capillaric, statistical, empiric, deterministic and network models. The simplest approaches based on the idea of conduit flow ignore the fact that different pores are interconnected with each other. These are called capillaric permeability models, among which one enjoys much greatest popularity: the so-called Carman-Kozeny model. In the Carman-Konzey theory or hydraulic radius theory, the porous medium was assumed to be equivalent to a conduit, in which the pore space is represented as an array of cylindrical tubes. If a probability law is used in the model, it is called statistical permeability model. One statistical permeability model is called cut-and-random-rejoin-type model. It was assumed that the fraction of the area of a section occupied by pore openings is deduced from the drainage capillary pressure curve. The sample is sectioned into two by a plane perpendicular to the direction of flow, and two parts are joined together again in a random fashion. The flow rate in the capillaries is assumed by a Hagen-Poiseuille type relationship. Due to the use of drainage capillary pressure curve, this model suffers from the shortcoming of assigning all the pore volume to entry pores. Some of the most successful permeability models are based on pure empiricism, even through attempts are often made to justify the good empiric correlation by a theoretical model. The deterministic permeability model offers the ability to study the micro-physical basis of macroscopic transport. But it is time consuming. The network models

have been used in the last four decades. But they are all based on the some information of pore structure, such as size distribution and coordination numbers. These data are almost assumed in the previous works. The 3-D skeleton of pore structure provides a real network. The hydraulic conductivity of the fluid in the network can be calculated from the local hydraulic radius. Therefore, the permeability can be calculated from the above data.

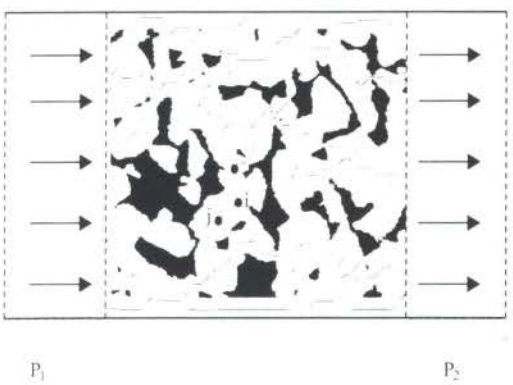

Figure 1: A 2-D graph representation for calculating permeability.

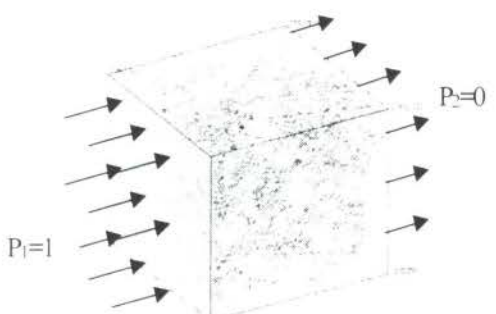

Figure 2: Simulation of fluid flow on the graph of pore space in a porous medium.

3.2. Calculation of permeability

The reconstructed 3-D porous medium is used to predict the permeability. It is usually a cube with size $N_x \times N_y \times N_z$. The x-axis of the medium is chosen to be parallel to the direction of macroscopic flow. Impervious boundary conditions are applied to the sides of the medium that are parallel to axes y and z. The graph of the pore structure is obtained by using a thinning algorithm, which preserves the connectivity. To simplify illustration of the process to calculate permeability, we use a 2-D graph of the pore space shown in Figure 1 (see also Figure 2). To calculate the conductivity of each points of the graph and save computer memory, the concepts of graph theory are used to describe the network. The link and nodes of the graph are composed of points with exactly two neighbors and three or more neighbors, respectively. A preferable way to describe a graph is by specifying the set of *nodes* and a *correspondence* that shows how the nodes are related to each other. The degree of a node is the number of links that connect it, which is also called coordination number.

To compute absolute permeability, we need to define the hydraulic conductivity of the fluid in the network. We make the assumption that the flow is sufficiently slow for the interaction between fluids to be negligible. Furthermore, we make the simplification that the resistance to the fluid flow in a pore link may be characterized in terms of an equivalent diameter d_H, which is four times the hydraulic radius r_H.

$$d_H = 4\ r_H . \tag{5}$$

The r_H is calculated from cross-sectional area and perimeter normal to the flow path, which can be represented by a parametric equation of curve. Thus, the conductivity of fluid in a pore link, g_L, is given by Poiseuille's equation and may be written as:

$$g_L = \frac{\pi\ d_H^4}{128\ \mu\ l} . \tag{6}$$

Where μ is the fluid viscosity and l is the length of the pore (here l =1 pixel). We also assume that the conductivity of fluid in a node, g_i, is given by Poiseuille's equation. According to the

definition of hydraulic radius, it is the minimum, which can be obtained by the distance from the solid. The overall resistance to flow of fluid between the two neighboring nodes i and j, g_{ij}, is the sum of resistance of two nodes and the link resistance, i. e.,

$$\frac{1}{g_{ij}} = \frac{1}{g_i} + \sum \frac{1}{g_L} + \frac{1}{g_j}. \tag{7}$$

Where g_L is the conductivity of the link and g_i and g_j are the conductivity of two nodes. The flow rate of fluid between the two nodes,

$$Q_{ij} = g_{ij} (P_i - P_j). \tag{8}$$

Where P_i and P_j are the nodal pressures. Since the fluid is incompressible, flux conservation requires that

$$\sum_j Q_{ij} = 0. \tag{9}$$

Where j runs over all the links connected to node i. Eq. (9) together with the appropriate boundary conditions form a complete solution to the steady flow of an incompressible fluid in the pore network. The equations are solved using successive over-relaxation:

$$P_i = \beta \frac{\sum_j g_{ij} P_j}{\sum_j g_{ij}} + (1-\beta) P_i, \tag{10}$$

Where β is the relaxation parameter.

The absolute permeability K of the pore network is calculated from Darcy's law by imposing a pressure drop across the network and computing the resulting single phase flow rate:

$$K = \frac{\mu L Q}{A \Delta P} = \frac{\mu (N_x - 4) Q}{(N_y - 4)(N_z - 4) \alpha \Delta P}. \tag{11}$$

Where Q, L, A, ΔP is the same as in Eq. (4), α is the length per pixel and N_x, N_y, and N_z are the side sizes of reconstructed porous medium. After the thinning operation, the sizes of the medium are N_x-4, N_y-4 and N_z-4.

4. RESULTS AND DISCUSSIONS

To predict the absolute permeability for a rock sample, a graph of 3-D pore space (skeleton) is extracted from 3-D pore structure by using a thinning algorithm, which preserves connectivity. Using thinning, the main flow path for a single flow is obtained, which is classified into nodes and links. The local cross-sectional area and perimeter normal to the flow path in each link is recorded to compute the local hydraulic radius. Resistance to flow may, then, be calculated by assigning hydraulic resistance to each link. A fluid pressure is computed at each node, and the total volumetric flux through the network is calculated. Then the absolute permeability is predicted from the corresponding network for the sample.

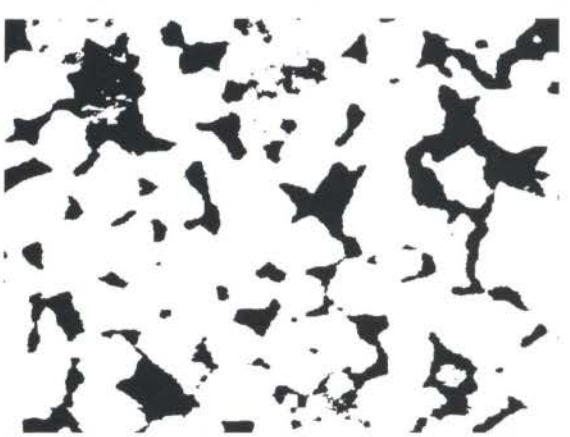

Figure 3: A binarized image of one thin section of 500 mD Berea sandstone, which is 609 × 458 pixels with magnification of 50 × . Each pixel is equal to 2.6 μm.

4.1. Sample

Figure 3 shows a binarized image of one thin section of a 500 mD Berea

sandstone sample, which is 609×458 pixels with magnification of 50×. A 3-D reconstructed porous medium is generated using truncated Gaussian method by using Fourier transform (Liang, 1997) as shown in Figure 4. The graph of reconstructed porous medium is obtained by the thinning algorithm and shown in Figure 5.

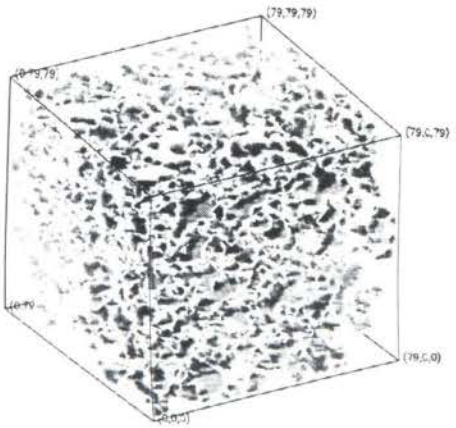

Figure 4: The isosurface of 3-D pore structure after removing the isolated regions of the solid and porous phase.

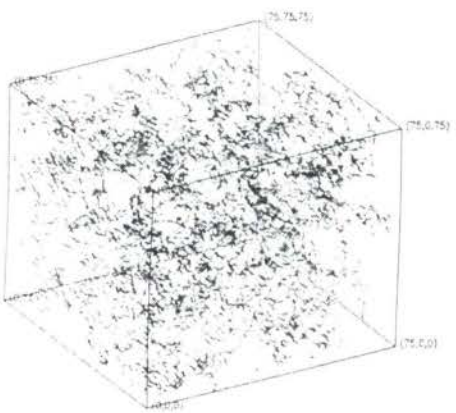

Figure 5: The graph of the reconstructed porous medium by thinning.

Table 1: Comparison of the present result for 500mD Berea sandstone with the experimental value and the results estimated by empirical correlations.

	K (mD)
1. $K=(\frac{D_b}{3.5})^2(\frac{\varepsilon}{32})\times 10^3$, *(From Dullien, 1992)* ε *=0.225* and* D_b *=31.25* μm*	560.5
2. $K=(\frac{85.63}{P_{cb}})^{2.71}$ *(From Dullien, 1992)* P_{cb} *=6.83* psi*	946.5
3. *Mendes (1997)*	632
4. *This work*	505.9
5. *Experimental value*	500*

* ε, P_{cb} *and* D_b are porosity, breakthrough capillary pressure and breakthrough diameter, respectively. These data were extracted from a report of Cenpes/PETROBRAS.

4.2. Prediction of permeability

When the skeleton is obtained, the simulation of flow is carried out on it, as is shown in Figure 1 and Figure 2. The permeability is calculated by using the process described in section 3.2. Mercury intrusion and corresponding pore size distributions from Laplace's equation were obtained for Berea samples in Brazilian Petroleum Company (Cenpes /PETROBRAS). Some empirical correlations described by Dullien (1992) were used to estimate the permeability. Mendes (1997) used the cut-and-random-rejoin-type model and calculated the permeability for the Berea sample. These values are given and compared with our results and with experimental ones in Table 1. It is shown that present results are in very good agreement with experimental ones.

5. CONCLUSIONS

1. The skeleton of 3-D pore structure is extracted by a thinning algorithm, which preserves connectivity. That is, it has the same topology as the pore space.
2. The skeleton gives a real network representation for 3-D porous medium. The main flow path for a single flow is obtained, which is classified into nodes and links. The local hydraulic radius normal to the flow path in each link can be recorded to predict the permeability.
3. The simulation of permeability is directly on the network. The effect of sample size N is important as it is directly associated to statistical homogeneity of the reconstructed structure.
4. The value of predicted permeability for a 500mD Berea sandstone sample is in good agreement with experimental results and empirical correlations.

References

Adler, P.M. *Porous Media: Geometry and Transports*, Butterworth-Heinemann, New York, 1992.

Adler, P.M., Jacquin C.G. & Quiblier J.A. Flow in Simulated Porous Media, *Int. J. Multiphase Flow*, vol.16, pp.691-712, 1990.

Bakke, S. & Øren P.E. 3-D Pore-Scale Modeling of Heterogeneous Sandstone Reservoir Rocks and Quantitative Analysis of the Architecture, Geometry and Spatial Continuity of the Pore Network, Paper *SPE 35479* presented at the European 3-D Reservior Modeling Conference, Stavanger, Norway, 1996.

Dullien, F.A.L. *Porous Media - Fluid Transport and Pore Structure*, San Diego: Academic Press, 1992.

Hilfer, R. Transport and Relaxation Phenomena in Porous Media, *Adv. Chem. Phys.*, vol.92, pp.299, 1996.

Ioannidis, M.A. & Chatzis I. Network Modeling of Pore Structure and Transport Properties of Porous Media, *Chem. Eng. Sci.*, vol.48, pp.951-972, 1993.

Liang, Z.R. *Computer Generation and Application of 3-D Reconstructed Porous Structure: From 2-D Images to the Prediction of Permeability*, Ph.D. thesis, Federal University of Santa Catarina, Florianópolis, 1997.

Ma, C.M. On Topology Preservation in 3D Thinning, *CVGIP: Image understanding*, vol.59, pp.328-339, 1994.

Ma, C.M. A 3D Fully Parallel Thinning Algorithm for Generating Medical Faces, *Patt. Recog. Lett.*, vol.16, pp.83-87, 1995.

Mendes, N. *Desenvolvimento de um Código Genérico para a Previsão da Transferência de Calor e de Umidade em Elementos Porosos de Edificações*, Ph. D. thesis, Federal University of Santa Catarina, Florianópolis, 1997.

Philippi, P.C., Yunes, P.R., Fernandes, C.P. & Magnani, F.S. The Microstructure of Porous Building Materials: Study of A Cement and Lime Mortar, *Transport in Porous Media*, vol.14, pp.219-245, 1994.

Pieritz, R.A. *Desevolvimento das Técnicas do Gráfico da Linha Mediana e da Binarização por Regiões Conexas Aplicadas à Caracterização Geométrica de Meios Porosos*, MS thesis, Federal University of Santa Catarina, Florianópolis, 1994.

Serra, J. *Image Analysis and Mathematical Morphology*, Academic Press, New York, 1982.

Thovert, J.F., Salles, J. & Adler, P.M. Computerized Characterization of the Geometry of Real Porous Media: Their Discretization, Analysis and Interpretation, *Journal of microscopy*, vol.170, pp.65-79, 1993.

XIV Brazilian Congress of Mechanical Engineering
Obeid Plaza Hotel Convention Center - Bauru - SP/Brazil
December 08-12th 1997

PAPER CODE: COB1447

INCOMPRESSIBLE FLUID FLOWS THROUGH A NONSATURATED SPHERICAL SURFACE

M.L. MARTINS COSTA† & R.M. SALDANHA DA GAMA‡
‡ *Laboratório de Mecânica Teórica e Aplicada - LMTA,*
Departamento de Engenharia Mecânica, Universidade Federal Fluminense
Rua Passo da Pátria no.156, 24210-240 Niterói/RJ, Brazil
†*Laboratório Nacional de Computação Científica*
Rua Lauro Müller, 455 22290-160, Rio de Janeiro, Brazil

Abstract

This work studies a nonsaturated flow of a newtonian fluid through a rigid porous spheric matrix, using a mixture theory approach in its modelling. The mixture consists of three overlapping continuous constituents: a solid (porous medium), a liquid and an inert gas, included to account for the compressibility of the mixture as a whole. A set of two nonlinear partial differential equations describes the problem which is approximated by means of a Glimm's scheme, combined with an operator splitting technique.

Keywords

Nonsaturated Flow, Mixture Theory, Glimm's Method

1. PRELIMINARIES

Transport phenomena in porous media have become a subject of increasing interest nowadays mainly due to the importance attached to problems that impact the energy self-sufficiency and the environmental state. They play an important role in countless practical applications such as groundwater flows, oil extraction, enhanced oil recovery processes, contamination of soils by hazardous wastes, storage of nuclear waste material in deep earth rock layers or deep ocean seabeds and pollution movement, just to mention a few of them.

This work presents a local model for the nonsaturated flow of a newtonian fluid through a rigid porous sphere, based on the Theory of Mixtures, a convenient method of modelling multicomponent systems, whose basic assumption is that, at any time, all the constituents are present in every point of the mixture. The nonsaturated porous medium is modelled as a mixture of three overlapping continuous constituents: a solid (a rigid, homogeneous and isotropic porous matrix), a liquid (an incompressible newtonian fluid) and an inert gas, assumed with zero mass density; which was included to account for the compressibility of the system as a whole, since the mixture is compressible but the fluid constituent is incompresssible. This model describes the dynamics of the

filling-up of a porous medium.

Additional terms, playing the role of momentum sources, absent in the classical approach, must be considered in the balance equations. (Besides the so called darcian term, the spherical geometry gives rise to another source term.) Assuming the porous matrix rigid and at rest, the momentum and mass balance equations must be solved for the fluid constituent only. No equation will be used to describe the behaviour of the gas constituent once that its presence is only for allowing changes in the liquid fraction (or liquid concentration). The resulting mathematical representation consists of a set of two nonlinear partial differential equations subjected to initial data and boundary conditions, whose unknowns are the fluid constituent velocity and the saturation.

A special numerical approach is used to simulate the radial flow throgh the porous spherical matrix. The problem is approximated by means of the Glimm's Scheme, combined with an operator splitting technique, which accounts for the nonhomogeneous part of the differential equations.

2. Mathematical Model

Assuming a chemically nonreacting continuous mixture, in which the solid constituent is rigid and at rest and the third (gas) constituent is inert, it suffices to solve mass and momentum balance equations for the fluid (liquid) constituent only. The mass balance for the fluid constituent may be expressed as (Atkin and Craine, 1976):

$$\frac{\partial \rho_F}{\partial t} + \mathrm{div}(\rho_F \mathbf{v}_F) = 0 \tag{1}$$

in which ρ_F is the fluid constituent mass density and $\mathbf{v}_F$ its velocity in the mixture.

The balance of linear momentum for the fluid constituent is given by (Atkin and Craine, 1976):

$$\rho_F \left[\frac{\partial \mathbf{v}_F}{\partial t} + (\mathrm{grad}\mathbf{v}_F)\mathbf{v}_F \right] = \mathrm{div}\mathbf{T}_F + \mathbf{m}_F + \rho_F \mathbf{b}_F \tag{2}$$

where $\mathbf{T}_F$ is the partial stress tensor associated to the fluid constituent, $\mathbf{b}_F$ is a specific body force acting on it and $\mathbf{m}_F$ is a momentum interaction force, per unit volume, acting on the fluid constituent due to its interaction with the remaining constituents of the mixture.

Defining the saturation ψ as the ratio between the fluid fraction φ and the porosity it may be expressed as:

$$\psi = \frac{\varphi}{\varepsilon} = \frac{\rho_F}{\varepsilon \rho} \qquad 0 \leq \psi \leq 1 \text{ everywhere} \tag{3}$$

where ρ is the actual mass density of the liquid (regarded as a single continuum) ρ_F is the liquid constituent mass density and ε the porous medium porosity (a constant).

Considering an incompressible newtonian fluid, the momentum source, which accounts for the dynamic interaction among the constituents, is given by (Williams, 1978; Saldanha da Gama and Sampaio, 1987):

$$\mathbf{m}_F = -\alpha\psi^2\mathbf{v}_F - \beta\psi\mathrm{grad}\psi \quad ; \quad \text{with} \qquad \alpha = \frac{\varepsilon^2\eta}{K} \qquad \beta = \frac{\varepsilon^2\eta\mathcal{D}}{K} \tag{4}$$

where η is the fluid viscosity (considering a continuum mechanics point of view), K is the specific permeability and $\mathcal{D}$ is the diffusion coefficient.

The partial stress tensor for the fluid constituent will be stated as (Williams, 1978; Allen, 1986):

$$\mathbf{T}_F = -\varepsilon^2\overline{p}\psi^2\mathbf{1} \tag{5}$$

where $\overline{p}$ is a constant pressure and $\mathbf{1}$ is the identity tensor.

2.1 Onedimensional Phenomena

Assuming now that all the quantities depend only on the time t and on the position r, and that v is the only nonvanishing component of the fluid constituent velocity $\mathbf{v}_F$, the governing equations may be expressed as:

$$\frac{\partial\psi}{\partial t} + \frac{\partial}{\partial r}(\psi v) = -2\frac{\psi v}{r} \tag{6}$$

$$\rho\varepsilon\left[\psi\frac{\partial v}{\partial t} + \psi v\frac{\partial v}{\partial r}\right] = -\frac{\partial}{\partial r}(\varepsilon^2\psi^2\overline{p}) - \frac{\beta}{2}\frac{\partial}{\partial r}(\psi^2) - \alpha\psi^2 v \tag{7}$$

At this point it is convenient to introduce the following definition, considering a reference pressure p_0 :

$$\frac{\partial}{\partial r}(\varepsilon^2\psi^2\overline{p}) + \frac{\beta}{2}\frac{\partial}{\partial r}(\psi^2) = \varepsilon^2 p_0\frac{\partial}{\partial r}(\psi^2) \tag{8}$$

The set of equations (6-8) may be rewritten as:

$$\frac{\partial\psi}{\partial\tau} + \frac{\partial}{\partial\xi}(\psi u) = -2\frac{\psi u}{\xi+\lambda} \tag{9}$$

$$\frac{\partial}{\partial\tau}(\psi u) + \frac{\partial}{\partial\xi}\left(\psi u^2 + \psi^2\right) = -\gamma\psi^2 u - 2\frac{\psi u^2}{\xi+\lambda} \tag{10}$$

provided that the following dimensionless quantities are defined:

$$u = v\sqrt{\frac{\rho}{\varepsilon p_0}} \quad \tau = \frac{t}{r_e - r_i}\sqrt{\frac{\varepsilon p_0}{\rho}} \quad \gamma = \frac{\alpha(r_e - r_i)}{\rho\varepsilon}\sqrt{\frac{\rho}{\varepsilon p_0}} \quad \xi = \frac{r - r_i}{r_e - r_i} \quad \lambda = \frac{r_i}{r_e - r_i} \tag{11}$$

in which r_e and r_i are the external and internal radia.

It is to be noticed that, in order to solve the above problem, initial data and boundary conditions for ψ and u are required.

3. Numerical Procedure

The scheme used to obtain numerical approximations of the nonlinear hyperbolic system of partial differential equations described in the previous section employs an operator splitting technique together with the Glimm's scheme. This procedure has already been used with success in other nonlinear hyperbolic problems: Sod (1977) studied wave propagation in fluids, Marchesin and Paes-Leme (1983) solved a gas dynamics problem, Saldanha da Gama and Sampaio (1978) simulated the filling-up of a porous matrix, Freitas Rachid et al. (1994) modelled the wave propagation in a damageable elasto-viscoplastic pipe and Martins-Costa et al. (1995) studied the flow of a newtonian fluid through an unsaturated porous matrix.

Starting from the fields ψ and u at time τ_n on equations (9) and (10) and assuming that $F \equiv \psi$ and $G \equiv \psi u$, their approximations at time τ_{n+1} are described as:

$$\begin{aligned} &\frac{\partial F}{\partial \tau} + \frac{\partial G}{\partial \xi} = -2\frac{G}{\xi + \lambda} \\ &\frac{\partial G}{\partial \tau} + \frac{\partial}{\partial \xi}\left(\frac{G^2}{F} + F^2\right) = -\gamma F G - 2\frac{G^2/F}{\xi + \lambda} \\ &F = \hat{F}_n(\xi) \quad \text{and} \quad G = \hat{G}_n(\xi) \qquad \text{at} \quad \tau = \tau_n \end{aligned} \tag{12}$$

in which $F = \hat{F}_n(\xi, \tau)$ and $G = \hat{G}_n(\xi, \tau)$.

An approximation for the fields F and G at the time τ_{n+1} is obtained by employing an operator splitting, (Martins-Costa et al., 1995), which consists in solving the following problem:

$$\begin{aligned} &\frac{\partial F}{\partial \tau} = -2\frac{G}{\xi + \lambda} \\ &\frac{\partial G}{\partial \tau} = -\gamma F G - 2\frac{G^2/F}{\xi + \lambda} \\ &F = \hat{F}_{n+1}(\xi) \quad \text{and} \quad G = \hat{G}_{n+1}(\xi) \qquad \text{at} \quad \tau = \tau_n \end{aligned} \tag{13}$$

as follows:

$$F = \hat{F}_{n+1}(\xi) \approx \overline{F}_{n+1}(\xi) - 2\frac{\overline{G}_{n+1}(\xi)}{\xi + \lambda}\Delta\tau \tag{14}$$

$$G = \hat{G}_{n+1}(\xi) \approx \overline{G}_{n+1}(\xi) \; - \left(\overline{F}_{n+1}(\xi)\overline{G}_{n+1}(\xi) + 2\frac{[\overline{G}_{n+1}(\xi)]^2\overline{F}_{n+1}(\xi)}{\xi + \lambda}\right)\Delta\tau$$

evaluated at $\tau = \tau_{n+1}$ and considering $\Delta\tau = \tau_{n+1} - \tau_n$.

The fields $\overline{F}_{n+1}$ and $\overline{G}_{n+1}$ used as initial data in (13) are obtained from the homogeneous problem:

$$\frac{\partial F}{\partial \tau} + \frac{\partial G}{\partial \xi} = 0$$

$$\frac{\partial G}{\partial \tau} + \frac{\partial}{\partial \xi}\left(\frac{G^2}{F} + F^2\right) = 0 \tag{15}$$

$$F = \hat{F}_n(\xi) \quad \text{and} \quad G = \hat{G}_n(\xi) \qquad \text{at} \quad \tau = \tau_n$$

In other words, $\overline{F}_{n+1}$ and $\overline{G}_{n+1}$ are the solutions of (15) evaluated at the time $\tau = \tau_{n+1}$.

Problems like (15) may be numerically solved by means of the Glimm's Scheme, which preserves the shock waves magnitude and position, within an uncertainty of $\Delta\xi$ (width of each step). Such features are not found in the usual numerical procedures (e.g. finite elements and finite differences). The first step to employ this scheme is to approximate the initial data by a piecewise constant function as follows:

$$F = \hat{F}_n(\xi) \approx F_{n_i} = \hat{F}_n(\xi_i + \theta_n \Delta\xi) \qquad \text{for} \quad \xi_i - \frac{\Delta\xi}{2} < \xi < \xi_i + \frac{\Delta\xi}{2} \tag{16}$$

$$G = \hat{G}_n(\xi) \approx G_{n_i} = \hat{G}_n(\xi_i + \theta_n \Delta\xi) \qquad \text{for} \quad \xi_i - \frac{\Delta\xi}{2} < \xi < \xi_i + \frac{\Delta\xi}{2}$$

in which θ_n is a number randomly chosen in the open interval $(-1/2, 1/2)$ and $\Delta\xi$ is the width of each step ($\Delta\xi = \xi_{i+1} - \xi_i$).

The above approximations for the initial data give rise, for each two consecutive steps, to the Riemann problem given by (Smoller,1983; Martins-Costa et al, 1995):

$$\frac{\partial F}{\partial \tau} + \frac{\partial G}{\partial \xi} = 0$$

$$\frac{\partial G}{\partial \tau} + \frac{\partial}{\partial \xi}\left(\frac{G^2}{F} + F^2\right) = 0 \tag{17}$$

$$(F, G) = (F_{n_i}, G_{n_i}) \qquad \text{for} \quad \tau = \tau_n \quad , \qquad -\infty < \xi < \xi_i + \frac{\Delta\xi}{2}$$

$$(F, G) = (F_{n_{i+1}}, G_{n_{i+1}}) \qquad \text{for} \quad \tau = \tau_n \quad , \qquad \xi_{i+1} - \frac{\Delta\xi}{2} < \xi < \infty$$

Denoting by $F^R_{n_i}$ and $G^R_{n_i}$ the generalized solution of (17), the approximation for the solution of (15) at the time τ_{n+1} is given as follows:

$$F = \hat{F}_{n+1}(\xi) \approx F^R_{n_i}(\xi, \tau_{n+1}) \qquad G = \hat{G}_{n+1}(\xi) \approx G^R_{n_i}(\xi, \tau_{n+1}) \qquad \text{for} \quad \xi_i < \xi < \xi_{i+1} \tag{18}$$

in which τ_{n+1} must be such that the Courant-Friedrich-Lewy (Smoller, 1983) condition is satisfied:

$$\tau_{n+1} - \tau_n \leq \frac{\Delta\xi}{2|\lambda|_{max}} \tag{19}$$

where $|\lambda|_{max}$ is the maximum (in absolute value) propagation speed, considering all the Riemann problems. The complete solution procedure, described in details by Martins-Costa et al. (1995), will be omitted for lack of space.

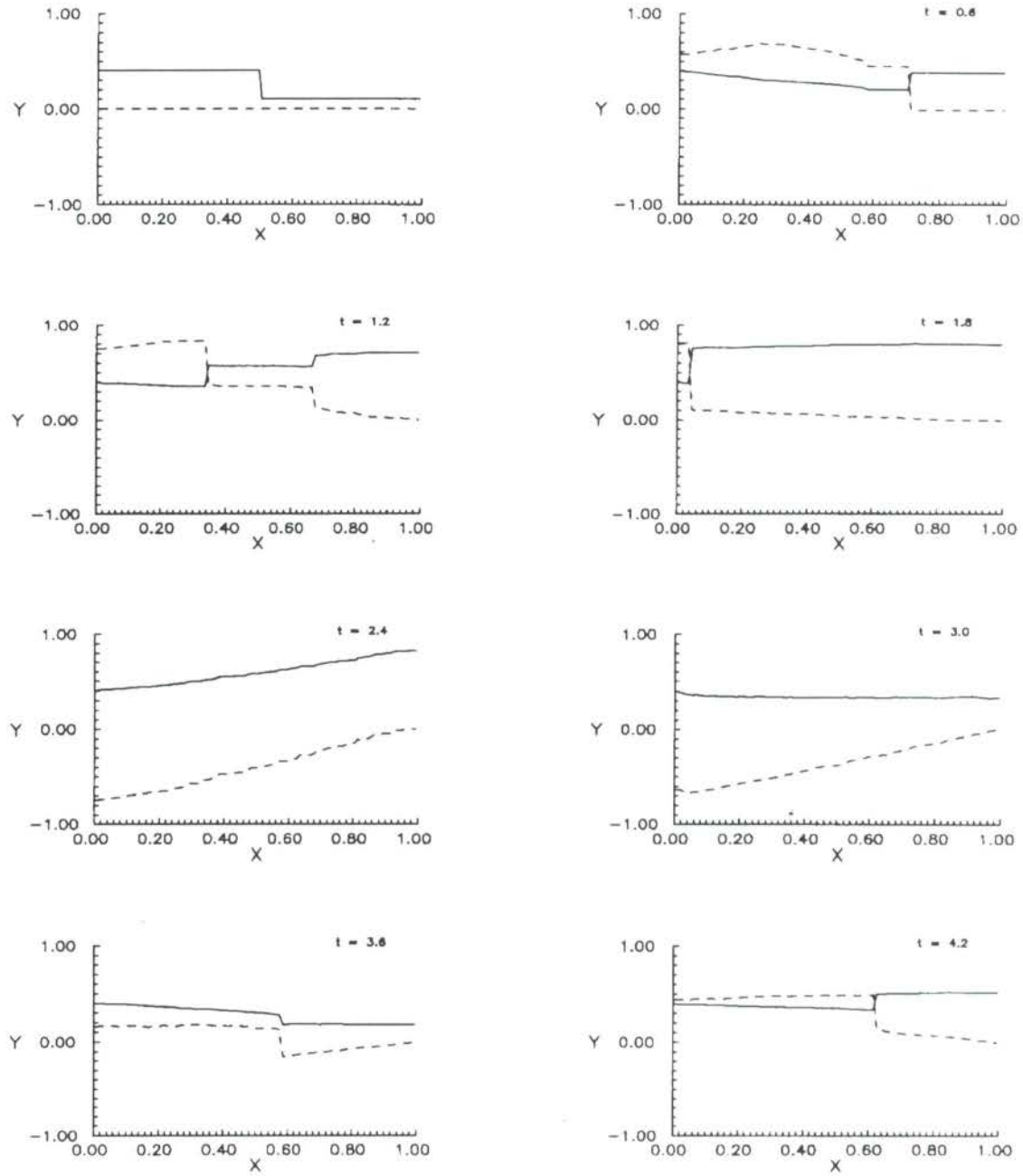

Figure 1. Saturation and fluid constituent velocity for $\gamma = 0$, $\lambda = 0.1$
$Y \equiv \psi$ for dashed curves; $Y \equiv u$ for solid curves and $X \equiv \xi$

4. Numerical Results

The procedure pointed out in the previous section is now employed for simulating the following spherical shell with a prescribed saturation at $\xi = 0$ and an impermeable surface at $\xi = 1$:

$$\frac{\partial \psi}{\partial \tau} + \frac{\partial}{\partial \xi}(\psi u) = -2\frac{\psi u}{\xi + \lambda}$$

$$\frac{\partial}{\partial \tau}(\psi u) + \frac{\partial}{\partial \xi}\left(\psi u^2 + \psi^2\right) = -\gamma \psi^2 u - 2\frac{\psi u^2}{\xi + \lambda} \tag{20}$$

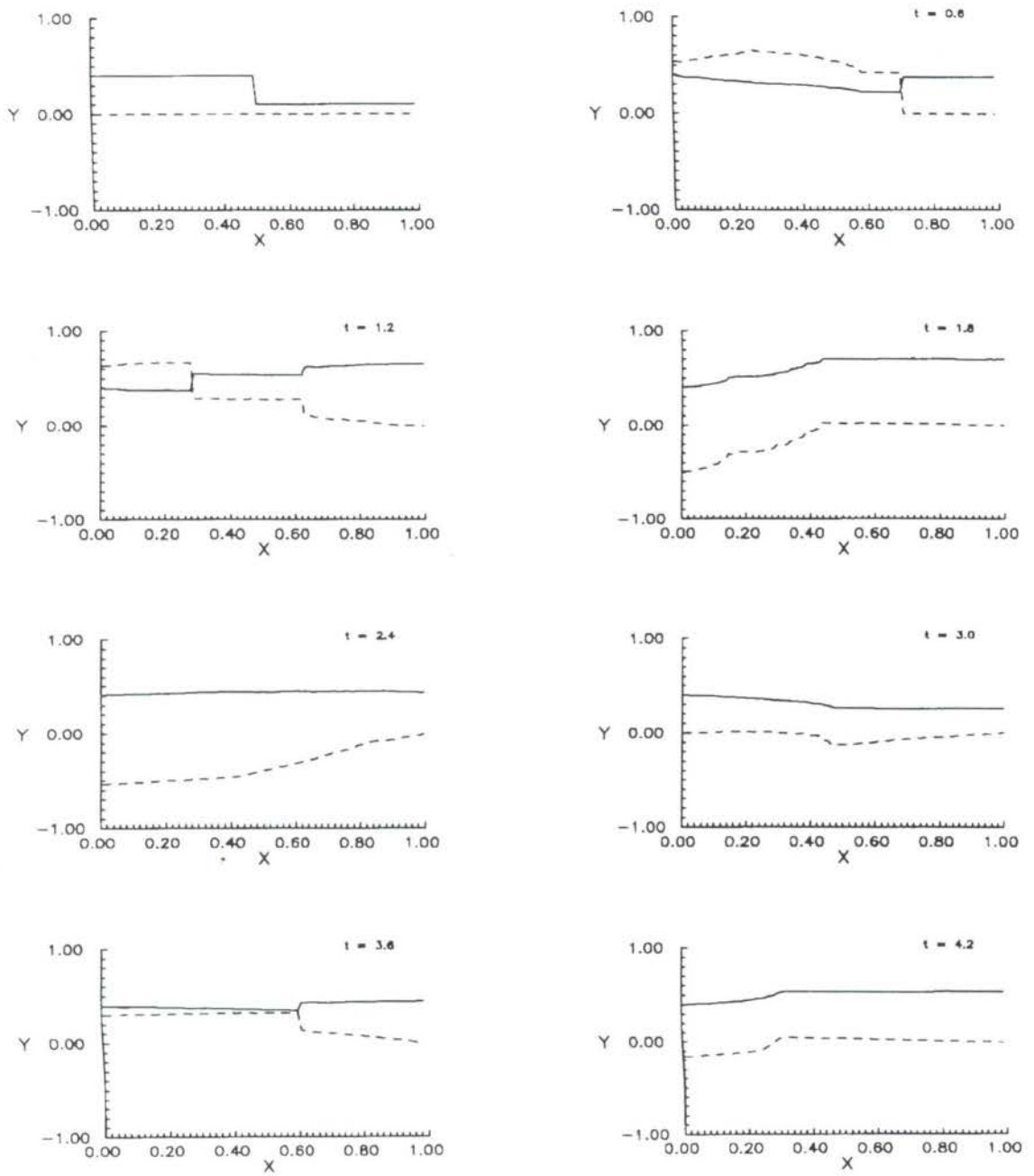

Figure 2. Saturation and fluid constituent velocity for $\gamma = 1$, $\lambda = 0.1$
$Y \equiv \psi$ for dashed curves: $Y \equiv u$ for solid curves and $X \equiv \xi$

$$\psi = \hat{\psi}_0(\xi) \quad \text{and} \quad u = \hat{u}_0(\xi) \qquad \text{for} \quad \tau = 0$$

$$\xi = 0 \quad \Rightarrow \quad \psi = 0.4 \qquad \text{for} \quad \tau > 0$$

$$\xi = 1 \quad \Rightarrow \quad u = 0 \qquad \text{for} \quad \tau > 0$$

The boundary conditions are imposed on the first and last steps after each advance in time.

Some selected results are presented in Figures 1 and 2, each of them consisting of eight graphs, each one representing a distinct time instant and the first graph in each

figure presents the initial data $\tau = 0$. Two curves are plotted in each graph: saturation (ψ) for solid lines and fluid constituent velocity (u) for dashed lines.

In figure 1 the parameter $\gamma = 0$ - this is equivalent to consider an inviscid flow through the nonsaturated porous medium - while a newtonian behaviour is shown in figure 2 making $\gamma = 1$. A strong influence of the γ parameter is verified on the saturation ψ and the fluid constituent velocity u. When $\gamma = 0$ the shock amplitudes - present in the saturation and fluid constituent velocity - are preserved, while a strong dissipation may be verified when $\gamma = 1$, for all considered cases. As it would be expected, the referred dissipation would be less evident for smaller values of γ ($\gamma = 0.1, for instance$) while for higher values of γ, the shock amplitudes almost disappear. The edge effect on the shock waves reflection may be clearly observed for the variables ψ and u.

5. Final Remarks

In the present work a specific and powerful procedure is employed in the simulation of the flow through a nonsaturated porous spherical surface: a Glimm's scheme, combined with an operator splitting technique, allowing very accurate results (Smoller, 1983; Martins-Costa et al., 1995).

Acknowledgments

This work has been partially supported by FAPERJ (Grant E-26/151.157).

6. References

Allen, M.B., Mechanics of Multiphase Fluid Flows in Variably Saturated Porous Media, *Int. J. Engng. Sci*, vl. 24, 339-351, 1986.

Atkin, R.J., & Craine, R.E., Continuum Theories of Mixtures. Basic Theory and Historical Development, *Quart. J. Mech. Appl. Math.*, vl. 29, pp. 209-244, 1976.

Freitas Rachid, F.B., Saldanha da Gama, R.M. & Costa Mattos, H., Modelling the Hydraulic Transients in Damageable Elasto-Viscoplastic Piping Systems, *Appl. Math. Modelling*, vl. 182, pp. 207-215, 1994.

Marchesin , D. & Paes-Leme, P.J., Shocks in Gas Pipelines, *SIAM J. Sci. Stat. Comput., vl. 4, pp. 105-116, 1983.*

Martins-Costa, M.L., Saldanha da Gama, R.M. & Sampaio, R., Incompressible Fluid Flows through a Nonsaturated Porous Medium, In Beiträge zur Mekanik, pp. 283-303, Universität Gesamthochschule Essen, Essen, 1995.

Saldanha da Gama, R.M. & Sampaio, R., Simulation of the Filling-up of a Porous Slab against Gravity, Proc. Int. Conf. on Comp. Mech. vl. 7, pp. 273-278, Tokyo, Japan, 1978.

Saldanha da Gama, R.M. & Sampaio, R., A Model for the Flow of an Incompressible Newtonian Fluid Through a Nonsaturated Infinite Rigid Porous Medium, Comput. Appl. Math.. vl. 6/2, pp. 195-205, 1987.

Smoller, J., Shock-Waves and Reaction-Diffusion Equations, Springer-Verlag, New York, 1983.

Williams, W.O., Constitutive Equations for a Flow of an Incompressible Viscous Fluid through a Porous Medium, Quart. J. Appl. Math, vl. 36, pp. 255-267, 1978.

XIV Brazilian Congress of Mechanical Engineering
Obeid Plaza Hotel Convention Center - Bauru - SP/Brazil
December 08-12th 1997

PAPER CODE: COB691

RESFRIAMENTO POR TRANSPIRAÇÃO: INFLUÊNCIA DA ESPESSURA E COMPRIMENTO DA PAREDE POROSA E DA RADIAÇÃO TÉRMICA INCIDENTE / *TRANSPIRATION COOLING: THE INFLUENCE OF THE POROUS WALL THICKNESS AND LENGTH AND OF THE INCIDENT THERMAL RADIATION*

GERALDO AUGUSTO CAMPOLINA FRANÇA[1], RITA CÉLIA MACIEL MENDONÇA NEVES[1], JEAN CLAUDE RODET[2] & ANDRÉ LALLEMAND[2]

[1]*Departamento de Engenharia Mecânica - UFMG, Av. Antônio Carlos ,6627 -CEP 31270-010 Belo Horizonte, MG, Brasil - E-mail: franca@vesper.demec.ufmg.br*

[2]*Institut National des Sciences Appliquées de Lyon - INSA/UCBL, Centre de Thermique de Lyon - CETHIL -20, avenue Albert Einstein - 69621 Villeurbanne Cedex (France) Lyon, França - E-mail: a.lal@cethil.insa-lyon.fr*

Abstract

In this work, some theoretical and experimental results related with the air transpiration cooling of a porous wall are presented and analyzed. The channel test has a length of 2 meters and a rectangular section 0,2 high by 0,5 wide. A porous plate with a porosity of 30% and dimensions 0,6mx0,3mx0,003 is installed in the bottom wall of the channel. The Reynolds number at the edge of the porous plate is always greater than $2x10^5$. The analysis show that neither the length nor the thickness of the porous wall modify greatly the cooling efficiency when the air blowing rate is equal or greater than 0,01. On the other hand, the experimental results show that thermal radiation may reduce in more than 50% the transpiration cooling efficiency. Furthermore, the fresh air injection has a little effect on the cooling of the impermeable plate upstream the blowing region.

Keywords

Transpiration - Porous wall - Cooling - Injection
Transpiração - Parede porosa - Resfriamento - Injeção

1. INTRODUÇÃO

A transpiração é comprovadamente um dos métodos mais eficientes para o resfriamento de paredes porosas sujeitas a fontes intensas de calor. Consiste na injeção de um gás ou líquido, em geral à temperatura ambiente, através da parede a ser resfriada. No caso do fluido injetado ser um líquido, pode haver evaporação do mesmo durante o processo. O esquema da figura 1 representa o mecanismo de resfriamento por injeção de gás de uma parede porosa sobre a qual escoa um outro gás quente. O exame desta figura permite identificar os dois principais fenômenos responsáveis pela diminuição da temperatura da parede (Grootenhuis, 1959), (Beveridge e Haughey, 1972), (Moffat e Kays, 1984), (Andoh *et al.*, 1994) e (França, 1996):

1^0 - ao passar através da parede porosa, o fluido injetado retira parte do calor transmitido da face quente para a face fria da parede

2^0 - ao sair, o fluido injetado modifica sensivelmente o perfil de velocidade do escoamento principal na região próxima da parede e induz o estabelecimento de uma camada de fluido que reduz a transferência de calor para a parede.

A análise detalhada do processo de resfriamento por transpiração envolve estudos dos mecanismos acoplados de transferência de quantidade de movimento, energia e massa na parede porosa e no escoamento principal. Diversos trabalhos teóricos e experimentais têm sido feitos nesta área e a compilação de uma boa parte deles pode ser encontrada em Jeromin (1970), Moffat e Kays (1984), Georgiou e Louis (1984), Kutateladze e Leont'ev (1990), Nicoud (1993) e França (1996). Estes estudos mostram que a eficiência do processo de resfriamento, definida por $\eta = \frac{T_e - T_{sp}}{T_e - T_f}$, depende de vários fatores como:

- taxa de injeção, ou seja, razão entre as densidades de fluxo do fluido injetado e do fluido principal
- rugosidade e porosidade da parede
- gradiente de pressão e intensidade da turbulência no escoamento potencial
- massa molecular do fluido injetado
- variação das propriedades termodinâmicas do fluido no interior e nas proximidades da face quente da parede porosa

Um dos resultados mais importantes dos estudos sobre escoamentos turbulentos com injeção, levemente acelerados, é que, para taxas de injeção iguais ou superiores a 0,01, a tensão de cisalhamento e o transporte convectivo de calor na parede porosa são praticamente nulos.

Os resultados do estudo de Yamamoto (1990) sobre o efeito da injeção de dióxido de carbono e de hélio no resfriamento de uma parede aquecida unicamente por radiação permitem concluir que os fluidos mais pesados são, neste caso, mais eficientes que os mais leves. Por outro lado, os estudos de Landis e Mills (1972), Shcherbenko (1988) e França *et al.* (1994) mostram que, para uma mesma taxa de injeção, a eficiência do resfriamento diminui com o aumento do peso molecular, nos casos em que o o transporte de calor por convecção é predominante.

Além disto, os estudos de Koh e Colony (1974), Koh et. al (1977) e Kar (1980) mostram que, a consideração da parede porosa como um trocador de calor em contracorrente e a utilização da temperatura média logarítmica na determinação de propriedades termodinâmicas, conduzem a bons resultados de cálculo do perfil de temperatura na parede. Portanto, a espessura e o comprimento da parede porosa, que são características geométricas do trocador de calor, podem também ter influência na eficiência do resfriamento.

Neste trabalho, alguns resultados teóricos e experimentais obtidos por França (1996) são apresentados e analisados com o objetivo de se extrair deles informações sobre a influência da espessura e do comprimento da parede e da radiação térmica incidente sobre a eficiência do resfriamento por transpiração.

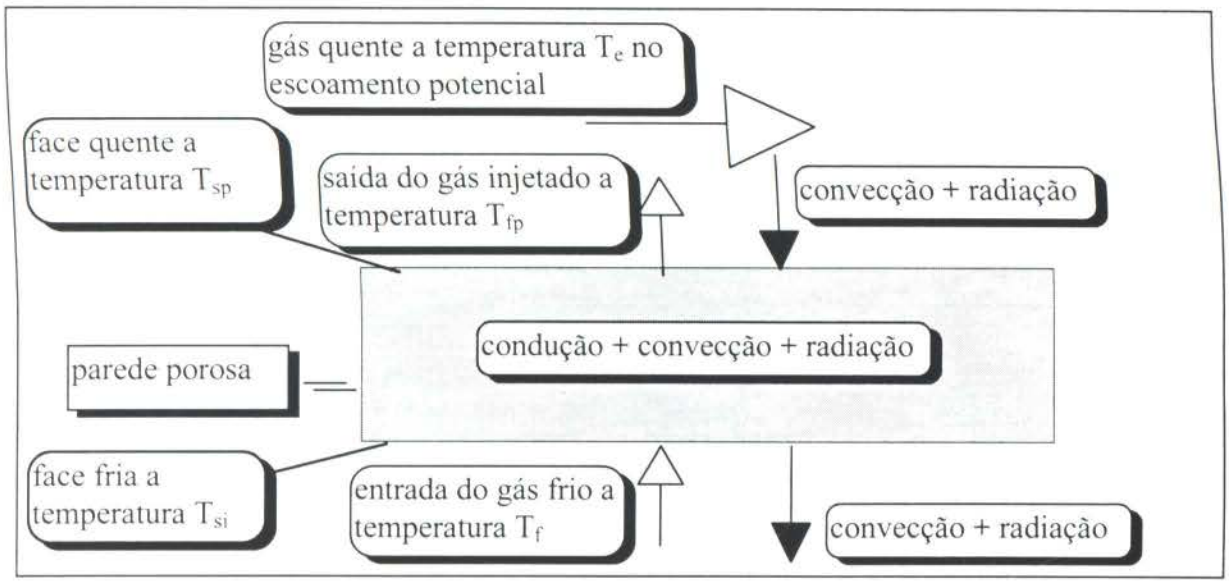

Figura 1 - Esquema térmico e hidrodinâmico do processo de resfriamento por transpiração de uma parede porosa sobre a qual escoa um gás quente.

2. DESCRIÇÃO SUCINTA DA MONTAGEM EXPERIMENTAL

Os resultados experimentais e teóricos usados neste trabalho referem-se a um canal de testes de aproximadamente 2 metros de comprimento com seção retangular de 0,2 metros de altura pôr 0,5 metros de largura. Ar aquecido em um trocador de calor e com intensidade de turbulência controlada pôr um retificado de fluxo do tipo colmeia passa no interior do canal, enquanto ar ambiente é injetado uniformemente na face inferior de uma placa porosa instalada na parede inferior do canal. Uma vista de topo da parede inferior do canal com a localização da placa porosa é apresentada na figura 2. As placas de aço hinos que compõem a parede inferior possibilitam o deslocamento discreto da placa porosa. A localização desta placa dentro do canal é tal que um escoamento turbulento do tipo camada limite, levemente acelerado, com número de Reynolds pouco superior a $2x10^5$ se estabelece em sua borda de ataque.

As medidas de velocidade do ar no interior do canal são feitas por meio de um tubo de pitot e de um anemômetro LASER-DOPPLER, enquanto tomadas de pressão e termopares instalados adequadamente fornecem medidas de pressão do ar e de temperatura do ar e da face inferior da parede porosa. Uma câmara infravermelho instalada na parede superior do canal permite o mapeamento da temperatura da face superior da placa porosa. A vazão do ar injetado é determinada por uma placa de orifício.

3. MODELOS ADOTADOS NA SIMULAÇÃO DO ESCOAMENTO COM INJEÇÃO

No estudo teórico do resfriamento por transpiração, o modelo k-ε a baixo número de Reynolds de Lam e Bremhost com a correção de Yap (Yap, 1987, França *et al.*, 1995) foi usado no escoamento turbulento dentro do canal, enquanto o modelo de equilíbrio térmico (Nield e Bejan, 1992) foi usado na parede porosa. A distribuição de pressão no interior do meio poroso foi obtida com o modelo de Andoh *et al.* (1994).

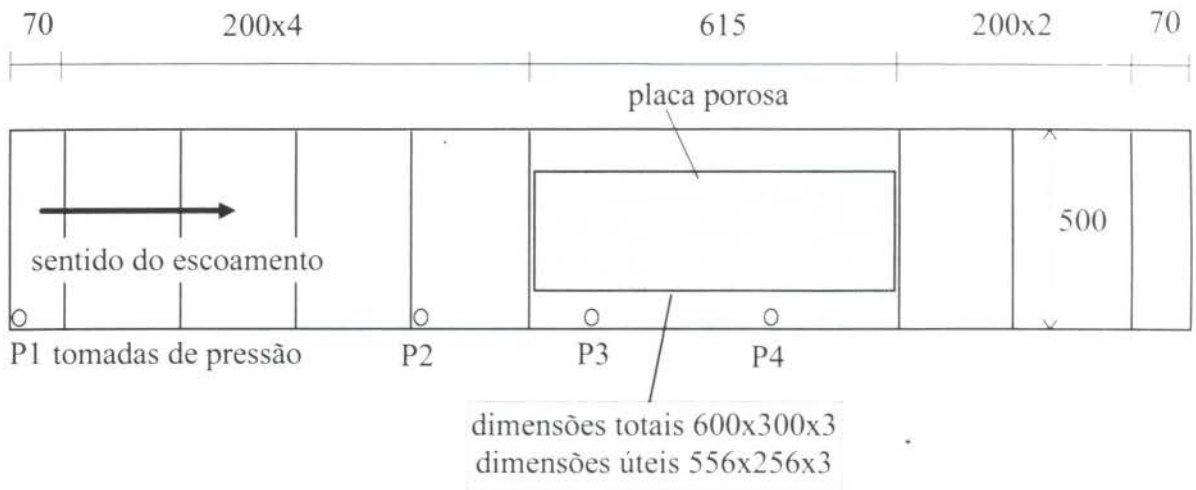

Figura 2. - Vista de topo da parede inferior do canal com a localização de uma placa porosa de duralumínio com 3 mm de espessura e 30% de porosidade (dimensões em mm).

4. APRESENTAÇÃO E ANÁLISE DOS RESULTADOS EXPERIMENTAIS E TEÓRICOS

Na figura 3 são comparados os perfis de temperatura teórico e experimental do ar dentro do canal, na região de injeção, a 0,5 mm de distância da parede inferior. A taxa de injeção é, neste caso, de 0,02 e as temperaturas do ar injetado e do ar no escoamento potencial são, respectivamente, 18 e 202°C. Verifica-se uma boa concordância entre os resultados do modelo e os resultados experimentais. Uma análise da figura 3 permite concluir que a temperatura do ar saindo sobre a face quente da parede porosa fica praticamente constante a partir de uma distância de cerca de 170 mm da borda de ataque da parede porosa (aproximadamente 30% do comprimento útil da placa). Isto sugere que a eficiência do resfriamento é menor neste trecho da placa. Entretanto, uma outra explicação para o fato seria uma maior iteração térmica e dinâmica, nesta região, da camada de ar quente com o jato de ar saindo da parede. Outra observação que pode ser feita pela análise da figura 3 é que o efeito

da transpiração sobre a temperatura da placa sólida a jusante da placa porosa tende a se anular rapidamente.

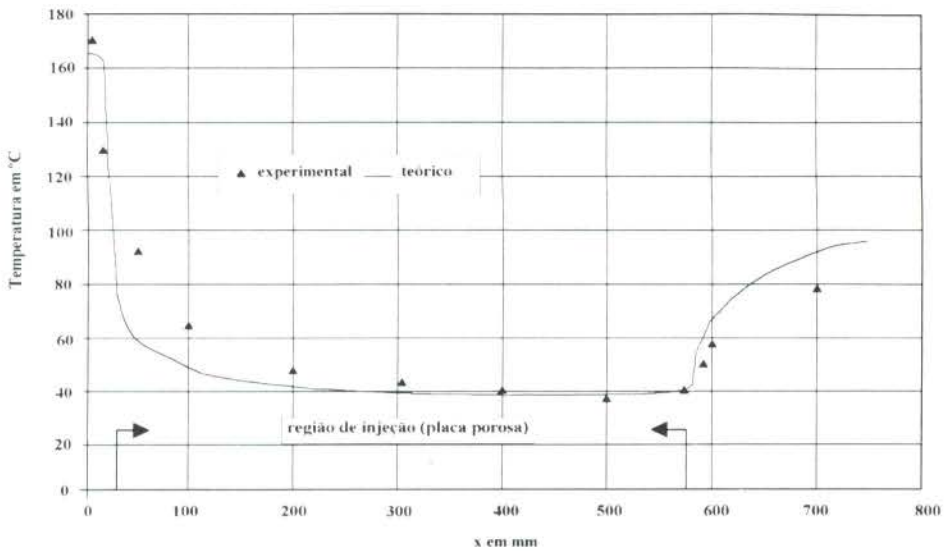

Figura 3 - Comparação entre os perfis experimental e teórico de temperaturas do ar a 0,5 mm da parede inferior do canal para uma taxa de injeção de 0,02.

A figura 4 apresenta uma comparação entre perfis de temperatura teóricos numa seção transversal do canal situada no meio da placa porosa, para 3 taxas de injeção. As temperaturas do ar injetado e do ar no escoamento potencial são, neste caso, iguais a 27 e 300°C respectivamente. O transporte de calor por radiação térmica não foi considerado nos cálculos. Assim, para escoamentos turbulentos com injeção e com efeitos de radiação térmica desprezíveis, os resultados desta simulação confirmam que:

- taxas de injeção superiores a 0,01 aumentam muito pouco a eficiência do resfriamento em relação a esta última
- a transferência de calor no interior da parede é o principal mecanismo responsável pelo seu resfriamento para baixas taxas de injeção (inferiores a 0,004)
- para altas taxas de injeção, praticamente toda a transferência de calor no interior da parede ocorre numa distância, medida a partir da face quente, igual a cerca de 20% da espessura total da parede porosa
- para taxas de injeção superiores a 0,01, a espessura da parede não tem influência sobre a eficiência do resfriamento por transpiração.

A tabela 1 apresenta valores médios de temperaturas do ar e da placa porosa determinadas com a câmara infravermelho e com termopares, durante testes experimentais com taxas de injeção de 1% e 2%. A nomenclatura da figura 1 foi utilizada. A temperatura, T_{fp}, do ar saindo sobre a face quente da parede porosa foi medida a uma distância de 0,5 mm da parede. A temperatura média, T_{sp}, da face superior da placa porosa foi estimada com o auxílio da câmara infravermelho, considerando uma emissividade constante e igual a 0,85

para a superfície da placa. Este valor médio foi obtido em testes de laboratório à temperatura ambiente.

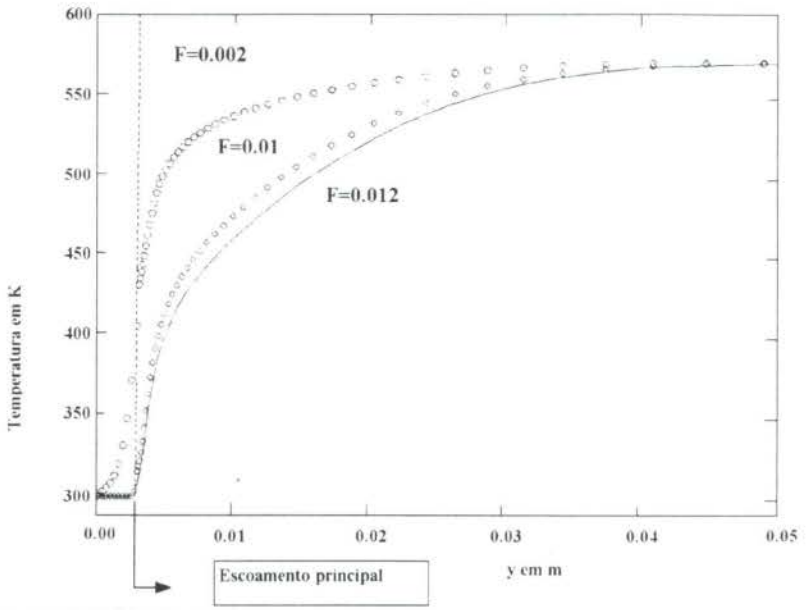

Figura 4 - Perfis teóricos de temperaturas na seção transversal do canal de testes situada no meio da placa porosa, para três taxas de injeção.

Tabela 1 - Temperaturas médias experimentais em graus Celsius e eficiência na região de injeção para escoamentos não isotérmicos no canal de testes e para duas taxas de injeção.

T_e	T_f	T_{si}	T_{sp}	T_{fp}	taxa de injeção	eficiência, η
200	29	34	128	77	1%	0,42
200	27	31	126	45	2%	0,43
250	46	54	154	110	1%	0,47
250	39	43	151	63	2%	0,47

A análise dos resultados da tabela 1 permite concluir que:

- não obstante os efeitos da radiação térmica, as eficiências de resfriamento para taxas de injeção de 1 % e 2% são praticamente iguais
- a eficiência do resfriamento por transpiração, que deveria ser igual a 1 sem a radiação térmica, é reduzida em mais de 50% pelo efeito da radiação térmica
- as diferenças acentuadas entre a temperatura do ar que atravessa a parede porosa (T_{fp}) e a temperatura da face quente da parede porosa (T_{sp}) indicam que a suposição de equilíbrio térmico entre o ar e o sólido no interior desta parede não é correta.

Além disto, o mapeamento com a câmara infravermelho da superfície superior da placa porosa, ao longo de sua linha mediana, mostrou um campo de temperatura praticamente

homogêneo. Isto indica que, para taxas de injeção superiores a 0,01, o comprimento da parede tem pouca influência sobre a eficiência do resfriamento por transpiração.

5. CONCLUSÕES

A análise de alguns dos resultados do estudo de França (1996) sobre o escoamento não isotérmico de ar quente num canal retangular, com injeção de ar ambiente através de uma placa porosa instalada na parede inferior do canal, conduz às seguintes conclusões, consideradas as mais importantes:

1. a espessura e o comprimento da parede porosa têm pouca influência sobre a eficiência do resfriamento por transpiração para taxas de injeção iguais ou superiores a 0,01. Para taxas inferiores, os resultados não são conclusivos
2. para taxas de injeção inferiores a 0,004, verifica-se que a maior parcela do transporte de calor para o ar injetado ocorre no interior da parede porosa; para taxas maiores, este transporte ocorre quase que integralmente numa distância da ordem de 20% da espessura da parede, contada a partir da sua face quente
3. confirma-se experimentalmente que uma taxa de injeção da ordem de 0,01 é suficiente para maximizar a eficiência do resfriamento por transpiração, mesmo em escoamentos onde os efeitos da radiação térmica são importantes
4. para temperaturas de ar quente no canal entre 200 e 300°C, os efeitos da radiação térmica diminuem em mais de 50% a eficiência do resfriamento por transpiração de ar ambiente
5. a suposição de equilíbrio térmico entre o ar e o sólido no interior da parede porosa, no modelamento teórico do resfriamento por transpiração, não é correta.
6. a transpiração tem efeito bastante limitado sobre o resfriamento da parede sólida imediatamente a jusante da região de injeção.

6. REFERÊNCIAS

Andoh,H.Y.,Lips,B.& Lallemand, A. Couplage transferts de masse e de chaleur dans une paroi poreuse. Application à la détermination des coefficients d'échange interne.. *Entropie,* N° 182, pp. 21-33,1994.

Beveridge, G.S.G. e Haughey, D.P. Axial heat transfer in packed beds. Gas flow through beds beween 20 and 650°C. *Int. J. Heat Mass Transfe*, Vol. 15, pp. 953-968*r*, 1972.

França, G.A.C.. Contribution a l'étude des écoulements pariétaux avec effusion. Application au refroidissement de parois. Tese de doutorado, INSA de Lyon, 197 pp, 1996.

França, G.A.C., Li, C. e Lallemand, **A.** Simulação, por volume finitos, do escoamento turbulento incompressível, não-isotérmico, no interior de um duto retangular, com injeção. *XV CILAMCE, Belo Horizonte, Brasil,* pp. 323-332, 1994.

França, G.A.C., Tedeschi, G. e Lallemand, A. Turbulent incompressible flow within a channel with transpiration : solution of the coupled problem porous wall - main flow. *13th Brasilian*

Congress and 2nd Iberian American Congress of Mechanical Engineering, 12-15 December, Belo Horizonte, Brasil. Proc,.pp.4, 1995.

Georgiou, D.P. e Louis, J.F. The transpired turbulent boundary layer in various pressure gradients and the blow-off condition *The American Sociey of Mechanical Engineers, Winter Annual Meeing*, ASME PAPER N° 84-WA/HT-71, pp.8, 1984.

Grootenhuis, P. The mechanism and application of effusion cooling. *The Journal of the Royal Aeronautical Sociey*, Vol. 63, N° 578, pp. 73-89, 1959.

Jeromin, L.O.F. The status of research in turbulent boundary layers with fluid injection. *Progress in Aeronautical Sciences*, Vol. 10, pp. 65-189, 1970.

Kar, K.K. *Heat and mass transfer caracteristics of the transpiration cooling.* Ph D. Thesis : Case Western Reserve University,. pp.337, 1980.

Koh, J.C.Y. e Colony, R. Analysis of cooling effectiveness for porous material in a coolant passage. *Transactions of ASME, Journal of Heat Transfer*, Vol. 96, pp. 324-330, 1974.

Koh, J.C., Dutton J.L., Benson, B.A. e Fortini, A. Friction factor for isothermal and nonisothermal flow through porous media. *Transactions of ASME, Journal of Heat Transfer*, Vol. 99, N° 3, pp. 367-373, 1977.

Kutateladze, S.S. e Leont'ev, A.I. *Heat transfer, mass transfer, and friction in turbulent boundary layers*. New York : Hemisphere Publishing Corporation, pp.302 , 1990..

Landis, R.B. e Mills, A.F. The calculation of turbulent boundary layers with foreign gás intestino. *Int. J. Heat Mass Transfer,* Vol. 15, pp. 1905-1932, 1972.

Moffat, R.J. e Kays, W.M. A review of turbulent boundary layer heat transfer research at Stanford, 1958-1983. *Advances in Heat Transferr*, Vol. 16, pp. 241-345, 1984.

Nicoud, F. *Prevision des transferts convectifs sur les protections thermiques d'un propulseur à propergol solide.* Toulouse : ONERA, 1993, pp. 282. N.T. 1993-15.

Nield, D.A. e Bejan, A. *Convection in porous media.* New York : Springer-Verlag, pp. 408, 1992.

Shcherbenko, I.V. Calculation for coefficients of heat and mass transfer in injection of a gas into a turbulent boundary layer of a different gas. *Heat Transfert - Soviet Research*, Vol. 20, N° 1, pp. 31-39, 1988.

Yap, C. *Turbulent heat and momentum transfer in recirculating and impinging flows.* Ph.D. Thesis : Faculty of Technology, University of Manchester, U.S.A, pp. 187, 1987.

Yammamoto, S. Effect of porosity in transpiration cooling system. *17th Int. Symposium on Space Technology and Sciences, Tokyo, Japan, ,20-25 mai* Vol. 2, pp. 2355-2360, *1990.*

Tema 34

Escoamentos Multifásicos

XIV Brazilian Congress of Mechanical Engineering
Obeid Plaza Hotel Convention Center - Bauru - SP/Brazil
December 08-12th 1997

PAPER CODE: COB758

ESTUDO DA MOVIMENTAÇÃO DO LEITO DE INERTES EM SECADOR ROTATÓRIO / *STUDIES OF INERTS BED DYNAMICS IN ROTARY DRYER*

MAURO MARQUES BURJAILI* & THEO GUENTER KIECKBUSCH**

* *Departamento de Engenharia Química - UFU - Uberlândia*
cep 38400-902 - Uberlândia, MG - E-mail: mmburjaili@ufu.br

** *Departamento de Termofluidodinâmica - Faculdade de Engenharia Química - Unicamp - Campinas*
cep 13081-920 - Campinas, SP

Abstract

Studies of the bed behaviour of a rotary dryer packed with inerts, utilized to drying pastelike materials, was performed as a function of rotation and geometrical parameters of the internal parts of the equipment, like the width, thickness, number and inclination of longitudinal flights, by film recording, made for a better visualization of the bed dynamics, composed by polyethylene and ceramic spheres.

Keywords

Rotary Dryer; Bed of Inerts Behaviour; Drying in Inert Bed; Pastelike Materials / Secador Rotatório; Comportamento de Leito de Inertes; Secagem em Leito de Inertes; Materiais Pastosos.

1. INTRODUÇÃO

O secador rotatório com recheio de inertes (SRRI) é um equipamento utilizado no processamento de materiais pastosos, utilizando-se simultaneamente das operações unitárias de secagem e moagem (Burjaili et al., 1994; Burjaili & Finzer, 1991; Finzer et al., 1992).

Consta de um cilindro horizontal ocupado por aletas dispostas longitudinalmente, chicanas e esferas de material inerte (polietileno, aço ou cerâmica). As aletas e chicanas formam um corpo único fixado à parede interna do cilindro, ao longo de todo o seu comprimento. As esferas, que constituem o leito de inertes, ocupam parcialmente o volume do cilindro (Burjaili et al., 1987; Álvares, 1990; Finzer et al., 1992).

O equipamento compõe uma instalação de secagem tradicional, que consta de sistemas de alimentação e aquecimento de ar; de alimentação de material a ser processado (materiais pastosos); de rotação do cilindro e de separação e coleta do material em forma de pó produzido (Burjaili, 1996).

A ação combinada da rotação do cilindro e das aletas leva à formação contínua de uma cortina de inertes na seção transversal do cilindro, uma vez que os inertes são levados continuamente da parte inferior para a superior do mesmo, como ocorre nos secadores

rotativos, em que se verificam os efeitos cascata e rolagem dos sólidos submetidos à secagem (Baker, 1988). Caracteriza-se, assim, a formação de uma área importante para a troca de calor e massa, com aproveitamento do calor convectivo do ar em escoamento. Além disso, a movimentação dos inertes permite que ocorra a operação de moagem do material seco que reveste as esferas, após a secagem.

Adicionalmente ao aproveitamento do calor convectivo do ar de secagem, o SRRI utiliza-se do princípio da secagem via contato, à medida que os corpos inertes, aquecidos pelo ar, transferem calor condutivo ao material pastoso que os reveste (Kudra, 1992).

A movimentação dos inertes, além de induzir a troca de calor e massa, é responsável pela operação de moagem no secador. Ela é importante para o desenvolvimento e renovação contínuos da interface gás-sólido que deve ocorrer na secagem com o SRRI, característica dos secadores de película: seco o material que reveste os inertes, a camada endurecida de revestimento é destruída pela ação de impacto e atrito dos inertes, expondo novamente a superfície dos inertes para a nova alimentação pastosa (Strumillo et al., 1983).

Outra vantagem associada à movimentação do leito de inertes no SRRI é a atenuação da aglomeração e aderência do material pastoso ao corpo interno do secador, muito comuns nos secadores de material pastoso (Strumillo et al., 1983).

O objetivo do trabalho é a determinação da velocidade de rotação do secador, correspondente à melhor distribuição dos inertes pela seção transversal do cilindro. Como a distribuição radial dos inertes depende do corpo interno do secador, a determinação da velocidade exigiu o estudo do seu arranjo interno, resultando no estudo do dimensionamento das aletas e do leito de inertes. Os resultados foram transpostos para o secador real através do emprego do princípio da similaridade geométrica.

2. MATERIAIS E MÉTODOS

2.1 Instalação Experimental

A instalação experimental consta de um "secador" modelo acoplado a um sistema motor com variador de velocidade. Neste estudo não houve movimentação de ar pelo leito de inertes.

O modelo era composto de um cilindro de PVC (cloreto de polivinil), com diâmetro de 0,195m e comprimento de 0,2m; um corpo interno formado por duas placas circulares (uma de acrílico e a outra de PVC, ambas com encaixes) e um conjunto de aletas de PVC, com comprimento de 0,195m, larguras de 0,039m, 0,049m ou 0,059m e em número de 3, 4, 6 ou 8; um volume de corpos inertes (esferas) de polietileno (diâmetro 0,017m) e de cerâmica (diâmetro 0,02m).

As extremidades das aletas adentravam os respectivos encaixes das placas, compondo o corpo interno do modelo (Figura 1). Esses encaixes permitiram que o corpo interno fosse montado com diversos arranjos, podendo-se variar o número e também a inclinação das aletas (70°, 90° e 110°). A placa de acrílico permitiu a visualização da movimentação dos inertes.

Ao sistema motor (0,5cv, 1710rpm e 60Hz) foi acoplado um variador eletrônico de velocidade, com variação conjunta de tensão/frequência, com torque constante (Figura 1).

2.2 Procedimento Experimental

Uma vez estabelecido o arranjo do corpo interno (número, largura e inclinação das aletas), o mesmo era introduzido no cilindro, juntamente com os corpos inertes. O cilindro acoplava-se ao sistema motor e a movimentação do leito, em função da rotação do cilindro e observada via placa de acrílico, era registrada com uma filmadora. Quantificava-se o tempo

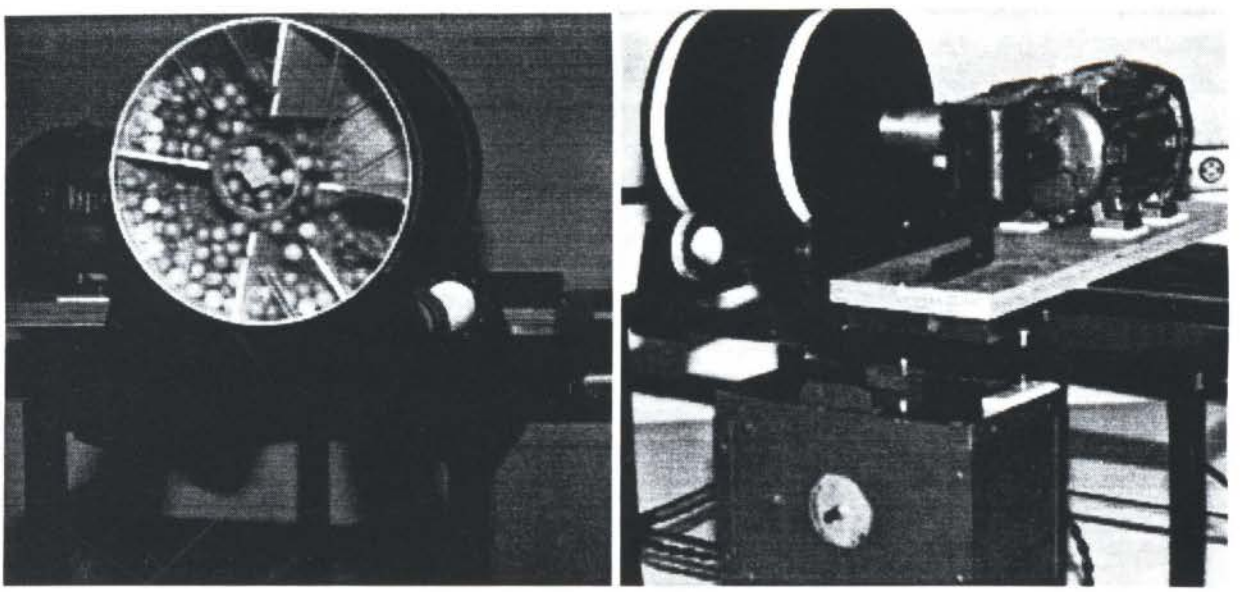

Figura 1: Instalação experimental do secador modelo.

gasto (medido por meio de um cronômetro digital com resolução de centésimo de segundos) até a ocorrência de um determinado número de voltas do cilindro. O procedimento era repetido para outros arranjos do corpo interno e outros volumes do leito de inertes.

Em seguida, visualizavam-se as filmagens geradas, utililizando-se, particularmente, o recurso de câmaras lenta e rápida, que permitiu a realização de observações pormenorizadas da trajetória das partículas do leito ao longo da seção transversal do cilindro.

A constatação visual da ocorrência dos efeitos cascata e rolagem dos inertes, com varredura da seção transversal, foi o critério empregado para caracterização de dinâmica adequada do leito.

Um item adicional para uma dinâmica adequada do sistema foi a necessidade de se manter livre a região próxima ao eixo do cilindro para não dificultar o jateamento da alimentação do material pastoso, quando da operação de secagem do equipamento real.

O volume do leito, representado por z (distância da base do cilindro até o nível dos inertes), referenciou-se à carga relativa à dos moinhos de bola, cerca de 50,0% do volume interno do cilindro (McCABE et al., 1993). Assim, utilizaram-se leitos com volume ligeiramente superior (z=0,115m), ligeiramente inferior (z=0,08m) e consideravelmente inferior (0,05) à metade do volume do cilindro.

Os ensaios foram realizados em duas etapas. Inicialmente, utilizaram-se inertes de polietileno e, posteriormente, de cerâmica, para averiguação da influência da massa específica das partículas na movimentação do leito.

3. RESULTADOS

3.1 Ensaios com Inertes de Polietileno

A massa específica das esferas foram determinadas, resultando o valor de 160kg/m^3, com incerteza de 8,55kg/m^3 (Holman, 1989).

Para todos os arranjos, foram realizados ensaios com pelo menos quatro rotações diferentes, varrendo-se uma faixa entre 10 a 90rpm, de modo a se poderem observar diversas movimentações do leito de inertes.

Verificou-se a situação de predomínio da rolagem das esferas inertes (baixas rotações), seguindo-se do efeito cascata progressivo, à medida que a velocidade de rotação aumentava e, finalmente, a tendência - e em alguns casos a consumação - da centrifugação do leito, quando as rotações eram muito elevadas.

Foram também constatadas as combinações rolagem e cascata, com varredura (ocupação contínua da secão transversal do cilindro) dos corpos inertes nos dois primeiros quadrantes da seção transversal do cilindro, caracterizando a dinâmica adequada do leito de inertes.

O volume correspondente ao z=0,08m caracterizou o leito com melhor dinâmica. O leito com z=0,115m apresentou uma dinâmica em que predominou a rolagem das partículas, mesmo a rotações elevadas; o leito com z=0,05m, embora favorecendo o efeito cascata, permitiu a ocorrência de muitos vazios na seção transversal do cilindro, o que comprometeria a área do leito disponível tanto para a recobrimento da alimentação quanto para a transferência de calor, na operação de secagem do equipamento.

As velocidades de rotação correspondentes às melhores movimentações dos inertes, para diversos arranjos, são apresentadas na Tabela 1. Essas velocidades, embora conduzissem às melhores movimentações do leito, não necessariamente representaram condições de dinâmica adequadas, com base no critério adotado. Constatou-se que o aumento da rotação do cilindro melhorava o comportamento geral do sistema; porém, para aletas de 110° e 90° e largura de 0,039m, os níveis de velocidades de rotação empregados foram elevados, relativamente aos comumente utilizados em secadores rotativos, em torno de 15rpm (STRUMILLO et al., 1983).

Tabela 1: . Velocidade de rotação do cilindro em função da inclinação (α), largura (L) e do número de aletas (esferas de polietileno, z=0,08m).

α	L	Rotação do cilindro (rpm)			
(°)	(m)	8 aletas	6 aletas	4 aletas	3 aletas
	0,039	76,6	-	-	-
110	0,049	72,9	-	-	-
	0,059	-	-	-	-
	0,039	65,5	64,7	71,2	72,6
90	0,049	54,9	50,2	65,2	68,2
	0,059	55,7	55,6	55,5	55,5
	0,039	36,6	38,6	38,6	-
70	0,049	29,9	32,7	32,7	41,2
	0,059	-	31,7	31,7	37,7

Os níveis de velocidade necessários, ainda que altos, decresceram, quando aletas mais largas foram empregadas. Para as mesmas 8 aletas de 110°, nas condições mencionadas, o aumento da largura (L) para 0,049m requereu uma velocidade de 72,9rpm, menor que a anterior; para 8 aletas de 90°, a velocidade necessária também diminuiu, sendo 54,9rpm. O aumento da largura das aletas elevou o *holdup* de esferas (quantidade de esferas presentes na aleta), melhorando a distribuição das mesmas ao longo da seção transversal do cilindro, particularmente na região correspondente ao primeiro quadrante. Verificou-se, porém, que esse aumento da largura das aletas, por causa da consequente diminuição da distância entre as extremidades das aletas contíguas, favorecia a retenção das esferas no espaço entre aletas. Em consequência, reduziu-se o efeito cascata dos inertes. Esta sobrecarga poderia levar a uma possível aglutinação do leito pastoso, durante a operação de secagem. Por outro lado, ficou implícita a existência de um limite mínimo para a largura das aletas, que permite a manutenção

de espaços vazios na seção transversal do cilindro. Esta condição é contornável com o uso de velocidades de rotação mais altas, como pode ser verificado na Tabela 1, para 3 aletas.

O número de aletas influenciou significativamente a dinâmica das partículas. O uso de muitas aletas tendeu a agravar a sobrecarga de inertes no espaço entre aletas, principalmente quando combinadas com larguras grandes. Um número pequeno de aletas provocou incidência acentuada de espaços vazios na seção transversal do cilindro, principalmente no primeiro e quarto quadrantes, exigindo a elevação das velocidades requeridas para revolver o leito.

A queda nos níveis de velocidade adequados a uma dinâmica satisfatória foi também verificada quando a inclinação das aletas foi reduzida, como indicado na Tabela 1. Nota-se que as velocidades em torno de 55 a 65rpm caem para 30 a 37rpm, quando o ângulo das aletas passa de 90 para 70°. Este efeito, certamente, é devido ao aumento do tempo de retenção dos inertes nas aletas, em consequência do decréscimo na inclinação das mesmas, de modo que os inertes puderam alcançar o primeiro quadrante do cilindro.

A visualização dos filmes dos ensaios da dinâmica do leito revelou que dois dos trinta arranjos geométricos testados produziram movimentações adequadas no leito: (a) 4 aletas, largura de 0,059m, inclinação de 70° e z=0,08m, cilindro a 31,7rpm; (b) 6 aletas, largura de 0,039m, inclinação de 70° e leito com z=0,08m, cilindro 31,0rpm. Selecionou-se o arranjo (a) como o melhor, sobretudo porque se observou uma varredura contínua das partículas ao longo dos dois primeiros quadrantes da seção transversal do cilindro (Figura 2). Além disso, uma menor quantidade de aletas (4) estabelece um maior volume disponível para o leito, permitindo que ele seja composto de maior número de inertes. Isto é de grande valia na operação do SRRI, pois, além de incrementar a área do leito para recebimento da alimentação e troca térmica com o ar, diminui a área total do conjunto aletas-chicanas, potencialmente retentora de material pastoso processado na operação do secador real.

3.2 Ensaios com Inertes de Cerâmica

Com base nos resultados com esferas de polietileno utilizaram-se arranjos com 6 e 4 aletas; inclinações de 90 e 70°; larguras de 0,039m, 0,049m e 0,059m e volume do leito dado por z=0,08m. As rotações empregadas foram 10rpm, 20rpm e 30rpm.

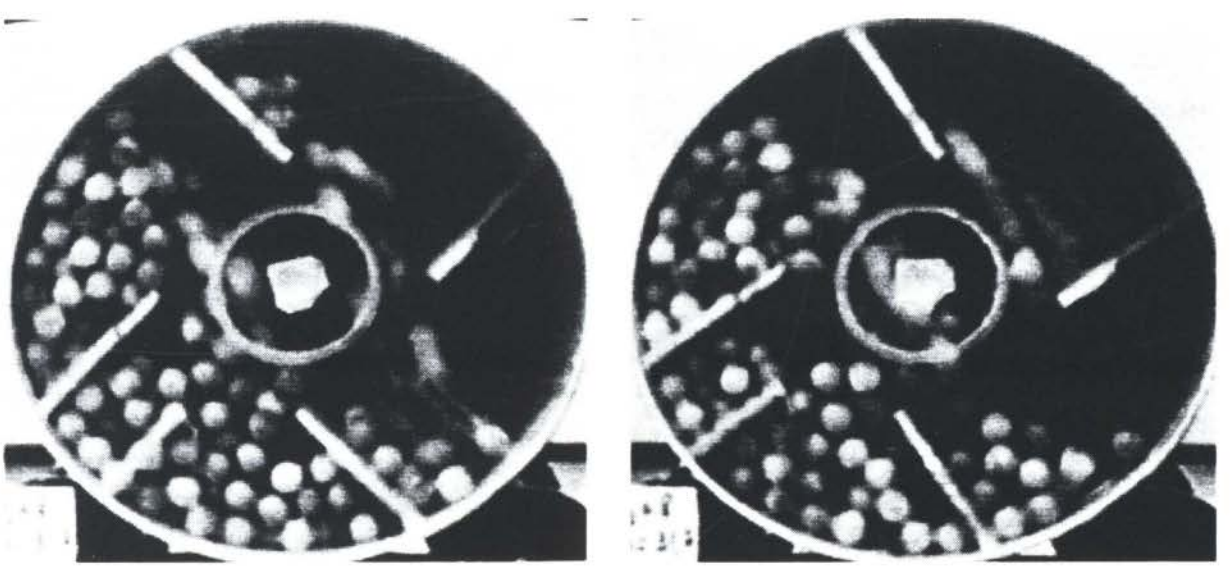

Figura 2: Distribuição do leito de inertes de polietileno para duas posições do cilindro.

Verificou-se a ocorrência de varredura na movimentação dos inertes. Para os arranjos com aletas de 90°, porém, mesmo nas velocidades da ordem da máxima (30rpm), observaram-se muitos vazios na seção transversal do cilindro, particularmente no primeiro quadrante. Isso confirmou a má capacidade das aletas desses arranjos em reter inertes, impossibilitando a ocorrência de cascatas no primeiro quadrante.

Com as aletas de 70°, constatou-se o transporte dos inertes até o primeiro quadrante, favorecido pela menor inclinação das aletas.

As mesmas observações feitas nos ensaios com recheio de polietileno são aplicáveis, em relação à largura das aletas.

O arranjo de 4 aletas inclinadas de 70°, largura de 0,059m, volume do leito equivalente a z=0,08m e velocidade de rotação do cilindro de 33rpm produziu uma movimentação considerada a mais próxima da adequada (Figura 3).

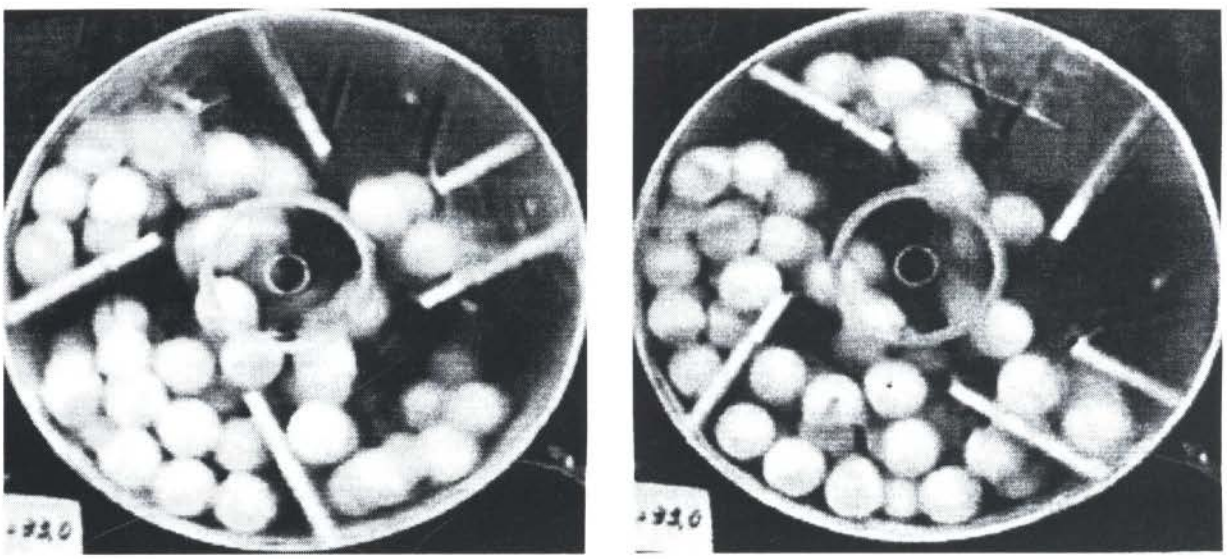

Figura 3: Distribuição do leito de inertes de cerâmica para duas posições do cilindro.

Houve boa distribuição dos inertes por toda seção transversal do cilindro: rolagem no segundo quadrante e cascata no primeiro; adiantamento da varredura das partículas na seção transversal do cilindro, a partir do segundo quadrante; transporte de partículas até o primeiro quadrante, devido ao menor ângulo das aletas. Observou-se, ainda, liberação intermitente desejável dos inertes da região axial do cilindro, para alimentação na operação de secagem.

3.4 Secador Real

Os resultados obtidos com o secador modelo foram utilizados para especificação do arranjo interno do secador real (diâmetro 0,25m e comprimento 0,60m).

Assim, o número de aletas determinou-se como 4 e a inclinação como 70°. Quanto ao comprimento delas, utilizou-se a similaridade geométrica entre o secador modelo e o real. Obteve-se o comprimento de 0,075m, considerando-se a razão entre os diâmetros de ambos os secadores e o comprimento das aletas do secador modelo determinado nos ensaios de dinâmica do leito (z=0,08m).

O diâmetro das esferas do secador real também foram determinados por similaridade geométrica. Obteve-se o valor de 0,025m, considerando-se novamente os diâmetros de ambos os secadores e o das esferas utilizadas nos experimentos com o secador modelo.

O volume do leito de inertes, do mesmo modo, calculou-se por similaridade, resultando z=0,10m. Esse valor foi obtido, aplicando-se a razão entre o diâmetro e o comprimento z, referentes ao secador modelo, ao diâmetro do secador real (0,25m). Após a construção do secador real, ensaios da dinâmica do leito de inertes nele realizados confirmaram o valor determinado de z.

4. CONCLUSÕES

O secador rotatório modelo associado à utilização da técnica de filmagem foi metodologicamente fundamental para a interpretação dos dados experimentais.

A ação de rolagem e impacto dos inertes foi melhorada pela utilização de esferas de maior massa específica (esferas de cerâmica).

O critério de estabelecimento da dinâmica adequada dos inertes deve levar em conta que a região axial não deve ficar obstruída, para evitar problemas na alimentação do material pastoso, quando da operação de secagem no secador real.

Os resultados obtidos com o secador modelo permitiram dimensionar, por similaridade geométrica, o secador real: rotação do cilindro igual a 33rpm, 4 aletas de largura igual a 0,075m e inclinação de 70°.

Esse arranjo propiciou uma movimentação adequada do leito de inertes, caracterizando uma área importante para troca de calor e massa na operação de secagem, verificada quando da movimento do leito no secador real.

5. REFERÊNCIAS

Álvares, C.M. Secagem de Melaço de Cana-de Açúcar em Secador Rotatório com Recheio de Inertes, *Dissertação (Mestrado)*, Universidade Federal de Uberlândia, Uberlândia, MG, 1990. 122p.

Baker, C.G.J. The Design of Flights in Cascating Rotary Dryers, *Drying Technology*, vol. 6, n. 4, pp. 631-654, 1988.

Burjaili, M.M. Desenvolvimento de um Secador Rotatório com Recheio de Inertes, *Tese de Doutorado*, Universidade Estadual de Campinas, Campinas, 1996. 218p.

Burjaili, M.M.; Finzer, J.R.D. Desempenho de um secador rotatório com recheio de nertes na secagem de dispersões, Anais do XIX Encontro Sobre Escoamento em Meios Porosos, pp. 556-567, Campinas, 1991.

Burjaili, M.M.; Finzer, J.R.D.; Limaverde, J.R. Secador rotatório com recheio de inertes. Int. Cl. A63B 11/00. BR n. PI8804812. 14 set. 1988; 29 mar. 1994. Revista da Propriedade Industrial, Rio de Janeiro, RJ, n. 1217, p. 36, 29 mar., 1994.

Burjaili, M.M.; Limaverde, J.R.; Finzer, J.R. Secador rotatório com recheio de inertes: I-Desempenho do equipamento, Anais do XV Encontro Nacional Sobre Escoamento em Meios Porosos, pp. 493-499, Uberlândia, 1987.

Finzer, J.R.; Burjaili, M.M.; Limaverde, J.R. Alternativa Tecnológica de Secagem de Materiais Pastosos - secador rotatório com recheio de inertes, *Ciência e Engenharia*, vol. 2, n. 2, pp. 97-120, Uberlândia, 1993.

Finzer, J.R.; Burjaili, M.M.; Limaverde, J.R.; Kieckbusch, T.G. Produção de milho verde em pó desidratando-se os grãos ou a pasta do material, Anais do XX Encontro Nacional Sobre Escoamento em Meios Porosos, pp. 543-554, São Carlos, 1992.

Holman, J.P. Experimental methods for engineers, McGraw-Hill, Singapura, 514p., 1989.

Kudra, T. Novel Drying Technologies for Particulates, Slurries and Pastes, *Drying 92*. Mujundar, A.S. (ed.), Elsevier Science Publishers B.V., p. 224-239, 1992.

McCabe, L.W.; Smith, C.J.; Harriot, P. Unit operations of chemical engineering, McGraw-Hill, New York, 130p, 1993.

Strumillo, C.; Markowski, A.; Kaminski, W. Modern Developments in Drying of Pastelike Materials, *Advances in Drying*, Mujundar, A.S. (ed.), Editora McGraw Hill, vol.2, pp.193-231, 1983.

XIV Brazilian Congress of Mechanical Engineering
Obeid Plaza Hotel Convention Center - Bauru - SP/Brazil
December 08-12th 1997

PAPER CODE: COB1119

ANÁLISE DA ACELERAÇÃO EM SISTEMAS DE TRANSPORTE PNEUMÁTICO VERTICAL EM FASE DILUÍDA/ *ANALYSIS OF THE ACCELERATION IN VERTICAL PNEUMATIC TRANSPORT SYSTEM IN DILUTE PHASE*

NAPOLEÓN GONZÁLEZ BENITEZ & ANDRÉ LUIZ AMARANTE MESQUITA
Grupo de Turbomáquinas - Departamento de Engenharia Mecânica - Universidade Federal do Pará
CEP - 66075-900 Guamá, Brasil E-mail: gtdem@amazon.com.br

Abstract

This work presents a model to analysis the gas-solid vertical flow in dilute phase based on one-dimensional, isothermal and steady-state on balances equation. With this model the length of the acceleration region is calculated and the pressure loss can be analyzed. The results from the present model are confronted with experimental data available in the literature, and a good agreement is observed.

Palavras Chaves

Pneumatic Transport/ Transporte Pneumático
Gas-Solid Flow/Escoamento Gás-Sólido
Dilute Phase/Fase Diluída
Acceleration Region/Região de Aceleração

1. INTRODUÇÃO

A perda de energia na região de aceleração em sistema de transporte pneumático em fase diluída é geralmente desprezada, principalmente pela complexidade que envolve o estudo das variáveis nesta região, o que requer um bom entendimento da dinâmica do escoamento da mistura gás-sólido em tubos e capacidade para predizer tal comportamento.

Sempre que partículas sólidas são introduzidas em um escoamento de um fluido ou mesmo quando a mistura encontra um acidente como válvula, cotovelos, etc., ocorre uma região onde os fluidos e as partículas possuem variação de velocidade até a região de escoamento completamente estabelecido, provocando, portanto, uma perda de carga adicional na linha de transporte.

A Figura 1 mostra a queda de pressão ao longo do sistema de transporte pneumático vertical em um fluxo de suspensão da mistura gás-sólido em fase diluída, onde ΔP_A e ΔP_T correspondem a queda de pressão na região de aceleração e a total, respectivamente.

Somente na década de sessenta surgiram as primeiras correlações considerando a queda de pressão na região de aceleração. Devido a complexidade da determinação do limite entre as duas regiões de escoamento distinto e a dificuldade de se determinar os parâmetros que descrevem o tipo de escoamento da mistura, as correlações propostas apresentam grandes limitações quanto a consistência do resultado de suas aplicações, ficando restritas a uma pequena faixa de condições.

Neste presente trabalho, utilizando os modelos para escoamento da mistura gás-solido em fase diluída apresentados por Benitez (1997), foi feita uma análise da perda de carga na região de aceleração, comparando os resultados teóricos com os dados experimentais de Silva (1984).

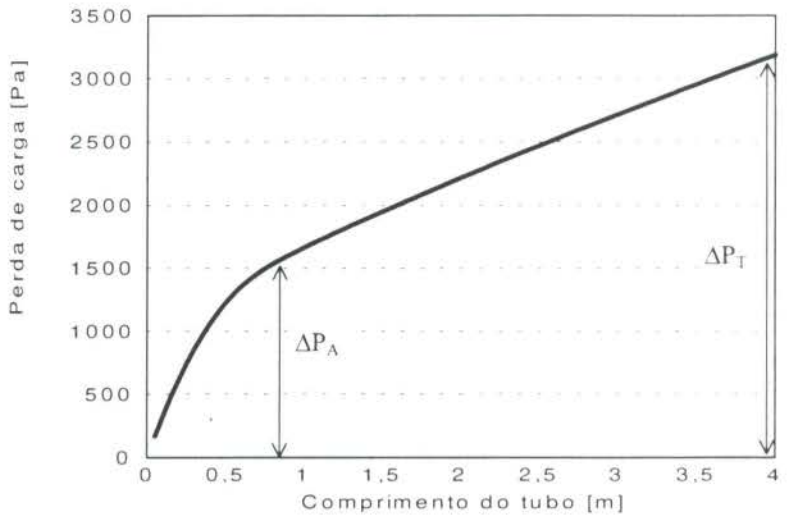

Figura 1 – Variação da perda de carga ao longo da tubulação

2. PERDA DE CARGA NA REGIÃO DE ACELERAÇÃO EM UM TUBO VERTICAL

Para a determinação da perda de carga na zona de aceleração em um tubo vertical, com escoamento em fase diluída, a equação do momento para a mistura gás-sólido na forma integral é geralmente adotada e é expressa como:

$$\Delta P_A = \int_{v_{s1}}^{v_{s2}} \rho_s(1-\varepsilon)v_s dv_s + \int_0^{L_A} \rho_s(1-\varepsilon)g dL + \int_0^{L_A} \frac{2f_g\rho_g v_g^{\,2}}{D_T} dL + \int_0^{L_A} \frac{2f_s\rho_s(1-\varepsilon)v_s^{\,2}}{D_T} dL \quad (1)$$

onde ε é a porosidade ou fração volumétrica do gás, v_s é a velocidade do sólido, v_g é a velocidade do gás, ρ_g é a densidade do gás, ρ_s é a densidade do sólido, f_g é o coeficiente de atrito entre o gás e a parede do tubo; f_s é o coeficiente de atrito entre o sólido e a parede do tubo, g é a gravidade e D_T é o diâmetro do tubo. Os limites de integração para a velocidade do sólido foram estabelecidos levando em conta a aceleração desde uma condição inicial de velocidade dos sólidos v_{s1} até a velocidade do regime estabelecido v_{s2}.

A grande dificuldade encontrada em aplicar a equação (1) consiste em encontrar o valor do comprimento de aceleração L_A a ser utilizado. São poucos os trabalhos experimentais existentes na literatura propondo correlações para o comprimento de aceleração. As correlações apresentadas por Shimizu *et al.* (1968) e Rose e Ducworth (1969) são restritas a uma pequena faixa de condições.

Klinzing (1981) e Silva (1984), utilizando um balanço de momento para a fase sólida em sua forma integral, apresentaram, respectivamente, as seguintes expressões para L_A:

$$\int_0^{L_A} dL_A = \int_{v_{s1}}^{v_{s2}} F_1 dv_s = \int_{v_{s1}}^{v_{s2}} \frac{v_s dv_s}{\frac{3}{4} C_{Ds} \varepsilon^{-4,7} \frac{\rho_g (v_g - v_s)^2}{(\rho_s - \rho_g) d_p} - \frac{2 f_s v_s^2}{D_T} - g} \tag{2}$$

$$\int_0^{L_A} dL_A = \int_{v_{s1}}^{v_{s2}} F_2 dv_s = \int_{v_{s1}}^{v_{s2}} \frac{v_s dv_s}{\frac{m}{(1-\varepsilon)\rho_s} - \frac{2 f_s v_s^2}{D_T} - g} \tag{3}$$

onde m na equação (3) representa a força resistiva por unidade de volume. Correlações de Massarani e Santana (1980) foram utilizados por Silva (1984) para descrever este valor; C_{Ds} é o coeficiente de arrasto, e d_p é o diâmetro da partícula sólida.

As Figs. 2 e 3 mostram, respectivamente, o comportamento das funções F_1 e F_2.

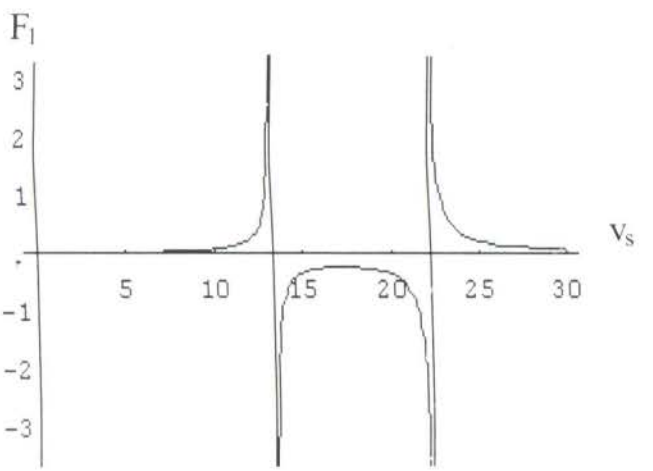

Figura 2 – Comportamento da função F_1.

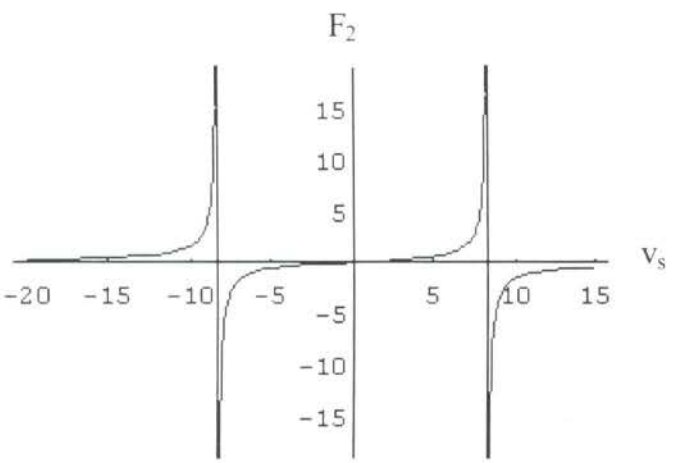

Figura 3 - Comportamento da função F_2

Observa-se nas Figs. 2 e 3 que as funções F_1 e F_2 apresentam pontos de singularidades, e, portanto, os métodos numéricos tradicionais de integração não são adequados na resolução dessas integrais. Além dessa limitação, os dois modelos utilizam o valor da porosidade calculado na região de regime estabelecido; requerem equações adicionais para o cálculo dos parâmetros ε, v_s, e v_g; a força resistiva por unidade de volume m na formulação de Silva (1984) é obtida a partir da resolução numérica de um conjunto de equações através de um processo iterativo.

Nos modelos estabelecidos por Benitez (1997), para o escoamento do gás-sólido em fase diluída, foi considerado que o tamanho das partículas sólida é uniforme e que as partículas possuam a mesma massa específica. O escoamento é considerado unidimensional, permanente, incompressível e isotérmico. Diante dessas considerações, o autor apresentou dois modelos para a análise de escoamento de gás-sólido em fase diluída, sendo compostos por dois sistemas de equações diferenciais ordinárias. O sistema de equações que utiliza a extensão do modelo de Gidaspow (1978) é referenciado como Modelo 1 e é formado por:

$$\frac{dv_g}{dx} = -\frac{v_g}{\varepsilon}\frac{d\varepsilon}{dx} \tag{4}$$

$$\frac{dv_s}{dx} = \frac{v_s}{(1-\varepsilon)}\frac{d\varepsilon}{dx} \tag{5}$$

$$\frac{dP}{dx} = -(1-\varepsilon)\rho_s v_s \frac{dv_s}{dx} - \varepsilon\rho_g v_g \frac{dv_g}{dx} - g[\rho_s(1-\varepsilon)+\rho_g\varepsilon]\operatorname{sen}\theta - \frac{2\varepsilon\rho_g v_g{}^2 f_g}{D_T} - \frac{2(1-\varepsilon)\rho_s v_s{}^2 f_s}{D_T} \tag{6}$$

$$\frac{d\varepsilon}{dx} = \frac{\left[F_D - g\rho_s \operatorname{sen}\theta - \dfrac{2\rho_s v_s{}^2 f_s}{D_T}\right]}{\rho_s(v_g - v_s)\left[\dfrac{v_g}{\varepsilon} + \dfrac{v_s}{(1-\varepsilon)}\right]} \tag{7}$$

e o segundo sistema de equações, referenciado como Modelo 2, envolve a extensão do modelo de SOO (1969) e é formado por (4), (5), (6) e

$$\frac{d\varepsilon}{dx} = \frac{\left[F_D - g\rho_s \operatorname{sen}\theta - \dfrac{2\rho_s v_s{}^2 f_s}{D_T}\right]}{\dfrac{\rho_s v_s{}^2}{(1-\varepsilon)}} \tag{8}$$

onde θ é o ângulo que forma o eixo do tubo com a linha horizontal e F_D é a força de arrasto por unidade de volume da partícula.

3. RESULTADOS

Os dois sistemas de equações diferenciais foram resolvidos pelo método tradicional de Runge Kutta de quarta ordem. Os números de Reynolds, Re e Re_s, o coeficiente de arrasto C_{Ds}, o fator de atrito entre gás-parede e sólido parede, f_g, e f_s, respectivamente, são recalculados para cada comprimento da malha ao longo da tubulação.

No sentido de validar os modelos, foram utilizados os valores experimentais obtidos por Silva (1984), em um sistema vertical de 4,0 m de altura e de 5 cm de diâmetro, com partículas sólidas de 0,4; 1,0; 1,2 e 1,7 mm de diâmetro médio e com a mesma densidade, 2500 Kg/m^3. Nesse experimento, o fluxo de massa do gás e do sólido e queda de pressão, tanto na região de aceleração como na região de escoamento estabelecido, foram medidos. Os valores de queda de pressão ao longo da seção de teste em cada transporte de mistura, foram colocados em gráficos sob a forma de pressão em função do comprimento do tubo determinado-se a partir dos quais o comprimento de aceleração. Este parâmetro foi definido pelo início da faixa de variação linear da pressão em função do comprimento do duto, como mostrado na Fig. 4.

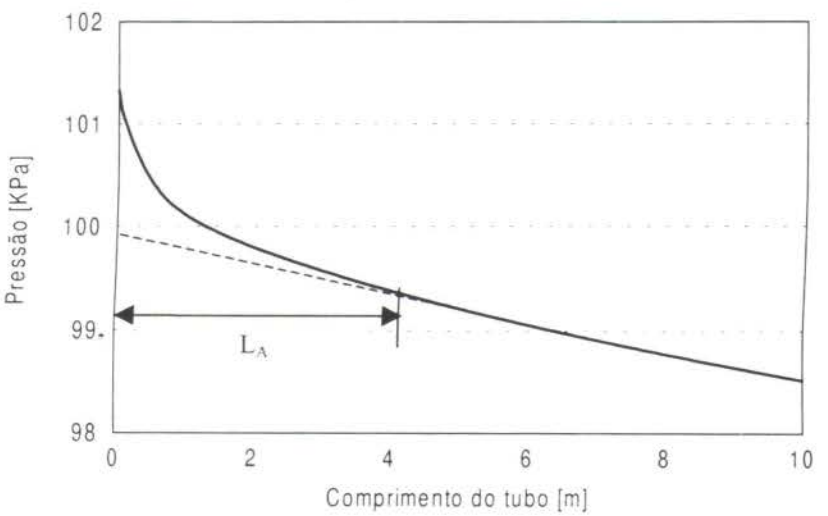

Figura 4 - Determinação do comprimento de aceleração L_A segundo SILVA (1984)

No escoamento gás-sólido em fase diluída quando a mistura atinge a região de escoamento estabelecido, os parâmetros ε, v_s e v_g permanecem aproximadamente constante. Assim, neste trabalho, o comprimento de aceleração foi determinado quando a variação no valor da porosidade é menor que 1%.

Nas Tabs. 1 e 2 estão listados alguns valores de L_A, ΔP_A experimentais de Silva (1984) e os valores calculados pelos modelos, para diversos diâmetros de partículas e carregamento de sólidos e gás. Foram também calculados os erros relativos percentuais para os parâmetros L_A e ΔP_A.

Considerando a complexidade do problema e o critério utilizado por SILVA (1984) na determinação do comprimento de aceleração, avalia-se como satisfatórios os resultados obtidos pelo Modelo 1, Tab. 1. Por outro lado, os valores da perda de carga e do comprimento de aceleração calculados pelo Modelo 2, Tab. 2, subestimam completamente os resultados experimentais.

Tabela 1 - Valores de L_A e ΔP_A experimentais de SILVA (1984) e calculados pelo Modelo 1.

W_s [g/s]	W_g [g/s]	L_A [m]			ΔP_A [Pa]		
		Mod. 1	Exp.	Erro %	Mod. 1	Exp.	Erro %
d_p = 0,4 mm							
103,400	32,500	1,254	1,730	27,51	804,304	804,420	0,01
101,300	32,100	1,249	1,780	29,83	789,242	804,420	1,88
109,100	27,100	1,319	1,980	33,38	816,835	941,700	13,25
105,200	46,200	1,180	1,860	36,55	902,520	902,520	0,00
101,800	44,400	1,175	1,780	33,98	850,992	863,280	1,42
d_p = 1,0 mm							
56,000	46,000	1,722	1,800	4,33	778,937	821,31	5,15
55,600	44,000	1,772	1,800	1,55	790,570	821,31	3,74
57,700	41,000	1,880	1,800	4,44	835,242	821,31	1,69
58,200	34,000	2,056	1,800	14,22	757,685	650,00	16,56
d_p = 1,2 mm							
117,600	49,000	1,781	1,920	7,23	849,867	935,960	9,19
127,200	40,100	1,942	1,880	3,29	884,672	843,660	4,86
129,500	42,800	1,913	1,720	11,22	894,625	755,370	18,44
128,000	34,800	2,053	2,200	6,68	917,031	824,000	11,28
123,500	33,500	2,057	1,940	6,03	904,922	716,130	26,36
d_p = 1,7 mm							
100,900	42,500	2,033	2,100	3,19	866,320	774,490	11,85
106,500	29,500	1,165	1,620	28,08	580,093	618,000	6,13
102,500	40,600	2,055	1,920	7,03	878,210	863,280	1,72
103,800	39,500	2,063	1,820	13,35	885,437	784,800	12,82
109,400	30,300	1,407	1,940	27,47	688,562	667,000	3,23

Tabela 2 - Valores de L_A e ΔP_A experimentais de SILVA (1984) e calculados pelo Modelo 2.

W_s [g/s]	W_g [g/s]	L_A [m]			ΔP_A [Pa]		
		Mod. 2	Exp.	Erro %	Mod. 2	Exp.	Erro %
d_p = 0,4 mm							
103,400	32,500	0,176	1,730	89,82	241,352	804,420	69,99
101,300	32,100	0,175	1,780	90,16	233,578	804,420	70,96
109,100	27,100	0,202	1,980	89,79	242,160	941,700	74,28
105,200	46,200	0,146	1,860	92,47	279,289	902,520	69,05
101,800	44,400	0,146	1,780	92,13	262,773	863,280	69,56
d_p = 1,0 mm							
56,000	46,000	0,147	1,800	91,83	100,672	821,31	87,74
55,600	44,000	0,153	1,800	91,50	99,632	821,31	87,86
57,700	41,000	0,166	1,800	90,77	104,765	821,31	87,24
58,200	34,000	0,195	1,800	89,16	105,54	650,00	83,76
d_p = 1,2 mm							
117,600	49,000	0,221	1,920	88,48	240,445	935,960	74,31
127,200	40,100	0,261	1,880	86,17	223,234	843,660	73,54
129,500	42,800	0,254	1,720	85,46	237,023	755,370	68,62
128,000	34,800	0,287	2,200	86,95	208,950	824,000	74,64
123,500	33,500	0,287	1,940	85,20	198,835	716,130	72,23
d_p = 1,7 mm							
100,900	42,500	0,229	2,100	89,09	150,914	774,490	80,51
106,500	29,500	0,853	1,620	47,34	39,984	618,000	93,53
102,500	40,600	0,234	1,920	88,02	146,359	863,280	83,04
103,800	39,500	0,236	1,820	87,36	143,757	784,800	81,68
109,400	30,300	0,126	1,940	93,50	62,125	667,000	90,68

4. CONCLUSÃO

Foram analisados dois modelos para o escoamento gás-solido em fase diluída na região de aceleração. A comparação dos resultados com os dados experimentais disponíveis na literatura indica que o Modelo 2 subestima completamente os resultados experimentais e o Modelo 1 apresenta resultado satisfatório para a queda de pressão e comprimento de aceleração.

Conclui-se que o Modelo 1 constitui-se como ferramenta adequada para análise do escoamento do sistema gás-sólido na região de aceleração.

5. REFERÊNCIAS

BENITEZ, N. G. Análise do Transporte Pneumático em Fase Diluida. *Tese de Mestrado apresentado ao Curso de Engenharia Mecânica da Universidade Federal do Pará*. Belém, 1997.

GIDASPOW, D. *Multiphase Flow and Fluidization : Continuum and Kinetic Theory Descriptions with Applications*. Academic Press, Inc., San Diego, 1994.

GIDASPOW, D. Hiperbolic Compressible Two-Phase Flow Equations Based on Stationary Princilples and the Fick's Law. p. 283 in T. N. Veziroglu and S. Kakac. Eds. *Two-Phase Transport and Reactor Safety*, v. 1. Hemisphere Publising Corp., 1978.

KLINZING, G. E. *Gas-Solid Transport*. Mc Graw Hill, New York, 1981.

MASSARANI, G. & SANTANA, C. C. Força Resistiva Sólido-Fluido em Sistemas Particulados de Porosidade Elevada. *Revista Brasileira de Tecnologia*, 11, 1980.

ROSE, N. E., DUCKWORTH, R. A. Transport of Solid Particules in Liquids and Gases. *The Engineer*, pp.392-396, 1969.

SHIMIZU, A. *et al.* Experimental Study on the Pressure Drop and the Entry Length of the Sas-Solid Suspensin Flow in a Circular Tube. *Int. J. Multiphase Flow*, vol. 4, pp.53-64, 1968.

SILVA , C. M. G. Dinâmica do Transporte Pneumático Vertical de Particulas. *Tese de mestrado apresentado à Faculdade de Engenharia de Campinas UNICAMP*. São Paulo, 1984.

SOO, S. L. *Fluid Dynamics of Multiphase Systems*. Waltham, Mass.: Blaisdell Publishing Co., 1967.

XIV Brazilian Congress of Mechanical Engineering
Obeid Plaza Hotel Convention Center - Bauru - SP/Brazil
December 08-12th 1997

PAPER CODE: COB1120

UM MÉTODO PARA A ANÁLISE DE TRANSPORTE PNEUMÁTICO VERTICAL EM FASE DILUÍDA/ *A METHOD FOR VERTICAL PNEUMATIC TRANSPORT ANALYSIS IN DILUTE PHASE*

NAPOLEÓN GONZÁLEZ BENITEZ & ANDRÉ LUIZ AMARANTE MESQUITA
Grupo de Turbomáquinas - Departamento de Engenharia Mecânica - Universidade Federal do Pará
CEP - 66075-900 Guamá, Brasil E-mail: gtdem@amazon.com.br

Abstract

This work presents a model for the gas-solid vertical flow analysis in dilute phase based on one-dimensional, isothermal and steady-state on balance equation. The model is an extension of some significant works. The results from the present model are confronted with experimental data available in the literature, and a good agreement is observed. The model is consistent and it is concluded that energy losses due the solid friction it is not important face the other loss energy sources.

Keywords

Pneumatic Transport/Transporte Pneumático Dilute Phase/Fase Diluida
Gas-Solid Flow/Escoamento Gás-Sólido

1. INTRODUÇÃO

O transporte pneumático de partículas sólidas é freqüentemente utilizados em diversas industrias. Atualmente, devido à preocupação com a higiene, poluição ambiental, manuseio e o custo, vem obtendo uma crescente posição de destaque nas indústrias químicas, alimentícias, processamentos de combustíveis sólidos e de minerais, no controle de emissão de poluição, secagem de sólidos, agroindústrias e outras.

A grande maioria dos modelos sobre o transporte pneumático em fase diluída é baseada em correlações inteiramente empíricas. Principalmente devido a esta característica, observa-se algumas discordância entre os modelos, gerando, portanto, dúvidas sobre a validade ou limites de confiabilidade dos mesmos.

Por outro lado, apenas um pequeno número de trabalhos foram desenvolvidos a partir das equações básicas de conservação. Nesta classe, algumas simplificações são introduzidas. Por exemplo, nos modelos analisados por Arastoopour & Gidaspow (1979), Rocha (1988), Paixão & Rocha (1993), o atrito entre as partículas sólidas e a parede do tubo não é levado em consideração.

Neste trabalho, fundamentando-se nos modelos de Soo (1969) e Gidaspow (1978), propõe-se uma modelagem para o transporte pneumático, que inclui o atrito sólido-parede, onde foi utilizado as correlações de Yang (1978) para o cálculo desse parâmetro. Além da modelagem e simulação do transporte pneumático, efetua-se uma comparação com os resultados experimentais obtidos por Zenz (1949).

2. MODELAGEM PARA O ESCOAMENTO GÁS-SÓLIDO EM FASE DILUÍDA

Para o estabelecimento do modelo, considerou-se que o tamanho das partículas é uniforme e que as partículas possuam a mesma massa especifica. O escoamento é considerado unidimensional, permanente, incompressível e isotérmico. Diante dessas considerações, para uma seção do tubo de comprimento diferencial Δx, as equações da continuidade e da quantidade de movimento para a mistura gás-solido são descritas como:

Equação da continuidade para a fase gasosa

$$\frac{d}{dx}[\varepsilon\rho_g v_g] = 0 \qquad (1)$$

Equação da continuidade para a fase sólida

$$\frac{d}{dx}[(1-\varepsilon)\rho_s v_s] = 0 \qquad (2)$$

Equação da quantidade de movimento para a mistura gás-solido

$$(1-\varepsilon)\rho_s v_s \frac{dv_s}{dx} + \varepsilon\rho_g v_g \frac{dv_g}{dx} + g[\rho_s(1-\varepsilon) + \rho_g\varepsilon]\operatorname{sen}\theta + \frac{dP}{dx} +$$

$$\frac{2\varepsilon\rho_g v_g{}^2 f_g}{D_T} + \frac{2(1-\varepsilon)\rho_s v_s{}^2 f_s}{D_T} = 0 \qquad (3)$$

onde ε é a porosidade ou fração volumétrica do gás, v_s é a velocidade do sólido, v_g é a velocidade do gás, ρ_g é a densidade do gás, ρ_s é a densidade do sólido, f_g é o coeficiente de atrito entre o gás e a parede do tubo; f_s é o coeficiente de atrito entre o sólido e a parede do tubo, θ é o ângulo que forma o eixo do tubo com a linha horizontal; g é a aceleração da gravidade e D_T é o diâmetro do tubo.

Como existem quatro incógnitas, ε, v_s, v_g e P, e somente 3 equações, há necessidade de mais uma equação.

No trabalho de Arastoopour & Gidaspow (1979), no sentido de completar o sistema de equações, foram analisados 4 modelos baseados na equação da quantidade de movimento para a fase sólida:

Caso A: queda de pressão em ambas as fases proposto por Kapes e Nakamura (1973),

$$\rho_s v_s \frac{dv_s}{dx} + \frac{dP}{dx} = F_D - \rho_s g \ \sin\theta \qquad (4)$$

onde F_D é a força de arrasto por unidade de volume da partícula.

Caso B: queda de pressão na fase fluida somente, proposto por Soo (1967),

$$\rho_s v_s \frac{dv_s}{dx} = F_D - \rho_s g \ \sin\theta \qquad (5)$$

Caso C: proposto por Gidaspow (1978), considera o efeito da velocidade relativa,

$$-\frac{1}{2}\frac{d}{dx}(v_g - v_s)^2 = \frac{F_D}{\rho_s} - g\ \sin\theta \tag{6}$$

Caso D: modelo proposto por Deich *et al.* (1974), supõe queda de pressão parcial em ambas as fases,

$$\rho_s U_s \frac{dU_s}{dx} - \frac{P}{(1-\varepsilon)}\frac{d\varepsilon}{dx} + \frac{dP}{dx} = F_D - \rho_s g\ \sin\theta \tag{7}$$

Na análise comparativa entre os resultados calculados pelos quatro modelos e os resultados experimentais de Hariu & Molstad (1949) e Zenz (1969), realizada pelos autores, foi concluído que o modelo da velocidade relativa, Caso C, apresentou melhor resultado, sendo que os modelos A e B são equivalentes e apresentaram também resultados satisfatórios. Contudo, a validade das equações (4) a (7) são questionadas, pois as mesmas desprezam o atrito dos sólidos com a parede do tubo e supõem que a queda de pressão devido ao atrito da mistura com a parede está relacionada diretamente com o coeficiente de atrito de Fanning para o fluxo de gás, f_g.

Portanto, os dois modelos analisados neste trabalho, no sentido de completar o sistema de equações, consideram o atrito dos sólidos com a parede do tubo e são:

1. Extensão do modelo de Gidaspow (1978), isto é, considerando o atrito sólido-parede a equação (6) é rescrita como:

$$-\rho_s(v_g - v_s)\frac{d(v_g - v_s)}{dx} = F_D - g\rho_s\sin\theta - \frac{2\rho_s {v_s}^2 f_s}{D_T} \tag{8}$$

2. Extensão do modelo de Soo (1967). Considerando também o atrito sólido-parede,

$$\rho_s v_s \frac{dv_s}{dx} = F_D - g\rho_s\sin\theta - \frac{2\rho_s {v_s}^2 f_s}{D_T} \tag{9}$$

As equações de continuidade, (1) e (2), podem ser rescritas, respectivamente, como

$$\frac{dv_g}{dx} = -\frac{v_g}{\varepsilon}\frac{d\varepsilon}{dx} \tag{10}$$

$$\frac{dv_s}{dx} = \frac{v_s}{(1-\varepsilon)}\frac{d\varepsilon}{dx} \tag{11}$$

Portanto,

$$\frac{d(v_g - v_s)}{dx} = -\left[\frac{v_g}{\varepsilon} + \frac{v_s}{(1-\varepsilon)}\right]\frac{d\varepsilon}{dx} \tag{12}$$

Substituindo (11) em (9) e (12) em (8) e rearrumando as equações tem-se, dois sistemas de equações diferenciais ordinárias. O primeiro é formado por (3), (10), (11) e

$$\frac{d\varepsilon}{dx} = \frac{\left[F_D - g\rho_s \sin\theta - \frac{2\rho_s v_s{}^2 f_s}{D_T}\right]}{\rho_s (v_g - v_s)\left[\frac{v_g}{\varepsilon} + \frac{v_s}{(1-\varepsilon)}\right]} \tag{13}$$

E o segundo sistema é formado por (3), (10), (11) e

$$\frac{d\varepsilon}{dx} = \frac{\left[F_D - g\rho_s \sin\theta - \frac{2\rho_s v_s{}^2 f_s}{D_T}\right]}{\frac{\rho_s v_s{}^2}{(1-\varepsilon)}} \tag{14}$$

O sistema de equações que envolve a extensão do modelo de GIDASPOW (1978), será referenciado como **Modelo 1** e o que envolve a extensão do modelo de SOO (1967), como **Modelo 2**.

A força de arrasto exercida pelo fluido sobre as partículas por unidade de volume das mesmas pode ser escrita como

$$F_D = \frac{3}{4} C_{Ds} \rho_g \frac{(v_g - v_s)^2}{d_p} \varepsilon^{-2,65} \tag{15}$$

onde o termo $\varepsilon^{-2.65}$ é o fator de correção para o coeficiente de arrasto C_{Ds} devido a presença de outras partículas no fluido (Gidaspow, 1994).

A correlação dada pela equação (15) é válida para partícula esférica, onde d_p é o diâmetro da partícula. O coeficiente de arrasto pode ser relacionado com o número de Reynolds (Rowe 1961 *apud* Gidaspow, 1994) por meio das expressões

$$C_{Ds} = \frac{24}{Re_s}(1 + 0{,}15 Re_s{}^{0,687}) , \qquad Re_s < 1000 \tag{16}$$

$$C_{Ds} = 0{,}44 \qquad Re_s > 1000 \tag{17}$$

onde

$$Re_s = \frac{\varepsilon \rho_g d_p (v_g - v_s)}{\mu} \tag{18}$$

e μ é a viscosidade do gás.

Considerou-se também que no transporte pneumático em fase diluída a fase gasosa não é afetada pela presença das partículas solidas, portanto, o coeficiente de atrito gás-parede do tubo na região laminar foi calculado pela expressão de Poiseulle:

$$f_g = 16/Re \quad \text{para} \quad Re \leq 2100; \tag{19}$$

pela fórmula de Blasius na região intermediária,

$$f_g = 0{,}0791/Re^{0{,}25},\ 2100 \leq Re \leq 1x10^5 \tag{20}$$

e para $Re > 1x10^5$ pela fórmula de Nikuradse

$$\frac{1}{\sqrt{f_g}} = 2\log(Re\sqrt{f_g}) - 0{,}8 \tag{21}$$

e para tubo rugoso foi utilizada a fórmula de Colebrook,

$$\frac{1}{\sqrt{f_g}} = -0{,}86\ln\left(\frac{\epsilon / D_T}{3{,}7} + \frac{2{,}51}{Re\sqrt{f_g}}\right) \tag{22}$$

onde o número de Reynolds é dado por

$$Re = \frac{D_T v_g \rho_g \varepsilon}{\mu}, \tag{23}$$

Para o cálculo do coeficiente de atrito sólido-parede do tubo, foram analisadas diversas correlações, comparando com os resultados experimentais de HARIU & MOLSTAD (1949) e foi concluído que as correlações de Yang (1978) e Ozbelge (1984) forneceram melhor resultado e são equivalentes. Neste trabalho, foi utilizada correlação de Yang (1978) e é dada por

$$fs = 0{,}00314\frac{1-\varepsilon}{\varepsilon^3}\left[\frac{(1-\varepsilon)U_t}{v_g - v_s}\right]^{-0{,}979} \tag{24}$$

onde U_t é velocidade terminal do sólido.

3. RESULTADOS

Os dois sistemas de equações diferenciais foram resolvidos pelo método tradicional de Runge Kutta de quarta ordem. Os números de Reynolds, Re e Re_s, o coeficiente de arrasto C_{Ds}, o fator de atrito entre gás-parede e sólido parede, f_g, e f_s, respectivamente, são recalculados para cada comprimento da malha ao longo da tubulação.

Nas Figs. 1 e 2 são apresentados a perda de carga em função da velocidade superficial do gás. Pode-se observar que a perda de carga obtida pelo Modelo 1, Fig. 1, cresce quando decresce o valor da porosidade inicial, como esperado fisicamente, por outro lado, o mesmo

não ocorre com a perda de carga calculada pelo Modelo 2, Fig. 2, ou seja, a perda de carga tende a diminuir com o decréscimo do valor da porosidade.

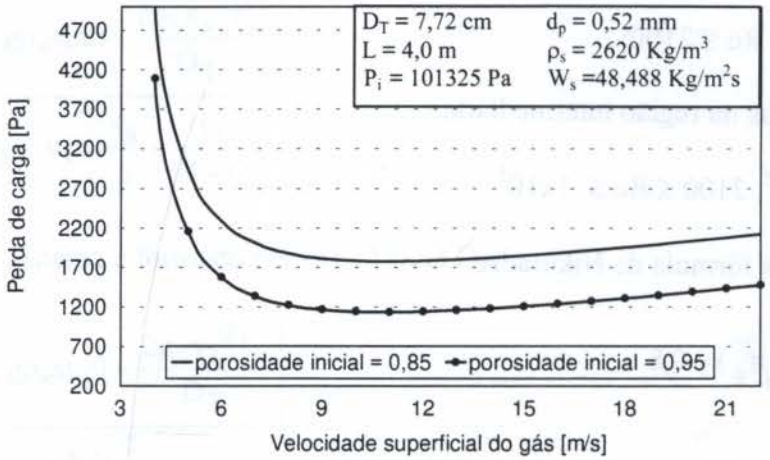

Figura 1 - Efeito do valor da porosidade inicial sobre a perda de carga segundo o Modelo 1.

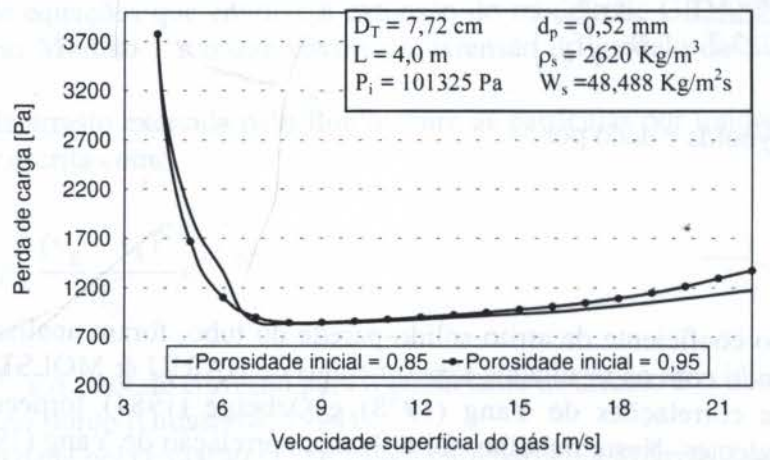

Figura 2 - Efeito do valor da porosidade inicial sobre a perda de carga segundo o Modelo 2.

No sentido de validar os modelos foram utilizados valores experimentais disponíveis na literatura. O conjunto de dados experimentais para escoamento de gás-sólido estudados foram os dados de Zenz (1949), o mesmo experimento estudado por Arastoopour & Gidaspow (1978).

As Figs. 3 e 4 mostram a comparação dos resultados da perda de carga com os dados experimentais de Zenz (1949). Pode-se observar que a baixa porosidade inicial, Fig. 3, os resultados obtidos pelo Modelo 1 mostram-se em boa concordância com os dados experimentais e os resultados obtidos pelo Modelo 2 divergem completamente dos dados experimentais, como já esperado segundo a Fig. 3. Para porosidade inicial mais elevada, Fig. 4, os modelos são equivalentes na região à direita do ponto mínimo de ΔP. À esquerda desse ponto mínimo somente o Modelo 1 fornece resultados satisfatórios.

No sentido de quantificar a contribuição da perda de carga devido ao atrito sólido-parede do tubo foi colocado na Fig. 5 o resultado da perda de carga em função da velocidade superficial do gás sem e com atrito sólido para duas densidades diferentes. Pode-se observar que a contribuição da perda de carga devido ao atrito sólido-parede do tubo é pequena.

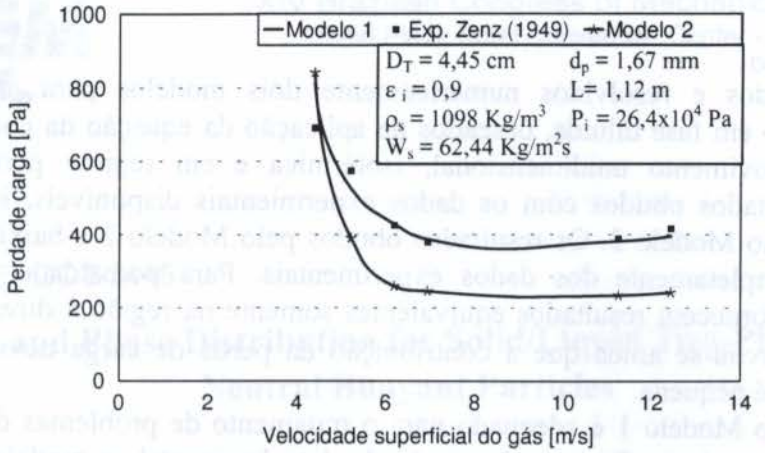

Figura 3 - Variação da perda de carga com a velocidade superficial do gás.

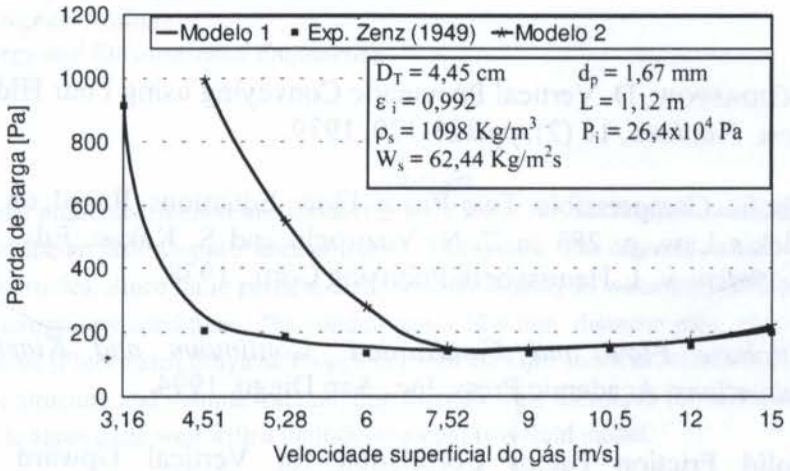

Figura 4 - Variação da perda de carga com a velocidade superficial do gás.

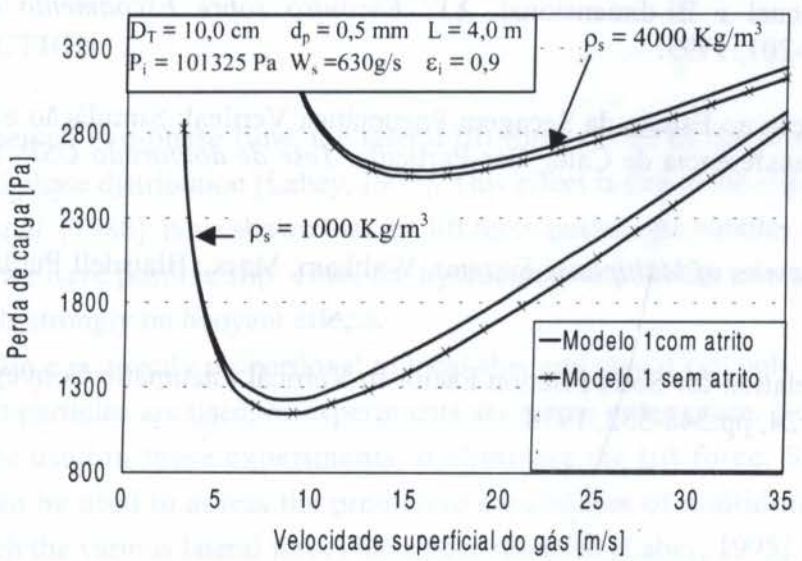

Figura 5 – Perda de carga com e sem arito sólido-parede do tubo segundo o Modelo 1.

4. CONCLUSÃO

Foram apresentados e resolvidos numericamente dois modelos para a análise do escoamento gás-sólido em fase diluída, baseados na aplicação da equação da continuidade e da quantidade de movimento unidimensional, isotérmica e em regime permanente. A comparação dos resultados obtidos com os dados experimentais disponíveis, indica que o Modelo 1 é superior ao Modelo 2. Os resultados obtidos pelo Modelo 2 a baixa porosidade inicial, divergem completamente dos dados experimentais. Para porosidade inicial mais elevada, os modelos fornecem resultados equivalentes somente na região à direita do ponto mínimo de ΔP. Observou-se ainda que a contribuição da perda de carga devido ao atrito sólido-parede do tubo é pequena.

Concluiu-se que o Modelo 1 é adequado para o tratamento de problemas de transporte pneumático em dutos verticais. Para configuração de duto horizontal, o modelo está sendo testado atualmente.

5. REFERÊNCIAS

ARASTOOPOUR, H. & GIDASPOW, D. Vertical Pneumatic Conveying using Four Hidrodynamic Models. *Ind. Eng. Chem. Fundam.*, 18 (2), pp.123-129, 1979.

GIDASPOW, D. Hiperbolic Compressible Two-Phase Flow Equations Based on Stationary Princilples and the Fick's Law. p. 283 in T. N. Veziroglu and S. Kakac. Eds. *Two-Phase Transport and Reactor Safety,* v. 1. Hemisphere Publising Corp., 1978.

GIDASPOW, D. *Multiphase Flow and Fluidization: Continuum and Kinetic Theory Descriptions with Applications*. Academic Press, Inc., San Diego, 1994.

ÖZBELGE, T. A. Solid Friction Factor Correlation for Vertical Upward Pneumatic Conveyings. *Int. J. Multiphase Flow*, vol. 10. No. 4. pp.459-465, 1984.

PAIXÃO, A. E. A. & ROCHA, S. C. S. Transporte Pneumático Vertical – Comparação entre Modelos Unidimensional e Bi-dimensional. *XXI Encontro sobre Escoamento em Meios Porosos*. vol. I, pp.89-201, 1993.

ROCHA, C. Contribuição ao Estudo da Secagem Pneumática Vertical: Simulação e Influência do Coeficiente de Transferência de Calor Gás-Partícula. *Tese de doutorado USP*. São Paulo, 1988.

SOO, S. L. *Fluid Dynamics of Multiphase Systems*. Waltham, Mass.: Blaisdell Publishing Co., 1967.

YANG W. C. A Correlation for Solid Friction Factor in Vertical Pneumatic Conveying Lines. *AICHE Journal*, vol. 24, pp.548-552, 1978.

XIV Brazilian Congress of Mechanical Engineering
Obeid Plaza Hotel Convention Center - Bauru - SP/Brazil
December 08-12th 1997

PAPER CODE: COB1445

Turbulence and Phase Distribution for Solid/Liquid Two-Phase Flow with Neutral Buoyant Particles

A. Assad[1] and R.T Lahey, Jr[2]

1- Purdue University, School of Mechanical Engineering
West Lafayette, IN 47907-1077. E-mail amir@ecn.purdue.edu
2- Rensselaer Polytechnic Institute
Department of Energy and Environmental Engineering
Troy, New York 12180

Abstract

Detailed local phase distribution measurements were made for solid/liquid two-phase flows in a horizontal pipe using a state-of-the-art laser Doppler anemometer (LDA) system. The disperse phase consisted of 2 mm neutral buoyant spherical particles. Since these particles had the same density as water particle/liquid slip was eliminated, thus simulating microgravity conditions. The conduit was a 30.6 mm diameter pipe, which was made of a special optically clear material (Fluorinated Ethylene Propylene) with the same index of refraction as water. A set of velocity profiles, turbulence structure and volume fraction distributions were measured for each phase. These experimental results were found to agree quite well with a multidimensional two-fluid model.

Keywords

Two-Phase Flow, Solid-Liquid Flow, Laser Doppler and Turbulence.

1. INTRODUCTION

In a dispersed two-phase flow, the lateral lift force is one of the most important effects affecting lateral phase distribution [Lahey, 1995]. This effect is due to the slip between the phases and Serizawa *et al.* [1988] have shown that the lift force pushes gas bubbles towards the wall for upflow, where we have positive slip. Thus, the hydrodynamic behavior of a turbulent multiphase mixture depends strongly on buoyant effects.

The lift force is directly proportional to local slip, and thus it can only be eliminated when neutral buoyant particles are used, or experiments are run in outer space. Neutral buoyant solid particles where used in these experiments to eliminate the lift force. Significantly, these experiments can be used to assess the predictive capabilities of multidimensional two-fluid models, in which the various lateral forces have been modeled [Lahey, 1995].

2. EXPERIMENTAL FACILITY

A special slurry loop was built in order to perform the experiments using neutral buoyant particles [Assad, 1995]. The test section consisted of a 30.6 mm ID horizontal pipe (length =1.52m) which was made of a special optically clear material (Fluorinated Ethylene Propylene) having the same index of refraction as water. The integrated local volume fraction obtained from the LDA measurements was compared against global quick-closing valve measurements to calibrate the measurements techniques used. Moreover, a unique phase separation system was designed and built for use with neutral buoyant particles (*i.e.*, a specific gravity of 1.03). Figure-1 shows a schematic of the loop where water coming from the slurry pump goes through a venturi in direction of the test section and a phase separator induces the particles to flow into to the venturi because of the drag force from the liquid, which returns to the pump through the bottom of the phase separator. Global quick-closing valve volume fraction measurements were also made after the test section and before the phase separator to obtain representative samples. A bypass was used when the quick-closing valves were activated to route the flow back to the pump. This bypass avoided an increase of pressure inside the experimental loop when the quick closing valves were activated.

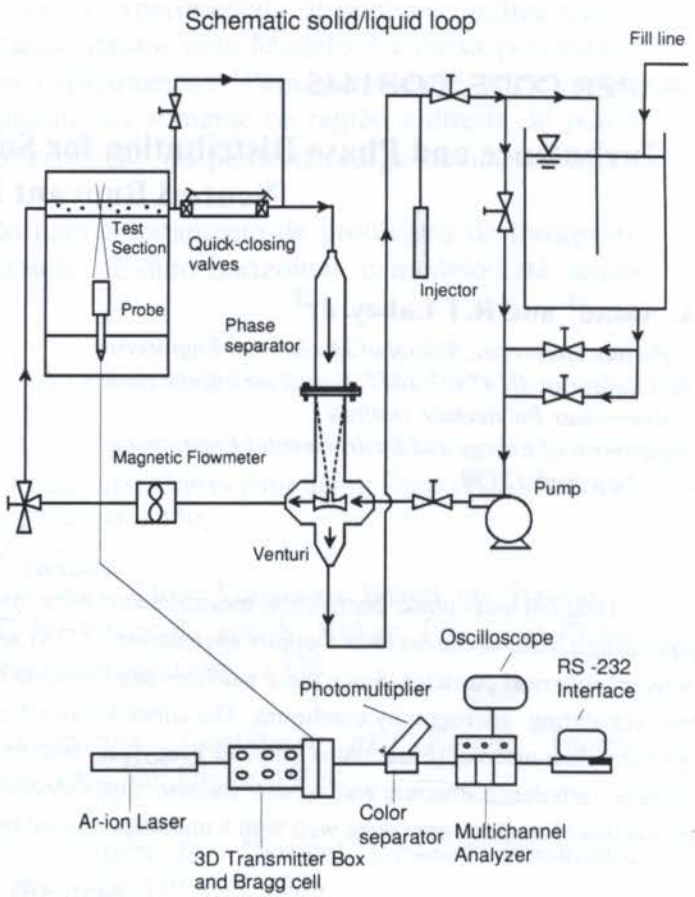

Figure 1. Loop utilized for neutral buoyant particles (water+polystyrene partcles

Air purges were installed in the upper part of the loop to avoid any possibility of entrapping small air bubbles. This was done to make sure that no air bubbles were present in the loop otherwise the LDA system would measure the velocities associated with these bubbles, and thus give erroneous data on particle velocity. Before each experiment, the Doppler burst signal was checked for the liquid phase since we could identify changes in this signal caused by air bubbles. A complete developed flow (L/D=140) were obtained to make sure that both phases were well mixed. A calibrated magnetic flow meter was installed before the test section, and was used to control the liquid flow coming from the slurry pump.

2.1 PHASE SEPARATION.

A unique, new phase separator with the capacity to separate the dispersed particles was designed and built [Assad, 1995]. This phase separator was able to separate the liquid from solid particles with 100% efficiency.

The principles behind this phase separator are:

(1) The pressure difference between two locations in a venturi.

(2) Use of the drag force from the continuous phase in order to induce the particles to flow into the venturi.

2.2 LASER DOPPLER AND ELETRONIC SETUP

A 4 watt Spectra Physics argon-ion laser was used, operating with three wavelengths: 514.5 nm (green), 488 nm (blue) and 477 nm (violet). To obtain the maximum power and the right path of the incident beams, the system was calibrated and aligned several times during the experiments, because even a small temperature variations can change the laser path and consequently the quality of the data.

The beam emanating from the laser was collimated as required for efficient coupling and so that it was parallel at the transmitter box. The beam was then separated into its component colors, and all but the three strongest beams were blocked. Each of these three beams was passed through a polarization plate so its axis of polarization could be oriented correctly with respect to its corresponding prism beamsplitter.

The beamsplitters separated each beam into a pair of beams of approximately equal intensity, and the stronger beam of each pair was frequency-shifted using a Bragg cell driven at 40 MHz. The beams were then aligned using DANTEC manipulators to route the beams to the optical fibers which transmit them to the submerged probes.

The submerged probe design was done in such a way that all optical surfaces were surrounded by a beam expander and a protective lens. After the beams reach the measurement volume the scattering light was sent to the photodetectors installed inside the probe.

Each photodetector used a narrow-band optical filter to pass only the appropriate wavelength, and the filtered, collimated beam was directly incident on the photomultiplier tube. All the scattering light was collected using a backscattering method which gave a good signal-to-noise ratio.

The electronic setup was software controlled via a RS-232 interface connected to an IBM/AT computer. The optimal configuration depends on what the laser is seeing inside the test section. If only one phase was present all parameters could be adjusted for that phase, but to balance the setup for both phases (i.e., two-phase flow) was a very difficult task. For example, the

best setup for 2mm particles (the solid particles) was a bad setup for very small seed particles in the liquid phase. To avoid this, some liquid seeding was necessary during these experiments, where the principal characteristic is that all particles was small enough to track the flow accurately but large enough to scatter sufficient light for the proper operation of the photodetector and the signal processing equipment. The bandwidth and voltage had to be carefully adjusted in order to get the best signal possible.

3. RESULTS AND DISCUSSION

In order to verify if the laser alignment was acceptable, the probe was submerged perpendicular to the test section and, with the laser beams working in a TEM_{00} (Transverse Electromagnetic) mode, several experiments were done using single-phase liquid. Figure-2 shows how the chordal measurements were performed. The axial direction (x) was in the direction of the flow. The lateral direction (y) was in the direction of the laser beams, and the vertical direction (r) was perpendicular to the flow direction inside the pipe.

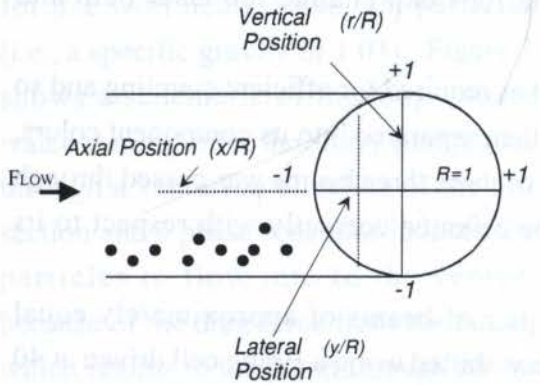

Figure 2. Nomenclature utilized for 2D experiments.

3.1 EXPERIMENTAL RESULTS AND TWO-FLUID MODELING.

3.1.1 LOCAL AXIAL VELOCITY PROFILE

Two-phase solid/liquid experiments were performed next using neutral buoyant particles (*i.e.*, particles having the same density as water). The absence of gravitational effects make these data applicable to microgravity studies. Significantly, the lateral lift force in this case is negligible since the slip between the phases is practically zero.

The local axial velocity for both phases are shown in Figure-4. The slip between the liquid and the particles is negligible and, near the wall, the particles have a slightly higher velocity due their finite size and the wall effects in the liquid phase.

The experiments with neutral buoyant particles can be considered to be microgravity simulations since slip and the lateral lift force can be neglected. Moreover, due to the absence of a deformable surface, the possibility of lateral forces were eliminated which would occur if distorted bubbles were the disperse phase.

3.1.3 LOCAL REYNOLDS STRESS.

The local measurements of the Reynolds stress for the liquid and neutral buoyant particles are shown in Figure-5 The Reynolds stresses for the liquid and neutral buoyant particles are almost identical when away from the wall, and they follow a linear trend until close to the wall where a pronounced wall effect is evident.

Also, since the particles were neutral buoyant, symmetry around the center line of the horizontal pipe was observed, with a zero value of Reynolds stress at this position.

3.2. TWO-FLUID MODELING

These data can be used to verify multidimensional two-fluid model predictions. The local instantaneous conservation equation for each phase are given by [Lahey, 1995]:

$$\frac{\partial}{\partial t}\rho\Psi + \nabla \cdot \rho\Psi\mathbf{v} = \nabla \cdot \mathbf{J} + \rho\mathbf{f} \tag{1}$$

Similarly, the jump conditions between phases k and l are:

$$[(\rho\Psi(\mathbf{v}-\mathbf{v}_i)+\mathbf{J})\cdot\mathbf{n}]_{kl} = M_i \tag{2}$$

Table 1 Variables utilized in the local conservation equations and jump conditions.

Balance Principle	Ψ Conserved quantity	$\mathbf{J}$ Conserved quantity's flux	$\mathbf{f}$ Conserved quantity's body source density	M_i Conserved quantity's interfacial source
Mass	1	0	0	0
Momentum	$\mathbf{v}$	$\mathbf{T}$	$\mathbf{g}$	$\underline{m}_i^{\sigma}$
Energy	$u+\frac{1}{2}(\mathbf{v}\cdot\mathbf{v})$	$\mathbf{T}\cdot\mathbf{v}-q'''$	$\mathbf{g}\cdot\mathbf{v}+r$	e_i^{σ}

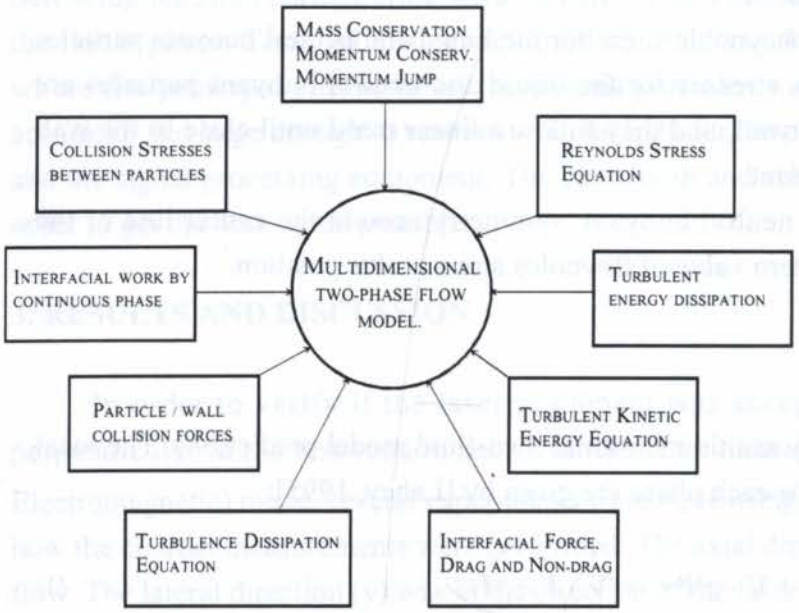

Figure 3. Overview of the two-fluid model.

where **T** is stress, **g** is gravity, u is internal energy, q''' is heat flux, and r is volumetric heat source. To obtain the conservation equations which govern the motion of turbulent dispersed solid/fluid flows. An overview of this model is presented in Figure-3 The two-fluid model utilized was evaluated using the PHOENICS code, which is suitable for solving all the equations obtained and allows ones to add appropriate closure laws. This model was developed considering only vertical upflow where the two-phase (solid/liquid) flow data were obtained in the horizontal test section. However, neutral buoyant particles were used, and thus gravitational effects were negligible. Hence these data can be compared with the model developed for vertical upflow. Indeed, Figures- 4 and 5 show that the agreement with the data is quite good.

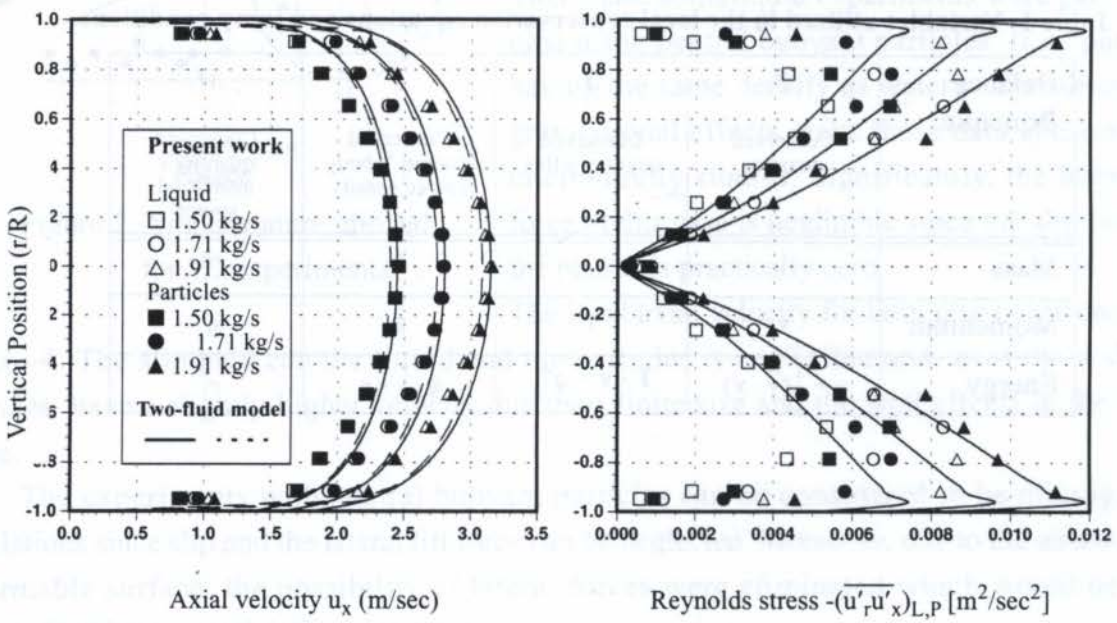

Figure 4 and 5. Data obtained for velocity profile and Reynolds stress for two-phase flow mixture using neutral buoyant particles compared with two-fluid model.

4. SUMMARY AND CONCLUSION

A complete set of data were taken for particle/liquid flow using neutral buoyant particles. These data represent a simulation of microgravity conditions and are useful for the assessment of multidimensional two-phase flow models.

It was found that a state-of-the-art two-fluid model was able to predict these data very well, thus supporting the validity of this modelling approach.

Acknowledgments - We wish to acknowledge the financial support given by NASA, CAPES-Brazilian Federal Agency and the National Science Foundation.

5. REFERENCES

Alajbegovic, A., Assad, A., Bonetto, F., Lahey, R.T., "Phase Distribution and Turbulence Structure for Solid/Fluid Upflow in a Pipe," *Int. J. Multiphase Flow*, 20(3), pp. 453-479, 1994.

Alajbegovic, A., "Phase Distribution and Turbulence Structure for Solid/Fluid Upflow in a Pipe," Ph.D. Thesis, Rensselaer Polytechnic Institute, Troy, New York, 1994.

Arnold, G.S., Drew, D.A., Lahey, R.T., Jr., "Derivation of Constitutive Equations for Interfacial Force and Reynolds Stress for Suspension of Spheres Using Ensemble Cell Averaging," *Chem. Eng. Comm.*, **86**, 43-54, 1989.

Assad, A., "An Experimental Study of Phase Distribution and Turbulence Structure for Solid/Liquid Flow in Horizontal and Vertical Pipes," Ph.D. Thesis, Rensselaer Polytechnic Institute, Troy, New York, 1995.

Drew, D.A., Lahey, R.T., Jr., "The Virtual Mass and Lift Force on a Sphere in Rotating and Straining Inviscid Flow," *Int. J. Multiphase Flow*, **13** (1), 113-121, 1987.

Drew, D.A., Lahey, R.T., Jr., "Some Supplemental Analysis on the Virtual Mass and Lift Force on a Sphere in Rotating and Straining Inviscid Flow," *Int. J. Multiphase Flow*, **16** (6), 1127-1130, 1990.

Drew, D.A., Passman, S.L., *Theory of Multicomponent Fluids*, To be published.,

Lahey, R.T., Jr., Drew, D.A., "The Current State-of-the-Art in the Modeling of Vapor/Liquid Two-Phase Flows," *ASME* 90-WA/HT-13, 1990.

Lahey, R.T., "The CFD Analysis of Multidimensional Phenomena in Multiphase Flow," *Proceedings of the 2nd International Conference on Multiphase Flow*, Kyoto, Japan, 1995.

Lopez de Bertodano, M., "Turbulent Bubbly Two-Phase Flow In a Triangular Duct," Ph.D. Thesis, Rensselaer Polytechnic Institute, Troy, New York, 1991.

Naot, D., Rodi, W., "Calculation of Secondary Currents in Channel Flow," *J. Hydraul. Div. ASCE*, **108** (HY8), 948-968, 1982.

Nigmatulin, R.I., "Spatial Averaging in the Mechanics of Heterogeneous and Dispersed Systems," *Int. J. Multiphase Flow*, **5**, 353-385, 1979.

Serizawa, A., Kataoka, I., "Phase Distribution in Two-Phase Flow," *Transient Phenomena in Multiphase Flow*, ed. by N.H. Afgan, Hemisphere, New York, pp. 179-225, 1988.

XIV Brazilian Congress of Mechanical Engineering
Obeid Plaza Hotel Convention Center - Bauru - SP/Brazil
December 08-12th 1997

PAPER CODE: COB1446

An Experimental Analysis of Pressure Drop and Entrainment in Annular Flow

A. Assad[1], M. de Bertodano[2] and Stephen Beus[3]

Purdue University, School of Mechanical Engineering[1] and School of Nuclear Engineering[2]
West Lafayette, IN 47907-1077. E-mail amir@ecn.purdue.edu

Bettis Atomic Power Laboratory Westinghouse Electric Corporation[3]
West Mifflin, PA 15122-0079

Abstract

The droplet entrainment and the interfacial shear are the most important phenomena that can exist in annular flow. Many of the available data were obtained for atmospheric condition neglecting high pressure effects where surface tension plays an important role. A unique vapor/liquid Freon experiments were designed and utilized to scale and simulate annular two-phase flow for high pressure data. The results were compared with two correlations available where Ishii and Mishima's dimensionless group was able to scale the data remarkably well. The pressure data obtained agreed well with Wallis and Asali's correlation for interfacial shear.

Keywords

Two-Phase Flow, Annular Flow and Vapor/Liquid Freon-113

1. INTRODUCTION

The fraction of liquid flow, which is dispersed in the gas core in annular flow, is the droplet entrainment. The experimental technique utilized in the present work is to extract the liquid film through a porous tube which allows to remove the droplet even near the liquid film.

Most of the data available has been obtained in air/water experiments at atmospheric pressure. However many applications operate under very different conditions. For the case of high pressure steam boilers the density ratio and the surface tension are quite different from these experiments.

The available correlations must rely on these data and therefore there is some uncertainty when they are applied to other situations. The present experiments employ air/water and Freon-113 data with the objective to bridge this gap in experimental data and reach steam/water conditions at high pressure.

2. PREVIOUS WORK

2.1 Available Data.

Cousins and Hewitt's (1968) experiments were carried out in adiabatic, upwards, air/water flows in tubes at near ambient temperature and low pressure, i.e. 0.14 to 0.24 MPa. A 9.5 mm (3/8 in) I.D. bore acrylic resin tube and a 31.8 mm (1 1/4 in) I.D. bore copper tube were employed.

The tube lengths used to attain equilibrium conditions are 2.2 m (7.17 ft.) for acrylic resin and 9.8 m (32 ft) for copper, respectively. The distance necessary to reach an equilibrium condition is given by Kataoka and Ishii (1982) as follows;

$$Z \approx 440 D \, We_f^{0.25} / \mathrm{Re}_f^{0.5} \tag{1}$$

where,

$$\mathrm{We}_l \equiv \frac{\rho_g j_g^2 D}{\sigma}\left(\frac{\Delta\rho}{\rho_g}\right)^{1/3} \tag{2}$$

$$\mathrm{Re}_f \equiv \frac{\rho_f j_f D}{\mu_f} \quad \text{where } j_{g,f} \text{ is the velocity for gas and liquid respectively} \tag{3}$$

For Cousins and Hewitt's experiments, the value of 440 $We_l^{0.25}$/ $Re_f^{0.5}$ lies between 50 and 150. Hence, the entrainment fractions measured at the tube exit can be regarded as the equilibrium value, since Z/D is greater than 230 at this point for all cases.

The flow rate of entrained liquid $(W_{LE})_1$, was determined by a mass balance equation:

$$W_L = (W_{LF})_1 + (W_{LE})_1 \tag{4}$$

Here, W_L is the inlet liquid flow rate, $(W_{LF})_1$ is the liquid film removal rate though porous wall section. The importance of this experiment is that the deposition rate is also measured with the second suction probe. Various deposition lengths were measured.

Keeys et al. (1970), measured the liquid entrainment in adiabatic annular steam/water flows at high pressures (3.447 and 6.894 MPa). The 12.6 mm I.D. test section was 3.66 m long. The value of 440 $We_l^{0.25}$/ $Re_f^{0.5}$ lies between 10 to 27 and Z/D is 290. This ensures equilibrium conditions at the liquid film extraction point. The liquid film flow rate is measured by extracting the film through a film removal device at the end of the test section. The steam, which is inevitably removed with the liquid film, is passed into a trace-heated cylinder and pumped back through another orifice. When the pressure difference across this orifice is increased, the liquid film removal rate increases until a plateau is reached. The true liquid film flow rate was taken as this value.

Since the Hewitt's data was obtained with entrainment fractions below 40% and Keeys' data above 70% there is a gap in the middle because the data did not overlap.

2.2 Available Correlations

Several correlations have been developed. Some of these correlations have been reviewed by Ishii and Mishima (1989). Two representative correlations are shown below: Dalman et. al. (1979) and Ishii and Mishima (1989).

Ishii and Mishima (1989) proposed a detailed correlation on the basis of an entrainment inception criterion and a force balance at the wavy interface as follows:

$$E_x = \tanh(7.25 \times 10^{-7} \, We_l^{1.25} \, \mathrm{Re}_f^{0.25}) \tag{5}$$

where We_l is defined in Equation (2).

This correlation indicates that the equilibrium entrainment fraction E_∞ depends on the total liquid Reynolds and gas Weber numbers.

Dallman et al. (1979) correlated the entrainment rate from a liquid film as:

$$\dot{\varepsilon} = k_A \left(\frac{W_{LF} - W_{LFC}}{P} \right) u_g^2 \rho_g^{1/2} \rho_f^{1/2} \tag{6}$$

where k_A is an entrainment coefficient, P is the perimeter of the wetted surface and W_{LFC} is the critical liquid mass flow rate required for the onset of entrainment. For air/water upflow k_A= 3.5 x 10^{-6} sec^2 /kg and W_{LFC}/P= 0.046 kg/m s.

The deposition rate is represented in terms of the concentration of droplets in the gas core, C, and the deposition coefficient, k_D (m/sec), as:

$$\dot{d} = k_D C \cong k_D \frac{\rho_g W_{LE}}{W_G} \tag{7}$$

At steady state, the rate of deposition from the gas core is equal to the entrainment rate from the liquid film, ie.,

$$\dot{d} = \dot{\varepsilon} \tag{8}$$

Inserting equations (6) and (7) into equation (8), Dallman obtained:

$$\frac{E}{E_M} = \frac{\frac{k_A \sigma j_g}{4k_D} We_D}{1 + \frac{\sigma j_g}{4k_D} We_D} \tag{9}$$

where we have defined:

$$We_D = \frac{\rho_g j_g^2 D}{\sigma} \sqrt{\frac{\rho_f}{\rho_g}} \quad \text{and} \quad E_M = 1 - \frac{W_{LFC}}{W_L} \tag{10}$$

Since equations (5) and (10) were developed using a limited set of experimental data in low pressure air/water flows, it is expected that the correlations may not apply directly to high pressure situations.

3. SCALING

The current experiments were designed to simulate steam/water flow at 13.6 MPa in a small diameter tube. The difficulty with scaling the interfacial phenomena in annular two-phase flow is that they are not well understood. The state-of-the-art correlations are empirical. We have chosen

the best known dimensionless correlations in the hope that the dimensionless numbers that they include are sufficient to scale the interfacial mechanisms.

The entrainment rate correlation was derived based on the correlation by Ishii and Mishima (1989). For fully developed annular flow they obtained:

$$\frac{\dot{\varepsilon D}}{\mu_f} = 6.6 \times 10^{-7}\, \mathrm{Re}_{lf}^{0.185}\, We_l^{0.925} \left(\frac{\mu_g}{\mu_f}\right)^{0.26} \tag{11}$$

where $\mathrm{Re}_{lf} = \mathrm{Re}_l\,(1\text{-}E)$. Combining equations (11) and (5) we obtain:

$$\frac{\dot{\varepsilon D}}{\mu_f} = \phi(We_g,\ \mathrm{Re}_l,\ \frac{\rho_f}{\rho_g},\ \frac{\mu_f}{\mu_g}) \tag{12}$$

The interfacial shear correlation of Wallis (1969) is based on the premise that the interfacial roughness is proportional to the film thickness:

$$c_{fi} = 0.005(1 + 300\frac{h}{D}) \tag{13}$$

Henstock and Hanratty (1976) used the approach that the flow in the film is similar to single-phase flow. The film was assumed to be uniform and the mixing length model was used to calculate the liquid velocity to obtain:

$$\frac{h}{D} = \frac{6.59F}{\sqrt{1+1400F}} \text{ where } F = \frac{\gamma(\mathrm{Re}_{lf})}{\mathrm{Re}_g^{0.9}} \frac{\mu_f}{\mu_g} \sqrt{\frac{\rho_g}{\rho_f}} \tag{14}$$

and $g(\mathrm{Re}_{lf})$ is an algebraic function.

By a similar argument as used for equations (12) it follows that:

$$c_{fi} = \psi(We_g,\ \mathrm{Re}_l,\ \mathrm{Re}_g,\ \frac{\rho_f}{\rho_g},\ \frac{\mu_f}{\mu_g}) \tag{15}$$

Equation (15) has one more dimensionless group than equation (12), Re_g.

To obtain similarity the five dimensionless groups on the RHS of equation (15) should be the same. Table 1 is a comparison between a steam/water reference case and six experimental cases. The hydraulic diameter is 6 mm for the reference case and 10 mm for the experiments. Freon-113 and air/water are used in this analysis.

The velocities, j_l and j_g, are chosen such that Re_l and We_g are similar. The only other variable that is controlled is the pressure.

There is one further advantage with Freon-113, that the surface tension is very low. In fact it is smaller than the reference condition. This is important in case that some significant dimensionless group was missed.

Table 1 Annular Flow Scaling

Fluids	P	T	j_l	j_g	Re_l	Re_g	We_g	ρ_l/ρ_g	μ_l/μ_g
	MPa	C	m/s	m/s					
Steam/Water	13.6	334	0.5	20	2.3 E+4	4.8 E+5	1.4 E+4	7.5	3.92
Freon (113)	2	180	0.357	7.347	2.3 E+4	7.3 E+5	1.4 E+4	7.1	10.92
Freon (113)	1	140	0.426	15.95	2.3 E+4	7.3 E+5	1.4 E+4	19.3	16.23
Freon (113)	0.5	100	0.503	27.49	2.3 E+4	7.3 E+5	1.4 E+4	40.9	23.65
Air/Water	2	20	2.327	84.47	2.3 E+4	1.0 E+6	1.4 E+4	42.4	52.63
Air/Water	1	20	2.327	119.5	2.3 E+4	7.4 E+5	1.4 E+4	84.7	52.63
Air/Water	0.5	20	2.327	168.9	2.3 E+4	5.2 E+5	1.4 E+4	169.5	52.63

4. EXPERIMENTS

4.1 Entrainment Measurement (Air/water).

As the liquid film flows up the tube, part of the liquid film is entrained as fine droplets in the gas core. When fully developed flow is established the entrainment rate is equal to the deposition rate and the entrainment fraction reaches its asymptotic value. Since the length between the top of the mixer to the inlet of the first extraction unit is about 440 diameters, fully developed annular flow is expected.

The entrainment fraction, E, can be calculated from the following expression:

$$E = 1 - \frac{W_{LF1}}{W_L} \tag{16}$$

For high water flows, it was hard to tell when the liquid film was extracted completely by visualization. The higher the inlet water flow, the greater percentage of the inlet air flow that needs to be extracted to reach the plateau. Once on the plateau it is assumed that the liquid film is extracted completely. The amount of extracted gas was always the minimum necessary to remove the liquid film. There are 121 experimental data points. The range of experimental data was extended on both air and water flows. The range of $\rho_f j_f^2$ is 5.5 to 289 kg/ms^2 and the range of $\rho_g j_g^2$ is 480 to 45000 kg/ms^2 (Pressure: 140 to 660 kPa).

4.2 Freon-113 Experiment.

In order to scale properly annular steam/water flow at high pressures and temperatures Freon has been shown to be one of the best fluids available. In Table 1 shows that it is possible to obtain the same density ratio as steam/water at 13.6 MPa using Freon-113 at 2MPa.

A unique annular two-phase loop (Figure 1) using vapor/liquid Freon was designed and built to scale the steam/water conditions. Vapor is produced inside a vapor generator (20 kw) and is mixed with Freon liquid in the inlet of the test section to produce annular flow. The pressure of the vapor generator is controlled automatically according to the set point established for the experiment. The first extraction unit works the same way as in the air/water loop. This liquid film goes to a flowmeter tank where the level can be read and the mass flow rate calculated. Two drain valves at the top of the flowmeter tank, with different discharge coefficients, were installed to control the optimal extraction point, i.e., when the plateau is reached. Thermocouples were installed before and along the test section to check that the data was obtained at steady-state saturated conditions. The range of the experiments were: $100 < \rho_g j_g^2 < 23000$ and $1.25 < \rho_f j_f^2 < 325$ at 2.5 and 10 bar.

5. RESULTS

Figure 2 shows a comparison of Ishii and Mishima's correlation (1989) and the four data sets: Cousins and Hewitt (1968), Keeys et. al. (1970), the present air/water data and the present Freon-113 data.

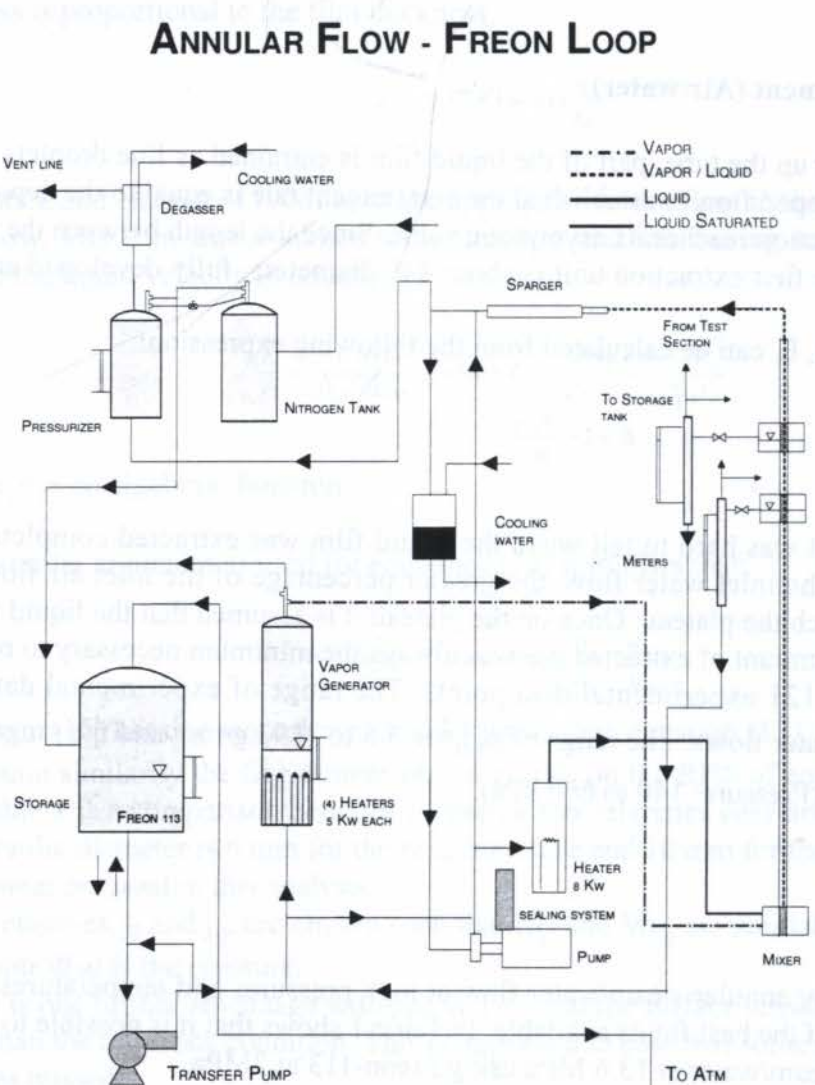

Figure 1 Two-phase annular Freon-113 loop.

The dimensionless group $We_l^{1.25} Re_l^{0.25}$ collapses all the data surprisingly well and it fits the data by Cousins and Hewitt very closely. This is not surprising since these data were use to obtain the correlation. Furthermore the correlation is in agreement with all the data for $We_l^{1.25} Re_l^{0.25} < 10^6$. The scatter observed in the new data at values of E below 0.1 is related to the uncertainty in the measurements and to the logarithmic scale which amplifies the effect. For $We_l^{1.25} Re_l^{0.25} > 10^6$ the correlation no longer fits the data. However the remarkable fact is that the low pressure air/water data, the high pressure steam/water data and the Freon-113 data are

collapsed in this region. The scatter of the air/water data set is systematic and depends on the liquid Reynolds number. This is not considered in Ishii and Mishima's correlation. Because of its significance, this phenomenon deserves to be studied separately and it will not be discussed any further at present.

Figure 3 shows the comparison of the correlation by Dallman et. al. (1979) with all the data. The correlation fits all the air/water data well with k_A=5.4 x 10^6 s^2/kg and W_{LFC}/P =0.046 kg/ms. Although the scatter is appreciable, Dallman et al.'s correlation does account for an asymptotic lower limit to the film flow, so the scatter is more random compared to Ishii and Mishima's correlation. However the correlation does not match the Freon-113 data. The pressure data is shown in Figures 4 and 5 compared with Wallis and Asali's correlation. A good agreement is observed.

6. CONCLUSION

New data sets have been obtained and they are consistent with previous entrainment data sets. The new data sets provide plenty of overlap between low pressure air/water data and high pressure Freon-113 data. It is now possible to show that the dimensionless group proposed by Ishii and Mishima (1989) scales data for a wide range of conditions, and in particular for high pressure steam/water flows. However the correlation by Ishii and Mishima is not properly calibrated for $We_l^{1.25}Re_l^{0.25} > 10^6$. Furthermore, it does not account for the asymptotic lower limit of the film flow rate observed at high gas flows. The new sets of data may be used to correct the correlation for these two effects and be used to improve the computer codes currently in operation.

7. REFERENCES

Asali, J. C., T. J. Hanratty, "Interfacial drag and film height for vertical annular flow," *AIChE Journal,* vol. 31, No. 6, pp 895-902, 1985.

Henstock, W. H. and T. J. Hanratty, "The interfacial drag and the height of the wall layer in annular flows," *AIChE Journal*, vol. 22, No 6, pp 990, 1976.

Cousins, L. B. and Hewitt, G. F., "Liquid Phase Mass Transfer in Annular Two-Phase Flow: Droplet Deposition and Liquid Entrainment", *UKAEA Report AERE-R5657*, 1968.

Dallman, J. C., Jones, B. G., and Hanratty, T. J.,"Interpretation of Entrainment Measurements in Annular Gas-Liquid Flows", *Two-Phase Momentum, Heat and Mass Transfer in Chemical, Process and Energy Engineering System*, Vol. 2, 681-693, Hemisphere, Washington, D.C., 1979.

Ishii, M. and Mishima, K., "Droplet entrainment correlation in annular two-phase flow", *Int. J. Heat and Mass Transfer*, Vol 32, n 10, pp 1835-1846, 1989.

Kataoka, I. and Ishii, M. "Mecanism and correlation of droplet entrainment and deposition in annular two-phase flow," *NUREG/CR-2885, ANL 82-44*, 1982.

Keeys, R. K. F., Ralph, J. C. and Roberts, D. N., "Liquid entrainment in adiabatic stream water flow at 500 and 1000 psi", *AERE-R-6293*, 1970.

Wallis, G. B., "*One Dimensional Two-Phase Flow*", McGraw-Hill, 1969.

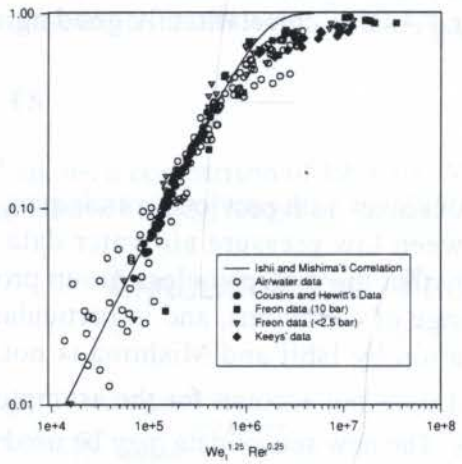

Figure 2. Comparison of Ishii and Mishima's (1989) correlation with data.

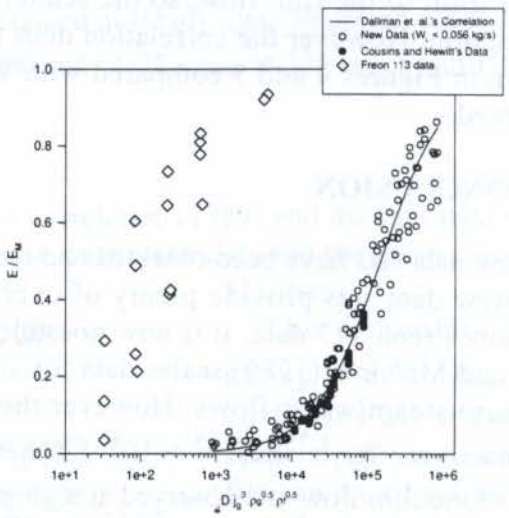

Figure 3. Comparison of Dallman et al. (1979) correlation with data.

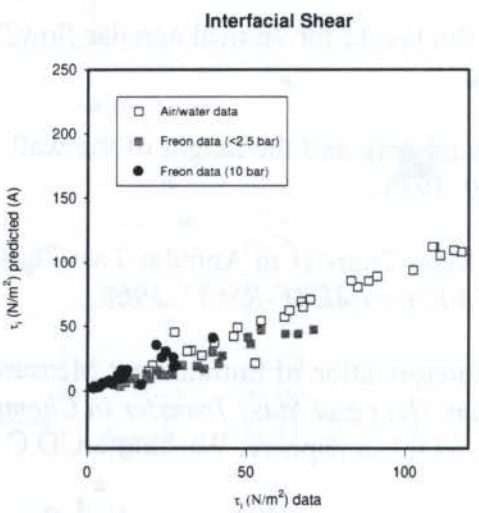

Figure 4.Data obtained compared with Wallis' (1969) correlation.

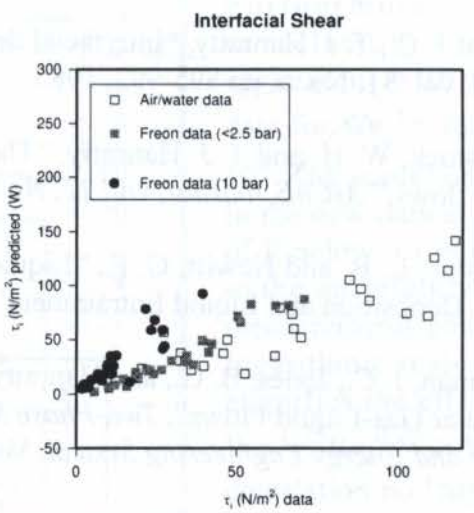

Figure 5. Data obtained compared with Asali's (1985) correlation.

XIV Brazilian Congress of Mechanical Engineering
Obeid Plaza Hotel Convention Center - Bauru - SP/Brazil
December 08-12th 1997

PAPER CODE: COB239

UMA ABORDAGEM MULTIESCALA NA SIMULAÇÃO NUMÉRICA DE RESERVATÓRIOS DE PETRÓLEO / *A MULTI-SCALE APPROACH IN PETROLEUM NUMERICAL RESERVOIR SIMULATION*

SOLANGE DA SILVA GUEDES
Exploração & Produção, Gerência de Reservas e Reservatórios - PETROBRAS
E-mail:solange@dep.fem.unicamp.br
DENIS JOSÉ SCHIOZER
Departamento de Engenharia de Petróleo - Faculdade de Engenharia Mecânica - UNICAMP
CEP 13083-970 - Cidade Universitária Zeferino Vaz - Campinas - SP -E-mail:denis@dep.fem.unicamp.br

Abstract

Advances in petroleum reservoir descriptions have provided an amount of data that can not be use directly during the simulations. This detailed geological information must be incorporated into a coarser model during the multiphase fluid flow simulations by means of some upscaling technique. The most used approach are the pseudo relative permeabilities and the more widely used is the Kyte and Berry method. In this paper it is proposed a multi-scale computational model for multiphase flow that implicitly treats the upscaling without using the pseudo functions. By solving a sequence of local problems on the more refined scale it is possible to achieve good agreement between a coarser grid and a more fine grid, without expensive computations on a fine grid model of the whole reservoir. The main characteristic of this new upscaling procedure is to overcome some practical difficulties related the use of traditional pseudo functions. Results of bidimensional two phase flow simulations considering homogeneous and heterogeneous porous media are presented. Three examples compare the results between this approach and the commercial upscaling program PSEUDO, a module of the reservoir simulation software ECLIPSE of Geoquest.

Keywords

Upscaling, Multiphase flow, Numerical simulations, Multi-scale computational model.

1. INTRODUÇÃO

A simulação numérica de reservatórios de petróleo é associada ao uso intensivo de recursos computacionais, principalmente nos tempos atuais quando técnicas geoestatísticas geram descrições de reservatórios heterogêneos com altíssimo grau de detalhe. No entanto as dificuldades computacionais decorrentes deste volume de dados leva a necessidade de mudança das propriedades envolvidas para uma escala menos refinada.

Na etapa de simulação, as equações do problema de transporte são discretizadas e o domínio de fluxo é então dividido em blocos, aos quais as propriedades de rocha são associadas. No caso de fluxo monofásico e/ou onde a heterogeneidade tem pouco efeito no fluxo, a mudança de escala envolvendo apenas a permeabilidade absoluta do meio pode ser suficiente para alcançar resultados satisfatórios. No entanto o fluxo multifásico em meios

porosos requer uso de técnicas específicas para ajustar os fluxos de cada fase através das faces dos blocos da malha de discretização.

Na presença de fluxo multifásico a técnica mais utilizada são as pseudo-curvas de permeabilidade relativa das fases, que substituem as relações originais, medidas em laboratório, e que são funções da saturações e do tipo de rocha reservatório.

A metodologia apresentada neste trabalho procura utilizar parâmetros obtidos com a simulação numérica de fluxo em algumas regiões como forma de criar uma equivalência entre a malha de simulação e outra bem mais refinada, mas sem utilizar os conceitos de pseudo-funções multifásicas e sem o custo computacional da malha fina. Os exemplos apresentados consideram problemas bidimensionais, bifásicos óleo-água e formulação Black-Oil.

2. MUDANÇA DE ESCALA ATRAVÉS DE PSEUDO-FUNÇÕES

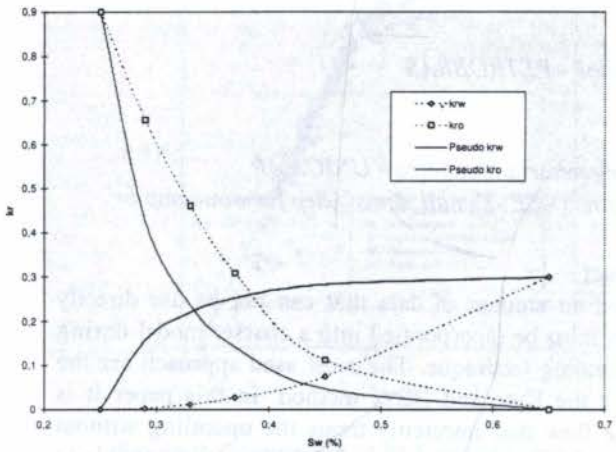

Figura 1: Curvas e pseudo-curvas de permeabilidades relativas

Modelos simplificados, analíticos ou numéricos, podem ser utilizados para obtenção destas pseudo-funções, exemplificadas na Fig.1. Métodos analíticos são válidos em situações onde algumas hipóteses simplificadoras, relativas ao mecanismo de produção ou a estrutura do reservatório, são atendidas. Exemplos destas condições idealizadas são a consideração de equilíbrio vertical (*Coats et al.* (1971)) e a seqüência de camadas não comunicantes (*Hearn* (1971)).

Métodos numéricos utilizam, de uma forma geral, simulações de fluxo, em parte do modelo fino, para construir as pseudo-funções para cada bloco da malha grossa. Desta forma, são geradas as pseudo-funções dinâmicas. *Jacks et al.* (1973) propuseram uma metodologia baseada em simulações de seções verticais, que gera diretamente um conjunto de pseudo-permeabilidades relativas para cada coluna vertical do modelo de malha fina, em situações onde o equilíbrio vertical não poderia ser adotado. Um dos métodos mais difundidos para o cálculo das pseudo-permeabilidades relativa dinâmicas foi proposto por *Kyte* e *Berry* (1975). Estes autores apresentaram um procedimento que se baseia na lei de Darcy para o cálculo das pseudo-funções, e pode ser considerado uma extensão da proposta de *Jacks et al.* (1973). *Stone* (1991) foi o primeiro a utilizar o parâmetro mobilidade total média, com o objetivo de evitar os problemas associados com a estimativa de pressões da malha grossa do método de *Kyte* e *Berry* (1975). Outros métodos também baseados em diferentes formas de se calcular a mobilidade total foram propostos por *Hewett* e *Berhens* (1991) e *Beier* (1992).

Guérillot e *Verdiére* (1995) e *Verdiére* e *Thomas* (1996) desenvolveram um esquema de mudança de escala baseado no uso de uma malha grossa para solução da equação da pressão e outra refinada para solução da equação da saturação, denominado *Dual Mesh Method* (*DMM*). Este trabalho considera apenas fluxo incompressível, o que permite o desacoplamento do sistema de equações não lineares em uma equação envolvendo apenas a variável saturação e outra envolvendo apenas a variável pressão, o que facilita o esquema de solução. Outra hipótese simplificadora destes trabalhos é a representação dos poços apenas como uma

condição de contorno associada a um bloco especifico, sem considerar as propriedades geométricas dos mesmos.

Uma revisão geral do uso de pseudo-funções, suas propriedades e limitações, pode ser encontrada no trabalho de *Barker* e *Thibeau* (1996). Além desta revisão, uma comparação entre cinco métodos dinâmicos de mudança de escala foi apresentada por *Barker* e *Dupouy* (1996).

3. MODELO COMPUTACIONAL MULTIESCALA

Este trabalho apresenta uma metodologia para a obtenção de soluções para o problema de escoamento em meios porosos, numa escala menos refinada do que a escala de descrição geológica, que pode considerar até dezenas de milhares de blocos. As vantagens deste procedimento sobre os processos tradicionais, que utilizam as pseudo-funções, são várias. A principal delas é permitir que a tarefa de mudança de escala seja executada de forma implícita pelo código computacional e ao mesmo tempo obter soluções próximas a solução da malha fina, sem que o problema seja resolvido nesta escala. Muitas vezes a descrição do reservatório é realizada com tal refinamento que soluções neste nível são impraticáveis. Outra característica importante desta metodologia é evitar a necessidade de reconstrução do modelo numérico toda vez que as linhas de fluxos do reservatório são alteradas. Quando se utiliza pseudo-funções, para cada simulação da malha grossa que incorpore mudanças, seja nas vazões, seja nas posições dos poços, novas pseudo-funções têm que ser geradas. Isto constitui uma das principais desvantagens na utilização das pseudo-curvas.

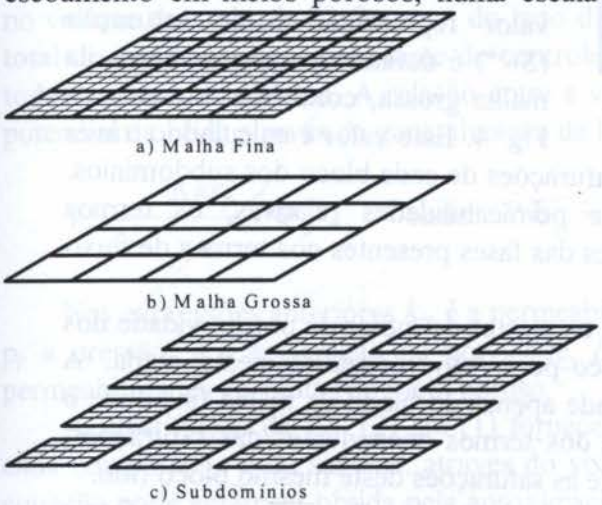

Figura 2 : Representação das escalas de simulação

A idéia central da metodologia é a utilização de parâmetros obtidos com a simulação numérica de fluxo, em algumas regiões refinadas, denominadas subdomínios (SD), onde são consideradas as propriedades físicas originais do meio, como forma de criar uma equivalência entre a malha de simulação, a malha grossa, e a malha fina onde o problema foi descrito. Para isto as escalas, mostradas na Fig. 2, estão sempre presentes no modelo numérico de simulação.

O esquema mostrado na Fig. 3 representa um fluxograma dos principais processos executados, num passo de tempo, no modelo computacional multiescala:

I - Inicialização da malha grossa: nesta etapa, os blocos da malha fina são agrupados em subdomínios, criando assim cada bloco da malha grossa. Os parâmetros de rocha e fluido são definidos através de média ponderada pelos volumes porosos, no caso de porosidades, pressões e saturações e através de métodos específicos no caso das permeabilidades absolutas.

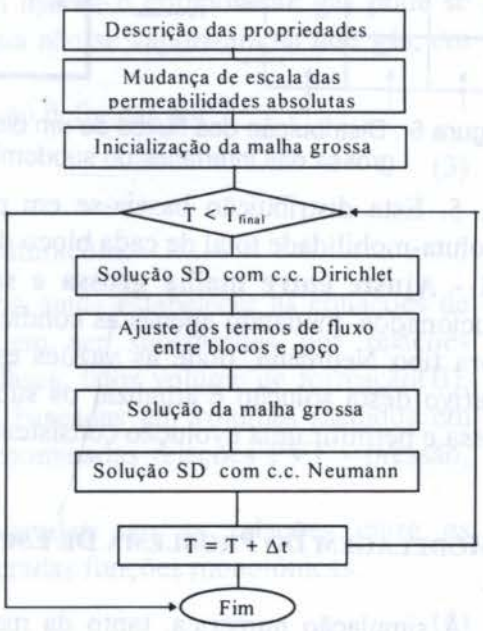

Figura 3 : Modelo computacional multiescala

Foram implementados o Método de Le Loc'h (*Le Loc'h* (1987)) e a obtenção da permeabilidade equivalente através da solução da equação de Laplace, que considera fluxo monofásico, aplicada a cada bloco e a cada direção.

II - Solução de uma seqüência de problemas locais: nesta etapa, que tem o objetivo de obter informações relativas ao fluxo das fases na malha fina, todos os subdomínios são resolvidos como um problema local definido por condições de contorno tipo Dirichlet e condições iniciais iguais ao do passo de tempo anterior.

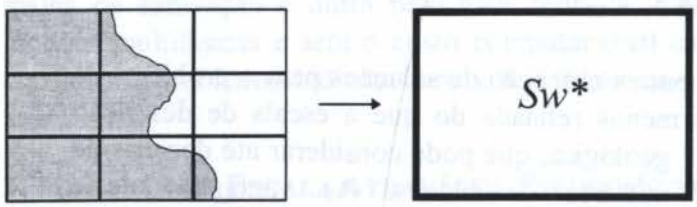

Figura 4 : Representação de *Sw** para cada bloco da malha grossa

III - Ajuste dos termos de fluxo entre blocos da malha grossa: através da solução aproximada nos subdomínios obtida na etapa II, um valor representativo de saturação (*Sw**) é definido para cada bloco da malha grossa, conforme esquema da Fig. 4. Este valor é calculado através de diferentes esquemas de ponderação aplicados às saturações de cada bloco dos subdomínios. Utilizando estes valores e as curvas originais de permeabilidades relativas, os termos dependentes da saturação, isto é, as transmissibilidades das fases presentes nos termos de fluxo da malha grossa, são ajustados.

IV - Ajuste dos termos fonte para a malha grossa: os ajustes do índice de produtividade dos poços e das transmissibilidades das conexões bloco-poço são realizados nesta etapa. A produtividade é ajustada considerando a permeabilidade apenas do bloco da malha fina onde o poço encontra-se completado, enquanto os cálculos dos termos dependentes das saturações, presentes nas transmissibilidades, utilizam diretamente as saturações deste mesmo bloco fino.

V - Solução da malha grossa: esta etapa corresponde à solução do problema de forma tradicional, com a diferença que aqui os fluxos das fases respeitam as correções efetuadas nos termos de fluxo nas etapas anteriores.

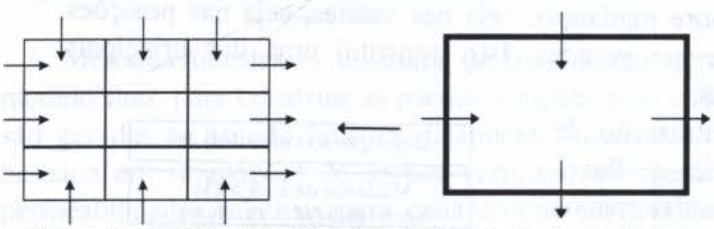

Figura 5 : Distribuição dos fluxos de um bloco da malha grossa nas interfaces do subdomínio

VI - Distribuição dos fluxos das conexões da malha grossa entre as conexões dos subdomínios: uma vez corrigidos os fluxos através das conexões das malha grossa, estes fluxos são distribuídos entre as conexões externas dos subdomínios associados a cada bloco, conforme Fig. 5. Esta distribuição baseia-se em ponderações que utilizam o produto permeabilidade absoluta-mobilidade total de cada bloco do subdomínio.

VII - Ajuste entre malha grossa e subdomínios: todos os subdomínios são novamente solucionados, mudando apenas as condições de contorno das conexões externas, consideradas agora tipo Neumann, onde as vazões especificadas são aquelas distribuídas na etapa VI. O objetivo desta solução é atualizar os subdomínios a partir dos resultados de fluxos da malha grossa e permitir uma evolução consistente das duas escalas.

4-MODELAGEM DO PROBLEMA DE ESCOAMENTO MULTIFÁSICO EM MEIOS POROSOS

A simulação numérica, tanto da malha grossa quanto da malha fina, é feita através do balanço de massa aplicado a cada componente c do fluxo que atravessa um volume arbitrário no domínio do fluxo, V, associado a uma área A. Este balanço é expresso por:

$$-\oint_A \sum_{p=1}^{n_p} x_{cp}\,\rho_p\,\vec{v}_p\cdot\vec{n}\,dA-\int_V \sum_{p=1}^{n_p} x_{cp}\,\rho_p\,\tilde{q}_p\,dV=\frac{\partial}{\partial t}\left(\int_V \sum_{p=1}^{n_p} x_{cp}\,\rho_p\,S_p\phi\,dV\right), \qquad (1)$$

onde o subscrito p refere-se a cada uma das n_p fases, x_{cp} é a fração mássica do componente c na fase p, ρ_p é a densidade, $\vec{v}_p$ é o vetor velocidade, $\vec{n}$ o vetor unitário normal a área A, $\tilde{q}_p$ o fluxo volumétrico, por unidade de volume, que é injetado em V, S_p é a saturação e ϕ é a porosidade.

A primeira parcela do lado esquerdo da Eq. (1) representa a razão mássica de fluxo do componente c que atravessa a superfície A , num sentido de fluxo oposto a direção do vetor normal unitário. A segunda parcela representa a razão de injeção de massa do componente c no volume de controle V. O termo do lado direito da Eq. (1) representa a variação da massa total do componente c no volume de controle V, ou seja a acumulação do componente c em todas as fases do sistema. A relação entre a velocidade superficial da fase p e o gradiente de potencial é obtida através da generalização da lei de Darcy

$$\vec{v}_p=-\frac{Kkr_p}{\mu_p}\vec{\nabla}\Phi_p\ , \qquad \text{onde:}\ \ \vec{\nabla}\Phi_p=\nabla p_p+\rho_p g\nabla D. \qquad (2)$$

Nas expressões anteriores k_{rp} é a permeabilidade relativa, μ_p a viscosidade, Φ_p o potencial, p_p a pressão, g a aceleração da gravidade, D a profundidade e **K** é o tensor diagonal de permeabilidades absolutas do meio poroso.

A substituição da Eq. (2) em (1) fornece a equação integral para o fluxo multifásico de cada componente c do sistema, através do volume representativo V. A forma discretizada da equação pode então ser obtida pela aproximação por diferenças finitas e constitui num sistema de equações não lineares. Este sistema é linearizado pelo método de Newton-Raphson e solucionado através de métodos iterativos.

O modelo Black-Oil, utilizado neste trabalho, considera três fases: a fase do hidrocarboneto líquido (o), a fase do hidrocarboneto gasoso (g) e a fase aquosa (w). Apenas três componentes são considerados: óleo ($\overline{o}$), água ($\overline{w}$) e gás ($\overline{g}$). Outras considerações do modelo são: o óleo e a água são imiscíveis e não trocam massa; o componente gás pode se dissolver nas fases óleo e água; os componentes óleo e água não se vaporizam na fase gás, em condições de reservatório e o fluxo é isotérmico.

As relações empíricas envolvendo pressões capilares são definidas por:

$$p_{cow}=p_o-p_w; \qquad p_{cog}=p_g-p_o, \qquad (3)$$

onde as pressões capilares p_c são funções conhecidas das saturações.

Para a completa formulação do problema é necessário ainda estabelecer as equações de equilíbrio de fases que na formulação Black-Oil podem ser substituídas por relações envolvendo propriedades das fases como densidades das fases, fator volume de formação(B), solubilidades e frações mássicas. Estas propriedades são baseadas em volumes medidos em condições normais, que são obtidas em laboratórios e denominadas relações PVT - pressão, volume e temperatura.

As últimas relações constitutivas a serem consideradas são as relações entre as permeabilidades relativas e as saturações das fases, consideradas funções monotônicas.

$$k_{rw}=k_{rw}(S_w);\quad k_{rg}=k_{rg}(S_g);\quad k_{ro}=k_{ro}(S_w,S_g) \qquad (4)$$

5. EXEMPLOS

Os três exemplos a seguir ilustram a aplicação do processo de mudança de escala proposto. Em todos os três casos a porosidade do meio é 30% e os parâmetros dos fluidos são os mesmos adotados por *Aziz* e *Odeh* (1981). As dimensões de cada bloco em todas as malhas de discretização mais refinadas são 304,8 m x 304,8 m.

5.1 Caso HERA

Este exemplo representa um meio homogêneo com permeabilidade constante igual a 700 mD. A malha fina é composta por 45 blocos, numa configuração de 15 por 3, enquanto a malha grossa é formada por 5 blocos, numa disposição 5x1. Neste exemplo um poço injetor de água esta localizado na posição (2,2) e um poço produtor na posição (14,2). As restrições de produção nestes poços são: vazão de injeção constante e igual a 6360 m^3/d no poço injetor e pressão de fundo especificada igual a 20670 kPa no poço produtor.

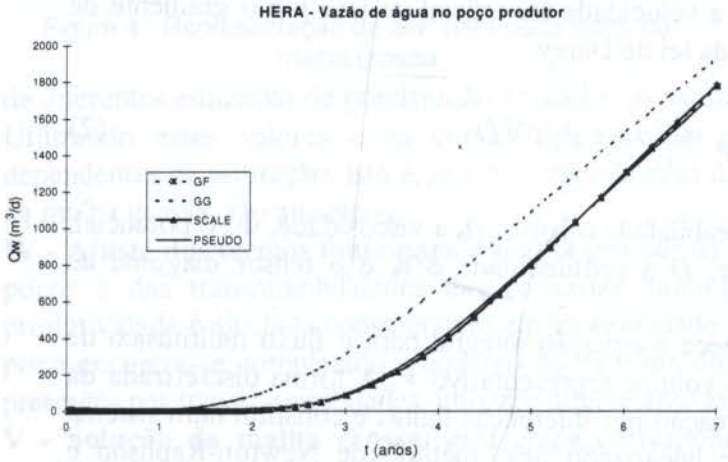

Figura 6 : Caso HERA - Comparação entre SCALE e PSEUDO

O gráfico da Fig. 6 compara resultados em termos de vazão de água no poço produtor obtidos pela simulação envolvendo todos os blocos da malha fina (GF), apenas os blocos da malha grossa sem qualquer alteração nas curvas de permeabilidades relativas (GG), a simulação através do procedimento multiescala proposto (SCALE) e o módulo PSEUDO do simulador comercial ECLIPSE. No PSEUDO são utilizadas as funções de *Kyte* e *Berry* (1975) associadas a pseudo-funções para poços propostas por *Emanuel* e *Cook* (1974).

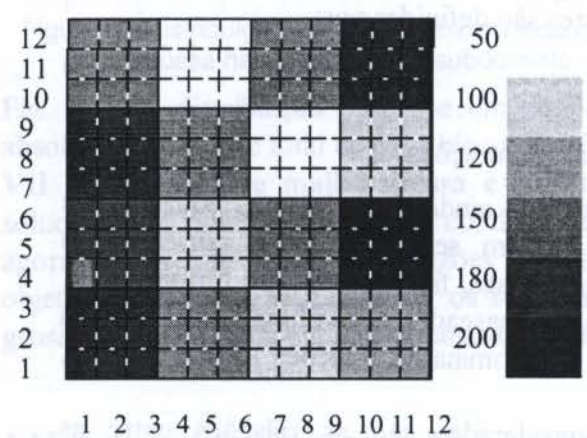

Figura 7 : Caso ZEUS - Malha fina e distribuição das permeabilidades, em mD.

5.2 Caso ZEUS

O caso ZEUS mostra um quarto de um esquema de injeção *five-spot*, com 3658 m de lado, onde a malha fina é composta por 144 blocos enquanto a malha grossa é formada por 16 blocos, conforme Fig. 7.

Neste exemplo o poço produtor esta situado na posição (2,2) operando com pressão de fundo constante igual a 20670 kPa enquanto o poço injetor, localizado em (11,11), opera com vazão de injeção constante e igual a 3180 m^3/d. Os resultados, em termos de vazão de água no poço produtor, para o GF, GG, SCALE e PSEUDO são apresentados na Fig.8.

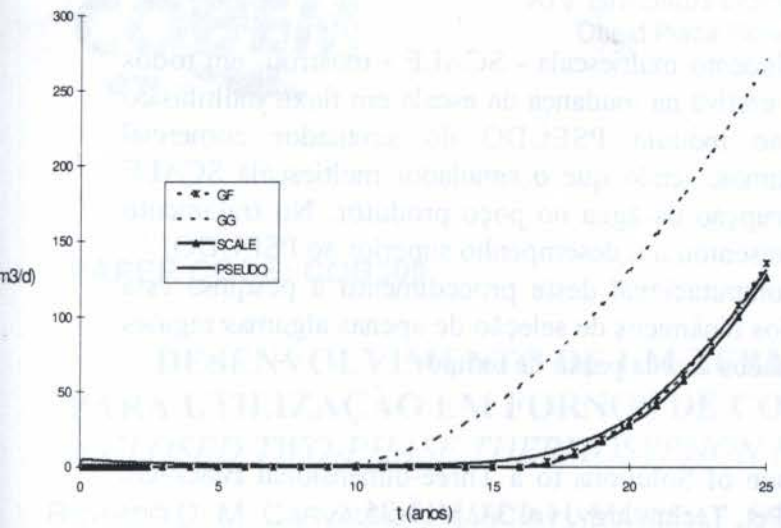

Figura.8 : Caso ZEUS - Comparação entre SCALE e PSEUDO

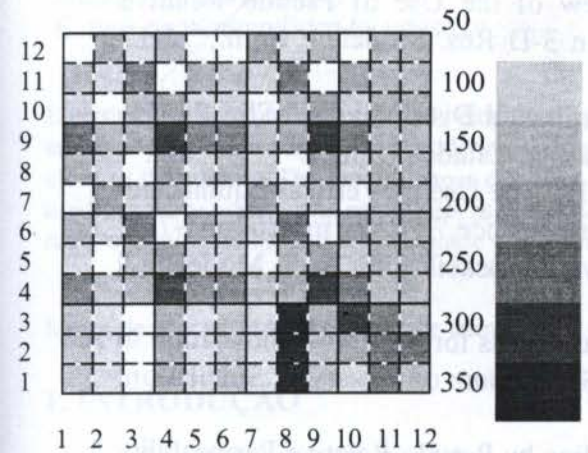

Figura 9 : Caso AJAX - Malha fina e distribuição das permeabilidades , em mD.

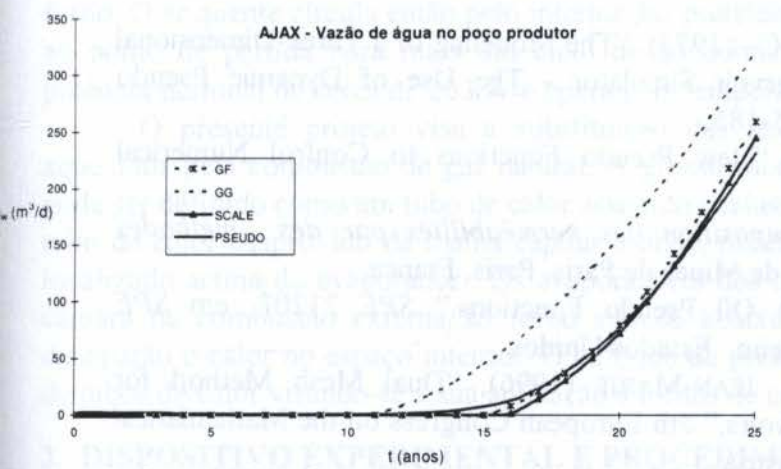

Figura 10 : Caso AJAX - Comparação entre SCALE e PSEUDO

5.3 Caso AJAX

O caso AJAX difere do caso ZEUS pela presença de heterogeneidade em todos os blocos da malha fina, como apresentado na Fig. 9. Para efetuar a mudança de escala das permeabilidades absolutas durante etapa de inicialização da malha grossa foi utilizado o Método de Le Loc'h (1987). Os resultados para este exemplo são apresentados na Fig. 10, mostrando a influência da heterogeneidade dos blocos da malha fina no ajuste do fluxo das fases nos blocos da malha grossa.

5.4 Comentários

Os casos apresentados mostraram boa concordância entre o procedimento proposto e a solução completa na malha fina. Em todos os exemplos observa-se um melhor desempenho do SCALE, quando comparado com PSEUDO, na obtenção do instante da irrupção da água no poço produtor. Além disto, a metodologia proposta também trata a mudança de escala em meios heterogêneos de forma mais precisa que o PSEUDO, como mostra o exemplo AJAX.

Uma análise do custo computacional, envolvendo o número de operações executado pelo método iterativo de solução do sistema de equações, mostra que, para problemas com razoável número de blocos, este procedimento executa menos operações que a solução da malha fina. A continuidade das pesquisas nesta área está concentrada na busca de critérios de seleção de subdomínios a serem resolvidos a cada passo de tempo, de forma a obter boas soluções a um custo menor do que aquele obtido com soluções em todos os subdomínios, como mostrado nos exemplos deste trabalho.

6. CONCLUSÕES

Os resultados obtidos com o procedimento multiescala - SCALE - mostrou, em todos os exemplos testados, ser esta metodologia efetiva na mudança da escala em fluxo multifásico em meios porosos. Comparativamente ao módulo PSEUDO do simulador comercial ECLIPSE, os resultados são bastante próximos, sendo que o simulador multiescala SCALE obtém com maior precisão o instante de irrupção da água no poço produtor. No tratamento das heterogeneidades o SCALE também apresentou um desempenho superior ao PSEUDO.

Com o objetivo de reduzir o custo computacional deste procedimento a pesquisa está atualmente direcionada para busca de critérios dinâmicos de seleção de apenas algumas regiões refinadas, os subdomínios, a serem solucionados a cada passo de tempo.

7. REFERÊNCIAS

AZIZ, K., ODEH, A. S., (1981), "Comparison of Solutions to a Three-dimensional Black-Oil Reservoir Simulation Problem," Journal of Pet. Technology, vol 33, p 13-25.

BARKER, J. W., DUPOUY, P. (1996), "An Analysis of Dynamic Pseudo Relative Permeabilities Methods ," 5th European Conf. on the Math. of Oil Recovery, 3-6 setembro, Leoben, Austria.

BARKER, J. W., THIBEAU, S. (1996), "A Critical Review of the Use of Pseudo Relative Permeabilities for Upscaling ," *SPE* 35491, em European 3-D Res. Modeling Conf., 16-17 abril, Stavanger, Noruega.

BEIER, R. A. ,(1992), "Pseudorelative Permeabilities From Fractal Distributions," *SPE* 24371, em *SPE* Rocky Moutain Regional Meeting, 18-21 maio, Casper, Estados Unidos.

COATS, K. H., DEMPSEY, J. R., HENDERSON, J. H. , (1971) "The Use of Vertical Equilibrium in Two Dimens. Simulation of Three-Dimensional Res. Performance," *SPEJ* , março, p63-71.

EMANUEL, A. S., COOK, G. W. , (1974), "Pseudo-Relative Permeability for Well Modeling," *SPE* 4731, *SPEJ*, fevereiro

GUÉRILLOT, D. R. , VERDIERE S. (1995), "Different Pressure Grids for Reservoir Simulation in Heterogeneous Reservoirs," *SPE* 29148 , em 13th SPE Symposium on Reservoir Simulation, 12-15 fevereiro, San Antonio , Estados Unidos.

HEARN, C. L. (1971), "Simulation of Stratified Waterflooding by Pseudo Relative Permeability Curves," Journal of Petroleum Technology, n 23, julho, p 805-813.

HEWETT, T. A., BERHENS, R. A., (1991), " Scaling Laws in Reservoir Simulation and Their Use ina Hybrid Finite Difference/Streamtube Approach to Simulating the Effects of Permeability Heterogeneity," Reservoir Characterization II, eds. L. W. Lake, H. B. Carrol e T. C. Wesson, Academic Press, p 402-411.

JACKS, H.H., SMITH, O. J. E., MATTAX, C.C., (1973) "The Modeling of a Three-Dimensional Reservoir With a Two-Dimensional Reservoir Simulator - The Use of Dynamic Pseudo Functions ," *SPE* 4071, *SPEJ*, junho, p 175-185.

KYTE, J. R., BERRY, D. W. ,(1975) , "New Pseudo Functions to Control Numerical Dispersion", *SPEJ*, agosto, p 269-276.

LE LOC'H, G, (1987), *Étude de la composition des perméabilités par des méthodes variationnelles*,- Thése de Doctorat, École de Mines de Paris, Paris, França.

STONE, H. L., (1991), "Rigorous Black Oil Pseudo Functions," *SPE* 21207, em *SPE* Symposium on Reservoir Simulation, Anaheim, Estados Unidos.

VERDIERE S., GUERILLOT, D., THOMAS, JEAN-MARIE (1996), "Dual Mesh Method for Multiphase Flows in Heterogeneous Reservoirs," 5th European Congress on the Mathematical of Oil Recovery, 3-6 setembro, Leoben, Austria

XIV Brazilian Congress of Mechanical Engineering
Obeid Plaza Hotel Convention Center - Bauru - SP/Brazil
December 08-12th 1997

PAPER CODE: COB309

DESENVOLVIMENTO DE UM TERMOSSIFÃO BIFÁSICO PARA UTILIZAÇÃO EM FORNOS DE COCÇÃO / *DEVELOPMENT OF A CLOSED TWO-PHASE THERMOSYPHON FOR USE IN BAKERY OVENS*

RICARDO D. M. CARVALHO[1], MÁRCIA H. MANTELLI[2], SÉRGIO COLLE[2] & JOSÉ A. S. LIMA[1]

[1]*Departamento de Engenharia Mecânica*
Faculdade de Engenharia de Joinville
89223-100 Joinville, SC
E-mail: dem2rdmc@dcc.fej.udesc.br

[2]*Departamento de Engenharia Mecânica*
Universidade Federal de Santa Catarina
88000-000 Florianópolis, SC
E-mail: marcia@labsolar.ufsc.br

Abstract

Electricity-powered ovens are largely employed by bakeries in Brazil, which constitutes a misuse of this form of energy. This is even more so considering that hydroelectric energy resources in the country might be coming close to their limit. The present paper describes the design, manufacture, and testing of thermosyphons to be used in bakery ovens using natural gas as the heat source. The design geometrical parameters, working fluid fill ratio, operation limits, and the two-phase flow pattern are discussed.

Keywords

fornos de cocção, projeto e ensaio de termossifões / bakery ovens, thermosyphon design and testing

1. INTRODUÇÃO

Um forno de padaria típico possui um espaço interno com dimensões H = 900 mm, W = 500 mm e D = 850 mm e comporta uma prateleira para nove bandejas com dimensões H = 890 mm, W = 400 mm e D = 800 mm. Na parede traseira, encontram-se um ventilador e resistências elétricas para circulação e aquecimento do ar. O ar é insuflado sobre as resistências, de onde é direcionado para o vão lateral entre a prateleira e a superfície interna do forno. O ar quente circula então pelo interior das prateleiras, cedendo calor aos pães, e retorna ao ponto de partida para mais um ciclo de aquecimento/resfriamento. O forno tem uma potência nominal de cerca de 20 kW e opera com temperaturas do ar entre 150 °C e 220 °C.

O presente projeto visa a substituição das resistências elétricas por termossifões aquecidos pela combustão de gás natural. A grosso modo, um termossifão bifásico fechado pode ser definido como um tubo de calor assistido exclusivamente pela gravidade, ou seja, um tubo de calor desprovido da malha capilar e onde, necessariamente, o condensador deve ser localizado acima do evaporador. Os evaporadores dos termossifões serão mantidos em uma câmara de combustão externa ao forno situada abaixo deste, enquanto os condensadores dissiparão o calor no espaço interno. O enfoque do presente artigo é a fabricação e os testes de tubos de calor visando-se a sua aplicação a fornos de cocção conforme descrito acima.

2. DISPOSITIVO EXPERIMENTAL E PROCEDIMENTO DE TESTE

Projeto do Termossifão: Considerou-se que o comprimento do condensador devesse ser aproximadamente igual à altura do espaço interno do forno, enquanto o comprimento do

evaporador requer a consideração da carga térmica aplicada a cada termossifão. Para tal, deve-se determinar o número total de tubos de calor que devem ser introduzidos no interior do forno. A este respeito, para a fabricação dos termossifões optou-se por utilizar tubos de aço inoxidável com D_o = 19,05 mm e D_i = 17,05 mm. Estes tubos são facilmente encontrados no comércio e não apresentam problemas quanto à sua utilização em laboratório ou, eventualmente, no protótipo do forno de cocção. Portanto, para uma profundidade de 810 mm do vão entre a parede interna do forno e as prateleiras, podem ser instalados 21 tubos de calor deixando-se entre eles um espaço de aproximadamente 10 mm, isto é, 29,05 mm de centro a centro. Tem-se 42 tubos de calor com carga térmica individual de cerca de 476 W.

Conforme será visto mais adiante, o limite operacional para o fluxo de calor aplicado ao termossifão, tendo-se a água como fluido de trabalho, é de aproximadamente 220 kW/m^2. Logo, para q = 476 W a área mínima do evaporador para cada termossifão deve ser 2,16 x 10^{-3} m^2, a qual corresponde um comprimento L_e = 36 mm. Optou-se por utilizar L_e = 220 mm por questões de facilidade de construção do protótipo de teste e da câmara de combustão da aplicação real. Os comprimento do termossifão utilizado são então L_c= 1000 mm e L_e=220 mm, ou seja, um comprimento total de 1220 mm.

Com relação ao volume de fluido de trabalho utilizado, um termossifão é caracterizado pela razão de enchimento, $F = V_l / V_e$; onde V_l é o volume total de fluido de trabalho e V_e é o volume do evaporador. Cálculos preliminares mostraram que o volume mínimo de fluido requerido para uma carga térmica de 500 W é de aproximadamente 5 ml, a qual corresponde uma razão de enchimento F = 0,10. Este é o volume mínimo para se manter apenas um filme de líquido nas paredes do termossifão, isto é, não se prevê a existência de um reservatório de líquido (Faghri, 1994). Por outro lado, Groll e Rösler (1992) recomendam que o valor de F esteja entre 0,4 e 0,6 para termossifões orientados verticalmente e entre 0,6 e 0,8 para termossifões inclinados. Destas considerações, decidiu-se utilizar para o presente protótipo, que operará orientado verticalmente, F = 0,6.

Construção do Protótipo: Uma vez determinados os valores apropriados para os parâmetros geométricos e para o volume do fluido de trabalho, procedeu-se à construção do termossifão. O primeiro passo é a limpeza do tubo de aço inoxidável e das outras peças constituintes do termossifão de modo a se assegurar a não contaminação do fluido de trabalho por impurezas. Isto é feito em um banho ultra-sônico durante aproximadamente 15 minutos utilizando-se tricloroetileno como solvente à temperatura aproximada de 35 °C.

Este procedimento é repetido até se obter um alto nível de limpeza do tubo e das demais peças. A soldagem das peças constituintes do termossifão é então feita em atmosfera inerte (argônio) a fim de se evitar a formação de óxidos que contaminariam o fluido de trabalho. Este óxidos, por sua vez, ocasionariam a formação de gases não condensáveis que se acumulariam no interior do termossifão, diminuindo a sua eficiência.

Neste ponto, está-se apto à evacuação e enchimento do termossifão com o fluido de trabalho. Para tal, dispõe-se de uma linha de evacuação e carga de tubos de calor (Fig. 1). O projeto deste sistema foi baseado principalmente na descrição apresentada por Dunn e Reay (1982) e consiste basicamente de uma bomba turbomolecular de alto vácuo que atua diretamente sobre o tubo de calor ou sobre tanques de depuração do fluido de trabalho. O direcionamento do vácuo para os tubos ou para os tanques é feito através de válvulas. Primeiramente procede-se à evacuação das linhas de conexão e à depuração do fluido dos gases inertes nele dissolvidos. Este processo de purificação consiste no congelamento do fluido a níveis criogênicos, evacuação da linha e posterior liquefação do fluido. Este ciclo é repetido até se obter o vácuo desejado (10^{-5} Torr). O tubo de calor é então ligado ao sistema para evacuação e carregamento com o fluido de trabalho. O procedimento de evacuação é

análogo ao descrito anteriormente. A bureta permite a medição precisa do volume de líquido a ser transferido para o tubo de calor. Uma vez carregado, o tubo de calor é então selado.

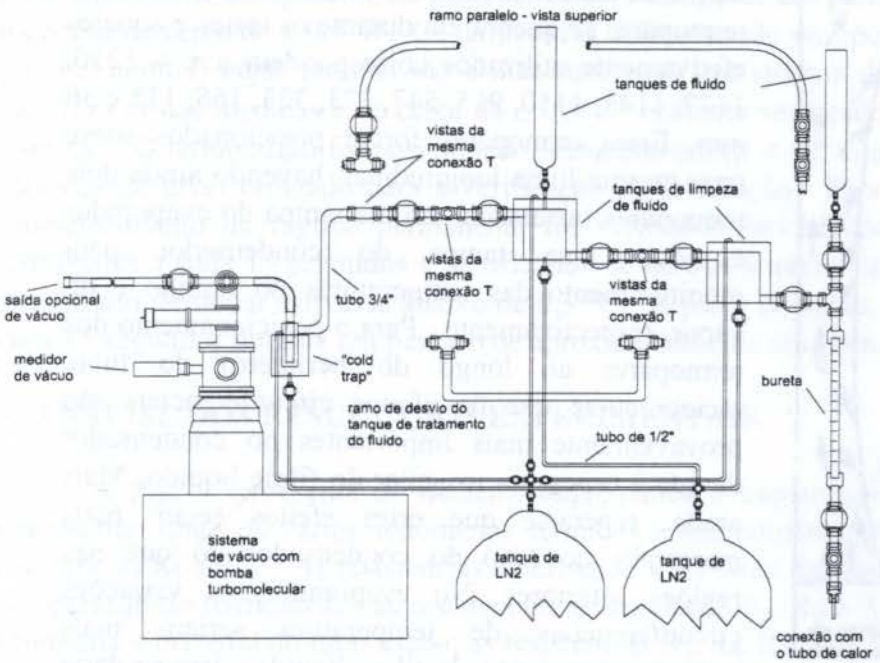

Fig. 1 : Linha de evacuação e carga de tubos de calor (NCTS-LABSOLAR-UFSC).

A função da armadilha criogênica é melhorar o vácuo da linha e proteger a bomba turbomolecular de partículas indesejáveis. O sistema de evacuação prevê ainda uma saída optativa para evacuação de outros dispositivos como, por exemplo, bombas capilares. Há também a possibilidade de conexão a um tanque de argônio quando da construção de tubos de calor de condutividade térmica variável, ou seja, tubos de calor contendo uma massa conhecida de gás inerte misturada ao fluido de trabalho.

Instrumentação do Protótipo: Concluída a construção o tubo de calor, este foi devidamente instrumentado com termopares. Os pontos de medida foram escolhidos de modo a se poder inferir a configuração do escoamento bifásico no interior do termossifão a partir dos valores de temperatura. Referindo-se à Fig. 2, observa-se que a espessura do filme de condensado aumenta de cima para baixo em L_c, o que implica em uma resistência de condução radial do filme crescente neste sentido. Como a temperatura do vapor, T_v, e da água de refrigeração, T_∞, são essencialmente constantes, a variação da temperatura da parede do condensador, T_{co}, seguirá a variação da resistência de condução do filme de condensado. Espera-se que no topo do condensador, onde se dá a formação inicial do filme de líquido, e nas regiões próximas ao evaporador, onde ocorre a mudança súbita da condição de contorno, estas variações sejam maiores. Nas regiões centrais do condensador, as variações da espessura do filme provavelmente não são altas a ponto de causarem variações substanciais da temperatura T_{co}.

No evaporador, há fenômenos térmicos e hidrodinâmicos ocorrendo em um comprimento de apenas 220 mm. Espera-se que a temperatura da parede do evaporador, T_{eo}, aumente de cima para baixo não somente pela proximidade com o condensador, mas também porque a vaporização do filme líquido em L_f muitas vezes remove calor mais eficazmente do que a ebulição em reservatório em L_p. O comprimento L_f é o comprimento total do filme de líquido no evaporador, incluindo o comprimento do filme que penetra no reservatório de líquido, $L_{f,p}$. Este último vem compensar a perda de massa por evaporação na superfície do reservatório de líquido. Os comprimentos L_f e L_p dependem da carga térmica aplicada, mas acredita-se que estas variações só sejam significativas para cargas térmicas muito diferentes. Isto é, não se espera poder detectar variações destes comprimentos a partir das medidas de temperatura.

O espaçamento entre os termopares foi definido a partir das considerações acima. Optou-se por uma maior concentração dos termopares ao longo de todo o evaporador e no topo e na base do condensador. Infelizmente vários termopares se quebraram durante os testes e aqueles efetivamente utilizados correspondem a x = 1210, 1177, 1143, 1110, 915, 547, 373, 323, 168, 115 e 36 mm. Estes termopares foram posicionados sobre uma mesma linha longitudinal, havendo ainda dois termopares instalados, um, na tampa do evaporador e, outro, na tampa do condensador para monitoramento das temperaturas do líquido e do vapor, respectivamente. Para o posicionamento dos termopares ao longo do perímetro do tubo, raciocinou-se que os efeitos circunferenciais são provavelmente mais importantes no condensador devido à espessura irregular do filme líquido. Mais ainda, espera-se que estes efeitos sejam mais marcantes no topo do condensador do que nas regiões inferiores. No evaporador, as variações circunferenciais de temperatura seriam mais marcantes na região do filme líquido. Isto se daria pela proximidade com o condensador e também pelas perturbações causadas pela agitação no reservatório de líquido. A escolha das posições circunferenciais para a fixação dos termopares adveio destas considerações. Mais uma vez, foram instalados termopares em várias posições mas vários deles se quebraram durante os testes. Os termopares efetivamente utilizados para a verificação de variações circunferenciais de temperatura estão localizados em x = 1210, 1177 e 1143 mm.

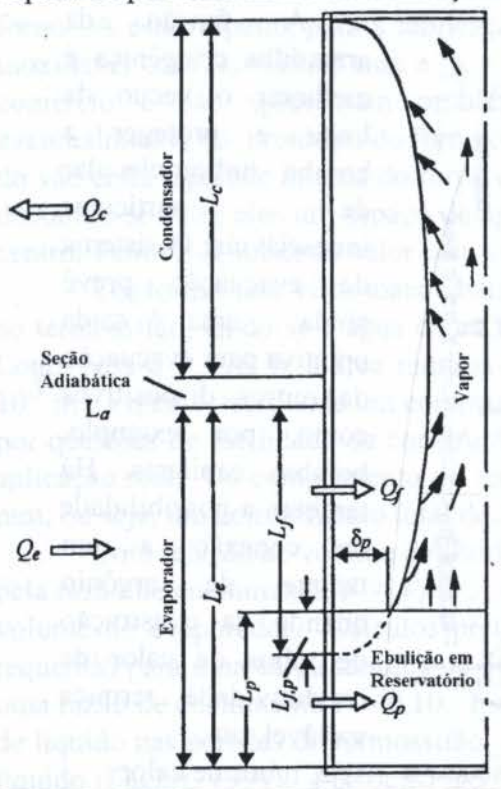

Fig. 2. : Configuração do escoamento bifásico no interior do termossifão (Faghri, 1994).

Dispositivo Experimental e Procedimento de Teste: Os dados experimentais foram obtidos utilizando-se as instalações do Núcleo de Controle Térmico de Satélites (NCTS) da Universidade Federal de Santa Catarina (UFSC). A Fig. 3 mostra esquematicamente o dispositivo experimental utilizado para a obtenção destes dados. O condensador é resfriado por água que escoa no espaço anular entre o condensador e uma tubulação de PVC que o envolve. A temperatura desta água de resfriamento foi fixada em 15 °C ± 0,1 °C por um banho térmico com capacidade de absorção de 1000 W de potência. A máxima carga térmica aplicada ao termossifão foi 500 W, representativa da aplicação real. Os níveis de pressão e temperatura no termossifão associados a esta carga térmica mantêm-se seguramente abaixo dos valores máximos tolerados pelo tubo de aço inoxidável (13,20 MPa a 204 °C). O evaporador do termossifão é

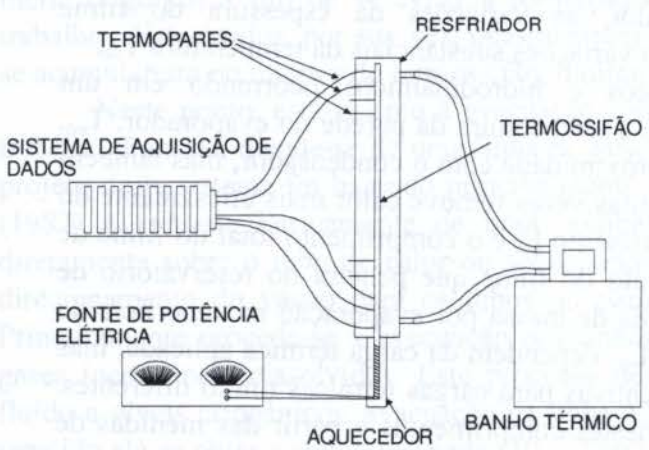

Fig. 3 - Dispositivo de teste do termossifão.

aquecido por uma resistência do tipo lâmina ("skin heater") especialmente fabricada para este fim (Güths *et al.*, 1995).A potência transmitida pelo tubo de calor foi admitida igual à potência elétrica dissipada. Esta pode ser calculada a partir dos parâmetros elétricos com uma incerteza de cerca de ± 0,5 W. Os termopares utilizados são do tipo T (cobre-constantan) e K (cromel-alumel) cujas leituras são armazenadas em um sistema de aquisição de dados. A incerteza nestas medidas é de cerca de ± 0,5°C conforme verificado por calibração prévia do sistema . O termossifão foi posicionado verticalmente ($\beta = 90°$) durante os testes, sendo um medidor de nível utilizado para a verificação da orientação. Para cada potência testada, o estabelecimento do regime permanente foi verificado procedendo-se à leitura dos vários termopares a cada 15 segundos e certificando-se de que a maior variação de temperatura em um mesmo termopar estivesse abaixo de 0,3 °C. A partir de então, os dados foram obtidos a cada 15 segundos durante um período de aproximadamente uma hora.

3. ANÁLISE DOS RESULTADOS EXPERIMENTAIS

A Fig. 4 representa de maneira esquemática o escoamento bifásico no interior do termossifão onde os vários fenômenos térmicos e hidrodinâmicos são representados pelas resistências R_1 a R_{10}. As resistências externas R_1 e R_9 estão ligadas diretamente às condições de operação do termossifão; as resistências de condução R_2, R_8 e R_{10} são determinadas pela geometria e material do tubo usado; as resistências R_3, R_4, R_5, R_6 e R_7 são determinadas pelas características do escoamento bifásico no interior do tubo, que por sua vez dependem diretamente da carga térmica aplicada. As resistências R_4 e R_6 ocorrem na interface líquido-vapor do evaporador e condensador, respectivamente. A resistência R_5 está associada à queda da temperatura de saturação entre o evaporador e o condensador causada pela perda de carga do escoamento de vapor. Normalmente, as resistências R_4, R_5 e R_6 podem ser desprezadas (Groll e Rösler, 1992), o que será feito neste trabalho.

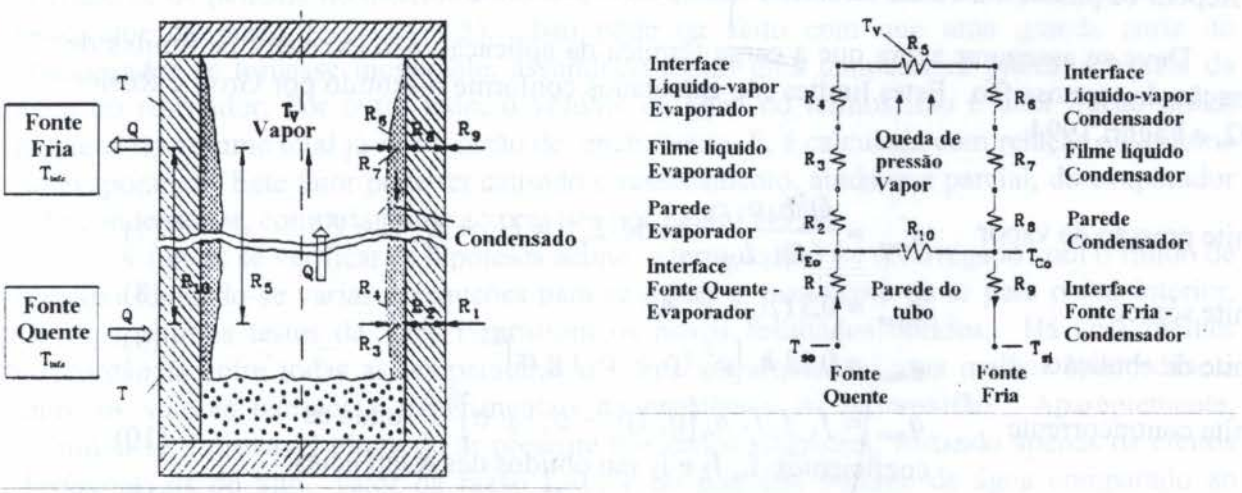

Fig. 4 - Circuito térmico representativo do termossifão bifásico fechado (Brost, 1996).

Para este problema particular envolvendo uma carga térmica conhecida, tem-se por objetivo determinar as temperaturas de operação T_{eo}, T_v, T_p e T_{co} bem como a resistência térmica global do termossifão. A comparação destas com as medidas experimentais permitirá validar os procedimentos de projeto, fabricação e teste dos tubos de calor.

O procedimento de cálculo dos parâmetros de operação do termossifão foi baseado naquele dado por Brost (1996). Os passos deste procedimento são descritos a seguir.

1. Cálculo de R_9 utilizando-se correlações clássicas de convecção forçada.
2. Cálculo de $R_2 = \ln (D_o/D_i)/2\pi k L_e$, $R_8 = \ln (D_o/D_i)/2\pi k L_c$ e $R_{10} = [L_a + 0{,}5(L_l + L_c)]/A_x k_x$.
3. Estimativa inicial de T_v: $T_v = T_{sat} = T_\infty + q(R_8 + R_9)$ admitindo-se $R_7 = 0$ e $R_{10} \to \infty$.
4. Avaliação das propriedades físicas da água à temperatura de saturação T_v.
5. Estimativa de p_p no evaporador: $p_p = p_v + \rho_l g F L_e \operatorname{sen}\beta$
6. Cálculo de $R_3 = R_{3p}$ para $R_{3p} < R_{3f}$ ou $R_3 = R_{3p}F + R_{3f}(1-F)$ onde,

$$R_{3f} = \frac{0{,}235\, q^{1/3}}{D_i^{4/3} g^{1/3} L_e \Phi_2^{4/3}};\quad \Phi_2 = \left[\frac{h_{lv} k_l^3 \rho_l^2}{\mu_l}\right]^{0{,}25} \quad \text{e,} \tag{1}$$

$$R_{3p} = \frac{1}{\Phi_3 g^{0{,}2} q^{0{,}4} \left(\pi\, D_i L_e\right)^{0{,}6}};\quad \Phi_3 = \frac{\rho_l^{0{,}65} k_l^{0{,}3} c_{p_l}^{0{,}7}}{\rho_v^{0{,}25} h_{lv}^{0{,}4} \mu_l^{0{,}1}} \left[\frac{p_v}{p_{at}}\right]^{0{,}23} \tag{2}$$

7. Cálculo da resistência de condução do filme de condensado, R_7

$$R_7 = \frac{0{,}235\, q^{1/3}}{D_i^{4/3}\, g^{1/3} L_c \Phi_2^{4/3}} \tag{3}$$

8. Cálculo da resistência térmica global do termossifão, R_t

$$R_t = \left[\frac{1}{R_2 + R_3 + R_7 + R_8} + \frac{1}{R_{10}}\right]^{-1} + R_9 \tag{4}$$

9. Cálculo das temperaturas médias do condensador e do evaporador, T_{co} e T_{eo}

$$T_{co} = T_{si} + q \cdot R_9 \quad \text{e} \quad T_{eo} = T_{si} + q \cdot R_t \tag{5}$$

10. Novo cálculo de T_v

$$T_v = T_{co} + \left[q - \frac{T_{eo} - T_{co}}{R_{10}}\right](R_7 + R_8) \tag{6}$$

11. Repetir os passos 4 a 10 até se obter convergência para T_v ($\Delta T_v < 0{,}5$ °C)

Deve-se assegurar agora que a carga térmica da aplicação não excederá os limites de operação do termossifão. Estes limites são calculados conforme discutido por Groll e Rösler, 1992, e Faghri,1994.

Limite pressão de vapor $$q''_{max} = \frac{D_i^2 h_{lv} \rho_v p_v}{64 \mu_v L_{eff}} \text{ onde } L_{eff} = L_{co} + L_{eo}(1-F) \tag{7}$$

Limite sônico $$q''_{max} = 0{,}5\,(p_v \rho_v)^{0{,}5} h_{lv} \tag{8}$$

Limite de ebulição $$q''_{max} = 0{,}12\, h_{lv}\left[\rho_v^2\, (\rho_l - \rho_v)\, g\, \sigma\right]^{0{,}25} \tag{9}$$

Limite contracorrente $$q''_{max} = f_1\, f_2 f_3\, h_{lv}\left[\rho_v^2\, (\rho_l - \rho_v)\, g\, \sigma\right]^{0{,}25}$$ onde os coeficientes f_1, f_2 e f_3 são obtidos das referências. (10)

Para o termossifão em questão, o limite de operação mais baixo é o limite de ebulição (cerca de 440 kW/m^2). A razão de enchimento utilizada (F = 0,6) é suficientemente alta de modo a tornar o limite de ressecamento seguramente elevado quaisquer que sejam as condições de operação do termossifão (Faghri, 1994). Por outro lado, Brost (1996) recomenda que o termossifão seja projetado para operar abaixo de 50% do fluxo máximo permitido. Para uma carga térmica máxima de 500 W, tem-se q" = 38 kW/m^2 no evaporador. Estando este valor bastante abaixo de 220 kW/m^2 (metade do limite de ebulição no presente projeto), pode-se esperar que o termossifão operará seguramente em fornos de cocção.

A Tab. 1 apresenta os valores do principais parâmetros de operação do termossifão em função da carga térmica aplicada. Optou-se por utilizar a resistência global do termossifão propriamente dito ($R = R_2 + R_3 + R_7 + R_8$) devido à grande incerteza no valor de R_9.

Tabela 1: Parâmetros de operação do termossifão em função da carga térmica aplicada.

no.	q	T_{si}	Teo [°C]		Tco [°C]		Tv [°C]		Tp [°C]		$R_{termossifão}$ [°C/W]	
	[W]	°C	Teór.	Exp.	Teór.	Exp.	Teór.	Exp.	Teór.	Exp.	Teór.	Exp.
1	85,6	15	19,3	78,7	17,8	19,1	18,1	18,9	26,0	77,2	0,0160	0,695
2	97,0	15	19,8	84,5	18,1	19,0	18,4	23,2	26,1	80,3	0,0159	0,675
3	198,5	15	24,7	87,8	21,5	19,9	22,0	24,1	28,5	80,4	0,0148	0,342
4	299,2	15	29,3	90,0	24,7	21,0	25,6	24,3	30,9	80,6	0,0140	0,231
5	405,1	15	34,0	89,6	28,0	20,9	29,3	21,6	33,5	80,0	0,0135	0,170
6	499,8	15	38,2	91,9	31,0	21,7	32,7	23,0	36,0	80,0	0,0131	0,140
7	266,6	55	67,4	71,4	63,5	58,2	64,2	49,0	65,0	59,1	0,0133	0,063
8	411,6	15	34,3	41,5	28,2	20,5	29,5	22,2	33,5	32,5	0,0134	0,051

$R_{termossifão,\ teórico} = R_2 + R_3 + R_7 + R_8$ $\qquad$ $R_{termossifão,\ experimental} = (T_{eo} - T_{co}) / q$

Observa-se no seis primeiros testes uma enorme discrepância entre os valores teóricos e experimentais das temperaturas da parede do evaporador, T_{eo}, e do reservatório de líquido, T_p. Com relação à temperatura do vapor, T_v, e da parede do condensador, T_{co}, a discrepância é muito menor embora as tendências não sejam as mesmas. As discrepâncias nos valores de T_{eo} e T_{co}, por sua vez causam a discrepância entre os valores teóricos e experimentais da resistência do termossifão. Acredita-se que este comportamento tenha sido causado, em parte, pela presença de ar no termossifão devida a uma possível falha no carregamento do mesmo com o fluido de trabalho. O ar, pelo seu efeito isolante, causaria uma redução drástica no coeficiente de película no interior do tubo. Além disso, um outro fator a ser considerado é o alto valor da razão L_c/L_e (= 4,5). Isto pode ter feito com que uma grande parte do condensador se tornasse inoperante, assumindo assim uma temperatura próxima àquela da água no resfriador. Por outro lado, o volume de água no termossifão é uma fração muito pequena do volume total já que a razão de enchimento, F, é calculada com relação ao volume do evaporador. Este fator pode ter causado o ressecamento, ainda que parcial, do evaporador e do condensador, contrariamente ao previsto por Faghri (1994).

A fim de se verificar as hipóteses acima, o termossifão foi recarregado com o fluido de trabalho tomando-se várias precauções para se evitar o vazamento de ar para o seu interior. Os dois últimos testes da Tab. 1 mostram os novos resultados obtidos. Há uma melhor concordância entre todas as temperaturas e, como conseqüência, uma melhor concordância entre os valores teóricos e experimentais da resistência do termossifão. Aparentemente, eliminou-se o provável efeito do ar presente nos dados anteriores, restando apenas os efeitos desfavoráveis do alto valor da razão L_c/L_e e do pequeno volume de água comparado ao volume total do termossifão.

Embora não haja concordância entre os valores teóricos e experimentais para a resistência do termossifão, as tendências são as mesmas em ambos os casos. A diminuição da resistência com o aumento da potência se explica pelo aumento da pressão. A maiores pressões, há uma maior tendência da água em formar um filme líquido na parede do tubo, melhorando as condições de troca térmica com uma conseqüente diminuição da resistência do termossifão. Este fator também explica a melhor concordância entre experimento e teoria para valores crescentes da potência aplicada.

A Fig. 5 apresenta a distribuição de temperaturas ao longo do tubo para 405 W. Vê-se que as distribuições de temperaturas obtidas não correspondem exatamente àquelas antecipadas na seção *Instrumentação do Protótipo*. Isto se deve às condições desfavoráveis de transferência de calor no interior do termossifão, já discutidas. Há um aumento da temperatura na base do evaporador devido a um provável ressecamento, enquanto que no condensador há um aumento da temperatura nas regiões superiores. Este comportamento pode ser explicado pelo efeito isolante do ar acumulado no topo do termossifão. Finalmente, não foi detectada qualquer variação circunferencial de temperatura no termossifão.

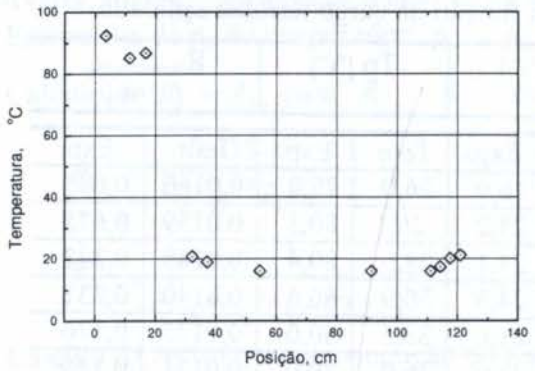

Fig. 5: Distribuição de temperaturas ao longo do tubo para q = 405 W.

4. CONCLUSÕES

Os dados experimentais mostraram valores excessivamente altos para a resistência do termossifão. Este comportamento seria explicado, sobretudo, pelo efeito desfavorável do alto valor da razão L_c/L_e e pelo pequeno volume de água comparado ao volume total do termossifão. Isto significa que o projeto do termossifão deverá ser modificado, aumentando-se o comprimento do evaporador (o que implicará em uma maior câmara de combustão na aplicação real). Como continuação desta investigação, serão testados termossifões assim projetados com diferentes valores da razão de enchimento.

Não se obteve a distribuição de temperaturas prevista ao longo do termossifão devido às condições desfavoráveis de troca térmica no seu interior. Espera-se que o novo projeto permita não simplesmente viabilizar a aplicação prática desejada, mas também proceder-se a um estudo sistemático do escoamento bifásico no interior do termossifão.

Embora mudanças no projeto do termossifão sejam necessárias, esta fase inicial deste projeto de pesquisa permitiu o aprimoramento no NCTS-LABSOLAR-UFSC dos procedimentos de fabricação e teste de tubos de calor.

5. REFERÊNCIAS

Brost, O., *Closed Two-Phase Thermosyphons*, Palestra Especial, LABSOLAR/NCTS-UFSC, 1996.

Dunn, P.D. e Reay, D.A. *Heat Pipes*, Elsevier Science Ltd., Pergamon, 4ª edição, 1994.

Faghri, A., *Heat Pipe Science and Technology*, pág. 341-440, 1994.

Groll, M e Rösler, S., *Operation Principles and Performance of Heat Pipes and Closed Two-Phase Thermosyphons*, J. of Non-Equilibrium Thermodynamics, Vol. 17, No. 2, págs. 91-151, 1992.

Güths, S., Philippi, P.C., Gaviot, E. e Thery, P., *Um Transdutor de Fluxo de Calor a Gradiente Tangential*, COBEM-CIDIM, 1995.

UNESP COBEM 97

XIV Brazilian Congress of Mechanical Engineering
Obeid Plaza Hotel Convention Center - Bauru - SP/Brazil
December 08-12th 1997

PAPER CODE: COB343

ESTIMATING THE THICKNESS OF THE LIQUID FILM GENERATED BY Y-JET ATOMIZERS

HERALDO DA SILVA COUTO & DEMÉTRIO BASTOS-NETTO

Laboratório Associado de Combustão e Propulsão, Centro Espacial de Cachoeira Paulista – INPE – SP

CEP 12630-000 Cachoeira Paulista, SP, Brasil – E-mail: demetrio@yabae.cptec.inpe.br

Abstract

Internal mixing twin fluid air blast (Y-jet) atomizers, in which liquid is injected into a mixing chamber with compressed air or steam, are extensively used in industry. It is well known that one of the main design parameters for pre filming blast atomizers is the thickness of the liquid film generated at the discharge orifice. This paper derives an expression for estimating that film thickness assuming that, apart from a small amount of droplets formed by the impact of the liquid on the air stream inside the pre-mixing chamber, the great majority of droplets is generated by the liquid film formed on the pre-mixing chamber wall through the deflection of the liquid jet by the high speed gas stream flowing through the center core of the pre-mixing chamber. That is, this Atomizer, usually classified as an "internal mixing, blast atomizer" behaves instead as a "pre filming blast atomizer". The results compared well with experiments.

Keywords

Atomizers, Y-Jet Atomizers, Liquid Films, Droplets and Sprays

1. INTRODUCTION

Internal mixing twin fluid air blast (Y-jet) atomizers, in which liquid is injected into a mixing chamber with compressed air or steam, are extensively used in industry. The principles of functioning of this atomizer were described in an experimental paper by Mullinger and Chigier , 1964, who used an empirical correlation obtained by Wigg,1964, to evaluate the effects of flow parameters on the spray droplet mean diameter. This correlation, however, is far from being of general use, as it does not offer satisfactory results in its estimate of the Sauter Mean Diameter (SMD) for fluids such as water, besides offering in general a sizable deviation from measured SMD's. The point is that the litterature on the subject treats the Y-Jet atomizer as an "internal mixing twin-fluid air blast atomizer". On the other side, it is well known that one of the main design parameters for prefiming blast atomizers is the thickness of the liquid film generated at the discharge orifice.

This paper derives an expression for estimating that film thickness assuming that, apart from a small amount of droplets formed by the impact of the liquid on the air stream inside the pre-mixing chamber, the great majority of droplets is generated by the liquid film formed on the pre-mixing chamber wall through the deflection of the liquid jet by the high speed gas

stream flowing through the center core of the pre-mixing chamber. This is to say that the Y-Jet Atomizer, usually classified as an "internal mixing air blast atomizer" behaves instead as a "pre filming air blast atomizer". This theory used to estimate the SMD, is then compared with LDV droplet size measurements.

2. PROBLEM DESCRIPTION

Figure 1 shows a schematic of a typical Y-Jet Airblast Atomizer. The liquid upon entering the mixing chamber is pushed against its walls by the incoming pressurized atomizing gas generating a liquid film.

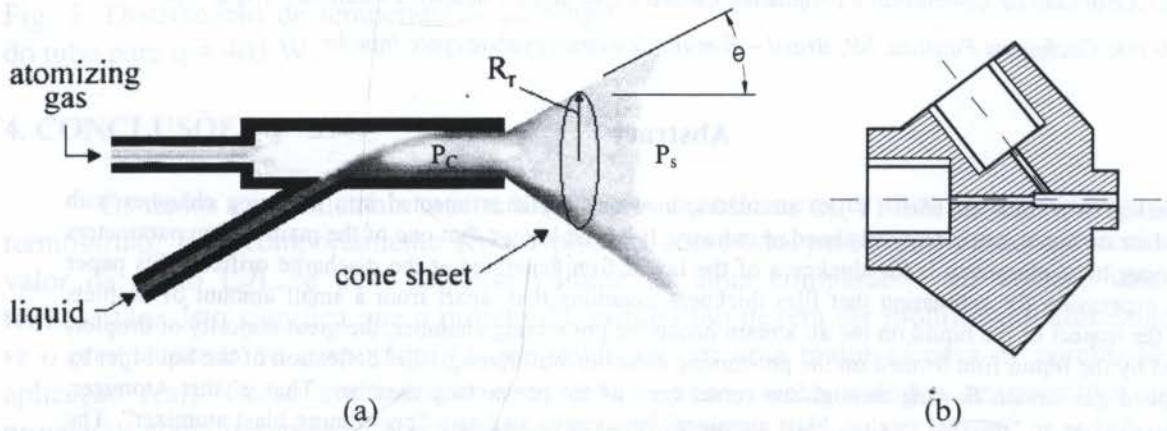

Figure 1 a - Schematic of a Y-Jet Atomizer and its assumed Conical Sheet
b - Y-Jet Injection Head

This liquid film is then ejected from the discharge orifice as a nearly conical sheet which disintegrates into fragments which form unstable ligaments that contract under the action of surface tension, forming droplets. Once the film thickness is estimated then, the SMD of these droplets is calculated using an analogy based upon the hypothesis of Dombrowski and Johns, (1963), regarding the behavior of a planar disintegrating liquid sheet, who showed that the main source of instabilities that causes sheet disintegration into droplets is related to the interaction between the sheet and the surrounding gaseous medium, when disturbances interact with the sheet. They derived an equation for the droplet size based on the concept of a planar liquid sheet and their theoretical values compared well with experimental results.

These ideas can be applied to the Y-Jet atomizer if one assumes that the conical liquid sheet formed from the atomizer discharge orifice possesses a much larger rupture radius than the sheet thickness and that the wavelength of the ripples formed in the liquid film grows until their amplitude equals the ligament radius, so that one droplet is produced per wavelength (Dombrowski and Johns, 1963). Once the thin conical sheet is established, the amplitude of the ripples away from the injector is assumed to be much smaller than the cone diameter so that disturbances "see" the conical sheet as a plane one.

3. GOVERNING EQUATIONS

As the atomizing gas and the liquid are discharged together in the surrounding medium the main parameter in this process is the difference between the chamber pressure, P_c, and the ambient pressure, P_s, which are the same for both fluids, i.e.,

$$\Delta P_l = \Delta P_{ar} = P_c - P_s \tag{1}$$

The liquid sheet velocity is given by:

$$U_f = C_d\left(\frac{2\Delta P_l}{\rho_l}\right) \tag{2}$$

where C_d is the discharge coefficient and ρ_l is the liquid density.
The continuity equation for incompressible fluids yields

$$\dot{m}_f = \rho_l U_f \frac{\pi}{4}\left[D_o^2 - (D_o - h_0)^2\right] \tag{3}$$

where $\frac{\pi}{4}\left[D_o^2 - (D_o - h_0)^2\right]$ is the area of the ring formed by the liquid film at the injector exit, D_o is the chamber exit diameter, h_0 is the liquid film thickness and $\dot{m}_f$ is the liquid mass flow rate. Then:

$$h_0 = \frac{D_0 - \left(D_0^2 - \frac{4\dot{m}_f}{\pi\rho_l U_f}\right)^{\frac{1}{2}}}{2} \tag{4}$$

Dombrowski and Johns (1963), derived the following expression for estimating the diameter of the ligaments, d_l, formed upon the breaking of a liquid film:

$$d_l = 2\left(\frac{4}{3f}\right)^{\frac{1}{3}}\left(\frac{K^2\sigma^2}{\rho_a\rho_l U_i^2}\right)^{\frac{1}{6}}\left[1 + 2{,}6\mu_l\sqrt{\frac{K\rho_a^4 U_i^8}{6f\rho_l^2\sigma^5}}\right] \tag{5}$$

Choosing f=12 as done by Dombrowski and Johns (1963) , one obtains

$$d_l = 0{,}9615\left(\frac{K^2\sigma^2}{\rho_a\rho_l U_i^2}\right)^{\frac{1}{6}}\left[1 + 2{,}6\mu_l\sqrt{\frac{K\rho_a^4 U_i^8}{72\rho_l^2\sigma^5}}\right]^{\frac{1}{5}} \tag{6}$$

where σ [dyn/cm] is the liquid surface tension, μ_l [cp] is the liquid dynamic viscosity, ρ_a [g/cm^3] is the density of the surrounding medium , ρ_l[g/cm^3] is the density of the liquid, K is the "nozzle parameter" which those authors calculated for fan-spray atomizers only and U_i [cm/s] is a velocity term which, in a general case, can be seen to be composed of three components: two of them relative to the air flowing on both sides of the liquid sheet , the third one being the velocity of the sheet itself (Shen and Li, 1996). Therefore, one may choose a mean value for the velocity field as

$$U_i = \left[\frac{1}{3}\left[U_f^2 + (U_{1a} - U_f)^2 + (U_{2a} - U_f)^2\right]\right]^{\frac{1}{2}} \quad (7)$$

where U_{1a} and U_{2a} are the air velocities on either side of the sheet and U_f is the sheet velocity.

As the air velocity outside the liquid sheet is taken to be zero in the Y-Jet atomizer, one may write:

$$U_i = \left[\frac{1}{3}\left[2U_f^2 + (U_{1a} - U_f)^2\right]\right]^{\frac{1}{2}} \quad (8)$$

It can be shown (Couto et al, 1996) that the nozzle parameter, K, for atomizers which generate nearly conical sheets is given by:

$$K = \left(\frac{h_0^2 \cos^3\theta}{U_f}\right) \quad (9)$$

where θ is the half cone angle formed by the liquid sheet upon leaving the atomizer.

Using equations (8) and (9) into equation (6), one obtains:

$$d_l = 0{,}9615\left(\frac{h_0^4 \sigma^2 \cos^6\theta}{\rho_a \rho_l U_f^2 U_i^2}\right)^{\frac{1}{6}}\left[1 + 2{,}6\mu_l\sqrt{\frac{h_0^2 \cos^3\theta \rho_a^4 U_i^8}{72 U_f \rho_l^2 \sigma^5}}\right]^{\frac{1}{5}} \quad (10)$$

for the diameter of the ligaments which, according to Rayleigh (apud Lefebvre, 1989), will generate droplets with a Sauter Mean Diameter, SMD, of

$$SMD = 1{,}89 d_l \quad (11)$$

4. EXPERIMENTAL SETUP AND PROCEDURE

A schematic of the Y-type atomizer used in this work is shown in figure1 Determination of the atomizer dimensions, basically the liquid and air injection orifices and the mixing chamber dimensions was based on Mullinger and Chigier's guidelines (Mullinger and Chigier, 1974) and on the following assumptions: a) isentropic flow through the atomization air orifice, b) Mach number equal to unity at the air orifice outlet section, c) stagnation air temperature of 298 K, and d) liquid injection discharge coefficient of 0.75. At

the design operation conditions, the ratio between the atomization air to the liquid flow rates was chosen to be 0,1.

Experiments with water were performed for atomization air injection pressures of 8, 15 and 25 psig. In these tests, the air mass flow rate was measured with a calibrated orifice plate and the water mass flow rate with a rotameter. The following parameters were then calculated, under the assumption of isentropic flow through the air injection orifice: injection Mach number, air density and stagnation pressure and temperature in the mixing chamber. The air velocity at the end of the mixing chamber was calculated from the chamber dimensions using the calculated air density, and the ratio between the air and liquid mass flow rates.

It should be pointed out that the injection pressure of 8 psig is out of atomizer assumed design point because 8 psig = 22,7 psia < 27,84 psia = (14,7/0528) psia, i.e., Mach = 1 at the injection port is a value that cannot be expected for such low air diferential pressure injection, even with no liquid in the mixing chamber. The atomizer operation with this air diferential pressure was investigated to provide extra discussion.

The Sauter mean diameters of water sprays generated by the atomizer were evaluated with a Phase Doppler Particle Analyzer (PDPA) system at the Mechanical Engineering Department of the Brigham -Young U., Utah, USA (Lacava, 1995).

TABLE 1 – SMD, calculated and measured, for ΔP_l = 8, 15, 25 psig
($T_0 = 20^0C$, $\theta = 7^\circ$ as measured from pictures of the Spray)

P_0 (psig	m_f (g/s)	m_{ar} (g/s)	Mach	T_c/T_0	P_c/P_0	ρ_{ar} g/cm^3 10^3	T_c (^{0}C)	P gage (bar)	U_a (m/s)	SMD calc. (μm)	SMD meas. (μm)
8	2,40	0.112	0.384	0.971	0.903	1,69	19,4	0.50	132	64	64
8	3,60	0,092	0,305	0,982	0,938	1,75	19,6	0,52	105	85	86
8	4,20	0,078	0,255	0,987	0,956	1,77	19,7	0,53	88	95	100
8	5,10	0,073	0,238	0,989	0,961	1,78	19,6	0,53	82	111	104
8	6,30	0,067	0,216	0,998	0,968	1,80	20,0	0,53	74	133	xxx
------	-----	-----	-----	-----	-----	-----	-----	-----	-----	-----	-----
15	2,40	0,176	0,485	0,955	0,851	2,10	19,1	0.88	166	47	45
15	3,60	0,146	0,382	0,972	0,904	2,22	19,4	0,93	131	61	56
15	4,20	0,131	0,336	0,978	0,925	2,26	19,6	0,95	115	68	74
15	5,10	0,114	0,287	0,984	0,944	2,30	19,7	0,97	98	77	82
15	6,30	0,105	0,263	0,986	0,953	2,32	19,7	0,98	90	91	86
-----	-----	-----	-----	-----	-----	-----	-----	-----	-----	-----	-----
25	2,40	0,235	0,479	0,956	0,855	2,85	19,1	1,48	164	34	42
25	3,60	0,231	0,469	0,958	0,860	2,86	19,2	1,49	161	47	46
25	4,20	0,216	0,431	0,964	0,880	2,91	19,3	1,52	148	52	54
25	5,10	0,190	0,337	0,978	0,924	3,27	19,6	1,60	116	58	61
25	6,30	0,168	0,319	0,980	0,932	3,05	19,6	1,61	109	68	67

5. COMPARISON OF THEORETICAL AND EXPERIMENTAL RESULTS

Table 1 presents the variation of several atomizer flow parameters as the water mass flow rate was varied, for air stagnation differential injection pressures of 8, 15 and 25 psig, respectively. It is observed that the water flow rate effectively obstructs the internal mixing

chamber, increasing the air discharge differential pressure and decreasing the atomization air flow rate.

Figure 2 shows the behavior of the SMD with the water mass flow rate for atomizing air differential injection pressures of 8, 15 and 25 psig. The SMD was obtained for the following cases: a) use of the formulation of film thickness developed in this paper, and b) determined experimentally with the PDPA system. The data were not extended for water mass flow rates above 5 g/s because, in this case, the SMD values obtained would be comparable to the PDPA measurement volume, leading to non-reliable experimental results.

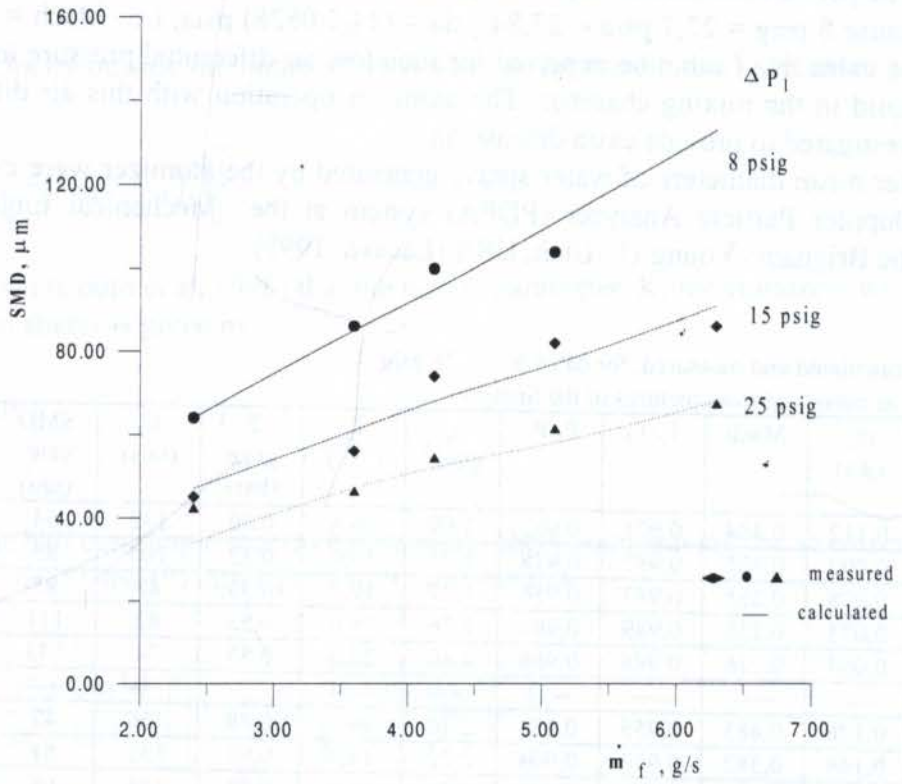

Figure 2 – SMD (calculated and measured) vs water mass flow rate, ΔP_l = 8, 15 and 25 psig

6. CONCLUSIONS

It is observed that the results obtained with the theoretical formulation derived in this work fit very well with the experimental data. One of the strong features of the formulation is that it takes into account the atomizer geometrical characteristics through the nozzle parameter K. The Sauter Mean Diameter has been shown to be very sensitive to K, which by its turn, is strongly dependent on the liquid film thickness, h_0. Therefore, by measuring the droplets SMD one may conclude that the expression derived for h_0, i.e., Equation (4), is satisfactory in describing the overall phenomenon of the liquid film generation. Finally, it is worth noticing that, even for the far off-design injection pressure of 8 psig, (a case included

just to provide extra discussion, as already mentioned), the formulation stood well compared with the experimental data as shown in Figure 2.

7. ACKNOWLEDGEMENTS

The authors are indebted to Prof. M. Q. McQuay of the BYU, Dr. J.A. Carvalho Jr. and Mr P.T. Lacava of INPE for the release of the experimental results shown in this work.

8. REFERENCES:

COUTO, H.S., CARVALHO Jr., J.A. and BASTOS-NETTO, D., Distribuição de Gotas Formadas por Jatos Múltiplos Não Coplanares, *Proccedings of the 6th Brazilian Congress of Engineering and Thermal Sciences (ENCIT 96)*, pp. 237-242, Florianópolis, 1996.

DOMBROWSKI, N. & JOHNS, W.R., The Aerodynamic Instability and Disintegration of Viscous Liquid Sheets, *Chem.Eng. Sci.*, vol.18, pp. 203-214, 1963.

LACAVA, P.T., *Influências de Parâmetros de Atomização na Geração de Instabilidades Acústicas na Combustão de Sprays em Tubos de Rijke.* MSc. Dissertation, INPE, Cachoeira Paulista, 1995.

LEFEBVRE, A.H., *Atomization and Sprays*, Hemisphere Publishing Co., New York, N.Y., 1989.

MULLINGER, P.J. & CHIGIER, N.A., The Design and Performance of Internal Mixing Multi-Jet Twin Fluid Atomizers, *J. Inst. Fuel*, vol. 47(393), pp. 251-261, 1974.

SHEN J.& LI, X., Breakup of Annular Viscous Liquid Jets in Two Gas Streams, *J. of Propulsion and Power,* vol.12, No.4, pp. 752-759, 1996.

WIGG, L. D., Drop Size Prediction for Twin-Fluid Atomizers, *J. Inst. Fuel*, vol.37(286), pp. 500-505, 1964.

XIV Brazilian Congress of Mechanical Engineering
Obeid Plaza Hotel Convention Center - Bauru - SP/Brazil
December 08-12th 1997

PAPER CODE: COB39

FREE SURFACE FLOW IN A HELICAL RECTANGULAR DUCT

EUGÊNIO SPANÓ ROSA, ANTONIO CARLOS BANNWART & FERNANDO DE ALMEIDA FRANÇA
Departamento de Energia, Faculdade de Engenharia Mecânica - UNICAMP
Cx.P. 6122 - CEP 13.083-970 - Campinas, SP - Brasil
E-mail: erosa, bannwart, ffranca@fem.unicamp.br

Abstract

Free surface flow in rectangular helical ducts is investigated experimentally. A liquid, driven by gravity, describes a descendent trajectory forming a curved free gas-liquid surface due to the centrifugal and gravity forces created by the duct curvature and torsion. The experiments were conducted in two different helical ducts, with liquids' viscosity varying from 1 cP to 150 cP and for duct Reynolds numbers ranging from 40 to 90000 performing a total of 18 experimental runs. The liquid height distributions across the duct were measured using a double wire probe. The results were transformed to an orthogonal system and then integrated across the flow orthogonal cross section to determine the averaged main flow velocity and liquid holdup. The friction factor is determined based on the experimental quantities and a correlation is proposed in the form of correction factors to the existing friction formulae for curved rectangular channels to express the effect of the free surface.

Keywords

Helical ducts, free surface flow, experimental techniques, friction factor, rectangular channel/
Dutos helicoidais, escoamento com superficie livre, técnicas experimentais, fator de atrito, canal retangular

1. INTRODUCTION

Fluid flow in helically coiled ducts has many engineering applications, including flow through turbomachinery blade passages, aircraft intakes, diffusers and heat exchangers. The key feature of this flow is the presence of secondary flows in a plane normal to its axial direction, which causes an increase in the friction factor with regard to the flow in straight tubes. Hence, the prediction of the flow quantities, in particular the friction factor, is important for the optimum design of industrial equipment.

The subject has drawn attention over the past 70 years, since the pioneering Dean's (1927) work, who investigated the flow in a toroidal pipe, i.e., a helical pipe with a zero pitch. A through review on single phase forced flow in curved ducts, discussing theoretical, computational and experimental aspects, was done by Berger and Talbot (1983), and more recently by Shah and Joshi (1987). Nonetheless, the challenges arising from the flow and geometrical complexities justify the effort still being spent nowadays. Recent works, which are tackled mainly by CFD methods, address to turbulence modeling, torsion effect on the flow structure and branching solutions (Hur, 1990; Jayanti, 1990; and Liu, 1993).

Despite the numerous works discussing the forced flow, there is a lack of studies on free surface flow in rectangular helical ducts. This type of flow geometry occurs, for example, inside compact gas-liquid separators. They are designed to take advantage of a centrifugal

field, in order to reduce the mean residence time of the fluids inside the equipment. The gas-liquid mixture enters the separator and flows downward driven by gravity describing a helical descendent trajectory. The phase segregation occurs establishing a curved free gas-liquid surface. The flow stratification is due to the combined action of the gravity and centrifugal force fields created by the curvature and torsion of the helical duct.

The present study deals only with the fully developed liquid flow, where the phase segregation already occurred and the gas has vented to gas outlet line. The phenomena then becomes similar to an open channel flow with no interfacial shear. The main objective is the development of a correlation representing the average friction factor of the free surface helical flow in rectangular ducts. The flow phenomena were analyzed from an experimental point of view feeding with liquid the helical duct. The liquid flow rate and the liquid height distribution were measured at an axial position where the flow was fully developed. The liquid height was then integrated across the duct width, rendering the liquid hold up over the measuring plane. In the helical duct, however, the plane orthogonal to the main flow direction is twisted regarding the measuring plane. The actual hold-up and hence the average flow velocity arose from the data conversion between the measuring and orthogonal planes. Finally, from the data reduction, the average friction factor was determined.

2. THE TEST LOOP AND EXPERIMENTAL TECHNIQUE

(collaborated Lourenço Gobira and Marcelo L. Morandin)

To generate a free surface flow in a rectangular helical duct a scaled-down model of a compact gas-liquid separator was used. The helical duct consisted of a stainless steel helix welded around a s.s. pipe of 89 mm in diameter inserted within a Plexiglas pipe of 137 mm in diameter. The inner and outer pipes define the inner and outer helical duct radius, IR and OR of 44.5 mm and 68.5 mm respectively. A thin rubber gasket was glued to the helix outer circumference to avoid any gap between the helix and the outer pipe. Therefore, the difference between the radii of the outer and inner pipes was the helix width (W), see Fig. 1. Two helices, having pitches of 58.5 mm and 121.5 mm were used, making up two geometrically different ducts hereafter denoted as duct I and II respectively. As the helical ducts were mounted vertically, their average inclination in relation to the horizontal were 9.4 and 18.9 degrees, respectively. The overall lengthwise dimension of the helical ducts were of 3500 mm which are equivalent to 60 and 29 pitches for ducts I and II, respectively. A summary of the helical duct geometrical dimensions is shown in Table 1.

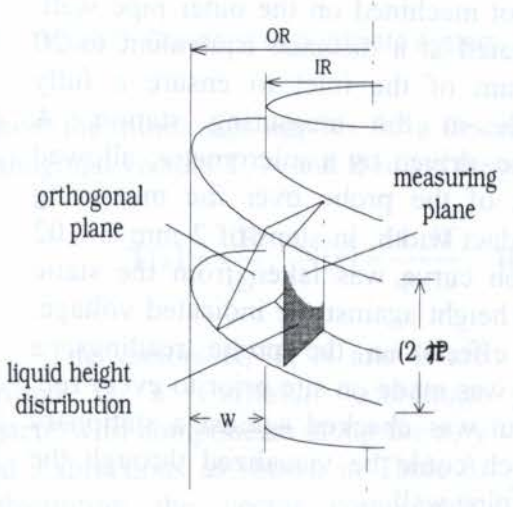

Figure 1: Helical duct schematic

The helical duct was connected to a test loop, which supplied, controlled and monitored the liquid flow rate. A centrifugal pump supplies the helical duct which had its flow rate measured by a turbine flow meter. The flow meter was carefully calibrated at every change of fluid. To avoid any change of the liquid properties during the tests, liquid temperature was monitored and kept constant connecting to the loop a heat exchanger.

The working liquids were tap water and three mixtures of water and corn syrup (Buffalo 1630®) under various concentrations, hereafter designated as fluids 1 through 4, as indicated in Table 1. The liquids viscosity ranged from 1 cP to 150 cP, keeping the Newtonian behavior even at the highest concentration of corn syrup. The density and viscosity of the liquids as well as the flow range applied during the runs, are also shown in Table 2. Considering the two helical ducts, liquids with four different viscosity and the set of flow rates applied, a total of 18 runs were performed.

Table 1: Duct dimensions

Dimension (mm)	Duct I	Duct II
Pitch	58.5	121.5
Inner Radius R_i	44.5	44.5
Mean Radius	56.5	56.5
Outer Radius R_o	68.5	68.5

Table 2: Liquid properties and flow range

Fluid	Composition	Density (kg/m^3)	Viscosity (cP)	Mass Flow (kg/s)
#1	Tap Water	1000	1	0.29 - 1.55
#2	Water +71% Corn Syrup	1285	46	0.48 - 0.91
#3	Water +82% Corn Syrup	1324	100	0.55 - 1.99
#4	Water +85% Corn Syrup	1338	150	0.14 - 0.32

The liquid height distribution was measured using a double-wire conductance probe (Koskie et al., 1989). The double-wire probe is composed by the wire probe itself and an electronic conditioning circuit. It measures the conductance of the liquid film between the two wires which is proportional to the liquid height. The wire probe consisted of two 0.01 mm parallel tungsten wires, 2.5 mm spaced, supported by a special fork, made of a stainless steel capillary tubes with 1.5 mm OD, Fig 2. The fork was inserted into the duct through a slot machined on the outer pipe wall. The slot was located at a distance equivalent to 20 pitches downstream of the inlet to ensure a fully developed profile at the measuring station. A positioning device, driven by a micrometer, allowed the displacement of the probe over the measuring plane across the duct width, in steps of 2 mm ± 0.02 mm. A calibration curve was taken from the static reading of liquid height against the indicated voltage. To avoid drift effects on the probe readings, a calibration check was made on site prior to every run. The probe readout was checked against a stationary liquid level, which could be visualized through the transparent outer pipe wall.

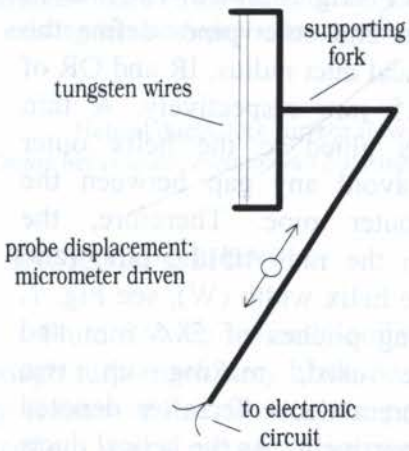

Figure 2: Wire probe sketch

3. MATHEMATICAL FORMULATION

The calculation of the averaged friction factor requires the knowledge of the actual mean flow velocity and of the liquid hold-up. The actual hold-up was determined by transforming the liquid height readings taken from the measuring plane, see Fig. 1, to the orthogonal plane and integrating them across the duct width. The orthogonal plane is defined with the help of an orthogonal coordinate system obtained from the Germano's (1982) transformation.

The helical rectangular duct is developed from the helix curve with s as the arc length, **R**(s) is the curve position vector, **T**(s) is the tangent vector and **N**(s) and **B**(s) are the normal and the bi-normal vectors, respectively. Germano (1982) constructed an orthogonal coordinate system (t,r,s) such that any Cartesian position vector **x**, joining the points M and O, is expressed as (see Fig. 3),

$$\mathbf{x} = P - O = \mathbf{R}(s) + \left[t\cdot\mathrm{Cos}\left(\phi(s)+\phi_0\right) - r\cdot\mathrm{Sin}\left(\phi(s)+\phi_0\right)\right]\cdot\mathbf{N}(s) + \left[t\cdot\mathrm{Sin}\left(\phi(s)+\phi_0\right) + r\cdot\mathrm{Cos}\left(\phi(s)+\phi_0\right)\right]\cdot\mathbf{B}(s) \quad (1)$$

Equation (1) sets the basis for transforming from the Cartesian plane (x,y,z) to the orthogonal plane (t,r,s). It is necessary, though, to define ϕ_0 and $\phi(s)$. Following Germano (1982), $\phi(s) = -\tau.s$ for a helix with a constant pitch where τ is the torsion to be defined below. Also, the value of ϕ_0 is arbitrary, and in particular, it is chosen to be $\phi_0 = \pi/2$. The helix curvature and torsion are respectively given by

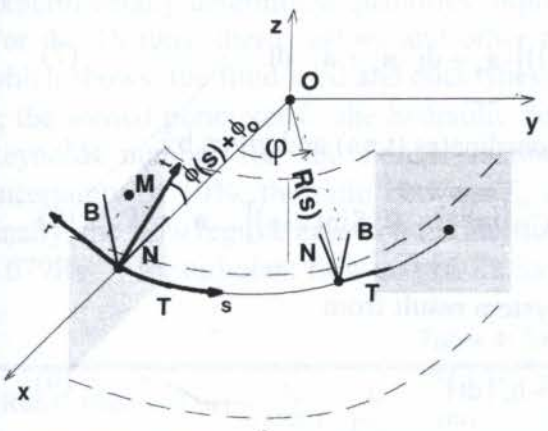

Figure 3: Germano's coordinate system

$$\kappa = \overline{R}/\left(\overline{R}^2 + P^2\right) \quad \text{and} \quad \tau = -P/\left(\overline{R}^2 + P^2\right) \quad (2)$$

where $\overline{R}$ and P are, respectively, the averaged radius defined as $(R_i+R_o)/2$ and the P is the helix pitch divided by 2π. It is convenient to express the arc length s in terms of the angle φ

$$s = \varphi/\sqrt{\kappa^2 + \tau^2} \quad (3)$$

and define the helix slope by means of angle α

$$\alpha = \mathrm{ArcTan}(-\tau/\kappa) \quad (4)$$

where the minus sign applies for a descending helix. The curve position vector **R**(s) and the orthogonal vectors **T**, **N** and **B** relate themselves through the relations:

$$\mathbf{T}(s) = \frac{d\mathbf{R}}{ds}, \quad \mathbf{N}(s) = \frac{1}{\kappa}\frac{d\mathbf{T}}{ds}, \quad \mathbf{B}(s) = \mathbf{T}\times\mathbf{N}, \quad \frac{d\mathbf{N}}{ds} = \tau\mathbf{B} - \kappa\mathbf{T}, \quad \frac{d\mathbf{B}}{ds} = -\tau\mathbf{N} \quad (5)$$

The vectors **R**, **T**, **N** and **B** are written in a Cartesian coordinate system with components along the x, y and z directions as shown in Table 3. Substituting the vector components from Table 1 into equation (1), collecting the terms along the proper directions and using the definitions of Equations (2)-(4) we obtain the transformation relationship between (x,y,z) and (t,r,s) coordinates as

Table 3: Vector components

	x component	y component	z component
$\mathbf{R}(\varphi)$	$+\overline{R}.\mathrm{Cos}(\varphi)$	$+\overline{R}.\mathrm{Sin}(\varphi)$	$-p.\varphi$
$\mathbf{T}(\varphi)$	$-\mathrm{Cos}(\alpha).\mathrm{Sin}(\varphi)$	$+\mathrm{Cos}(\alpha).\mathrm{Cos}(\varphi)$	$-\mathrm{Sin}(\alpha)$
$\mathbf{B}(\varphi)$	$-\mathrm{Sin}(\alpha).\mathrm{Sin}(\varphi)$	$+\mathrm{Sin}(\alpha).\mathrm{Cos}(\varphi)$	$+\mathrm{Cos}(\alpha)$
$\mathbf{N}(\varphi)$	$-\mathrm{Cos}(\varphi)$	$-\mathrm{Sin}(\varphi)$	0

$$x = \frac{\kappa}{\psi^2}\cdot\mathrm{Cos}(s\cdot\psi) - \left[r\cdot\mathrm{Sin}(\tau\cdot s) - t\cdot\mathrm{Cos}(\tau\cdot s)\right]\cdot\mathrm{Cos}(s\cdot\psi) + \left[r\cdot\mathrm{Cos}(\tau\cdot s) + t\cdot\mathrm{Sin}(\tau\cdot s)\right]\cdot\frac{\tau}{\psi}\cdot\mathrm{Sin}(s\cdot\psi) \quad (6a)$$

$$y = \frac{\kappa}{\psi^2}\cdot \mathrm{Sin}(s\cdot\psi) - \left[r\cdot\mathrm{Sin}(\tau\cdot s) - t\cdot\mathrm{Cos}(\tau\cdot s)\right]\cdot\mathrm{Sin}(s\cdot\psi) - \left[r\cdot\mathrm{Cos}(\tau\cdot s) + t\cdot\mathrm{Sin}(\tau\cdot s)\right]\cdot\frac{\tau}{\psi}\cdot\mathrm{Cos}(s\cdot\psi) \quad (6b)$$

$$z = +\frac{1}{\psi}\left(\tau\cdot s + \kappa\cdot\left[r\cdot\mathrm{Cos}(\tau\cdot s) + t\cdot\mathrm{Sin}(\tau\cdot s)\right]\right) \quad (6c)$$

where $\psi = \sqrt{\kappa^2 + \tau^2}$. A numerical routine, based on Eq. (6), transforms the coordinates (t,r,s) into (x,y,z), and vice-versa. The flow cross sectional area, as well as the liquid hold-up, both normal to the flow, arises transforming the (x,y,z) duct coordinates and the experimental liquid height data to a plane whose normal is coincident with the s direction and then performing the integration.

The metric for the (t,r,s) coordinate system is obtained taking the changes in the position vector d**x**, defined in Eq. (1):

$$d\mathbf{x} = ds\cdot\left[1 - \kappa\left(r\cdot\mathrm{Sin}(\tau\cdot s) - t\cdot\mathrm{Cos}(\tau\cdot s)\right)\right]\cdot\mathbf{a}_s + dr\cdot\mathbf{a}_r + \mathbf{a}_t\cdot dt \quad (7)$$

where the unit vectors, $\mathbf{a}_t$, $\mathbf{a}_r$ and $\mathbf{a}_s$ are parallel to the coordinates (t,r,s) and given by

$$\mathbf{a}_t = \left[\mathbf{N}\cdot\mathrm{Sin}(\tau\cdot s) + \mathbf{B}\cdot\mathrm{Cos}(\tau\cdot s)\right], \quad \mathbf{a}_r = -\left[\mathbf{N}\cdot\mathrm{Cos}(\tau\cdot s) + \mathbf{B}\cdot\mathrm{Sin}(\tau\cdot s)\right], \quad \mathbf{a}_s = \mathbf{T} \quad (8)$$

The metric coefficients for the (t,r,s) coordinate system result from

$$d\mathbf{x}\cdot d\mathbf{x} = h_s^2(ds)^2 + h_r^2(dr)^2 + h_t^2(dt)^2 \quad (9)$$

where the coefficients are:

$$h_t^2 = 1, \quad h_r^2 = 1, \quad h_s^2 = \left[1 - \kappa\left(r\cdot\mathrm{Sin}(\tau\cdot s) - t\cdot\mathrm{Cos}(\tau\cdot s)\right)\right]^2 \quad (10)$$

With the metric coefficients is possible to write the momentum equation along the flow direction, (s), Warsi (1993). Area averaging the momentum equation results the one-dimensional momentum equation:

$$\frac{\partial}{\partial t}\langle\rho w\rangle + \frac{\partial}{\partial s}\langle\rho w^2\rangle = -\frac{\partial}{\partial s}\langle P\rangle + \frac{\partial}{\partial s}\langle T_{ss}\rangle - \frac{\tau_w}{R_H} + \rho g\mathrm{Sin}(\alpha) \quad (11)$$

where $\langle\ \rangle$ denotes area averaged terms over the flow cross section area, w and T_{ss} are the velocity component and the shear stress along the s direction, respectively. R_H and τ_W are the hydraulic radius and the averaged wall shear stress as defined in Eq. (12),

$$R_H = \frac{A_S\cdot\varepsilon}{L_r + L_t}, \quad \tau_w = R_H\cdot\left[\frac{L_t\cdot\langle\tau_t\rangle_w + L_r\cdot\langle\tau_r\rangle_w}{A_s\cdot\varepsilon}\right] \quad (12)$$

where L_r and L_t refer to the wetted perimeter along the r and t directions; A_s is duct cross sectional area along the s direction and ε is the liquid holdup, defined as the ratio between the area occupied by the liquid and A_s. For a steady state and fully developed flow, Eq. (11) reduces to a balance between wall shear forces and body forces:

$$\frac{\tau_w}{R_H} = \rho g \mathrm{Sin}(\alpha) \tag{13}$$

Substituting in Eq. (13) the shear stress by a Fanning friction factor and defining the average flow velocity by means of the liquid flow rate, Q, gives

$$f_H = 2\frac{(A_s \cdot \varepsilon)^3 \cdot g \cdot \mathrm{Sin}(\alpha)}{(L_r + L_t) \cdot Q^2} \tag{14}$$

4. RESULTS

Equation (14) is employed to evaluate the friction factor f_H based on the experimentally determined quantities: liquid flow rate, wetted perimeter and liquid hold-up. For the 18 runs, these values and other parameters of interest are summarized in Table 4 which shows: the fluid used and duct types; the duct orthogonal section A_s; the liquid holdup ε; the wetted perimeter L; the hydraulic diameter D ; the average axial flow velocity w; the Reynolds number Re; the Froude number; the experimental friction factor f_H with an uncertainty of 10%; the ratio between f_H and the friction factor to a straight pipe f_s , and finally, the flow regime based on the Reynolds number. The friction factor f_s was estimated as $0.079Re^{0.25}$ for turbulent flow and 16/Re for laminar flow.

Table 4: Experimental values

Run #	Fluid #	Duct	A_s (mm^2)	ε (%)	L (m)	D (m)	w (m/s)	Re	Fr	$f_H \pm 10\%$	f_H/f_s	flow regime
1	1	I	1388	26.6	0.0708	0.0209	0.79	16389	1.10	0.0270	3.9	turb.
2	1	I	1388	40.7	0.0877	0.0258	1.27	32840	2.89	0.0127	2.2	turb.
3	1	I	1388	50.6	0.0900	0.0312	1.57	48893	4.37	0.0102	1.9	turb.
4	1	I	1388	57.4	0.0954	0.0334	1.73	57880	5.34	0.0089	1.7	turb.
5	1	I	1388	62.9	0.0976	0.0358	1.78	63550	5.62	0.0091	1.8	turb.
6	1	II	2765	12.9	0.0919	0.0156	1.23	19156	2.59	0.0163	2.4	turb.
7	1	II	2765	26.9	0.1317	0.0226	1.37	30984	3.22	0.0190	3.2	turb.
8	1	II	2765	41.5	0.1374	0.0334	1.88	62899	6.05	0.0150	3.0	turb.
9	1	II	2765	53.8	0.1429	0.0416	2.24	93485	8.60	0.0131	2.9	turb.
10	3	II	2765	23.7	0.0964	0.0272	0.63	242	0.69	0.1072	1.6	lam.
11	3	II	2765	37.2	0.1340	0.0307	0.72	303	0.88	0.0942	1.8	lam.
12	3	II	2765	53.0	0.1719	0.0341	0.81	369	1.12	0.0829	1.9	lam.
13	3	II	2765	67.3	0.2016	0.0369	0.81	405	1.11	0.0900	2.3	lam.
14	4	I	1388	52.5	0.0866	0.0337	0.14	41	0.04	1.3043	3.4	lam.
15	4	I	1388	68.0	0.1060	0.0356	0.25	77	0.11	0.4422	2.1	lam.
16	2	I	1388	35.4	0.0744	0.0264	0.76	560	1.03	0.0366	1.3	lam.
17	2	I	1388	55.9	0.0958	0.0324	0.76	679	1.04	0.0444	1.9	lam.
18	2	I	1388	71.5	0.1085	0.0366	0.71	718	0.91	0.0573	2.6	lam.

For the variables in Table 4 the following definitions apply: the average flow velocity is $w = Q/(A_s\varepsilon)$; the hydraulic diameter is $D = 4R_H$; the Reynolds and Froude numbers are, respectively $Re = \rho wD/\mu = 4Q/(\nu L)$, $Fr = w^2 \mathrm{Cos}(\alpha)/(g\overline{R})$. It can be shown that Fr controls the slope of interface in the channel cross section. The experimental uncertainty on f_H was evaluated based on the relative errors of the liquid holdup, wetted perimeter and volumetric flow rate , as given in Eq. (15):

$$(\delta f_H / f_H) = \sqrt{\left[3(\delta\varepsilon/\varepsilon)\right]^2 + (\delta L/L)^2 + \left[2(\delta Q/Q)\right]^2}. \quad (15)$$

These relative errors were estimated as: $\delta\varepsilon/\varepsilon = 3\%$, $\delta L/L = 5\%$ and $\delta Q/Q = 1\%$ and represent confidence intervals of 95%. Using these values Eq. (15) gives $\delta f_H/f_H \approx 10\%$.

The helical duct liquid height distributions are shown in Figs 4 and 5 for data taken on the measurement plane (X,0,Z) for the runs #3, #9, #13 and #18. Typical gas-liquid interfaces for turbulent regime are shown in Fig. 4, for laminar regime are in Fig. 5. One can notice that the interfaces for the turbulent flow regime are steeper than the laminar regime due to the higher averaged flow velocities expected in the turbulent flow regime.

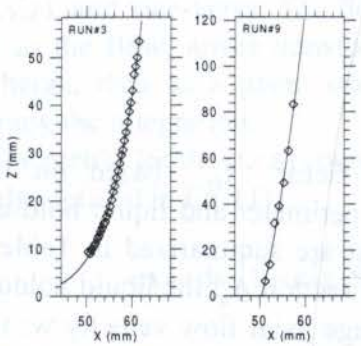

Figure 4: Liquid height for turbulent flow

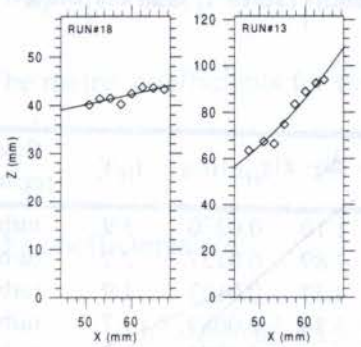

Figure 5: Liquid height for laminar flow

Correlations for friction in curved ducts found in the literature refer only to forced convection flows. No study on friction in free surface flows through curved channels seems to have been made to date. In their review paper, Shah & Joshi (1987) recommended Ito's correlation for turbulent flow and Chen's correlation for laminar flow in curved rectangular ducts. Thus we decided to correlate our data by introducing a correction factor to the recommended friction formula in each flow regime. Further, since this factor is intended to represent the effect of the free surface, it was expressed as a function of the Froude number in the form $m + n\,\mathrm{Fr}^p$.

The final correlations given below were obtained by minimizing the total relative deviation to the experimental friction data, with respect to the unknown constants *m, n, p* :

Turbulent flow: we corrected Ito's correlation (Shah & Joshi, 1987) to get

$$f_H = 0.076\,\mathrm{Re}_\infty^{-0.25}\left(1 + 0.0954\,\mathrm{Re}_\infty^{-0.25}\,\lambda_\infty^{0.5}\right)\left(1.039 + 2.053\mathrm{Fr}^{-1.437}\right) \quad (16)$$

where $\mathrm{Re}_\infty = 4Q/(\mu L_\infty)$, $L_\infty = 2\varepsilon(R_o - R_i)(1+\gamma_\infty)$, $\lambda_\infty = D_\infty \mathrm{Cos}^2(\alpha)/(2\overline{R})$, $D_\infty = 4\varepsilon A_s/L_\infty$ and γ_∞ is the aspect ratio defined by $\gamma_\infty = (\pi/\varepsilon)\sqrt{\overline{R}^2\mathrm{Sin}^2(\alpha) + P^2\mathrm{Cos}^2(\alpha)}/(R_o - R_i)$. The standard deviation shown by dashed lines in Fig. 6 is 25 %.

Laminar flow: Chen's correlation for rectangular curved ducts is corrected in the form

$$f_H = \frac{Po_\infty}{\mathrm{Re}_\infty}\left(\frac{f_c}{f_s}\right)\left(0.279 + 0.594\mathrm{Fr}^{-0.487}\right) \quad (17)$$

where Po_∞ is the Poiseuille number (White, 1991) for a rectangular cross section which can be approximated by $Po_\infty = 14.23 + 9.77\left(1-\gamma_\infty^*\right)^{2.217}/\left(1+\gamma_\infty^*\right)^{1.143}$, $\gamma_\infty^* = Min\left[\gamma_\infty; 1/\gamma_\infty\right]$ and

(f_c/f_s) is the function given by Chen's correlation (see Shah & Joshi, 1987) depending on the Dean number $Dn_\infty = Re_\infty \lambda_\infty^{0.5}$ and the aspect ratio γ_∞. The standard deviation is 30 %, shown by dashed lines in Fig. 7.

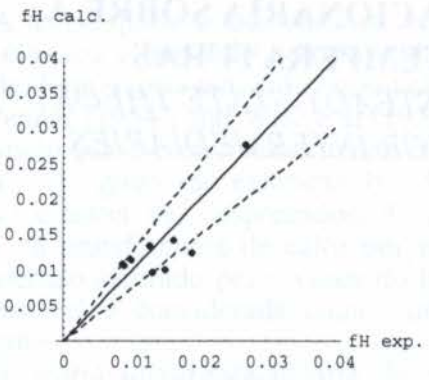

Figure 6: Friction factor data versus Eq.(16)

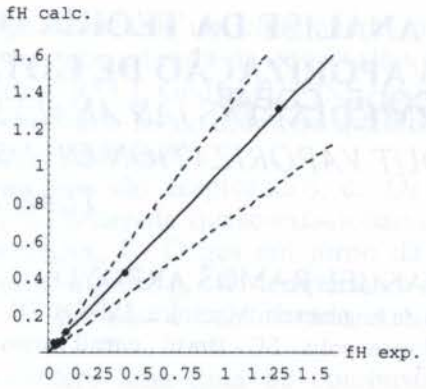

Figure 7: Friction factor data versus Eq.(17)

5. CONCLUSIONS

The experimentally determined friction factor exhibits an increase regarding the flow in straight tubes, in agreement with previous works. It was observed although that the correlations developed to forced flow in helical ducts can not be used when the flow has a free surface. This effect was introduced here as a correction factor depending only on a Froude number defined as the ratio of centripetal and gravitational forces. Many questions still remain open for the problem studied such as the effect of interfacial inclination and waves in secondary motions, the helix torsion effect on the flow structure, the number of recirculating cells, the development of a constitutive equation for the liquid height distribution, transition criteria in the helical rectangular channel and others.

6. REFERENCES

BERGER. S.A. & TALBOT, L. Flow in Curved Pipes, *Ann. Rev. Fluid. Mech.* **11**, 1983.

DEAN, W.R. Note on the Motion of Fluid in a Curved Pipe. *Phil. Mag. J.Sci.* **4**,208-23, 1927.

GERMANO,M. On the Effect of Torsion on a Helical Pipe Flow *J. Fluid Mech.*,**125**,1-8,1982.

HUR, N. & THANGAM, S. Laminar Secondary Flows in Curved Rectangular Ducts, *J. Fluid Mech.*, **217**, 421-440, 1990.

JAYANTI, S., HEWITT, G.F. & KIGHTLEY, J.R., Fluid Flow in Curved Ducts, *Int. J. Numerical Meth. in Fluids*, **10**, 569-589, 1990 .

KOSKIE, J. E., MUDAWAR, I. & TIETERMAN, W. G. Parallel Wire Probe for Measurement of Thick Liquid Films, *Int. J. Multiphase Flow*, 15, **4**, 521-530, 1989.

LIU, S. & MASLIYAH, J.H. , Axially Invariant Laminar Flow in Helical Pipes with a Finite Pitch, *J. Fluid Mech.*, **251**, 315-353,1993.

SHAH, R.K. & JOSHI, S.D., Convective Heat Transfer in a Curved Duct. In *Handbook of Single-Phase Convective Heat Transfer* (Edited by S. Kakac, R.K. Shah and W. Aung). John Wiley, NY, 1987.

WHITE, F.M., *Viscous Fluid Flow*, McGraw Hill, 2nd ed., 1991.

WARSI,Z.U.A.,*Fluid Dynamics - Theoretical and Computational Approaches*, CRC, 1993.

XIV Brazilian Congress of Mechanical Engineering
Obeid Plaza Hotel Convention Center - Bauru - SP/Brazil
December 08-12th 1997

UMA ANÁLISE DA TEORIA QUASE-ESTACIONÁRIA SOBRE A VAPORIZAÇÃO DE GOTAS, PARA TEMPERATURAS INTERMEDIÁRIAS

PAPER CODE: COB48

/AN ANALYSIS OF THE STEADY-STATE THEORY ABOUT VAPORIZATION OF DROPLLETS FOR INTERMEDIARIES TEMPERATURE

NARCISO ANGEL RAMOS ARROYO
Departamento de Engenharia Mecânica, UFSC/CTC
88.010-970 Florianópolis - SC - Brasil ; e-mail : arroyo@sinmec.ufsc.br

Abstract

This paper show a revision about the steady-state theory developed of Spalding, Godsave, Goldsmith and Penner. It show that the Lewis number can be obtain for the logarithmic relation of the transfer mass Spalding number and the transfer of heat Spalding number. This work show that intermediaries temperature between 310 K and 700 K, the Lewis number is not equal to the unit. It show experimental results for n-heptane drops in these temperatures range.

Keywords

Combustion, Vaporization , Sprays /Combustão, Vaporização, Sprays

1. INTRODUÇÃO

A vaporização é uma etapa importante que precede o processo de combustão dos combustíveis líquidos utilizados em diversas máquinas térmicas, tais como os motores de combustão interna, as turbinas a gás, caldeiras, fornos industriais e das câmaras de combustão de alguns motores de foguetes.

Geralmente o fornecimento de combustíveis líquidos nas câmaras de combustão é realizado em forma de jatos e sprays através de um atomizador ou injetor. O spray é constituído de pequenas gotas onde o tamanho e a distribuição dependem do tipo do injetor utilizado e das condições de operação.

Durante a vaporização das gotas se realizam simultaneamente o processo de transferência de calor e de transferência da massa. O calor de vaporização é transferido através da superficie da gota por condução e convecção do gás quente que a envolve. O vapor de combustível é transferido ao ambiente por convecção e difusão.

Para conhecer melhor o comportamento dos sprays é necessário conhecer o fenômeno da vaporização de uma gota pura isolada. Este estudo tem sido iniciado por Spalding [1953] e é conhecido como a teoria quase-estacionária da vaporização e combustão das gotas puras isoladas.

O objetivo deste trabalho é mostrar que o número de Lewis desenvolvido na teoria quase- estacionária não é igual à unidade em certas condições de temperatura, e mostrar como varia a temperatura interna de uma gota de um líquido puro quando é submerso em um ambiente de ar aquecido. Para realizar esta experiência, temos escolhido o combustível n-heptano por ser um combustível bem representativo dos combustíveis industriais.

No estudo experimental, temos utilizado uma bancada formada por um forno elétrico concêntrico a um tubo de quartzo de 30 mm de diâmetro interno, onde passa um fluxo de ar. A regulação da temperatura é realizada através de um termopar que é ligado num regulador de temperatura. A observação da temperatura interna da gota, foi feita através de um termopar fino de Cr-Al .

Para a obtenção da regressão do diâmetro da gota em função do tempo, a gota foi suspensa numa fibra de quartzo de 0,25 mm numa distância de 30 mm na saída do tubo. Foi

registrada a variação da gota, através de uma câmara CCD ligada num microcomputador, num vídeo cassete e num monitor de TV[Ramos-Arroyo, 1994]. Os resultados obtidos são apresentados em forma de gráficos e discutidos posteriormente.

2. TEORIA QUASE-ESTACIONÁRIA

A teoria quase-estacionária da vaporização da gota isolada de um componente puro é a mais clássica e tem sido desenvolvida simultaneamente com a teoria da combustão da gota isolada. Esta teoria tem sido desenvolvida por Spalding [1953], Godsave [1953], Goldsmith and Penner [1954] and Wise e al [1956], e nos tem fornecido a lei do diâmetro quadrado para um estado quase-estacionário, tendo em conta as seguintes hipóteses:

a .- As gotas são esféricas; b .- Os efeitos convectivos são desprezados; c.- Os efeitos Dufour e Soret são desprezados; d.- A fase gasosa é considerada quase-estacionária; e.- O efeito da transferência de calor por radiação é desprezados; f.- O gás em torno da gota é considerado saturado pelo vapor do líquido que constitui a gota; g.- A temperatura da gota combustível é considerada como uniforme; h .- A pressão é considerada constante e uniforme.

A teoria quase-estacionária da vaporização, considera uma gota de combustível de componente puro e isolada de raio "r_s", em um meio ambiente quente e a pressão atmosférica normal [Spalding, 1953], onde : m = fluxo de vaporização; q = fluxo de calor transmitido a gota; r_s = raio da gota; r = distância radial à partir do centro da gota; Y_f = concentração do vapor de combustível; Y_{fs} = concentração do vapor de combustível na superfície da gota; $Y_{f\infty}$ = concentração do vapor de combustível no meio ambiente; T_s = temperatura na superfície da gota.

A transferência de calor da região com maior temperatura em torno da gota, produz a transferência de massa da fase líquida para a fase vapor do combustível. O vapor formado é transferido ao meio ambiente por difusão molecular.

Da equação de conservação da massa :

$$r^2 \rho v = r_s^2 \rho_s v_s \qquad (1)$$

e na superfície da gota nos temos :

$$-\rho_l \, dr_s/dt = \rho_s v_s \qquad (2)$$

Da equação de conservação das espécies :

$$v_s = D_s [dY_f/dr]_s \qquad (3)$$

$$r_s v_s = D_s \ln [1 + B_M] \qquad (4)$$

Onde : $B_M = (Y_{fs} - Y_f)/(1-Y_{fs})$ = Número de Spalding de transferência de massa (5)

Da equação de conservação da energia :

$$r_s v_s = \alpha_s \ln [1 + B_T] \qquad (6)$$

Onde $B_T = Cp (T_\infty - T_s)/L$ = Número de Spalding de transferência de calor (7)

Comparando as equações (4) e (6) :

$$D_s \ln [1 + B_M] = \alpha_s \ln [1 + B_T] \qquad (8)$$

Para o número de Lewis igual a 1 temos : $\alpha_s = D_s$ (9)

Então, $B_M = B_T$ (10)

$$Cp(T_\infty - T_S)/L = (Y_f - Y_{fs})/(Y_{fs} - 1) \quad (11)$$

Esta equação mostra a relação entre a temperatura T_S e a fração de massa Y_{fs}

Das equações (2) e (6), temos :

$$r_S\, dr_S/dt = -\rho_s/\rho_l\ \alpha_s\ \ln[1 + B_t] \quad (12)$$

$$\text{Daí : } d^2 = do^2 - [8\ \rho_s\ \alpha_s\ \ln(1 + B_T)] \quad (13)$$

$$\text{Para } K = [8\ \rho_s/\rho_l\ \alpha_s \ln(1 + B_T)], \text{ ou} \quad (14)$$

$$K = [8\ \rho_s/\rho_l\ D_S \ln(1 + B_M)], \text{ então} \quad (15)$$

$$d^2 = do^2 - K.t \quad (16)$$

A equação (16), representa a lei do diâmetro quadrado para a vaporização de uma gota pura, onde K é conhecido como o coeficiente de vaporização. Para K constante, a regressão do diâmetro da gota em função do tempo é linear.

O tempo de vida da gota é definida :

$$tv = do^2/K = \rho_l\, do^2 / [8\ \rho_s\ \alpha_s \ln(1 + B_t)], \text{ ou} \quad (17)$$

$$tv = \rho_l\, do^2 / [8\ \rho_s\ D_S \ln(1 + B_M)] \quad (18)$$

As equações (17) e (18) mostram que o tempo de vida da gota é diretamente proporcional a massa específica e ao diâmetro inicial da gota, e inversamente proporcional ao coeficiente de difusão térmica e de massa na superfície da gota e ao termo $\ln(1+B_t)$.

3. EFEITO DA TEMPERATURA NO NÚMERO DE LEWIS

A temperatura na superfície de uma gota é um parâmetro importante no estudo da vaporização. Ela pode ser obtida experimentalmente ou teoricamente. Na obtenção experimental temos usado um termopar Cr-Al de 0,4 mm de diâmetro. Para determinar a temperatura na superfície teoricamente, temos usado a teoria quase-estacionária descrita anteriormente.

Assim da equação (8) temos :

$$(1 + B_T)^{Le} = (1 + B_M), \text{ ou} \quad (19)$$

$$Le = \frac{\ln(1 + B_M)}{\ln(1 + B_T)}. \quad (20)$$

onde Le é o número de Lewis. O termo B_T é função da temperatura ambiente T_∞, da temperatura da superfície T_S, do calor latente L e do calor específico Cp na fase gasosa, que depende também da fração dos componentes na fase gasosa. O termo B_M é função da fração em massa do vapor de combustível na região da temperatura ambiente, e da fração em massa do vapor de combustível na superfície da gota. A equação (19), pode ser solucionada se conhecermos a temperatura da superfície da gota, a temperatura ambiente e o número de Lewis. Geralmente a temperatura ambiente é conhecida, mas a temperatura da superfície da gota que depende dela, não é conhecida.

Como B_T e B_M são funções da temperatura da superfície da gota, a temperatura da superfície da gota será a temperatura correspondente aquela da interação dos termos $(1 + B_M)$ e $(1 + B_T)^{Le}$, para o número de Lewis conhecido, tal como mostra a figura 1.

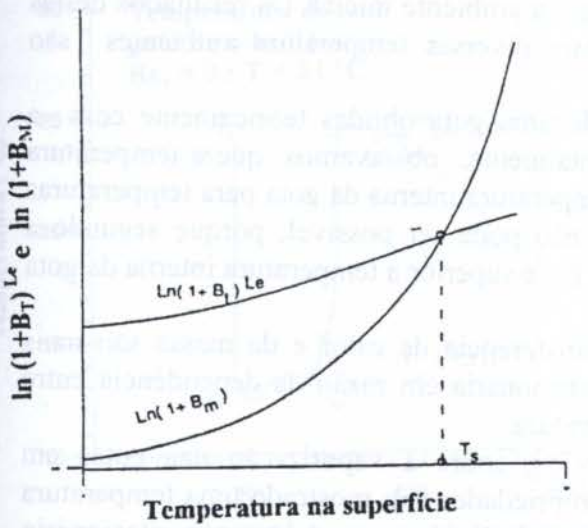

Fig. 1 Termos $(1 + B_M)$ e $(1 + B_T)^{Le}$ em função da temperatura da superfície.

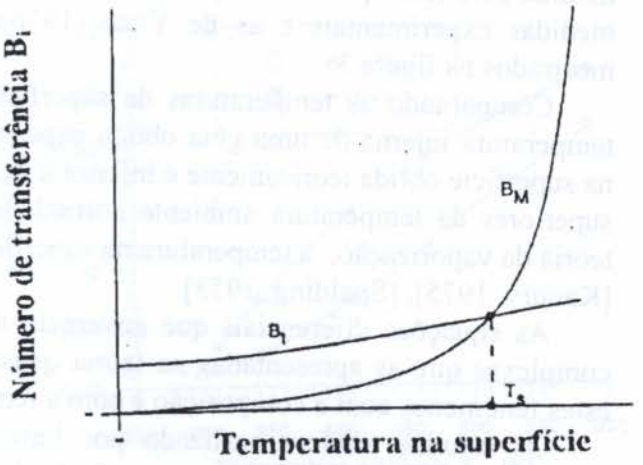

Fig. 2 Termos B_T e B_M em função da temperatura da superfície, para Le =1 de uma gota de n-heptano, numa temperatura ambiente de 400 °C.

Uma solução particular muito utilizada por diversos autores é de fixar o número de Lewis igual a 1. Nesse caso, da equação (19), temos : $B_T = B_M$, e a temperatura da superfície é então definida pela interseção das curvas B_T (T_s) e $B_M(T_s)$, como mostra a figura 2, sugerida por Lefebvre [1989].

Segundo este último procedimento, para Le = 1, temos determinado a temperatura da superfície do n-heptano. Os resultados são apresentados na figura 3.

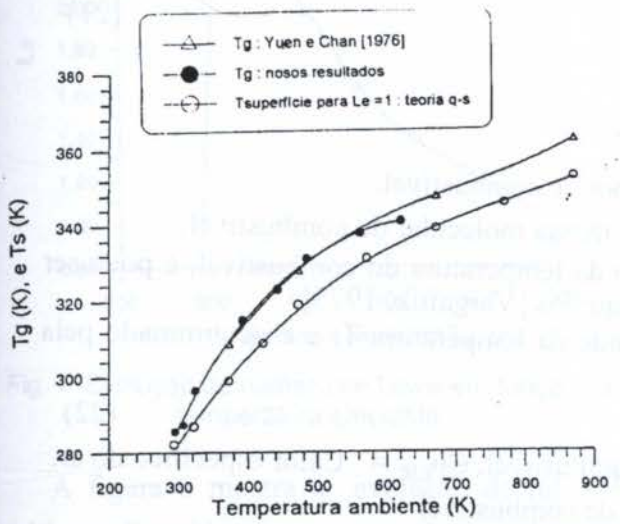

Fig. 3 Evolução da temperatura da superfície de uma gota segundo a teoria quase-estacionária para o n-heptano, com Le = 1 e as obtidas experimentalmente.

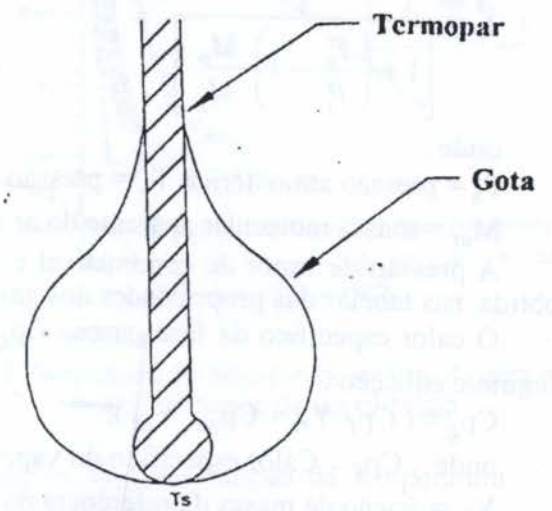

Fig. 4 Esquema da posição do termopar para medir a temperatura na superfície da gota.

Para medir a temperatura na superfície de uma gota temos utilizado um termopar de Cromel-Alumel, onde o contato entre ele e a gota tem sido tangente a superfície da gota, tal como mostra a figura 4. A figura 5 descreve a evolução da temperatura de uma gota de n-heptano de 1,3 mm de diâmetro, vaporizando-se num ambiente de 24 °C. No início da vaporização, quando é colocada a gota no termopar, se observa uma queda brusca da temperatura medida (parte AB da curva da figura 5). Durante a vaporização (parte BC), a temperatura se comporta quase constante, e ao final da vaporização (parte CD), a temperatura

medida pelo termopar volta rapidamente a temperatura ambiente inicial. Os resultados destas medidas experimentais e as de Yuen (1976), para diversas temperatura ambientes são mostrados na figura 3.

Comparando as temperaturas de superfície de uma gota obtidas teoricamente com a temperatura interna de uma gota obtida experimentalmente, observamos que a temperatura na superfície obtida teoricamente é inferior à da temperatura interna da gota para temperaturas superiores da temperatura ambiente normal. Isto não pode ser possível, porque segundo a teoria da vaporização, a temperatura na superfície T_s , é superior à temperatura interna da gota [Kanury, 1975], [Spalding, 1953].

As equações diferenciais que governam a transferência de calor e da massa são mais complexas que as apresentadas na teoria quase-estacionária em razão da dependência entre estes fenômenos com a composição e com a temperatura.

Os estudos teóricos realizado por Law [1975], sobre a vaporização das gotas em condições quase-estacionárias com variação das propriedades tem mostrado uma temperatura na superfície de uma gota de n-heptano maior do daquela obtida no modelo quase-estacionário com Le =1. Comparando estes resultados da temperatura na superfície com os nossos resultados experimentais e os resultados experimentais obtidos por Yuen [1976], vemos que eles possuem uma grande concordância.

Considerando então nosso resultado experimental como a temperatura na superfície da gota T_s , podemos obter o número de transferência B_T e B_M através da regra de "1/3" [Sparrow, 1958].

A fração em massa do vapor de combustível pode ser obtida em função das pressões parciais como mostra Lefebvre [1989] :

$$Y_s = \frac{1}{\left[1 + \left(\frac{P_a}{P_v} - 1\right)\frac{M_{ar}}{M_f}\right]}. \qquad (21)$$

onde :

P_a = pressão atmosférica, P_v = pressão de vapor de combustível.

M_{ar} = massa molecular aparente do ar e M_f = massa molecular do combustível.

A pressão de vapor de combustível é função da temperatura do combustível, e pode ser obtida nas tabelas das propriedades dos gases e líquidos [Vargaftik, 1975].

O calor específico da fase gasosa Cp_g depende da temperatura T_r e é determinado pela seguinte equação :

$$Cp_g = (Cp_f . Y_{fr} + Cp_{air} . Y_{ar}), \qquad (22)$$

onde : Cp_f = Calor específico do vapor de combustível, Cp_{air} = Calor específico do ar,

Y_{fr} = fração de massa de referência do vapor de combustível

Y_{ar} = fração de massa de referência do ar

Usando a regra de "1/3", sugerido por Sparrow [1958] temos :

$$Y_{fr} = Y_{fs} + \frac{Y_{f\infty} - Y_{fs}}{3}. \qquad (23)$$

$$T_r = T_s + \frac{T_\infty - T_s}{3}. \qquad (24)$$

Considerando $Y_\infty = 0$, então :

$$Y_{fr} = Y_{fs} \qquad (25)$$

e

$$Y_{ar} = 1 - Y_{fr} \qquad (26)$$

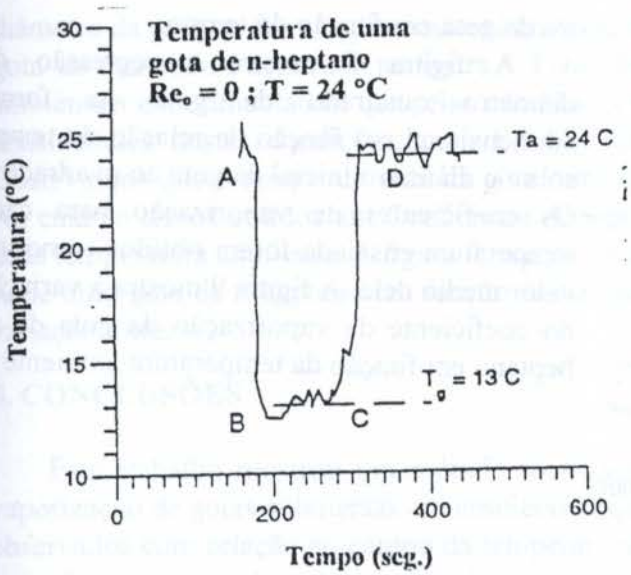

Fig. 5 Determinação da temperatura de uma gota de n-heptano, em um ambiente estacionário de uma gota de n-heptano., T_∞ = 24 °C.

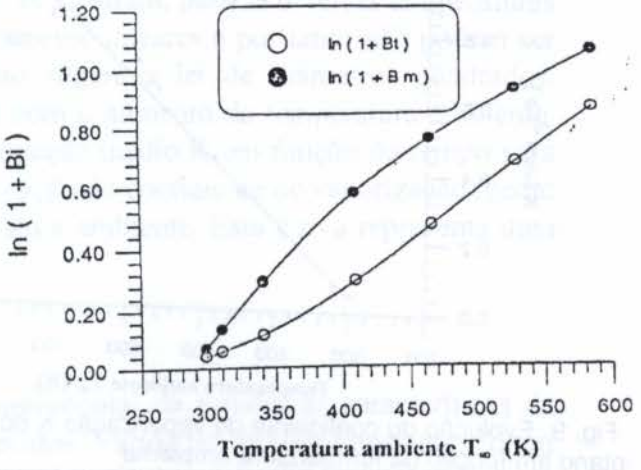

Fig. 6 Termos $\ln(1+B_T)$ e $\ln(1+B_M)$ em função da temperatura ambiente T_∞.

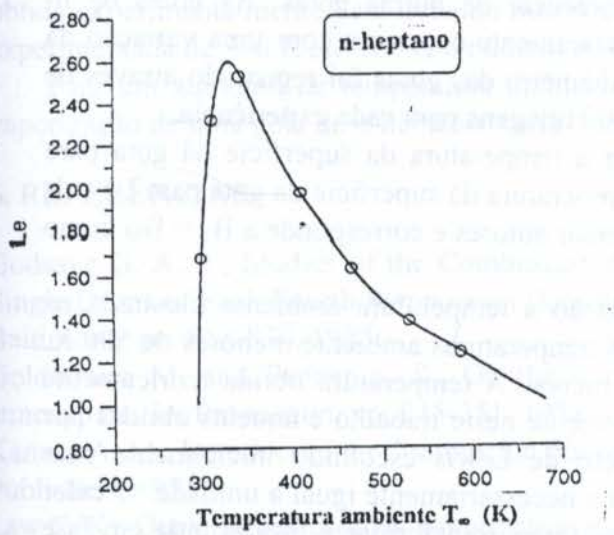

Fig. 7 Evolução do número de Lewis em função da temperatura ambiente

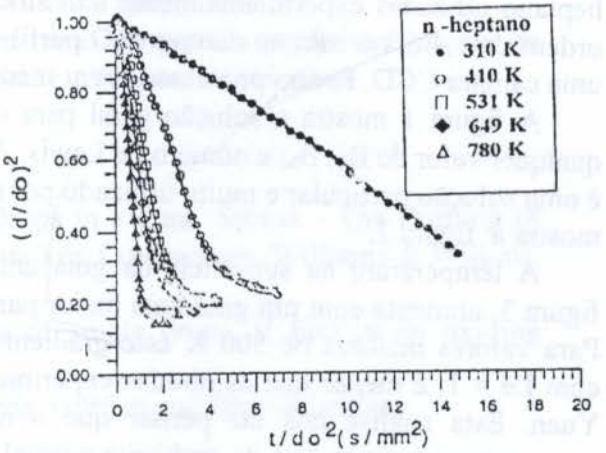

Fig. 8 Regressão do diâmetro quadrado da gota em função do tempo de vaporização

A figura 6 mostra a evolução de $\ln(1+B_T)$ e $\ln(1+B_M)$ em função da temperatura ambiente T_∞. Nestas curvas podemos observar que os termos $\ln(1+B_T)$ e $\ln(1+B_M)$ são convergentes em baixa e em alta temperaturas, mas são diferentes neste intervalo de temperatura. O número de Lewis é obtido usando a equação (20) e os resultados em função da temperatura ambiente são mostrados na figura 7. Esta curva mostra que a baixa temperatura o número de Lewis se aproxima de 1, logo aumenta até um valor máximo em torno de 2,6 para uma temperatura ambiente correspondente em torno de 360 K, e logo diminui conforme aumenta a temperatura. As regressões do diâmetro equivalente das gotas de n-heptano suspendidas em fibra de quartzo de 0,4 mm, foram obtidas através de uma câmara CCD ligada a um monitor, a um videocassete e a um microcomputador. Estas imagems foram processadas através de um programa de análise de imagem, obtemdo-se a variação do diâme-

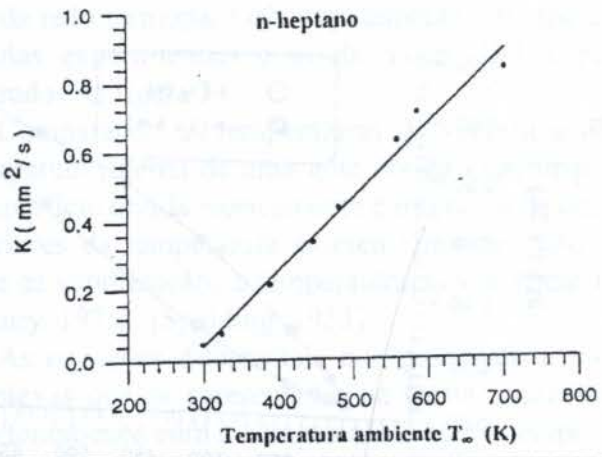

Fig. 9 Evolução do coeficiente de vaporização K do ndo
ptano em função da temperatura ambiente

tro da gota em função do tempo.

A figura 8 mostra a regressão do diâmetro quadrado da gota na forma adimensional em função da relação do tempo sobre o diâmetro inicial da gota ao quadrado. Os coeficientes de vaporização para cada temperatura ensaiada foram obtidos como um valor médio dele. A figura 9 mostra a variação do coeficiente de vaporização da gota de n-heptano em função da temperatura ambiente

4. RESULTADOS E DISCUSSÃO

Os resultados preliminares são apresentados e discutidos neste trabalho. Estes resultados se referem a vaporização das gotas combustíveis de componentes puros tratadas pela teoria quase-estacionária como gota isolada, sem interferência de outras gotas. As gotas de n-heptano utlizadas experimentalmente têm sido praticamente constante com uma variação da ordem de 1,4 á 1,6 mm no diâmetro. O perfil do diâmetro das gotas foi registrado através de uma câmara CCD. Foram processados em média 300 imagens para cada experiência.

A figura 1 mostra a solução geral para obter a temperatura da superfície da gota para qualquer valor de B_T, B_M e número de Lewis. A temperatura da superfície da gota para Le = 1, é uma solução particular e muito utilizado por diversos autores e corresponde a $B_T = B_M$ como mostra a figura 2.

A temperatura na superfície da gota em relação a temperatura ambiente mostrada na figura 3, aumenta com um gradiente maior para as temperaturas ambiente menores de 500 K. Para valores maiores de 500 K este gradiente é menor. A temperatura obtida teoricamente com Le = 1, é menor que as obtidas experimentalmente neste trabalho e àquelas obtidas por Yuen. Esta análise nos faz pensar que o número de Lewis escolhido inicialmente para temperaturas superiores à do ambiente normal não é necessariamente igual a unidade. O calor transferido para a gota não é totalmente aproveitado para transformar a fase líquida em fase vapor como sugere a teoria quasi-estacionária. Uma parte deste calor é utilizada para aquecer a gota.

A evolução de $\ln(1+ B_T)$ e $\ln(1+ B_M)$ em função da temperatura ambiente T_∞ obtida na figura 6 mostra que elas evoluem de forma diferente, e não são iguais, condição necessária para que o número de Lewis seja igual a unidade. Estas são convergentes em baixa e em alta temperaturas, o que indica que o número de Lewis é unitário nestas condições.

A figura 7 mostra a variação do número de Lewis. Ela apresenta um gradiente positivo até valores em torno de 360 K e gradientes negativos para temperaturas maiores. O valor máximo é de 2,6 para uma temperatura em torno de 360 K. Este fenômeno pode ser explicado pela aquecimento prévio da gota que não foi considerada na teoria quase-estacionária e a geração dos efeitos convectivos produzidos em torno da gota pelo mesmo aumento da temperatura ambiente e que também não foi considerado na teoria quase-estacionária.

Para o estudo da regressão do diâmetro da gota em função da temperatura ambiente foram realizadas cinco experiências para cada temperatura de 300K, 410 K, 531 K, 649 K e 780 K em um número de Reynolds que varivam entre 40 e 70. A regressão do quadrado do

diâmetro da gota na forma adimensional em função da relação tempo sobre diâmetro inicial da gota ao quadrado é mostrado na figura 8. Estas curvas mostram, para as diversas temperaturas ambientais experimentadas, que elas não são exatamente lineares e por tanto não podem ser consideradas nestas condições, com Le =1, como sugere a lei de diâmetros quadrados. Observamos que o tempo de vida da gota diminui com o aumento da temperatura ambiente. No entanto temos obtidos um Coeficiente de vaporização médio K em função do tempo para cada temperatura ambiente. A figura 9 mostra a evolução do coeficiente de vaporização médio K de uma gota de n-heptano em função da temperatura ambiente. Esta curva representa uma variação linear.

5. CONCLUSÕES

Este trabalho mostrou um método teórico-experimental de estudar as caracteríticas da vaporização de gotas submersas em ambientes aquecidos. Varios fenômenos transientes foram observados com relação ao campo da temperatura ambiente e da temperatura na superficie da gota. O comportamento das gotas submersas nas diversas temperatura ambientes foram bem diferentes, assim como o tempo de vida de cada uma delas. Foi verificado, para cada gota ensaiada, a existência de um período inicial de aquecimento. Foi mostrado que a temperatura na superficie da gota, obtida usando a teoria quase-estacionária com Le =1, é menor que a obtida experimentalmente.Este trabalho mostrou que para uma faixa de temperatura ambiente experimentada de 300 K até 780 K o número de Lewis não é igual a unidade.

Para um aumento da temperatura ambiente em torno da gota, o coeficiente médio da vaporização de uma gota de n-heptano varia linearmente com esta temperatura.

6. REFERÊNCIAS

Godsave G. A. E., Studies of the Combustion of Drops in a Fuel Sprays - The Burning of Single Drops of Fuel, Fourth Symposium (International) on Combustion, Williams & Wilkins, Baltimore, pp. 818-830, 1953.

Goldssmith M. and Penner S. S., On the burning of single drops of fuel in an oxiding atmosphere. Jet Propulsion, pp. 245-251, 1954.

Kanury A. M., Introduction to Combustion phenomena, Gordon and Breach Science Publishers, 1975.

Law C. K., Quasi-steady droplet vaporization theory with property variation, The Physics of fluids, vol 18, N° 11, 1975.

Lefebvre A. H., Atomization and Sprays , Taylor & Francis, 1989.

Ramos-Arroyo N. A., Etude de la vaporisation de gouttes en interaction. Influence de la convection et de la temperatura. PhD thesis, University of Orléans, Orléans,1994.

Spalding D. B., Combustion and Mass Transfer, Pergamon Press, 1979.

Spalding D. B., The Combustion of liquid fuels, Fourth Symposium (International) on Combustion, Williams and Wilkins, pp. 847-864, 1953.

E. M. Sparrow and J. L. Gregg, Trans ASME, vol 8,pp879-886, 1958.

Vargaftik N.B., Handbook of Physical Properties of Liquids and Gases, Hemispher Publishing Corporation, 1975.

Wise H., J. Lorell and B. J. Wood, The effects of chemical and physical parameters on burning rate of liquid droplet, Fifth Symposium (International) on Combustion, pp.132-141, 1955.

Yuen M. C. and L. W. Chen, On drag of evaporating liquid drops.Combustion Science and Technology, vol. 14, pp. 147-154, 1976

XIV Brazilian Congress of Mechanical Engineering
Obeid Plaza Hotel Convention Center - Bauru - SP/Brazil
December 08-12th 1997

PAPER CODE: COB505

INFLUÊNCIA DA RAZÃO DE VAZÕES NA TRANSFERÊNCIA DE CALOR DE UM ESCOAMENTO LAMINAR ANULAR DE DOIS LÍQUIDOS IMISCÍVEIS EM TUBOS CURVOS / *INFLUENCE OF THE FLOW RATE ON THE HEAT TRANSFER IN THE FLOW OF TWO INMISCIBLE LIQUIDS IN CURVED TUBES*

RICARDO JUNQUEIRA SILVA, MÁRCIO ZIVIANI & RAMÓN MOLINA VALLE
Departamento de Engenharia Mecânica, UFMG, Av. Antônio Carlos, 6627
CEP 31.270-910 - Belo Horizonte - MG - Brasil - E-mail: junco@demec.ufmg.br

Abstract

The present paper reports the influence of the flow rate on the flow and heat transfer in the fully developed region in a steady laminar annular flow of two inmiscible liquids inside horizontal and slightly curved tube with constant circular cross section. The liquids interface was considered without thickness, smooth, circular and concentric to the axis of the duct. The liquids properties were taken constant and calculated based on the mean temperature. The finite volume method was used to solve the mass, momentum and energy conservation equations. The influence of the flow rate on the flow, temperature profile and heat loss have been determined.

Keywords

Curved pipe, annular flow, heat transfer, tubo curvo, escoamento anular, transferência de calor.

1. INTRODUÇÃO

Estuda-se a influência da razão de vazões no escoamento e na troca convectiva de calor da região completamente desenvolvida do escoamento laminar anular de dois líquidos imiscíveis em trechos curvos de um tubo horizontal de seção circular constante. Escoamento anular é aquele em que os dois fluidos que o compõem escoam completamente segregados, um como um filme junto à parede e outro no núcleo da tubulação. Escoamentos multifásicos ocorrem em vários sistemas e equipamentos industriais. A presença de um outro fluido no escoamento pode ser inerente ao processo, como nos trocadores de calor por contato direto; inevitável, como nos vazamentos de óleo nas bombas e compressores, ou um segundo líquido pode ser propositadamente injetado no escoamento para formar um filme junto à parede do tubo.

A primeira solução do escoamento em tubo curvo se deve a Dean (1927), que mostrou que os efeitos centrífugos deslocam o pico da velocidade principal para o lado externo da curvatura e dão origem ao escoamento secundário. Além disso, estabeleceu a representação deste escoamento por um grupo adimensional, que hoje leva seu nome:

$$K = Re\sqrt{a/r_c}\,, \qquad (1)$$

onde K é o número de Dean, a o raio do tubo, r_c o raio de curvatura e Re o número de

Reynolds dado por

$$\mathrm{Re} = \overline{\rho} a \overline{w} / \overline{\mu}, \tag{2}$$

onde $\overline{w}$ é a velocidade principal média, $\overline{\rho}$ e $\overline{\mu}$ são a massa específica e a viscosidade médias na seção transversal, ponderadas pela área transversal de cada fluido. Genericamente:

$$\overline{p} = p_n\left((2\delta)^2\left(1-p^*\right)+p^*\right), \tag{3}$$

onde $\overline{p}$ é a propriedade média, p_n a propreidade do núcleo, p^* a razão entre seu valor no filme e no núcleo e δ é a posição da interface. O escoamento em tubos curvos é caracterizado pelo número de Dean e pela razão de curvatura (r_c/a).

O primeiro trabalho teórico sobre transferência de calor em tubos curvos deveu-se a Mori e Nakayama (1965) que utilizaram como condição de contorno o fluxo de calor prescrito na parede. Utilizaram o modelo de camada limite restrito a problemas completamente desenvolvidos e altos números de Dean. Resolveram também o problema com condição de contorno de temperatura de parede constante, além de apresentarem correlações para o número de Nusselt (1967). Patankar et al. (1974) resolvem numericamente as regiões de entrada e completamente desenvolvida, com condições de contorno de temperatura e fluxo de calor prescritos.

Bentwich e Sideman (1964) estudaram a transferência de calor no escoamento anular de dois líquidos em um tubo reto horizontal, nas regiões de entrada e completamente desenvolvidas, com condição de contorno de temperatura prescrita. Leib et al. (1977) investigam a transferência de calor no escoamento anular de dois líquidos em um tubo reto vertical, com condição de contorno de temperatura prescrita.

Recentemente, Nogueira (1993) estudou o escoamento completamente desenvolvido de fluidos imiscíveis em tubos retos. Ziviani et al. (1991) resolveram numericamente o problema do escoamento anular de dois líquidos imiscíveis em tubos retos e curvos, na região de entrada, considerando a interface entre eles circular e concêntrica ao eixo do tubo. Braga et al. (1995) estudaram a região completamente desenvolvida, com as mesmas considerações de Ziviani et al.

No presente trabalho estuda-se, para a região térmica e hidrodinâmicamente desenvolvida, o comportamento dos perfis de velocidade e a troca de calor com a razão de vazões, definida como

$$\dot{m}^* = \dot{m}_f / \dot{m}_n \tag{4}$$

onde $\dot{m}_f$ é a vazão do filme e $\dot{m}_n$ a vazão do núcleo. Considerou-se dois tipos de condição de contorno, temperatura axial constante (condição de contorno de 1ª espécie) e fluxo de calor axial constante (condição de contorno de 2ª espécie).

2. FORMULAÇÃO DO PROBLEMA

A configuração geométrica e o sistema de coordenadas utilizados na solução do problema estão representados na Fig. 1. O ângulo na direção axial do tubo (α) é retificado como

$$dz = r_c \, d\alpha \tag{5}$$

e as equações são escritas em um sistema de coordenadas cilíndrico (r, ω, z).

Considera-se que a pressão possa ser escrita como a soma de um valor médio na seção ($\overline{p}$) com uma flutuação na seção (p^{**}), ou seja,

$$p(r,\omega,z)=\overline{p}(z)+p^{**}(r,\omega,z) \quad (6)$$

e define-se uma pressão modificada que inclua os efeitos gravitacionais

$$p^{*}=p^{**}+\rho g r\,\mathbf{sen}\,\omega\,. \quad (7)$$

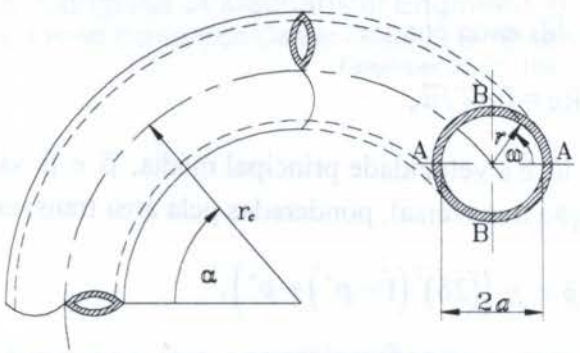

Figura 1 - Geometria e sistema de coordenadas.

O problema da transferência convectiva de calor nesta geometria pode então ser descrito pelo seguinte conjunto de equações diferenciais (Silva et al., 1996):

• equação da continuidade:

$$\frac{1}{r}\frac{\partial}{\partial r}(r\rho v)+\frac{1}{r}\frac{\partial}{\partial \omega}(\rho u)=0 \quad (8)$$

• equação da conservação da quantidade de movimento

- direção axial:

$$\frac{1}{r}\frac{\partial}{\partial r}(r\rho vw)+\frac{1}{r}\frac{\partial}{\partial \omega}(\rho uw)=-\frac{\partial \overline{p}}{\partial z}+\frac{1}{r}\frac{\partial}{\partial r}\left(r\mu\frac{\partial w}{\partial r}\right)+\frac{1}{r}\frac{\partial}{\partial \omega}\left(\frac{\mu}{r}\frac{\partial w}{\partial \omega}\right) \quad (9)$$

- direção radial:

$$\frac{1}{r}\frac{\partial}{\partial r}(r\rho vv)+\frac{1}{r}\frac{\partial}{\partial \omega}(\rho uv)=-\frac{\partial p^{*}}{\partial r}+\frac{1}{r}\frac{\partial}{\partial r}\left(r\mu\frac{\partial v}{\partial r}\right)+\frac{1}{r}\frac{\partial}{\partial \omega}\left(\frac{\mu}{r}\frac{\partial v}{\partial \omega}\right)+\mathrm{Sc}_v+\mathrm{Sp}_v v \quad (10)$$

$$\text{onde: } \mathrm{Sc}_v=\frac{\rho u^2}{r}+\frac{\rho w^2}{r_c}\mathbf{cos}\,\omega-\frac{2\mu}{r^2}\frac{\partial u}{\partial \omega} \text{ e } \mathrm{Sp}_v=-\frac{\mu}{r^2} \quad (11)$$

- direção angular:

$$\frac{1}{r}\frac{\partial}{\partial r}(r\rho vu)+\frac{1}{r}\frac{\partial}{\partial \omega}(\rho uu)=-\frac{1}{r}\frac{\partial p^{*}}{\partial \omega}+\frac{1}{r}\frac{\partial}{\partial r}\left(r\mu\frac{\partial u}{\partial r}\right)+\frac{1}{r}\frac{\partial}{\partial \omega}\left(\frac{\mu}{r}\frac{\partial u}{\partial \omega}\right)+\mathrm{Sc}_u+\mathrm{Sp}_u u \quad (12)$$

$$\text{onde: } \mathrm{Sc}_u=-\frac{\rho w^2}{r_c}\mathbf{sen}\,\omega+\frac{2\mu}{r^2}\frac{\partial v}{\partial \omega} \text{ e } \mathrm{Sp}_u=-\frac{\rho v}{r}-\frac{\mu}{r^2} \quad (13)$$

• equação da energia:

$$\frac{1}{r}\frac{\partial}{\partial r}(r\rho vc_p T)+\frac{1}{r}\frac{\partial}{\partial \omega}(\rho uc_p T)=\frac{1}{r}\frac{\partial}{\partial r}\left(rk\frac{\partial T}{\partial r}\right)+\frac{1}{r}\frac{\partial}{\partial \omega}\left(\frac{k}{r}\frac{\partial T}{\partial \omega}\right)+\mathrm{Sc}_T \quad (14)$$

$$\text{onde: } \mathrm{Sc}_T=-\rho c_p w\,\partial T/\partial z \quad (15)$$

As condições de contorno do problema são:

- Não deslizamento, impermeabilidade e temperatura superficial constante (T_w, condição de contorno de 1ª espécie) ou fluxo de calor constante (q_w, condição de contorno de 2ª espécie) na parede do tubo ($r = a$).

- No plano horizontal ($\omega = 0$ e $\omega = \pi$) não há fluxo de massa ou calor devido à simetria do problema.

- O eixo do tubo ($r = 0$) é um ponto singular com área igual a zero.

O termo $\partial T/\partial z$ na Eq. 15 é obtido através de um balanço de energia em um trecho do tubo, ou seja:

$$\frac{\partial T_b}{\partial z} = \frac{2q_w}{a\overline{\rho}\overline{c}_p\overline{w}}, \text{ assim temos,} \tag{16}$$

$$\left.\frac{\partial T}{\partial z}\right|_1 = \frac{T - T_w}{T_b - T_w}\frac{\partial T_b}{\partial z} \text{ e } \left.\frac{\partial T}{\partial z}\right|_2 = \frac{\partial T_b}{\partial z}, \tag{17}$$

para as condições de contorno de 1ª e 2ª espécie, respectivamente.

2.1 Simplificações do modelo

Devido à complexidade dos fatores que afetam a forma e a posição da interface foram feitas algumas simplificações no modelo. A interface foi modelada observando os trabalhos experimentais de Anderson e Hills (1974) e Maddock e Lacey (1974) sobre escoamento anular. O modelo utilizado considera que os dois líquidos escoam completamente segregados, não havendo penetração, formando uma interface sem espessura, lisa, circular e concêntrica ao eixo do tubo (Ziviani, 1991). São desconsiderados portanto os efeitos da instabilidade de Kelvin-Helmholtz provocada pelo salto de viscosidade na interface. A região ocupada por cada líquido é definida pela posição da interface (δ). Essa posição é tal que satisfaça a equação de conservação da massa para cada líquido.

O modelo apresentado é válido em todo ponto do domínio em que as propriedades sejam contínuas e continuamente diferenciáveis. No contato entre os dois líquidos ($r = \delta$), devido às descontinuidades nas propriedades físicas, as equações de conservação assumem formas específicas, representando continuidade de velocidade, de temperatura, de tensões de cisalhamento e de fluxo de calor.

2.2 Número de Nusselt

Para avaliação e comparação da troca de calor entre os vários casos estudados foi definido o seguinte número de Nusselt:

$$\mathrm{Nu} = \frac{h2a}{\overline{\mathrm{k}}} \tag{18}$$

onde h é o coeficiente convectivo e $\overline{\mathrm{k}}$ a condutividade térmica média dos fluidos, dados por:

$$h = \frac{-k\partial T/\partial r|_{r=a}}{T_w - T_b} \text{ e } \overline{\mathrm{k}} = \delta \mathrm{k}_n + (1-\delta)\mathrm{k}_f. \tag{19}$$

O número de Nusselt assim definido é influenciado tanto pelo coeficiente convectivo quanto pela posição da interface e pela condutividade térmica dos fluidos.

3. METODOLOGIA DE SOLUÇÃO

As equações foram discretizadas segundo o método de Diferenças Finitas com formulação em volumes de controle, conforme descrito por Patankar (1980). Foi utilizado o esquema de interpolação *Power-law* e o acoplamento pressão-velocidade nas direções angular e radial foi feito com o algoritmo SIMPLE (Semi-Implicit Metod for Pressure Linked Equations). Foi adotado um esquema desencontrado de alocação das variáveis (Patankar, 1980). A malha adotada foi não-homogênea, com refinamento nas regiões próximas à parede e à interface.

4. RESULTADOS E DISCUSSÕES

Não foram encontrados dados experimentais de escoamento anular, por isso o modelo foi validado simulando um escoamento monofásico. Os resultados obtidos no presente modelo foram comparados com os resultados experimentais de Mori e Nakayama (1965) e numéricos obtidos por Patankar et al. (1974) (Silva et al., 1996).

Tabela 1 - Propriedades físicas nas composições consideradas (filme / núcleo).

	Água / querosene	Querosene / água
ρ^*	0,9615	1,04
μ^*	0,4453	2,2459
k^*	3,1289	0,3196
c_p^*	2,1186	0,4762

Analisam-se os efeitos da razão de vazões sobre o escoamento e a troca de calor nas composições água / querosene e querosene / água, com o primeiro componente no filme, cujas propriedades físicas são mostradas na Tab. 1. O aumento da razão de vazões, como definido pela Eq. 5, afeta fortemente a posição da interface entre os líquidos, aumentando a espessura do filme. Nas figuras apresentadas a parte externa da curva está sempre do lado esquerdo e a linha vermelha representa a interface entre os líquidos.

Nota-se que no escoamento da composição água / querosene o líquido menos viscoso e com maior condutividade térmica escoa no filme. A forma do escoamento principal não é alterada de forma significativa com o aumento da razão de vazões, como mostrado na Fig. 2. Quando a interface está suficientemente afastada da parede ($\dot{m}^* > 1{,}0$), devido à pouca influência do núcleo, o escoamento principal se comporta como monofásico, sendo o efeito da parede todo absorvido pelo filme.

Neste trabalho consideraremos como camada limite do escoamento secundário a região em que o fluido contorna a parede do tubo, da parte externa para a interna da curva. Mostra-se na Fig. 3 que, se a interface está fora da camada limite as alterações na razão de vazões não levam a modificações no escoamento secundário ($\dot{m}^* > 1{,}0$). Conclui-se, então, que apenas nos casos em que o filme for muito estreito variações significativas serão observadas no escoamento secundário, com a variação da razão de vazões.

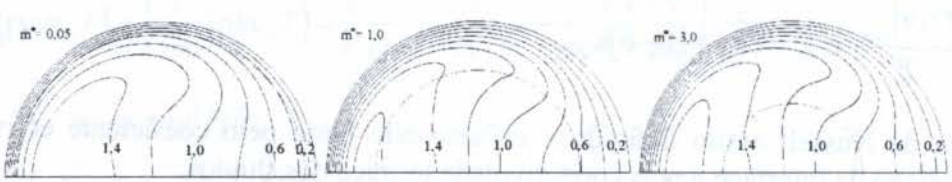

Figura 2 - Escoamento principal da composição água / querosene.

Figura 3 - Linhas de corrente do escoamento secundário da composição água / querosene.

Na Fig. 4, que mostra as isotermas para a condição de contorno de 1ª espécie, observa-se uma forte alteração dos perfis de temperatura com a variação da razão de vazões, quando o filme é estreito ($\dot{m}^* < 1{,}0$), devido às alterações do escoamento secundário nestas condições. A elevação da razão de vazões aumenta o gradiente de temperatura próximo à parede e o diminui na região central do tubo. Quando a camada limite é constituída por um único fluido

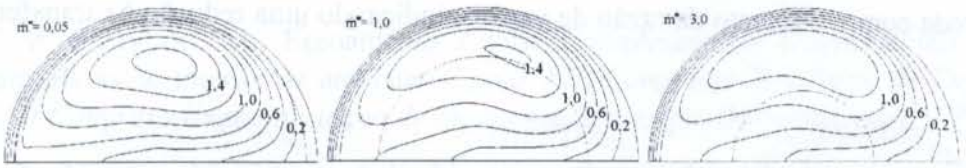

Figura 4 - Isotermas da composição água / querosene.

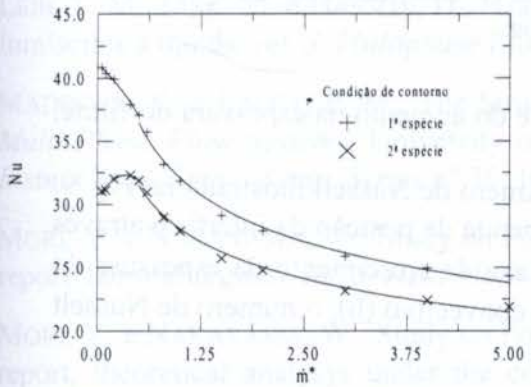

Figura 5 - Efeito da razão de vazões no número de Nusselt na composição água / querosene.

($\dot{m}^* > 1{,}0$), o perfil de temperatura praticamente não se altera. As isotermas para a condição de contorno de 2ª espécie apresentam um comportamento similar.

Para pequenos valores de razão de vazões o comportamento do número de Nusselt é diferente para as condições de contorno de 1ª e 2ª espécie, como mostra Fig. 5. Com a condição de contorno de 1ª espécie o número de Nusselt é sempre decrescente, mas a curva muda de concavidade para $\dot{m}^* \geq 0{,}5$. Com a condição de contorno de 2ª espécie o número de Nusselt é crescente para $\dot{m}^* \leq 0{,}4$ e depois decrescente, como observado na condição de contorno de 1ª espécie.

Na composição querosene / água o líquido mais viscoso e com menor condutividade térmica escoa no filme (Tab. 1). Nestas condições, para a mesma razão de vazões, o filme e a camada limite são mais espessos que no caso anterior (Fig. 3). Observa-se na Fig. 6 um comportamento dos perfis de velocidade semelhante ao da composição água / querosene.

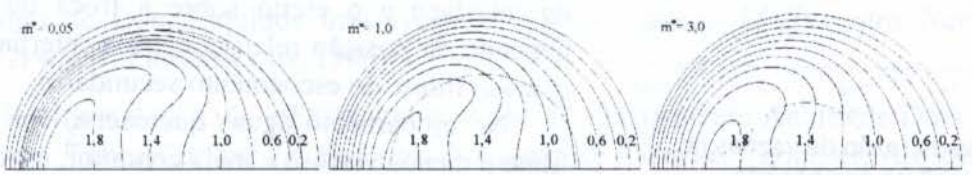

Figura 6 - Escoamento principal da composição querosene / água.

Figura 7 - Linhas de corrente do escoamento secundário da composição querosene / água.

Nota-se neste caso, no entanto, que o escoamento principal apresenta gradientes mais suaves e perfis de velocidade melhor distribuídos na seção.

O escoamento secundário, mostrado na Fig. 7, praticamente não é afetado pela variação da razão de vazões. Observa-se apenas um pequeno deslocamento para o lado de dentro da curva quando $\dot{m}^*$ é pequeno ($\dot{m}^* < 1{,}0$).

A Fig. 8 mostra o comportamento do perfil de temperatura, para a condição de contorno de 1ª espécie, com a razão de vazões. Observa-se uma diminuição do gradiente de temperatura próximo à parede com o aumento da razão de vazões, indicando uma redução na transferência

Figura 8 - Isotermas da composição querosene / água.

de calor por causa da redução do escoamento secundário e do aumento na espessura do filme, que funciona como isolante térmico (observe Tab. 1).

Este efeito não é observado no comportamento do número de Nusselt mostrado na Fig. 9. O número de Nusselt definido neste trabalho (Eq. 14) depende da posição da interface através da condutividade térmica média ($\bar{k}$) (Eq. 15). Como a taxa de crescimento da espessura do filme (δ) é maior que a taxa de decréscimo do coeficiente convectivo (h), o número de Nusselt é crescente, como mostra a Fig. 9.

6. CONCLUSÕES

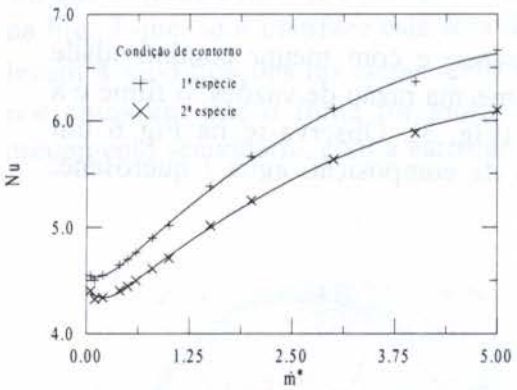

Figura 9 - Efeito da razão de vazões no número de Nusselt na composição querosene / água.

A troca de calor no escoamento em tubos curvos é comandada principalmente pelo escoamento secundário. A forma das isotermas se aproxima da forma das linhas de corrente em todos os casos analisados.

O escoamento secundário é afetado fortemente pela razão de vazões quando o filme é mais estreito que a camada limite.

A razão de vazões afeta fortemente a posição da interface e o efeito sobre a troca de calor depende da posição relativa entre a interface e a camada limite do escoamento secundário.

No escoamento água / querosene, em que o filme é menos viscoso e mais condutor, a troca de

calor diminui com o aumento da razão de vazões.

No escoamento querosene / água, ao contrário, a troca de calor aumenta, significando que a viscosidade do filme inflencia mais que sua condutividade térmica na troca de calor do escoamento.

O comportamento do número de Nusselt para as duas condições de contorno analisadas é o mesmo, exceto para os casos com filme muito estreito no escoamento água / querosene.

7. REFERÊNCIAS

ANDERSON, G. H. e HILLS, P. D., Two-Phase Annular Flow in Tube Bends. *Symps. Multi-Phase Flow Systems*, University of Stratechyde, Glasgow, Paper J1. Publicado como *Instn. Chem. Engrs. Symp. Series* nº 38, 1974.

BENTWITCH, M. e SIDEMAN, S., Temperature Distribution and Heat Transfer in Annular Two-phase (Liquid-Liquid) Flow. *The Canadian Journal of Chemical Engineering*, Fevereiro, pp. 9-13, 1964.

BRAGA, F. P. e ZIVIANI, M., Escoamento Anular Completamente Desenvolvido de Dois Líquidos Imiscíveis no Interior de um Tubo Curvo. *XIII Congresso Brasileiro de Engenharia Mecânica / II Congreso Iberoamericano de Ingenieria Mecánica*, Belo Horizonte, 1995.

DEAN, W. R., Note on the Motion of the Fluid in a Curved Pipe. *Philos. Mag.* nº. 20, pp. 208-223, 1927.

LEIB, T. M., FINK, M. e HASSON, D., Heat Transfer in Vertical Annular Laminar Flow of Two Inmiscible Liquids. *Int. J. Multiphase Flow*, vol. 3, pp. 533-549, 1977.

MADDOCK, C. e LACEY, P. M., The Structure of Two-Phase Flow in a Curved Pipe. *Symps. Multi-Phase Flow Systems*, University of Stratechyde, Glasgow, Paper J2. Publicado como *Instn. Chem. Engrs. Symp. Series* nº 38, 1974.

MORI, Y. e NAKAYAMA, W., Study on Forced Convective Heat Transfer in Curved Pipes. (1st report, laminar region). *Int. J. Heat Mass Transfer*, vol. 8, pp. 67-82, 1965.

MORI, Y. e NAKAYAMA, W., Study on Forced Convective Heat Transfer in Curved Pipes. (3rd report, theoretical analysys under the condition of uniform wall temperature and practical formulae). *Int. J. Heat Mass Transfer*, vol. 10, pp. 681-695, 1967.

NOGUEIRA, E., *Solução Analítica para Escoamento e Transferência de Calor em Regime Bifásico Anular Vertical*. Tese de Doutorado, COPPE/UFRJ, Rio de Janeiro, RJ, 1993.

PATANKAR, S. V., PRATAP, V. S. e SPALDING, D. B., Prediction of Laminar Flow and Heat Transfer in Helically Coiled Pipes. *Journal of Fluid Mechanics*, vol. 62, part. 3, pp. 539-551, 1974.

PATANKAR, S. V., *Numerical Heat Transfer and Fluid Flow*. Hemisphere Publishing Corp, 1980.

SILVA, R. J., ZIVIANI, M. e VALLE, R. M., Transferência de Calor no Escoamento Anular Desenvolvido de Dois Líquidos Imiscíveis em Tubos Curvos. *VI Encontro Nacional de Ciências Térmicas*, Florianópolis, 1996.

ZIVIANI, M., NIECKELE, A. O. e FIGUEIREDO, A. M. D., Escoamento Anular de Dois Líquidos Imiscíveis em Tubos Curvos. *IV Encontro Nacional de Ciências Térmicas*, Rio de Janeiro, 1992.

XIV Brazilian Congress of Mechanical Engineering
Obeid Plaza Hotel Convention Center - Bauru - SP/Brazil
December 08-12th 1997

PAPER CODE: COB52

DIRECT IMAGING OF TWO-PHASE FLOWS BY MEANS OF ELECTRICAL CONDUCTIVITY MEASUREMENTS

Paulo Seleghim Jr. & Antonio Moreira dos Santos
Departamento de Engenharia Mecânica, Escola de Engenharia de São Carlos - USP
Av. Dr. Carlos Botelho, 1465, CEP13560-970 São Carlos - SP - Brasil
E-mail : seleghim@sc.usp.br and asantos@sc.usp.br

Abstract

In this paper a two-phase flow direct imaging probe is presented. To do so, the electrode configuration is adapted in the sense that an imaged representation of the phase distribution within the probe's sensing volume can be obtained by simply plotting the signals corresponding to peripheral conductivity measurements without numerically reconstructing it from the experimental data. Several transient tests were performed in a two-phase loop aiming to demonstrate the the probe's capability in exhibiting not only large structures such as slugs and plugs, but also some finer details as for instance, the wavy or rugged interface in stratified flow and the drainage of the liquid film in the transition between intermittent and annular flow. The methodology proposed in this work is thus fully adapted to on line process monitoring, which is of crucial importance in order to assure ideal exploitation conditions and safety. It constitutes a simple and inexpensive alternative to tomographic imaging techniques.

Keywords

two-phase flow, imaging, visualisation, conductivity

1. INTRODUCTION

Process imaging techniques offers a unique possibility to accede the interior of complex structures such as the geometrical organization of the phases in multiphase flows. This allows one to obtain more detailed information about the associated phenomenology, which in turn can be used to improve the design and operation of multiphase fluids equipment as well as to explain their fundamental hydrodynamics. The main reason for this is the increasing need in process industry to utilize resources more efficiently, to reduce environmental emmissions, to satisfy more strict product quality norms, etc. A good ilustration of this situation is the problematic related to the fluidized bed coal combustion process. This technology allows a significant reduction of the emissions of several pollutants such as sulphur and nitrogen oxides. This is in fact the basic driving force of the research in this area. However, in its curent degree of development, the hydrodynamics of fluidized bed combustion is still not fully understood and one of the main reasons for this is an incomplete knowledge of the structure of the solid-gas flow in the reactor (Halow & Nicoletti, 1992; Milioli, 1996). There is a clear need for visualization techniques as one can conclude from the rapidly growing number of scientific publications on this subject.

This paper describes a direct two-phase flow qualitative imaging technique based on conductivity measurements. More specifically, in order to obtain an imaged representation of the flow pattern from peripheral measurements, generaly, one has to solve an inverse problem which is intrinsically a numerical ill-posed problem. In what concerns electrical sensing techniques, extremely promising due to its simplicity, the ill-posedness may become critical to the point that one is not sure of the uniqueness of the solution with respect to any set of measurements (Seo, 1996). Our approach is then to avoid the numerical image reconstruction procedure by adapting the geometry of the sensing device in a way that the main features of the flow pattern becomes evident by simply plotting the probe's unprocessed signals. This procedure is justified by the fact that in many multiphase systems monitoring tasks one needs only to have an approximate representation of the spacial distribution of the constituent phases of the fluid. The direct imaging approach is a simple and inexpensive alternative to tomographic imaging techniques.

2. TOMOGRAPHIC IMAGING

In order to obtain a phase profile corresponding to the multiphase flow pattern, the most common approach is to install a certain number of sensors aroud the pipe or vessel confining the flow. This is done in such a way that the output signals of the sensors depend on the constitution of the fluid within their sensing zones. In other words the basis of most imaging techniques is to exploit differences or contrasts in some physical property of the phases of the multiphase fluid. Subsequently a computer may be used to reconstruct from these signals a 2D or a 3D image of the flow by numerical techniques. The information that can be obtained from these images can be of great value. Good reviews on this subject can be found in the special issue of *Measurement Science & Technology* dedicated to process tomography (march 1996 , Vol. 7, No. 3).

Depending on the physical principle of the sensing system, the measured signals may contain information related to a well delimited region inside the sensing volume. Exemples of this are transmission/emission methods like nucleonic techniques (X-ray, γ-ray attenuation or single photon and positron emission) as well as some acoustic and optical methods. There are several reconstruction algorithms suited for this type of problem such as Fourier inversion, convolutional back-projection and algebraic reconstruction methods (Herman, 1980; Natterer, 1986). In contrast to transmission/emission methods, the peripheral signals obtained from diffraction (neutron, γ-ray and acoustic wave scattering) or electrical sensing systems result from undetermined regions within the sensing zone. How much each of these regions contributes to the measured values depends on the unknown phase distribution of the multiphase fluid. This feature, refered to as the soft-field effect, requires refined numerical reconstruction methods.

In general, constructing an image from peripheral signals by tomographic techniques involves solving an inverse problem. More specifically the measurements performed at the periphery provides a set of projected views of the process under investigation, which are then utilized to construct a cross section profile of the flow pattern. Inverse problems are characteristic of a very large number of mathematically ill-posed problems emerging in physical as well as in medical sciences and others. This ill-posed nature of the problem may, under certains circonstances, affect the quality of the final images. In what concerns multiphase flow tomographic imaging, experimental errors and noise, coupled with round-off and truncation errors inherent to the numerical reconstruction algorithms, may be amplified and corrupt the precision of the results. For instance, considering the spacial resolution attainable by different sensing methods it is known that transmission/emission techniques are in general capable of locating an object within 1% of the diameter of the cross section of the sensing zone, while

typical resolutions associated with acoustical and electrical techniques corresponds to 3% and 10% respectively (Williams & Beck, 1995). Another important feature is the distinguishability as defined by Gisser *et al.*, 1987, that is, the ability to distinguish between two different phase profiles. Unfortunately, a systematic study dedicated to this subject has not been published yet.

Imaging systems based on electrical sensing are, among other advantages, simple, robust and fast. This explains the current great interest in process imaging and, in particular, in multiphase flow visualization. However this technique has some drawbacks. In contrast to X-ray and other transmission/emission systems, the electrical field is "soft" in the sense that it depends on the phase distribution within the sensing zone. Thus the forward and the inverse problems are coupled, quantitative reconstruction algorithms are in general iterative and convergence may become a major source of problems. In fact, one observes that the reconstruction algorithm does not converge to the right solution (or not at all) for some sets of possible input data (Kühn *et al.*, 1996). In addition the algorithms available for image reconstruction assume in general the electrical field to be static and two-dimensional, thus not correcting for the soft field or 2D/3D effect. Consequently results from calculations may exhibit some over and under-shooting as for instance void fractions above 100% and under 0% (Xie *et al.*, 1992).

3. DIRECT IMAGING

In order to obtain an image of the flow directly from the measured physical quantities, *i.e.* without reconstructing it by solving an inverse problem, the sensing technique must be so to divide the sensing region in a certain number of independent sub-regions. This being done, the set of measured signals ideally reflects the constitution of the flow within each of these sub-regions independently of their surrounding.

Producing a partition of the sensing volume by means of non-intrusive sensing techniques is a very complex problem and, to our knowledge, no specific work on this subject has been published yet. In the context of electrical measuring principles, this task has an additional complicating factor which is the soft field effect. However, a particular configuration of the excitation and measurement device may be capable of sectorising the electrical field in a way that a default of the measured physical quantity in a specific electrode can be related to the presence of obstacles within its corresponding sensibility sector. This is effectively what has been done in this work as described in the following.

We started from a basic configuration which consists of two stainless steel ring electrodes flush mounted to the tube wall as ilustrated in Figure 1. This configuration have been already adopted by Asali *et al.* (1985) for the measurement of thin liquid films and by Andreussi *et al.* (1988) for the measurement of the liquid hold-up in gas-liquid pipe flows. The measurement principle is based, as mentioned before, on differences or contrasts in the electrical properties of the constitutive phases of the multiphase flow. Due to this fact, their spatial distribution affects the global impedance between the ring electrodes. More specifically, in two phase flows where only one of the phases is conductive, the impedance may be

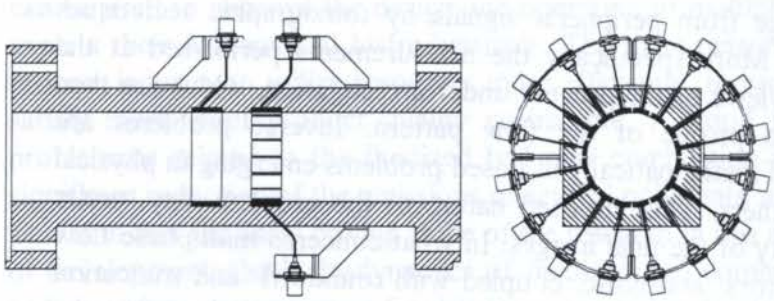

Figure 1 - Conductivity probe composed of an exitation and a measuring ring. The last one is segmented in 16 electrodes in order to partition the sensing volume.

reduced to a purely resistive term when the excitation source is of sufficiently high frequency so that the contact impedance resulting from electrochemical phenomena taking place near the electrodes becomes negligible (some kHz for conductances arround 0.3 $m\Omega^{-1}$ which corresponds to tap water). In addition, the exitation frequency must not be excessively high, say more than some MHz, so that inductive effects becomes preponderant. Under these conditions the problem can be discribed by relations governing the electrostatic field, that is the Poisson's equation

$$\nabla\cdot(\sigma\nabla\Phi) = 0 \qquad (1)$$

where Φ represents the potential and σ the local conductivity of the multiphase fluid. It is interesting to note that for non conducting fluids the direct imaging technique proposed in this work can still be implemented based on a capacitive sensing technique. In other words, in a non conducting multiphase fluid as for instance in gas-particle flows, the global impedance may be reduced to a purely capacituve term and the equation governing the electrostatic field is formally the same, that is

$$\nabla\cdot(\varepsilon\nabla\Phi) = 0 \qquad (2)$$

where ε stands for the local permittivity.

A fundamental characteristic of the ring electrodes geometry is that the global impedance is strongly coupled with the flow pattern within the sensing volume, as reported by both Asali *et al.* (1985) and Andreussi *et al.* (1988). This can be attributed to strong differences in the current flux distribution in the azimuthal sense with respect to distinct flow regimes. Consequently a partition of the sensing volume can be obtained by segmenting the measurement ring what results in a series of electrodes regularly disposed according to the perimeter of the tube, as schematised in Figure 1. A more detailed description of the probe as well as it's operating principles can be found in Seleghim (1996).

4. EXPERIMENTAL APPARATUS AND TESTS

In order to ilustrate the potentiality of the direct imaging methodology proposed in this work we performed several experimental tests at the facilities of the *Comissariat à l'Energie Atomique* in Grenoble - France. The measurements were carried out in a horizontal two-phase flow loop, basically composed of an air circuit, a water circuit, a mixer, an horizontal test section and a separator. The test section is 30 m long and has an internal diameter of 60 mm. It was constructed in Plexiglas in order to allow the flow visualisation. The loop's instrumentation includes temperature and pressure transducers and electromagnetic and turbine flow meters to measure respectively the water and the air flow rates. These parameters are used in two independent PID based regulation loops which are responsible for the control of the flow rates, and permits one to set their temporal variation. For a detailed description of the loop see Seleghim (1996).

The experimental procedure consists essentially in doing transient tests in which the flow regime slowly evolves from one established configuration to another, passing trough a transition in between. Three series of transient test were performed. The first one, aiming to exhibit the main stratified regimes, had a water flow rate fixed at 0.5 m^3/h and an air flow rate varying between 10 and 60 m^3/h. In order to show the evolution from intermittent to bubbly flow, a second transient test was definied: air flow rate fixed at 7.5 m^3/h and water flow rate varying from 5 to 50 m^3/h. The third series of tests, performed to show the transition from

intermittent to anular flow, was conducted with a constant water flow rate of 15 m^3/h and an air flow rate ranging from 70 to 250 m^3/h. The duration of each test was of 820 seconds.

5. RESULTS

In the following the results obtained from the tests described above will be presented. More specifically the signals delivered by the probe (normalized current intensities) will be plotted as a function of two co-ordinates: time and the angular position of the associated electrode. These time traces provide a plane or "unrolled" longitudinal view of the flow since the extent of the probe's sensing volume is negligible when compared to the length of the test section as well as to a characteristic length representative of the longitudinal evolution of the flow. The normalised current intensities are coded in grey levels ranging from white to black which corresponds respectively to 0 and 100% of the values obtained when only the conducting phase is present in the probe. Hence, water will appear in black and air in white in the following images.

5.1. Stratified flows

In stratified flow gravity predominates over other hydrodynamic forces which produce a separation between the liquid and the gas phases. Depending on the shape of the interface one can define the following sub-regimes: stratified smooth, where the interface is flat; stratified wavy, where the interface oscillates in a regular way; and stratified rugged, where the interface oscillates randomly. In the case of horizontal configurations, the energy necessary to the formation of interface waves comes from the gas flow. Stable waves are characteristic of lower gas flow rate values while a rugged interface appears at higher gas flow rates.

The following three plots in Figure 2 ilustrate the imaged representation corresponding to stratified smooth, wavy and rugged flows. As we can see, the flow patterns are easily recognisable by their main geometrical features. We can observe from the images that when the air flow rate increases the liquid film height decreases, which is in accordance to the stratified flow equilibrium equation (see Taitel & Dukler, 1976). Some finer details are also visible, for instance, the distinct wave packets in stratified wavy flow and the presence of solitary large amplitude waves in stratified rugged flow (Seleghim, 1996).

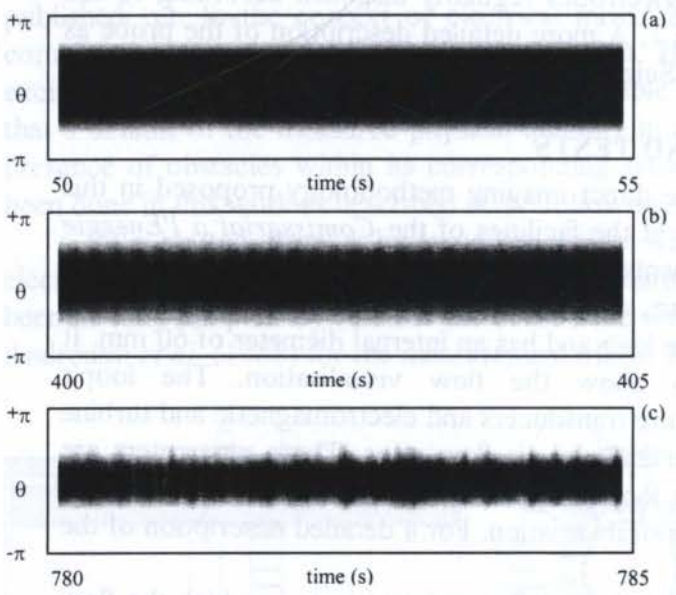

Figure 2 - Imaged representation of stratified flows at constant Qwater = 0.5 m3/h : a) smooth (Qair = 10 m3/h), b) wavy (Qair = 40 m3/h) and c) rugged (Qair = 60 m3/h). The liquid layer is localised around θ = 0 which corresponds to the bottom of the tube.

5.2. Intermittent to bubbly transition

Horizontal intermittent flow is characterised by a non-uniform liquid distribution in the axial direction. More precisely liquid slugs fill the pipe and separate zones in which the gas flows at the top and the liquid

flows on the bottom of the tube as in stratified flow. Consequently the area void fraction is highly intermittent, alternating from a lower value, associated with the presence of a liquid slug, to a higher one, associated with stratified zones.

At low water flow rates the liquid slug is not aerated and the corresponding area void fraction approaches zero. The stratified zones assume the form of elongated bubbles with a relatively sharp head and a biconvex tail. Depending on the values of the air flow rate the interface of the liquid layer within the stratified zone may assume a wavy form, as we can observe on Figure 3a.

When the water flow rate increases at constant air flow rate, the forces that maintain the integrity of the air plugs, *i.e.* surface tesion and Archimede's upthrust, start to compete with turbulent fluctuations which tend to entrain gas into the liquid slugs. This in fact constitutes the basic mechanism of the transition between intermittent and bubbly flow. Due to this, the water slugs become aerated with small bubbles, which increases the local void fraction. The air plugs become smaller and faster, also due to the fact that the average flow velocity increases with the water flow rate at the intermittent regime.

These important aspects of the intermittent to bubbly transition can be observed in Figure 3b and 3c. The bubbly flow regime is shown in figure 3d. Due to the relatively low air flow rate, the bubbles are concentrated at the upper region of the tube which corresponds to the neibouring of $\theta = \pi$.

5.3. Intermittent to annular transition

In the annular regime the liquid flows as a continuous film around the perimeter of the pipe and is also continuous in it's longitudinal direction. This liquid film surrounds a high speed air flow at the core of the tube which may contain entrained liquid droplets formed from waves at the liquid-gas interface. Due to gravity, the liquid film is usually thicker at the bottom of the pipe. Under certain conditions near the transition to annular flow, circular aerated waves may be so that the film thickness increases substantially at the bottom as well as at the top of the tube. This is usually described as a wavy-annular flow pattern.

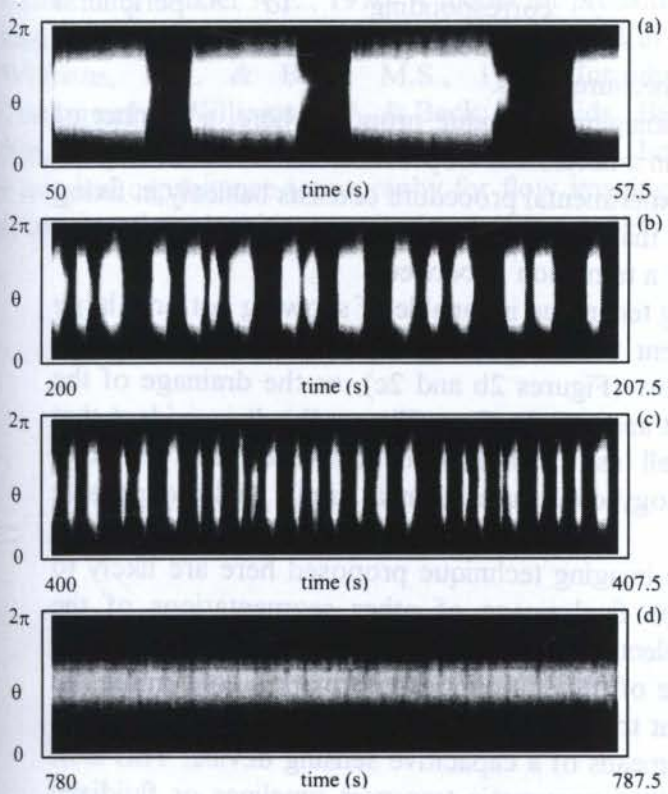

Figure 3 - Imaged representation of intermenttent and bubbly flows at constant Qair = 7.5 m3/h : a) elongated bubbles (Qwater = 5 m3/h), b) medium aerated slugs (Qwater = 15 m3/h), c) small aerated slugs (Qwater = 30 m3/h) and d) bubbly flow (Qwater = 50 m3/h).

Starting from an intermittent flow, the transition to annular flow takes place when the air flux is intense enough to break and traverse some of the water slugs, generating liquid structures that are currently designated pseudo-slugs or rolling waves which can be observed in Figure 4a. The slugs that are not destroyed are ejected at high velocities reaching that of the air flow.

An important effect associated to

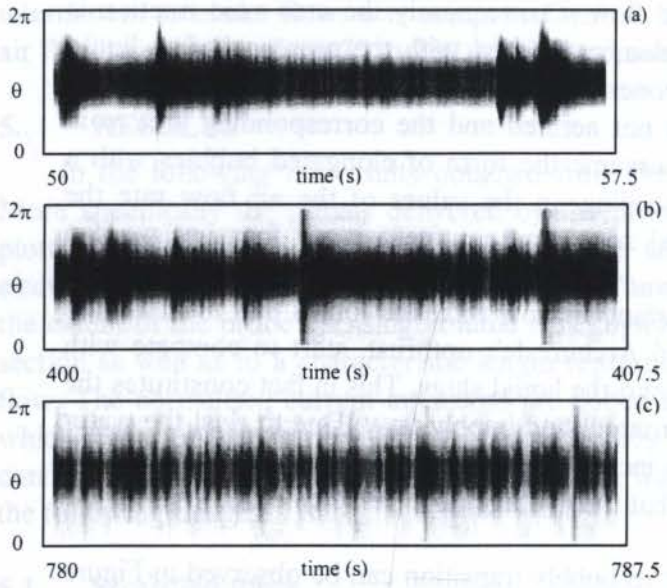

Figure 4 - Imaged representation of the interminttent to annular transition (constant Qwater = 15 m3/h) : a) pseudo-slugs or rolling waves (Qair = 70 m3/h), b) fast slugs and drainage of the peripheral liquid film (Qair = 175 m3/h) and c) established annular flow (Qair = 250 m3/h).

the presence of fast slugs is the deposition of a liquid film at the perimeter of the tube. If the gas velocity is not high enough to maintain this liquid film it may flow back to the bottom of the tube as can be observed in Figure 4b (white spots). If the gas velocity is high enough to destroy all slugs and to maintain a stable liquid film flowing at the walls of the pipe, then the annular regime may be considered fully installed. This situation is ilustrated in Figure 4c.

6. CONCLUSION

A direct imaging probe suited for air-water flows is presented in this work. An imaged representation of the phase distribution within the probe's sensing volume is obtained by simply plotting the signals corresponding to peripheral conductivity measurements, therefore without reconstructing it numerically from the measurements.

To demonstrate the potentiality of the imaging technique proposed here, a number of transient two-phase flow tests were conducted in a horizontal loop which allows one to impose the temporal variations of the flow rates. The experimental procedure consists basicaly in fixing one flow rate and slowly varying the other so that the flow regime slowly evolves from one established configuration to another, passing by a transition in between.

The results confirm that our direct imaging technique is capable of showing not only large structures such as slugs and plugs in intermittent flow (Figure 3) but also finer details as the wavy or rugged liquid interface in stratified flow (Figures 2b and 2c), or the drainage of the liquid film in the transition between intermittent and annular flow (Figure 4b). It is evident that the identification of the flow regime as well as the transitions between them is quite straightforward. Our direct imaging methodology constitutes then a simple and inexpensive alternative to tomographic imaging techniques.

In conclusion, future developments of the imaging technique proposed here are likely to include studies in which the influence on the final image of other segmentations of the measurement ring, as well as the number and electrodes geometry, is established. In particular this could lead to sensor configurations capable of providing more information concerning the flow in the core of the pipe. It is also important to stress that our imaging technique could be applied to nonconducting two-phase fluids by means of a capacitive sensing device. This is of particular interest in gas-particulate flows such as pneumatic transport pipelines or fluidized bed combustion since some basic aspects concerning their hydrodynamics are still poorly understood.

7. REFERENCES

Asali, J.C., hanratty, T.J. & Andreussi, p., 1985, Interfacial drag and film height for vertical

annular flow. AIChE J., Vol. 31, pp.895-902.
Andreussi, P., Di Donfrancesco, A. & Messia, M., 1988, An impedance method for the measurement of liquid hold-up in two-phase flow, International Journal on Multiphase Flow, Vol. 14, No. 6, pp.777-785.
Gisser, D.G., Isaacson, D. & Newell, J., 1987, Current topics in impedance imaging. Clin. Phys. Physiol. Meas. A, Vol.8, p36-46.
Halow, J.S. & Nicoletti, P., 1992, Observations of fluidized bed coalescence using capacitance imaging. Powder Technology, Vol.69, p.2243-2251.
Herman, G.T., 1980, Image Reconstruction from Projections - The Fundamentals of Computerised Tomography, Academic Press, New York.
Kühn, F.T., Schouten, J.C., Mudde, R.F., Van Den Bleek, C.M. & Scarlett, B., 1996, Analysis of chaos in fluidization using electrical capacitance tomography. Measurement Science & Technology, Vol.7, No.3, p.361-368.
Milioli, F. E., 1996, Atmospheric bubbling fluidized bed combustion: application to high ash coals and approach to scientific research. Revista Brasileira de Ciências Mecânicas - ABCM, Vol.XVIII, n.2, p.127- 142.
Netterer, F., 1986, The Mathematics of Computerised Tomography, Wiley, Chichester.
Seleghim P. Jr., 1996, Caracterisation des changements de configuration d'un écoulement diphasique horizontal par l'application de méthodes d'analyse temps-fréquence. Institut National Polytechnique de Grenoble - France, thése de doctorat.
Seo, J.K., 1996, On the uniqueness of the inverse conductivity problem. Journal of Fourier Analysis and Applications, Vol.2, No.2-4.
Taitel Y. & Dukler A.E., 1976, A model for predicting flow regime transitions in horizontal and near horizontal gas-liquid flow. AIChE Journal, Vol. 22, N°1, pp. 47-55.
Williams, R.A. & Beck, M.S., 1995, Introduction to process tomography. Process Tomography, Williams, R.A. & Beck, M.S. Eds., Butterworth-Heinemann.
Xie, C.G., Huang, S.M., Hoyle, B.S., Thorn, R., Lenn, C., Snowden, D. & Beck, M.S., 1992, Electrical capacitance tomography for flow imaging: system model for developmemt of image reconstruction algorithms and primary sensors. IEE Proc. G, Vol.139, p.89-98.

XIV Brazilian Congress of Mechanical Engineering
Obeid Plaza Hotel Convention Center - Bauru - SP/Brazil
December 08-12th 1997

PAPER CODE: COB67

SEARCH FOR FAVORABLE CONDITIONS OF ATMOSPHERIC FLUIDIZED-BED GASIFICATION OF SUGAR-CANE BAGASSE THROUGH COMPREHENSIVE SIMULATION

Marcio L. de Souza-Santos
IPT-Instituto de Pesquisas Tecnológicas de São Paulo e UNICAMP - Universidade Estadual de Campinas
FEM - Faculdade de Engenharia Mecânica, Departamento de Energia
Cidade Universitária Zeferino Vaz, C. Postal 6122, Campinas, SP 13083-970, Brasil
E-mail: souzasan@fem.unicamp.br

Abstract

A study to search for the most favorable condition of atmospheric fluidized-bed gasification of sugar-cane bagasse has been possible using a comprehensive computer simulator of fluidized bed equipment. A previous version of the simulation program has been improved to provide more precise results. In addition, the prediction of possible particle segregation in the bed has been implemented. "Cold" efficiency has been chosen as objective function. The following conditions have been set as constants: operational pressure, basic geometry of the reactor, bed height, particle size distribution of bagasse, particle size distribution of alumina (used as inert in the bed), and bagasse dry-basis composition. The parameters left as variables were: bagasse moisture and the oxygen ratio (fraction from the necessary oxidant for total or stoichiometric combustion). Future steps toward a more complete optimization are shown. The results are going to be used on studies of power generation systems employing gas turbine concepts.

Key Words

Fluidized-bed, gasification, simulation, optimization, sugar-cane bagasse

1. INTRODUCTION

Despite the use of bagasse for steam and power generation in the mills, improvements in the plants may increase the fraction that is diverted to power generation. Some calculations (Hollanda, 1991) demonstrate that, just in the state of São Paulo, 16 % of the power generation could be provided by that source. This represents something around 2 GW.

The effort to apply biomass, particularly sugar-cane bagasse, to advanced gas-turbine power generation system has required extensive studies. Optimization of the reactor is needed to assure the best possible conditions for the application of gasification in a given process. For each single optimization objective, the search involves several variables and a theoretical tool as comprehensive computer simulation saves time and money if compared with, for instance, search through experimental tests in pilot units.

The gasification is one of the most important points of any BIG/GT (Biomass Integrated Gasifier/Gas Turbine Systems) process. Of course, several techniques to achieve the gasification can be considered. Among these, the bubbling fluidized-bed is a serious candidate and has been chosen for the present investigation.

2. THE EXISTING PROGRAM

A simulation program (Souza-Santos, 1987, 1989) has been developed for cases of boilers and gasifiers operating with coal. Later it has been adapted to shale retorting (Souza-Santos, 1994a). After improvements, a new version was validated for simulations of wood gasification (Souza-Santos, 1994b).

The biggest deviation in computations when dealing with different biomass, is due to differences in the devolatilization profiles. For the present application to sugar-cane bagasse, it has been assumed that the bagasse devolatilization stoichiometry is similar to the wood. A test of this hypothesis has been made using IGT (Institute of Gas Technology, Illinois, USA) experimental data. Average deviations between simulation predictions and measured values (concentrations, temperatures, and carbon conversions) are in the same order of magnitude as the obtained for wood gasification (Souza-Santos, 1994b). Unfortunately, the results of that work with bagasse cannot be published due to contract conditions under which it was developed. Future developments will concentrate in adding bagasse devolatilization characteristics. This may improve the results even further.

Recently, the possibility to predict segregation between solids of different minimum fluidization velocities has been implemented in the mathematical model. The correlation by Nienow et al. (1978) was employed. This is an important information, mainly for biomass processing, because most of the reactors use inert solid particles and, very often, their average minimum fluidization velocities are much higher than the necessary by the carbonaceous particles. Therefore the eventually segregated biomass particles would concentrate at the top of the bed. A significant part of the released tar would pass straight to the freeboard, having little residence time for proper cracking and cocking processes. This may increase the probability of the undesirable high tar concentrations to appear in the produced gas. The presence of tar or heavy oils in the exit gas may bring serious problems for the cleaning system. Other problems that heterogeneous fluidization may bring are:

- Unstable fluidization process;
- Slug-flow;
- High temperature spots with consequent ash softening leading to particle agglutination and bed collapsing.

3. THE OPTIMIZATION STRATEGY

Having in mind the intended application for the produced gas, the "Cold" and the "Hot" gasification efficiencies could be set as optimization objectives. "Hot" efficiency would be the search objective for cases where the gas cleaning system does not impose significant temperature drop in the gas stream. Conversely, "Cold" efficiency is the proper parameter if, for instance, the removal of alkaline by condensation is required.

In the present work both parameters are analyzed, and the definitions used here are:

- "Cold" efficiency as

$$\varepsilon_c = \frac{F_G(1 - w_{H2O} - w_{TAR})_G H_{Gc}}{F_B H_B} \quad (1)$$

- "Hot" efficiency as:

$$\varepsilon_h = \frac{F_G H_{G_h}}{F_B H_B} \quad (2)$$

Here "F_G" represents the mass flow of produced gas and "F_B" the inlet mass flow of bagasse (kg/s); "H_G" represents the enthalpy of the produced gas and "H_B" the high heat value of the inlet bagasse (J/kg); "w" represents the mass fraction of the indicated component in the exit gas.

3.1. Range of Tested Conditions.

For the present search some parameters have been left as constants. Those are:

- The characteristics of the feeding bagasse (dry basis).
- Basic dimensions of the gasifier. The present work is part of the study for future experimental tests in a given pilot unit. Therefore, the dimensions such as bed and freeboard internal diameter, total height, distributor design, and cyclone geometry have been assumed as constants.
- Bed depth. The value of 2 m for the bed height has been selected. For some situations, shallower beds have shown that the bubbles could reach the top of the bed with some oxygen. Therefore, no reducing region is left in the bed. Of course, this jeopardizes the gasification efficiency. In order to maintain a uniform value for all tests, it has been decided to set it at the above mentioned value. Future investigations could refine this choice.
- Freeboard height. As the equipment is 6 m tall, the freeboard height has been set to 4 m. This is above of most of the computed TDH (Transport Disengaging Height).
- Mass flow of bagasse feeding. This is determined by the capacity of the feeding system in the existing pilot unit.
- Bagasse particle size distribution. The distribution is the same as the obtained from mills installed in typical sugar and alcohol plants.
- Gasifier nominal operational pressure. For the present it has been set equal to 1 atmosphere because the intended study considers a new process that would not require pressurized gas. Details of such a process will be described in a future paper.
- Temperature of the feeding air. Set to 343 K.
- No steam injection. Preliminary simulations have shown that the moisture contents of the bagasse are enough to provide the needed water as gasification agent.
- Inert characteristics (composition, densities, and particle size distribution). Alumina has been chosen as the inert. Its particle size distribution is such that feasible operational conditions were achieved for the whole studied range of air flow injected through the distributor.

The parameters adopted as variables are:

1. Bagasse moisture. Although the bagasse usually leaves the mill with 50% moisture, the present work considers the possibility of prior drying employing stack gas streams. In this case, it seems that the economic limit is around 30% moisture. Therefore, it has been decided to concentrate the study in three basic levels for the moisture: 20%, 30%, and 35%.
2. Mass flow of air injected through the bed distributor. This variable would be a consequence of each imposed "oxygen ratio". This parameter is given by the ratio between the mass

flow of injected oxygen and the mass flow of oxygen necessary for the stoichiometric combustion of the biomass.

To allow a quick reference to the set of tests, the following nomenclature has been adopted:

- The name of the test is indicated using six symbols.
- The numbers following the "u" letter indicates the moisture level. As commented before, these numbers are: 20, 30, and 35.
- The numbers following the "a" letter indicates the mass flow of injected air in g/s. The tested values were: 20, 25, 27, 30, 35, 40 and 45.

It is important to notice the results for some combinations do not appear because operational problems have been predicted. Among them the collapsing of the bed due to the agglomeration of particles that surpassed the ash softening point. Other conditions led to too low carbon conversion.

4. INPUT DATA

Some of the most important data, common to all cases, are presented below.

Table 1: Proximate analysis of bagasse at 20% moisture

Component	Mass % (w.b.)
Moisture	35.0
Volatile	56.2
Fixed-carbon	6.0
Ash	2.8
High Heat Value (MJ/kg) (dry basis)	16.7

Table 2: Ultimate analysis of the feeding bagasse

Comp.	Mass % (d.b.)
C	44.8
H	5.4
O	39.5
N	0.4
S	0.0
Ash	9.8

More details on the required data as well as information provided by of the present simulation program can be found elsewhere (Souza-Santos, 1987, 89, 94a, 94b).

Table 3: Basic geometry of the gasifier

Characteristics	Value
Internal diameter in the bed section	0.4 m
Bed height	2.0 m
Internal diameter in the freeb. section	1.0 m
Total equipment height	6.0 m
Insulation thickness (m)	0.2
Average thermal conductivity of the insulation (W m^{-1} K^{-1})	0.08
Diameter of the orifices in the distributor (mm)	2
Total number of orifices in the distributor	2688
Bagasse feeding position (from bed base)	0.1 m

As mentioned above, the feeding rate of dry bagasse was kept constant. Therefore, the values of 0.2000 kg/s, 0.22857 kg/s, 0.26667 kg/s, and 0.32000 kg/s where used for 20%, 30%, 40% and 50% moisture, respectively.

Table 4: Particle size distribution of the feeding solids

Bagasse		Alumina	
Sieve opening (mm)	Retained mass percentage	Sieve opening (mm)	Retained mass percentage
0.1	19	0.595	1.0
0.5	36	0.420	4.0
1.0	13	0.250	90.0
1.5	6	0.149	4.0
2.0	3.5	0.105	1.0
2.5	22.5		

5. DISCUSSION OF RESULTS

Table 5 presents the gas, dry basis, composition for the cases that led to the best gasification efficiencies . The program generates several other results which are listed in Table 6. Figure 1 summarizes the results for the "Cold" efficiencies.

Among all information provided by the simulation, the profile of bubble sizes has especial interest. For all cases, slugging flow (bubble occupies the whole cross section of the bed) has been predicted. Apart from the bubble coalescence process, large bubbles are also caused by large differences between the actual and the minimum fluidization velocity. Therefore, the slugging flow starts at a certain height in the bed. This may present a problem because such operations lead to excessive vibration of the equipment added to poor mass transfer between bubbles and emulsion. This can be avoided if the difference between actual and minimum fluidization velocities can be diminished by:

1. Employing pure oxygen, instead air, as oxidant;
2. Operating at pressurized conditions;
3. Pre-heating of the air combined with larger bed cross sections.

Some comments on those may be useful.

It has been verified that bubbles can reach points of temperature well above the average in the bed (Fig. 2). The main cause for this is the process of mass transfer of fuel gases from the emulsion to the relatively cold bubbles. Due to devolatilization, most of the fuel gases are released into the emulsion at points near the bagasse feeding position (0.1 m). Part of these gases reaches the cold bubbles before complete oxidation. Once the bubble phase temperature reaches a certain value, the burning is fast leading to the referred temperature surge. This provokes fast increase on bubble sizes and on the void fraction in the bed (Fig. 4). In addition, the gas flowing through the emulsion also suffers fast expansion at points near the distributor.

On the other hand, if the gas injected through the distributor is pre-heated (combined with larger bed cross sections), the bed can be operated at superficial velocities not too far from the minimum fluidization. This leads to smaller bubbles, smaller differences of temperature between bubbles and emulsion, and no process of fast increase in the void fraction as well as the superficial velocity. The option "3", above, is also the most attractive solution because can be implemented through heat recovery from a turbine exhaust stream.

Finally, as the determination of sulfur emissions was not the aim of the present work, some imbalance may be found for that element in the results. This is because the tolerance set for the integrations was just enough to obtain low deviations for all other elements. The alternative, e.g., using more stringent tolerances, would require much longer computational times. Such requirements can be set once the optimum condition is found.

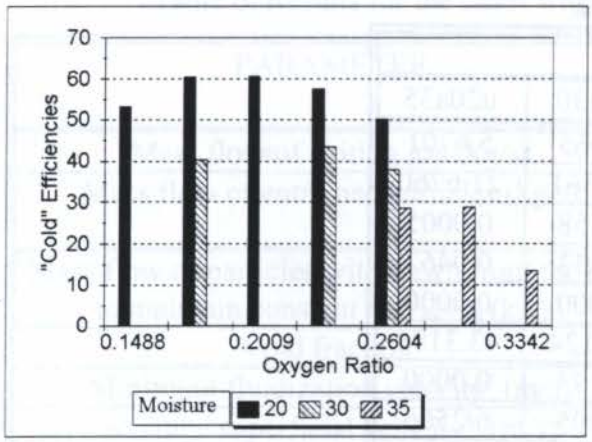

Figure 1: Cold efficiencies.

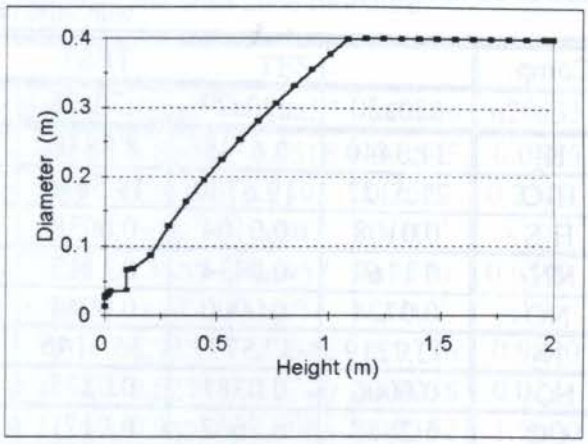

Figure 3: Bubble size profile for the best case.

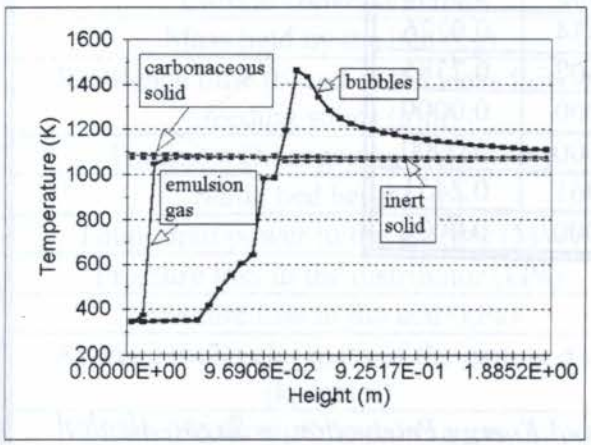

Figure 2: Temperature profiles for the best case.

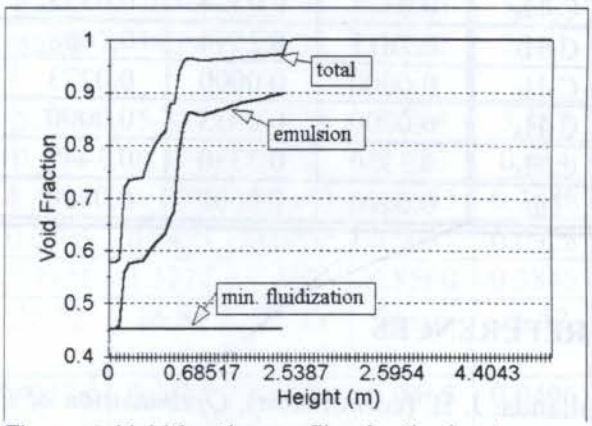

Figure 4: Void fraction profiles for the best case

6. CONCLUSIONS

The basic conclusions are:

- The program can be used as a tool for optimization.
- As the bagasse moisture increases, higher efficiencies are found for higher oxygen ratios.
- No test showed the possibility of segregation in the bed.
- Within the tested range, the best efficiencies were found for 20% moisture and bagasse processed under approximately 20% oxygen ratio (test u20a27).

Future studies intend to:

- Extend the analysis to pressurized systems (see companion paper).
- Repeat the present work for non-slugging conditions.
- Refine the present set of values of bagasse moisture and oxygen ratios.
- Verify the effects of recycling to the bed the particles collected by the cyclone system.
- Include the bed height and other operational parameters as variables in the optimization study.

Table 5: Compositions (molar, wet basis) of the exiting gas streams for tests where bagasse was fed with 20% moisture.

Comp.	TEST				
	u20a20	u20a27	u20a25	u20a30	u20a35
H_2	11.3440	7.6345	8.8848	7.4065	5.6701
H_2O	21.5122	19.6780	19.5690	20.2361	21.6760
H_2S	0.0108	0.0104	0.0038	0.0158	0.0005
NH_3	0.1169	0.0434	0.1113	0.0833	0.0467
NO	0.0724	0.0000	0.0044	0.0000	0.0000
N_2	32.7219	37.5777	36.1146	39.6124	43.3193
SO_2	0.0000	0.0381	0.0275	0.0193	0.0000
CO	5.2688	6.7662	6.9171	6.9895	6.2566
CO_2	20.1412	19.2867	19.3973	17.0403	16.8683
CH_4	8.1828	8.3360	8.2958	7.0403	5.6561
C_2H_4	0.0328	0.0334	0.0333	0.0434	0.0226
C_2H_6	0.2611	0.2594	0.2688	0.2307	0.2385
C_3H_6	0.0000	0.0000	0.0273	0.0000	0.0000
C_3H_8	0.0000	0.0033	0.0000	0.0000	0.0000
C_6H_6	0.3350	0.3330	0.3449	0.2961	0.2451
Tar	0.0000	0.0000	0.0000	0.0000	0.0000

7. REFERENCES

Hollanda, J. B. (coordinator), *Optimization of Electrical Energy Production in Sugar-Alcohol Mills* (in Portuguese), Eletrobrás, Copersucar, BNDES, CESP, CPFL, Eletropaulo, 1991.

Souza-Santos, M. L., Modelling and Simulation of Fluidized-Bed Boilers and Gasifiers for Carbonaceous Solids, *Ph.D. Thesis*, University of Sheffield, England, U.K., 1987.

Souza-Santos, M. L., Comprehensive Modelling and Simulation of Fluidized Bed Boilers and Gasifiers, *Fuel*, Vol. 68, 1507-1521,1989.

Souza-Santos, M. L., Application of Comprehensive Simulation to Pressurized Fluidized Bed Hydroretorting of Shale, *Fuel*, Vol. 73, 1459-1465,1994(a)..

Souza-Santos, M. L., Application of Comprehensive Simulation of Fluidized-Bed Reactors to the Pressurized Gasification of Biomass, *J. of the Braz. Soc. of Mechanical Sciences*, Vol. XVI, No. 4, 376-383, 1994(b).

Nienow, A. W., Rowe, P. N., and Cheung, L. Y. The Mixing/Segregation of a Dense Powder with Two Sizes of a Lighter One in a Gas Fluidized Bed, in *Fluidization*, ed. Davidson, J. F. and Keairns, D. L., Cambridge University Press, London, 1978.

Table 6. Results for the cases where bagasse was fed with 20% moisture.

PARAMETER	TEST				
	u20a20	u20a25	u20a27	u20a30	u20a35
Mass flow of exiting gas (kg/s)	0.0424	0.0494	0.0518	0.0545	0.0586
Mass flow of entrained particles (kg/s)	0.3625 $x10^{-4}$	0.2947 $x10^{-4}$	0.2595 $x10^{-4}$	0.2627 $x10^{-4}$	0.2217 $x10^{-4}$
Mass flow of particles withdrawn from the bed to maintain constant bed level (kg/s)	0.7728 $x10^{-2}$	0.5867 $x10^{-2}$	0.5457 $x10^{-2}$	0.5770 $x10^{-2}$	0.6599 $x10^{-2}$
Void fraction[a]	0.9226	0.9551	0.9642	0.9756	0.9890
Minimum fluidization velocity[a] (m/s)	0.0304	0.0279	0.2700	0.0258	0.0241
Average superficial velocity[a] (m/s)	0.7420	0.9853	1.8082	1.2152	1.5600
Mixing index	1.0000	1.0000	1.0000	1.0000	1.0000
Carbon conversion (%)	63.88	74.72	76.72	75.16	71.60
Mass held by the bed (kg)	83.43	70.08	65.46	59.43	51.13
Residence time (based of the mass flow of feeding solid) (min)	46.36	38.94	36.38	33.02	28.41
Transport Disengaging Height (m)	5.266	5.337	5.373	5.364	5.387
Static bed height (m)	0.677	0.570	0.532	0.483	0.414
Total input power to the gasifier (MW)	0.3881	0.3883	0.3884	0.3885	0.3888
Pressure loss in the distributor (kPa)	0.0303	0.0473	0.0552	0.0681	0.0928
Pressure loss in the bed (kPa)	2.7121	1.5737	1.2563	0.8560	0.3845
Average molecular mass of the exiting gas (kg/kmol)	25.32	26.04	26.33	26.26	26.52
Volumetric flow of the exiting gas (m^3/s) (standard conditions: 273.15K, 1bar)	0.0376	0.0425	0.0441	0.0465	0.0495
Mass concentration of tar in the gas leaving the bed and entering the freeboard (%)	0.0128	0.0019	0.0000	0.0000	0.0000
Enthalpy of exiting gas ("hot, wet") (MJ/kg)	5.8767	5.9398	5.7871	5.4214	4.7972
Enthalpy the exiting gas ("cold, dry") (MJ/kg)	5.7446	5.4955	5.2441	4.7663	3.9114
"Hot" efficiency	**64.23**	**75.59**	**77.25**	**76.02**	**72.26**
"Cold" efficiency	**53.18**	**60.47**	**60.57**	**57.56**	**50.24**
Average bubble diameter at the distributor (m)	0.011	0.013	0.013	0.014	0.019
Aver. bubble diameter at the middle of bed (m)	0.332	0.343	0.377	0.384	0.400
Average bubble diameter at the top of bed (m)	0.400	0.400	0.400	0.4000	0.400
Height at which the bubble diameter is the same as the reactor internal diameter (m)	1.390	1.180	1.165	1.025	0.896
Temperature of carbonaceous particles[a] (K)	924.3	1029.3	1063.5	1110.5	1183.5
Temperature of inert particles[a] (K)	928.3	1037.1	1072.9	1121.7	1196.5
Emulsion gas temperature in the bed[a] (K)	929.0	1038.0	1074.1	1123.5	1199.9
Bubble phase temperature[a] (K)	994.3	1106.6	1165.3	1253.1	1439.1
Aver. temperature at the middle of the bed (K)	927.8	1036.1	1071.7	1120.3	1195.0
Average temperature at the top of the bed (K)	928.4	1036.5	1072.2	1120.7	1195.2
Aver. temperat. at the top of the freeboard (K)	912.6	1021.0	1059.6	1106.0	1204.0

(a): at the middle of the bed.

XIV Brazilian Congress of Mechanical Engineering
Obeid Plaza Hotel Convention Center - Bauru - SP/Brazil
December 08-12th 1997

PAPER CODE: COB68

SEARCH FOR FAVORABLE CONDITIONS OF PRESSURIZED FLUIDIZED-BED GASIFICATION OF SUGAR-CANE BAGASSE THROUGH COMPREHENSIVE SIMULATION

Marcio L. de Souza-Santos
IPT-Instituto de Pesquisas Tecnológicas de São Paulo e UNICAMP - Universidade Estadual de Campinas
FEM - Faculdade de Engenharia Mecânica, Departamento de Energia
Cidade Universitária Zeferino Vaz, C. Postal 6122, Campinas, SP 13083-970, Brasil
E-mail: souzasan@fem.unicamp.br

Abstract

An updated comprehensive simulator for fluidized-bed equipment has been employed to perform studies aiming the optimization of sugar-cane bagasse gasification. The present work for pressurized systems follows one where the atmospheric option was focused. Improvements on the calculations of physical-chemical properties provided more precise computations for operations at high pressures. Gasification "Cold" efficiency has been chosen as the objective function. For this first round of studies, the operational pressure was fixed at 2 MPa. The basic geometry of the reactor, the particle size distribution of the alumina (used as inert in the bed), and the bagasse dry-basis composition are assumed as constants. Bagasse moisture and the injected air mass flow (or oxygen ratio) are left as variables. Detailed data of the reactor internal as well as overall operational conditions are discussed. The results are going to be used on studies of power generation systems employing gas turbine concepts.

Key Words

Fluidized-bed, gasification, simulation, optimization, biomass

1. INTRODUCTION

The motivation for studies on utilization of sugar-cane bagasse as power source has been described in the companion paper (Souza-Santos, 1997).

The present study follows another where atmospheric gasification has been focused. The results are going to be applied to studies on power generation systems.

2. THE EXISTING PROGRAM

A previous version (Souza-Santos 1989, 94a) of the simulation program has been updated to expand its range of applicability as well as to provide more precise results.

Although the first version of the program was already prepared to face pressurized processing, improvements in computations of physical-chemical properties of gases and their mixtures have been introduced. These corrections employed the Redlich-Kwong-Soave

equations. Among the corrected properties are the Gibbs free energy, used to more precise computations of reaction equilibria (Reid et al. 1977). Therefore, the kinetics of the various involved reaction also benefited from these improvements.

This new version has also been validated for pressurized gasification of wood (Souza-Santos, 1994b). The biggest deviation in computations when dealing with different biomass, is due to differences in the devolatilization profiles. For this first approach, it has been assumed that the bagasse devolatilization stoichiometry is similar to that of the wood. A test of this hypothesis has been made using IGT (Institute of Gas Technology, Illinois, USA) results for pressurized gasification of sugar-cane bagasse. Average deviations between simulation predictions and measured values (concentrations, temperatures, and carbon conversions) are in the same order of magnitude as the obtained for wood gasification. Unfortunately, the results of the work with bagasse cannot be published due to contract conditions under which it was developed. Future developments will concentrate in adding specific correlation for bagasse devolatilization. This may improve the results even further.

3. THE OPTIMIZATION STRATEGY

For the present search, "Cold" efficiency is the proper parameter because the removal of alkaline (by condensation) from the exit gas is normally required.

The definitions of "Hot" and "Cold" efficiencies have already been given in the companion paper (Souza-Santos, 1997)

3.1. Range of Tested Conditions

For the present search some parameters have been left as constants, such as:

- Gasifier nominal operational pressure. This first study assumes the conclusion from Hollanda (1991) which shows that pressures around 2 MPa should be near the optimum for processes aiming power generation. A possible confirmation of this comes from the fact that this range of pressure has been chosen by IGT (Evans et al., 1986) for developments.
- The characteristics of the feeding bagasse (dry basis). The adopted composition (Tables 1 and 2) and properties are well within typical values for this biomass.
- Basic dimensions of the gasifier. The present work is part of a study for future experimental tests in a pilot unit. Therefore, the dimensions such as bed and freeboard internal diameter, total height, distributor design, and cyclone geometry have been assumed as constants. Some of the most important values are described in Table 3.
- Bed depth. The value of 2 m has been selected. Preliminary tests showed that short regions of the bed are left at reducing conditions if beds shallower than that were used. Of course, scarce reducing regions lead to poor gas composition and to relatively low gasification efficiency. Future investigations could refine this choice.
- Bagasse particle size distribution. The distribution is the same as the obtained from mills installed in typical sugar and alcohol plants.
- Bagasse feeding rate. The feeding rates of biomass per unit of reactor cross section used here, are around 1 kg s^{-1} m^{-2}, which is the same range arrived through experimental tests at IGT (Evans et al., 1986). A more detailed study on this parameter will be conducted in the near future.
- Inert characteristics (composition, densities, and particle size distribution). Alumina has been chosen as the inert solid in the bed due to its resistance to attrition and high

temperatures. Differently from the bagasse, which is fed continuously, just a make-up is necessary to compensate for losses due entrainment. Its particle size distribution is such that feasible bubbling operational conditions (without leading to pneumatic transport) were achieved for the complete studied range of air flow injected through the distributor.

- The temperature of the feeding air was set to 650 K, which is around the value obtained after compression of ambient air.
- No steam injection. Preliminary simulations have shown that the moisture contents of the bagasse are enough to provide the needed water as gasification agent.

The parameters adopted as variables are:

1. Bagasse moisture. Although the bagasse usually leaves the mill with 50% moisture, the present work considers the possibility of prior drying employing stack gas streams in the mill or through controlled fermentation. This last technique allows to reach a 20% moisture level (Camargo et al., 1990). Values below 20% have not been included in this study because it seems unlikely that they could be economically obtained. The tested cases included moisture levels of 20%, 30%, 40%, and 50%.
2. Oxygen ratio, which is the ratio between the mass flow of injected air and the mass flow of air necessary for the stoichiometric combustion of the biomass. The tested cases were carried out within the range from 16% to 28%.

It is important to notice that even within those ranges, some combinations do not appear in the results either because operational problems have been predicted or too low efficiencies have been obtained. Among the operational problems there are:

- Relatively high or relatively low average bed temperatures. The first led to collapse of the bed due to the agglomeration of particles that surpassed the ash softening point. The second caused low carbon conversion which led to extremely low gasification efficiencies.
- Unfeasible operation because the superficial gas velocity was too high or too low. The first led to total pneumatic transport of the particles in the bed. The second could not meet minimum fluidization requirements.

4. INPUT DATA

Some of the most important inputs, common to all cases, are presented below.

Table 1: Proximate analysis of bagasse at 20% moisture

Component	Mass % (w.b.)
Moisture	20.000
Volatile	65.249
Fixed-carbon	12.105
Ash	2.646
High Heat Value (MJ/kg) (dry basis)	19.04

Table 2: Ultimate analysis of the feeding bagasse

Comp.	Mass % (d.b.)
C	49.66
H	5,71
O	41.08
N	0,21
S	0,03
Ash	3.31

More details on the required data as well as information provided by of the present simulation program can be found in Souza-Santos (1989, 94a, 94b) and in the companion paper.

Table 3: Data on basic geometry of gasifier and operation

Characteristics	Value
Internal diameter in the bed section	0.5 m
Bed height	2.0 m
Internal diameter in the freeb. section	1.0 m
Total equipment height	7.0 m
Bagasse feeding position (from bed base)	0.5 m

To maintain equivalence between different conditions, the feeding rate of dry bagasse was kept constant. Therefore, the values of 0.2000 kg/s, 0.22857 kg/s, 0.26667 kg/s, and 0.32000 kg/s where used for 20%, 30%, 40% and 50% moisture, respectively. The mass of bagasse initially put into the bed was 800 kg.

5. DISCUSSION OF RESULTS

Table 4 presents several operational data for the most favorable range of oxygen ratio, i.e., 24%. The gas composition obtained from that test is reproduced in Table 5.

Figures 1 and 2 summarize the results for the efficiencies (Hot and Cold).

As can be seen in Fig. 1, the maximum "Cold" efficiencies occur for the lowest tested moisture (20%). The maximum value was obtained in the vicinity of 24% oxygen ratio and this is valid for the entire range of bagasse moistures.

Figure 2 shows that "Hot" efficiency increases with the oxygen ratio and no maximum was obtained for values within the tested range. As said before, it was not possible to report higher oxygen ratios because ash-softening temperatures were reached for values with relatively low moisture of the bagasse.

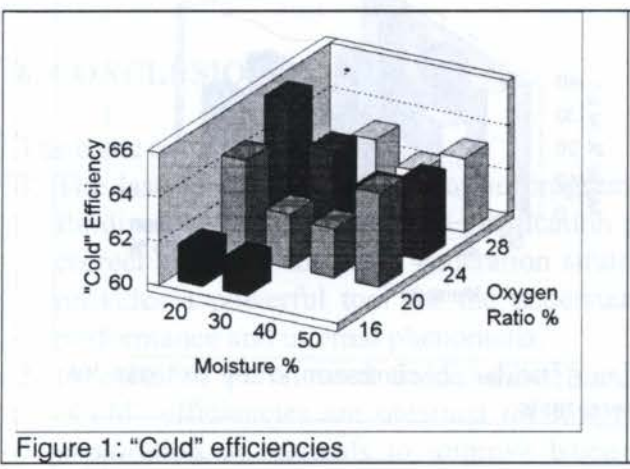

Figure 1: "Cold" efficiencies

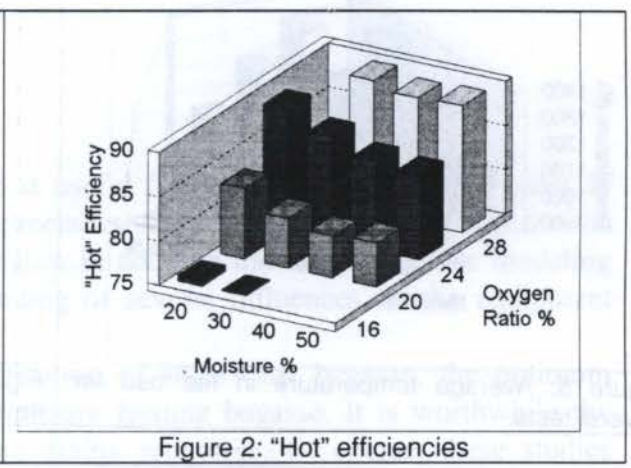

Figure 2: "Hot" efficiencies

Back to Fig. 1, it is interesting to notice a "valley" shape with lowest values for moistures around 40%. This can be explained on the basis of conflicting tendencies:

1. The increase on heat value of the exit gas due to higher concentrations of fuel gases, particularly hydrogen (Fig. 3).
2. The decrease in the carbon conversion due to lower average temperatures (Figs. 4 and 5).

The rate of Carbon-Water reaction increases with higher concentration of water in the system (Fig. 6) brought with wetter bagasse. To a certain degree, the increase in hydrogen concentration overcompensates the relative decrease on carbon monoxide (Fig. 7) and methane (Fig. 8). On the other hand, due to highly endothermic carbon-water reaction, high-moisture operations decrease the average temperature in the bed. Lower temperatures lead to a decrease in the rate of carbon-water reaction as well as the other reactions. From the point of

view of oxygen ratios, lower values allow relatively high hydrogen concentrations because hydrogen combustion rates are much faster than the rates for other fuel gases.

In the whole range of cases, no segregation of bagasse has been verified, i.e., all mixing indexes were above 0.5.

For the best case (20% moisture and 24% oxygen ratio) Figs. 9 to 12 are presented. In Fig. 9 the decrease of temperature near 0.5 m is due to bagasse feeding. For the same case, Fig. 10 shows some concentration profiles in the bubble phase and it is possible to verify that the oxygen was completely consumed at 0.5 m from the distributor.

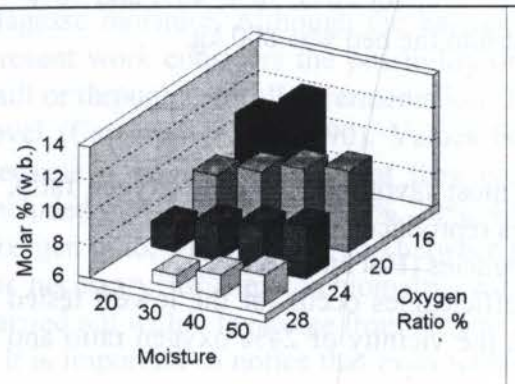

Figure 3: Hydrogen concentration in the exit gas for several tests.

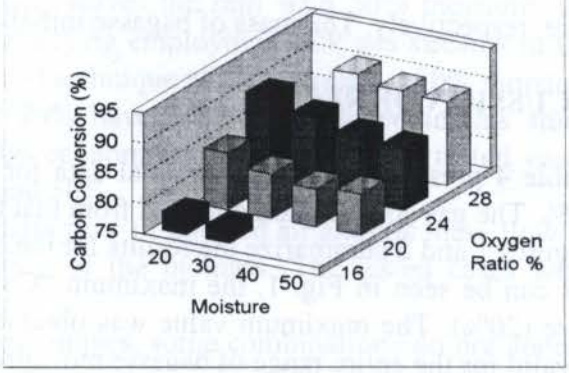

Figure 4: Carbon conversion for several tests

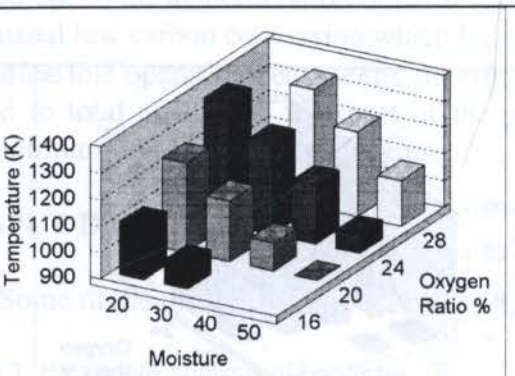

Figure 5: Average temperature in the bed for several tests.

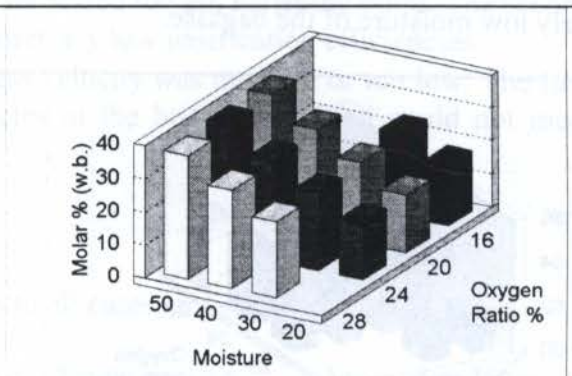

Figure 6: Water concentration in the exit gas for several tests.

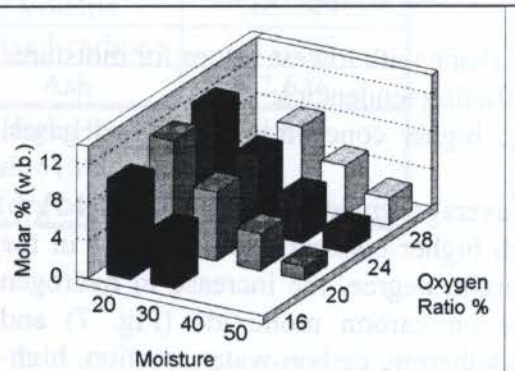

Figure 7: Carbon Monoxide concentration in the exit gas for various tests.

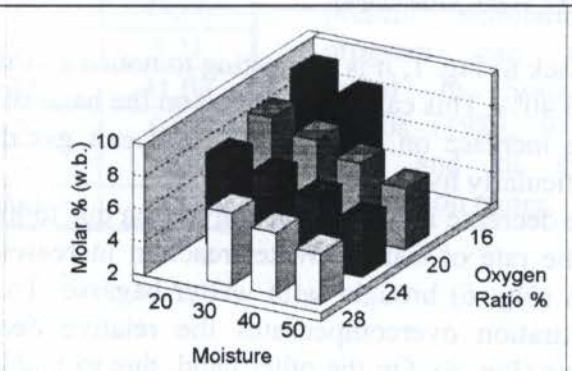

Figure 8: Methane concentration in the exit gas for various tests.

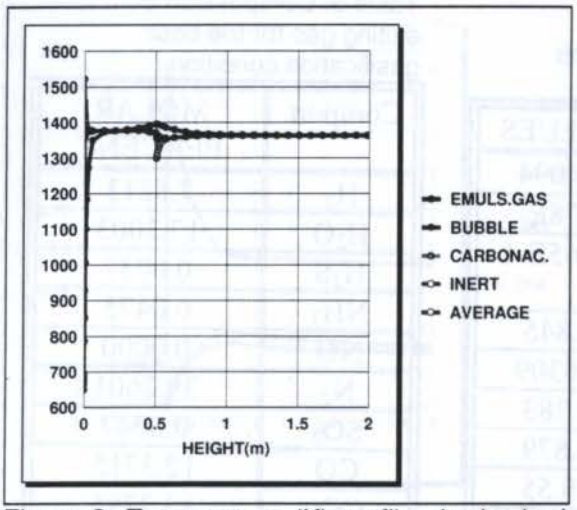

Figure 9: Temperature (K) profiles in the bed for the best case.

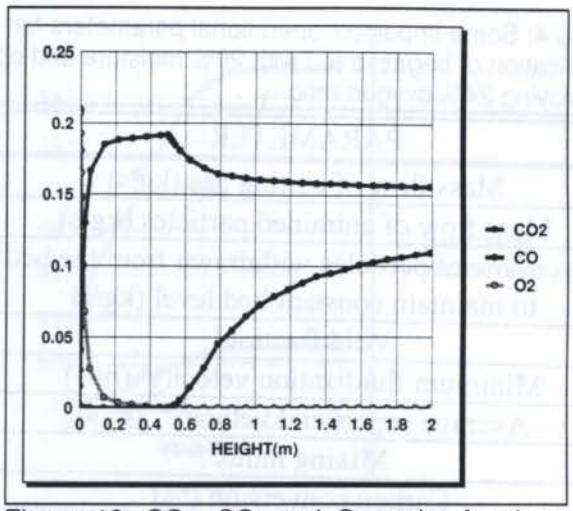

Figure 10: CO_2, CO, and O_2 molar fractions (w.b.) profiles in the bubble phase for the best case.

The surge of water concentration in the emulsion is due to the release of moisture from the bagasse which is being fed at 0.5 m from the bed base (Fig. 11). After that, water is consumed mainly by reaction with carbon.

It is interesting to notice that the bubble maximum stable diameter is smaller than the bed internal diameter (Fig. 12). This agrees with the comments made in the companion paper concerning methods of avoiding slugging-flow.

6. CONCLUSIONS

The basic conclusions are:

1. The last version of the simulation program is useful for detailed optimization studies of fluidized-bed combustion and gasification processes. These studies are important for the correct approach to power generation strategies. In addition the comprehensive modeling provides a powerful tool for the understanding of several influences on the equipment performance and internal phenomena.
2. In cases of pressurized fluidized-bed gasification of sugar-cane bagasse, the optimum "Cold" efficiencies are obtained for low moisture feeding bagasse. It is worthwhile the exploration of methods to improve bagasse drying processes. Of course, these studies should be combined with economic considerations. Regarding the oxygen ratio, the maxima of "Cold" efficiencies are in the neighborhood of 24%. This was around the same condition found for the atmospheric gasification, with conditions described in the companion paper. Refinement of the grid, as well as inclusion of other parameters as variables, will be tried in a near future work.
3. When the gas-utilization process employs cold gas and the pre-drying of bagasse do not reach values below 30%, it is preferable to feed the gasifier with bagasse as produced by the mill, i.e., with 50% moisture.

Table 4: Some important operational parameters for gasification of bagasse fed with 20% moisture and operations employing 24% oxygen ratio.

PARAMETER	VALUES
Mass flow of exiting gas (kg/s)	0.4094
Mass flow of entrained particles (kg/s)	0.278E-5
Mass flow of particles withdrawn from the bed to maintain constant bed level (kg/s)	0.165E-1
Void fraction[a]	0.845
Minimum fluidization velocity[a] (m/s)	0.0309
Average superficial velocity[a] (m/s)	0.383
Mixing index	0.879
Carbon conversion (%)	89.55
Mass held by the bed (kg)	508
Residence time (based of the mass flow of feeding solid) (min)	42
Transport Disengaging Height (m)	5.726
Static bed height (m)	1.130
Total input power to the gasifier (MW)	3.058
Pressure loss in the distributor (kPa)	0.010
Pressure loss in the bed (kPa)	13.56
Average molecular mass of the exiting gas (kg/kmol)	26.01
Volumetric flow of the exiting gas (m^3/s) (standard conditions: 273.15K, 1bar)	0.353
Mass concentration of tar in the gas leaving the bed and entering the freeboard (%)	0.000
Enthalpy of exiting gas ("hot, wet") (MJ/kg)	6.6300
Enthalpy the exiting gas ("cold, dry") (MJ/kg)	5.5909
"Hot" efficiency	**88.78**
"Cold" efficiency	**65.89**
Average bubble diameter at the distributor (m)	0.15E-2
Aver. bubble diameter at the middle of bed (m)	0.246
Average bubble diameter at the top of bed (m)	0.276
Temperature of carbonaceous particles[a] (K)	1362.9
Temperature of inert particles[a] (K)	1362.9
Emulsion gas temperature in the bed[a] (K)	1362.9
Bubble phase temperature[a] (K)	1366.0
Aver. temperature at the middle of the bed (K)	1362.9
Average temperature at the top of the bed (K)	1362.8
Aver. temperat. at the top of the freeboard (K)	1315.1

(a): at the middle of the bed.

Table 5: Composition of exiting gas for the best gasification condition.

Compon.	MOLAR PERCENT
H_2	7.5813
H_2O	17.3003
H_2S	0.0037
NH_3	0.0475
NO	0.0000
N_2	39.2601
SO_2	0.0047
CO	12.3715
CO_2	15.2795
CH_4	7.5684
C_2H_4	0.0303
C_2H_6	0.2421
C_3H_6	0.0000
C_3H_8	0.0000
C_6H_6	0.3107
Tar	0.0000

4. Regarding the equipment operation, it is important to notice the following. The biomass feeding position is an important parameter. Most of the carbonaceous solids go through fast drying and devolatilization near the feeding point. This last process yields important fuel gases. If these gases find an oxidant atmosphere they burn with low or no addition of fuel gases to the upward gas stream. On the other hand, if the feeding occurs too near the top of the bed, the produced tar may escape to the freeboard without enough residence time for cracking and coking. The tar, even in small concentration, causes severe problems for the gas cleaning system.

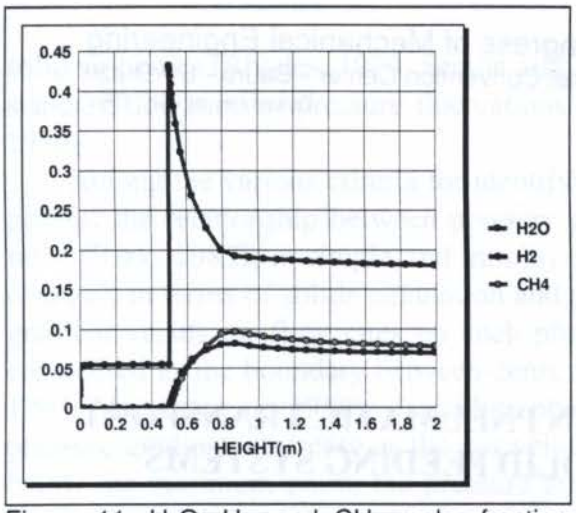

Figure 11: H_2O, H_2, and CH_4 molar fraction profiles (w.b.) in the emulsion for the best case.

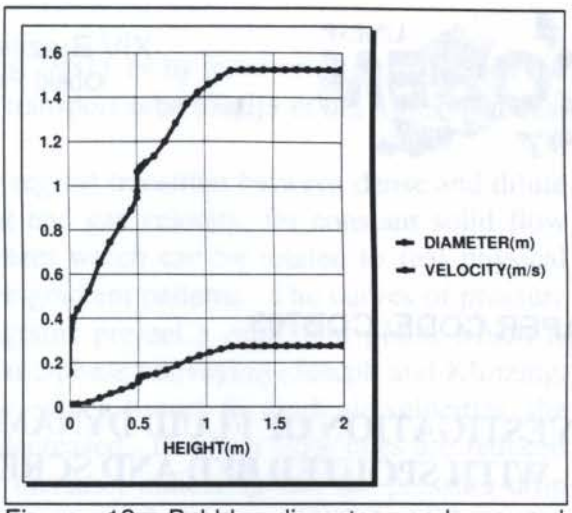

Figure 12: Bubble diameter and upward velocity for the best case.

7. REFERENCES

CAMARGO, A. C., USHIMA, A. H., RIBEIRO, A. M. M., SOUZA, M. E. P. & SANTOS, N. F. *Energy Conservation in the Sugar and Alcohol Industry* (in Portuguese), IPT- Technical Research Institute, São Paulo, Brazil, pp. 730, 1990.

EVANS, R. J., KNIGHT, R. A., ONISCHAK, M. & BABU, S. P. Process and Environmental Assessment of the Renugas® Process, *Symposium on Energy from Biomass and Wastes X*, Institute of Gas Technology, Washington, D.C., USA, April 6-10, 1986.

HOLLANDA, J. B. (coordinator), *Optimization of Electrical Energy Production in Sugar-Alcohol Mills* (in Portuguese), Eletrobrás, Copersucar, BNDES, CESP, CPFL, Eletropaulo, 1991.

REID, C. R., PRAUSNITZ, J. M., SHERWOOD, T. K. *The Properties of Gases and Liquids*, 3rd. ed., McGraw-Hill, N. Y., pp. 629-675, 1977.

SOUZA-SANTOS, M. L., Comprehensive Modelling and Simulation of Fluidized Bed Boilers and Gasifiers, *Fuel*, **68**, pp. 1507-1521, 1989.

SOUZA-SANTOS, M. L. Application of Comprehensive Simulation to Pressurized Fluidized Bed Hydroretorting of Shale, *Fuel*, **73**, pp. 1459-1465, 1994(a)

SOUZA-SANTOS, M. L. Application of Comprehensive Simulation of Fluidized-Bed Reactors to the Pressurized Gasification of Biomass, *J. of the Braz. Soc. of Mechanical Sciences*, **XVI**, No. 4, pp. 376-383, 1994(b).

SOUZA-SANTOS, M. L. Search for Favorable Conditions of Atmospheric Fluidized-Bed Gasification of Sugar-Cane Bagasse Through Comprehensive Simulation. Paper submitted to the *14th Brazilian Congress of Mechanical Sciences*, Bauru, São Paulo, 7-9 December 1997.

XIV Brazilian Congress of Mechanical Engineering
Obeid Plaza Hotel Convention Center - Bauru - SP/Brazil
December 08-12th 1997

PAPER CODE: COB703

INVESTIGATION OF FLUID DYNAMICS IN PNEUMATIC TRANSPORT WITH SPOUTED BED AND SCREW SOLID FEEDING SYSTEMS

Élcio M. V. Silva, Maria do Carmo Ferreira & José Teixeira Freire
Departamento de Engenharia Química, Universidade Federal de São Carlos
C.P. 676 –CEP 13.569-265 - São Carlos - SP – Brazil- E-mail: mariaf@power.ufscar.br

Abstract

The use of a spouted bed for feeding solids in a pneumatic transport tube allows for a wide range of operational conditions. However, as the solid flow rates become dependent on the air flow rates, the flow diagrams available in literature for flow regime identification cannot be applied for such a equipment. In present work, fluid dynamic characterization of pneumatic transport with a spouted bed type solid feeding system has been extended by comparing its fluid dynamic behavior with the one provided by using a classical feeder, which allowed for independent variation of gas and solid flow rates. Experimental data of pressure gradients versus air velocities have been obtained using the same transport pipe (4.0 m long and 104.8 mm in diameter) and using both a spouted bed and a screw conveyor as solid feeding devices. Experimental values of the air velocities at the transition from dilute to dense-phase regimes have been obtained for both systems. The data obtained using the screw feeder have been compared with data from literature. Also investigated was the validity of using the correlations for predicting the transition air velocities developed for classical feeders for the data obtained using the spouted bed feeder. The results allow the conclusion that the transition point can be predicted using the same criterion for both systems.

Keywords

Pneumatic transport, solid feeding systems, flow regime identification.

1. INTRODUCTION

The pneumatic bed with a spouted bed type solid feeding system has been investigated by authors such as Ferreira and Freire (1992), Littman *et al.* (1993) and Garic *et al.* (1995). This system allows for a wide range of operational conditions, but it makes fluid dynamic characterization more difficult, particularly the identification of flow regime. This is because the solid flow rates become dependent on the air flow rates. It is well known that the identification of flow regimes, as well as of their transitions, is essential for better design and operation of vertical transport lines, and also for its fluid dynamics modeling, since the flow structure governs the various transfer mechanisms between the two-phase mixtures. The dilute and dense phase conveying represent the two main flow regimes on gas-solid transport, but different sub-regimes can be identified, as discussed by Satija *et al.* (1985) and Chong and Leung (1986). Selection of the proper gas velocity determines the flow regime of solids conveying, with the dilute transport being the most common (Arastoopour, 1985). A complete identification of flow regimes usually involves extensive experimental measurements. This can be done, for instance, by using suction probes or laser techniques for measuring radial

solid velocities (Rhodes, 1990, Semiat and Dukcler, 1981), or by monitoring variations in the standard deviation of pressure fluctuations in the transport tube (Satija *et al.*, 1985; Rhodes, 1996).

Among the various criteria for identifying the regime transition between dense and dilute phases, the relationship between pressure gradient and gas velocity, for constant solid flow rates (Rizk, 1985), is simple and employ parameters which can be related to real physical changes, in terms of solids circulation and pressure gradient patterns. The curves of pressure gradient versus air flow rates on such phase diagrams present a minimum point, which is considered as the boundary between dense and dilute-phase conveying (Joseph and Klinzing, 1983; Marcus *et al.*, 1990). On dilute-phase flow, which occurs for high air velocities, the pressure gradients decrease as the gas velocity is decreased. If the air flow rates are reduced below the minimum point, the pressure gradients increase, indicating that the pressure drop due to the solids hold-up predominate. So the minimum air flow rates at which solids can be conveyed in the dilute phase regime is set by the air velocity at the minimum pressure drop in the state diagram, which will be referred to as the minimum velocity. Hong *et al.* (1995) reported that the locations of the minima in this phase diagram should change depending on the particle diameter, transport pipe diameter and solid flow rates, so the determination of the minimum under different conditions is complicated. It is nevertheless important because the best operation point for dilute vertical pneumatic transport should be carried out at air velocities slightly above the minimum velocity (Arastoopour, 1985).

Despite their simplicity, such phase diagrams cannot be applied directly for the pneumatic bed with a spouted bed feeding system, since the solid flow rates can not be maintained constant while the air flow rates are varied (Ferreira and Freire, 1992; Littman *et al.*, 1993; Garic *et al.*, 1995). Until now, very few experimental data have been reported aiming at the investigation of flow transitions for the pneumatic bed with a spouted bed feeder. In their former work, Ferreira and Freire (1992) reported the existence of different flow regimes in this bed, namely a slug flow (usually associated with dense-phase conveying) and a typical dilute transport. However, their analysis was only qualitative and their results did not allow for any specific conclusions about the flow transitions to be reached. Garic *et al.* (1995) employed the method proposed by Satija *et al.* (1995) for regime identification in a bed similar to that of Ferreira and Freire (1992). They identified a dilute phase flow, and two types of slug flow—one of which was stable while the other was unstable. This unstable slug flow occurred for low air flow rates, next to the transport collapse point. Such a regime map, however, could not be extended for the results obtained in the present work, probably because the bed used by Garic *et al.* (1993) operates semi-continuously and the transport is carried out in a plexiglass transport tube, resulting in flow conditions very different from those obtained here. The solid feeding system may also affect the fluid dynamic behavior of flow (Arastoopour, 1985), but no experimental work have been reported comparing the spouted bed feeder to different ones.

The purpose of this work is to extend the fluid dynamics characterization of pneumatic transport with a spouted bed type solid feeding system by comparing its fluid dynamics behavior with the one provided by using a classical solid feeding system, which allowed for independent variation of gas and solid flow rates. For that, experimental fluid dynamic data have been obtained using the same pneumatic transport tube, with both a spouted bed and a screw conveyor as solid feeding devices. Experimental values of the minimum air velocities for both systems have been obtained and the data for the screw conveyor have been compared with data from the literature. Also investigated was the validity of using pressure gradient versus air velocity phase diagrams for the pneumatic bed with spouted bed type solid feeding system.

2. EXPERIMENTAL METHODOLOGY

The same transport pipe and measuring systems were used for all experiments, but two types of solid feeding systems have been employed, the spouted bed and a screw feeder. The pneumatic bed with the spouted bed type feeder is shown in Figure 1(a). Spherical glass particles with ρ_p=2503 kg/m^3 and mean diameters of 1.00 and 2.05 mm, belonging to group D on Geldart's (1973) classification, were transported in a galvanized iron pipe, 4.0 m long and with internal diameter equal to 104.8 mm. Air to the system was supplied by a 20 HP fan and its volumetric flow rate was measured by means of an orifice plate flowmeter. After being pneumatically transported (1), the particles returned through a standpipe (2) with diameter equal to 104.8 mm. A reduction nozzle was placed at the air inlet, aiming at reducing both the gas flow rates deviated through the standpipe and the length of the acceleration region on the transport pipe (Silva *et al.*, 1996). The solids flow rates were measured by diverting the flow and collecting the solids in the sample collector (3). The static pressures along the pipe were measured at seven points by pressure taps connected to U-type manometers. While in operation, the standpipe was kept filled with solids and the gas flow rates through it were estimated from the Forchheimer equation, with the pressure drop measured between two points of the pipe. The gas flow rates in the transport pipe are then obtained from a mass balance which considered the difference between the air supplied by the fan and the air deviated through the standpipe, which in most cases was negligible. The distance between the air inlet and the bottom end of the transport tube (z_0) is a parameter for controlling the solid flow rates and could be changed by a set of flanges of different thicknesses placed in the transport tube. The mean voidages at the transport pipe were measured by means of two pneumatically operated traps (4) which closed off a 2.05 m long section of the pipe. The solids accumulated on the bottom trap were collected by a suction pump and subsequently weighted, providing the average voidage. The accuracy of voidage measurements was estimated using a statistical quality control procedure (Montgomery, 1991) as being ±0.15%. The length of the acceleration region was obtained from experimental data, by plotting the pressures versus axial distances of transport tube and taking the linear portion of the curves. For all the conditions investigated, this length was found to be less than 2.1 m, and the bottom slip valve was placed above such a distance. A glass section was placed at the top end of the transport tube for visual observation of the flow. The air velocity was initially fixed at a maximum value, and the fluid dynamics measurements were carried out. After that, the gas velocity was slowly decreased and the experimental procedure repeated, until reaching a condition for which the transport was ceased.

The replacement of the spouted bed feeding system by a screw feeder was performed by eliminating the bottom reservoir (5) and changing the standpipe configuration, resulting in the apparatus shown in Figure 1(b). All measuring systems are the same described above. The solid flow pattern is also essentially the same, except that the solids are now returned to the screw conveyor. Additional data, similar to those previously described, were obtained for this feeding system. The air velocity was initially fixed at a maximum value and the solid flow rates were varied by changing the screw rotating velocity (maximum solid flow rates were limited by construction of the feeder). The air velocity was subsequently reduced and the experimental procedure repeated until reaching the minimum value for transport. An additional glass section was placed just above the solids feeding point, for visual observations of the flow at the bottom end of transport pipe.

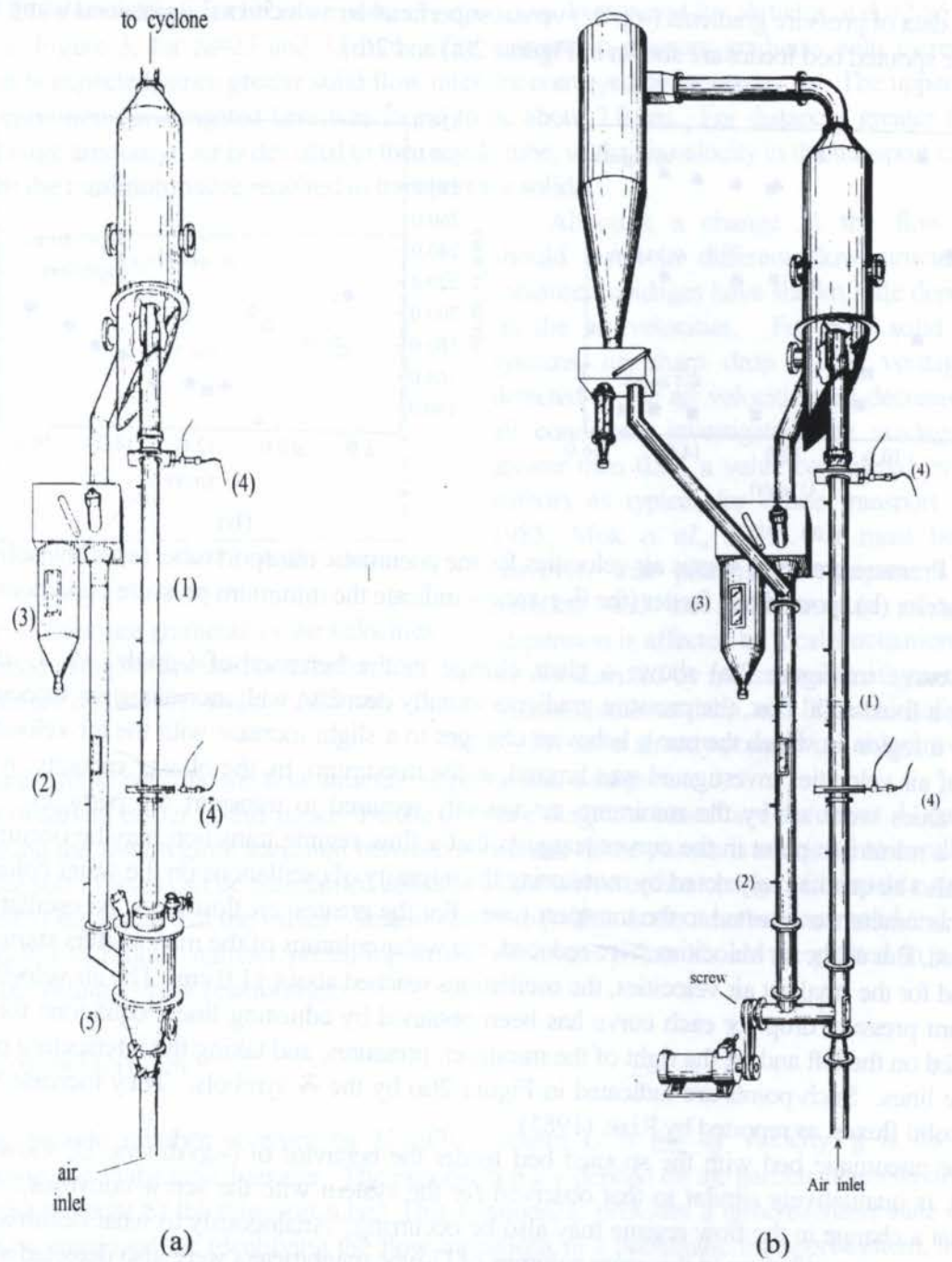

Figure 1 - Experimental apparatus; (a) system with the spouted bed feeder; (b) system with the screw feeder. (1) transport tube, (2) recycle, (3) solids sampler, (4) pneumatic trap valves, (5) bottom reservoir in the spouted bed feeder.

In all experiments, the transport pipe was grounded in order to eliminate electrostatic effects. The range of experimental conditions investigated and accuracy for the measurements are shown in Table 1.

Table 1: Range of operational conditions

	Spouted bed feeder	Screw feeder	Accuracy (%)
d_p (mm)	1.00; 2.05	1.00	-
w_f (kg/s)	0.080-0.155	0.082-0.136	2.5
w_p (kg/s)	0.207-1.39	0.363-0.796	6.0
-dp/dz(Pa/m)	154-514	153-305	7.0

3. RESULTS

Typical data of pressure gradients (-dp/dz) versus superficial air velocities (U) obtained using the screw and the spouted bed feeder are shown in Figures 2(a) and 2(b).

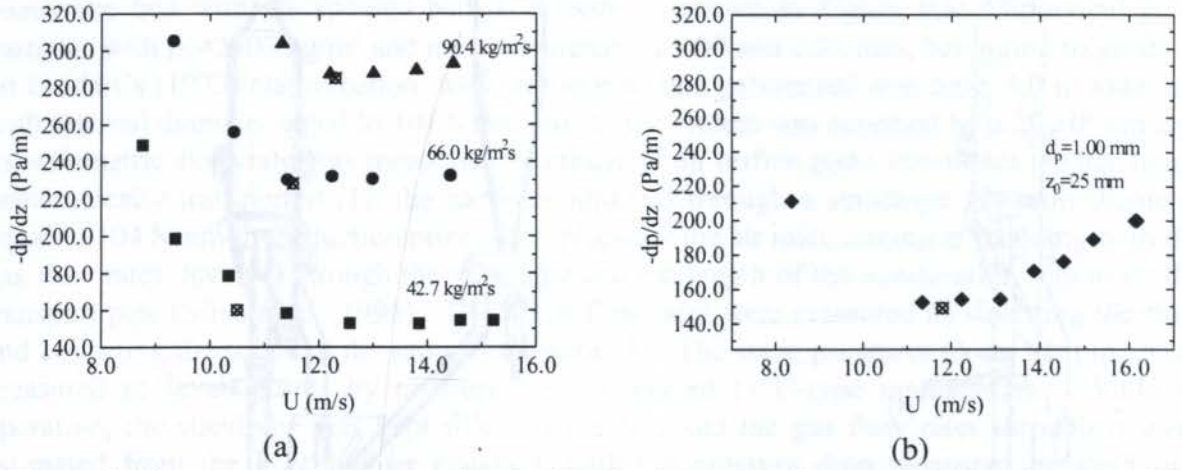

Figure 2 - Pressure gradients versus air velocities for the pneumatic transport tube; (a) screw solid feeding system; (b) spouted bed feeder (the ✇ symbols indicate the minimum pressure conditions).

Every curve in Figure 2(a) shows a clear change in the behavior of (-dp/dz) vs. U data. Considering a fixed solid flux, the pressure gradients initially decrease with increasing air velocities, followed by a region in which the curve behavior changes to a slight increase with the air velocities. The range of air velocities investigated was limited, at the maximum, by the blower capacity, while the lower values were set by the minimum air velocity required to transport the particles. The presence of a minimum point in the curves suggests that a flow regime transition may be occurring. This could also be qualitatively noted by monitoring the intensity of oscillations on the water columns of U-type manometers connected to the transport tube. For the greatest air flow rates, no oscillations were detected. But as the air velocities were reduced, the water columns of the manometers started to increase, and for the smallest air velocities, the oscillations reached about ±1.0 cm. The air velocity at the minimum pressure drop for each curve has been obtained by adjusting linear equations for the points located on the left and on the right of the minimum pressures, and taking the intersecting point between the lines. Such points are indicated in Figure 2(a) by the ✇ symbols. They increase with increasing solid fluxes, as reported by Rizk. (1985).

For the pneumatic bed with the spouted bed feeder the behavior of (-dp/dz) vs. U, shown in Figure 2(b), is qualitatively similar to that observed for the system with the screw conveyor. This indicates that a change in the flow regime may also be occurring. Analogously to what occurred for the screw conveyor, oscillations in the water columns of U-type manometers were also detected as the gas velocity was reduced. It must be noted, however, that in this case the solid fluxes are not constant. Hence the curves of Figures 2(a) and (b) are not equivalent, since the data shown in Figure 2(b) have distance z_0 as a constant parameter, instead of solid fluxes. For the range of air velocities investigated with z_0=25 mm, the solid fluxes varied from 24.0 to 49.4 kg/m^{2}s. Additional data have been obtained with this particle diameter at different z_0 distances, but due to a limitation in the blower capacity, the data were restricted to narrow ranges of air velocities. The minimum point in pressure drop could not be detected, although the dependence on z_0 was reproducible. It is interesting to observe that the solid flow rates conveyed increase as z_0 is increased. Solid fluxes up to 160.7 kg/m^{2}s have been obtained (for z_0=55 mm, d_p=1.00 mm and U=13.6 m/s), demonstrating that this system really provides greater flexibility for operational conditions in pneumatic transport if compared to the screw feeder The

distance z_0 can be described as a non-mechanical valve and clearly represents a parameter for controlling the solid flow rates, as already shown by Ferreira and Freire (1992) and Littman *et. al.* (1993). For illustrating such behavior, data of (-dp/dz) vs. U obtained for particles of d_p=2.05 mm are shown in Figure 3, for z_0=25 and 35 mm. The increase in pressure gradients with increasing z_0 distances is expected, since greater solid flow rates are conveyed by increasing z_0. The upper z_0 limit for the conditions investigated here was found to be about 7.0 cm. For distances greater than this value, a large amount of air is deviated to the recycle tube, so the air velocity in the transport tube does not reach the minimum value required to transport the solids.

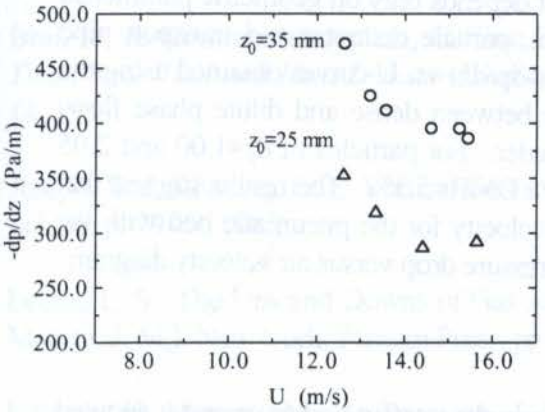

Figure 3 - Pressure gradients vs. air velocities obtained using the spouted bed feeder, for different z_0 distances and d_p=2.05 mm.

Although a change in the flow regime should result in different flow structures, the measured voidages have shown little dependence on the air velocities. For both solid feeding systems, no sharp drop in the voidages was detected as the air velocities are decreased. For all conditions investigated, the voidages were greater than 0.97, a value considered by several authors as typical for dilute transport (Leung, 1985; Mok *et al.*, 1989). It must be noted, however, that pneumatic transport is highly turbulent and the flow structure of gas-solid suspension is affected by local fluctuations which are not detected by measurement of mean values. Authors such as Ishii and Kocamustafaogullari (1983) have already pointed out that this is not a good parameter to describe the flow structure in pneumatic transport.

As observed earlier in this paper, the use of phase diagrams based on (-dp/dz) vs. U curves for determining the flow regime transition between dense and dilute phases is restricted to conditions in which the solid fluxes can be maintained constant as the air velocities change. For such a condition, Rizk (1985) suggested that the values of mass load ratio (which is the ratio between solid and air flow rates, w_p/w_f) vs.Froude number prevailing at the minimum points should be plotted in a log-log format, providing a linear relationship:

$$w_p/w_f = \left(1/10^{\delta}\right) Fr^{\chi} \qquad (1)$$

The Froude number is given by $U/(gD)^{0.5}$, where U is the air velocity, g is the gravity acceleration and D the tube diameter. The exponents δ e χ depend on the particle diameter and shape and on the material of the transport tube. This relationship provides a dimensionless state diagram that can be employed for identifying the flow transitions in a pneumatic transport system, since the Froude number for experimental conditions can be compared to those obtained for the minimum pressure conditions. The coefficients δ e χ can be obtained from empirical expressions proposed by Rizk (1985):

$$\delta = 1.44\, d_P + 1.96 \qquad (2)$$

$$\chi = 1.1\, d_p + 2.5 \qquad (3)$$

The comparison of experimental and predicted minimum air velocities was carried out by estimating the root-mean-square relative deviation (DMR), defined as:

$$DMR = \sqrt{\frac{1}{n}\sum_{i=1}^{n}\left(\frac{U_{exp\,i} - U_{cal\,i}}{U_{exp\,i}}\right)^2} \times 100 \qquad (4)$$

Initially, the experimental minimum velocities obtained using the screw feeder were compared with values predicted using Equation (1). The aim was to verify if the results were consistent with literature data for similar feeders. An excellent adjustment was obtained for the particles investigated with DMR=14.8 %. Equation (1) provides a relationship that depends only on geometric parameters and operational conditions, such as air and solid flow rates, particle diameter and transport pipe diameter. Considering that the minimum points observed in (-dp/dz) vs. U curves obtained using the spouted bed feeder might also represent the flow transition between dense and dilute phase flow, Equation (1) was applied for the data obtained using this feeder. For particles of d_p=1.00 and 2.05 mm, this equation predicted the minimum air velocities with a DMR=5.3%. The results suggest that this criterion can be employed for predicting the minimum velocity for the pneumatic bed with the spouted bed feeder, even though the solid fluxes vary in the pressure drop versus air velocity diagram.

4. CONCLUSIONS

The use of two interchangeable solid feeding devices (namely a screw conveyor and a spouted bed), in a pneumatic transport tube allowed a comparison between fluid dynamic behavior provided by the spouted bed feeder and the data reported in the literature for classical devices. The results obtained using the screw conveyor are consistent with literature data for similar systems. The criterion suggested by Rizk (1985) for identifying the air velocity at minimum pressure drop conditions provided very good predictions for the conditions investigated. For the pneumatic bed with spouted bed feeder, the results show that, transition points between dense and dilute phase transport can be predicted using the same criterion. This occurs in spite of the fact that solid fluxes do not remain constant as the air flow rates are changed. The results allow the conditions of dilute-phase flow to be identified by only knowing the operational conditions and geometric parameters.

Concerning the performance of the two feeding systems investigated, the spouted bed is more flexible than the screw feeder, since for similar air velocities, a wider range of solid fluxes can be obtained only by changing the z_0 distances. Besides, the variation of z_0 acts as a non-mechanical valve and, as it does not have mechanical parts, it is expected to operate well for several particle diameters, while the range of particle diameters for the screw feeder is limited because of building features.

5. ACKNOWLEDGEMENTS

The authors thank CNPq, PRONEX and FAPESP (proc. n°. 1997/2256-8) for the financial assistance given to this work.

6. REFERENCES

Arastoopour, H. Pneumatic Transport of Solids, *Encyclopedia of Fluid Mechanics*, (ed. Cheremisinoff), N. P., Gulf Publishing Company, Houston, Texas, vol. 1, pp.349-382, 1986.

Chong, Y. O. & Leung, L. S. Comparison of Choking Velocity Correlations in Vertical Pneumatic Conveying, *Powder Technol.*, vol. 47, pp. 43-50, 1986.

Ferreira, M. C. & Freire, J. T. Fluid Dynamics Characterization of a Pneumatic Bed with a Spouted Bed Type Solid Feeding System, *Can. J. Chem. Eng.*, vol. 70, pp. 905-909, 1992.

Garic, R.; Grbavcic, Z.; Vukovic, D. V.; Hadzismajlovic, Dz. E. & Littman, H. Hydrodynamic Modeling of Vertical Non-Accelerating Gas Solids Flow, *Powder Technol.*, vol. 84, pp. 65-74, 1995.

Geldart, D. Types of Gas Fluidization, *Powder Technol.*, vol. 7, pp. 285-292, 1973.

Hong, J.; Shen, Y. & Tomita, Y. Phase Diagrams in Dense Phase Pneumatic Transport, *Powder Technol.*, vol. 84, pp. 213-219, 1995.

Ishii, M. & Kocamustafaogullari, G. Two Phase Flow Models and Their Limitations, *Advances in Two Phase Flow and Heat Transfer-Fundamentals and Applications*, vol. 1, M. Nijhoff Pub., pp. 1-14, 1983.

Joseph, S. & Klinzing, G. E. Vertical Gas-solid Transition Flow with Eletrostatics, *Powder Technol.*, vol. 36, p. 79-87, 1983.

Leung, L. S. The Ups and Downs of Gas-solid Flow-A Review. In: *Fluidization*, (eds: Grace, J. R.; Matsen, J. M.). New York, Plenum Press, pp. 25-68, 1989.

Littman, H; Morgan, M. H.; Paccione, J. D.; Jovanovic, S. Dj; Grbavcic, Z. B. Modeling and Measurement of the Effective Drag Coefficient ..., *Powder Technol,* vol. 77, pp. 267-283, 1993.

Marcus, R. D.; Leung, L. S.; Klinzing, G. E. & Risk, F. *Pneumatic Conveying of Solids: A Theoretical and Practical Approach*, St. Edmundsbury Press, Great Britain, 1990.

Mok, C. L.; Molodtsof, Y.; Large, J.-F. & Bergougnou, M. A. Characterization of Dilute and Dense Phase Vertical Upflow Gas-Solid Transport Based on Average Concentration and Velocity Data, *Can. J. Chem. Eng.*, vol. 67, pp. 10-16, 1989.

Montgomery, D. C. *Introduction to Statistical Quality Control*, John Wiley & Sons Inc., 1991.

Rhodes, M. J. Modeling the Flow Structure of Upward-flowing Gas-solids Suspensions. *Powder Technology*, v. 60, p. 27-38, 1990.

Rhodes, M. What is Turbulent Fluidization?, *Powder Technol.*, vol. 88, pp. 3-14, 1996.

Rizk, F. Principles of Pneumatic Conveying, *Encyclopedia of Fluid Mechanics*, (ed. Cheremisinoff, N. P.), Gulf Publishing Company, Houston, Texas, vol. 1, pp.311-348, 1985.

Satija, S.; Young, J. B. & Fan, L-S. Pressure Fluctuations and Choking Criterions for Vertical Pneumatic Conveying of Fine Particles, *Powder Technol.*, vol. 43, pp. 257-271, 1985.

Semiat, R. & Duckler, A. E. Simultaneous Measurements of Size and Velocity of Bubbles or Drops: a New Optical Technique, *AIChE Journal*, vol. 27, p. 148-159, 1981.

Silva, E.M.V., Ferreira, M. C. & Freire, J. T. Análise da Influência do Bocal de Entrada no Comportamento Fluidodinâmico do Leito Pneumático com Alimentador Tipo Jorro. *J. of the Braz. Soc. Mechanical Sciences*, vol.18, pp. 67-73, 1996.

XIV Brazilian Congress of Mechanical Engineering
Obeid Plaza Hotel Convention Center - Bauru - SP/Brazil
December 08-12th 1997

PAPER CODE: COB71

ANALYSIS OF SCALE REDUCTION EFFECTS IN ANNULAR SOLID-LIQUID FLOWS

ANDRÉ LEIBSOHN MARTINS & FELIPE SANTOS LIPORACE
PETROBRAS / CENPES / DIPLOT - Ilha do Fundão Q.7 - Cidade Universitária
CEP 21949-900 Rio de Janeiro, Brasil - E-mail: Aleibsohn@cenpes.petrobras.com.br

Abstract

This paper presents and discusses results of solids transport experiments run in two different flow loops (5 in OD x 4 in ID and 8 in OD x 7.5 in ID external pipes), built in PETROBRAS Research Center and University of Tulsa, respectively. The tests represent the annular stratified flow of solid - non Newtonian fluid mixtures for different operational parameters, such as: fluid and solid properties, annular eccentricity and inclination and fluid flow rate. Based on the experimental data, several recommendations are drawn about the usefulness of running reduced scale solid-liquid flow experiments and its applicability to real oilwell drilling operations.

Keywords

Petroleum Engineering, Drilling, Dimensional Analysis, Similarity Theory, Pilot Plants.

1. INTRODUCTION

Scaling down is a common technique for the analysis of industrial processes. The construction of reduced models allow the optimization of operational parameters with smaller effort and expenses and the use of dimensionless analysis and similarity theories is widespread in several areas of engineering.

There is a lot of controversy, though, in the use of scaling down techniques for the representation of two phase flows. In these cases, due the complexity of the phenomena involved, it may be difficult to reproduce all the required dimensionless numbers in the reduced scale. This fact may lead to the representation of different configurations, or flow patterns, between the two phases and, consequently, to inaccurately predict the real case behavior.

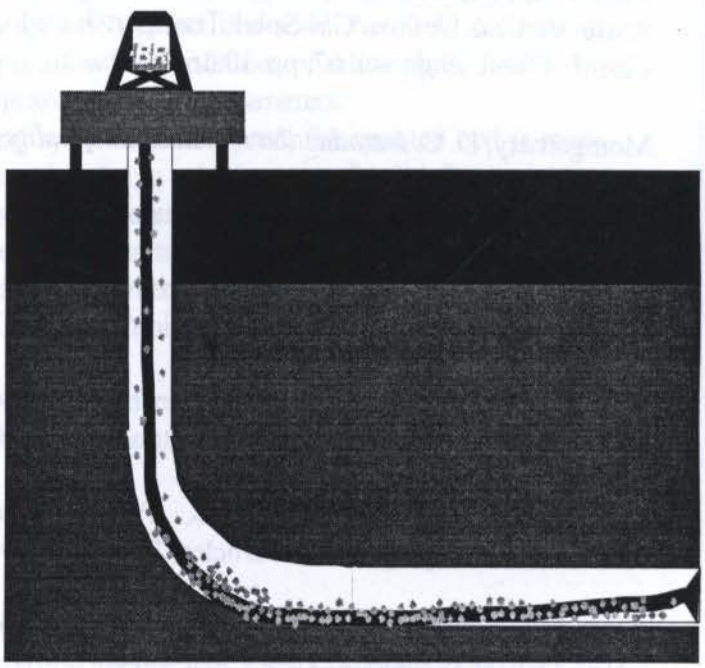

Figure 1- Horizontal Well Drilling

The study of stratified solid liquid annular flows is of great interest for petroleum engineering, specifically in the drilling area. This kind of flow describes the phenomena involved in the transport of solids generated by the bit during the drilling of a horizontal or highly inclined well. This technique is being used worldwide as an economic way of oilfield development. Figure 1 illustrates schematically the drilling of a horizontal well. Due to gravitational segregation, both solids and drill pipe will have the tendency to be in the lower portion of the annulus formed by the well walls and the drill column. The fluid is generally composed by a polymeric solution . This process, is then characterized by a stratified solid - non Newtonian fluid flow in eccentric annuli.

If hydraulic conditions permit, the solids may be kept in suspension avoiding operational problems such as abnormal torque and drag during drill string movement. This situation, however, is impossible to be reached in many phases of an oilwell and drilling has to be performed in the presence of a cuttings bed.

Iyoho (1980) presented a qualitative flow pattern map of solid liquid horizontal pipe flow. In his study, he divided the flow in four different configurations called stationary bed, moving bed, heterogeneous suspended flow and homogeneous suspended flow, as illustrated in figure 2. Later, other authors (Sanchez et al., 1997 and Peden et al., 1990), observed more detailed flow patterns, such as dune formation and the occurrence of a rolling region above the stationary bed (figures 3 and 4, respectively).

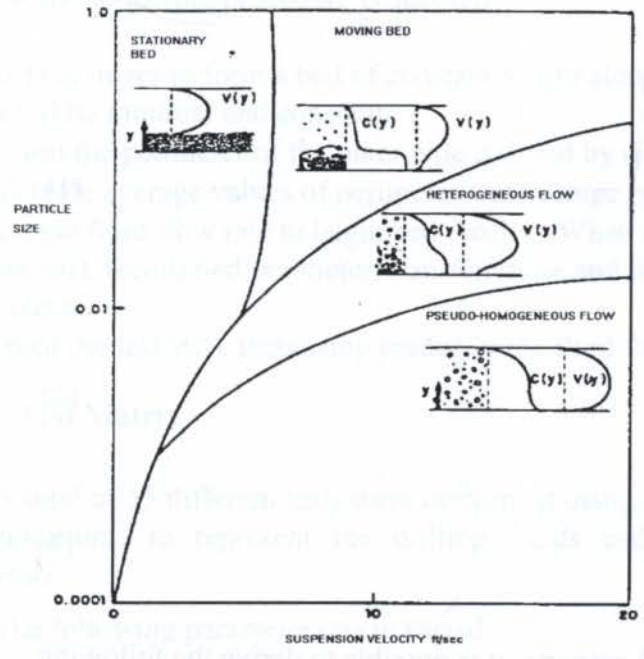

Figure 2- Flow patterns in solid liquid flow (Iyoho,1980).

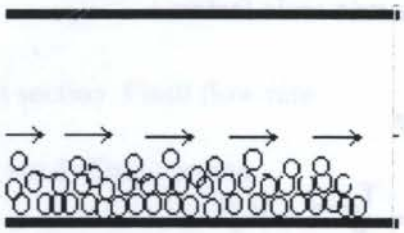

Figure 3- Transport by rolling mechanism.

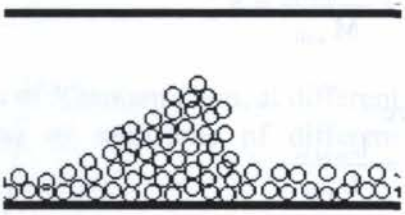

Figure 4- Transport by dunes mechanism

A lot of discussion has been presented on the difficulty of running representative reduced scale experiments concerning compressible two-phase flows. The main point is that the flow pattern transition is deeply influenced by the geometry. In the case of incompressible solid liquid flows, this effect is probably less important. In this study, two different scale results for stratified flow and for the transition stratified-suspended flow will be presented and discussed.

2. SCALING METHODOLOGY

A very important step for conducting a reduced scale experiment is to ensure the reproduction of the real situation. Scaling down and scaling up techniques are often neglected and may lead to erroneous quantification of variables.

The basic tool for the physical simulation of processes is the theory of similarity. With this, it is possible to establish the design conditions for the reduced model, that will reproduce the same behavior of the real situation. The first, but not sufficient, condition for physical simulation, is geometric similarity. Dynamic similarity is required for the reproduction of non-static phenomena.

The basis of the methodology consists in defining a scale factor for each of the basic dimensions which characterize the problem, namely length, mass and time, and use these factors to scale down/up the involved parameters. The length (geometric) scale factor is previously defined by the dimensions of the model, which is determined based on technical, operational and economic considerations. The geometric scale factor is defined by the ratio of length (diameter) in the reduced model and in the real situation.

Several different criteria can be used to define mass and time scale factors, depending on the phenomena to be simulated. In the specific case of cuttings transport in inclined/horizontal annuli, it is difficult to scale down fluid density and acceleration of gravity. These parameters will be equal in the real and in the reduced situations. These conditions restrict the definition of the mass and time scale factors, as functions of the geometric scale factor:

Time

$$K_T = \frac{T_{model}}{T_{well}} = K_L^{1/2} \qquad (1)$$

Mass:

$$K_M = \frac{M_{model}}{M_{well}} = K_L^3 \qquad (2)$$

where

$$K_L = \frac{L_{model}}{L_{well}} \qquad (3)$$

So, if we define as "A" any relevant physical property, it is possible to derive the following expression:

$$\frac{A_{model}}{A_{well}} = K_L^{(n_1+3n_2+n_3/2)} \qquad (4)$$

where

$$A = L^{n_1} M^{n_2} T^{n_3} \quad (5)$$

3. EXPERIMENTAL WORK

3.1 Part 1 - 5 inches pipe tests

3.1.1 Flow Loop Description

The experimental apparatus, consists of a test section 12m long acrylic pipe where a PVC pipe is introduced concentrically or eccentrically. The acrylic pipe, representing the wellbore, is 5 in OD X 4 in ID and allows flow visualization. Certainly the relevant variable for scale reduction is the internal diameter of the outer pipe. The internal pipe, representing the drill string, accounts for different phases of the drilling operation, depending on its diameter. Helical pumps are used to bring fluid into movement at controlled flow rates, while solids are fed in the test section through an auger. Instrumentation includes flow meters, differential pressure transducers, temperature sensors and a densitometer. Results are collected through a data acquisition system which allows checking the reliability of the results during the test.

3.1.2 Test Procedure

Once the operational parameters (geometry, eccentricity, fluid and solid properties) are chosen, the following procedure is adopted:

- Start the auger to form a bed of constant height along the test section. Fluid flow rate should be minimal and constant;
- Record the perimeter of the outer pipe covered by the bed in ten different points.
- Calculate average values of perimeter and average bed;
- Increase fluid flow rate to begin bed erosion. When steady state is reached (no more solids removal), record bed perimeter, transient time and friction loss; observe removal flow patterns;
- Repeat the last step, increasing gradually the fluid flow rate until complete bed removal.

3.1.3 Test Matrix

A total of 55 different tests were performed using solutions of Xhantam Gum, at different concentrations, to represent the drilling fluids and particles of sandstone of different diameters.

The following parameters were varied:

- Annular diameter ratio : 0.408 and 0.588
- Annular eccentricity : 0 (concentric) and 1 (fully eccentric)
- Fluid relative density: 1.0, 1.1, 1.2, 1.3
- Fluid rheology : water, thin, average and thick (dial readings and rheological parameters are shown on table 2)
- Solids diameter: 0.081, 0.117, 0.163 and 0.234 in
- Wellbore inclination: 40, 65 and 90 degrees from vertical

3.2 Part 2 - 8 inches pipe tests

3.2.1 Design Criteria

The TUDRP flow loop was designed and constructed by Stenevick (1991) and later modified by Bassal (1996) . It was designed to simulate a drilling rig in full scale and the main purpose is to perform cuttings transport research. The flow loop is made up of a test loop section which is composed of a 4 1/2 in drillpipe and an 8 in OD x 7.5 in ID transparent acrylic outer pipe of total length of 84 ft, a mud tank with an agitator of 85 bbls volume capacity, two parallel duplex mud pumps (one is driven by a six cylinder diesel engine and another the other by an electric motor), flow lines that connect pumps via test loop section to mud tank, a cuttings injection tank which can simulate the rate of penetration and a cuttings collection tank.

Two pressure taps are installed near the ends of the test loop section, they were connected by plastic tube filled with tap water to a differential pressure transducer. Mud flow rate, temperature and density are monitored by a Coriolis Type flow meter.

Parameters of pressure, flow rate, pipe rotary speed, torque, mud weight, injection tank weight and collection tank weight, pump pressure and mud temperature are displayed in the control room, and can be recorded every second by a data acquisition system.

3.2.2 Test Matrix

A second set of 28 experiments was performed with XCD polymer solutions and 0.25 in cuttings with the variation of the following parameters:

- Drillpipe rotation: 0, 75, 100, 125 RPM
- Flow rate: 200, 300, 400 GPM
- Wellbore inclination: 40, 65 and 90 degrees from vertical

4. RESULTS AND DISCUSSION

4.1.1 Proposed Correlations

Martins et al. (1996) present a detailed study on the experimental results and on the physical phenomena involved in the problem. Based on the experimental results the authors proposed the following correlations for bed height and critical velocity prediction as functions of the different dimensionless groups:

For bed height prediction:

$$\Pi_1 = 1 - (K_1.\Pi_2 + .K_2).\Pi_3.\Pi_4^a.\Pi_5^b.\Pi_6^d.\Pi_7^e \qquad (6)$$

For critical flow rate predictions:

$$\log \Pi_7^{CRIT} = K_1 + K_2.\log(\Pi_5 + K_3.K_6) + K_4.\Pi_2 + K_5.\Pi_3 + K_6.\Pi_4 \qquad (7)$$

where Π_i are dimensionless groups, defined by Martins et al (1996), and K_i, a, b, c, d, e are regression coefficients.

The first three dimensionless groups, Π, are shape factors which express ratios between bed height and internal diameter of outer pipe, internal diameter and annular gap and particle diameter and annular gap. The next dimensionless group represents the buoyancy forces. The last three groups represent the ratios between yield point effects and particle weight, viscous effects and particle weight and inertial and viscous forces. The last group is the Reynolds Number.

The least squares method was used in the search for optimum coefficients. The effects of drillpipe rotation (RPM) and wellbore inclination (θ) were incorporated in the model by the adjustment of polynomial functions (*f*) (Bassal, 1996), as follows

$$h / d_e = (h / d_e)_{horizontal} \cdot (f_{incl}) \cdot (f_{rpm}) \tag{8}$$

and

$$Q = (Q)_{horizontal} \cdot (f_{incl}) \cdot (f_{rpm}) \tag{9}$$

where:

$$f_{incl} = \frac{\mathrm{h} / \mathrm{d_e}}{\mathrm{h} / \mathrm{d_{ehorizontal}}} = a \cdot (90-\theta)^3 + b \cdot (90-\theta)^2 + c \cdot (90-\theta) + 1 \tag{10}$$

$$f_{RPM} = \frac{\mathrm{h}_{\mathrm{RPM}}}{h} = 1 - a \cdot RPM^b \tag{11}$$

h is the bed height, d_e the external diameter, Q the flowrate and a, b, and c regression coefficients.

Table 1 shows the variation of each dimensionless parameter in the experiments run in both flow loops. Since the range of variation of each dimensionless group, excepting the scale factor, in the 8 in tests is included in the range of the 5 in tests, the experiments can be considered dinamically quite similar. The following analysis will concentrate in the fitness of the method developed using the 5 in experiments to represent the 8 inch experiments.

Table 1:Range of Variation of dimensionless Parameters in the Experiments

	5 in Tests		8 in Tests	
Dimensionless Groups	Minimum	Maximum	Minimum	Maximum
π_2	*0,724*	*1,5*	*1,89*	*1,89*
π_3	*0,035*	*0,149*	*0,11*	*0,11*
π_4	*0,979*	*1,61*	*1,6*	*1,6*
π_5	*0*	*0,337*	*0,0193*	*0,0465*
π_6	*8,90*10 -6*	*6,40*10 -4*	*1,10E-5*	*2,27E-5*
π_7^{CRIT}	*10500*	*169000*	*13511,6*	*16558,6*

Figure 5 shows the results of applying equations 6 and 8 to calculate relative bed heights in the second set of tests. There is clear tendency to underprediction. The shape proposed for eq 6 proved to be inadequate for extrapolation due to excessive increase in the product term. Other shapes of function were tested and the following form was found to be more adequate for scale extrapolation, as can be seen in figure 6.

$$\Pi_1 = (K_1 . \Pi_2 + . K_2) . \Pi_3 . \Pi_4^a . \Pi_5^b . \Pi_6^d . \Pi_7^e \tag{12}$$

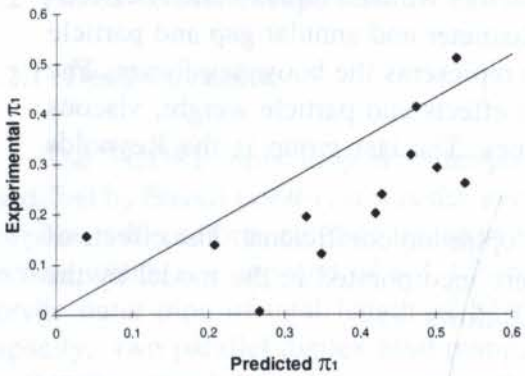

Figure 5- Fitness of Equation 6 in Scale Up Analysis.

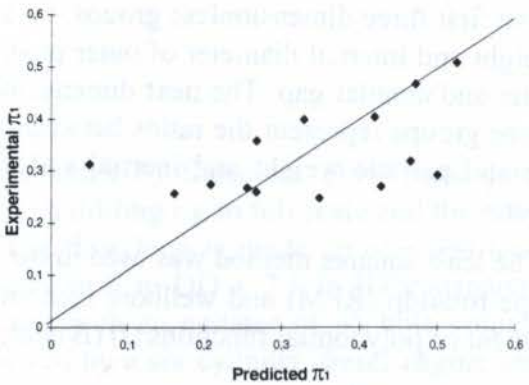

Figure 6 - Fitness of Equation 12 in Scale Up Analysis.

The most important approach in this work is, the evaluation of the critical flow rate equations. They define conditions where drilling will take place without the existence of a cuttings bed and consequently, with minimum risk of operational problems. With this goal, eqs 7 and 9 were used in the prediction of critical flow rates for set of experiments number two. Table 2 shows the results for tests conducted below critical conditions, where solids remained in the test section after the end of tests. From the 20 tests listed, the procedure predicted correctly in 13. In 4 of the other 7, there was indication of dune formation, meaning that solids would be removed if the tests were continued. Consequently, only in 3 of the 20 tests the predictions were inaccurate. Table 3 shows the results of the tests conducted above critical conditions. In all 5 tests the critical flow rate predicted was smaller than the test flow rate, indicating perfect fitness of the method.

Table 2: Subcritical 8 in Loop Tests

Flowrate (gpm)	Drillpipe Rotation (RPM)	Wellbore Inclination (degree)	Flowrate / Critical Flowrate	Observed Flow Patterns
300	*0*	*65*	*0,566830375*	*Bed*
300	*75*	*65*	*0,848693327*	*Bed*
200	*125*	*40*	*0,840099685*	*Bed*
400	*0*	*65*	*0,72939908*	*Bed*
200	*0*	*90*	*0,363693681*	*Bed*
200	*0*	*90*	*0,407239366*	*Bed*
200	*100*	*90*	*0,578169556*	*Bed*
200	*125*	*90*	*0,620544381*	*Bed*
200	*125*	*90*	*0,705454957*	*Bed*
400	*0*	*90*	*0,828038106*	*Bed*
400	*75*	*90*	*1,179093804*	*Bed*
400	*100*	*90*	*1,249605995*	*Dune*
400	*125*	*90*	*1,25029193*	*Dune*
400	*125*	*90*	*1,431889535*	*Dune*
300	*0*	*40*	*0,812523881*	*Bed*
300	*75*	*40*	*1,074480975*	*Bed*
300	*125*	*40*	*1,260149528*	*Bed*
300	*0*	*90*	*0,625628019*	*Bed*
300	*100*	*90*	*0,963711413*	*Bed*
300	*125*	*90*	*1,04818788*	*Dune*

Table 3: Critical 8 in Loop Tests

Flowrate (gpm)	Drillpipe Rotation (RPM)	Wellbore Inclination (degree)	Flowrate / Critical Flowrate	Observed Flow Patterns
400	*75*	*65*	*1,128811661*	*Suspended*
400	*125*	*65*	*1,366299506*	*Suspended*
400	*0*	*40*	*1,19211155*	*Suspended*
400	*75*	*40*	*1,432641301*	*Suspended*
400	*125*	*40*	*1,705114171*	*Suspended*

5. Conclusions

1. An analysis of the use of scale down techniques to represent solid-liquid two phase flow was conducted. The phenomenon is of great importance in petroleum engineering.
2. The model developed using reduced scale experiments in stratified flow conditions, proved to be reasonably adequate if some changes in the shape of original correlations are performed. This changes aimed the achievement of an adequate shape for extrapolation use.
3. The model developed in reduced scale proved to be very accurate in predicting critical conditions for bed removal. This is the most important factor to be monitored, since the absence of a solids deposit greatly enhances the chances of success in oilwell drilling operations.

6. References

BASSAL, A. *The Effect of Drillpipe rotation on Cuttings Transport in Inclined Wellbores*, MS thesis, U. of Tulsa, 1996.

IYOHO, A.W. *Drilled Cuttings Transport by Non-Newtonian Drilling Fluids Through Inclined, Eccentric Annuli,* PhD. Thesis, U. of Tulsa, Tulsa, USA, 1980.

MARTINS, A.L., SÁ C.H.M., LOURENÇO, A.M.F. & CAMPOS, W. Optimizing Cuttings Circulation in Horizontal Well Drilling, *Proceedings of the SPE Intl. Pet. Conf of Mexico*, Villahermosa, Mexico, Mar 5-7, 1996.

PEDEN, J.M., FORD, J.T. & OYENEYIN, .B.: Comprehensive Experimental Investigation of Drilled Cuttings Transport in Inclined Wells Including the Effects of Rotation and Eccentricity, *Proceedings of the EUROPEC 90*, The Hague, Netherlands, oct 22-24,1990.

SANCHEZ, R.A., AZAR, J.J., BASSAL, A.A. & MARTINS, A.L. *The Effect of Drillpipe rotation on Hole Cleaning During Directional Well Drilling,* Proceedings of the SPE/IADC Drilling Conference, Amsterdam,Netherlands, Mar 4-6., 1997.

STENEVIK, B. C., *Construction of a Full Scale Flow Loop Simulator*, MS Thesis, U. of Tulsa,1991.

Tema 35

Turbulência e Camada Limite

XIV Brazilian Congress of Mechanical Engineering
Obeid Plaza Hotel Convention Center - Bauru - SP/Brazil
December 08-12th 1997

PAPER CODE: COB886

MASS FLOW IN A TWO-PHASE FLOW WITH BOILING THERMAL SIPHON LOOP / *VAZÃO MÁSSICA EM ESCOAMENTO BIFÁSICO COM EBULIÇÃO EM UM CIRCUITO DE TERMOSSIFÃO*

MARIA EUGÊNIA VIEIRA, HUGO LEONARDO DE BRITO BUARQUE & PÚBLIO OTÁVIO OLIVEIRA DUARTE
Laboratório de Energia Solar, Centro de Tecnologia, Bloco 710, Campus do Pici - UFC
CEP 60455-760 - Fortaleza, Brazil - E-mails: eugenia@les.ufc.br / hugo@les.ufc.br

Abstract

This work presents a model to determine the total mass flow rate in a two phase flow with boiling closed circuit. This system is used to collect solar energy by the formation of vapor bubbles in a solar collector and to release this energy in condensation by heating a second fluid. The model assumes that the total frictional drop equals the pressure gain due to the difference in gravity in the single phase and the two phase vertical parts of the loop. Using the definition of the void fraction, a second expression could be written and the two equations were solved simultaneously for the void fraction and the total mass rate. The results indicated that the two phase flow was bubbly, what was expected considering the relatively low intensity of the solar flux and the experimental values for the temperature difference between the heated wall and the fluid saturation temperature.

Keywords

Thermal siphon, two-phase flow, mass rate, void fraction / Termossifão, escoamento bifásico, fração de void

1. INTRODUCTION

The grounds for this work rests upon the necessity to determine the total mass flow rate and the void fraction in a two-phase flow with boiling thermal siphon circuit. The system is used to absorb solar energy by boiling part of the mass flow of the working fluid through the collector and to deliver this energy in a heat exchanger in condensation. This energy heats up water which flows in the opposite direction through the heat exchanger.

A study on the thermal siphon operation of a boiling solar collector has been presented by Vieira and Reinaldo (1996), as shown in Figure 1. In its operation, liquid refrigerant is gravity fed from an accumulator tank to the collector. As it flows through the absorber plate, part of it boils and forms vapor bubbles which rise dragging liquid and starting the two-phase flow. When the flow leaves the collector, it moves through a tee-type connection where the liquid returns to the collector and the vapor moves upward to the heat exchanger to condense and heat the storage fluid.

In order to determine the collector thermal efficiency, the total mass flow rate and the void fraction of the flow are needed. Even though various researchers have worked on this system, a model for the collector efficiency factor based on these two flow variables has not been presented.

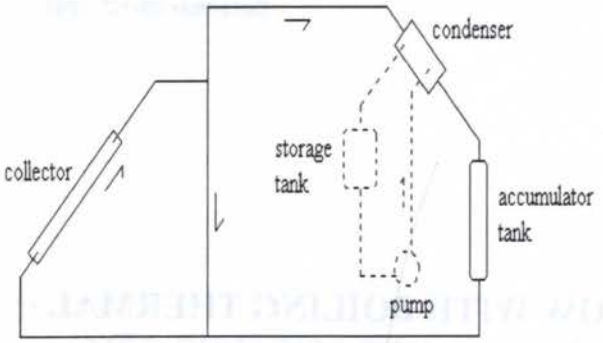

Figure 1 - Schematic view of the thermal siphon circuit.

The purpose of this work is to develop a numerical procedure to estimate the total mass flow rate through the closed circuit by equating the pressure change due to friction to that due to momentum changes. To solve this equation, experimental values for the vapor mass flow rate through the condenser were used to calculate the void fraction of the flow and thus, the total mass flow rate. To estimate the total pressure drop due to friction in the two-phase part of the system, two models based on the Martinelli and Nelson (1948) work were used and the results from these two models compare well. The values found for the void fraction fall in the range of bubbly flow, which was expected considering the low heat flux in solar radiation and also the low experimental values for the temperature difference between the tube wall and the fluid saturation.

2. LITERATURE REVIEW

Since the work by Vieira and Reinaldo (1996), presented a review of the boiling collector in thermal siphon operation where no results for the total mass flow rate nor the void fraction, this section comments on the models used to estimate the pressure drop in a two-phase flow system.

The first largely accepted method for the calculation of the two-phase flow pressure drop was proposed by Martinelli and Nelson (1948). In this method, the two-phase frictional pressure drop is determined by multiplying the pressure which would exist were the flow of liquid only, ΔP_o, by the ratio of the two-phase pressure drop to the single-phase drop, $\Delta P_{tpf} / \Delta P_o$, plotted versus the absolute pressure for the different exit. The curves are applicable to a horizontal tube of constant diameter.

Owens (1961) presented a solution theoretical in nature, which is not limited to any specific flow problem or substance to determine the two-phase pressure gradient for isothermal and non-isothermal flow. He assumed homogeneous flow and that the two-phase friction factor being the same as for single-phase liquid flow.

Marchaterre (1961) developed a model based on the work presented by Levy (1960) for vertical two-phase flow with each phase satisfying a momentum equation of the Bernoulli type. An expression for the frictional pressure drop in a vertical two-phase flow was presented based on the single phase flow.

3. METHODOLOGY

This section presents the analytical equations and the numerical procedure used to estimate the mass flow rate and void fraction in the two-phase flow system described in Figure 1. The Experimental data used were measured at the Solar Energy Applications Laboratory (Vieira, 1992). The total mass flow rate through the circuit could not be measured due to limitations in the instrument available. At first, a turbine flow meter calibrated by the manufacturer was installed, but it was not possible to obtain reasonable readings. This meter

introduced too large a pressure drop in the circuit. The mass flow rate of vapor through the system was determined as the ratio of the rate of sensible heat transferred in the condenser to a water-glycol solution to the latent heat of the working fluid. This value was used to estimate the total mass flow rate and void fraction in this model.

3.1 Analytical Model

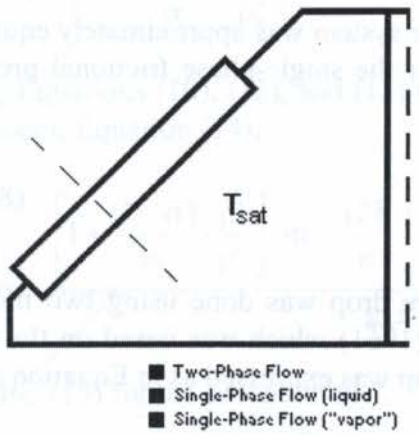

Figure 2 - Closed system in two-phase flow with boiling.

Figure 2 shows the closed thermal siphon loop and identifies the regions for single and two-phase flow. The position where boiling started was experimentally determined by thermocouples attached to the back of the flow channel.

To calculate the total mass flow rate of this system, it is assumed that frictional pressure drop in the closed loop is equal the pressure gain due to the difference in gravity in single-phase and the two-phase vertical sections of the loop. That is, the total pressure change for a complete cycle through the closed system is zero.

$$\Delta P_T^g + \Delta P_T^f = 0 \tag{1}$$

The pressure change due to the difference in density, ΔP_T^g, can be estimated using the expression,

$$\Delta P_T^g = g \cdot \sin\theta \cdot \left(\rho_l^s - \rho_{mix}^s\right) L_i \tag{2}$$

Using the definition of the void fraction, the density of the two-phase mixture can be expressed as in Equation (3),

$$\rho_{mix}^s = (1-\alpha)\rho_l^s + \alpha\rho_v^s \tag{3}$$

and this pressure change is re-written as,

$$\Delta P_T^g = g \cdot \sin\theta \cdot \alpha\left(\rho_l^s - \rho_v^s\right) L_i \tag{4}$$

To obtain the expression of frictional pressure drop, it must be divided into two parts, one for two-phase flow and the other for single-phase flow, as in Equation (5).

$$\Delta P_T^f = \Delta P_{spf}^f + \Delta P_{tpf}^f \tag{5}$$

The calculation of the single-phase frictional pressure drop was done using the well-known expression,

$$-\Delta P^{f}_{spf} = \frac{f_{spf} \cdot \rho^{s}_{l} \cdot \bar{v}^{2}}{2D} \cdot L_{spf} \tag{6}$$

and its friction factor was determined assuming that the single-phase flow was laminar.

$$f_{spf} = \frac{64}{Re} \tag{7}$$

Considering that the total mass flow rate through the system was approximately equal the mass flow rate of single-phase (liquid), the equation for the single-phase frictional pressure drop was re-written as,

$$-\Delta P^{f}_{spf} = \frac{128}{\pi} \cdot \frac{\mu^{s}_{l}}{\rho^{s}_{l} \cdot D^{4}} \cdot \dot{m}_{T} \cdot L_{spf} \tag{8}$$

The calculation of the two-phase frictional pressure drop was done using two models. The first used an expression presented by Marchaterre (1961) which was based on the work presented by Levy (1960). In this model, the pressure drop was expressed as in Equation (9)

$$\left(\frac{\Delta P}{L}\right)_{tpf} = \left(\frac{\Delta P}{L}\right)_{o} \cdot \left[\frac{(1-x)^{2}}{1-\alpha} + \frac{2g \cdot \sin\theta \cdot \alpha\left(\rho^{s}_{l} - \rho^{s}_{v}\right)\rho^{s}_{l} \cdot D}{f_{o} \cdot G^{2}}\right] \tag{9}$$

where the second term in brackets was set equal to zero to account for just the frictional losses. Combining the equations (1), (3), (4), (8) and (9), the total mass rate can be written as,

$$\dot{m}_{T} = \frac{\alpha\left(\rho^{s}_{l} - \rho^{s}_{v}\right)L_{i} \cdot g \cdot \sin\theta}{\frac{128}{\pi} \cdot \left(\frac{\mu^{s}_{l}}{D^{4} \cdot \rho^{s}_{l}}\right) \cdot \left\{L_{spf} + \frac{(1-\alpha) \cdot \left(\rho^{s}_{l}\right)^{2}}{\left[(1-\alpha)\rho^{s}_{l} + \alpha\rho^{s}_{v}\right]^{2}} L_{tpf}\right\}} \tag{10}$$

In the second model, the expression presented by Owens (1961) was used. The frictional pressure drop was written as in Equation (11),

$$\left(\frac{\Delta P}{L}\right)_{tpf} = \left(\frac{\Delta P}{L}\right)_{o} \cdot \left[1 + x \cdot \left(\frac{\rho^{s}_{l}}{\rho^{s}_{v}} - 1\right)\right] \tag{11}$$

Combining the equations (1), (3), (4), (8) and (11), the total mass rate can be written as

$$\dot{m}_{T} = \frac{\alpha\left(\rho^{s}_{l} - \rho^{s}_{v}\right)L_{i} \cdot g \cdot \sin\theta}{\frac{128}{\pi} \cdot \left(\frac{\mu^{s}_{l}}{D^{4} \cdot \rho^{s}_{l}}\right) \cdot \left\{L_{spf} + \frac{\rho^{s}_{l}}{(1-\alpha)\rho^{s}_{l} + \alpha\rho^{s}_{v}} L_{tpf}\right\}} \tag{12}$$

Equations (10) and (12) are the two expressions that were to calculate the total mass flow rate and the void fraction in the system.

3.2 Numerical Procedure

In order to validate the model, it is necessary find a second equation for the mass flow rate as a function of void fraction. From the definition of the void fraction, the total mass flow rate was expressed as in Equation (13),

$$\dot{m}_T = \left[1 + \frac{(1-\alpha)}{\alpha} \cdot \frac{\rho_l^s}{\rho_v^s}\right] \cdot \dot{m}_v \tag{13}$$

Using Equations (10), (12), and (13) the expressions found for the void fraction were for the first model, Equation (14),

$$\alpha = \frac{\left[1 + \frac{(1-\alpha)}{\alpha} \cdot \frac{\rho_l^s}{\rho_v^s}\right] \cdot \dot{m}_v \cdot \frac{128}{\pi} \cdot \left(\frac{\mu_l^s}{D^4 \cdot \rho_l^s}\right) \cdot \left\{L_{spf} + \frac{(1-\alpha)\cdot(\rho_l^s)^2}{\left[(1-\alpha)\rho_l^s + \alpha\rho_v^s\right]^2} L_{tpf}\right\}}{g \cdot \sin\theta \cdot (\rho_l^s - \rho_v^s) \cdot L_i} \tag{14}$$

and Equation (15) for the second model.

$$\alpha = \frac{\left[1 + \frac{(1-\alpha)}{\alpha} \cdot \frac{\rho_l^s}{\rho_v^s}\right] \cdot \dot{m}_v \cdot \frac{128}{\pi} \cdot \left(\frac{\mu_l^s}{D^4 \cdot \rho_l^s}\right) \cdot \left\{L_{spf} + \frac{\rho_l^s}{(1-\alpha)\rho_l^s + \alpha\rho_v^s} L_{tpf}\right\}}{g \cdot \sin\theta \cdot (\rho_l^s - \rho_v^s) \cdot L_i} \tag{15}$$

Using the experimental data collected, the numerical procedure developed was tested.

3.3 Experimental Measurements

Experimental measurements were made for the incident solar radiation on horizontal and tilted planes, the temperature of the absorber plate and of the outside walls of the connecting lines, the temperature of the ambient air, the working fluid pressure and temperature at collector inlet and pressure at outlet. On the storage side, the volumetric flow rate of the glycol-water solution through the condenser and the temperature difference of this heat exchanger were measured. A data acquisition system collected the raw data and was programmed with a scan interval of twenty seconds and pseudo channels were defined to give average values.

4. RESULTS

Using the experimental values for the mass flow rate of vapor in the system, the void fraction calculation using the two models for the frictional pressure drop agree well. A sample calculation for a day is presented in Figure 3, where I represent the solar radiant heat flux, $\dot{m}_v$ the mass flow rate of vapor through the collector and condenser, and α the void fraction of the flow. This vapor rate is important because it represents the useful energy gain in the collectors. It flows to the heat exchanger to release its latent heat in the condensation process by heating up water which flows in a second circuit through the heat exchanger.

In Figure 4, the values for $\dot{m}_T$, the total mass flow rate that circulates through the system are used instead of the mass flow rate of vapor.

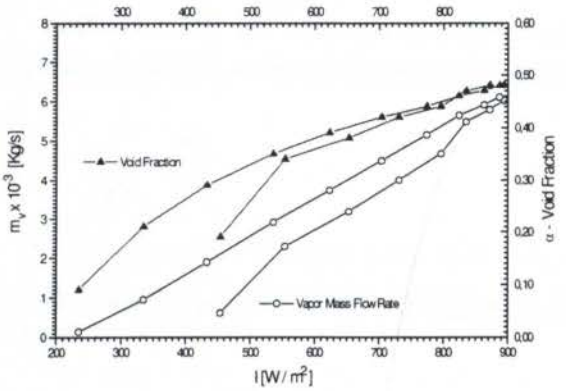

Figure 3 - Results for the void fraction and the mass flow rate of vapor as a function of the solar flux.

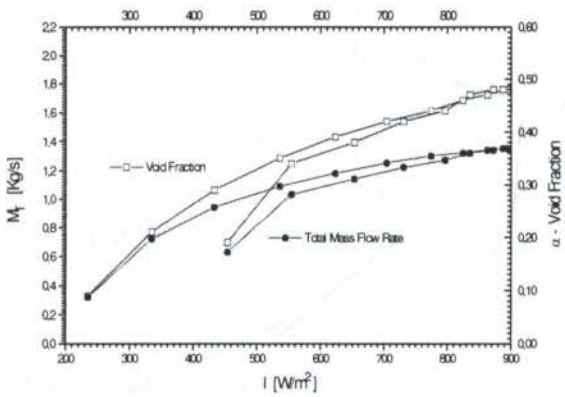

Figure 4 - Results for the void fraction and the total mass flow rate as a function of the solar flux.

Looking at these two figures, it is seem that the values for the total mass flow rate are much higher than those for the vapor mass rate. This confirm the assumption that, even at the collector exit, the vapor quality is very small, as considered in the development of Equation (7).

Due to limitations in the instrumentation, it was not possible to measure the total mass flow rate through the collector. To correctly measure this flow, a non-intrusive instrument should be used. This is a extremely important because the pressure drop across the meter influences the mass flow rate.

5. CONCLUSION

From the results in Figures 3 and 4, the values for the void fraction indicate that the two-phase flow is bubbly. This is reasonable considering the relatively low rates of heat flux in solar radiation and also the experimental values for the difference between the temperature of the channel wall and the fluid saturation temperature.

These results also show that the total mass flow rate through the circuit does not boil in the collector flow channels, as considered in various model presented in the literature. Indeed, only a very small portion of this total mass flow rate becomes vapor.

Even though the values for the void fraction seem reasonable and the results from the pressure drop models agree well, the total mass flow rate through the system could not be checked as this experimental values were not available. Actually, when this measurements be made, as intended in the system prototype that is being built at the Applied Solar Energy Laboratory [LES], a correlation for the void fraction based on the drift flux model with the total mass flux as a known variable will be used.

6. ACKNOWLEDGEMENTS

We would like to thank FINEP for sponsoring the new system to be installed at LES and CNPq for a six month undergraduate student research fellowship. We would like to very much thank Dr. J. H. Davidson and Dr. G.O.G. Löf from the Solar Energy Applications Laboratory at Colorado State University and also all its staff members for all the support given.

7. REFERENCES

Levy, S. Steam-Theorical Predicton From Momentum Model, *Journal of Heat Transfer*, Trans. ASME, Series C, vol. 82, pp.113-124, 1960.

Marchaterre, J.F. Two-Phase Frictional Pressure Drop Prediction From Levy's Momentum Model, *Trans. ASME, Series C. Journal of Heat Transfer*, pp. 503-505, 1961.

Martinelli, R.C., Nelson, D.B., Prediction of pressure Drop Forced-Circulation Boiling of Water, *Trans. ASME.*, Vol. 70, pp.695-702, 1948.

Owens, W.L. Two-Phase Pressure Gradient, *ASME International Developments in Heat Transfer*, Part II, pp. 363-368, 1961. American Society of Mechanical Engineers, New York, 1962.

Vieira, M.E. Experimental and Analytical Study of a Boiling Collector in Thermal Siphon Operation, *Ph.D. Thesis*, CSU, USA, 1992.

Vieira, M.E. & Reinaldo, R. F. Efficiency Analysis of a Boiling Collector in Thermal Siphon Operation, *ENCIT96* and *LATCYM96*, vol.III, pp.1615-1619, Florianópolis, 1996.

8. NOMENCLATURE

D ≡ equivalent diameter of tube, [m]
f ≡ friction factor, [non-dimensional]
g ≡ gravitational acceleration, [m/s^2]
G ≡ mass flow rate per unit area, [$Kg/s/m^2$]
L ≡ length of tube, [m]
$\dot{m}$ ≡ mass flow rate, [Kg/s]
ΔP ≡ pressure drop, [N/m^2]
Re ≡ Reynolds number, [non-dimensional]
$\bar{v}$ ≡ average velocity, [m/s]
x ≡ quality, [non-dimensional]
α ≡ void fraction, [non-dimensional]
μ ≡ viscosity, [Kg/s/m]
θ ≡ angle of inclination, [degrees]
ρ ≡ density, [Kg/m^3]

8.1 Subscripts

i ≡ two-phase flow non-horizontal
l ≡ liquid
mix ≡ mixture liquid-vapor
o ≡ flow of liquid only
spf ≡ single-phase flow (liquid)
T ≡ total
tpf ≡ two phase flow (liquid and vapor)
v ≡ vapor

8.2 Superscripts

f ≡ frictional
g ≡ acceleration
s ≡ saturated

XIV Brazilian Congress of Mechanical Engineering
Obeid Plaza Hotel Convention Center - Bauru - SP/Brazil
December 08-12th 1997

PAPER CODE: COB074

GÖRTLER VORTICES/TOLLMIEN-SCHLICHTING WAVES INTERACTION: REASSESSMENT OF PREVIOUS RESULTS WITH A SPATIAL/NONPARALLEL MODEL

Márcio T. Mendonça, Philip J. Morris †, and Laura L. Pauley ‡
Centro Técnico Aeroespacial - Instituto de Atividades Espaciais.
São José dos Campos, SP 12228-904 - Brazil,
The Pennsylvania State University, Dept. of Aerospace Eng. and Dept. of Mechanical Eng.
University Park, PA 16802 - USA. E-mail: † pjm@cac.psu.edu, ‡ lpauley@psu.edu

Abstract

The interaction between Görtler vortices and Tollmien-Schlichting waves is studied with a spatial, nonparallel model based on the Parabolized Stability Equations. A reassessment of previous results obtained with temporal, parallel models is performed showing that the main conclusions obtained with those models are valid but the parallel flow assumption does influence the results. New results not previously available in the literature for Tollmien-Schlichting wave amplitudes of the same order of magnitude as the vortices are also presented.

Keywords

Görtler vortices, instability, boundary layer, Tollmien-Schlichting waves, vortices de Görtler, instabilidade, camada limite, ondas de Tollmien-Schlichting

1. INTRODUCTION

The study of transition to turbulence in flows over curved surfaces finds applications in problems such as the flow over laminar flow wings, the flow over axial turbine and compressor blades, and the flow inside supersonic converging diverging nozzles. The main consequence of a concave surface curvature is the generation of Görtler vortices (GV) that can anticipate transition to turbulence. In certain flow conditions, besides the presence of the vortices, the flow becomes unstable to other perturbations and the nonlinear interaction between the Görtler vortices and these other perturbations may result in even earlier breakdown to turbulence.

Using the method of multiple scales Nayfeh (1981) found that the vortices strongly destabilize Tollmien-Schlichting (TS) waves. His results were not confirmed by Malik (1986) who used a temporal/parallel model and found an inconsistent length scale in Nayfeh's formulation. Malik found that TS waves with spanwise wavelength half the wavelength of the vortices are destabilized by the nonlinear interaction. Nayfeh reworked his formulation and presented new results in Nayfeh and Al-Maaitah (1988). They showed that the TS waves have two components, one growing slower, and the other growing faster

than the unexcited mode. Their results agree with Malik (1986) in the sense that resonance occurs when the spanwise wavelength of the oblique wave is half that of the wavelength of the vortices. They also presented some parametric studies on the effect of Reynolds number and frequency. Malik and Hussaini (1990) investigated the necessary vortex amplitude for the interaction to take place. They also studied the growth of a two-dimensional wave and concluded that the growth rate is larger than the growth of the unperturbed wave. They confirmed Nayfeh and Al-Maaitah' s (1988) results that interactions take place only at relatively large GV amplitudes. Malik and Godil (1990) using the same formulation used by Malik (1986) showed that the GV/2D TS wave interaction leads to the development of oblique waves with a spanwise wavelength equal to that of the vortices. All previous studies were limited to small amplitude TS waves.

So far the investigations on GV/TS wave interaction have used local models and temporal/parallel models. Local models are not suitable to study the development of Görtler vortices that are governed by parabolic equations which rigorously can not be simplified to ordinary differential equations, except at large wavenumbers. In this way, local models have been used to study the development of TS waves in boundary layer flows with embedded streamwise vortices. Temporal/parallel models are not the most appropriate to describe the physics of spatially developing vortices; nonparallel effects are important both for low spanwise wavenumber vortices and for three-dimensional TS waves. Only results for TS waves with amplitudes one order of magnitude smaller than the vortices have been presented in previous works. The present investigation studies GV/TS wave nonlinear interactions with a spatial/nonparallel model. The model is based on the Parabolized Stability Equations (PSE) developed by T. Herbert and F. P. Bertolotti at The Ohio State University (Bertolotti, 1991). The goal of the present investigation is to verify if the results obtained with temporal/parallel models are valid and to present new results for TS wave amplitudes of the same order of magnitude as the vortices.

2. FORMULATION

The coordinate system used in the present work is the same coordinate system presented by Floryan (1980). It is based on the streamlines (ψ^*) and potential lines (ϕ^*) of the inviscid flow over a constant radius of curvature wall. This coordinate system has the advantage of considering the decay of the curvature away from the wall such that at the wall it is surface oriented, but away from the wall it approaches a Cartesian system.

The Navier-Stokes equations for an incompressible flow of a Newtonian fluid are simplified by assuming that the dependent variables are decomposed into a mean component and a fluctuating component as follows:

$$\vec{u^*} = \vec{U^*} + \vec{u'^*}, \qquad \text{and} \qquad p^* = P^* + p'^*. \tag{1}$$

where $\vec{u^*} = [u^*, v^*, w^*]^T$ is the velocity vector and p^* is the pressure. The superscript * indicates dimensional variables.

The equations are nondimensionalized using δ_0^* and U_∞^* as the length and velocity scaling parameters, where $\delta_0^* = (\nu^* \phi_0^* / U_\infty^*)^{1/2}$ is the boundary layer thickness parameter, U_∞^* is the free stream velocity, ϕ_0^* is a reference length taken as the streamwise location where initial conditions are applied, and ν^* is the kinematic viscosity.

Floryan (1980) derived the equations for the zeroth order and first order approximation for the mean flow and for the perturbation quantities He concluded that for the

zeroth order approximation the mean flow equations reduce to the Prandtl boundary layer equations for the flow over a flat plate. The only remaining curvature term for the perturbation equations zeroth order approximation is the term on the normal momentum equation given by:

$$\frac{Go^2}{Re^2}(2Uu' + u'^2), \qquad \text{where} \qquad Go = Re(k^*\delta_0^*)^{(1/2)}, \qquad Re = \frac{U_\infty^*\delta_0^*}{\nu^*}. \tag{2}$$

Go is the Görtler number, k^* is the curvature of the wall, and Re is the Reynolds number.

The resulting momentum and continuity equations are written in vector form.

$$A\frac{\partial\Phi'}{\partial t} + B_1\frac{\partial\Phi'}{\partial\phi} + C_1\frac{\partial\Phi'}{\partial\psi} + D_1\frac{\partial\Phi'}{\partial z} + E\left(\frac{\partial^2\Phi'}{\partial\phi^2} + \frac{1}{g^2}\frac{\partial^2\Phi'}{\partial\psi^2} + \frac{\partial^2\Phi'}{\partial z^2}\right) + F_1\Phi' = G, \tag{3}$$

where $\Phi' = [u', v', w', p']^T$, and the expressions for the coefficient matrices can be found in Mendonça (1997).

The boundary conditions are given by:

$$u' = v' = w' = 0 \qquad \text{for} \qquad \psi = 0,$$

$$\frac{\partial u'}{\partial\psi}, \frac{\partial v'}{\partial\psi}, \frac{\partial w'}{\partial\psi}, p' \to 0 \qquad \text{for} \qquad \psi \to \infty. \tag{4}$$

The boundary condition for pressure at the wall is given by the momentum equation in the normal direction applied at $\psi = 0$.

2.1 Parabolized Stability Equations

The governing equations for the perturbation variables are simplified, leading to the Parabolized Stability Equations (PSE) developed by Herbert and Bertolotti (Bertolotti, 1991). The resulting set of equations describes the spatial evolution of disturbances, and allows nonparallel nonlinear effects to be accounted for without the heavy demands of a direct numerical simulation.

The set of equations represented by Eq. (3) are elliptic and the perturbations propagate in the flow field as wave structures. The governing equations can be simplified if the wavelike nature of the perturbations are represented by their frequency, wavenumber, and growth rate. The perturbation Φ' is assumed to be composed of a slowly varying shape function and an exponential oscillatory wave term. It is represented mathematically as a Fourier expansion truncated to a finite number of modes:

$$\Phi' = \sum_{n=-N}^{N}\sum_{m=-M}^{M}\Phi_{n,m}(\phi,\psi)\chi_{n,m}(\phi,z,t), \tag{5}$$

where $\Phi_{n,m}(\phi,\psi) = [u_{n,m}, v_{n,m}, w_{n,m}, p_{n,m}]^T$ is the complex shape function vector, and

$$\chi_{n,m}(\phi, z, t) = \exp\left[\int_{\phi_0}^{\phi} a_{n,m}(\xi)d\xi + im\beta z - in\omega t\right], \tag{6}$$

$$a_{n,m}(\phi) = \gamma_{n,m}(\phi) + in\alpha(\phi). \tag{7}$$

This procedure is similar to a normal mode analysis, but, in this case, the shape function $\Phi_{n,m}$ is a function of both ϕ and ψ.

The streamwise growth rate $\gamma_{n,m}$, the streamwise wavenumber α, and the spanwise wavenumber β were nondimensionalized using the boundary layer thickness parameter δ_0^*. The frequency ω was nondimensionalized using the free stream velocity U_∞^* and the boundary layer thickness parameter δ_0^* .

For linear problems only the fundamental mode is significant. With the growth of the amplitude of the fundamental, higher harmonics become significant as well as the mean flow distortion (MFD) $n = 0$, $m = 0$. As the nonlinearities become stronger, higher harmonics are considered by increasing the number of modes N, M in the truncated Fourier expansion. The choice for $a_{n,m}$ for higher harmonics reflects the fact that their phase speed should be the same as the phase speed of the fundamental mode to avoid dispersion of the wave structure.

The perturbation variable Φ', as defined in Eq. (5), is substituted in the governing Eq. (3). The equation is then simplified by assuming that the shape function, wavelength, and growth rate vary slowly in the streamwise direction. In this way, second order derivatives and products of first order derivatives can be neglected.

After substituting these terms in Eq. (3) and performing an harmonic balance in the frequency, a set of coupled nonlinear equations is obtained. For each mode (n, m) the equation is given in vector form by:

$$\overline{A}_{n,m}\Phi_{n,m} + \overline{B}_{n,m}\frac{\partial\Phi_{n,m}}{\partial\phi} + \overline{C}_{n,m}\frac{\partial\Phi_{n,m}}{\partial\psi} + \overline{D}_{n,m}\frac{\partial^2\Phi_{n,m}}{\partial\psi^2} = \frac{\overline{E}_{n,m}}{e^{\left(\int_{\phi_0}^{\phi} a_{n,m}(\xi)d\xi\right)}}, \tag{8}$$

where the coefficient matrices can be found in (Mendonça, 1997)

The resulting equations are parabolic in ϕ and the solution can be marched downstream given initial conditions at a starting position ϕ_0. This is true as long as the instabilities are convected instabilities such that they propagate in the direction of the mean flow and do not affect the flow field upstream.

The pressure gradient in the streamwise momentum equation also makes the system of equations nonparabolic. For incompressible flow Malik and Li (1993) suggest that sufficiently large steps in the streamwise direction will avoid the elliptic behavior of the problem. They also show that dropping the pressure gradient term altogether does not change the results for the level of approximation given by the PSE equations. In the present model the pressure gradient term is not included.

The boundary conditions for Eq. (8) are derived from Eq. (4). At the wall, homogeneous Dirichlet no-slip conditions are used. In the far field, Neumann boundary conditions are used for the velocity components and homogeneous Dirichlet condition are used for pressure.

For the parabolic formulation, it is necessary to specify initial conditions at a starting position ϕ_0 downstream of the stagnation point at the leading edge of the curved plate. For TS waves the initial data is obtained from the solution of the eigenvalue problem

posed by the Orr-Sommerfeld equation. For GV the initial conditions are also given by a local normal mode analysis.

2.2 Normalization Condition

The splitting of $\Phi'(\phi, \psi, z, t)$ into two functions, $\Phi_{n,m}(\phi, \psi)$ and $\chi_{n,m}(\phi, \psi, z, t)$, is ambiguous, since both are functions of the streamwise coordinate ϕ. It is necessary to define how much variation will be represented by the shape function $\Phi_{n,m}(\phi, \psi)$, and how much will be represented by the exponential function $\chi_{n,m}(\phi, \psi, z, t)$. This definition has to guarantee that rapid changes in the streamwise direction are avoided so that the hypothesis of slowly changing variables is not violated. The objective is to transfer fast variations of $\Phi_{n,m}(\phi, \psi)$ in the streamwise direction to the streamwise complex wavenumber $a_{n,m}(\phi) = \gamma_{n,m}(\phi) + in\alpha(\phi)$. If this variation is represented by $b_{n,m}$, for each step in the streamwise direction it is necessary to iterate on $a_{n,m}(\phi)$ until $b_{n,m}$ is smaller than a given threshold. At each iteration k, $a_{n,m}(\phi)$ is updated according to:

$$(a_{n,m})_{k+1} = (a_{n,m})_k + (b_{n,m})_k \tag{9}$$

The variation $b_{n,m}$ of the shape function can be monitored in different ways. In the present implementation the following is used:

$$b_{n,m} = \frac{1}{\int_0^\infty \|\vec{u}_{n,m}\|^2 d\psi} \int_0^\infty \left(\vec{u}_{n,m}^{\dagger} \cdot \frac{\partial \vec{u}_{n,m}}{\partial \phi} \right) d\psi, \tag{10}$$

where $u_{n,m}^{\dagger}$ is the complex conjugate of $u_{n,m}$. The integral of $\|\vec{u}_{n,m}\|^2$ was used to assure that the variation is independent from the magnitude of $\vec{u}_{n,m}$.

2.4 Numerical Method

The system of parabolic nonlinear coupled equations given by Eq. (8) is solved numerically using finite differences. The partial differential equation is discretized implicitly using a second order backward differencing in the streamwise direction, and fourth order central differencing in the normal direction. The resulting coupled algebraic equations form a block pentadiagonal system which is solved by LU decomposition.

To start the computation a first order backward differencing is used. The first order approximation is used, also, in a few subsequent steps downstream in order to damp transients more efficiently. For the points neighboring the boundaries, second order central differencing in the normal direction was used.

The nonlinear terms are evaluated iteratively at each step in the streamwise direction. The iterative process is used both to enforce the normalization condition and to enforce the convergence of the nonlinear terms. A Gauss-Siedel iteration with successive overrelaxation is used. The nonlinear products are evaluated in the time domain. The dependent variables in the frequency domain are converted to the time domain by an inverse Fast Fourier Transform subroutine. The nonlinear products are evaluated and the results are transformed back to the frequency domain.

The complex wavenumber is updated at each iteration according to Eq. (9), and the variation in the shape function is monitored through Eq. (10). The iteration is considered converged when the normalization condition is no larger than a given small threshold. In

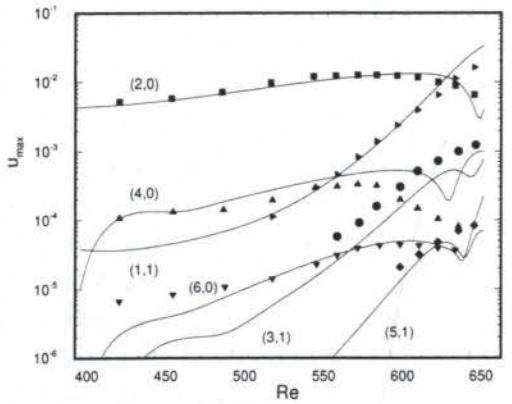

Figure 1: Subharmonic breakdown. Comparison between the PSE results and experimental results from Kachanov and Levchenko (1984)

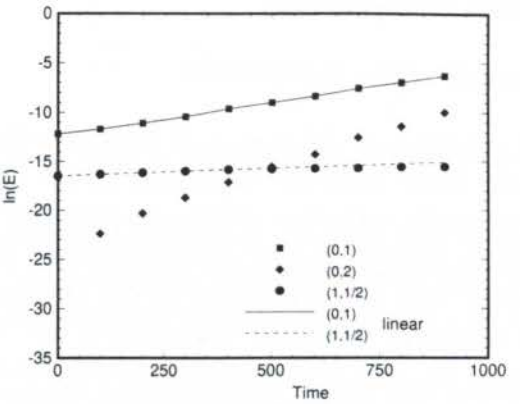

Figure 2: GV/3D-TS interaction. Temporal results from Malik's computation (1986). Symbols — nonlinear results, lines — linear results.

the present implementation this threshold is 10^{-8}.

2.5 Code Validation

A comparison between PSE results and the experimental results from Kachanov and Levchenko (1984) for subharmonic breakdown is presented. The subharmonic breakdown is characterized by the nonlinear interaction between a finite amplitude two-dimensional TS wave and small amplitude three-dimensional waves with half the frequency of the 2D TS wave. The starting conditions are: $Re = 400$, frequency $\omega_{2,0} = 0.0496$, spanwise wavenumber $\beta_{1,1} = 0.1333$, frequency $\omega_{1,1} = 0.0248$, initial amplitudes $\epsilon_{2,0} = 0.439\%$, and $\epsilon_{1,1} = 0.0039\%$.

Figure 1 presents a comparison between the PSE results and the experimental results from Kachanov and Levchenco (1984) for the amplitude of different harmonics. It shows that the PSE is able to reproduce the development of all harmonics with good accuracy. According to Joslin, Street and Chang (1993), the small differences between experimental and computational results observed for higher harmonics can be attributed to small differences between the experimental conditions reported by Kachanov and Levchenco and the actual experimental conditions in their experiment. Those differences were due to a small streamwise pressure gradient and a larger frequency.

Good comparison was also obtained with numerical results from Bertolotti (1991) for K-type breakdown and with numerical and experimental results from Malik and Li (1993) and Swearingen and Blackwelder (1987) respectively for nonlinear GV development

3. GV/TS WAVE INTERACTION

3.1 Reassessment of Previous Results

First a result from Malik (1986) is reproduced. The test case considered is defined by the following initial conditions: $Re = 950$, $\omega = 0.038$, $\alpha = 0.103$, $\beta_{TS} = 0.15$, $Go = 14$, $\beta_{GV} = 0.3$, $\epsilon_{TS} = 0.1\%$, $\epsilon_{GV} = 1\%$. Figure 2 shows temporal/parallel results from Malik, and Figure 3 shows the results obtained with the present model. They confirm that the TS wave is not strongly destabilized by the nonlinear interaction. Other comparisons with Malik's results confirm this conclusion. Figure 3 also shows that, in the

present case, nonparallel effects are present, but are not strong.

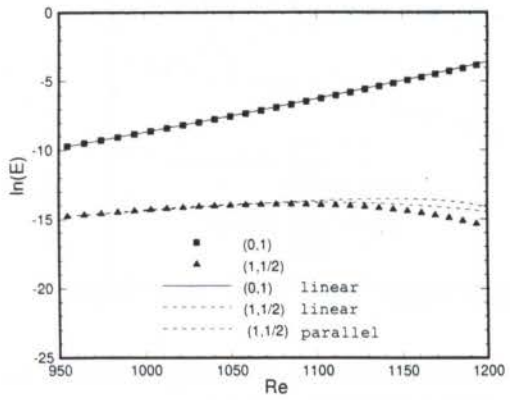

Figure 3: GV/3D-TS wave interaction. Comparison between nonlinear and linear results.

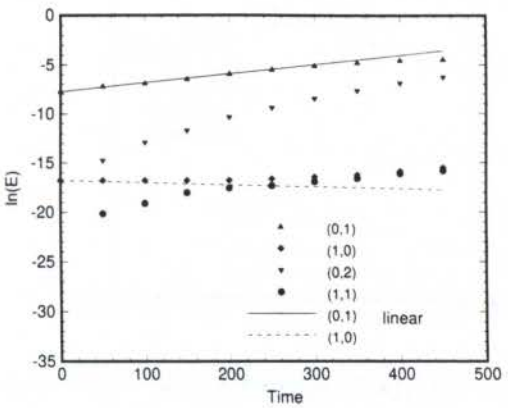

Figure 4: GV/2D-TS wave interaction Temporal, parallel results from Malik and Hussaini (1990).

The following test case is taken from Malik and Hussaini (1990). The initial conditions are specified by $Go = 14.$, $Re = 950.$, $\beta_{GV} = 0.5$, $\alpha = 0.2$, $\omega = 0.0697$, $\epsilon_{TS} = 0.1\%$, $\epsilon_{GV} = 1\%$. The temporal/parallel results from (Malik & Hussaini, 1990) presented in Figure 4 are in good qualitative agreement with the present spatial/nonparallel results presented in figure 5. The TS wave is weakly destabilized by the nonlinear interaction and the development of the oblique wave given by mode (1,1) is confirmed by the spatial model. This oblique wave grows to energy levels of the same order as the TS wave (1,0). In this case the nonparallel effects are considerably higher than observed in the previous case.

Results for a stable 2D TS wave presented by Malik and Godil (1990) are presented in Figure 6. The initial conditions are specified by: $Go = 12.$, $Re = 600.$, $\beta_{GV} = 0.4$, $\beta_{TS} = 0.0$, $\alpha = 0.2$, $\omega = 0.0738$, $\epsilon_{TS} = 0.1\%$, $\epsilon_{GV} = 1\%$. Figure 7 shows the corresponding results obtained with the present model. Again the results are in good qualitative agreement in the sense that the nonlinear interaction weakly destabilizes the 2D TS wave given by wave mode (1,0) and that an oblique TS wave given by mode (1,1) develops and grow to energy levels of the 2D TS wave. The comparison between spa-

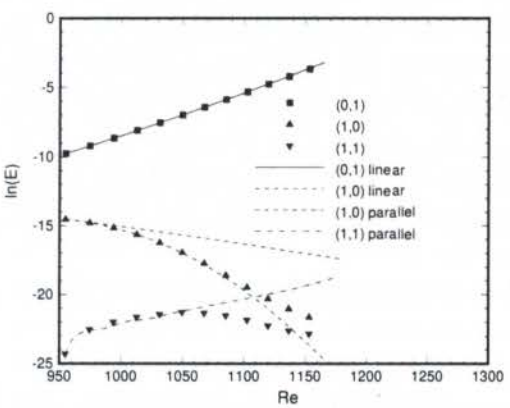

Figure 5: GV/2D-TS interaction. Spatial, nonparallel results obtained with the present model.

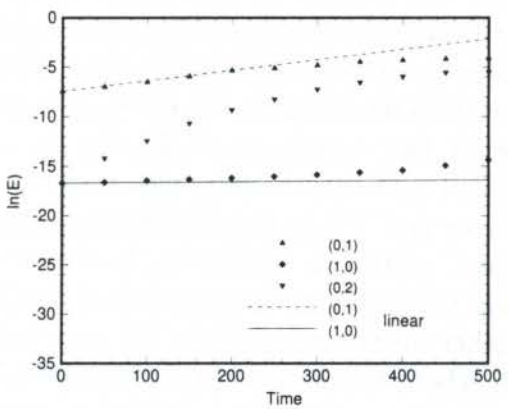

Figure 6: GV/2D-TS interaction. Temporal, parallel results from Malik and Godil (1990).

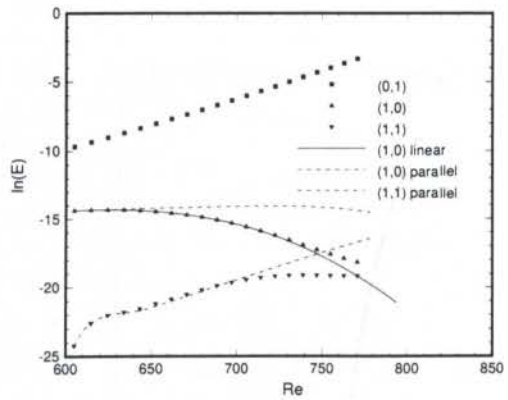

Figure 7: GV/2D-TS interaction. Spatial, nonparallel results.

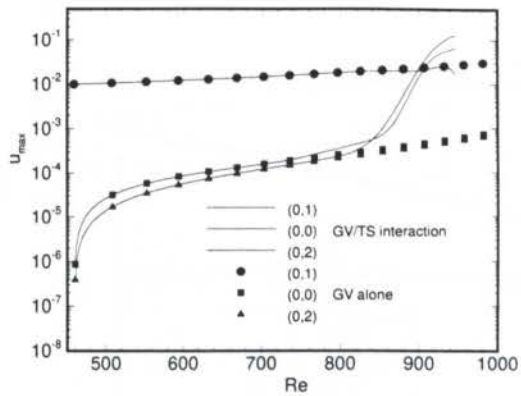

Figure 8: GV/2D-TS wave interaction. Comparison with nonlinear GV.

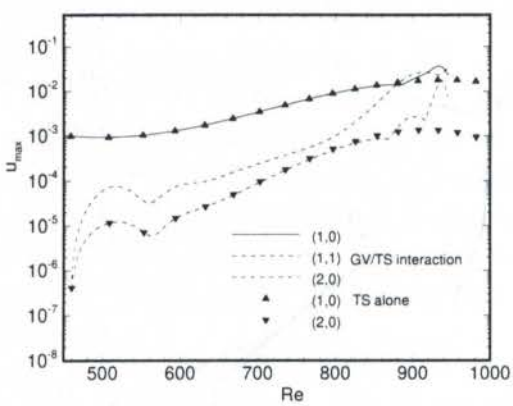

Figure 9: GV/2D-TS wave interaction. Comparison with nonlinear TS wave.

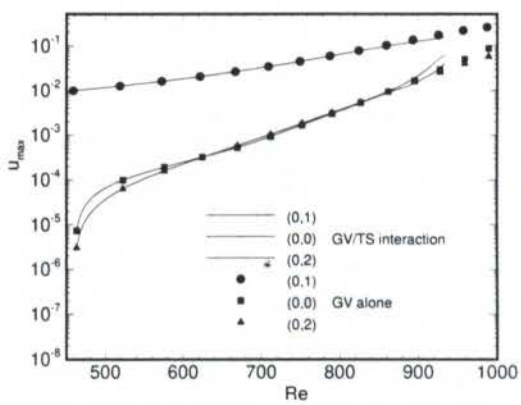

Figure 10: GV/2D-TS wave interaction. Comparison with nonlinear GV.

tial/nonparallel model and spatial/parallel model show a strong influence of nonparallel effects.

3.2 Higher TS Wave Amplitudes

The conclusion that the GV always dominate the transition is valid if the TS waves do not grow to amplitude levels of the same order of magnitude as the vortices. Figures 8 and 9 show results for unstable TS waves interacting with GV defined by the following initial conditions: $Re = 459$, $F = 75$, $Go = 1.5$, $\beta = 0.25$, $\epsilon_{GV} = 1\%$, $\epsilon_{TS} = 0.1\%$. The growth of the TS waves with respect to the growth of the GV results in amplitude levels for vortices and TS waves of the same order of magnitude. In this case the nonlinear interaction results in significant nonlinear effects on the development of the vortices, especially through the development of the MFD and mode (0,2). This result also shows that neither the vortices nor the TS wave dominate the transition and that the streamwise position where breakdown to turbulence takes place is anticipated. The same TS wave would not have such strong nonlinear effect on stronger vortices. To show that, the previous test case is repeated with the same initial conditions and TS wave, but with initial vortices with higher Görtler number ($Go = 3.5$). Figure 10 shows the development

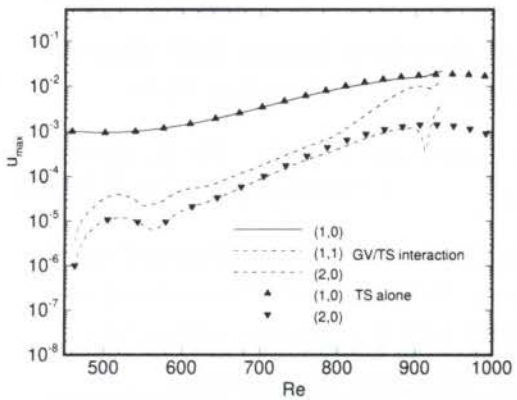

Figure 11: GV/2D-TS wave interaction and the nonlinear development of a TS wave without interaction.

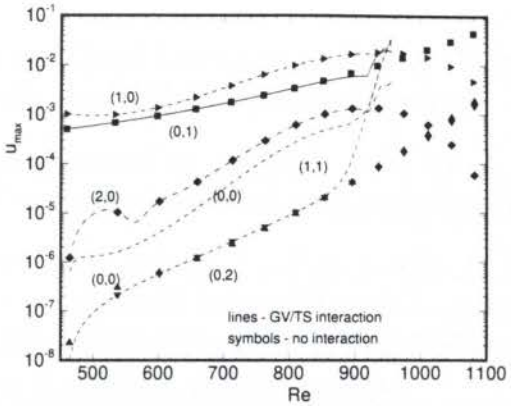

Figure 12: GV/2D-TS wave interaction and the nonlinear development of a TS wave without interaction.

of the GV fundamental mode (0,1), the MFD, and the first harmonic (0,2). Unlike the results for $Go = 1.5$ the MFD and mode (0,2) are less sensitive to the presence of the TS wave. Figure 11 shows the development of the TS wave, its first harmonic and of the oblique wave. It shows that the stronger vortices results in weaker effect on the TS wave when compared to the results presented in figure 9, but the stronger nonlinear interaction anticipates the streamwise position where the computation fails to converge. To show that the main controlling parameter is not the Görtler number but the relative strength of the vortices and TS wave, the same test case was run with initial vortices amplitudes reduced to $\epsilon_{GV} = 0.05\%$. Figure 12 shows that the stronger nonlinear effect on the development of the first harmonic (0,2) is similar to the effect found for $Go = 1.5$. The mean flow distortion is also stronger than the MFD due to the vortices and after approximately $R\epsilon = 900$ the MFD starts to grow at a higher rate due to the nonlinear interaction.

4. CONCLUSIONS

Previous results on GV/TS wave interaction obtained with local models and temporal/parallel models are reassessed with a spatial/nonparallel model and the conclusions obtained with those models were verified. New results considering the effect of the TS waves on the development of the vortices are presented. The conclusions obtained with local and temporal/parallel models are shown to be valid, but the assumption of parallel mean flow does influence the results. The development of the disturbances in the streamwise direction, and the ability of the model to take into consideration the nonlinear effects of the TS waves on the vortices, shows the importance of the initial amplitudes and growth rates as controlling parameters in GV/TS wave interaction. For TS wave amplitudes of the same order of magnitude as the vortices amplitudes, strong nonlinear interaction takes place and the breakdown to turbulence is anticipated.

5. ACKNOWLEDGEMENT

We would like to acknowlege the financial support from FAPESP for the presentation of this article at the XIV COBEM.

6. REFERENCES

Bertolotti, F. P. 1991. *Linear and Nonlinear Stability of Boundary Layers With Streamwise Varying Properties.* Ph.D. thesis, Ohio State University, Columbus, Ohio.

Floryan, J. M. 1980. *Stability of boundary layer flows over curved walls.* Ph.D. thesis, Virginia Polytechnic Institute and State University.

Joslin, R. D., Street, C. L., & Chang, C.-L. 1993. Spatial Direct Numerical Simulation of Boundary-Layer Transition Mechanics: Validation of PSE Theory. *Theoretical and Computational Fluid Dynamics*, **4**(6), 271–288.

Kachanov, Y. K., & Levchenko, V. Y. 1984. The Resonant Interaction of Disturbances at Laminar-Turbulent Transition in a Boundary Layer. *J. Fluid Mechanics*, **138**, 209–247.

Malik, M. R. 1986. Wave Interaction in Three-Dimensional Boundary Layers. *AIAA Paper 86-1129.*

Malik, M. R., & Godil, A. A. 1990. Nonlinear Development of Görtler and Crossflow Vortices and Görtler/ Tollmien-Schlichting Wave Interaction. *NTIS, AD A 221 107.*

Malik, M. R., & Hussaini, M. Y. 1990. Numerical Simulation of Interactions Between Görtler Vortices and Tollmien-Schlichting Waves. *J. Fluid Mechanics*, **210**, 183–199.

Malik, M. R., & Li, F. 1993. Transition Studies for Swept Wing Flows Using PSE. *AIAA Paper, 93-0077.*

Mendonça, M. T. 1997. *Numerical Analysis of Görtler Vortices /Tollmien-Schlichting Waves Interaction With a Spatial Nonparallel Model.* Ph.D. thesis, The Pennsylvania State University.

Nayfeh, A. H. 1981. Effect of Streamwise Vortices on Tollmien-Schlichting Waves. *J. Fluid Mechanics*, **107**, 441–453.

Nayfeh, A. H., & Al-Maaitah, A. 1988. Influence of Streamwise Vortices on Tollmien-Schlichting Waves. *Physics of Fluids*, **31**(12), 3543–3549.

Swearing, J. D., & Blackwelder, R. F. 1987. The Growth and Breakdown of Streamwise Vortices in the Presence of a Wall. *J. Fluid Mechanics*, **182**, 255–290.

XIV Brazilian Congress of Mechanical Engineering
Obeid Plaza Hotel Convention Center - Bauru - SP/Brazil
December 08-12th 1997

PAPER CODE: COB1011

AN ASSESSMENT OF THE RNG k-ε TURBULENCE MODEL APPLIED TO THE FLOW IN RADIAL DIFFUSERS

CÉSAR J. DESCHAMPS, ÁLVARO T. PRATA & ROGÉRIO T.S. FERREIRA
Department of Mechanical Engineering
Federal University of Santa Catarina
88040-900 - Florianópolis - SC - Brazil - E-mail: deschamps@emc.ufsc.br

Abstract

The present work considers the turbulent flow modeling in a radial diffuser with axial feeding using the RNG k-ε model of Orzag et al. (1993). The model has been recommended for flows including features such as stagnation and recirculation regions, curvature and adverse pressure gradients (all of them are not properly taken into account by the standard k-ε model). The flow through radial diffusers possesses all the aforementioned flow features and therefore is a good test case to further assess the RNG k-ε model. Numerical results of pressure distribution along the surface of one of the diffuser disks are compared to experimental data and show that the RNG k-ε model can predict quite successfully the flow.

Keywords

Turbulence modeling, radial diffusers, valves.

1. INTRODUCTION

The flow through radial diffuser has an special importance in the analysis of several technological applications such as hermetic compressors valves and air thrust bearings. The flow geometry considered in this work is composed of two concentric parallel circular disks. Figure 1(a) gives a three dimensional schematic view of the flow whereas Figure 1(b) shows the flow geometric parameters. The flow supplied by the orifice of diameter d and length e, placed in one of the disks, occurs initially in the axial direction and after being deflected by the frontal disk of diameter D becomes radial.

The few works dealing with turbulent flow for this geometry focused on pure radial flow between parallel disks without considering the inlet region (Ervin et al., 1989 and Tabatabai and Pollard, 1987). Apparently, the first attempt to solve the turbulent flow in axial feeding radial diffusers was made by Deschamps et al. (1988). There it was found that the high Reynolds number k-ε model used to close the averaged Navier-Stokes equations was unable to predict the flow, even with the inclusion of correction terms to take into account effects such as flow curvature on turbulence. The poor performance of the numerical solution was attributed to the wall-functions used in the model, which could not render an adequate

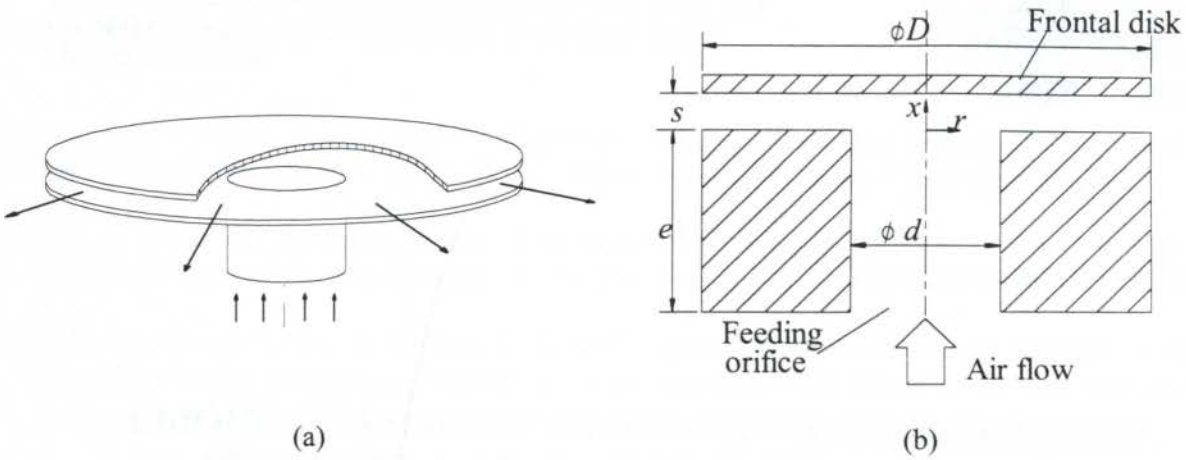

Figure 1: Flow geometry.

computational grid refinement in the wall vicinity. This was confirmed later when a low Reynolds number k-ε model, which does not use wall-functions, produced better flow predictions (Deschamps et al. 1989). Nevertheless, even for this model there were significant differences between experiments and computations that were thought to be originated by an overprediction of turbulence levels by the model.

Recently, Orzag et al. (1993) have proposed a new form of k-ε model. According to those authors, the new model, hereafter called RNG k-ε model, is capable of predicting flows including features such as stagnation and recirculation regions, curvature and adverse pressure gradients (all of them are not properly taken into account by the standard k-ε model). Since all the aforementioned flow features are present in the radial diffuser, such a flow geometry is therefore an excellent test case to further assess the RNG k-ε model performance.

2. TURBULENCE MODELING

2.1 Preliminary Remarks

The Boussinesq's hypothesis that turbulence is proportional to the velocity gradient, with a 'turbulent' or 'eddy' viscosity ν_t acting like the viscous stresses, is written in the following generalized form:

$$\overline{u_i u_j} = -\nu_t \left[\frac{\partial U_i}{\partial x_j} + \frac{\partial U_j}{\partial x_i} \right] + \frac{2}{3}\delta_{ij}\, k \qquad (1)$$

where δ_{ij} is the Kronecker delta and the kinetic energy of the turbulent motion, k, is defined as $k = (\overline{u_i u_i})/2$.

The Averaged Navier-Stokes equations for isothermal and incompressible flow, with the Reynolds stresses modeled via equation (1), can be written as:

Mass conservation,

$$\frac{\partial U_i}{\partial x_i} = 0 \quad , \qquad (2)$$

Momentum conservation for the x_i component of velocity,

$$U_j \frac{\partial U_i}{\partial x_j} = -\frac{1}{\rho}\frac{\partial}{\partial x_i}\left(p+\frac{2}{3}\rho k\right)+\frac{\partial}{\partial x_j}\left[\nu_{eff}\left(\frac{\partial U_i}{\partial x_j}+\frac{\partial U_j}{\partial x_i}\right)\right], \qquad (3)$$

where the effective viscosity $\nu_{eff}(=\nu+\nu_t)$ takes into account the 'turbulent' or 'eddy' viscosity ν_t and the molecular viscosity ν. By far the most common choice for calculating of ν_t has been that in terms of the turbulence kinetic energy k and its rate of dissipation ε, i.e.

$$\nu_t = c_\mu \frac{k^2}{\varepsilon}, \qquad (4)$$

Models of this kind were extensively tested and refined by Launder and Spalding (1974). Due to its robustness, economy and acceptable results for a considerable amount of flows the k-ε model version of Launder and Spalding (1974) has been the most used model for numerical predictions of industrial flow. However, it is acknowledged its deficiencies in situations of streamline curvature, acceleration and separation; all of them are present in the case of flow through radial diffusers. For instance, turbulence is very sensitive to small amounts of curvature of the streamlines. The effects of curvature tend to increase the magnitude of the turbulence shear stress where the angular momentum of the flow decreases in the direction of the radius of curvature and to decrease when the angular momentum increases with the radius. Such effects cannot be accounted for neither by the k-ε model nor by any other turbulence model based on the simple eddy-viscosity hypothesis of equation (1) unless some ad hoc extra term is introduced into the model equations. Another well known problem associated with the k-ε model is the excessive high levels of length scales returned by the dissipation rate ε equation in the presence of adverse pressure gradients. As a consequence, skin friction coefficients are usually found overpredicted and the calculated flow to remain attached where experimental data indicate separation occurs (Rodi and Scheuerer, 1986). Several proposals have been put forward to remedy the problem. Hanjalic and Launder (1980), proposed an extra term to the dissipation equation in a attempt to reduce turbulence levels in the case of adverse pressure gradient. Despite the term did work well for the flow Hanjalic and Launder were interested in, some authors have recently reported that in some situations the use of the term acts exactly contrary to what is required and returns unrealistic flow patterns. A more recent proposal, this time by Yap (1987), consisted also in adding an extra term to the dissipation equation to bring the predicted value of dissipation ε in the near-wall region towards a value giving the length scale according to $\ell_\varepsilon=2.44\ y$. A dramatic improvement in the numerical results have been observed in some flow cases, such as the impinging jet, but in many others the term has produced just a marginal benefit.

2.2 The RNG k-ε Model

The new form of k-ε model proposed by Orzag et al (1993) was derived according to mathematical techniques called Renormalization Group (RNG) methods. The novelty of the so called RNG k-ε model, compared to the standard k-ε model, is that constants and functions are evaluated by the theory and not by empiricism and that the model can be applied to the near-wall region without recourse to wall-functions or ad-hoc function in the transport equations of the turbulence quantities. Due to this mathematical foundation, compared to the semi-

empirical approaches adopted in the standard k-ε, Orzag and his colleagues argue that the RNG k-ε model offers a wider range of applicability. Some examples of flows where the RNG k-ε model has been seen to return better predictions than the standard k-ε are those including flow separation, streamline curvature and flow stagnation.

The effective viscosity in the RNG k-ε model is given by

$$\nu_{eff} = \nu\left[1+\sqrt{\frac{C_\mu}{\nu}}\frac{k}{\sqrt{\varepsilon}}\right]^2 , \tag{5}$$

which is valid across the full range of flow conditions from low to high Reynolds numbers. The turbulence kinetic energy k and its dissipation ε appearing in (5) are obtained from the following transport equations:

$$U_j\frac{\partial k}{\partial x_j} = \frac{\partial}{\partial x_j}\left[\alpha\nu_t\frac{\partial k}{\partial x_j}\right] + \nu_t S^2 - \varepsilon , \tag{6}$$

$$U_j\frac{\partial \varepsilon}{\partial x_j} = \frac{\partial}{\partial x_j}\left[\alpha\nu_t\frac{\partial \varepsilon}{\partial x_j}\right] + C_{\varepsilon 1}\frac{\varepsilon}{k}\nu_t S^2 - C_{\varepsilon 2}\frac{\varepsilon^2}{k} - R , \tag{7}$$

where the values of $C_{\varepsilon 1}$ e $C_{\varepsilon 2}$ are equal to 1.42 and 1.68; respectively. The inverse Prandtl number α for turbulent transport is given by the following relationship:

$$\left|\frac{\alpha-1.3929}{\alpha_o-1.3929}\right|^{0.6321}\left|\frac{\alpha+2.3929}{\alpha_o+2.3929}\right|^{0.3679} = \frac{\nu}{\nu_{eff}} , \tag{8}$$

with α_o = 1.0. Equations (6) and (7) resemble those of the standard k-ε model. The main difference brought about by the RNG k-ε model is the rate of strain term, R, given by

$$R = \frac{C_\mu\eta^3\left(1-\eta/\eta_0\right)}{1+\beta\eta^3}\frac{\varepsilon^2}{k} , \tag{9}$$

where $\eta = Sk/\varepsilon$, $\eta_o \approx 4.38$ and $S^2 = 2S_{ij}S_{ij}$ is the modulus of the rate-of-strain tensor. According to Orzag et al. (1993), in regions of small strain rate, the term R acts to increase ν_{eff}, but even though the values of ν_{eff} are still typically smaller than values that would be returned by the standard k-ε model in the same situation. On the other hand, in regions of high strain rate the sign of R becomes negative and ν_{eff} is considerably reduced. It is precisely this reduction in ν_{eff} verified in the RNG k-ε that offers a considerable improvement in the prediction of separation flow regions. Finally, the reduced value of $C_{\varepsilon 2}$ (=1.62) in the RNG k-ε model, compared to the value of 1.9 in the standard k-ε turbulence model, contributes also to produce smaller values of ν_{eff}, by decreasing the rate of dissipation of ε.

2.3 Boundary Conditions

For the inlet boundary it was recognized by Ferreira et al. (1989) that, as the flows exits the feeding orifice of area A_f and enters the diffuser of area A_d, the strong reduction of the passage area given by the ratio $A_d / A_f = 4$ s/d brings about a strong flow acceleration next to the orifice wall for small values of *s/d*. Due to this phenomenon the inflow velocity profile plays no role in the solution of the flow field in the diffuser and hence the inlet boundary condition was specified as $U = \overline{U}_{in}$ and $V = 0$. Despite no information is available for the turbulence kinetic energy, numerical tests indicated that when the level of the turbulence intensity was changed from 3% to 6% no significant change was observed in the predicted flow. Therefore, a value of 3% of turbulence intensity was used in the calculation of all results shown in this work. Finally, the distribution of the dissipation rate was estimated based on the assumption of equilibrium boundary layer, that is, $\varepsilon = \lambda^{3/4} k^{3/2} / \ell_m$, where $\ell_m = 0.07\, d/2$ and $\lambda = 0.09$.

At the solid boundaries the condition of non-slip and impermeable boundary condition were imposed for the velocity components, that is, $U = V = 0$, with calculations being extended up to the walls across the viscous sublayer. For the turbulence quantities k and ε rather than prescribing a condition at the walls, they were calculated in the control volume adjacent to the wall following a non-equilibrium wall-function.

In the plane of symmetry, the normal velocity and the normal gradients of all other quantities were set to zero.

At the outlet boundary two different procedures had to be adopted. For the diameter relation $D/d = 3$ the diffuser exit is far enough downstream that a condition of parabolic flow can be assumed; that is $\partial U/\partial r = \partial(rV)/\partial r = \partial k/\partial r = \partial \varepsilon / \partial r = 0$. Yet for the much smaller relation $D/d = 1.45$ also considered in the present work this is not possible and, therefore, the solution domain had to be extended well beyond the diffuser exit and the atmospheric pressure verified in the experiment set to the outlet. The boundary condition for k in this case was fixed according to a turbulence intensity of 3% whereas the dissipation rate was estimated based on the same assumption of equilibrium boundary layer used at the inlet, as indicated above. Given the wall jet characteristic of the flow exiting the diffuser it is expected that any eventual inaccuracy of the above outlet conditions will not have a significant impact on the numerical solution.

3. NUMERICAL METHODOLOGY

The numerical solution of the governing equations was performed using the commercial computational fluid dynamics code FLUENT, version 4.2 (1993). In this code the conservation equations for mass, momentum and turbulence quantities are solved using the finite volume discretization method. The resulting system of algebraic equations is solved using the Gauss Seidel method and the SIMPLE algorithm.

In the finite volume method, schemes used to evaluate property transport by convection across each volume surface can be of primary importance to the accuracy of the numerical results. In the present work, the QUICK scheme was adopted in the solution of momentum equations, yielding a second order accuracy for the interpolated values. Yet, for the transport equations of turbulence quantities the PLDS was adopted since the unboundness of the QUICK scheme usually introduces serious numerical instabilities. Nevertheless, there is some evidence in the literature that in the case of these equations the source terms are dominant, with the convective terms playing only a secondary role.

4. RESULTS

Results for the flow depicted in Figure 1 are presented for two gaps s/d (=0.05 and 0.07) and two diameter ratios D/d (=1.45 and 3). In all situations the Reynolds number was the maximum value that could be obtained in the experimental setup, that is $Re \approx 20{,}000$. Due to limitation of space no detail on the experimental setup will be given here but can be found in Ferreira et al. (1989).

Sensitivity tests of the numerical results with respect to grid refinement and boundary conditions were fully addressed before the assessment of the turbulence model, which was carried out through comparisons between experimental data and computations.

Figures 2 and 3 show the radial pressure distribution on the frontal disk surface according to experimental data and computations for a variety of flow geometries. In all situations there is a plateau of pressure on the central part of the curve ($r/d < 0.5$), as verified previously in the laminar flow by Ferreira et al. (1989). Similar to the laminar flow is also the sharp drop of pressure at the radial position $r/d \approx 0.5$, which is due to the change of the flow direction. For the outer part of the curve ($r/d > 0.5$) the pressure level never recovers a positive value, a situation which is also verified in the laminar flow for combinations of large gaps and Reynolds number.

The good agreement between experiments and computations seen in Figures 2 and 3 provides some confidence in the turbulence model capability. It should however be mentioned that the success of the RNG k-ε model verified here is not certain in the case of three-dimensional flows. For instance, the appearance of turbulence driven secondary flow in non-circular ducts for fully developed flow, which occurs due to the difference between the normal Reynolds stresses, can only be predicted by an anisotropic model. Of course, neither the standard k-ε model nor the RNG k-ε model fall in this category and would therefore predict equal normal stresses.

The next step in the analysis was to generate numerical simulations for flow situations not included in the experimental investigation. In Figure 4 dimensionless stream-function contours are plotted at the entrance of the diffuser for Re = 10,000 and 40,000. The flow is seen to separate at $r/d \approx 0.5$ and to reattach downwards inside the diffuser. As the Reynolds number is increased to 40,000, the flow inertia becomes stronger, the separation region is increased and the recirculating zone moves into the valve exit. Since the flow passage area at the entrance of the diffuser has a direct effect on the pressure distribution shown in Figures 2 and 3 it is agreed that any successful turbulence model must correctly predict these separated flow regions.

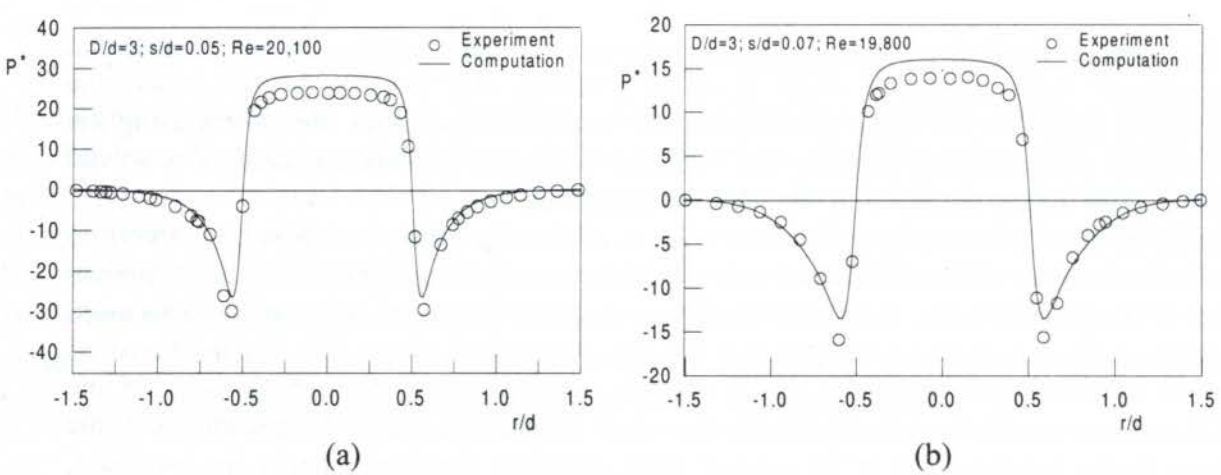

Figure 2: Numerical results and experimental data of pressure distribution; D/d=3.

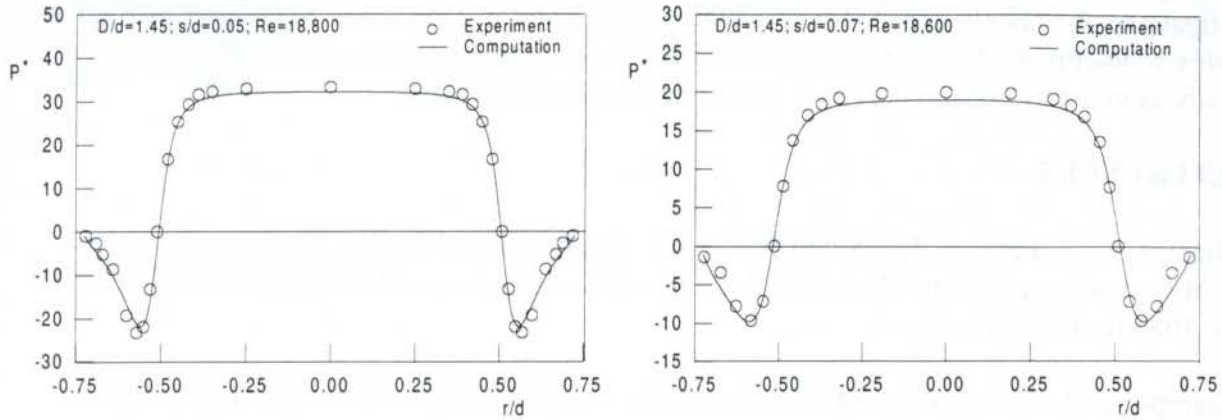

Figure 3: Numerical results and experimental data of pressure distribution; D/d=1.45.

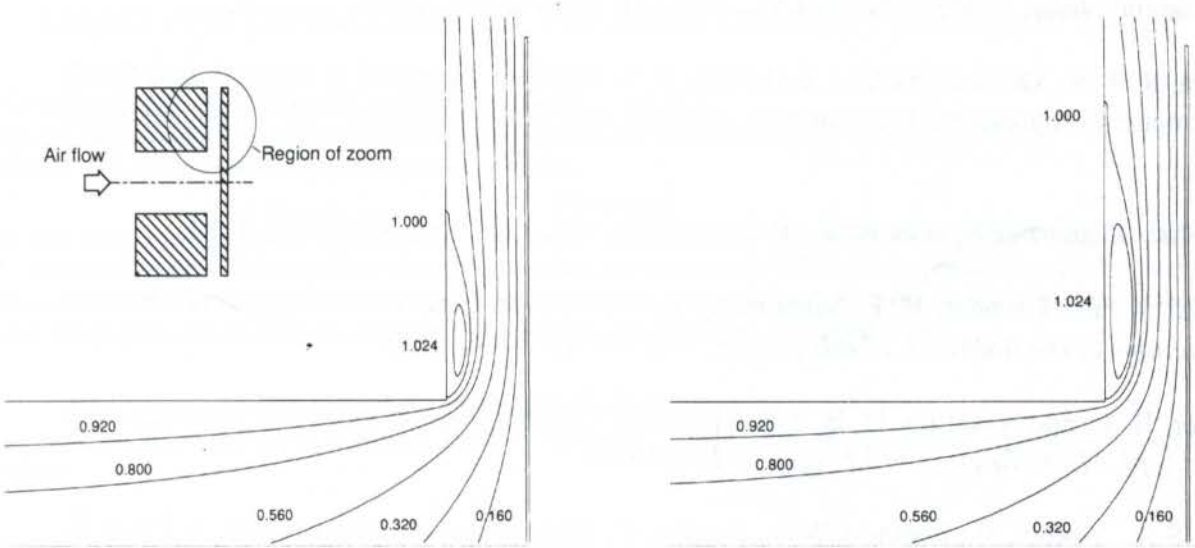

(a) s/d=0.05; Re=10,000 (b) s/d=0.05; Re=40,000

Figure 4 - Stream-function contours at the diffuser entrance, D/d=1.45.

A further step in the assessment of the RNG k-ε model would require comparisons between numerical predictions and experimental data of mean velocities and turbulence quantities. Another possible analysis could also be carried out by comparing predictions of such quantities given by the RNG k-ε model and the standard k-ε model. Both steps in the model assessment will be considered in a future work.

5. CONCLUSIONS

The present work has presented an assessment of the RNG k-ε turbulence model applied to the incompressible turbulent and isothermal flow in radial diffuser. The flow was analyzed for different geometric parameters and in all situations the RNG k-ε model was found to reproduce well the experimental results. Despite the success observed in the present

investigation, one should proceed with caution when applying the RNG k-ε model in more complex problems, such as three dimensional flows. In these situations, the concept of eddy viscosity as given by equation (1) may prove to be totally inadequate.

6. REFERENCES

Deschamps, C. J., Ferreira, R.T.S and Prata, A.T. Application of the k-ε Model to Turbulent Flow in Compressor Valves, *Proc. 2nd Brazilian Thermal Science Meeting*, pp.259-262, São Paulo, 1988 (in Portuguese).

Deschamps, C. J., Prata, A.T. and Ferreira, R.T.S. Turbulent Flow Modeling in Presence of Stagnation, Recirculation, Acceleration and Adverse Pressure Gradient, *Proc. X Brazilian Congress of Mechanical Engineering*, v. I, pp. 57-60, Rio de Janeiro, 1989 (in Portuguese).

Ervin, J. S., Suryanarayana, N. V. and Ng, H. C. Radial, Turbulent Flow of a Fluid Between Two Coaxial Disks, *ASME J. Fluids Eng.*, Vol. 111, pp. 378-383, 1989.

Ferreira, R. T. S., Deschamps, C. J. and Prata, A. T. Pressure Distribution Along Valve Reeds of Hermetic Compressors, *Experimental Thermal and Fluid Sciences*, Vol. 2, pp. 201-207, 1989.

Fluent Inc., Centerra Resource Park, 10 Cavendish Court, Lebanon, NH 03766, 1993.

Hanjalic, K. and Launder, B. E. Sensitizing the Dissipation Equation to Irrotational Strains, *Transactions of the ASME–J. Fluids Engng.*, Vol.102, pp.34-40, 1980.

Launder, B. E. and Spalding, D. B. The Numerical Computation of Turbulent Flows, *Comp. Meths. Appl. Mech. Engng.*, Vol.3, pp.269-289, 1974.

Orzag, S.A., Yakhot, V., Flannery,W.S., Boysan, F., Choudhury, D., Marusewski, J., Patel, B. Renormalization Group Modeling and Turbulence Simulations. In So, R.M.C., Speziale, C.G., Launder, B.E. (editors), *Near-Wall Turbulent Flows*. Elsevier Science Publisher, 1993.

Rodi, W. and Scheuerer, G. Scrutinizing the k-ε Turbulence Model under Adverse Pressure Gradient Conditions, *Transactions of the ASME–J. Fluids Engng.*, Vol. 108, pp. 174-179, 1986.

Tabatabai, M. and Pollard, A., Turbulence in Radial Flow between Parallel Disks at Medium and Low Reynolds Numbers, *J. Fluid Mechanics*, Vol. 185, pp. 483-502, 1987.

Yap, C. R. Turbulent Heat and Momentum Transfer in Recirculating and Impinging Flows, Ph.D. Thesis, UMIST, England, 1987.

XIV Brazilian Congress of Mechanical Engineering
Obeid Plaza Hotel Convention Center - Bauru - SP/Brazil
December 08-12th 1997

PAPER CODE: COB1215

UM MODELO ALGÉBRICO DE TURBULÊNCIA PARA ESCOAMENTO EM CAMADA LIMITE SUJEITA A UM FORTE GRADIENTE DE PRESSÃO ADVERSO/*AN ALGEBRAIC TURBULENCE MODEL FOR STRONG ADVERSE PRESSURE GRADIENT BOUNDARY LAYER*

DANIEL O DE ALMEIDA CRUZ & NELSON KUWAHARA
Grupo de Turbomáquinas Departamento de Engenharia Mecânica do Centro Tecnológico. UFPa
66075-900 Belém-PA-Brasil -gtdem@amazon.com.br

Abstract

In this work a new algebraic turbulence closure model, developed for adverse pressure gradient boundary layer, is presented. A new characteristic velocity which takes into account the effects of the pressure gradient as well as the influence of the shear stress at the wall is also presented. A comparison with experimental data clearly shows that the proposed model is superior to the Cebeci-Smith one in treating separating flows.

Palavras-chave/*keywords*

Camada Limite, turbulência, separação, modelo algébrico / *boundary layer, turbulence, separation, algebraic model.*

1. INTRODUÇÃO

A representação adequada de escoamentos turbulentos permanece ainda hoje como um dos principais desafios à ciência da mecânica dos fluidos. Embora nos últimos anos grandes progressos tenham sido alcançados com o desenvolvimento de vários modelos de turbulência (Hanjalic, 1994), uma descrição de baixo custo, de grande precisão, de implementação simples e que seja geral o suficiente para resolver a maioria dos problemas encontrados em engenharia ainda permanece desconhecida. Nesse contexto, o aprimoramento de modelos de turbulência, que embora não sendo de grande generalidade descrevam de maneira simples e acurada certos tipos específicos de escoamento, torna-se necessário. Dentre estes fenômenos podemos citar o escoamento na camada limite turbulenta o qual, devido a grande freqüência com que ocorre em problemas de engenharia, deve ser tratado de forma precisa e barata. Atualmente um grande número de modelos de turbulência para a região da camada limite pode ser encontrada na literatura (Pletcher, 1978), muitos deles considerando inclusive os casos em que a camada limite está sujeita à interação com outros fatores como onda de choque (Johnson e King,1985), transpiração e fortes gradientes de pressão.

Dentre esses modelos podemos destacar o de Cebeci-Smith.(1969) como estando entre os mais populares, principalmente devido a sua simplicidade de implementação, embora em muitos casos não descreva de maneira adequada o escoamento, principalmente na região de

separação da camada limite. Essa discrepância ocorre basicamente devido ao fato de os parâmetros utilizados nesse modelo não são adequados para a região de separação, como acontece com a velocidade de fricção a qual é nula no ponto de descolamento.

No presente trabalho um novo modelo algébrico de turbulência será proposto para escoamentos em camada limite sujeita a um gradiente de pressão adverso. Nesse novo modelo uma nova velocidade característica, a qual considera os efeitos do gradiente de pressão além dos efeitos causados pela tensão de cisalhamento na parede será utilizada (Cruz e Silva Freire, 1994). Essa nova velocidade não se anula quando a tensão na parede tende a zero, podendo ser utilizada inclusive na região de separação. A obtenção dessa velocidade é feita através de um equação polinomial cúbica, não exigindo a solução de uma equação diferencial adicional, o que torna o modelo proposto pelo menos tão prático quanto os mais simples encontradas na literatura. Será mostrado, através de uma comparação com dados experimentais, que o modelo proposto reproduz com precisão alguns parâmetros de interesse no escoamento, como a tensão na parede, principalmente na região de separação. Os resultados obtidos serão comparados com o modelo de Cebeci-Smith (1969) apresentando um melhor desempenho.

2. O MODELO DE TURBULÊNCIA

O escoamento na região da camada limite turbulenta é descrito pela seguinte equação :

$$u\frac{\partial u}{\partial x}+v\frac{\partial u}{\partial y}=-\frac{1}{\rho}\frac{dP}{dx}+\frac{\partial \tau_{xy}}{\partial x}+\nu\frac{\partial^2 u}{\partial y^2}\,, \qquad (1)$$

$$\frac{\partial u}{\partial x}+\frac{\partial v}{\partial y}=0\,, \qquad (2)$$

onde, u e v são velocidades na direção de x e y respectivamente, P é a pressão, ν é a viscosidade cinemática e ρ representa a massa especifica do fluído.

As equações acima estão sujeitas as seguintes condições de contorno :

$u(x,0)=0,\ v(x,0)=0$
$u(x_1,y)=u_1(y)$
$u(x,y)\rightarrow U_\infty(x),$ com $y\rightarrow\infty$

O termo τ_{xy} representa a tensão turbulenta a qual será modelada de formas diferentes dependendo da região do escoamento.

Na região próxima à parede o modelo de comprimento de mistura será empregado juntamente com o termo de amortecimento proposto por Van Driest(1956), como pode ser visto na equação abaixo :

$$\tau_{xyl}=\kappa^2 y^2\left(1-exp(-\frac{y^+}{A})\right)^2\frac{\partial u}{\partial y}\left|\frac{\partial u}{\partial y}\right|\,, \qquad (3)$$

onde : $y^+ = \frac{yu_R}{\nu}$, $A = 26$ e $\kappa = 0{,}41$

A principal diferença entre a equação (3) e o modelo de Cebeci-Smith(1969) está na velocidade u_R que é definida como sendo a maior raiz real da seguinte equação :

$$u_R{}^3 - \frac{\tau_w}{\rho} u_R - \frac{\nu}{\rho}\frac{dP}{dx} = 0 \ , \qquad (4)$$

onde τ_w representa a tensão de cisalhamento na parede. Longe do ponto de descolamento temos que $\frac{\nu}{\rho}\frac{dP}{dx} << \frac{\tau_w}{\rho}$. Neste caso a velocidade u_R é dada por :

$$u_R \cong \sqrt{\frac{\tau_w}{\rho}} = u_\tau \ ,$$

ou seja a velocidade de fricção clássica, isto indica que a equação (3) reduz-se a modelagem de Cebeci-Smith(1969) longe da região de separação. Próximo ao ponto de descolamento onde $\tau_w = 0$ temos que o valor de u_R torna-se:

$$u_R \cong \sqrt{\frac{\nu}{\rho}\frac{dP}{dx}} \ .$$

Isto mostra que o valor de u_R não se anula mesmo quando a tensão na parede tende a zero, sugerindo que esta velocidade pode ser utilizada como referência ao longo de todo o escoamento próximo à parede, tanto na região de separação quanto longe desta.

Na região externa da camada limite a tensão turbulenta assume a seguinte forma :

$$\tau_{xy2} = 0{,}44\delta^* u_R \frac{\partial u}{\partial y} \ . \qquad (5)$$

Nesse caso a velocidade de referência u_R foi utilizada no lugar da velocidade do escoamento externo para compor a viscosidade turbulenta ($\nu_{t2} = 0{,}44\delta^* u_R$) juntamente com a espessura de deslocamento (δ^*). A expressão (5) difere da relação proposta por Clauser(1956) para a região externa da camada limite, a qual é empregada em muitos modelos de turbulência, basicamente pela introdução da velocidade u_R, essa diferença contudo não se mostra muito evidente longe do ponto de descolamento, ficando mais importante na região de separação, como será mostrado.

Uma descrição da tensão turbulenta válida nas regiões interna e externa da camada limite pode ser obtida da seguinte forma (Johnson e King,1985):

$$\tau_{xy} = \nu_{tur} \frac{\partial u}{\partial y} \ , \qquad (6)$$

$$\nu_{tur} = \nu_{t2}(1 - exp[(-\frac{\nu_{t1}}{\nu_{t2}})^{2,0}])^{\frac{1}{2}} , \qquad (7)$$

$$\nu_{t1} = \kappa^2 y^2 (1 - exp(-\frac{y^+}{A}))^2 \frac{\partial u}{\partial y} , \qquad (8)$$

$$\nu_{t2} = 0{,}44\delta^* u_R . \qquad (9)$$

3. COMPARAÇÃO DOS RESULTADOS

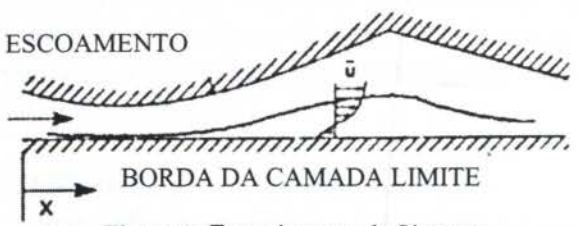

Figura 1: Experimento de Simpson.

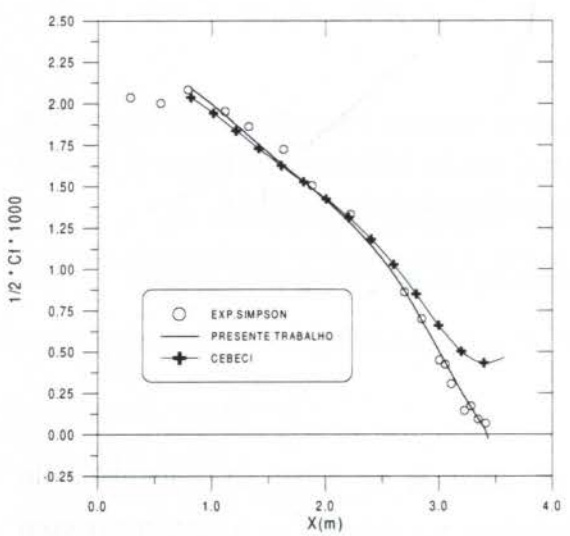

Figura 2: Comparação do coeficiente de atrito na parede.

As equações (1) e (2) foram resolvidas numericamente através do método de diferenças finitas utilizando a transformação de variáveis proposta por Cebeci-Smith(1969). Os resultados foram comparados com os dados de Simpson *et al.*(1981), para camada limite submetida a um gradiente de pressão do tipo presente no escoamento sobre aerofólios, (ver figura (1)).A técnica de anemometria a laser foi empregada na determinação dos parâmetros cacterísticos desse tipo de escoamento na região de separação. Os valores experimentais obtidos para a velocidade no escoamento fora da camada limite, foram utilizados como condição de contorno a cada passo da variável x.

A figura (2) mostra uma comparação entre o coeficiente de atrito na parede experimental e o calculado numericamente. Os resultados previstos pela presente teoria e pelo modelo de Cebeci-Smith.(1969) são apresentados. Fica claro que a presente formulação reproduz com precisão os valores de C_f (coeficiente de atrito = $\tau_w / (1/2)\rho U_\infty^2$) tanto longe quanto próximo da região de separação, prevendo inclusive a localização do ponto de descolamento, o mesmo não acontece com o modelo de Cebeci-Smith(1969) o qual, embora apresente um comportamento adequado longe do ponto de descolamento, mostra grandes discrepâncias com relação aos dados experimentais quando valor de C_f tende a zero, não prevendo a existência da separação de camada limite.
Na figura (3) aparecem os valores da espessura de deslocamento da camada limite. Ambos os modelos são capazes de prever com precisão os dados experimentais longe do ponto de

$$l = \kappa y[1 - exp(-y^+ \frac{1}{26}(1 + \frac{\nu}{\rho}\frac{dP}{dx}\frac{11,8}{u_\tau^3})^{\frac{1}{2}}] \ . \qquad (12)$$

No limite quando $u_\tau \to 0$ $(u_\tau = \sqrt{\frac{\tau_w}{\rho}})$ e com $\frac{dP}{dx} \neq 0$ temos que :

$$l = \kappa y \ . \qquad (13)$$

Ou seja, o termo de amortecimento ("damping") desaparece próximo ao ponto de descolamento, provocando um crescimento na tensão turbulenta calculada próximo à parede. Isto contribui para um aumento da tensão de cisalhamento na parede (τ_w) tornando menos provável que ocorra separação. O mesmo não acontece com a equação (3) devido à utilização de u_R como velocidade característica.

2 - Na região externa da camada limite a viscosidade turbulenta é, em muitos modelos, obtida através da formulação de Clauser (1956), que foi deduzida para escoamentos sobre uma placa plana e é mostrada abaixo.

$$\nu_{t2} = 0,016 U_\infty \delta^* \ . \qquad (14)$$

Próximo ao ponto de descolamento a espessura de deslocamento da camada limite (δ^*) apresenta um acentuado crescimento, ver figura (3). Como a ordem de grandeza da velocidade no escoamento externo U_∞ não se altera, a viscosidade turbulenta também cresce provocando um aumento na tensão de cisalhamento na parede. Na presente formulação esse efeito é anulado pela utilização da velocidade u_R, que apresenta o seu valor mínimo no ponto de descolamento, evitando que a viscosidade turbulenta na região externa sofra grandes modificações com o crescimento da espessura de deslocamento.

5. CONCLUSÃO

No presente trabalho um novo modelo algébrico de turbulência para escoamentos em camada limite sujeita a um forte gradiente de pressão adverso foi apresentado. Nesse modelo uma velocidade característica do fenômeno (u_R). Foi introduzida. foi mostrado que a presente formulação reproduz melhor os dados experimentais que o modelo de Cebeci-Smith(1969) na região de separação da camada limite. Cabe ressaltar que a presente formulação é de implementação tão simples quanto a dos demais modelos algébricos existentes na literatura, não necessitando que nenhuma equação diferencial adicional seja resolvida.

Em futuros trabalhos uma comparação mais detalhada com um número maior de dados experimentais e com outros modelos de turbulência será feita.

6. AGRADECIMENTOS

Os autores agradecem a A.P. Silva Freire pelas proveitosas discussões durante a realização deste trabalho e ao CNPq pelo apoio financeiro.

7. BIBLIOGRAFIA

Cebeci, T. & Smith, A.M.O. A Finite-difference Solution of the Incompressible Turbulent Boundary Layer Equations by an Eddy Viscosity Concept, in (Coles and Hirst) Computation of Turbulent Boundary Layers - *1968 AFOSK-IFP-Stanford Conference*. Stanford University Press, Stanford, Calif. 1969.

Clauser, F.H. The Turbulent Boundary Layer, in Advances in Applied Mechanics, Academic Press, New York, 1956.

Cruz, D.O.A. & Silva Freire, A.P. The Asymptotic Structure of the Thermal Turbulent Boundary Layer Near a Separation Point, *Proceedings of the International Symposium on Turbulence Heat and Mass Transfer*, Portugal, 1994.

Hanjalic, K. Advanced Turbulence Closure Models: a View of Current Status and Future Prospects, *International Journal Heat and Fluid Flow*, vol.15, pp.178-203, 1994.

Johnson, D.A. & King, L.S. A Mathematically Simple Turbulence Closure Model for Attached and Separated Turbulent Boundary Layers, *AIAA Journal*, vol.23, pp.1684-1692, 1985.

Pletcher, R.H. Prediction of Incompressible Turbulent Separating Flow, *Journal of Fluids Engineering*, vol. 100, pp.427-433, 1978.

Simpson, R.L.,Chew, Y.-T. & Shivaprasad, B.G. The Structure of a Separating Turbulent Boundary Layer. Part 1. Mean Flow and Reynolds Stresses, *Journal of Fluid Mechanics*, vol.113, pp. 23-51, 1981.

Van Driest, E.R. On Turbulent Flow near a Wall, *J. Aerosp. Sci.*, vol.23, pp. 1007-1012, 1956.

XIV Brazilian Congress of Mechanical Engineering
Obeid Plaza Hotel Convention Center - Bauru - SP/Brazil
December 08-12th 1997

PAPER CODE: COB1221

O PROBLEMA DA CAMADA LIMITE PARA AVALIAÇÃO DE PERDAS: UMA METODOLOGIA ALTERNATIVA / *BOUNDARY-LAYER FORMULATION FOR LOSS CALCULATION: AN ALTERNATIVE APPROACH*

DANIEL O. ALMEIDA. CRUZ E ANDRÉ.L. AMARANTE MESQUITA
Grupo de Turbomáquinas, Depto. de Engenharia Mecânica, Universidade Federal do Pará
66075-900 Belém-PA-Brasil - E:mail: gtdem@amazon.com.br

Abstract

In this work, an alternative approach for loss calculation in external flows is proposed, by applying Kaplun limits to the Navier-Stokes equations, obtaining a generalized boundary layer formulation. It is shown that this alternative formulation can be reduced into a 'quasi similar' differential equation that can be solved as an ordinary one. Numerical solutions of this equation are presented showing that it contains the Falkner - Skan equation as a particular case.

Palavras-chave / *Keywords*

Análise assintótica, camada limite, similaridade / asymptotic analysis, *boundary-layer, similarity,*

1. INTRODUÇÃO

O cálculo da perda de energia em escoamentos ao redor de corpos é de fundamental importância para o projeto hidrodinâmico de equipamentos, como por exemplo no dimensionamento de turbomáquinas. A análise completa desse fenômeno somente pode ser realizada através da utilização das equações gerais de Navier-Stokes juntamente com um modelo de turbulência adequado (Amano *et al.*, 1996). Essa metodologia contudo, resulta em elevados custos computacionais, não sendo indicada para as etapas iniciais de um projeto de turbomáquina.

Nesse caso, a utilização de formulações simplificadas, como a representada pelas equações da camada limite, aparecer como uma alternativa viável para o tratamento desse problema.

A formulação de camada limite necessita contudo, em muitos problemas, da solução do escoamento potencial (não viscoso) para que possa ser implementada. Além disso em alguns casos, como no ponto de descolamento, ocorre o aparecimento de singularidades que somente podem ser removidas através de um processo interativo viscoso - não viscoso

No presente trabalho, a técnica da variável intermediária desenvolvida por Kaplun (1967) será utilizado para fornecer uma formulação alternativa para os escoamentos na camada

limite, na qual a clássica divisão do escoamento em duas regiões distintas desaparece, sendo portanto desnecessários os processos de interação viscosa - não viscosa.

Será mostrado que, para o caso laminar, esta formulação apresenta a propriedade de "quase similaridade", significando que, através de uma mudança adequada de variável, o conjunto de equações diferenciais parciais pode ser resolvido como uma equação diferencial ordinária de modo semelhante ao conceito de similaridade aplicado à camada limite clássica. Entretanto na presente formulação, essa equação é de quarta ordem, diferente da equação de Falkner-Skan (terceira ordem) obtida através da formulação de camada limite clássica (Schilichting, 1967).

A solução numérica dessa equação "quase similar" será mostrada para o caso de escoamentos sujeitos a diversos tipos de gradientes de pressão adversos, assim como para o escoamento sobre uma placa plana.

2. ANÁLISE DAS EQUAÇÕES DE CONSERVAÇÃO

Será aplicado o método da variável intermediária às equações de Navier-Stokes para o caso laminar, incompressível e estacionário. Para maiores detalhes sobre o método ver Silva Freire (1996) e Cruz e Silva Freire (1994). Sejam as equações do conservação:

$$u\frac{\partial u}{\partial x} + v\frac{\partial u}{\partial y} = -\frac{\partial P}{\partial x} + \frac{1}{R_e}\left[\frac{\partial^2 u}{\partial x^2} + \frac{\partial^2 u}{\partial y^2}\right] \quad , \tag{1}$$

$$u\frac{\partial v}{\partial x} + v\frac{\partial v}{\partial y} = -\frac{\partial P}{\partial y} + \frac{1}{R_e}\left[\frac{\partial^2 v}{\partial x^2} + \frac{\partial^2 v}{\partial y^2}\right] \quad , \tag{2}$$

$$\frac{\partial u}{\partial x} + \frac{\partial v}{\partial y} = 0. \tag{3}$$

Nas equações acima u e v foram adimensionalizadas por uma velocidade U_∞ característica do escoamento não perturbado, x e y por um comprimento característico do fenômeno L e $P= (P_1 - P_0)/\rho\, U_\infty^2$, onde P_0 é uma pressão de referência O parâmetro R_e representa o número de Reynolds. Estudaremos agora o caso do escoamento sobre uma superfície sólida onde $R_e >> 1$, para isso definiremos agora as seguintes variáveis intermediárias:

$$\hat{y} = y / \hat{\eta}(\varepsilon) \ , \tag{4}$$

$$\hat{v} = v / \hat{\eta}(\varepsilon) . \tag{5}$$

onde $\varepsilon = 1/R_e$.

Substituindo as equações (4) e (5) nas equações (1), (2) e (3) tem-se:

$$u\frac{\partial u}{\partial x} + \hat{v}\frac{\partial u}{\partial \hat{y}} = -\frac{\partial P}{\partial x} + \frac{1}{R_e}\left[\frac{\partial^2 u}{\partial x^2} + \frac{1}{\hat{\eta}^2}\frac{\partial^2 u}{\partial \hat{y}^2}\right] \tag{6}$$

$$\hat{\eta}u\frac{\partial \hat{v}}{\partial x} + \hat{\eta}\,\hat{v}\frac{\partial \hat{v}}{\partial \hat{y}} = -\frac{1}{\hat{\eta}}\frac{\partial P}{\partial \hat{y}} + \frac{1}{R_e}\left[\hat{\eta}\frac{\partial^2 \hat{v}}{\partial x^2} + \frac{1}{\hat{\eta}}\frac{\partial^2 \hat{v}}{\partial \hat{y}^2}\right] \tag{7}$$

$$\frac{\partial u}{\partial x} + \frac{\partial \hat{v}}{\partial \hat{y}} = 0 \tag{9}$$

Variando o parâmetro $\hat{\eta}$ tem-se no limite com $\varepsilon \to 0$ o seguinte conjunto de equações:

Conservação de quantidade de movimento na direção de x:

$$O(\hat{\eta}) = O(1): u\frac{\partial u}{\partial x} + \hat{v}\frac{\partial u}{\partial \hat{y}} = -\frac{\partial P}{\partial x} \tag{10}$$

$$O(1) > O(\hat{\eta}) > O(\sqrt{\varepsilon}): u\frac{\partial u}{\partial x} + \hat{v}\frac{\partial u}{\partial \hat{y}} = -\frac{\partial P}{\partial x} \tag{11}$$

$$O(\hat{\eta}) = O(\sqrt{\varepsilon}): u\frac{\partial u}{\partial x} + \hat{v}\frac{\partial u}{\partial \hat{y}} = -\frac{\partial P}{\partial x} + \frac{\partial^2 u}{\partial \hat{y}^2} \tag{12}$$

$$O(\hat{\eta}) < O(\sqrt{\varepsilon}): \frac{\partial^2 u}{\partial \hat{y}^2} = 0 \tag{13}$$

Conservação da quantidade de movimento na direção de y:

$$O(\hat{\eta}) = O(1): u\frac{\partial \hat{v}}{\partial x} + \hat{v}\frac{\partial \hat{v}}{\partial \hat{y}} = -\frac{\partial P}{\partial \hat{y}} \tag{14}$$

$$O(\hat{\eta}) < O(1): \frac{\partial P}{\partial \hat{y}} = 0 \tag{15}$$

Observando-se os conjuntos de equações (10)-(13) e (14)-(15) pode-se notar a existência de duas equações que se destacam das demais. As relações (12) e (14) são chamadas 'equações principais' desses conjuntos, pois contém todas as demais equações sem estarem contidas em nenhuma delas. Deste modo, no limite com $\varepsilon \to 0$, o sistema (1)-(3) pode ser reduzido, em uma primeira ordem de aproximação, ao seguinte sistema de equações

$$u\frac{\partial u}{\partial x} + v\frac{\partial u}{\partial y} = -\frac{\partial P}{\partial x} + \frac{1}{R_e}\frac{\partial^2 u}{\partial y^2} \tag{16}$$

$$u\frac{\partial v}{\partial x} + v\frac{\partial v}{\partial y} = -\frac{\partial P}{\partial y} \tag{17}$$

$$\frac{\partial u}{\partial x} + \frac{\partial v}{\partial y} = 0 \tag{18}$$

O sistema de equações acima foi obtido considerando-se simultaneamente es equações principais dos conjuntos (10)-(13) e (14)-(15). De outro modo, caso fosse considerada somente a equação principal do conjunto (10)-(13) ($O(\hat{\eta})=O(\sqrt{\varepsilon})$), a aproximação de camada limite seria obtida (equações (12) e (15)). No caso da equação principal ser a do conjunto (14)-(15) então o sistema de Euler surgiria ($O(\hat{\eta})=O(1)$, equações (14) e (10)). Ambos os casos acima citados estão contidos no sistema (16)-(18), o qual representa um "sistema principal" das equações (10)-(13) e (14)-(15). A solução das equações de Navier-Stokes corresponde assintoticamente à solução das equações (16)-(18) no limite quando $\varepsilon = 1/R_e \to 0$.

As equações (16)-(18) representam uma aproximação de ordem superior às equações de camada limite e imediatamente inferior à aproximação de camada fina - TSL ("Thin Shear Layer), a qual contém ainda um termo difusivo na equação do momento na direção y.

O modelo proposto pode ser aplicado à problemas de escoamento em torno de aerofólios, constituindo-se uma solução superior ao procedimento da interação viscosa - não viscosa. Por exemplo, Pulliam e Steger (1985) utilizando a aproximação TSL resolvem o escoamento turbulento ($Re = 5{,}7 \times 10^6$) em torno de um aerofólio, apresentando resultados satisfatórios. Isto sugere que a formulação apresentada deva também fornecer uma solução adequada para problemas semelhantes.

Como primeiro resultado numérico da aplicação do modelo proposto, este trabalho resolve o problema de placa plana, com e sem gradiente de pressão, utilizando um método quase-similar , o qual é apresentado a seguir.

3. A EQUAÇÃO QUASE-SIMILAR

Utilizando-se a definição de função corrente pode-se rescrever o sistema de equações (16)-(18) de seguinte forma:

$$\frac{\partial \psi}{\partial y}\frac{\partial^3 \psi}{\partial y^2 \partial x} - \frac{\partial \psi}{\partial x}\frac{\partial^3 \psi}{\partial y^3} + \frac{\partial \psi}{\partial y}\frac{\partial^3 \psi}{\partial x^3} - \frac{\partial \psi}{\partial x}\frac{\partial^3 \psi}{\partial x^2 \partial y} = \frac{1}{R_e}\frac{\partial^4 \psi}{\partial y^4} \tag{19}$$

A equação (19) pode ser transformada em uma equação diferencial ordinária através da seguinte mudança de variável:

$$\eta = y\sqrt{\frac{m+1}{2} R_e x^{m-1}} \tag{20}$$

$$\xi = \frac{1}{R_e x^{m+1}} \tag{21}$$

$$\lambda = 1 - \xi \tag{22}$$

$$\psi = \sqrt{\frac{2}{m+1} \frac{1}{R_e} x^{m+1}} F(\eta,\lambda) \tag{23}$$

Substituindo-se as equações (20)-(23) em (19) tem-se:

$$\left(\frac{3m-1}{2}\right)F''F' - \left(\frac{m+1}{2}\right)(F'''F + F'''') -$$

$$\left[\frac{1}{R_e x^{m+1}}\right]\left[\left(\frac{m^2-1}{2}\right)\left(\frac{3m-2}{4}\right)F'F + (m-1)\left(2m^2+7m+11\right)\eta F'^2 + m\left(\frac{m-1}{2}\right)^2 \eta^2 F'F'' +\right.$$

$$\left.\left(\frac{m^2-1}{4}\right)\left(\frac{5m-3}{2}\right)\eta F F'' + \eta^2 F F''' \left(\frac{m+1}{2}\right)\left(\frac{m-1}{2}\right)^2\right] = 0 \tag{24}$$

onde $F^{(n)} = \dfrac{\partial^n F}{\partial \eta^n}$.

A equação acima está sujeita às seguintes condições de contorno:

$$F(0,\lambda) = 0 \tag{25}$$

$$F'(0,\lambda) = 0 \tag{26}$$

$$F'(\eta_0,\lambda) = 1 \qquad (27)$$

$$F''(\eta_0,\lambda) = 0 \qquad (28)$$

Onde η_0 é um valor de η considerado no infinito. As equações (25)-(27) representam as condições de contorno clássicas aplicadas aos escoamentos em camada limite com similaridade. A condição adicional (equação (28)), caracteriza o comportamento assintótico dos perfis de velocidade em $\eta=\eta_0$. As transformações (20)-(23) são semelhantes às transformações aplicadas no caso da equação de camada limite para se obter a relação de Falkner-Skan. A equação (24) não pode ser considerada como uma equação similar, para o caso geral, pois não possui todos os seus coeficientes constantes. Isto contudo não impede que essa equação possa ser resolvida como uma equação diferencial ordinária, pois todas as suas derivadas estão relacionadas a apenas uma variável. As derivadas com relação a λ foram desprezadas por somente serem relevantes para $O(\lambda)=O(1)$, caso este aqui não considerado de forma análoga ao procedimento clássico de camada limite.

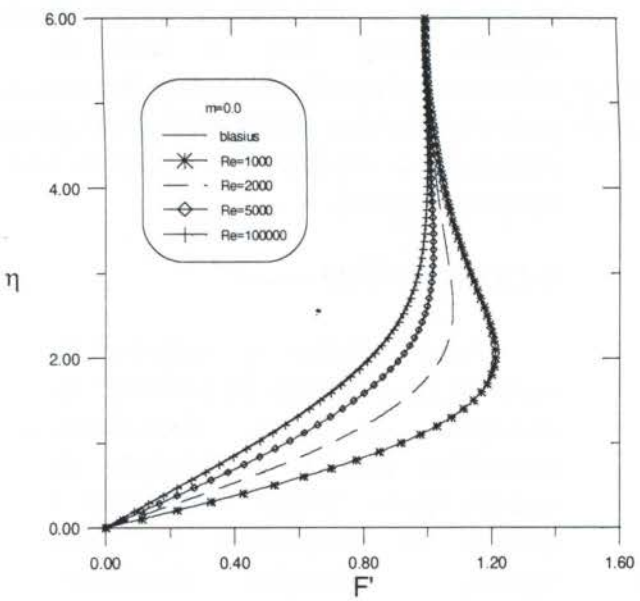

Figura 1: Perfis de velocidade para m = 0

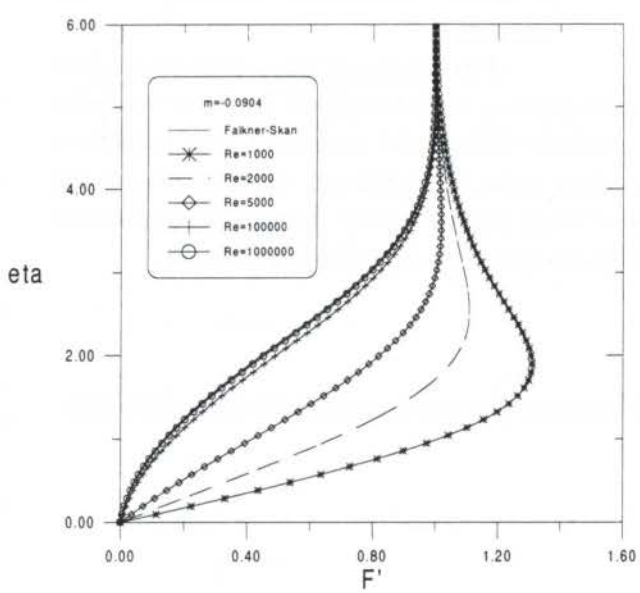

Figura 2: Perfis de velocidade m = -0,0904

A equação de Falkner-Skan, representa um caso particular da expressão (24), como pode ser observado pelos resultados apresentados nas figuras (1) e (2). A figura (1) mostra a solução da equação (24) para m = 0 (placa plana sem gradiente de pressão) e para vários valores de R_e, fixando-se x = 1. Como se pode notar, os perfis de velocidade tendem assintoticamente para a solução de Blasius (Schilichting, 1967). Os demais perfis mostram os estágios intermediários de desenvolvimento do escoamento. Na figura (2) são mostrados os perfis de velocidade para m = -0,0904 (gradiente de pressão adverso), para o qual a solução de Falkner-Skan fornece uma tensão nula na parede. Novamente é observada a tendência assintótica para a solução da equação (24). Para $R_e\to\infty$ ($\xi\to 0$) a solução reproduz o valor nulo para a tensão na parede, como mostrado na figura (3).

Convém ressaltar que o único caso em que a equação (24) apresenta similaridade completa é dado por m = -1, que representa o

escoamento em um canal convergente de paredes retas.

4. ANÁLISE DOS RESULTADOS

As figuras (1)-(3) mostram que a equação de Falkner-Skan representa o limite assintótico da equação (24) para $R_e \to \infty$ ($\xi \to 0$). Os perfis correspondentes aos estágios intermediários apresentam um comportamento similar à solução de Navier-Stokes para a região de entrada hidrodinâmica para o escoamento entre placas.

Um ponto importante a ser destacado é o fato da equação (24) fornecer a posição do ponto de descolamento, como pode ser visto na figura (3) para m = -0,095 e m = -0,1. Isto nos sugere que o sistema (16)-(18) fornece uma descrição mais geral dos escoamentos próximos a uma superfície sólida que a formulação clássica de camada limite. Assim, melhores resultados poderão ser alcançados no cálculo de parâmetros de interesse de engenharia, como por exemplo os coeficientes de arrasto e sustentação.

O modelo apresentado pode ser estendido para o caso do escoamento turbulento, partido das equações médias de Reynolds. A aplicação da técnica da variável intermediária acarreta o surgimento de um termo adicional na equação (16). Para o caso do escoamento instacionário, esta técnica pode ainda ser aplicada com a introdução de um fator de escala para a variável temporal.

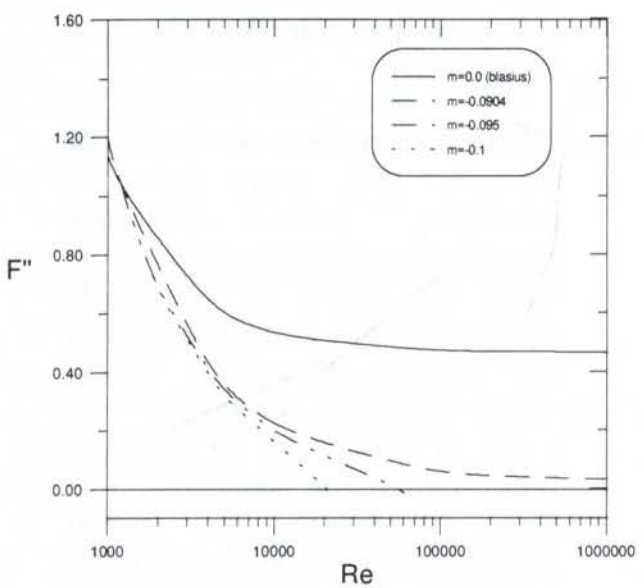

Figura 3: Segunda derivada de F na parede para vários valores de m, x = 1

5. CONCLUSÃO

Neste trabalho o método da variável intermediária foi utilizado na obtenção de uma formulação alternativa para o escoamento de camada limite. Nessa formulação a divisão do escoamento em duas regiões distintas desaparece eliminando assim a necessidade do processo interativo viscoso - não viscoso.

Foi mostrado que, através de uma mudança adequada de variáveis esta formulação alternativa transforma-se em uma equação quase-similar, podendo ser resolvida como uma equação diferencial ordinária, que contém a equação de Falkner-Skan como caso particular. Uma solução numérica dessa equação foi apresentada e comparada com a solução de Falkner-Skan para diversos valores do parâmetro m. É a primeira vez dentro do conhecimento dos autores que essa equação é mostrada.

6. AGRADECIMENTOS

Os autores agradecem ao CNPq pelo apoio financeiro durante a realização deste trabalho.

7. REFERÊNCIAS

Amano, R.S., Rieger, N.F. & Hesler, S. An Aerodynamic Analysis of Turbine Cascade by Using a Second - Order Closure of Turbulence, *Int. J. Heat and Fluid Flow*, vol.17, pp.276-282, 1996.

Cruz, D.O.A. & Silva Freire, A.P. The Asymptotic Structure of the Thermal Turbulent Boundary Layer Near a Separation Point, *Proceeding of the International Symposium on Turbulence Heat and Mass Transfer*, Portugal, 1994.

Kaplun, S. *Fluid Mechanicas and Singular Pertubation*, Academic Press, 1967.

Pulliam, T.H. & Steger, J. L. Recents Improvements in Efficiency Accuracy and Convergence for Implicit Approximate Factorization Algorithms, *AIAA Paper 85-0360, AIAA 23rd Aerospace Sciences Meenting,* 1985.

Schlichting, H. *Boundary Layer Theory*, McGraw-Hill Book Company, New York, 1967.

Silva Freire, A.P. On Kaplun Limits and the Asymptotic Structure of the Turbulent Boundary Layer, *Journal of the Brazilan Society for Mechanical Sciences*, vol.XVIII, n. 1, pp.80-87, 1996.

XIV Brazilian Congress of Mechanical Engineering
Obeid Plaza Hotel Convention Center - Bauru - SP/Brazil
December 08-12th 1997

PAPER CODE: COB1226

COHERENT VORTICES IN SOLID PROPELLANT ROCKET MOTORS USING LARGE-EDDY SIMULATION

JORGE HUGO SILVESTRINI[1,2], PIERRE COMTE[1] & MARCEL LESIEUR[1]

[1] *Equipe Modelisation et Simulation de la Turbulence, Laboratoire des Ecoulements Geophysiques et Industriels, INPG, BP 53X, 38041 Grenoble-Cedex 9, France*

[2] *Departamento de Matematica Pura e Aplicada, UFRGS, Av. Bento Gonçalves 9500, 91501-970 Porto Alegre - RS, Brasil, E-mail: silvestr@mat.ufrgs.br (Present address)*

Abstract

Coherent vortices in solid propellant rockets motors are investigated by numerical experimentation, via full Navier-Stokes solution in two-dimensional configurations and Large-Eddy Simulation (LES) in a three-dimensional one. Particular attention is paid to the vortex shedding phenomena of Kelvin-Helmholtz vortices and their interaction with the chamber's acoustic. The LES results show that streamwise secondary vortices of mixing layers and Dean-Görtler type vortices may be also present in these kind of geometries.

Keywords

Coherent Vortices - Large-Eddy Simulation - Subgrid Scales Models - Solid Propellant Rocket Motors

1. INTRODUCTION

The existence of pressure and thrust oscillations in segmented solid propellant rocket motors, like Ariane V boosters and others motors (U.S. Space Shuttle and Titan SRM) were reported in several studies (Culick, 1966; Brown *et al.*, 1981). In particular, recent studies developed in the Aerodynamics of Segmented Solid Motor program (ASSM), supported by CNES and coordinated by ONERA (CNES-ONERA, 1991), show that these oscillations are provoked by the interaction between the chamber's acoustic and the periodical shedding of vortices. The vortices are induced by the segmented design which employs inhibitor rings to separate adjacent loads of solid propellant (Fig. 1).

In such complex situations, the available linear methods, like acoustic balance, fail to predict motor instability (Lupoglazoff & Vuillot, 1992). Therefore, full unsteady simulations solving the complete Navier-Stokes equations are a real need to assess the level of oscillations. On the other hand, all that is known about numerical simulations in these types of motors, comes from two-dimensional simulations. Hence, the objective of this paper is to present results from full three-dimensional simulations to improve the understanding on the formation and evolution of coherent vortices.

LES consists of simulating explicitly and in three dimensions all motion larger than a certain cut-off scale, accounting for the contribution of the smaller scales through a *sub-*

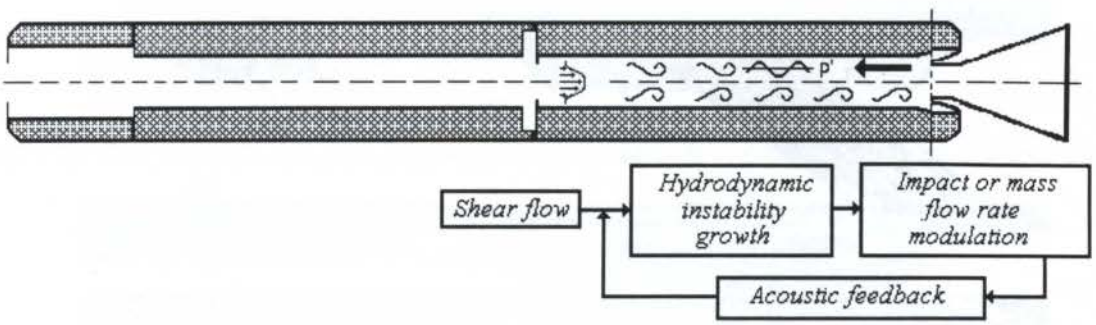

Figure 1: Illustration of possible coupling between hydrodynamics and acoustics modes in a solid propellant rocket motor (from Lupoglazoff & Vuillot, 1992).

grid model. This presupposes that the large scales are more important than the small ones, which is certainly true for turbulence but is more doubtful for combustion, for example. Our calculation strategy was to undertake two-dimensional numerical simulations without artificial (or eddy) viscosity or limiters, and only for a 3D simulation introduce a sub-grid model.

2. LES FOR COMPRESSIBLE FLOWS

The LES formalism for three dimensional Cartesian co-ordinates can be found in Comte *et al.* (1994). The numerical code used can also consider two dimensional axisymmetric geometries and is written in curvilinear co-ordinates. The formalism for cylindrical coordinates is presented in Silvestrini (1996).

2.1. LES governing equations

In Cartesian co-ordinates and after several simplifications, the compressible continuity, momentum and energy equations, in LES sense, can be cast in the conservation-like form :

$$\frac{\partial}{\partial t}\begin{pmatrix} \rho \\ \rho u_1 \\ \rho u_2 \\ \rho u_3 \\ \rho e \end{pmatrix} + \frac{\partial}{\partial x_i}\begin{pmatrix} \rho u_i \\ \rho u_i u_1 + \rho RT\delta_{i1} - (\mu + \rho\nu_t)S_{i1} \\ \rho u_i u_2 + \rho RT\delta_{i2} - (\mu + \rho\nu_t)S_{i2} \\ \rho u_i u_3 + \rho RT\delta_{i3} - (\mu + \rho\nu_t)S_{i3} \\ \rho(e + RT)u_i - \mu S_{ij}u_j - c_p(\mu Pr^{-1} + \rho\nu_t Pr_t^{-1})\dfrac{\partial T}{\partial x_i} \end{pmatrix} = 0 \quad (1)$$

in which ρe stands for the resolved (or filtered) total energy defined, for an ideal gas, by

$$\rho e = \rho\ c_v\ T + \tfrac{1}{2}\rho(u_1^2 + u_2^2 + u_3^2), \quad (2)$$

and

$$S_{ij} = \left[\frac{\partial u_j}{\partial x_i} + \frac{\partial u_i}{\partial x_j} - \frac{2}{3}(\vec{\nabla}.\vec{u})\delta_{ij}\right], \quad (3)$$

is the deviatoric part of the resolved strain-rate tensor. Molecular viscosity is prescribed through Sutherland's law, the molecular conductivity is derived from the constant Prandtl number assumption, and the turbulent diffusivity is calculated assuming a constant turbulent Prandtl number.

2.2. Sub-grid models

To determine eddy viscosities in physical space, the kinetic energy at the smallest resolved scale $\Delta = \pi/k_c$ (k_c being the cut-off wave number) should be measured. One of

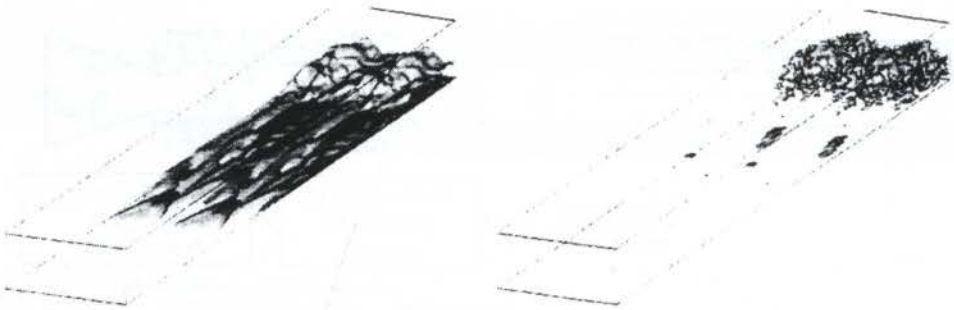

Figure 2: Isosurfaces $\nu_t = 2/3\ \nu$ given by the SF (left) and FSF (right) models in the transitional portion of a spatially-growing boundary layer at Mach 0.5. The same velocity field was used for the two plots (a priori test).

these local spectra is $F_{2\Delta}(\vec{x},t)$, the second-order structure function of the resolved velocity field defined as :

$$F_{2\Delta}(\vec{x},t) = \left\langle \|\vec{u}(\vec{x}+\vec{r},t)) - \vec{u}(\vec{x},t)\|^2 \right\rangle_{\|\vec{r}\|=\Delta}. \tag{4}$$

In the case of infinite Kolmogorov spectra, energy-conservation arguments yield the *structure-function model* (SF model) (Métais & Lesieur, 1992), defined by

$$\nu_t^{SF}(\vec{x},t) = 0.105\ C_K^{-3/2}\ \Delta\ \sqrt{F_{2_\Delta}(\vec{x},t)}, \tag{5}$$

where C_K is the Kolmogorov constant. As it involves velocity increments instead of derivatives, the SF model has the advantage of being defined independently of the numerical scheme used. It is nevertheless not much better for transitional flows than the Smagorinsky model: low wave number velocity fluctuations corresponding to unstable modes yield ν_t's so large that affects the growth rate of weak instabilities like Tollmien-Schlichting waves. One way of remedying this is to apply a high-pass filter onto the resolved velocity field before computing its structure function. With a triply-iterated second-order finite-difference Laplacian filter denoted $\tilde{}$, one finds $\tilde{E}(k)/E(k) \approx 40^3\ (k/k_c)^9$ for all k, almost independently of the velocity field and resolution. With the same formalism used for the structure-function model, this yields the *filtered structure-function model* (FSF model), defined by (Ducros et al, 1996)

$$\nu_t^{FSF}(\vec{x},t) = 0.0014\ C_K^{-3/2}\ \Delta\ \sqrt{\tilde{F}_{2_\Delta}(\vec{x},t)}. \tag{6}$$

Fig. 2 presents a comparison between the SF and FSF models in a transitional boundary layer. While the FSF model do not react to Λ-vortices, the SF model does.

2.3. Numerical scheme and boundary conditions

The system (1) is solved by means of a "two-four" extension of the fully-explicit McCormack scheme devised by Gottlieb and Turkel (1976). The boundary conditions are based on a decomposition into characteristics, in the spirit of Thompson (1987) and Poinsot and Lele (1992). The Riemann invariants of outgoing characteristics are extrapolated, whereas the incoming ones are prescribed (*e.g.* at the inflow boundary).

3. VORTEX SHEDDING IN 2D CONFIGURATIONS

Two 2D simulations undertaken to characterize the vortex shedding phenomenon in solid propellant rocket motors will be described here. All the test used were defined by ONERA (CNES-ONERA, 1991).

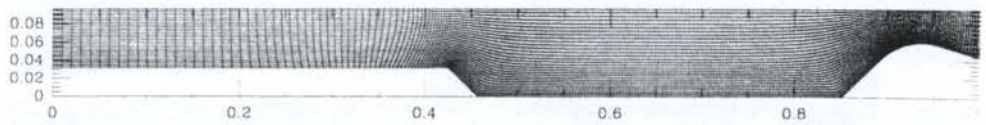

Figure 3: Grid of the C1 test case (length $L = 0.47m$, radius $H = 0.045m$, resolution 318×31 points).

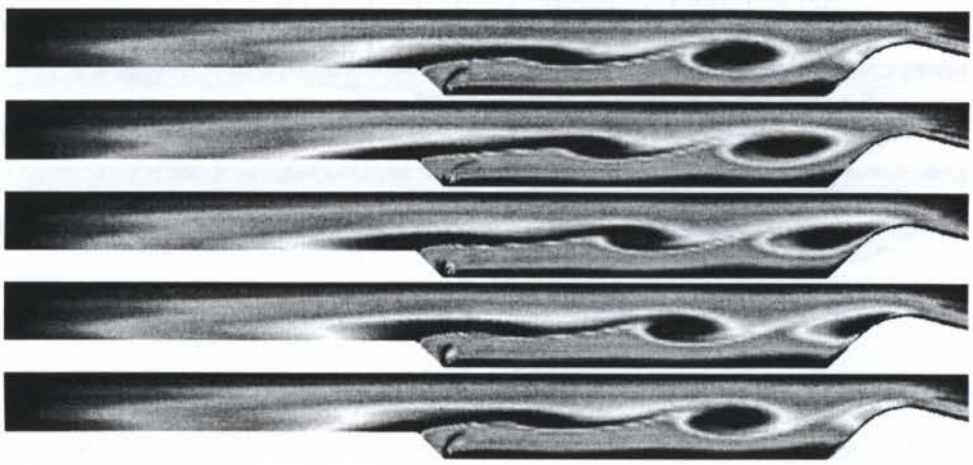

Figure 4: Contour maps of vorticity during one period of the most amplified mode predicts by linear stability theory - C1 test case.

3.1. Test case in a two-dimensional plane configuration

In this first simulation, called C1 test case (see Fig. 3), the geometrical configuration is plane. As for the boundary conditions, the lateral wall is composed by a step of burning propellant at a flame temperature of 3387 K and a mass flow rate, normal to the walls, of 21.2 $kg/s/m^2$. After the step and at the head-end boundary no-slip conditions are prescribed. At the outlet nozzle, free supersonic boundary conditions are imposed and on the upper boundary, symmetry conditions are used. The head-end average pressure is $\overline{p}_{FAV} = 4.66\ bar$.

Recorded signals at the head-end shows a self sustained oscillation with a average head-end pressure of $\overline{p}_{FAV} = 4.62\ bar$ and a fluctuation level of $p'_{FAV} = 0.015\ \overline{p}_{FAV}$. Spectral analysis of the signals shows a peak at a frequency of $f_o = 2670\ Hz$ and its harmonics $2f_o, 3f_o$ and $4f_o$. The frequency f_o is very near to the most amplified mode (the fundamental one) predicted by linear stability theory ($f_{cr} = 2640\ Hz$) (Lupoglazoff & Vuillot, 1992). It corresponds also to the second axial acoustic mode of the chamber.

Fig. 4 shows the temporal evolution of vorticity during one period of the second axial mode ($T_2 = 0,38\ ms$). A shear layer is formed due to the separation of a boundary layer at the end of the horizontal part of the burning surface. The shear layer induces, through Kelvin-Helmholtz (KH) instability, the roll-up of KH vortices (also called primary vortices). When these vortices impact the nozzle, they produce an acoustic reflected wave that excites new KH vortices. After that, the vortices are expelled from the chamber. It is important to note that no perturbation was added to the mean velocity flow, therefore the mixing layer is formed only by the perturbation imposed by the acoustic field.

3.1. Test case in a two-dimensional axisymmetric configuration

The C1x test case was developed from an experimental set-up called LP2/C1-x (Dupays *et al.*, 1995). This test case, with a similar geometry to the C1, is now axisymmetric, with a total length of 0.785 m, a diameter of 0.085 m and the solid propellant step has 0.018 m The mass flow rate is 6.63 $kg/s/m^2$ and the flame temperature is 2224 K. The resolution

Table 1: Measured ($\overline{p}_o$) and calculated ($\overline{p}_c$) mean pressure at four locations - C1x test case

	(i,j)	x (mm)	$\overline{p}_o$ (bar)	$\overline{p}_c$ (bar)
PFAV	1,12	0.0	9.50	9.436
PC 1	240,1	400.0	9.10	9.141
PC 6	457,1	650.0	9.22	9.136
PFAR	523,1	720.5	9.02	9.158

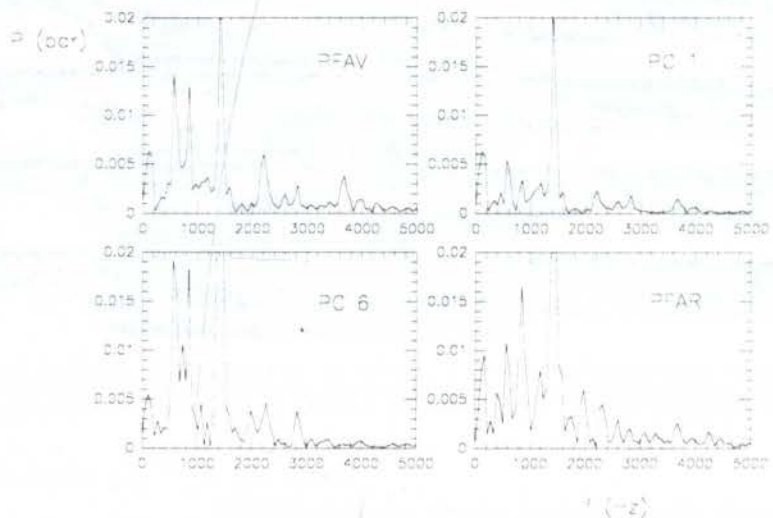

Figure 5: Pressure spectra - C1x test case.

was of 597×49.

Time series of pressure were recorded during 20 ms. In Table 1 the mean pressure is compared with the experimental data. The head-end pressure is very near to the observed value; the error is of 0.67%. The values of calculated pressure are in good agreement with the data. Nevertheless the difference between observed and calculated pressure seems to increase at the nozzle (1.5%). It should be noted that the calculated mean pressure has increased from the location PC6 to the nozzle PFAR, that is, a adverse pressure gradient seems to establish. It would indicate the presence of a zone of recirculation at the entrance of the nozzle. The measured mean pressures, between PC1 and PC6, also show a weak adverse pressure gradient.

The spectral analysis of the time series is presented in Fig. 5. At all the locations, a frequency peak of 1400 Hz is dominant. This frequency is very near to the second axial mode. At the head-end the pressure spectrum is very rich with a second peak at 570 Hz, probably corresponding to the first axial mode. The third (2200 Hz) and fourth (2800 Hz) axial modes are also identifiable in the spectrum. The presence of a peak at 850 Hz at the head-end and near the nozzle is unexpected and we have no explication for the time being.

Fig. 6 shows the evolution of vorticity during two periods of the second axial mode ($2T_2 = 1.33\ ms$). The vortex shedding phenomena is evident from the pictures, while the shear layer is thinner than the C1 test case. The KH vortices are more elliptical than before and pairing (or merging) of these vortices are also observed. In this figure can be seen that the vortex shedding due to Kelvin-Helmholtz instability is established at a frequency of $f_o = 1400\ Hz$. This frequency is present over all the chamber and is determined by the thickness of the shear layer, which is defined by the velocity profile and therefore by the

Figure 6: Vorticity evolution for two periods correspond of the second longitudinal acoustic mode - C1x test case.

motor diameter and the propellant load thickness.

Another interesting issue from Fig. 6 is a recirculation zone at the entrance of the nozzle, which had been suspected in the examination of the calculated mean pressure registered at neighborhood locations (see Table 1). This is probably the cause of the frequency peak at 850 Hz observed at the spectra, but this is still to be confirmed. It is believed that this recirculation, that do not seems to occur in the experiments (there is no measured adverse pressure gradient between PC6 and PFAR in Table 1) is due to the two-dimensional approximation that forced the recirculation to happen.

4. COHERENT VORTICES IN 3D CONFIGURATION

The C1 test case is now analyzed by LES using the FSF model in a simplified 3D plane configuration. For this geometry it was taken a spanwise resolution of 90 points equally spaced over the span $L_z = \pi\ H \approx 0.141\ m$, with periodic boundary conditions. The initial condition consists of the 2D flow shown above (Fig. 4), taken at the end of the simulation, with low-amplitude white noise of amplitude 10^{-4} the speed of sound, at the surface of the propellant on all the velocity components. Without this perturbation, the flow would have remained 2D.

After having reached the steady state, which took 50 hours of Cray 90 at 450 Mflops (corresponding to 8 ms of real time), time series are recorded for 5 ms, that corresponds to $12T_2$. From the sample, it was calculated the mean velocity and pressure at three positions at the chamber: after the step ($i = 170$), before the entrance of the nozzle ($i = 224$) and between the entrance of the nozzle and the sonic troast ($i = 270$) (Fig. 7). The figure shows that small negatives mean streamwise velocities are measured at the low part of the chamber, that seems to denote a low-frequency recirculation zone in this part of the motor. In particular the streamwise component of the velocity field recorded after the step near the lateral wall, shows a oscillating behavior with change of sign (see Silvestrini, 1996). In a rough estimation, during $\frac{1}{3}T_2$ the instantaneous axial velocity is positive while for the other $\frac{2}{3}T_2$, the instantaneous axial velocity is negative. This might explain the measured adverse pressure gradient observed in Table 1.

An "animation" of an isosurface of vorticity norm during one period of the vortex shedding is shown in Fig. 8. The figure is taken at the end of the simulation ($t_o = 13\ ms$). This figure (and also Fig. 9) enables us to identify that, along with the primary Kelvin-Helmholtz vortices, streamwise secondary vortices can also be observed. These streamwise

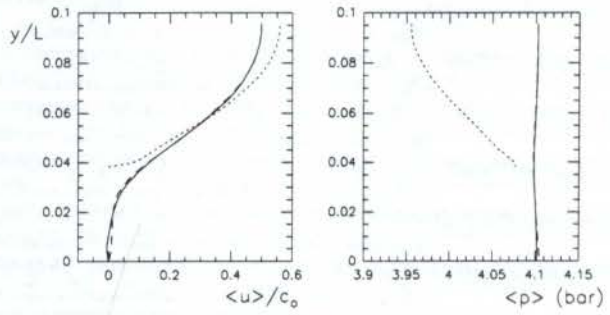

Figure 7: Mean axial velocity profiles (left) and pressure (right) at $i = 170$ (—), 224 (- - -), et 270 (...)

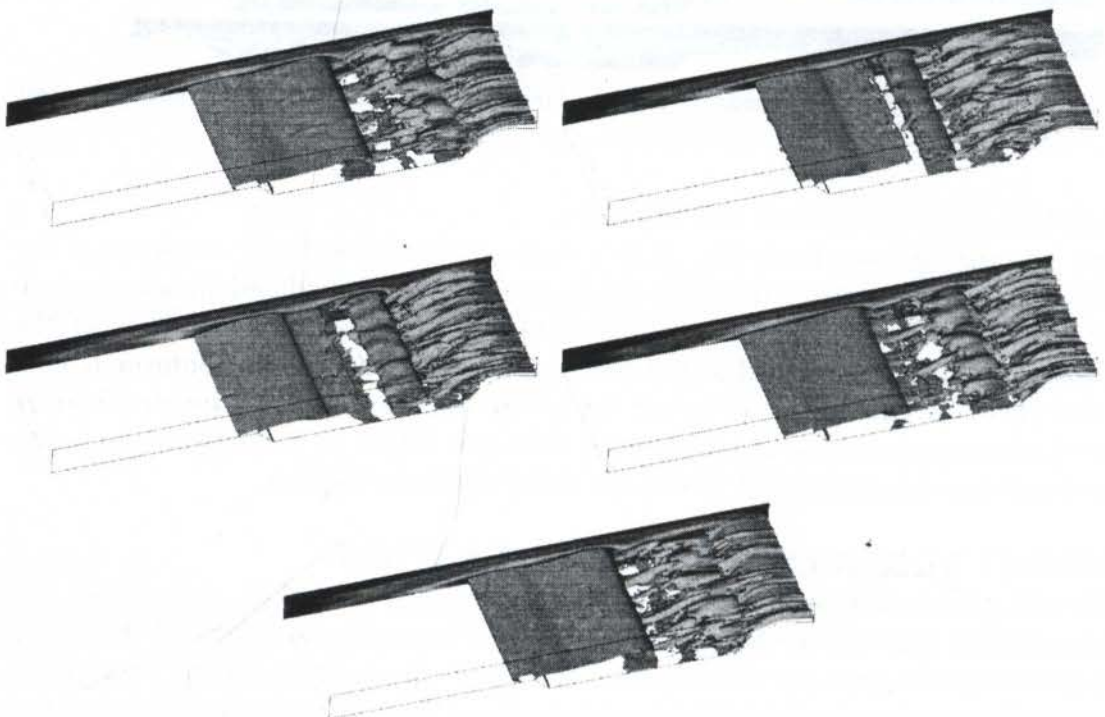

Figure 8: Isosurface of vorticity norm at t_o, $t_o + T_2/4$, $t_o + T_2/2$, $t_o + 3T_2/4$ and $t_o + T_2$, T_2 being the period of the most amplified mode predicted by linear stability theory.

vortices not only appear in between the large Kelvin-Helmholtz billows, as can be seen in mixing layers experiments (Silvestrini, 1996), but also at the wall of the nozzle. In the first case, they are formed by the stretching of vorticity lines due to the strain field imposed by the primary vortices. In the second case, they are likely to result from a Dean-Görtler instability of the detached boundary layer, which re-attaches in the convergent part of the nozzle (Fig. 9).

5. CONCLUSIONS

The coherent vortices of segmented solid propellant rocket motors were assessed by full 2D Navier-Stokes solution and LES. Their strength as a prediction tool for the study of the unsteady characteristic of the vortex shedding phenomenon is to be remarked. The possibility of representing the complex geometries that are common in almost all the "industrial configurations", is another feature which makes LES useful for industrial applications. As far as coherent vortices dynamic is concerned, the LES enables us to assess complex vorticity structures and quantify oscillations levels where experiments may

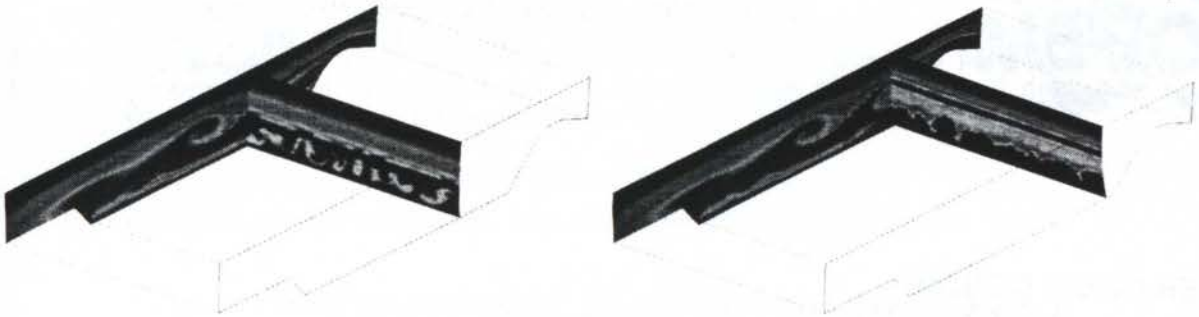

Figure 9: Maps of the entropy field. The left view shows a cross section of the streamwise vortices which connect the KH billows and the right view the Görtler-type vortices.

be impossible. The knowledge of these levels is of crucial importance for the design of the anti-vibration protections of the rocket's control systems.

6. REFERENCES

BROWN, R., DUNLAP, R., YOUNG, S. & WAUGH, R. Vortex shedding as a source of acoustic energy in segmented solid rockets. *J. of Spacecraft and Rockets*, **18**, 217–221, 1981.

CNES-ONERA. Fonctionnement des moteurs à propergol solide segmentés pour lanceurs spatiaux. Rapport CNES, 1992.

COMTE, P., DUCROS, F., SILVESTRINI, J., DAVID, E., LAMBALLAIS, E., MÉTAS, O. & LESIEUR, M. *Simulation des grandes échelles d'écoulements transitionnels*, AGARD 74th Fluid Dynamics Panel Meeting and Symposium on "Application of direct and large eddy simulation to transition and turbulence", 14.1–14.12, Crete, Grèce, 1994

CULICK F.E.C. Acoustic oscillations in solid propellant rocket chambers. *Astronautica Acta*, **12** (2), 113–125, 1966.

DUCROS, F., COMTE, P. & LESIEUR, M. Large-eddy simulations of transition to turbulence in a weakly-compressible boundary layer over a flat plate, submitted to *J. Fluid Mech.*, 1996.

DUPAYS J. & DELFOUR A. Description du montage LP2/C1x et resultats de la campagne d'essais 1994. Rapport technique RT 61/6133 EY, ONERA, 1995.

GOTTLIEB, D., & TURKEL, E. Dissipative two-four methods for time-dependent problems. *Math. Comp.*, **30** (136), 703–723, 1976.

LUPOGLAZOFF, N. & VUILLOT, F. Numerical simulation of vortex shedding phenomenon in 2D test case solid rocket motors. *AIAA Paper 92-0776*, 30th AIAA Aerospace Sciences Meeting Reno, USA, 1992.

MÉTAIS, O. & LESIEUR, M. Spectral large-eddy simulation of isotropic and stably stratified turbulence, *J. Fluid. Mech.* **239**, 157–194, 1992.

POINSOT, T.J. & LELE, S.K. Boundary conditions for direct simulations of compressible viscous reacting flows, *J. Comp. Phys.* **101**, 104–129, 1992.

SILVESTRINI J.H. *Simulations des grandes échelles des zones de mélange; application à la propulsion solide des lanceurs spatiaux*, Thèse INPG, 1996.

THOMPSON, K.W. Time-dependant boundary conditions for hyperbolic systems, *J. Comp. Phys.* **68**, 1–24, 1987.

XIV Brazilian Congress of Mechanical Engineering
Obeid Plaza Hotel Convention Center - Bauru - SP/Brazil
December 08-12th 1997

PAPER CODE: COB246

A NEW LAW OF THE WALL FORMULATION

Atila P. Silva Freire
Mechanical Engineering Program (COPPE/UFRJ),
C.P. 68503, 21945-970 Rio de Janeiro, Brazil.

Abstract

The present work introduces a new expression for the velocity profile in the near wall region of a turbulent boundary layer. The new theory uses asymptotic arguments and considerations of the mixing length type to find a local analytical solution which presents the correct asymptotic behaviour both close to wall in the laminar sub-layer and in the logarithmic region of the flow. Next, heuristic arguments are evoked to add a damping function to the local solution. This function provides an excelent correction to the original analytical solution, furnishing a solution valid for the whole range of inner scales. The resulting expression is compared with ten other different formulations for the problem. The results are also compared with some experimental test cases.

Keywords
Law of the Wall, Turbulence, Boundary Layer.
Palavras Chave
Lei da Parede, Turbulncia, Camada Limite.

1. INTRODUCTION

The turbulent boundary layer has a distinct structure with a number of regions having characteristic properties. This fact was acknowledged very early in this century by several researchers including Prandlt(1910), Taylor(1916) and Von Karman(1939). The important realization at the time was that the flow in the wall region was determined by conditions at the wall, as expressed by the local shear stress and roughness. The region which comprises most of the flow, the outer region, on the other hand, has its properties determined by scales related to the main flow.

Most of the work that followed in this period was aimed at finding a local velocity solution for the wall region. This solution was termed by Coles "the law of the wall". Many expressions describing the velocity behaviour in the near wall viscous region were soon advanced through different methods. Dimensional analysis and experimental evidence established a logarithmic functional form for the velocity profile. This form was subsequently confirmed by mixing length arguments and asymptotic matching considerations. Since this formulation could not be extended down to the wall, several authors found it necessary to use at least two functions to describe adequately the velocity profile. This introduced some inconveniences in the formulation, notably, the necessity of patching the solutions.

As a result, the interest shifted to find a single expression to describe the velocity for the whole range of inner lengths. Several expressions were soon proposed by a host of authors. These expressions were more aesthetical and convenient from a numerical implementation point of view.

The purpose of this work is twofold. First, we review ten different theories advanced in the past for the problem comparing them with the test case data of Andersen et al.(1972) and of Purtell, Klebanoff and Buckley(1981). Second, we propose a new expression for the description of the wall layer flow based on an exact approximated local solution for the equations of motion together with some purely heuristic arguments. The new equation is different from all those presented in literature, and is shown to provide a very good match with the experimental data.

2. THE UNIVERSAL TURBULENT VELOCITY PROFILE

The flow in the wall layer is postulated to depend on the wall shear stress τ_w, on the distance y to the wall, on a roughness parameter K, and on the fluid properties ρ and μ. Then, from dimensional considerations, it follows that the the functional dependence of u on the flow parameters can be expressed as

$$u = f(\tau_w, y, K, \rho, \mu). \tag{1}$$

This equation can be re-written, in a non-dimensional form, as

$$\frac{u}{u_\tau} = g\left(\frac{u_\tau\, y}{\nu}, \frac{u_\tau\, K}{\nu}\right), \tag{2}$$

where $u_\tau (= \sqrt{\tau_w/\rho})$ denotes the wall friction velocity and $\nu = \mu/\rho$.

Equation (2) should be a universal function valid in the whole of the wall viscous region. Using a limit expansion argument, Prandtl(1910) found that in the very vicinity of the wall the following relation applied

$$u^+ = y^+; \quad 0 \le y^+ < 11.5. \tag{3}$$

where $u^+ = u/u_\tau$ and $y^+ = y u_\tau/\nu$.

Further out, in the turbulence dominated part of the wall layer, the commom assumption is that the local shear stress deviates only slightly from the wall value. Hence, we may write

$$\nu_t \frac{\partial u}{\partial y} = \frac{\tau_w}{\rho}, \tag{4}$$

where the eddy viscosity ν_t is a quantity related with the diffusion of momentum between adjacent layers due to turbulence. For diffusion times short with respect to the Lagrangian integral time scale, the diffusion has a linear behaviour with respect to time and the eddy viscosity varies linearly with distance. At a short distance from the wall, the diffusion of particles is restricted to short distances, so that the eddy viscosity may be considered proportional to the distance y. Thus, we write

$$\nu_t = k\, u_\tau\, y, \tag{5}$$

where u_τ is a characteristic velocity and k is a constant.

Integration of equations (4) and (5) gives

$$u^+ = \frac{1}{k} \ln y^+ + A; \quad y^+ > 11.5. \tag{6}$$

where the values of k(=0.4) and of A(= 5.5) were determined experimentally.

This expression was first derived by Taylor in 1916, and subsequently by Prandtl in 1925 and Von Karman in 1930. The last two authors resorted, again, to arguments of the mixing length type.

Later on, in 1939, equation (6) was split into two by Von Karman to cover the regions $5 \le y^+ < 30$ and $30 \le y^+$. In this case, the constants assume respectively the values (k, A) = (0.2,-3.05) and (k, A) = (0.4,5.5).

In fact, expression (6) can be obtained without introduction of a closure condition. Using overlap arguments of the asymptotic type, Millikan(1939) obtained the logarithmic law; thus, he only needed to resort to assumptions of a general nature, without any considerations about the detais of the turbulence to find expression (6). This result set the logarithmic law as a definitive "truth" in the theory of turbulence.

The law has been widely used to test new theories, calibrate experimental apparatus, and validate computer codes, having become one of the great paradigms of turbulence theory. Validated by a large number of experimental data, the law has become a bench mark result to which all simulations of wall flow have to conform to. Evidence in favour of the law is, therefore, strong. Some authors, however, have placed the law under a severe scrutiny, claiming the velocity profile to be power-like, and not logarithmic-like!

In fact, the derivation of both laws is equally consistent and rigorous. However, they are based on entirely different assumptions. Both derivations start from similarity and asymptotic considerations. The log-law is obtained from the assumption that for

sufficiently large *local* Reynolds number and sufficiently large *flow* Reynolds number, the dependence of the velocity gradient on the molecular viscosity disappears completely. In the alternative approach that leads to the power-law, the velocity gradient is assumed to possess a power-type asymptotic behaviour, where the exponent and the multiplying parameter are supposed to depend somehow on the *flow* Reynolds number. Thus, the velocity gradient dependence on molecular viscosity does not disappear however large the *local* and the *flow* Reynolds numbers may be. The form of the power-like scaling law yields a family of curves whose parameter is the Reynods number. The resulting envelop of curves is shown to be very close to the universal log-law.

The original result, the logarithmic law, however, has remained central to the theory of turbulence. The fact that the log-law can be obtained from formal asymptotic methods and that it has been shown to apply to a variety of flows, has firmly silenced its critics. In fact, the large body of useful services covered by the law has made it to transcend in importance. The universal laws of friction for smooth and rough pipes are just one of the pungent examples of application of the log-law.

Typical examples of application of the law include cases with wall transpiration, roughness, transfer of heat, compressibility, three-dimensionality, and even separation of flow. Of course, for all of these situations, some modifications need to be made in the original formulation to comply with specific flow requirements. However, the essence of the law and its general form are the same for all cases.

3. A SHORT REVIEW OF THE ANALYTICAL FUNCTIONS FOR THE INNER VELOCITY PROFILE

All previous authors have found it necessary to use at least two expressions for the description of the near wall flow. In what follows, we will show how this can be circumvented by using alternative approaches to the solution.

3.1 The theory of Reichardt(1940)

The equation of continuity implies that for the very near wall region, $v \sim y^2$. Then, as shown by Reichardt, it results from the momentum equation that $\nu_t \sim y^3$. On the other hand, we have seen (Eq. 5) that for large values of y^+ the eddy viscosity must present a linear behaviour. Thus, it was only natural to Reichardt to assume that

$$\frac{\nu_t}{\nu} = k\left(y^+ - \delta_l^+ \tanh\frac{y^+}{\delta_l^+}\right). \tag{7}$$

The velocity profile can then be obtained from

$$(\mu + \rho\nu_t)\frac{\partial u}{\partial y} = \tau_w. \tag{8}$$

Unfortunately, this equation cannot be solved analytically. An approximated solution is given by

$$u^+ = \frac{1}{k}\ln(1 + k\,y^+) + c\left[1 - \exp(-y^+/\delta_l^+) - \frac{y^+}{\delta_l^+}\exp(-0.33y^+)\right], \tag{9}$$

where $k = 0.41$, $\delta_l^+ = 11$ and $c = 7.4$.

3.2 The theory of Rotta(1950)

Rotta assumed that, for the flow in the region $5.0 < y^+$, the total shear stress is determined through both viscous and turbulence effects. Thus, a direct application of the mixing-length hypothesis leads to

$$\rho\left(\nu + I_m^2\left|\frac{\partial u}{\partial y}\right|\right)\frac{\partial u}{\partial y} = \tau_w\,, \tag{10}$$

where $I_m = k(y - \delta_l)$.

The solution to the above equation can be written as

$$u^+ = \frac{1}{2kI_m^+}\left(1 - \sqrt{1 + 4I_m^{+2}}\right) + \frac{1}{k}\ln\left(2I_m^+ - \sqrt{1 + 4I_m^{+2}}\right) + \delta_l^+, \tag{11}$$

with $l_m^+ = u_\tau l_m/\nu$ and $\delta_l^+ = u_\tau \delta_l/\nu$.

The main difficulty with this formulation is that it requires the correct especification of the value of the thickness of the viscous sublayer δ_l^+. The abrupt distinction made between the viscous sublayer and the turbulent region, however, does not reflect the true physics of the flow where the turbulent fluctuations are continuosly damped by viscous effects. In our calculations we will use $\delta_l^+ = 5.0$.

3.3 The theory of Van Driest(1956)

Van Driest was the first to consider the inclusion of a damping function into the mixing length theory of Prandtl. As a result, he wrote

$$\nu_t = k^2 y^2 \left(1 - \exp(-y^+/a)\right)^2 \left|\frac{\partial u}{\partial y}\right|. \tag{12}$$

The rate at which the flow velocity approaches zero at the wall is now controlled by the damping exponential function. In this case, $\nu_t \sim y^4$ as $y \to 0$.

Integration of equations (8) and (12) gives

$$u^+ = 2 \int_0^{y^+} \frac{dy^+}{1 + [1 + 4\,k^2\, y^{+2}(1 - \exp(-y^+/a))^2]^{1/2}}. \tag{13}$$

where Van Driest considered $a = 26$.

3.4 The theory of Rannie(1956)

As the wall is approached, all previous expressions for the non-dimensional eddy viscosity show a functional behaviour of the form either y^{+3} or y^{+4}. However, for finite values of y^+ a more appropriate behaviour would be of form y^{+2}. To satisfy this requirement, Rannie proposed for the region $y^+ \leq 27.5$ the following expression

$$\frac{\nu_t}{\nu} = \sinh^2(\sigma y^+). \tag{14}$$

The resulting mean velocity profile is then given by

$$u^+ = \frac{1}{\sigma} \tanh(\sigma\, y^+), \tag{15}$$

where $\sigma = 0.0688$.

3.5 The theory of Spalding(1961)

The motivation for Spalding was to find a good formula for the representation of the the velocity profile which presented at the same time a simpler form than the formulas of Reichardt and of Van Driest. This formula should, according to the author himself, fit the experimental data closely, contain a sufficient number of constants to permit modification in the light of the experimental data, and have a simple analytical form. He then sought at establishing a formula that satisfied the following conditions:

i) passes through the point: $y^+ = 0, u^+ = 0$;
ii) is tangential at this point to: $u^+ = y^+$;
iii) is asymptotic at large y^+ to: $u^+ = 2.5\ \ln y^+ + 5.5$;
iv) fits the experimental points at intermediate y^+ values.

The equation that immediately becomes a candidate is

$$y^+ = u^+ + C\left[\exp(k\,u^+) - 1 - k\,u^+ - \frac{(k\,u^+)^2}{2!} - \frac{(k\,u^+)^3}{3!} - \frac{(k\,u^+)^4}{4!}\right], \tag{16}$$

where $C = \exp(-kA)$, with A the standard constant in the law of the wall. For $A = 5.5$, the value suggested by Spalding, $C = 0.1108$.

Expression (16) furnishes, for large values of y^+, the asymptotic behaviour $\nu_t/\nu \sim y^{+4}$.

3.6 The theory of Rasmussen(1975)

Following the same line of thought of Spalding, Rasmussen introduced a similar expression but with fewer terms. In his formulation we have

$$y^+ = u^+ + \exp^{-A}\left[2\ \cosh(ku^+) - (ku^+)^2 - 2\right]. \tag{17}$$

The above equation satisfies the two boundary conditions specified by Spalding at the wall. In addition, conditions $(y = \delta, u = u_\infty)$ and $(y = \delta, \partial u/\partial y = 0)$ are satisfied. Only the requirement $(y = \delta, u = u_\infty)$ is not satisfied exactly. However, it is easily shown that the error becomes vanishingly small for $u^+ > 20$.

3.7 The theory of Musker(1979)

Observing the limiting behaviour of the eddy viscosity for small and large values of y^+, Musker proposed the following interpolating formula

$$\frac{1}{\nu_t/\nu} = \frac{1}{C\,y^{+3}} + \frac{1}{k\,y^+}, \tag{18}$$

where $C(= 0.001093)$ is a proportionality constant.

Using equation (8), it results that

$$\frac{du^+}{dy^+} = \frac{k + C\,y^{+2}}{k + C\,y^{+2} + C\,k\,y^{+3}}. \tag{19}$$

An integration of this equation gives

$$u^+ = 5.454\ \tan^{-1}\left[\frac{2y^+ - 8.15}{16.7}\right] + \log_{10}\left[\frac{(y^+ + 10.6)^{9.6}}{(y^{+2} - 8.15y^+ + 86)^2}\right] - 3.52 + 2.44. \tag{20}$$

3.8 The theory of Haritonidis(1989)

In the sixties, the structure of the turbulent boundary layer was shown to consist of a set organized large scale motions that was responsible for the bulk of turbulence production. The motions occur in a quasi-periodic fashion, giving rise to a sequence of events which is termed "the burst". To incorporate these facts into a simple algebraic model for the eddy viscosity, Haritonidis considered not the details of the flow instability that leads to a burst but the net result of the burst.

The resulting expression was

$$\nu_t = \frac{1}{2} n\, l_m^2\, f. \tag{21}$$

where n is the number of ejections of equal strength and duration over the period Δt_b between bursts, $f = 1/\Delta t_b$ is the bursting frequency, and l_m is the distance traveled by the bursts.

An integration of equations (8) and (21) gives

$$u^+ = (1/\lambda)\ \tan^{-1}(\lambda\, y^+), \tag{22}$$

where $\lambda^2 = \alpha f^+ = 0.00877$.

3.9 The theory of Yakhot(1993)

In the renormalization group approach (RNG), a systematic elimination of the small scales of motion from the Navier-Stokes equation is obtained. By eliminating the small-scale modes from the wave-number interval $\Lambda_f < k < \Lambda_0$, the following expression for the eddy viscosity follows:

$$\frac{\nu_t}{\nu} = \left[1 + H\left(a\frac{\epsilon\,\Lambda_f^4}{\nu^3} - C\right)\right]^{1/3}, \tag{23}$$

where H is the ramp function defined by $H(x) = max(x, 0)$, $a = 0.12$, and $C = 160$.

The RNG eddy viscosity is, therefore, written as a funcion of the mean dissipation rate, ϵ, and the length scale, $\Delta = 2\pi\Lambda_f^{-1}$, corresponding to the smallest fluctuating scales. Appealing to well known correlations for the $k - \epsilon$ transport model of turbulence, to a equilibrium hypothesis between production and dissipation near the wall, and to mixing-length type arguments, equation (23) becomes:

$$\frac{\nu_t}{\nu} = \left[1 + H\left(k^4 \frac{u_\tau^4 l^4}{\nu_t \nu^3} - C\right)\right]^{1/3}. \tag{24}$$

Considering that $H(x) = x$, equation (24) can be written as

$$Q4(\hat{\nu}) = \hat{\nu}^4 + (C-1)\hat{\nu} - \hat{\nu}_m^4 = 0, \tag{25}$$

where, $\hat{\nu} = \nu_t/\nu$, $\hat{\nu}_m = ky^+$, $y^+ = u_\tau y/\nu$.

The quartic equation (25) is solved under the constraint $\hat{\nu} = max(\hat{\nu}, 1)$, so that the eddy viscosity is turned on for $y^+ > C^{1/4}/k$.

In the fully turbulent region, the flow is governed by equation (4). An integration of this equation with equation (25) gives

$$u^+(y^+) = \frac{1}{3k}\left[4C^{1/4} - z + \ln\left(\frac{z+1}{z-1}\right) + 2\tan^{-1}(z) - \ln\left(\frac{C^{1/4}+1}{C^{1/4}-1}\right) - 2\tan^{-1}(C^{1/4})\right], \tag{26}$$

where $z = (\hat{\nu}^3 - 1 + C)^{1/4}/\hat{\nu}^{3/4}$ and $\hat{\nu} = \hat{\nu}(y^+)$ is the solution of the quartic equation (25).

3.10 The theory of Barenblat(1993)

In a completely different approach to the problem, Barenblat proposed a velocity scaling law that involves a special dependence of the power exponent and multiplicative factor on the flow Reynolds number. Based on arguments related to general fractal properties of vortex dissipative structures in turbulent flow and on the experimental data of Nikuradze(1932) for pipe flow, he proposed

$$\frac{u}{u_\tau} = C\,\eta^\alpha, \tag{27}$$

where

$$C = \frac{1}{\sqrt{3}}\ln R + \frac{5}{2} = \frac{\sqrt{3}+5\alpha}{2\alpha}, \quad \alpha = 3/2\ lnR.$$

4. A NEW LAW OF THE WALL FORMULATION

As we shall see, the results provided by most of the above formulations are in general good. The underlying hipotheses in the derivation of the equations, however, are quite different. In fact, we have just seen that they can be of a dimensional type, of a mixing length type, of an heuristic nature, of the RNG type, of an asymptotic type, or even a combination of all these possibilities.

For all formulations, however, the following shortcomings were observed. The theories of Reichardt and of Van Driest propose modifications in the mixing-length theory which lead to quadratures requiring numerical integration. The theories of Spalding and of Rasmussen, present their solution in an inverse form. Rotta, Rannie and Haritonidis present solutions with a limited range of validity. The theory of Yakhot requires the solution of a quartic equation. Barenblat's solution has been developed for pipe flow. The remaining theory, due to Musker, is seen by the present author as the easiest to implement, which still provides a solution with a wide enough range of validity and good accuracy.

To find a new, alternative solution we will combine some of the ideas of Rotta, of Spalding and of Van Driest. First, we resort to Cruz and Silva Freire(1995), to identify a specific region of the flow where equation (8) holds. Next, using equation (5), we perform a first integral to obtain

$$u^+(y^+) = \frac{1}{k}\left(\frac{1 - \sqrt{1 + 4k^2 y^{+2}}}{2k y^+} + \ln\left(2k y^+ + \sqrt{1 + 4k^2 y^{+2}}\right)\right). \tag{28}$$

This exact result is similar to the one found by Rotta, equation (11). The only difference here is the omittion of the thickness of the viscous sublayer δ_l^+. The asymptotic behaviour of equation (28) is

$$u^+ \to y^+, \quad y^+ \to 0$$

$$u^+ \to 2.5\, ln\, y^+ - 1.325, \quad y^+ \to \infty.$$

The result is that the single-variable profile, equation (28), fails in the high y^+ limit. To insure a good curve fitting for the whole range of inner scales, we add the function

$$D_A(y^+) = \frac{d}{2}\left[1 + \tanh\left(\frac{2\,k\,y^+ - y_c^+}{y_r^+}\right)\right], \tag{29}$$

to equation (28), where $d = 6.7$ and $y_c^+ = y_r^+ = 8$.

This function substitutes the need for the specification of δ_l^+ in Rotta's theory fixing the wrong asymptotic behaviour of equation (28). It has been selected on a purely empirical basis, very much in the same fashion of Spalding and of Rasmussen. In addition, it has the advantage of being written in a direct form.

5. DISCUSSION

The theories will be compared with the data of Andersen et al.(1972)and of Purtel, Klebanoff and Buckley(1981). Curves corresponding to all theories are plotted in figure 1. The main comments are: i) the theory of Reichardt overshoots the experimental data; ii) the solution of Rannie is good but limited to $y^+ < 27.5$; iii) Rotta's solution clearly suffers from an ill definition of δ_l^+; iv) the agreement with the experimental data provided by Van Driest's solution is very good, the same occuring with Spalding' solution; v) the theory of Rasmussen undershoots the data; vi) the agreement with the data yielded by Musken's expression is very good; vii) Haritonidis'solution is good but limited to $y^+ < 27.5$; viii) the results provided by the RNG theory are not good in the transition region; ix) the theory of Barenblat developed for pipe flows needs a better definition of the Reynolds number for boundary layer flows; x) the present formulation compares well with the data, being also comparable with the solutions of Van Driest and of Musker.

6. CONCLUSION

We have here presented a new formulation for the law of the wall which can be used to represent the flow in the inner part of a turbulent boundary layer within the accuracy of the experimental data. The law was derived based on concepts of the mixing length type together with an empirically chosen function. The results were compared with ten other different formulations for the problem.

Acknowledgements. The author thanks the Brazilian National Research Council (CNPq) for the financial support received through the Research Grant No 350183/93-7.

7. REFERENCES

Andersen, P. S., Kays, W. M. and Moffat, R. J. The Turbulent Boundary Layer on a Porous Plate: an Experimental Study of the Fluid Mechanics for Adverse Free-Stream Pressure Gradients,*HMT Report No 15, Stanford University*, 1972.

Barenblatt, G. I. Scaling Laws for Fully Developed Turbulent Shear Flows. Part 1. Basic Hypotheses and Analysis,*J. Fluid Mechanics*, vol. 248, pp. 513-520, 1993.

Cruz, D. O. A. & Silva Freire, A. P. The Asymptotic Structure of the Thermal Turbulent Boundary Layer Near a Separation Point, *in Turbulence, Heat and Mass Transfer*, Begell House Inc. Publishers, 1995.

Van Driest, E. R. On Turbulent Flow Near a Wall,*Journal of the Aeronautical Sciences*, vol. 23, pp. 1007, 1956.

Haritonidis, J. H. A Model for Near Wall Turbulence,*Phys. Fluids A*, vol 1, pp. 302-306, 1989.

Von Karman, T. Mechanische Ähnlichkeit u. Turbulenz,*Nachr. Ges. der Wiss. Göttingen, Math. Phys. Klasse*, vol. 58, 1930.

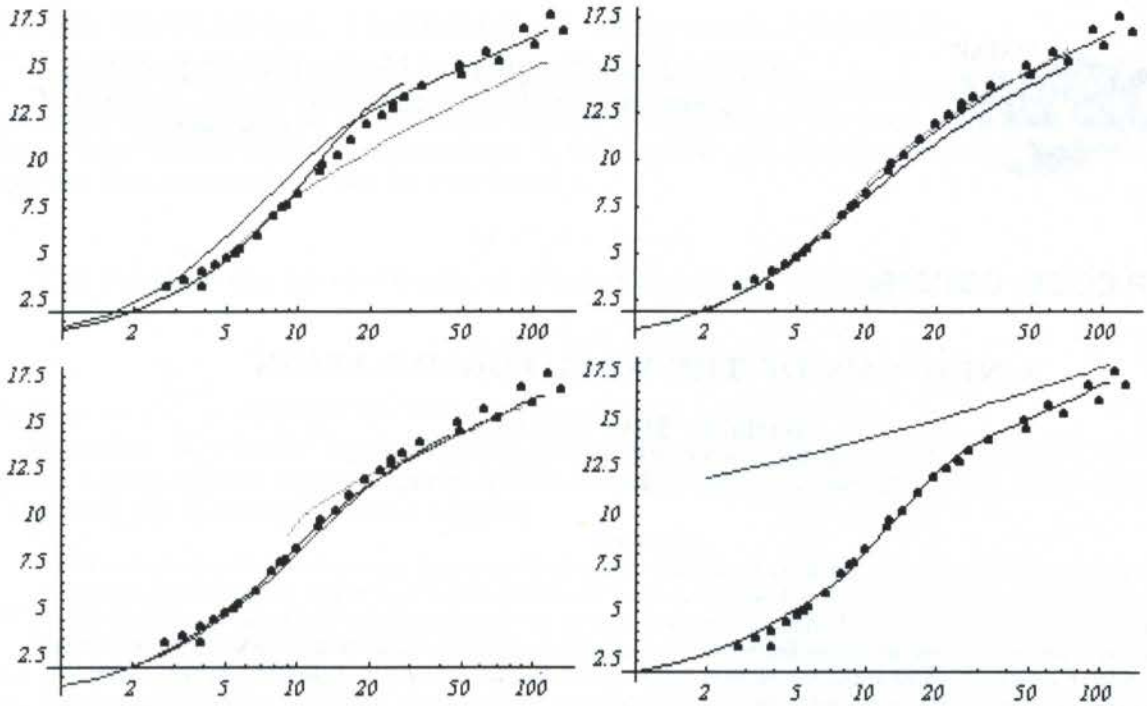

Figure 1. Law of the wall formulation. Coordinates are y^+ and u^+. Top left: theories of Reichardt(red line), Rotta(green line) and Rannie(blue line). Top right: theories of Van Driest(red line), Spalding(green line) and Rasmussen(blue line). Bottom left: theories of Musker(blue line), Haritonidis(red line) and Yakhot(green line). Bottom right: theories of Barenblat(red line) and present.

Von Karman, T. The Analogy Between Fluid Friction and Heat Transfer, *Trans. ASME*, vol. 61, pp. 705-710, 1939.

Musker, A. J. Explicit Expression for the Smooth Wall Velocity Distribution in a Turbulent Boundary Layer, *AIAA Journal*, vol. 17, pp. 655-657, 1979.

Nikuradse, J. Gesetzmässigkeiten der Turbulenten Strömung in Glatten Rohren, *Forschung a.d. Geb. Ing.*, No 356, 1930.

Prandtl, L. Über die Ausgebildete Turbulenz, *ZaMM*, vol. 5, pp. 136, 1925.

Purtell, L. P., Klebanoff, P. S. & Buckley, F. T. Turbulent Boundary layer at Low Reynolds Number, *Phys. Fluids*, vol. 24, pp 802-811, 1981.

Rannie, W. D. Heat Transfer in Turbulent Shear Flow, *Journal of the Aeronautical Sciences*, vol. 23, pp. 485, 1956.

Rasmussen, M. L. On Compressible Turbulent Boundary Layers in the Presence of Favorable Pressure Gradients, *ASME Paper 75-WA/HT-53*, 1975.

Reichardt, H. Die Wärmeübertragung in Turbulenten Reibungschichten, *ZaMM*, vol. 20, pp. 297, 1940.

Rotta, J. *J. Ing.-Archiv.*, vol. 18, pp-277, 1950.

Spalding, D. B. A Single Formula for the Law of the Wall, *Journal of Applied Mechanics*, vol. 83, pp. 455-458, 1961.

Taylor, G. I. Conditions at a Surface of a Hot Body Exposed to the Wind, *Brit. Aero. Res. Comm. R & M No 272*, pp. 423, 1916.

Yakhot, A., Khait, V. D. & Orszag, S. A. Analytic Expression for the Universal Logarithmic Velocity Law, *Journal of Fluids Engineering*, vol. 115, pp. 532-534, 1993.

XIV Brazilian Congress of Mechanical Engineering
Obeid Plaza Hotel Convention Center - Bauru - SP/Brazil
December 08-12th 1997

PAPER CODE: COB246c

A NEW LAW OF THE WALL FORMULATION

Atila P. Silva Freire
Mechanical Engineering Program (COPPE/UFRJ),
C.P. 68503, 21945-970 Rio de Janeiro, Brazil.

Abstract

The present work introduces a new expression for the velocity profile in the near wall region of a turbulent boundary layer. The new theory uses asymptotic arguments and considerations of the mixing length type to find a local analytical solution which presents the correct asymptotic behaviour both close to wall in the laminar sub-layer and in the logarithmic region of the flow. Next, heuristic arguments are evoked to add a damping function to the local solution. This function provides an excelent correction to the original analytical solution, furnishing a solution valid for the whole range of inner scales. The resulting expression is compared with ten other different formulations for the problem. The results are also compared with some experimental test cases.

Keywords
Law of the Wall, Turbulence, Boundary Layer.
Palavras Chave
Lei da Parede, Turbulncia, Camada Limite.

1. INTRODUCTION

The turbulent boundary layer has a distinct structure with a number of regions having characteristic properties. This fact was acknowledged very early in this century by several researchers including Prandlt(1910), Taylor(1916) and Von Karman(1939). The important realization at the time was that the flow in the wall region was determined by conditions at the wall, as expressed by the local shear stress and roughness. The region which comprises most of the flow, the outer region, on the other hand, has its properties determined by scales related to the main flow.

Most of the work that followed in this period was aimed at finding a local velocity solution for the wall region. This solution was termed by Coles "the law of the wall". Many expressions describing the velocity behaviour in the near wall viscous region were soon advanced through different methods. Dimensional analysis and experimental evidence established a logarithmic functional form for the velocity profile. This form was subsequently confirmed by mixing length arguments and asymptotic matching considerations. Since this formulation could not be extended down to the wall, several authors found it necessary to use at least two functions to describe adequately the velocity profile. This introduced some inconveniences in the formulation, notably, the necessity of patching the solutions.

As a result, the interest shifted to find a single expression to describe the velocity for the whole range of inner lengths. Several expressions were soon proposed by a host of authors. These expressions were more aesthetical and convenient from a numerical implementation point of view.

The purpose of this work is twofold. First, we review ten different theories advanced in the past for the problem comparing them with the test case data of Andersen et al.(1972) and of Purtell, Klebanoff and Buckley(1981). Second, we propose a new expression for the description of the wall layer flow based on an exact approximated local solution for the equations of motion together with some purely heuristic arguments. The new equation is different from all those presented in literature, and is shown to provide a very good match with the experimental data.

2. THE UNIVERSAL TURBULENT VELOCITY PROFILE

The flow in the wall layer is postulated to depend on the wall shear stress τ_w, on the distance y to the wall, on a roughness parameter K, and on the fluid properties ρ and μ. Then, from dimensional considerations, it follows that the the functional dependence of u on the flow parameters can be expressed as

$$u = f(\tau_w, y, K, \rho, \mu). \tag{1}$$

This equation can be re-written, in a non-dimensional form, as

$$\frac{u}{u_\tau} = g\left(\frac{u_\tau\, y}{\nu}, \frac{u_\tau\, K}{\nu}\right), \tag{2}$$

where $u_\tau (= \sqrt{\tau_w/\rho})$ denotes the wall friction velocity and $\nu = \mu/\rho$.

Equation (2) should be a universal function valid in the whole of the wall viscous region. Using a limit expansion argument, Prandtl(1910) found that in the very vicinity of the wall the following relation applied

$$u^+ = y^+; \quad 0 \le y^+ < 11.5. \tag{3}$$

where $u^+ = u/u_\tau$ and $y^+ = y u_\tau/\nu$.

Further out, in the turbulence dominated part of the wall layer, the commom assumption is that the local shear stress deviates only slightly from the wall value. Hence, we may write

$$\nu_t \frac{\partial u}{\partial y} = \frac{\tau_w}{\rho}, \tag{4}$$

where the eddy viscosity ν_t is a quantity related with the diffusion of momentum between adjacent layers due to turbulence. For diffusion times short with respect to the Lagrangian integral time scale, the diffusion has a linear behaviour with respect to time and the eddy viscosity varies linearly with distance. At a short distance from the wall, the diffusion of particles is restricted to short distances, so that the eddy viscosity may be considered proportional to the distance y. Thus, we write

$$\nu_t = k\, u_\tau\, y, \tag{5}$$

where u_τ is a characteristic velocity and k is a constant.

Integration of equations (4) and (5) gives

$$u^+ = \frac{1}{k} \ln y^+ + A; \quad y^+ > 11.5. \tag{6}$$

where the values of k(=0.4) and of A(= 5.5) were determined experimentally.

This expression was first derived by Taylor in 1916, and subsequently by Prandtl in 1925 and Von Karman in 1930. The last two authors resorted, again, to arguments of the mixing length type.

Later on, in 1939, equation (6) was split into two by Von Karman to cover the regions $5 \le y^+ < 30$ and $30 \le y^+$. In this case, the constants assume respectively the values (k, A) = (0.2,-3.05) and (k, A) = (0.4,5.5).

In fact, expression (6) can be obtained without introduction of a closure condition. Using overlap arguments of the asymptotic type, Millikan(1939) obtained the logarithmic law; thus, he only needed to resort to assumptions of a general nature, without any considerations about the detais of the turbulence to find expression (6). This result set the logarithmic law as a definitive "truth" in the theory of turbulence.

The law has been widely used to test new theories, calibrate experimental apparatus, and validate computer codes, having become one of the great paradigms of turbulence theory. Validated by a large number of experimental data, the law has become a bench mark result to which all simulations of wall flow have to conform to. Evidence in favour of the law is, therefore, strong. Some authors, however, have placed the law under a severe scrutiny, claiming the velocity profile to be power-like, and not logarithmic-like!

In fact, the derivation of both laws is equally consistent and rigorous. However, they are based on entirely different assumptions. Both derivations start from similarity and asymptotic considerations. The log-law is obtained from the assumption that for

sufficiently large *local* Reynolds number and sufficiently large *flow* Reynolds number, the dependence of the velocity gradient on the molecular viscosity disappears completely. In the alternative approach that leads to the power-law, the velocity gradient is assumed to possess a power-type asymptotic behaviour, where the exponent and the multiplying parameter are supposed to depend somehow on the *flow* Reynolds number. Thus, the velocity gradient dependence on molecular viscosity does not disappear however large the *local* and the *flow* Reynolds numbers may be. The form of the power-like scaling law yields a family of curves whose parameter is the Reynods number. The resulting envelop of curves is shown to be very close to the universal log-law.

The original result, the logarithmic law, however, has remained central to the theory of turbulence. The fact that the log-law can be obtained from formal asymptotic methods and that it has been shown to apply to a variety of flows, has firmly silenced its critics. In fact, the large body of useful services covered by the law has made it to transcend in importance. The universal laws of friction for smooth and rough pipes are just one of the pungent examples of application of the log-law.

Typical examples of application of the law include cases with wall transpiration, roughness, transfer of heat, compressibility, three-dimensionality, and even separation of flow. Of course, for all of these situations, some modifications need to be made in the original formulation to comply with specific flow requirements. However, the essence of the law and its general form are the same for all cases.

3. A SHORT REVIEW OF THE ANALYTICAL FUNCTIONS FOR THE INNER VELOCITY PROFILE

All previous authors have found it necessary to use at least two expressions for the description of the near wall flow. In what follows, we will show how this can be circumvented by using alternative approaches to the solution.

3.1 The theory of Reichardt(1940)

The equation of continuity implies that for the very near wall region, $v \sim y^2$. Then, as shown by Reichardt, it results from the momentum equation that $\nu_t \sim y^3$. On the other hand, we have seen (Eq. 5) that for large values of y^+ the eddy viscosity must present a linear behaviour. Thus, it was only natural to Reichardt to assume that

$$\frac{\nu_t}{\nu} = k\left(y^+ - \delta_l^+ \tanh\frac{y^+}{\delta_l^+}\right). \tag{7}$$

The velocity profile can then be obtained from

$$(\mu + \rho\nu_t)\frac{\partial u}{\partial y} = \tau_w. \tag{8}$$

Unfortunately, this equation cannot be solved analytically. An approximated solution is given by

$$u^+ = \frac{1}{k}\ln(1 + k\,y^+) + c\left[1 - \exp(-y^+/\delta_l^+) - \frac{y^+}{\delta_l^+}\exp(-0.33y^+)\right], \tag{9}$$

where $k = 0.41$, $\delta_l^+ = 11$ and $c = 7.4$.

3.2 The theory of Rotta(1950)

Rotta assumed that, for the flow in the region $5.0 < y^+$, the total shear stress is determined through both viscous and turbulence effects. Thus, a direct application of the mixing-length hypothesis leads to

$$\rho\left(\nu + I_m^2\left|\frac{\partial u}{\partial y}\right|\right)\frac{\partial u}{\partial y} = \tau_w\,, \tag{10}$$

where $I_m = k(y - \delta_l)$.

The solution to the above equation can be written as

$$u^+ = \frac{1}{2kI_m^+}\left(1 - \sqrt{1 + 4I_m^{+2}}\right) + \frac{1}{k}\ln\left(2I_m^+ - \sqrt{1 + 4I_m^{+2}}\right) + \delta_l^+, \tag{11}$$

with $l_m^+ = u_\tau l_m/\nu$ and $\delta_l^+ = u_\tau \delta_l/\nu$.

The main difficulty with this formulation is that it requires the correct especification of the value of the thickness of the viscous sublayer δ_l^+. The abrupt distinction made between the viscous sublayer and the turbulent region, however, does not reflect the true physics of the flow where the turbulent fluctuations are continuosly damped by viscous effects. In our calculations we will use $\delta_l^+ = 5.0$.

3.3 The theory of Van Driest(1956)

Van Driest was the first to consider the inclusion of a damping function into the mixing length theory of Prandtl. As a result, he wrote

$$\nu_t = k^2 y^2 \left(1 - \exp(-y^+/a)\right)^2 \left|\frac{\partial u}{\partial y}\right|. \tag{12}$$

The rate at which the flow velocity approaches zero at the wall is now controlled by the damping exponential function. In this case, $\nu_t \sim y^4$ as $y \to 0$.

Integration of equations (8) and (12) gives

$$u^+ = 2 \int_0^{y^+} \frac{dy^+}{1 + [1 + 4\,k^2\, y^{+2}(1 - \exp(-y^+/a))^2]^{1/2}}. \tag{13}$$

where Van Driest considered $a = 26$.

3.4 The theory of Rannie(1956)

As the wall is approached, all previous expressions for the non-dimensional eddy viscosity show a functional behaviour of the form either y^{+3} or y^{+4}. However, for finite values of y^+ a more appropriate behaviour would be of form y^{+2}. To satisfy this requirement, Rannie proposed for the region $y^+ \leq 27.5$ the following expression

$$\frac{\nu_t}{\nu} = \sinh^2(\sigma y^+). \tag{14}$$

The resulting mean velocity profile is then given by

$$u^+ = \frac{1}{\sigma} \tanh(\sigma\, y^+), \tag{15}$$

where $\sigma = 0.0688$.

3.5 The theory of Spalding(1961)

The motivation for Spalding was to find a good formula for the representation of the the velocity profile which presented at the same time a simpler form than the formulas of Reichardt and of Van Driest. This formula should, according to the author himself, fit the experimental data closely, contain a sufficient number of constants to permit modification in the light of the experimental data, and have a simple analytical form. He then sought at establishing a formula that satisfied the following conditions:

i) passes through the point: $y^+ = 0, u^+ = 0$;
ii) is tangential at this point to: $u^+ = y^+$;
iii) is asymptotic at large y^+ to: $u^+ = 2.5\ \ln y^+ + 5.5$;
iv) fits the experimental points at intermediate y^+ values.

The equation that immediately becomes a candidate is

$$y^+ = u^+ + C\left[\exp(k\,u^+) - 1 - k\,u^+ - \frac{(k\,u^+)^2}{2!} - \frac{(k\,u^+)^3}{3!} - \frac{(k\,u^+)^4}{4!}\right], \tag{16}$$

where $C = \exp(-kA)$, with A the standard constant in the law of the wall. For $A = 5.5$, the value suggested by Spalding, $C = 0.1108$.

Expression (16) furnishes, for large values of y^+, the asymptotic behaviour $\nu_t/\nu \sim y^{+4}$.

3.6 The theory of Rasmussen(1975)

Following the same line of thought of Spalding, Rasmussen introduced a similar expression but with fewer terms. In his formulation we have

$$y^+ = u^+ + \exp^{-A}\left[2\ \cosh(ku^+) - (ku^+)^2 - 2\right]. \tag{17}$$

The above equation satisfies the two boundary conditions specified by Spalding at the wall. In addition, conditions $(y = \delta, u = u_\infty)$ and $(y = \delta, \partial u/\partial y = 0)$ are satisfied. Only the requirement $(y = \delta, u = u_\infty)$ is not satisfied exactly. However, it is easily shown that the error becomes vanishingly small for $u^+ > 20$.

3.7 The theory of Musker(1979)

Observing the limiting behaviour of the eddy viscosity for small and large values of y^+, Musker proposed the following interpolating formula

$$\frac{1}{\nu_t/\nu} = \frac{1}{C\,y^{+3}} + \frac{1}{k\,y^+}, \tag{18}$$

where $C(= 0.001093)$ is a proportionality constant.

Using equation (8), it results that

$$\frac{du^+}{dy^+} = \frac{k + C\,y^{+2}}{k + C\,y^{+2} + C\,k\,y^{+3}}. \tag{19}$$

An integration of this equation gives

$$u^+ = 5.454\ \tan^{-1}\left[\frac{2y^+ - 8.15}{16.7}\right] + \log_{10}\left[\frac{(y^+ + 10.6)^{9.6}}{(y^{+2} - 8.15y^+ + 86)^2}\right] - 3.52 + 2.44. \tag{20}$$

3.8 The theory of Haritonidis(1989)

In the sixties, the structure of the turbulent boundary layer was shown to consist of a set organized large scale motions that was responsible for the bulk of turbulence production. The motions occur in a quasi-periodic fashion, giving rise to a sequence of events which is termed "the burst". To incorporate these facts into a simple algebraic model for the eddy viscosity, Haritonidis considered not the details of the flow instability that leads to a burst but the net result of the burst.

The resulting expression was

$$\nu_t = \frac{1}{2} n\, l_m^2\, f, \tag{21}$$

where n is the number of ejections of equal strength and duration over the period Δt_b between bursts, $f = 1/\Delta t_b$ is the bursting frequency, and l_m is the distance traveled by the bursts.

An integration of equations (8) and (21) gives

$$u^+ = (1/\lambda)\ \tan^{-1}(\lambda\, y^+), \tag{22}$$

where $\lambda^2 = \alpha f^+ = 0.00877$.

3.9 The theory of Yakhot(1993)

In the renormalization group approach (RNG), a systematic elimination of the small scales of motion from the Navier-Stokes equation is obtained. By eliminating the small-scale modes from the wave-number interval $\Lambda_f < k < \Lambda_0$, the following expression for the eddy viscosity follows:

$$\frac{\nu_t}{\nu} = \left[1 + H\left(a\frac{\epsilon\,\Lambda_f^4}{\nu^3} - C\right)\right]^{1/3}. \tag{23}$$

where H is the ramp function defined by $H(x) = max(x, 0)$, $a = 0.12$, and $C = 160$.

The RNG eddy viscosity is, therefore, written as a funcion of the mean dissipation rate, ϵ, and the length scale, $\Delta = 2\pi\Lambda_f^{-1}$, corresponding to the smallest fluctuating scales. Appealing to well known correlations for the $k - \epsilon$ transport model of turbulence, to a equilibrium hypothesis between production and dissipation near the wall, and to mixing-length type arguments, equation (23) becomes:

$$\frac{\nu_t}{\nu} = \left[1 + H\left(k^4 \frac{u_\tau^4 l^4}{\nu_t \nu^3} - C\right)\right]^{1/3}. \tag{24}$$

Considering that $H(x) = x$, equation (24) can be written as

$$Q4(\hat{\nu}) = \hat{\nu}^4 + (C-1)\hat{\nu} - \hat{\nu}_m^4 = 0, \tag{25}$$

where, $\hat{\nu} = \nu_t/\nu$, $\hat{\nu}_m = k y^+$, $y^+ = u_\tau y/\nu$.

The quartic equation (25) is solved under the constraint $\hat{\nu} = max(\hat{\nu}, 1)$, so that the eddy viscosity is turned on for $y^+ > C^{1/4}/k$.

In the fully turbulent region, the flow is governed by equation (4). An integration of this equation with equation (25) gives

$$u^+(y^+) = \frac{1}{3k}\left[4C^{1/4} - z + \ln\left(\frac{z+1}{z-1}\right) + 2\tan^{-1}(z) - \ln\left(\frac{C^{1/4}+1}{C^{1/4}-1}\right) - 2\tan^{-1}(C^{1/4})\right], \tag{26}$$

where $z = (\hat{\nu}^3 - 1 + C)^{1/4}/\hat{\nu}^{3/4}$ and $\hat{\nu} = \hat{\nu}(y^+)$ is the solution of the quartic equation (25).

3.10 The theory of Barenblat(1993)

In a completely different approach to the problem, Barenblat proposed a velocity scaling law that involves a special dependence of the power exponent and multiplicative factor on the flow Reynolds number. Based on arguments related to general fractal properties of vortex dissipative structures in turbulent flow and on the experimental data of Nikuradze(1932) for pipe flow, he proposed

$$\frac{u}{u_\tau} = C\,\eta^\alpha, \tag{27}$$

where

$$C = \frac{1}{\sqrt{3}}\ln R + \frac{5}{2} = \frac{\sqrt{3}+5\alpha}{2\alpha}, \qquad \alpha = 3/2\ lnR.$$

4. A NEW LAW OF THE WALL FORMULATION

As we shall see, the results provided by most of the above formulations are in general good. The underlying hipotheses in the derivation of the equations, however, are quite different. In fact, we have just seen that they can be of a dimensional type, of a mixing length type, of an heuristic nature, of the RNG type, of an asymptotic type, or even a combination of all these possibilities.

For all formulations, however, the following shortcomings were observed. The theories of Reichardt and of Van Driest propose modifications in the mixing-length theory which lead to quadratures requiring numerical integration. The theories of Spalding and of Rasmussen, present their solution in an inverse form. Rotta, Rannie and Haritonidis present solutions with a limited range of validity. The theory of Yakhot requires the solution of a quartic equation. Barenblat's solution has been developed for pipe flow. The remaining theory, due to Musker, is seen by the present author as the easiest to implement, which still provides a solution with a wide enough range of validity and good accuracy.

To find a new, alternative solution we will combine some of the ideas of Rotta, of Spalding and of Van Driest. First, we resort to Cruz and Silva Freire(1995), to identify a specific region of the flow where equation (8) holds. Next, using equation (5), we perform a first integral to obtain

$$u^+(y^+) = \frac{1}{k}\left(\frac{1 - \sqrt{1 + 4k^2 y^{+2}}}{2k y^+} + \ln\left(2k y^+ + \sqrt{1 + 4k^2 y^{+2}}\right)\right). \tag{28}$$

This exact result is similar to the one found by Rotta, equation (11). The only difference here is the omittion of the thickness of the viscous sublayer δ_l^+. The asymptotic behaviour of equation (28) is

$$u^+ \to y^+, \quad y^+ \to 0$$

$$u^+ \to 2.5\, ln\, y^+ - 1.325, \quad y^+ \to \infty.$$

The result is that the single-variable profile, equation (28), fails in the high y^+ limit. To insure a good curve fitting for the whole range of inner scales, we add the function

$$D_A(y^+) = \frac{d}{2}\left[1 + \tanh\left(\frac{2\,k\,y^+ - y_c^+}{y_r^+}\right)\right], \tag{29}$$

to equation (28), where $d = 6.7$ and $y_c^+ = y_r^+ = 8$.

This function substitutes the need for the specification of δ_l^+ in Rotta's theory fixing the wrong asymptotic behaviour of equation (28). It has been selected on a purely empirical basis, very much in the same fashion of Spalding and of Rasmussen. In addition, it has the advantage of being written in a direct form.

5. DISCUSSION

The theories will be compared with the data of Andersen et al.(1972)and of Purtel, Klebanoff and Buckley(1981). Curves corresponding to all theories are plotted in figure 1. The main comments are: i) the theory of Reichardt overshoots the experimental data; ii) the solution of Rannie is good but limited to $y^+ < 27.5$; iii) Rotta's solution clearly suffers from an ill definition of δ_l^+; iv) the agreement with the experimental data provided by Van Driest's solution is very good, the same occuring with Spalding' solution; v) the theory of Rasmussen undershoots the data; vi) the agreement with the data yielded by Musken's expression is very good; vii) Haritonidis'solution is good but limited to $y^+ < 27.5$; viii) the results provided by the RNG theory are not good in the transition region; ix) the theory of Barenblat developed for pipe flows needs a better definition of the Reynolds number for boundary layer flows; x) the present formulation compares well with the data, being also comparable with the solutions of Van Driest and of Musker.

6. CONCLUSION

We have here presented a new formulation for the law of the wall which can be used to represent the flow in the inner part of a turbulent boundary layer within the accuracy of the experimental data. The law was derived based on concepts of the mixing length type together with an empirically chosen function. The results were compared with ten other different formulations for the problem.

Acknowledgements. The author thanks the Brazilian National Research Council (CNPq) for the financial support received through the Research Grant No 350183/93-7.

7. REFERENCES

Andersen, P. S., Kays, W. M. and Moffat, R. J. The Turbulent Boundary Layer on a Porous Plate: an Experimental Study of the Fluid Mechanics for Adverse Free-Stream Pressure Gradients,*HMT Report No 15, Stanford University*, 1972.

Barenblatt, G. I. Scaling Laws for Fully Developed Turbulent Shear Flows. Part 1. Basic Hypotheses and Analysis,*J. Fluid Mechanics*, vol. 248, pp. 513-520, 1993.

Cruz, D. O. A. & Silva Freire, A. P. The Asymptotic Structure of the Thermal Turbulent Boundary Layer Near a Separation Point, *in Turbulence, Heat and Mass Transfer*, Begell House Inc. Publishers, 1995.

Van Driest, E. R. On Turbulent Flow Near a Wall,*Journal of the Aeronautical Sciences*, vol. 23, pp. 1007, 1956.

Haritonidis, J. H. A Model for Near Wall Turbulence,*Phys. Fluids A*, vol 1, pp. 302-306, 1989.

Von Karman, T. Mechanische Ähnlichkeit u. Turbulenz,*Nachr. Ges. der Wiss. Göttingen, Math. Phys. Klasse*, vol. 58, 1930.

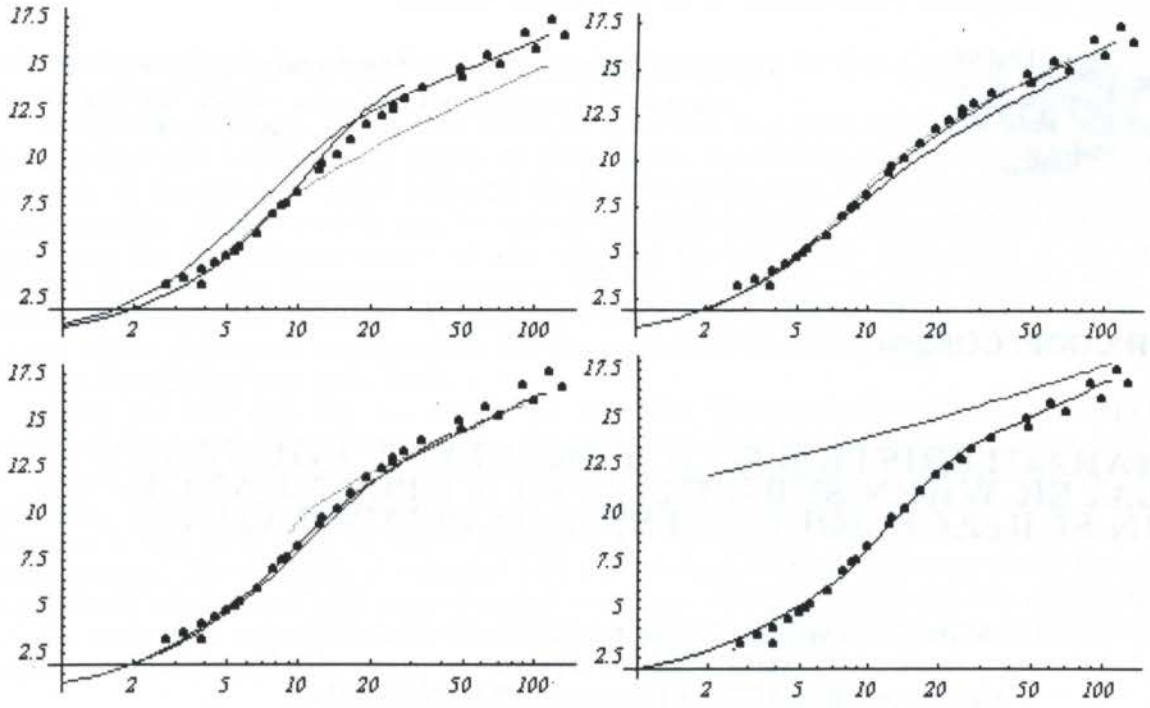

Figure 1. Law of the wall formulation. Coordinates are y^+ and u^+. Top left: theories of Reichardt(red line), Rotta(green line) and Rannie(blue line). Top right: theories of Van Driest(red line), Spalding(green line) and Rasmussen(blue line). Bottom left: theories of Musker(blue line), Haritonidis(red line) and Yakhot(green line). Bottom right: theories of Barenblat(red line) and present.

Von Karman, T. The Analogy Between Fluid Friction and Heat Transfer, *Trans. ASME*, vol. 61, pp. 705-710, 1939.

Musker, A. J. Explicit Expression for the Smooth Wall Velocity Distribution in a Turbulent Boundary Layer, *AIAA Journal*, vol. 17, pp. 655-657, 1979.

Nikuradse, J. Gesetzmässigkeiten der Turbulenten Strömung in Glatten Rohren, *Forschung a.d. Geb. Ing.*, No 356, 1930.

Prandtl, L. Über die Ausgebildete Turbulenz, *ZaMM*, vol. 5, pp. 136, 1925.

Purtell, L. P., Klebanoff, P. S. & Buckley, F. T. Turbulent Boundary layer at Low Reynolds Number, *Phys. Fluids*, vol. 24, pp 802-811, 1981.

Rannie, W. D. Heat Transfer in Turbulent Shear Flow, *Journal of the Aeronautical Sciences*, vol. 23, pp. 485, 1956.

Rasmussen, M. L. On Compressible Turbulent Boundary Layers in the Presence of Favorable Pressure Gradients, *ASME Paper 75-WA/HT-53*, 1975.

Reichardt, H. Die Wärmeübertragung in Turbulenten Reibungschichten, *ZaMM*, vol. 20, pp. 297, 1940.

Rotta, J. *J. Ing.-Archiv.*, vol. 18, pp-277, 1950.

Spalding, D. B. A Single Formula for the Law of the Wall, *Journal of Applied Mechanics*, vol. 83, pp. 455-458, 1961.

Taylor, G. I. Conditions at a Surface of a Hot Body Exposed to the Wind, *Brit. Aero. Res. Comm. R & M No 272*, pp. 423, 1916.

Yakhot, A., Khait, V. D. & Orszag, S. A. Analytic Expression for the Universal Logarithmic Velocity Law, *Journal of Fluids Engineering*, vol. 115, pp. 532-534, 1993.

XIV Brazilian Congress of Mechanical Engineering
Obeid Plaza Hotel Convention Center - Bauru - SP/Brazil
December 08-12th 1997

PAPER CODE: COB248

CHARACTERISTICS OF A TURBULENT BOUNDARY LAYER WHEN SUBJECTED TO A STEP CHANGE IN SURFACE ROUGHNESS AND TEMPERATURE

Mila R. Avelino, Philippe P. M. Menut and Atila P. Silva Freire
Mechanical Engineering Program (COPPE/UFRJ),
C.P. 68503, 21945-970 Rio de Janeiro, Brazil.

Abstract

The present work uses asymptotic and heuristic arguments to develop a theory for the description of turbulent boundary layer flows over surfaces with a step change in roughness and in temperature. Based on the concept of the displacement in origin, the theory proposes a new expression for the near wall logarithmic temperature profile, which is then used as a boundary condition for a k ϵ modelling of the external flow. The results are tested for a sea breeze that advances over dry land. Simulations of velocity and temperature profiles, and of skin-friction and of Stanton number profiles are presented.

Keywords

Turbulent, Boundary Layer, Surface Roughness, Atmospheric Flows, k ϵ model.

Palavras Chave

Turbulncia, Camada Limite, Rugosidade Superficial, Escoamento Atmosfrico, modelo k ϵ.

1. INTRODUCTION

The earth surface presents large variations in topography due to changes in the nature of the terrain. These changes are basically of two types, changes in the land surface and hills. In the real world, these conditions normally occur at the same time giving rise to flow configurations that are really difficult to treat theoretically.

In this work, we will be solely concerned with atmospheric flows that develop over flat terrain with changing surface conditions. In particular, we will be looking at flows which present abrupt changes in surface conditions from one extensive uniform surface to another. Two types of changes will be dealt with here: changes in surface roughness and changes in surface temperature.

Important differences occur in flow behaviour depending on whether the wind blows from one type of rough surface to another, and on whether it blows from a hot to a cold surface or vice-versa. The theory to be developed here is expected to account for all these effects. The atmospheric boundary layer will be split into different regions where different characteristics are attained. For a neutrally stable boundary layer, the flow is normally separated into two regions. In the inner layer, where the flow is insensitive to the earth's rotation and the wind properties are primarily determined by the local surface friction and scalar fluxes, the velocity profile is observed to have a logarithmic form. For more stable or unstable flows, the velocity profile deviates from its logarithmic behaviour. For all applications, however, asymptotic techniques can be evoked to show

that the velocity profile always assume a logarithmic form for distances sufficiently close to the wall.

At the larger scale, convective motions give rise to a near uniform distribution of the velocity and temperature fields. In this region the flow is nearly insensitive to the presence of the surface below and can be described through gradient transport turbulence models. These models can be expressed algebraically or may involve differential equations for the determination of the relevant characteristic properties of the flow. Models that use two transport equations for the description of the turbulent field are termed two-equation models. A classical example of a two-equation model is the k–ϵ model where equations are specified for the turbulent kinetic energy, k, and the overall viscous dissipation per unit mass, ϵ.

Here, we will use the k–ϵ model to describe the properties of the atmospheric boundary layer in the outer region. In addition, a local analytical solution will be developed for the inner region which will be used as a boundary condition for the outer solution. This inner solution must, as just argued above, take into account for local changes in the flow such as those provoked by changes on the surface roughness and temperature. The analytical solution will be developed on an heuristic basis, based on asymptotic arguments and experimental evidence. Corroboration on the applicability of this analytical expression to atmospheric flows is seen by the present authors as the main contribution of this work.

2. THE FLOW OVER ROUGH WALLS

Theoretical and experimental studies on the development of turbulent boundary layer flows over rough surfaces have a long history, having being stimulated by such diverse applications as naval architecture, aeronautics and micrometeorology. The fundamental concepts and ideas on the problem were established by Nikuradse(1933) who investigated the flow in sand-roughened pipes. He found that, at high Reynolds number, the near wall flow becomes independent of viscosity, and is a function of the roughness scale, K, and of the pipe diameter, D. He also found that, for the defect layer, the universal laws apply to the bulk of the flow irrespective of the conditions at the wall. The roughness effects are, therefore, restricted to a thin wall layer.

From dimensional arguments and comparison with Prandtl's law of the wall, Nikuradse wrote:

$$\frac{u}{u_\tau} = \frac{1}{k} \ln \frac{y}{K} + B\left[\frac{K u_\tau}{\nu}\right], \tag{1}$$

where all symbols in the above equation attain their classical meaning, that is, u_τ is the friction velocity, k the Von Karman constant, and ν the kinematic viscosity. The square brackets stand for functional dependence.

Equation (1) was written in an alternative form by Clauser(1954), who cast it as

$$\frac{u}{u_\tau} = \frac{1}{k} \ln \frac{y u_\tau}{\nu} + A - \frac{\Delta u}{u_\tau}\left[\frac{K u_\tau}{\nu}\right]. \tag{2}$$

After an extensive experimental program, Hama(1954) showed that

$$\frac{\Delta u}{u_\tau} = \frac{1}{k} \ln \frac{K u_\tau}{\nu} + C, \tag{3}$$

which immediately shows that equations (1) and (2) are just the same but written in a different form.

Flows that follow the behaviour set by equations (1) to (3) are said to occur over surfaces of the type "K". Flows, on the other hand, which are apparently insensitive to the characteristic scale K, but depend on other global scale of the flow are termed

"D" type flows. In the latter case, the roughness is geometrically characterized by a surface with a series of closely spaced grooves within which the flow generates stable vortical configurations. To describe the part of the velocity profile that deviates from the logarithmic law in the defect region, we consider that, in the flow region above the rough elements, the mean motion is independent of the characteristic scales associated with the near wall flow. Thus equation (2) may be re-written as

$$\frac{u}{u_\tau} = \frac{1}{k} \ln \frac{y u_\tau}{\nu} + A - \frac{\Delta u}{u_\tau} \left[\frac{D u_\tau}{\nu} \right]. \tag{4}$$

In principle, there is no reason why the functions appearing in equations (2) and (4) should have the same form. In fact, the distinct length scales used in the representation of the "K" and "D" type rough wall flows may suggest that a single framework for the description of both types of roughness cannot be devised. However, Moore(1951) showed that a similarity law can be written in a universal form provided the origin for measuring the velocity profile is set some distance below the crest of the roughness elements. A detailed method for locating the displaced origin is described in Perry and Joubert(1964). The displacement is normally referred to as the error in origin, ε.

To write an expression valid for both types of roughness we make

$$\frac{u}{u_\tau} = \frac{1}{k} \ln \frac{(y_T + \varepsilon) u_\tau}{\nu} + A - \frac{\Delta u}{u_\tau}, \tag{5}$$

where,

$$\frac{\Delta u}{u_\tau} = \frac{1}{k} \ln \frac{\varepsilon u_\tau}{\nu} + C_i, \tag{6}$$

and $C_i, i = K, D$; is a constant characteristic of the roughness.

Having shown how an universal similarity law was established for the velocity profile according to other authors, we now turn our attention to the temperature field. A serious difficulty with most studies on the problem is the absence of measurements of the active scalars, temperature and humidity. This is particularly true in micrometeorology. In the wind tunnel, some investigations were carried out to assess the effects that a step change in surface roughness and temperature will have on the flow. These are important works that, however, suffer from the impossibility of reproducing the coupling between the surface fluxes of radiant energy and sensible and latent heat so important in real atmospheric flows. The works of Gowen and Smith(1968), of Healzer et alli(1974), of Ligrani et alli(1979) and of Taylor et alli(1989), all deal with flows over uniformly heated rough surfaces and will be used here to extend the previous formulation to the temperature field. The work of Ligrani and Moffat(1985) is the only one to give results for a step change in both roughness and temperature at the wall and should, for this reason, be used to validate the theory developed here. These experimental data are the most important for meteorological applications, providing results for the surface flux of heat. Unfortunately, at the time this work was being written, Ligrani and Moffat's data were not available to the present authors. This, in fact, is being provided and will be available soon. In fact, this would be an important contribution to the present article. However, the data of Ligrani and Moffat requires a great effort for their complete compilation and reduction; they are not presented in tabular form and with some vital missing information in what concerns their experimental conditions. The present authors are engaged in a great effort to obtain all the pieces and bits of the missing information, in a laborous task which will not be completed soon. As a result, full comparison of the present developments with these data will have to be published some other time.

To extend expressions (5) and (6) to the thermal turbulent boundary layer we will follow the procedure of Silva Freire and Hirata(1990a). Alternatively, we could have used dimensional arguments.

The very first requirement for the correct assessment the asymptotic structure of the flow is the determination of the order of magnitude of the fluctuating quantities. For the velocity field, a classical result is that, for flow over a smooth surface, both the longitudinal and the transversal velocity fluctuation components scale with the friction velocity, u_τ. The direct implication of this result is that the fully turbulent region is limited by the scales $(u_\tau^2/U_\infty^2)L$ and ν/u_τ. The temperature fluctuations, on the other hand, are shown (Orlando et alli 1974) to scale with the friction temperature, t_τ. The implication here is that the temperature fully turbulent region is limited by the scales $(u_\tau t_\tau/U_\infty(T_w - T_\infty))L$ and $\nu/u_\tau P_r$, where P_r denotes Prandtl number. Now, the lower limiting scales are a property of both the fluid and the flow, and, as a result, should have different values except for the fortuitous case of $P_r = 1$. The mixing properties of a turbulent flow, however, ensure that the friction velocity and the friction temperature have the same order of magnitude. The implication of this is that the upper limiting scales for the velocity and the temperature fields always coincide irrespective of the flow conditions, provided the flow is turbulent.

All these arguments can easily be formalized through application of the single limit concept of Kaplun(1967). Indeed, an application of the theory of Kaplun (Silva Freire and Hirata(1990a)) to the equations of motion, shows that the flow structure consists of two distinct regions determined by specific regions of validity obtained through passage of the single limiting process. The domains defined by the limits quoted above are just the overlap domains of the inner and the outer regions.

For flows over rough surfaces, we have seen that the lower bound of the overlap regions must change, being now a function of the surface geometry. Indeed, in this situation, the viscosity becomes irrelevant for the determination of the inner wall scale because the stress is transmitted by pressure forces in the wakes formed by the crests of the roughness elements. We have seen that the characteristic length scale for the near wall region must be the displacement in origin. It is also clear that, in either case, roughness of the type "K" or roughness of the type "D", the roughness elements penetrate well into the fully turbulent region so that the displaced origin for both the velocity and the temperature profiles will always be located in the overlap fully turbulent region. The similarity in transfer processes for turbulent flows then suggests that

$$\frac{t - t_w}{t_\tau} = \frac{1}{k_t} \ln P_r \frac{(y_T + \varepsilon)u_\tau}{\nu} + B - \frac{\Delta t}{t_\tau}. \tag{7}$$

where,

$$\frac{\Delta t}{t_\tau} = \frac{1}{k_t} \ln P_r \frac{\varepsilon u_\tau}{\nu} + D_i. \tag{8}$$

and $D_i, i = K, D$; is a constant characteristic of the roughness.

Equations (7) and (8) are the law of the wall formulation for flows over rough surfaces with transfer of heat. They were initially proposed and tested by Silva Freire and Hirata(1990b) for flows over uniformly heated surfaces. The results were very satisfactory. Validation at that time was, however, achieved only through predictions of the global parameter $\ln((\delta + \varepsilon)/\varepsilon)$. Here, we will apply, for the first time, the above formulation for a problem with a step change in roughness and in temperature. Equations (5) to (8) will be used to specify the boundary conditions on a k–ϵ formulation of the problem. These equation are, then, numerically solved to provide predictions of the velocity and temperature profiles.

3. THE TEST CASE

In nature, simultaneous changes in roughness and in temperature typically occur when the wind blows from the sea to the land. In the simplest possible modelling of the phenomenon, the velocity and scalar fluxes are considered uncoupled and the momentum

and energy equations are solved separately. Here we will adopt this procedure, seeking to discuss the effects of local advection and of downwind development.

The many possible combinations of these two effects furnishes a host of conditions to be studied. To simplify our discussion, we will refrain our simulation to flows where an abrupt change from one type of extensive surface to another occurs. The air flow will also be supposed to encounter a new surface where it is slowed down (smooth-rough change) and suffers an increase of temperature at the wall. This situation was chosen so as to emulate a sea breeze that blows over dry land. The flow conditions are: i) external flow velocity, $10m/s$; ii) external flow temperature, $25C$; iii) boundary layer thickness at $x = 0$, $\delta = 50m$; iv) initial values, $Pr = 0.7$, $\nu = 1.510^{-5}m^2/s$, $k = 0.41$, $k_t = 0.43$. The roughness was characterized through the constants: $A = 5.0$, $C_1 = 0.1$ e $C_2 = 1.4$. The conditions at the wall are shown in Table 1.

Table 1. Conditions at the wall

	Region 1	Region 2
Total Length (m)	120	280
Displacement in Origin (m)	0.1	3.0
Temperature (C)	15.0	50.0

The present theory was numerically implemented through the computer code CAST (Computer Aided Simulation of Turbulence, Peric and Scheuerer(1989)). This program has the same structure of other existing fluid flow prediction schemes such as TEAM and TEACH. It is thus a conservative finite-volume method in primitive variables. Differences from those codes arise in the co-located variable arrangement, the discretization scheme, the solution algorithms for the linear equation systems resulting form the discretization, and in the pressure coupling which is adopted to the co-located variable storage

For turbulent flow, the code solves the Reynolds averaged Navier-Stokes equations in connection with the k–ϵ differential turbulence model of Launder and Spalding(1974). The five empirical constants appearing in the code take on the standard values. Since CAST uses the wall function method for specification of the boundary conditions at the wall, an extension of the program to our case of interest was a relatively straightforward affair. Changes were basically made in the momentum and energy balances at the control volumes adjacent to the wall. Here, we will spare the reader the main implementation details. We just point out that the concept of a turbulent Prandtl number was used. A grid of 100x100 points was used for the calculations. The results converged to a 10^{-3} error within 900 iterations. The boundary conditions for K and ϵ at the wall are automatically evaluated by CAST considering the former quantity to vary quadratically with the distance from the wall, and the latter quantity linearly. For more details on the implementation of the program, the interested reader is refered to Peric and Scheuerer(1989).

Figure 1 illustrates the flow geometry and the resulting streamlines. Note the streamline deflection at the roughness change. Figures 2 to 5 show, in linear and logarithmic graphs, the effects of surface change on the velocity profiles. The smooth surface case, figures 4 and 5, were run to validate the code and to permit a comparison with the undisturbed case. For both conditions, smooth and rough surfaces, a good reproduction of the law of the wall was obtained. The changes in temperature are shown in figures 6 to 9. Again, nice log profiles are obtained. In all velocity and temperature profiles, the correct behaviour is observed. As we mentioned before, only one data set is currently available in literature which deals with step changes in both roughness and temperature, and this is not available to the present authors. Comparison of the numerical results with the data of Gowen and Smith(1968), of Healzer et alli(1974), of Ligrani et alli(1979) and of Taylor et alli(1989) shows that the expected flow behaviour is certainly met here by the computations. Graphs of the friction coefficient and of the Stanton number are shown in figures 10 and 11. The skin-friction results are very impressive for they stand a close resemblance with the experimental results obtained by

Bradley(1968). In his experiments Bradley found $C_{f1}/C_{f2} = 2.8$, whereas we found here $C_{f1}/C_{f2} = 2.3$. The Stanton number results also follow the expected trend.

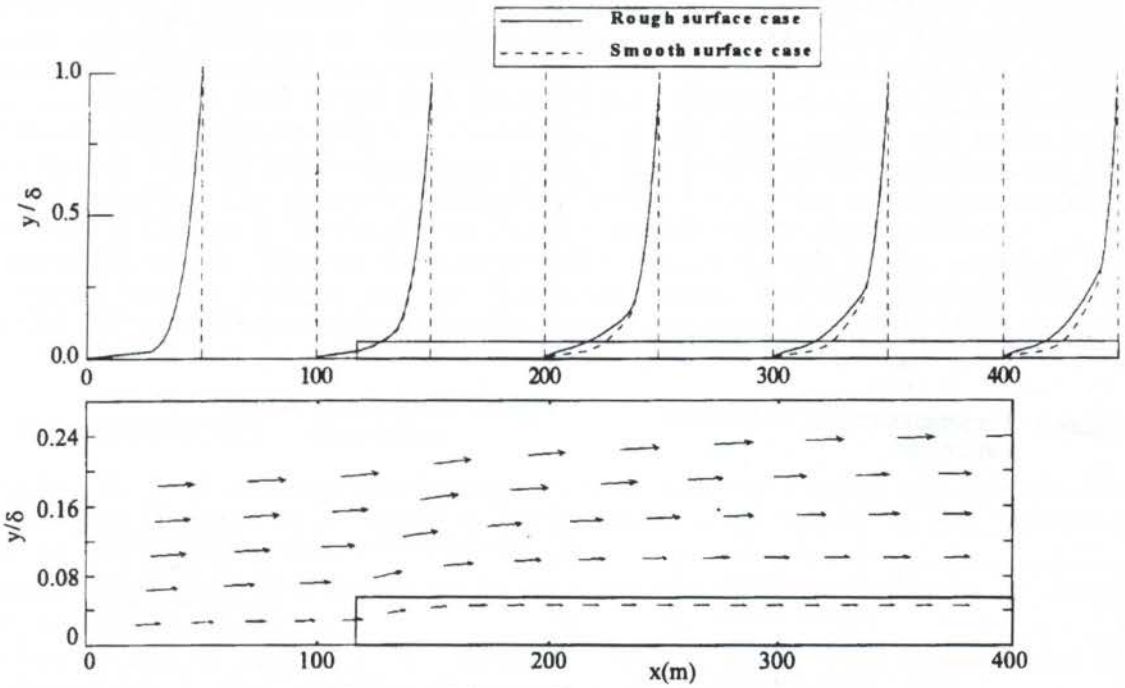

Figure 1 - Flow configuration and streamlines.

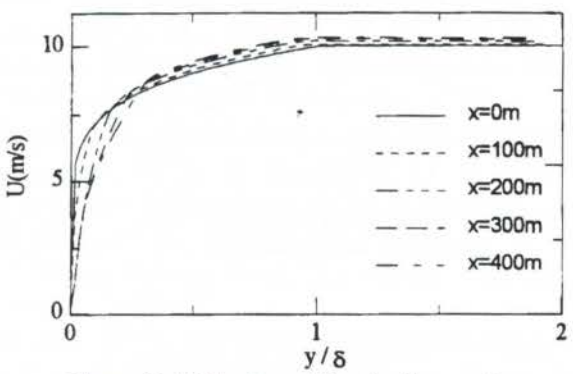

Figure 2 - Velocity profiles for the rough surface case.

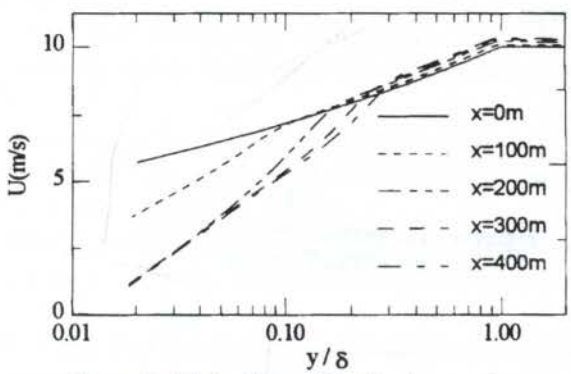

Figure 3 - Velocity profiles for the rough surface case.

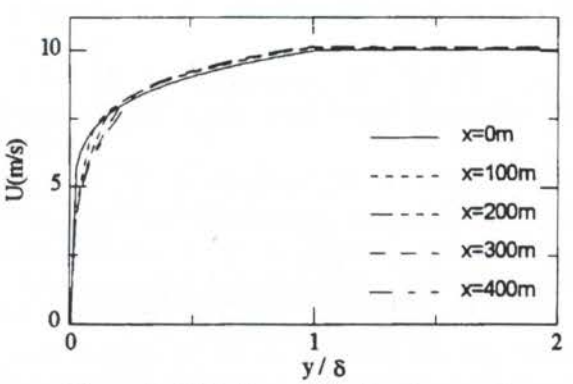

Figure 4 - Velocity profiles for the smooth surface case.

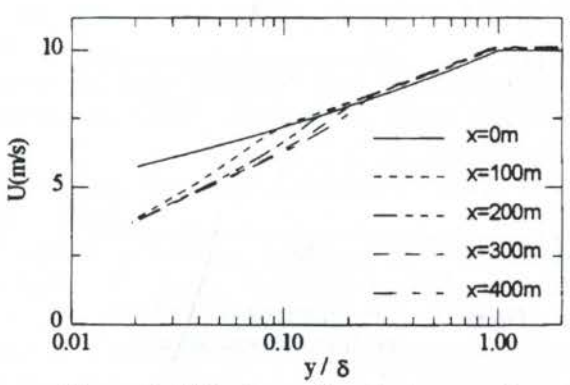

Figure 5 - Velocity profiles for the smooth surface case.

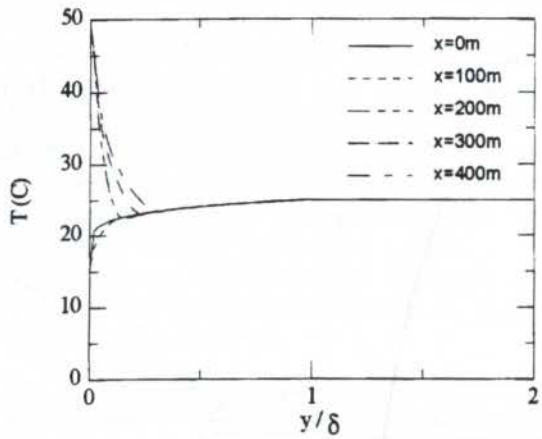

Figure 6 - Temperature profiles for the rough surface case.

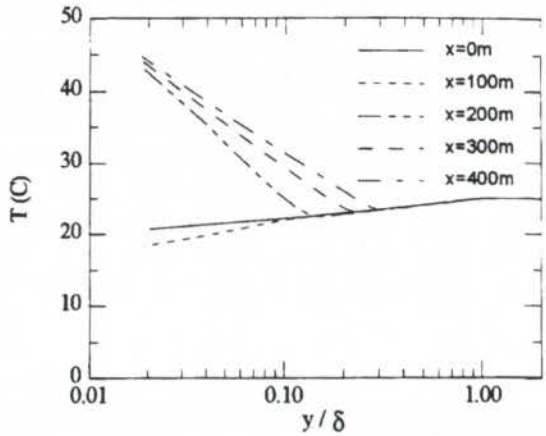

Figure 7 - Temperature profiles for the rough surface case.

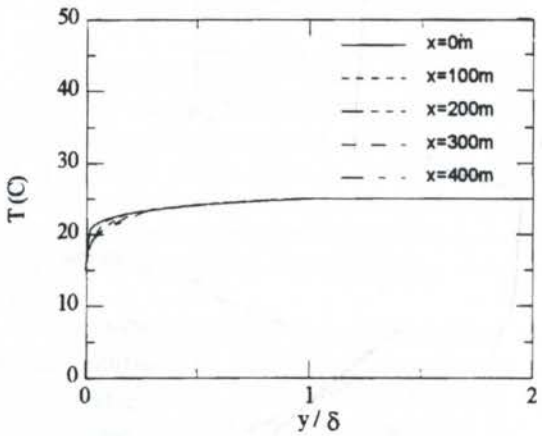

Figure 8 - Temperature profiles for the smooth surface case.

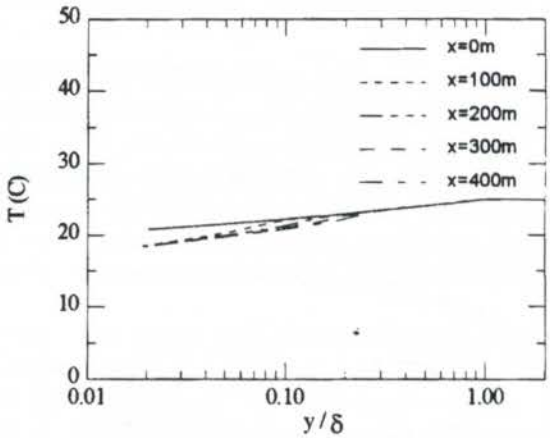

Figure 9 - Temperature profiles for the smooth surface case

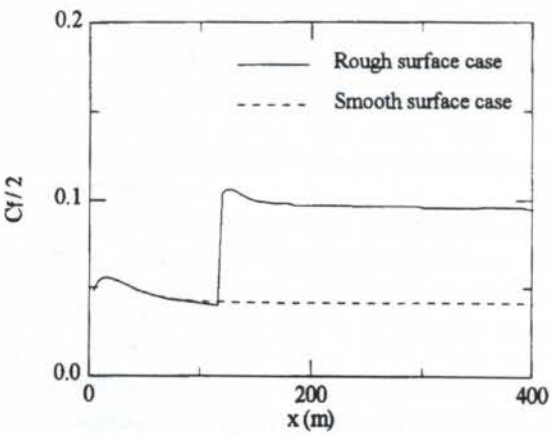

Figure 10 - Skin friction profile for both rough and smooth surfaces.

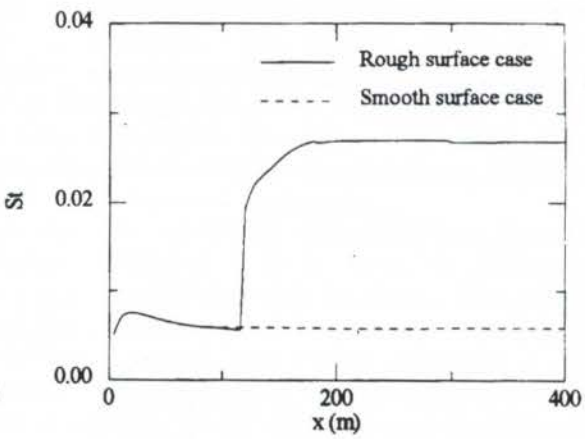

Figure 11 - Stanton number profiles for both rough and smooth surfaces.

4. CONCLUSION

We have developed a theory for the treatment of turbulent boundary layer flows subjected to a step surface change in roughness and in temperature. The theory is based on late concepts by Nikuradse(1933), Clauser(1954) and Moore(1951), being extended to the thermal case through asymptotic and heuristic arguments according to the reasonings of Silva Freire and Hirata(1990a, 1990b). A numerical implementation of the theory, together with a $k-\epsilon$ modelling of the outer region, was made, resulting in coherent velocity and temperature profiles, and skin-friction coefficient and Stanton number profiles. The theory is undergoing further tests, being currently compared with the data of Ligrani & Moffat(1985). Further results will be reported later.

Acknowledgements. During the execution of this work, one of the authors, PPMM, benefited from a Visiting Scholar Scholarship from FAPERJ (Process Number E-26/151.087-96). The work was also financially supported by CNPq through grant No 350183/93-7.

5. REFERENCES

Bradley, E. F. A Micrometeorological Study of Velocity Profiles and Surface Drag in the Region Modified by a Change in Surface Roughness. *Quart. J. Roy. Meteor. Soc.*, vol. 94, pp. 361-379, 1968.

Clauser, F. H. Turbulent Boundary layers in Adverse Pressure Gradients. *J. Aero. Sci.*, vol. 21, pp. 91, 1954.

Gowen, R. A. & Smith, J. W. Turbulent Heat Transfer from Smooth and Rough Surfaces. *Int. J. Heat and Mass Transfer*, vol. 11, pp. 1657-1673, 1968.

Hama, F. R. Boundary Layer Characteristics for Smooth and Rough Surfaces. *Trans. Soc. Nav. Arch. Mar. Engrs.*, vol. 62, pp. 333, 1954.

Healzer, J. M., Moffat, R. J. & Kays, W. M. The Turbulent Boundary Layer on a Rough, Porous Plate: Experimental Heat Transfer with Uniform Blowing. *Report No HMT-18*, Stanford University, 1974.

Kaplun, S. Fluid Mechanics and Singular Perturbations, *Academic Press*, 1967.

Launder, B. E. & Spalding, D. B. The Numerical Computation of Turbulent Flows, *Computer Methods in Applied Mechanics*, vol. 3, pp. 269-289, 1974.

Ligrani, P. M., Moffat, R. J. & Kays, W. M. The Thermal and Hydrodymanic Behaviour of Thick Rough-Wall Turbulent Boundary Layers. *Report No HMT-29*, Stanford University, 1979.

Moore, W. L. An Experimental Investigation of the Boundary Layer Development Along a Rough Surface. *Ph. D. Thesis*, State University of Iowa, 1951.

Nikuradse, J. Stromungsgesetze in Rauhen Rohren. *V. D. I. Forshungsheft* No 361, 1933.

Orlando, A. F., Moffat, R. J. & Kays, W. M. *Report No HMT-*, Stanford University, 1974.

Peric, M. & Scheuerer, G. CAST - A Finite Volume Method For Predicting Two-Dimensional Flow and Heat Transfer Phenomena, *GRS- Technische Notiz Srr-89-01*, 1989.

Perry, A. E. & Joubert, P. N. Rough-Wall Boundary layers in Adverse Pressure Gradients. *J. Fluid Mechanics*, vol. 17, pp. 193-211, 1963.

Silva Freire, A. P. & Hirata, M. H. Approximate Solutions to Singular Perturbation Problems: the Intermediate Variable Technique. *J. Math. Analysis and Applications*, vol. 145, pp. 241-253, 1990a.

Silva Freire, A. P. & Hirata, M. H. Analysis of Thermal Turbulent Boundary Layers Over Rough Surfaces. *Proceedings of the 3rd Brazilian Meeting on Thermal Sciences*, pp. 313-316, Florianópolis, 1990b.

Taylor, R. P., Coleman, H. M. & Hodge, B. K. Prediction of Heat Transfer in Turbulent Flow Over Rough Surfaces. *Journal of Heat Transfer*, vol. 111, pp. 568-572, 1989.

XIV Brazilian Congress of Mechanical Engineering
Obeid Plaza Hotel Convention Center - Bauru - SP/Brazil
December 08-12th 1997

PAPER CODE: COB249

AN ALGEBRAIC TURBULENCE MODEL FOR THE DESCRIPTION OF BUBBLE PLUMES

Andréa C. Alves, Jian Su† and Atila P. Silva Freire
Mechanical Engineering Program (COPPE/UFRJ)
C.P. 68503, 21945-970 Rio de Janeiro, Brazil
†Department of Mechanical and Material Engineering
Military Engineering School (IME/RJ)
22290-270, Rio de Janeiro, Brazil

Abstract

The present work advances a new algebraic turbulence model for the description of bubble plumes. The model is based on the eddy viscosity and bubble diffusity concepts, resorting to dimensional arguments and experimental data to arrive at functional relationships involving only primitive variables of the flow. The model is an improvement over other algebraic models in literature, providing better results at lower computational cost. The results include predictions of the velocity profiles, of the void fraction and of the plume radius. The four constants that appear in the theory are determined through comparison with the data of Milgram and Van Houten(1982) and of Milgram(1983), for depths ranging from 6 to 20 meters. The agreement is shown to be very good.

Keywords

Multiphase Flows, Turbulence Modeling, Bubble Plumes,
Algebraic Turbulence Models, Finite Difference Methods

Palavras Chave

Escoamento Multiffico, Modelagem Turbulenta, Pluma de Bolhas,
Mtodo de Diferenas Finitas

1. Introduction

The development of models for the description of turbulent two-phase flows has basically followed two lines of thought. In the integral models, some *ad hoc* assumptions concerning the functional form of the flow parameters are made; additionally, constitutive equations are unleashed to reduce the original set of partial differential equations that govern the phenomenon to a simplified set of ordinary differential equations. A classical example of integral method is the entrainment method developed by G. I. Taylor to describe jets and plumes. We recall that, in these methods, the details of the turbulence must be embodied in the extra hypotheses for the specification of the constitutive equations and that, in many situations, they are simply not enough to perceive all subtleties of the flow. The differential methods on the other hand, aim at solving the

equations of motion in their original form provided they are averaged and complemented with constitutive equations for the resulting Reynolds stresses. Several possibilities are then in order. One can use simplified algebraic models of the mixing length type, or two-equation differencial models, or even transport equations for direct modelling of the Reynolds tensor components. The advantage of the differential methods is that, in theory, all properties of the flow, mean and fluctuating, are resolved at the same time giving a procedure which is deemed more general and precise.

The purpose of this paper is to propose a new algebraic turbulence model for the description of bubble plumes. After the introduction of the concepts of eddy viscosity and of effective diffusivity of bubbles, an exact set of equations is derived for these parameters. The equations are obtained directly from the equations of motion after some algebraic manipulations are made and some hypotheses are introduced. The hypotheses are advanced to render the turbulence model explicit, that is, to yield functional relationships involving only primitive variables of the flow. In other words, the turbulence model to be here determined is independent on the flow parameters to be resolved. The result is a new model which represents an improvement over of the algebraic model of Iguchi and Morita(1990). The derivation of the model of Iguchi and Morita follows the some procedure presented here but does not make any assumption about the values of the liquid phase velocity and the void fraction in the centerline of the flow. The same holds for the position of the plume radius. The implication is that the resulting models for the eddy viscosity and for the effective diffusity of bubbles are dependent on flow parameters that are yet to be calculated.

The governing equations for the bubbly two phase flow are given in the next section. In section 3 we describe the new algebraic turbulence model and make some comments about other available models in literature.

In section 4 we will give a brief explanation of the finite difference method used to implement the turbulence model here derived. Then, we will show how the model stands comparatively with some experimental data. The results include predictions of the velocity profiles, of the void fraction and of the plume radius. The theory is compared with the data of Fanneløp and Sjøen(1980), of Milgram and Van Houten(1982) and of Milgram(1981), for depths ranging from 6 to 60 meters. The agreement is shown to be very good.

2. The Equations of Motion

In what follows we will be interested in describing the flow properties at a specific region of the plume, the zone of established flow. Thus, realizing that in this region the dominant force is the buoyancy force, several simplifications are in order.

The small characteristic radial scale of the plume - its radius - implies that the boundary layer approximation can be applied here. Then, invoking Boussinesq approximation, the equations of motion can be written in classical notation as:

a) continuity equation:

$$\frac{\partial u}{\partial z} + \frac{1}{r}\frac{\partial (r\, v)}{\partial r} = 0; \tag{1}$$

b) momentum equation for the liquid phase:

$$u\frac{\partial u}{\partial z} + v\frac{\partial u}{\partial r} = \frac{1}{r}\frac{\partial}{\partial r}\left(\nu_{eff} r \frac{\partial u}{\partial r}\right) + \alpha g; \tag{2}$$

b) momentum equation for the gas phase:

$$(u + u_s)\frac{\partial \alpha}{\partial z} + v\frac{\partial \alpha}{\partial r} = \frac{1}{r}\frac{\partial}{\partial r}\left(D_{eff} r \frac{\partial \alpha}{\partial r}\right). \tag{3}$$

We point out to the reader that all quantities depicted in the above equations are mean quantities. The bar have been omitted for the sake of brevity.

These equations are subjected to the following boundary conditions:

$$\frac{\partial u}{\partial r}(z,0) = 0, \quad \frac{\partial \alpha}{\partial r}(z,0) = 0, \quad v(z,0) = 0,$$

$$\lim_{r\to\infty} u(z,r) = U_e, \quad \lim_{r\to\infty} \alpha(z,r) = 0. \tag{4}$$

3. The Algebraic Turbulence Model

The effects provoked by dispersed bubbles on the turbulence structure of two-phase flows are very complex. Typically, the mixing resulting from the bubbles increase the turbulence in the flow by a factor of at least fifty percent. In the integral theories, this increase is taken into account by the amplification momentum factor, which is pretty much an empirically determined parameter. To obtain more general procedures, some authors (Lopez de Bertodano *et. al.*(1990) and Lopez de Bertodano *et. al.*(1994)) have developed two-equation differential models for the description of two-phase bubbly flows. In the latter work, Lopez de Bertodano and co-workers discussed two possible variations of the $\kappa - \epsilon$ model for two-phase flows. The more interesting one, the two time-constant model, considers that the shear induced turbulence and the bubble induced turbulence can be linearly superposed. This approach for a phenomenon which is inherently non-linear must be considered an approximation valid only for low void fraction flows. In fact, six types of non-linear coupling were identified in literature (Lance *et. al.*(1992), Serizawa and Kataoka(1990) and Squires and Eaton(1989)) depending on the flow conditions. For flows where non-linear coupling effects are important, further improvements on the model are required. The model to be developed here is expected to performe, at least for the same flow conditions, as well as the differential models but with a much lower computational cost.

Algebraic models are normally derived in literature by analogy with the mixing length theory of Prandtl. Dimensional arguments and heuristic considerations are also commomly evoked. A typical example is the model proposed by Sahai and Guthrie(1982), which can be cast as

$$\nu_{eff} = C \left[Q_g (1-\alpha) g / D \right]^{1/3}, \tag{5}$$

where all symbols above have their classical meaning and the value of the constant $C(= 0.00049)$ has been recently established by Mazumdar(1989). Thus, Q_g stands for the gas flow rate, g for the gravity acceleration and D for the diameter of the cylinder. Comparison with experimental data shows this equation to overestimate the effective viscosity and consequently the velocity of the liquid phase. This discrepacy is inputed to the disregard of the bubble induced turbulence.

An alternative formulation was proposed by Taniguchi *et. al.*(1988), who considered both the eddy viscosity and the effective diffusity of bubbles constant throughout the flow region. Then, considering the liquid phase velocity and the void fraction to have a Gaussian curve form, and resorting to some experimental data, they wrote

$$\nu_{eff} = 0.0783\, g^{0.056}\, u_s^{-0.36}\, Q_g^{0.528}. \tag{6}$$

where u_s is the slip velocity.

This equation is valid for flows in the interior of cylinders where wall effects are negligible.

Other equations were proposed for the mean values of ν_{eff} averaged over the whole bath. Examples are the expressions of Pun and Spalding(1967) and of Mazumdar(1989).

To find a more general turbulence model which can be applied locally to the whole of the plume, we consider first that the velocity and void fraction profiles can be written as:

$$u = u_{cl}\ exp\big(-c(r/b_u)^2\big), \tag{7}$$

$$\alpha = \alpha_{cl}\ exp\big(-c(r/b_\alpha)^2\big), \tag{8}$$

where $c = ln\,2$, cl denotes a centerline value, and b_u and b_α are the half-value radii of u and α respectively.

Next, we re-write equation (2) in its integral form as

$$ru\Big(-\frac{1}{r}\frac{\partial}{\partial z}\int_0^r ru\,dr\Big) + \frac{\partial}{\partial z}\int_0^r ru^2\,dr = r\nu_{eff}\,\frac{\partial u}{\partial r} + \int_0^r \alpha g r\,dr. \tag{9}$$

Substitution of equations (7) and (8) into equation (9), yields

$$\nu_{eff} = \Big(\frac{1}{2c}\Big)^2 \frac{b_u^2}{ur^2}\Big[gb_\alpha^2(\alpha_{cl}-\alpha) - b_u^2\frac{du_{cl}}{dz}(u_{cl}-u) - b_u\frac{db_u}{dz}(u_{cl}-u)^2\Big]. \tag{10}$$

The same procedure can now be applied to the gas phase momentum equation. Substitution of equations (7) and (8) into the integral form of equation (3) yields

$$\begin{aligned} D_{eff} = &-\Big(\frac{b_\alpha}{2c}\Big)^2\Big(\frac{B^2}{u_{cl}}\frac{du_{cl}}{dz} + \frac{B^2}{\alpha_{cl}}\frac{d\alpha_{cl}}{dz} + 2B\frac{dB}{dz}\Big)\frac{1}{r^2\alpha}(u_{cl}\alpha_{cl} - u\alpha) + \\ &\Big(\frac{b_\alpha}{2c}\Big)^2\Big(\frac{b_\alpha^2}{\alpha_{cl}}\frac{d\alpha_{cl}}{dz} + 2b_\alpha\frac{db_\alpha}{dz}\Big)\frac{1}{r^2\alpha}(\alpha_{cl}-\alpha)u_s + \\ &\Big(\frac{b_\alpha}{2c}\Big)^2\Big(\frac{b_u^2}{u_{cl}}\frac{du_{cl}}{dz} + 2b_u\frac{db_u}{dz}\Big)\frac{1}{r^2}(u_{cl}-u) + \\ &\Big(\frac{b_\alpha}{2c}\Big)^2\Big(\frac{u}{B}\frac{dB}{dz} + \frac{u_s}{b_\alpha}\frac{db_\alpha}{dz} - \frac{u}{b_u}\frac{db_u}{dz}\Big), \end{aligned} \tag{11}$$

where

$$B = b_u b_\alpha/(b_u^2 - b_\alpha^2)^2,$$

$$\frac{dB}{dz} = B^3\,\frac{b_\alpha^2}{2c}\Big(\frac{1}{b_u^3}\frac{db_u}{dz} + \frac{1}{b_\alpha^3}\frac{db_\alpha}{dz}\Big).$$

Expressions for the values of ν_{eff} and of D_{eff} in the centerline of the plume can be obtained through passage of the limit $r \to 0$. It results that

$$\nu_{eff,cl} = \frac{1}{4c}\frac{b_u^2}{u_{cl}}\Big(g\alpha_{cl} - u_{cl}\frac{du_{cl}}{dz}\Big), \tag{12}$$

and

$$D_{eff,cl} = -\frac{b_\alpha^2}{4c}\,\frac{u_{cl}+u_s}{\alpha_{cl}}\,\frac{d\alpha_{cl}}{dz}. \tag{13}$$

All equations derived so far for ν_{eff} and D_{eff} are dependent on the flow parameters themselves which are, at this stage, unknowns. Therefore, the next step in our modelling must be to find functional relationships to ν_{eff} and D_{eff} which are dependent only on the flow variables. This will be made in two stages. First, we will consider that ν_{eff} and D_{eff} obey certain functional relationships that involve only flow parameters measured at the centerline and primitive flow variables. Next, the centerline parameters will be determined through similarity arguments and an analysis of some experimental data.

The Gaussian curve behaviour of the liquid phase velocity and of the void fraction is a well documented fact. Equations (7) and (8) can, therefore, be considered a truth expression of the actual behaviour of u and of α. For ν_{eff} and D_{eff}, however, an analysis of the experimental data leads to a distinct result. Iguchi and Morita(1992) have shown that, in the zone of established flow, the eddy viscosity exhibits a parabolic behaviour, whereas the effective diffusity of bubbles exhibits a nearly constant behaviour. Thus, we may write

$$\nu_{eff} = \frac{1}{4c}\frac{b_u^2}{u_{cl}}\left(g\alpha_{cl} - u_{cl}\frac{du_{cl}}{dz}\right)\left(1 - 0.5\left(\frac{r}{b_u}\right)^2\right), \tag{14}$$

and

$$D_{eff} = -\frac{(0.8b_u)^2}{4c}\frac{u_{cl} + u_s}{\alpha_{cl}}\frac{d\alpha_{cl}}{dz}, \tag{15}$$

where we have used the fact that $b_\alpha = 0.8b_u$.

Further, a dimensional analysis of the problem (Ditmars and Cederwall(1974)) suggests that the mean flow parameters at the centerline can be written as

$$u_{cl} = C_1\left(Q_g\, g\right)^{1/3} z^{-1/3}, \tag{16}$$

$$\alpha_{cl} = C_2\left(\frac{z}{H + H_o}\right)^{c_3}, \tag{17}$$

$$b_u = C_4\, z. \tag{18}$$

In the above equations, H represents the height of the zone of established flow and H_o the manometric pressure.

Finally, substitution of equations (16) to (18) into equations (14) and (15) yields the turbulence model here proposed, that is,

$$\nu_{eff} = \frac{C_4}{4c}\left(\frac{C_2\, g^{2/3} z^{7/3+C_3}}{C_1\, Q_g^{1/3}\,(H + H_0)^{C_3}} + \frac{1}{3} z^{2/3} C_1\, Q_g^{1/3}\, g^{1/3}\right), \tag{19}$$

and

$$D_{eff} = -\frac{0.8^2}{4c} C_4\, C_3\left(C_1\, Q_g^{1/3}\, z^{1/3} + u_s\, z\right). \tag{20}$$

The two equations shown above are clearly independent of the flow parameters, as intended before. In the next section, constants C_1 to C_4 will be determined.

The last parameter to be defined is the slip velocity u_s. The slip velocity was observed (Iguchi and Morita(1992))to increase slightly in the radial direction and decrease as the air flow rate increases. Most authors, however, for the sake of simplicity, consider u_s constant; this will be, indeed, the consideration adopted here.

4. Finite Difference Solution

The momentum equations for liquid and gas phases are solved through a general solution procedure for transport equations, in a conservative form

$$\frac{\partial u\phi}{\partial x} + \frac{\partial v\phi}{\partial y} = \frac{\partial}{\partial y}(\Gamma_\phi \frac{\partial \phi}{\partial y}) + S_\phi, \tag{21}$$

where Γ_ϕ denotes the generalised diffusion coefficient and S_ϕ the source term.

Equation(21) is solved by using the explicit finite-difference scheme of Dufort-Frankel. The scheme is a two-step explicit centered difference method with a uniform grid in the radial direction. The flow parameters at the centerline were found through a Taylor series expansion using a second order approximation for the velocity and the void fraction profiles. The Dufort-Frankel formulation applied to jet and plume flows presented stability restrictions. This restriction has allowed the user of relatively coarse grids without any prejudice to accuracy. Here, the dependent variable is taken to be u and h for the solution respectively of the momentum and the energy equations. The continuity equation is integrated the usual way and iterations are needed to treat the nonlinear coupling among the equations.

The code was qualified against a laminar jet flow test case. For this flow, the numerical solution was in agreement with the similarity solution up to six significant figures, which was considered to be satisfactory for the purpose of this work.

5. Numerical Results

The variation in centerline void fraction with axial distance for the Milgram and Van Houten(1982) case is shown in Fig.1. Note that the predictions given by the present turbulent model compare favorably with the experimental data. The curve fitting was made considering equation(17). This gives the following expression:

$$\alpha_{cl} = 0.00151 z^{-1.37}. \tag{22}$$

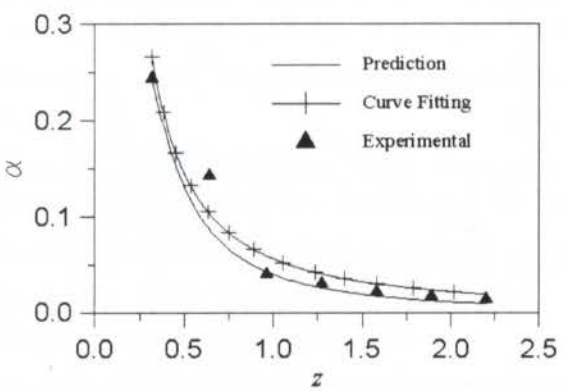

Fig.1 Axial variation of centerline void fraction, α_{al}, compared with experimental data (Milgram and Van Houten, 1982).

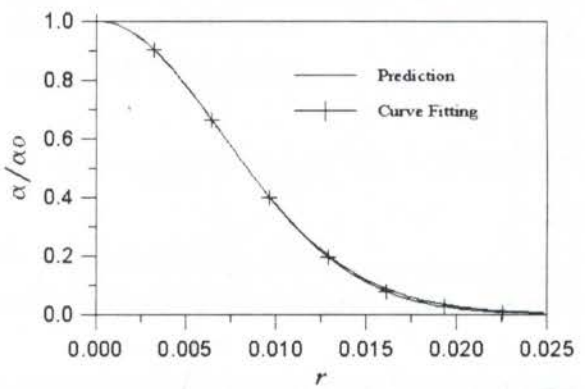

Fig.2 Radial distribution of void fraction, $\alpha(r)$.

The radial distribution of the void fraction is shown in Fig.2 together with the curve fitting provided by Equation(8). Observe that the predicted radial distribution fits well the Gaussian distribution, except for a very small difference at large radial positions. This is probably due to the application of the infinite boundary condition at a finite radial position.

The variation of the plume radius with the axial distance for the Milgram and Van Houten(1982) case is given in Fig.3. The bubble plume radius is defined as the radial position where the mean velocity profile attains half of its value at the centerline. The numerical results should, according with equation(18), be a linear function of the axial coordinate. In fact, the present model predicts a reasonably linear variation of the plume radius. This variation, however, differs appreciably from the experimental data. We suspect this to happen due to the relatively short total axial length of the experimental case; in such situation, free surface effects should be important. The present model is not capable of predicting free surface effects, nor even the flow in the surface region.

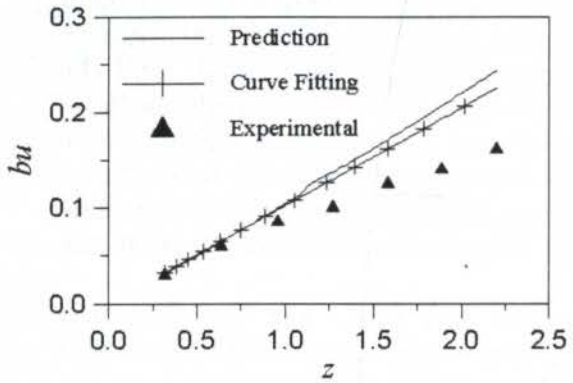

Fig.3 Axial variation of bubble plume, b_u, compared with experimental data (Milgram and Van Houten, 1982).

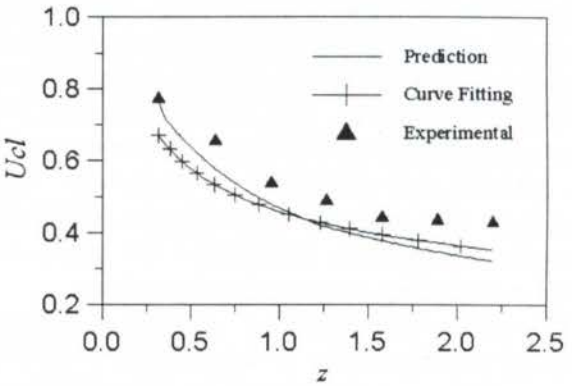

Fig.4 Axial variation of centerline velocity compared with experimental data (Milgram and Van Houten, 1982).

The axial variation of the mean centerline velocity is shown in Fig.4. The numerical results follow, indeed, the trend set by equation(16). We conclude from the four preceeding figures that the present algebraic turbulence model predicts correctly the expected axial and radial distributions of important two phase flow parameters.

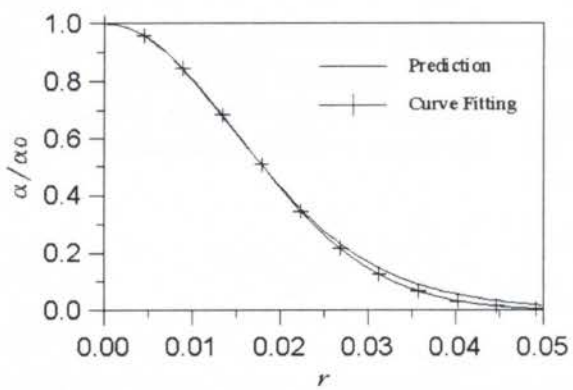

Fig.5 Radial distribution of void fration ration $\alpha(r)$.

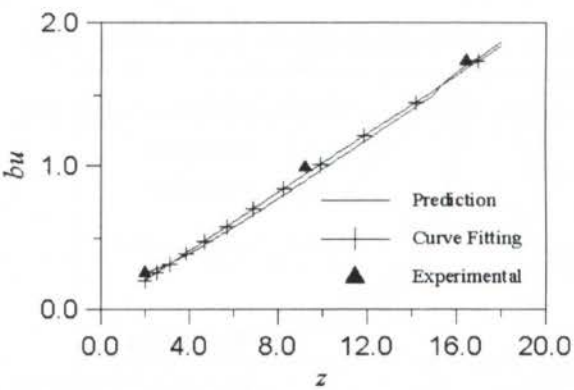

Fig.6 Axial variation of bubble plume, b_u, compared with experimental data(Milgram, 1983)

In Fig. 5 and Fig. 6 we show selected results for the test case of Migram(1983). Here, only the first 20 meters of his 60 meter experiment are shown. For this case, the predicted plume radius is in excellent agreement with the experimental data. The radial profile of the void fraction is seen to fit well to a Gaussian distribution.

We close this section by pointing out to the reader that in all above developments we have used $C_1 = 2.70$, $C_2 = 0.0015$, $C_3 = -1.37$ and $C_4 = 0.102$.

6. Conclusion

We have here developed a simple algebraic turbulence model for the description of bubble plumes which was shown to performe well for a range of flow conditions. The model, to the authors' knowledge, is the simplest available in literature for this class of problem. The model is now been tried at more complex flow configurations which involve more than one plume and where wall effects are important.

Acknowlegements. The present work has been financially supported by CNPq through grant No.350183/93-7. JS is gratefull to FAPERJ for the award of a Research Fellowship No E26-151.113/96. During the course of the research ACA benefited from a CNPq Scholarship.

7. References

Ditmars, J. D. & Cederwall, K. Analysis of Air Bubble Plumes, *Proc. Coastal Engng. Conf.*, chap. 128, pp.2209–2226, 1974. Fanneløp, T.K. & Sjøen, K. Hydrodynamics of Underwater Blowouts. *AIAA paper 80-0219*, 1980.

Iguchi, M and Morita, Z-I, The Effective Viscosity and Effectice Diffusity of Bubbles in an Air-Water Vertical Bubbling Jet, *ISIJ Intl*, vol.32, pp.857–864, 1990.

Lance, M. & Lopez de Bertodano, M. Phase Distribution Phenomena and Water Effects in Bubbly Two-Phase Flows, *3rd Int. Workshop on Two-Phase Flow Fundamentals*, Imperial College, London, 1992.

Lopez de Bertodano, M., Lee, S.-J., Lahey, R. T. Jr. & Drew, D. A. The Prediction of Two-Phase Turbulence and Phase Distribution Phenomena Using a Reynolds Stress Model, *ASME J. Fluids Engrg.*, vol.112, pp.107–113, 1990.

Lopez de Bertodano, M., Lahey, R. T. Jr. & Jones, O. C. Development of a $k-\epsilon$ Model for Bubbly Two-Phase Flow, *ASME J. Fluids Engrg.*, vol.116, pp.128–134, 1994.

Mazumdar, D. *Metall. Trans. B*, vol.13, pp.125, 1989.

Milgram, J.H & Van Houten, R.J. Plumes from Sub-Sea Well Blowouts. In *Proc. of the 3rd Intl Conf., BOSS*, vol.1, pp.659–684, 1982.

Milgram, J. H., Mean Flow in Round Bubble Plumes, *J. Fluid Mech.*, vol. 133, pp.345–376, 1983.

Pun, W. M. & Spalding, D. B. *Proc. XVIII Int. Astronautical Cong.*, vol. 3, Pergamon Press/OWN-Polish Sci. Publ., vol. 3, 1967.

Sahai, Y & Guthrie, R. I. L. *Metall. Trans. B*, vol. 13, pp 125, 1982.

Serizawa, A. & Kataoka, I. Turbulence Supression in Bubbly Two-Phase Flow, *Nuclear Engineering and Design*, 1991.

Squires, K. D. & Eaton, J. K., Study of the Effects of Particle Loading on Homogeneous Turbulence Using Direct Simulation, *ASME, Fluids Engng. Division, FED*, vol. 80, pp 37-44, 1989.

Tanigushi, S., Kikuchi, A., Matsuzaki, H. & Bessho,*N. Trans. Iron Steel Inst. Japan*, vol.28, pp.262, 1988.

XIV Brazilian Congress of Mechanical Engineering
Obeid Plaza Hotel Convention Center - Bauru - SP/Brazil
December 08-12th 1997

PAPER CODE: COB250

FURTHER RESULTS ON THE ASYMPTOTIC BEHAVIOUR OF INTERACTING TURBULENT BOUNDARY LAYERS AND SHOCK WAVES

Guilherme S. Terra, Jian Su† and Atila P. Silva Freire
Mechanical Engineering Program (COPPE/UFRJ),
C.P. 68503, 21945-970 Rio de Janeiro, Brazil.
†Department of Mechanical and Material Engineering,
Military Engineering School (IME/RJ),
22290-270, Rio de Janeiro, Brazil.

Abstract

The present work makes a critical compilation of some experimental data to corroborate the physical validity of the theoretical asymptotic structure resulting from an application of Kaplun limits to the shock-wave/turbulent boundary layer interaction problem. The interaction of a shock wave with a turbulent boundary layer is a very complex and rich phenomenon, where the steep pressure gradient imposed to the boundary layer by the shock wave gives rise to an inviscid interaction process in a region which would be otherwise viscous dominated. Thus, in a classical three deck asymptotic model of the compressible turbulent boundary layer (Silva Freire(1989a)), the turbulent region must change so as to comply to this constraint. In fact, according to the single limit concept of Kaplun, in the interaction region the turbulent region completely disappears. The new arising asymptotic structure consists then of two distinct regions: the wall viscous region and the outer inviscid region. Here, these two regions are clearly identified by a careful processing of some experimental data. Considering some flow measurements, one is capable of evaluating the dominant terms in the Navier-Stokes, from which the asymptotic structure can then be ascertained. With the new asymptotic structure, a simplified theory can then be developed for the inner regions of the flow. The results obtained through the simplified theory are compared with calculations provided by a full Navier-Stokes code and with some experimental data for velocity, pressure and skin-friction. The full N-S code uses a finite difference explicit scheme. In the numerical simulation, the turbulent shear stresses are evaluated through an algebraic model and a half-equation differential model.

Keywords

Interaction, Turbulence, Boundary Layer, Shock Wave, Kaplun Limits.

Palavras Chave

Interação, Turbulência, Camada Limite, Onda de Choque, Limites de Kaplun.

1. INTRODUCTION

In a previous work by the present authors (Terra et alli(1996)), the asymptotic structure resulting from the interaction between a normal shock-wave and a turbulent boundary layer was studied. In a straightforward application of Kaplun limits to the problem, a new two-layered structure consisting of a set of two principal equations and two characteristic scales was deducted. In fact, we have shown that for the interaction problem the turbulent boundary layer presents a changeable asymptotic structure, resuming his classical two-layered structure into an one-layered structure at the foot of the shock. A continuous and slow shrinking of the turbulent region is predicted by the new theory, resulting from the application of Kaplun limits in the stream-wise direction. The new structure, as derived, is thus completely different from those found in the literature, being, however, fully compatible with the observed data.

With the new asymptotic structure for the interaction region, a simplified theory can be developed (Terra et alli(1996)) for the inner regions of the flow which is capable of completely describing the main flow features and yet avoid the complications involved in the matching processes required by the classical approaches. The theory, as advanced, avoids the specification of a turbulence model, using asymptotic arguments for the construction of a wall solution. This wall solution is then patched to a defect layer solution.

The defect layer is modelled by an inviscid set of equations that is numerically solved through a finite difference code. The theoretical results include the specification of an algebraic skin-friction coefficient equation.

The purpose of this work is to obtain complete experimental evidence that the asymptotic structure discussed at length in Terra et alli(1996) is correct. This will be achieved by a careful compilation of the experimental data of Sawyer and Long(1982). Through this compilation, a map that displays the dominant region of every term in the equations of motion is constructed, which is then compared with the theoretical results. The results obtained through the simplified theory will also be compared with calculations provided by a full Navier-Stokes code and with the experimental data of Sawyer and Long(1982) for velocity, pressure and skin-friction. The full N-S code uses a finite difference procedure based on the explicit scheme of Bralovskaya(1965). In the numerical simulation, the turbulent shear stresses are evaluated through the algebraic model of Cebeci-Smith(1970) and the half-equation differential model of Johnson and King(1985).

The simplified model is an advance to the previous asymptotic analyses of the problem by Melnik and Grossmann(1974), Adamson and Feo(1975), Messiter(1980), Liou and Adamson(1980) and Silva Freire(1988). In these classical works, the matched asymptotic expansion method was used to develop specific theories for specific values of a small parameter that relates the velocity change across the shock wave with the velocity change across the boundary layer (see Silva Freire(1989b)). Depending on the order of magnitude of this small parameter, four cases were identified for study. In all cases, particular solutions were proposed which could not be extended to the other situations. The theory here presented treats the two relevant small parameters of the problem in a completely independent manner, giving an asymptotic description of the flow field that can be reduced to all those derived by the previous authors. In particular, the present theory shows how the logarithmic region of the flow is affected by the foot of the shock, giving rise to a new asymptotic structure for the turbulent boundary layer in the interaction region.

2.THEORETICAL ASYMPTOTIC STRUCTURE

The new asymptotic structure for the interaction problem can be obtained through a straightforward application of Kaplun limits to the equations of motion. The definition of Kaplun limits, their theoretical foundations, and application to the problem under study, are discussed in Terra et alli(1996). More details on the method can be found in Silva Freire and Hirata(1990). In what follows we will summarize the main findings for the interaction problem.

The resulting asymptotic structure is depicted in figure 1. Please, note that as the shock is approached, that is, as the order of magnitude of Δ – the x-wise streatching function – increases, the validity domain of the turbulent region changes position until it merges at $(\Delta, \eta) = (\epsilon/(u_\tau^3 R), 1/(u_\tau R))$ with the viscous region. Here, η stands for the y-wise streatching function. Indeed, as shown by the calculations (Terra et alli(1996)), at the beginning of the interaction the outer edge of the turbulent region is positioned at $(\Delta, \eta) = (\epsilon, u_\tau^2)$. However, as the order of magnitude of η varies from u_τ^2 to $1/u_\tau R$, the dominance of the turbulent terms moves along the path $(\epsilon\eta/u_\tau^2, \eta)$ until reaching the point $(\epsilon/u_\tau^3 R, 1/u_\tau R)$. The flow structure is then shown to reduce from a classical two deck structure to an one deck structure near to the foot of the shock wave. According to these results, there is a region at the foot of the shock where the full boundary layer equations are recovered. The simplified theory is developed on that basis.

In the simplified theory, the flow is divided into a rotational and an irrotational part. Next, appropriate asymptotic expansions are chosen to represent the flow variables. Substitution of these expansions into the approximate equations of motion and collection of the terms of same order of magnitude then provides three sets of approximated equations (Terra et alli(1996)). These equations are numerically solved and patched to an inner viscous layer solution. The result is a complete description of the velocity and pressure profiles in the inviscid flow region, and the specification of a skin friction equation.

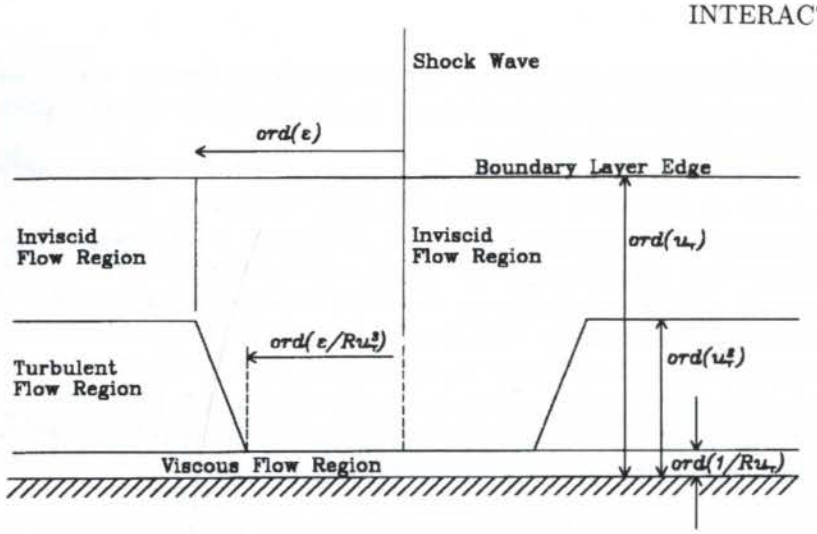

Figure 1. Flow asymptotic structure

3. NUMERICAL ANALYSIS

The results yielded by the simplified theory will be compared in section 4 with the experimental data of Sawyer and Long(1982) and with the results provided by a full Navier-Stokes code developed specifically for the interaction problem.

In this section we will briefly describe some implementation features of both the simplified inviscid theory numerical code and the full N-S numerical code. The N-S code can be run with either an algebraic turbulence model or a half-equation differential model. A brief explanation on the turbulence models will also be given here.

Since the equations yielded by the simplified model are similar to the transonic small disturbance equation, they were discretised through a mixed finite difference scheme. Centered difference was used in the subsonic region whereas a second-order upwind difference was used in the supersonic region. The algebraic equations that arise from the discretisation were solved by a successive line over-relaxation(SLOR) technique.

Two models were used to represent the Reynolds shear stress terms in the full Reynolds averaged Navier-Stokes equations, the algebraic model of Cebeci and Smith(1970) and the half equation model of Johnson and King(1985).

The governing Reynolds-averaged Navier-Stokes equations for steady two-dimensional flows were solved, in a conservative form, using the finite-difference scheme of Brailovskaya (1965). The Brailovskaya scheme is a two-step explicit centered difference method. The formal accuracy and stability limits of the scheme are given by Carter(1972). Artificial dissipative terms were added to the discretised finite difference equations to provide stability against spatial oscillations caused by the centered diffences. A non-uniform grid spacing was used in both spatial directions, so as to get a minimum number of grid points without compromising the accuracy of the solution. A separate compressible boundary layer code was devised to generate a smooth inflow profile. When the boundary layer had reached the correct experimental values, the numerical profiles were transferred to the main solver. The experimental data of Sawyer and Long(1982)were used to specify the main flow velocity variation. Linear extrapolation was used for specification of the outflow boundary conditions.

The full N-S code was tested against non-interacting and interacting flows. For laminar compressible flow, the code was compared with the the similarity solution of Illingworth-Stewartson. For turbulent flow, the code was compared with the test case data of Mabey et alli(1974) and with the law of the wall formulation of East(1972). The agreement was very good for both flow simulations, for both turbulence models.

For interacting flow, the results were also good for both turbulence models. The fact that part of the experimental data was used to specify the boundary conditions certainly made it easier for the code to converge to a solution which was close to the experimental data. From the two tried cases, the first, $M = 1.27$, showed a remarkable agreement between the numerically predicted velocity profiles and the experimental data. For the second case, $M = 1.37$, the agreement was only bad in a ten centimeters x-wise vicinity of

the shock wave. This corresponds to about 40% of the interaction region. The boundary layer thickness at the beginning of the interaction was four centimeters.

Therefore, for most of the flow region, the numerical code was considered to provide good results.

4. RESULTS AND DISCUSSION

Before considering the experimental data of Sawyer and Long(1980), we will briefly explain the reason why they were selected as our test case data.

First, we should recognize that the phenomenon of the interaction manifests itself in diverse forms and hence a single experimental framework which embraces all aspects of the problem is very difficult to devise. The experimental investigations have been conducted with two basic configurations: i) isolated aerofoils and ii) wall mounted models. In the former configuration the shock-wave/boundary layer interaction and the trailing edge flow are strongly coupled, whereas in the latter the coupling effect is eliminated. For interactions occuring on an aerofoil, investigations on the development of shock induced separation with several changing conditions such as the increase in Mach number, the increase in Reynolds number, the changing conditions on the boundary layer nature and on the shock strength, can be found in literature. For flows over wall mounted models, the same effects have been studied; now with the advantage of eliminating any misleading influence of the coupling effects.

Experiments aimed at understanding the detailed structure of the normal shock-wave/boundary layer interaction have often been performed with flat plate flows. Measurements of the boundary layer profiles, their variation through the interaction, and the pressures and velocities in the external flow were made by Sawyer and Long(1982). This work is, to these authors' knowledge, the most detailed experimental analysis of the interaction problem for the Mach number range 1.3-1.5. Besides, their flow is certainly two-dimensional and non-separated, for the range $M = 1.3, 1.4$. For this reason, we have here decided to compare our theoretical predictions with this work.

Two of the cases of Sawyer and Long(1982), here identified by 1.3A and 1.4A, were chosen to test the simplified theory and the full Navier-Stokes solver. The flow conditions are given in Table 1.

Table 1. Flow Conditions

flow	M	Re
1.3A	1.270	3.66×10^6
1.4A	1.370	3.66×10^6

We start our comparison by looking at the predicted flow asymptotic structure. Figure 2 reproduces, from the experimental data, a map which indicates the dominant region of every term in the equations of motion. Both cases, 1.3A and 1.4A are shown. The meaning of the shades in gray is clear. Thus, the outer tone corresponds to the inertia and pressure gradient terms, the intermediate tone to the turbulent terms and the inner tone to the viscous terms. The shock wave is located at $x = 0$. Observe, as predicted by the asymptotic theory, the complete dominance of the inertia and pressure terms in the vicinity of the shock. This feature is particularly striking in case 1.4A where the influence of the shock extends down to the viscous layer. The consequence is that the phenomenon is, for most of the interaction region, and, to a leading order, governed by inviscid equations.

The predicted velociy profiles are shown in figures 3 and 4. Since the full N-S numerical computations have taken the boundary conditions directly from the data of Sawyer and Long(1982), their conditions downstream of the shock never reach the asymptotic levels predicted by the shock wave jump conditions, even at great distances from the shock. Therefore, as the simplified asymptotic theory does satisfy the jump conditions, discrepancies between both were expected to occur. In any case, the agreement between the predicted velocity variation along the streamwise direction for both theories is not bad (figure 4). In fact, the velocity behaviour at the first grid line is predicted quite faithfully by both approaches.

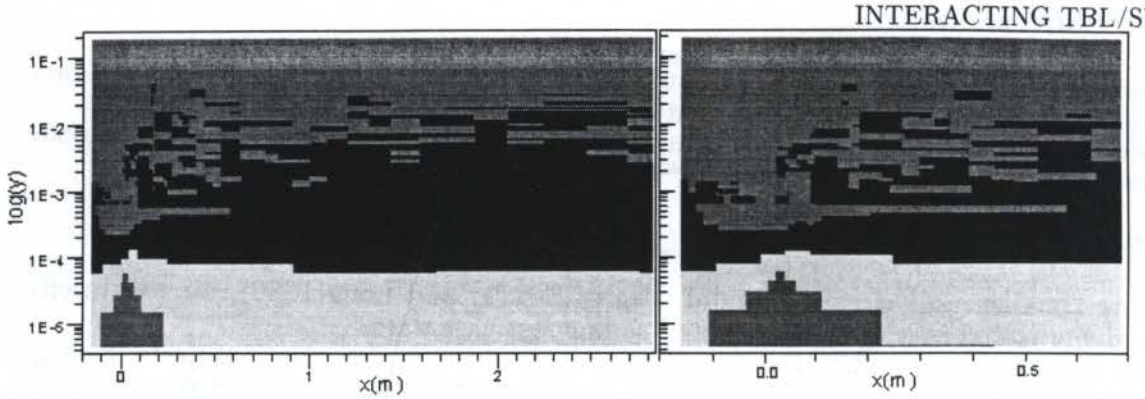

Figure 2a. Flow structure according to data of Sawyer and Long: (a) case 1.3A; (b) case 1.3A, zoom in at the interaction region.

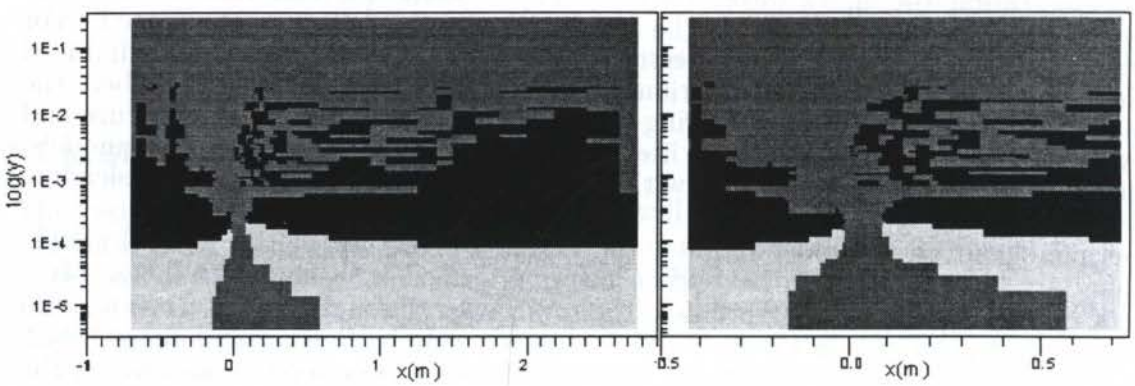

Figure 2b. Flow structure according to data of Sawyer and Long: (c) case 1.4A; (d) case 1.4A, zoom in at the interaction region.

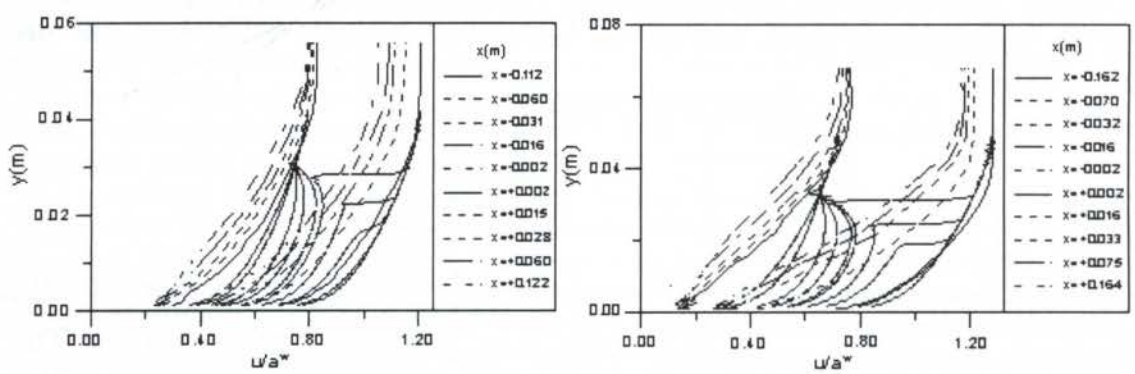

Figure 3. Velocity profile for several x-station: (a) case 1.3A; (b) case 1.4A

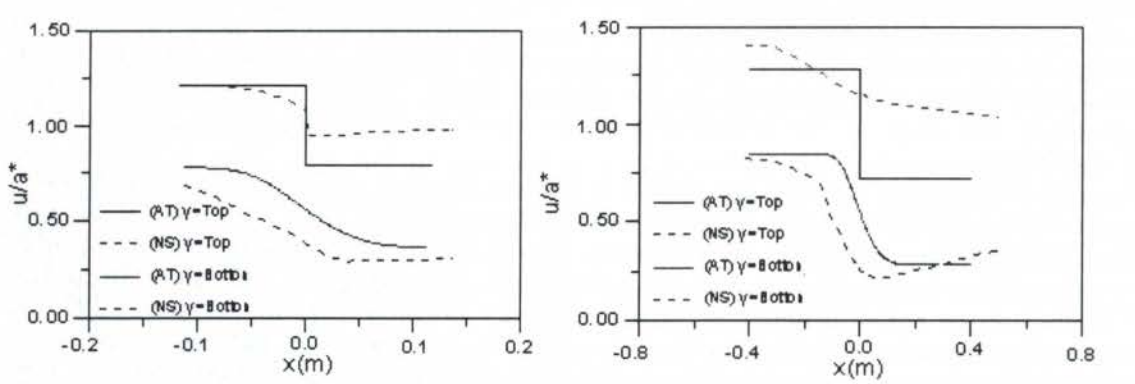

Figure 4. Velocity profiles at the bottom and top of the computational grid: (a) case 1.3A; (b) case 1.4A

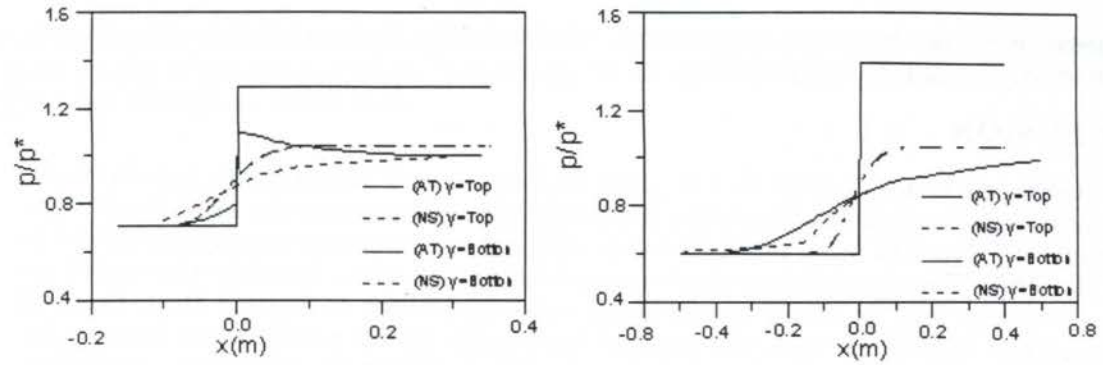

Figure 5. Pressure profiles at the bottom and top of the computational grid: (a) case 1.3A; (b) case 1.4A

In figures 3 and 4, only the data obtained with the algebraic model of Cebeci, Smith and Mosinski(1970), are shown. The algebraic model proved to be much easier to run, and since the discrepancies from the experimental data were minimum, except for a very narrow range in the vicinity of the shock at the higher Mach number, we decided here to plot just the data obtained with Cebeci, Smith and Mosinski's model. The data given by the Johnson and King(1985) model will only be explored in figure 6.

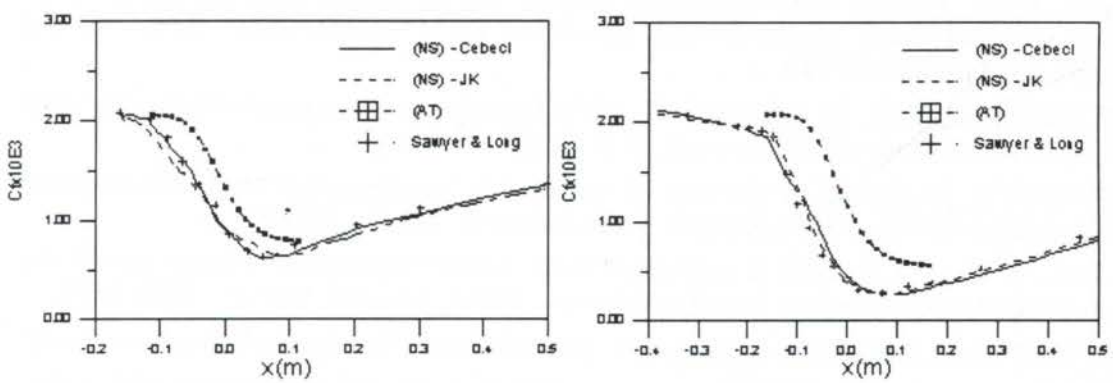

Figure 6. Skin-frictin results: (a) case 1.3A; (b) case 1.4A

The pressure profile results are shown in figure 5. Again, the same remarks concerning the shock wave jump conditions apply here.

Finally, the skin friction results are presented in figure 6. This was one of the main objectives of this work. The agreement for C_f prediction is very favorable for the simplified theory. The results are well inside an aceptable level, being, in fact, comparable with the most advanced and complex approaches.

A 155 (streamwise) by 145 (transversal) grid was used in the finite difference solution of the simplified model (Eq.5-2). Four hundred iterations were necessary to reach a converged solution. This took 4 minutes of computational time in a PC 486 DX2-66, with 8M RAM. A 93(x-wise) by 55(y-wise) grid was used to find the finite difference solution of the full Navier-Stokes equations. In this case, the calculations needed 2000 iterations to reach a time independent solution, with 200 minutes of computational time being used in the same PC for the Cebeci-Smith model. About 50% more of computational time was spent by the Johnson and King model. We estimate a factor of about 50 times between the computational time used by the simplified model and the full Navier-Stokes equations.

The full Navier-Stokes code with the two different turbulent models was observed to compare very well with the experimental results of Sawyer and Long(1982), provided the boundary conditions were correctly specified. Considering the computational costs of both approaches, we conclude that the simplied theory proposed in this work provides a much more economic and efficient approach to the turbulent boundary layer/shock wave interaction problem.

One should also observe that the specification of a turbulence model is not required by the simplified theory. This is just a realization that, as confirmed by the numerical

results, the asymptotic structure suggested in this work for the main interaction region of the flow is predominantly non-viscous.

5. CONCLUSION

The present work has, based on the data of Sawyer and Long(1982), convincingly demonstrated that the flow configuration resulting from the interaction of a shock wave with a turbulent boundary layer resembles very much the asymptotic structure derived in Terra et alli(1996). The conclusion is that an application of Kaplun limits to the equations of motion shows the flow to attain an one deck structure, which is distinct from those of other authors but consistent with the general knowledge of the problem we have. Our results have also successfully shown that the simplified theory is consistent, providing good results for the velocity and pressure profiles and for the skin-friction cofficient.
Acknowledgments. This work has been financially supported by CNPq through grant No. 350183/93-7. JS is grateful to CNPq for a research fellowship through grant No. 301476/92-6. In the course of this research GST benefited from a CAPES scholarship.

6. REFERENCES

Adamson, T.C.Jr. & Feo, A. 1975 Interaction between a shock wave and a turbulent boundary layer at transonic speeds. SIAM J Appl Math,**29**, 121-145.

Brailovskaya, I.Yu. 1965 A finite-difference scheme for numerical solution of the two-dimensional non-stationary Navier-Stokes equations for a compressible flow. Soviet Physics-Doklady, **10** (2), 107-110.

Cebeci, T., Smith, A.M.O. & Mosinski, G. 1970 Calculation of compressible adiabatic turbulent boundary layers. AIAA Journal, **8** (11), 1974-1982.

East, L. F. 1972 A prediction of the law of the wall in compressible three-dimensional turbulent boundary layers. Royal Aircraft Establishment TR No 72178.

Johnson, D.A. & King, L.S. 1985 A mathematically simple turbulence closure model for attached and separated turbulent boundary layers. AIAA Journal, **23**(11), 1684-1692.

Kaplun, S. 1967 Fluid mechanics and singular perturbation. Academic Press New York.

Liou, M.S. & Adamson, T.C. 1980 Interaction between a normal shock wave and a turbulent boundary layer at high transonic speeds. Part II: Wall shear stress. ZaMP, **31**, 227-246.

Mabey, D. G., Meier, H. U. & Sawyer, W. G. 1974 Experimental and theoretical studies of the boundary layer on a flat plate at Mach numbers from 2.5 to 4.5. Royal Aircraft Establishment TR No 74127.

Melnik, R.E. & Grossmann, B. 1974 Analysis of the interaction of a weak normal shock wave with a turbulent boundary layer. AIAA paper No. 74-598.

Messiter, A.F. 1980 Interaction between a normal shock wave and a turbulent boundary layer at high transonic speeds. Part I: Pressure distribution. ZaMP **31**, 204-227.

Sawyer, W.G. & Long, C.J. 1982 A study of normal shock-wave turbulent boundary-layer interactions at Mach numbers of 1.3, 1.4 and 1.5. Royal Aircraft Establishment, Technical Report No 82099.

Silva Freire, A.P. 1988 An asymptotic approach for shock-wave/transpired turbulent boundary layer interaction. ZaMP, **39**, 478-503.

Silva Freire, A.P. 1989a On the matching conditions for a two-deck compressible turbulent boundary layer model. ZaMM, **69**(2), 100-104.

Silva Freire, A. P. 1989b A detailed review of a solution procedure for shock-wave/turbulent boundary layer interaction problems. Revista Brasileira de Ciências Mecânicas, **4**, 210-246.

Silva Freire, A.P. & Hirata, M.H. 1990 Approximate solutions to singular pertubation problems: the intermediate variable technique. J. Math. Analysis and Appl., **145**, 245-253.

Terra, G. S., Su, J. & Silva Freire, A. P. 1996 The asymptotic structure of the turbulent boundary layer when subject to an interacting shock-wave. Anais do VI Encontro Nacional de Ciências Térmicas, 1833-1838.

XIV Brazilian Congress of Mechanical Engineering
Obeid Plaza Hotel Convention Center - Bauru - SP/Brazil
December 08-12th 1997

PAPER CODE: COB328

LAMINAR-TURBULENT TRANSITION: THE NONLINEAR EVOLUTION OF THREE-DIMENSIONAL WAVETRAINS IN A LAMINAR BOUNDARY LAYER

MARCELLO A. FARACO DE MEDEIROS [1]
Departamento de Engenharia Mecânica
Escola de Engenharia de São Carlos - Universidade de São Paulo
Rua Dr. Carlos Botelho, 1465, São Carlos, 13560-250 - SP - Brazil
E-mail:mafdm@sc.usp.br

Abstract

This paper presents results of an experimental study of the transition in boundary layers. The experiments were conducted in a low-turbulence wind tunnel. The process was triggered by a three-dimensional Tollmien-Schlichting wavetrain excited by a harmonic point source in the plate. Hot-wire anemometry was used to measure the signal and investigate the nonlinear regime of these waves. It was observed that the three-dimensional wavetrain behaved very differently from two-dimensional ones. In particular, it did not involve the growth of subharmonics or higher harmonics. The first nonlinear signal to appear was a mean flow distortion. This had a spanwise structure consisting of regions of positive and negative mean distortion distributed like streaks, which became more complex as the nonlinearity developed. Elsewhere studies have revealed the existence of streak-structures in turbulent flow. It is conjectured that the current experiments may provide a link between early wave-like instabilities and some coherent structures of turbulent boundary layers.

Keywords

Laminar-turbulent transition, hydrodynamic instability, boundary layer, hot-wire anemometry, nonlinear systems.

1 Introduction

Laminar-turbulent transition in boundary layers is a subject in fluid mechanics that has gained increasing interest in recent years. It is known that the process usually involves waves of small amplitude, the so called Tollmien-Schlichting (TS) waves, which amplify as they travel downstream. These waves are excited by disturbances in the flow such as wall vibrations, acoustic waves, free-stream turbulence or wall roughness. When the waves reach some finite size they cause the breakdown of the laminar flow structure

[1] Current Address: Departamento de Engenharia Mecânica - Pontifícia Universidade Católica de Minas Gerais - Av. Dom José Gaspar, 500, Belo Horizonte, 30535-610 - SP - Brazil.

creating a turbulent flow. For small enough amplitudes the evolution of these waves can be described by a linear version of the Navier-Stokes equation, the Orr-Sommerfeld equation (Lin 1955). However, experiments show that prior to transition the TS waves behave nonlinearly (Klebanoff, Tidstrom & Sargent 1962). Moreover, the amplification rates are often considerably larger in the nonlinear regime and therefore the transition point is ultimately determined by this stage. However, scientists have not been able to explain entirely the nonlinear regime of the TS waves, and this remains a very active field of research.

Most of the research on nonlinear TS waves has concentrated on the evolution of plane two-dimensional wavetrains. This effort has been able to established that when a two-dimensional TS wave reaches some threshold amplitude a secondary instability sets is causing strong amplification of three-dimensional modes (Kachanov 1987, Herbert 1988, Corke & Mangano 1989). The mechanism is of a parametric resonant nature and saturates in the form of a staggered pattern of λ vortices that, for some yet unclear reason, breakdown into turbulence. If the primary TS wave is very large, the process involves the generation of harmonics producing an aligned arrangement of λ vortices (Kachanov 1994).

The situation of more practical interest, however, involves highly three-dimensional modulated waves. Moreover, experiments have shown that these waves cause transition in a way that is remarkably different from that of two-dimensional regular wavetrains, and often the appearance of turbulence spots is observed (Shaikh 1997). As an example of this more generic type of waves, three-dimensional wavepackets have been studied a number of times (Gaster & Grant 1975, Gaster 1975, Cohen, Breuer & Haritonidis 1991, Konzelmann 1990, Medeiros & Gaster 1995, Medeiros 1996, Medeiros. & Gaster 1997, Medeiros 1997). These studies however have not been able to explain the complicated nonlinear behaviour observed. Research is now concentrating on a simpler three-dimensional wave, namely the three-dimensional wavetrain (Mack 1985, Kachanov 1985, Seifert 1990, Seifert & Wygnanski 1991, Wiegand, Bestek, Wagner & Fasel 1995) in the hope that this could bring some insight into the more complex cases. These works were mainly concentrated on the linear evolution. The work by Wiegand included the nonlinear regime, but the investigation was restricted to flow visualization. The objective of our current work is to investigate the nonlinear regime of these waves in a more detailed and quantitative way. This paper presents some preliminary findings.

2 Experimental set-up

Experiments on transition in boundary layers are usually carried out in wind tunnels in which the levels of disturbances of the flow are kept to a minimum. This in turn excites very small amplitude TS waves which take a long downstream distance to reach the amplitudes that cause breakdown to turbulence. It is then possible to disturb the flow with some controlled wave-maker and excite TS waves artificially. If the artificially excited waves are substantially larger than the naturally arising ones, the transition process can be controlled and repeated to a considerable degree even at the highly nonlinear stages. This provides a fundamental tool for research in this subject.

The experiments here presented were carried out in a 0.9m x 0.9m low-turbulence wind tunnel in which the free-stream velocity was 16.7m/s. The RMS free-stream turbulence level was of about .008%. The boundary layer studied developed on a 2m long elliptic nosed plate placed vertically at the centre of the tunnel. The plate was slightly

inclined to the tunnel wall on the working side in order to compensate for the boundary layer growth so as to ensure a constant pressure in the streamwise direction. Fine adjustment of the pressure gradient was achieved by flaps at the trailing edge of the plate. The artificial excitations were produced by a loudspeaker embedded in the plate and coupled to the flow via a .3mm hole located on the centre line of the plate 203mm from the leading edge. A more detailed description of the set up is given by Medeiros (1996).

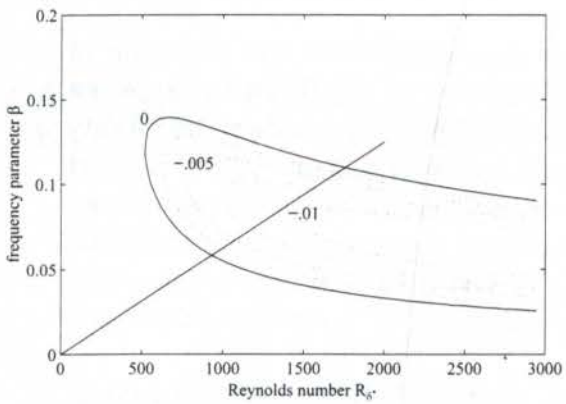

Figure 1: The instability diagram showing the path of the 200Hz TS wave.

First the loudspeaker was driven continuously by a 200Hz sine wave and the disturbance flow field was studied. The streamwise velocity fluctuations were detected by a constant temperature hot-wire anemometer. The anti-aliases filter was adjusted at 600Hz. Measurements were taken at a constant nondimensional distance from the wall, namely $y/\delta^* = .58$ (δ^* = displacement thickness), which is close to the inner peak of the streamwise velocity eigenfunction. Figure 2 shows velocity records taken along the centreline of the flow at different distances from the leading edge of the plate. These results can best be interpreted with the help of figure 1. This figure shows the stability diagram of the flat plate boundary layer obtained by solving the Orr-Sommerfeld equation. It indicates in a Reynolds number(R)×nondimensional frequency ($\beta = 2\pi f\delta^*/U_\infty$) plane the region of flow instability. The curve indicates the neutrally unstable waves and separate the unstable region (the inner part) from the stable region. The picture also displays, inside the loop, curves of constant amplification rates. Waves traveling downstream in the boundary layer follow straight lines that irradiate from the origin of the coordinate system. The line displayed in figure 1 corresponds to the wave in figure 2. It is observed that the first measuring station ($R = 1312$) is located within the unstable region. This is confirmed by the observation that the wave amplifies from station x=500 to x=600mm. From stations x=800 to 900mm the signal starts to decays. That corresponds to the region where the waves cross the upper part of the neutral curve and return to the stable region.

3 The nonlinear three-dimensional wavetrain

A more detailed study of the linear evolution the wavetrain was carried out, but this paper focuses on the more interesting nonlinear regime. Previous studies have used a continuous wavetrain to excite the flow. Here the excitation used to study the nonlinear regime was a finite wavetrain. However, the finite wavetrain was made long enough so as to behave like a continuous one. Also, care was taken that the ends of the wavetrain were very smooth in order that the modulation did not affect the results. In this way, the hot-wire records obtained were composed of two parts, a disturbed part and an undisturbed one, figure 3. The background noise in the experiment was very low, but the random part of the signal was further reduced by ensemble averaging a set of 64 records generated by identical excitations. Analysis of the signals revealed no sign of subharmonic or higher harmonic. In fact, the first sign of nonlinearity was clearly a mean flow distortion also indicated in the picture.

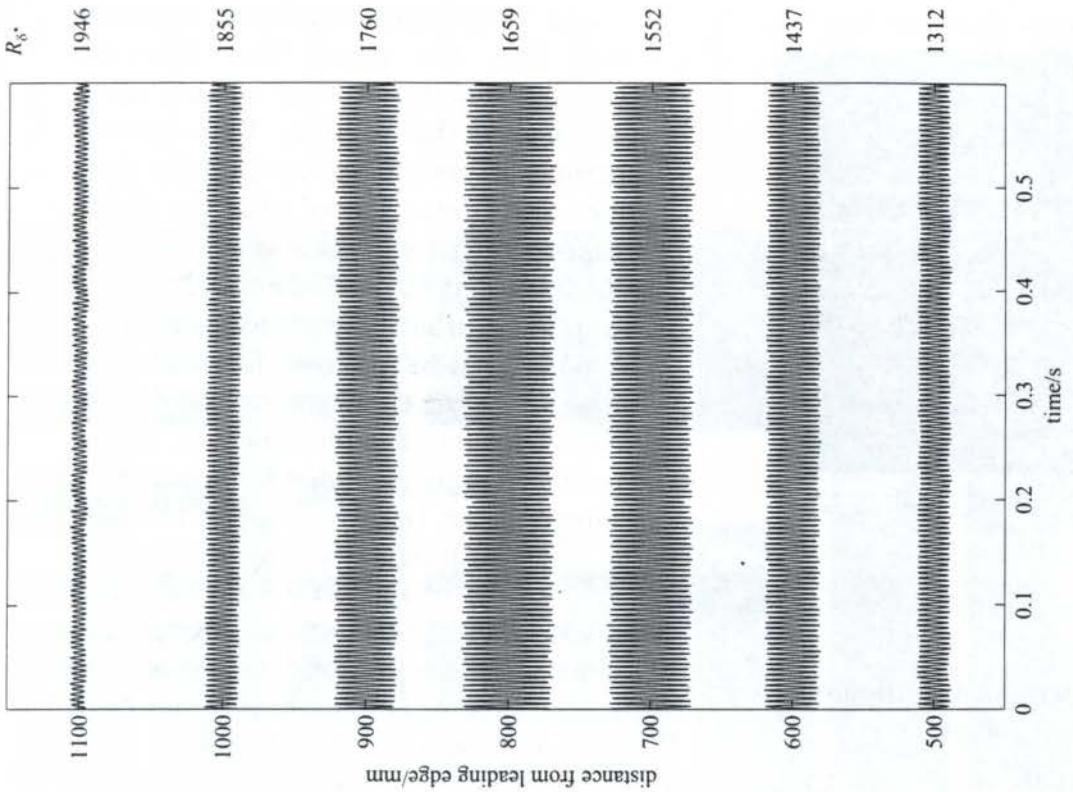

Figure 2: Centreline linear evolution of a continuous wavetrain excited by a point source.

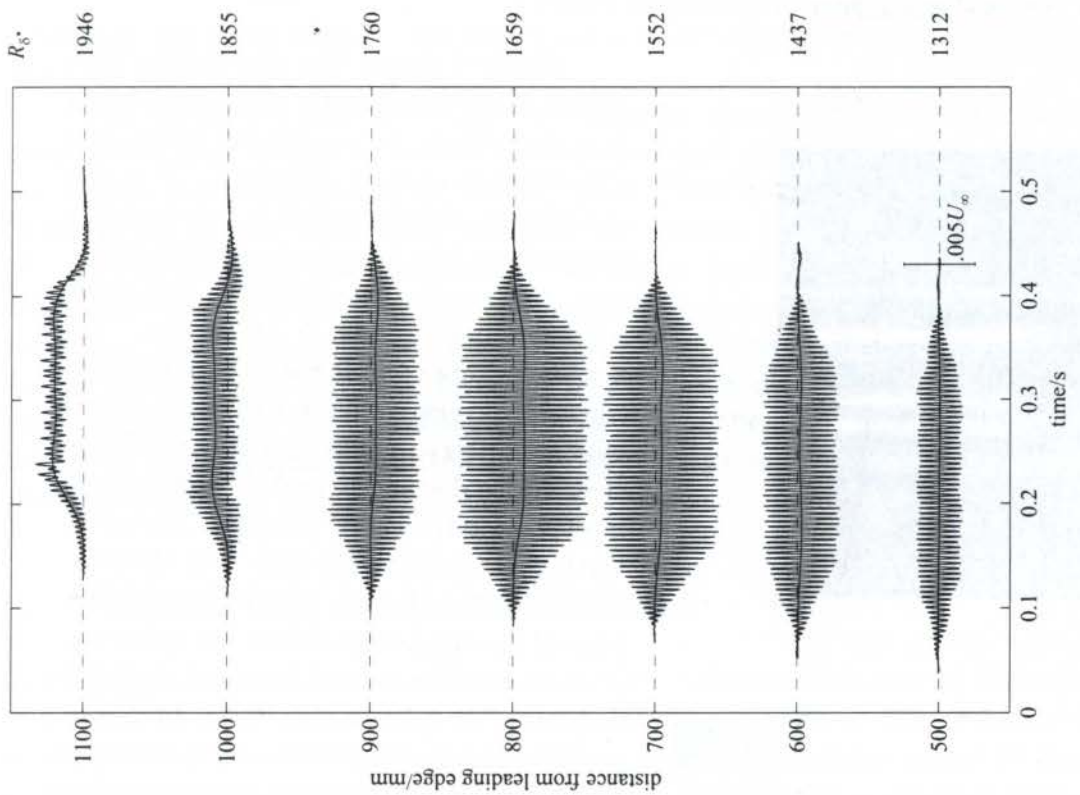

Figure 3: Centreline nonlinear evolution of a wavetrain excited by a point source.

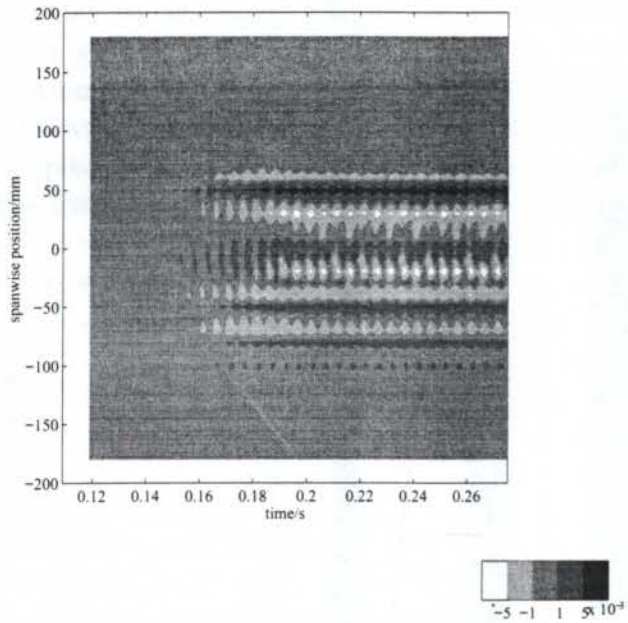

Figure 4: Spanwise distribution of the disturbance field at x=1100mm.

A somewhat surprising behaviour was that the mean flow distortion changed from negative to positive somewhere along the evolution. Under this experimental conditions, the positive mean flow distortion occurred after the disturbances had crossedthe second branch of the instability loop. Although the fundamental disturbances were decaying in this region, the positive mean flow distortion was larger then the negative one. To shed more light into the phenomenon, the experiments were extended to include measurements off the centreline of the flow, in order to produce a three-dimensional view of the disturbance field. Figure 4 shows contour plots of the wave field as it passes a downstream station, namely x=1100mm. It is important to note that this view was constructed from 41 spanwise equally spaced time series measured by hot-wire anemometer and it should not be taken as a snap-shot of the flow at a particular time. Figure 4 shows some streak structures which developed nonlinearly in the flow. A clearer view of streak structures is obtained by filtering out the oscillating part of the signal, figure 5.

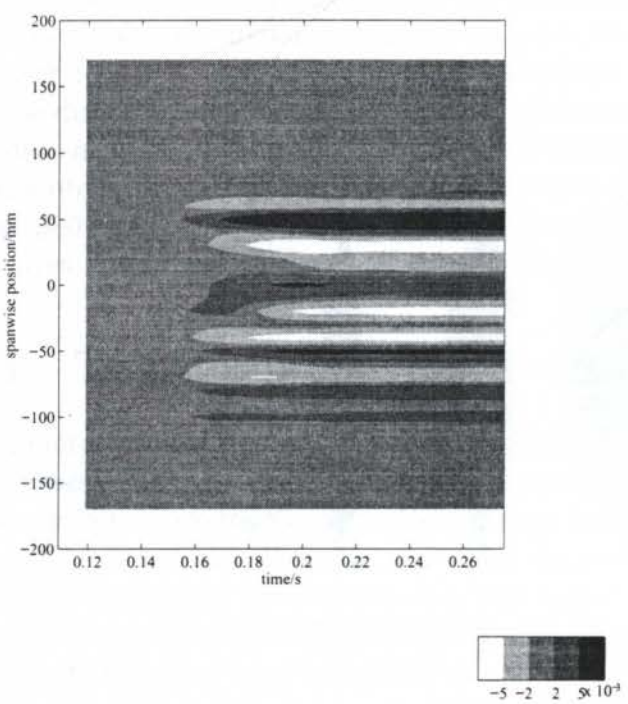

Figure 5: Spanwise distribution of the mean flow distortion caused by the disturbance field at x=1100mm.

Figure 6 shows the streamwise evolution of the nonlinearly generated mean flow distortion. At x=.7m the mean flow distortion is already apparent. It is observed that the distortion is not negative everywhere, but has some spanwise structure. At x=.8m the distortion is larger, but remains similar in structure. At x=.9m a more complex structure is forming. It is very difficult to obtain spanwise symmetry in experiments at so large streamwise distances, and this affects the interpretation of the results. However, the picture conveys the idea that the positive lumps of mean distortion on the edge of the disturbance field are splitting. At x=1.0m the central lump of negative distortion is split in two by a localized positive mean distortion. It is remarkable that the phenomenon occurs exactly at the centreline of the flow, although the disturbance field appears to be asymmetrical. After x=1.0m the spanwise distribution of the streak structures remains

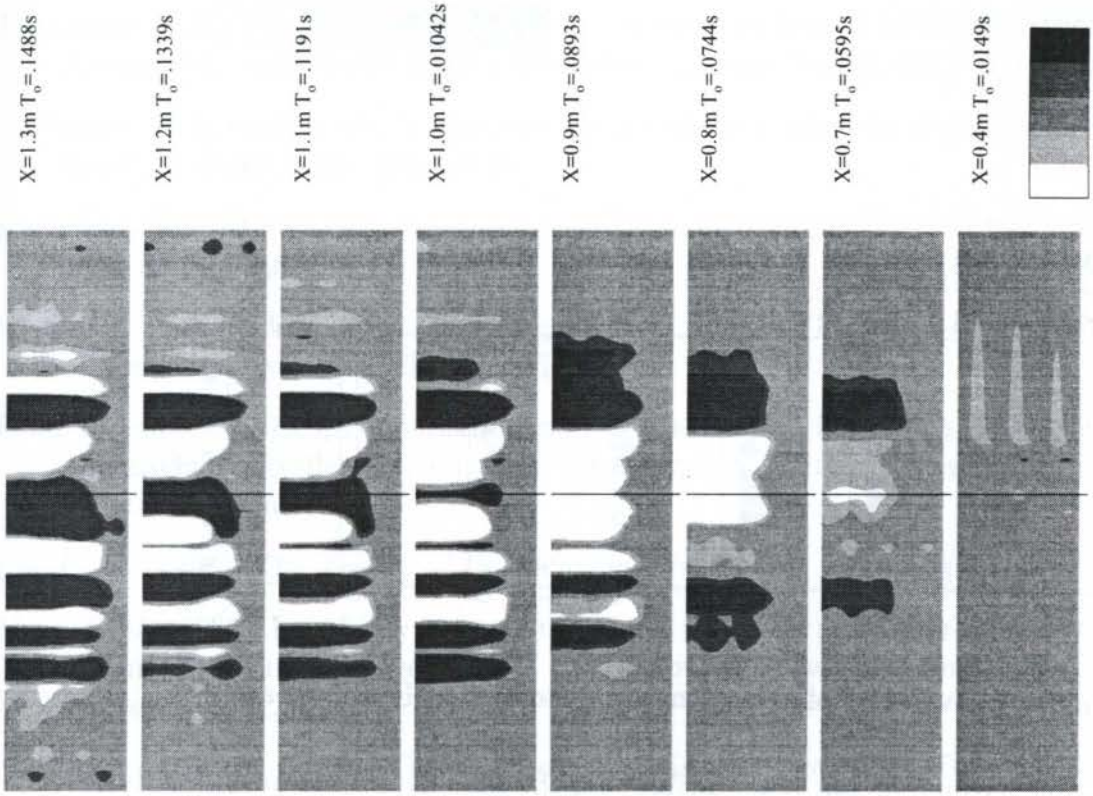

Figure 6: Evolution of the mean flow distortion.

essentially the same with a widening of the positive distortion generated at the centre of the wave field.

From figure 6 it appeared that the spanwise wavelength at station x=1.3m is approximately half of that at x=.7m. To try and gain more insight into the phenomenon the signals were also studied in Fourier space. Two dimensional discrete Fourier transforms of the signals were taken mapping the spectra onto a nondimensional frequency ($F = 10^4\beta/R$)×spanwise wavenumber (α_z)plane, figure 7. In the figure the frequency coordinate was stretched and only the frequencies close to zero were shown. Initially the mean flow distortion appears as a double peak of symmetrical spanwise wavenumbers. As the nonlinearity developed the spanwise distribution became more complex and more peaks appear in the spectra. The change of sign of the mean flow distortion on the centreline at x=1.0m manifests itself in the appearance of spanwise modes of even higher wavenumbers.

4 Discussion and conclusions

The current experiments have shown that the nonlinear evolution of three-dimensional wavetrains does not seem to be linked with the appearance of sub or higher harmonics as occurs with two-dimensional ones. In fact, the first nonlinear signal to appear was a mean flow distortion. The experiment was not designed for a detailed investigation of the origin of this distortion, but some conjectures can be made. It is possible that the nonlinearity arises from the Reynolds stresses terms ($u'v'$) that are neglected in the linear approximation. It is known that this terms can produce both harmonics and mean flow distortion (Stuart 1960). In a three-dimensional case this mechanism would produce both

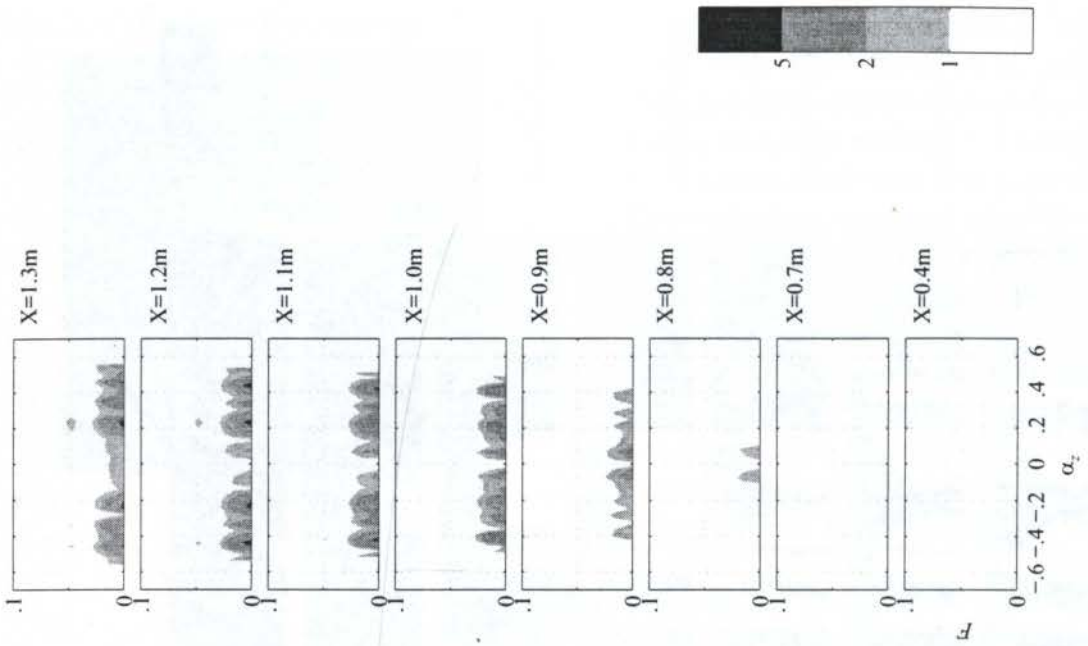

Figure 7: Evolution of the mean flow distortion in Fourier space.

spanwise and time harmonics, but it is possible that the time harmonics have been highly dumped because of their high frequency and only the mean distortion remained. The appearance of the higher spanwise wavenumber number modes might be connect with a secondary Reynolds stress interaction which would produce even higher harmonics. A similar mechanism has been found in the so called oblique transition (Elofsson & Alfredsson 1997). Our experiment, however, did not have enough spanwise resolution for a definitive conclusion. In any case, the results appear to provide a link between the early wave-like instability and streak structures which seem to be a key ingredient of boundary layer transition (Monkewitz 1997).

References

Cohen, J., Breuer, K. S. & Haritonidis, J. H. (1991), 'On the evolution of a wave packet in a laminar boundary layer', *J. Fluid Mech.* **225**, 575–606.

Corke, T. C. & Mangano, R. A. (1989), 'Resonant growth of three-dimensional modes in transitioning Blasius boundary layers', *J. Fluid Mech.* **209**, 93–150.

Elofsson, P. A. & Alfredsson, P. H. (1997), 'An experimental study of oblique transition in plane poiseuille flow'. (submitted to the J. Fluid Mech.).

Gaster, M. (1975), 'A theoretical model of a wave packet in the boundary layer on a flat plate', *Proc. R. Soc. London A* **347**, 271–289.

Gaster, M. & Grant, I. (1975), 'An experimental investigation of the formation and development of a wavepacket in a laminar boundary layer', *Proc. Royal Soc. of London A* **347**, 253–269.

Herbert, T. (1988), 'Secondary instability of boundary layers', *Ann. Rev. Fluid Mech.* **20**, 487–526.

Kachanov, Y. S. (1985), Development of spatial wave packets in boundary layer, *in* V. V. Kozlov, ed., 'Laminar-turbulent transition', springer-Verlag, pp. 115–123.

Kachanov, Y. S. (1987), 'On the resonant nature of the breakdown of a laminar boundary layer', *J. Fluid Mech.* **184**, 43–74.

Kachanov, Y. S. (1994), 'Physical mechanisms of laminar boundary layer transition', *Ann. Rev. Fluid Mech.* **26**, 411–482.

Klebanoff, P. S., Tidstrom, K. D. & Sargent, L. M. (1962), 'The three-dimensional nature of boundary layer instability', *J. Fluid Mech.* **12**, 1–34.

Konzelmann, U. (1990), Numerische Untersuchungen zur räumlichen Entwicklung dreidimensionaler Wellenpakete in einer Plattengrenzschichtströmung, PhD thesis, Universität Stuttgart.

Lin, C. C. (1955), *The Theory of Hydrodynamic Instability*, Cambridge University Press.

Mack, L. M. (1985), Instability wave patterns from harmonic point sources and line sources in laminar boundary layers, *in* V. V. Kozlov, ed., 'Laminar-turbulent transition', springer-Verlag, pp. 125–132.

Medeiros, M. A. F. (1996), The nonlinear behaviour of modulated Tollmien-Schlichting waves, PhD thesis, Cambridge University - UK.

Medeiros, M. A. F. (1997), 'Experiments on nonlinear wavepackets in laminar boundary layers: the possibility of subharmonic resonance'. (submitted to the J. Fluid Mech.).

Medeiros, M. A. F. & Gaster, M. (1995), The nonlinear behaviour of modulated Tollmien-Schlichting waves, *in* 'IUTAM Conference on nonlinear instability and transition in tri-dimensional boundary layers', Manchester, pp. 197–206.

Medeiros., M. A. F. & Gaster, M. (1997), 'Experiments on nonlinear wavepackets in laminar boundary layers: the possibility of near field influence'. (submitted to the J. Fluid Mech.).

Monkewitz, P. (1997), personal communication.

Seifert, A. (1990), On the interaction of small amplitude disturbances emanating from discrete points in a Blasius boundary layer, PhD thesis, Tel-Aviv University.

Seifert, A. & Wygnanski, I. (1991), On the interaction of wave trains emanating from point sources in a Blasius boundary layer, *in* 'Proc. Conf. on Boundary Layer Transition and Control', The Royal Aeronautical Society, Cambridge, pp. 7.1–7.13.

Shaikh, F. N. (1997), Investigation of transition to turbulence using white noise excitation, (to be published in J. Fluid Mech.).

Stuart, J. T. (1960), 'On the nonlinear mechanisms of wave disturbances in stable and unstable parallel flows', *J. Fluid Mech.* **9**, 1–21.

Wiegand, T., Bestek, H., Wagner, S. & Fasel, H. (1995), Experiments on a wave train emanating from a point source in a laminar boundary layer, *in* '26th AIAA Fluid Dynamics Conference', San Diego, CA.

XIV Brazilian Congress of Mechanical Engineering
Obeid Plaza Hotel Convention Center - Bauru - SP/Brazil
December 08-12th 1997

PAPER CODE: COB544

SUPERSONIC AND HYPERSONIC LAMINAR BOUNDARY LAYERS

P.G.P. Toro, Z. Rusak, H.T. Nagamatsu, L.N. Myrabo
Department of mechanical Engineering, Aeronautical Engineering and Mechanics
Rensselaer Polytechnic Institute, Troy, NY 12180-3590 - USA
torop@rpi.edu, rusakz@rpi.edu, nagamh@rpi.edu, myrabl@rpi.edu

Abstract

A new set of self-similar solutions of a compressible laminar boundary layer is used for air as perfect gas and where the viscosity is a power function of the temperature. Modified Levy-Mangler and Dorodnitsyn-Howarth transformations are presented to solve the flow in a thin laminar boundary layer with no external pressure gradients on a smooth flat plate. This results in an explicit relation between the stream function and the enthalpy fields described by a closed coupled system of nonlinear ordinary differential equations. In the present work boundary layer flows with external Mach numbers up to 15 are studied and the skin friction and heat transfer coefficients for a hot wall case are presented. The present solution methodology provides a straight forward way of comparing results using the viscosity-temperature linear relation, Sutherland's law and the relation according to the kinetic theory. Also, the results may provide important data needed for the design of future hypersonic vehicles.

Keywords

Self-Similar Equations, Compressible Laminar Boundary Layer, Supersonic and Hypersonic Flows.

1. INTRODUCTION

High supersonic Mach number and high stagnation temperature flows are characterized by the phenomena of vibrations and dissociation of molecules and ionization of atoms and molecules. For supersonic and hypersonic cases, the flow can be considered as low enthalpy condition and may be modeled by a calorically or thermally perfect gas equation of state.

In a calorically perfect gas the specific heats, c_p and c_v, are considered as constant. A thermally perfect gas is one in which the specific heats are functions of only the temperature. This is a result of the vibrational energy within the gas molecules and the electronic energy associated with the electron motion within the atoms or molecules. In both cases the perfect gas equation of state may be used. In the more general case of a purely compressible gas at thermodynamic equilibrium, the specific heats are functions of two thermodynamic properties, for example the pressure and the temperature. The real gas equation of state should be used for such cases. This relation may be applied in high enthalpy flows where dissociation and ionization occur.

A hypersonic flow over a flat plate can be divided into four distinct regions, Figure 1 (see also Anderson et al. 1984).

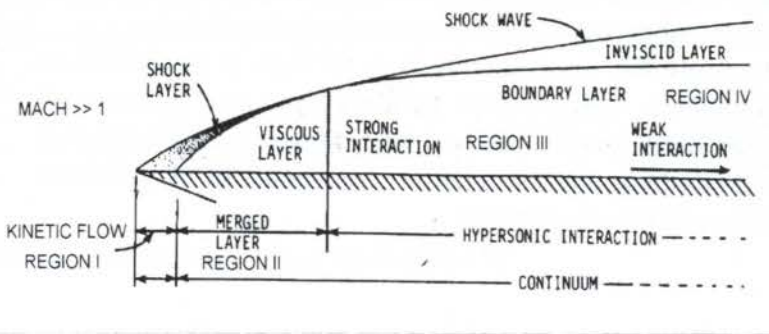

Figure 1.Flowfield on a flat plate at hypersonic flow.

Near the plate leading edge, there exists a delay in the formation of the shock layer and the boundary layer as a result of the slip phenomena in this region (Nagamatsu and Sheer, 1960). Close to the leading edge, region I, the slip condition is stated and the flow is not a continuum, so that the Navier-Stokes equations are not valid, and the first order kinetic flow theory should be applied (Nagamatsu and Li, 1960).

Immediately after the noncontinuum region, there exists a strong interaction continuum region, where the shock layer and the boundary layer are merged and the no-slip condition exists at the surface of the plate, region II. In this region the pressure gradient in the y-direction may be ignored, $\frac{\partial p}{\partial y} = 0$, but the pressure gradient in the x-direction can not be neglected, due to the presence of the shock wave inside the viscous layer.

Far from the leading edge region, a weaker interaction region may be found. In this region, which is close to the strong interaction (region III) the pressure gradients in the x- and y-directions inside the boundary layer are very small and may be ignored. However, outside the boundary layer, in the inviscid layer between the shock wave and the boundary layer, the pressure gradient in the y-direction can not be neglected.

Downstream of the strong interaction region, in region IV, the classical approach of Prandtl incompressible boundary layer theory can be applied to the compressible boundary layer. In this region the pressure gradients in the x- and y-directions may be neglected, both inside as well as outside the boundary layer.

Van Driest (1952) used the Crocco's method and derived a set of ordinary differential equations to describe the compressible laminar boundary layer. He studied flows with Mach numbers up to 25 on a flat plate assuming a perfect gas obeying Sutherland's viscosity law. The main results presented are the skin-friction and heat-transfer coefficients as function of Reynolds number, Mach number, and wall-to-free stream temperature ratio.

Cohen and Reshotko (1957) studied self-similar solutions for a two-dimensional steady compressible laminar boundary layer with heat transfer and pressure gradients. They used the perfect gas assumption, with a unit Prandtl number and a linear viscosity-temperature relation across the boundary layer.

Mirels (1955) studied the shock wave as it advances into a stationary fluid bounded by a wall. A boundary-layer flow is established along the wall behind the shock. He employed a Blasius equation to solve the heat transfer behind the shock wave, with a modified boundary condition at $f'(0) = \frac{u_w}{u_e}$, where u_w and u_e are the velocity of the shock wave relative to the wall and the velocity outside the boundary layer, respectively. He stated that with increasing the Reynolds numbers, the laminar boundary layer behind the shock becomes unstable and the transition to turbulent flow occurs.

Toro et al. (1997) have recently developed new self-similar solutions for a compressible laminar boundary layers over a flat plate. The influence of the flow Prandtl number, wall to free-stream temperature ratio, and the power of the viscosity-temperature law for supersonic flows with external Mach numbers up to 4 have been investigated.

The purpose of this work is to apply the new methodology of Toro et al. (1997) to study self-similar supersonic and hypersonic compressible laminar boundary layers with external Mach numbers up to 15. The resulting skin friction and heat transfer coefficients will be presented. The work is limited to cases where the dissociation phenomena do not present, and where the viscosity is a power function of the temperature.

2. Mathematical Model

A steady compressible flow of a viscous, heat conducting, Newtonian fluid is considered. For this flow at the limiting case of a high Reynolds number, or a small dynamic viscosity, the Navier-Stokes equations may be simplified to the classical Prandtl laminar boundary layer. Following Van Driest (1952), the steady, compressible, viscous, thin boundary layer, with two-dimensional flow, and zero pressure gradients in the x- and y-directions, over a smooth flat plate may be described by the following conservative equations:

$$\frac{\partial(\rho u)}{\partial x}+\frac{\partial(\rho v)}{\partial y}=0, \tag{1}$$

$$\rho u\frac{\partial u}{\partial x}+\rho v\frac{\partial u}{\partial y}=\frac{\partial}{\partial y}\left(\mu\frac{\partial u}{\partial y}\right), \qquad \frac{\partial p}{\partial y}=0 \tag{2}$$

$$\rho u\frac{\partial i}{\partial x}+\rho v\frac{\partial i}{\partial y}=\frac{\partial}{\partial y}\left(\frac{1}{Pr}\mu\frac{\partial i}{\partial y}\right)+\mu\left(\frac{\partial u}{\partial y}\right)^2. \tag{3}$$

Here, ρ is the flow density, p is the pressure, p=const., (u, v) are the axial and transverse velocity components, μ is the viscosity, Pr is the Prandtl number, $Pr=\frac{\mu c_p}{k}$, c_p is the gas specific heat coefficient, k is the gas conductivity, and i is the enthalpy.

The boundary conditions needed to solve the problem are no penetration and no slip condition on an isothermal wall (at $y=0,\ x\geq 0$) and the free stream conditions as $y\to\infty$:

$$u(x,0)=0, \quad v(x,0)=0, \quad i(x,0)=i_w, \quad u(x,\infty)=u_\infty, \quad i(x,\infty)=i_\infty. \tag{4}$$

We assume a power law for the viscosity change as function of temperature given by

$$\frac{\mu}{\mu_r}=\left(\frac{T}{T_r}\right)^\alpha \tag{5}$$

Here μ_r and T_r are reference viscosity and temperature, respectively and α is a given power.

3. Self-Similar Solution

We seek self-similar solutions of equations (1) - (5). The boundary layer equations may be reduced to self-similar solutions by introducing a modified change of variables that combines the Levy and Mangler and the Dorodnitsyn-Howarth transformations, and the power α that accounts for the variation of viscosity with temperature. Let

$$\xi(x) = \int_0^x \rho_w \mu_w u_\infty d\xi', \qquad \eta(x,y) = \frac{\rho_w u_\infty}{\sqrt{2\xi}} \int_0^y \left(\frac{\rho}{\rho_w}\right)^\alpha dy' \tag{6}$$

The stream function $\psi(x,y)$ is defined by

$$\rho u = \rho_w \frac{\partial \psi}{\partial y} \qquad \rho v = -\rho_w \frac{\partial \psi}{\partial x}. \tag{7}$$

We assume a self-similar relation:

$$\psi(x,\eta) = \sqrt{2u_\infty \nu_w x} f(\eta), \qquad \frac{i(x,\bar{y})}{i_\infty} = \theta(\eta) \tag{8}$$

Replacing equations (6) - (8) into the momentum and energy equations, we obtain the self-similar compressible boundary layers given by

$$f''' + ff'' = \frac{\alpha - 1}{\theta}\left[f'\theta'' + 2\theta' f'' + ff'\theta' - \alpha \frac{f'(\theta')^2}{\theta}\right] \tag{9}$$

$$\theta'' + \Pr f\theta' = -(\gamma - 1) M_\infty^2 \Pr \left[\left(\frac{\theta_w}{\theta}\right)^{\alpha-1}\right]^2 \left[f'' - (\alpha - 1)\frac{f'\theta'}{\theta}\right]^2. \tag{10}$$

where $M_\infty = \frac{u_\infty}{a_\infty}$ is the Mach number of the external flow. The boundary conditions (4) result in

$$f(0) = 0, \qquad f'(0) = 0, \qquad f'(\infty) = \theta_w^{-(\alpha-1)}, \qquad \theta(0) = \theta_w, \qquad \theta(\infty) = 1. \tag{11}$$

Here $\theta_w = \frac{i_w}{i_\infty} = \frac{T_w}{T_\infty} = \frac{\rho_\infty}{\rho_w}$ is the ratio of the wall enthalpy (temperature) and the free-stream enthalpy (temperature). This parameter strongly affects the behavior of the flow. When $\theta_w < 1$ we have a cold wall and when $\theta_w > 1$ we have a hot wall. For more detail of this theoretical approach see Toro et al. (1997). Toro et al. (1997) also present results for various hot and cold walls with Mach numbers of external flow up to 4.

The system (9), (10) and (11) is a system of nonlinear ordinary differential equations that explicitly describes the relations between the stream function and the temperature fields. Due to the compressibility effects, density is used here as a variable. The momentum equation in the x-direction and the energy equation are coupled by enthalpy, as one would expect. For the special case where viscosity changes as a linear function of temperature (i.e., α=1), the

compressible laminar boundary layer represented by Blasius and Pohlhausen equations are recovered.

Notice that according to (7) and (8) the streamwise velocity, u, is given by $u = u_\infty f'(\eta)\left(\frac{\rho}{\rho_w}\right)^{\alpha-1}$, i.e., u given by $f'(\eta)$ and also related to the density. One would expect therefore, that the local skin friction coefficient c_f is not only related to $f''(0)$ (as Blasius equation). However, the local heat transfer rate at the surface c_H is still related to $\theta'(0)$ as in the classical compressible Pohlhausen self-similar equation. Then, the local skin friction and the local heat transfer coefficients based on free-stream velocity and the wall condition can be calculated, respectively, by

$$c_f = \sqrt{\frac{2}{Re}}\left[f''(0) - (\alpha - 1)\frac{f'(0)'\theta'(0)}{\theta(0)}\right], \qquad C_H = \frac{i_\infty}{i_{aw} - i_w}\frac{1}{Pr}\left(\frac{\theta_\infty}{\theta_w}\right)^{\alpha+1}\frac{\theta'(0)}{\sqrt{2\,Re}} \tag{12}$$

where the Reynolds number, Re, and the adiabatic enthalpy, i_{aw}, are given, respectively, by

$$Re = \frac{\rho_w u_\infty x}{\mu_w}, \qquad \frac{i_{aw}}{i_\infty} = 1 + \frac{\gamma - 1}{2}M_\infty^2. \tag{13}$$

4. Results

The system of equations (9), (10) and (11) may now be used to study the behavior of self-similar compressible boundary layers. This system is solved by a standard Runge-Kutta fourth order integration technique using MATLAB. There are four parameters that affect the solution: the Mach number of the external flow, M_∞; the temperature ratio, θ_w; the Prandtl number, Pr; and the power α of the viscosity-temperature relation.

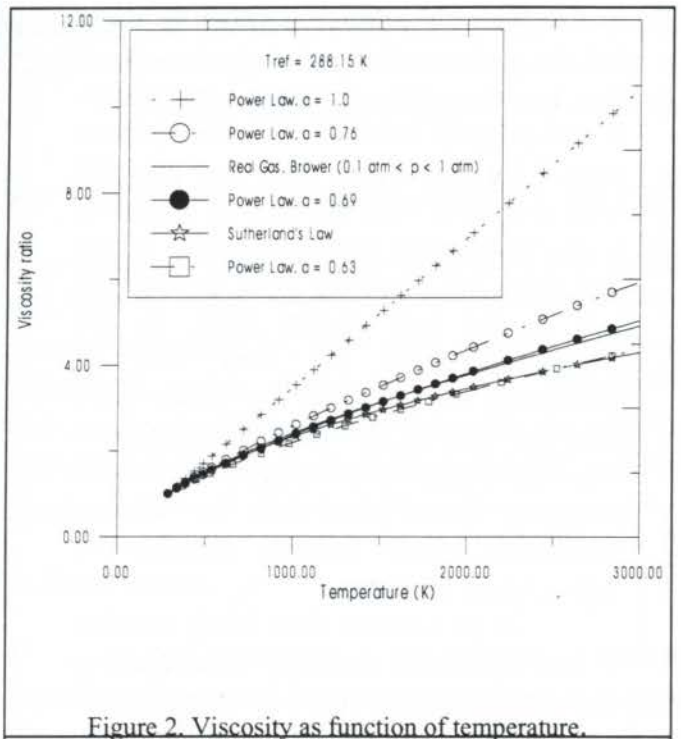

Figure 2. Viscosity as function of temperature.

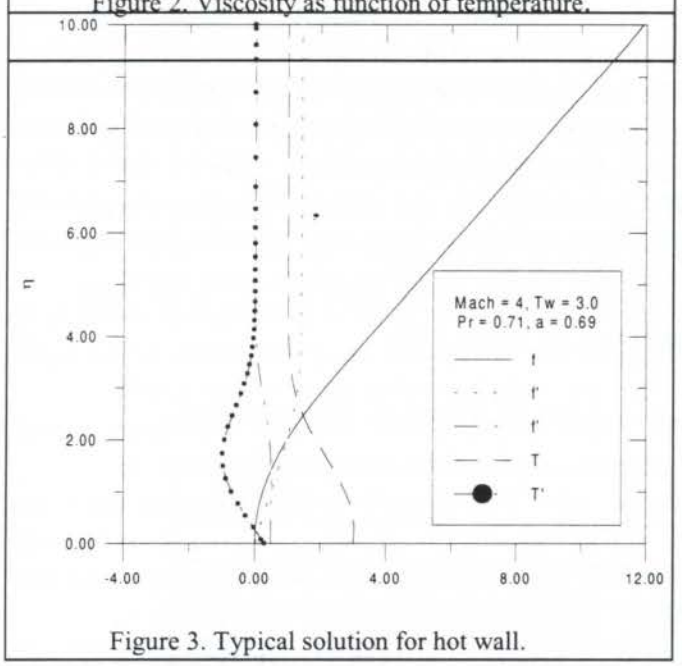

Figure 3. Typical solution for hot wall.

Figure 2 displays the variation of viscosity-temperature law at pressures between 0.1 and 1 atmosphere. Note that α=0.69 matches the numerical real gas values of Brower (1990) better than the other powers for a wide range of temperatures, up to 3000 K. The power α=0.76 is a typical value used for air at relatively low temperatures, less than 1000 K. Also, notice that the power α=0.63 provides a close match with Sutherland's law,

$$\frac{\mu}{\mu_{ref}} = \left(\frac{T}{T_{ref}}\right)^{3/2} \frac{T_{ref}+S}{T+S}$$

with T_{ref} = 288.15 K and S = 110 K, that is commonly used for air at temperatures, up to 2000 K.

A typical solution of the self-similar equations (11-13) for $M_\infty = 4$, $\alpha = 0.69$, Pr=0.71, and $\theta_w = 3.0$ (hot wall) is shown in Figure 3. Note that the temperature increases within the boundary layer, which demonstrates that viscous dissipation is an important aspect at high Mach number flows. It results in this case in a heat flux into the wall.

Flows with a external Mach number about 4 ($3 < M_\infty < 4$) represent a near adiabatic wall case for θ_w=3 (the enthalpy gradient at the changes its sign, Table I).

Figure 4 presents the influence of the changing external flow Mach number for the streamwise velocity and enthalpy profiles for the hot wall, θ_w=3, power viscosity-temperature law with α=0.69, and Pr = 0.71. As the Mach number increases, for a fixed η, the streamwise velocity decreases and the enthalpy (temperature) increases. For Mach number less than about 3.5 the boundary layer is colder than the wall, and there exists heat flux from the wall to the flow due to only the temperature difference. For Mach numbers less than 3.5 the surface is hotter than boundary layer, and the temperature gradient at the wall , $\theta'(0)$, is negative, see Table I.

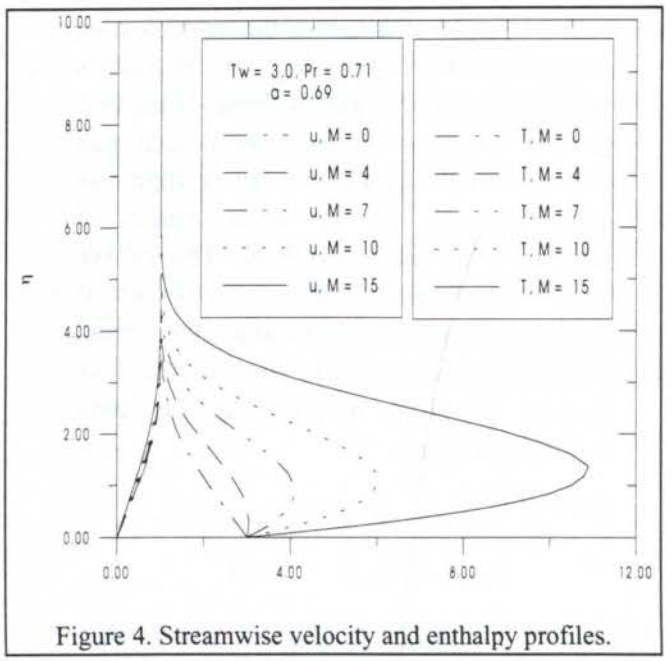

Figure 4. Streamwise velocity and enthalpy profiles.

When the Mach number is about 3.5 the viscous dissipation creates a heat flux into the wall, see Table I and Figure 4. For external flow Mach number greater than 4 the free stream flow and also the wall are colder than the flow in boundary layer. This means that there exists a heat flux from the boundary layer to the wall and to the free stream flow. In the supersonic cases the heat flux is dominated not only by the temperature ratio but also by the viscous dissipation, since the temperature increases within the boundary layer. Note that the viscous dissipation effects become stronger for higher Mach numbers.

At an external flow Mach number 15 the maximum enthalpy (temperature) ratio in the boundary layer is about 11, and when the external temperature is about 220 K (flight at altitude of 10 - 30 km), the maximum temperature in the flow will be about 2500 K. Therefore, for Mach number high as 15, the free stream temperature must be sufficiently low to assure that dissociation of the molecules will not occur. For higher Mach numbers or temperature ratios θ_w the flow may reach temperatures above 3000 K where the real gas effects become important and where the present analysis is not valid anymore.

Finally, we would like to comment on the effect of α on the velocity boundary layer thickness at M_∞=0. For a hot wall, θ_w=3, u reaches 99% of u_∞ at $\eta_u \approx 3.12$ for α= 0.69 and Pr = 0.71, whereas in the well-known Blasius solution for α=1 and Pr=0.71, $\eta_u \approx 3.5$. One can see that the hydrodynamic boundary layer decreases by about 11%.

Table I. Values of f''(0), θ'(0), $u(\eta_u)/u_\infty$, f'(∞), θ(∞) and η_∞ for various M_∞.

M_∞	f''(0)	$\eta_{\infty f}$	η_u	$u(\eta_u)/u_\infty$	θ'(0)	$\eta_{\infty\theta}$	$\sqrt{2\,\mathrm{Re}}C_H$
15	0.39940	6.6885	3.97	0.9907	12.64320	7.4773	0.0326
10	0.43445	6.2696	3.57	0.9883	5.68680	6.2696	0.0350
7	0.45916	5.9318	3.52	0.9919	2.52970	5.9318	0.0359
4	0.48363	5.5327	3.28	0.9901	0.29055	5.7998	0.0268
3	0.49040	5.7734	3.15	0.9872	-0.21645	5.4940	0.1200
2	0.49579	5.4432	3.07	0.9854	-0.58790	5.7313	0.0543
1.2	0.49875	5.2740	3.14	0.9887	-0.78157	5.5499	0.0506
0.8	0.49970	5.2619	3.13	0.9886	-0.84260	5.8535	-0.0467
0.3	0.50035	5.5208	3.12	0.9882	-0.88470	6.2005	-0.0491
0.0	0.50045	5.5181	3.12	0.9882	-0.89160	5.8319	-0.0494

Although in the present investigation the viscosity-temperature is not a linear relation, i.e, $\alpha \neq 1$, the local skin friction is only function of $f''(0)$, since $f'(0) = 0$. Note from

equation (14) that in the supersonic cases when Mach number increases, the velocity boundary layer thickness $\eta_{\infty f}$ increases and the skin friction c_f decreases, since $f''(0)$ also decreases.

The local heat transfer rate, C_H, (Stanton number) represents the ratio of heat flux to the fluid and the heat transfer capacity of the fluid flow, and it is given by $C_H = \frac{k\,\partial T/\partial y}{\rho c_p u_\infty \Delta T}$. The change of C_H with the external flow Mach number is also given in Table I. It is found that for subsonic cases, where $M_\infty < 1$, the dissipation effects are not dominant, and as the Mach number increases the local heat transfer coefficient decreases, since $\theta'(0)$ decreases. In the supersonic cases, where $M_\infty > 1$, C_H increases because the fluid can transfer heat by convection. As Mach number increases the enthalpy (temperature) gradient increases, and C_H should increase but for high Mach number (hypersonic $M_\infty > 5$) the heat transfer capacity of the fluid flow is higher than the surface can transfer at same time, therefore the C_H decreases.

5. Conclusion

A new methodology for calculating self-similar solutions of a compressible laminar boundary layer, considering the viscosity as a power function of the temperature is applied. The modified Levy-Mangler and Dorodnitsyn-Howarth transformations describe the similarity variables in terms of a power of the density that takes into account the viscosity-temperature power law. These transformations result in an explicit relation between the stream function and the temperature fields. Solutions are presented for boundary layer flows over hot walls with Mach number of the external flow up to 15. The present solution methodology also provides a straight forward way of comparing results using the viscosity-temperature linear relation, Sutherland's law and the relation according to the kinetic theory.

These self-similar solutions are applicable to subsonic and supersonic flows. They may also apply to hypersonic flows with low enthalpy, as long as the flow is far from the leading edge and is described by a continuum calorically or thermally perfect gas relation.

These self-similar solutions may provide important data needed for the design of future hypersonic vehicles. It may also be applied in two important areas, as follows:

1) Most of the Hypersonic Shock Tunnels operate at the cold flow condition, where the total enthalpy is low enough and there are no chemical reactions within the boundary layer; here the real gas effects may be ignored. For this particular experimental work one can utilize the present analyses to compare with the experimental data.

2) The Navier-Stokes equations as well as Reynolds-averaged Navier-Stokes equations for supersonic or hypersonic flows must be solved by numerical methods since there are no exact solutions for them. The present self-similar solutions can be used as a tool to validate these numerical simulations.

6. Acknowledgments

This report was prepared under contract no. NCC9-112 for NASA Marshall Space Flight Center. The first author wishes to thank the Brazilian Foundation (FAPESP) for supporting his graduate studies, and the Aeronautic and Space Institute (IAE) which allowed him to pursue graduate studies at Rensselaer Polytechnic Institute (RPI).

7. References

Anderson, D.A.; Tannehill, J.C. and Pletcher, R.H. "Computational Fluid Mechanics and Heat Transfer," MacGrawhill, 1984.

Brower, W.B. "Theory, Tables, and Data for Compressible Flow," NY: Hemisphere Publishing Co., 1990.

Cohen, C. B. and Reshotko, E. "Similar Solutions for the Compressible Laminar Boundary Layer with Heat Transfer and Pressure Gradient," NACA Report 1293, 1957.

Mirels, H. "Laminar Boundary behind Shock Advancing into Stationary Fluid," NACA TN 3401, 1955.

Nagamatsu, H. T.; Sheer, R.E., Jr. "Hypersonic shock wave-boundary layer interaction and leading edge slip," ARS J., vol. 30, no. 5, pp. 454-462, 1960.

Nagamatsu, H.T. and Li, T.Y. "Hypersonic Flow near the Leading Edge of a Flat Plate," The Physics of Fluids 3, no. 1, pp. 140-141, 1960.

Toro, P.G.P.; Rusak, Z.; Nagamatsu, H.T. and Myrabo, L.N. "Self-Similar Compressible Laminar Boundary Layers," AIAA 97-0797, Jan. 97.

Van Driest, E.R. "Investigations of Laminar Boundary Layer in Compressible Fluids using the Crocco Method," NACA TN 2597, 1952.

XIV Brazilian Congress of Mechanical Engineering
Obeid Plaza Hotel Convention Center - Bauru - SP/Brazil
December 08-12th 1997

PAPER CODE: COB686

SIMULATION AND TESTING OF A SATELLITE SOLAR ARRAY GENERATOR WING DEPLOYMENT

ANTONIO CLARET PALEROSI
Instituto Nacional de Pesquisas Espaciais - INPE
Divisão de Mecânica Espacial e Controle - DMC

SÉRGIO FRASCINO M. DE ALMEIDA
Instituto Tecnológico de Aeronáutica - ITA
Divisão de Engenharia Mecânica e Aeronáutica - IEM

PETRÔNIO NORONHA DE SOUZA
Instituto Nacional de Pesquisas Espaciais - INPE
Divisão de Mecânica Espacial e Controle - DMC

Abstract

This work studies the solar panels deployment of the Chinese-Brazilian satellite CBERS. The problem solution demands some deployment tests and the development of two different dynamic simulation models: one more complex related to the laboratory and another one related to orbit conditions. This work begins with a description of the deployment mechanisms, of the test device and of the deployment dynamic problem. The problem formulation is discussed and the use of a computer package for dynamic analysis of mechanisms is justified. The dynamic simulation models, the test results, the adjustment of the model parameters to fit the simulation to the test results, the laboratory and the in-orbit simulation results are presented. The importance of the inclusion in the dynamic models of the solar panel synchronizing mechanisms, of the aerodynamic forces of the solar panels due to the laboratory atmosphere, and of the solar panels initial deformations are discussed.

Keywords

Satellite, solar array deployment, dynamic simulation model, dynamic of multibody systems, model adjustment.

1. INTRODUCTION

A satellite to be launched must be assembled in the launcher nose cone which has a geometry designed to minimize the aerodynamic forces. The satellite envelope is determined by the launcher nose cone design. Therefore, in the launching configuration, the satellite must be as compact as possible. Specifications like the power supply, the satellite stabilization, the positioning of sensors far from the satellite main structure and large antennas can be against the envelope constraints requiring structures exceeding the satellite main structure size. This problem is solved by means of foldable structures. These structures are held stowed to the satellite sidewall during launching phase and, after the satellite separation from the launcher, they are moved to a deployed and locked position. The motion from a stowed to a deployed position is provided by a set of deployment mechanisms. In the case of solar arrays, the power

to be generated may require a large area to be covered with solar cells. This is supplied by solar panels which can have different designs. In this work we will be concerned with the deployment of a solar array wing with three stiff and flat solar panels. This is the case of the CBERS (China-Brazil Earth Resources Satellite) satellite which has been developed by INPE (Brazilian National Institute for Space Research) and CAST (Chinese Academy of Science and Technology). Figure 1 shows the CBERS' structural model.

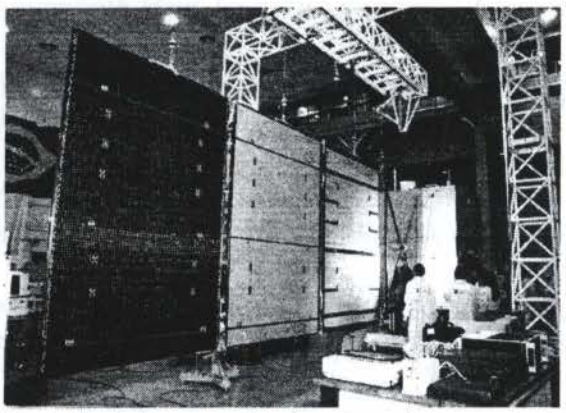

Figure 1: CBERS' structural model.

The CBERS satellite has no active deployment control. At the end of the movement the solar panels latch-up and stops suddenly. This implies in a transfer of kinetic to potential energy which characterizes an impact in the solar panels and in the deployment mechanisms. The dynamic problem consists (1) in guaranteeing that there is enough energy to initiate and conclude the deployment and (2) in determining the angular velocity at panel latch-up. The solution requires some deployment tests and the development of dynamic models to simulate the problem in laboratory and orbital conditions. The laboratory dynamic model must take into account the characteristics of the test device and of the solar panels and deployment mechanisms. The results from the deployment tests are used to adjust the parameters of the laboratory dynamic model. The in-orbit condition can be simulated when the influences of the laboratory are removed from the calibrated laboratory model. Also, the data from the mechanisms friction must be updated to those of orbit environment.

A brief description of the deployment mechanisms and of the test device is done in the next section. The purpose is to give the reader a better understanding on the problem. The description of the problem, based on the simulation parameter, is done in section 3. The problem formulation, including a justification to use a computer package for dynamic analysis of mechanisms and the dynamic simulation models are described in section 4. The test results, the adjustment to fit the simulation to the test results, the laboratory and in-orbit simulation results are present in section 5. Finally the conclusions are in last section.

2. DEPLOYMENT MECHANISMS AND TEST DEVICE DESCRIPTION

The CBERS's solar array is a deployable single wing type configuration with the following characteristics: three solar panels (inner, center and outer) assembled over a flat composite substrate with aluminum honeycomb core and carbon fibber facesheet; one positioning structure (yoke) to support and positioning the solar panels away from the satellite main structure; and a set of deployment mechanisms. The functions of the deployment mechanism are (1) to keep the wing in the stowed position against the side wall of the satellite during the launching phase, (2) to release the solar panels allowing the wing deployment motion in orbit and (3) to fully deploy the wing in a synchronized motion and latch the wing in the deployed position. The deployed wing is about 6.5 meters long and 2.6 meters wide (Vaz and Palerosi, 1992). Figures 2 and 3 show the solar array wing at its stowed and deployed positions, respectively.

The deployment mechanisms are composed by the following parts: (1) Hinge mechanisms.

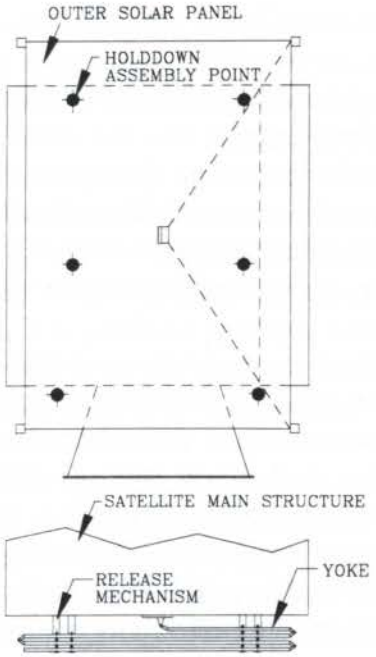

Figure 2: CBERS's solar array at stowed position.

These mechanisms connect one solar panel to another one, the inner panel to the yoke and this to the satellite main structure. At end of deployment a locking lever slides into a slot, latching the wing at full deployed position. They are composed by spherical bearings, each one with one Archimedes spring. These springs provide the energy to deploy the wing; (2) Close cable loop (CCL) mechanisms. They synchronize the deployment angles applying a passive control torque by means of cables and pulleys assembled in each rotation axis; (3) Holddown mechanisms. These are composed by six strengthened pins that hold, by means of solar panel and yoke contact bushings the three solar panels and the yoke in a folded condition against the side wall of the satellite; and (4) Release mechanisms. These cut the holddown pins by means of pyrocutter devices. Figures 2 and 3 show the assembly position in the wing of the deployment mechanisms.

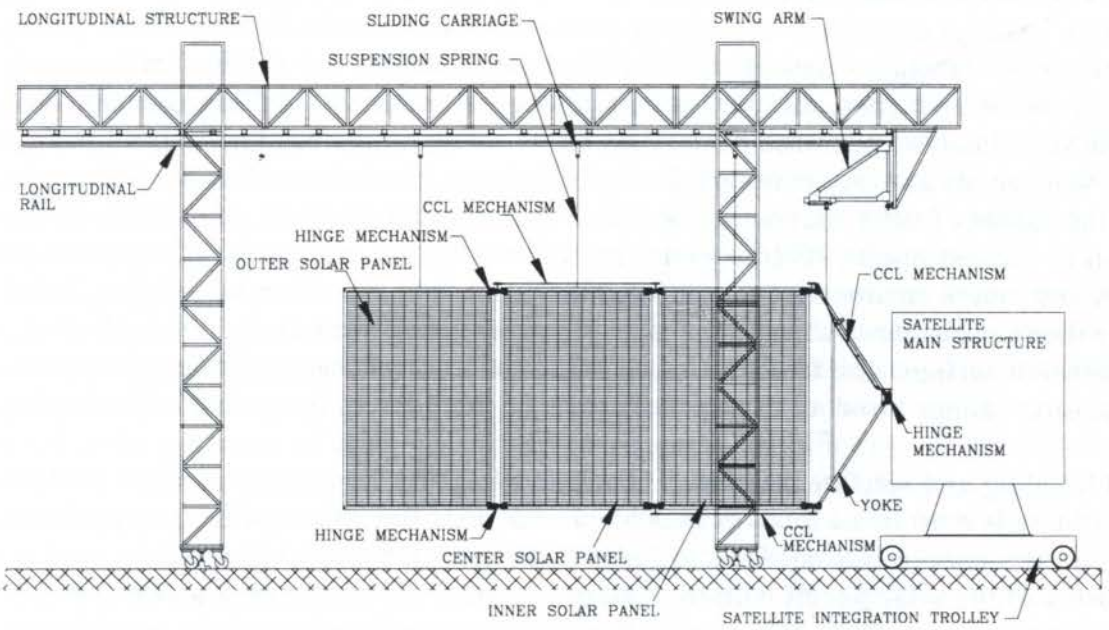

Figure 3: CBERS's solar array at deployed position and test device.

The test device is used to simulate the deployment without the gravity force. This is provided by suspension devices which hang the solar panels and yoke during the deployment. Also, the wing is assembled in this device. The test device is depicted in Figure 3.

The test device has a longitudinal structure which supports a rail. Sliding carriages, one for each solar panels, are assembled in the longitudinal rail. A suspension device is mounted in the sliding carriage holding the solar panels by means of a suspension spring. So, the sliding carriages translate in the rail carrying the solar panels during the deployment. A structure, called swing arm, hangs the yoke. A suspension device similar to that of solar panels is used. The satellite is assembled in a integration trolley as shown in Figure 3.

3. DESCRIPTION OF THE PROBLEM

The problem will be described in terms of the simulation parameters. At end of this section the degrees of freedom and the problem simplifications are presented.

Mass and inertias: The inertias of the problem in orbit condition are: the translational and rotational inertias of the solar panels and hinge mechanisms, and the mass and rotational inertia of the yoke. The translational inertias of the sliding carriages, the mass and rotational inertia of the swing arm are the mass and inertias of the problem in laboratory condition in addition to those of orbit conditions previously listed.

Torques and forces: The energy to deploy the wing comes from the deployment springs assembled in the hinge mechanisms, from the torques applied by the electrical harness which connects one solar panel to another one until the satellite main structure and from the solar panel structural deformations. In the stowed configuration the deployment springs are assembled with a pre-load and at end of deployment the springs have a residual torque due to reliability requirements. The electrical transfer harness apply a motor torque in the beginning of the deployment and, at end, it becomes a resistant torque. This is due to the viscoelastic behaviour of the electrical harness. The solar panels present geometric imperfections due to the manufacturing of the substrate and to the solar cells bonding. As the wing is set in the stowed configuration, the solar panels deform elastically storing potential energy which provide energy in the beginning of the deployment.

Friction torques and forces: These are from the friction torques in the hinge mechanisms bearings (laboratory and orbital condition) and from the friction forces in the sliding carriages (laboratory condition). The friction forces in the sliding carriages are obtained by means of friction tests performed with the rail inclined. The bearings are coated with solid M_oS_2 (molybdenum disulphide) The forces acting on the bearings depend mainly on the wing assembly and they may vary during deployment. So, it is not possible to know in advance the values of these friction torques. This is the parameter to be adjusted to fit the simulation to the test results. It is necessary to perform friction tests in the mechanisms at laboratory and orbital environment to estimate the friction torque at orbital condition. These results are then compared and a mathematical expression relating them can be obtained.

Suspension springs: The forces acting on the hinge bearings change during deployment. The suspension springs avoid an excessive increase of these forces by storing and releasing energy.

Rail levelling and satellite position: The rail levelling and the inclination of the satellite related to the rails must be as small as possible to minimize the effects of the gravity force. These parameters must be measured and included in the laboratory dynamic model.

Iteration of the solar panels with the laboratory air: This is a complex problem due to the unfolding movement of the solar panels. There is turbulent flow around the panels. This makes the determination of the aerodynamic forces very difficult.

Degrees of freedom (DOF) and problem simplification: There are four deployment angles: α_1, between the yoke and the satellite main structure; α_2, between the yoke and the inner panel; α_3, between the inner and the center panels and α_4, between the center and the outer panels. These angles are synchronized by the CCL mechanisms. The angle differences during deployment are due to the flexibility of the CCL cables. So, there are four DOF related to the CCL mechanisms. The laboratory environment adds complexity to the problem. During deployment, each sliding carriage has a different angular position with respect to its solar panel. This adds three more DOF to the problem (β_2, β_3 and β_4). Also, the yoke and the swing arm have different angular position during the deployment, which adds one more DOF (β_1).

The following simplifications are done to define and simplify the problem: (1) the mass of the hinge mechanisms can be considered to be distributed among the solar and yoke; (2) the solar panels and yoke are rigid elements; (3) the angular differences from the flexibility of the CCL cable are very small and do not have influence in the simulation results; (4) the forces due to the panels deformation are assumed to act on the outer panel and (5) the influence of the aerodynamic forces on the outer panel is predominant in relation to the aerodynamics effects on the other panels. The simplification number 3 reduces the four deployment angles to only one, α . Therefore, the problem in laboratory condition has five DOF, β_1, β_2, β_3, β_4 and α. The problem in orbital condition has only one DOF, α.

4. PROBLEM FORMULATION AND MODEL DESCRIPTION

It is possible to find a set of independent generalized coordinates which describes the system configuration. The number of generalized coordinates is equal to the number of degrees of freedom (five in laboratory and one in in-orbit condition). No additional equations are necessary to solve the problem (Meirovitch, 1970). However, the analytical formulation using the Lagrange equations for this problem, which has several elements, constraints and applied forces is cumbersome, difficult to visualize, time consuming and subject to errors. This is mainly due to the time differentiation of those equations which depends on the generalized velocities. Programs of symbolic calculations like Mathematica® are useful, but the handling of equations remains difficult. Moreover, if any change is necessary in the mechanical configuration, significant part of the work must be redone.

A computer package for dynamic analysis of multibody system improves the design activities. The user can be concentrated in modelling the problem, analysing the results and several configurations can be rapidly tested. This kind of computer tool provides, in a graphic-iterative environment, the time-history solution for all displacements, velocities, accelerations and reaction forces in a mechanical system that is driven by a set of applied excitations. The program ADAMS® was used to solve the dynamic problem of CBERS's solar array.

In this program the mechanical system modelling is based on the mathematical description of the behaviour of each element (parts, constraints and forces) and Cartesian coordinates are used instead of generalized coordinates. The software adds constraint equations to the problem set of equations. The resulting equations of motion are greater in number but are simpler compared to the approach of using generalized coordinates. The efficiency of the software is enhanced by taking advantages of sparse matrices numerical techniques. The resulting formulation is a set of equations including the state variables and the mathematical equations relating these variables. The formulation used in this program is described by Wielenga (1994).

A dynamic simulation model for laboratory and another one for orbital environment were prepared. The in-orbit is a simplification of the laboratory model. The model construction in ADAMS® was performed using existing standard types of parts, constraints and applied forces. Simplified geometries were used to model the system components. The actual inertia properties of each component was either measured or computed and imposed on the dynamic model.

The wing synchronization was modelled using an artifice. During deployment the solar panels rotate and translate. A point located at the panel top (synchronization point), follows a straight path along the deployment axis. The synchronization was modelled by an additional massless block assembled on the solar panel synchronization point. This block allows the solar panel rotation and drives the panel according to the defined path. The rail levelling and the satellite inclination related to the rail were modelled by changing the direction of the gravity force. The vertical component was decreased and a horizontal component was added to the model.

5. TEST AND SIMULATION RESULTS

Seven deployment tests were performed. Angular transducers were assembled in each rotating axis. The software Labview® was used to release the wing from the stowed position and to acquire the angular position during deployment. A data acquisition calibration was previously done with the angular transducers assembled in a precision table device. A numerical operator, representing the calibration curves, was included into Labview®. Figure 4 shows the results from the test number 1.

The angular differences among the wing elements (yoke and solar panels) are due to the compliance of the synchronizing mechanism cable and the force variations on this system. The center panel shows a more uniform behaviour and is used as the reference axis.

Seven deployment tests were performed to characterize the system repeatability. For each test there was a different set up for the wing in the stowed configuration. So, the forces due to the solar panels deformations differs from one test to another. This causes a small difference among the resulting curves of angular position as a function of time. Test number seven, which has an average behaviour, was used as test reference to adjust the simulation parameters to fit the simulation to the test results. Figure 5 shows the test result and simulations using different values for the friction torques.

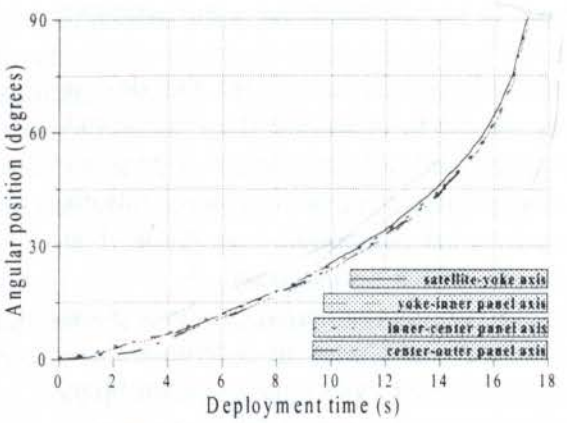

Figure 4: Angular position as a function of time for the deployment test 1.

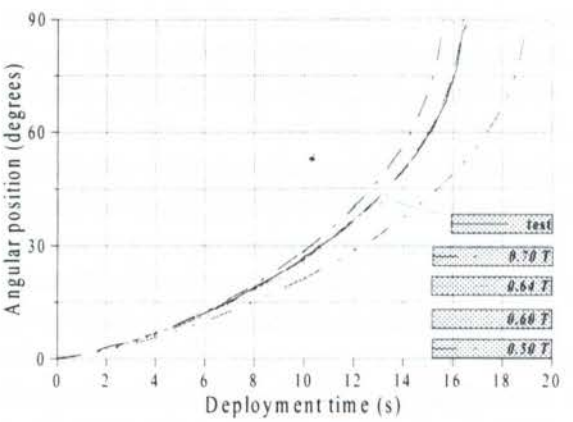

Figure 5: Test results and simulation with different values of friction torques.

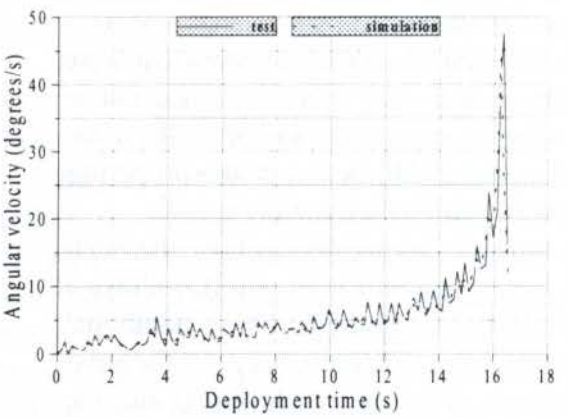

Figure 6: Comparison between test and simulation angular velocity.

In Figure 5 the total motor torque are multiplied by constants which represent the friction torques in the hinge bearings at laboratory environment. The better approximation is obtained using the torque *0.64 T*. This implies that the friction torque represents *36%* of the total available torque calculated. The simulation and test angular velocities are compared in Figure 6. The test angular velocity was calculated using the central difference differentiation method.

At end of deployment the angular velocity presents a sudden change and there is a discrepancy between the simulation and test results. Better agreement would be obtained if a higher data acquisition frequency was used. Also, it can be seen that the test curve presents *saw tooth* oscillations about the simulation curve during deployment. These small oscillations in the angular displacements can be attributed to the compliance of the CCL mechanism cables, which were not included in the simulation model, and measurement errors.

There was no available friction test results from the hinge bearing in the laboratory and orbital environment at the time this work was prepared. So, it was decided to simulate the in-orbit deployment according to two limit situations: (1) in-orbit friction torque equal to the laboratory and (2) in-orbit friction torque equal to zero. Under vaccum condition, the dry film of M_oS_2 applied to the hinge bearings has a better performance than laboratory condition (Roberts, 1989). So, in the first situation is possible to predict, in a conservative way, if the torque margin is large enough to guarantee the deployment. In situation two, the angular velocity is greater than the actual one and the latch-up analysis can be done based on this conservative value. Figures 7 and 8 show the results for both situations for the in-orbit condition.

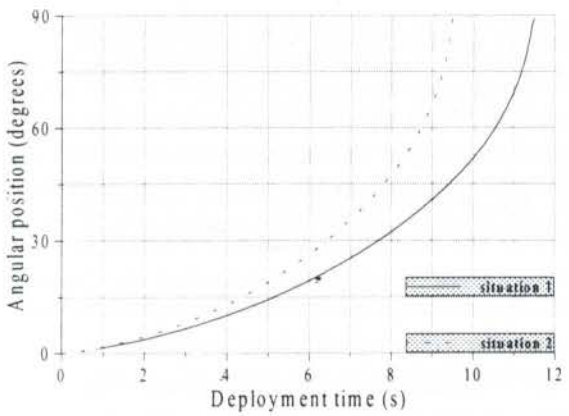

Figure 7: Angular position as function of time for the in-orbit simulation.

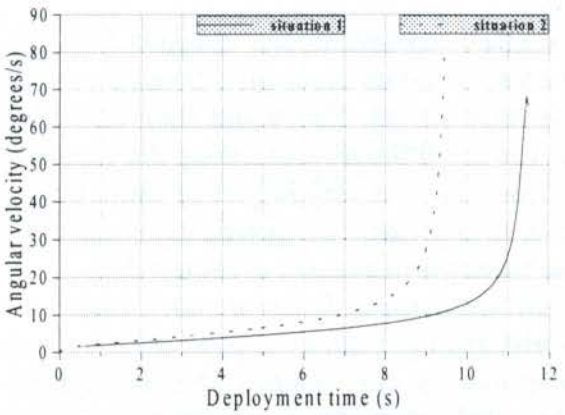

Figure 8: Angular velocity as function of time for the in-orbit simulation.

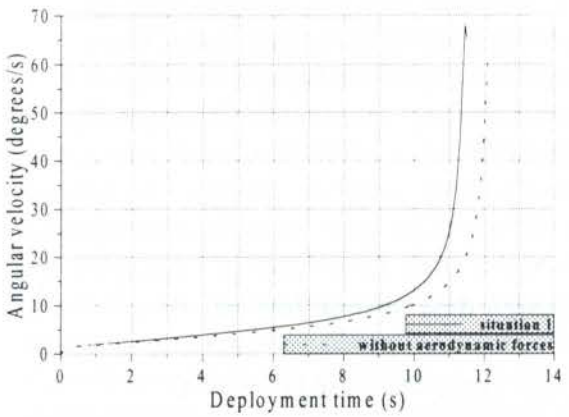

Figure 9: Comparison between the in-orbit simulated angular velocity for the friction torque adjustment with and without the aerodynamic forces

If the aerodynamic forces are not taken into account in the laboratory model, the adjustment of the friction torque will be biased. This error affects the in-orbit simulation results. A new adjustment of the friction torque to fit the simulation to the test results without the aerodynamic force was performed. A comparison between the in-orbit simulation for the friction torque adjustment with and without the aerodynamic forces is presented in Figure 9. The friction torque situation 1 is used in this comparision. The figure shows that the error is non-conservative.

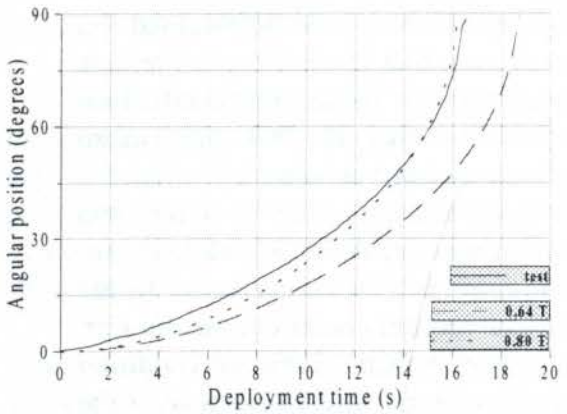

Figure 10: Tentatives to adjust the simulation to the test results without considering the solar panels deformations.

The importance of modelling the forces due to the solar panels deformations is indicated in Figure 10. Tentatives to adjust the simulation to the test results are presented. It can be seen that adjustment is not possible. The best approximation is obtained with the curve *0.80 T*, which is slow in the beginning of the deployment because the energy from the solar panels deformations is not included in the analysis.

6. CONCLUSIONS

Excellent agreement was obtained between the adjusted simulation model and the test results. A higher data acquisition frequency is recommended during the deployment test of the satellite flight model. This could show the effect of the compliance of the CCL mechanism cables. The small differences among the deployment angles do not have influence in the model adjustment. This is a very important simplification because the deployment angles are reduced from four to only one. The specification of the CCL mechanism cables and its initial tension can be done based on an analysis of the test data.

If the aerodynamic forces are not included in the simulation model, an error of about *8%* in the in-orbit angular velocity at panel latch-up occurs. The angular velocity obtained in this case is smaller than the one obtained when aerodynamic forces are included in the model adjustment procedure. This represents an error against safety conditions.

It is not possible to adjust the simulation model if the solar panel initial deformations are not included in the model. Measurements of these deformations and corresponding forces during the set-up of the solar panels in the stowed position must be carefully done.

The problem must be analyzed under a general view. A structural transient analysis must be performed and stress safety margins due to the solar panels latch-up must be calculated. Once these models are available, the influence of each parameter in the in-orbit angular velocity at latch-up can be better analyzed using the dynamic simulation models developed. Moreover, it will be possible to determine tolerances to each model parameters.

REFERENCES

VAZ, C. C.; PALEROSI, A. C. **CBERS's solar array design description**. Internal document of INPE, 1992 (CBDQ-ITRP-022).

MEIROVITCH, L. **Methods of analytical dynamics**, New York, McGraw Hill, 1970.

WIELENGA, T. J. **Analysis methods and model representation in ADAMS**. Internal document of Mechanical Dynamics, Inc., 1994.

ROBERTS, E. W. The advantages and limitations of sputtered molybdenum disulphide as a space lubrificant. In: EUROPEAN SYMPOSIUM ON SPACE MECHANISMS AND TRIBOLOGY, 4., Cannes, Sept., 1989. **Proceedings**. ESA, p. 59-65. (ESA SP-299).

XIV Brazilian Congress of Mechanical Engineering
Obeid Plaza Hotel Convention Center - Bauru - SP/Brazil
December 08-12th 1997

PAPER CODE: COB695

UMA SOLUÇÃO PARA A CAMADA-LIMITE DE CONCENTRAÇÃO JUNTO A SUPERFÍCIES LIVRES EM ESCOAMENTOS TURBULENTOS

HARRY EDMAR SCHULZ & SELVA AMARAL GARCIA SCHULZ
Departamento de Hidráulica e Saneamento, Escola de Engenharia de São Carlos - USP - São Carlos
CEP 13560-250 São Carlos, Brasil - E-mail:heschulz@sc.usp.br

Resumo

O presente trabalho descreve uma solução analítica para a camada-limite de concentração junto a superfícies livres em escoamentos turbulentos, obtida a partir de aproximações convenientes para a difusividade turbulenta nesta região e de uma adimensionalização particular aplicada à equação governante do fenômeno espacial-temporal de transferência de massa. A adimensionalização permitiu gerar uma equação governante para o fenômenos de transferência de massa na interface gás-líquido que conduziu a uma solução geral para a geometria estudada. A análise dos fluxos de massa através da interface gás-fluido permitiu obter, a partir de uma equação aproximada para a solução do equacionamento proposto, uma expressão que envolve os coeficientes adimensionais clássicos para os problemas de transferência de massa, como o número de Reynolds, Schmidt e Sherwood. Esta expressão segue a forma tradicional de relacionar o número de Sherwood ao produto de potências dos dois outros parâmetros adimensionais.

Palavras-chave/ Key words

Absorção de Gases, Dessorção de Gases, Turbulência Interfacial, Transferência Interfacial de Massa, Camada-Limite de Concentração, Gas Absorption, Gas Desorption, Interfacial Turbulence, Interfacial Mass Transfer, Concentration Boundary Layer.

1. INTRODUÇÃO

A transferência interfacial de massa entre gases e líquidos é um problema complexo que tem ocupado os pesquisadores ao longo dos anos. Atualmente o tema tem crescido em importância devido aos processos de transferência na superfície de corpos de água poluídos, como rios, lagos, estuários e oceanos. Assim, em termos ambientais, há maior interesse em estudar o sistema ar-água, pois vincula-se este sistema particular aos processos de transferência de gases nocivos na interface de águas residuárias com a atmosfera e à absorção de oxigênio em corpos de água naturais e em esgotos. Como exemplo podemos citar o processo de auto-depuração dos rios, que consiste em absorver oxigênio da atmosfera enquanto o rio escoa, fornecendo este gás para o metabolismo das bactérias que consomem materiais poluentes orgânicos. A partir das primeiras décadas deste século, com o aparecimento de modelos matemáticos suportados em modelos físicos mais consistentes, a questão da transferência interfacial de massa tornou-se bastante polêmica justamente no que concerne à validade destes modelos físicos. Parâmetros novos, nem sempre possuindo uma explicação ou existência física real, surgiram e passaram a enriquecer o vocabulário dos estudiosos do assunto e a fomentar a polêmica. Termos como camada superficial laminar, penetração, renovação superficial, foram incorporados à literatura da área. No presente

trabalho a atenção é concentrada na absorção de gases pouco solúveis pela água, como é o caso do oxigênio. A formulação obtida vale, evidentemente, tanto para processos de absorção como para processos de dessorção desses gases. Em geral é aceito que a taxa de transferência de gases interfacial, em um processo de absorção, pode ser representada pela equação (1):

$$\frac{dC_b}{dt} = K(C_S - C_b) \tag{1}$$

C_b é a concentração média de gás dissolvido no seio do líquido (kg/m^3), C_s é a concentração do mesmo na superfície do líquido (kg/m^3) e K é denominado de coeficiente de transferência interfacial de massa (s^{-1}). A integração desta equação produz a variação temporal:

$$\frac{C_b - C_S}{C_0 - C_S} = exp(-Kt) \tag{2}$$

C_0 é a concentração média no instante inicial (kg/m^3). A equação (2) sugere que a evolução da concentração normalizada de gás no seio líquido independe de qualquer coordenada espacial. Entretanto, há de fato uma grande variação da concentração média na região imediatamente abaixo da superfície, na camada-limite de concentração, entre as concentrações extremas da superfície e do seio líquido. Lee e Luk (1982), Chu e Jirka (1991) e Schulz e Schulz (1991) sugerem uma forma normalizada também para a variação da concentração no espaço:

$$\frac{C(x) - C_b}{C_S - C_b} = f(x) \tag{3}$$

$C(x)$ é a concentração média na posição x no líquido (função do tempo) e $f(x)$ é uma função genérica para a variação espacial da concentração. Chu e Jirka (1991), baseados em dados experimentais, utilizaram uma aproximação exponencial para $f(x)$. Nota-se que a concentração normalizada da equação (3) independe agora da variável tempo. As equações (2) e (3) são formas de análise comumente encontradas na literatura. Neste estudo é mostrado que ambas as equações estão relacionadas com a equação geral de transferência de massa e que uma equação governante para $f(x)$ pode ser obtida a partir da equação geral. Uma solução para $f(x)$ é também apresentada, seguindo a proposta de Schulz e Schulz (1992)

2. EQUAÇÃO GOVERNANTE PARA $f(x)$

Considerando o balanço de massa para fluidos incompressíveis, sem termos advectivos, sem fontes e sumidouros que não sejam a atmosfera e com turbulência estacionária, tem-se:

$$\frac{\partial C(x)}{\partial t} = \frac{\partial}{\partial x}\left(D_E(x) \frac{\partial C(x)}{\partial x} \right) \tag{4}$$

$D_E(x)$ é o coeficiente de difusividade efetiva, ou seja, a soma das difusividades molecular e turbulenta. Nesta formulação considerou-se que a difusividade turbulenta varia, que se contrapõe à proposta de Kishinevsky e Serebriansky (1955). Subtraindo C_S de cada membro a igualdade não se altera. Definindo $C^+ = C(x) - C_S$ e admitindo separação de variáveis, isto é, $C^+ = X(x).T(t)$, onde $X(x)$ é uma função apenas de x e $T(t)$ é uma função apenas de t, obtém-se:

$$\frac{1}{T(t)}\frac{dT(t)}{dt}=\sigma \qquad \text{ou} \qquad T(t)=T_0.exp(\sigma t) \qquad \text{onde} \qquad T_0=C_0-C_S \tag{5}$$

$$D_E(x)\frac{d^2X(x)}{dx^2}+\frac{dD_E(x)}{dx}\frac{dX(x)}{dx}-\sigma X=0 \tag{6}$$

As equações (5) mostram que o déficit do gás considerado é proporcional ao déficit inicial e evolui exponencialmente no tempo, o que coincide com a equação (2). A presente abordagem, portanto, produz a evolução temporal geralmente aceita. A equação (6), por sua vez, é a equação governante para $X(x)$, isto é, para a evolução espacial da concentração. Esta equação independe de como a difusividade efetiva varia com x, mas sua solução envolve a definição prévia da difusividade efetiva. Uma equação com a mesma forma pode ser obtida das equações (2) e (3), de cuja união resulta:

$$\frac{C(x)-C_S}{C_0-C_S}=\left[1-f(x)\right].exp(-Kt) \tag{7}$$

Das equações (4) e (7), por sua vez, resulta:

$$D_E(x)\frac{d^2f(x)}{dx^2}+\frac{dD_E(x)}{dx}\frac{df(x)}{dx}+K\left[f(x)-1\right]=0 \tag{8}$$

Comparando as equações (6) e (8), vê-se que ambas são equivalentes e que:

$$\sigma=-K \qquad \text{e} \qquad X(x)=1-f(x)$$

As equações (2) e (3) são casos particulares da equação geral (4). Para obter uma avaliação de $f(x)$, é preciso encontrar uma expressão aceitável para a difusividade efetiva.

3. A DIFUSIVIDADE EFETIVA

Representando a difusividade efetiva expandida em série de potências de x e restringindo a aplicação da formulação para a camada-limite de concentração (uma região muito delgada, abaixo da superfície), pode-se truncar a série no termo de primeira ordem em x. Tem-se então:

$$D_E(x)=\alpha_0+\alpha_1 x \tag{9}$$

α_0 e α_1 são coeficientes da expansão efetuada. Como a difusividade efetiva é a soma das difusividades molecular (constante) e turbulenta (variável), a equação (9) é escrita como:

$$D_E(x)=D+a\,x \tag{10}$$

A difusividade molecular, D, substitui a constante α_0, e a escala de velocidade a substitui a constante α_1. A difusividade turbulenta, D_t, é representada, na camada-limite, como uma variação linear com a distância, $D_t=ax$. Esta aproximação é considerada válida na literatura da área para pequenos valores de x (Hinze, 1959). A equação (8) passa então a assumir a forma:

$$(D+ax)\frac{d^2f(x)}{dx^2}+a\frac{df(x)}{dx}+K\left[f(x)-1\right]=0 \tag{11}$$

4. CONDIÇÕES DE CONTORNO E SOLUÇÃO PARA *f(x)*

Considerando a figura 1, para absorção de gás, as condições de contorno são:

-A concentração é C_S na superfície, ou $f(x=0)=1$

-A concentração é C_b no seio líquido, ou $f(x=e)=0$

-A derivada da concentração é zero na fronteira inferior da camada-limite, $\left.\frac{df(x)}{dx}\right|_{x=e} = 0$

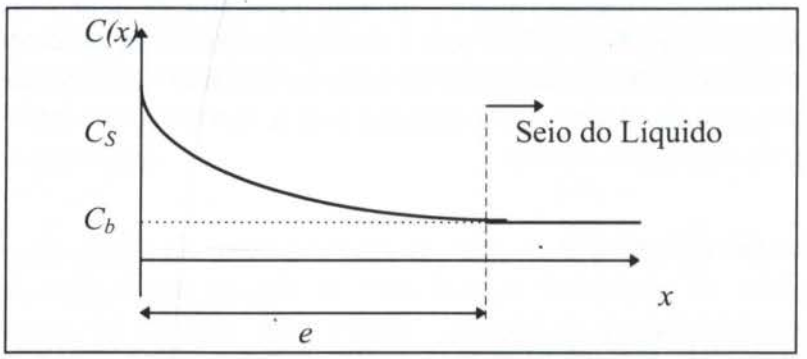

Figura 1: Contornos para a função *f(x)* na resolução do problema de camada-limite

Para obter uma forma simplificada da equação (11), com coeficientes que não envolvem as variáveis *D, a* e *K*, foi sugerida a seguinte transformação:

$$x^* = \frac{K(ax+D)}{a^2} \qquad \text{e} \qquad Y(x^*) = f(x^*) - 1 \tag{12}$$

x^* é uma distância normalizada para a dimensão perpendicular à superfície, x. A aplicação das transformações (12) na equação (11), produz a nova equação governante:

$$x^* \frac{d^2Y}{dx^{*2}} + \frac{dY}{dx^*} + Y = 0 \tag{13}$$

Os novos contornos, envolvendo as variáveis adimensionais, passam a ser:

$$Y(x^*) = 0 \qquad \text{em} \qquad x^* = x^*_{min} = \frac{KD}{a^2} \tag{14a}$$

$$Y(x^*) = -1 \qquad \text{em} \qquad x^* = x^*_{max} = \frac{K(D+ae)}{a^2} \tag{14b}$$

$$\frac{dY(x^*)}{dx^*} = 0 \qquad \text{em} \qquad x^* = x^*_{max} = \frac{K(D+ae)}{a^2} \tag{14c}$$

x^* é o parâmetro adimensional associado a distância normal à superfície x.

x^*_{min} define a posição da interface no novo sistema de coordenadas.

x^*_{max} define a fronteira da camada superfcial para a variação da concentração.

A solução da equação (13) envolve funções de Bessel de primeira e segunda espécies, e pode ser expressa por uma série de potências, na forma:

$$Y(x^*) = C_1 Y_1(x^*) + C_2 Y_2(x^*) \tag{15a}$$

$$Y_1(x^*) = 1 - x^* + \frac{x^{*2}}{(2!)^2} - \frac{x^{*3}}{(3!)^2} + \frac{x^{*4}}{(4!)^2} - \ldots \tag{15b}$$

$$Y_2(x^*) = Y_1(x^*)\ln(x^*) + 2\left\{x^* - \frac{x^{*2}}{(2!)^2}\left[1+\frac{1}{2}\right] + \frac{x^{*3}}{(3!)^2}\left[1+\frac{1}{2}+\frac{1}{3}\right] - \right.$$

$$\left. - \frac{x^{*4}}{(4!)^2}\left[1+\frac{1}{2}+\frac{1}{3}+\frac{1}{4}\right] + \frac{x^{*5}}{(5!)^2}\left[1+\frac{1}{2}+\frac{1}{3}+\frac{1}{4}+\frac{1}{5}\right] - \ldots\right\} \qquad (15c)$$

C_1 e C_2 são constantes determinadas pelas condições de contorno. De posse do perfil de concentração, o fluxo de massa na interface ($x=0$, $x^*=x^*_{min}$) é obtido pela lei de Fick. Como o gradiente de concentração é adimensionalizado, também se adimensionalizou o fluxo. Tem-se:

$$m^* = \frac{ma}{DK\left(C_S - C_b\right)} = -\left.\frac{dY(x^*)}{dx^*}\right|_{x^*=x^*_{min}} \qquad (16)$$

O fluxo de massa não adimensionalizado, m, surge como incógnita. Assim, uma expressão para m deve ser obtida. Reconhecendo que a massa que varia no volume pode apenas ter atravessado a interface ar-água, tem-se:

$$m = \frac{d\,(Massa\ de\ soluto)}{d\,t}\frac{1}{'\,Area\ Interfacial} \qquad (17a)$$

A massa de soluto, por sua vez, pode ser representada pelo produto entre a concentração média da mesma no seio do líquido, C_b, e o volume (V, constante) deste líquido. Considerando ainda a altura média (H) do volume de líquido com relação à área interfacial (A_i), resulta:

$$m = \frac{1}{A_i}\frac{d\left(C_b V\right)}{d\,t} = H\frac{d\,(C_b)}{d\,t} \qquad (17b)$$

Unindo as equações (1) e (17b), resulta:

$$m = KH(C_S - C_\infty) \qquad (18)$$

Das equações (16) e (18), tem-se, por sua vez:

$$m^* = \frac{Ha}{D} = Pe = -\left.\frac{dY(x^*)}{dx^*}\right|_{x^*=x^*_{min}} \qquad (19)$$

Pe, na equação (16), representa o número de Peclét, definido com a escala de velocidade da difusividade turbulenta. Assim, o fluxo adimensionalizado de massa pode ser visto como este número de Peclét. As constantes C_1 e C_2 da equação (15a) foram quantificadas com os contornos (14b) e (14c). O contorno (14a) permite o estabelecimento de x^*_{min}, que corresponde à situação na qual $Y(x^*)=0$. A tabela (1) apresenta valores dos diferentes parâmetros mencionados, utilizando x^*_{max} como parâmetro de controle (valor arbitrado)

5. Resultados obtidos da solução analítica

Com base na tabela 1, traçaram-se os perfis de concentração normalizados, para as diferentes situações de agitação turbulenta, indicadas por x^*_{max}. Frisa-se que x^*_{max} é a posição da fronteira da região de variação de concentração, que se posiciona de acordo com o estado

de movimento do fluido, sendo um bom parâmetro de controle nos cálculos efetuados. As figuras 2a e 2b mostram os perfis obtidos. A representação gráfica do fluxo de massa normalizado m^* em função de x^*_{min} está mostrado nas figuras 3a e 3b onde se vê que m^* e x^*_{min} podem ser relacionados por uma lei de potência, como mostra a equação (20): Nota-se a grande região com declividade -1 na figura 3a e a tendência à declividade -1/2 na figura 3b.

$$m^* = \omega\, x^{*n}_{min} \qquad \text{ou} \qquad x^*_{min} = \left(\frac{m^*}{\omega}\right)^{1/n} \tag{20}$$

Tabela 1: Valores de C_1, C_2, x^*_{min} e m^* calculados para diferentes valores de x^*_{max}

x^*_{max}	C_1	C_2	x^*_{min}	m^*
0,010	-1,0557	$-9{,}9501.10^{-3}$	$8{,}3493.10^{-47}$	1,1917.10 44
0,035	-1,1488	$-3{,}4391.10^{-2}$	$4{,}7229.10^{-15}$	7,3840.10 12
0,050	-1,1930	$-4{,}8760.10^{-2}$	$2{,}3684.10^{-11}$	2,0588.10 9
0,080	-1,2662	$-7{,}6842.10^{-3}$	$6{,}9760.10^{-8}$	1.1015.10 6
0,100	-1,3067	$-9{,}5082.10^{-2}$	$1{,}0753.10^{-6}$	8,8423.10 4
0,300	-1,5044	-0,25719	$2{,}8651.10^{-3}$	9,0026.10 1
0,500	-1,4874	-0,38499	$2{,}0154.10^{-2}$	1,9493.10 1
0,800	-1,2476	-0,51993	$7{,}7173.10^{-2}$	7,2890
1,000	-1,0020	-0,57672	$1{,}3195.10^{-1}$	5,0103
3,000	1,9118	$-2{,}6401.10^{-2}$	1,0548	1,2980
5,000	2,7418	0,49965	2,2847	8,1678.10-1
8,000	0,40657	0,93030	4,3694	5,6151.10-1
10,00	-1,7149	0,63793	5,8510	4,7605.10-1
30,00	4,0301	0,92853	$2{,}2236.10^{1}$	2,2907.10-1
50,00	-4,4931	-1,0947	$3{,}9738.10^{1}$	1,6823.10-1
85,00	-0,24714	1,5819	$7{,}1369.10^{1}$	1,2375.10-1
100,0	-5,9712	-0,66833	$8{,}5144.10^{1}$	1,1289.10-2
200,0	3,1306	-1,4654	$1{,}7864.10^{2}$	7,6983.10-2
300,0	3,9861	-1,4883	$2{,}7373.10^{2}$	6,1843.10-2

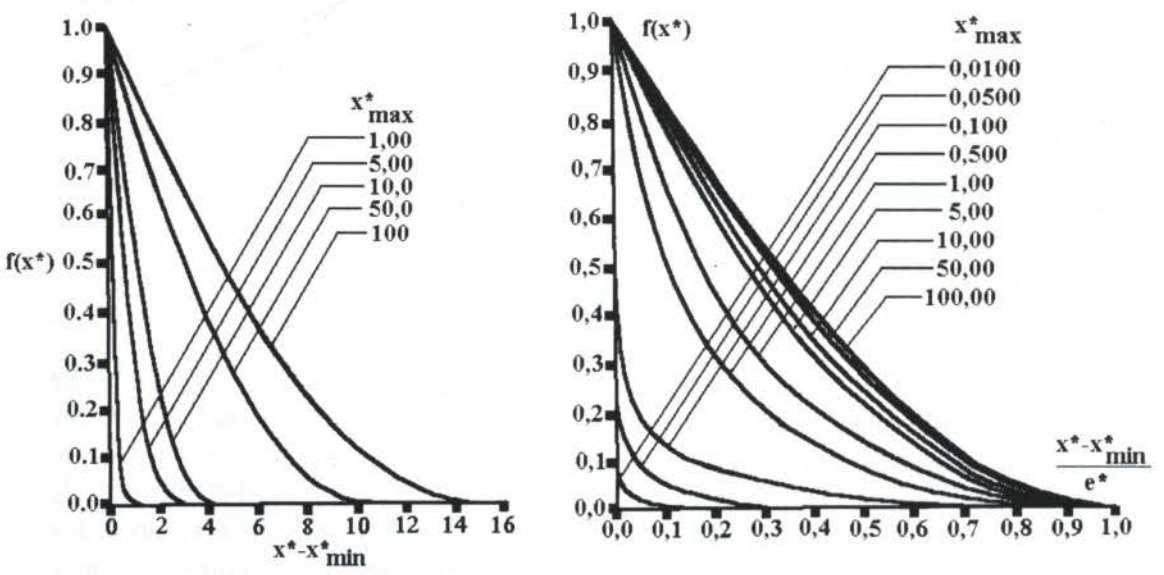

Figura 2: (a) Perfis de concentração normalizados $f(x^*)$ representados como função da distância normalizada sem considerar a dimensão e^*.(b) Perfis de concentração normalizadosconsiderando ainda a dimensão e^*.

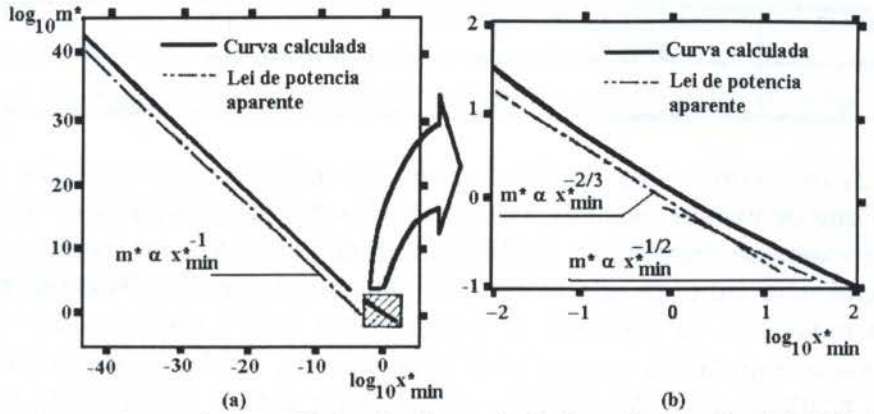

Figura 3: (a) m^* como função de x^*_{min}. (b) Quadro destacado da figura 3a. Tendência à declividade -1/2.

ω é uma constante de proporcionalidade. O índice n varia com à agitação do líquido. De acordo com a faixa de trabalho estudada, $-1<n<-1/2$. A partir da lei de potência (20) e das definições de m^* e x^*_{min}, anteriormente apresentadas, tem-se:

$$\frac{aH}{D} = \omega\left(\frac{KD}{a^2}\right)^n \tag{21}$$

Rearranjando os termos, pode-se escrever:

$$KH = \theta\, a^{\beta}\left(\frac{D}{H}\right)^{1-\beta} \qquad \beta = \frac{2n+1}{n} \tag{22}$$

θ é uma constante de proporcionalidade e β é uma função do expoente n. Para o intervalo teórico de n, tem-se que $0<\beta<1$. O primeiro membro da equação (22) é também um coeficnete de transferência de massa denominado usualmente de coeficiente de película (ver equação 18). O que se observa é que o coeficiente de transferência de massa pode ser expresso como um produto conveniente entre a difusividade molecular e a escala de velocidade característica da difusividade turbulenta. Utilizando os parâmetros adimensionais clássicos em problemas de transferência de massa, (ver, por exemplo, Chu e Jirka, 1991) obtém-se:

$$Sh = \theta\, Pe^{\beta} = \theta\, Re^{\beta}\, Sc^{\beta} \tag{23}$$

Neste caso $Sh = (KH)H / D$ é o número de Sherwood, $Re = aH / \nu$ é o número de Reynolds e $Pe = aH / D$ é o número de Peclét já anteriormente definido. Um aspecto positivo da formulação apresentada é o seu caráter unificador, no que tange a alguns aspectos das teorias antagônicas relacionadas à transferência interfacial de massa. Particularmente no que concerne ao expoente da difusividade molecular, o intervalo teórico de n permite obter tendências que englobam as variações de todas as teorias precedentes, conforme indicado na tabela (2).

Tabela 2: Tendências para o coeficiente de transferência de massa (KH) para diferentes faixas de agitação (diferentes valores de m^*)

m^*	n	β	KH
Baixo $m^*<0,295$	-1/2	0,0	$a\ (D/H)$
Intermediário	-2/3	0,5	$a\ (Ds)^{0,5}$

$0{,}295<m^*<89{,}12$	(valor intermediário genérico)		$s=a/H$
Alto $89{,}12<m^*<10^{13}$	-1	1,0	$a\ a$

Na tabela (2) os valores altos do fluxo de massa indicam altas agitações do meio líquido, enquanto que os menores valores indicam baixas agitações. Vê-se que a tendência obtida, quanto ao expoente unitário da difusividade molecular, para as baixas agitações, coincide com a tendência indicada pela teoria dos dois filmes (Lewis e Withmann, 1924). Para as agitações moderadas, o resultado ½ é semelhante àquele obtido pelas teorias de penetração e renovação superficial, quando n=-2/3 (Dankwerts, 1951), enquanto que para as altas agitações, o resultado de independência de KH para com a difusividade molecular coincide com a proposta de Kishinevsky e Serebriansky (1955). Os valores de β indicados na tabela (2) podem ser utilizados nas equações (22) e (23), de acordo com a situação de agitação estudada. Evidentemente toda a faixa de variação de 0,0 a 1,0 pode ser utilizada.

6. Conclusões

O equacionamento apresentado permitiu obter tendências analíticas para a evolução da concentração de gás dissolvido em um líquido, na região de camada-limite de concentração junto à interface gás-líquido. A partir dos perfis de concentração foram calculados fluxos de massa, cujos resultados permitiram unificar tendências anteriormente antagônicas encontradas na literatura da área. O potencial de unificação é um aspecto altamente positivo desta formulação.

6. Agradecimentos

Os autores são gratos à FAPESP e ao CNPq pelos auxílios e bolsas que permitiram a realização desta pesquisa e a publicação dos resultados.

7. Referências bibliográficas

CHU, C.R. & JIRKA, G.H. Turbulence Velocity and Gas Concentration Measurements in the Near Surface Layer. - In: Wilhelms, S.C. & Gulliver, J.S. (ed), *Air-Water Mass Transfer*, ASCE, American Society of Civil Engineering, New York, pp. 160-172, 1991.

DANKWERTS, P. V. Significance of Liquid-film Coefficients in Gas Absorption. *Industrial and Engineering Chemistry*, 43(6); pp. 1460-1467; june, 1951.

KISHINEVSKY, M. KH. & SEREBRIANSKY, V.T. The Mechanism of Mass Transfer at the Gas-Liquid Interface With Vigorous Stirring. *Journal Applied Chemistry*, U.S.S.R, 29: pp. 29-33, 1955.

LEE, Y. H. & LUK, S. Characterization of Concentration Boundary Layer in Oxygen Absorption, *Ind. Eng. Chem. Fundam.*, 21(4), pp. 428-434, 1982.

LEWIS, W. K. & WHITMAN,W. G. Principles of Gas Absorption, *Absorption Simposium, Industrial and Engineering Chemistry*, 16(12), pp.1215-1220, dec, 1924.

SCHULZ, H. E. & SCHULZ, S. A. G. Modelling Below Surface Characteristics in Water Reaeration, In Wrobel L.E. and Brebia. C. A. (ed), *Water Pollution, Modelling, Measuring and Prediction*, Computational Mechanics Publications and Elsevier Applied Sciences, pp 441-454, 1991

SCHULZ, H. E. & SCHULZ, S. A. G Water aeration: An Approach For the Near -Surface Region, *Proceedings of the IX International Conference of Computational Methods in Water Resources*, Denver, U.S.A., June,1992.

XIV Brazilian Congress of Mechanical Engineering
Obeid Plaza Hotel Convention Center - Bauru - SP/Brazil
December 08-12th 1997

PAPER CODE: COB697

ESTUDO EXPERIMENTAL DE ESCOAMENTOS TURBULENTOS EM DUTOS CURVOS COM GRANDES RAIOS DE CURVATURA

Paper code: 697 Theme n° 35

Abstract

This work presents experimental results of fully developed turbulent flows in two curved rectangular duct sections with small curvature. Mean velocity and turbulent intensity profiles are measured using Pitot tubes and a hot wire anemometer system along a 3000 mm x 460 mm x 50 mm rectangular duct and also along the central longitudinal positions af the curved duct sections of 1500 mm and $1800/\pi$ mm curvarture radii, respectively.

Keywords

Turbulence, Hot-Wire Anemometer, Wind Tunnel, Data Acquisition System, Curved Ducts

1. INTRODUÇÃO

Este trabalho tem como objetivo o estudo experimental dos perfis de velocidade média e de intensidade de turbulência, em escoamentos turbulentos plenamente desenvolvidos, no interior de dutos curvos de seção retangular, com grandes raios de curvatura.

A necessidade de caracterização dos escoamentos em dutos curvos, segundo o tamanho de seus raios de curvatura deve-se, conforme demonstram ao estudos de Hunt e Joubert (1979) e de Ellis e Joubert (1974), à natureza diversificada das forças atuantes, devido à presença da curvatura, na geometria estudada.

Os escoamentos que se desenvolvem em dutos com grandes raios de curvatura são caracterizados como escoamentos governados, predominantemente, por forças cisalhantes. Nos escoamentos em geometrias com pequenos raios de curvatura, as forças governantes são basicamente inerciais.

A predominância das forças cisalhantes nos escoamentos turbulentos internos, em dutos com grandes raios de curvatura, é demonstrada pelos trabalhos de Hunt e Joubert (1979) e Ellis e Joubert (1974). Apesar de constatarem a formação de vórtices de Taylor-Goertler na região central do escoamento, os estudos mostram que a estrutura do escoamento na região interna da camada limite é preservada, conservando desta forma sua similaridade com os perfis convencionais de parede plana.

O escoamento no interior de dutos curvos com seção não-circular é sempre tridimensional, coexistindo dois tipos distintos de escoamentos secundários: os gerados pela geometria não-circular da seção e os vórtices celulares conhecidos como vórtices de Taylor-Goertler.

Considerando a complexidade do escoamento e o caracter inicial deste estudo, o trabalho concentra sua análise apenas sobre a seção longitudinal média do escoamento, onde não são sensíveis os efeitos das recirculações ocasionadas pelos cantos do duto, evidenciando dessa forma somente o efeito da curvatura sobre o fluxo.

O túnel de vento construído para a realização deste trabalho é dotado de um canal retangular reto, capaz de permitir o completo desenvolvimento do escoamento e de dois segmentos curvos, caracterizados por diferentes raios de curvatura, onde foi feito o levantamento experimental.

2. MONTAGEM EXPERIMENTAL

2.1 O TÚNEL DE VENTO

O túnel de vento de circuito aberto empregado na realização deste trabalho foi composto a partir de um equipamento Tecnovate no qual a seção de teste original foi substituída por um canal reto de seção retangular, destinado a provocar o desenvolvimento completo do escoamento e por dois segmentos curvos que se constituem nas seções de teste e que trabalham conectadas à seção de saída do canal de desenvolvimento através de um sistema de encaixe por flanges.

O canal de desenvolvimento, todo construído em madeira e revestido internamente por fórmica branca lisa, tem seção retangular de 460 mm por 50 mm e comprimento de 3000 mm.

As dimensões da seção retangular do canal de desenvolvimento foram impostas pela seção de saída do bocal convergente que serve para conectá-lo ao túnel de vento.

O bocal convergente instalado à montante do canal de desenvolvimento tem seção de entrada de 460 mm por 460 mm, comprimento de 450 mm e está equipado com tomadas de pressão estática em suas seções de entrada e saída destinadas a medir a vazão de ar que alimenta o canal de desenvolvimento.

O comprimento de 3000 mm do canal foi dimensionado para permitir um desenvolvimento completo do escoamento em função do diâmetro hidráulico do duto e de escoamentos com números de Reynolds da ordem de 10^5.

No canal de desenvolvimento foram intaladas dez tomadas para pressão estática e quatro tomadas de velocidade. As tomadas de pressão estática foram locadas sobre a linha central da superfície inferior e as de velocidade, no mesmo eixo, sobre a superfície superior do canal que trabalha com o lado maior da seção retangular nivelada paralelamente ao solo. As tomadas de velocidade e pressão estão destribuidas uniformemente ao longo do canal, considerando que a primeira tomada está a 350 mm de seu início e a última a 375mm de sua extremidade final.

O acesso ao interior do túnel é feito através de sua parede superior que, dotada de dobradiças externas, articula-se como uma porta. A vedação é mantida por espuma auto-adesiva colocada nos batentes da abertura.

As seções de teste foram construídas com dois materiais distintos. As laterais, com 50 mm de altura, e as flanges de encaixe no canal de desenvolvimento foram construídas em madeira. As superfícies, superior e inferior, foram feitas de placas de PVC transparente com objetivo de possibilitar a visualização do escoamento.

Duas seções de teste, com diferentes dimensões, foram usadas. As seções de teste são canais curvos com seção reta retangular, de dimensões iguais a do canal de desenvolvimento.

A seção de teste, denominada doravante curva 1, apresenta na sua linha de centros um comprimento de 600 mm e um raio de curvatura de 1500 mm. A seção de teste, denominada doravante curva 2, apresenta na sua linha de centros um comprimento de 600 mm e um raio de curvatura de $1800/\pi$ mm.

Sobre a parede superior das curvas 1 e 2 foram feitos cinco furos, equidistantes e posicionados sobre sua linha média, para a instalação dos sensores de velocidade.

O sistema de acionamento do túnel de vento original foi substituido por um motor elétrico trifásico Weg com potência de 2,0 Hp, controlado por um variador de frequência

WEG de 20 kW. O ventilador axial de marca Buffalo, com diâmetro de 400 mm, é acionado por um sistema convencional de polias.

2.2 O EQUIPAMENTO DE MEDIÇÃO

Três tipos de sensores foram empregados na medição: sensor de pressão estática, tubo de Pitot e anemômetro de fio quente.

Os sensores de pressão estática, em número de 14, são conectadas por mangueiras de borracha a um multimanômetro inclinavel marca TEM, com resolução de 2 mm e fundo de escala de 600 mm, com possibilidade de trabalhar com ângulos de inclinação entre 20° e 90°. O fluido manométrico usado foi água.

O tubo de Pitot, de construção própria, é constituído por um tubo metálico com 5mm de diâmetro e dotado de orifícios sensores com 1 mm de diâmetro, sendo ligado por mangueira de borracha a um manômetro inclinado, tendo como fluido de trabalho álcool etílico, com resolução de 1/25 mm de coluna d'água e fundo de escala de 25 mm.

O anemômetro de fio quente usado é de temperatura constante modelo 55 D01, acoplado a um voltímetro digital modelo 55 D31, com uma sonda de fio quente modelo 55 P11, fabricados pela DISA, acoplado a um sistema de aquisição de dados .

A fixação dos sensores de velocidade ao túnel, bem como seu deslocamento e posicionamento no levantamento dos perfis de velocidade média e de intensidade de turbulência, é feito através de um suporte concebido e construído especialmente para este experimento, com capacidade para medir deslocamentos de até 0,1 mm, ao longo dos 50 mm de altura do canal de desenvolvimento e seções de teste.

Na calibração do anemômetro de fio quente foi usado um micro manômetro de construção própria com resolução de 0,05 mm de coluna d'água e fundo de escala de 300 mm. O fluido de trabalho usado foi água.

A curva de calibração utilizada, para o anemômetro de fio quente, é dada pela equação

$$V^2 = A + B\sqrt{U} \qquad (1)$$

onde V é a diferênca de potencial, U a velocidade média, A e B são os coeficientes da Lei de King, cujos valores para o equipamento empregado neste trabalho foram A = 12,68 e B = 3,52

2.3 AQUISIÇÃO E PROCESSAMENTO DE DADOS

Para a aquisição e tratamento da massa de dados analógicos gerados pelo anemômetro de fio quente foi empregado um sistema digital baseado no conversor analógico-digital de 12 bits Daqbook 112, com acesso de entrada para 20 canais analógicos e frequência máxima de aquisição de 100 kHz, uma conexão cabo/interface projetada e construída por Rebello (1996), que permite a comunicação entre o conversor analógico-digital e um PC 486 DX2/66. O controle e operação do conversor analógico-digital é feito a partir do micro-computador pelo software DaqView.

A configuração usada para a aquisição do sinal gerado pelo anemômetro de fio quente foi baseada no uso de apenas um canal trabalhando com uma frequência de aquisição de 100 kHz gerando para cada posição no espaço, 25000 leituras (tempo de aquisição de 0,25 s para cada ponto do perfil). Por meio de configuração implementada no Daqbook, via hardware, foi

viabilizada a aquisição do sinal analógico em voltagem unipolar na faixa de 0 a 10 volts, gerada pelo anemômetro de fio quente.

A frequência de aquisição de 100 kHz é o dobro da frequência máxima característica para escoamentos turbulentos internos (Simon 1996). Desta forma é respeitado o teorema de Nyquist (apud Simon 1996) que prevê para a captação de todas as informações de um sinal analógico, para uma dada frequência, uma taxa de aquisição digital com o dobro da frequência analógica considerada.

O número de pontos lidos no tempo, 25000, para cada ponto no espaço, foi selecionado após análise estatística de variação da velocidade média e intensidade de turbulência. Com 12000 pontos a variação encontrada era de 5% entre duas medidas repetidas. Com 25000 a variação é menor que 1%.

Considerando que a medida de cada ponto do perfil de velocidade gera um arquivo ASCII de aproximadamente 1 MB e que para cada seção reta analisada foram medidos 50 pontos, foi necessário o desenvolvimento de um programa capaz de linearizar os dados obtidos em volts, transformando-os em velocidades através da Lei de King, calculando em seguida a velocidade média estatística $\overline{U}$, seu desvio padrão RMS e a intensidade de turbulência κ através das expressões (2) e (3):

$$RMS = \frac{\sum_{i=1}^{N} \sqrt{\left(u_i - \overline{U}\right)^2}}{N} \qquad (2)$$

$$\kappa = \frac{RMS}{\overline{U}} \qquad (3)$$

O código numérico foi escrito em FORTRAN 90, com o compilador Microsoft Fortran Powerstation 4.0, gerando um executável para o sistema operacional Windows 95.

2.4 ENSAIOS

A primeira etapa de medição teve como objetivo a avaliação de desempenho do duto reto, destinado ao completo desenvolvimento do escoamento turbulento, na faixa de velocidades prevista.

Os números de Reynolds que caracterizam esta faixa de velocidades são respectivamente 18500, 20000 e 22500. A dimensão característica usada para o cálculo do número de Reynolds foi o diâmetro hidráulico do duto,

$$d_h = \frac{4A}{P} \qquad (4)$$

onde A é a área da seção reta do duto e P o perímetro da mesma.

Os perfis de velocidade média e de intensidade de turbulência, a 375 mm da extremidade de saída do duto reto e segundo sua seção longitudinal média, para os três números de Reynolds testados, estão apresentados na figura 1.

Na segunda etapa de medição foram obtidos os resultados correspondentes aos perfis de velocidade média e de intensidade de turbulência bem como suas evoluções em função da

curvatura do canal e do número de Reynolds do escoamento, em quatro pontos equidistantes, situados sobre a seção longitudinal média de cada uma das duas curvas. Estes resultados estão contidos nas figuras 2, 3 e 4.

3. RESULTADOS

3.1 DUTO RETO

O escoamento que se estabelece no duto reto, para números de Reynolds entre 18500 e 22500, se desenvolve completamente depois de percorrer aproximadamente dois terços de seu comprimento total, conforme indicam as medidas de pressão e velocidade feitas com o canal livre das seções curvas.

As medidas de velocidade média e de intensidade de turbulência, na última estação do duto reto, estão apresentadas na figura 1 para regimes de escoamento caracterizados por números de Reynolds de 18500 e 22500.

Na figura 1 os resultados obtidos para os perfis de velocidade média adimensional (curva convexa) estão apresentados no eixo esquerdo de ordenadas, ficando o eixo direito destinado à quantificação dos perfis de intensidade de turbulência (curva côncava).

Os resultados obtidos são típicos de perfis turbulentos totalmente desenvolvidos, notadamente o perfil de intensidade de turbulência.

O eixo das abcissas, adimensionalisado em relação à altura da seção útil do túnel, tem sua origem na parede interna inferior do túnel.

A discreta assimetria dos pontos situados na vizinhança imediata das paredes (y/ymáx≅0 e y/ymáx≅1) deve-se à dificuldades de posicionamento do sensor de fio quente na região adjacente à parede inferior (y/ymáx≅0).

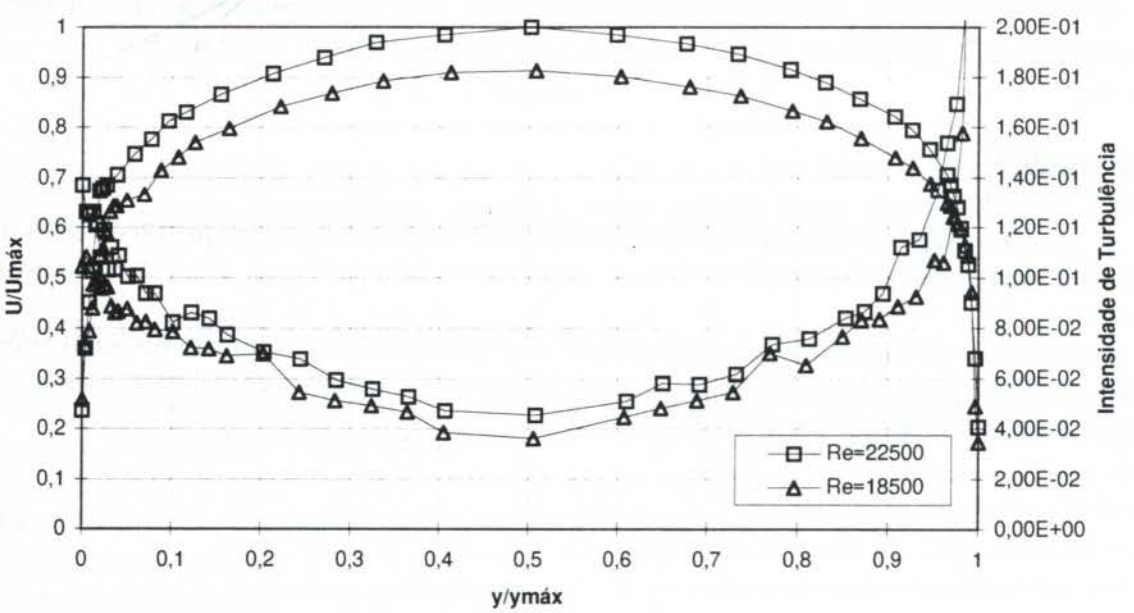

Figura 1 - Perfis de velocidade média adimensional e intensidade de tubulência para canal reto

A diminuição dos valores de intensidade de turbulência na vizinhança imediata das paredes não pode ser detectada, em nehuma das duas paredes, por diferentes motivos. Na

parede interna superior do túnel existe uma perturbação no escoamento causada pela presença do orifício de introdução do sensor. Na parede interna inferior o sensor de fio quente não pode, sob pena de danos físicos, aproximar-se o suficiente para detectar a queda na intensidade de turbulência.

3.2 DUTOS CURVOS

As medidas de velocidade, nas seções curvas 1 e 2, foram feitas com a sonda de fio quente deslocando-se ao longo da seção longitudinal média dos dutos, em cinco posições diferentes. Na curva 1 os cinco pontos são posicionados da seguinte forma: o primeiro ponto, identificado como TV1, está posicionado a 10 mm do início da curva. O segundo ponto de medida, identificado como TV2, está a 140 mm do ponto TV1. Os outro três pontos, identificados como TV3, TV4 e TV5 estão também separados, entre si e em relação a TV2, por 140 mm. O ponto TV5 está localizado a 50 mm do fim do duto. Na curva 2 uma distribuição similar é adotada. A distância de separação entre os pontos TV1, TV2, TV3, TV4 e TV5 passa para 145 mm, o ponto TV1 permanece a 10 mm do início do duto e o ponto TV5 está locado a 60 mm da extremidade final do duto.

Na figura 2 estão apresentados os perfis de velocidade média que se estabelecem nas curvas 1 e 2. São mostrados os resultados correspondentes às estações de medida TV2, TV4 e TV5 para um número de Reynolds de 22500.

Nesta figura o eixo das ordenadas representa a velocidade média, adimensionalisada pela velocidade máxima. O eixo das abcissas representa um comprimento na direção normal às paredes superior e inferior do duto, adimensionalisado pela altura da seção útil dos dutos. A origem das abcissas é posicionada na parede interna das curvas 1 e 2.

Os resultados da figura 2 mostram a evolução do perfil de velocidade média ao longo das curvas 1 e 2 e justificam a seleção do perfil de velocidades correspondente à estação TV4 como sendo o mais conveniente para a análise dos efeitos da curvatura sobre o escoamento.

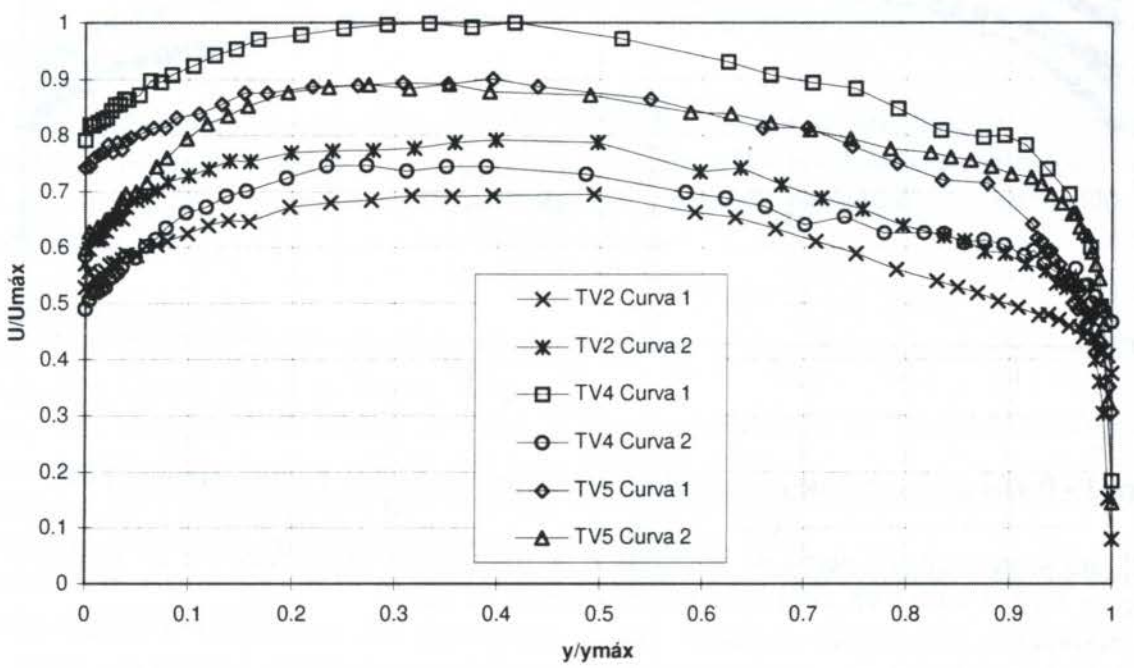

Figura 2 - Curvas de velocidade média em 3 pontos das curvas 1 e 2. Re=22500.

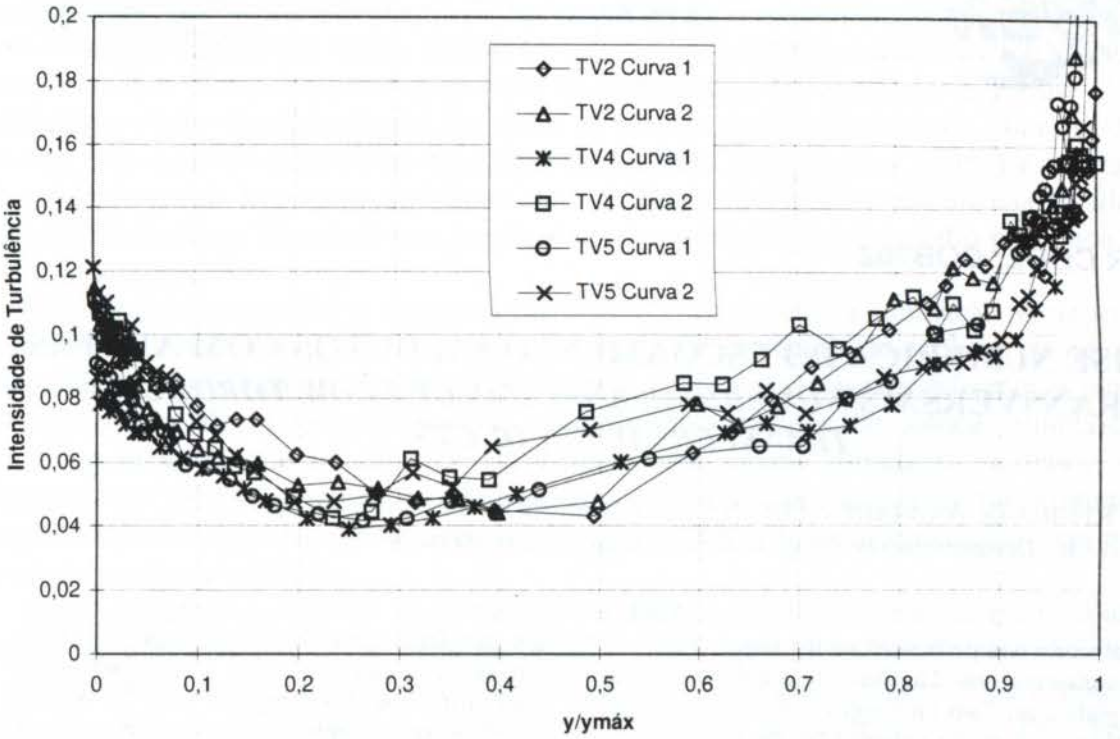

Figura 4 - Perfis de intensidade de turbulência para as curvas 1 e 2. Re=22500.

Este resultado é coerente e pode ser interpretado da seguinte forma: na parede externa as partículas de fluido mais rápidas são impulsionadas, centrifugamente, para o interior da camada limite e ao misturarem-se com as partículas mais lentas aumentam a intensidade de turbulência. De forma contrária, na parede interna, o mesmo mecanismo tende a afastar da parede as partículas mais rápidas, diminuindo assim, a intensidade de turbulência nesta região.

4. CONCLUSÕES

Este trabalho apresenta o início, a nível experimental, de um estudo sobre escoamentos turbulentos parietais. A coerência qualitativa e quantitativa dos resultados encontrados avaliza a metodologia e a instrumentação adotadas no trabalho, permitindo e orientando sua continuação.

5. BIBLIOGRAFIA

Ellis, L.B., Joubert, P.N. Turbulent Shear Flow in a Curved Duct, *Journal of Fluid Mechanics*, vol 62, part 1, pp. 65-84, 1974.

Hunt, I.A., Joubert, P.N. Effects of Small Streamline Curvature on Turbulent Duct Flow, *Journal of Fluid Mechanics,* vol. 91, part 4, pp. 633-659, 1979.

Rebello, E.P.C. Instrumentação para Medição de Camada Limite Atmosférica, Dissertação de Mestrado, Depto. Eng. Mecânica, Universidade de Brasília, 1996.

Simon, T.W. Acquiring and ProcessingTurbulent Flow Data, *Fluid Mechanics Measurements*, Taylor & Francis, 1996.

XIV Brazilian Congress of Mechanical Engineering
Obeid Plaza Hotel Convention Center - Bauru - SP/Brazil
December 08-12th 1997

PAPER CODE: COB762

ANÁLISE NUMÉRICA DO ESCOAMENTO EM DUTOS COM ALETAS TRANSVERSAIS/*NUMERICAL ANALYSIS OF FLOW THROUGH TRANSVERSAL FIN DUCTS*

CLÁUDIA REGINA de ANDRADE e EDSON LUIZ ZAPAROLI
CTA - ITA - IEM - Departamento de Energia - E-mail: zaparoli@mec.ita.cta.br

Abstract

A numerical study was performed on the augmentation of the heat transfer for internal flow through flat plates containing transversal fins. The duct width and the fins spacing were kept constant and 17 fins were affixed along the heated plate side. Two fin heights were simulated and the heat transfer rate was compared with the smooth duct case. Numerical results obtained for the mean heat transfer coefficients and experimental data showed good agreement. Also reported was the grid refinement effect on the numerical solution accuracy.

Keywords

Dinâmica de Fluidos Computacional/Computational Fluid Dynamics, Escoamento Turbulento/Turbulent Flow, Aletas/Fins, Intensificação da Transferência de Calor/Enhanced Heat Transfer.

1. INTRODUÇÃO

As técnicas de intensificação da transferência de calor tem inúmeras aplicações na engenharia, tanto no que se refere à redução do consumo de energia como à economia nos custos de fabricação. Deste modo, o projeto de trocadores de calor mais eficientes pode ser feito através da ampliação do coeficiente de transferência de calor. No entanto, a otimização de equipamentos de troca térmica envolve diversos fatores como a superfície de troca de calor, o peso e/ou volume do equipamento, o custo dos materiais utilizados, etc. De acordo com a aplicação do trocador de calor são estabelecidos critérios de otimização (função objetivo) que se desejam maximizar ou minimizar. Além disso, existem diversas técnicas utilizadas para se ampliar a transferência de calor em dutos (circulares ou não). Pode-se aumentar a rugosidade da superfície, ou ainda introduzir dispositivos como a colocação de espirais ou de aletas.

Existem diversos trabalhos experimentais que mostram a utilização de aletas para intensificar as trocas de calor no escoamento em dutos. Apesar disso, ainda não se dispõem de correlações unificadas que reproduzam de forma universal todas as características dos processos de transferência de momento e calor, principalmente no caso de escoamentos turbulentos. No estudo do escoamento turbulento como não é possível conhecer e prever todos os processos físicos envolvidos, as correlações existentes são obtidas através de dados experimentais e possuem validade restrita à geometria e condições predeterminadas. Como exemplos de trabalhos que fizeram uso de aletas para intensificar a transferência de calor, tem-se Knudsen e Katz (1950) que estudaram os processos de trocas de calor e queda de pressão do escoamento de água em dutos, com aletas circulares de perfil triangular. Weiss (1964)

analisou a influência da altura das aletas no escoamento de ar, para pequenas razões entre a altura e o espaçamento das aletas. Brauer (1961) também estudou o efeito da introdução de aletas em tubos circulares como geradoras de turbulência. Já Obermeier e Henne (1993) analisaram o efeito do espaçamento das aletas de mesma altura nas trocas de calor em dutos anulares. No caso do escoamento em dutos retangulares, Boelter *et al.* (1951) estudaram o efeito da variação da largura do duto bem como da altura das aletas na turbulência gerada em um escoamento de ar. São obtidos os coeficientes de convecção local e médio para cada uma das configurações.

Pode-se também estudar o comportamento de fluidos através da simulação numérica dos escoamentos. Neste caso, faz-se uso de técnicas de discretização do sistema de equações governantes do problema, transformando o sistema original de equações diferenciais parciais em um sistema algébrico onde possam ser aplicados métodos de solução numérica. É importante ressaltar que no caso de escoamentos em regime turbulento os modelos de turbulência se aplicam a situações padrão, com validade comprovada para configurações específicas. Portanto, os resultados obtidos quando se utilizam novas geometrias devem passar por um processo de validação.

Neste contexto, o objetivo deste trabalho é utilizar a análise numérica para estudar o escoamento turbulento em dutos, onde é analisado o efeito da introdução de aletas transversais na geração de turbulência e na intensificação das trocas de calor (aumento da temperatura média de mistura do fluido). As simulações numéricas utilizam a opção para regime permanente de um programa de CFD (Computational Fluid Dynamics) baseado na técnica de elementos finitos para a solução de problemas de escoamentos de fluidos e transferência de calor e que aplica o modelo $K-\varepsilon$ padrão no estudo do escoamento turbulento. Neste trabalho a análise do problema térmico é feita utilizando-se uma abordagem de transferência de calor conjugada (Gill e Davis, 1970), onde a condução nas aletas e a convecção no fluido são estudadas de forma acoplada. As propriedades do sólido e do fluido são consideradas constantes. Os resultados da análise numérica são comparados com os dados experimentais de Boelter *et al.* (1951), e revelam boa concordância dos valores obtidos para o coeficiente de convecção. Estuda-se também o efeito do refinamento da malha computacional na acuidade da solução numérica obtida.

2. MODELO MATEMÁTICO E GEOMETRIA DO PROBLEMA

2.1 Equações e Condições de Contorno

Neste trabalho simula-se a convecção forçada do ar em um duto de placas paralelas, com as equações da continuidade, quantidade de movimento e energia, válidas para um escoamento em regime permanente incompressível, expressas por:

$$\frac{\partial(\rho Vx)}{\partial X}+\frac{\partial(\rho Vy)}{\partial Y}=0 \qquad (1)$$

$$\frac{\partial(\rho VxVx)}{\partial X}+\frac{\partial(\rho VyVx)}{\partial Y}=-\frac{\partial P}{\partial X}+\frac{\partial}{\partial X}\left(\mu e\frac{\partial Vx}{\partial X}\right)+\frac{\partial}{\partial Y}\left(\mu e\frac{\partial Vx}{\partial Y}\right) \qquad (2)$$

$$\frac{\partial(\rho VxVy)}{\partial X}+\frac{\partial(\rho VyVy)}{\partial Y}=-\frac{\partial P}{\partial Y}+\frac{\partial}{\partial X}\left(\mu_e\frac{\partial Vy}{\partial X}\right)+\frac{\partial}{\partial Y}\left(\mu_e\frac{\partial Vy}{\partial Y}\right) \quad (3)$$

$$\frac{\partial}{\partial X}(\rho\, VxCpT)+\frac{\partial}{\partial Y}(\rho\, VyCpT)=\frac{\partial}{\partial x}\left(k_e\frac{\partial T}{\partial x}\right)+\frac{\partial}{\partial y}\left(k_e\frac{\partial T}{\partial y}\right) \quad (4)$$

onde ρ é a densidade do fluido, **Vx** e **Vy** são as componentes de $\vec{V}$, **T** é a temperatura, k_e é condutividade térmica efetiva, Cp é o calor específico a pressão constante e μ_e é a viscosidade dinâmica efetiva.

As viscosidade e condutividade efetivas são definidas como a soma da parcela laminar com a turbulenta, indicadas por:

$$\mu_e = \mu + \mu_t \quad e \quad k_e = k + k_t \quad (5)$$

onde as parcelas turbulentas são calculadas de acordo com o modelo K-ε de Launder e Spalding (1974).

As condições de contorno são Vx e Vy iguais a zero junto às fronteiras sólidas (parede do duto e superfícies das aletas). Na parte central da face aquecida do duto tem-se uma condição de temperatura constante (Tw) enquanto as regiões de entrada e final estão isoladas. As condições de entrada são perfis de velocidade (Ve), temperatura (Te), K e ε uniformes. Na saída do duto impõe-se um valor para a pressão (P=0) e condições livres para as demais variáveis. Nas proximidades das fronteiras sólidas, o programa utiliza a Lei de Parede para estabelecer os valores de K e ε. Uma representação esquemática do experimento é indicada na Fig.1, onde **h** indica a altura das aletas fixadas ao longo da porção aqüecida do duto e **p** o espaçamento entre elas.

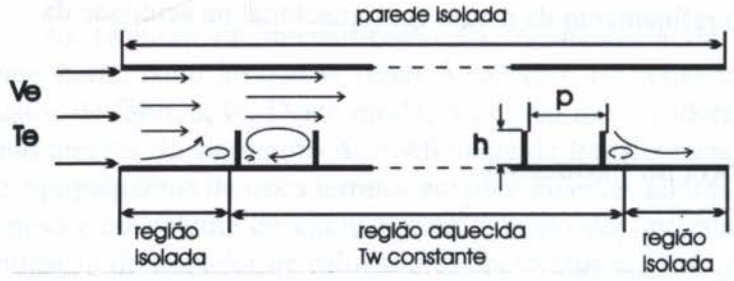

Fig.1 - Representação esquemática do experimento.

2.2 Simulações Numéricas

As simulações numéricas foram realizadas seguindo a geometria do aparato experimental especificado em Boelter et al. (1951), para um escoamento de ar, em regime permanente, com Pr=0,7 e $Re=10^4$. Os parâmetros adimensionais foram definidos por:

$$Pr = \mu Cp/k \quad e \quad Re=2|Ve|b/\mu, \quad (6)$$

onde **b** representa a distância entre as placas. A Tabela 1 traz um resumo das simulações.

Tabela 1: Resumo e nomenclatura das simulações numéricas.

SIMULAÇÃO	ALTURA DAS ALETAS	NOMENCLATURA
experimento com duto liso	----------	exp-h0
duto com 17 aletas	$3{,}175\cdot10^{-3}$ m	exp-h1
duto com 17 aletas	$9{,}525\cdot10^{-3}$ m	exp-h2

Em todos os experimentos as 17 aletas acopladas ao duto possuem 0,001 m de espessura e são fixadas em intervalos de 0,0254 m. As partes isoladas do duto tem um comprimento de 0,3048 m. Foram utilizados os seguintes valores numéricos para as propriedades do fluido (ar): ρ= 1,06 Kg/m^3 , Cp =1,006 kJ/Kg·K, μ = 1,98 W/(m·K) e k = 2,845 Kg/(m·s).

3. SOLUÇÃO NUMÉRICA DO PROBLEMA

3.1 Formulação em Elementos Finitos

A solução numérica do problema foi obtida utilizando-se um código de **CFD**, baseado no método de elementos finitos. As equações governantes(1)-(4) para o escoamento do fluido os foram resolvidas aplicando-se uma formulação segregada (onde calculam-se separadamente os campos de Vx, Vy, P, T, K e ε) conforme detalhado em Rice e Schnipke (1986). O domínio de interesse foi discretizado com uma malha estruturada, refinada nas regiões onde as variáveis apresentaram maiores gradientes, a fim de que pudessem ser reproduzidos os efeitos de camada limite (térmica ou hidrodinâmica). Os sistemas de equações algébricas foram resolvidas através de métodos iterativos como o TDMA (*Tri-diagonal Matrix Algorithm*) e o PCG (*Preconditioned Conjugate Gradient Algorithm*), dependendo das dificuldades de convergência. Para a solução do campo de temperatura, utilizou-se uma abordagem de *problema-conjugado* (Davis e Gill, 1970), onde a condução no sólido e a convecção no fluido são resolvidas de forma acoplada. É importante ressaltar que o código atribui valores nulos para as componentes de velocidade no sólido, de modo que nesta região não são resolvidas as equações para o problema hidrodinâmico.

3.2 Etapas das Simulações Numéricas

As simulações numéricas foram realizadas utilizando um microcomputador Pentium-Pro (200 MHz , 128 MBytes de memória RAM) e foram compostas de 3 etapas:

- *Pré-processamento*: representada pela construção da geometria do problema , aplicação das condições de contorno e geração da malha, isto é, a representação do domínio em termos dos elementos finitos;
- *Análise numérica*: nesta etapa foram aplicados os algoritmos de solução numérica para a configuração estabelecida na etapa 1;
- *Pós-processamento*: uma vez que a solução numérica foi obtida (dentro dos critérios de convergência pré-estabelecidos), nesta etapa foi feita a visualização dos resultados obtidos. O programa possui uma interface gráfica que permite a obtenção de campos básicos (pressão, velocidade, temperatura) além de grandezas derivadas como linhas de corrente (2D) e fluxo de calor.

4. RESULTADOS E DISCUSSÃO

4.1 Efeito do refinamento da malha e comparação com resultados experimentais

A utilização de programas de CFD na solução de problemas de escoamento e transferência de calor normalmente fornece um conjunto de dados que precisam ser analisados quanto à sua acuidade. Neste trabalho foram realizadas diversas simulações numéricas a fim

de se estudar o efeito do refinamento da malha, e os resultados foram validados através da comparação com dados experimentais e correlações existentes (para o caso do duto liso).

Analisou-se o efeito do refinamento da malha na simulação da configuração exp-h1 (tabela 1). A comparação dos resultados obtidos para o coeficiente de convecção médio ($h_{médio}$), é indicada na Tabela 2. Verifica-se que para uma malha grossa (10.000 nós) a porcentagem de erro da solução numérica em relação ao valor experimental atinge mais de 50%, o que compromete a validade desta solução. Isto ocorre porque neste caso o número de pontos da malha é insuficiente para reproduzir a complexidade do escoamento (recirculações) na região entre as aletas.

Tabela 2: Efeito do refinamento da malha na simulação exp-h1 (aleta de altura $3{,}175 \cdot 10^{-3}$ m)

MALHA COMPUTACIONAL	VALOR DE $h_{médio}$ OBTIDO (exp-h1)	ERRO RELATIVO AO VALOR EXPERIMENTAL
10.000 nós	5.74	57,5%
20.000 nós	8.48	37,2%
40.000 nós	12.78	5,3%

À medida que a malha vai sendo refinada, principalmente junto à parede do duto e na vizinhança das aletas, a solução converge para valores próximos aos resultados experimentais, chegando a uma diferença de 5% para a simulação com 40.000 nós. É importante lembrar que como o programa faz uso de uma abordagem elíptica do problema, a cada nova iteração global é preciso recuperar os valores de todas as variáveis em todo o domínio do problema. Isto exige uma maior capacidade de armazenamento das matrizes de dados conforme cresce o número de nós na malha. Outro fator a ser considerado é o comprometimento entre o refinamento da malha e o esforço computacional requerido (tempo de CPU). O coeficiente de convecção médio ($h_{médio}$) apresentado na Tabela 2 foi calculado segundo a expressão:

$$h_{médio} = Q/(A\,\Delta Tln), \qquad (7)$$

onde:

ΔTln é a média logaritmica das diferenças de temperatura,

A representa a área de troca de calor e

Q = ρ_e (Ve) Cp $[T_m(x=1) - T_m(x=0)]$, indica a taxa de transferência de calor.

Para a obtenção da taxa de transferência de calor (Q) utilizou-se o conceito de temperatura média de mistura do fluido (T_m) definida por:

$$T_m(x) = \frac{1}{(Ve)b}\int_y (Vx)Tdy\,. \qquad (8)$$

Na simulação numérica do caso de duto liso (exp-h0) os resultados obtidos para o número de Nusselt (Nu) são apresentados na Tabela 3. A solução numérica foi comparada com os dados experimentais de Boelter *et al.* (1951) e com a correlação de Gnielinski (1992), com o fator de correção para tubo curto e conversão para escoamento em duto de placas paralelas com uma parede aquecida e outra isolada. O valor de Nusselt mostrado na Tabela 3 foi obtido utilizando-se um nível de turbulência de 5% na entrada do duto e apresentou uma melhor

concordância com o dado experimental do que com o valor obtido quando se utilizou a correlação.

Tabela 3: Comparação dos resultados para o duto liso.

exp-h0	Nu - numérico	Nu - Gnielinski (1992)	Nu - Boelter et al. (1951)
	33,4	30,1	33,6
erro	-----	10,8 %	0,6 %

No entanto, quando se utilizou um nível de turbulência de 1% na entrada do duto, o valor de Nusselt obtido numericamente se aproximou mais da correlação de Gnielinski (1992), com um erro 3,7%, do que com o dado experimental. Isto indica que ocorre uma interação entre o nível de turbulência e a transferência de calor na entrada do duto, pois os casos simulados se referem a um duto curto. O valor de Nu numérico foi calculado a partir do valor de $h_{médio}$ (equação 7), de modo que:

$$Nu = \frac{h_{medio}(2b)}{k} . \qquad (9)$$

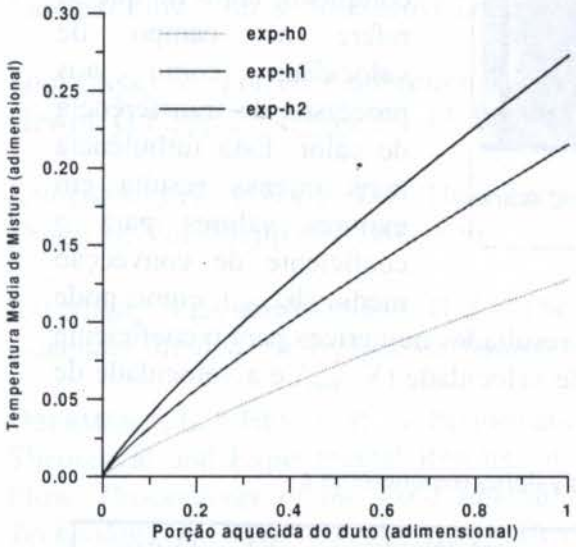

Fig 2 - Variação da Temperatura Média de Mistura ao longo do duto.

4.2 Comparação entre as simulações

Os resultados obtidos para as 3 simulações referenciadas na Tabela 1 foram comparados tanto no que se refere ao efeito das aletas como promotoras de turbulência (configuração dos campos de velocidade) como no aumento das trocas de calor (aumento da temperatura média de mistura do fluido).

Em notação adimensional podemos escrever:

$$\theta_m(x) = \frac{T_m(x) - Te}{Tw - Te}, \qquad (10)$$

onde Tw indica a temperatura na parede do duto e Te a temperatura de entrada. Na fig.2 são mostrados os perfis de temperatura média de mistura (θ_m) ao longo da porção aquecida do duto. Verifica-se que com a introdução das aletas transversais ocorre um aumento significativo da temperatura média do fluido em relação ao experimento com o duto liso (exp-h0), chegando a 100% no caso das aletas mais longas (simulação exp-h2). A comparação entre os dois casos de dutos aletados mostra que o aquecimento do fluido é maior quando são introduzidas aletas mais longas do que na simulação exp-h1. Isto ocorre porque na simulação exp-h2 aumenta-se a área de troca de calor (superfície aletada) em relação ao caso da aletas mais curtas, mas ainda não se atinge uma razão de altura-espaçamento das aletas que bloqueie as trocas de calor para o fluido escoando na área livre. Este bloqueio se deve a uma região de recirculação de baixa intensidade entre as aletas.

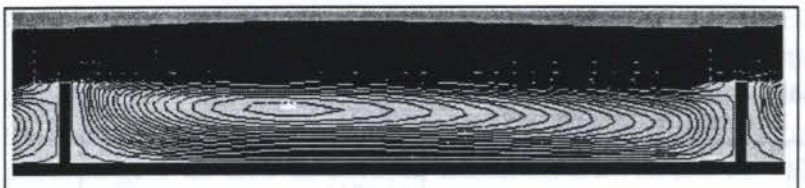

Fig.3 - Configuração das linhas de corrente para o intervalo entre duas aletas curtas.

As figuras 3 e 4 mostram a configuração das linhas de corrente relativas ao escoamento para o mesmo intervalo entre duas aletas dos experimentos exp-h1 e exp-h2. Na fig. 4, como as aletas são mais longas, formam-se duas zonas de recirculação mais intensas quando comparadas com a da fig.3, onde se configura uma única bolha. A simulação das características gerais do escoamento mostram que o modelo matématico e o método computacional são adequados para o estudo do problema. No entanto, para reproduzir os detalhes do escoamento (como a segunda bolha da fig. 4) e o cálculo preciso do coeficiente de transferência de calor são necessários um número grande de nós na malha (justificando os dados da tabela 2).

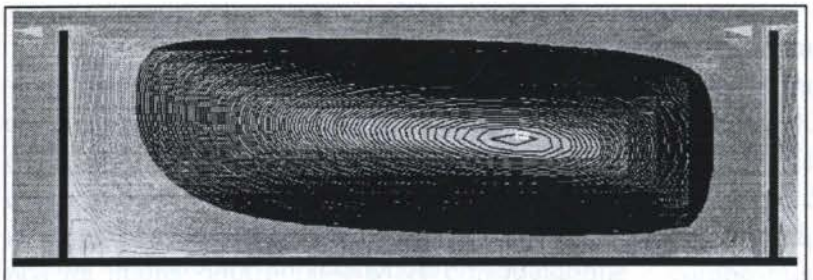

Fig.4 - Configuração das linhas de corrente para o intervalo entre duas aletas longas.

Quando as aletas transversais são acopladas ao duto, o escoamento torna-se muito mais complexo, tanto no que se refere ao campo de velocidade como aos processos de transferência de calor. Esta turbulência mais intensa resulta em maiores valores para o coeficiente de convecção médio ($h_{médio}$), como pode ser confirmado pela análise da Tabela 4 que mostra os resultados numéricos para o coeficiente $h_{médio}$ e para a razão entre a componente horizontal de velocidade ($Vx_{máx}$) e a velocidade de entrada (Ve).

Tabela 4: Comparação entre as simulações numéricas e os valores experimentais

SIMULAÇÃO	hmédio numérico	hmédio Boelter *et al.*(1951)	erro relativo	$Vx_{máx}$ /Ve
exp-h0	5,27	5,3	0,5%	1,2
exp-h1	12,78	13,5	5,3%	1,5
exp-h2	17,06	18,0	5,2%	3,6

Verifica-se que o valor de $Vx_{máx}$ /Ve é maior nos dutos aletados do que no duto liso, e a comparação das simulações exp-h1 e exp-h2 confirmam que o escoamento é mais intenso no experimento com aletas mais longas. Os resultados das simulações numéricas apresentados na Tabela 4 também mostraram boa concordância com os dados experimentais para o coeficiente de convecção médio ($h_{médio}$) apresentados em Boelter *et al.*(1951).

Os resultados foram considerados consistentes com os valores experimentais uma vez que diversos fatores físicos foram desprezados na simulação numérica do problema, tais como: as

propriedades do fluido foram consideradas constantes, os efeitos de rugosidade da parede do duto são desprezados, e além disso o modelo de turbulência utilizado pelo programa k-ε padrão possui constantes que foram ajustadas para situações padrão, como o escoamento em dutos lisos.

5. REFERÊNCIAS BIBLIOGRÁFICAS

BOELTER, L. M. K., YOUNG, G., GREENFIELD, M. L., SANDERS, V.D. e MORGAN, M. An Investigation of Aircraft Heaters. XXXVII - Experimental Determination of Thermal and Hydrodynamical Behavior of Air Flowing Along a Flat Plate Containing Turbulence Promoters. *NACA TN 2517*, 1951.

BRAUER, H. Strömungswiderstand und Wärmeübergang bei Ringspalten mit rauhen Kernrohren., *Atomkernenegie,* vol 6, pp.207-211, 1961.

FEUSTEIN, G. E RAMPF, H. Der Einfluβ rechteckiger Rauhigkeiten auf den Wärmeübergang und den Druckabfall in turbulenter Ringspaltströmung., *Wärme-und Stoffübertragung*, Vol. 2, pp. 19-30, 1969.

GILL, W.N. E DAVIS, E.J. The Effcts of Axial Conduction In The Wall On Heat Transfer With Laminar Flow", *Int. J. Heat Mass Transfer*, Vol. 13, pp 459-470, 1970.

GNIELINSKI,.V. Forced Convection in Ducts, *Handbook of Heat Exchanger Design,* ed. Hewitt, G.F., pp.2.5.1-1 a 2.5.1-13, Begell House, Inc, New York, 1992.

KNUDSEN, J.G., E KATZ, D.L. Heat Transfer and Pressure Drop In Annuli, *Chem. Engng. Progress*, Vol. 56, pp.490-500, 1950.

LAUNDER, B.E., E SPALDING, D.B. "The Numerical Computation of Turbulent Flows", *Computer Methods In Applied Mechanics And Engineering,* Vol.3, pp 269-289, 1974.

OBERMEIER, E, E HENNE, R. A. Performance Analysis of Augmented Heat Transfer Surfaces-Theoretical and Experimental Results for Tubes with Circunferencial Fins in Longitudinal Flow. *Proceedings of the First International Conference on Aerospace Heat Exchanger Technology,* pp. 329-345, Palo Alto, USA, 1993.

RICE, J.G. e SCHNIPKE, R.J. An Equal-Order Velocity-Pressure Formulation That Does Not Exhibit Spurious Pressure Modes. *Computer Methods In Applied Mechanics And Engineering,* Vol.58, pp 135-149, 1986.

WEISS, S. Wärmeübergang und Strömungswiderstand bei Rippenrohen im Längsstrom., *Chem. Techn.,* 16, pp. 7-17, 1964.

Tema 36

Hidrodinâmica

XIV Brazilian Congress of Mechanical Engineering
Obeid Plaza Hotel Convention Center - Bauru - SP/Brazil
December 08-12th 1997

PAPER CODE: COB774

MIXING OF CONFINED COAXIAL TURBULENT JETS IN DUCTS OF VARYING CROSS SECTION

MARCELO J.S. DE LEMOS*
Dept. de Energia, ITA-CTA
*12228-900 - São José dos Campos, SP, Brasil - * E-mail: mlemos@tecsat.com.br*

AMARILDO MILAN
EMBRAER - GEA -EAD/APC

Abstract

Computations for the mean and turbulent fields for the flow field formed by two coaxial streams confined in a duct of varying cross section are presented. The widely-used marching-forward method of Patankar-Spalding was used for sweeping the computational domain. The standard k-ϵ model was applied for handling turbulence. Results are presented for developing and fully-developed diverging and converging ducts of straight and sinusoidal wall shape.

Keywords

Duct Flow, Turbulence Modeling, CFD

1. INTRODUCTION

Confined coaxial jets in ducts constitute an important class of engineering flows. Applications of such configuration are found in jet-pumps, rockets boosters and in equipment for mixing streams with different velocity and temperatures.

Equally important, the use of numerical tools for design and analysis of complex geometries can provide such useful engineering information as turbulent transport rates and film coefficients. Accordingly, the adequate employment of numerical predictions, carefully combined with experimental work, can bring, in most cases, substantial savings to the overall process of analysis and optimization of a new design concept.

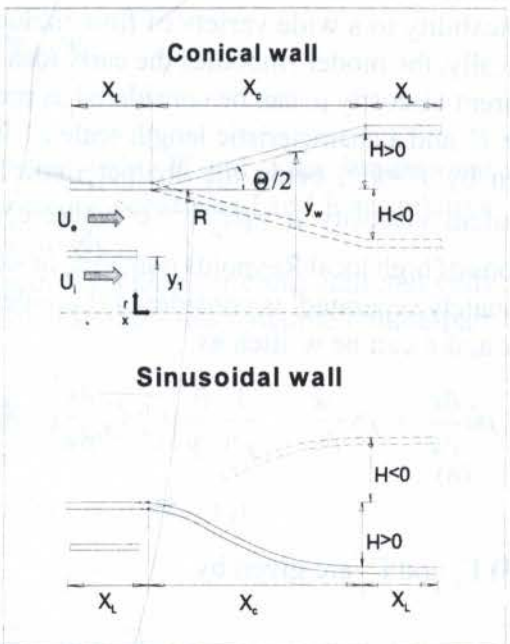

Figure 1 - Notation for general duct flow with *diverging* (H>0) and *converging* (H<0) walls.

Based on the foregoing, the work of Matsumoto & de Lemos (1990) presented results for the developing *time-averaged* and *turbulent* fields in a coaxial jet along a circular duct of constant area The present contribution extends the results therein by considering now the duct shape of Figure 1. The duct wall in the figure is assumed to be described by a function of a sinusoidal form and the applicability of the used numerical scheme used is investigated in *diverging* (positive H) and *converging* (negative H) ducts.

2. Mathematical Model and Numerics

The equations of continuity of mass and x-momentum for a two-dimensional planar/axi-symmetric turbulent mixing layer can be readily written as,

$$\frac{\partial (y^{\eta}\rho u)}{\partial x} + \frac{\partial (y^{\eta}\rho v)}{\partial y} = 0 \qquad (1)$$

$$\rho u\frac{\partial u}{\partial x}+\rho v\frac{\partial u}{\partial y} = -\frac{\partial P}{\partial x}+\frac{1}{y^{\eta}}\frac{\partial}{\partial y}\left[y^{\eta}\,\mu_{eff}\frac{\partial u}{\partial y}\right] \qquad (2)$$

In **(1)**-**(2)** u and v are the velocity components in the axial and transverse direction, respectively, ρ the fluid density, P the static pressure and μ_{eff} the effective coefficient of exchange given as $\mu_{eff}= \mu_t + \mu$ where μ is the molecular viscosity and μ_t the turbulent viscosity given below. As usual, equations **(1)** and **(2)** are written in a compact notation embracing planar (η=0) and axi-symmetric (η=1) cases.

It is worth noting that applicability of the model above is limited to parabolic flow analyses, so that recirculating motion induced by boundary layer separation in fast diverging ducts or *"vena contract"* regions in after duct constrictions are not considered here. With these restrictions applied, the axial momentum equation can be solved with well-known marching-forward numerical techniques for computation of parabolic and partially-parabolic flows.

The statistical turbulence model k-ϵ (Jones & Launder, 1972) has been extensively used in the literature for its characteristics of robustness and numerical stability. Recent extensions of its applicability to a wide variety of flow includes the so-called **RNG** and **non-linear** approaches. Basically, the model embodies the early idea of Prandtl/Kolmogorov that, in a turbulent flow, the apparent viscosity μ_t can be considered as proportional to the product of a characteristic velocity scale V' and a characteristic length scale L'. In the k-ϵ model, the characteristic velocity scale is given by $V'=k^{1/2}$, being the characteristic length scale written as $L'=k^{3/2}/\epsilon$, implying for the turbulent viscosity $\mu_t = \rho c_{\mu} k^2/\varepsilon$ where c_{μ} is a constant. Here, only the case involving flow regions of high local Reynolds numbers, or say, regions with Kolmogorov and macroscopic scales adequately separated, is considered (Launder & Spalding, 1974). With this, transport equations for k and ϵ can be written as,

$$\rho u\frac{\partial k}{\partial x} + \rho v\frac{\partial k}{\partial y} = \frac{1}{r^{\eta}}\frac{\partial}{\partial y}\left[r^{\eta}\,\Gamma_k\frac{\partial k}{\partial y}\right] + S_k \;;\quad \rho u\frac{\partial \varepsilon}{\partial x} + \rho v\frac{\partial \varepsilon}{\partial y} = \frac{1}{r^{\eta}}\frac{\partial}{\partial y}\left[r^{\eta}\,\Gamma_{\varepsilon}\frac{\partial \varepsilon}{\partial y}\right] + S_{\varepsilon} \qquad (3)$$

In **(3)** Γ_k and Γ_ϵ are given by

$$\Gamma_k = \mu + \frac{\mu_t}{\sigma_k} \;;\quad \Gamma_{\varepsilon} = \mu + \frac{\mu_t}{\sigma_{\varepsilon}} \qquad (4)$$

where the σ's are the turbulent Prandtl/Schmidt numbers for k and ϵ, respectively. The last terms in **(3)** are known as "source" terms and are given by:

$$S_k = \rho(P-\varepsilon) \; ; \quad S_\varepsilon = \rho\frac{\varepsilon}{k}(c_1 P - c_2\varepsilon) \tag{5}$$

being c_1=1,47, c_2=1,92 and c_μ=0.09. The production term in **(5)** reads

$$P = \frac{\mu_t}{\rho}\left(\frac{\partial U}{\partial y}\right)^2 \tag{6}$$

The numerical approach here adopted is the well-known parabolic solver technique of Patankar (1972,1980). Details of this method can be found elsewhere and for that only general ideas are here presented. The method consists of first recasting **(2)**-**(3)** onto a general transport equation of the form,

$$\frac{\partial \phi}{\partial x} + (a + b\,\omega)\frac{\partial \phi}{\partial \omega} = \frac{\partial}{\partial \omega}\, c\, \frac{\partial \phi}{\partial \omega} \tag{7}$$

where

$$a = -\frac{d\Psi_I}{dx}/\Psi_{EI} \; ; \quad b = -\frac{d\Psi_{EI}}{dx}/\Psi_{EI}$$

$$c = r^2 \rho U \Gamma_\phi/\Psi_{EI}^2 \; ; \quad \Psi_{EI} = \Psi_E - \Psi_I$$

Equation **(7)** is written in the so-called ***x-ω*** coordinate system, being Ψ and ω the dimensional and non-dimensional stream functions, respectively. Accordingly, subscripts I and E are relative to the "internal" an "external" boundary layer limits, respectively.

The second step is then to integrate **(7)** over the Control-Volume (or computational cell) shown in Figure 1. The conservation laws are then rewritten in their macroscopic counterpart form over the volume giving,

$$\begin{aligned}&[\Psi_{EI,P}-\Psi_{EI,P}](\omega_n-\omega_s) + [m''\phi-\Gamma_\phi\frac{\partial\phi}{\partial y}]_n r_n^\eta(x_P-x_A)- \\ &[m''\phi-\Gamma_\phi\frac{\partial\phi}{\partial y}]_s r_s^\eta(x_P-x_A) = (S_c+S_P\phi_P)[r_n^\eta(y_n-y_s)]_P(x_P-x_A)\end{aligned} \tag{8}$$

In **(8)** the subscripts "P" and "A" are relative to downstream and upstream x-positions, respectively. Also, for numerical stability, source term linearization (S_ϕ=S_C+$S_P\phi$) has been used (Patankar 1080). After incorporating the linear formulation for the diffusion term, one finally gets,

$$a_P\phi_P = a_N\phi_N + a_S\phi_S + a_{PA}\phi_{PA} + b_P \tag{9}$$

where the a's and b are coefficients. The system **(9)** of algebraic equations can then be solved for each dependable variable ϕ at each downstream position x_P.

Inlet flow for the central and annular jets are given a uniform distribution defining the velocity ratio U_e/U_i, where U_e and U_i are the inlet velocities for the annular and central regions, respectively. The values of k and ϵ at the inlet section were giving by,

$$k_{in} = 1.0x10^{-3}U_m \; ; \quad \epsilon_{in} = k_{in}^{3/2}/\mathrm{K}y' \tag{10}$$

where U_m is the overall mean velocity, K is the von Karman constant (K=0.4) and y' the distance to the wall. For the centerline (y=0) the symmetry condition is implemented for all dependent variables (ϕ=U, k and ϵ) as,

$$\left.\frac{\partial\phi}{\partial y}\right)_{y=0} = 0 \tag{11}$$

Wall proximity is handled by the usual **Wall Function** approach (Launder & Spalding, 1972,1974), giving for the wall shear stress,

$$\tau_w = \left(U_N\, c_\mu^{1/4} k_N^{1/2}\right) \Bigg/ \frac{1}{\kappa}\ln\left[E\, y_N \frac{\mu(c_\mu^{1/2}k_N)^{1/2}}{\rho}\right] \tag{12}$$

being $U^* = \left(\tau_w/\rho\right)^{1/2}$ and E a constant. Also, $U_N^+ = U_N/U^*$ and $y_N^+ = (\mu y_N^{'} U^*)/\rho$. In **(12)** the subscript "N" identifies the grid point closest to the wall. In that region, the use of the **Wall Function** approach associated with the assumption of "local equilibrium" for turbulence (P=ϵ) gives,

$$k_N = \tau_w/\left(\rho c_\mu\right)^{1/2} \; ; \quad \varepsilon_N = \left(k_N^{3/2}\right)\Big/\left(\kappa y_N^{'}\right) \tag{13}$$

Determination of the unknown pressure gradient is handled exactly as explained in Patankar (1988). That approach consists basically in finding the "zero" of a function f (dp/dx) defined as;

$$f(dp/dx) = \left(A_{calc} - A_{duct}\right) \Big/ \Psi_{EI} \tag{14}$$

where the left hand side represents the discrepancy, at the downstream position, between the *calculated* and *real* duct areas. Solution of **(14)** can be achieved with an iterative Newton-Raphson method of the form

$$f^* + f^{*'}[(dp/dx) - (dp/dx)^*] = 0 \tag{15}$$

where "starred" values are estimate quantities later improved in subsequent iterations. Typically, 3 to 4 iterations are necessary in solving **(15)** at each axial station.

3. Results and Discussion

Computational details. The duct shown in Fig. 1 was calculated with two sets of input data. The first one consisted of a long inlet region followed by a converging/diverging duct before another long outlet sector was calculated. In this case, at entrance, the concentric jets were of equal value, or say U_e/U_i=1. The second case involves the use of a short tube length before any change in the duct initial cross sectional area. This short duct case had a small entrance length of x/D= 5 with the jet velocity ratio U_e/U_i equal to 1.3. The former situation aimed the analysis of fully developed flow passing by an obstruction or expansion whereas the later case was used to simulate the mixing of streams through a varying cross section. Either expansion or contraction of the initial duct area was based on a variation of ±20% of the initial duct radius. Data used in all cases are summarized in Table 1.

Table 1 - Input data for geometry of Figure 1.

	Long duct - U_i/U_e=1		Short duct - U_i/U_e=1.3, y_1/D=0.5	
	Diverging:	Converging	Diverging	Converging
H/D	+.2	-.2	.2	-.2
X_L/D	100		5	
Xc/D	25			

Long duct. Figures 2 and 3 show the developing mean velocity field passing over the variation of area. One can clearly see in Fig. 2 that, in relation to the mean flow rate, the flow accelerates in the core region (y/R_w<0.5) whereas it slows down close to the wall. In a contraction, Fig. 3 shows the opposite trend. Corresponding results for turbulence are shown in Figures 4 and 5. The figures present the non-dimensional turbulent kinetic energy along the duct and at different radial positions. It is interesting to note that in the diverging duct, Figure 4 indicates that in all the flow cross section an increase in k/U^{*2} takes place across the area change section. Yet, this perturbation in the stabilized profiles reaches a maximum value at around the end of the diverging section, requiring nearly another 25 to 30 diameters downstream the flow in order to attain again stable values. Radial plots for both expansion and contraction are shown in Figures 6 and 7, respectively. Enhancement of turbulent kinetic energy over a diverging section (Fig. 6) and damping in a contracting duct (Fig. 7) are also shown in the figures. Further, inspecting Fig. 1 and Table 1 one can see that although the last curve in the figures correspond to the exit of the diverging/contracting section (x/D=125), the values of k/U* are still quite different than those at the incoming stabilized flow. Another 30 to 50 additional diameters downstream in the duct are further necessary for the induced oscillations to be damped out.

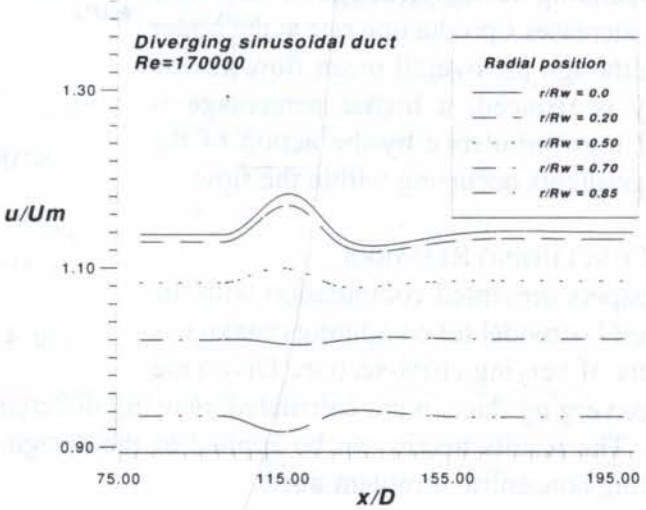

Fig. 2 - Axial mean velocity over a expansion.

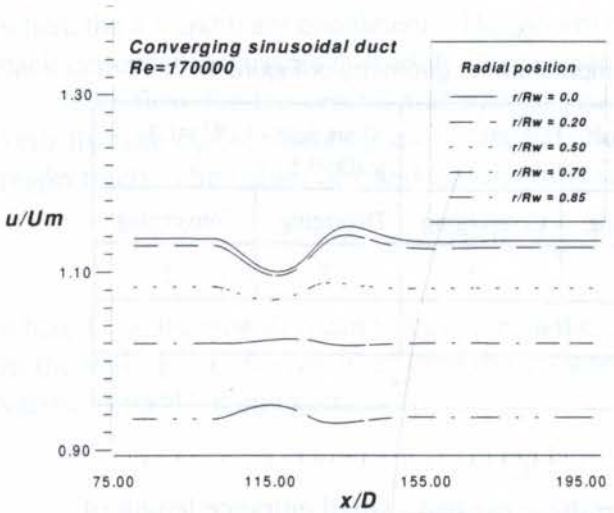

Fig. 3 -Axial mean velocity over a contraction.

Short duct. As mentioned before, calculations were also performed in a 25 diameters long diverging/converging section preceded and followed by a length equal to x/D=5. In this situation, an internal jet with velocity 30% higher than the concentric external stream promotes radial mixing along the channel. Mean velocity is presented in Figures 8 and 9. Deceleration of the central flow in Fig. 9 is much stronger than in Fig. 8 in a similar fashion with results already presented for the long duct case (Figs. 2-3) Stronger flattening of the velocity profile in converging ducts may suggest the use of this geometry for quickly mixing coaxial jets with higher inner velocity. The behavior of corresponding turbulent fields is shown in Figs. 10 for the contracting duct. The steep velocity gradient at the duct entrance promotes turbulence production increasing the level of k within the mixing layer. (see Eqn. **(6)**). Later, downstream the flow, this energy level is dissipated by diffusion to the center and wall fluid layers.

Finally, Figure 11 compares the centerline development of k/U^{*2} for the mixing of streams in different channels. In this radial position, a reduction on the level of the turbulent kinetic energy in the converging duct occurs due to the retardation of the core velocity (Fig. 3) causing a flatter U profile at the center and, consequently, a lower production rate of k. The mean field acquires more kinetic energy but a lower fraction is made available for generating turbulence. On the other hand, in the expanding duct, retardation of wall fluid layers increases k production rate at the center and, although the overall mean flow kinetic energy is reduced, a higher percentage is turned into turbulence by the action of the steep gradients occurring within the flow.

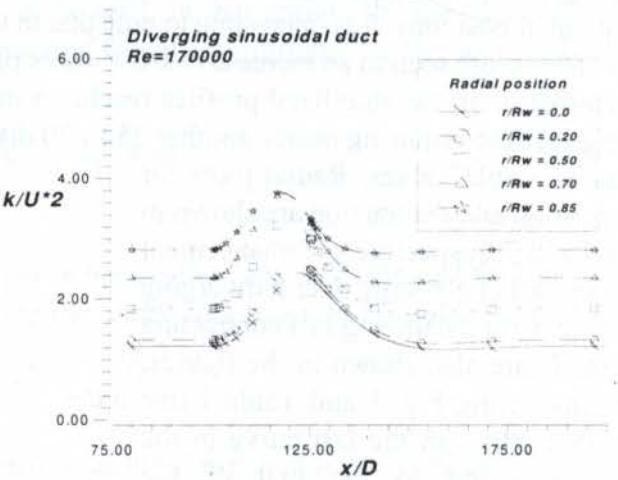

Fig. 4 - Effect of duct expansion on k/U^{*2}

4. CONCLUDING REMARKS

This papers presented computation with the standard k-ϵ model for computing coaxial jets in ducts of varying cross-section. Diverging and converging ducts were calculated *showing* different behavior for the mean and turbulent fields. The results herein can be applied to the design ad analysis of engineering equipment *involving* concentric turbulent ducts.

5. ACKNOWLEDGMENTS

MJS deLemos is thankful to CNPq, Brazil, for financial support during the preparation of

this work.

6. References

Matsumoto, E., de Lemos, M.J.S., DEVELOPMENT OF AN AXI-SYMMETRIC MIXING LAYER IN A DUCT OF CONSTANT CROSS SECTION, *Proc. of 3rd Braz. Therm. Sci. Meet.*, vol. I, pp. 381-385, Itapema, December 10-12 (1990).

Jones, W.P., Launder, B.E., THE PREDICTION OF LAMINARIZATION WITH A TWO-EQUATION MODEL OF TURBULENCE, Int. J. Heat & Mass Transfer, vol. 15, pp. 301-314 (1972).

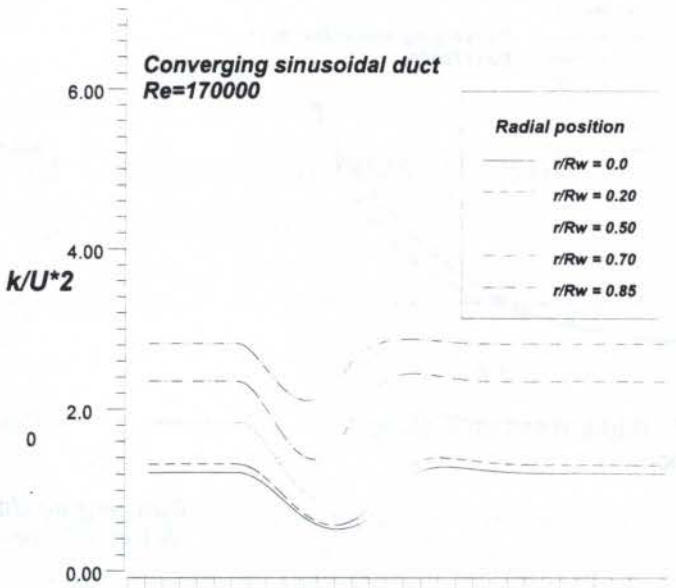

Fig. 5 - Effect of contraction on k/U^{*2}

Launder, B.E., Spalding, D.B., THE NUMERICAL COMPUTATION OF TURBULENT FLOWS, Comp. Meth. App. Mech. Eng., vol. 3, pp. 269-289 (1974)

Patankar, S.V., Spalding, D.B., A CALCULATION PROCEDURE FOR HEAT, MASS AND MOMENTUM TRANSFER IN THREE-DIMENSIONAL PARABOLIC FLOWS, Int. J. Heat & Mass Transf., vol. 15, pp. 1787-1806 (1972)

Patankar, S.V., NUMERICAL HEAT TRANSFER AND FLUID FLOW, Mc-Graw Hill (1980)

Launder, B.E., Spalding, D.B., LECTURES IN MATHEMATICAL MODELS OF TURBULENCE, Academic Press, New York (1972).

Patankar, S.V., PARABOLIC SYSTEMS, cap. 2 de HANKBOOK OF NUMERICAL HEAT TRANSFER, Rohsenow ed., John Wiley & Sons, New York (1988).

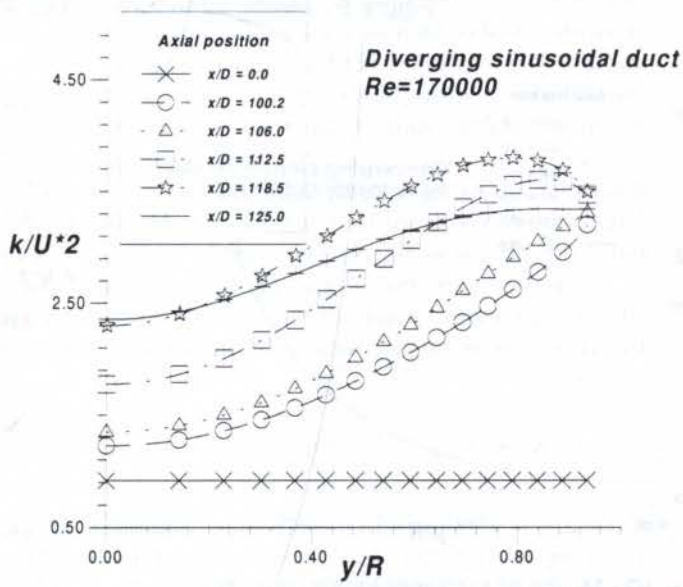

Figure 6 -Radial distribution along expansion.

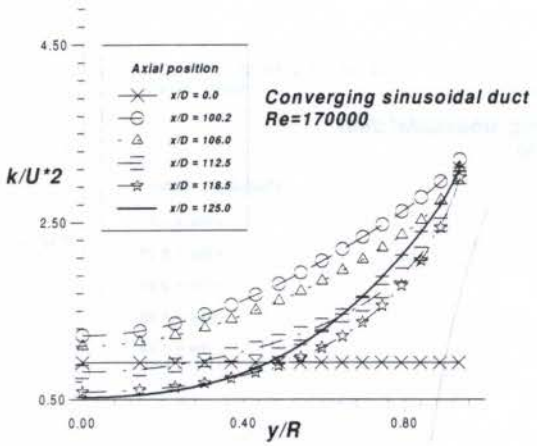

Figure 7 - Radial distribution along contraction.

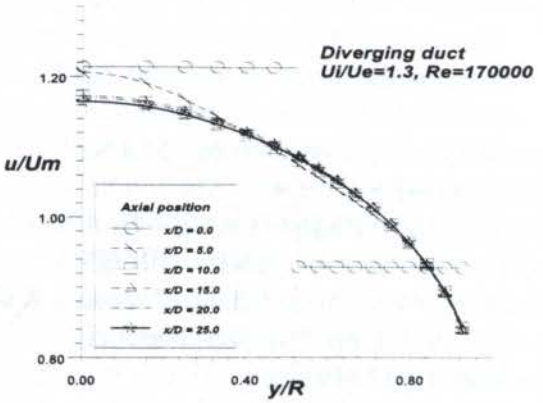

Figure 8 - Mixing streams along expansion.

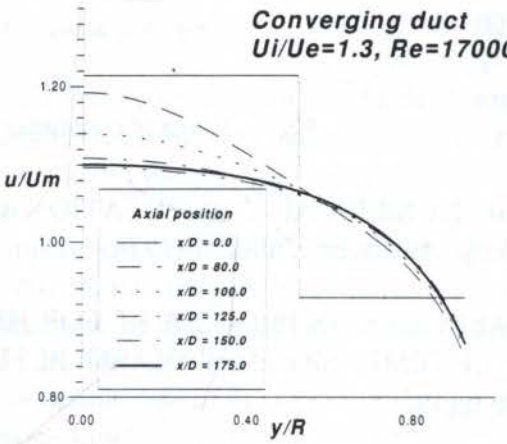

Figure 9 - Mixing streams along contraction.

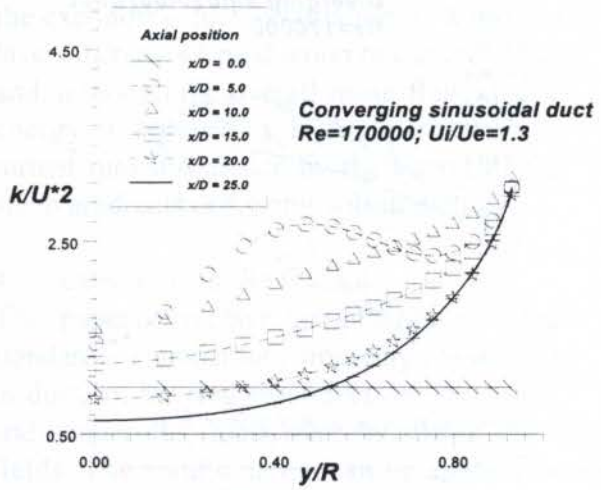

Figure 10 - Mixing of turbulent kinetic energy along contraction

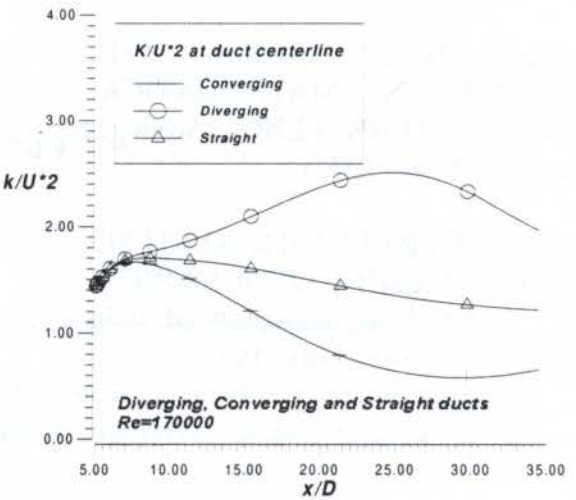

Figure 11 - Comparison of centerline turbulent knetic energy development.

XIV Brazilian Congress of Mechanical Engineering
Obeid Plaza Hotel Convention Center - Bauru - SP/Brazil
December 08-12th 1997

PAPER CODE: COB1515

Particle Weighted schemes for Conservation laws. Recent developments and Applications.

J.P. Vila*

1 Introduction

In the last ten years new Particle Weighted methods for Partial Differential Equations have been introduced. There is a lot of applications in the field of Fluid dynamic, and we must quote Vortex and Vortex-like methods for inviscid Euler equations and Navier Stokes equations. PIC (Particle in Cell) methods are also well known in the field of compressible gas dynamic. Together with Vortex methods they use a specific numerical or semi-analytical methods to compute differential terms such as pressure terms :

- Green kernels for Vortex methods
- particle grid coupling for PIC methods

In this conference we are concerned with a class of methods which use only particle weighted approximations to compute such differential terms. The SPH method (Smooth Particle Hydrodynamics) is our starting point.

It has been "discovered "in 1977 by Lucy ([18]) a British astrophysicist. At this time his computation only require 100 particles. The effective development of the method is due to J. Monaghan, an Australian applied mathematician ([7], [8], [20]). We are also imbedded to him for most of extensions of the original technics to multifluid equations, MHD....

Until 1985, the SPH method was specialized in Astrophysics applications, W. Benz (yet an astrophysicist) is among the first which use SPH methods for complex applications such as high velocity impacts problems with damage models ([5],[6]). Actually, a lot of research center use SPH methods ([24], [12]) as an efficient alternative to Finite Element Lagrangian codes in the field of high velocity impacts. Industrial codes using SPH methods have been available only recently. This is partly due to some difficulties in the theoretical and numerical basis for handling with boundary conditions.

In this paper, I first give an overview of classical recipes for designing SPH methods. I then introduce a new approach - a weak discrete formulation - which provides an efficient tool for understanding and solving problems related with the global conservation property of the method and new efficient (and necessary) tools in the field of SPH methods such as Variable smoothing length, Renormalization.

With this new approach we overcome usual restrictions on the ratio of the smoothing length to the size of the mesh which needs to be large enough (or equal to some specific value depending on the kernel function)

2 Classical Recipes

The design and analysis of weighted particle methods for transport equations and Euler inviscid equations is a well documented field. Thus we briefly discuss the main tools necessary for a comprehensive study of our results. We refer for example to the book of P. A. Raviart ([26]) for an exhaustive study of the different points reviewed here.

*Mathématiques pour l'Industrie et la Physique, UMR 5640, CNRS-UPS-INSA, Département de Génie Mathématique, INSA, Complexe Scientifique de Rangueil, 31077 Toulouse Cedex 4, France, email vila@mip.ups-tlse.fr

2.1 Particle Approximation of functions

The first tool is to obtain a quadrature formula on a set of moving particles. Let us take such a set $(x_i(t), w_i(t))_{i\in P}$, indexed by $i \in P$, where $x_i(t)$ is the position of the particle and $w_i(t)$ its weight. Let $\vec{v}$ a regular vector field in $\mathbb{R}^d$, we classically move the particles along the characteristic curves of the field $\vec{v}$ and also modify the weights in order to take account of deformations due to the field $\vec{v}$:

$$\begin{array}{ll} \frac{d}{dt}x_i = v(x_i,t) & \frac{d}{dt}w_i = \text{div}\ (v(x_i,t))\, w_i \\ x_i(0) = \xi_i & w_i(0) = \omega_i \end{array}$$

(ξ_i, t) are the Lagrangian coordinates of the particle i. We thus have the following quadrature formula where $J(\xi,t)$ is the Jacobian of $(\xi,t) \longrightarrow (x,t)$:

$$\int_{\mathbb{R}^d} f(x)dx = \int_{\mathbb{R}^d} f(x(\xi,t))J(\xi,t)d\xi \approx \sum_{j\in P} w_j(t)f(x_j(t)) \tag{1}$$

Weighted particle Approximation :
The previous quadrature formula, together with the following tools :

- Smoothing kernel,
- convolution,

leads in 3 steps to the smoothed (or regularized) particle approximation of a function :

. Smoothing kernel $W(x,h)$

$$W(x,h) = \frac{1}{h^d}\theta(\frac{\|x\|}{h})$$

We take usually θ as a positive function with compact support $\subset [0,2]$ (d is the space dimension), for example :

$$\theta(y) = C \times \begin{cases} 1 - \frac{3}{2}y^2 + \frac{3}{4}y^3 & \text{if } 0 \le y \le 1, \\ \frac{1}{4}(2-y)^3 & \text{if } 1 \le y \le 2 \end{cases}$$

$C = \frac{2}{3}, \frac{10}{7\pi}, \frac{1}{\pi}$ (d=1,2 or 3). $W(x,h) \longrightarrow \delta$ when $h \longrightarrow 0$. h is the "smoothing length".

. Régularization of f

Convolution of f with the kernel W :

$$< f(x) >= f * W(x) = \int f(y)W(x-y,h)dy \tag{2}$$

. Quadrature of (2)

We provide a quadrature of the integral in (2) with the help of (1), we thus define $\Pi^h(f)$ the smoothed (or regularized) particle approximation of a function f as :

$$\Pi^h(f)(x) = \sum_{j\in P} w_j f(x_j)W(x - x_j(t), h)$$

We shall use the following notations :

$$W_{ij} \equiv W(x_j - x_i, h) \qquad \nabla W_{ij} \equiv grad_x[W(x_i - x_j, h)]$$

Particle approximation of derivatives is easily handled by taking direct derivation of smoothed particle approximations which gives at the point x_i :

$$\nabla \Pi^h(f)_i = \sum_{j \in P} w_j f(x_j) \nabla W_{ij}$$

Remark 1 *Here we use the standard notations in SPH literature. The smoothing length is h, the kernel is W and we have chosen Δx as the characteristic size of the mesh. In most of the mathematical papers related to particle weighted methods, the smoothing length is denoted ε, the kernel or cut-off function is ζ^ε and h is the characteristic size of the mesh. The reader has to take account of that in some of the references quoted in this paper.*

In classical discretization methods such as finite differences, finite volumes or finite elements we have a unique discretization parameter which is Δx the characteristic size of the mesh. Here we get an additional parameter h , the so-called "smoothing length", which is the characteristic size of the regularizing kernel W.
The combined effect of these 2 parameters can be studied accurately. We refer to the book of P.A. Raviart [26] for a detailed analysis of interpolation errors in various Sobolev norms and semi-norms. We just recall some results of [26] (see also [19]) which will be useful for our analysis. We restrict ourselves to compactly supported symmetric kernels such that $W \in \mathcal{C}^{m+1}$, $m \geq 2$. Then, there exists a constant $C > 0$ just depending on the transport field $\vec{v}$ (supposed regular enough) such that :

$$\begin{aligned} &\forall u \in W^{\mu,p}(I\!R^d), \quad s \geq 0, \mu = \max(r+s, m), \\ &\qquad r = 1, 2, \frac{d}{m} \leq p \leq \infty, \qquad q = \frac{p-1}{p} \\ &|u - \Pi^h(u)|_{s,p,I\!R^d} \leq \\ &\qquad C\left(h^r |u|_{r+s,p,I\!R^d} + (1 + \frac{\Delta x}{h})^{\frac{d}{q}} \frac{(\Delta x)^m}{h^{m+s}} ||u||_{m,p,I\!R^d}\right) \end{aligned} \tag{3}$$

Note that we need that the ratio $\frac{(\Delta x)}{h} \longrightarrow 0$, in order that $\Pi^h(u) \longrightarrow u$. In these formulae Δx is the characteristic scale of the mesh. That means - taking account that W is compactly supported - that the number of neighbors of any particles, i.e. the number of particles located at a distance less than a length of order h, needs to go to infinity when h et Δx go to 0.

2.2 Particle Approximation of a model Partial Differential Equation

We consider the following model PDE in conservation form :

$$L_v(\Phi) + \text{div } F(x, t, \Phi) = S \tag{4}$$

where $L_v(\Phi)$ is the transport operator :

$$L_v(\Phi) = \frac{\partial \Phi}{\partial t} + \sum_{l=1,d} \frac{\partial}{\partial x^l}(v^l \Phi)$$

For the mathematical analysis v is supposed to be known and not depending on Φ. Such a dependency is possible and classical in applications. We thus look for an approximation $(\Phi_i(t))_{i \in P}$ of (4) defined on the particle moving along the characteristic curves of v :

$$\Phi_i := \Phi(x_i(t), t)$$

We thus have

$$\frac{1}{w_i} \frac{d}{dt}(w_i \Phi_i) = L_v(\Phi)_i$$

In order to compute an approximation of div $F(x, t, \Phi)$, we naturally smooth F, which leads to:

(5) $$L_v(\Phi)_i + \nabla\Pi^h(F)_i + F_i\nabla\Pi^h(1)_i = S_i$$

or equivalently

(6) $$\frac{d}{dt}(w_i\Phi_i) + w_i\sum_{j\in P} w_j(F_j + F_i)\nabla W_{ij} = w_iS_i$$

We have add $\nabla\Pi^h(1)_i$ in order to satisfy the global conservation. We first remark that this term is small (due to(3)), we then use $\nabla W_{ij} = -\nabla W_{ji}$ to prove easily that :

(7) $$\frac{d}{dt}\left(\sum_{i\in P} w_i\Phi_i\right) = \sum_{i\in P} w_iS_i,$$

discrete version of the continuous conservation of Φ :

$$\frac{d}{dt}\left(\int_{\mathbb{R}^d}\Phi dx\right) = \int_{\mathbb{R}^d} S dx$$

Note that (6) is a centered scheme, we thus need some upwinding or equivalently some artificial viscosity in order to stabilize the method. We practically introduce Π_{ij} ,an artificial viscosity term satisfying $\Pi_{ij} = \Pi_{ji}$ - we need to satisfy conservation-an the scheme is :

(8) $$\frac{d}{dt}(w_i\Phi_i) + w_i\sum_{j\in P} w_j(F_j + F_i + \Pi_{ij})\nabla W_{ij} = w_iS_i$$

We then perform a suitable time discretization to get an efficient numerical scheme.

2.3 Applications to Euler equations

Thanks to the set of approximation rules described in the previous section we are now able to design the SPH approximation of Euler equations of a compressible fluid. We detail the simplest case of a single compressible gas in 2 dimensions:

$$\Phi = \begin{pmatrix} \rho \\ \rho v^1 \\ \rho v^2 \\ E \end{pmatrix} \quad F^1(\Phi) = \begin{pmatrix} 0 \\ p \\ 0 \\ v^1 p \end{pmatrix} \quad F^2(\Phi) = \begin{pmatrix} 0 \\ 0 \\ p \\ v^2 p \end{pmatrix}$$

$p = p(\rho, u)$ $\quad E = \rho(u + \frac{1}{2}||\vec{v}||^2)$

$$L_v(\Phi) + \sum_{l=1,d}\left(\frac{\partial\Pi^h(F^l(\Phi))}{\partial x^l}\right) = 0$$

We use the following particle approximation :

$$L_v(\Phi)_i + \sum_{l=1,d} F^l(\Phi)_i\left(\frac{\partial\Pi^h(1)}{\partial x^l}\right)_i + \left(\frac{\partial\Pi^h(F^l(\Phi))}{\partial x^l}\right)_i = 0$$

to get the system of ordinary differential equations :

$$(i) \quad \frac{d\vec{x_i}}{dt} = \vec{v_i}, \qquad (ii) \quad \frac{d}{dt}(w_i\rho_i) = 0,$$

$$(iii) \quad \frac{d}{dt}(w_i\rho_i\vec{v_i}) + w_i\sum_{j\in P} w_j(p_i + p_j)\nabla W_{ij} = 0,$$

$$(iv) \quad \frac{d}{dt}(w_iE_i) + w_i\sum_{j\in P} w_j(p_i\vec{v_i} + p_j\vec{v_j}).\nabla W_{ij} = 0$$

$(ii) \Longrightarrow w_i(t)\rho_i(t) = cst \equiv m_i$.The quantity m_i is constant with the time, its dimension is a mass, thus it is natural to call it the mass of the particle i. Taking account of that in the two others equations, we get finally :

$$\left\{ \begin{array}{l} \frac{d}{dt}(\vec{v_i}) = -\sum_{j\in P} m_j(\frac{p_i+p_j}{\rho_i\rho_j})\vec{\nabla}W_{ij} \\ \frac{d}{dt}(u_i) = -\sum_{j\in P} m_j \frac{p_j}{\rho_i\rho_j}(\vec{v_j}-\vec{v_i}).\vec{\nabla}W_{ij} \end{array} \right. \tag{9}$$

The more popular way to add such contribution in SPH is to take a pseudo-viscous pressure of the type proposed by Von Neumann and Richtmeyer ([28]), p is modified in $p + \Pi_v$, with :

$$\Pi_v = \left\{ \begin{array}{ll} \beta\rho l^2(\mathrm{div}\vec{v})^2 - \alpha\rho lc\mathrm{div}\vec{v} & \text{si } \mathrm{div}\vec{v} < 0 \\ 0 & \text{sinon} \end{array} \right.$$

where α and β are nondimensional coefficients whose value is of order 1, c is the sound velocity and l is the characteristic width of the shock we want to compute (of order Δx or h).

This set of equation is not the standard set of equation used in SPH codes. The classical formulation of SPH ([20],[5],[27]) is :

$$\left\{ \begin{array}{l} \frac{d}{dt}(\vec{v_i}) = -\sum_{j\in P} m_j(\frac{p_i}{\rho_i^2}+\frac{p_j}{\rho_j^2}+\Pi_{ij})\nabla W_{ij} \\ \frac{d}{dt}(u_i) = -\frac{p_i}{\rho_i^2}\sum_{j\in P} m_j(\vec{v_j}-\vec{v_i}).\nabla W_{ij} \\ \qquad\qquad -\frac{1}{2}\sum_{j\in P} m_j\Pi_{ij}(\vec{v_j}-\vec{v_i}).\nabla W_{ij} \end{array} \right. \tag{10}$$

$$\Pi_{ij} = \left\{ \begin{array}{ll} \frac{\mu_{ij}(\beta\mu_{ij}-\alpha\bar{c})}{1/2(\rho_i+\rho_j)} & \text{si } (\vec{v_i}-\vec{v_j}).(\vec{x_i}-\vec{x_j}) < 0, \\ 0 & \text{sinon} \end{array} \right.$$

where $\bar{c} = 1/2(c_i + c_j)$ is the mean sound velocity and μ_{ij} given by :

$$\mu_{ij} = \frac{h(\vec{v_i}-\vec{v_j}).(\vec{x_i}-\vec{x_j})}{|\vec{x_i}-\vec{x_j}|^2+\epsilon h^2}$$

We refer to [32] for more details. Note anyway that the formulation (9) is rather robust when we compute high density gradients.

2.4 Comments

Time Discretization Most SPH codes use Runge et Kutta explicit in time discretization, and thus need to satisfy CFL type restriction for the time step.

Structural Data. Cost SPH codes, due to the particles , do not need heavy data structures. Nevertheless, we need to compute at any time step some minimal structural data. In order to compute efficiently the summation in (8) we build the list of neighbors of any particles i. In usual codes - with no large distance forces as gravitational effects- the most efficient algorithm is the "linked list" algorithm. Its cost is less than 50% of the total cost of one time step. Tree algorithm (cf. [11]) are also used in some complex situations.

Although actually the SPH codes seems to be more expensive than Finite Volume schemes. They can compute with the advantages of Lagrangian methods some computations only possible previously with Eulerian FV codes. One interest of the method is also the availability of the method to complex physics situations such as multifluid ([5], [20]), multiphases flows ([21]), including viscoplastic effects, damage ([6])... The methods looks consequently very attractive due to its efficiency at a reasonable cost.

Conservativity. Variable smoothing length Variable smoothing length is a basic ingredient in performing efficient computations with weighted particle methods. The original computations made by Monaghan for standard test problems such as shock tubes have proven that keeping the smoothing length to be constant introduces numerical instabilities inside rarefaction waves. These difficulties are clearly consequences of the decrease in the number of neighboring particles in these area. Variable smoothing length has then been introduced by Monaghan ([20], cf. also[5]) to overcome this problem, and it reveals as a very performing and essential tool. We modify the approximation principles according to :

$$< f(x) >_g = \int f(y) W(x-y, h(x)) dy$$

$$\Pi_g^h(f)_i = \sum_{i \in P} w_i f_i W(x_i - x_j, h_i)$$

$$W_{ij} \equiv W(x_j - x_i, h_i) \cdot \quad \nabla W_{ij} \equiv grad_x[W(x_j - x_i, h_i)]$$

$$\nabla^h \Pi_g^h(f)_i = \sum_{j \in P} w_j f_j \nabla W_{ij}$$

and we use the usual formulae (5) where we take $\nabla^h \Pi_g^h(f)$ instead of $\nabla^h \Pi(f)$. h evolves according to

$$\frac{dh_i}{dt} = \frac{1}{d} h \mathrm{div} v$$

in order that the number of neighbors to be constant.

We do not have yet $\nabla W_{ij} = -\nabla W_{ji}$ and global conservation is not exactly satisfy.

Boundary Conditions This is one of the main difficulties when we deal with industrial applications. The usual technics use ghost particles. Boundary forces have also been introduced by Monaghan ([22]). We refer to section 3.4 for more details.

Gap Theoretical analysis- Practise In practical computations, the parameters h and Δx are chosen so that the number of neighbors of any particles, i.e. the number of particles located at a distance less than a length of order h, is almost constant all other the computational domain ($\approx$ 25 for 2D computations, and $\approx$ 50 in 3D). We thus have $\frac{h}{\Delta x} \simeq \mathcal{O}(1)$, which does not agree with theoretical results which require at least that $\frac{\Delta x}{h} \longrightarrow 0$. The renormalization technics - see section 3.3 - overcome this difficulty..

An example of a complex application In order to emphasize on the ability of the method to handle with complex situations, I present here a simulation, with the code SmartFluid of XRS and Simulog. This is the disintegration of a liquid jet (nearly incompressible) in a gas flow at high velocity. The computation is 3D according to the scheme :

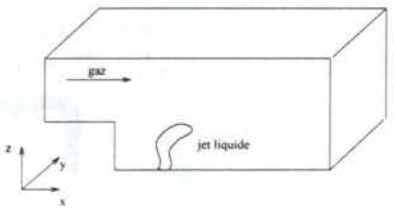

Figure 1: Experimental device

3 cases are studied and compared with experimental data performed at CORIA ([29]).

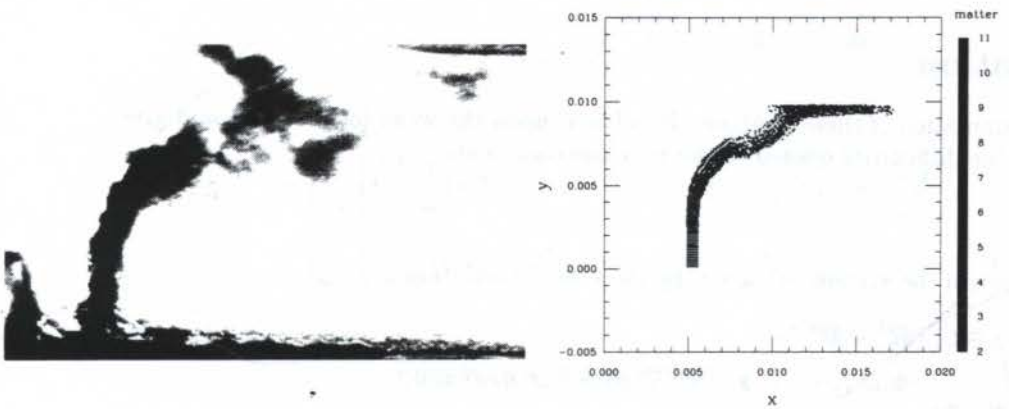

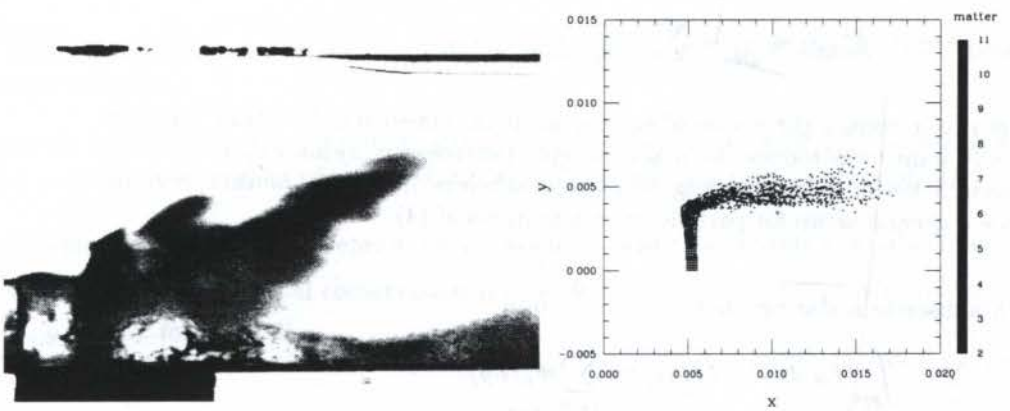

We only present the liquid particles. The photography represent the experimental distribution of drops at the same time, the qualitative agreement is clear. These results are representative of what we can expect of SPH computation in complicated situations. We refer to [16] for more details.

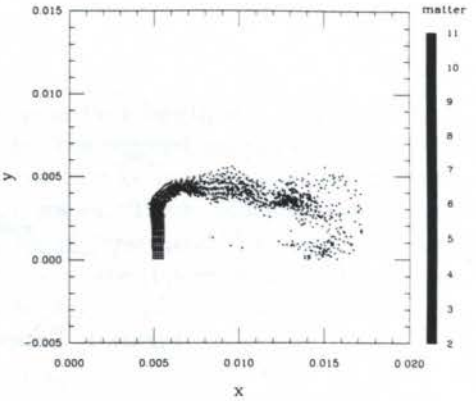

Figure 2: Comparison Experiment- Computation

3 Weak Formulation

We now introduce a new formulation of these methods. It is based upon the weak formulation, and gives an efficient tool for solving the difficulties quoted in the previous comments.

3.1 Basic Principle

We look for an approximation of the system (4), given by its weak formulation :

$$\begin{aligned} &\forall \varphi \in C_0^2(\mathbb{R}^d \times \mathbb{R}^{+,*}) \\ &\int_{\mathbb{R}^d \times \mathbb{R}^+} (\Phi . L_v^*(\varphi) + F(x,t,\Phi).\nabla(\varphi) + S.\varphi)\, dxdt = 0 \end{aligned} \tag{11}$$

where $-L_v^*$ is the adjoint operator of L_v :

$$L_v^*(\varphi) = \frac{\partial \varphi}{\partial t} + \sum_{l=1,d} v^l \frac{\partial \varphi}{\partial x^l}$$

To get uniqueness we need to introduce the notion of entropy solution, classical in this field, but it is not essential here since we only want to introduce the main concepts (we refer to [2] for a more detailed analysis). In order to provide a better understanding of particle schemes like those of the previous sections, let us now introduce a general setup for particle approximations of (4).

We proceed in 3 steps :

- We provide the space with a discrete scalar product :

$$\int_{\mathbb{R}^d} f.g\ dx \longrightarrow (f,g)_h := \sum_{j \in P} w_j f_j . g_j$$

  which is clearly an approximation of the scalar product in $L^2(\mathbb{R}^d)^m$ thanks to the quadrature formula.

- We also introduce the linear operator $D_{h,S}$ which is supposed to approximate strongly the derivative, i.e. for any φ regular enough

$$\sup_{i \in P} \|D_{h,S}\varphi_i - D\varphi_i\| \to 0 \text{ as } h \to 0$$

  and let us define $-D_{h,S}^*$ as the adjoint operator of $D_{h,S}$. We thus have

$$(D_{h,S}\varphi, \Psi)_h = -\left(\varphi, D_{h,S}^* \Psi\right)_h \tag{12}$$

- A discrete version of (4) is provided by just replacing the integration over $\mathbb{R}^d$ by the discrete scalar product $(.,.)_h$ and the derivative $\vec{\nabla}(\varphi)$ by its approximation $D_{h,S}\varphi$:

$$\int_{\mathbb{R}^+} \left[(\Phi, L_v^*(\varphi))_h + (F(\Phi), D_{h,S}\varphi)_h + (S, \varphi)_h \right] dt = 0$$

We thus get

$$\begin{aligned} \int_{\mathbb{R}^+} (\Phi, L_v^*(\varphi))_h \, dt &= \int_{\mathbb{R}^+} \left(\Phi, \frac{d}{dt}(\varphi) \right)_h dt \\ &= -\int_{\mathbb{R}^+} [\sum_{i \in P} \frac{d}{dt}(w_i \Phi_i)\varphi_i] dt \\ &= -\int_{\mathbb{R}^+} \left(\frac{1}{w}\frac{d}{dt}(w\Phi), \varphi \right)_h dt \end{aligned}$$

and

$$\begin{aligned} & -\int_{\mathbb{R}^+} \left[\left(\frac{1}{w}\frac{d}{dt}(w\Phi), \varphi \right)_h + (D_{h,S}^* F(\Phi), \varphi)_h - (S, \varphi)_h \right] dt \\ = & -\int_{\mathbb{R}^+} \left(\frac{1}{w}\frac{d}{dt}(w\Phi) + D_{h,S}^* F(\Phi) - S, \varphi \right)_h dt = 0 \end{aligned}$$

which leads to the scheme

(13) $$\frac{d}{dt}(w_i \Phi_i) + w_i D_{h,S}^*(F)_i = w_i S_i$$

where

$$\frac{d}{dt}(\Phi_i) + \Phi_i \text{div } (v_i) + D_{h,S}^*(F)_i = S_i$$

The schemes (13) satisfy automatically a result similar to Lax-Wendroff ([17]) theorem for Finite difference schemes :

Theorem 1 *If* $\overline{\Phi}^{0,h}(x,t) = \sum_{j \in P} w_j \Phi_j(t) \chi_{B_i(t)}(x) \longrightarrow \Phi$ *a.e. where* $(\Phi_j)_{j \in P}$ *is solution of (13) and if* $D_{h,S} f \longrightarrow \nabla f$ *for* f *regular when* h *and* Δx *go to* 0, *then* Φ *is a weak solution of (4).*

It remains to define the operator $D_{h,S}$. With the same computation as above we easily see that the scheme (13) satisfy global conservation (i.e. $\frac{d}{dt}(\Phi, 1)_h = (S, 1)_h$) if $1(x)$ is in the null space of $D_{h,S}$ (i.e. $D_{h,S} f = \nabla f$ for $f \in P0$).

We recover the standard scheme by taking $D_{h,S} f = \nabla \Pi^h(f) - f \nabla \Pi^h(1)$. We thus have

$$D_{h,S} f_i = \sum_{j \in P} w_j (f_j - f_i) \nabla W_{ij}$$

with $P0 \subset \ker(D_{h,S})$ and

$$D_{h,S}^* f_i = \sum_{j \in P} w_j (f_j + f_i) \nabla W_{ij} = \nabla \Pi^h(f)_i + f_i \nabla \Pi^h(1)_i$$

I refer to [32] and [3] for a detailed analysis.

We now discuss the technical features in relation with use of Variable Smoothing Length and Renormalization.

3.2 Variable Smoothing Length

We use the Variable Smoothing Length formalism of paragraph 2.4 :

$$< f(x) >_g = \int f(y) W(x-y, h(x)) dy \qquad \Pi_g^h(f)_i = \sum_{i \in P} w_i f_i W(x_i - x_j, h_i)$$

$$W_{ij} \equiv W(x_j - x_i, h_i) \qquad \nabla W_{ij} \equiv grad_x[W(x_j - x_i, h_i)]$$

It is the so called "gather" formulation in the SPH papers (see [11]). The only difficulty is to define a suitable linear operator $D_{h,S}$ with sufficient consistency properties. We achieve that by taking first

$$\nabla^h \Pi_g^h(f)_i = \sum_{j \in P} w_j f_j \nabla W_{ij}$$

which is not - as in the standard case- the exact derivative of $\Pi^{h,g}(f)$. In this case, we can prove similar approximation results to (3). I refer to the PHD thesis of J.L. Lacome ([13]) for a detailed study (see also [32], [14]). We then define $D_{h,S}$:

(14)
$$D_{h,S} f = \nabla^h \Pi_g^h(f) - f \nabla^h \Pi_g^h(1)$$

$$D_{h,S} f_i = \sum_{j \in P} w_j (f_j - f_i) \nabla W_{ij}$$

It satisfies the hypothesis on the kernel suitable for global conservation and $D^*_{h,S}$ is given by :

$$D^*_{h,S} f_i = \sum_{j \in P} w_j (f_i \nabla W_{ij} - f_j \nabla W_{ji})$$

Note that we do not recover the usual formulae (unless $\nabla W_{ij} = -\nabla W_{ji}$).

3.3 Renormalization

Renormalization is a technic recently appeared in SPH literature ([25]), it is supposed to improve accuracy of the method. We prove here that, with the help of the general setup of section 3.1 it is also conservative in the sense of (7). All the approximation and convergence results can be extended by using renormalized particle weighted approximation, this is precisely studied in [30]. In particular we are able to relax the assumption that the ratio $\frac{\Delta x}{h}$ goes to zero, and we just need that $\frac{\Delta x}{h} = \mathcal{O}(1)$. Numerical tests in [?] (due to N. Lanson) prove that classical SPH scheme converge to a wrong solution unless we take well chosen value of the ratio $\frac{\Delta x}{h}$

Formally, renormalization is a tool which provides new formulae for $D_{h,S} f(x)$ with the help of a weight matrix (the renormalization matrix) in the following way:

$$D_{h,S} f(x) = B(x) . \nabla^h \Pi_g^h(f)(x) - f(x) B(x) \nabla^h \Pi_g^h(1)(x)$$

We aim to increase the accuracy, thus instead of $P0 \subset \ker(D_{h,S})$ we ask for $P1 \subset \ker(D_{h,S})$. It can be easily proved that

Proposition 2 *We have $P1 \subset \ker(D_{h,S})$ or equivalently $D_{h,S} f = \nabla f$ for any polynomial f of in $P1$, if and only if $B(x) = E(x)^{-1}$ with*

$$E(x)^{\alpha\beta} = \sum_{j \in P} w_j (x_j^\beta - x^\beta) \, \partial^\alpha W(x, x_j)$$

We the have $E(x)^{\alpha\beta} = \partial^{\alpha,h}\Pi_g^h(x^\beta) - x^\beta\partial^{\alpha,h}\Pi_g^h(1)$.

Approximation results (??) easily prove that $E(x)^{\alpha\beta} \simeq \delta^{\alpha\beta}$ and consequently that $B(x)$ makes sense, if $\frac{(\Delta x)}{h} \longrightarrow 0$. More precisely it can be proved (see [30]) that:

Proposition 3 *Let us suppose that B is uniformly bounded (with respect to h_0 and Δx) then we have*

$$\|D_{h,S}\varphi(x) - D\varphi(x)\| \leq Ch_0\|B(x)\|\|D^2\varphi\|_\infty$$

where h_0 is the characteristic scale of the smoothing length (i.e. $\eta_- h_0 \leq h \leq \eta_+ h_0$ with η_- and η_+ two constants > 0)

The consistency of the method is thus satisfied at the only condition that the smoothing length goes to zero. Moreover, it can be proved that, if $\frac{\Delta x}{h}$ is bounded and if the initial distribution of particles is regular enough the matrix $B(x)$ is uniformly bounded and that :

$$\left|(\varphi, D_{h,S}(\varphi))_h\right| = \left|\left(\varphi, D^*_{h,S}(\varphi)\right)_h\right| \leq C\|\varphi\|_h^2.$$

This also insure stability and convergence of the method (at least in the linear case of symmetric first order systems). The discrete operators are defined according to :

$$\begin{aligned} D_{h,S}f_i &= \sum_{j\in P} w_j(f_j - f_i)B_i.\nabla W_{ij} \\ D^*_{h,S}f_i &= \sum_{j\in P} w_j(f_iB_i.\nabla W_{ij} - f_jB_j.\nabla W_{ji}) \end{aligned} \tag{15}$$

and the scheme is :

$$\frac{d}{dt}(w_i\Phi_i) + w_i\sum_{j\in P} w_j(f_iB_i.\nabla W_{ij} - f_jB_j.\nabla W_{ji}) = w_iS_i$$

We refer to [30] for more details . For operators $D_{h,S}$ given by

$$D_{h,S}\varphi_i := \sum_{j\in P} w_j(\varphi_j - \varphi_i)A_{ij}$$

with

$$\begin{aligned} &(i)\sum_{j\in P} w_j\|A_{ij}\| \leq \frac{C}{h_0} \\ &(ii)\|\sum_{j\in P} w_jA_{ij}\| \leq C \\ &(iii)\|A_{ij} + A_{ji}\| \leq Ch_0(\|A_{ij}\| + \|A_{ji}\|) \\ &(iv)A_{ij} = 0 \text{ si } \|x_i - x_j\| \leq Ch_0 \end{aligned} \tag{16}$$

where h_0 is the characteristic scale of the mesh, the scheme given by (13) is convergent (case of linear symmetric systems). We also prove that conditions (16) are true for (??) at the only condition that $\frac{\Delta x}{h} = \mathcal{O}(1)$, which insures the convergence of the method.

We now present some numerical tests -due to N. Lanson ([15])- on a simple test problem - the Sod shock tube -. We compare the result of the standard method with the renormalized method (see [1],[15] for details) for different values of $\frac{\Delta x}{h}$.

The results with the renormalized method do not depend on $\frac{\Delta x}{h}$. The value of the different level in the solution of the Riemann problem, computed with the SPH standard method agree with the exact solution only for values of the ratio $\frac{\Delta x}{h}$ closed to 1.2.

To understand this result, we remark that for $\frac{\Delta x}{h} = 1.2$ and for a regular mesh the approximation $\nabla\Pi^h(x)$ of 1 is exact. This fact explain the good behavior of the standard method for values of $\frac{\Delta x}{h}$ closed to 1.2.

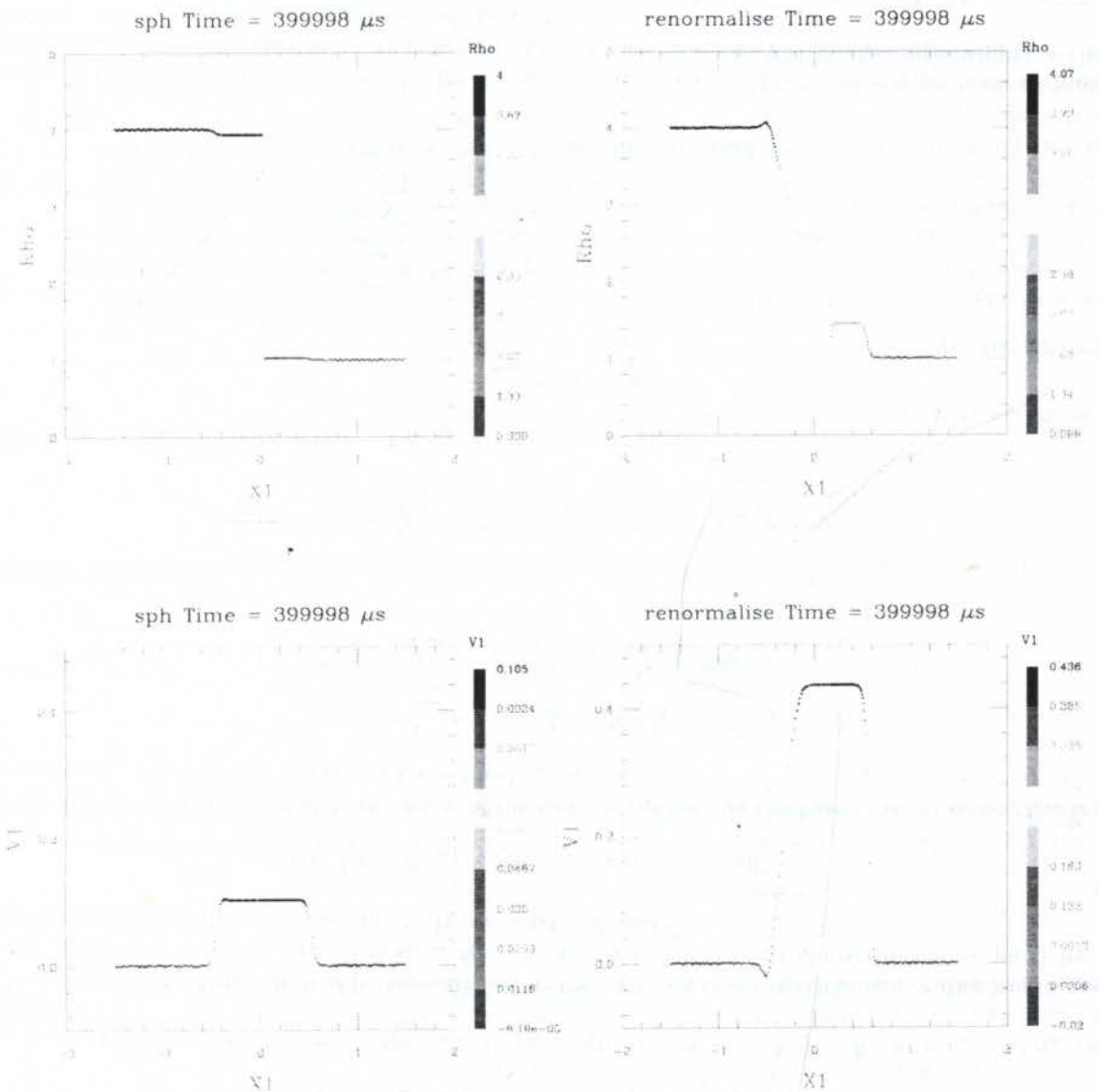

Figure 3: Comparison SPH-Renormalized $\frac{\Delta x}{h} = 1.666$

The resulting renormalized method turns out to be more robust than standard methods, and also less expensive since we can use smaller values of the ratio $\frac{(\Delta x)}{h}$. This makes decrease the number of neighbors (a factor 2 or 3 is possible) and the cost of the method also decrease with a similar ratio. This is particularly true in situation with complex physics since the additional cost due to the computation of renormalization matrices is no more than the computation of an additional physical unknown.

3.4 Boundary Conditions

3.4.1 General Recipes

We deal here with the particle approximation of a function f defined over an open bounded set Ω in $I\!R^d$. Let us denote by $P(\Omega)$, the set of index of the particles of Ω. The weights associated with each particle need to define a good quadrature formula over Ω. We define the approximation Π_Ω in the following way :

$$\Pi_\Omega(f)(x) = \sum_{i \in P(\Omega)} w_i(t) f(x_i(t)) \delta(x - x_i(t))$$

The consistency of this approximation is satisfied if and only if :

$$\sum_{i \in P(\Omega)} w_i(t) f(x_i(t)) \approx \int_\Omega f(x) dx$$

This property will remain true if we move the particles with the field $\vec{v}$ together with modifying the weights according to :

$$\frac{d}{dt}(w_j) = w_j \div \vec{v}$$

From a practical point of view we need to insure initially the accuracy of the quadrature formula. In most of practical computations the particles are initially distributed on a regular grid (for instance cubic grids) and it is quite easy to find suitable weights and positions. A minimum rule could be the following : find some control volume for each particle close to the boundary, take the mid point formula for quadrature and move the particle at this point. This choice is not very accurate but sufficient in most of cases.

As in the unbounded case it is useful to introduce the discrete scalar product

$$(\varphi, \Psi)_{h,\Omega} := \sum_{i \in P(\Omega)} w_i \varphi_i . \Psi_i = \int_\Omega \overline{\varphi}^\Delta . \overline{\Psi}^\Delta dx \tag{17}$$

which approximates the standard one in $L^2(\Omega)$.

To define a Smoothed Particle approximation on a bounded domain requires a convolution by a regularizing kernel :

$$\Pi^h_\Omega(f)(x) = \sum_{i \in P(\Omega)} w_i(t) f(x_i(t)) W(x - x_i(t)) = \Pi_\Omega(f) * W(x)$$

Different approaches are then possible to define particle approximations which takes account of boundary conditions, we shall detail three solutions :

- the classical approach of ghost particles. This very well known approach for plane boundaries is generalized to the case of general curved boundaries. We thus propose new treatments of polyhedral boundaries as those we encounter in industrial problems. This will be detailed in the section ??.
- a technique based on boundary particles and boundary forces, which is related to the approach proposed by Monaghan [20]. Our general tool deals with the consistency of the method at the boundary.

- a semi-analytic approach which uses approximation of integrals of the kernel and its derivatives. This approach is detailed in [32]. It was first proposed by Benz ([5], see also Herand [10]), we give there a more general treatment which in particular deals with some difficulties due to the boundary conditions at free surfaces.

We finally refer to [3] where B. Ben Moussa studies in the scalar nonlinear case the convergence of the particle approximation on bounded domains developed according to the ideas of the following sections. Here we are just interested in the designing of particle methods suitable to approximate such a weak solution, thus we limit ourselves to a model situation where the weak solution of the problem :

$$(18) \qquad \begin{cases} L_v(\Phi) + \mathrm{div} F(x,t,\Phi) = S & \text{for } x \in \Omega \\ F(x,t,\Phi).n = g(x,t,\Phi).n & \text{for } x \in \partial\Omega \end{cases}$$

is defined as :

$$(19) \qquad \begin{array}{l} \forall \varphi \in C^2(\Omega \times I\!R^{+,*}) \\ \displaystyle\int_{\Omega \times I\!R^+} (\Phi . L_v^*(\varphi) + F(x,t,\Phi).\nabla(\varphi) + S.\varphi)\, dxdt \\ \displaystyle -\int_{\partial\Omega \times I\!R^+} g(x,t,\Phi).n\varphi d\sigma(x)dt = 0 \end{array}$$

$n(x)$ is the outward normal to $\partial\Omega$.

We have supposed here that the transport field v is such that $v.n = 0$ at the boundary $\partial\Omega$, otherwise, additional terms must be needed in the weak formulation (19), we do not detail these points, we just point out that all the technics developed here can be extended to these situation.

As in the unbounded case it is useful to introduce the discrete scalar product

$$(20) \qquad (\varphi, \Psi)_{h,\Omega} := \sum_{i \in P(\Omega)} w_i \varphi_i . \Psi_i = \int_\Omega \overline{\varphi}^{\Delta} . \overline{\Psi}^{\Delta} dx$$

which approximates the standard one in $L^2(\Omega)$.

We also use the same discrete operators as in the unbounded case. In the unbounded case, the unknown Φ, evolves at each particle according to the derivative of the field F which acts as a volume source term. To take account of any boundary condition on the flux F we need to compute a specific volume source term. To this ends, let us first suppose that we get a regularized approximation, $G_{h,\Omega}$, of the boundary flux $g.n$ in the sense that (when $h \longrightarrow 0$) : $\forall \varphi \in C^2(\Omega \times I\!R^{+,*})$:

$$(G_{h,\Omega}, \varphi)_{h,\Omega} \longrightarrow \int_{\partial\Omega} g.n\ \varphi dx$$

The particle approximation of the new system in the following way : $\forall \varphi \in C^2(\Omega \times I\!R^{+,*})$,

$$(21) \qquad \int_{I\!R^+} \left[(\Phi, L_v^*(\varphi))_{h,\Omega} + (F(\Phi), D_{h,S}\varphi)_{h,\Omega} + (S, \varphi)_{h,\Omega} - (G_{h,\Omega}, \varphi)_{h,\Omega} \right] dt = 0$$

which gives

$$(22) \qquad \frac{d}{dt}(w_i \Phi_i) + w_i D_{h,S}^*(F)_i = w_i (S_i - G_i)$$

We have a result similar to Theorem 1 :

Theorem 4 *If* $\overline{\Phi}^{0,h}(x,t) = \sum_{j \in P} w_j \Phi_j(t) \chi_{B_i(t)}(x) \longrightarrow \Phi$ *a.e., where* $(\Phi_j)_{j \in P}$ *is solution of (22), if* $D_{h,S} f \longrightarrow \nabla f$ *for* f *regular with compact support in* Ω *and if* $(G_{h,\Omega}, \varphi)_{h,\Omega} \longrightarrow \int_{\partial\Omega} g.n\ \varphi dx$ *for* φ *regular when* h *and* $\Delta x \longrightarrow 0$, *then* Φ *is a weak solution of (18).*

3.4.2 Ghost Particles

It remains to give practical algorithms for designing $G_{h,\Omega}$. The most classical technics is Ghost Particles. In case of plane boundaries the techniques of ghost particles allows us to compute boundary conditions in an interesting way. For simplicity let us suppose that our computational domain is the half space $x^1 < 0$. Let us define the symmetry F_0 with respect to our boundary (the hyperplane $x^1 = 0$) by :

$$F_0 \begin{pmatrix} x^1 \\ x^2 \\ \vdots \\ x^d \end{pmatrix} = \begin{pmatrix} -x^1 \\ x^2 \\ \vdots \\ x^d \end{pmatrix}$$

Let us suppose that the set $P(\Omega)$ of particles (x_j, w_j) gives a consistent quadrature formula in Ω. Clearly the set of particles $P(\Omega) \cup F_0(P(\Omega))$ where particles of $F_0(P(\Omega))$ are $(F_0(x_j), w_j)$, defines now a consistent quadrature formula over the set $\Omega \cup F_0(\Omega) = I\!R^d$. We define a modified approximation $\widetilde{D}_{h,S}$

$$\widetilde{D}_{h,S}\varphi_i := \sum_{j\in P} w_j(\varphi_j - \varphi_i)A_{ij} + \sum_{j\in G} w_j(\varphi_j - \varphi_i)A_{ij} = D_{h,S}\varphi_i + \sum_{j\in G} w_j(\varphi_j - \varphi_i)A_{ij}$$

The additional term insure that for φ with compact support in $\widetilde{\Omega}$, $\widetilde{D}_{h,S}\varphi \to D\varphi$.

$\widetilde{D}^*_{h,S}\varphi$ is given by

$$\widetilde{D}^*_{h,S}\varphi_i = \sum_{j\in P\cup G} w_j(\varphi_i A_{ij} - \varphi_j A_{ji})$$

and $\widetilde{D}^*_{h,S}\varphi \to D\varphi$ in the sense of distribution in $\mathcal{D}'(\widetilde{\Omega})$. Note anyway that $-\widetilde{D}^*_{h,S}$ is not the adjoint of $\widetilde{D}_{h,S}$ with respect to the scalar product (20).

Let us describe the numerical scheme. We define an extension $G(x(\bar{x}, y), t)$ of the boundary data.

$$\int_{\partial\Omega} G(x,t).n\varphi d\sigma = \int_\Omega \varphi \mathrm{div} G(x,t)dx + \int_\Omega G(x,t)\vec{\nabla}(\varphi)dx$$

We thus have

$$\left(\varphi, \widetilde{D}^*_{h,S}G\right)_{h,\Omega} \longrightarrow \int_\Omega \varphi \mathrm{div} G(x,t)dx$$

$$(G, D_{h,S}\varphi)_{h,\Omega} \longrightarrow \int_\Omega G(x,t)\vec{\nabla}(\varphi)dx$$

and we define $G_{h,\Omega}$ in the following way :

$$(G_{h,\Omega}, \varphi)_{h,\Omega} := \left(\varphi, \widetilde{D}^*_{h,S}G\right)_{h,\Omega} + (G, D_{h,S}\varphi)_{h,\Omega} = \left(\varphi, \widetilde{D}^*_{h,S}G - D^*_{h,S}G\right)_{h,\Omega}$$

The final scheme is given by :

$$\frac{d}{dt}(w_i\Phi_i) + w_i \sum_{j\in P} w_j(F_i A_{ij} - F_j A_{ji}) + w_i \sum_{j\in G} w_j(G_i A_{ij} - G_j A_{ji}) = w_i S_i$$

3.4.3 Boundary Particles and Boundary forces

It is possible to avoid Ghost Particles. The first idea is to look for a volume approximation of the outward normal. By using Theorem 4 and using an extension G - uniquely in Ω (i.e. $y > 0$) - of the boundary data. We have

$$(1, D_{h,S}G\varphi)_{h,\Omega} \to \int_\Omega \mathrm{div}\,(G(x,t)\varphi)\,dx = \int_{\partial\Omega} G(x,t).n\varphi d\sigma$$

which leads to $G_{h,\Omega}$:

$$(G_{h,\Omega},\varphi)_{h,\Omega} := (1, D_{h,S}G\varphi)_{h,\Omega} = -\left(\varphi, GD^*_{h,S}1\right)_{h,\Omega}$$

The scheme is :

$$\frac{d}{dt}(w_i\Phi_i) + w_i\sum_{j\in P} w_j(F_iA_{ij} - F_jA_{ji}) + w_iG_i\sum_{j\in P} w_j(A_{ij} - A_{ji}) = w_iS_i$$

We can compute the extension G by using Surface Finite Elements, for example :

$$G_i = \mu(y_i)\sum_{l\in N_{\partial\Omega}} G(x(\bar{x}_l,0))\psi_l(x(\bar{x}_i,0))$$

where ψ_l is the shape function associated with the node l of a triangulation of $\partial\Omega$. We chose $\mu(y)$ in a way that we insure the consistency of the extension G, at least continuity and $\theta(0) = 1$. I refer to [32] and [4] for more details.

3.5 Hybrid schemes Finite Volumes- Weighted Particles

Finally, I report how we can use Godunov type schemes - similar to those used in the field of Finite Volume schemes- inside the methodology of Wp schemes. We have :

$$\begin{aligned}\nabla_x W(x_i - x_j) &= -D\theta_{ij}n_{ij} \qquad n_{ij} = \frac{x_j - x_i}{\|x_j - x_i\|},\\ D\theta_{ij} &= D\theta(\|x_i - x_j\|)\end{aligned}$$

In order to simplify, let us take $S = 0$, the standard scheme is given by

$$\frac{d}{dt}(w_i\Phi_i) - w_i\sum_{j\in P} w_j\left(F_i + F_j\right).n_{ij}D\theta_{ij} = 0$$

which makes appear a conservation law in the direction n_{ij} :

$$\frac{\partial}{\partial t}(\Phi) + \frac{\partial}{\partial x}(F(x_{ij},t,\Phi).n_{ij}) = 0 \tag{23}$$

Therefore it is natural to introduce a 1-dimensional finite difference scheme in conservation form associated to (23), which brings a sufficient numerical viscosity.. Such a scheme consists in replacing the centered approximation $(F(\Phi_i) + F(\Phi_j)).n_{ij}$ by the numerical flux of a Finite Difference scheme $2g(n_{ij},\Phi_i,\Phi_j)$, which is required to satisfy :

$$\begin{aligned}&(i) \quad g(n,u,u) = F(u).n\\ &(ii) \quad g(n,u,v) = -g(-n,v,u)\end{aligned}$$

The numerical viscosity $Q(n,u,v)$ is classically defined in the scalar case (i.e. $\Phi \in \mathbb{R}$) as :

$$Q(n,u,v) = \frac{F(u).n - 2g(n,u,v) + F(v).n}{v-u}$$

The new system is written

$$\begin{aligned}\frac{d}{dt}(w_i\Phi_i) - w_i\sum_{j\in P} w_l 2g(n_{ij},\Phi_i,\Phi_j)D\theta_{ij} &= 0\\ \Phi_i(0) &= \Phi^0(\xi_i)\end{aligned}$$

or equivalently

$$\frac{d}{dt}(w_i\Phi_i) - w_i \sum_{j\in P} w_j(F(x_{ij},t,\Phi_i) + F(x_{ij},t,\Phi_j)).n_{ij}$$
$$+Q(n_{ij},\Phi_i,\Phi_j)(\Phi_i - \Phi_j)D\theta_{ij} = 0$$
$$\Phi_i(0) = \Phi^0(\xi_i)$$

This form is very closed to the one classically used in SPH literature (8), where $Q(n_{ij},\Phi_i,\Phi_j)(\Phi_i - \Phi_j)$ replace here Π_{ij}. We can expect more robustness, as it is the case in the field of FV schemes. Mathematical analysis of the convergence is possible (cf. [2]).

This approach is connected with the notion of Arbitrary Lagrange Euler approximation (A.L.E.), it is also in some sense a generalization of ideas develop by Harten and Hymann ([9]) in their work on self adjusting grid methods for conservation laws. We refer to([31], [23]) for a more detailed analysis and applications to Euler equations.

4 Conclusion

We have reviewed in this paper some recipes for designing particle weighted schemes, and particularly SPH like schemes. These methods are not yet very well known in the field..I believe that they bring some new direction for complex simulation in various field of continuum mechanics. I expect they can open the way for efficient cooperation between applied mathematician and physicists.

References

[1] Ben Moussa B., Lanson N., Vila J.P. "Gridless methods for conservation laws, application to Euler equations" en préparation

[2] Ben Moussa B., Vila J.P. "Convergence of SPH method for scalar nonlinear conservation laws", preprint MIP 1996

[3] Ben Moussa B. PHD thèse INSA Toulouse MIP à soutenir 09 1997

[4] Ben Moussa B., Vila J.P."Convergence of SPH method for scalar nonlinear conservation laws on bounded domains" rapport interne MIP à paraitre Juillet 97

[5] Benz W. "Smooth Particle Hydrodynamics : a Review." Harvard-Smithsonian Center for Astrophysics preprint 2884, 1989

[6] Benz W., Asphaug A. "Impact Simulations with Fracture : I. Methods and Tests"Icarus, 1993

[7] Gingold R.A., Monahghan, 1977, MNRAS, 181-375

[8] Gingold R.A., Monahghan J.J., "Shock simulation by the particle method S.P.H." J.C.P. 52, 374-389 (1983)

[9] Harten A., Hyman J.M. "Self adjusting grid methods for one-dimensional hyperbolic conservation laws" J. Comp. Phys (1983)

[10] Herant "Dirty Tricks for SPH" Mem. S. A. It., Vol. XX,1993

[11] Hernquist L., Katz N. "'TREESPH : a unification of SPH with the hierarchical tree method" The Astr. J. S.S., 70 : 419-446, 1989

[12] Johnson G. R. "Artificial viscosity effects for SPH computations" Int. J. Impact Engng Vol 18, 5, pp. 477-488, 1996

[13] Lacôme J.L. thèse INSA Toulouse MIP CEG à soutenir 09 1997

[14] Lacôme J.L., Vila J.P. en préparation

[15] Lanson N. rapport de DEA juin 97, MIP INSAT

[16] Larrey E., Vich G., Merlo A., Ledoux M., Rompteaux A., Vila J.P. "Liquid Jet disintegration in a gas stream" ICLAS, Seoul, 1997

[17] Lax P.D.,Wendroff B. "Systems of Conservation Laws" CPAM,13,pp.217-237 (1960)

[18] Lucy .L. 1977 ,Astrono. J., 82,1013

[19] Mas-Gallic S., Raviart P.A. "A Particle Method for First-order Symmetric Systems" Numer. Math. 51, 323-352 (1987)

[20] Monaghan J.J. "Smooth Particle Hydrodynamics" Annu. Rev. Astron. Astrop., 1992, 30,543-74

[21] Monaghan J.J., Kocharyan "SPH simulation of multi-phase flow" Comp. Physics Comm. 87 (1995) 225-235

[22] Monahghan J.J., lecture notes, Kaiserslautern University 1995

[23] Paris L. Rapport de Fin d'étude, INSA GMM, 1996

[24] Petschek A.G., L.D. Libersky "Cylindrical Smooth Particle Hydrodynamics" J. Comp. Phys. 109, 76-83 (1993)

[25] Randles R.W., Libertsky L.D. "Smoothed Particle Hydrodynamics, Some recent improvements and Applications" Comp. Meth. Appli. Mech. Eng;, 139 (1996) 375-408

[26] Raviart P.A. "An analysis of particle methods" in Num. method in fluid dynamics, F. Brezzi ed.. Lecture Notes in Math., vol 1127, Berlin, Springer 1985

[27] Raviart P.A. "Particle approximation of first order systems", Journal of Comp. Mathematics, Vol 4, 1,1986

[28] Richtmeyer R.D., Morton K.W., "Difference methods for initial value problems" Interscience Publishers, New York, 1967

[29] Vich G., Ledoux M., "Disintegration of a liquid jet by a subsonic crossflow" ICLAS, Seoul 1997

[30] Vila JP. "Gridless Methods for Conservation Laws" rapport MIP juin 1997

[31] Vila JP. "Weighted Particle-Finite Volume Hybrid schemes" in Finite Volumes for Complex Applications ed. F. Benkhaldoun, R. Vilsmeier, HERMES, Paris, 1996.

[32] Vila JP. "Particle Weighted methods and Smooth Particle Hydridynamics" Soumis à M3AS

XIV Brazilian Congress of Mechanical Engineering
Obeid Plaza Hotel Convention Center - Bauru - SP/Brazil
December 08-12th 1997

PAPER CODE: COB331

ROLL WAVE FORMATION IN NON-NEWTONIAN FLOWS

GERALDO DE FREITAS MACIEL[1], JEAN PAUL VILA, GILBERT MARTINET & GERALDINE GIRARD

INSA/TOULOUSE, MIP/CNRS, Complexe Scientifique de Rangueil - 31077 Toulouse cedex 4

E-mail : maciel@gmm.insa-tlse.fr, vila@gmm.insa-tlse.fr

Abstract

The purpose of this paper is first to determine the criteria for the occurrence of discontinuous roll waves in the non-Newtonian fluids such as debris and dense snow avalanche flows. These are periodic waves separated by hydraulic jumps. Using shallow water equations applied to a Bingham fluid, a flow down an inclined infinite plane is considered. The conditions for the development of such instabilities are discussed to justify the field observations of such waves in these geophysical flows. Special attention is given to the Froude and the Reynolds numbers. The influences of the wavenumber and the fluid cohesion are also adressed. We limited to present the mathematical development of the phenomenon and a few numerical results which should be appreciated by engineers. The numerical model was elaborated using a finite volume technique and the Godunov -VanLeer (2^{nd} order) scheme was applied.

Keywords

shallow water equations, Bingham fluid, roll waves, numerical simulations
equações de água rasa, fluido de Bingham, "roll waves", simulações numéricas

1. INTRODUCTION

Fluids can flow in inclined channels of uniform cross sections such that the depth and the velocity profiles are not changing with downstream distance. If the channel is steep enough, the development of instabilities can occur, resulting in long waves separated by bores or hydraulic jumps. These waves are called roll waves. While roll waves are not frequent in natural water channels, they occur more frequently in artificial hydraulic structures as dam spillways.

On the one hand, roll waves in the clear water was already studied by several authors in past and is still nowadays a subject of great interest of the hydraulic researches.We mention briefly the works on roll waves due to Jeffreys (1925), the photographs illustrating the periodic nature of roll waves published by Cornish (1934), the extend work of Dressler (1949), the experimental work of Mayer (1949) and others. In the last decade, we point out the papers of Needham and Merkin (1984, 1986) that extend the shallow water equations by adding a diffusive term to the momentum equation. More recently, we point out the numerical results published by Kranenburg (1992) on the evolution of roll waves.

[1] Supported by a Posdoctoral grant from FAPESP (São Paulo, Brazil)

On the other hand, roll waves in non-Newtonian fluids is a recent subject of research, and no theories of this phenomenom is yet available from the engineering point of view. If numerous experiments existing on the rheological properties of this sort of fluid, it appears that the purpose of a Bingham model is still an idealization of debris and dense snow avalanche flow reality. Our proposal is using Saint Venant model based on shallow water equations, and assuming that the yield stress along the depth of the flow is a constant, show that this procedure can be validated to simulate debris flow evolution and, in particular, generate roll waves. In this context, we can mention the field observations done by Davies (1986) that suggest that roll waves develop in the debris flow and dense snow avalanches. Davies (1986) has reviewed field observations of debris flows and hypothesised that the pulsating flow of the Jiang-jia Gulley and other similar events in China were the result of roll waves in highly viscous laminar flows. Recently, Takawashi (1991) from the experiments undertaken in the laboratory proves the existence of roll waves in debris flow.

2. MATHEMATICAL MODEL FOR SIMULATING NON-NEWTONIAN FLOWS - SHALLOW WATER EQUATIONS

2.1 Rheological model

The rheology studies the relationship between a shear stress and its velocity gradient. Many hypotheses can be considered; for example, the Newtonian model expresses the linearity between the shear stress and the resulting deformations. However the behaviour of the materials involved in that flow is very different from clear water. Debris flow exhibits the property of requiring a minimum stress to initiate deformation. The existence of a cohesion gives to these fluids a heavily non-Newtonian behaviour, and so, another model must be used. Among the existing models let us point out the Bingham model. The Bingham fluid is a good model because it adds to a classical diffusion effect a critical shear stress τ_c that is necessary to exceed to initiate deformation. For a one-dimensional deformation it is given by :

$\frac{\partial u}{\partial y} = 0$ if $\tau < \tau_c$, and $\tau - \tau_c = \mu \frac{\partial u}{\partial y}$ if $\tau > \tau_c$ where μ is the dynamic viscosity.

This critical shear stress τ_c homogeneous to a static cohesion, depends on the density and the humidity for snow avalanches, for instance, and on the concentration of fine particles for debris flow (Martinet, 1992). The main interest of this modelisation consists in describing faithfully the starting movement of the flows, when the material from a solid phase sets to a liquid one. Because the flow of a Bingham fluid starts when the internal shear exceeds the critical shear τ_c, as long as the height of the fluid is lower than the critical value h_c, no deformations occur, and so, no movement can begin.

$h_c = \frac{\tau_c}{\rho.g.\sin(\theta)}$ movement if $h > h_c$, where θ is the slope of the long profile.

2.2 Mathematical model

2.2.1 Hypothesis and equations

For a finite mass of isotropic material, in which density variations can be neglected, and supposing that the height of the flow is large enough compared to the particles's diameter, an incompressible model can be established from the equations of conservation of mass and momentum. The shallow water equations system are then obtained from the general fluid mechanic equations by introducing the rheological behaviour laws, and by integrating the equations in the vertical. If we suppose that the height of the flow is small compared with the length of the flow and if the ratio of the Froude number and the Reynolds number is also small compared to unity, the pressure is hydrostatic (Martinet, 1992). The system is then constituted with the continuity equation (1); the depth averaged momentum equation (2) and also of the two hydraulic jumps equations ((3) and (4)).

$$\frac{\partial h}{\partial t} + \frac{\partial (hu)}{\partial x} = 0 \qquad (1)$$

$$\frac{\partial (hu)}{\partial t} + \frac{\partial (hu^2)}{\partial x} + g.h.\cos(\theta).\frac{\partial h}{\partial x} = g.h.\sin(\theta) - \frac{\tau_c}{\rho} - \frac{g.u^2}{C^2} \qquad (2)$$

$$\rho.h.(w-u) = \rho_0.h_0.w \qquad (3)$$

$$\rho_0.h_0.w.u = \frac{1}{2}.\rho.g.h^2.\cos(\theta) - \tau_c.h_0 \qquad (4)$$

with h : height of the flow, h_o : height of the static fluid, u : vertically averaged velocity , w : propagation velocity of the front of the flow, C : Chézy coefficient, τ_c : critical shear stress, θ : slope of the bed, ρ: density of the fluid.

2.3 Existence of discontinuous roll waves

The purpose of this paragraph is to give necessary conditions for discontinuous roll waves that are solutions of the shallow water equations without diffusion terms. This analysis generalizes the work of Dressler (1949) to a Bingham fluid.

Let us consider the Bingham fluid flow on an infinite plane. First we define dimensionless variables and chose scales. The dimensionless quantities are :

length scales : $H = \frac{h}{h_o}$ and $X = \frac{x.\tan(\theta)}{h_o}$, velocity scales : $U = \frac{u}{\sqrt{g.h_o.\cos(\theta)}}$

and $W = \frac{w}{\sqrt{g.h_o.\cos(\theta)}}$, time scale : $T = \frac{t}{\frac{h_0}{tg(\theta)}\frac{1}{\sqrt{g.h_0.\cos(\theta)}}}$

If we introduce the dimensionless variables in the equations, we finally obtain the dimensionless equations :

$$\frac{\partial H}{\partial T} + \frac{\partial (H.U)}{\partial X} = 0 \qquad (5)$$

$$\frac{\partial H}{\partial T} + U\frac{\partial H}{\partial X} + \frac{\partial H}{\partial X} = 1 - \frac{C^*}{H} - \beta.\frac{U^2}{H} \qquad C^* = \frac{\tau_c}{\rho.g.h_0.\sin(\theta)} ; \beta = \frac{g}{C^2.\tan(\theta)} \qquad (6)$$

$$W = H.(W-U) \quad \text{and} \quad W.U = \frac{1}{2}.H^2 - C^* \qquad (7.1,7.2)$$

The determination of the criteria for roll wave existence requires solution of the free surface profile equation. First of all, we have to write the equations in a moving coordinate system fixed with the front discontinuity of the flow. Let us define $\zeta = X - W.T$, where W represents the dimensionless front velocity propagation. We obtain two linear equations with two unknowns U' and H'. The resolution of this system gives two differential equations between H', U' :

$$H' = \frac{\partial H}{\partial \zeta} = -\frac{H.(1 - \frac{C^*}{H} - \beta.\frac{U^2}{H})}{(U-W)^2 - H} \quad \text{and} \quad U' = \frac{\partial U}{\partial \zeta} = \frac{(U-W).(1 - \frac{C^*}{H} - \beta.\frac{U^2}{H})}{(U-W)^2 - H} \qquad (8, 9)$$

The ratio between the (8) and (9) equations allows us to verify that the relative discharge is a constant : $\frac{H'}{U'} = \frac{H}{W-U}$, and $H\,(W-U) = K = \text{constant}$ (10)

If we insert (10) in the H' expression (8), we finally obtain the non-linear first order equation :

$$\frac{\partial H}{\partial \zeta} = -\frac{H.\left(1 - \frac{C^*}{H} - \beta.\frac{(H.W - K)^2}{H^3}\right)}{\left(\frac{K}{H}\right)^2 - H} \qquad (11)$$

The resolution of this equation will give the profile of the surface. No continuous periodic solutions exist for this equation. We will construct discontinuous periodic solutions piecing together different continuous profiles with hydraulic jumps. We must find the continuous solution having the property that in one section of the flow must be supercritical and subcritical in the remainder. By continuity, there exists a point at the abscissa ζ_0 with fluid's height H_0 and a speed U_0, where the Froude number equals unity (Dressler, 1949) : $W - U_0 = \sqrt{H_0}$. For that point, the denominator of equation (11) is zero. This means that the discontinuity of the free surface is situated at that point, except in the special case when the numerator vanishes also. The critical point is necessarily different from the hydraulic jump, so it may be possible to construct roll-waves only in the special case when the numerator and denominator both vanish. This condition gives the two parameters U_0 and H_0 as a function of nondimensional variables of the flow :

$$H_0 = \left(\frac{-\beta.W + \sqrt{C^*.(1-\beta) + \beta.W^2}}{1-\beta}\right)^2 \qquad (12.1)$$

$$U_0 = \frac{W - \sqrt{C^*.(1-\beta) + \beta.W^2}}{1-\beta} \qquad (12.2)$$

$$K = (W - U_0).H_0 = (H_0)^{(3/2)} \qquad (12.3)$$

Relation (10) is now introduced in the equation (11) to suppress the indetermination. The differential equation for the free surface profile in the continuous zone is given, after some calculations, by :

$$\frac{\partial H}{\partial \zeta} = \frac{H^2 + H.(H_0 - C^* - W^2.\beta) + \beta.H_0^2}{(H_0^2 + H.H_0 + H^2)} \qquad (13)$$

To construct roll waves from equation (13), it is necessary that $(\frac{\partial H}{\partial \zeta})_{H = Ho} > 0$. We finally obtain the following condition for roll-wave formation :

$$2.\beta. \frac{1 - \sqrt{\beta + \frac{C^*.(1-\beta)}{W^2}}}{-\beta + \sqrt{\beta + \frac{C^*.(1-\beta)}{W^2}}} < 1 \qquad (14)$$

3. DISCUSSION OF RESULTS

The inequality (14) defines a domain for the formation of roll-waves. The results are reported in Figure 1, where $X = \frac{C^*.(1-\beta)}{W^2}$:

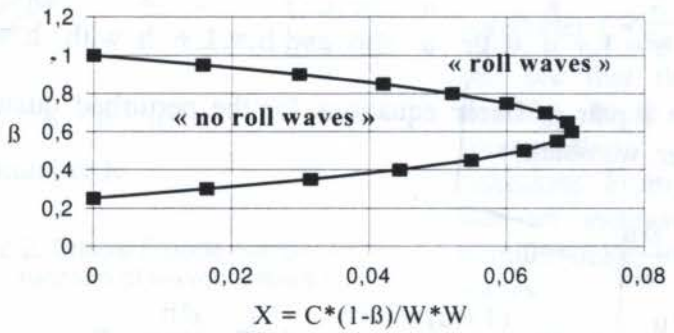

Figure 1: Domain of the roll waves existence

We can see that if the fluid cohesion increases, roll waves can occur more easily because the critical inclination of the long profile decreases. If the fluid's cohesion C* sets to zero, the inequality (14) becomes : $\beta < 0.25 \Leftrightarrow \tan(\theta) > 4\ g / C^2$ and we recover the development conditions of the roll-waves generation defined by Dressler (1949) for clear water.

4. CRITERIA FOR ROLL WAVE FORMATION

The equations used to describe the flow are the same as the previous, but augmented with an additional term υ that represents the viscous dissipation. This additional term allows to take an other dimensionless number into account : the Reynolds number. The α coefficient in the momentum equation takes into account the different velocity profiles.

$$\frac{\partial h}{\partial t} + \frac{\partial (hu)}{\partial x} = 0 \qquad (15)$$

$$\frac{\partial (hu)}{\partial t} + \frac{\partial (\alpha h u^2)}{\partial x} + gh\cos(\theta)\frac{\partial h}{\partial x} = g.h.\sin(\theta) - \frac{\tau_c}{\rho} - \frac{g.u^2}{C^2} + \frac{\partial}{\partial x}\left(h\upsilon\frac{\partial u}{\partial x}\right) \qquad (16)$$

Using the uniform flow to make the equations nondimensional, we obtain length scales : $x = L.x'$, $h = h_n.h'$; velocity scales : $u = u_n.u'$, and shear scale $C^{*\prime} = \frac{\tau_c}{\rho.g.h_n.\sin(\theta)}$ with L is the wavelength. On substituting the dimensionless variables and omitting the ('), we obtain the system :

$$\frac{\partial h}{\partial t} + \frac{\partial (hu)}{\partial x} = 0 \qquad (17)$$

$$\frac{\partial u}{\partial t} + \alpha.u.\frac{\partial u}{\partial x} - (\alpha-1).\frac{u}{h}.\frac{\partial h}{\partial t} + \frac{1}{F^2}.\frac{\partial h}{\partial x} = \frac{\tan(\theta)}{\varepsilon.F^2}.\left((1-C^*).\frac{u^2}{h}\right) + \frac{1}{Re}.\left(\frac{\partial^2 u}{\partial x^2} + \frac{1}{h}.\frac{\partial u}{\partial x}.\frac{\partial h}{\partial x}\right) \qquad (18)$$

with : $F = \frac{u_n}{\sqrt{g.h_n.\cos(\theta)}}$, Froude number ; $Re = \frac{u_n.L}{\nu}$ Reynolds number and $\varepsilon = \frac{h_n}{L}$

We examine first the temporal stability of the uniform flow to small amplitude disturbances by putting : $u = 1 + \hat{u}$ with $\hat{u} << 1$ and $h = 1 + \hat{h}$ with $\hat{h} << 1$. Substituting (17) into (18), we obtain a pair of linear equations for the perturbed quantities $\hat{h}$ and $\hat{u}$. Omitting the (^) character, we obtain :

$$\frac{\partial h}{\partial t} + \frac{\partial h}{\partial x} + \frac{\partial u}{\partial x} = 0 \qquad (19)$$

$$\frac{\partial u}{\partial t} + \alpha.(1+u).\frac{\partial u}{\partial x} - (\alpha-1).\frac{(1+u)}{(1+h)}.\frac{\partial h}{\partial t} + \frac{1}{F^2}.\frac{\partial h}{\partial x} = \qquad (20)$$

$$= \frac{tg(\theta)}{\varepsilon.F^2}\left(1 - \frac{C^*}{(1+h)}(1-C^*)\frac{(1+2.u)}{1+h}\right) + \frac{1}{Re}.\left(\frac{\partial^2 u}{\partial x^2} + \frac{1}{(1+h)}.\frac{\partial u}{\partial x}.\frac{\partial h}{\partial x}\right)$$

Equation (19) is used to eliminate u from (20) to obtain a single equation in h. First of all, it is necessary to differentiate in space equation (20). If we retain only the first order terms, we obtain:

$$\frac{\partial^2 h}{\partial t^2} + 2.\alpha\nu.\frac{\partial^2 h}{\partial x \partial t} + (\alpha - \frac{1}{F^2}).\frac{\partial^2 h}{\partial x^2} = \frac{1}{Re}.\left(\frac{\partial^3 h}{\partial t \partial x^2} + \frac{\partial^3 h}{\partial x^3}\right) - \left(\frac{tg(\theta)}{\varepsilon.F^2}\right)\left(C^*\frac{\partial h}{\partial x} - (1-C^*).\left(-2.\frac{\partial u}{\partial x} - 3\frac{\partial h}{\partial x}\right)\right) \qquad (21)$$

A solution is sought in the form : $h(x,t) = H(k).e^{(ikx-wt)}$ where $w = w_r + i.w_i$, and where for stability we require $w_r \geq 0$. Substitution into (21) gives a quadratic equation with complex

coefficients. Separating real and imaginary parts, we obtain two equations for w_r and w_i that allow us to calculate a fourth-order polynomial $P(w_r)$ in which w_r is the only unknown . After some calculations, we demonstrate that $P(w_r)$ has three turning points (positive values) and $P(w_r)$ is a monotonic decreasing function for] -∞; 0]. A necessary and sufficient condition for all the roots of $P(w_r)$ to be positive is $P(0) \geq 0$. In this case, the mathematical development shows that the critical Froude number is given by :

$$Fc = \sqrt{\frac{1}{\left(\frac{1}{2.(1-C^*) + \frac{k^2.\sigma}{Re}} - (\alpha - 1) \right)^2 - \alpha(\alpha - 1)}} \qquad (22)$$

4.1 Discussion of results

The figures 2 and 3 point out the influence of the wavenumber and Reynolds number on the critical Froude number F_c for different dimensionless cohesion C*. The first one (Fig. 2) shows the influence of the wavenumber k. The parameter $\xi = \frac{\sigma}{Re}$ is set to 0.05. We can see that the disturbances can develop more easily for small wavenumbers and for high cohesions. From figure 3 we can see that an increase in the Reynolds number helps the formation of roll waves.

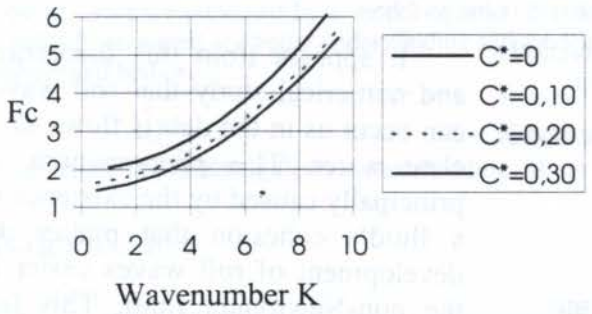

Figure 2: Critical Froude number as a function of wavenumbers k

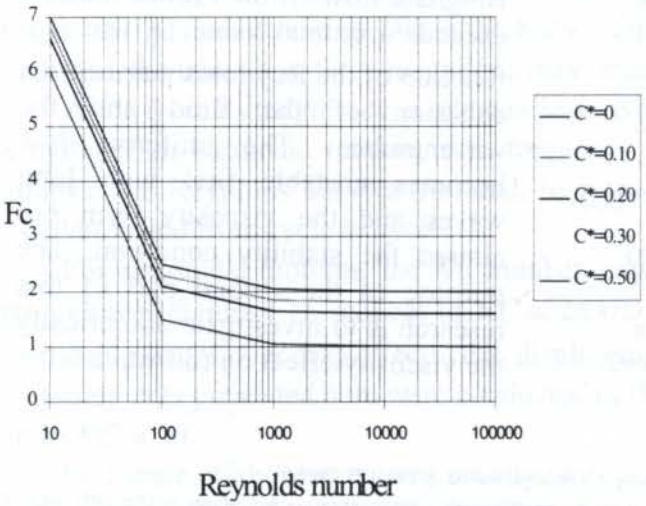

Figure 3: Critical Froude number as a function of the Reynolds number (α=1)

5. NUMERICAL SIMULATIONS

The numerical model was elaborated using a finite volume technique and the Godunov-VanLeer schemes was applied. The two-dimensional model is then used to simulate the development of roll-waves in a 1000 meter long rectangular channel. Firstly, in the clear water (C* = 0), β parameter is constant (β = 0.028) with slope of the channel tan (θ) = 0.30, Chézy number C = 30, and a constant discharge of 800 l/s is imposed at the upstream boundary. A small perturbation (less that 1%) is

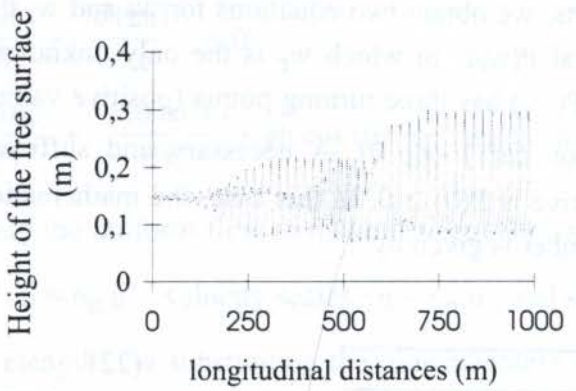

Figure 4: Surface profile with a sinusoidal perturbation (C*=0,ν=0)

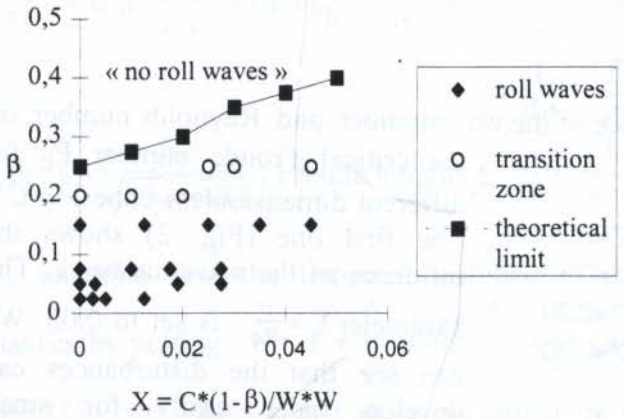

Figure 5: β versus Bingham parameter generating discontinuous roll waves(ν=0)

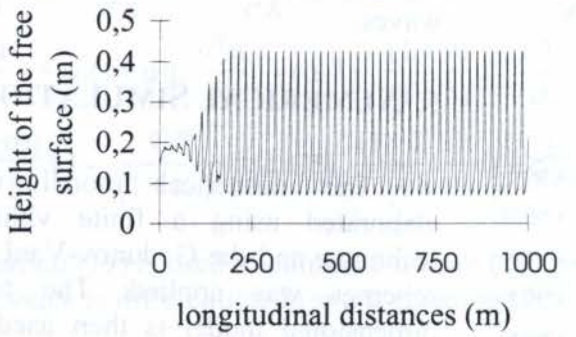

Figure 6: Surface profile with a sinusoidal perturbation (C*=0.2 ,ν=0)

superposed to the average discharge to develop instabilities. We present here the essential results, such as the possibility to generate discontinuous roll waves with certain accuracy using a Saint Venant model. The figure 4 shows the free surface profile generated by a sinusoidal perturbation (with periods T = 3.14 (L=25m); 1.57 (L=12.5m) and 1.00 sec (L=8m) after 200 seconds of calculation time. The roll wave generated presented L=25m(T=3.14)

Secondly, we verified the aptitude of the model generate roll waves taking into account the Bingham parameter ($0 < C^* < 1$) - case of debris flow- whose the results are illustrated in the figure 5 and 6.

6. CONCLUSIONS

It appears from this theoretical and numerical study that roll waves can occur as in the debris flows as in clear water. This phenomenom is principally caused by the existence of a fluid's cohesion that makes the development of roll waves easier in the non-Newtonian fluid. This last result is in according to the experiments performed by Takahashi (1991). Roll waves can appear in Bingham flows if the Froude number exceeds a critical value F_c that is a function of the Reynolds number, the cohesion of the fluid and the wavenumber . The uniform flow becomes unstable first with long waves and the viscosity term not altered the stability condition. The purpose of the second part of this research is to investigate numerically the viscosity effect on roll waves.

7. REFERENCES

Davies, T.R.H Large debris flows : a macro-viscous phenomenon. *Acta Mechanica*, vol 63, p 161-178,1986.

Dresller, R.F Mathematical solution of the problem of roll waves in inclined open channels, *Communs pure appl. Math.*, vol2,p 149-194,1949.

Kranenburg, C. On the evolution of roll waves, *J. Hydraulic Research*, vol. 245, 249-261, 1992.

Martinet, G. Contribution à la modélisation numérique des avalanches de neige dense et des laves torrentielles. Dissertation Univ. Joseph Fourier Grenoble I,1992

Needham, D.J., Merkin, J.H. On roll waves down an open inclined channel, *Proc. R. Soc. Lond* A 394, p 259-278,1984.

Takahashi, T. *Debris Flow*, Monograph, IAHR, Balkema, Rotterdam,1990.

UNESP COBEM 97
XIV Brazilian Congress of Mechanical Engineering
Obeid Plaza Hotel Convention Center - Bauru - SP/Brazil
December 08-12th 1997

PAPER CODE: COB507

LIFT FORCE OF A CYLINDER IN A REVERSING FLOW – MEASUREMENTS AND MODELING

ELYAS FERREIRA DE MEDEIROS, MAURÍCIO PAZINI BRANDÃO, AND RICHARD W. MIKSAD
Instituto de Aeronáutica e Espaço - Centro Técnico Aeroespacial - IAE - CTA
12228-904 - São José dos Campos, Brasil
E-mail: elyasfm@intervale.com, pazini@aer.ita.cta.br, and rwmiksad@virginia.edu

Abstract

Reduced measurements and a semi-empirical equation are presented for the hydrodynamic lift of a circular cylinder in a harmonically oscillating flow. Characteristic loading features associated with vortex shedding and wake returns are clearly shown from the experimental data. The relationship between the flow near the cylinder and the lift is well represented by a model-equation based on added-mass and circulation concepts. This study may help efforts aimed at a better understanding and modeling of the transverse force induced by oscillatory flows on submerged bodies.

Keywords

Hydrodynamic lift, reversing flow, vortex shedding, lift on cylinder.

1. INTRODUCTION

Lift is the hydrodynamic force component normal to the direction of motion of a body. It may be important even for symmetrical shapes, depending upon the nature of motion. A circular cylinder in steady translation may experience lift as a result of the continuous supply of kinetic energy to the trailing vortices as they grow and shed with some asymmetry with respect to the line of motion. When the body moves unsteadily, in particular with reversing of direction, the transverse force magnitude may be as large as the inline force.

Aside from its magnitude, a relevant feature of the lift is the frequency of fluctuation. For a cylinder in harmonic motion, this frequency varies with the Keulegan-Carpenter (KC) number, the Reynolds number (Re) and, to a lesser extent, with the time during a cycle of oscillation and from cycle to cycle.

For sinusoidal motions, the KC number, expressing the flow displacement A relative to the cylinder diameter D, reduces to $KC = 2\pi A/D$. In the range of KC between 1 to about 8, inertia dominates over drag effects. For displacements larger than 25, drag predominates. The measurements presented here were conducted in the inertia and drag-inertia flow regimes, i.e., up to $KC = 20$.

Full-scale offshore structures usually work at Re numbers of the order of 10^6. Here they vary from 1,263 to 25,260, indicating that the experiments are performed in the subcritical regime during which the cylinder's boundary layer is laminar, whereas low-scale turbulence is expected in the wake.

Figure 1 shows time histories of the lift force over the test cylinder for *KC*s up to 20 and frequency parameter $\beta = Re/KC = 1{,}263$. The cylinder is mounted perpendicularly to the incident flow into a square test section of an oscillating water tunnel. One end of the cylinder is attached to a water-proof high-sensitivity load-cell, while the other is kept free. Precautions have been taken to minimize disturbances of the near-cylinder flow by end effects. Besides the lift, inline forces and fluid measurements, with the aid of laser velocimetry, have been simultaneously acquired for mappings and modeling purposes (Medeiros, 1995).

In Figure 1 one notices the randomly fluctuating character of the lift trace. Despite the sinusoidal variation of the driving flow, as indicated by the farflow velocity trace at the bottom, it is very unlikely that the nearflow structures repeat periodically. Even at flow oscillations as small as one diameter of amplitude, turbulence and vortices formation can trigger nonstationary lift fluctuations as shown.

These fluctuations have challenged modelers (Justesen, 1991, Sibetheros *et al.*, 1997) of wave forces on cylindrical structures. An approach to represent the main features of the fluctuating lift has been the development of models based on time-averaged data (Bearman *et al.*, 1984, Lambrakos *et al.*, 1987).

In this paper, reduced measurements of the lift show the degree of its fluctuations about representative time-averaged histories of the flow loading. A sound data processing operation on the lift even allows the identification of the phenomenon of wake returns intermittently upwashing and downwashing the cylinder. To the authors best knowledge, information regarding a steady state component of the lift on a circular cylinder is here first time published. In addition, statistical quantities are shown along with discussions of a model-equation for the lift over representative flow oscillation patterns.

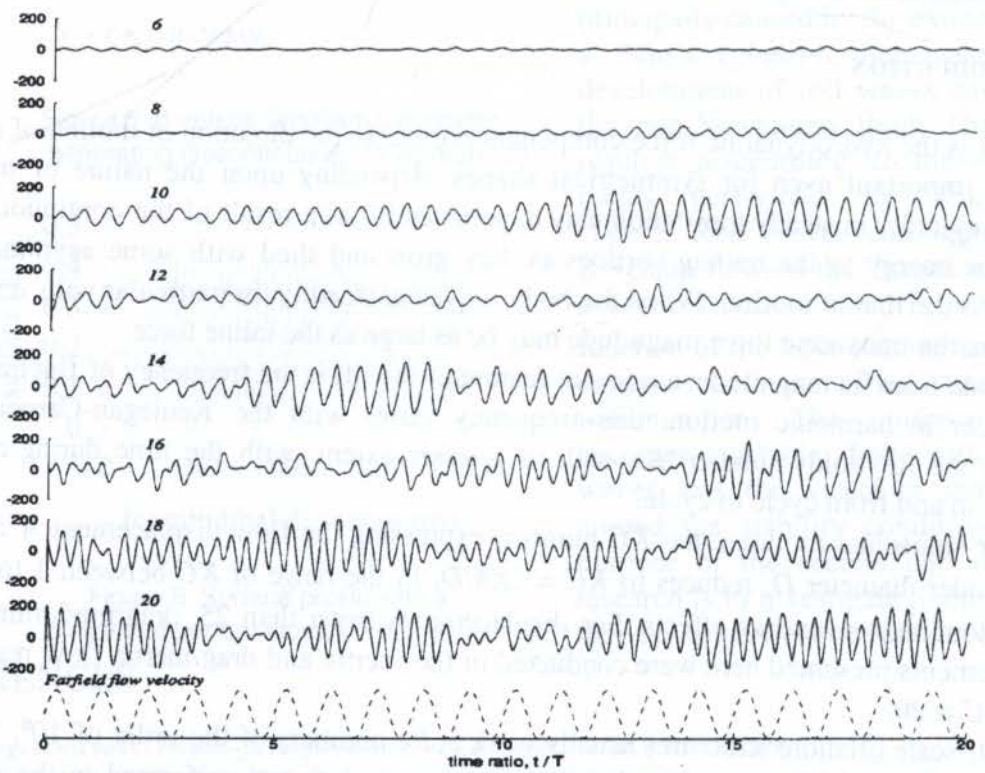

Figure 1 - Time traces of lift force on the stationary test cylinder in a harmonically oscillating flow of period $T=1/f_o$. The force coefficient C_L is made dimensionless by $1/2\rho D^3 f_o^2$.

2. LIFT FREQUENCY SPECTRA

As seen in Figure 1, the lift force on the circular cylinder shows random-like time traces. An important part of the study of these time histories is the description of the distribution of energy content with frequency. This description is obtained with the help of auto-power spectrum plots.

The power spectra of the lift for a range of *KC*s up to 20 are shown in Figure 2. This Figure presents as representives of this range, *KC*s equal to 6, 12, 16, and 20. It is seen that weak fluctuating lift on the cylinder appears as early as $KC = 6$ at f_o and $2f_o$ (where f_o is the oscillating water frequency) with both peaks having the same order of magnitude. The f_o component for any *KC* is the effect of the transverse contribution of the near-cylinder flow loading the structure at the frequency of the farflow. The power at f_o remains the lowest among the spectral components because it is the vortex shedding at multiples of f_o that plays a dominant loading role.

The $2f_o$ fluctuation dominates for *KC*s up to about 15. This signifies that the cylinder experiences two alternating pressure pulses in the transverse direction during a half-cycle. Basing on flow visualization findings (Bearman, 1985, Ventre, 1993, Williansom, 1985) and the flow mappings of Medeiros, 1995, one may associate this loading frequency to flow activity as follows:

- In the asymmetric regime $4 < KC < 8$, one dominant vortex is formed and sheds at each half-cycle. Therefore, the first pressure pulse in a half-cycle is due to the return of the bulk recirculating flow from the previous half-cycle, whereas the second pulse is caused by the shedding of the single vortex near the end of the half-cycle. This loading pattern is associated with a return-shedding sequence of vortex activity.
- In the transverse regime $8 < KC < 15$, one pair of vortices sheds during a whole cycle. This means that the pair of lateral vortices grows asymmetrically in a half-cycle and sheds at the beginning of the next. Therefore, the first lift peak is associated with the shedding of the vortices newly grown in the previous half-cycle, whereas the second peak is due to the growth of a pair of vortices in the current half-cycle. This pattern establishes a shedding-growth sequence during a half-cycle.

The power spectrum of the lift for $KC = 16$ distinctly shows two spikes at $2f_o$ and $3f_o$ of the same order of magnitude. Because on both sides of $KC = 16$ the power is predominantly single-peaked, this *KC* behaves as a boundary between two regimes of the flow. Beyond *KC* equal to 16, the spectrum becomes single peaked again, but with different behavior.

The lift force for *KCs* from 17 to 20 fluctuates mainly at $3f_o$. These *KC*s are in the diagonal flow regime in which two vortices are shed sequentially per half-cycle. Therefore, the first peak of the lift is caused by the return of the recirculating flow, and the next two peaks in the half-cycle is due to either the shedding of sequential vortices from the shoulders of the cylinder or the reaching of instantaneous maximum flow asymmetry while the vortices grow. The loading pattern is then established by a return-shedding-shedding sequence or by a return-outgrowth-growth sequence of the lower-upper-lower vortices.

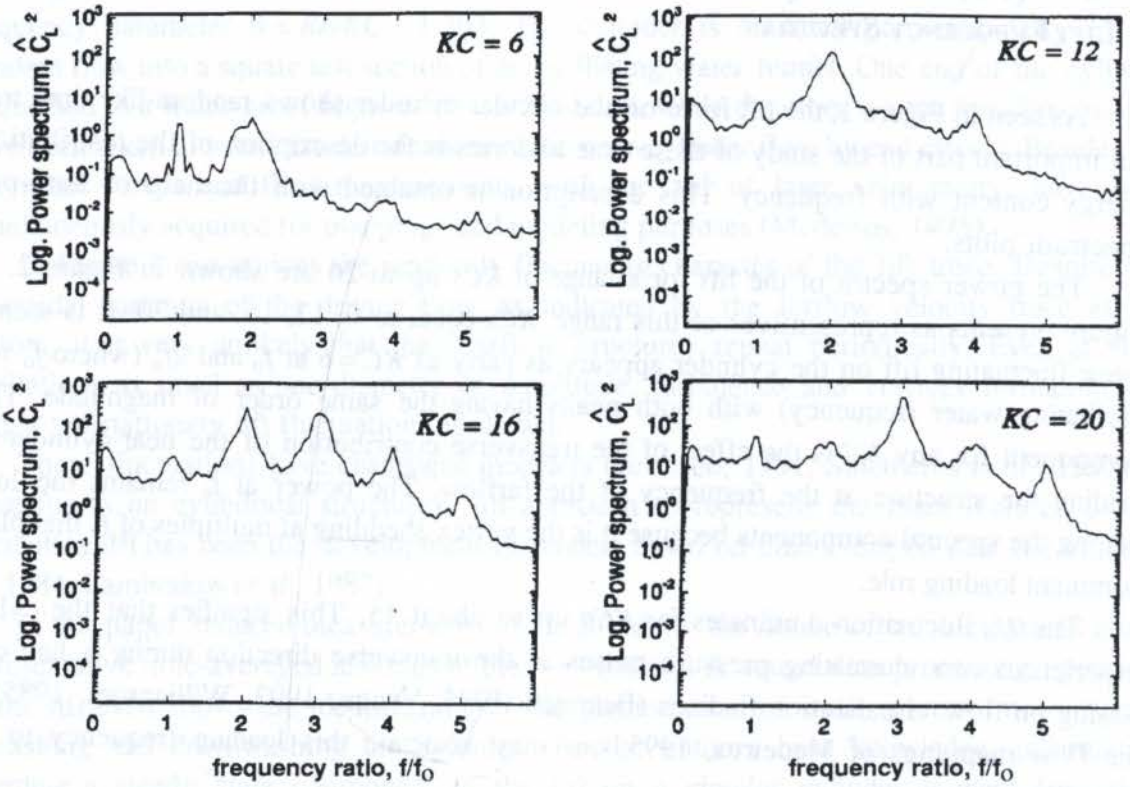

Figure 2 - Autopower spectra of the lift force $C_L^2=L^2(t)/(1/2\rho D^3 f_o^2)^2$ for *KC*s up to 20.

3. STATISTICAL DESCRIPTION OF THE LIFT

Figure 3 shows the standardized probability density function of lift along with statistical quantities for the evaluation of the non-Gaussian nature of the fluctuating lift. The non-dimensional lift magnitude $x = L/L_{max}$ is replaced by the standardized variable $z = (x-\mu_x) / \sigma_x$ which has zero mean and unit standard deviation. For all *KC*s in the range studied, it was found that the lift signals tend to a Gaussian distribution except by a negligible skewness and small positive kurtosis. Considering that no random data can be truly Gaussian (Bendat and Piersol, 1986), the present results imply that the fluctuating lift force of a cylinder in harmonic flows can be considered Gaussian distributed to a good extent. This assumption has important facilitating consequences regarding linear mathematical operations, integration and the taking of Fourier transforms in modeling procedures.

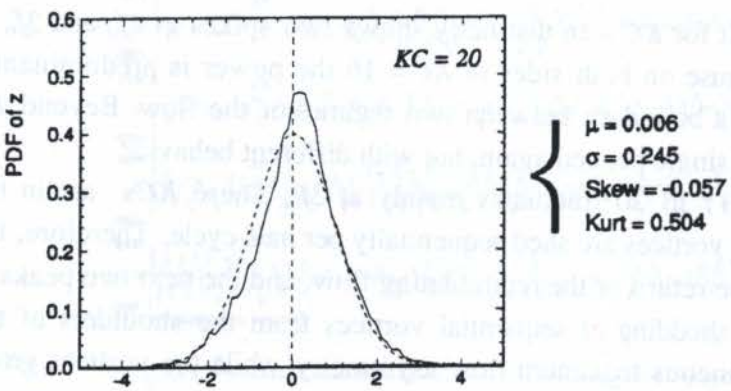

Figure 3 - Standardized probability density function of the lift force contrasted to the Gaussian one. Statistical quantities (mean μ_x, standard deviation σ_x, skewness and kurtosis) of the lift

4. TIME-AVERAGED LIFT WAVEFORMS

Efforts have been dedicated to the modeling of lift on cylinders (Bearman, *et al.*, 1984, Justesen, 1991). As previously shown through the statistical analysis, the lift on a circular cylinder in a planar harmonic flow fluctuates randomly. These fluctuations are related to changes in the spectral frequencies, phase angles and/or amplitudes. Although not discussed here, time traces of the lift are quite invariant in frequency for a flow at any constant *KC* number. Thus, the irregularity of the lift magnitude may be primarily caused by changes in the initial phases and/or in the amplitudes of the lift's harmonic components.

To determine how phase of the dominant spectral component is distributed over the cycles of oscillations, the probability density function of phase of the lift force is being presented. Figure 4 shows the probability density functions of phase computed using Equation 1. The total number of cycles per *KC* number and the phase resolution $\Delta\alpha_o$ used in the computation were 480 and 10°, respectively.

$$P(\alpha) \equiv \frac{\text{Number of cycles for which } \alpha \text{ lies in the range } \alpha - \frac{1}{2}\Delta\alpha_0 \le \alpha \le \alpha + \frac{1}{2}\Delta\alpha_0}{(\text{Total number of cycles}) \times \Delta\alpha_0} \qquad (1)$$

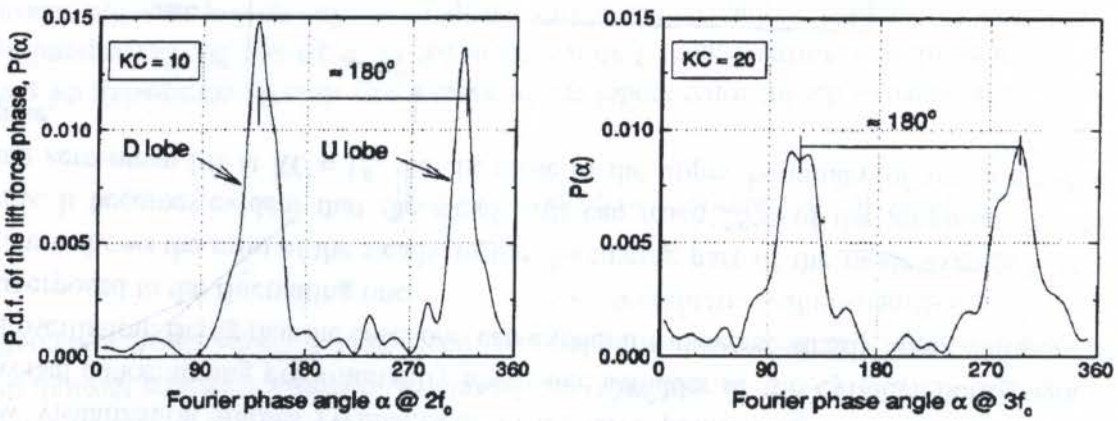

Figure 4 - Probability density functions of phase of the lift force computed according to Eq. 1.

Figure 4 is showing that the phase α of the predominant harmonic component $A_n \sin(2\pi\, nf_o\, t + \alpha)$ of the lift assumes in an average sense two values which differs by approximately 180 degrees. This particular behavior of reversing flows about circular cylinders means that, as the wake returns, it can intermittently upwash or downwash the body. The resulting lift would then alternate sign at same cycle times, as Figure 5 illustrates.

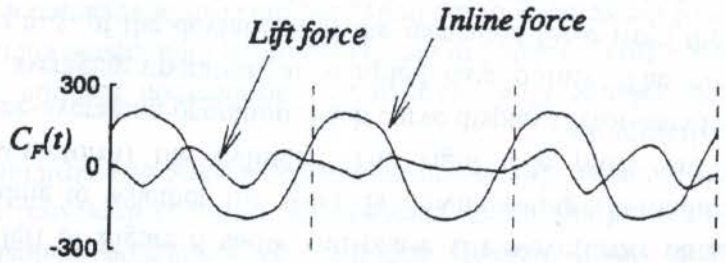

Figure 5 - Sign change of the lift due to the wake switching from a downwash to an upwash of

Being able to discriminate the mirror-image upwash and downwash modes of wake returns, enables more accurate time-averaging of the measurements. Otherwise, conventional ensemble averaging would cancel out data in the image flow modes.

The plots on the left of Figure 6 show anti-phase lift waveforms obtained by time-averaging the lift according to whether the wake is downwashing (*D*-mode waveform) or upwashing (*U*-mode waveform) the cylinder. The right side plots are from a non-discriminating global time-averaging operation. Each curve displays error-bars for an indication of the accuracy of the averaging operation at sampled data points. The error-bars' semi-lengths are equal to the r.m.s. of the deviations of the measured force from the time-averaged force multiplied by the absolute value of a scaling factor $r' = (r.m.s._{cycle} - r.m.s._{series})/r.m.s._{series}$. The $r.m.s._{series}$ is the true r.m.s. computed over the entire time series, and $r.m.s._{cycle}$ is the estimated r.m.s. of the corresponding averaged waveform. That is, r' factor is actually a figure-of-merit of the averaging technique.

5. STEADY STATE COMPONENT OF THE LIFT

Flow visualization studies (Williamson, 1985) have pointed out vortex shedding and wake reversal concentrating predominantly about one shoulder of the cylinder during whole cycles of oscillation. Being that the case, one can expect a transverse steady force component acting superposed to the fluctuating one.

Figure 6 shows the ratio of the steady to the fluctuating part of the mode-averaged force waveforms. It becomes evident that the steady lift can reach 25% of the amplitude of the fluctuating zero-mean lift at $KC = 15$, that is, close to the upper boundary of the transverse flow regime.

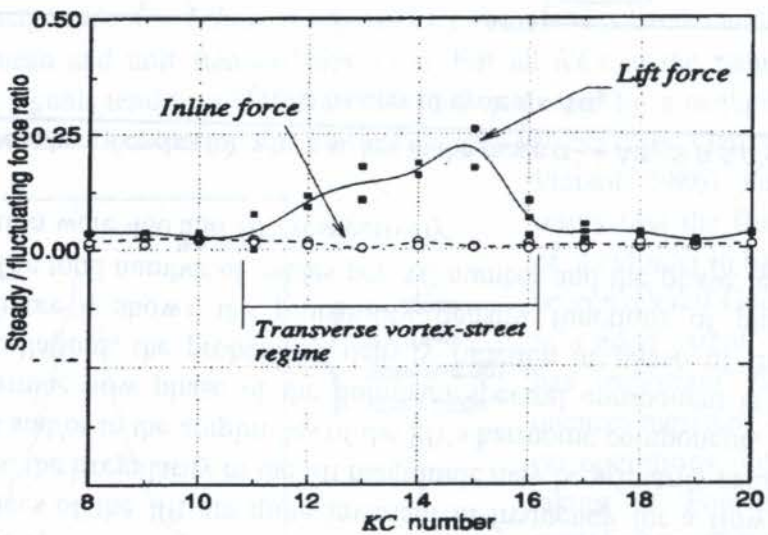

Figure 6 - Ratio of the steady magnitude to the fluctuating amplitude of the lift and inline force mode-averaged waveforms.

6. LIFT MODEL-EQUATION

In theoretical aerodynamics, the relationship between the lift force on an airfoil translating with steady velocity and the flow circulation evaluated from the irrotational velocity field around any circuit enclosing the airfoil is expressed by the Kutta-Joukowsky circulation-lift theorem. Circulation models the loading of a structure due to momentum flux and pressure distribution.

When the relative flow is unsteady, acceleration reaction needs modeling as well. Acceleration reaction is related to the change of the total kinetic energy of the fluid in response to the change of the velocity of the body, and thus can be regarded as an added-mass effect. In situations where the flow has some asymmetry about the centerline, the added-mass force contributes to the lift force too. Therefore, in a reversing planar flow, such as the case studied here, the lift force combines cross-stream momentum, pressure distribution, and added-mass effects; all three being time-dependent.

To carry out a predictive equation for the lift over a characteristic cycle of oscillation, the unsteady momentum flux and pressure distribution is here modeled through a generalized unsteady circulation. Being kinetic energy a quadratic function of velocity, it suggests that the added-mass force can be modeled through a squared relation of the fluid's velocity. Putting these information together, the lift force on a two-dimensional body in a sinusoidal flow of far-field velocity $U(t) = U_o \sin(2\pi f_o t)$ can be related to flow kinematics through the equation below, where C_A is the cross-flow added-mass coefficient, C_Γ is the circulation coefficient, and $K(t)$ is the dimensionless circulation.

$$C_L(t) = KC\left[C_A \pi^2 \cos(2\pi n f_o t) + C_\Gamma \sin(2\pi f_o t)\, K(t)\right] \qquad (2)$$

The merit of the lift force model can be assessed by directly contrasting the predicted and measured lift waveforms. Figure 7 shows them for $KC = 10$ and 20. Corresponding values of C_A and C_Γ are also displayed. From direct inspection, the agreement with measurements is good.

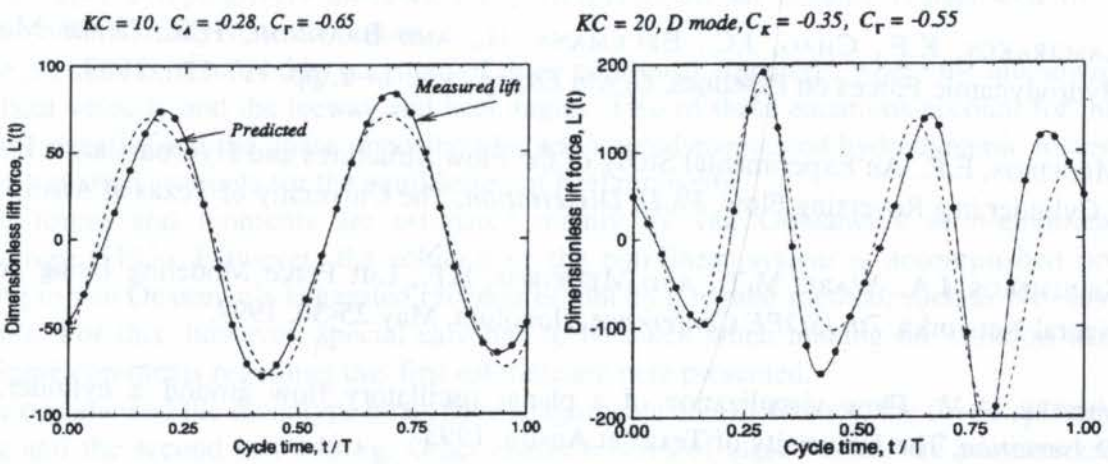

Figure 7 - The use of Eq. 2 to predict the lift at KCs = 10 and 20 compared with measurements

7. CONCLUSION

Reduced measurements of the lift with discrimination between the intermittent upwash and downwash modes of wake returns over the cylinder have been presented. The good performance of the lift expression suggests added-mass and circulation as potentially helpful elements to model unsteady forces on submerged bodies.

8. ACKNOWLEDGMENTS

This material represents results of research supported in part by the US National Science Foundation Engineering Research Center Program, the Texas Offshore Technology Research Center and the Brazilian Air Ministry. The second author would also like to acknowledge research support received from the Brazilian Council of Scientific and Technological Development (CNPq), under grant 300675/96-8.

9. REFERENCES

BEARMAN, P.W., GRAHAM, J.M.R., AND OBASAJU, E.D., A Model Equation for the Transverse Forces on Cylinders in Oscillatory Flows, *Applied Ocean Research,* vol. 6-3, pp. 166-172, 1984.

BEARMAN, P.W., Vortex Trajectories in Oscillatory Flow, *Proceedings of Separated Flow Around Marine Structures*, NIT, Trodheim, Norway, 1985.

BENDAT, J.S. AND PIERSOL, A.G., Random Data – Analysis and Measurements Procedures, *John Wiley,* New York, 1986.

JUSTESEN P., A Numerical Study of Oscillating Flow Around a Circular Cylinder, *J. Fluid Mech.,* vol. 222, pp. 157-196, 1991.

LAMBRAKOS, K.F., CHAO, J.C., BECKMANN, H., AND BRANNON, H.R., Wake Model of Hydrodynamic Forces on Pipelines, *Ocean Engng.,* vol. 14-2, pp. 117-136, 1987.

MEDEIROS, E.F., An Experimental Study of the Flow Structures and Hydrodynamic Forces of a Cylinder in a Reversing Flow, *Ph.D. Dissertation*, The University of Texas at Austin, 1995.

SIBETHEROS, I.A., WARE, M.T., AND MEDEIROS, E.F., Lift Force Modeling Using Artificial Neural Networks, *7th ISOPE Conference,* Honolulu, May 25-30, 1997.

VENTRE, A.V., Flow visualization of a planar oscillatory flow around a cylinder, *M.Sc. Dissertation*, The University of Texas at Austin, 1993.

WILLIAMSON, C.H.K., Sinusoidal flow relative to circular cylinders, *J. Fluid Mech.,* vol. 155, pp. 141-174, 1985.

XIV Brazilian Congress of Mechanical Engineering
Obeid Plaza Hotel Convention Center - Bauru - SP/Brazil
December 08-12th 1997

PAPER CODE: COB726

APPLICATION OF A SAILING YACHT VELOCITY PREDICTION PROGRAM TO A MONOTYPE AND AN OCEANIC SAILBOAT

MARDEL BONGIOVANNI DE CONTI
RODRIGO CÉSAR FRANCESCHINI DE OLIVEIRA
Departamento de Engenharia Naval e Oceânica - EPUSP
Av. Prof. Mello Moraes, 2231 - São Paulo (SP) - CEP 05508-900 - E-mail: mbdconti@usp.br

Abstract

This paper analyses the steady-state performance of an oceanic yacht cruiser and of a monotype sailboat. The first one is here considered with three sails, namely the main, the jib and the spinnaker, and the last one just with a main sail. True wind incidence angle is varied from 0 to 180 degrees. Three wind velocity amplitudes are considered: 9, 15 and 20 knots. The boat velocity and the leeway and heel angles are determined by solution of three non-linear equations. Two of these equations express magnitude equality and phase opposition between aerodynamic and hydrodynamic forces, and the third expresses equilibrium of heel moments. Suggestions for the first guess of the boat velocity, leeway and heel are made, in order to initialize the solution of the non-linear system. Some discussion about the shadow zone, the heel angles on close-hauled, the spinnaker rising effect and the true wind magnitude effect is presented.

Keywords

Naval Architecture, Yacht Design, Sail Propulsion, Sail Boat Performance

1. INTRODUCTION

This paper comparatively analyses the performance of an oceanic cruiser and of a monotype hull in steady-state conditions.

The problem is described by a system of three non-linear equations, where the unknowns are the boat velocity and the leeway and heel angles. Two of these equations account for the magnitude equality and the phase opposition between aerodynamic and hydrodynamic forces. The third equation accounts for the equilibrium of heel moments.

The forces and moments are estimated mainly by van Oossanen's semi-empirical methodology (1993). However, the solution of the non-linear system is accomplished not according to van Oossanen's suggested procedures, but by a regular method, such as Newton-Raphson's. For this, however, special care had to be taken when making the solution first guess. Some comments regarding this first estimate are here presented.

The oceanic and the monotype boats have a significant size difference, the first displacing 5200 kg and the second just 140 kg. Other characteristics of these vessels are presented in section 3, table 1.

One may question if the solution first guess depend significantly on whether the boat type is oceanic or laser, or just on the wind characteristics.

Other questions of interest may concern the wind incidence angles for which the boats do

not navigate (shadow zone), the heel angles assumed by the boats on close-hauled (situation where the heel angles are specially high), spinnaker rising effect on boat performance, effect of true wind magnitude on boat velocity.

This paper includes some discussion about the aforementioned questions.

2. FORMULATION OF THE PROBLEM AND METHODOLOGY

The boat is supposed to be under constant wind conditions in a steady-state navigation.

The true wind velocity, v_{TW}, and the true wind angle relative to the path of the boat, β'_{TW}, are known.

Figure 1 shows the adopted nomenclature for wind incidence. Figure 2 shows an schematic plan view of the hull with close-reach apparent wind incidence angle.

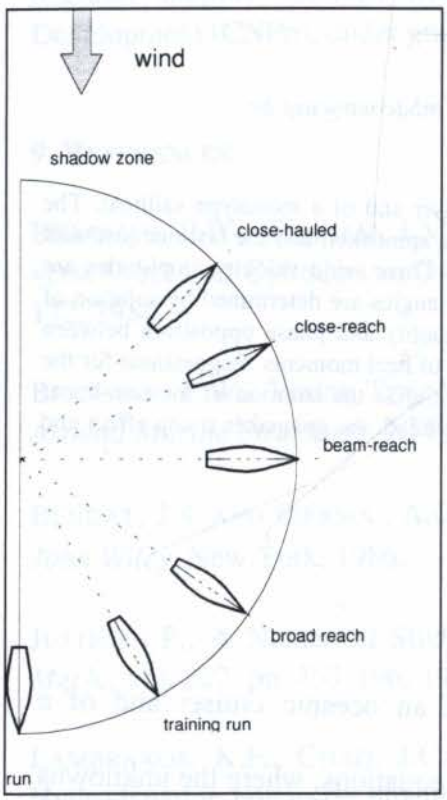

Fig. 1 - Nomenclature for wind incidence.

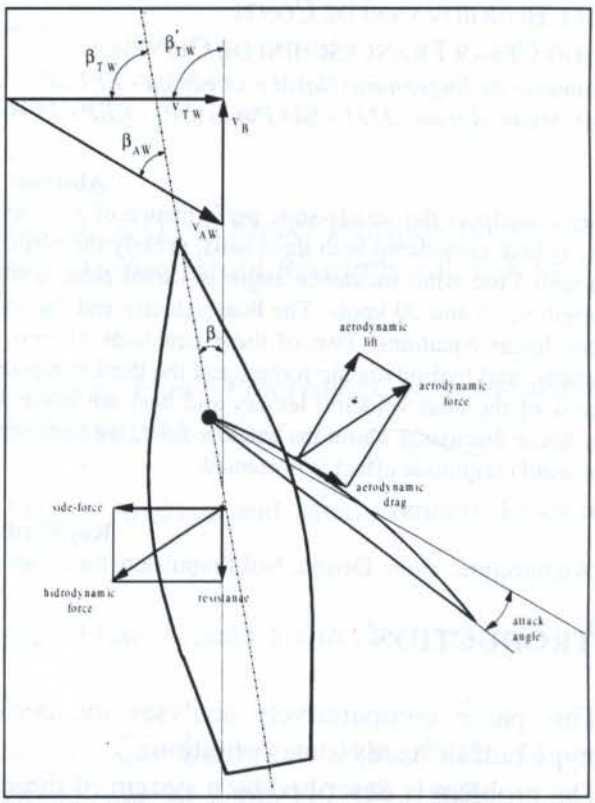

Fig. 2 - Schematic plan view of the hull with close-reach apparent wind incidence angle.

Three parameters are to be determined:

-the boat velocity: v_B;

-the leeway angle (the angle that the boat makes with its path, enabling the generation of lift on the hull and on the keelboard): β;

-the heel angle: ϕ.

The dynamic trim and yaw as well as the vertical displacement of the boat are ignored.

The true wind incidence angle relative to the boat centerline is $\beta_{TW} = \beta'_{TW} - \beta$.

It is interesting to remark the following:

-the angle of attack of the water flow on the boat and keelboard is not just β; it is approximately given by $\beta \cos\phi$, because of the heel;

-the wind conditions felt by the boat are not those in respect to Earth; the so called apparent wind conditions are influenced by the boat velocity; the apparent wind velocity, v_{AW}, and the apparent wind angle relative to the boat centerline, β_{AW}, are determined by:

$$v_{AW} = \sqrt{\left(v_{TW}\cos\beta'_{TW} - v_B\right)^2 + \left(v_{TW}\,\mathrm{sen}\,\beta'_{TW}\right)^2} \;;\; \beta_{AW} = \tan^{-1}\frac{v_{TW}\,\mathrm{sen}\,\beta'_{TW}}{v_{TW}\cos\beta'_{TW} - v_B} - \beta \;;$$

-just the apparent wind velocity component normal to the mast is responsible for the aerodynamic lift;

-optimum main sail trim and sheeting angles are assumed, meaning that for apparent wind close-hauled, close-reach and beam reach incidence, the main sail remains almost aligned to the wind, while for apparent wind broad-reach, training-run and run incidence, it remains at beam.

The determination of v_B, β and ϕ is achieved by the imposition of three equilibrium equations:

-magnitude equality between aerodynamic and hydrodynamic forces;

-phase opposition between aerodynamic and hydrodynamic forces;

-heel moments due to aerodynamic and hydrodynamic forces equal to hydrostatic restoring heel moment plus crew moment.

Expressing the aerodynamic and the hydrodynamic forces and moments in terms of the boat geometric and weight characteristics, of the wind parameters v_{TW} and β'_{TW}, and of the unknowns v_B, β and ϕ, is not so simple. Here the semi-empirical methodology proposed by van Oossanen (1993) is mainly followed, including:

-low aspect ratio formulation for hull lift and induced drag estimation;

-high aspect ratio formulation for keelboard lift estimation;

-Delft series data for residual resistance estimation;

-International Measurement Systems (IMS) data for sail lift and drag coefficients estimation.

The resulting system in v_B, β and ϕ is non-linear, and it is solved iteratively. When using a regular method, such as Newton-Raphson's or some "library routine" based on this method, special care has to be taken to make a good first estimate of the unknowns, so that proper convergence is achieved. This is commented in section 3.

3. RESULTS AND ANALYSIS.

Results for the steady-state performance of an oceanic yacht cruiser and of a monotype sailboat are presented. Some characteristics of these boats are shown in table 1.

Table 1 - Characteristics of the sailboats

	Waterline length (m)	Beam (m)	Draft (m)	Sail area (m^2)	Displacement (kg)	Keel chord (m)	Keel height (m)
Laser	3,50	1,4	0,1	7	140	0,3	0,6
Oceanic	11,6	2,6	0.6	118	5200	1,5	1,5

The oceanic cruiser is here considered with three sails, namely the main, the jib and the spinnaker, and the monotype boat just with a main sail.

True wind incidence angle is varied from 0 to 180 degrees. Three wind velocity amplitudes are considered: 9, 15 and 20 knots.

Figures 3 and 4 show β versus β_{TW} for the oceanic boat with the spinnaker and for the monotype hull.

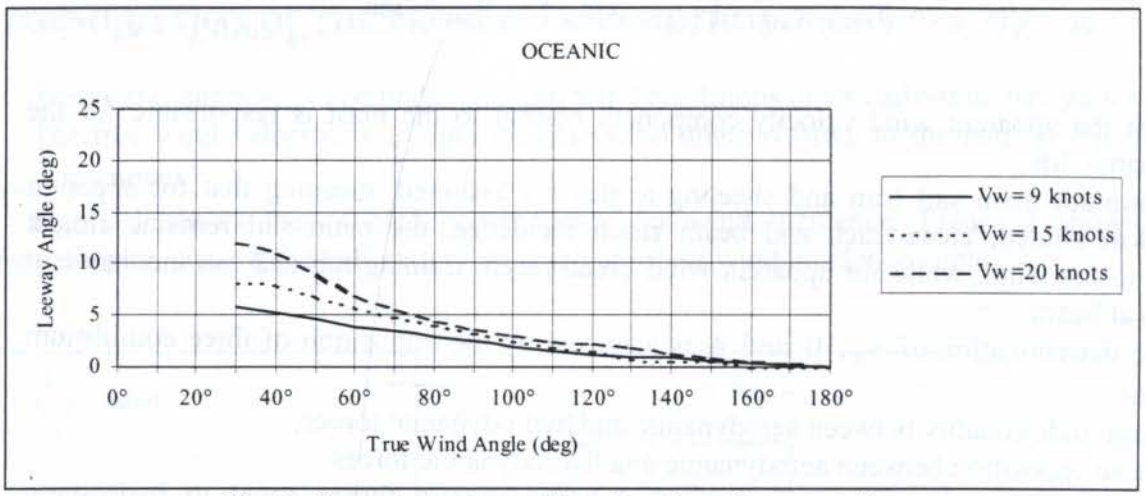

Fig. 3- Oceanic cruiser with spinnaker: β versus β_{TW}.

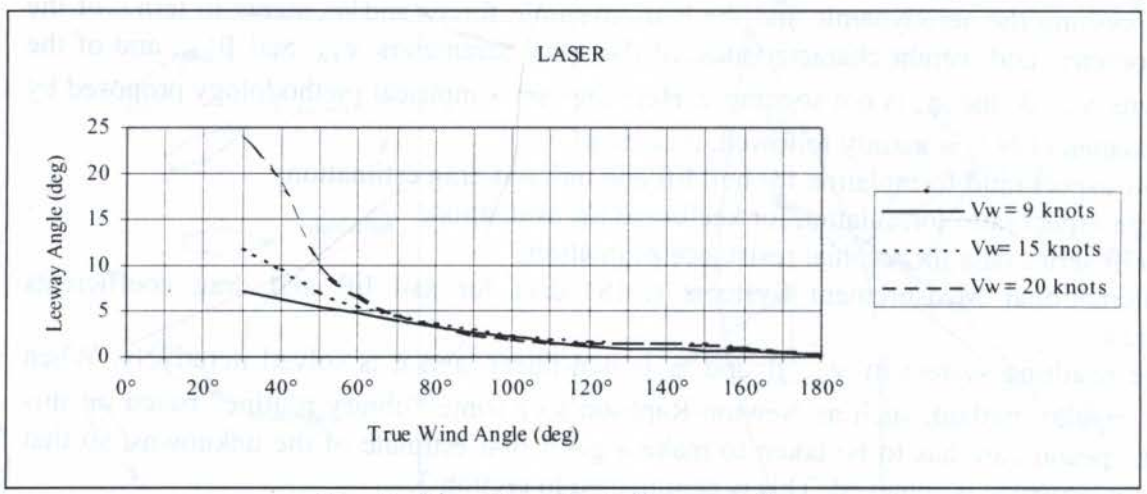

Fig. 4 - Monotype boat: β versus β_{TW}.

The leeway angle β enables that a hydrodynamic lift counterbalances the aerodynamic side force (see figure 2).

Since the aerodynamic side force is most intense for close hauled wind incidence, it is expect that in this case β assumes the higher values.

For incidence angles from beam reach to run, the sails remain almost transverse to the boat, and the generated aerodynamic side force is small. Thus, in this case β is also expected to be small.

These tendencies are confirmed both for the oceanic and for the laser boats. The oceanic boat, however, presents lower leeway angles than the monotype for β_{TW} =30 and 40 degrees. This is related to the better performance of the oceanic hull and keelboard in generating lift.

It can also be noted that the velocity increase from 15 to 20 knots causes a high leeway increase for the laser, that possibly prevents its operation for close hauled.

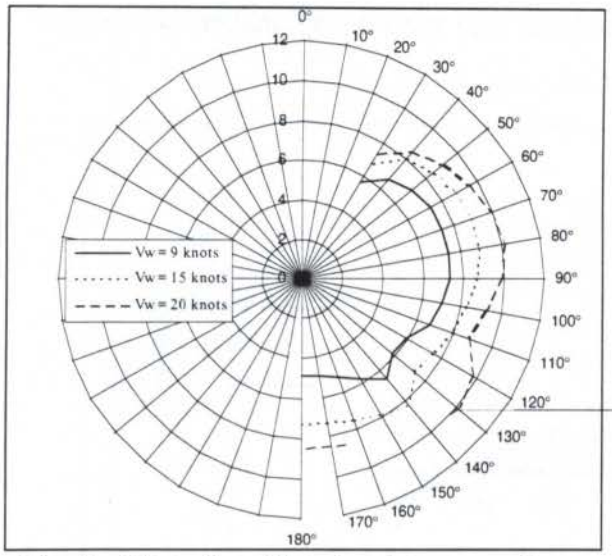

Fig. 5 - Oceanic with spinnaker: $v_B \times \beta_{TW}$.

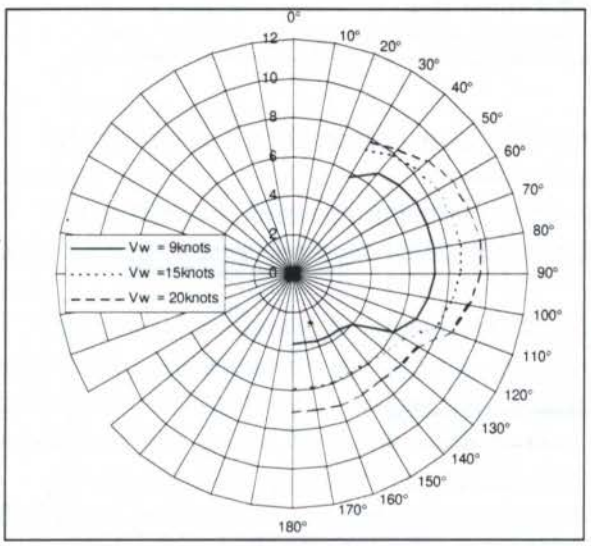

Fig. 6 - Oceanic without spinnaker: $v_B \times \beta_{TW}$.

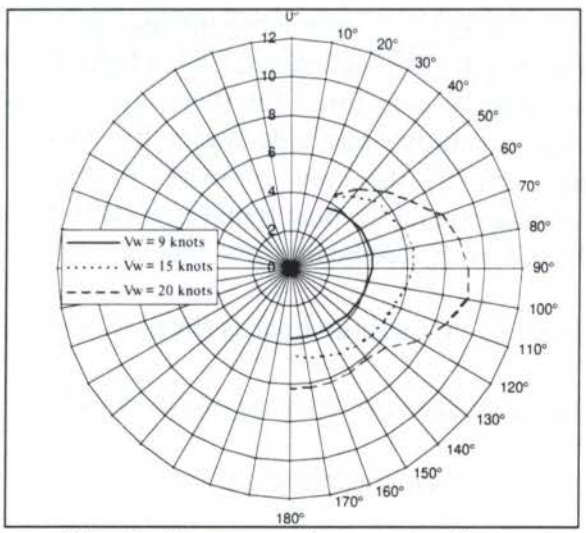

Fig. 7 - Monotype boat: $v_B \times \beta_{TW}$.

Figures 5 to 7 show v_B versus β_{TW} for the oceanic boat with and without the spinnaker, and for the monotype hull. In these figures, v_B is the radial coordinate, β_{TW} is the polar angle, and each curve refer to each value of v_{TW}.

Comparing figures 5 and 6, one notes a subtle increase in boat velocity on broad reach, due to spinnaker raising. On broad reach the spinnaker is responsible for more than 2 knots of increase in boat velocity when v_{TW}=20 knots.

For true wind incidence angles between 0 and circa 30 degrees there is a shadow zone, where the boats cannot navigate. This is due to the fact that the propulsive component of the aerodynamic lift is less intense than the longitudinal component of the aerodynamic drag plus the hydrodynamic resistance.

The best performance of the laser is on beam reach. As for the oceanic yacht, its best performance round close reach is again obtained on broad reach, due to the spinnaker.

The oceanic boat performance for higher velocities is not so efficient as for lower ones. This effect is not so evident for the laser.

For oceanic yachts, higher boat velocities are more difficult to be reached as the wind velocity grows. Therefore special care must be taken in the hydrodynamic boat design so as to minimize hydrodynamic resistance.

It is interesting to notice that both types of boats reaches comparable velocities, despite their significant size difference.

Figures 8 and 9 show ϕ versus β_{TW} for the oceanic boat with the spinnaker and for the monotype hull.

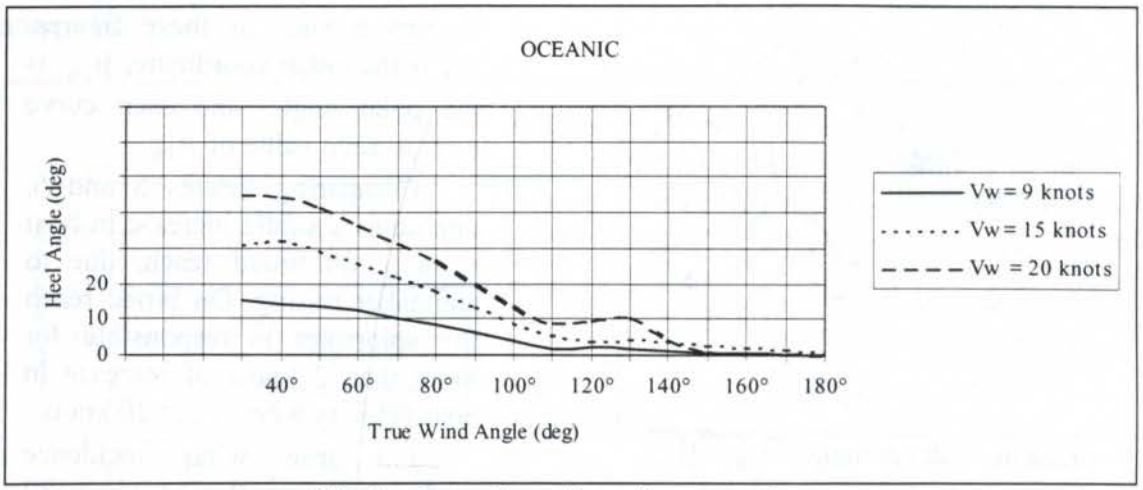

Fig. 8 - Oceanic cruiser: ϕ versus β_{TW}.

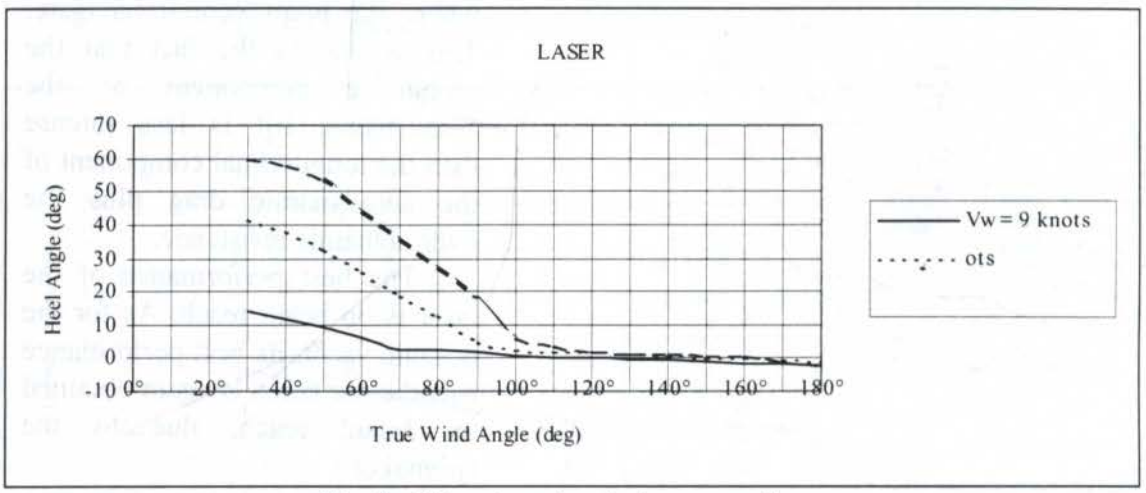

Fig. 9 - Monotype boat: ϕ versus β_{TW}.

Heel angles are largest on close hauled (see figures 8 and 9), being more intense for the laser than for the oceanic yacht. This confirms the tendency for the leeway angle (see figures 3 and 4), and is related to the higher values of aerodynamic side force for these incidence angles. The heel moment due to the hydrodynamic and aerodynamic side forces has to be counterbalanced by the hydrostatic righting moment and by the crew moment. Righting moment is in fact low for the laser, being crew positioning crucial for boat transverse stability. The oceanic boat can be also fitted with a bulb and with keelboard low ballast which contribute to stability.

The increase in heel angles for the laser in respect to the oceanic boat is proportionally not so intense as the increase in leeway angles.

For true wind velocity of 20 knots, it is not expected that the laser navigates on close hauled, since heel and leeway angles are very large.

Figure 10 shows the relation between β_{AW} and β_{TW} for the oceanic yacht for v_{TW} equal to 15 knots.

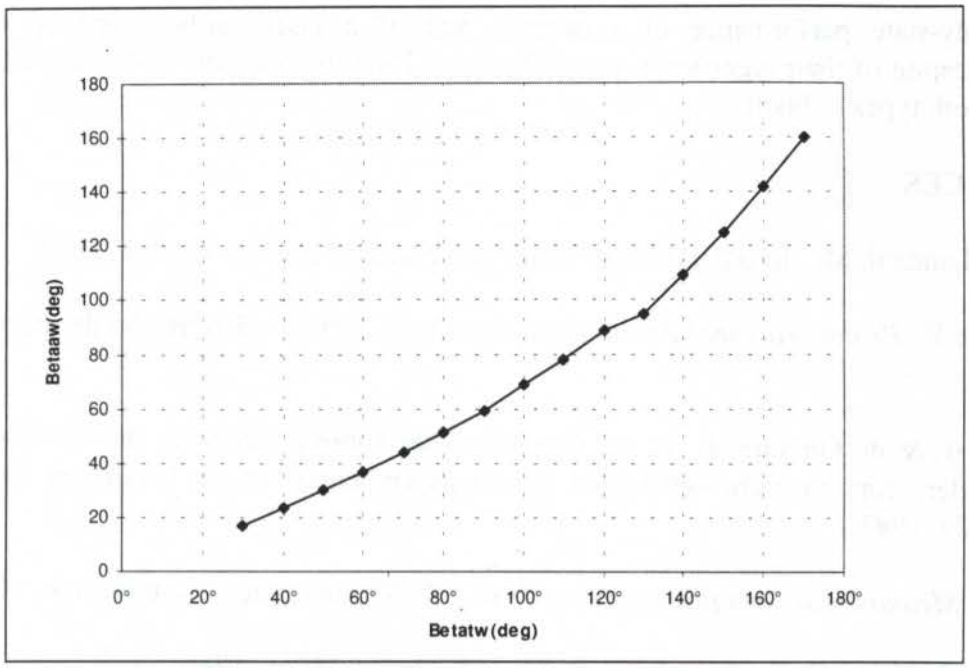

Fig. 10 - Oceanic cruiser β_{AW} versus β_{TW}.

Just the curve for the oceanic boat has been shown in figure 10, but the laser has a similar behavior.

The difference between apparent wind and true wind angles is more pronounced for clause hauled, where the boat navigates upwind. For downwind these angles tend to be the same.

Eventually, it should be remarked that the solution of the non-linear set of equations could be accomplished for the oceanic and the laser sailboats, except for the shadow zone. A regular Newton-Raphson's method may in fact be used, but care shall be taken when making the solution first guess. It is suggested that:

-the steady-state performance prediction begins for run and training run, where the leeway and heel angles are approximately null; the initial value for the boat velocity may be estimated to be circa 25 to 35% of the wind velocity;

-the performance prediction is conducted for lower wind incidence angles (broad reach, beam reach, close reach and close hauled), adopting the initial heel and leeway estimates as the last ones obtained, plus some increase; this increase shall be more intense for β_{TW} <100 degrees.

The steady-state performance of a oceanic and of a laser sailboat proved to be comparable, despite of their significant size difference. Thus the solution first guess may be the same for both types of boats.

5. REFERENCES

Ashley, H. & Landahl, M.. *Aerodynamics of wings and bodies*. Addison-Wesley, 1965.

Campos, M. de P.. *Projeto racional de embarcações a vela*. EPUSP, dissertação de mestrado, 1995.

de Conti, M. B. & de Oliveira, R. C. F.. Considerações sobre a dinâmica de veleiros tipo "laser" e "holder" com base em verificação de seu desempenho "in situ". *Boletim Técnico PNV-USP* n. 29, 1997.

Guedes, P. L.. *Metodologia para projeto de veleiros*. EPUSP, dissertação de mestrado, 1997.

Kuethe, A. M. & Chow, C.-Y.. *Foundations of Aerodynamics*. Wiley, 1986.

van Oossanen, P.. Predicting the speed of sailing yachts. *Transactions of the SNAME* (Society of Naval Architects and Marine Engineers), v. 101, 1993.

Tema 37

Aerodinâmico

XIV Brazilian Congress of Mechanical Engineering
Obeid Plaza Hotel Convention Center - Bauru - SP/Brazil
December 08-12th 1997

ODINÂMICAS SOBRE UM CILINDRO DE SEÇÃO

/ AERODYNAMIC LOADS ACTING ON A CYLINDER WITH A RECTANGULAR SHAPE

ATA & VANESSA GONÇALVES GUEDES
Mecânica - COPPE/UFRJ
, Brasil - E.mail: hirata@serv.com.ufrj.br

Abstract

body with a complex shape possesses much scientific interest, since it presents ly understood, such as the shadow effect and the blockage effect. In particular, the mic loads on the body is of great technological importance in the analysis and design res, etc. In a previous work it has been shown that the estimate of the drag coefficient hen it is assumed that the body is formed of a combination of simpler bodies. The find alternative and efficient methods to estimate the aerodynamic loads that act on a hape and different aspect ratios, for any value of the Reynolds number. The approach ic to estimate the loads, as well as genetic algorithms to improve the accuracy of the

Keywords

fuzzy logic, genetic algorithm, interference

imento ao redor de um corpo e o cálculo das grandezas a ele associadas mais importantes problemas estudados na Mecânica dos Fluidos e, odinâmica; esta análise desperta um grande interesse científico pelos envolvidos. Do ponto de vista tecnológico, os resultados obtidos

ais complexa. É comum, realizar-se esta análise com a utilização de
s de vento. Com os avanços na área computacional torna-se mais
stas análises com a utilização de simulações numéricas. Uma
ara se realizar simulações numéricas (do escoamento ao redor de
e em se utilizar o método de vórtices, Hirata (1991) e Lewis (1991);
nâmica na região de vorticidade acompanhando, de uma maneira
retos que se originam na superfície do corpo.
o possuir formas complexas, as dificuldades para se analisar o
aumentam consideravelmente. Fenômenos como o efeito de sombra,
n presentes em adição à separação do escoamento e à formação de
. Existe um grande interesse científico em se conhecer e equacionar
são tecnológica para a obtenção de resultados cresce, uma vez que,
engenharia, predominam este tipo de situação. Nestes problemas,
necessita-se conhecer apenas uma grandeza, a força de arrasto, por
s a procura de procedimentos alternativos à análise completa do
ar resultados imediatos e de boa qualidade.
Guedes *et al.* (1996) apresentaram um procedimento eficiente para
te de arrasto de um corpo rombudo de formas complexas; o
nentos de lógica nebulosa para estimar a grandeza procurada.
utilizados para calibrar o procedimento numa fase preliminar e,
lhorar a precisão do valor estimado a cada utilização (ou n
ho os autores utilizam um enfoque global, procurando estimar
eficiente de arrasto, ou seja, o coeficiente de arrasto é tratado como
omo conseqüência o procedimento fica associado a uma geometria
7) mostra a possibilidade de se utilizar um procedimento
nte da geometria. No procedimento composicional o corpo é visto
outros de formas simples, como ilustra a figura (1).

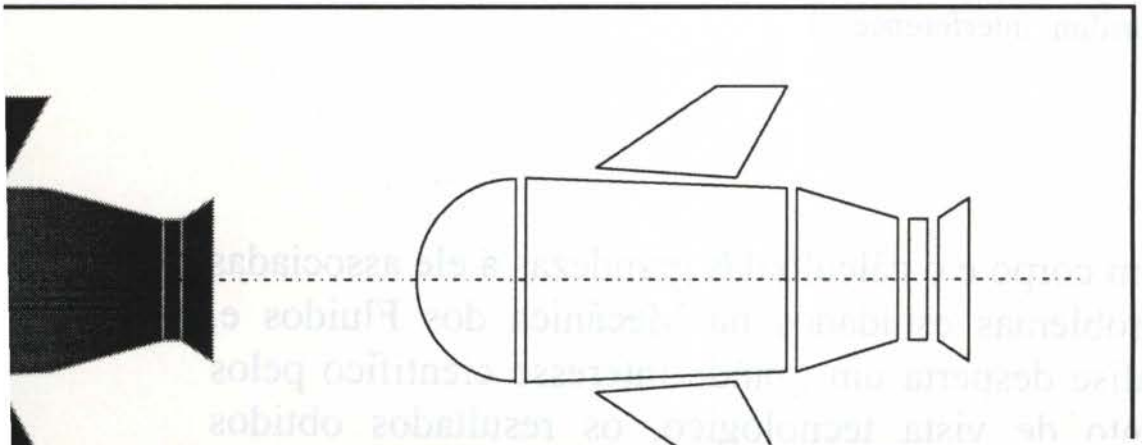

eficiente de arrasto de um corpo simples (i). Por sua vez, cada C_D^i é

coeficiente de arrasto do corpo simples (i) quando isolado e S_{ij} o cia do corpo (j) sobre o corpo (i). O coeficiente S_{ij} depende da posição e assumir valores positivos, negativos ou nulos , não é simétrico e é vel nebulosa.

m sempre está disponível na literatura e, freqüentemente, os valores todas a condições necessárias. Esta é a motivação básica deste n procedimento para se estimar $C_{D\infty}^i$. Com esta finalidade escolheu-se gular, por ser esta uma das formas mais básicas na composição de um s resultados obtidos por Guedes *et al.* (1996), embora não incluam os tivam o desenvolvimento de um procedimento que tenha como gica nebulosa combinada com os algoritmos genéticos. Com este stimar o valor de $C_{D\infty}^i$ para um retângulo, em função do número de te de esbeltez ou razão de aspecto. Evidentemente os procedimentos icados para outros corpos rombudos que possuam arestas vivas.

sumida aos elementos da lógica nebulosa e dos algoritmos genéticos n Guedes (1997), enquanto que uma abordagem mais completa é 95) e Goldberg (1989).

TO DE UM CORPO ROMBUDO

D, é a componente da força aerodinâmica que atua sobre um corpo, nento. Esta pode ser calculada integrando-se a tensão que atua sobre a malmente, pode-se dizer que ela possui uma componente associada à ão, D_f, doravante componente viscosa, e outra à parte normal, D_p, a de pressão. A análise dimensional mostra que

(1)

s aspectos, a expressão (1) é re-escrita como:

$$\frac{D_f}{\frac{1}{2}\rho U^2 h} = C_{dp}^h + C_{df}^h \qquad (2)$$

ma forma mais conveniente

$$\frac{\alpha(\varepsilon)}{\varepsilon} C_f \qquad (3)$$

coeficiente de atrito de uma placa plana e $\alpha(\varepsilon)$ é uma função que

sbeltez.

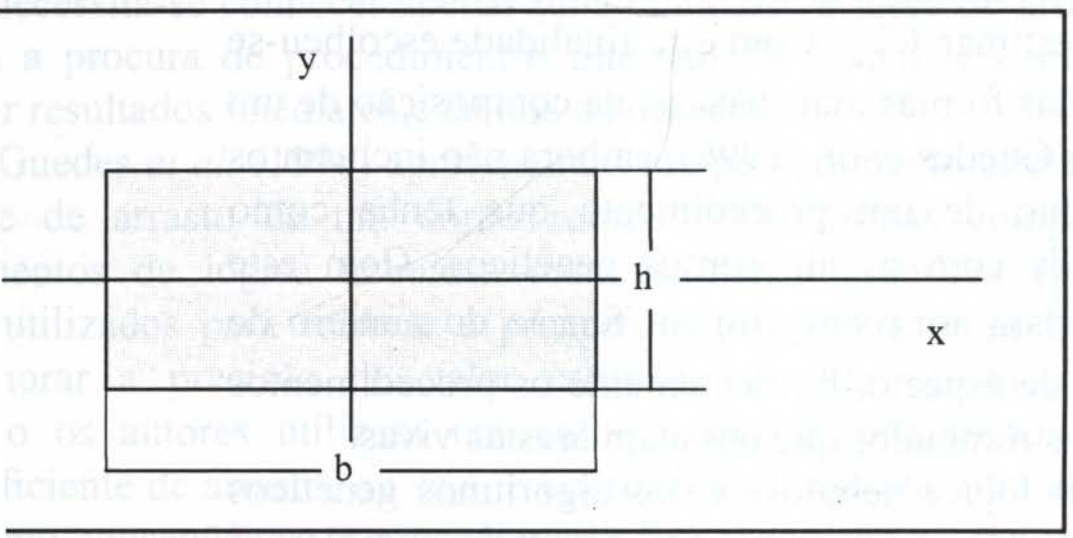

Figura 2 : Cilindro de seção retangular.

pecto baixa: $\varepsilon < \varepsilon_o$

$\rightarrow 0$ a forma do corpo tende para uma placa plana, orientada scoamento e, de uma maneira geral, tem-se $D \approx Dp$ e,

(4)

rmente com Re_h, assumindo os valores 4.0 e 6.0, respectivamente

Tabela 1: Valores Assumidos por C_{dp}^{h} , ε e Re_h

	Re_h		ε	
	SÍMBOLO	VALOR	SÍMBOLO	VALOR
AIXO	CR	CREEPING	EB	EXTREM. BAIXO
IXO	L1	LAMINAR 1	MB	MUITO BAIXO
	L2	LAMINAR 2	B	BAIXO
	TR	TRANSIÇÃO	M	MÉDIO
	T1	TURBULENTO 1	A	ALTO
TO	T2	TURBULENTO 2	MA	MUITO ALTO
ALTO			EA	EXTREM.ALTO

Tabela 2 : Matriz Relacional para cálculo de C_{d}^{h}

EB	MB	B	M	A	MA	EA
MB	MB	MB	EB	EB	BX	BX
MB	M	MB	MB	EB	EB	BX
M	A	M	MB	MB	EB	EB
A	MA	A	M	MB	MB	EB
MA	EA	MA	A	M	B	MB
MA	EA	MA	A	M	B	MB

le aspecto muito alta: ε→∞

o deforma-se numa placa plana alinhada com o escoamento, logo ente, tem-se

arte relativa ao arrasto de forma, as seguintes observações são feitas
e Re_h , o valor de C_{dp}^h deve continuar a sua tendência de queda suave
de ε, anulando-se quando $\varepsilon \to \infty$
, o valor de C_{dp}^h assume uma variação suave e contínua ao passar pelas

ε , o valor de C_{dp}^h deve aumentar suavemente com o valor de Re_h
omponente viscosa é estimada levando-se em conta que:
do corpo tende para uma placa plana alinhada com o escoamento e

ne valores menores a importância relativa de D_f para o arrasto total

estimado para $\varepsilon \to \infty$, em princípio, só é válido para a placa plana;
ue ele pode ser utilizado para valores finitos de ε com uma pequena
$\alpha(\varepsilon)$ na expressão (3).
nponente viscosa é estimada como

$$\frac{\alpha(\varepsilon)}{\varepsilon} C_f$$

- ε_o) como uma forma adequada para a função α.

isponíveis na literatura e que permitiram uma comparação sistemática
os estão associados aos valores elevados de Reynolds, isto é, $Re_h >$
ltados referem-se a situação analisada no item (2.1), talvez a de maior
a concordância obtida é mostrada na tabela (3).

Tabela 3 : Coeficiente de arrasto para $Re_h > 10^4$

0.5	0.6	0.8	1.0	1.2	1.5	2.0	2.5	3.0	6.0
2.5	2.8	2.3	2.2	2.1	1.8	1.6	1.4	1.3	0.89
2.47	2.82	2.33	2.28	2.17	1.81	1.76	1.45	1.27	0.97

ssumir. O comportamento inesperado que ocorre para $Re=10^4$, no cil tratamento. Conjectura-se que este comportamento possa ser que C_{dp}^{h} é estimado; no momento, um procedimento alternativo imento.

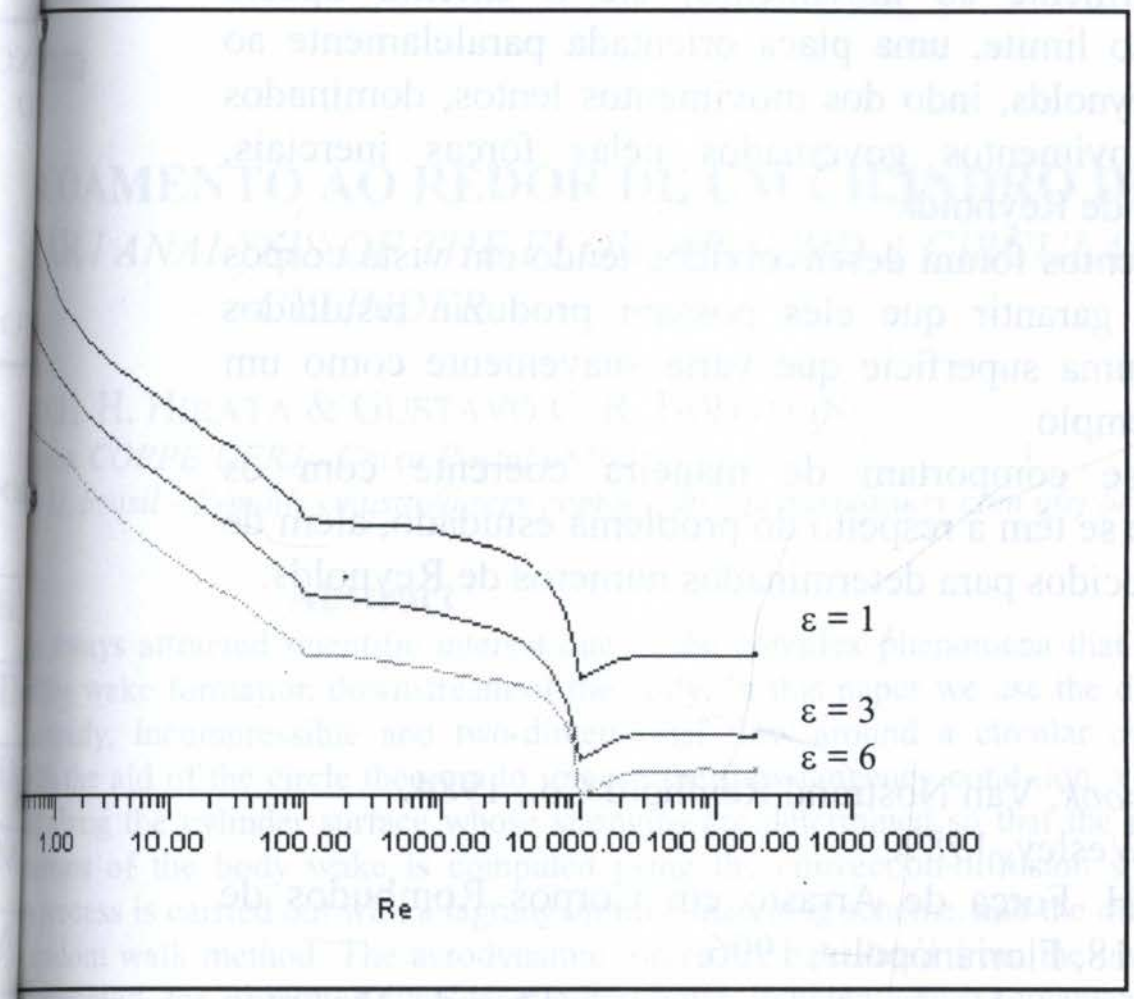

Comportamento do coeficiente de arrasto em função de Re.

a o comportamento de C_{dp}^{h} em função do coeficiente de esbeltez, ero de Reynolds.

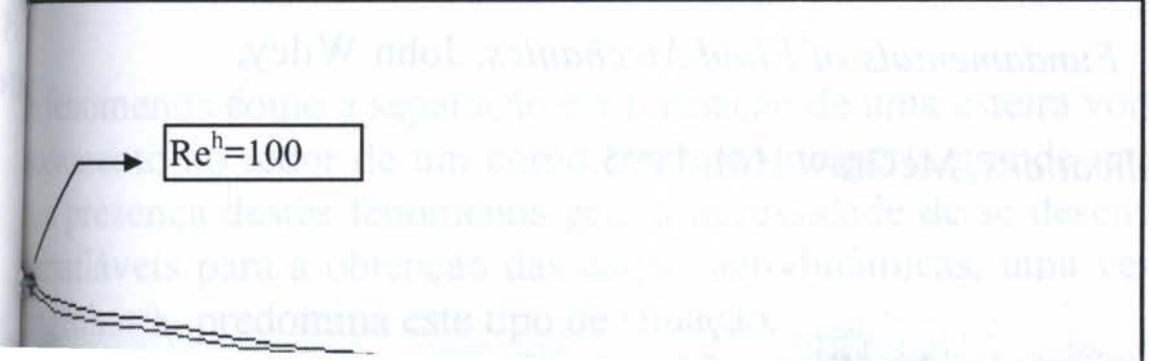

tados permite formular, de uma maneira simples e compatível com as
os procedimentos necessários para se estimar a força de arrasto que
corpo. Os procedimentos incluem desde formas rombudas (no caso
entada perpendicularmente ao movimento) até o extemo oposto
pos esbeltos (no caso limite, uma placa orientada paralelamente ao
n toda a faixa de Reynolds, indo dos movimentos lentos, dominados
osidade, até os movimentos governados pelas forças inerciais,
os valores do número de Reynolds
var que os procedimentos foram desenvolvidos tendo em vista corpos
vivas; não se pode garantir que eles possam produzir resultados
o rombudo possuir uma superfície que varia suavemente como um
ar ou elíptica, por exemplo.
s nos resultados se comportam de maneira coerente com os
ínica dos Fluidos que se têm a respeito do problema estudado, além de
guns valores já conhecidos para determinados números de Reynolds.

luid Dynamic Handbook, Van Nostrand Reinhold Co., 1984.

lgorithms, Addison-Wesley, 1989.

L.P. & Hirata, M.H. Força de Arrasto em Corpos Rombudos de
ENCIT, vol.1, pp.13-18, Florianópolis, 1996.

s da Lógica Nebulosa na Mecânica dos Fluidos, Tese de Mestrado
a de Eng. Mecânica da COPPE/UFRJ, 1997.

o Escoamento de um Fluido Viscoso Utilizando Elementos da Teoria
le Vórtices, *I Congresso Norte-Nordeste de Engenharia Mecânica*,

ment Methods for Fluid Dynamic Analysis of Engineering Systems,

D.F. & Okiishi, T.H. *Fundamentals of Fluid Mechanics*, John Wiley,

vith Engineering Applications, McGraw Hill, 1995.

XIV Brazilian Congress of Mechanical Engineering
Obeid Plaza Hotel Convention Center - Bauru - SP/Brazil
December 08-12th 1997

B1380

SCOAMENTO AO REDOR DE UM CILINDRO DE LAR / *ANALYSIS OF THE FLOW AROUND A CIRCULAR CYLINDER*

MIGUEL H. HIRATA & GUSTAVO C. R. BODSTEIN
ecânica, COPPE/UFRJ - Caixa Postal 68503
, RJ, Brasil - E-mails: mustto@serv.com.ufrj.br; gustavo@serv.com.ufrj.br

Abstract

have always attracted scientific interest due to the complex phenomena that occur, esulting wake formation downstream of the body. In this paper we use the discrete unsteady, incompressible and two-dimensional flow around a circular cylinder . With the aid of the circle theorem to impose the flow-tangency condition, vortices ated along the cylinder surface whose strengths are determined so that the no-slip dynamics of the body wake is computed using the convection-diffusion splitting tion process is carried out with a lagrangian time-marching scheme, and the diffusion he random walk method. The aerodynamic forces are calculated from the unsteady re presented for a high Reynolds number flow, showing good agreement with

Keywords

ema do Círculo, Corpo Rombudo, Esteira, Separação / *Vortex Method, Circle Separation.*

de fenômenos como a separação e a formação de uma esteira vorticosa escoamento ao redor de um corpo rombudo desperta grande interesse do, a presença destes fenômenos gera a necessidade de se desenvolver confiáveis para a obtenção das cargas aerodinâmicas, uma vez que, engenharia, predomina este tipo de situação.

ces, que na última década teve um grande desenvolvimento, apresenta mplementações diferentes e, desta maneira, sente-se a necessidade de ação que sirva de referência. O escoamento ao redor de um cilindro lidato, uma vez que o cilindro é um típico corpo rombudo, possui uma análise do escoamento ao seu redor apresenta inúmeros resultados ser utilizados nas comparações, como, por exemplo, o teorema do on, 1955). Adicionalmente a análise do escoamento ao redor de um nta grande interesse, tendo em vista as inúmeras variações possíveis, n rotação, presença de uma superfície nas proximidades etc., sem etrias não-circulares que podem ser analisadas através da técnica de a partir da solução para um círculo. Estes fatos motivaram a escolha de um cilindro circular como objeto de estudo neste trabalho.

edor de um cilindro circular já foi analisado por outros pesquisadores, ação do método de vórtices, como, por exemplo, Silva (1992). No faz-se uso do teorema do círculo que viabiliza satisfazer, de uma eta (procedimento não iterativo), à condição de impenetrabilidade da velocidade), e, simultaneamente, impõe-se a condição de componente tangencial) em alguns pontos da superfície do corpo. . (1996) utilizaram o método de painéis compostos por fontes para otencial e, a cada incremento do tempo, gerava dois novos vórtices ados no fluido em posições pré-estabelecidas; com este procedimento mento nulo não podia ser garantida; mesmo assim os resultados foram A abordagem de Kamemoto e Kawamata (1986) utiliza painéis stribuição de vórtices que permitem satisfazer apenas à condição de perfície do corpo; porém faz uso da teoria integral de camada limite separação e a intensidade dos vórtices gerados nestes pontos, além de para efetuar a metamorfose de elementos lineares de vorticidade em is (1991) utiliza uma abordagem totalmente numérica, baseada no n distribuição linear de vórtices, para satisfazer simultaneamente às bilidade e escorregamento nulo na superfície do cilindro.

ns a difusão da vorticidade pode ser simulada com a utilização do dômico ou do crescimento do núcleo (Hirata, 1991); no presente utilização do método de avanço randômico porque o método do é essencialmente determinístico. A abordagem utilizada por Arkell e o método de vórtice em célula para acompanhar eficientemente o discretos; com esta abordagem, porém, os efeitos da difusão viscosa ndo uma malha, o que descaracteriza o enfoque lagrangeano.

das fórmulas generalizadas de Blasius, independentemente do buição de pressão na superfície do corpo. Esta característica serve, de se ter uma situação que sirva como termo de comparação para

REDOR DE UM CILINDRO CIRCULAR

argumentos apresentados acima, elegeu-se analisar o escoamento uido newtoniano que ocupa uma região fluida de grandes dimensões, um cilindro de seção circular (bidimensional) e diâmetro d. Esta figura 1. O movimento do fluido é governado pela equação da ções de Navier-Stokes, que podem ser escritas como

(1)

$$\frac{1}{\mathrm{Re}}\nabla^2\mathbf{u}, \qquad (2)$$

de velocidade, p o campo de pressão, e $\mathrm{Re} \equiv Ud/\nu$ o número de metro do cilindro, onde ν é a viscosidade cinemática do fluido. Todas), (2) e nas equações abaixo foram adimensionalizadas por d e U, niforme que incide sobre o cilindro. Sobre a superfície do corpo deve- de aderência, que por conveniência futura é expressa em termos das ngencial da velocidade, isto é,

$r = 1/2$ (condição de impenetrabilidade) (3a)

$r = 1/2$ (condição de escorregamento nulo). (3b)

deve tender ao escoamento uniforme, ou seja,

$r \to \infty$. (3c)

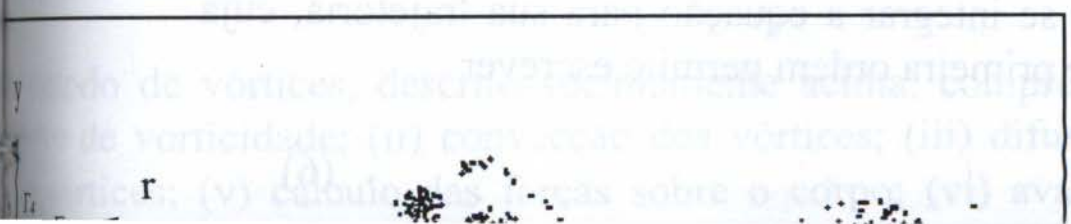

ovimento do fluido, governada pelas Eqs. (1) e (2) e condições de
calculada de forma mais conveniente substituindo-se as equações de
ação de transporte de vorticidade, obtida tomando-se o rotacional da
a equação da continuidade. No caso bidimensional, esta equação é
essa na forma

$$\nabla^2\omega, \qquad (4)$$

onente não-nula do vetor vorticidade (na direção normal ao plano do
de vantagem de se trabalhar com esta equação é a eliminação do termo
requer tratamento especial em métodos numéricos eulerianos.

OLUÇÃO

ces

problema proposto acima foi obtida com a utilização do Método de
ata, 1991). Este método baseia-se na Eq. (4), e faz uso de um algoritmo
erador diferencial convectivo-difusivo, na forma

(5a)

(5b)

scoamento real é gerada na superfície do corpo de modo a satisfazer à
ento nulo, Eq. (3b), e é, então, transportada por convecção e difusão,
. O método de vórtices discretos representa a vorticidade por meio de
discretizar a vorticidade gerada no corpo, cujo transporte a cada
ealizado em duas etapas. Na primeira, utiliza-se uma abordagem
ever o processo de convecção, que é governado pela Eq. (5a). O
tice é determinado ao se integrar a equação para sua trajetória, cuja
m esquema de Euler de primeira ordem permite escrever

(6)

$/P)]$, e $\Delta\theta = 2\pi Q$. (8)

números randômicos entre 0 e 1, calculados segundo o algoritmo

).

dade pode ser construído de modo a satisfazer automaticamente às

g). A partir do teorema do círculo (Milne-Thompson, 1955), a

o, escrita na forma de uma velocidade complexa, é dada por

$$\frac{i}{2\pi}\sum_{k=1}^{N_v}\frac{\Gamma_k}{z-z_k(t)}+\frac{i}{2\pi}\sum_{k=1}^{N_v}\frac{\Gamma_k}{z-z_{k_{im}}(t)}, \quad (9)$$

onentes de **u** nas direções x e y, respectivamente; $i \equiv \sqrt{-1}$; $z \equiv x+iy$ é qualquer do escoamento no plano complexo; z_k e $z_{k_{im}} \equiv 1/(4\bar{z}_k)$ são de intensidade Γ_k e suas imagens no ponto inverso, respectivamente na denota o complexo conjugado); e N_v é o número total de vórtices o (excluindo suas imagens). Observe que as imagens no centro, do círculo, foram desprezadas, uma vez que sua presença afeta a o infinito para um escoamento assimétrico em relação ao eixo x

micas são obtidas a partir da Fórmula de Blasius generalizada para Milne-Thompson, 1955), a qual, aplicada para o problema em questão, 89)

$$[(u_k + iv_k) - (u_{k_{im}} + iv_{k_{im}})], \quad (10)$$

oeficientes de arrasto e sustentação, respectivamente. A fórmula de neira mais conveniente para a determinação das forças aerodinâmicas, e uma integração numérica do campo de pressão.

Método de Solução

o método de vórtices, descrito sucintamente acima, compreende o ração de vorticidade; (ii) convecção dos vórtices; (iii) difusão dos o de vórtices; (v) cálculo das forças sobre o corpo; (vi) avanço no

exista uma soma nos índices repetidos k, sendo j um índice livre. A
o N×N, possui elementos que dependem apenas da posição onde os
da posição dos pontos do corpo onde se impõe a condição de
ndo, portanto, calculada apenas uma vez. O vetor b_j, que é atualizado
po, inclui a contribuição de todo o escoamento sobre os pontos da
ou seja, escoamento uniforme, dipolo, vórtices da esteira e suas
quações (11) é resolvido utilizando-se um algoritmo de eliminação de

rticidade é executado por convecção e difusão, de acordo com as
Para eliminar as singularidades representadas pelos vórtices potenciais
os da Eq. (9), utiliza-se vórtices de Lamb, cuja expressão para a
um vórtice k na direção circunferencial, u_{θ_k}, é

$$\text{xp}[-C(r^2/\sigma_o^2)]\}. \qquad (12)$$

distância entre o centro do vórtice e o ponto do escoamento onde a
alculada, $C = 5.02572$ é uma constante, e σ_o é o núcleo do vórtice,
a diferença entre a Eq. (12) e a expressão para a velocidade induzida
(primeiro termo do lado direito da Eq. (12)) seja desprezível.
etram no corpo ou que ultrapassam uma distância na direção do eixo
a jusante do corpo são eliminados. Uma alternativa ao primeiro
s vórtices que penetram no corpo de volta ao escoamento. Entretanto,
inação é mais freqüentemente utilizado na literatura, uma vez que
mo um modelo ao processo de destruição de vorticidade que ocorre
as regiões de gradiente de pressão adverso da superfície do corpo
o de eliminação a jusante do corpo objetiva apenas reduzir o tempo
justifica devido ao fato de que estes vórtices já se encontram a uma
o corpo, e, portanto, sua influência direta sobre o cálculo das forças é

ONCLUSÕES

entados na seção abaixo foram obtidos para $Re = 4\times10^4$. Este valor
meio da faixa onde o coeficiente de arrasto e o número de Strouhal,
oximadamente constantes, sendo f a freqüência de desprendimento
Blevins (1984), $C_D = 1.1$ e $S = 0.2$ para $Re = 10^4$, e $C_D = 1.2$ e

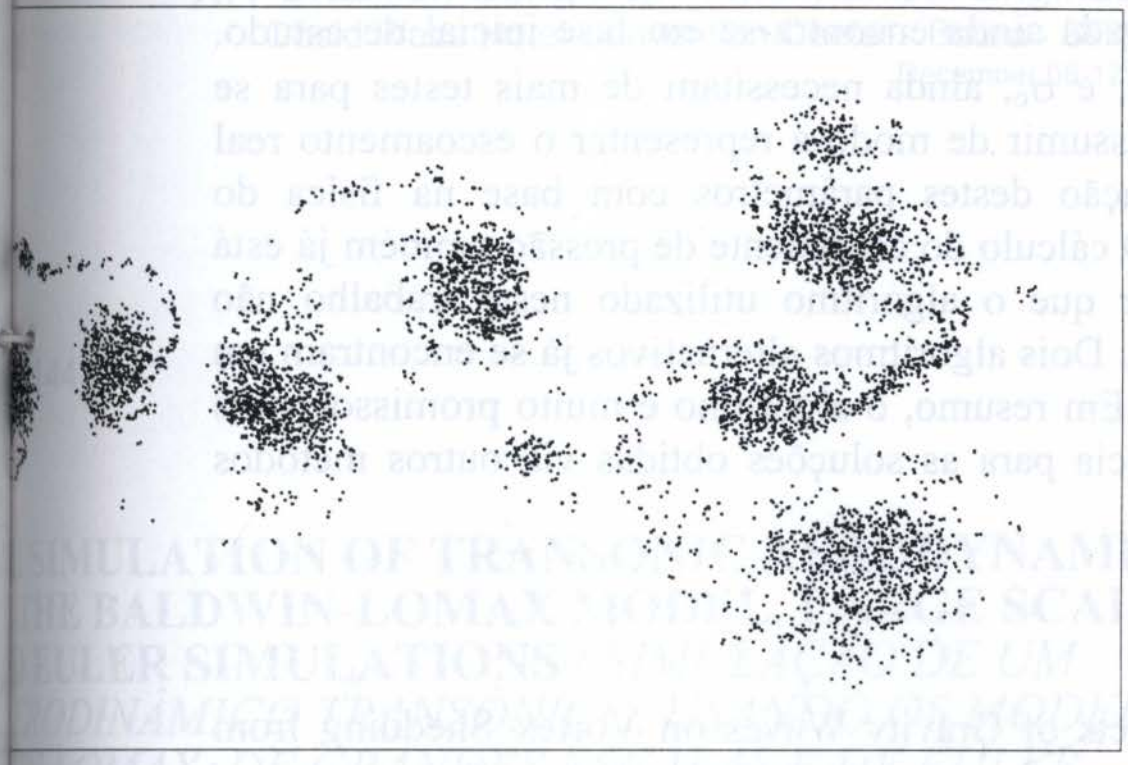

2: Posição dos vórtices na esteira do cilindro em t = 22.5.

das forças aerodinâmicas, calculadas pela Eq. (10), está apresentada
desprendimento dos vórtices pode ser visto na oscilação das forças de
pós o "transiente" ter acabado e o "regime permanente periódico" ter
t = 5.0), o coeficiente de sustentação mostra uma variação entre -1.5
, com uma freqüência adimensional (número de Strouhal) de 0.17,
ente de arrasto apresenta um valor médio de 1.02, e oscila com
aior que o de sustentação, o que está de acordo com os fenômenos
oamento. A simulação, portanto, produziu resultados relativamente
ntais, onde o erro no coeficiente de arrasto é 14% e no número de

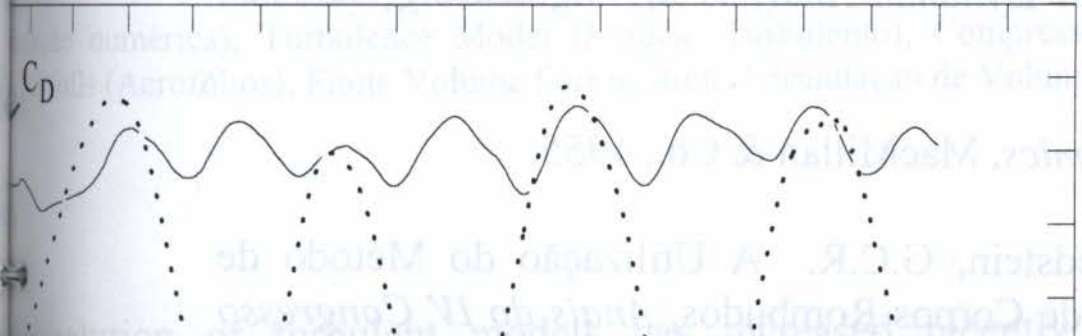

metodologia empregada ainda encontra-se em fase inicial de estudo. tais como N, Δt, ε, e σ_o, ainda necessitam de mais testes para se valores que podem assumir de modo a representar o escoamento real os para a determinação destes parâmetros com base na física do ndo desenvolvidos. O cálculo do coeficiente de pressão também já está Cabe ainda ressaltar que o algoritmo utilizado neste trabalho não global do escoamento. Dois algoritmos alternativos já se encontram em to e implementação. Em resumo, o algoritmo é muito promissor, pois servir como referência para as soluções obtidas via outros métodos

n, J.M.R. The Effects of Gravity Waves on Vortex Shedding from *s of the IUTAM Simposium on Bluff-Body Wakes, Dynamics and* Gottingen, 1992.

Fluid Dynamics Handbook, Van Nostrand Reinhold Co., 1984.

l Study of Slightly Viscous Flow, *Journal of Fluid Mechanics*, Vol. 57,

do Escoamento de um Fluido Viscoso Utilizando Elementos da Teoria de Vórtices, *Anais do I Congresso de Engenharia Mecânica Norte-*

amata, Y. Representation of Two-Dimensional Boundary Layers by *eedings of the International Conference on Computational Mechanics*,

lement Method for Fluid Dynamic Analysis of Engineering Systems, Press, Cambridge, 1991.

Theoretical Hydrodynamics, MacMillan & Co., 1955.

N., Hirata, M.H. & Bodstein, G.C.R. A Utilização do Método de Escoamento ao Redor de Corpos Rombudos, *Anais do IV Congresso*

XIV Brazilian Congress of Mechanical Engineering
Obeid Plaza Hotel Convention Center - Bauru - SP/Brazil
December 08-12th 1997

L SIMULATION OF TRANSONIC AERODYNAMIC THE BALDWIN-LOMAX MODEL, LARGE SCALE D EULER SIMULATIONS / *SIMULAÇÃO DE UM ERODINÂMICO TRANSÔNICO, USANDO OS MODELOS IN-LOMAX, DE GRANDES ESCALAS E DE EULER*

A.
deral University of Uberlândia
ax: (55)(34)239-4106 and e-mail: mbiage@ufu.br
, Brazil

Abstract

rical simulation study to compute a turbulent compressible aerodynamic flows. The the finite volume formulation for spatial discretization and a stepping time procedure iscretiztion. Also, a multigrid procedure is used with aim for speeding up the steady dynamic flows solutions around airfoils in transonic state were performed using Euler ge scale field simulation (LES) and Baldwin-Lomax model. The results achieved are l data available for two kinds of airfoils (NACA0012 and RAE2822), in the transonic equal to $9{,}0 \times 10^6$ and for large variation of attack angles. Some supersonic results pared with analytical evaluations. All computations were made for the three models, icy of the solutions and how expensive they are.

Key words

nulação numérica), Turbulence Model (Modelo Turbulento), Compressible Flows , Airfoils (Aerofólios), Finite Volume Formulation (Formulação de Volumes Finitos).

the solution of turbulent models has increased recently and the

nodels, there are large interest in the use of the algebraic models, due nt simplicity, but especially to the straightforward extension from ses by merely an alternate definition of the viscosity coefficient. It is leling assumption is not satisfactory to model the complex flows. t algebraic models, as that one of Baldwin-Lomax model, have been ss, when applied to evaluate the aerodynamic flows in boundary layer r over solid boundary almost flat. In these cases, the whirling effects or criticism that can be addressed to all algebraic turbulence models, is oo tightly linked to the mean field. Turbulence is described only by ther than by the turbulence properties themselves.

arge Eddy Simulation(LES) model allows to obtain the large scale field lution with the grid filter and the subgrid scales are modeled from the scale field. The definition of what we call the large eddies and what the are, is not trivial and deserves special discussion in view of different the literature. The general reasoning is that the numerical simulation riginal turbulent field rather than a filtered field with a certain filter if the Navier-Stokes equations are approximated by a finite volume luces an approximation-filter, which filters out all subgrid-scales with x, where dx is the mesh spacing, while longer waves are also filtered So this filter is not sharply defined. As a consequence, the subgrid- nsitive to the type of numerical approximation (Moin et al. 1991). Due cale is evaluated from the smoothing solution approach the average ale part is resolved by the numerical method used. Then, we have simulation model with aim to model only the large scale field. The n this work neglects the effect of the subgrid stress and the turbulent he large scale field. The subgrid stress and the transport energy go to idth h goes to zero. In this case, we suppose that the mesh spacing is hese terms can be negligible. Finally, we have proceed the calculation tion.

ations to perform this study was to analyze the transonic flow over E2822), and compare the behavior of flow structure from the solutions Baldwin-lomax with the Large Scale Solution and Euler solution.

L FORMULATION

mean governing equations, we applied the ordinary time average d in Reynolds 1894 and Boussinesq 1897, spliting the instantaneous

total enthalpy and the velocities fluctuations upon the weighting

the $\overline{\tau_{ij}^t}$ and $\overline{q_j^t}$ as general terms for all formulations. For instance,

these terms are modeled appropriately as a function of the large
mulate both the diffusive and the dissipation effect accurately. For
pplied here we neglected these terms.

were used as characterist scales to parametrize the variables in

r the lengths, $\frac{\sqrt{P_\infty^*/\rho_\infty^*}}{L^*}$ for the time, $\sqrt{\frac{P_\infty^*}{\rho_\infty^*}}$ for the velocities, $\frac{P_\infty^*}{\rho_\infty^*}$

y totals, ρ_∞^* for the density, P_∞^* for pressure, μ_∞^* for the dynamic
k_∞^* for the thermal conductivity coefficient. For commodity the
denoted for an asterisk upper-index, the properties of the free-
y the ∞ sub-index and the L^* is the characteristic length (airfoil
ds number.

cterist scale parameters defined above upon the two-dimensional
ions to obtain their dimensionless vectorial form (Lopes 1996).

used to model turbulent transport terms is to establish an analogy
ss and the turbulent stresses (sub-grid scale components). In this
n viscosity law is established for the turbulent stress tensor as

close the energy equation, $\overline{q_j^t}$ must be modeled. Also, is established
olecular heat flux and the eddy diffusivity, as described by Eq. 4.

$$-\frac{2}{3}\delta_{ij}\bar{\rho}K \quad \text{and} \quad \bar{q}_j = \left(-\gamma\frac{\mu_t}{Pr_t}\frac{\partial\tilde{e}}{\partial x_j}\right)\frac{\sqrt{\gamma}M_\infty}{Re_L} \qquad (3,4)$$

scosity coefficient and the K is the mean kinetic energy of the
The Baldwin-Lomax turbulent model is an algebraic model, in
oefficient is express as a function of the quantities of the large-scale
, the turbulent kinetic energy term in the Eq. 3 (the last term of the
le (Baldwin and Lomax 1978).

the stationary solution of turbulent compressible flows. For this, the
ular for each cell of the mesh, in according to the Courant condition.
ed with the three simulations are compared with experimental data
2 airfoil (Harris 1981) and for RAE airfoil (Cook et al. 1979). The
d for an attack angles interval that covers the stol regime and for all
vs. The set graphics of results are standardize in the way where the
ribution over the superior line of airfoil is always the higher line in the

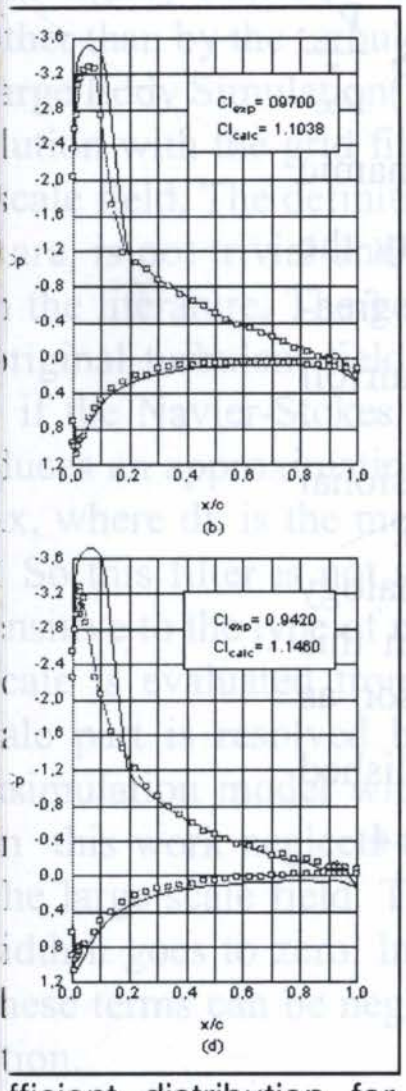

fficient distribution for
$0x10^6$, Ma=0.55; —— EU and —□— 6^0 , (b) $a=8.86^0$, (c)

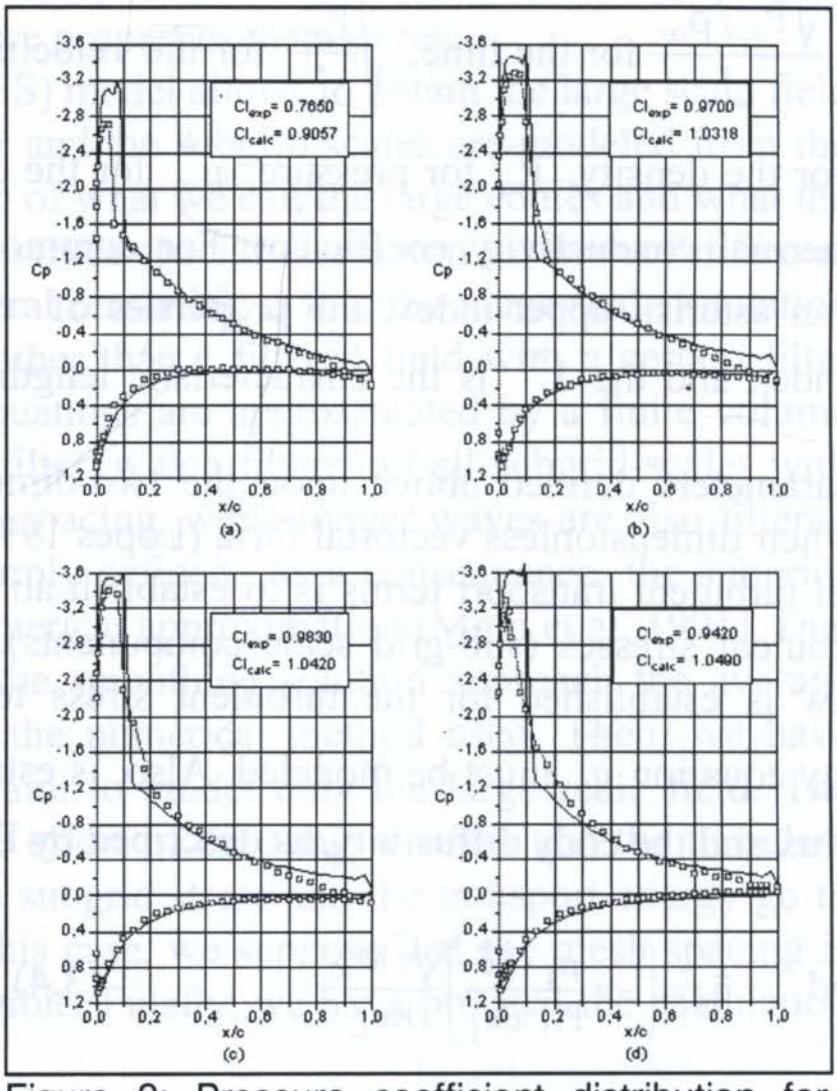

Figure 2: Pressure coefficient distribution for NACA0012 airfoil ($Re=9.0x10^6$, Ma=0.55; —— Theoretical calculation, LES and —□— experimental). (a) $a=6.86^0$, (b) $a=8.86^0$, (c) $a=9.86^0$ and (d) $a=10.86^0$.

results, Figs. 1 and 2 show the pressure coefficient distribution for
$=9.0x10^6$, Ma=0.55, for $\alpha=6.86^0$, $\alpha=8.86^0$, $\alpha=9.86^0$ and $\alpha=10.86^0$,
ngle), using the Euler formulation, EU and Large Scale Simulation,

meric model, using in the computational code, was first order in the on, with aim to dumping the effect of round-off errors, which are n. It was of third order in other regions. We can expect that the anti-ed over-dissipation in the expansion region;
n the Mach number increases the shock waves occur in the expansion discontinuities, the anti-diffusive flux was first order, causing over-on.

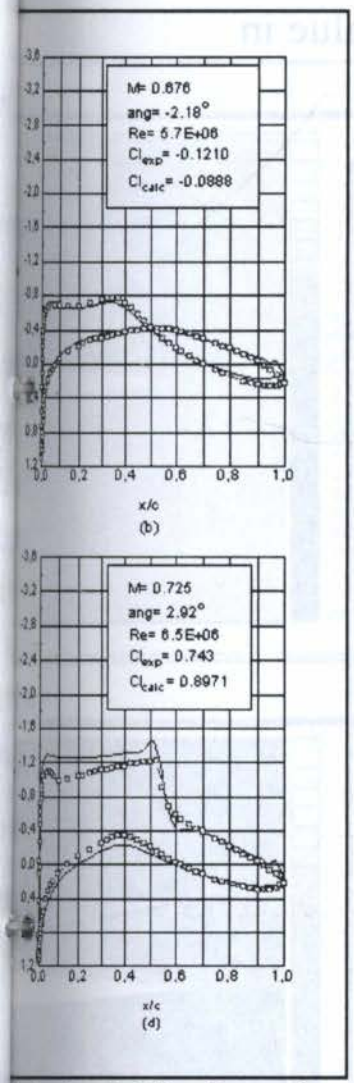

ficient distribution for heoretical calculation, ital). (a) a=2.40^0 , (b) d) a=2.92^0.

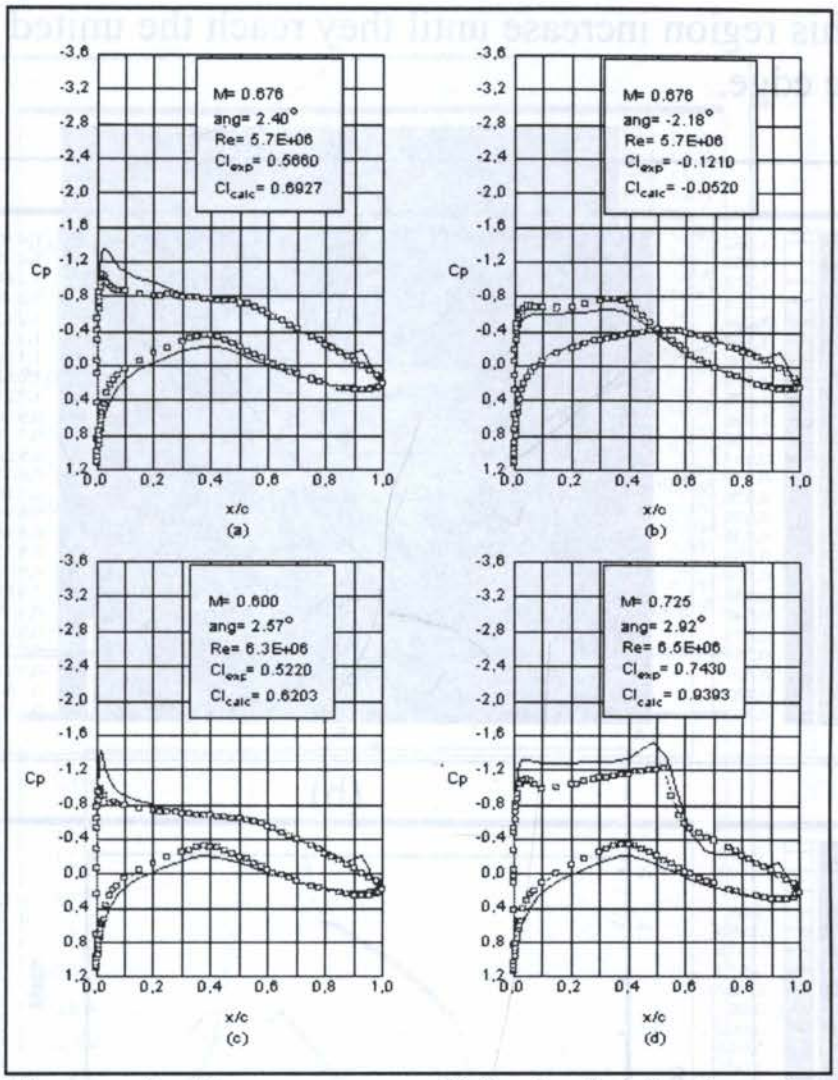

Figure 4- Pressure coefficient distribution for RAE2822 airfoil (—— Theoretical calculation, BL and —□— experimental). (a) a=2.40^0 , (b) a=-2.18^0, (c) a=2.57^0 and (d) a=2.92^0.

ll be presented with aim to enhance the qualitative flow features, formulations. The flow structure evolution over airfoil will be ion of the Mach number and attack angle. Figs. 5 to 7 show some figures are presented the pressure, local Mach number and entropy of the Mach number in horizontal position over the airfoil as showed

s larger when the attack angle increases. For the LES and Baldwin-
ts showed an expansion region larger than that one presented for the
is physically consistent, because of the Euler formulation one neglects
ulent stresses. We suggest that these differences presented in the LES
odel, deriving from the molecular and turbulent stresses, cause a better
re coefficient, as one can remark in Figs. 1 to 4 (essentially by the lift
airfoil middle, the flow is compressed, also upon the inferior and
ts structure maintains as compressing pressure waves that originated in
essure values in this region increase until they reach the united value in
the airfoil escape edge.

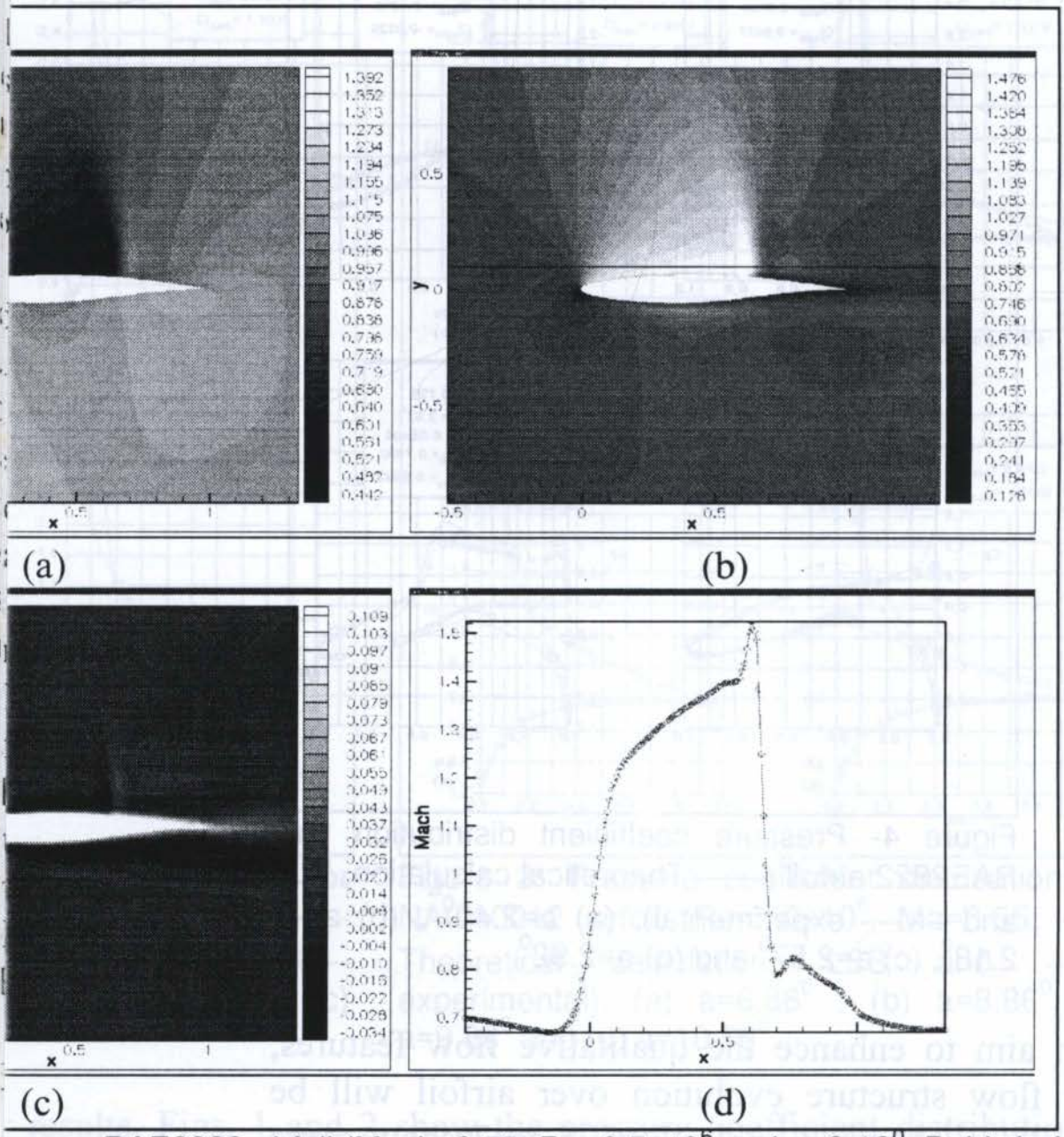

over a RAE2822 airfoil (Mach=0.75, Re=6.5x10^6 and a=3.19^0, Baldwin-Lomax
) local Mach number, (c) entropy and (d) evolution of the Mach number in
e airfoil as showed by black line in Fig. 5.b.

ents the flow disorder degree. One remarked in our results that the the Mach number and with the attack angle provoking disturbance in ect for lower Mach number or smaller attack angle is that where the d, thus the entropy level is lower. The results obtained with LES and tion enhance a boundary layer flow. This flow region and the wake s with the larger entropy values. However, the Euler results showed ent the larger entropy values. The Euler model does not define the

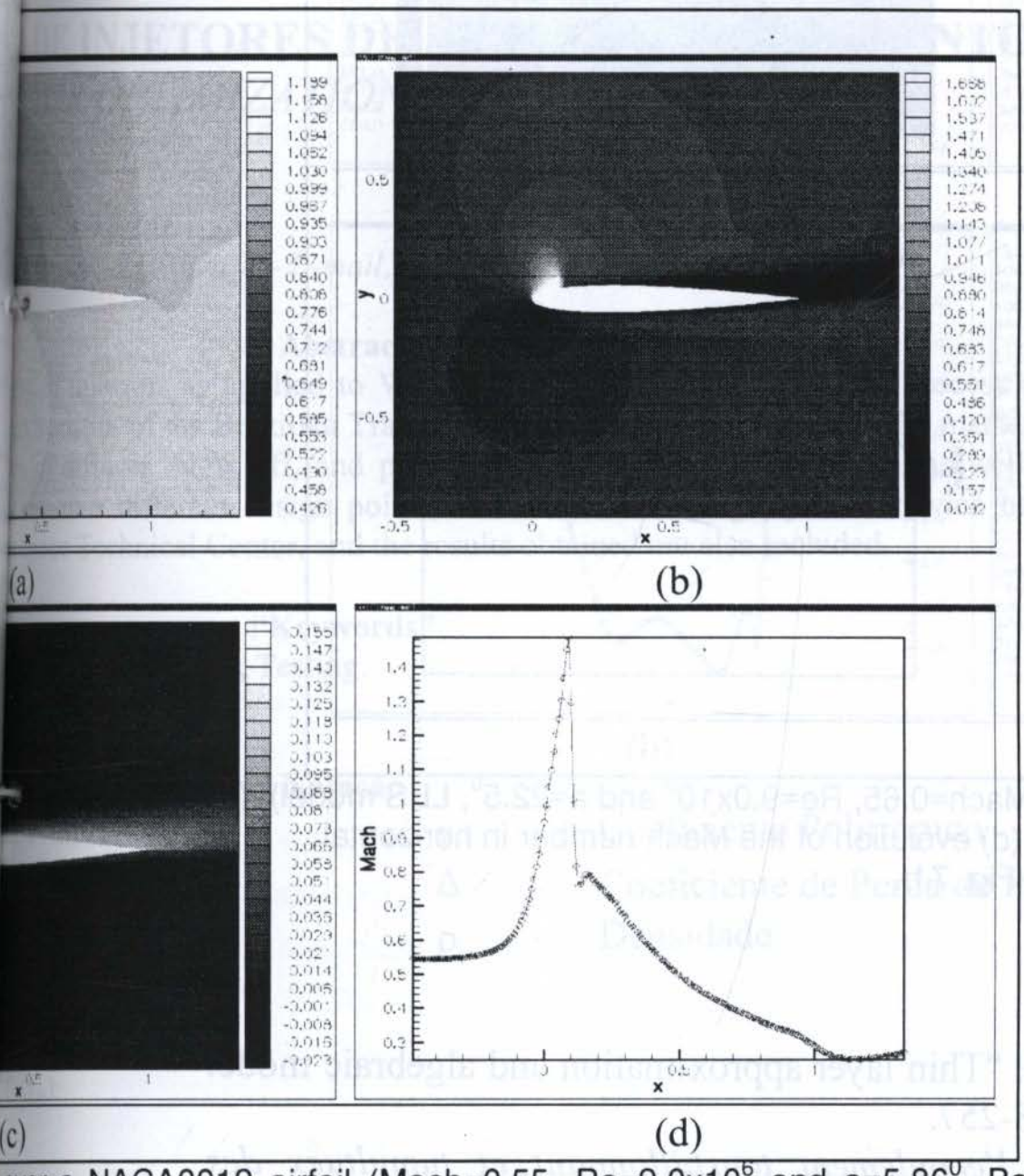

over a NACA0012 airfoil (Mach=0.55, Re=9.0x10^6 and a=5.86^0, Baldwin-ure, (b) local Mach number, (c) entropy and (d) evolution of the Mach number the airfoil as showed by black line in Fig. 6.b.

iscosity dissipation in the boundary layer flow that is responsible for

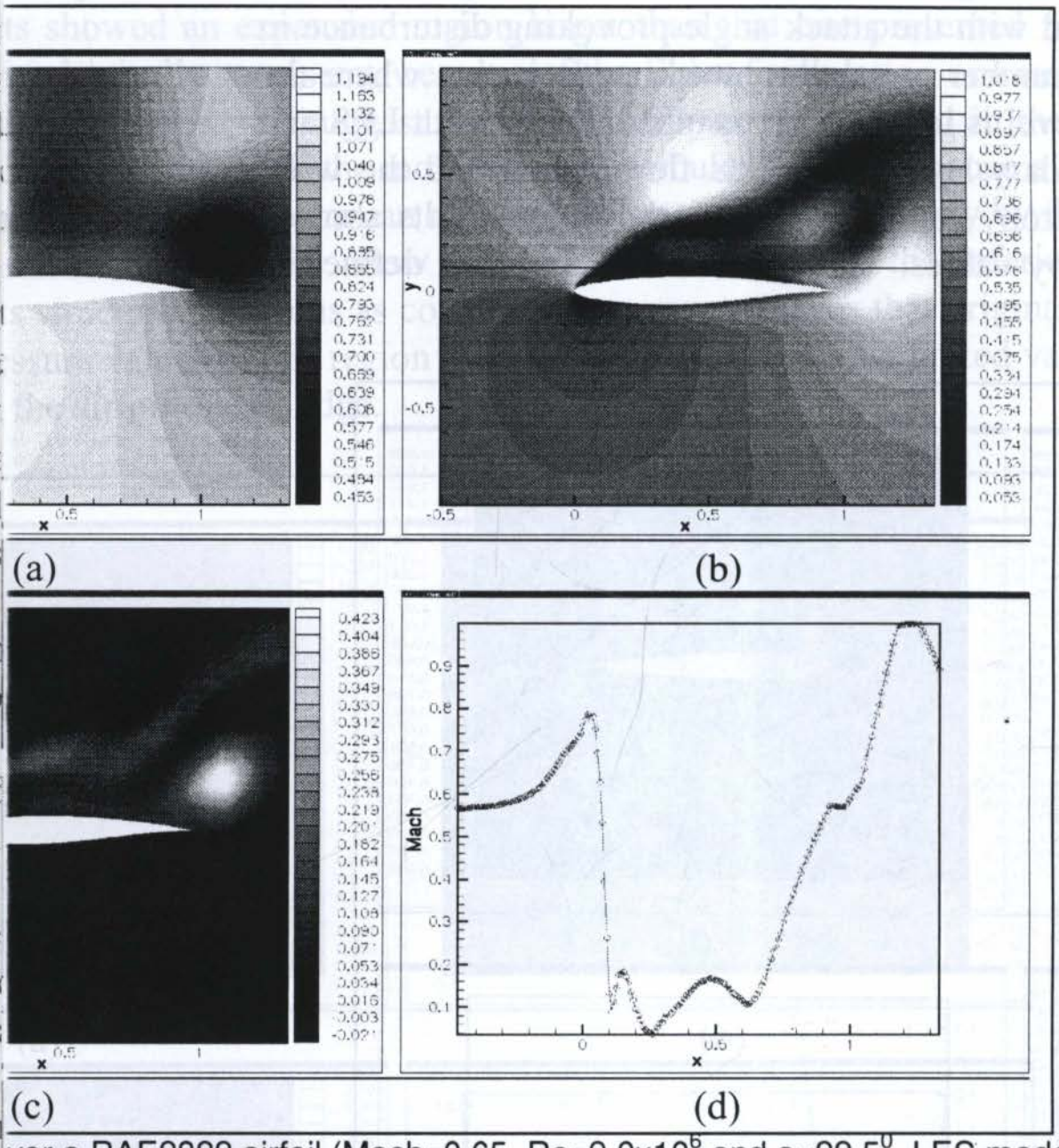

ver a RAE2822 airfoil (Mach=0.65, Re=9.0x10^6 and a=22.5^0, LES model). (a) umber, (c) entropy and (d) evolution of the Mach number in horizontal showed by black line in Fig. 7.b.

& LOMAX, H., 1978. "Thin layer approximation and algebraic model lows". *AIAA paper* 78-257.

1897. *Théorie de l'ecoulement tourbillonnant et tumultuex des tilignes à grande section*. Tome I-II, Gautier-Villars, Paris.

:DONALD, M. A., FIRMIN, M. C. P., 1979, Aerofoil RAE2822 undary layer and wake measuments, *AGARD Ad. Report* No. 138.

)81. Two dimensional aerodynamics characteristics of the Naca 0012

XIV Brazilian Congress of Mechanical Engineering
Obeid Plaza Hotel Convention Center - Bauru - SP/Brazil
December 08-12th 1997

B238

) DE INJETORES DE AR EM TÚNEIS DE VENTO/
CTOR OPTIMIZATION FOR WIND TUNNEL

A
spaço- CTA/IAE
s Campos, S.P., Brasil - E-mail, tts@iconet.com.br

Abstract

ory of injectors as applied to Wind Tunnels, and the optimization process used to aracteristics of the Brazilian Transonic Wind Tunnel Project-TTS. The mathematical on of diffuser, blow off, and pressures losses of the configuration, as well as the ctors on a different design point. A Pilot Tunnel using injectors device has been ospace Technical Center, and the results obtained are also included.

"Keywords"

sign, Pressure Loss, Testing.

Notação

o Tranversal
lach
ica

Estática
Total

γ	-	Coeficiente Politrópico
Δ	-	Coeficiente de Perda de P_t
ρ	-	Densidade

lizadas no texto encontram-se definidas na figura 1 ou ao longo do

instalações eficientes para simular em laboratório o comportamento

ECANISMO DE INJEÇÃO

ente de ar comprimido é introduzida no circuito através de injetores de
co, conforme Figura 1.
seguintes funções.

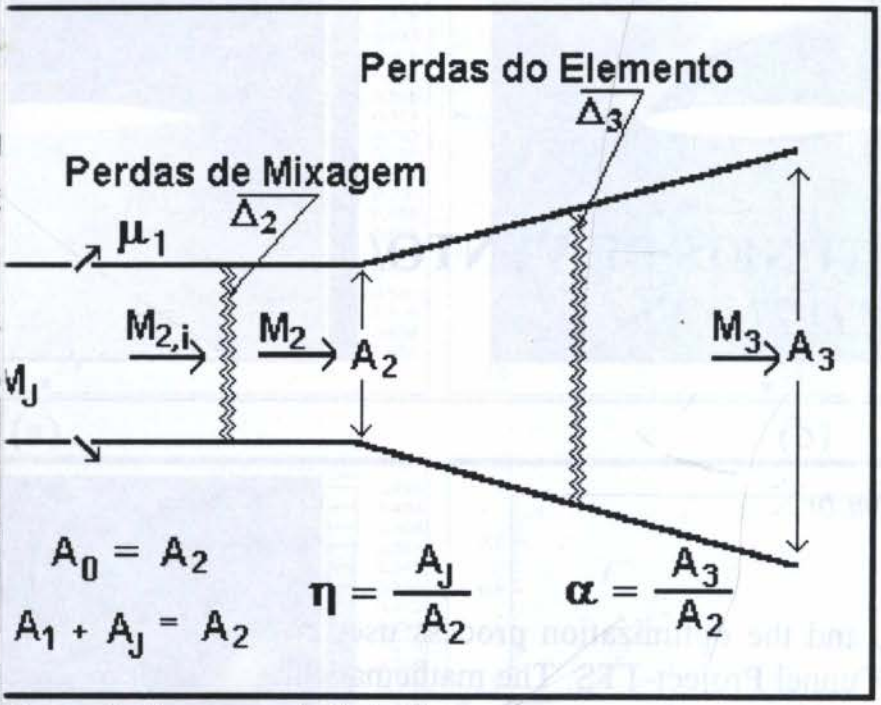

Parâmetros de Injeção

$$\lambda = \frac{Pt_{2,i}}{Pt_1} \quad \Omega = \frac{Pt_J}{Pt_1}$$

$$\beta = \frac{P_J}{P_1} \quad \omega = \frac{\dot{m}_J}{\dot{m}_1}$$

$$\mu = \frac{\dot{m}_{BLOW\ OFF}}{\dot{m}_1}$$

$$\theta_J = \frac{Tt_J}{Tt_1} \quad \theta_2 = \frac{Tt_2}{Tt_1}$$

Figura 1- Esquema de Injeção

$$\frac{-1)}{2}M^2) - (\gamma/(\gamma-1)) \qquad (1)$$

$$\frac{1}{+\frac{(\gamma-1)}{2}M^2)} \qquad (2)$$

(3)

enta a razão de fluxo de massa pela área da seção considerada, levando
s do coeficiente Δ, e variação de área dada por α, descritas adiante.
'J", representa a injeção de um jato de ar em regime supersônico na
ncipal do túnel na região "1". A partir desta injeção inicia-se um
com a ocorrência de uma perda de pressão total "Pt"do sistema. Esta
ticular geometria da câmara de mixagem, das relações de Mach M_1 e
e injeção apresentados na Figura 1. O modelo considera que esta perda
l da câmara, transitando-se então das condições ideais de perdas nulas,
"2,i", para as condições na seção "2", onde as perdas de mixagem
nodelo também admite a existência de extração de ar "blow off"antes

$$^2)+\eta.P_J.(1+\gamma.M_J^2) = P_2.(1+\gamma.M_{2,i}^2) \quad (5)$$

$$\omega).Tt_2 \quad (6)$$

estão já consideradas as extrações de massa. A função Φ do fluxo de ortamento nos trechos 2,i -2 e 2-3.

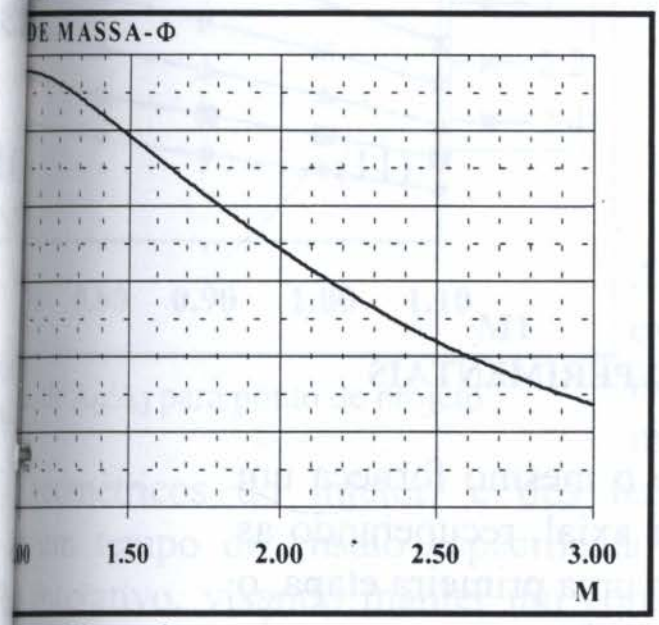

Figura 2

As perdas Δ, são determinadas através de experiências. Para estas seções resultam as seguintes equações.

$$\frac{\pi_2.M_2}{\psi_2} = \frac{1}{(1-\Delta_2)}.\frac{\pi_{2,i}.M_{2,i}}{\psi_{2,i}} \quad ..(7)$$

$$.\alpha.\frac{\pi_2 M_2}{\psi_2} \quad (8)$$

dependem de forma complexa da relação de M_1, M_J, da geometria do Mixagem, assim como das relações de pressão entre os fluidos em ara a faixa de operação na qual se pretende empregar o injetor do com dados experimentais obtidos na literatura Rússia, estima-se Δ_2 no

adas pela Figura 3 e mostradas a seguir.

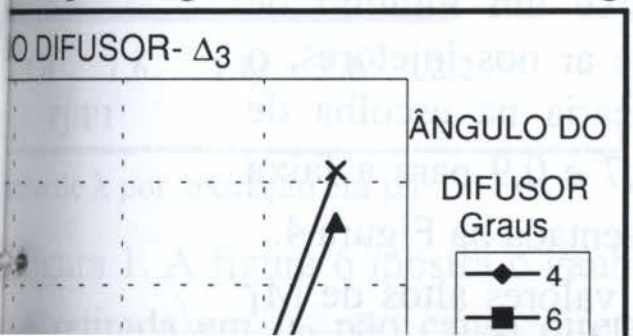

O sistema de equações de conservação é não linear, mas admite uma solução analítica. Trabalhando algébricamente o mesmo determina-se $M_{2,i}$, como solução da equação

$$-)\,]\,M_{2,i}^{4} + [\,2y^2.\gamma - z^2\,]\,M_{2,i}^{2} + y^2 = 0 \qquad (9)$$

$$\frac{-\mu_1}{0}(1-\eta) + \eta.\beta.\frac{\psi_1}{\psi_J}.\frac{M_j}{\sqrt{\theta_J}}\,].\,\frac{\sqrt{\theta_2}}{\psi_1} \qquad (10)$$

$$\frac{{}^{2})+\eta.\beta.(1+\gamma.M_J^{2})}{{}^{+\gamma.M_{2,i}^{2})}} \qquad (11)$$

ETOR PARA O PROJETO TTS E RESULTADOS EXPERIMENTAIS

ı de utilizar injetor consiste em fazer com que o mesmo forneça um capaz de compensar a limitação do compressor axial, recuperando as ito como um todo. Considerou-se ainda que, em uma primeira etapa, o mo um circuito aberto, e que portanto a injeção, sem o uso do capaz de manter um determinado regime de velocidade na seção de

ariação do Mach se faz através da variação da pressão total do injetor. ɔressões estáticas $\beta=P_J/P_1$ sofre também uma variação. Para P_J muito ıa abertura excessiva da corrente de ar injetado, com o aparecimento ɛrda de eficiência. Valor de $P_J < P_1$ produz o efeito indesejável de ição de mixagem e também perda de eficiência. Balanceando estes e que o ponto de projeto do injetor para $\lambda = 0.95$, $\beta=1$.
alor dependeu de uma análise de engenharia levando em conta a ɔressores axiais e as perdas estimadas para o Túnel. Após a definição rocedeu-se ao estudo paramétrico exemplificado nas figuras 4 e 5.

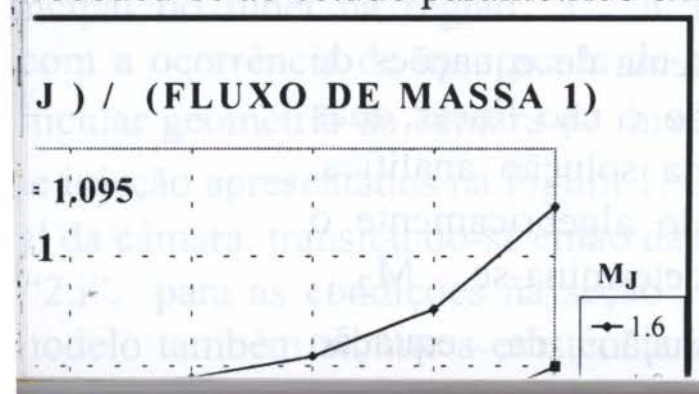

Deseja-se um mínimo de consumo de ar nos injetores, o que significaria na escolha de M_1 entre 0,7 e 0,9 para a faixa de M_J apresentada na Figura 4.

Porém valores altos de M_1

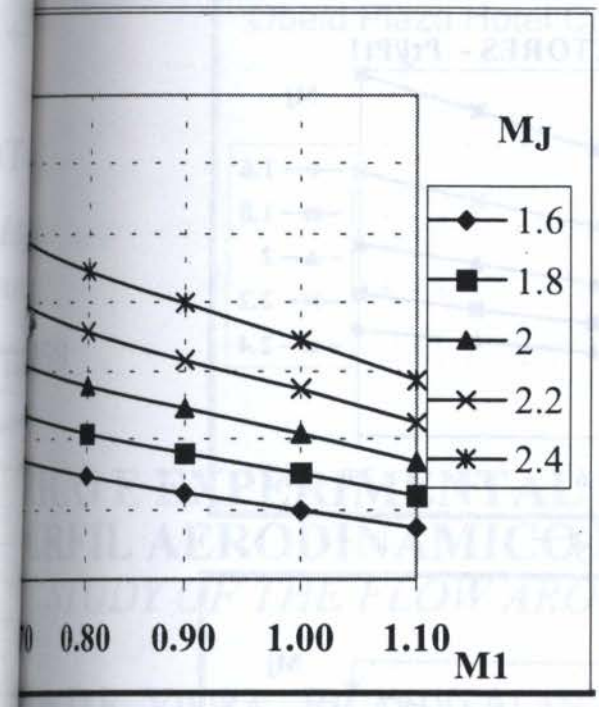

o de A_0/A_J para ponto de projeto

Outro parâmetro a selecionar é a área do injetor, o que é feito através da Figura 5. Desta combinação de critérios das figuras 4 e 5, foram selecionados os valores de:

$$A_0/A_1 = 30 \quad \text{e} \quad M_1 = 0.5$$

Antes de ser uma questão exclusiva de determinação matemática de pontos de mínimo, a seleção atendeu ainda geométricos do injetor, e dos recursos de reservatórios de ar um tempo de ensaio especificado. Na verdade estas definições interativo, visando manter um compromisso com outras áreas do da solução acima seriam também admissíveis.

finição do injetor, passou-se ao estudo do funcionamento do mesmo considerando os demais parâmetros envolvidos. Por exemplo, ao injetar ar na corrente do túnel, caso o mesmo seja de circuito fechado, é imprescindível que também haja uma retirada do ar injetado em algum ponto do circuito, ou este se pressurizará de forma indesejável e catastrófica.

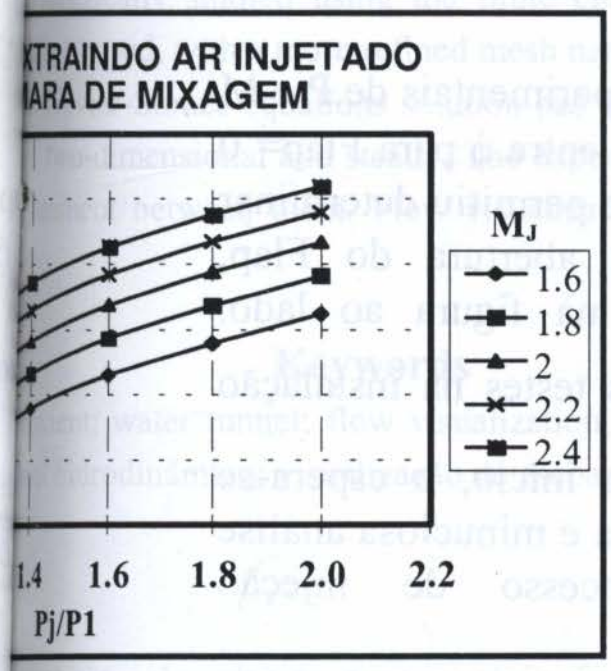

nho de λ por extração em μ1

Esta extração, ou "Blow off" pode ser feita antes ou

Figura 1. A figura 6 mostra o ganho obtido na pressão Pt_2 ao retirar

A retirada em μ_0 não causa diretamente aumento de λ, mas uma

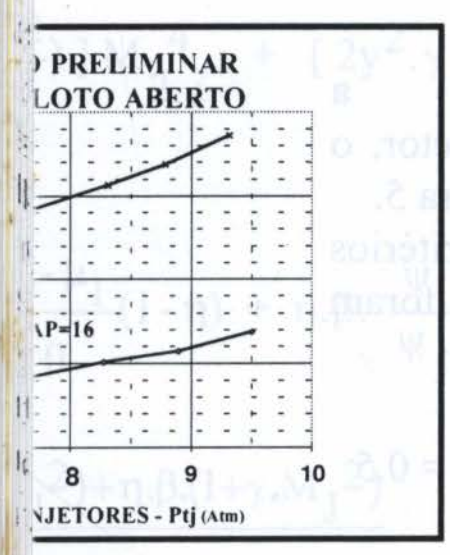

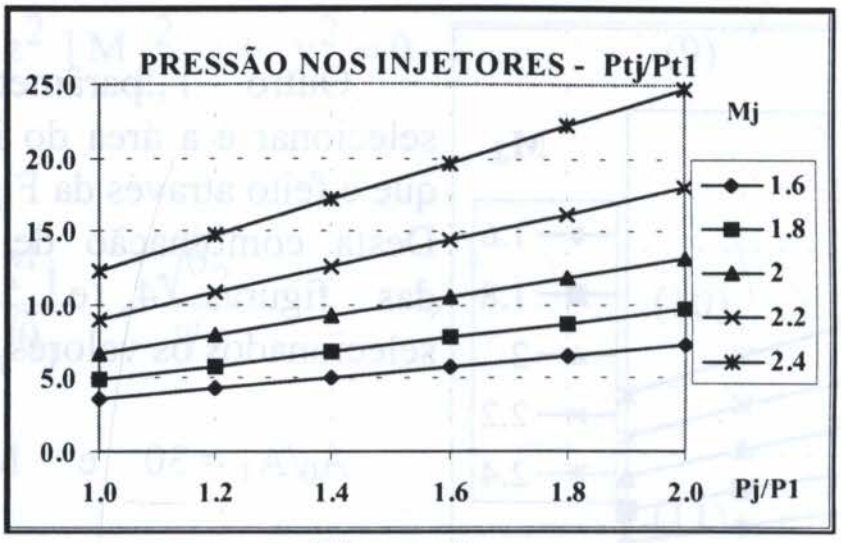

Figura 8

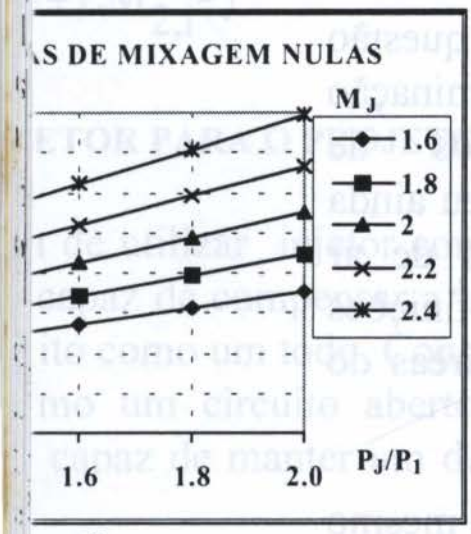

ra 9

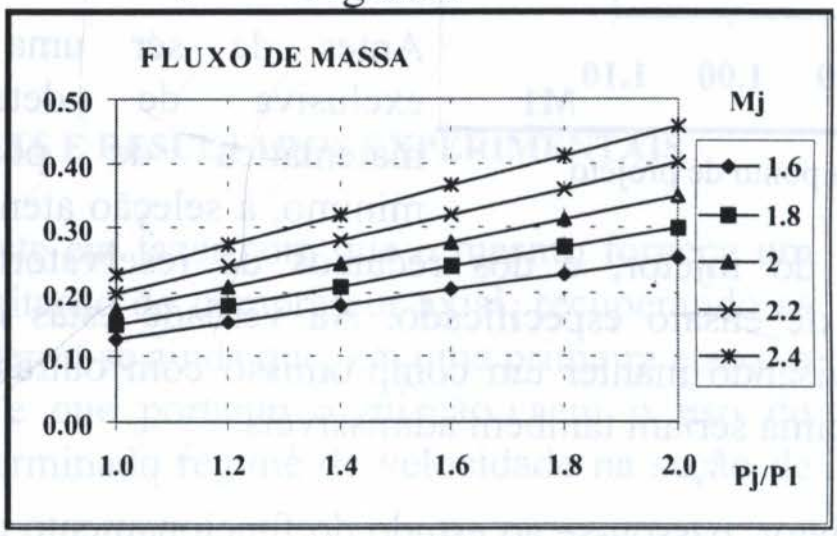

Figura 10

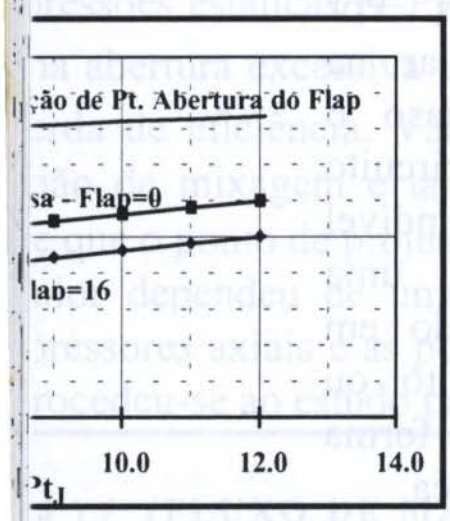

ga da abertura do Flap

A partir das medidas experimentais de P e M determinou-se a relação entre ϕ para Flap= 0 e Flap = 16. O resultado permitiu determinar a perda de carga da abertura do Flap, conforme apresentado na figura ao lado, onde $\sigma = \frac{1}{(1-\Delta).\alpha}$. Os testes na instalação piloto estão apenas no início, e espera-se através dele uma extensa e minuciosa análise experimental do processo de injeção descrito.

XIV Brazilian Congress of Mechanical Engineering
Obeid Plaza Hotel Convention Center - Bauru - SP/Brazil
December 08-12th 1997

B258

RICO E EXPERIMENTAL DO ESCOAMENTO AO PERFIL AERODINÂMICO NACA 0012 / *NUMERICAL AL STUDY OF THE FLOW AROUND A NACA 0012 AIRFOIL*

DSON D.R. VIEIRA, RICARDO ALAN V. RAMOS & SÉRGIO S. MANSUR
a Mecânica, Faculdade de Engenharia - UNESP - Ilha Solteira
- SP, Brasil, E-mail: mansur@feis.unesp.br

Abstract

ie wake of a NACA 0012 airfoil have been made with hot wire anemometer in a tunnel, which has a test section of 146 × 146 × 500 mm. The drag coefficient of the , employing the momentum equation on a control volume that encloses the airfoil. n numerically studied using the finite control volumes method. In this study, a as been used, with a more refined mesh near the airfoil, where pressure and velocity ed. Navier-Stokes equations solution has been obtained with the SIMPLE method, nar, two-dimensional and steady. The experimental and numerical results have been agreement between them. Flow visualization has also been performed, using the e.

Keywords

efficient; water tunnel; flow visualization; numerical simulation; aerofólio NACA túnel hidrodinâmico; visualização de escoamento; simulação numérica.

io patenteado que se tem notícia foi desenvolvido por volta de 1884 hillips que, já naquela época, conduziu estudos pioneiros envolvendo xperimentais em túnel de vento. Desde então, perfis aerodinâmicos

oltados para o aprimoramento de perfis aerodinâmicos. Dentre estas a famosa NACA (*National Advisory Committee for Aeronautics*), SA, cujas investigações resultaram na criação de famílias consistentes las de maneira racional e sistemática.

ılias – conhecida como NACA 4 dígitos – insere-se o perfil no âmbito do presente trabalho, por se tratar de um perfil simétrico e ilizado pela indústria aeronáutica, cujas características geométricas e er facilmente encontradas na literatura especializada. O presente artigo scoamento ao redor deste aerofólio, concentrando-se na determinação al do coeficiente de arrasto aerodinâmico que o caracteriza. O artigo ns do escoamento obtidas através da técnica de visualização em meio por injeção direta de corantes líquidos.

O PROBLEMA

rrasto (C_D) de um corpo sólido imerso em um escoamento permanente e ser determinado aplicando-se a forma integral da equação da ento ao volume de controle (VC) que o confina, representado na

e de controle.

Pode-se demonstrar que, sob estas condições, a força de arrasto por unidade de comprimento do perfil (F_D) é dada por:

$$F_D = \rho \int v_2 (v_1 - v_2)\, dx \qquad (1)$$

e o coeficiente de arrasto pode ser escrito como:

$$C_D = \frac{F_D}{\frac{1}{2}\rho v_1^2 A} \qquad (2)$$

onde: F_D = força de arrasto [N/m]
C_D = coeficiente de arrasto
ρ = densidade do fluido [kg/m^3]
v_1 = velocidade na entrada do VC [m/s]
v_2 = velocidade na saída do VC [m/s]
A = área frontal projetada [m^2/m]

eterísticas geométricas do perfil e as propriedades físicas do fluido

lado no *Laboratoire de Visualisation Hydrodynamique* do *Office herches Aéroespatiales – ONERA,* localizado em Chantillon, França. modo contínuo ou intermitente (*blow-down*), sempre pela ação da o foi construído em material composto de fibra de vidro e resina ado sobre estrutura metálica. Sua seção de ensaios, com dimensões otada de janelas de observação confeccionadas em acrílico de boa

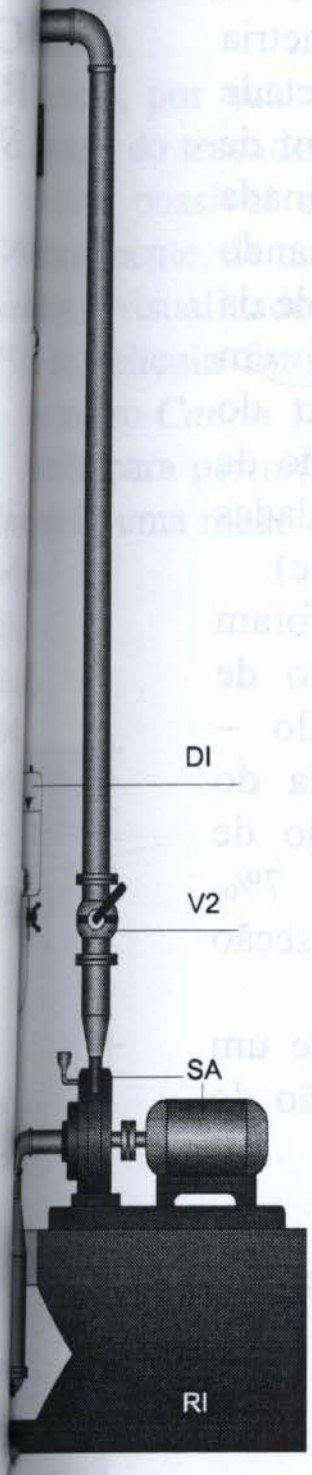

Ensaios preliminares realizados com anemômetro de fio quente, para velocidades do fluxo não perturbado compreendidas entre 0,05 e 0,20 m/s, comprovaram a excelente qualidade do escoamento na seção de testes, que alia boa uniformidade do perfil de velocidade e reduzida intensidade turbulenta – inferior a 1 %, mesmo nas condições mais adversas de operação. Este baixo nível de turbulência, quando comparado com instalações similares operando à mesma velocidade média, deve-se ao projeto acurado da contração (CT) e à presença de telas e colmeias (TC) no reservatório superior (RS), que agem como atenuadores de turbulência.

A operação em modo contínuo é executada regulando-se as válvulas (V1) e (V2), de maneira que o nível de água do reservatório superior se mantenha constante. Nesta condição, a velocidade média na seção de testes (ST) deve permanecer inalterada durante toda a realização dos ensaios.

A operação em modo intermitente (*blow-down*), por sua vez, é realizada fechando-se totalmente a válvula (V1), até que o nível do reservatório superior atinja seu ponto máximo. Neste instante, o sistema de acionamento do túnel (SA) é desligado, aguardando-se o tempo

na de injeção de corantes líquidos (DI) utilizado para a visualização do
o perfil consiste, basicamente, de uma garrafa pressurizada, ligada a
lérmica de 0,6 mm de diâmetro externo, dobrada em forma de cotovelo
50 mm a montante do modelo.

tagem do Modelo de Ensaio

icação do modelo de ensaio compreende três etapas distintas, podendo
como segue.

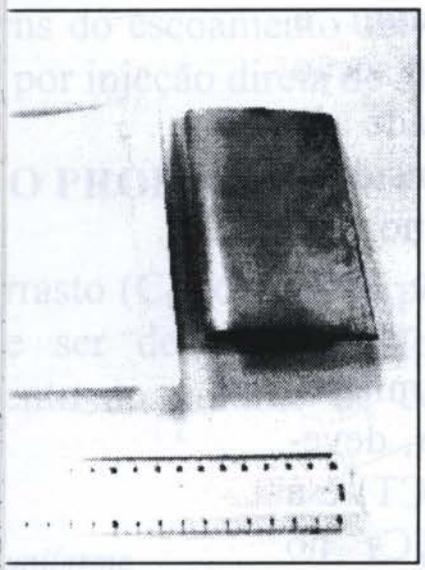

(b) (c)

e confecção do perfil:

em alumínio;
ina epoxi;
tivo em resina epoxi.

Inicialmente, aproveitando-se a simetria do perfil NACA 0012, apenas uma metade de modelo – Figura 3(a) –, com 80 mm de corda e 146 mm de envergadura, foi usinada em alumínio numa fresadora de comando numérico. A partir deste modelo, o molde da Figura 3(b) pôde ser confeccionado em resina epoxi, permitindo a produção do modelo definitivo de ensaio, constituído de duas metades idênticas coladas, moldadas com o mesmo tipo de resina – Figura 3(c).

As dimensões do modelo foram especificadas de maneira que a razão de bloqueio para ângulo de ataque nulo – relação entre a área frontal projetada do modelo e a área transversal da seção de testes –, fosse mantida inferior a 7%, limitando a influência das paredes da seção de testes sobre o escoamento.

aio foi aferido quanto à sua forma e dimensões, verificando-se um
áximo de apenas 0,07 mm na espessura, relativamente à equação do
bott & von Doenhoff (1959), é dada por:

$$\left(\sqrt{x} - 0{,}126x - 0{,}3516x^2 + 0{,}2843x^3 - 0{,}1015x^4\right) \qquad (3)$$

ıda da superfície superior e inferior do perfil
sura máxima do perfil, em fração da corda

anemométrica foi introduzido na seção de ensaios através da parede
itir o levantamento do perfil de velocidade na seção localizada a
do modelo, utilizando-se um anemômetro Dantec tipo CTA, modelo
sonda 55R11. A aferição deste dispositivo de medição foi realizada
livre gerado por um pequeno túnel hidrodinâmico horizontal,
por Pluister (1975), especialmente construído para esta finalidade.
izados em regime de funcionamento contínuo, com a velocidade
s ajustada em 6,55 cm/s, que corresponde a um número de Reynolds,
il, da ordem de 5300. A repetição deste procedimento revelou a boa
rimento.

alização, por sua vez, foram executados em modo *blow-down* de
injeção do traçador líquido com velocidade e pressão controladas, a
mínimo possível de perturbação sobre escoamento principal. Este
sencialmente, de uma solução aquosa de pigmentos a base de PVA.
amento visualizado - para dois diferentes ângulos de ataque, $\alpha = 0^o$ e
s em película fotográfica, com uma câmera *SLR Canon Elan II-e*
iva macro *Canon* 100mm f2.8 e filme negativo *Kodak GPX* ISO 160.
olhido para permitir a ocorrência de um acentuado descolamento da
, ainda, uma razão de bloqueio moderada – inferior a 17%.

4. SIMULAÇÃO NUMÉRICA

As equações governantes – conservação da massa e da quantidade de movimento –, sem a presença de termos transitórios, foram discretizadas no espaço bidimensional pela técnica dos volumes finitos e resolvidas pelo método SIMPLE (*Semi-Implicit Method for Pressure-Linked Equations*), desenvolvido por Patankar (1980).

O pacote computacional utilizado, implementado em linguagem FORTRAN, permite a programação de diversos esquemas convectivos. No caso da presente simulação, optou-se pela utilização de um esquema baseado na lei das potências que, segundo vários autores, atenua o problema da difusão

nensional entre duas malhas adjacentes foi mantida inferior a 10% em
ılo, evitando uma deterioração desnecessária nos resultados.
ções de contorno foram utilizadas na solução numérica do problema:
: velocidade prescrita (u = 0 e v = –6,55 cm/s);
uerda: parede impermeável e aderente (u = 0 e v = 0);
eita: simetria do perfil de velocidade (du/dx = 0);
escoamento plenamente estabelecido (dv/dy = 0);
orpo sólido (u = 0 e v = 0).

DISCUSSÃO

5(b), respectivamente, representam as linhas de corrente e o campo de
vés da simulação numérica, para as mesmas condições em que foram
perimentais.
lade na seção localizada 40 mm à jusante do bordo de fuga do modelo
mentalmente, revelando uma excelente simetria em relação ao plano
e centro do perfil (x = 0,073 m) - Figura 6. A boa concordância entre
experimentais refletem o bom desempenho do programa de simulação
a malha computacional e das condições de contorno utilizadas. Além
s asseguram a obtenção de coeficientes de arrasto numérico e
róximos, como mostra a Tabela 1.

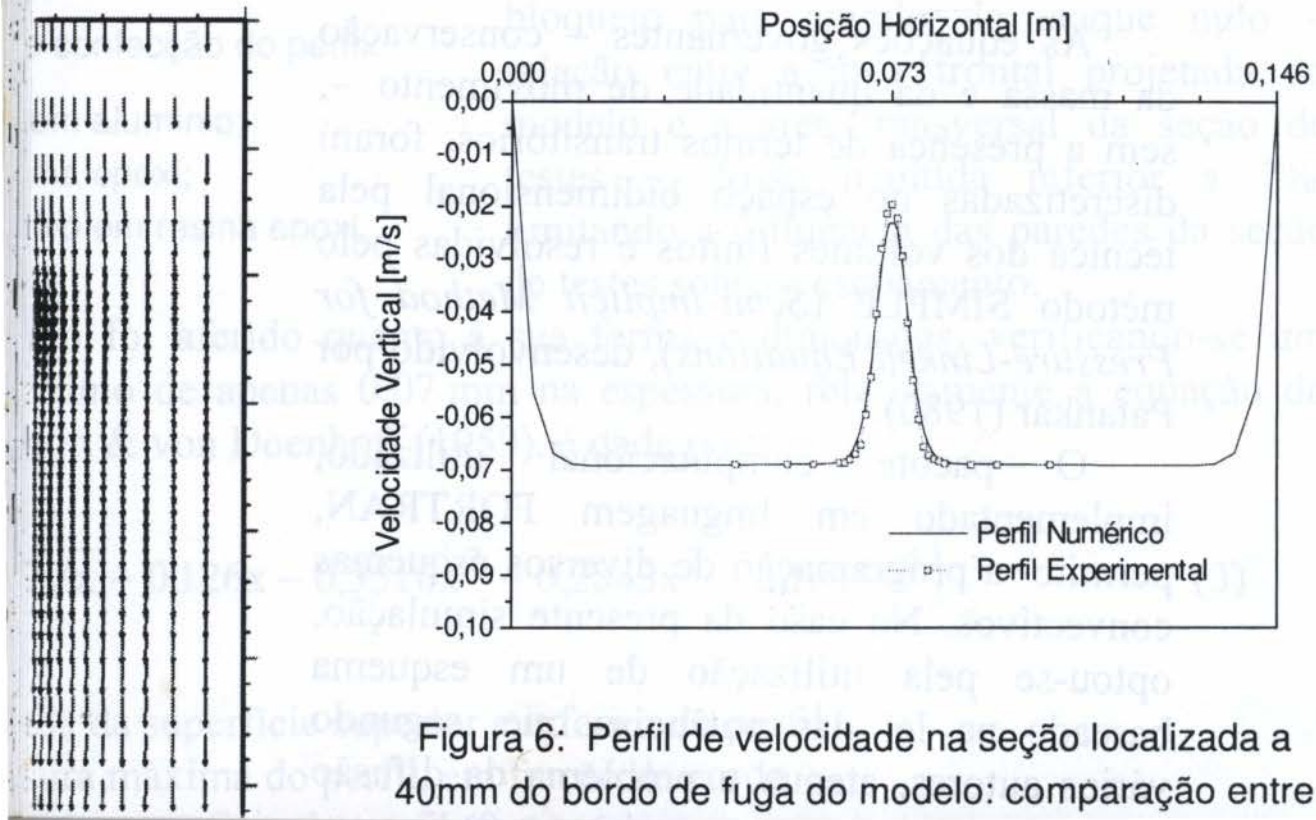

Figura 6: Perfil de velocidade na seção localizada a 40mm do bordo de fuga do modelo: comparação entre

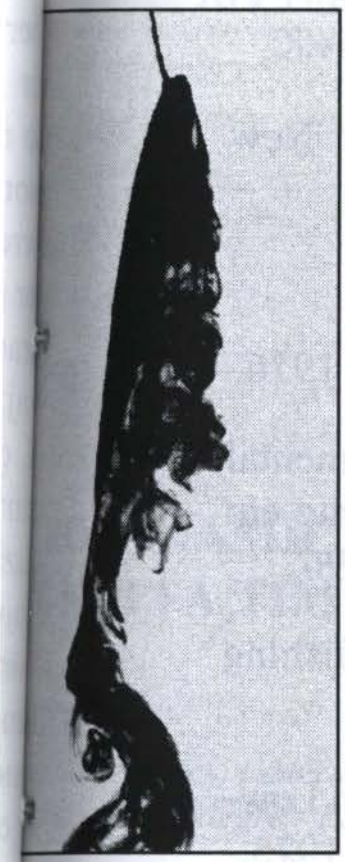

(b) $\alpha = 12^{\circ}$

escoamento ao redor
para $Re = 5 \times 10^3$:
erimentais.

As imagens fotográficas obtidas através da visualização do escoamento ao redor do modelo, com dois diferentes ângulos de ataque (α), podem ser observadas na Figura 7.

Na Figura 7(a), nota-se que o escoamento acompanha os contornos do perfil até um ponto localizado próximo ao bordo de fuga, onde ocorre o descolamento da camada limite. Este resultado encontra-se em perfeito acordo com os dados numéricos da Figura 5.

Na Figura 7(b), ao contrário, observa-se uma região de grande turbulência localizada no dorso do perfil, devido ao descolamento prematuro da camada limite, próximo ao bordo de ataque. Na linguagem aeronáutica, esta situação é conhecida como *stall*, implicando em perda significativa da sustentação. Evidentemente, este tipo de escoamento não pôde ser estudado numericamente no âmbito deste trabalho, por envolver a ocorrência de fenômenos
itos, de características notadamente transitórias. É importante observar
nto, o programa utilizado ainda não contém os termos temporais das
o. Sua inclusão deverá ser efetuada numa próxima etapa desta

ca do problema, a solução das equações de Navier-Stokes forneceu
da simulação direta, sem a necessidade de utilização de modelos de
tilizada mostrou-se adequada para o cálculo do escoamento global,
tamanho compatíveis para o uso de computadores do tipo PC,
dor Pentium 133 MHz.

perimental e a metodologia de ensaio empregados revelaram-se
à realização dos testes envolvendo pequenos ângulos de ataque. O
entretanto, implica em um crescimento rápido da razão de bloqueio

BLIOGRÁFICAS

)OENHOFF, A.E. *Theory of Wing Sections*, Dover Publications, New

undamentals of Aerodynamics, McGraw-Hill, Singapura, 1988.

Mechanics Measurements, Hemisphere Publishing Corporation, 1976.

E.D.R., SAITO, M. & ESPERANÇA, G.A.S. Visualização Experimental or de Cilindros de Base Quadrada Posicionados Transversalmente em ipal, *Anais do VI ENCIT*, vol.2, pp.1103-1108, Florianópolis, 1996.

umerical Heat Transfer and Fluid Flow, Hemisphere Publishing on, 1980.

GIB, H.M. Evaluation of a Hot-Film Calibration Tunnel for Low- *DISA Information – Measurement and Analysis*, n.17, pp.29-33, 1975.

acional Fluid Mechanics, Hermosa Publisher, New Mexico, 1976.

eau Laboratoire de Visualisation Hydrodynamique de la Direction de *'echerche Aérospatiale*, vol.5, pp.289-311, 1982.

ion Quantitative des Visualisations par Traceurs Obtenues dans les ques de l'ONERA, *Colloque National de Visualisation et de Traitement* 8, 15-17, 1985.

XIV Brazilian Congress of Mechanical Engineering
Obeid Plaza Hotel Convention Center - Bauru - SP/Brazil
December 08-12th 1997

3290

ERODYNAMICAL SIMULATIONS BASED ON GE-KUTTA TIME-STEPPING SCHEMES

RTOLI
lied Mathematics, Federal University of Rio Grande do Sul
-900 - Porto Alegre - RS - Brazil
br

Abstract

ol in the development of today's automobile. This technology allows to reduce the te the design, development and manufacture of vehicles. However, there are no ions. This work employs a method to solve compressible and almost incompressible me explicit Runge-Kutta multistage scheme, with central spatial discretization. The e cell-centered arrangement of the control volume for the flow variables. Numerical le configurations and airfoils for Mach-numbers ranging from 0.002 to 0.63.

Keywords

rical simulation, finite volume, Runge-Kutta / Veículo, aerodinâmica, simulação nge-Kutta

of computational fluid dynamics has been driven by the need of faster thods for the calculation of flow fields around configurations of powerful computers and user facilities are enabling technologies for day's vehicles. Aerodynamics, confort and safety are topics which are re important. Besides, increasing quality of transportation systems, to growing, continues to emphasise the need of additional studies to

e energy, the mass conservation equation to calculate the density and culate the pressure.

be easily extended for the solution of almost incompressible flows conditioning, which consists in the transformation of the governing that are better conditioned. Results are obtained for bi and three e configurations and the NACA 0012 airfoil for Mach-numbers .63 using the Euler equations.

JATIONS

quations for non viscous flows are the Euler equations. The three tions for unsteady compressible flows in differential form reads

$$\frac{\partial \vec{F}_3}{\partial z} = 0 \tag{1}$$

$$\overline{\vec{F}} = \begin{Bmatrix} \rho\vec{q} \\ \rho u\vec{q} + p.\vec{i} \\ \rho v\vec{q} + p.\vec{j} \\ \rho w\vec{q} + p.\vec{k} \\ \rho H\vec{q} \end{Bmatrix}, \qquad \overline{\vec{F}} = \vec{F}_1\vec{i} + \vec{F}_2\vec{j} + \vec{F}_3\vec{k} \tag{2}$$

y, $\vec{q}$ the velocity vector ($\vec{q} = u\vec{i} + v\vec{j} + w\vec{k}$) and p the pressure.

orm allow discontinuities, the approach is suitable for capturing shocks e flow field. The total energy E and total enthalpy H are given by

$$\frac{}{}, \qquad H = E + \frac{p}{\rho} \tag{3}$$

em of equations the state equation for a perfect gas is employed

$$o[E - \frac{u^2 + v^2 + w^2}{2}] \tag{4}$$

$$\frac{\partial \vec{F}_3}{\partial z} = 0 \qquad (6)$$

$$\begin{bmatrix} 0 & 0 & 0 & 0 \\ 1 & 0 & 0 & 0 \\ 0 & 1 & 0 & 0 \\ 0 & 0 & 1 & 0 \\ (M^{-2}-1) & u(1-M^{-2}) & v(1-M^{-2}) & w(1-M^{-2}) & M^{-2} \end{bmatrix}$$

matrix indicates that the energy equation is transformed into h-numbers. Thus, the eigenvalues of the resultant system of equations the Mach-number goes to zero, laying the basis of construction of d Merkle, 1985) to solve incompressible flows (De Bortoli, 1994).

THE NUMERICAL METHOD

ces among the various finite volume formulations known in the ent of the control volume and update points for the flow variables The most frequently used schemes are the cell-centered, cell-vertex ch. Each of these schemes has its advantages and disadvantages. The d on the cell-centered arrangement (Blazek, 1994).

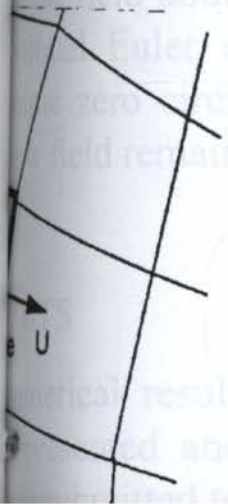

$$\frac{\partial \vec{W}_{i,j,k}}{\partial t} = -\frac{1}{V_{i,j,k}} \int_S (\bar{\bar{F}}.\vec{n}) dS \qquad (7)$$

The finite volume discretization based on the central averaging is not dissipative. The numerical procedure does not converge to the steady state solution when the high frequency oscillations of error in

perator is a blend of second and fourth differences and is defined
, 1989)

$$_{i-1/2,j,k} + d_{i,j+1/2,k} - d_{i,j-1/2,k} + d_{i,j,k+1/2} - d_{i,j,k-1/2} \tag{9}$$

icient is given by

$$\varepsilon^{(2)}_{i+1/2,j,k}\delta_x \vec{W}_{i,j,k} - \varepsilon^{(4)}_{i+1/2,j,k}\delta_{xxx}\vec{W}_{i-1,j,k}\} \tag{10}$$

ators of first and third order are δ_x and δ_{xxx}, respectively, and α is the
written for the i direction as (Blazek, 1994)

$$+\lambda^{i*}_{i+1,j,k}) \tag{11}$$

$$\phi^{i}_{i,j,k} = 1 + max\left[\left(\frac{\lambda^{j}_{i,j,k}}{\lambda^{i}_{i,j,k}}\right)^{w}, \left(\frac{\lambda^{k}_{i,j,k}}{\lambda^{i}_{i,j,k}}\right)^{w}\right]. \tag{12}$$

apted to the local pressure gradients $\varepsilon^{(2)}$ and $\varepsilon^{(4)}$, needed to obtain the
are written as

$$\upsilon_{max}), \qquad \varepsilon^{(4)}_{i+1/2,j,k} = max(0, k^{(4)} - \varepsilon^{(2)}_{i+1/2,j,k}), \tag{13}$$

$$_{i,j,k}, \upsilon_{i,j,k}, \upsilon_{i-1,j,k}),$$
$$\left|\frac{p_{i,j,k} + p_{i-1,j,k}}{p_{i,j,k} + p_{i-1,j,k}}\right|, \tag{14}$$

$$\frac{1}{128} \le k^{(4)} \le \frac{1}{48}.$$

λ is defined for the i direction according to (Choi and Merkle, 1985)

$$\frac{\sqrt{u^2(1-M^2)^2 + \beta^2 c^2}}{2} \tag{15}$$

ssical fourth order Runge-Kutta method requires the evaluation of lissipative terms, what leads to storage problems. Therefore, the eme, which requires few computational storage, is employed (Kroll

$$\bar{R}^{(r-1)}_{i,j,k} \tag{16}$$

$$r = 0,1,2,\cdots,m = 5 \tag{17}$$

ITIONS

ment of boundary conditions in the physical domain is one of the ing the Euler equations. Inappropriate conditions can substantially nd convergence of the computed solution. Numerical conditions undary should assure that the outgoing waves are not reflected back

n efficient numerical implementation of the boundary conditions the surrounded by dummy cells. The body coinciding with a coordinate by straight lines. On a solid body the physical condition of no-osed. Since the numerical treatment of the flow exterior to a body s a bounded domain, an artificial far field has to be introduced.
t far field boundaries (Whitfield, 1983) is based on the characteristic nsional Euler equations normal to the boundary. As the far field sume zero circulation, they have to be placed sufficiently far away low field remains undisturbed.

ULTS

umerical results for the bi and three dimensional vehicle and the presented and compared. First computations were performed for le submitted to almost incompressible flow. A grid containing 50x26

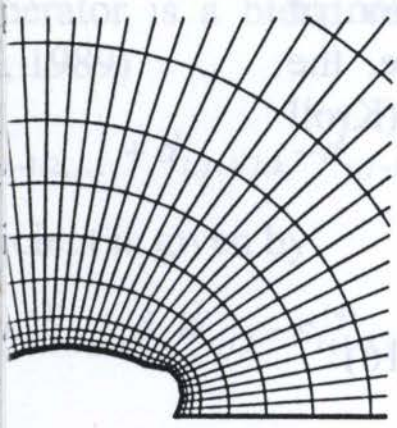

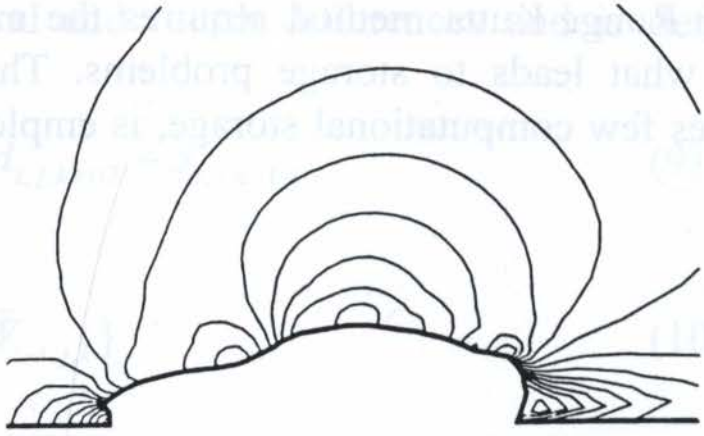

ıicle, 50x26 cells

Fig. 3 Mach contours for 2D vehicle, Mach = 0.25

umerical results for three dimensional (3D) vehicle are presented. The till coarse, but helps to analyse the aerodynamical behaviour. Results rid topology which consists of 30x22x22 cells as shown in Fig. 5.

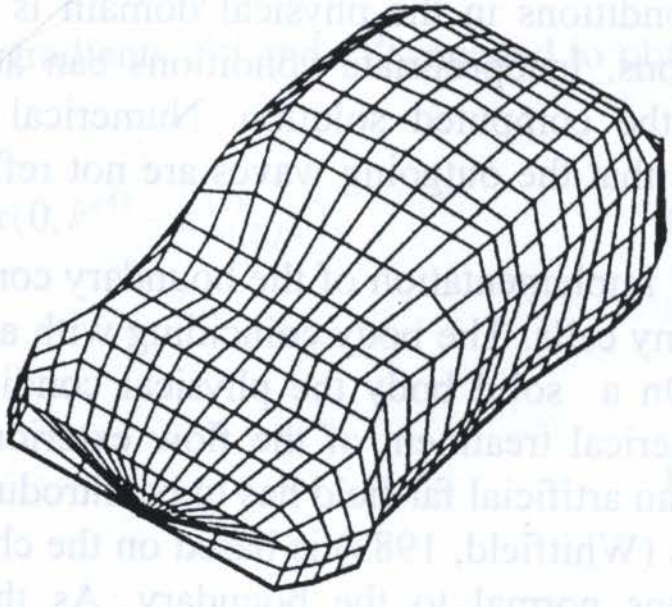

for 2D vehicle, = 0.25

Fig. 5 Grid for 3D vehicle, 30x22x22 cell

ector field computed for Mach 0.25 in the proximity of the surface of

multigrid process (256x64 - fine grid, 128x32 - second grid, 64x16 - third grid, 32x8 - fourth grid, 16x4 - fifth grid).

s for NACA 0012 airfoil are compared to a solution obtained by the ethod (Blazek, 1989) for incompressible flows and with experiments Fig. 8 shows the pressure coefficient computed for Mach = 0.63 and the pressure coefficient computed for Mach = 0.002 and $\alpha = 5°$ obtained by Blazek (1989).

ent for NACA 0012,
nd $\alpha = 2°$

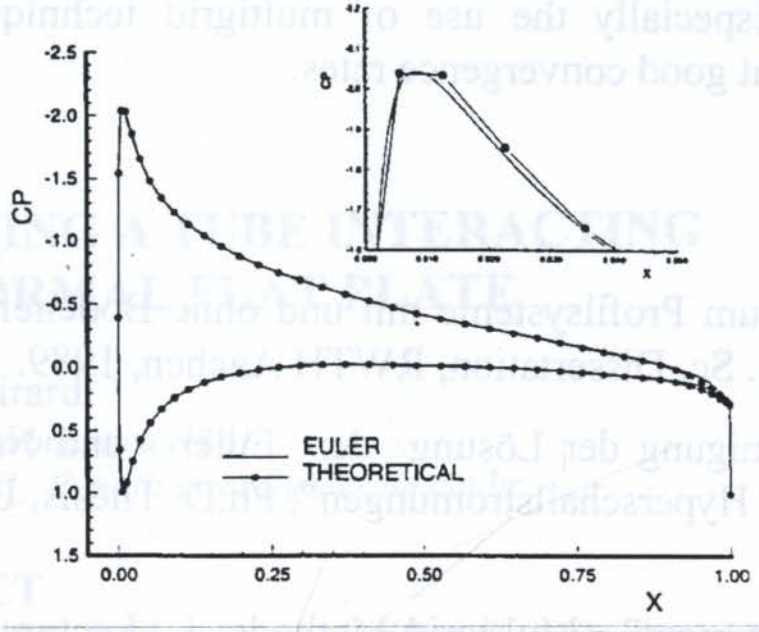

Fig. 9 Pressure coefficient for NACA 0012, Mach = 0.002 and $\alpha = 2°$

10 compares the
r Mach = 0.1 with
multigrid techniques
rms out that the
gases with the grid
according to these
solve compressible
le flows with the
essure coefficient
cisions lower than
with less than 300

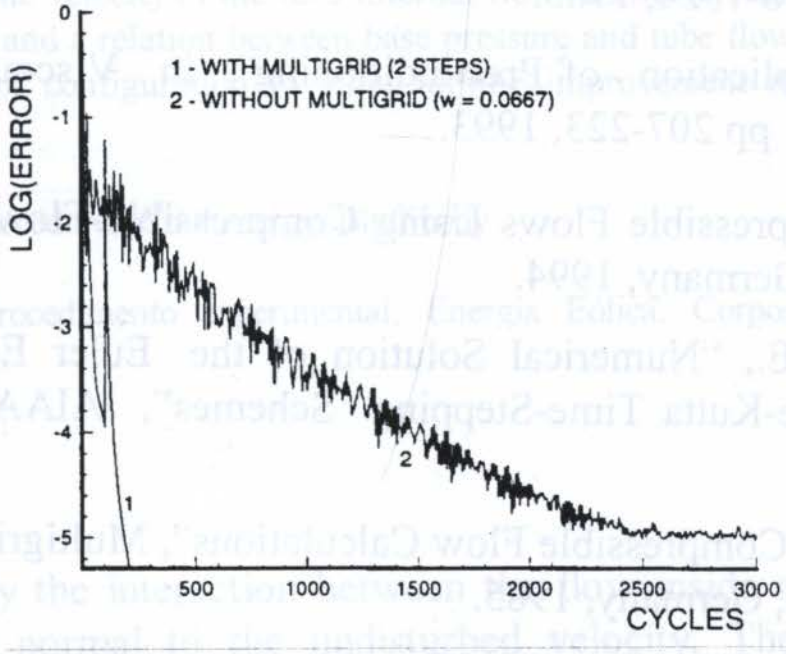

Fig. 10 Convergence history for NACA 0012 with and without multigrid techniques, Mach = 0.1

o the steady state is accelerated using local time-stepping, residual d for the NACA 0012 airfoil. With these acceleration techniques the quations can be obtained in few seconds on today supercomputers for

inion that the comparison between the theoretical/experimental and encouraging. Especially the use of multigrid techniques and its nditioning present good convergence rates.

g der Strömung um Profilsysteme mit und ohne Bodeneffect mit der n Abbildung", M. Sc. Dissertation, RWTH Aachen, 1989.

zur Beschleunigung der Lösung der Euler- und Navier-Stokes nären Über- und Hyperschallströmungen", Ph.D. Thesis, University of

Multigrid Development", Multigrid Methods I, Lecture Notes in

, "Application of Time-Iterative Schemes to Incompressible Flow", Nr. 10, pp. 1518-1524, 1985.

C.L., "The Application of Preconditioning in Viscous Flows", nal Physics 105, pp 207-223, 1993.

ition of Incompressible Flows Using Compressible Flow Solvers", Braunschweig, Germany, 1994.

, W., Turkel, E., "Numerical Solution of the Euler Equations by s Using Runge-Kutta Time-Stepping Schemes", AIAA Paper 81-

l Algorithm for Compressible Flow Calculations", Multigrid Methods, matics, Cologne, Germany, 1985.

Solution of Two-Dimensional Euler Equations - Experience with a orschungsbericht, DFVLR-FB 87-41, Braunschweig, Germany, 1987.

-Vertex Multigrid Method for the Navier-Stokes Equations", NASA n, 101557, 1989.

XIV Brazilian Congress of Mechanical Engineering
Obeid Plaza Hotel Convention Center - Bauru - SP/Brazil
December 08-12th 1997

3746

A JET FLOW LEAVING A TUBE INTERACTING THE WAKE OF A NORMAL FLAT PLATE

Roberto M. Girardi
Instituto Tecnológico de Aeronáutica (ITA)
São José dos Campos, SP, Brasil - E-mail: girardi@aer.ita.cta.br

ABSTRACT

in the present paper is constituted by a tube connected with a flat plate normal to placed inside a wind tunnel and the undisturbed flow is aligned to the tube axis. ork is to study the interaction occurring between the flow leaving the tube and the late, which is dominated by the wake flow. Pressure distributions on the flat plate xis were measured, as well as the velocity of the tube internal flow. Using screens ternal flow velocity was varied and a relation between base pressure and tube flow lly, application of this kind of configuration to wind turbine improvement is aper.

Aerodynamics; Experimental procedure; Wind energy; Bluff body

o em tubo; Aerodinâmica: Procedimento experimental; Energia Eólica; Corpos

e present work is to study the interaction between the flow inside a ion flow of a flat plate normal to the undisturbed velocity. The in this work is constituted by a rectangular flat plate connected to the f a tube, as shown in the Fig. 1. The tube axis is aligned to the) and, therefore, the flat plate is positioned normal to such direction. exploit the low pressure (which is always lesser than the undisturbed

ve, the internal and external flows are connected and can be described
e base pressure coefficient and the non dimensional velocity of the flow
elation is a function of the dynamics and topology of the formation
nan 1967), and changes of the flow rate inside the tube cause new
number, for the dimensions of the formation region, as well as, for the
arman vortex street).

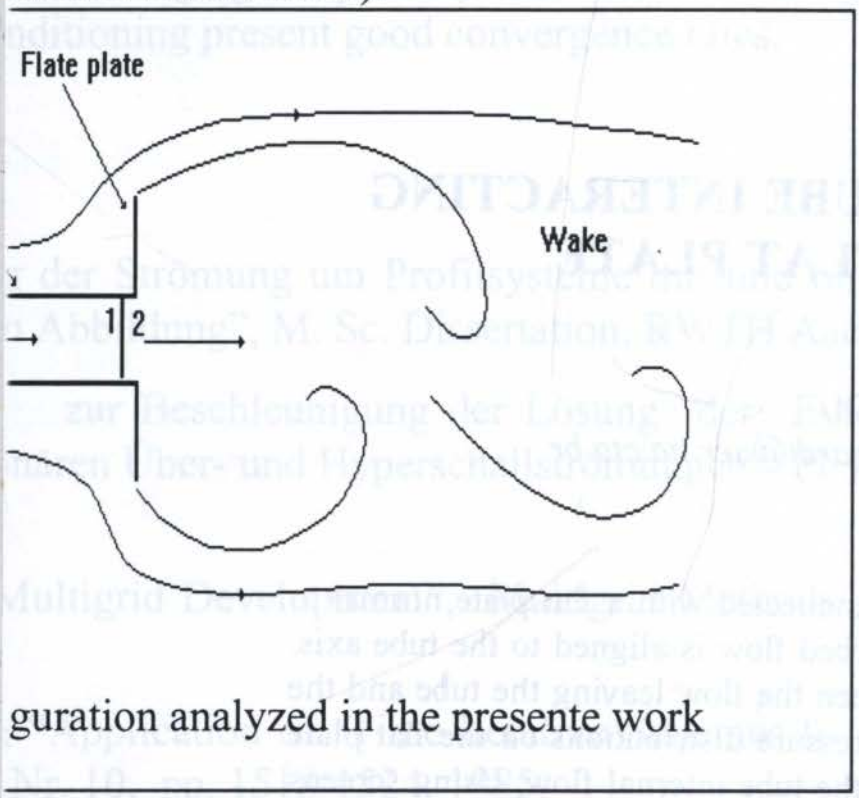

guration analyzed in the presente work

Analitical or numerical study of such kind of flow is very difficulty due to the complex pattern of the near wake of the flat plate, where the rolling up of the shear layers interacts with a jet leaving the tube exit section. On the other hand, the experimental approach can be used and, in the present

n under study is placed inside a small wind tunnel with square test
different meshes are used to change the flow rate inside the tube.
n the flat plate surface and along the tube axis are measured and the
ressure coefficient and the non dimensional velocity inside the tube is
y. Measurements of the Strouhal number and of the characteristic
flow are left to future works.

studied in this work can have some practical applications, and wind
e possibility. In order to verify such possibility, the actuator disk theory
1987) is used to obtain information about the behavior a wind turbine
ced inside the tube of the configuration described above. The interest is
would have greater efficiency than the classical wind turbine, whose
fficiency is 59.3%, as stated by Glauert (see Eggleston & Stoddard
s to use the low pressure established in the flat plate wake region as a
ble for increasing the mass flow rate passing by the actuator disk and
power generated by a wind turbine confined inside the tube.
en the configuration under study and the flow over a wind turbine is

ARATUS

; used in this work. The flow velocity can vary from 8 m/s to 33 (defined by the ratio between fluctuating velocity and test chamber imately 0.5% at the maximum test chamber velocity. The test section with 460 mm and the device considered (see Fig. 1) is the test chamber exit, as shown in the Fig. 2. In this case, the in an open test section. The model dimensions are shown in the

six pressure taps were distributed to verify the internal flow lifficulties, only the tube extremities were considered in this first vas made of aluminum and pressure taps were installed along the al (12 taps) directions, as can be seen in the Fig. 2. Additionally, 8 ong the central hole perimeter and they were used to measure the p_b) of the rectangular flat plate through an average process. Inside to measure the velocity at the cross section center. Other Pitot g of the test section, was used to obtain the free stream dynamic , the velocity V_∞. ed at the tube and ted to a scan valve mm diameter. The by a transducer, rated with a Betz ual to 0.1 mm of nal was sent to a ital voltmeter was

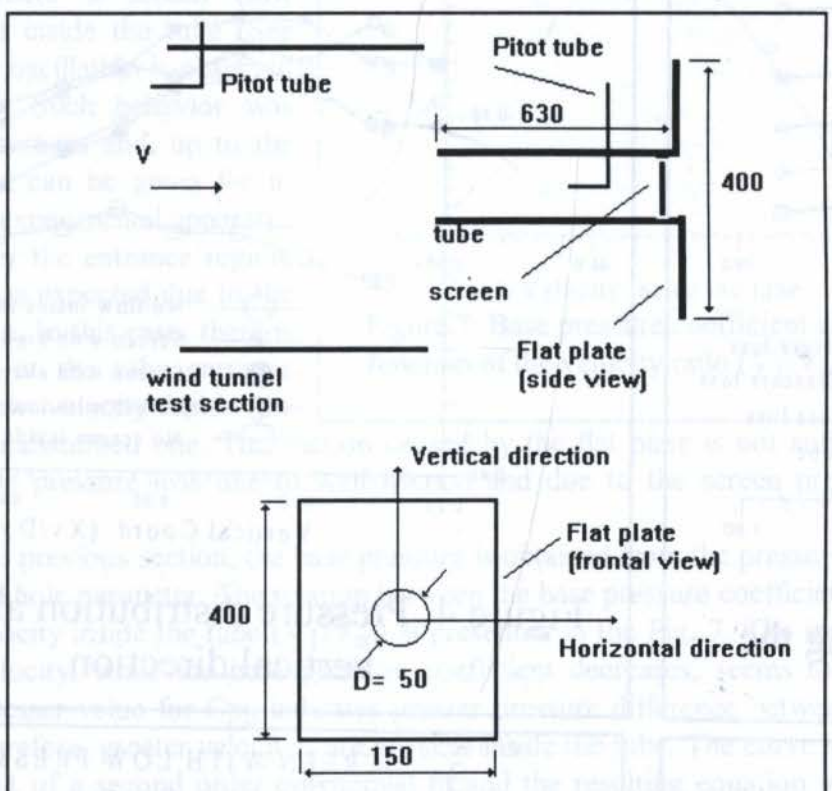

Figure 2: Geometric aspects of the model and its position related to the wind tunnel.

(least count equal sed to measure the disturbed flow and ow. A previous Pitot tube located section. For this ube was placed at tunnel, where the e experiments.

ed inside the tube diameter (loads of the wind turbine) in order to

tainty analysis was made by using the Kline & McClintock (1953) case of the pressure transducer calibration, the standard deviation was t square method, as explained in Doeblin (1990).

RESULTS

ve, at the rear of the flat plate two sets of pressure taps were distributed ertical directions. The horizontal pressure distribution is shown in the number 6.8 x 10^5 (the greater value in the present work). Five curves each series mentioned in the previous section. When the flow inside the kade, the pressure coefficient is nearly constant, as it is usual for bluff here the fluid is free to flow inside the tube (screens are not used) the is a little variation, with lower values near the hole perimeter. Finally, lled inside the tube, a pronounced variation is observed in the region

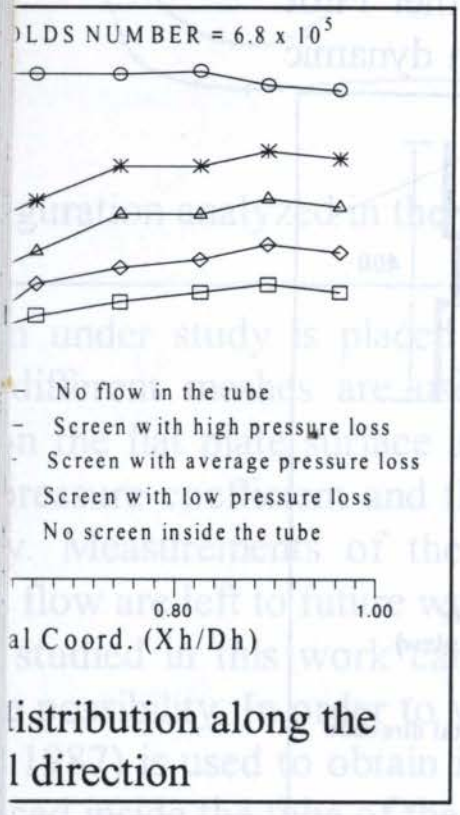

istribution along the l direction

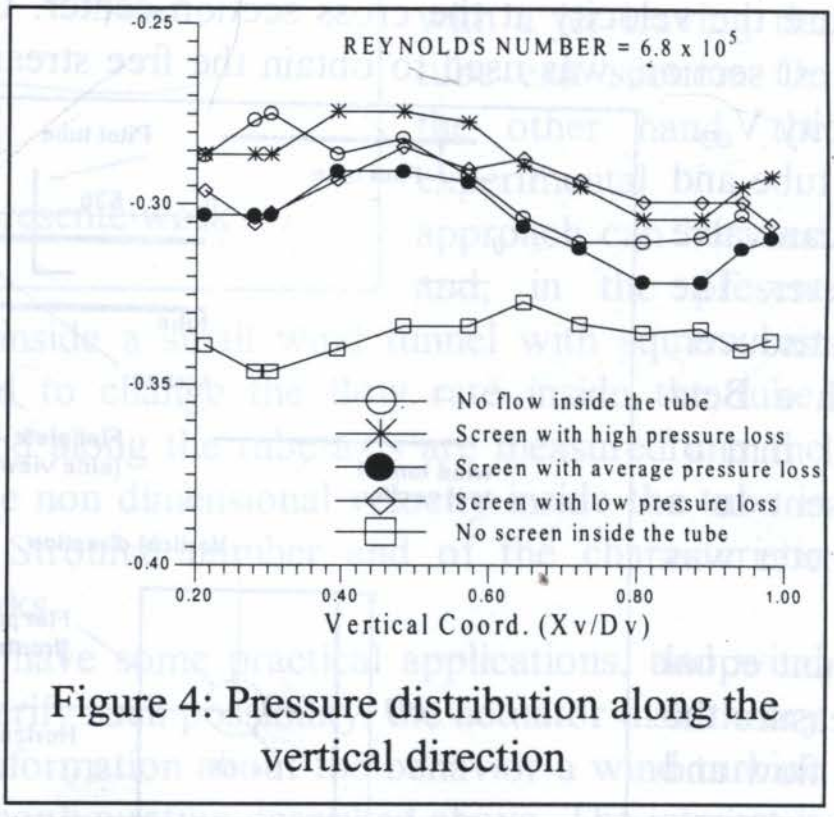

Figure 4: Pressure distribution along the vertical direction

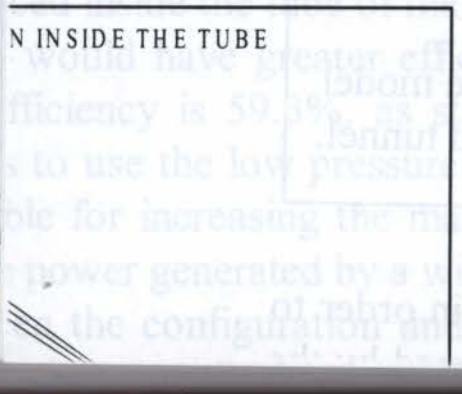

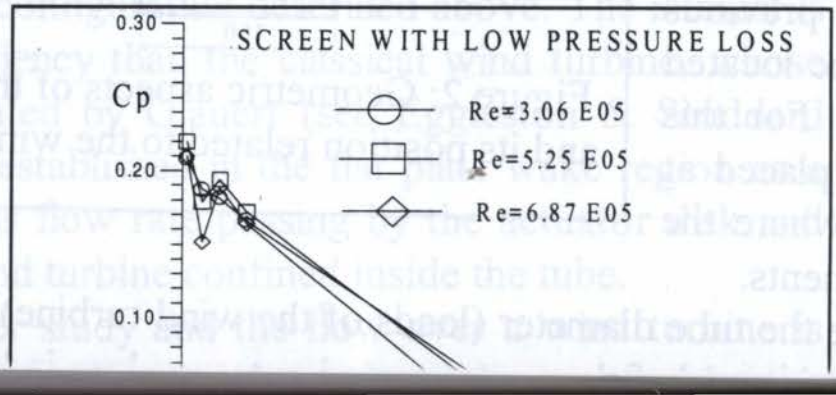

The above results show that the flow leaving the hole has an influence in the pressure distribution, as well as in the value for the base pressure coefficient. As can be seen in the Fig. 3, Cp_b is more negative for greater values of velocity inside the tube, which is related to the screen characteristics.

The vertical pressure distribution is presented in the Fig. 4. Except for the case where the fluid is free to flow inside the tube (no obstructions are placed in the tube), the pressure distributions have greater values in the region near the hole and a small decrease is observed when the taps are followed to the plate extremity. Here, the flow leaving the hole seems to have no influence in the base pressure coefficient, unless for the case mentioned above. Considering the Figs. 3 and 4, one can conclude that vortices formed at the plate vertical edges seem to be more affected by the flow leaving the tube. This conclusion may be explained considering that such vortices must interact strongly than the ones formed at the horizontal edges, because the distance between vertical edges is lesser than the other characteristic dimension (see Fig. 2). Moreover, as the vertical edges are closer to the hole, it seems natural a greater interaction between the internal flow and the vortices formed from the vertical edge.

The pressure distributions related to the flow inside the tube is shown in the Fig. 5. For the case where no obstructions are placed inside the tube, the internal flow velocity is greater than the undisturbed flow velocity (V_∞). This result is a consequence of a flow suction at the tube entrance, which is caused by the flat plate placed at the other tube extremity. Such suction results in a recirculating bubble at the tube entrance, which is related to the pressure peak (great negative values at the entrance section) observed in the Fig. 5. Just after the entrance region, the pressure distribution decreases slowly due to the pressure losses caused by the wall friction along the tube length.

For the case, where a screen (low pressure loss) is placed inside the tube (See Fig. 6), a small pressure oscillation is observed at the entrance region. Such behavior was verified for the other screens and, up to the moment, no explanation can be given for it. Some problem with the experimental apparatus was not discarded. After the entrance region, the pressure decreases, as expected due to the tube internal wall friction. In this case, there is no recirculating region at the tube entrance section because the flow velocity inside the tube is lesser than the undisturbed one. The suction caused by the flat plate is not sufficient enough to overcome the pressure loss due to wall friction and due to the screen presence inside the tube.

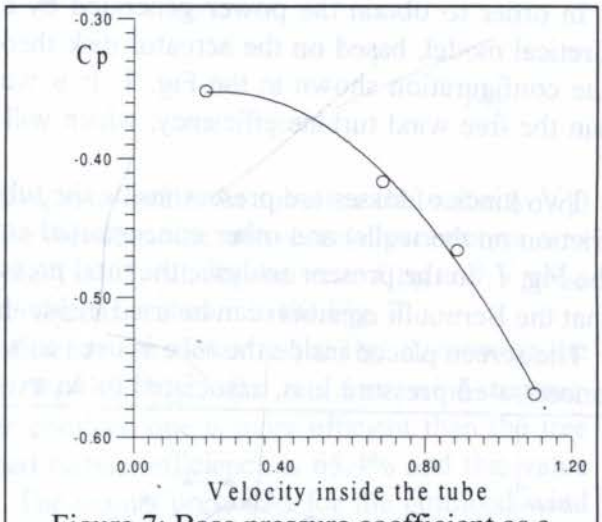

Figure 7: Base pressure coefficient as a function of the velocity ratio (V_1/V_∞).

As mentioned in the previous section, the base pressure is obtained from the pressure taps located along the central hole perimeter. The relation between the base pressure coefficient and the non-dimensional velocity inside the tube (V_1/V_∞) is presented in the Fig. 7. The increase of the internal flow velocity, while the base pressure coefficient decreases, seems to be a natural result, because lesser value for Cp_b indicates greater pressure difference between the tube extremities and, therefore, greater velocities are possible inside the tube. The curve shown in the Fig. 7 is the result of a second order polynomial fit and the resulting equation will be used in the next section.

4. ANALYSIS OF CONFINED WIND TURBINE

In this section a possible practical application of the configuration studied in the present paper will be analyzed. As mentioned previously, due to the suction effect caused by the flat plate presence at the downstream tube extremity, a wind turbine placed inside the tube (confined wind turbine) could be more efficient than a free one. The main objective of this section is to apply the same theory (disk actuator theory) to confined and to free wind turbines, verifying if this new concept has a potential for practical application.

A theoretical model for the confined wind turbine is developed in order to verify the flow parameters that are important to increase the wind energy extraction. In this model the interaction between the external flow in the wake region of the flat plate and the air flowing inside the tube must be considered. Such interaction was obtained by the experimental procedure described above.

The experiments conducted in this work were performed in a small wind tunnel, and the installation of a wind turbine would be a difficulty task. (Blockage effects must be considered - see Glauert 1933 and Maskell 1963). On the other hand, to verify if the flat plate placed at the downstream tube extremity is capable of making a suction, sufficient to increase the wind turbine efficiency, it is only necessary to simulate the pressure loss caused by the wind turbine presence inside the tube. In this case, the screens used in this experimental investigation are used to simulate a wind turbine subjected to different loads.

In order to obtain the power generated by a confined wind turbine and its efficiency, a theoretical model, based on the actuator disk theory (Eggleston & Stoddard 1987), is applied to the configuration shown in the Fig. 1. It is worth to note that the same theory is used to obtain the free wind turbine efficiency, which will be compared to the confined one (See Fig. 8).

Two kinds of losses are present inside the tube: one distributed along the tube length (due to friction on the walls) and other concentrated at the screen located at the tube end as shown in the Fig. 1. In the present analysis, the total pressure loss is considered as a concentrated one, so that the Bernoulli equation can be used inside the tube between points ∞ and 1.

The screen placed inside the tube is used to simulate the wind turbine effect, which causes a concentrated pressure loss, associated to an axial force, while energy is withdrawn from the wind. This axial force can be calculated through the momentum equation applied between points 1 and 2,

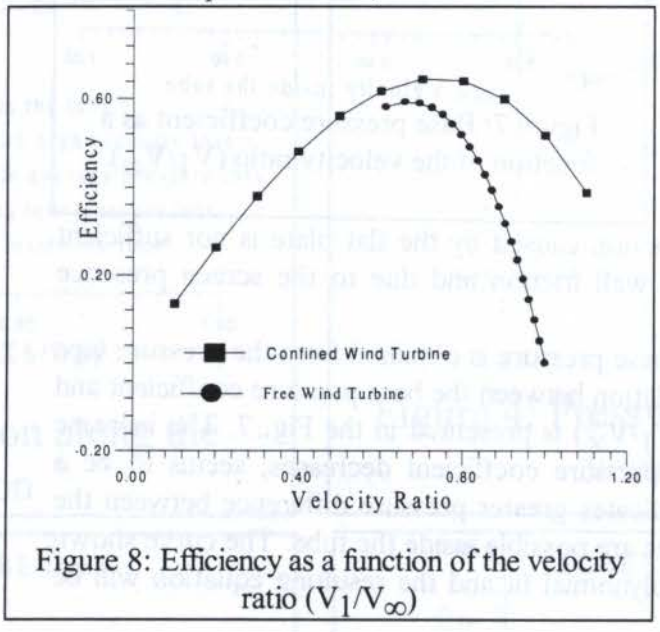

Figure 8: Efficiency as a function of the velocity ratio (V_1/V_∞)

The power generated by a wind turbine can be calculated by using energy equation between points 1 and 2

$$W_e = \rho V_1 S \left(\frac{P_1 - P_2}{\rho} \right) \qquad (1)$$

where W_e is the power, $\rho V_1 S$ is the mass flow rate, which pass through the wind turbine, p_1 and p_2 are the pressure at sections 1 and 2, as shown in the Fig. 1, and S is the cross section area of the tube.

The external flow over the apparatus in the Fig. 1 is dominated by the separated flow in the base of the flat plate normal to the free stream. Such complex flow is characterized by the rolling up of the shear layers shed

from the separation points, which form strong vortices responsible by the low base pressure coefficient (Cp_b) found in the base region. Internal and external flows are coupling in the wake region and in the present model the pressure p_2 (inside the tube) is made equal to the base pressure p_b, so that

$$Cp_b = \frac{P_2 - P_\infty}{\frac{1}{2}\rho V_\infty^2} \tag{2}$$

The above assumption is the main difference between the present work and the classical actuator disk theory (see Eggleston & Stoddard 1987), where the pressure just downstream the disk is increased to the free stream pressure due to a decrease of the flow velocity.

Considering equations (1), (2) the Bernoulli equation, the power generated by the confined wind turbine can be expressed by

$$W_e = Sq_\infty V_\infty \left(\frac{V_1}{V_\infty}\right)\left[1 - Cp_b - \left(\frac{V_1}{V_\infty}\right)^2\right] \tag{3}$$

where q_∞ is the dynamic pressure of the undisturbed flow. Finally, the efficiency of the confined wind turbine can be given by

$$\eta = \left(\frac{V_1}{V_\infty}\right)\left[1 - Cp_b - \left(\frac{V_1}{V_\infty}\right)^2\right] \tag{4}$$

Here it is important to note that the mass flow rate inside the tube (or the velocity V_1) affects the base pressure coefficient. The relation between the above two parameters was obtained by experiments, and as mentioned previously, such relation between Cp_b and V_1/V_∞ was obtained by a second order polynomial fitting (see curve shown in the Fig. 7).

Equation (4) and the classical wind turbine efficiency are plotted in the Fig. 8, showing the maximum efficiency (η=59.3%) for a velocity V_1=2/3 V_∞., for the free wind turbine. Comparing the two wind turbine conceptions, the confined one is more efficient than the free wind turbine. The maximum value for the confined turbine efficiency is 65,4% and this value occurs to non dimensional velocity equal to 0.7. The results presented for the confined wind turbine have some uncertainty, due to the few experimental data presented in the Fig. 7. More experiments are necessary, mainly for low velocities inside the tube. Such velocities can be obtained by using other screens, which were not available during the present experimental work.

Some interesting characteristics can be observed in the Fig. 8: For the free wind turbine, the non-dimensional velocity at the disk plane varies from 0.5 to 1.0 and the maximum efficiency occurs for a velocity equal to 0.667, which is related to a great axial force (or a great pressure loss). For the confined wind turbine, velocities greater than the undisturbed flow velocity can be reached due to the suction caused by the low pressure in the base region of the flat plate. Moreover, the minimum value for the non-dimensional velocity (0.5) at the actuator disk plane (free turbine) occurs because the pressure behind this disk has to be recovered to the undisturbed flow pressure. For the confined case, the base pressure is fixed by the flow in the flat plate wake and, then, the velocity inside the tube (passing through a wind turbine) can be lower than the limit mentioned above.

5. CONCLUDING REMARKS

An important result is the relation between the base pressure coefficient and the velocity inside the tube. This relation is the result of the coupling between the external flow in the wake region (downstream the flat plate) and the flow inside the tube, which passes through the screens. The theoretical calculation of this relation is very difficult to be obtained due to the complex nature of a wake flow interacting with a jet. On the other hand, the experimental procedure is relatively simple and will be used to additional investigations, as described below.

A simple model, based on the actuator disk theory, was developed for the case of a confined wind turbine. The relation between the base pressure and the non dimensional velocity of the tube internal flow can be used to complete the theoretical model, and to determine the efficiency of a confined wind turbine. On the basis of the experimental results obtained in the present work, an improvement of nearly 10% was observed for the confined wind turbine efficiency. For the configuration with the internal flow totally blockade, the base pressure has a value equal to -0.3, which can be compared to the value (Cp_b = -1.1) for the base pressure coefficient of a two dimensional flat plate. This comparison is interesting because a two dimensional flow would perform more suction than the three dimensional flat plate used in the present work, and therefore, a confined wind turbine would have greater efficiency.

The present reported is only a first work of this research program, where the interaction of internal and external flow is the main objective. The confined wind turbine would be a practical application for such class of flows, but much more work has to be done before a final conclusion. Further experiments are already scheduled in order to investigate practical as well as fundamental aspects.

6. REFERENCES

Bearman, P.W. On vortex street wakes, *J. fluid Mech.*, Vol. 28, pp. 625-641, 1967.

Doebelin, E.O., *Measurement Systems: Application and Design*, McGraw-Hill, New York, 1990.

Eggleston, D.M. & Stoddard, F.S., *Wind Turbine Engineering Design*, Van Nostrand, New York, 1987.

Fage, A. & Johansen, F.C., On the flow behind an inclined flat plate of infinite span, *Proc. Roy. Soc. A*, pp. 380-388, 1927.

Glauert, H., Wind tunnel interference on wings, bodies and airscrews, *A.R.C. & M.*, No. 1566, 1933.

Kline, S.J. & McClintock, F. A., Describing uncertainties in single-sample experiments, *Mechanical Eng.*, pp. 3-8, 1953.

Maskell, E.C.,A theory of the blockage effects on bluff bodies and stalled wings in a closed wind tunnel, *A.R.C.&M.*, No. 3400, 1963.

XIV Brazilian Congress of Mechanical Engineering
Obeid Plaza Hotel Convention Center - Bauru - SP/Brazil
December 08-12th 1997

PAPER CODE: COB747

AVALIAÇÃO DA INTERFERÊNCIA DAS PAREDES DE UM TÚNEL DE VENTO SOBRE RESULTADOS EXPERIMENTAIS / *EVALUATION OF WIND TUNNEL WALL INTERFERENCE ON EXPERIMENTAL RESULTS*

ROBERTO DA MOTA GIRARDI & BRENO MOURA CASTRO
CTA - ITA - Divisão de Engenharia Aeronáutica - Praça Mal. Eduardo Gomes, 50
CEP 12.228-900 - São José dos Campos - SP - Brasil - E-mail: girardi@aer.ita.cta.br

Abstract

A method for correction of the blockage effect of the wind tunnel walls on the experimental results, based on the panel technique, is presented. The method is valid only for subsonic flows (Mach≤0,3). Some comparisons with the worldwide adopted method proposed in Rae & Pope (1984) are made and some contributions of the present work are discussed.

Keywords

Wind tunnel, blockage corrections, panel method, tridimensional flow, complex geometries.

1. INTRODUÇÃO

O problema de corrigir-se os resultados obtidos em túneis aerodinâmicos tem preocupado os operadores desde o início deste século, após o aparecimento dos primeiros túneis aerodinâmicos. Teorias baseadas no método das singularidades (Rae & Pope, 1984) foram formuladas para auxiliar as correções dos resultados experimentais, de forma a retirar a interferência no escoamento sobre os modelos, devido à presença das paredes do túnel de vento. Estas teorias tiveram sucesso no caso de corpos esbeltos simples (teoria do perfil fino), porém, para o caso de configurações mais complexas com espessuras relativas maiores, estes resultados teóricos simples tiveram que ser corrigidos através de extensos programas experimentais. Outro problema que afeta a confiabilidade dos resultados experimentais obtidos em túnel aerodinâmico é a interferência causada pelos suportes do modelo (mastros). Para avaliar esta interferência devem ser feitos ensaios adicionais, deslocando-se a posição do mastro, acarretando em custo mais alto para obter-se as informações necessárias para o desenvolvimento do projeto associado ao modelo que está sendo ensaiado.

No presente trabalho foi desenvolvido um código computacional, baseado no método dos painéis, para uma geometria complexa (por exemplo, um avião), instalada no interior de um túnel de vento e considerando-se a presença dos mastros. A idéia consiste em executar o código computacional, considerando-se todos os elementos mencionados acima e, em seguida, realizar novamente os cálculos considerando-se somente a geometria complexa. Com estes dois conjuntos de resultados numéricos pode-se avaliar a interferência das paredes do túnel de vento e também dos mastros. A grande vantagem deste método com relação ao aplicado

atualmente (Rae & Pope, 1984) é a possibilidade de promover-se a correção dos resultados em cada ponto da superfície do modelo. Neste artigo são apresentados os resultados das validações feitas para o código computacional desenvolvido.

Este trabalho representa o primeiro passo no desenvolvimento de um método de correção de ensaios em túnel de vento. No estágio atual do método, apenas as correções do efeito de bloqueio estão implementadas. Trabalhos futuros devem ser conduzidos para uma validação do método de correção desse efeito através de comparações com resultados experimentais. Além disso, existe a possibilidade de implementação de outros tipos de correção tais como correções do efeito de bloqueio devido à esteira do modelo e correções de perda de carga ao longo da seção de ensaios.

2. FORMULAÇÃO E MÉTODO DE CÁLCULO

O problema em questão é a determinação das características do escoamento sobre um modelo colocado no interior de um túnel de vento. Neste caso, considerando-se o escoamento no início da seção de testes com perfil uniforme, para alto número de Reynolds e para número de Mach menor que 0,3 (Karamcheti, 1966), o escoamento pode ser considerado como potencial.

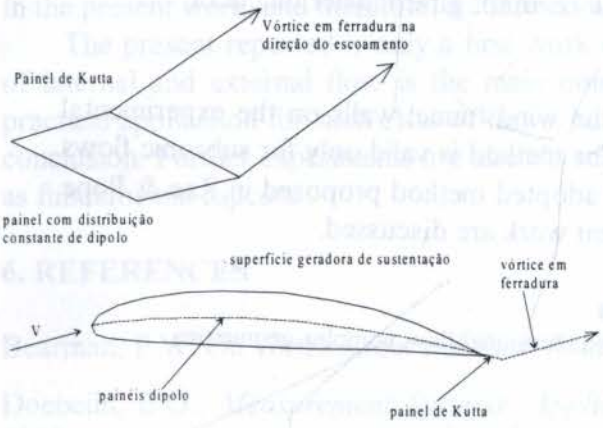

Figura 1 - Esquema do painel de Kutta

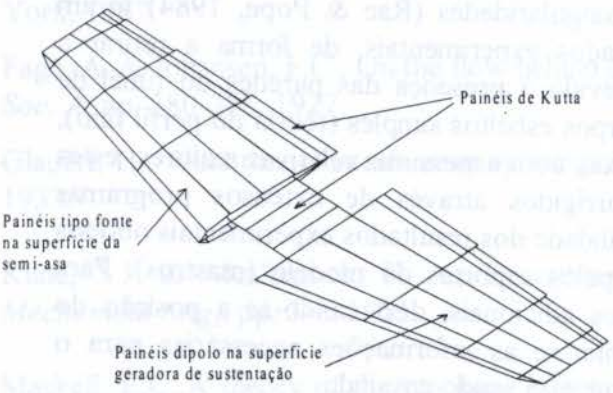

Figura 2 - Discretização de uma asa mostrando a superfície geradora de sustentação

A solução numérica utilizada neste trabalho consiste em dividir as superfícies do modelo, das paredes do túnel e dos mastros em painéis do tipo fonte, dipolo e vórtices em ferradura, que são soluções simples da equação de Laplace. Todos os painéis utilizados neste trabalho são quadriláteros e possuem distribuição constante de singularidade (Katz & Plotkin, 1991, fornecem todas as equações). As condições de contorno empregadas em todos os painéis correspondem ao Problema de Neumann, ou seja, velocidade normal nula em todos os pontos de controle, localizados no centro geométrico dos quadriláteros.

As fuselagens dos modelos são consideradas como corpos sem sustentação. As superfícies de corpos deste tipo são modeladas de forma semelhante ao método de Hess & Smith (1966), ou seja, painéis tipo fonte com intensidade constante.

As asas são discretizadas com painéis fonte na sua superfície e por painéis dipolo na sua linha de arqueamento. Além desses, são colocados painéis de Kutta no bordo de fuga da asa para impor a condição de Kutta. O painel de Kutta consiste de um painel dipolo acoplado a um vórtice em ferradura (vide figura 1). Os vórtices em ferradura, constituintes dos painéis de Kutta, são responsáveis pela simulação da esteira da asa. O presente método é semelhante ao de Hess (1972), com a diferença de que neste trabalho a distribuição de dipolos ao longo da superfície geradora de sustentação é uma conseqüência da

imposição da condição de contorno nos pontos de controle dessa superfície. O método de Hess (1972), no entanto, considera uma distribuição de dipolos pré-estabelecida no interior da asa, não necessitando, assim, de impor condições de contorno adicionais, como no caso deste trabalho. A utilização de painéis dipolo no interior de um corpo com sustentação corresponde à aplicação de um esquema do tipo Vortex Lattice internamente ao corpo.

No caso de configurações compostas por partes que geram sustentação (como uma asa) e partes que não geram (como uma fuselagem), deve-se estender a superfície geradora de sustentação para o interior das partes que não geram sustentação, de modo a evitar-se erros numéricos na intersecção asa-fuselagem. O detalhe da geometria adotada neste trabalho para a extensão da superfície geradora de sustentação é mostrado na figura 2.

As paredes do túnel são modeladas apenas por painéis dipolo, com excessão da faixa adjacente à seção de saída, que é preenchida com painéis de Kutta. Não existem painéis fechando as seções de entrada e de saída do túnel, de tal forma que a superfície total fique fechada.

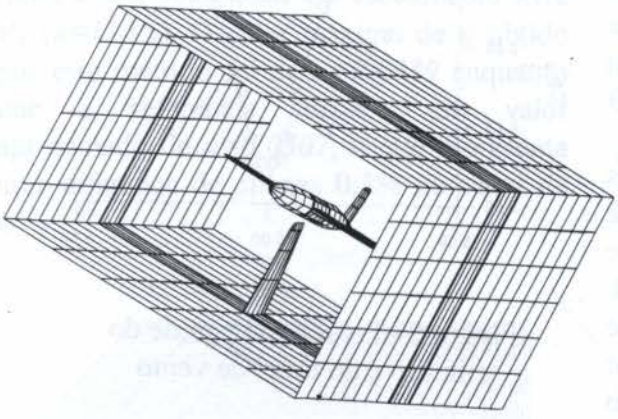

Figura 3 - Exemplo de configuração para aplicação deste método

O modelamento do túnel corresponde, assim, ao modelamento de uma asa sem espessura. Os painéis dipolo correspondem a um esquema do tipo "Vortex Lattice" e os painéis de Kutta simulam a esteira.

O mesmo modelamento das asas é utilizado para os painéis dos mastros. A figura 3 apresenta um exemplo de configuração com a qual é possível a utilização deste método.

O cálculo dos coeficientes aerodinâmicos pode ser feito de duas formas distintas: (i) através da integração da pressão na superfície do modelo e (ii) utilizando-se as intensidades dos vórtices das esteiras das superfícies geradoras de sustentação das asas, usando-se o chamado plano de Trefftz (veja, Karamcheti, 1966, e Kroo & Smith, 1990). Esta técnica foi implementada no presente trabalho e, como relatado por Letcher Jr. (1989), apresenta resultados melhores para o caso do arrasto induzido.

3. APLICAÇÃO DO MÉTODO

Nesta seção do artigo serão apresentados exemplos utilizados para a validação do método de cálculo e para ilustrar a metodologia proposta para a correção de resultados experimentais, de modo a eliminar os efeitos causados pela interferência das paredes de um túnel de vento.

3.1. Cilindro em túnel bidimensional (bloqueio=30%) - exemplo 2-D sem sustentação

Aproveitando a possibilidade de se modelar o mastro do túnel, foi utilizada uma configuração apresentando apenas as paredes e um mastro circular para simular um cilindro, com diâmetro d, em um túnel bidimensional, com altura H. Este caso foi estudado analiticamente e constitui um excelente teste para validação do modelamento utilizado para os painéis da parede do túnel. O corpo no interior do túnel é um cilindro que vai de uma parede lateral à outra. O bloqueio estudado foi de 30% (d/H=0,30). A discretização para este caso é apresentada na figura 4. As paredes do túnel foram divididas em 30 faixas com 22 painéis

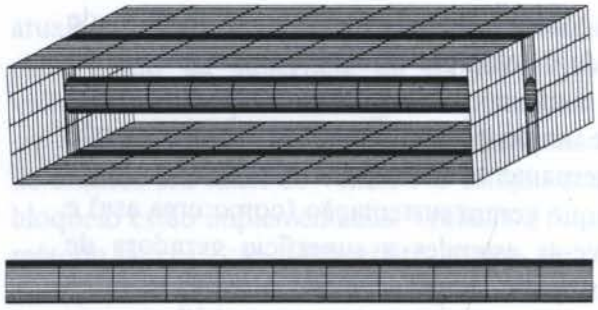

Figura 4: Discretização do cilindro em um túnel bidimensional

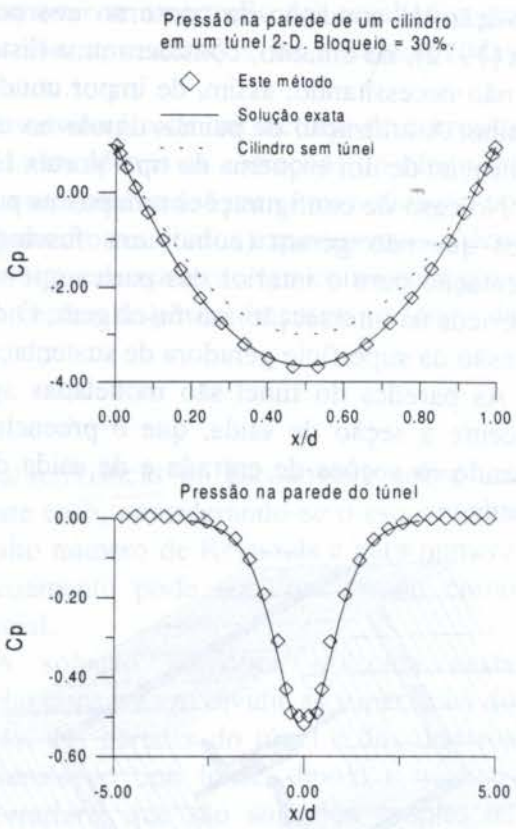

Figura 5 - Pressão na parede do cilindro e do túnel de vento

dipolo cada. Na saída do túnel foram colocados 22 painéis de Kutta. O cilindro foi modelado em 11 faixas, cada uma com 48 painéis fonte, 24 painéis dipolo na linha de arqueamento (já que se trata de um mastro) e um painel de Kutta. Assim, foram utilizados 924 painéis dipolo, 528 painéis fonte e 33 painéis de Kutta, totalizando 1485 painéis.

A figura 5 mostra a comparação dos resultados obtidos com a solução exata (Rae & Pope, 1984). A aproximação entre os valores é muito grande. Apenas a pressão na parede do túnel, em torno de x/d=0,0 é que ficou ligeiramente diferente. Isso se deve à variação brusca do tamanho dos painéis na região do mastro (x/d=0,0), como pode ser observado na figura 4.

3.2. Esfera em túnel de seção circular (bloqueio=7,5%) - exemplo 3-D sem sustentação

O segundo estudo foi um caso apresentado por Holst (1984). Consiste de uma esfera localizada no centro de um túnel de vento circular. O bloqueio, definido como a relação entre a área da seção máxima da esfera e a área da seção transversal do túnel, é de 7,5%.

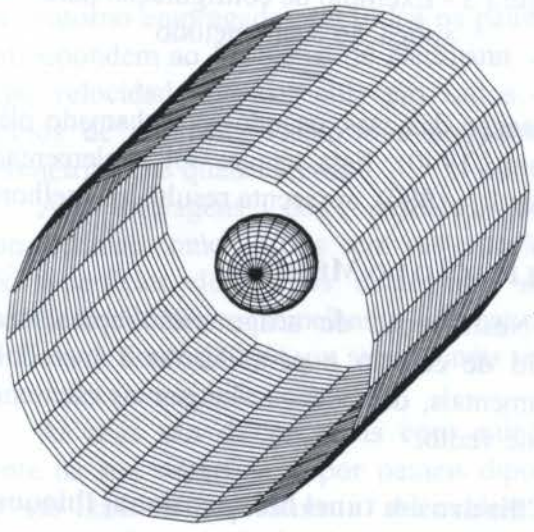

Figura 6: Discretização da esfera em um túnel circular

O modelamento do túnel foi feito utilizando-se 40 faixas com 24 painéis dipolo cada. A saída foi dividida em 24 painéis de Kutta. A esfera foi discretizada em 24 faixas com 24 painéis fonte cada. Foram utilizados, então, 576 painéis fonte, 960 painéis dipolo e 24 painéis de Kutta, em um total de 1560, os quais podem ser observados na figura 6. O comprimento do túnel foi feito igual a duas vezes o diâmetro da seção transversal (L=2,0D ou L=4,0R). Este é o menor valor que faz com que a velocidade na saída do túnel seja igual a V_∞, conforme pode ser observado na figura 7.

A comparação dos resultados obtidos pelos dois métodos encontra-se na figura 7. Há uma ligeira discrepância entre os valores de u/V_∞ devido à discretização utilizada e à forma como foi modelada a esfera. Holst (1984) utilizou um método numérico com um dipolo no centro da esfera para simulá-la e vórtices em ferradura no túnel. Neste trabalho foram utilizados painéis fonte na superfície da esfera e dipolo no túnel. Cabe salientar que o que se está comparando são valores de u/V_∞, onde u é a velocidade de perturbação do escoamento definida como a diferença entre a velocidade na superfície do túnel U e a velocidade do escoamento livre V_∞ ($u=U-V_\infty$). O valor máximo de u obtido por este método foi de $u=0.0339$ enquanto que a referência fornece um valor aproximado de $u=0.0307$, o que representa uma diferença de apenas 0,3% no valor de U.

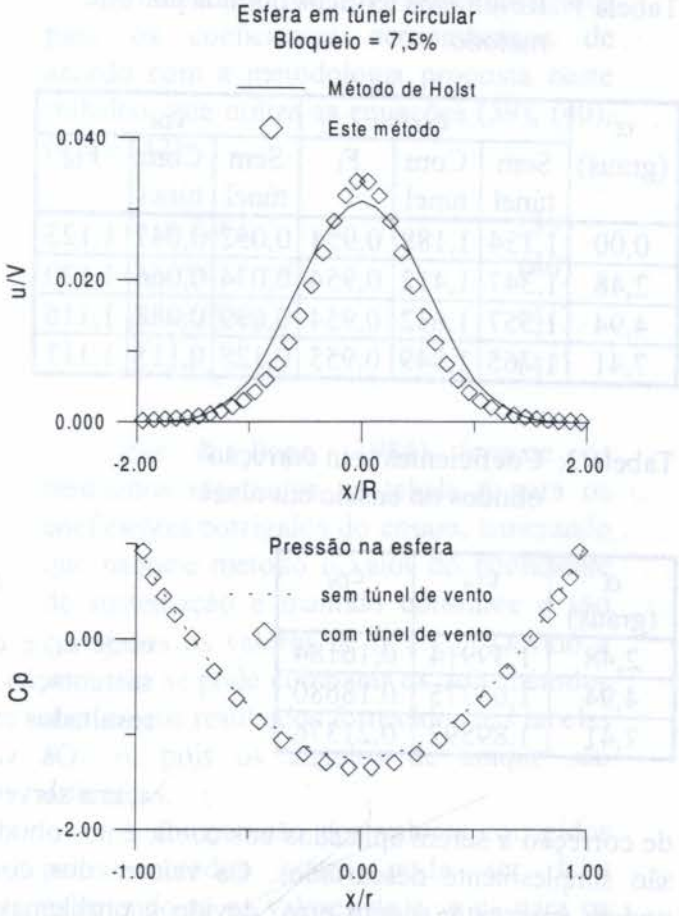

Figura 7: Pressão na superfície da esfera e nas paredes do túnel

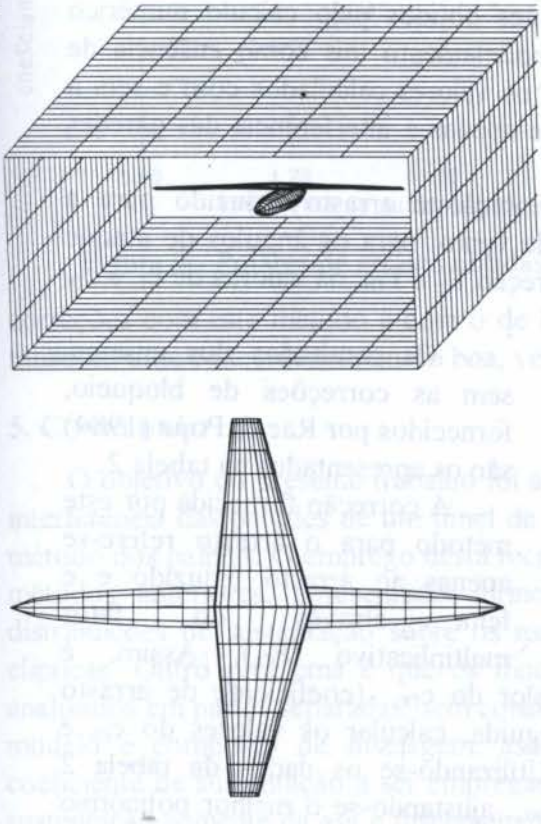

Figura 8: Discretização da configuração asa e fuselagem em um túnel de vento retangular

3.3. Asa-fuselagem em túnel de vento

Este exemplo consiste da aplicação da metodologia de correção da interferência das paredes de um túnel de vento, proposta neste trabalho, para um caso prático. Os resultados experimentais obtidos para uma configuração asa-fuselagem, encontrada em Rae & Pope (1984), foram utilizados. Estes resultados foram corrigidos pelo método usado pelos autores da referência acima e, também, pelo método proposto no presente trabalho.

A figura 8 mostra o modelo utilizado e sua discretização, na qual empregou-se um total de 1390 painéis.

O valor de b/B utilizado neste ensaio foi de b/B=0,6124, ou seja, a envergadura do modelo, b, ocupa 61% da largura do túnel, B, sendo o valor de H/B=0,6667 (H é a altura do túnel de vento). Todos os detalhes da configuração e da

Tabela 1: Resultados teóricos obtidos por este método

α (graus)	c_L			c_{Di}		
	Sem túnel	Com túnel	F_L	Sem túnel	Com túnel	F_{Di}
0,00	1,134	1,188	0,954	0,052	0,047	1,123
2,48	1,347	1,412	0,954	0,074	0,066	1,120
4,94	1,557	1,632	0,954	0,099	0,088	1,116
7,41	1,765	1,849	0,955	0,128	0,115	1,111

Tabela 2: Coeficientes sem correção obtidos no ensaio em túnel

α (graus)	c_{Lu}	c_{Du}
2,48	1,39914	0,16184
4,94	1,65775	0,18680
7,41	1,89592	0,21376

Tabela 3: Coeficientes corrigidos por este método

α (graus)	c_L Eq. (39)	c_{Diu} Eq. (40)	c_{Di} Eq. (41)	c_D Eq. (42)
2,48	1,33505	0,06195	0,06940	0,16929
4,94	1,58199	0,08691	0,09698	0,19687
7,41	1,80975	0,11387	0,12647	0,22636

Tabela 4: Coef. corrigidos por Rae & Pope (1984)

α (graus)	c_L	c_D
3,15	1,39914	0,17819
5,74	1,65775	0,20981
8,32	1,89592	0,24391

discretização podem ser encontrados no trabalho de Castro (1997).

O método proposto neste trabalho consiste em calcular numericamente os coeficientes aerodinâmicos do modelo dentro do túnel de vento e, depois, sem a presença das paredes. A relação entre os coeficientes obtidos em cada condição fornece o fator de correção a ser utilizado para o ensaio, segundo as equações (35) e (36).

$$F_L = \frac{c_L}{c_{Lu}} \qquad (35)$$

$$F_{D_i} = \frac{c_{D_i}}{c_{D_i u}} \qquad (36)$$

onde c_L e c_{Di} são os coeficientes, já corrigidos, de sustentação e arrasto induzido. O sub-índice, u, indica resultados experimentais sem correção.

Os valores obtidos nos cálculos numéricos acima servem apenas para a determinação dos fatores de correção a serem aplicados nos coeficientes obtidos nos ensaios. Após a sua utilização eles são simplesmente descartados. Os valores dos coeficientes obtidos pelo cálculo numérico podem apresentar algum erro, devido a problemas de modelamento tais como ausência de camada limite e erros numéricos, porém, a relação entre os valores calculados com e sem a presença do túnel apresenta valores confiáveis pois reflete apenas a interferência das paredes sobre o modelo.

Assim, foram calculados os coeficientes de sustentação e arrasto induzido para a configuração admitida, com e sem a presença do túnel de vento, para os ângulos de ataque constantes da tabela 1. Após o cálculo dos fatores de correção F_L e F_{Di}, os valores de c_L e c_{Di} são descartados.

Os resultados dos ensaios, sem as correções de bloqueio, fornecidos por Rae & Pope (1984) são os apresentados na tabela 2.

A correção fornecida por este método para o arrasto refere-se apenas ao arrasto induzido e é feita através do fator multiplicativo (F_{Di}). Assim, é necessário obter o valor do c_{D0} (coeficiente de arrasto parasita) para, em seguida, calcular os valores do c_{Di} e fazer as correções. Utilizando-se os dados da tabela 2 pode-se determinar c_{D0}, ajustando-se o melhor polinômio de segundo grau que passa pelos pontos obtidos nos ensaios, já que a polar de arrasto de uma asa é, aproximadamente, uma parábola (veja Karamcheti 1966).

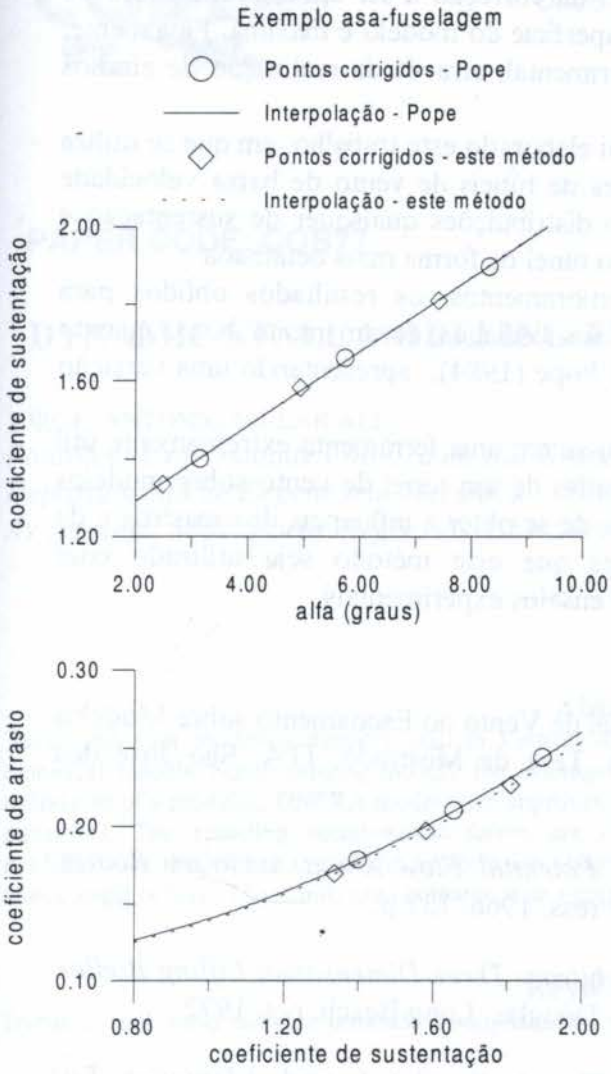

Figura 9 - Polares de arrasto obtidas

A tabela 3 fornece os valores corrigidos para os coeficientes aerodinâmicos de acordo com a metodologia proposta neste trabalho, que utiliza as equações (39), (40), (41) e (42).

$$c_L = F_L c_{Lu} \tag{39}$$

$$c_{D_i u} = c_{Du} - c_{D_0} \tag{40}$$

$$c_{D_i} = F_{D_i} c_{D_i u} \tag{41}$$

$$c_D = c_{D_i} + c_{D_0} \tag{42}$$

Rae & Pope (1984) fornece os resultados mostrados na tabela 4 para os coeficientes corrigidos do ensaio, lembrando que naquele método o valor do coeficiente de sustentação é mantido constante e são corrigidos os valores de α e C_D. Devido a isso, não se pode comparar os dois métodos através dos resultados fornecidos nas tabelas 5 e 6, pois os ângulos de ataque são diferentes.

A comparação dos valores corrigidos pelos métodos acima pode ser feita calculando-se os valores de c_L e c_D para os pontos intermediários de ângulo de ataque. Para tanto, ajusta-se um polinômio do segundo grau sobre os pontos da tabela 4 para a representação da polar de arrasto do modelo. As curvas de sustentação vs. ângulo de ataque e polar de arrasto, para as correções com este método e com o de Rae & Pope (1984), são apresentadas na figura 9, e mostram uma concordância muito boa, verificando-se diferenças menores que 3%.

5. CONCLUSÃO

O objetivo do presente trabalho foi apresentar um método mais elaborado de avaliação da interferência das paredes de um túnel de vento sobre modelos tridimensionais utilizando-se o método dos painéis. O emprego desta técnica foi motivado pelas simplificações admitidas pelos métodos anteriores, apresentados principalmente por Rae & Pope (1984), em que as distribuições de sustentação sobre os modelos são consideradas como sendo constantes ou elípticas. Outro problema é que os modelos, quando compostos de asas e fuselagem, são analisados em partes separadas, sem considerar as interferências mútuas. Além disso, quando o modelo é composto de fuselagem, asa e empenagem, existe uma dúvida a respeito do coeficiente de sustentação a ser empregado nas correções. Pode-se empregar o coeficiente de sustentação somente da asa e fuselagem, sem a presença da empenagem, ou o da configuração completa. Esta dúvida gera imprecisão na aplicação do método e implica na realização de ensaios adicionais, da configuração sem a empenagem, acarretando aumento dos custos do ensaio. Outro aspecto importante é que não se estabelece uma correção do coeficiente de pressão para cada ponto do modelo. No caso de se desejar obter a distribuição de pressão

sobre um perfil, por exemplo, não haveria distinção da correção a ser aplicada no ponto de estagnação e no extradorso, onde a velocidade na superfície do modelo é máxima. Finalmente, a interferência dos mastros é obtida de forma experimental, através da realização de ensaios adicionais com mastros imagem.

Para contornar as limitações desses métodos, foi elaborado este trabalho, em que se utiliza o método dos painéis, possibilitando aos operadores de túneis de vento de baixa velocidade obterem correções para seus ensaios, considerando distribuições quaisquer de sustentação e interferências entre as diversas partes do modelo e do túnel de forma mais detalhada.

Apesar do método necessitar de alguns aprimoramentos, os resultados obtidos para correções de ensaios de configurações tipo asa e asa-fuselagem foram muito bons, quando comparados com as correções propostas por Rae & Pope (1984), apresentando uma variação máxima em torno de 3%.

Diante do exposto, o presente método constitui-se em uma ferramenta extremamente útil para uma correta avaliação da interferência das paredes de um túnel de vento sobre modelos complexos, contando, inclusive, com a possibilidade de se obter a influência dos mastros e de diminuir os custos do ensaio. No entanto, antes que este método seja utilizado com confiabilidade, deve-se testá-lo na prática através de ensaios experimentais.

6. REFERÊNCIAS BIBLIOGRÁFICAS

CASTRO, B.M. Interferência das Paredes de um Túnel de Vento no Escoamento sobre Modelos Tridimensionais Utilizando o Método dos Paineis. Tese de Mestrado, ITA, São José dos Campos, SP, 1997.

HESS, J. L. & SMITH, A. M. O. *Calculation of Potential Flow About Arbitrary Bodies*. Progress in Aeronautical Sciences, v. 8. Pergamon Press. 1966. 137 p.

HESS, J. L. *Calculation of Potential Flow About Arbitrary Three-Dimensional Lifting Bodies*. Final Technical Report, MDC J5679-01, McDonnel Douglas, Long Beach, oct. 1972.

HOLST, H. *Wind Tunnel Wall Interference in Closed, Ventilated, and Adaptative Test Sections*. Separata de Wind Tunnel Wall Interference Assessment/ Correction 1983. NASA Conference Publication 2319, p. 61-78, 1984.

KARAMCHETI, K. *Principles of Ideal-Fluid Aerodynamics*. New York: John Wiley and Sons, 1966. 636 p. ISBN 0-471-45852-X.

KATZ, J. & PLOTKIN, A. *Low-Speed Aerodynamics - From Wing Theory to Panel Methods*. New York: McGraw-Hill, Inc., 1991. 632 p. ISBN 0-07-050446-6.

KROO, I. & SMITH, S. C. *The Computation of Induced Drag with Nonplanar and Deformed Wakes*. SAE Technical Paper Series. Long Beach: SAE, 1990.

LETCHER JR., J. S. Convergence of Lift and Drag Predictions by a Morino Panel Method (VSAERO). *AIAA Journal*, v. 27, n. 8, p. 1019-1021, aug. 1989.

RAE JR., W. H. & POPE, A. *Low-Speed Wind Tunnel Testing*. 2. ed. New York: John Wiley & Sons, 1984. 534 p. ISBN 0-471-87402-7.

SMITH, S. C. & KROO, I. M. Computation of Induced Drag for Elliptical and Crescent-Shaped Wings. *Journal of Aircraft*, Washington, v. 30, n. 4, p. 446-452, july/aug. 1993.

XIV Brazilian Congress of Mechanical Engineering
Obeid Plaza Hotel Convention Center - Bauru - SP/Brazil
December 08-12th 1997

PAPER CODE: COB77

DYNAMIC STALL MODELING TECHNIQUES IN WIND TURBINES

JORGE ANTONIO VILLAR ALÉ
Pontificia Universidade Católica do Rio Grande do Sul - PUCRS
Departamento de Engenharia Mecânica - Eólus - Grupo de Energia Eólica
Av Ipiranga 6681, Porto Alegre, RS, CEP 90.619-900 - E-mail: villar@music.pucrs.br

Abstract

Techniques for modeling dynamic stall in Vertical Axis Wind Turbines (VAWT) are analyzed using semi-empirical models. Some existing models, the Boeing-Vertol, MIT and Indicial are reviewed. Is proposed the utilization of a modified ONERA model with improved performance. The model is based on a set of differential equations. The resulting aerodynamic forces are presented with the proposed model, after including modifications that extend the model to operation at low tip speed ratio where the amplitude oscillation of the attack angle is high. The results are compared with experiment showing good agreement.

Keywords

Dynamic stall, wind turbines, unsteady aerodynamics.

1. INTRODUCTION

The determination of aerodynamic forces on VAWT blades operating in dynamic stall condition is a complicated problem because of the difficulties of the characterization of its physical phenomenon on experimental investigation and consequently the adaptation of an effective model to describe the phenomenon in all its extension. In VAWT at low Tip Speed Ratio (defined as $\lambda=\Omega R/U_\infty$, where U_∞, is the non-perturbed velocity, Ω is rotational velocity and R the turbine radius) the cyclic variation of the angle of incidence reaches high amplitude extending beyond the stall angle manifesting the typical effects that occurs at dynamic stall phenomenon. It is characterized by the development and displacement of the vortices on the suction side of the airfoil causing deformation of the pressure distribution. This phenomenon substantially modifies the aerodynamic forces affecting the turbine performance and also endangers the turbine structure.

Although there exist models based on the Navier-Stokes equations and vortex theory that describe the phenomenon of dynamic stall, the only viable solution for engineering application is to approach the problem by using models originating from the helicopter. These models are semi-empirical in nature based on the coefficients obtained from the wind tunnel tests. Previously four models have been utilized in VAWT: the Boeing-Vertol model, the MIT model, the Indicial model and the ONERA model. It is observed that the largest divergence of the existing models with the experimental data is found to occur in the aerodynamic forces at the downwind side of the blade trajectory that get disturbed by the forwarding blades, especially on the characteristics of the tangential forces. This work improves the ONERA model adequately for the conditions appropriate to the phenomenon encountered by the VAWT blades.

2. MODELS USED IN VAWT

2.1 Boeing-Vertol Model

This model was developed by Gormont (1973) to analyze the aerodynamics of helicopter blades. The linear domain of the model is based on the classic theory of Theodorsen and in the dynamic stall region works with a semi-empirical formula. The temporal lag to attain dynamic stall is given as a function of the dynamic stall parameter equivalent to the reduced frequency. The model was introduced by Strickland *et al.* (1979) for VAWT with the vortex development in the wake. Paraschivoiu and Allet (1988) utilized it in VAWT with the strip theory in multiple stream tubes of the flow field. Vanderbergue and Dick (1991) also used it with the vortex model. It is observed that the results obtained by all these models do not agree with experimental results when the amplitude of oscillation is high, specially for the tangential forces. Figure 1 shows the results for λ=2.0, in which the discrepancy is clearly visible.

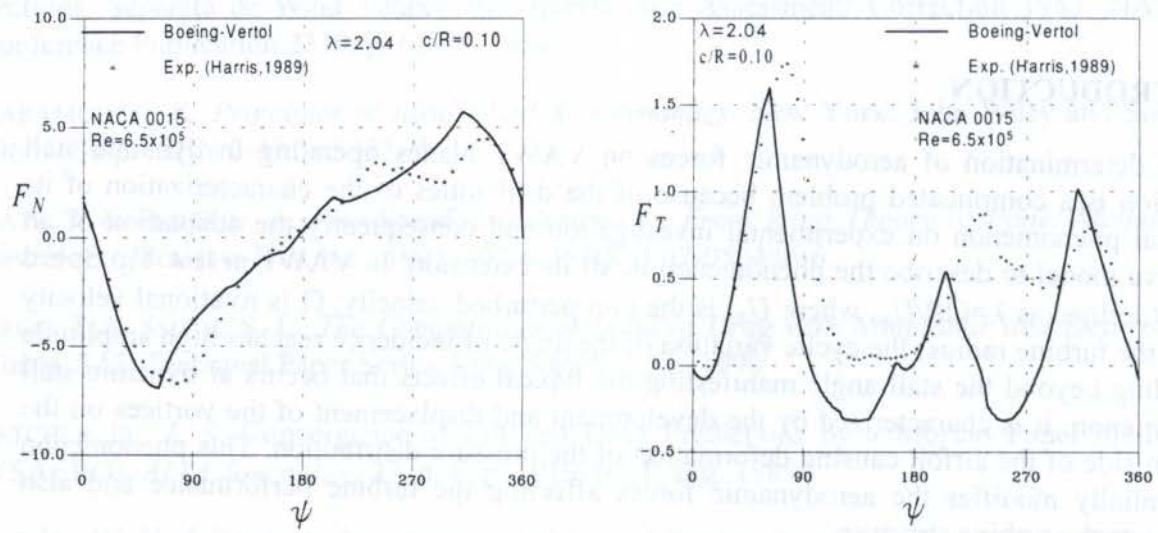

Figure 1 - Boeing-Vertol model to nondimensional forces in VAWT

2.2 MIT Model

This model was developed at the Massachusetts Institute of Technology (MIT) by Noll and Ham (1982) adapting the empirical relations of the Boeing-Vertol model to determine the angle of attack in dynamic stall. Up to the separating regime steady state data are used for lift and drag coefficients of the blade. When the angle of attack exceeds the static stall the aerodynamic coefficients are assumed to increase linearly until reach the maximum value, depending on the dynamic stall parameter. After reaching the maximum value the lift is determined using the classical theory of oscillating blades, assuming exponential law of the lift decrement as a function of azimuth angle until reaches the static stall angle. Paraschivoiu and Allet (1988) used this model in VAWT and compared results with that of the Boeing-Vertol. Figure 2 shows the results applying with MIT model.

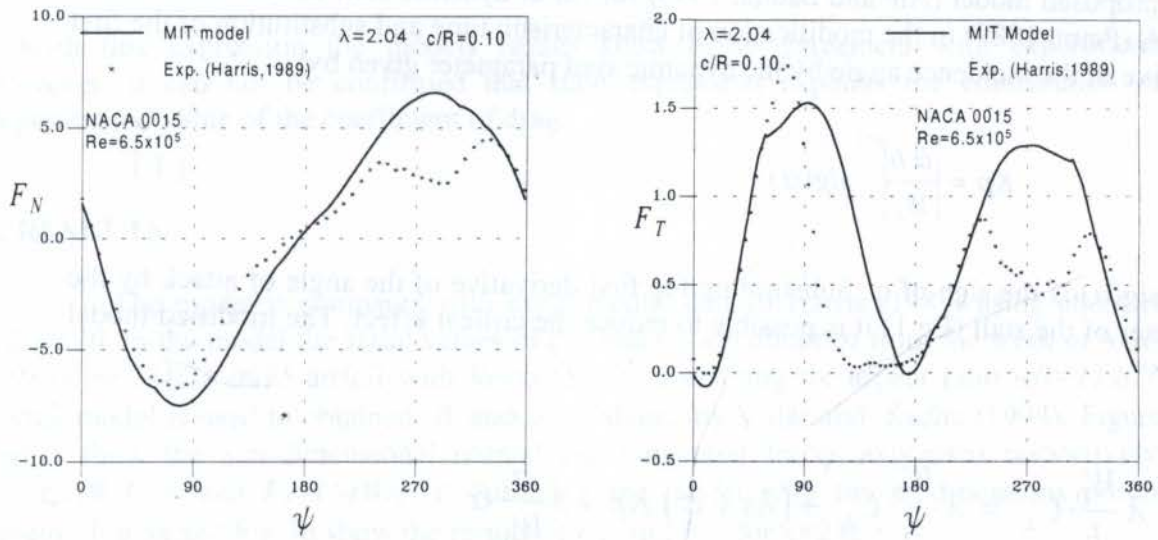

Figure 2 - MIT model at nondimensional forces in VAWT

2.3 Indicial Model

The model by Leisman and Beddoes (1986) presents three different solutions of the flow regime: (a) flow without separation involving unsteady forces with linear characteristics; (b) flow without separation for nonlinear aerodynamic forces; and (c) dynamic stall provoked by the vortex emission. Harris et al. (1989) presented the results with this model. It showed good agreement with the normal forces, but exhibited a large divergence for tangential forces. This model is also applied by Jiang *et al.* (1991) and Liu *et al.* (1992) for VAWT but the results are limited to determination directly the turbine power output.

3. PROPOSED MODEL

The proposed model is based in the ONERA model (Petot, 1989) and is a semi-empirical model developed to analyze the aerodynamic forces of helicopter blades. It can also be applied to the blades of the Horizontal Axis Wind turbine (HAWT) by Bierbooms (1989) and for the VAWT by Alé and Sadhu (1993). The dynamic stall phenomena is modeled as a

combination of differential equations that include coefficients obtained from the wind tunnel tests. When applied to the blades of helicopter and to the HAWT, the model produces satisfactory aerodynamic forces. However, in case of VAWT, in which the blades are subjected to high angles of attack, it also fails to produce a satisfactory model (see Alé and Sadhu, 1995). This work aimes to extend the model for the most adverse dynamic stall conditions. Various factors are studied that contribute in improving the model. To cite some of them : i) Appropriate use of the static lift and drag coefficients ii) Proper definition of the characteristic time iii)Modifying the equations by the characteristic parameter phenomena iv) Inclusion of an expression for the drag that allows better adjustment of the tangential forces. Modifications are explained in detail in Alé and Sadhu (1995) and Alé and Sadhu (1996).

3.1 Lift Model

The proposed model (Alé and Sadhu, 1996) for lift at dynamic stall differs from that of ONERA (Petot, 1989) in the modification of characteristic time and substitution of the first derivative of the incidence angle by the dynamic stall parameter given by:

$$Kp = \left| \frac{\dot{\alpha}\, b}{W_0} \right|^{1/2} sig(\alpha) \qquad (1)$$

where sig(α) is the sign of α. Substituting the first derivative of the angle of attack by the parameter of the stall (Eq.1) it is possible to reduce the critical effect. The modified model stays as:

$$\dot{C}_{L_1} + \lambda \frac{W_0}{b} C_{L_1} = \lambda \frac{W_0}{b} C_{L_I} + (\lambda s + \sigma)\, Kp + s \frac{b}{W_0} \ddot{\alpha}$$

$$\ddot{C}_{L_2} + a \frac{W}{b} \dot{C}_{L_2} + r \left(\frac{W}{b} \right)^2 C_{L_2} = -r \left(\frac{W}{b} \right)^2 \Delta C_L + EKp \qquad (2)$$

$$C_L = C_{L1} + C_{L_2}$$

the coefficients involved in the above expressions depend on the type of airfoil and could be found from Petot (1989).

3.2 Drag Model

The magnitude of the normal force (non-dimensional) presents similar order as C_L, showing little sensitivity to modification of C_D. This does not occur with tangential force. Hence, attention is focused to the study of modeling the drag aiming to improve the models for the tangential force. In the ONERA model, the drag is given by:

$$C_{D_1} = C_{D_I} + (\lambda s + \sigma) \frac{W}{b} \dot{\alpha} + s \left(\frac{W}{b} \right)^2 \ddot{\alpha}$$

$$\ddot{C}_{D_2} + a\frac{W}{b}\dot{C}_{D_2} + r\left(\frac{W}{b}\right)^2 C_{D_2} = -r\left(\frac{W}{b}\right)^2 \Delta C_D - E\frac{W}{b}\dot{\alpha} \qquad (3)$$

$$C_D = C_{D1} + C_{D2}$$

A expression for drag (Alé and Sadhu, 1996) is proposed as:

$$C_D^* = C_D \frac{sin^2\alpha}{\cos\alpha} \qquad (4)$$

With this expression the models results show better agreement with experiment. However, it can not be confirmed that such expression explains the contribution of experimental value of the coefficient of drag.

4. RESULTS

The model is compared with experimental data of Harris (1989) using chord ratio $c/R=0.10$. In the model the static values of C_L and C_D are obtained from the work of Madsen (1983) for *NACA 0015* airfoil with $Re=6.55x10^5$, correcting for aspect ratio $AR=11.8$. The vortex model is used to obtained W and α as shown by Villar and Sadhu (1994). Figures 3 and 4 show the non-dimensional normal and tangential forces expressed respectively as $F_N=C_N(W/U_\infty)^2$ and $F_T=C_T(W/U_\infty)^2$ utilizing the model with the modifications proposed herein Fig.3a and Fig.3b show the results of F_N and F_T for λ=2.0.

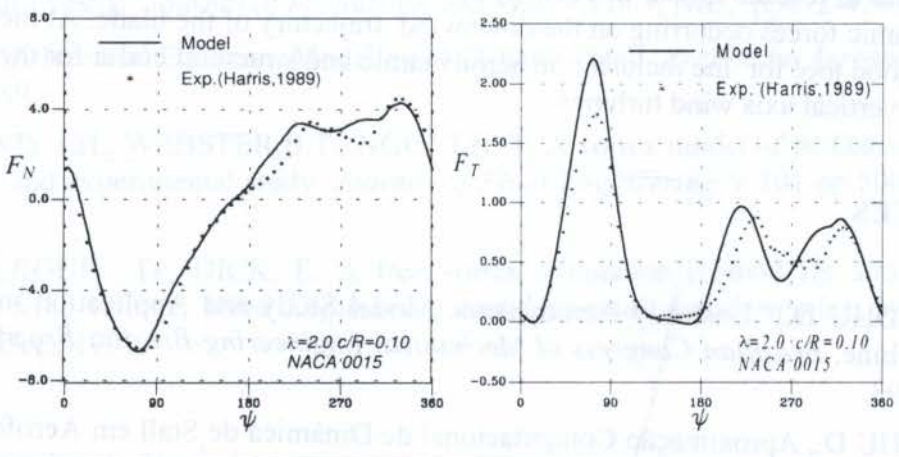

Figure 3. Proposed model for nondimensional aerodynamic forces in VAWT

For high amplitude oscillations, Figure 4 presents the typical hysteresis loop of dynamic stall of F_T with respect to incidence in which the model overestimates F_{Tmax} in the upwind region. In the downwind region, F_T obtained from the model deviates from the experimental

data. Figure 4b shows the results for λ=2.64. It can be seen that there is a good agreement with the experimental data with divergence occurring mainly on the downward trajectory.

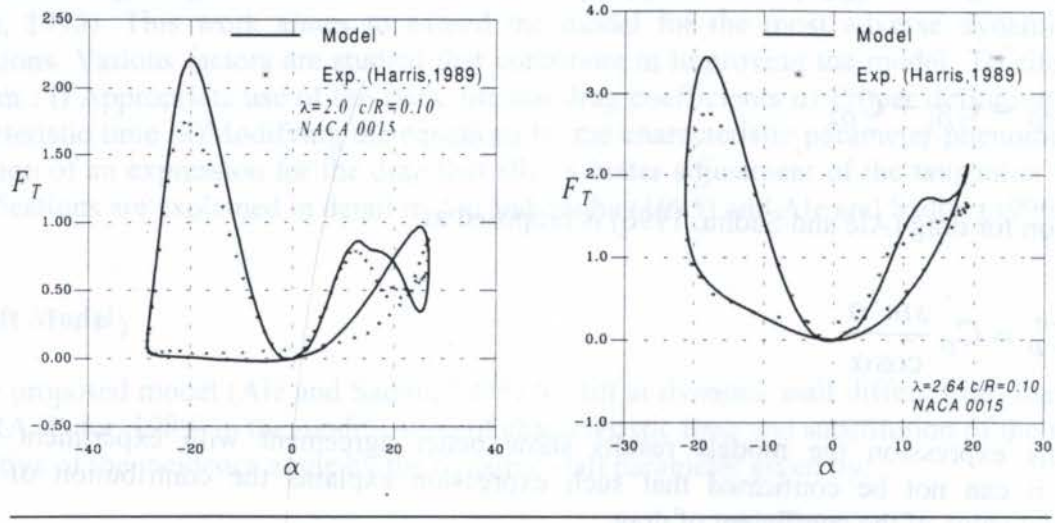

Figure 4. Proposed model for nondimensional aerodynamic forces in VAWT

5. CONCLUSION

The model presented permit the determination of the aerodynamic forces in VAWT in dynamic stall conditions. The modifications improve the original model at low tip speed ratio where there exists high variation of the angle of incidence and the phenomenon of dynamic stall is manifested in the aerodynamic forces. Perhaps the introduction of the parameter of stall in the diferential equations is not an elegant solution but, at the moment, is an effective way to extend the model to these critical conditions. The drag coefficient used permits the reduction of the high values obtain directly with the ONERA model and give a good agreement of the tangencial force at different tip speed ratios. It is necessary to have more experimental data to test the model in other dynamic stall conditions and to study the effects of the aerodynamic forces occurring on the downwind trajectory of the blade. At the moment the model is a good tool for the inclusion in aerodynamic and structural codes for the study of performance in vertical axis wind turbines.

6. REFERENCES

ALÉ V. J., SADHU D., Unsteady Aerodynamic Model Study and Application in Vertical Axis Wind Turbine. *Brazilian Congress of Mechanical Engineering-Brasilia Brazil*, Vol. I, pp.825-827, 1993.

ALÉ V.J. SADHU D., Aproximação Computacional de Dinâmica de Stall em Aerofólios com Movimento Cíclico Rotacional. VIII SENESE, *Anais do Seminario Nacional e Congreso Internacional de Energias Renovables*. Tarapaca, Chile., 1994.

ALÉ V.J. SADHU D., Determination of Aerodynamic Forces on VAWT Blade at Dynamic Stall. *Anais do 12th Brazilian Congress of Mechanical Engineering* Brazilia, Brazil, 1995

ALÉ V.J. SADHU D., Dynamic Stall Model in Vertical Axis Wind Turbines, VIII SENESE, *Anais do Seminario Nacional e Congreso Internacional de Energias Renovables*. pp. 188-193, Antofagasta, Chile, 1996.

BIERBOOMS W.A.M., *A Dynamic Model of Flexible Rotor Including Unteady Aerodynamics*; EWEC'89, European Wind Energy Conference, Glasgow, pp.278-282, 1989.

GORMONT, R.E., *A mathematical model of unsteady aerodynamics and radial flow for application to helicopter rotors*; Philadelphia: U.S., Army Air Mobility R&D Laboratory, Vertol Division, (Report on Boieng-Vertol ContractJ02-71-C00045) May,1973.

HARRIS A., CLAYTON B.R., MCD GALBRAITH R.A., GRASIDE A.J., ANGELL R.K., FOSTER J,E., Vertical Axis Wind Turbine/Aerodynamics in U.K.; EWEC'89, *European Wind Energy Conference,* Vol. I pp.64-69, 1989.

HARRIS A. Report on 25m VAWT at Camarthan Bay; VAWT MacAlpine Ltd, UK, 1989.

JIANG. D., COTON F.N., GALBRAITH MCD., A Fixed Wake Vortex Model fo Vertical Axis Wind Turbines Including Unsteady Aerodynamics; *Wind Engineering* Vol.15, No6, pp.348-360., 1991.

LIU W.Q., PARASCHIVOIU I., MARTINUZZI R., Calculation of Dynamic Stall on SANDIA 34M VAWT Using an Indicial Model; *Wind Engineering*, Vol.16, No6, pp. 313-325, 1992.

LEISHMAN, J.G. BEDDOES, T.S., A generalised for airfoil unsteady aerodynamics behaviour and dynamic stall using indicial method; *Annual Forum of the American Helicopter Society*, No42, p.243-265., 1982.

MADSEN H.A. On The Ideal and Real Energy Conversion in a Straight Bladed Vertical Axis Wind Turbine; Aalborg University Centre, Report, April, 1983.

NOLL, R.B. HAM, N.D., Effects of dynamics stall on Swecs; *Journal of Solar Energy Engineering*, Vol.104, pp.96-101., May.,1982.

PARASCHIVOIU I., ALLET A., Aerodynamic Analysis of Darreius Wind Turbine Including Dynamic Stall Effects; *Journal of Propulsion and Power* Vol.4, No5, pp472-477, 1988.

PETOT, D., Differential Equation Modeling of Dynamic Stall, *Recherche Aerospatiale*, No5, pp.59-72, 1989.

STRICKLAND, J.H., WEBSTER,B.T., NGUYEN, T. A vortex model of de Darrieus turbine: an analytical and experimental study. *Journal of Fluid Engineering* V.101 pp.500-505, Dec., 1979.

VANDERVERGUE , D., DICK, E. A free vortex simulation method for straight bladed vertical axis wind turbine. *Wind Engineering and Industrial Aerodymamics*. Vol.26 No.3, pp.307-324, Dec., 1991.

XIV Brazilian Congress of Mechanical Engineering
Obeid Plaza Hotel Convention Center - Bauru - SP/Brazil
December 08-12th 1997

PAPER CODE: COB785

UNSTEADY AIRFOIL INVISCID FLOW SIMULATIONS USING UNSTRUCTURED DYNAMIC MESHES

CARLOS FREDERICO CASTRO SIMÕES
EMBRAER - Empresa Brasileira de Aeronáutica, Av. Brigadeiro Faria Lima, 2170
12227-901 - São José dos Campos - SP - BRAZIL - E-mail: fred@aer.ita.cta.br
JOÃO LUIZ FILGUEIRAS AZEVEDO
Instituto de Aeronáutica e Espaço, CTA/IAE/ASE-N
12228-904 - São José dos Campos - SP - BRAZIL - E-mail: joaoaze@darwin.cesup.ufrgs.br

Abstract

The efforts for the simulation of unsteady airfoil flows using an unstructured finite volume algorithm are described. The flowfield is modeled using the inviscid equations of gasdynamics, i.e., the Euler equations, which are discretized in a cell centered unstructured grid made up of triangles. Time integration uses an explicit, second-order accurate, hybrid scheme which evolved from the consideration of Runge-Kutta time stepping schemes. Steady state and unsteady calculations for NACA 0012 and NACA 64A010 airfoils at transonic flow conditions are presented. The results obtained are discussed and the implications of using the present time stepping scheme for unsteady calculations are highlighted.

Keywords

Unsteady flow, unstructured mesh, finite volume method, aerodynamic hysteresis.

1. INTRODUCTION

Computational methods for the treatment of aerodynamic and fluid problems have evolved to a point in which the simulation of rather realistic flow situations is attainable with acceptable accuracy and computational costs. Historically, the vast majority of the work performed with finite difference and finite volume methods have been based on structured meshes. However, as the configurations to be analyzed become more complex, the number of grid points that may be required in a structured mesh can be quite large in order to achieve the desired spatial resolution. Moreover, there could exist some configurations for which it would be extremely difficult even to generate a good structured mesh.

The treatment of a truly complex configuration would usually require the use of one of the two approaches. The first option would be the use of multiple block grid strategies, if one would insist on working with structured meshes. But even with such an approach, it could be difficult to avoid the waste of many grid points in regions of negligible spatial gradients. A much more general approach for the treatment of complex geometries would be the use of unstructured grids composed, for instance, of triangles in two-dimensions or tetrahedra in 3-D.

The present work is concerned with the development of a two-dimensional, unstructured, finite volume Euler solver with the capability of treating unsteady aerodynamic flows. The emphasis of the work is on airfoil flow simulations, and some unsteady motions are considered with the objective of demonstrating the capability implemented. As it is usually the

case with unsteady calculations, an initial steady state solution for the mean flight condition of interest has to be obtained. Therefore, steady solutions are also presented and discussed. The unstructured triangular mesh generation capability, developed in the context of the present work will also be described here. Finally, some concluding remarks will be drawn indicating the current status of the work and the proposed lines for extension of the present effort.

2. THEORETICAL FORMULATION AND SPACE DISCRETIZATION

The two-dimensional, time-dependent Euler equations can be written in integral form for 2-D Cartesian coordinates as

$$\frac{\partial}{\partial t}\iint_V Q\, dxdy + \int_S (Edy - Fdx) = 0 \tag{1}$$

Here, V represents the area of the control volume and S is its boundary. The vector of conserved quantities, Q, is written as

$$Q = \begin{Bmatrix} \rho \\ \rho u \\ \rho v \\ e \end{Bmatrix} \tag{2}$$

For a non-stationary mesh the inviscid flux vectors, E and F, are given by

$$E = \begin{Bmatrix} \rho U \\ \rho u U + p \\ \rho v U \\ (e+p)U + x_t p \end{Bmatrix} \qquad F = \begin{Bmatrix} \rho V \\ \rho u V \\ \rho v V + p \\ (e+p)V + y_t p \end{Bmatrix} \tag{3}$$

The contravariant velocity components are defined as

$$U = u - x_t \qquad V = v - y_t \tag{4}$$

where x_t and y_t represents the Cartesian velocity components of the mesh.

The 2-D Euler equations in integral form are discretized by a finite volume procedure in an unstructured grid made up of triangles. The present algorithm is a cell centered scheme in which the variables actually stored represent an average over the control volume of the conserved quantities. The Euler equations can, then, be rewritten for each i-th control volume as

$$\frac{\partial}{\partial t}(V_i Q_i) + \int_{S_i} (Edy - Fdx) = 0 \tag{5}$$

We must point out that the interface flux computation used in the present work is somewhat different from that used by Jameson *et al.* (1981). For a cell centered scheme, these authors compute the average of the conserved variables at the interface and, then, form the interface

flux using these averaged quantities. In the present work, we are computing fluxes using the properties at each of the two adjacent cells, and averaging them in order to obtain the interface flux.

The Euler equations are a set of nondissipative hyperbolic conservation laws. Hence, their numerical solution requires the introduction of artificial dissipation terms in order to avoid oscillations near shock waves and to damp high frequency uncoupled error modes. In the present work, the numerical dissipation terms are formed as a careful blend of undivided Laplacian and biharmonic operators (Batina, 1989). Hence, the artificial dissipation operator, $D(Q_i)$, can be written as

$$D(Q_i) = d^{(2)}(Q_i) - d^{(4)}(Q_i) \tag{6}$$

where $d^{(2)}(Q_i)$ represents the contribution of the undivided Laplacian operator, and $d^{(4)}(Q_i)$ the contribution of the biharmonic operator.

The biharmonic operator is responsible for providing the background dissipation to damp high frequency uncoupled error modes and the undivided Laplacian artificial dissipation operator prevents oscillations near shock waves.

Therefore, the Euler equations, fully discretized in space and after the explicit addition of artificial dissipation terms, can be written as

$$\frac{d}{dt}(V_i Q_i) + C(Q_i) - D(Q_i) = 0 \tag{7}$$

3. TIME DISCRETIZATION

The semi-discrete equations are advanced in time using a second-order accurate, 5-stage, explicit, hybrid scheme which evolved from the considerations of Runge-Kutta time stepping schemes. This scheme, already including the necessary terms to account for changes in cell area due to mesh motion or deformation, can be written as

$$\begin{aligned} Q_i^{(0)} &= Q_i^{(n)} \\ Q_i^{(l)} &= \frac{V_i^n}{V_i^{n+1}} Q_i^{(0)} - \alpha_l \frac{\Delta t_i}{V_i^{n+1}} \left[C(Q_i^{(l-1)}) - D(Q_i^{(m)}) \right] \quad , \quad l = 1,\ldots,5 \rightarrow \begin{cases} l = 1 \rightarrow m = 0 \\ l > 1 \rightarrow m = 1 \end{cases} \\ Q_i^{(n+1)} &= Q_i^{(5)} \end{aligned} \tag{8}$$

The values used for the α coefficients, as suggested by Mavriplis (1990), are

$$\alpha_1 = \frac{1}{4}, \quad \alpha_2 = \frac{1}{6}, \quad \alpha_3 = \frac{3}{8}, \quad \alpha_4 = \frac{1}{2}, \quad \alpha_5 = 1 \tag{9}$$

We observe that the convective operator, $C(Q)$, is evaluated at every stage of the integration process, but that the artificial dissipation operator, $D(Q)$, is only evaluated at the two initial stages. As discussed by Jameson *et al.* (1981), this type of procedure is known to provide adequate numerical damping characteristics while achieving the desired reduction in computational cost.

It is important to emphasize that the above time stepping scheme has been extensively tested for steady state problems (Jameson *et al.*, 1986; Mavriplis, 1988; Mavriplis, 1990).

However, to the authors knowledge, this scheme has been used in unsteady calculations only by Azevedo *et al.* (1994).

As previously mentioned, steady state solutions for the mean flight condition of interest must be obtained before the unsteady calculation can be started. Therefore, it is also important to guarantee an acceptable efficiency for the code in steady state mode. The objective in implementing a local time stepping option is to keep an approximately constant CFL number throughout the whole field. In the present work, the time step used to update the conserved variables in the i-th cell, i.e., Δt_i, in steady state mode, is calculated as

$$\Delta t_i = \frac{(CFL)(\Delta s)_i}{(|q|+a)_i} \tag{10}$$

where Δs_i is the characteristic length associated to the i-th cell, a is the local speed of sound and $|q|$ is the magnitude of the local velocity vector. The least well defined quantity is certainly the characteristic length for a triangular mesh. In the present approach, we have taken Δs_i as

$$(\Delta s)_i = min(l_{min}, c_{min}) \tag{11}$$

Here, l_{min}, represents the smallest side of the i-th triangle, and c_{min}, represents the smallest distance between the centroid of the i-th cell and that of its neighbors.

4. BOUNDARY CONDITIONS

All boundary conditions were implemented with the use of "ghost", or "slave", cells. These are fictitious control volumes which are defined outside the computational domain of interest and which serve the solely purpose of implementing boundary conditions. Two types of boundary conditions must be considered for the airfoil applications emphasized in the present work. These are solid wall and far field boundary conditions.

At a solid wall boundary, the flow must be tangent to the wall in the inviscid case. This is enforced here by imposing that the velocity component normal to the wall in the ghost volume has the same magnitude and opposite sign of the normal velocity component in its adjacent interior volume, whereas the ghost volume velocity component tangent to the wall is exactly equal to its internal cell counterpart. The other two conditions are obtained by assuming a zero normal pressure gradient and a zero normal temperature gradient at the wall. However, since we are not averaging the conserved variables at the interface prior to computing the interface flux, but we are averaging the fluxes themselves, it happens that the convective flux would be nonzero across a wall boundary if only the above condition was used. Hence, in addition to that, we are also explicitly enforcing that the normal components of the E and F fluxes are zero across a wall interface, except, of course, for the pressure terms in the momentum and energy equations.

Two forms of treating the far field boundary conditions were implemented here. The easiest approach is to assume freestream conditions at a far field boundary. However, this is known to introduce errors in the solution, unless the boundary is located very far away form the body of interest. The correct treatment of these boundaries should implement non-reflective boundary conditions that should allow for the undisturbed propagation of outward going waves. This was accomplished in the present work with the use of one-dimensional Riemann invariants (Jameson *et al.*, 1983).

5. GRID GENERATION AND DYNAMIC MESH ALGORITHM

An advancing front type grid generation scheme was implemented which is capable of automatic generation of 2-D unstructured meshes composed of triangles. The procedure can be divided in four separated phases, which are the generation of nodes, triangulation, grid smoothing and adaptative refinement. Moreover, the procedure is also able to handle non-convex domains, and domains with any number of internal boundaries which are quite often encountered in aerodynamic applications.

Unsteady calculations involve airfoil motion and, therefore, the computational grid should be somehow adjusted to take this motion into account. The approach adopted here is to keep the far field boundary fixed and to move the interior points in order to accommodate the prescribed motion of the airfoil points. This was done following the ideas presented by Batina (1989), in which each side of the triangle is modeled as a spring with stiffness constant proportional to the length of the side. Hence, once points on the airfoil surface have been moved, and if we assume that far field points are held fixed, a set of static equilibrium equations can be solved for the position of the interior grid points. Fig. 1 presents a partial view of the grid generated for a NACA 0012 airfoil using the previously described advancing front technique. The resulting mesh after a 10° pitch displacement in the original grid is shown in Fig. 2. It is clear that grid quality is maintained by the present approach of deforming the mesh in order to account to airfoil motion.

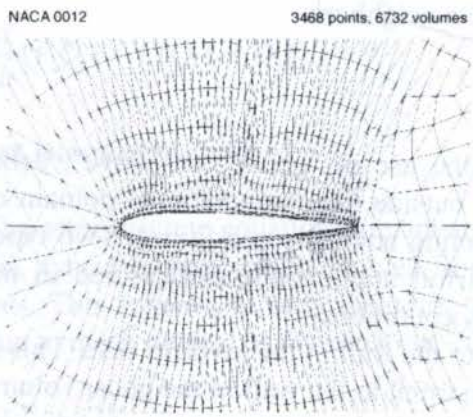

Fig. 1: Partial view of an unstructured mesh for a NACA 0012 airfoil

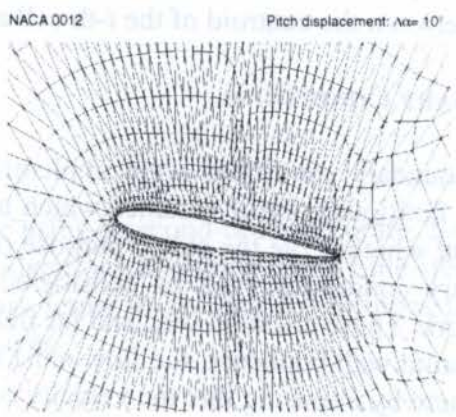

Fig. 2: Partial view of unstructured mesh for a NACA 0012 airfoil with 10° pitch displacement

6. CALCULATION OF STEADY AIRFOIL FLOWS

The steady flow cases treated here considered both fully subsonic and transonic airfoil flows. A typical computational mesh used for these simulations has already been shown in Fig. 1. Steady state pressure coefficient distributions are shown in Fig. 3 for a subcritical flow case over a NACA 0012 airfoil. In this case, a freestream Mach number M_∞=0.63 and a angle of attack α=2° were considered. Results for a transonic case are shown in Fig. 4 and consider M_∞=0.80 and α=1.25°. The present results for both cases are compared to the calculations of Kroll *et al.* (1987). The agreement between the two sets of results is very good, as it is clear from those figures. Several other transonic airfoil cases were run and their agreement with the data in the literature was as good as for the cases previously shown.

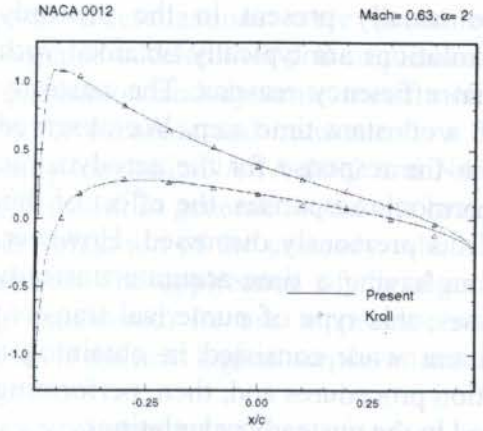

Fig. 3: Steady pressure coefficient distributions for a NACA 0012 airfoil at $M\infty$=0.63 and α=2°.

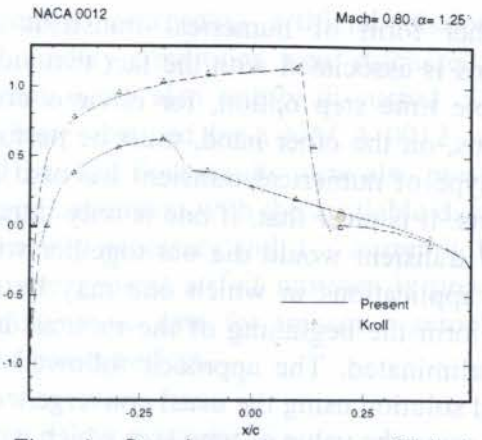

Fig. 4: Steady pressure coefficient distributions for a NACA 0012 airfoil at $M\infty$=0.80 and α=1.25°.

7. SIMULATIONS OF UNSTEADY FLOWS

Unsteady calculations were performed for NACA 0012 airfoils at various transonic flow conditions. The simulations have considered harmonic oscillations about the airfoil quarter-chord. In all cases, the airfoil motion was prescribed and the interest was in calculating the aerodynamic response in terms of unsteady pressure distributions and aerodynamic coefficients. Both plunge and pitch motions were simulated for most cases. The usual procedure followed in the present work was to obtain a steady state solution for a certain flight condition of interest and, then, to start the unsteady motion from this converged solution.

In the case of harmonic motion, it is clear that this procedure will cause some initial numerical transients since the initial conditions for the unsteady motion are not exactly equal to those of the converged steady state solution. These initial transients were evaluated for the case of a sinusoidal pitch motion about the quarter-chord of the airfoil (NACA 0012, M_∞=0.755, α_0=0.016°). The reduced frequency considered in this case was k=0.0814 and the half-amplitude of oscillation in this case was $\Delta\alpha$=2.51°. The most interesting form of visualizing the results is in terms of the hysteresis loops for the aerodynamic coefficients. This is shown in Figs. 5 and 6 for both the lift and the moment coefficients for the same case previously discussed. The important conclusion from these results is that the data on the first cycle of oscillation are contaminated by the initial transients and they should not be used to provide harmonic airfoil response.

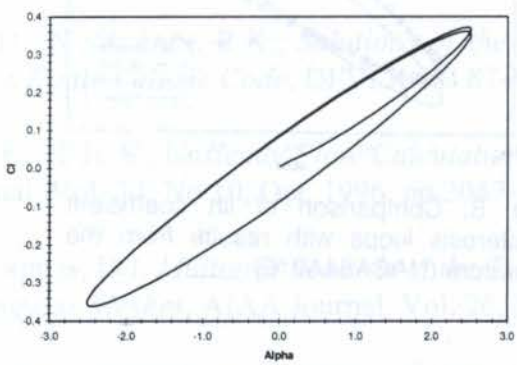

Fig. 5: Effect of initial transients on lift coefficient hysteresis loops for a sinusoidal pitch motion

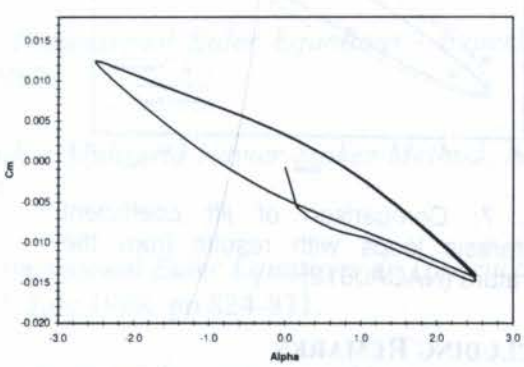

Fig. 6: Effect of initial transients on moment coefficient hysteresis loops for a sinusoidal pitch motion

Another form of numerical transients which are usually present in the unsteady calculations is associated with the fact that steady state solutions are typically obtained with the variable time step option, for obvious computational efficiency reasons. The unsteady calculations, on the other hand, must be performed with a constant time step. We observed that this type of numerical transient has also appeared in the response for the aerodynamic coefficients. It is clear that, if one is only interested in harmonic responses, the effect of this numerical transient would die out together with the effects previously discussed. However, there are applications in which one may be interested in having a time-accurate unsteady response form the beginning of the motion. In these cases, this type of numerical transient must be eliminated. The approach followed in the present work consisted in obtaining a converged solution using the usual convergence acceleration procedures and, then, performing iterations using the value of time step which would be used in the unsteady calculations.

A comparison of the aerodynamic lift coefficient hysteresis curve obtained in the present calculations and those available in the literature (Batina, 1989), for the same case discussed in the previous paragraph, is shown in Fig. 7. A similar comparison is presented in Fig. 8, for a pitching NACA64A010 airfoil (M_∞=0.796, α_0=0°, $\Delta\alpha$=1.01°, k=0.202). In this figure, results are compared to those of Liu *et al.*(1996). It is clear from the figures that the agreement is not as good as one would like to have. The actual cases for these discrepancies are still being investigated. At present the authors believe that the discrepancies could be associated to the fact that Batina (1989) uses a 4-stage scheme in which the artificial dissipation terms are evaluated only at the first stage, and Liu (1996) uses a implicit time marching method. In the present calculations, a 5-stage scheme, with artificial dissipation evaluated at both the first and the second stages, is being used. The exact implications of this fact have not yet been fully explored at this point. The first test to be performed would be a simulation of the same cases using a better triangular mesh. However, it seems that phase errors in the Runge-Kutta scheme may also be causing the discrepancies observed, and that it might also be interesting to run the same examples using a standard Runge-Kutta scheme instead of the hybrid scheme here implemented. Finally, it must be pointed out that the aerodynamic coefficients are very sensitive to shock location and the details of shock/boundary layer interaction may affect them significantly, causing the discrepancies between the present results and the experimental ones.

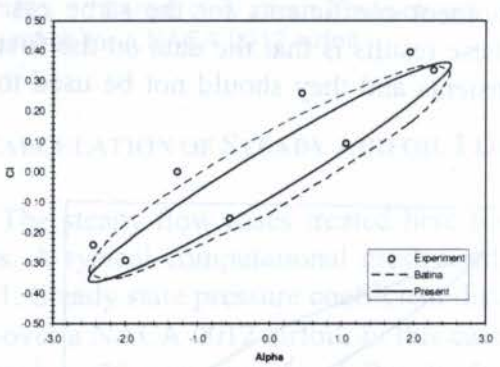

Fig. 7: Comparison of lift coefficient hysteresis loops with results from the literature (NACA0012)

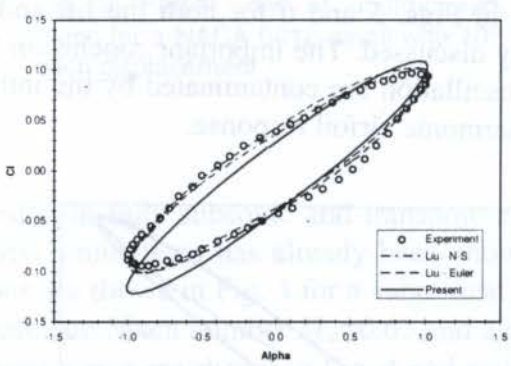

Fig. 8: Comparison of lift coefficient hysteresis loops with results from the literature (NACA64A010)

8. CONCLUDING REMARKS

A finite volume procedure based on triangular unstructured grids was developed for the solution of the 2-D unsteady Euler equations in conservation form. Details of the spatial and

temporal discretizations were presented, and aspects concerning artificial dissipation, convergence acceleration and implementation of boundary conditions were discussed. The grid generation and dynamic mesh motion algorithms were also briefly discussed. Steady results for subsonic and transonic flow conditions were obtained for a NACA 0012 airfoil. Unsteady transonic NACA 0012 and NACA 64A010 airfoil flow results were also presented and discussed. In general, the results have shown good agreement with the available data, but further validation of the unsteady calculations is certainly necessary and it is currently being performed. The application of the algorithm for more general airfoil motions is presently being considered. Its use to provide unsteady aerodynamic data for transonic aeroelastic analyses is the next logical step as an extension of the present effort.

9. ACKNOWLEDGMENTS

The present work was partially supported by CNPq under the Integrated Project Research Grant No. 522413/96-0. Partial support has also been provided by EMBRAER - Empresa Brasileira de Aeronáutica S.A.

9. REFERENCES

AZEVEDO, J.L.F., & OLIVEIRA, L.C. *Unsteady Airfoil Flow Simulations Using the Euler Equations*, AIAA Paper 94-1892-CP, Proceedings of the 12th AIAA Applied Aerodynamics Conference, Colorado Springs, CO, June 1994, pp. 650-660.

BATINA, J.T. *Unsteady Euler Airfoil Solutions Using Unstructured Dynamic Meshes*, AIAA Paper 89-0115, 27th Aerospace Sciences Meeting, Reno, NV, Jan. 1989.

JAMESON, A., & BAKER, T.J. *Solution of the Euler Equations for Complex Configurations*, AIAA Paper 83-1929, July 1983.

JAMESON, A., & MAVRIPLIS, D. *Finite Volume Solutions of the Two-Dimensional Euler Equations on a Regular Triangular Mesh*, AIAA Journal, Vol. 24, No. 4, April 1986, pp. 611-618.

JAMESON, A., SCHMIDT, W., & TURKEL, E. *Numerical Solution of the Euler Equations by Finite Volume Methods Using Runge-Kutta Time-Stepping Schemes*, AIAA Paper 81-1259, AIAA 14th Fluid and Plasma Dynamics Conference, Palo Alto, CA, June, 1981.

KROLL, N., & JAIN, R.K., *Solutions of the Two-Dimensional Euler Equations - Experience with a Finite Volume Code*, DFVLR-FB 87-41, 1987.

LIU, F., & JI, S., *Unsteady Flow Calculations with a Multigrid Navier-Stokes Method*, AIAA Journal, Vol. 34, No.10, Oct. 1996, pp.2047-2053.

MAVRIPLIS, D.J. *Multigrid Solution of the Two-Dimensional Euler Equations on Unstructured Triangular Meshes*, AIAA Journal, Vol. 26, No. 7, July 1988, pp.824-831.

MAVRIPLIS, D.J. *Accurate Multigrid Solution of the Euler Equations on Unstructured and Adaptative Meshes*, AIAA Journal, Vol. 28, No. 2, Feb. 1990, pp. 213-221.

XIV Brazilian Congress of Mechanical Engineering
Obeid Plaza Hotel Convention Center - Bauru - SP/Brazil
December 08-12th 1997

PAPER CODE: COB789

SIMULAÇÃO NUMÉRICA DE PROBLEMAS AEROESPACIAIS NO CONTEXTO DE MALHAS ESTRUTURADAS E NÃO ESTRUTURADAS

/ *NUMERICAL SIMULATIONS OF AEROSPACE PROBLEMS ON STRUCTURED AND UNSTRUCTURED MESHES*

JOÃO L. F. AZEVEDO[1] & EDISSON S. G. MACIEL[2]
[1] *Instituto de Aeronáutica e Espaço, Centro Técnico Aerospacial - CTA/IAE - azevedo@ase2.iae.cta.br*
[2] *Instituto Tecnológico de Aeronáutica, Centro Técnico Aerospacial - CTA/ITA - mesg@aer.ita.cta.br*
12228-904 - São José dos Campos - SP - Brasil

Abstract

The paper presents comparisons between different algorithms used for the solution of the Euler equations for typical aerospace applications. The schemes considered include a cell centered, unstructured, explicit method and an implicit, unfactored algorithm constructed on structured grids. The unstructured method is based on Jameson and Mavriplis' work and it yelds a centered, spatially 2nd-order accurate scheme. The structured algorithm is based on MacCormack's flux vector splitting scheme, but it is only 1st-order accurate in space. The particular applications considered were transonic nozzle flows and supersonic blunt body flows. The aspects emphasized in the present comparison were the final solution quality for steady state applications, the overall easiness of code implementation, and the method's computational efficiency.

Keywords

Equações de Euler, Esquemas Explícito e Implícito, Comparação de Eficiência Computacional / Euler Equations, Implicit and Explicit Schemes, Computational Efficiency Comparison.

1. INTRODUÇÃO

Na indústria aeronáutica, a necessidade de experimentação prática dos vários dispositivos aerodinâmicos que compõem uma aeronave durante a fase de projeto é uma realidade que encontra muitas vezes limites no excessivo custo dispendido para elaboração de protótipos em escala reduzida e na montagem destes em túneis de vento. Isto é agravado, principalmente, em vista do grande número de ensaios que são necessários durante o processo de otimização desses componentes. Devido ao crescente aumento da tecnologia dos computadores, propiciando o surgimento de máquinas com grande poder de processamento de dados e de armazenamento de informações, a área de dinâmica dos fluidos computacional (em inglês: "CFD", "Computational Fluid Dynamics") vem ocupando um espaço cada vez mais significativo na indústria, instituições e centros de pesquisa brasileiros. Baseado neste fato, o presente trabalho realizará um estudo comparativo entre o esquema implícito de MacCormack (1985), com separação de vetores de fluxo de Steger e Warming (1981), no contexto de malhas estruturadas, e o esquema explícito de Jameson e Mavriplis (1986), no contexto de malhas não estruturadas, aplicados a problemas cotidianos da indústria aeronáutica, a fim de

avaliar as características de cada algoritmo. Serão resolvidas as equações de Euler, segundo o formalismo de volumes finitos, e o interesse nos problemas físicos a serem estudados será na obtenção da solução de estado estacionário.

2. FORMULAÇÃO TEÓRICA

As equações de Euler em forma conservativa diferencial no sistema de coordenadas cartesiano bidimensional, são:

$$\frac{\partial Q}{\partial t}+\frac{\partial E_e}{\partial x}+\frac{\partial F_e}{\partial y}=0\,, \tag{1}$$

onde: Q é o vetor de variáveis conservadas; E_e e F_e são os vetores de fluxo de Euler nas direções x e y, respectivamente. As grandezas presentes na Eq. (1) são definidas conforme:

$$Q=\begin{Bmatrix}\rho\\ \rho u\\ \rho v\\ e\end{Bmatrix},\qquad E_e=\begin{Bmatrix}\rho u\\ \rho u^2+p\\ \rho uv\\ (e+p)u\end{Bmatrix}\qquad \text{e}\qquad F_e=\begin{Bmatrix}\rho v\\ \rho uv\\ \rho v^2+p\\ (e+p)v\end{Bmatrix}, \tag{2}$$

com ρ sendo a densidade do meio; u e v os componentes cartesianos de velocidade nas direções x e y, respectivamente; p a pressão estática do meio; e e a energia total por unidade de volume. A equação de estado dos gases perfeitos é utilizada para fechar a Eq. (1).

No contexto do algoritmo de MacCormack (1985), a Eq. (1) em forma integral e em coordenadas generalizadas, é escrita como:

$$\frac{\partial Q}{\partial t}+\frac{1}{V}\int_V \vec{\nabla}\cdot\vec{P}\,dV=0, \tag{3}$$

em que V representará a área de cada célula (bidimensional); $\vec{\nabla}=(\partial/\partial x)\vec{i}+(\partial/\partial y)\vec{j}$ representa o operador gradiente; e, $\vec{P}=E_e\vec{i}+F_e\vec{j}$ representa o vetor de fluxo de Euler. Utilizando o teorema de Green na Eq. (3) e adotando uma notação estruturada, é possível escrever que:

$$\frac{\partial Q_{i,j}}{\partial t}=-\frac{1}{V_{i,j}}\int_{S_{i,j}}(\vec{P}\cdot\vec{n})_{i,j}\,dS_{i,j}\,, \tag{4}$$

com $\vec{n}$ sendo o versor normal direcionado para fora da respectiva área de fluxo. Uma dada célula nesta notação é formada pelos nós: (i,j), (i+1,j), (i+1,j+1) e (i,j+1).

Utilizando Euler explícito para a marcha no tempo e após discretização espacial da integral de superfície, a Eq. (4) pode ser reescrita como:

$$Q_{i,j}^{n+1}=Q_{i,j}^{n}-\frac{\Delta t}{V_{i,j}}\left[(\vec{P}\cdot\vec{S})_{i,j-1/2}+(\vec{P}\cdot\vec{S})_{i+1/2,j}+(\vec{P}\cdot\vec{S})_{i,j+1/2}+(\vec{P}\cdot\vec{S})_{i-1/2,j}\right]^n\,, \tag{5}$$

onde, por exemplo, $\vec{S}_{i,j-1/2}$ tem a direção e sentido de $\vec{n}_{i,j-1/2}$ e magnitude igual ao valor da área $S_{i,j-1/2}$. No presente sistema de coordenadas, MacCormack (1985) sugere o uso de vetores de área normalizados s_x' e s_y', que são sempre orientados no sentido positivo das direções coordenadas. Uma boa vantagem neste procedimento é a economia computacional no cálculo dos vetores de área. É necessário apenas calcular, por exemplo, os vetores em (i+1/2,j) e (i,j+1/2) e realizar o recuo ou avanço de uma unidade nos índices adequados para determinar os termos de fluxo. Assim, os termos de fluxo da Eq. (5) são redefinidos, por exemplo, como:

$$(\vec{P}\cdot\vec{S})_{i+1/2,j}=\left(E_e s_x+F_e s_y\right)_{i+1/2,j}\left\|\vec{S}\right\|_{i+1/2,j} \quad \text{e} \quad (\vec{P}\cdot\vec{S})_{i-1/2,j}=-\left(E_e s_x+F_e s_y\right)_{i-1/2,j}\left\|\vec{S}\right\|_{i-1/2,j}. \tag{6}$$

O esquema de MacCormack (1985) leva em consideração a separação de vetores de fluxo proposta por Steger e Warming (1981). Segundo o enfoque da separação de vetores de fluxo e sendo consistente com a metodologia implementada por MacCormack em seus esquemas, os vetores E_e e F_e na face (i+1/2,j), bem como o termo de fluxo em (i+1/2,j), são escritos como:

$$(E_e)_{i+1/2,j}=A^+_{i+1/2,j}Q_{i,j}+A^-_{i+1/2,j}Q_{i+1,j} \quad \text{e} \quad (F_e)_{i+1/2,j}=B^+_{i+1/2,j}Q_{i,j}+B^-_{i+1/2,j}Q_{i+1,j},$$

$$(\vec{P}\cdot\vec{S})_{i+1/2,j}=\left[\left(A^+ s_x+B^+ s_y\right)_{i+1/2,j}Q_{i,j}+\left(A^- s_x+B^- s_y\right)_{i+1/2,j}Q_{i+1,j}\right]\left\|\vec{S}\right\|_{i+1/2,j}. \tag{7}$$

em que A^+, A^-, B^+ e B^- são as matrizes jacobianas não viscosas reconstruídas positivas e negativas. Desta forma, o esquema implícito de MacCormack (1985), utilizando Euler implícito para marcha no tempo, pode ser escrito como:

- Passo preditor:

$$\Delta Q^n_{i,j}=-\frac{\Delta t}{V_{i,j}}\Big[(B^+_{i,j}Q_{i,j-1}+B^-_{i,j}Q_{i,j})\left\|\vec{S}_{i,j-1/2}\right\|+(A^+_{i+1,j}Q_{i,j}+A^-_{i+1,j}Q_{i+1,j})\left\|\vec{S}_{i+1/2,j}\right\|$$
$$+(B^+_{i,j+1}Q_{i,j}+B^-_{i,j+1}Q_{i,j+1})\left\|\vec{S}_{i,j+1/2}\right\|+(A^+_{i,j}Q_{i-1,j}+A^-_{i,j}Q_{i,j})\left\|\vec{S}_{i-1/2,j}\right\|\Big]^n$$

$$\left(-\frac{\Delta t}{V_{i,j}}B^+_{i,j}\left\|\vec{S}_{i,j-1/2}\right\|\right)^n\delta Q_{p_{i,j-1}}^{n+1}+\left\{I+\frac{\Delta t}{V_{i,j}}\Big[-B^-_{i,j}\left\|\vec{S}_{i,j-1/2}\right\|+A^+_{i+1,j}\left\|\vec{S}_{i+1/2,j}\right\|+B^+_{i,j+1}\left\|\vec{S}_{i,j+1/2}\right\|-A^-_{i,j}\left\|\vec{S}_{i-1/2,j}\right\|\Big]\right\}\delta Q_{p_{i,j}}^{n+1}$$
$$+\left(\frac{\Delta t}{V_{i,j}}B^-_{i,j+1}\left\|\vec{S}_{i,j+1/2}\right\|\right)\delta Q_{p_{i,j+1}}^{n+1}+\left(-\frac{\Delta t}{V_{i,j}}A^+_{i,j}\left\|\vec{S}_{i-1/2,j}\right\|\right)\delta Q_{p_{i-1,j}}^{n+1}+\left(\frac{\Delta t}{V_{i,j}}A^-_{i+1,j}\left\|\vec{S}_{i+1/2,j}\right\|\right)\delta Q_{p_{i+1,j}}^{n+1}=\Delta Q^n_{i,j}$$

$$Q_{p_{i,j}}^{n+1}=Q^n_{i,j}+\delta Q_{p_{i,j}}^{n+1} \tag{8}$$

- Passo corretor:

$$\Delta Q_{c_{i,j}}^{n+1}=-\frac{\Delta t}{V_{i,j}}\Big[(B^+_{i,j-1}Q_{i,j-1}+B^-_{i,j-1}Q_{i,j})_p\left\|\vec{S}_{i,j-1/2}\right\|+(A^+_{i,j}Q_{i,j}+A^-_{i,j}Q_{i+1,j})_p\left\|\vec{S}_{i+1/2,j}\right\|+$$
$$(B^+_{i,j}Q_{i,j}+B^-_{i,j}Q_{i,j+1})_p\left\|\vec{S}_{i,j+1/2}\right\|+(A^+_{i-1,j}Q_{i-1,j}+A^-_{i-1,j}Q_{i,j})_p\left\|\vec{S}_{i-1/2,j}\right\|\Big]^{n+1}$$

$$\left(-\frac{\Delta t}{V_{i,j}}B^+_{i,j-1}\left\|\vec{S}_{i,j-1/2}\right\|\right)_p^{n+1}\delta Q_{c_{i,j-1}}^{n+1}+\left\{I+\frac{\Delta t}{V_{i,j}}\Big[-B^-_{i,j-1}\left\|\vec{S}_{i,j-1/2}\right\|+A^+_{i,j}\left\|\vec{S}_{i+1/2,j}\right\|+B^+_{i,j}\left\|\vec{S}_{i,j+1/2}\right\|-A^-_{i,j-1}\left\|\vec{S}_{i-1/2,j}\right\|\Big]\right\}_p^{n+1}\delta Q_{c_{i,j}}^{n+1}$$
$$+\left(\frac{\Delta t}{V_{i,j}}B^-_{i,j}\left\|\vec{S}_{i,j+1/2}\right\|\right)_p^{n+1}\delta Q_{c_{i,j+1}}^{n+1}+\left(-\frac{\Delta t}{V_{i,j}}A^+_{i-1,j}\left\|\vec{S}_{i-1/2,j}\right\|\right)_p^{n+1}\delta Q_{c_{i-1,j}}^{n+1}+\left(\frac{\Delta t}{V_{i,j}}A^-_{i,j}\left\|\vec{S}_{i+1/2,j}\right\|\right)_p^{n+1}\delta Q_{c_{i+1,j}}^{n+1}=\Delta Q_{c_{i,j}}^{n+1}$$

$$Q_{i,j}^{n+1}=\frac{1}{2}\left(Q^n_{i,j}+Q_{p_{i,j}}^{n+1}+\delta Q_{i,j}^{n+1}\right) \tag{9}$$

Assim, o método implícito de MacCormack (1985) utiliza o desenvolvimento com separação de vetores de fluxo de Steger e Warming (1981) para obter um sistema linear

pentadiagonal de blocos cheios em que a diagonal principal é dominante sobre as demais. Este sistema linear é resolvido por relaxação tipo Gauss-Seidel de linha com duas varreduras: uma para frente e outra para trás, resultando em um sistema tridiagonal de blocos em j.

No esquema explícito de Jameson e Mavriplis (1986), as equações de Euler, no contexto de malhas não estruturadas, são escritas como:

$$\frac{\partial}{\partial t}\int_V Q dx dy + \int_S \left[E_e dy - F_e dx\right] = 0. \qquad (10)$$

Os autores propõem uma discretização espacial centrada e uma discretização no tempo segundo um método explícito híbrido de Runge-Kutta de segunda ordem de precisão e cinco estágios. Do exposto, a Eq. (10) pode ser discretizada no espaço e no tempo conforme abaixo:

$$\begin{aligned} Q_i^{(0)} &= Q_i^{(n)} \\ Q_i^{(k)} &= Q_i^{(0)} - \alpha_k \frac{\Delta t_i}{V_i}\left[C(Q_i^{(k-1)}) - D(Q_i^{(m)})\right], \\ Q_i^{(n+1)} &= Q_i^{(5)} \end{aligned} \qquad (11)$$

em que k = 1,...,5; m = k-1, se $k \le 2$, e m = 1, se k > 2; $C(Q_i) = \sum_{k=1}^{3}\left[E_e(Q_{i,k})\Delta y_{i,k} - F_e(Q_{i,k})\Delta x_{i,k}\right]$ é a aproximação discreta da integral de fluxo; D é o operador de dissipação artificial introduzido explicitamente a fim de prover estabilidade ao esquema centrado; e $\alpha_1 = 1/4$, $\alpha_2 = 1/6$, $\alpha_3 = 3/8$, $\alpha_4 = 1/2$ e $\alpha_5 = 1$. Segundo Swanson e Radespiel (1991), a dissipação artificial é atualizada apenas nos dois primeiros estágios a fim de permitir uma economia de tempo de CPU, resultando no esquema híbrido acima. No presente trabalho, foram admitidos ainda os seguintes procedimentos:

$$Q_{i,k} = \frac{Q_i + Q_k}{2}, \quad \Delta y_{i,k} = y_{n2} - y_{n1}, \quad \text{e} \quad \Delta x_{i,k} = x_{n2} - x_{n1}, \qquad (12)$$

com i representando o volume i e k seu respectivo vizinho; e n1 e n2 representam nós consecutivos do elemento de área triangular em sentido anti-horário. O operador de dissipação artificial utilizado segue os trabalhos de Mavriplis (1990) e Azevedo (1992b) e é definido por:

$$D(Q_i) = d^{(2)}(Q_i) - d^{(4)}(Q_i), \qquad (13)$$

em que $d^{(2)}(Q_i) = \sum_{k=1}^{3} \varepsilon_{i,k}^{(2)} \times \frac{(A_i + A_k)}{2} \times (Q_k - Q_i)$, denominado de operador laplaciano não dividido, com a função de estabilizar o esquema em regiões de formação de ondas de choque; e $d^{(4)}(Q_i) = \sum_{k=1}^{3} \varepsilon_{i,k}^{(4)} \times \frac{(A_i + A_k)}{2} \times \left(\nabla^2 Q_k - \nabla^2 Q_i\right)$, denominado de operador bi-harmônico, que é responsável pela estabilidade de "background" (por exemplo, desacoplamento de soluções do tipo par-ímpar) do esquema. Neste último termo, $\nabla^2 Q_i = \sum_{k=1}^{3}(Q_k - Q_i)$. Os termos ε's possuem expressões definidas em Azevedo (1992b) e o termo $\underline{A}$ é definido conforme a seguir:

$$A_i = \sum_{k=1}^{3}\left[\left|u_{i,k}\Delta y_{i,k} - v_{i,k}\Delta x_{i,k}\right| + a_{i,k}\sqrt{\left(\Delta x_{i,k}\right)^2 + \left(\Delta y_{i,k}\right)^2}\right], \qquad (14)$$

onde $u_{i,k}$, $v_{i,k}$ e $a_{i,k}$ são grandezas médias avaliadas entre o volume i e seu vizinho k. A grandeza $\underline{a}$ representa a velocidade do som no meio.

5. PROBLEMAS ESTUDADOS E CONDIÇÕES INICIAL E DE CONTORNO

No presente estudo comparativo, foram propostos os seguintes problemas físicos: bocal transônico convergente-divergente e corpo rombudo em escoamento supersônico. A adimensionalização da Eq. (1) para o problema do bocal transônico é realizada em termos das propriedades de estagnação (MacCormack, 1985) e para o problema do corpo rombudo em relação às propriedades de escoamento livre (Jameson e Mavriplis, 1986).

A condição inicial adotada para o problema do bocal transônico convergente/divergente é a de estagnação para todo o domínio de cálculo, com exceção da saída onde existirá uma redução no valor da pressão e da densidade a fim de inicializar o escoamento (Basso e Azevedo, 1996). Para o problema envolvendo o corpo rombudo, a condição inicial adotada é a de escoamento livre (Jameson e Mavriplis, 1986) para todo o domínio de cálculo.

O bocal transônico será resolvido considerando metade deste dispositivo ao longo da linha de centro, aproveitando características de simetria do escoamento convergido. As condições de contorno, válidas também para o caso do corpo rombudo, são:

a) Condição de Parede: O caso Euler impõe a condição de tangência de fluxo. Além disso, o gradiente de pressão na direção normal à parede é igual a zero, o mesmo acontecendo com o gradiente de temperatura.

b) Condição de Simetria: As células de contorno (denominadas "ghost", em inglês) adjacentes à linha de centro possuem o vetor de variáveis conservadas igual ao da célula real vizinha com excessão do termo ρv que possue sinal oposto a fim de garantir a condição de fluxo nulo. Esta condição de contorno é aplicada apenas no problema do bocal transônico.

c) Condições de Entrada e Saída do Bocal: Estas condições foram impostas baseadas no conceito de relações características unidimensionais (ver Azevedo, 1990, e Azevedo, 1992a).

6. RESULTADOS

6.1 Caso 1: Bocal Transônico

Neste problema foi utilizada uma malha gerada algebricamente com 41 pontos na direção ao longo da parede e 20 pontos na direção perpendicular a esta. Foi utilizado um estiramento exponencial de 10% em ambas as direções coordenadas. O bocal apresenta a região convergente com um ângulo de inclinação de 22,33° e a região divergente com ângulo de 1,21°. O comprimento total do bocal é de 0,1158m (0,380ft), com a garganta sendo localizada na metade deste. O raio de curvatura da garganta do bocal é de 0,0274m (0,090ft). As Figs. 1 e 2 exibem as curvas de contorno de pressão obtidas, respectivamente, pelo método implícito de MacCormack (1985) e pelo método explícito de Jameson e Mavriplis (1986).

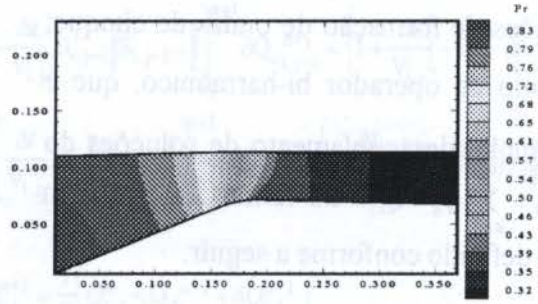

Figura 1 - Contornos de pressão (Mac).

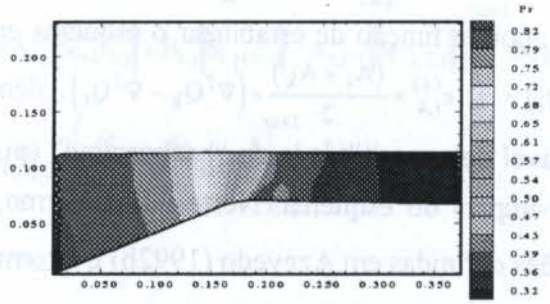

Figura 2 - Contornos de pressão (Jam/Mav).

As Figs. 3 e 4 exibem as curvas de contorno de número de Mach obtidas também pelo método implícito de MacCormack (1985) e pelo método de Jameson e Mavriplis (1986).

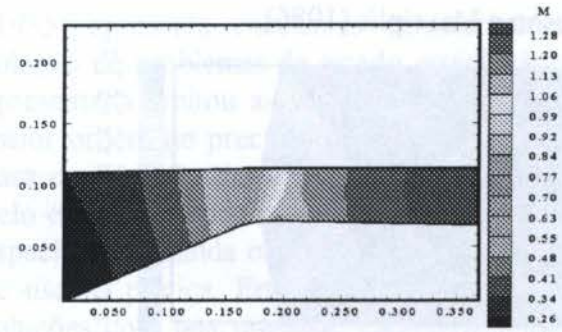

Figura 3 - Contornos de No. de Mach (Mac).

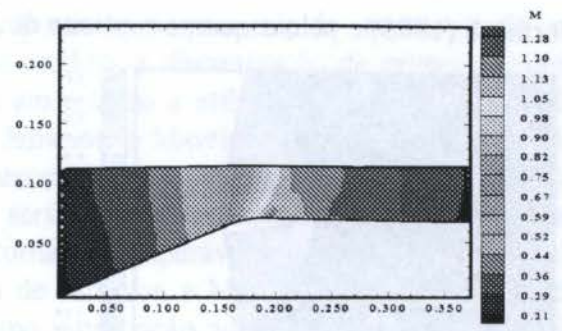

Figura 4 - Contornos de No. de Mach (Jam/Mav).

No tocante à qualidade da solução, é clara a melhor precisão do esquema de Jameson e Mavriplis (1986), tendo em vista ser um esquema de segunda ordem de precisão espacial, em comparação com o esquema implícito de MacCormack (1985) apresentado, que corresponde a uma discretização espacial de primeira ordem. Com relação às características de convergência, o esquema implícito de MacCormack pode utilizar um número de CFL igual a 175,0 enquanto o esquema de Jameson e Mavriplis utilizou um número de CFL igual a 0,9. Ambos os esquemas foram executados em uma estação de trabalho IBM 6091-19. Uma convergência excelente foi obtida para o primeiro algoritmo, resultando em um total de 100 iterações para atingir uma convergência de 10^{-10} sobre o valor do máximo resíduo no campo. O tempo total de convergência deste esquema foi de 1'36,52", a um custo de aproximadamente 0,0012s de CPU por iteração por ponto da malha enquanto o esquema explícito de Jameson e Mavriplis (1986) apresentou um custo próximo a 0,0009s de CPU por iteração por ponto da malha computacional em um tempo total de 53'25,69" e 4470 iterações foram necessárias para obter a solução de estado estacionário. Fica evidenciado que a diferença de custo por iteração por ponto computacional entre os dois algoritmos é pequena e, portanto, o desempenho computacional do esquema implícito de MacCormack (1985) é muito superior. As Figs. 5 e 6 exibem as histórias de convergência para o esquema implícito de MacCormack (1985) e para o esquema explícito de Jameson e Mavriplis (1986), no tocante ao problema do bocal transônico.

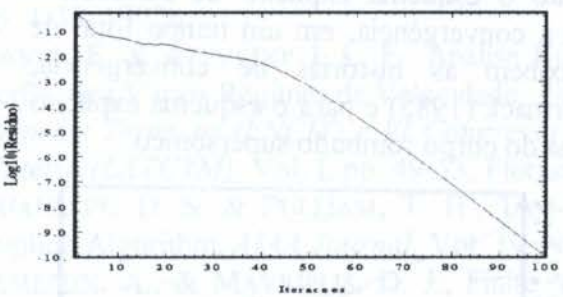

Figura 5 - Convergência Caso 1 (Mac).

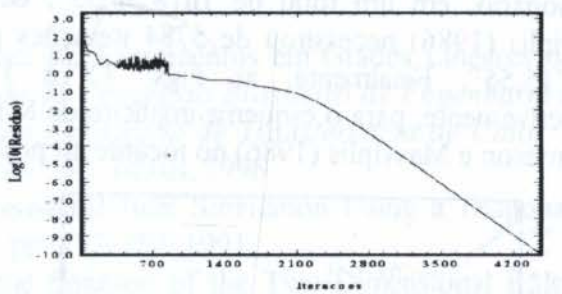

Figura 6 - Convergência Caso 1 (Jam/Mav).

6.2 Caso 2: Corpo Rombudo

Para o problema do corpo rombudo, foi utilizada uma malha algébrica suavizada por um gerador elíptico com 113 pontos na direção ao longo do corpo rombudo e 40 pontos na direção perpendicular ao corpo. O corpo rombudo é representado por uma geometria esfera/cone no plano com ângulo de inclinação da geratriz cônica de 10°. O número de Mach de escoamento livre para a condição inicial foi adotado igual a 2,0 e o ângulo de ataque foi admitido igual a 0°. As Figs. 7 e 8 exibem as curvas de contorno de pressão e as Figs. 9 e 10 as curvas de contorno de número de Mach obtidas, respectivamente, pelo esquema implícito de

MacCormack (1985) e pelo esquema explícito de Jameson e Mavriplis (1986).

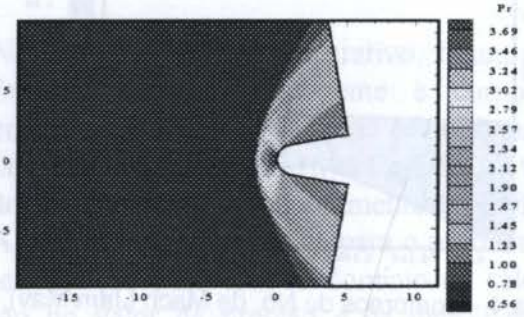

Figura 7 - Contornos de pressão (Mac).

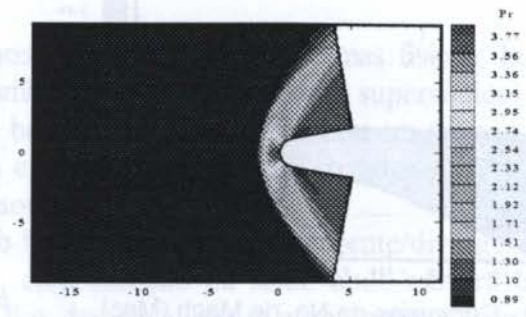

Figura 8 - Contornos de pressão (Jam/Mav).

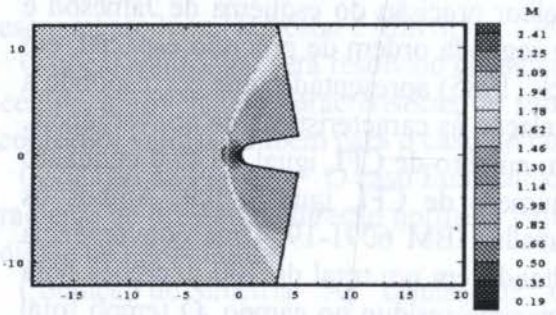

Figura 9 - Contornos de No. de Mach (Mac).

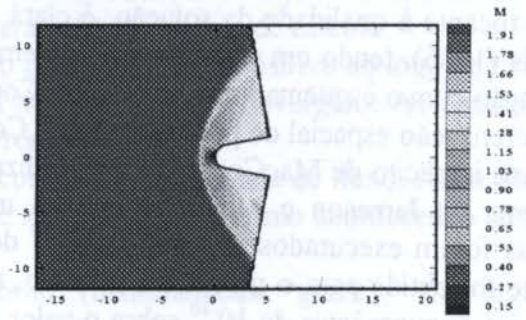

Figura 10 - Contornos de No. de Mach (Jam/Mav).

Novamente, é verificada a melhor qualidade da solução do esquema de Jameson e Mavriplis (1986) em comparação com o esquema implícito de MacCormack (1985). Em relação às características de convergência, o método implícito de MacCormack (1985) pode utilizar um número de CFL igual a 8,2 enquanto o método de Jameson e Mavriplis (1986) manteve o mesmo número de CFL de 0,9. Os esquemas foram executados no mesmo modelo de estação de trabalho. Uma convergência muito boa foi obtida para o esquema implícito de MacCormack (1985), apresentando 868 iterações para obtenção da solução de estado estacionário, em um total de 1h18'38,55", enquanto o esquema explícito de Jameson e Mavriplis (1986) necessitou de 5784 iterações para a convergência, em um tempo total de 6h43'15,55". Finalmente, as Figs. 11 e 12 exibem as histórias de convergência, respectivamente, para o esquema implícito de MacCormack (1985) e para o esquema explícito de Jameson e Mavriplis (1986) no tocante ao problema do corpo rombudo supersônico.

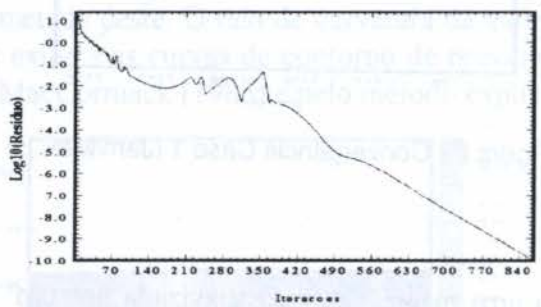

Figura 11 - Convergência Caso 2 (Mac).

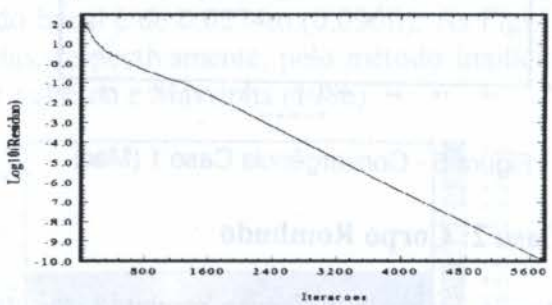

Figura 12 - Convergência Caso 2 (Jam/Mav).

7. CONCLUSÕES

Foram discutidos neste trabalho alguns aspectos teóricos e práticos da implementação numérica do esquema implícito de MacCormack (1985) e do esquema explícito de Jameson e Mavriplis (1986). Os resultados demonstraram que o esquema implícito de MacCormack

(1985) apresenta excelentes características computacionais para rápida convergência na solução de problemas de estado estacionário. No entanto, a discretização de primeira ordem apresentada limitou as vantagens deste esquema em relação a utilização de um esquema de maior ordem de precisão como o algoritmo de Jameson e Mavriplis (1986). Uma proposta para continuação deste trabalho, motivado pelo excelente desempenho computacional obtido pelo esquema implícito de MacCormack (1985), seria a implementação de uma discretização espacial de segunda ordem de precisão a fim de torná-lo comparável aos esquemas numéricos de uso na prática. Em contrapartida, o esquema de Jameson e Mavriplis (1986) apresentou soluções com boa precisão, caracterizando-o como uma opção adequada para resolução de problemas de estado estacionário ou transiente, devido principalmente a maior facilidade de implementação.

AGRADECIMENTOS

Este trabalho faz parte de um projeto de pesquisa financiado parcialmente pela Fundação de Amparo à Pesquisa do Estado de São Paulo (FAPESP), através de uma bolsa de Doutorado, nível I, sob o Processo Nº 96/02601-4. Os autores também agradecem o suporte parcial do Conselho Nacional de Desenvolvimento Científico e Tecnológico, CNPq, através do Projeto Integrado de Pesquisa associado ao Processo Nº 522413/96-0.

REFERÊNCIAS BIBLIOGRÁFICAS

AZEVEDO, J. L. F., Euler Solutions of Transonic Nozzle Flows, *Anais do III Encontro Nacional de Ciências Térmicas (III ENCIT)*, Vol. I, Itapema, SC, Brazil, pp. 243-48, 1990.

AZEVEDO, J. L. F., A Finite Difference Method Applied to Internal Axisymmetric Flows, *Boletim da Sociedade Brasileira de Matemática Aplicada e Computacional*, Vol. 3, No. 1, Série II, pp. 1-20, 1992a.

AZEVEDO, J. L. F., On the Development of Unstrutured Grid Finite Volume Solvers for High Speed Flows, NT-075-ASE-N/92, Nota Técnica do Intituto de Aeronáutica e Espaço, CTA, pp. 1-33, 1992b.

BASSO, E. & AZEVEDO, J. L. F., Análise Numérica de Escoamentos em Grades Lineares de Perfis para Vários Regimes de Velocidade, *Anais do VI Congresso Brasileiro de Engenharia e Ciências Térmicas (ENCIT) e VI Congresso Latino Americano de Transferência de Calor Y Matéria (LATCYM)*, Vol. I, pp. 49-53, Florianópolis, SC, Brasil, 1996.

CHAUSSEE, D. S. & PULLIAM, T. H., Two-Dimensional Inlet Simulation Using a Diagonal Implicit Algorithm, *AIAA Journal*, Vol. 19, No. 2, pp. 153-159, 1991.

JAMESON, A., & MAVRIPLIS, D. J., Finite Volume Solution of the Two-Dimensional Euler Equations on a Regular Triangular Mesh, *AIAA Journal*, Vol. 24, No. 4, pp. 611-618, 1986.

MACCORMACK, R. W., Current Status of Numerical Solutions of the Navier-Stokes Equations, AIAA Paper 85-0032, *AIAA 23rd Aerospace Sciences Meeting*, Reno, Nevada, EUA, pp. 14-17, 1985.

MAVRIPLIS, D. J., Accurate Multigrid Solution of the Euler Equations on Unstructured and Adaptive Meshes, *AIAA Journal*, Vol. 28, No. 2, pp. 213-221, 1990.

STEGER, J. L., & WARMING, R. F., Flux Vector Splitting of the Inviscid Gasdynamic Equations with Application to Finite-Difference Methods, *Journal of Computational Physics*, Vol. 40, pp. 263-293, 1981.

SWANSON, R. C., & RADESPIEL, R., Cell Centered and Cell Vertex Multigrid Schemes for the Navier-Stokes Equations, *AIAA Journal*, Vol. 29, No. 5, pp. 697-703, 1991.

XIV Brazilian Congress of Mechanical Engineering
Obeid Plaza Hotel Convention Center - Bauru - SP/Brazil
December 08-12th 1997

PAPER CODE: COB790

SLOTTED TRANSONIC WIND TUNNEL FLOW SIMULATIONS USING THE EULER EQUATIONS

RENATO VIEIRA[1], JOÃO L.F. AZEVEDO[2] & NIDE G.C.R. FICO, JR.[3]
[1] *Faculdade de Engenharia de Guaratinguetá, FEG/UNESP - mec94125@lccp1.feg.unesp.br*
[2] *Instituto de Aeronáutica e Espaço, Centro Técnico Aerospacial - IAE/CTA - azevedo@ase2.iae.cta.br*
[3] *Instituto Tecnológico de Aeronáutica, Centro Técnico Aerospacial - ITA/CTA - nide@aer.ita.cta.br*
12228-904 - São José dos Campos - SP - Brasil

Abstract

The paper presents flow simulations relevant to transonic wind tunnel design and operation. A three-dimensional, finite difference, computational code which solves the Euler equations in a general, body conforming, curvilinear grid has been developed and used for these simulations. This code incorporates the capability of including test section wall slots for realistic simulation of a transonic wind tunnel facility. Test cases considered include a tunnel contraction alone and a complete high speed tunnel segment. Both cases with closed and open slots were considered. The results obtained adequately reproduced the expected flow features for the conditions analyzed and indicated that the particular configuration studied holds promise of providing very good test section flow quality.

Keywords

Transonic Wind Tunnel, TTS Project, Slotted Walls, Inviscid Flow Simulation, Finite Difference Method.

1. INTRODUCTION

Transonic wind tunnels usually operate from low subsonic Mach numbers ($M \cong 0.25$) to the supersonic regime ($M \cong 1.6$). The tunnel nozzle is a key element in achieving the desired test-section Mach number, M_{TS}. Mach numbers up to unity are obtained using a sonic nozzle. There are two possible solutions for M_{TS} above this value: *(i)* the installation of a flexible Laval nozzle or *(ii)* a sonic nozzle used in conjunction with test-section mass extraction. In the case of test-section evacuation, about 2.5% of the tunnel total mass flow enters the plenum chamber through ventilated walls. While the first option is mechanically complex and much more expensive, it yields better test-section flow quality than the second one. Moreover, the second option is also limited to $M_{TS} \leq 1.3$, since above this test section Mach number value the mass extraction needed is prohibitive as it would demand very large auxiliary compressors and it would also have an adverse impact upon the tunnel flow quality.

The Centro Técnico Aeroespacial (CTA) is designing a large transonic wind tunnel facility with a 2.0×2.4 test section (TTS Project). To minimize the technical risks involved in such an enterprise, the project's first phase consists of the construction and operation of a pilot facility (TTP). Moreover, Computational Fluid Dynamics (CFD) methods are enjoying increasing application assisting in the selection of tunnel airline component geometry (Davis *et al.*, 1986).

These techniques have been used to design diffusers and flexible nozzles as well as investigate other aspects of the tunnel flow. Therefore, the major objective of the present work is to study, using CFD techniques, flowfields which are relevant for the TTP design and operation. This has the long term goal of developing reliable computational tools that could be used for flow simulation inside transonic wind tunnel facilities, including the effect of ventilated walls.

The work will briefly describe the formulation of the codes used and it will concentrate on the discussion of the results. Simulations were initially performed for the tunnel contraction alone, since results were available for comparison and validation. Afterwards, the tunnel test section was included in the computational domain and simulations were performed both with and without ventilated walls. Clearly, in the actual operating conditions, the slots are present in the test section and some mass extraction is necessary in order to maintain good test section flow quality. However, the non-porous wall is a limiting case which is also interesting to be tested in the code validation process. In the present simulations, the amount of mass extracted through the slots is controlled by the specified plenum chamber pressure.

2. THEORETICAL FORMULATION AND NUMERICAL IMPLEMENTATION

The flow simulations here reported are performed using the three-dimensional, compressible Euler equations. These equations can be written in strong conservation-law form for general, body-conforming, curvilinear coordinates (Pulliam & Steger, 1980) as

$$\frac{\partial \overline{Q}}{\partial \tau}+\frac{\partial \overline{E}}{\partial \xi}+\frac{\partial \overline{F}}{\partial \eta}+\frac{\partial \overline{G}}{\partial \zeta}=0 \qquad (1)$$

The definition of the vector of conserved quantities, $\overline{Q}$, and the flux vectors, $\overline{E},\overline{F},\overline{G}$, can be found in Fico *et al.* (1994).

The spatial discretization adopted in the present work uses a central difference type algorithm plus explicitly added artificial dissipation terms in order to control nonlinear instabilities. The equations, fully discretized in space, can be written as:

$$\frac{\partial \overline{Q}}{\partial t}_{i,j,k}=-RHS_{i,j,k} \qquad (2)$$

The right-hand side operator of Eq. (2) is defined as

$$RHS_{j,k}=\frac{1}{\Delta\xi}(\overline{E}_{i+1/2,j,k}-\overline{E}_{i-1/2,j,k})+\frac{1}{\Delta\eta}(\overline{F}_{i,j+1/2,k}-\overline{F}_{i,j-1/2,k})+\frac{1}{\Delta\zeta}(\overline{G}_{i,j,k+1/2}-\overline{G}_{i,j,k-1/2}) \qquad (3)$$

where $\Delta\xi=\Delta\eta=\Delta\zeta=1$ for the general curvilinear coordinate case. The artificial dissipation terms were implemented as described in Turkel & Vatsa (1994). Time march uses an explicit, 2nd-order, 5-stage Runge-Kutta scheme (Jameson *et al.*, 1981), which can be written as

$$\begin{aligned}
&\overline{Q}^{(0)}_{i,j,k}=\overline{Q}^{n}_{i,j,k}\\
&\overline{Q}^{(l)}_{i,j,k}=\overline{Q}^{(0)}_{i,j,k}-\alpha_l\cdot\Delta t_{i,j,k}\cdot RHS^{(l-1)}_{i,j,k}, \qquad l=1,2,\ldots,5\\
&\overline{Q}^{n+1}_{i,j,k}=\overline{Q}^{(5)}_{i,j,k}
\end{aligned} \qquad (4)$$

In the above expressions Δt stands for the time step, and n and $(n+1)$ are the properties values at the start and end of each time step. A variable time step convergence acceleration technique is

used to accelerate convergence to steady state results. Considerable effort was invested in the accurate implementation of entrance and exit boundary conditions through the use of one-dimensional characteristic relations (Azevedo *et al.*,1992 and Fico, 1991).

3. GRID GENERATION

The initial simulations for the convergent-divergent nozzle were performed using a 100 × 20 × 29 point mesh, respectively in the ξ, η and ζ directions. The curvilinear coordinate system is set such that ξ is the longitudinal coordinate, η is the coordinate from the centerline to the tunnel wall, and ζ is the azimuthal direction. A typical longitudinal plane of this mesh is shown in Fig. 1. Moreover, when the tunnel test section was introduced in the simulations, another 50 grid points were added to the longitudinal direction. The meshes here used were all generated by algebraic methods after the data on the tunnel wall geometry was obtained from a CAD system.

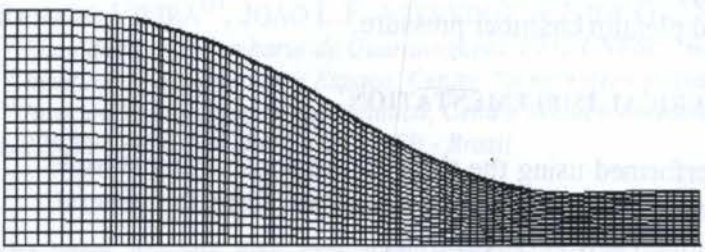

Figure 1 - View of a longitudinal plane of the mesh

The complete wind tunnel has four slots in the top and bottom test section walls, positioned at regular intervals. The tunnel lateral walls do not have the two central slots, because the space is needed for the observation windows. Therefore, the lateral walls have two slots each, located at the corresponding positions of the outer slots in the top and bottom walls. The slots have an approximate width of 5 to 6 mm. Previous experience has shown that one needs at least three computational points inside the slot width in order to obtain an adequate resolution of flow through the slots. However, the particular tunnel configuration under consideration has two symmetry planes. Therefore, one has to solve only for one-fourth of the complete tunnel, indicating that only three slots are present in the computational domain considered.

The initial simulations with the above mesh indicated that the resolution in the ζ direction was not adequate. This experience has shown that a mesh spacing at the tunnel wall (in the azimuthal direction) of at least 5 mm was necessary, aside from further refinement at the slots themselves. This spacing would imply that 55 points were required in this direction. It must be pointed out that the ideal solution would be to have a complete refinement in the ζ direction, because this would provide a smoother mesh. However, considering that three computational points would be required within each slot and that the slots had a 5 mm width, this would imply a mesh with about 211 points in the azimuthal direction. The computational costs of a solution in such a grid, even assuming that the refinement in the other directions would remain as previously cited, were well beyond the available computational resources at the time.

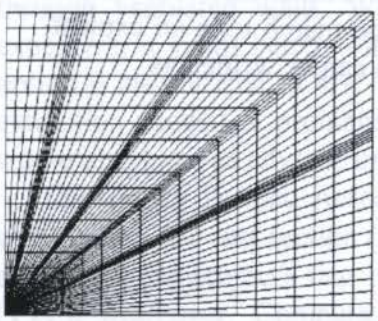

Figure 2 - View of a crossflow plane of the mesh

Therefore, the decision adopted was to have a mesh with an average spacing at the wall in the ζ direction of approximately 5 mm and to perform a localized refinement at the slots in order to recover the necessary resolution. This mesh was generated by a linear interpolation process on the previous grid, which had 29 points in the azimuthal direction. This yielded a mesh with 55 grid points. Afterwards, and still using linear interpolation at the wall, further refinement was performed at the slots adding 12

points to the mesh. The final mesh had, therefore, 150 × 20 × 67 in the (ξ, η, ζ) directions, respectively, which provides the minimum resolution required to perform simulations with the ventilated wall wind tunnel. A typical crossflow plane of the grid in the slotted test section portion of the tunnel in shown in Fig. 2. One can clearly see in this figure the additional refinement at the slot locations and, also, some additional refinement in order to resolve the kink in the tunnel wall.

4. RESULTS

As previously discussed, the initial simulations performed considered only the tunnel contraction, i.e., the convergent-divergent nozzle portion of the tunnel. These calculations were performed with the objective of validating the code developed against results available in the literature for this configuration (Fico *et al.*, 1994). Moreover, there was also interest in comparing the present code computational efficiency against that provided by the previous implicit code (Fico *et al.*, 1994). This phase of the work used the original 100 × 20 × 29 point mesh. Results for this simulation for a nominal test section Mach number of 1.3 are shown in Fig. 3. In particular, this figure presents Mach number contours along four crossflow sections at different longitudinal locations along the tunnel. The planes represent the nozzle entrance section (i=1), two intermediate planes (i=25 and i=75) and the nozzle exit plane (i=100), which corresponds to the entrance of the tunnel test section.

One can clearly observe from Fig. 3 that the Mach number variation within each crossflow section is very small, indicating a very uniform acceleration of the flow through the nozzle. The overall quality of these solutions is in very good agreement with the results reported by Fico *et al.* (1994). The authors emphasize that the reader should pay attention to the color coding of each plot in order to observe that Mach number variations within each section are indeed very minor. Figure 4 presents the Mach number contour plots (top) and the velocity vectors (bottom) along the tunnel horizontal symmetry plane. One can observe a very uniform and smooth expansion of the flow along the nozzle. Moreover, one can also observe that the Mach contours are orthogonal to the nozzle axis and uniformly spaced along the nozzle. This conclusion that the flow is very smooth along the nozzle is further emphasized by the velocity vector plot, which indicates that the flow follows the nozzle geometry without any shocks or discontinuities. Figure 5 presents the pressure distribution along the nozzle wall in the longitudinal direction. This figure again indicates that there are no sharp variations in the pressure along the longitudinal direction, thus showing that there are no shock waves in the flowfield for this case. This is clearly the desired behavior since shock waves would degrade the flow quality for the tunnel test section.

Simulations were also performed for the tunnel including both the contraction and the test section, but without including the effect of the wall slots. This case will be denoted here as the closed slots case. The computational mesh used in these simulations is already the final grid with 150 X 20 X 67 points, especially because the present solution provides the necessary initial condition for the simulation with the slots open, which will be discussed latter in the paper. Figure 6 presents the Mach number contours for three crossflow planes, namely the plane at the end of the contraction (i=100), an intermediate plane along the test section (i=125) and the test section exit plane (i=150), for the case of nominal test section Mach number of 1.3. One can observe from the top figure in Fig. 6 that the tunnel nozzle is providing a very uniform flow to the test section. Moreover, it is also fulfilling its design objective which was to provide, in this case, the tunnel test section with a M = 1.3 flow. Furthermore, if one compares the three plots in Fig. 6, it is clear that test section Mach number variations about the nominal value of 1.3, throughout the entire test section, are extremely small. This indicates that, despite the fact that the test section is fairly long, its Mach number remains essentially constant. A similar conclusion

could be reached by analyzing the pressure distribution in the test section. The pressure results are not shown here for the sake of brevity.

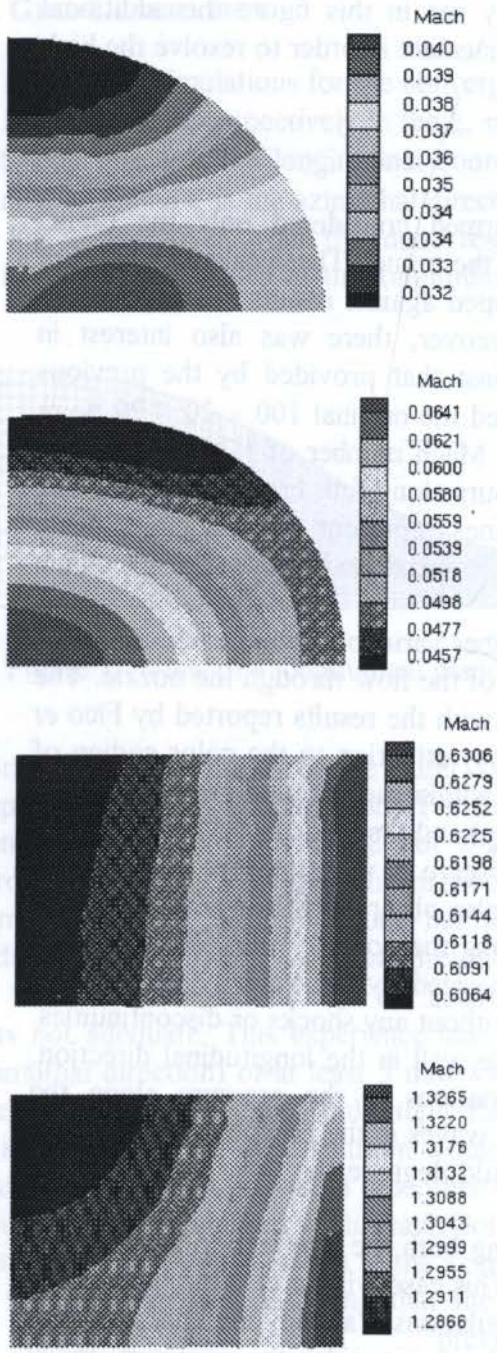

Figure 3 - Mach number contours at planes perpendicular to the nozzle axis

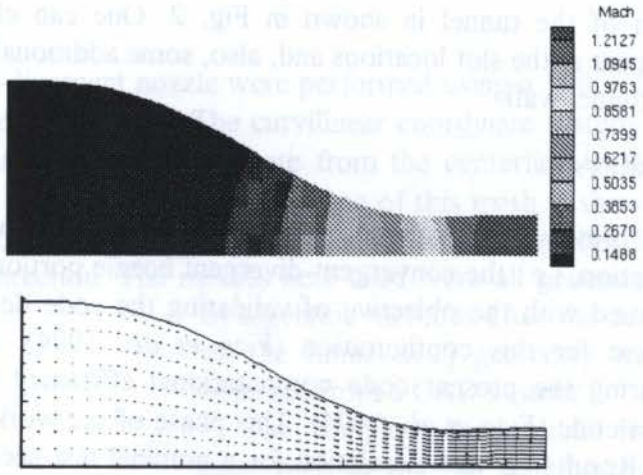

Figure 4 - Nozzle horizontal simetry plane

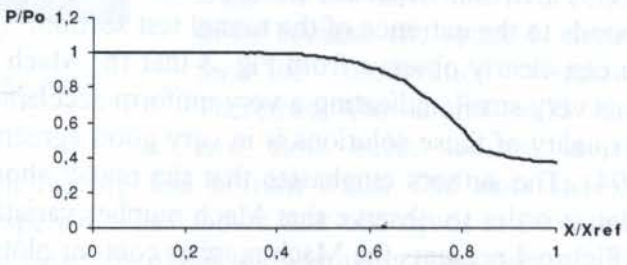

Figure 5 - Wall pressure distribution in the streamwise direction

The forthcoming discussion considers the case of open slots for a nominal test section Mach number of 1.3. The basic boundary condition imposed at the slots is a fixed pressure boundary condition. This is consistent with a characteristic analysis in which the slots are treated as a subsonic exit boundary (see, for instance, Azevedo *et al.*, 1995, for more details on the use of characteristic relations for boundary condition enforcement for the Euler equations). The static pressure imposed at the slots was varied between 90 and 98% of the average static pressure at the test section entrance, i.e., plane i=100, obtained from the simulation with closed slots. It should be emphasized that this is a somewhat artificial form of enforcing the slot boundary conditions because what one usually regulates in these facilities is the percentage of mass flow extracted from the test section. However, this would require the inclusion of the plenum chamber in the simulations, which is still a future step in the present development process. Therefore, the approach adopted in the present case is to impose the slot pressure and to compute the extracted mass flow as a result of

the simulation. By varying the slot pressure, one can obtain the correct mass flow ratio and, hence, validate the simulations.

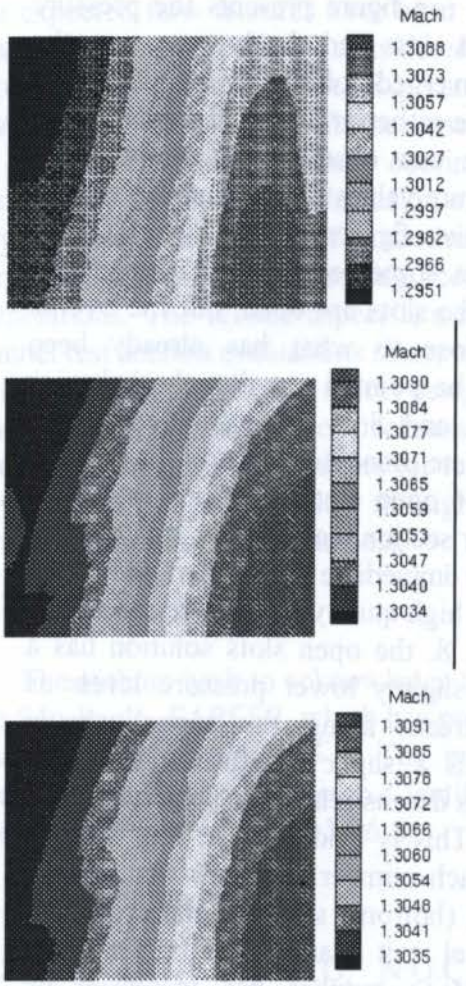

Figure 6 - Mach numbers contours at planes perpendicular to the wind tunnel axis

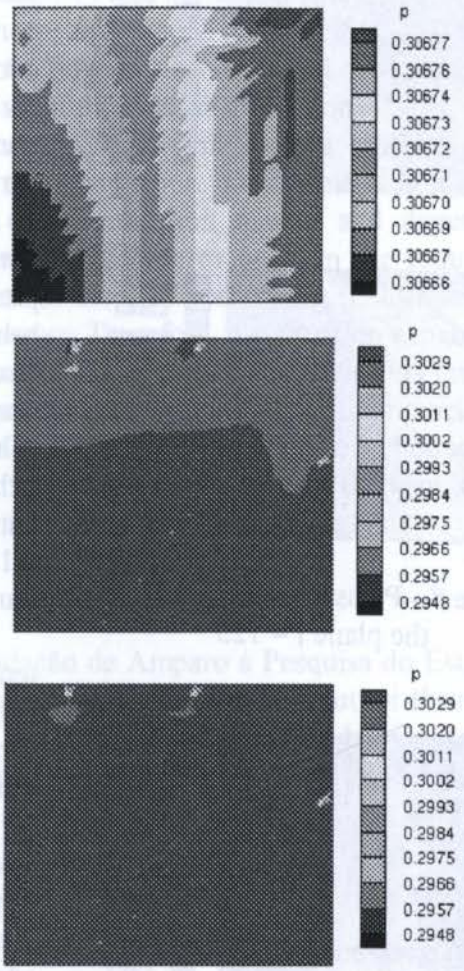

Figure 7 - Pressure distribution at the plane i = 107

As an example of the results obtained in the open slot case, Fig. 7 presents the pressure distribution along the crossflow plane i=107, for three instances along the numerical convergence process, for a slot static pressure equals to 95% of the average pressure at the test section entrance. This crossflow plane corresponds to the second computational plane (in the longitudinal direction) in the slotted portion of the test section. The top figure in Fig. 7 presents the section pressure distribution with the slots closed, the figure in the middle represents an instant of time just after the slots were open, and the bottom figure is the converged solution for that section with open slots. It should be, again, emphasized that, for example, the top figure may give a false impression of wild pressure variations in this particular section. However, if one observes the figure color coding, it becomes clear that the section pressure distribution is extremely uniform with an average value of 0.306. The authors point out that the quantity plotted is the dimensionless static pressure, referred to the stagnation pressure at the entrance of the tunnel contraction. The second (middle) figure shows some reduction in the pressure level throughout the section, but especially in the region closer to the upper wall which has two slots. This pressure variation within the section tends to disappear as the solution converges, and the bottom figure evidences that by showing again a very constant pressure distribution throughout the section except, obviously, in the immediate vicinity of the slots.

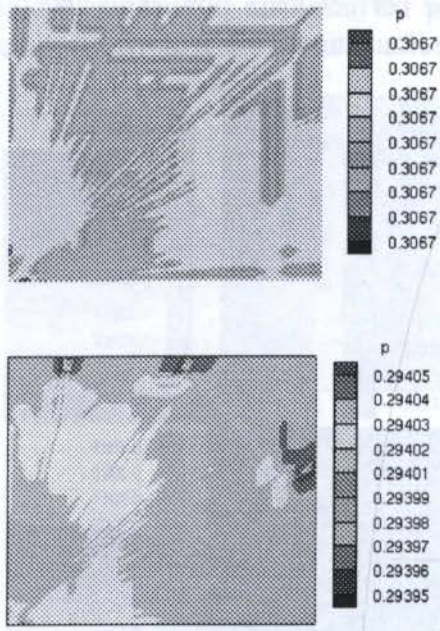

Figure 8 - Pressure distribution at the plane i = 125

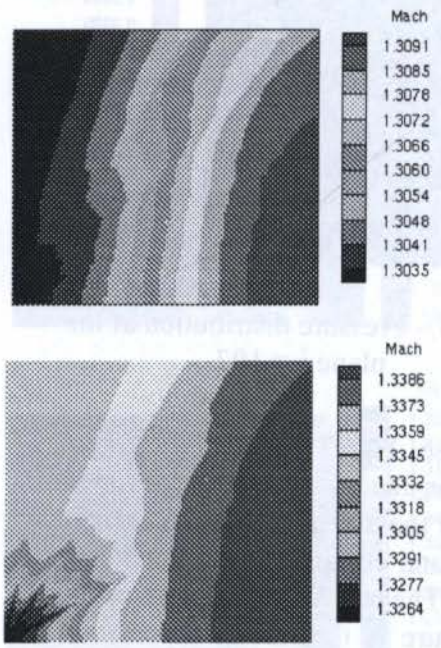

Figure 9 - Mach number contours at the plane i = 125

Figure 8 presents dimensionless pressure contours for a crossflow section halfway through the tunnel test section (i=125). The top figure presents the pressure contours with closed slots and the bottom one, the contours for the converged solution with open slots. As before, despite the rather erratic appearance of the contour colors, one can observe that there is no variation in the pressure values throughout the section up to four significative figures in the top plot. The bottom plot indicates some reduction in the section pressure level after the slots are open, but the overall behavior is very close to what has already been discussed. It should be pointed out that the behavior observed in Figs. 7 and 8 is representative of the solution in the complete tunnel test section. In general, either with closed or open slots, pressure variations within each particular section were always smaller than 0.1%, except in the immediate vicinity of the slots, thus demonstrating a high quality flow in the tunnel.

As shown in Fig. 8, the open slots solution has a tendency of having slightly lower pressure levels as one moves downstream along the tunnel. As a consequence, there is a slight increase in the flow velocity as one moves downstream along the tunnel for the open slot case. This is evidenced in Fig. 9. This figure shows the Mach number contours with closed (top) and with open (bottom) slots for the crossflow section at the tunnel exit plane (i=150). One can observe that the Mach number has increased by approximately 0.03 for the open slot case, in comparison with the closed slot solution which indeed reproduces the nominal test section Mach number of 1.3. Although there is some acceleration of the flow in the open slot case, the flowfield is still very uniform within each crossflow plane. Moreover, this slight acceleration of the flow with open slots is exactly the result one should expect to find in an empty wind tunnel. Due to mass extraction through the slots, and considering that there are no viscous effects in the simulations, the test section behaves as a divergent nozzle in supersonic flow and the flow must accelerate. Furthermore, an analysis of several crossflow planes further indicates that crossflow velocities are negligible throughout the entire test section, except in the immediate vicinity of the slots.

5. CONCLUDING REMARKS

The paper has presented flow simulations relevant to transonic wind tunnel design and operation. Initial tests reproduced some existing tunnel contraction results with the objective of validating the computational code developed. Afterwards, the tunnel test section was included in

the computational domain and simulations with both closed and open test section slots were performed. The overall assessment of the results obtained so far is very positive in the sense that all expected flow features have been adequately reproduced by the numerical simulations. The particular tunnel geometry considered models the pilot transonic tunnel, TTP facility, currently under construction at CTA. Experimental results for the flow in this facility should soon be available which will allow further assessment of the quality of the present simulations.

Moreover, the immediate continuation of the present effort will include further grid refinement studies and the inclusion of viscous terms in the formulation. The former will mainly try to assess the effect of smoother, refined meshes in the solution quality and depends, primarily, of the authors getting access to enough computer power to perform the required simulations. The second aspect is a must from the point of view of performing realistic wind tunnel test section evaluations since, clearly, reality is viscous. Therefore, a simulation capability which intends to aid wind tunnel design and operation must include the effect of viscous terms. In particular, boundary layer thickness and boundary layer thickness growth along the tunnel are extremely important parameters for test section flow quality assessment. Furthermore, boundary layer interaction with the flow through the slots is also critical for the efficiency of the ventilated wall concept in transonic tunnels.

6. ACKNOWLEDGMENTS

The authors wish to acknowledge the support of Fundação de Amparo à Pesquisa do Estado de São Paulo, FAPESP, which has provided a Research Scholarship to the first author through the Process No. 96/0565-0. The present work was also partially supported by Conselho Nacional de Desenvolvimento Científico e Tecnológico, CNPq, under the Integrated Project Research Grant No. 522413/96-0.

7. REFERENCES

AZEVEDO, J.L.F., FICO, N.G.C.R., Jr. & ORTEGA, M.A., Two-Dimensional and Axisymmetric Nozzle Flow Computations Using the Euler Equations, *J. of the Braz. Soc. Mechanical Sciences*, Vol. 17, No. 2, pp. 147-170, 1995.

AZEVEDO, J.L.F., FICO, N.G.C.R., Jr., ORTEGA, M.A. & LUNA, G.C., Nozzle Flow Calculations Using the Euler Equations, ICAS Paper 92-4.1.2. *Proceedings of the 18th Congress of the International Council of Aeronautical Sciences*, Vol. 1, pp. 97-107, Beijing, China, 1992.

DAVIS, M.W., GUNN, J.A., HERRON, R.D. & KRAFT, E.M., Optimum Transonic Wind Tunnel, *AIAA 14th Aerodynamic Testing Conference*, West Palm Beach, Florida, 1986.

FICO, N.G.C.R., Jr., AZEVEDO, J.L.F. & ORTEGA, M.A., Use of CFD Methods for Transonic Wind Tunnel Nozzle Selection, ICAS Paper N°94-2.5.4, *Proceedings of the 19th Congress of the International Council of the Aeronautical Sciences,* Vol. 2, pp. 1587-1596, Anaheim, California, 1994.

FICO, N.G.C.R., Jr. Simulation of the Flow in the Reentry Flap Region of a Transonic Wind Tunnel, *Doctoral Dissertation*, Instituto Tecnológico de Aeronáutica, São José dos Campos, SP, Brazil, 1991 (in Portuguese).

JAMESON, A., SCHMIDT, W. & TURKEL, E., Numerical Solutions of the Euler Equations by Finite Volume Methods Using Runge-Kutta Time-Stepping Schemes, *AIAA Paper 81-1259*, 1981.

PULLIAM, T.H. & STEGER, J.L., Implicit Finite-Difference Simulations of Three-Dimensional Compressible Flow, *AIAA Journal*, Vol. 18, No. 2, pp. 159-167, 1980.

TURKEL, E. & VATSA, V.N., Effect of Artificial Viscosity on Three-Dimensional Flow Solutions, *AIAA Journal*, Vol. 32, No. 1, pp. 39-45, 1994.

XIV Brazilian Congress of Mechanical Engineering
Obeid Plaza Hotel Convention Center - Bauru - SP/Brazil
December 08-12th 1997

PAPER CODE: COB876

SIMULATION OF UNSTEADY TRANSONIC FLOW OVER A FIGHTER WING USING A ZONAL NAVIER-STOKES/FULL-POTENTIAL METHOD

OLYMPIO ACHILLES DE FARIA MELLO†
Instituto de Aeronáutica e Espaço, Centro Técnico Aeroespacial
12228-904 - São José dos Campos - SP, Brazil - e-mail: oamello@iconet.com.br

LAKSHMI N. SANKAR
School of Aerospace Engineering, Georgia Institute of Technology
Atlanta, Georgia 30332, U.S.A. - e-mail:lakshmi.sankar@ae.gatech.edu

Abstract

An improved hybrid method for computing unsteady compressible viscous flows is presented. This method divides the computational domain into two zones. In the inner zone, the Navier-Stokes equations are solved using a diagonal form of an alternating-direction implicit (ADI) approximate factorization procedure. In the outer zone, the unsteady full-potential equation (FPE) is solved. The two zones are tightly coupled so that steady and unsteady flows may be efficiently solved. Characteristic-based viscous/inviscid interface boundary conditions are employed to avoid spurious reflections at that interface. The resulting CPU times are about 60% of the full Navier-Stokes CPU times for unsteady flows in non-vector processing machines. Applications of the method are presented for a F-5 wing in steady and unsteady transonic flows. Steady surface pressures are in very good agreement with experimental data and are essentially identical to the full Navier-Stokes predictions. Density contours show that shocks cross the viscous/inviscid interface smoothly, so that the accuracy of full Navier-Stokes equations can be retained with a significant savings in computational time.

Keywords

Transonic flow, zonal methods, viscous/inviscid interaction, unsteady flow, finite-difference methods.

1. INTRODUCTION

Transonic flow is characterized by the presence of regions of supersonic flow embedded in a subsonic region. Mathematically, the governing equations are inherently non-linear, a fact that has prevented the application of traditional analytical tools and early numerical methods to the analysis of such a flow condition. In addition, transonic flows tend to be more unsteady and three-dimensional than purely subsonic and supersonic flows (Ballhaus, 1978).

In non-steady flow situations, The presence of a supersonic region embedded in a subsonic region causes downstream disturbances to be propagated upstream with a considerable time lag, which results in significant out-of-phase forces. It has been known for quite some time (Landahl, 1951) that transonic flow conditions are critical for flutter, with the flutter dynamic pressure being substantially reduced for Mach numbers near unity, in a phenomenon that has been called "transonic dip" (Whitlow, 1987). The severity of flutter at transonic speeds is linked to the presence of moving shock waves over the wing surface

† The first author was supported by the Conselho Nacional de Desenvolvimento Científico e Tecnológico (CNPq) and the Fundação de Amparo à Pesquisa do Estado de São Paulo (FAPESP), Brazil.

(Ashley, 1980). From these considerations, it is clear that accurate flutter predictions depend on the ability of the computational fluid dynamics procedure to predict correct shock strength and location, in a time-accurate fashion.

Transonic Small Disturbance equation (TSD)- and Full-Potential Equation (FPE)-based methods have been extensively used to compute complex configurations. These methods, in some cases, have been coupled to interactive boundary layer analyses to allow solution of problems where viscous effects can be included in a limited way.

For problems where substantial separation occurs, the TSD and FPE techniques coupled with interactive boundary-layer analysis are not adequate, since the concept of a boundary layer is no longer applicable. For these cases, Navier-Stokes methods are clearly needed. However, these are still computationally expensive and have seen limited practical use for complete configurations due to this factor. This becomes especially evident for problems where extensive computations are needed, such as the prediction of transonic flutter (Whitlow, 1987).

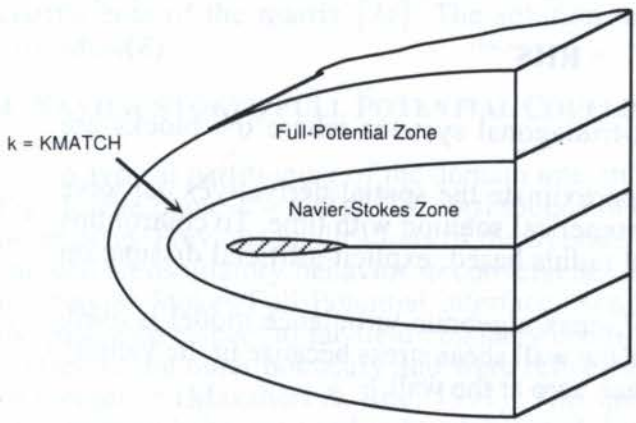

Fig. 1: Partitioning of Computational Domain into Inner and Outer Zones

The present method is an extension of the work initiated by Sankar *et al.* (1993), who developed a zonal Navier-Stokes/Full-Potential method. The approach used here is to solve the Full-Potential Equation in an outer zone, away from solid surfaces and viscous regions, and solve the Navier-Stokes equations in an inner zone, where viscous effects are essential. This approach is schematically illustrated in Fig. 1. This results in a highly efficient solver that retains the accuracy of the Navier-Stokes methodology near the solid surface, and the simplicity of a potential flow solver away from solid surfaces.

The mathematical formulation used here is described in detail by Mello (1994) and only a brief outline is presented next.

2. NAVIER-STOKES FORMULATION

The Navier-Stokes solver used in the present work was developed by Sankar & Kwon (1990). The vector form of the full Reynolds-averaged, 3-D Navier-Stokes equations based on an arbitrary curvilinear coordinate system can be written in non-dimensional form as:

$$\mathbf{Q}_\tau + \mathbf{E}_\xi + \mathbf{F}_\eta + \mathbf{G}_\zeta = \frac{1}{\mathrm{Re}}\left(\mathbf{R}_\xi + \mathbf{S}_\eta + \mathbf{T}_\zeta\right) \qquad (1)$$

where $\mathbf{Q}$ is the vector of unknown flow properties; $\mathbf{E}$, $\mathbf{F}$, $\mathbf{G}$ are the inviscid flux vectors; $\mathbf{R}$, $\mathbf{S}$, $\mathbf{T}$ are the viscous flux vectors and $\mathrm{Re} = \rho_\infty a_\infty c/\mu_\infty$ is the Reynolds number based on the free-stream speed of sound a_∞, density ρ_∞, viscosity μ_∞ and reference chord c.

The time derivative, $\mathbf{Q}_\tau$, of equation (1) is approximated using two-point backward difference at the new time level $n+1$. All spatial derivatives are approximated by standard second-order central differences and are represented by the difference operators δ. The streamwise and normal derivatives, $\mathbf{E}_\xi$ and $\mathbf{G}_\zeta$, are evaluated implicitly at the new time level $n+1$. The spanwise derivative, $\mathbf{F}_\eta$, is evaluated explicitly at the old time level n but uses the $n+1$ values as soon as they become available. This semi-explicit treatment of the spanwise derivative enables the scheme to solve implicitly for $\Delta\mathbf{Q}^{n+1}$ at all points at a given spanwise station at a time. To eliminate any dependency the solution may have on the sweeping direction, the solver reverses the direction of spanwise sweeping with every sweep.

The viscous terms $\mathbf{R}_\xi$, $\mathbf{S}_\eta$ and $\mathbf{T}_\zeta$ are evaluated explicitly, using half-point central differences denoted here by the difference operator $\bar{\delta}$, so that the computational stencil for the stress terms uses only three nodes in each of the three directions. Explicit treatment of the

stress terms still permits the use of large time steps since the Reynolds numbers of interest here are fairly large.

With the above described time and space discretizations, Eq. (1) becomes:

$$\Delta\mathbf{Q}^{n+1} + \Delta\tau\left(\delta_\xi \mathbf{E}^{n+1} + \delta_\eta \mathbf{F}^{n,n+1} + \delta_\zeta \mathbf{G}^{n+1}\right) = \frac{\Delta\tau}{\mathrm{Re}}\left(\bar{\delta}_\xi \mathbf{R}^{n,n+1} + \bar{\delta}_\eta \mathbf{S}^{n,n+1} + \bar{\delta}_\zeta \mathbf{T}^{n,n+1}\right) \quad (2)$$

Application of Eq. (2) to the grid points leads to a system of non-linear, block penta-diagonal matrix equations for the unknown $\Delta\mathbf{Q}^{n+1} = \mathbf{Q}^{n+1} - \mathbf{Q}^n$, Eq. (2), since the convection fluxes **E**, **F**, **G** are non-linear functions of the vector of unknown flow properties **Q**. Equation (2) is then linearized using the Jacobian matrices $\mathbf{A} = \partial\mathbf{E}/\partial\mathbf{Q}$ and $\mathbf{C} = \partial\mathbf{G}/\partial\mathbf{Q}$. This results in a system of linear, block penta-diagonal matrix equations, which is considerably expensive to solve. The approach used here is to employ an approximate factorization and the diagonal algorithm of Pulliam and Chaussee (1981), to diagonalize **A** and **C**. This approach yields:

$$\mathbf{T}_\xi^n\left[\mathbf{I} + \Delta\tau\,\delta_\xi \Lambda_\xi^n\right]\mathbf{N}^n\left[\mathbf{I} + \Delta\tau\,\delta_\zeta \Lambda_\zeta^n\right]\left(\mathbf{T}_\zeta^{-1}\right)^n \Delta\mathbf{Q}^{n+1} = \mathbf{RHS}^{n,n+1} \quad (3)$$

The solution of Eq. (3) involves two block-tridiagonal systems where the blocks are diagonal matrices.

The use of standard central differences to approximate the spatial derivatives can give rise to the growth of high frequency errors in the numerical solution with time. To control this growth, a set of 2nd/4th order non-linear, spectral radius based, explicit artificial dissipation terms are added to the discretized equations.

A slightly modified version of the Baldwin-Lomax algebraic turbulence model is used, where the maximum shear stress is used instead of the wall shear stress because in the vicinity of separation points, the shear stress values approach zero at the wall.

3. FULL-POTENTIAL FORMULATION

The Full-Potential solver used in the present work was developed by Sankar *et al.* (1981). The 3-D unsteady compressible potential flow equation, in a body-fitted coordinate system, may be written as a second order hyperbolic partial differential equation for the perturbation potential φ:

$$\frac{\rho}{a^2 J}\left[\varphi_{\tau\tau} + U\varphi_{\xi\tau} + V\varphi_{\eta\tau} + W\varphi_{\zeta\tau}\right] = \left(\frac{\rho U}{J}\right)_\xi + \left(\frac{\rho V}{J}\right)_\eta + \left(\frac{\rho W}{J}\right)_\zeta \quad (4)$$

where ρ is the density, U, V and W are the contravariant components of velocity and J is the Jacobian of the transformation between Cartesian and curvilinear coordinates.

At a given time level n, the disturbance velocity potential φ and its temporal derivative φ_τ are known, and consequently all velocity components, speed of sound and density are also known. Eq. (4) is a partial differential equation for φ with nonlinear coefficients. To circumvent the nonlinearities, the coefficients ρ, a^2, J, U, V and W appearing on the left side, and the density ρ appearing on the right side of equation (4) are computed at the time level n. The remaining quantities in (4) are kept at the new time level $n+1$. In the process of evaluating the contravariant velocities U, V and W, two-point central differences are used to evaluate the derivatives of φ and the transformation metrics at the grid points and locations mid distance between the grid points.

The temporal derivatives on the left hand side of Eq. (4) are discretized using two-point backward finite-difference operators. The mixed space-time derivatives appearing in Eq. (4) are discretized using two-point upwind-differencing for the spatial derivative, and two-point backward-differencing for the temporal derivative. The flux-like terms appearing on the right hand side of Eq. (4) are evaluated using two-point central-difference formulas with half intervals, using the density ρ computed at the time level n, while the contravariant components of velocity are computed using mixed information from time level n and the new time level $n+1$, in order to reduce the number of diagonals in the final matrix of coefficients.

In order to maintain numerical stability in regions of supersonic flow, the numerical formulation must be constructed in such a way that it is consistent with the physical domain of dependence. For that purpose, the artificial compressibility method is used. Here, the density values ρ that appear in $(\rho U/J)$ on the right side of equation (4) are biased in the direction of the flow .

When the above discretizations are employed, at each grid point a linear equation results for the change in the solution in two consecutive time steps $\Delta\varphi^{n+1} = \varphi^{n+1} - \varphi^{n}$. Application of this linear equation at the grid points result in a sparse pentadiagonal matrix system which may be expressed as:

$$[M]\{\Delta\varphi\}^{n+1} = \{R\}^{n} \tag{5}$$

The matrix $[M]$ is approximately factored as the product of two sparse lower ($[L]$) and upper ($[U]$) matrices each having four diagonals, with their elements recursively related to the coefficients of the matrix $[M]$. The solution to Eq. (5) is then obtained using a two-step procedure.

4. NAVIER-STOKES/FULL POTENTIAL COUPLING

A typical partitioning of the domain into an inner zone and an outer zone is illustrated in Fig. 1. The plane $k = KMATCH$ corresponds to the interface between the inner zone and the outer zone. Previous applications of the hybrid NS/FPE solver to an iced wing configuration showed an oscillatory behavior in convergence histories that indicated false reflections from the Navier-Stokes/Full-Potential interface. Similar numerical phenomena were observed in the past with respect to far-field boundary conditions: Acoustic waves traveled from the solid surface to the outer boundary and were reflected back to contaminate the solution and delay convergence (Mazaheri & Roe, 1991). The spurious waves responsible for the oscillatory convergence behavior need to be eliminated. In unsteady flows this is even more important since these spurious waves will compromise the time accuracy of the solution.

Non-reflecting far-field boundary conditions would not be directly applicable to the viscous/inviscid interface discussed here because perturbations in one zone must be transmitted to the other zone. The disturbances in the inner region should contribute to the outgoing waves only, while the disturbances in the outer region should contribute to the ingoing waves only, so that there is no reflection at the interface.

Following a development analogous to Giles' derivation of approximate non-reflecting boundary conditions (Giles, 1990), a set of characteristics $\mathbf{c}$ normal to a ζ=constant surface was obtained. These characteristics were related to small perturbations on the primitive variables. The resulting characteristic equations are integrated according to the signs of the corresponding eigenvalues. This corresponds to the eigenvalue splitting $\Lambda_\zeta = \Lambda_\zeta^+ + \Lambda_\zeta^-$ and corresponding characteristic splitting $\mathbf{c} = \mathbf{c}^+ + \mathbf{c}^-$:

$$\mathbf{c}_\tau^+ + \Lambda_\zeta^+ \mathbf{c}_\zeta^+ = 0 \quad ; \quad \mathbf{c}_\tau^- + \Lambda_\zeta^- \mathbf{c}_\zeta^- = 0 \tag{6}$$

For the Navier-Stokes solver, the vector $\mathbf{Q}$ at the viscous/inviscid interface is updated using the characteristics obtained from the integration of Eqs. (6). For the Full Potential solver, two of the characteristics are expressed in terms of the Riemann invariants, which are computed according to the signs of the corresponding eigenvalues. The flow properties at the interface are then updated from the Riemann invariants.

The above procedure has been successful in suppressing the oscillatory behavior observed in previous version of the hybrid method. Although the procedure is strictly valid only for steady flows (Mello, 1994), it was used also for unsteady flows with results similar to those obtained by full Navier-Stokes computations.

5. RESULTS AND DISCUSSION

In the present work, the F-5 wing in transonic flow undergoing pitch oscillations was investigated. This is a very rigorous test for the present method, due to the development of

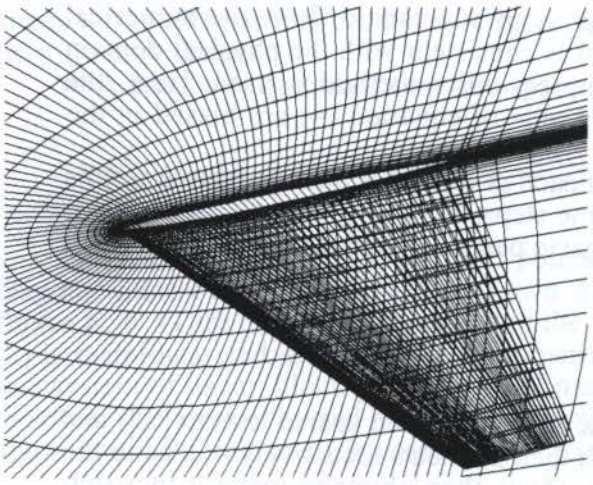

Fig. 2: Computational Grid for the F-5 Wing

shock waves which cross the viscous/inviscid interface. The interface boundary conditions are therefore required to propagate significant disturbances. In the unsteady flow simulations, these disturbances have to be propagated in a time-accurate fashion, which presents an even more rigorous test. The experimental results used here were obtained by Tijdeman *et al.* (1979), who measured steady and time-dependent pressures at eight spanwise stations.

The computational grid used in the present study is illustrated in Fig. 2. The Navier-Stokes and Full-Potential solvers were interfaced so that about half of the number of points were located in each zone.

5.1 Steady Flow Simulations

Steady pressure coefficient ($C_P = 2p/\rho_\infty V_\infty^2$) distributions for M_∞=0.95, zero angle of attack, at spanwise stations 35.2%, 72.1% and 97.7% are shown in Fig. 3. Here the dominating feature is the shock that forms over most of the wing, on both upper and lower

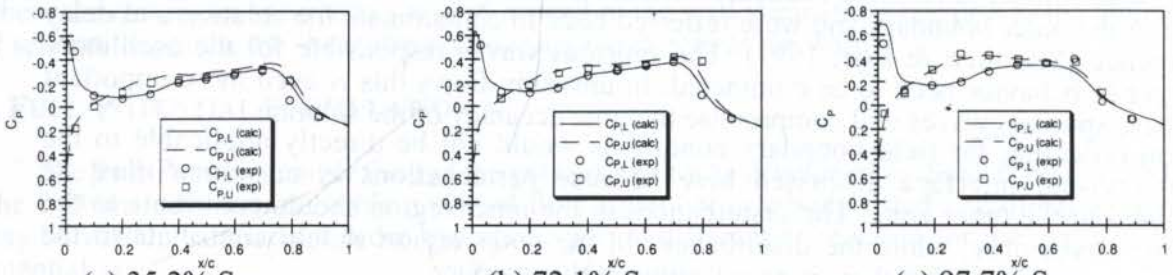

(a) 35.2% Span (b) 72.1% Span (c) 97.7% Span

Fig. 3: Steady Surface Pressure Distributions, M_∞ = 0.95

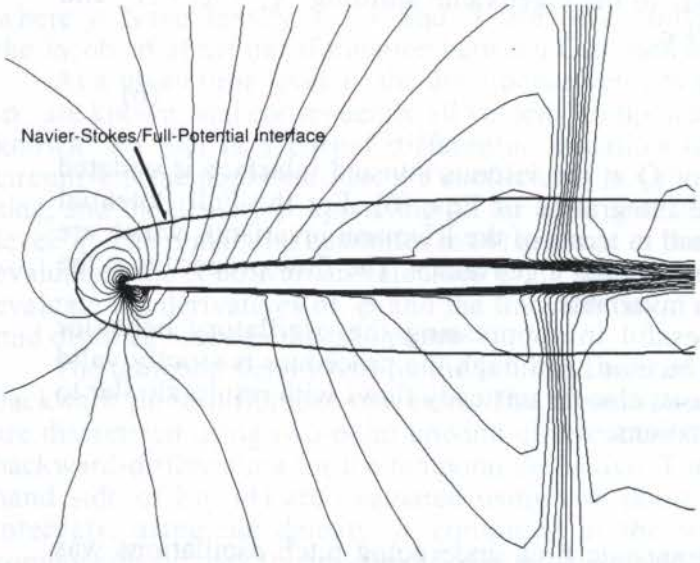

Fig. 4: Density Contours at 81.7% Span, M_∞ = 0.95

surfaces. The upper surface shock is stronger and aft of the lower surface shock. These features were well predicted by the current method. The suction peaks and location of matching upper and lower surface pressures are again well predicted, except at the station 97.7%, where the experimental data indicate a lower suction peak. This test case was demanding in the sense that the shock crosses the Navier-Stokes/ Full-Potential interface, and the results presented here indicate that the hybrid method is able to predict adequately both shock location and strength even when the discontinuities due to the shock are propagated through the Navier-Stokes/ Full-Potential interface.

Further evidence to support this conclusion is presented in Fig. 4, where the density contours at station 81.7% of span are shown. In this figure, the Navier-Stokes/Full-Potential interface is drawn to facilitate the analysis. It can be seen that the contours smoothly cross the interface, and in particular the shock is well captured across the interface.

The results presented here show that the hybrid method can be successfully applied to steady transonic flows, even when the shock crosses the Navier-Stokes/Full-Potential interface. The differences between the computed and measured data are of the same order of, or lower than, the more costly Navier-Stokes solutions presented by other researchers (e.g. Obayashi *et al.*, 1991).

5.2 Unsteady Flow Simulations

Unsteady transonic flows are very challenging to the present method, due to the presence of strong disturbances generated by unsteady shock motion, which need to be propagated through the Navier-Stokes/Full-Potential interface in a time-accurate fashion.

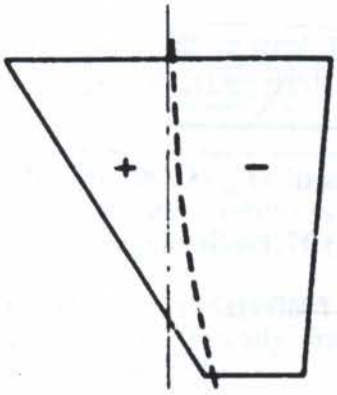

Fig. 5: Nodal Line

For the unsteady flow simulations presented here, the Mach number was 0.95. The wing was in pitching oscillations with a frequency of 40 Hz about half-chord, and around α_0=0°. Under these pitching oscillations, the F-5 wing deforms aeroelastically. During the investigation reported by Tijdeman *et al.* (1979), the wing vibration mode was measured for the various test runs using eight accelerometers. These measurements were used to obtain an approximate analytical expression for the vertical wing displacement at various points, assuming no chordwise deformation (rigid rotation) and parabolic spanwise deformation. This approximation to the elastic deformation allows a consistent representation by a rigid rotation about the node corresponding to each spanwise station. The nodal line corresponding to the case presented here is illustrated in Fig. 5, from Tijdeman *et al.* (1979).

The nondimensional time step was 0.005. An additional computation to assess the effect of the time step was made with a nondimensional time step of 0.002. The real and imaginary parts of the unsteady pressure coefficient distributions at spanwise stations 35.2%, 72.1% and 97.7% are shown in Fig. 6. As occurred in the previous test case, at all spanwise stations strong leading edge peaks are present in the lower surface both in the in-phase and out-of phase component and they seem to be well predicted by the present method. The steady flow results, shown in Fig. 3, indicate a strong shock on both upper and lower surfaces around 80% of the chord. The experimental data for the unsteady case, seen in Fig. 6, show significant peaks around this chordwise location, mostly in the real (in-phase) component, but also in the imaginary (out-of-phase) component. These peaks are very localized, which indicates that they result more from shock strength variations than shock movement. The numerical results presented in Fig. 6 show that the present method was unable to correctly predict the peak in the real part, but predicted the peak in the imaginary part. The computations with a smaller time step show some improvement in the real part, which indicate that the time step might have to be further reduced to yield a better correlation. Further reductions in time step were not attempted because of the large CPU resources that would be needed. It should also be noted that the current coarse grid presents some smearing in the shock, therefore small changes in the shock strength are not likely to be well captured, even with a smaller time step.

Except for the above discussed discrepancy, the unsteady pressure coefficient distribution is well predicted. It should be noted that this is a very rigorous test for the present method, due to the strong shock crossing the Navier-Stokes interface, as seen in Fig. 4. The results presented here indicate that the discrepancies observed in this test case are inherent to the Navier-Stokes module, and can probably be overcome by using an upwind Navier-Stokes module capable of capturing sharper shocks.

Overall the unsteady pressure coefficient distributions correlate well with experimental data and are similar to those obtained with equivalent full Navier-Stokes computations, with a fraction of the computational cost. The savings in CPU time were found to depend on the

vector capability of the CPU, ranging from 27% on the Cray Y/MP-L up to 40% on a HP Apollo 730 workstation.

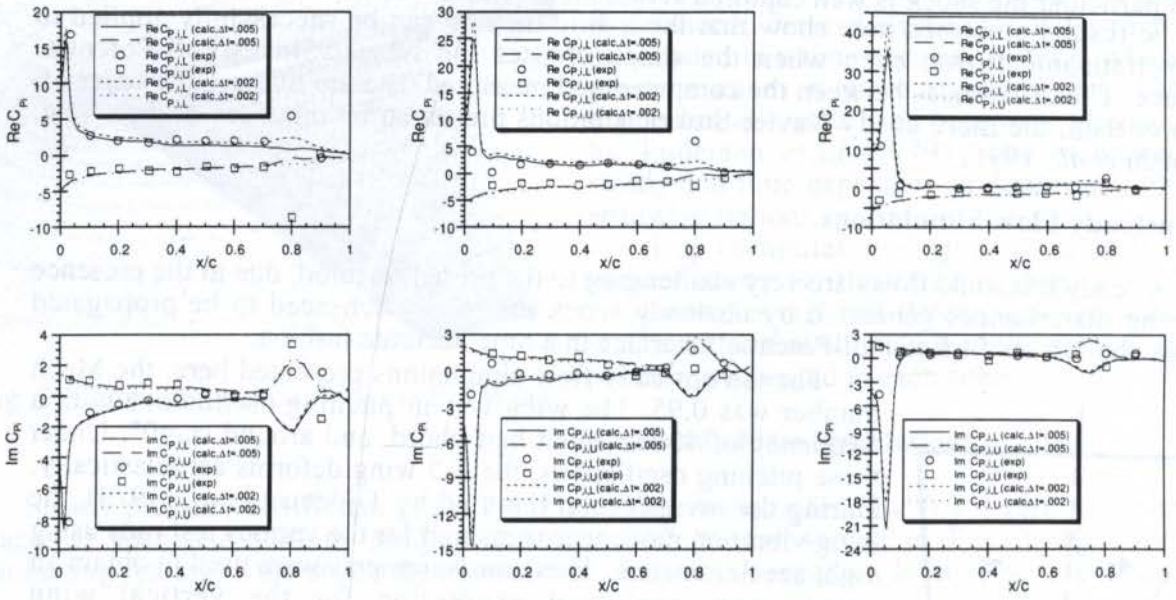

(a) 35.2% Span (b) 72.1% Span (c) 97.7% Span

Fig. 6: Unsteady Surface Pressure Distributions, $M_\infty = 0.95$, f=40 Hz

6. CONCLUSION

An improved hybrid Navier-Stokes/Full-Potential method has been successfully applied to transonic steady and unsteady flow around an F-5 fighter wing. It was found that the present technique allowed flow parameters to change smoothly across the viscous/inviscid interface. Pressure coefficient distributions agreed very well with experimental data. It should be noted that the shocks considered here have been virtually normal to the Navier-Stokes/Full Potential interface. For this reason, further investigation should be carried out before applying the present method to flow situations where significantly oblique shocks are present.

For the computations presented here, the two zones had the same number of grid points. With this configuration, the savings in total CPU time were found to depend on the vector capability of the CPU, ranging from 27% on the Cray Y/MP-L up to 40% on a HP Apollo 730 workstation. For steady flow cases, the computational savings were slightly higher, because the hybrid method presented convergence rates higher than the full Navier-Stokes method.

The location of the viscid/inviscid interface is a major factor in determining the actual savings for practical applications. For problems where massive separation occurs, this interface would have to be located farther away from solid surfaces, with a larger number of points in the inner zone. For these cases, the savings in CPU times would be reduced and might not be significant enough to justify the use of the present method. For problems where little or no separation occurs, the interface can be located closer to solid surfaces, so that less than half of the grid points would be located in the inner zone, and the computational savings could be increased even further. For helicopter rotor blades, dynamic partitioning between the viscous and inviscid domains (Berezin, 1995) allows optimal computational savings.

The present hybrid technique, which combines the accuracy of Navier-Stokes methods in the viscous regions with the economy of potential flow methods in inviscid regions, may be used as a stepping stone for more ambitious efforts involving aeroelastic and unsteady aerodynamic analysis of complete aircraft configurations.

8. REFERENCES

ASHLEY, H. "Role of Shocks in the 'Sub-Transonic' Flutter Phenomenon," *Journal of Aircraft*, Vol. 17, No. 3, March 1980, pp. 187.

BALLHAUS, W.F. "Some Recent Progress in Transonic Flow Computations," In: *Numerical Methods in Fluid Dynamics*, Edited by H. J. Wirz and J. J. Smolderen, Hemisphere Publishing Co., Washington, DC, 1978, pp. 155–235.

BEREZIN, C. "A Coupled Navier-Stokes/Full-Potential Analysis for Rotors," Ph.D. Dissertation, Georgia Institute of Technology, Atlanta, May 1995.

GILES, M. "Nonreflecting Boundary Conditions for Euler Equation Calculations," *AIAA Journal*, Vol. 28, No. 12, December 1990, pp. 2050–2058.

LANDAHL, M.T. *Unsteady Transonic Flow,* Pergamon Press, New York, 1951.

MAZAHERI, K. & ROE, P.L. "New Light on Numerical Boundary Conditions," AIAA Paper 91-1600-CP, AIAA 10th Computational Fluid Dynamics Conference, Honolulu, Hawaii, June 1991.

MELLO, O.A.F. "An Improved Hybrid Navier-Stokes/Full-Potential Method for Computation of Unsteady Compressible Viscous Flows," Ph.D. Dissertation, Georgia Institute of Technology, Atlanta, November 1994.

OBAYASHI, S., GURUSWAMY, G.P. & GOORJIAN, P.M. "Streamwise Upwind Algorithm for Computing Unsteady Transonic Flows Past Oscillating Wings," *AIAA Journal,* Vol. 29, No. 10, October 1991.

PULLIAM, T.H. & CHAUSSEE, D.S. "A Diagonal Form of an Implicit Approximate-Factorization Algorithm," *Journal of Computational Physics*, Vol. 39, 1981, pp. 347–363.

SANKAR, L.N., BHARADVAJ, B.K. & TSUNG, F.-L. "A Three-Dimensional Navier-Stokes/Full-Potential Coupled Analysis for Viscous Transonic Flow," AIAA Paper 91-1595-CP, AIAA 10th Computational Fluid Dynamics Conference, Honolulu, Hawaii, June 1991; also *AIAA Journal*, Vol. 31, No. 10, October 1993.

SANKAR, L.N. & KWON, O.J. "High-Alpha Simulation of Fighter Aircraft," Proceedings of the NASA High Angle-of-Attack Technology Conference, Vol. 1, NASA CP-3149, Pt. 2, NASA Langley Research Center, Hampton, VA, November 1990, pp. 689–702.

SANKAR, L.N., MALONE, J.B. & TASSA, Y. "An Implicit Conservative Algorithm for Steady and Unsteady Three-Dimensional Transonic Potential Flows," AIAA Paper 81-1016. Proceedings of the AIAA Fifth Computational Fluid Dynamics Conference, Palo Alto, CA, June 1981, pp. 199–212.

TIJDEMAN, H., VAN NUNEN, J.W.G., KRAAN, A.N., PERSOON, A.J., POESTKOKE, R., ROOS, R., SCHIPPERS, P. & SIEBERT, C.M. "Transonic Wind Tunnel Tests on an Oscillating Wing with External Stores, Part II: Clean Wing," Air Force Flight Dynamics Laboratory, AFFDL-TR-78-194, Part II, Wright-Patterson AFB, Ohio, March 1979. (Also NLR-TR-78106-U, Part II)

WHITLOW, W., JR. "Computational Unsteady Aerodynamics for Aeroelastic Analysis," NASA TM-100523, December 1987.

XIV Brazilian Congress of Mechanical Engineering
Obeid Plaza Hotel Convention Center - Bauru - SP/Brazil
December 08-12th 1997

PAPER CODE: COB908

TRANSONIC TURBULENT FLOW CALCULATIONS OVER THE VLS FOREBODY

Cesar A. Buonomo & João L. F. Azevedo

Instituto de Aeronáutica e Espaço, Centro Técnico Aeroespacial - CTA/IAE/ASE-N CEP 12228-904 - São José dos Campos - SP - Brasil - E-mail: azevedo@ase2.iae.cta.br

Abstract

A detailed study of transonic, turbulent flow conditions over the first Brazilian satellite launcher, the VLS, is described. The emphasis of the work is in developing the capability of accurately simulating realistic rocket flowfields and in understanding the behavior of two turbulence models in such conditions. The flowfields over the VLS at zero angle of attack are modeled by the axisymmetric, thin layer Navier-Stokes equations, and turbulence closure is obtained with the implementation of two different eddy viscosity models. A comparison of the characteristics of these two models is performed. Accurate solutions for the transonic flight regime are obtained. Non-reflective boundary conditions are also implemented, improving the representation of far field boundaries and the code's convergence characteristics in most cases.

Keywords

Transonic Flow, VLS, Turbulence Modeling, Finite Difference Method, Improved Boundary Conditions.

1. INTRODUCTION

A substantial amount of work has been devoted to the development of reliable computational tools for flow simulation in the context of the aerodynamic design of the VLS system, the first Brazilian satellite launcher. The VLS is a four-stage vehicle in which the first stage is composed of four strap-on boosters around a central core. The vehicle has a hammerhead-type payload shroud which is a configuration known to be prone to flow separation during the transonic flight regime. The experience with similar launchers has shown that the payload acoustic excitation loads due to the separated flow condition in the transonic regime can be as large as those experience by the payload at takeoff. Therefore, there is particular importance in having a thorough understanding of the vehicle's forebody flow condition in this regime.

Of special interest in the present case, previous work by Azevedo *et al.* (1995) has performed quite an extensive study of transonic and supersonic flowfields over the VLS at zero angle of attack. In that particular case, the primary concern was the flowfield around the vehicle forebody and the study had been motivated by the need to obtain boundary layer thickness information. The computations performed at that time presented very good agreement with the available experimental data for the majority of the conditions analyzed, except that the transonic case at $M_\infty = 0.90$ seemed to converge to the wrong shock position as the mesh was refined. The Baldwin and Lomax model (Baldwin & Lomax, 1978) was used for those simulations, and the grid refinement studies were performed by increasing the number of points in the longitudinal direction. Therefore, in this context, the major purpose of the present work is to extend the previous study in order to fully understand the VLS forebody flow characteristics at transonic flight conditions and to further the validation the present flow simulation capability.

2. THEORETICAL FORMULATION

The flowfield over the complete VLS vehicle, even at zero angle of attack, is certainly three dimensional. However, the effect of the four strap-on boosters is not considered in the present work. This is done because the vehicle forebody and satellite fairing are the primary regions of concern for the present transonic solutions. Thus, the azimuthal-invariant, Reynolds-averaged, thin-layer Navier-Stokes equations (Nietubicz *et al.*, 1979, Deiwert, 1984) are employed and, for the case of no body rotation, they can be written in general curvilinear coordinates as

$$\frac{\partial \overline{Q}}{\partial \tau} + \frac{\partial \overline{E}}{\partial \xi} + \frac{\partial \overline{F}}{\partial \eta} + \overline{H} = \frac{M_\infty}{\mathrm{Re}} \frac{\partial \overline{S}}{\partial \eta} \ , \tag{1}$$

where $\overline{Q}$ is the vector of conserved variables, $\overline{E}$ and $\overline{F}$ are the inviscid flux vectors, $\overline{S}$ is the thin-layer viscous flux vector, and $\overline{H}$ is the axisymmetric source term. A suitable nondimensionalization (Pulliam & Steger, 1980) of the governing equations has been assumed in order to write Eq. (1). The form of the previously defined algebraic vectors can be found, for instance, in Zdravistch & Azevedo (1990) and Fernández (1990). In the previous expression, M_∞ is the freestream Mach number and the Reynolds number is defined in its usual form as

$$\mathrm{Re} = \frac{\ell \rho_\infty q_\infty}{\mu_\infty} \ , \tag{2}$$

where ℓ is the reference length, ρ_∞ is the freestream density, q_∞ is the magnitude of the freestream velocity vector, and μ_∞ is the molecular viscosity coefficient at the freestream temperature. Expressions for the required metric terms and for the Jacobian of the coordinate transformation can be found in Deiwert (1984) and Fernández (1990), among other references.

The correct account for the viscous effects in the present case involves the implementation of an appropriate turbulence closure model. Two models have been implemented and were tested in this study, the Baldwin and Lomax (1978) algebraic model and the Baldwin and Barth (1990) one-equation model. For a complete description of these models, the interested reader is referred to the original references previously cited. It is important to emphasize, however, that the specific implementation of the Baldwin and Lomax model adopted here is a straightforward extension to the axisymmetric case of the work of Menezes (1994). The Baldwin and Barth model was implemented in present code precisely as described in Baldwin and Barth's (1990) original work. The extension for compressible flows was obtained simply by multiplying the kinematic turbulent viscosity coefficient by the local density, as also described in the original reference. Moreover, the turbulence model equation is solved separately from the other governing equations in a loosely coupled fashion. This procedure was adopted in order to avoid having to modify the flux Jacobian matrices and the overall structure of the flow solution algorithm which had been previously implemented.

3. NUMERICAL IMPLEMENTATION

The governing equations were discretized in a finite difference context on a structured quadrilateral mesh which would conform to the body. The Beam and Warming implicit approximate factorization scheme (Beam & Warming, 1978 and Pulliam & Steger, 1980) was used, with the implicit Euler method selected for the time march. As usual with the Beam and Warming algorithm, the spatial derivatives were centrally differenced using three-point, second-order, finite difference operators. Discretization of the viscous terms uses the so-called midpoint operators in order to obtain a compact finite difference stencil at each point and to avoid the need for a different discretization of these terms close to computational boundaries.

Artificial dissipation terms were added to the formulation in order to control nonlinear instabilities. All results reported in the present work have used Pulliam's nonlinear artificial

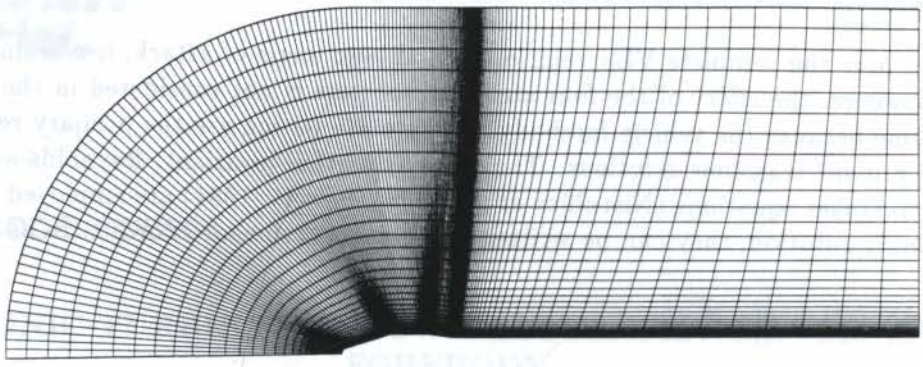

Figure 1: Typical computational mesh (156 × 65 points).

dissipation model (Pulliam, 1986). Implicit artificial dissipation terms were implemented as described in Azevedo *et al.* (1992). The axisymmetric source term was treated fully explicitly in the present case. This was done because previous experience (Zdravistch & Azevedo, 1990 and Fernández, 1990) has shown that this is sufficient for the applications at hand.

Four types of boundary conditions were implemented. These are wall, upstream centerline, far field and exit plane (downstream) boundary conditions. Wall boundary conditions are obtained by imposing no slip at the wall, zero normal pressure gradient and by assuming the wall to be adiabatic. The upstream centerline is a singularity of the coordinate transformation in the axisymmetric case. Hence, the governing equations are never solved at the centerline itself. The present approach considers a line of computational points "on the other side" of the centerline in order to impose symmetry boundary conditions along the centerline. Far field conditions are treated in two different forms. The initial approach was to simply assume freestream values specified at this computational boundary. Latter, non-reflective boundary conditions (Azevedo & Oliveira, 1994), based on Riemann invariants, were used which improved the code's convergence characteristics. Downstream conditions are based on the concept of one-dimensional characteristic relations (Azevedo *et al.*, 1992) in order to determine the number of variables which should be extrapolated at this boundary. For a subsonic downstream boundary, the static pressure is fixed and all other quantities at the boundary are obtained by zero-th order extrapolation of their respective values in the adjacent interior point. All flow variables are extrapolated from the adjacent interior point for a supersonic outflow.

4. RESULTS AND DISCUSSION

The computational grids used in the present work were generated algebraically, using the four-surface method as described in Fletcher (1988). An example of a typical grid used is shown in Fig. 1. This particular grid has 156 × 65 mesh points. Other meshes were generated, typically increasing the number of grid points in the nominally normal direction, in order to evaluate mesh convergence of the various solutions calculated. Specific details of the studies performed regarding mesh refinement and computational domain extension are discussed in the forthcoming paragraphs.

The assessment of the predictions of the two turbulence models was performed through comparisons of pressure and eddy viscosity coefficient (μ_t) contours, velocity fields and pressure coefficient (Cp) along the body. The simulations considered freestream Mach numbers in the range from $M_\infty = 0.73$ to $M_\infty = 1.05$. As one can see in Fig. 2, there are no large differences between the pressure coefficient distributions along the body for the solutions with the different turbulence models. This figure shows the results for freestream Mach number $M_\infty = 0.85$ and Reynolds number of 20 million. The same comment would be true if one would look at the

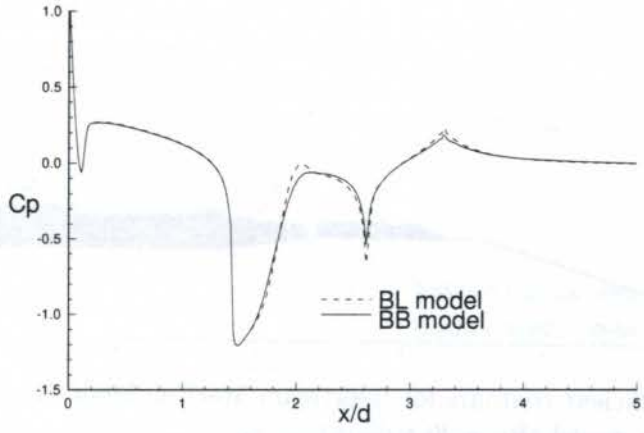

Figure 2: Comparison of pressure coefficient distributions obtained with different turbulence closure models for freestream Mach number $M_\infty = 0.85$ and Re = 20 million.

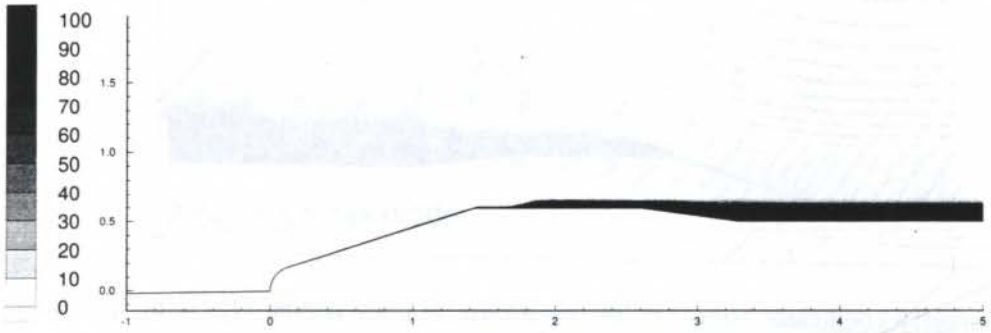

Figure 3: Eddy viscosity coefficient contours for freestream Mach number $M_\infty = 0.85$ obtained with the Baldwin and Barth model (Re = 20 million).

pressure contours (not shown) in the field for this case. This trend is observed in the freestream Mach number range of $M_\infty = 0.73$ up to 0.90.

In the same Mach number range, however, it is possible to see large differences between the eddy viscosity coefficient, μ_t, contours computed by the two models. This is evidenced in Figs. 3 and 4. Figure 3 shows the μ_t field obtained in the solution with the Baldwin and Barth model. As one can see, a very smooth and well behaved eddy viscosity coefficient distribution is obtained. It is also possible to observe the thickening of the boundary layer at the shock impingement point along the forebody cylindrical section. Moreover, after the boattail region, the thickness of the region with large values of μ_t remains approximately unchanged. This is in contrast with the results obtained for this case with the Baldwin and Lomax model, which are shown in Fig. 4. In the latter case, one can see the boundary layer thickening at the forebody cylindrical section and also downstream of the boattail-afterbody cylinder intersection. Actually, the behavior of the eddy viscosity coefficient contours is fairly erratic for the Baldwin and Lomax solution. The μ_t profile essentially vanishes at the expansion corner of the forebody cylinder-boattail intersection, which is clearly wrong. One should expect some thinning of the boundary layer and, therefore, a reduction of μ_t levels at such intersection, due to the expansion, but clearly the boundary layer or the turbulent effects cannot completely disappear.

It is interesting to observe that this anomalous behavior in the eddy viscosity coefficient distribution for the Baldwin and Lomax solution only occurs when the flow is supersonic at the corner. This can be verified by observing the solution for the $M_\infty = 0.73$ case, which is shown in Fig. 5. In this case, the flow is subsonic at the forebody cylinder-boattail intersection and one can see that there is no anomalous behavior of the μ_t distribution at this corner. Moreover,

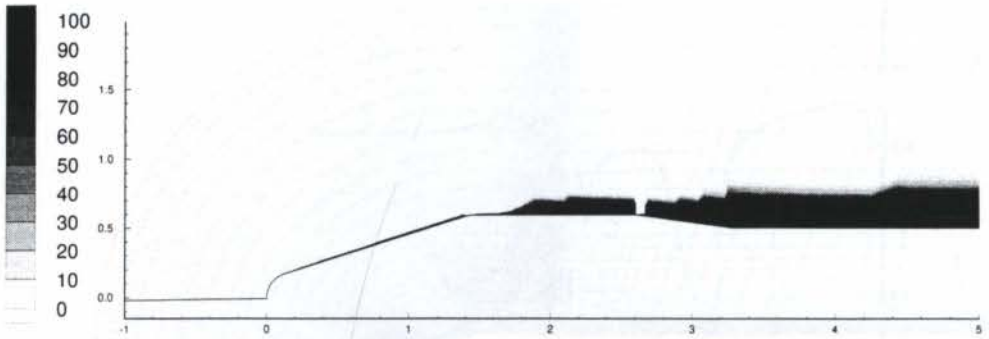

Figure 4: Eddy viscosity coefficient contours for freestream Mach number $M_\infty = 0.85$ obtained with the Baldwin and Lomax model (Re = 20 million).

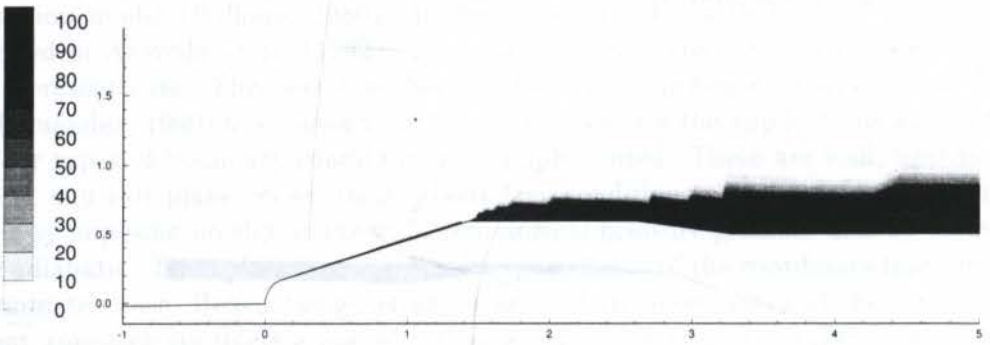

Figure 5: Eddy viscosity coefficient contours for freestream Mach number $M_\infty = 0.73$ obtained with the Baldwin and Lomax model (Re = 20 million).

the flow at the forebody cone-cylinder intersection is supersonic on both cases, i.e., Figs. 4 and 5, and one can see that the μ_t distribution vanishes at this supersonic corner for both solutions.

The only flow condition studied in which significant differences, between the results of the two turbulence models, were observed both on μ_t and pressure coefficient distributions was the $M_\infty = 0.95$ case (and still considering Re = 20 million). The pressure coefficient distributions for the two cases are shown in Fig. 6. The results with the Baldwin and Barth model are indicating a much larger separation region in the boattail than the corresponding results with the Baldwin and Lomax model. The physical explanation for this behavior is quite clear in this case. For the $M_\infty = 0.95$ case, the transonic shock impinges over the body in the boattail region. Therefore, not only this shock is stronger than the one present in the previous cases analyzed, but it also impinges on the body in a region of adverse pressure gradient due to the boattail-afterbody cylinder intersection. Hence, the flow separates at the foot of the shock. The Baldwin and Lomax model is known to add more μ_t than what would be correct in reality. Thus, it tends to numerically prevent the occurence of flow separation or the reduce the extension of the separated region. In this case, the separation is severe enough that even the Baldwin and Lomax model is able to capture it, although its prediction indicates a much smaller separated region. On the other hand, the Baldwin and Barth model predicts lower levels of μ_t and, hence, allows for a more extensive flow separation. Velocity vector plots for the boattail region are shown in Fig. 7 for these two cases. This figure clearly demonstrates the aspects just discussed.

As previously mentioned, typical initial grids had 156×65 points, and the external boundary was located 10 afterbody diameters away from the body. As the Mach number was increased, the transonic shock on the cylindrical portion of the payload shroud became stronger and it moved downstream. Moreover, a second shock began to form in the boattail-cylindrical afterbody intersection. As this second shock became stronger, there was a need to extend the position

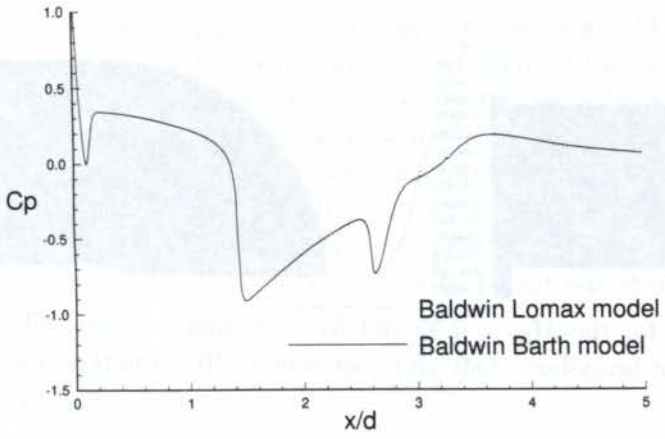

Figure 6: Comparison of pressure coefficient distributions obtained with different turbulence closure models for freestream Mach number $M_\infty = 0.95$ and Re = 20 million.

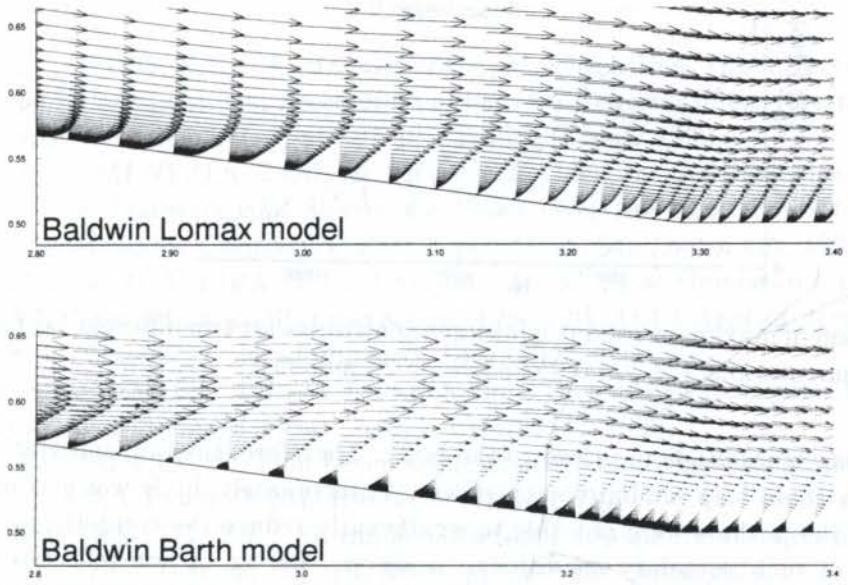

Figure 7: Velocity vectors in the boattail region for simulations with different turbulence closure models for freestream Mach number $M_\infty = 0.95$ and Re = 20 million.

of the far field boundary. Tests were performed with this boundary placed up to 15 afterbody diameters away from the body. This originated a need to increase the number of points in the normal direction up to 100 points, in order to maintain the y^+ value of the first point away from the body still small enough while keeping the grid stretching within acceptable levels. An example of the type of problem which can occur if the far field boundary is too close to the body in these cases is shown in Fig. 8. This figure shows results for the $M_\infty = 0.95$ and Re = 20 million case for two different positions of the far field boundary. In the left plot, the far field boundary is located 10 afterbody diameters from the body whereas, in the right plot, it is located at 15 diameters. Clearly, the boundary is causing interference in the pressure contours in the left-hand plot, indicating that it is too close in that case. Both calculations were performed with the Baldwin and Lomax model for the results shown in Fig. 8.

Another study performed considered the implementation of non-reflective boundary conditions at the far field boundary. The basic idea was to avoid the need of extending the computational boundary further away from the body in order to prevent the interference described in the previous paragraph. The rationale behind these tests was that the interference problem could be associated with the reflection of outward going waves due to the imposition of fixed

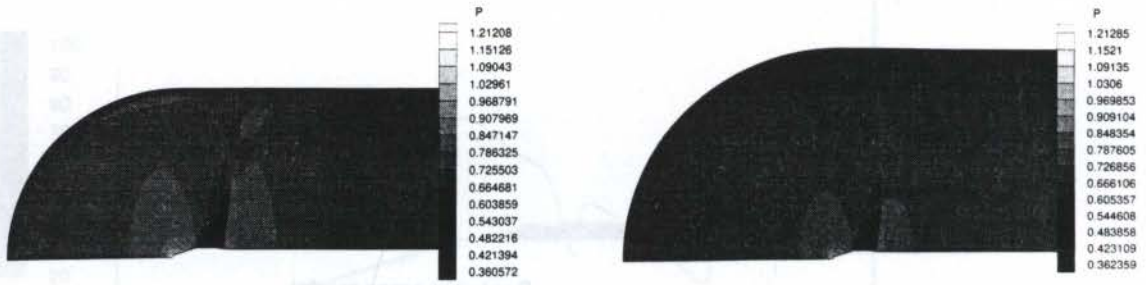

Figure 8: Pressure contours for the $M_\infty = 0.95$ and Re = 20 million case, indicating the effect of the position of the far field boundary. Left plot: far field at 10 diameters; right plot: far field at 15 diameters.

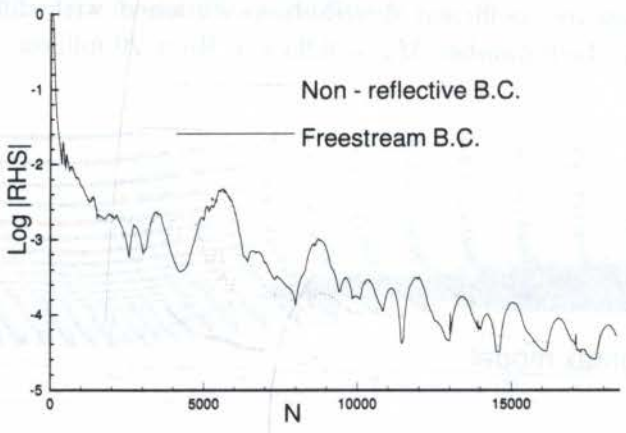

Figure 9: Comparison of maximum residue convergence histories for two different far field boundary condition implementations ($M_\infty = 0.95$ and Re = 20 million).

(freestream) boundary conditions too close to the body. Therefore, the implementation of non-reflective conditions could help minimize such effects. Unfortunately, little was accomplished in this sense, because the authors were not able to significantly reduce the computational domain with the adoption of such boundary conditions. However, the use of non-reflective boundary conditions has yielded an improvement in the smoothness of the code's convergence history, as one can see in Fig. 9. This seems to be an indication that non-reflective boundary conditions have indeed allowed for a more correct treatment of the outward going waves and, therefore, they have increased the robustness of the code.

5. CONCLUDING REMARKS

The paper presented a study of transonic, turbulent flow conditions over the first Brazilian satellite launcher, the VLS. The turbulence models considered included the Baldwin and Lomax algebraic eddy viscosity model and the Baldwin and Barth one-equation model. The results have indicated that there are no large differences between the pressure distributions on the body obtained with the different models, provided that the flow remains attached. The values of the eddy viscosity coefficient in the field, on the other hand, are quite different for the two models in all cases simulated. The behavior of μ_t for the Baldwin and Barth predictions is smoother and more consistent with the expected results than the one observed with the Baldwin and Lomax model solutions. For the cases with flow separation, the predictions obtained with the Badwin and Barth model are substantially better than those offered by the algebraic model. This difference is basically associated with the ability of determining the onset of flow separation. Since the Baldwin and Lomax model adds more μ_t to the solution, this has a tendency of delaying, or even eliminating, flow separation.

Systematic grid studies have indicated that, as the freestream Mach number approaches 1, there is a need to position the far field boundary at least 15 afterbody diameters from the vehicle. Failure to position this boundary sufficiently far away from the body has resulted in oscillations and spurious behavior of the pressure contours about the vehicle. Attempts to overcome this difficulty with the implementation of non-reflective boundary conditions at far field boundary have yielded mixed results. In one sense, the solutions remained sensitive to the far field boundary position. However, non-reflective conditions have made maximum residue convergence histories smoother, which seems to be an indication of a more robust code implementation.

6. ACKNOWLEDGMENTS

The present work was partially supported by Conselho Nacional de Desenvolvimento Científico e Tecnológico, CNPq, under the Integrated Project Research Grant No. 522413/96-0.

7. REFERENCES

AZEVEDO, J.L.F., FICO, N.G.C.R., Jr., ORTEGA, M.A. & LUNA, G.C., Nozzle Flow Computations Using the Euler Equations, *Proceedings of the 18th Congress of the International Council of the Aeronautical Sciences*, Vol. 1, pp. 97-107, Beijing, China, 1992.

AZEVEDO, J.L.F., MENEZES, J.C.L. & FICO, N.G.C.R., Jr., An Assessment of Boundary Layer Properties for Transonic and Supersonic Flows Over the VLS, *Proceedings of the 13th AIAA Applied Aerodynamic Conference*, Part 1, pp. 41-51, San Diego, CA, 1995.

AZEVEDO, J.L.F. & OLIVEIRA, L.C., Unsteady Airfoil Flow Simulations Using the Euler Equations, AIAA Paper 94-1892-CP, *Proceedings of the 12th AIAA Applied Aerodynamics Conference*, Part 2, pp. 650-660, Colorado Springs, CO, 1994.

BALDWIN, B.S. & BARTH, T.J., A One-Equation Turbulence Transport Model for High Reynolds Number Wall-Bounded Flows, NASA TM-102847, 1990.

BALDWIN, B.S. & LOMAX, H., Thin Layer Approximation and Algebraic Model For Separated Turbulent Flows, AIAA Paper 78-257, Huntsville, Ala., 1978.

BEAM, R.M. & WARMING, R.F., An Implicit Factored Scheme for the Compressible Navier-Stokes Equations, *AIAA Journal*, Vol. 16, No. 4, pp. 393-402, April 1978.

DEIWERT, G.S., Supersonic Axisymmetric Flow over Boattails Containig a Centered Propulsive Jet, *AIAA Journal*, Vol. 22, No. 10, pp. 1358-1365, Oct. 1984.

FERNÁNDEZ, F.Z., Simulation of Aerodynamic Flows Over Cluster Type Configurations, Master Dissertation, Instituto Tecnológico de Aeronáutica, São José dos Campos, SP, Brazil, Nov. 1990 (in Portuguese).

FLETCHER, C.A.J., *Computational Techniques for Fluid Dynamics. 2 - Specific Techniques for Different Flow Categories*, Springer-Verlag, New York, 1988.

MENEZES, J.C.L., Numerical Analysis of Transonic Turbulent Flows About Airfoils, Master Dissertation, Instituto Tecnológico de Aeronáutica, São José dos Campos, SP, Brazil, July 1994 (in Portuguese).

NIETUBICZ, C.J., PULLIAM, T.H. & STEGER, J.L., Numerical Solution of the Azimuthal-Invariant Thin-Layer Navier-Stokes Equations, AIAA Paper 79-0010, *17th Aerospace Sciences Meeting*, New Orleans, LA, Jan. 1979.

PULLIAM, T.H., Artificial Dissipation Models for the Euler Equations, *AIAA Journal*, Vol. 24, No. 12, pp. 1931-1940, Dec. 1986.

PULLIAM, T.H. & STEGER, J.L., Implicit Finite-Difference Simulations of Three-Dimensional Compressible Flow, *AIAA Journal*, Vol. 18, No. 2, pp. 159-167, Feb. 1980.

ZDRAVISTCH, F. & AZEVEDO, J.L.F., Numerical Simulation of High Speed Flows Over Complex Satellite Launchers, *Proceedings of the 3rd Brazilian Thermal Sciences Meeting*, Vol. I, pp. 233-238, Itapema, SC, Brazil, Dec. 1990.

XIV Brazilian Congress of Mechanical Engineering
Obeid Plaza Hotel Convention Center - Bauru - SP/Brazil
December 08-12th 1997

PAPER CODE: COB909

MULTIBLOCK SIMULATIONS OF TURBULENT VISCOUS FLOWS OVER THE VLS AFTERBODY REGION

Daniel Strauss[1] & João L. F. Azevedo[2]
[1]*Instituto Tecnológico de Aeronáutica, Centro Técnico Aeroespacial -CTA/ITA/IEAA - daniels@aer.ita.cta.br*
[2]*Instituto de Aeronáutica e Espaço, Centro Técnico Aeroespacial - CTA/IAE/ASE-N - azevedo@ase2.iae.cta.br*
12228-904 - São José dos Campos - SP - Brasil

Abstract

Axisymmetric, turbulent, viscous flow simulations over the first Brazilian satellite launcher, the VLS, are presented. The emphasis of the work is on multiblock calculations for afterbody flows. The details of the multiblock implementation are presented together with a brief description of the numerical method. The implementation is validated against previous solutions for forebody flows over the same vehicle and through comparisons with experimental data for afterbody flows. The increased resolution of the multiblock calculations for the afterbody region is evidenced through comparisons with previous single block grid solutions.

Keywords

Axisymmetric Formulation, Multiblock Methods, Viscous Flow, Turbulent Flow.

1. INTRODUCTION

The present work arose from the need to numerically investigate afterbody flows for the VLS system and, in particular, the interaction between the external flow and the plumes from the rocket motor nozzles. Due to the complexity of the geometry in the afterbody region, and with the objective of keeping the codes as modular as possible while still remaining with a structured grid approach, the decision was made to extend the existing capability (Azevedo *et al.*, 1995b, 1996) in the direction of implementing multiblock techniques.

For the present axisymmetric case, the complexity of the geometry is not an overwhelming issue as it could be for realistic 3-D cases. Therefore, one could probably deal with the present problem using a single block grid. However, in the present context, there was interest in developing tools that could be used as building blocks to handle even more complicated configurations in the future. Based on the group's previous experience, it seemed that the best approach would be to use block structured grids.

The work describes the general ideas of the multiblock extension, with applications to forebody flow cases for which results were previously available with a single block formulation (Azevedo *et al.*, 1996). After this initial validation, the code is applied to afterbody flow cases without a propulsive jet. However, the long term objective of the development is to create the ability to include jets at realistic pressure and temperature ratios.

The forthcoming sections describe the theoretical formulation and numerical method, with emphasis on the details of the multiblock implementation. The computational results are presented together with their discussion and comparison with available data.

2. THEORETICAL FORMULATION

The first Brazilian Satellite Launch Vehicle (VLS) is of the cluster type with four strap-on boosters around the central core. Further description of this vehicle can be seen in Azevedo *et al* (1996). The flowfield over the complete VLS vehicle, even at zero angle of attack, is certainly three dimensional. The effect of the four strap-on boosters, however, will not be considered in the present work and only the geometrically axisymmetric central body is considered. Thus, the flowfields are modeled by the azimuthal-invariant, Reynolds-averaged, thin-layer Navier-Stokes equations (Nietubicz *et al.*, 1979, Deiwert, 1984), that can be written for the case of no body rotation in general curvilinear coordinates as

$$\frac{\partial \overline{Q}}{\partial \tau} + \frac{\partial \overline{E}}{\partial \xi} + \frac{\partial \overline{F}}{\partial \eta} + \overline{H} = \frac{M_\infty}{\mathrm{Re}} \frac{\partial \overline{S}}{\partial \eta} , \qquad (1)$$

where $\overline{Q}$ is the vector of conserved variables, $\overline{E}$ and $\overline{F}$ are the inviscid flux vectors, $\overline{S}$ is the thin-layer viscous flux vector, $\overline{H}$ is the axisymmetric source term, and M_∞ is the freestream Mach number. A suitable nondimensionalization of the governing equations is assumed in order to write Eq. (1). In the present case, the choice of reference state proposed in Pulliam & Steger (1980) is adopted. The form of the previously defined algebraic vectors can be found, in Zdravistch & Azevedo (1990). Expressions for the required metric terms and for the Jacobian of the coordinate transformation can be found in Deiwert (1984).

The correct account for the viscous effects in the present case involves the implementation of an appropriate turbulence closure model. Three different eddy viscosity models were available in the single block code (Azevedo *et al.*, 1996). These were the Baldwin and Lomax algebraic model (Baldwin & Lomax, 1978), the Johnson and King half-equation model (Johnson & King, 1985) and the Baldwin and Barth one-equation model (Baldwin & Barth, 1990). For a complete description of each of these models, the interested reader is referred to the original references previously cited.

3. SPATIAL AND TEMPORAL DISCRETIZATION

The governing equations were discretized in a finite difference context on a structured quadrilateral mesh which would conform to the body. The Beam and Warming implicit approximate factorization scheme (Pulliam & Steger, 1980) was used, with the implicit Euler method selected for the time march. As usual with the Beam and Warming algorithm, the spatial derivatives were centrally differenced using three-point, second-order finite difference operators. All results reported in the present work have used Pulliam's nonlinear artificial dissipation model (Pulliam, 1986). Implicit artificial dissipation terms were implemented as described in Azevedo *et al.* (1995a).

Variable time stepping was used in order to accelerate convergence to steady state. The implementation of the variable time step option also follows the work in Azevedo *et al.* (1995a). All boundary conditions were treated explicitly in the cases analyzed in this work, including boundaries between computational blocks. Further discussion of the boundary conditions implemented in the present work can be seen in Azevedo *et al.* (1996).

4. MULTIBLOCK IMPLEMENTATION

An initial attempt to treat afterbody flows over the VLS is described in Gregório (1995). This work used the available forebody flow simulation codes (Azevedo *et al.*, 1995b) and extended the computational mesh to also include the afterbody region. However, in an attempt to continue to use the available single block approach, the meshes had a "half-O" type of topology. Although results with and without jets have been computed and are shown in Gregório (1995), the quality of the solutions clearly reflects the lack of adequate resolution in the wake region of the flow. These results, although qualitatively correct, do not contain all the phenomena that should be present in the body wake or in the jet mixing layer.

The use of multiblock grids, however, allow for a much greater control of grid refinement in the regions of interest, without having to increase the number of grid points in regions where there is no need for such refinement. Therefore, one can improve the solution quality without excessive computational cost penalties. Moreover, a multiblock approach alleviates the burden of generating structured meshes over very complex configurations.

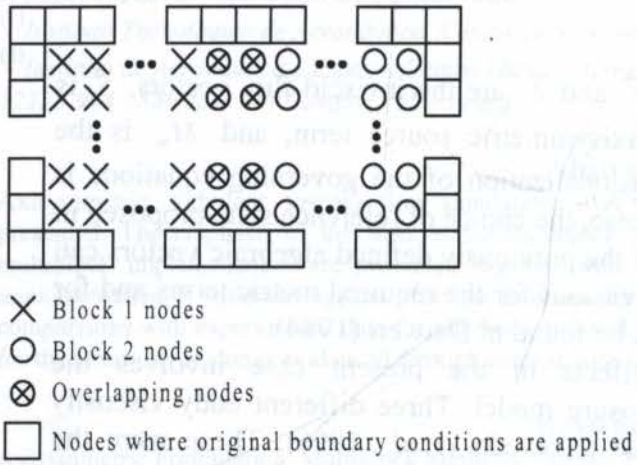

Figure 1: Sketch indicating the communication of information between grid blocks.

In the present case, a patched multiblock approach has been adopted in this first stage of the capability implementation. The basic ideas underlying the present development were that each block should be able to internally identify the types of boundaries on its four sides and that each side should consist of one single type of boundary. Moreover, another basic assumption in the present development was that the solution procedure within each block should be implemented in a completely independent fashion. Therefore, additional details of a given configuration could be added on to the simulation simply by creating new grid blocks that would describe such features.

The present code only applies the algorithm previously described for interior grid points. Boundary points are always updated through boundary conditions. The mesh is generated such that there is an overlap of two grid points between the adjacent blocks as indicated in Fig. 1. Hence, the block interfaces are perceived by the block currently being operated as boundaries with Dirichlet-type boundary conditions. The first overlapped point is an interior point of the block being operated. Therefore, the governing equations are solved at this point. The second overlapped point is the actual boundary point of the current block, and its property values are not changed during the current block solution. It should be noted that this second point is an interior point for the other block. Its properties are, therefore, updated through the actual solution of the governing equations when the other block is operated on. After the solution within the block is completed, the information on the first overlapped point is passed on to the neighboring blocks such that their boundary information is updated.

5. RESULTS AND DISCUSSION

The first tests performed with the multiblock capability were an attempt to reproduce results which were previously calculated (Azevedo *et al.*, 1996) with the single block code, in

order to validate the present implementation. These are results for the forebody portion of the vehicle and the single block grid used in these calculations is shown in Fig. 2. This particular grid has 156 × 65 points in the longitudinal and nominally normal directions, respectively, and a value y^+ of approximately 3 for the first grid point off the wall. All forebody computations presented here used the Baldwin and Lomax (Baldwin & Lomax, 1978) algebraic eddy viscosity model.

Multiblock computations have been performed for this configuration using four blocks. The computational mesh for this case is shown in Fig. 3. This mesh is essentially equivalent to the one presented in Fig. 2, except that it is topologically divided into four blocks. Fig. 3 shows these blocks separated solely to facilitate the reader's understanding of the block breakup. Simulations for freestream Mach number of 0.73 were performed with the four-block grid. Results for this case are shown in Fig. 4 in terms of pressure contours.

The Reynolds number for this calculation was 20 million, based on the afterbody diameter. One can observe from Fig. 4 that there is very good continuity of pressure contour lines across block interfaces. Incidentally, the block interfaces with their two overlapped points are also indicated in Fig. 4. The good continuity characteristics of the property contour lines across block interfaces is an indication of the correction and efficiency of the communication between computational blocks.

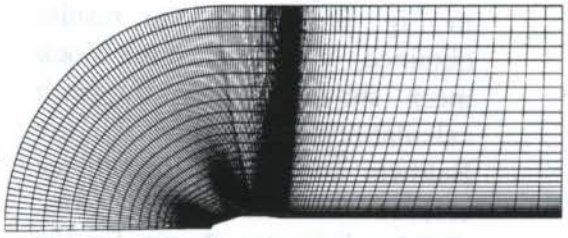

Figure 2: Single block computational mesh for vehicle forebody used to provide results for validation.

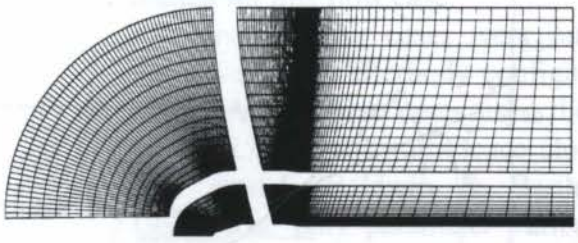

Figure 3: Four-block grid for the VLS forebody.

The pressure coefficient distributions along the body for this case are shown in Fig. 5. The figure compares the current multiblock solution with the single block solution reported in Azevedo *et al.* (1996). One can observe a very good agreement between the two results, indicating that the multiblock calculation is as good as the previous single block result. Moreover, at least for this case, these results indicate that the need to pass information across blocks has not caused any deterioration in the numerical solution.

Both computations were run with the same CFL number, using the variable time step option previously discussed. The results indicates that the explicit treatment of the internal boundary conditions are not reducing the rate of convergence to steady state in this case. Furthermore, this is an indication that the present multiblock implementation does not cause any degradation in the level of solution convergence possible with the algorithm.

The previous results provided confidence in the correct implementation of the multiblock procedure in the present case. Therefore, the forthcoming tests will consider the afterbody flows which are the major motivation for the present work. The initial comparison is performed with some of the results available in Gregório (1995). The first simulated case considers freestream flow with $M_\infty = 0.5$, Re = 20 million, and no rocket jets in the vehicle afterbody. In other words, there is simply a base on the back of the vehicle. The computational mesh used in the simulations of Gregório (1995) is shown in Fig. 6, whereas the present multiblock mesh is shown in Fig. 7. This mesh has 3 computational blocks. The 1st block comprises the complete vehicle up to the base, and it is somewhat equivalent to the mesh shown in

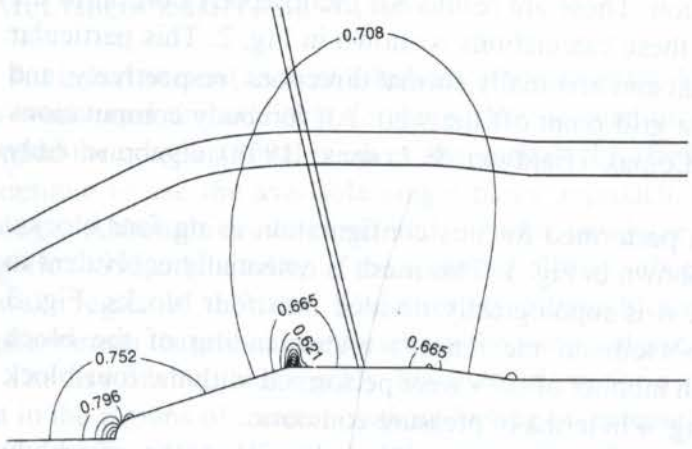

Figure 4: Pressure contours over the VLS forebody for M_∞ = 0.73. Simulation uses a four-block grid.

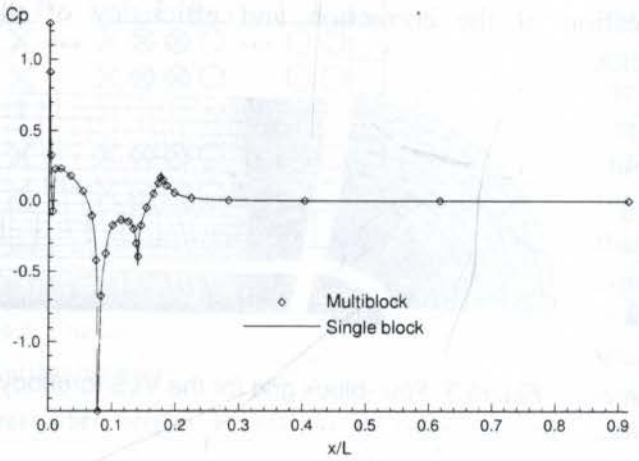

Figure 5: Comparison of single block and multiblock pressure coefficient distributions along the body for $M_\infty = 0.73$ and $Re = 20 \times 10^6$.

Fig. 2, except for some additional grid clustering in the longitudinal direction as the base region is approached. The 2nd block includes the region from the vehicle base until the downstream boundary, with a "height" equal to the base height. The 3rd block completes the computational domain in this case.

A comparison of the results obtained with the two different approaches can be seen in Fig. 8. These figures show pressure contours in the base and near wake regions. The top figure presents the results obtained with the single block, O-type mesh shown in Fig. 6. The middle case in Fig. 8 presents the results obtained with the three-block mesh shown in Fig. 7. Both calculations have used the Baldwin and Lomax turbulence closure model. The block division lines are shown for the multiblock cases in the figure and these give an idea of the continuity of pressure contours across the interfaces. In general, for the afterbody results with the Baldwin and Lomax model, continuity is very good in regions of high mesh density. However, it is also evident that, further downstream of the vehicle base, the continuity of pressure contours is not as good. Nevertheless, it is correct to state that the multiblock calculation yields an increased resolution of the flow features in the vicinity of the vehicle base.

In an attempt of improving the contour continuity across block interfaces, the same physical problem was solved using the multiblock code with the Baldwin and Barth turbulence closure model. The results are presented in the bottom case in Fig. 8. Clearly, there is good continuity of pressure contour lines throughout the near-wake region for this case. As a general assessment, one could state that the Baldwin and Barth solution is fairly different from

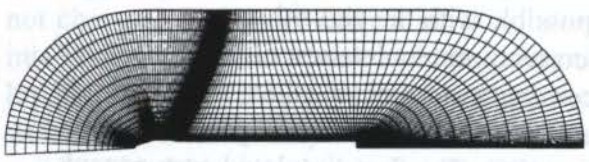

Figure 6: Single block grid including the afterbody region.

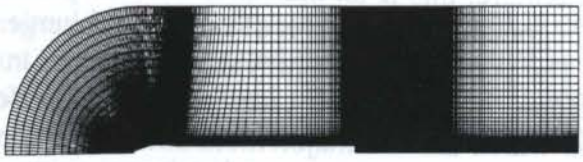

Figure 7: A typical multiblock grid used for the afterbody flow simulations.

the other two. In particular, the middle and bottom results in Fig. 8 use the same computational mesh and the solution is quite different. On the other hand, the two calculations with the Baldwin and Lomax model, although using very different meshes, have a somewhat similar pattern for the pressure contour plots. Moreover, one can clearly observe a backward motion of the rear stagnation point for the Baldwin and Barth solution, as compared to the other two previous cases.

A more quantitative comparison of the rear stagnation point position for these three cases is presented in Table 1. This table presents the axial position along the centerline of the rear stagnation point nondimensionalized by the afterbody diameter. The computational results are also compared in Table 1 with experimental data for cylindrical afterbodies obtained from Merz *et al.* (1978). These results indicate that the numerical solution with the Baldwin and Barth model provides a much better correlation with the experimental for this flow case.

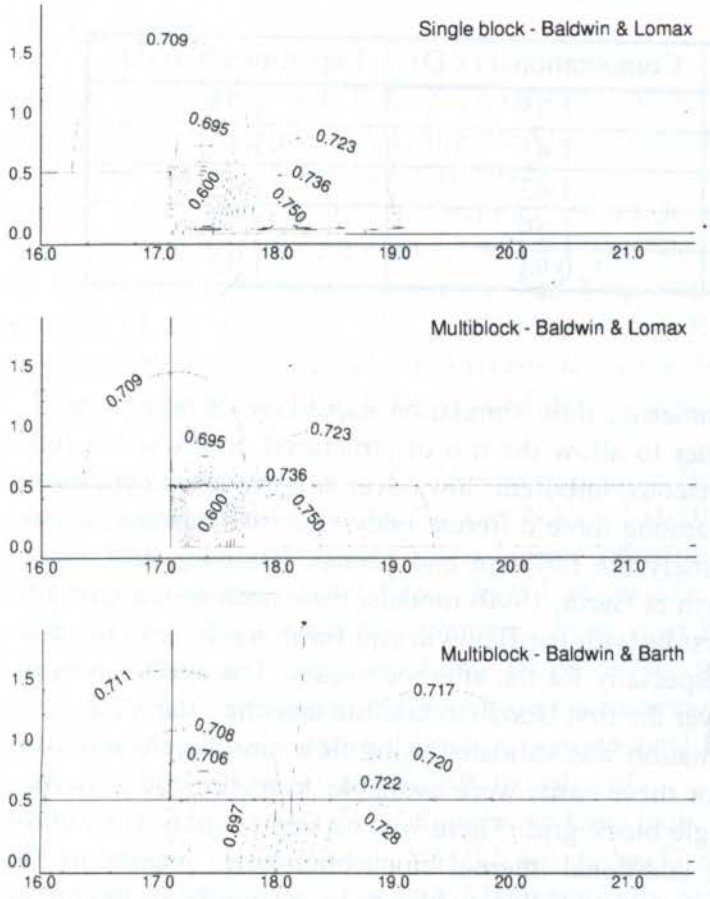

Figure 8: Pressure contours in the base region for $M_\infty = 0.5$ and $Re = 20 \times 10^6$. **(a)** Single block results; **(b)** Multiblock results using the Baldwin and Lomax turbulence model; and **(c)** Multiblock results using the Baldwin and Barth turbulence model.

Several other cases were run for this all-base afterbody configuration. All of these cases used the Baldwin and Barth turbulence closure model (Baldwin & Barth, 1990). The only parameter varied in these studies was the freestream Mach number. The results reproduce the general trend of the expected behavior and some validation of these afterbody simulations was obtained through comparisons of the rear stagnation point positions with experimental data. The data used was obtained from Merz *et al.* (1978) for the subsonic freestream cases and from Herrin & Dutton (1994) for the supersonic case. This comparison is presented in Table 2

The errors in the prediction of the rear stagnation point position are at most of 10% in the subsonic freestream cases. This error, however, is higher for the supersonic case. In general, one observes that the rear stagnation point moves downstream as the Mach number is increased in the subsonic cases, which is the expected behavior according to Merz *et al.* (1978). However, this movement is less pronounced in the computational results than in the actual experiments. Hence, for the lower Mach numbers, the computational stagnation points are further downstream than the experimental results, whereas for the higher Mach numbers (in the subsonic regime) the opposite occurs.

Table 1: Position of rear stagnation point behind body base for M_∞ = 0.5 and Re = 20 × 10^6 (D is the afterbody diameter and x is measured along the downstream centerline).

Case Description	Position (x/D)
Computation, single block, Baldwin-Lomax model	0.97
Computation, multiblock, Baldwin-Lomax model	0.82
Computation, multiblock, Baldwin-Barth model	1.35
Experimental data (Merz et al., 1978)	1.21

Table 2: Position of rear stagnation point behind body base (D is the afterbody diameter and x is measured along the downstream centerline).

Freestream Mach Number (M_∞)	Computational (x/D)	Experimental (x/D)
0.50	1.35	1.21
0.73	1.41	1.39
0.80	1.43	1.47
0.94	1.59	1.76
2.50	0.94	1.32

6. CONCLUDING REMARKS

An extension of an existing axisymmetric, flow simulation capability (Azevedo *et al.*, 1995b, 1996) has been performed in order to allow the use of structured, multiblock grids. The implemented formulation includes viscous, turbulent flows over axisymmetric configurations. The original code offers a choice among three different eddy viscosity turbulence closure models, but only two of them, namely the Baldwin and Lomax (Baldwin & Lomax, 1978) and the Baldwin and Barth (Baldwin & Barth, 1990) models, have been tested with the multiblock implementation so far. The results with the Baldwin and Barth model provide better comparison with the available data, especially for the afterbody cases. The applications of major interest concern afterbody flows over the first Brazilian satellite launcher, the VLS.

The multiblock capability implementation was validated using flow simulations over the VLS forebody. Computational results for these cases were available from previous calculations (Azevedo *et al.*, 1996) using a single block grid. There was no degradation in solution accuracy that could be attributed to the additional internal block boundaries present in the multiblock simulations. Property contours cross block boundaries in a completely seamless fashion. No oscillations or discontinuities in the contours could be observed in the forebody results run. Moreover, the use of multiblock grids has not degraded the convergence rate for these forebody simulations.

Afterbody simulation results with the present code were compared with those obtained using the single block code described in Gregório(1995) and with experimental data for general cylindrical afterbodies at zero angle of attack. In general, the multiblock results show a marked improvement in the resolution of flow features, as compared to the previous single block solutions. Moreover, the computational results reproduce the trends observed in the experimental data in terms of the location of the rear stagnation point as a function of the Mach number. For subsonic freestream Mach number cases, the discrepancies between computational and experimental values for this parameter were at most of 10%. The quantitative agreement in the supersonic case was poorer, but again the correct trend was captured.

Computational results for the afterbody cases calculated with the Baldwin and Barth model indicated very good property contour continuity across block interfaces. Moreover, in the overall sense, the rate of convergence to steady state remained essentially unaltered with

the introduction of the multiblock capability. Both the number of iterations for convergence and the level of maximum residue reduction are not significantly different from the cases computed with a single block grid. On the other hand, the additional resolution of flow details provided by the multiblock grids are evident from the results presented.

7. ACKNOWLEDGMENTS

The present work was partially supported by Conselho Nacional de Desenvolvimento Científico e Tecnológico, CNPq, under the Integrated Project Research Grant No. 522413/96-0.

8. REFERENCES

AZEVEDO, J.L.F., FICO, N.G.C.R., Jr., e ORTEGA, M.A., "Two-Dimensional and Axisymmetric Nozzle Flow Computations Using the Euler Equations," *J. of the Braz. Soc. Mechanical Sciences*, Vol. 17, No. 2, pp. 147-170, 1995a.

AZEVEDO, J.L.F., MENEZES, J.C.L., and FICO, N.G.C.R., Jr., "Accurate Turbulent Calculations of Transonic Launch Vehicle Flows," AIAA Paper No. 96-2484-CP, *Proceedings of the 14th AIAA Applied Aerodynamics Conference*, Part 2, pp. 841-851, New Orleans, LA, 1996.

AZEVEDO, J.L.F., MENEZES, J.C.L., and FICO, N.G.C.R., Jr., "An Assessment of Boundary Layer Properties for Transonic and Supersonic Flows Over the VLS," AIAA Paper 95-1769-CP, *Proceedings of the 13th AIAA Applied Aerodynamics Conference*, Part 1, pp. 41-51, San Diego, CA, 1995b.

BALDWIN, B.S., and BARTH, T.J., "A One-Equation Turbulence Transport Model for High Reynolds Number Wall-Bounded Flows," NASA TM-102847, 1990.

BALDWIN, B.S., and LOMAX, H., "Thin Layer Approximation and Algebraic Model for Separated Turbulent Flows," AIAA Paper 78-257, Huntsville, Ala., 1978.

DEIWERT, G.S., "Supersonic Axisymmetric Flow over Boattails Containing a Centered Propulsive Jet," *AIAA Journal*, Vol. 22, No. 10, pp. 1358-1365, 1984.

GREGÓRIO, E.L., "Simulação Numérica de Escoamentos em Regiões Traseiras de Veículos Lançadores," Graduation Project, Dept. of Aeronautical Engineering, Instituto Tecnológico de Aeronáutica, São José dos Campos, SP, Brazil, 1995.

HERRIN, J.L., and DUTTON, J.C., "Supersonic Base Flow Experiments in the Wake of a Cylindrical Afterbody," *AIAA Journal,* Vol. 32, No. 1, pp. 77-83, 1994.

JOHNSON, D.A., and KING, L.S., "A Mathematically Simple Turbulence Closure Model for Attached and Separated Turbulent Boundary Layers," *AIAA Journal*, Vol. 23, pp. 1684-1692, 1985.

MERZ, R.A., PAGE, R.H., and PRZIREMBEL, C.E.G., "Subsonic Axisymmetric Near-Wake Studies," *AIAA Journal*, Vol. 16, No. 7, pp. 656-662, 1978.

NIETUBICZ, C.J., PULLIAM, T.H., and STEGER, J.L., "Numerical Solution of the Azimuthal-Invariant Thin-Layer Navier-Stokes Equations," AIAA Paper 79-0010, 17th Aerospace Sciences Meeting, New Orleans, LA, 1979.

PULLIAM, T.H., "Artificial Dissipation Models for the Euler Equations," *AIAA Journal*, Vol. 24, No. 12, pp. 1931-1940, 1986.

PULLIAM, T.H., and STEGER, J.L., "Implicit Finite-Difference Simulations of Three-Dimensional Compressible Flow," *AIAA Journal*, Vol. 18, No. 2, pp. 159-167, 1980.

ZDRAVISTCH, F., and AZEVEDO, J.L.F., "Numerical Simulation of High Speed Flows Over Complex Satellite Launchers," *Proceedings of the 3rd Brazilian Thermal Sciences Meeting*, Vol. I, pp. 233-238, Itapema, SC, Brazil, 1990.

Tema 38

Métodos Experimentais em Mecânica dos Fluídos

UNESP COBEM 97

XIV Brazilian Congress of Mechanical Engineering
Obeid Plaza Hotel Convention Center - Bauru - SP/Brazil
December 08-12th 1997

PAPER CODE: COB1211

UM EXPERIMENTO DIDÁTICO EM CONVECÇÃO NATURAL / *A DIDACTIC EXPERIMENT ON FREE CONVECTION*

SAULO GÜTHS & VICENTE DE PAULO NICOLAU
Laboratório de Meios Porosos e Propriedades Termofisicas de Materiais (LMPT)
Departamento de Engenharia Mecânica, Universidade Federal de Santa Catarina
CEP 88040-900 Florianópolis/SC, Brasil - E-mail: saulo@lmpt.ufsc.br

Abstract

This paper describes a didactical experiment on natural convection along a vertical flat plate at constant temperature. It describes a methodology to determine the heat transfer coefficient based on the use of heat fluxmeters. The effect of radiant exchanges on the heat transfer coefficient is presented. A new type of heat fluxmeter, the "tangential heat fluxmeter", is presented as well the calibration technique.The experiment is very useful to ilustrate heat transfer concepts.

Keywords

convecção, convecção natural, fluxo de calor, fluxímetro / convection, free convection, heat flux, heat fluxmeter

1. INTRODUÇÃO

Em numerosas aplicações os problemas de controle e medição da transferência de calor por convecção natural ou forçada são muito importantes. Pode-se citar o dimensionamento de dissipadores de calor de componentes eletrônicos, condensadores de refrigeradores domésticos e industriais, aquecedores de ambientes, ou ainda no projeto térmico de edificações. Em muitos casos é difícil uma aproximação teórica, então a experimentação é inevitável. Este artigo apresenta uma metodologia para determinar o coeficiente de transferência de troca calor por convecção natural baseado no uso de transdutores de fluxo de calor (ou fluxímetros).

Particularmente é apresentado o caso clássico da convecção natural ao longo de uma placa plana vertical a temperatura constante. Esta configuração foi escolhida pelo grande número de resultados experimentais e teóricos (Eckert, 1950; Oostrach,1952; Gregg e Sparrow, 1956). É possível analisar o número de Nusselt para diferentes valores de Rayleigh (modificando a temperatura da placa e/ou altura da região de medição), a influência da emissividade da superficie e a influência da região de entrada. Um transdutor de fluxo de calor a gradiente tangencial será apresentado, e igualmente um método de calibração. O experimento é excelente para fixar os conceitos de transferência de calor além de ser um instrumento importante no estudo da transferência de calor, não só em ar, mas também em líquidos e escoamento multifásico.

2. O DISPOSITIVO EXPERIMENTAL

2.1 A Placa Plana Vertical

O placa plana vertical é uma placa de cobre (250 x 150 x 2 mm) aquecida por um filme resistivo em Constantan alimentado por uma fonte de tensão constante. A condição de regime estacionário é obtida em aproximadamente quinze minutos. A diferença de temperatura ao

longo da placa é menor que 0.1 K. A face posterior é isolada por 10 mm de fibra de vidro prensada com uma fina placa em fibra epoxy. A altura da placa em relação à base pode ser ajustada, possibilitando o estudo da influência da região de entrada.

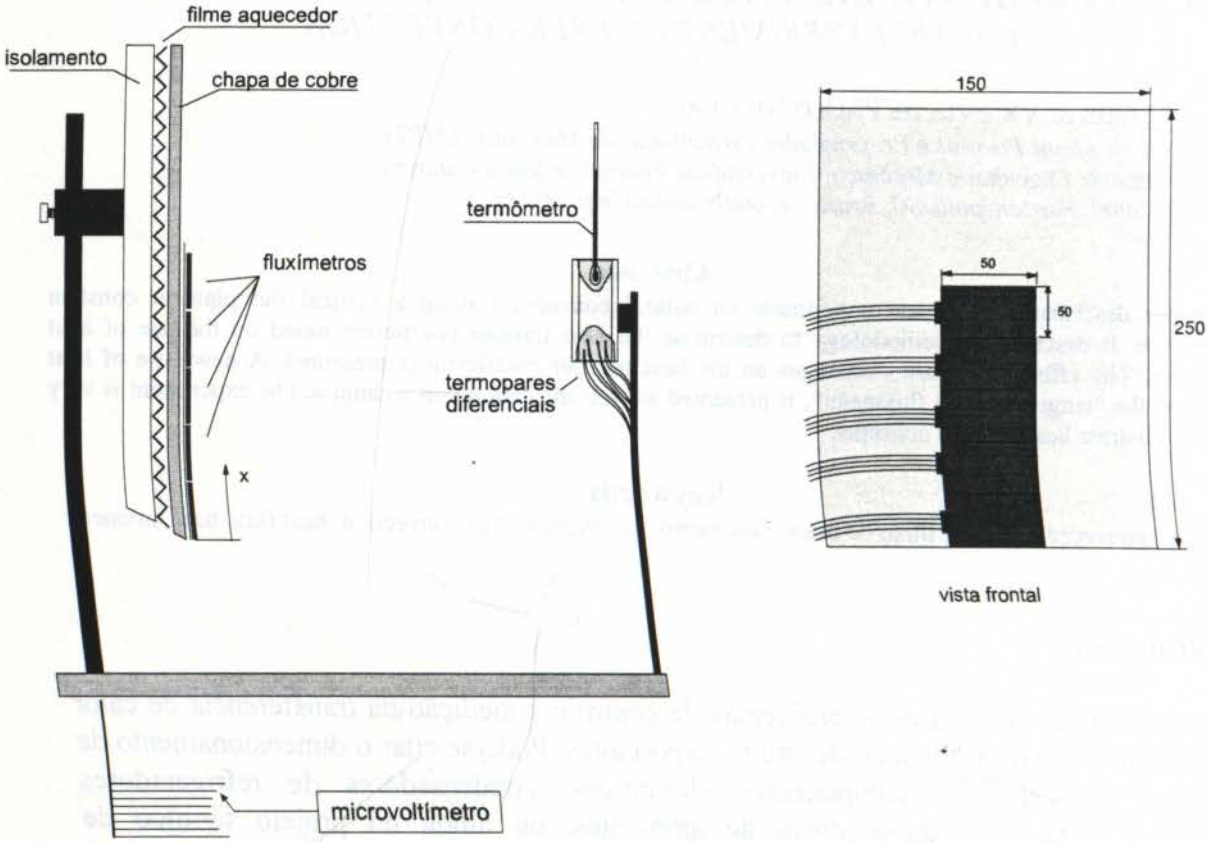

Figura 1 - A placa plana vertical

O sistema é protegido de perturbações adjacentes por uma caixa de vidro (1 m x 1 m x 0.6 m e 4 mm de espessura). A caixa deve assegurar uma boa evacuação do calor produzido pela placa plana, isto é, ela deve possuir uma baixa resistência térmica. Um ventilador externo pode ser implementado para aumentar o coeficiente global de transferência de calor. E um ventilador interno pode ser implementado possibilitando o estudo do coeficiente de transferência de calor por convecção forçada.

2.2 O Transdutor de Fluxo de Calor

O sensor, desenvolvido por Thery *et al.*(1980) e Güths (1994) chamado "transdutor de fluxo de calor a gradiente tangencial" tem como característica principal a pouca espessura (300 μm) e uma alta sensibilidade (20 mV/(W/m^2)) para um sensor com superfície de 50 x 50 mm^2. O princípio de funcionamento dos transdutores de fluxo de calor a gradiente tangencial consiste em desviar as linhas de fluxo de calor de modo a gerar uma diferença de temperatura sobre uma termopilha planar (Güths et al.,1996). O desvio das linhas de fluxo é causado pelo contato pontual entre a superfície isotérmica superior e a parede auxiliar conforme o esquema representado na Figura 2. As células termoelétricas, colocadas em série, geram uma força eletromotriz proporcional ao fluxo térmico. Vários artigos (Leclercq e Thery,1983; Lassue *et al.*,1993) foram publicados mostrando a baixa perturbação gerada pelo sensor em diversas aplicações.

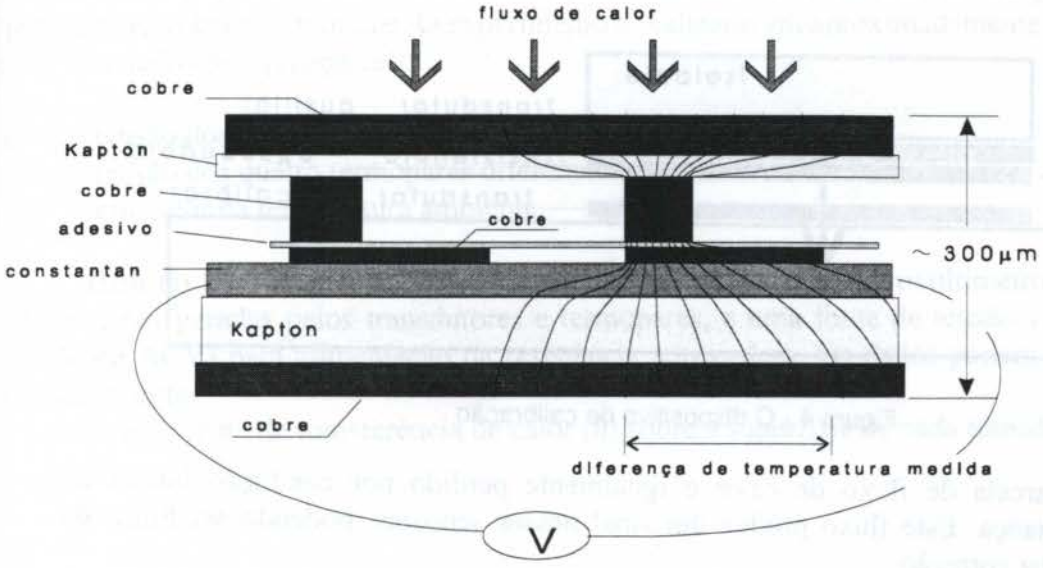

Figura 2 - O transdutor de fluxo de calor a gradiente transversal

Quatro sensores são aplicados lado a lado sobre uma folha de alumínio (espessura = 100 µm). Um pequeno espaço é deixado entre os sensores a fim de reduzir a transferência lateral de calor, fonte de erro na calibração. Esse espaço é preenchido com resina epoxy (Fig.3) para não perturbar o escoamento.

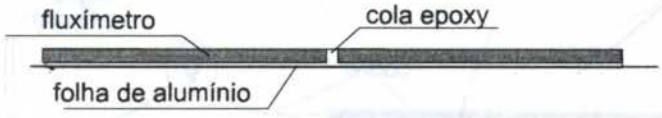

Figura 3 – Montagem dos transdutores

2.3 A Calibração do Transdutor de Fluxo de Calor

A técnica de calibração apresentada pode ser realizada in situ, e pode ser utilizada como uma parte da experimento. O sinal de saída é uma tensão em DCV proporcional ao fluxo de calor.

$$\ddot{q} = c\,V \tag{1}$$

onde $\ddot{q}$ é o fluxo de calor [Wm^{-2}], c é a constante de calibração [$Wm^{-2}\,V^{-1}$] e V a tensão de saída [V]. A calibração consiste em submeter o transdutor a um fluxo de calor gerado por um filme resistivo em Constantan com a mesma superfície (S) do sensor (50 x 50 mm^2). O fluxo de calor é obtido pela pela medição da corrente elétrica (I) e resistividade (R) do filme. A constante de calibração fica igual a:

$$c = \frac{R\,I^2}{S\,V} \tag{2}$$

O fluxo de calor perdido pela superfície oposta (em torno de 5 %) pode ser determinado através de um transdutor auxiliar, previamente calibrado, conforme mostrado na Figura 4.

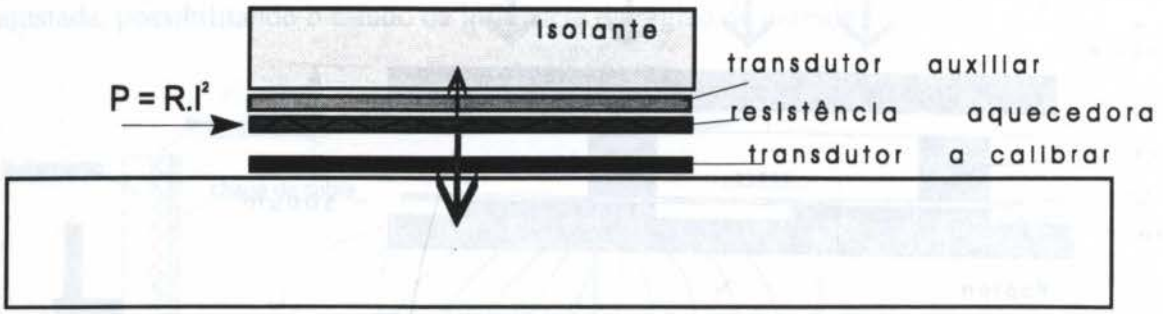

Figura 4 - O dispositivo de calibração

Uma certa parcela de fluxo de calor é igualmente perdido por condução lateral ao sensores da vizinhança. Este fluxo produz um sinal nesses sensores, podendo ser utilizado como informação na correção.

2.4 Medição da Temperatura

As temperaturas de superfície (T_s) são medidas no centro de cada transdutor. Um fio de Constantan (ϕ = 25 μm) é soldado no lado posterior da chapa de cobre, conforme mostrado na Figura 5.

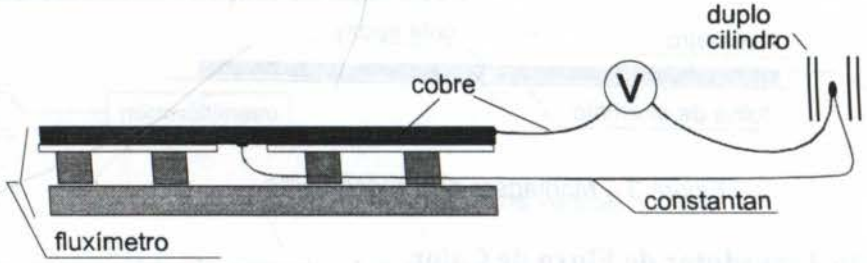

Figura 5 - A medição da temperatura

As medidas estão em modo de diferencial com a temperatura do ar (T_∞). As quatro junções são protegidas da radiação por um cilindro duplo com baixa emissividade. Além das temperaturas diferenciais, mede-se a temperatura ambiente através de um termômetro de bulbo, também protegido da radiação pelo duplo cilindro. Essa informação é utilizada na determinação das propriedades do fluido.

3. METODOLOGIA E RESULTADOS

Antes de iniciar a experimentação, o aluno necessita procurar na literatura as principais correlações do número de Nusselt para o caso estudado. Ele será confrontado com diferentes formas de apresentação (Nusselt local, Nusselt médio) e diferentes condições de validade (laminar, turbulento, número de Prandt). É um bom estímulo para comparar as diferenças entre as várias correlações.

A experimentação padrão é com os transdutores polidos, a placa distante da base e o escoamento em regime laminar. Somente a transferência de calor convectiva é analisada. A

resistência aquecedora é alimentada a tensão constante. Ela alcança o regime permanente em aproximadamente 15 minutos. O experimento é realizado em aproximadamente 50 minutos.

Os dados de aquisição são:

- tensão dos quatro transdutores de fluxo de calor,
- tensão dos quatro termopares diferenciais, e,
- um valor da temperatura ambiente.

Além do termômetro de bulbo, o experimento requer um microvoltímetro para medição das tensões geradas pelos transdutores e termopares, e uma fonte de tensão variável (0 - 30 DCV ou ACV) para alimentação da resistência aquecedora. Os dados podem ser adquiridos manualmente.

O coeficiente de transferência de calor (h) sobre a superfície de cada transdutor é igual a:

$$h = \frac{c\,V}{T_s - T_\infty} \tag{3}$$

onde c e V são, respectivamente, as constantes de calibração e a tensão fornecida por cada transdutor, T_s é a temperatura superficial e T_∞ é a temperatura ambiente.

Um segundo passo consiste em analisar a influência da transferência de calor por radiação. Um papel de carbono pode ser aplicado sobre os fluxímetros com o objetivo de obter uma superfície com alta emissividade ($\varepsilon \approx 0.95$). Cola hidrosolúvel ou gel aquoso podem fixar o papel de carbono. Uma parcela do calor é transferida por radiação ($\ddot{q}_r$) e outra parcela por convecção ($\ddot{q}_c$),

$$\ddot{q} = \ddot{q}_r + \ddot{q}_c \tag{4}$$

onde

$$\ddot{q}_c = h_c(T_s - T_\infty) \tag{5}$$

Uma linearização da expressão de radiação fornece:

$$\ddot{q}_r = h_r(T_s - T_\infty) \tag{6}$$

com

$$h_r = \varepsilon\sigma(T_s + T_\infty)(T_s^2 - T_\infty^2) \tag{7}$$

onde ε é a emissividade da superfície, σ é a constante de Stefan-Boltzmann. O ambiente é considerado um corpo negro. O coeficiente global de transferência de calor (h) é definido por:

$$h = \frac{\ddot{q}}{(T_s - T_\infty)} \tag{8}$$

sendo $\ddot{q}$ o fluxo de calor medido pelo transdutor. O coeficiente de transferência de calor por convecção (h_c) pode ser obtido por:

$$h_c = \frac{\ddot{q}}{(T_s - T_\infty)} - h_r \tag{9}$$

A literatura apresenta o coeficiente de troca como um valor local em L (h_L) ou como um valor médio até a distância L ($\bar{h}_L$). Cada transdutor dá uma informação do fluxo de calor médio sobre a superfície (comprimento de L_1 a L_2). Uma transformação faz-se então necessária.

$$\bar{h}_L = \frac{1}{L}\int_0^L h_x dx \tag{10}$$

então

$$\bar{h}_{L2} = \frac{1}{L_2}\int_0^{L2} h_x dx = \frac{1}{L_2}\left(\frac{L_1}{L_1}\int_0^{L1} h_x dx + \frac{(L_2 - L_1)}{(L_2 - L_1)}\int_{L1}^{L2} h_x dx\right) \tag{11}$$

Contudo

$$\bar{h}_{L1} = \frac{1}{L_1}\int_0^{L1} h_x dx \quad \text{e} \quad \bar{h}_{L1,L2} = \left(\frac{1}{(L_2 - L_1)}\int_{L1}^{L2} h_x dx\right) \tag{12}$$

então

$$\bar{h}_{L1,L2} = \frac{L_2 \bar{h}_{L2} - L_1 \bar{h}_{L1}}{L_2 - L_1} \tag{13}$$

onde $\bar{h}_{L1,L2}$ é o coeficiente médio de troca de calor entre as distâncias L_1 e L_2.

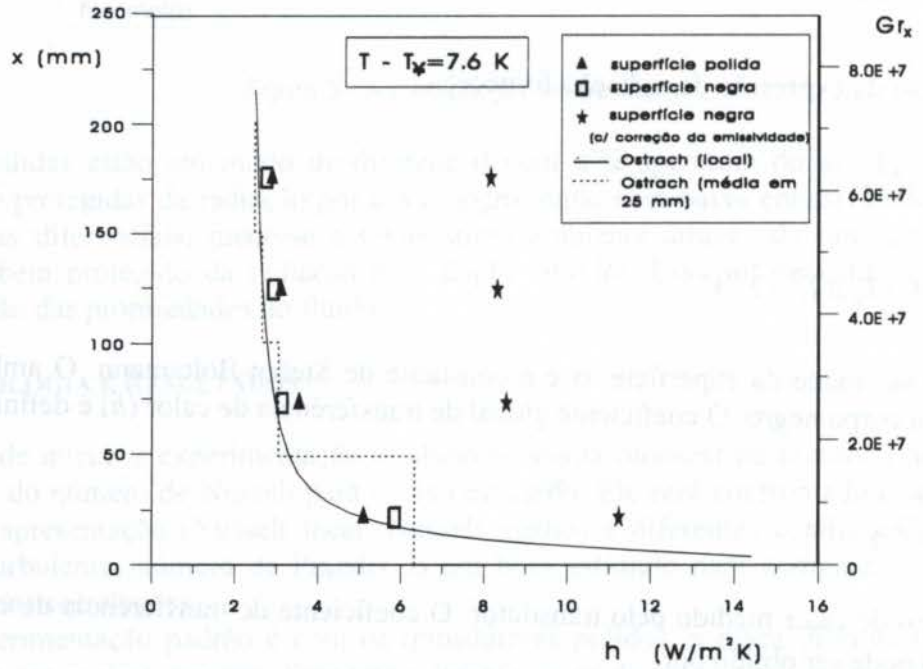

Figura 6 - O coeficiente de transferência de calor

A Figura 6 mostra o coeficiente de transferência de calor (h) determinado experimentalmente com a placa a 7.6 K acima da temperatura ambiente ($Ra \approx 10^7$). Duas condições são apresentadas: i) com a superfície dos fluxímetros polida, e, ii) com a superfície dos fluxímetros recoberta por um papel de carbono ($\varepsilon \approx 0.95$). A parcela referente à radiação foi subtraída de acordo com a Equação 9. O aluno pode analisar a forte influência das trocas radiantes no fenômeno e o boa concordância entre os resultados experimentais e o proposto por Oostrach (1952).

4. Conclusão

A experiência da placa plana vertical demonstrou ser uma ferramenta útil para ilustrar os conceitos de transferência de calor por convecção natural. A simplicidade da experiência incentiva o aluno a analisar outras configurações experimentais. O uso de transdutores de fluxo de calor abre vários campos na análise experimental dos fenômenos de troca de calor. A compreensão do princípio de funcionamento e procedimentos de calibração dos transdutores são, igualmente, exercícios importantes. Esse experimento está sendo atualmente incrementado com fluxímetros mais estreitos, possibilitando uma análise mais discreta do coeficiente de troca de calor.

5. Referências

ECKERT E.R.G. *An introduction to the transfer of heat and mass*. E. MacGraw Hill Book Company Inc, New York, 1950.

GREGG J.L. & SPARROW E.M. *Laminar free convection from a vertical plate with uniform surface heat flux* . Trans A.S.M.E., pp. 735-440, Feb. 1956.

GÜTHS, S. *Anémemomètre a effet Peltier et fluxmètre thermique: conception et réalisation. Application a l'étude de la convection naturelle* . Doctor thesis at Université D'Artois, FR, 1994.

GÜTHS, S, PHILIPPI, P.C., GAVIOT, E. E THERY, P. - *Um Transdutor de Fluxo de Calor a Gradiente Tangencial.* XI Congresso Brasileiro em Engenharia Mecânica (COBEM), Belo Horizonte/MG, 1995.

LASSUE, S., GÜTHS, S., LECLERCQ, D. & DUTHOIT, B. *Contribution to the experimental study of natural convection by heat flux measurement and anemometry using termoelétric effects* . Proceedings of the Third World Conference on Experimental Heat Transfer, Fluid Mechanics and Thermodynamics, USA, pp.831-838, 1993.

LECLERCQ, D. & THERY, P. *Apparatus for simultaneous temperature and heat flux measurements under transient conditions* . Rev. Sci. Instrum, vol 54, pp.374-380, 1983.

OOSTRACH S. *An analysis of laminar free convection flow and heat transfer about a flat plate parallel to the generating force* NACA-TN2635, Feb.1952.

THERY, P., DUTHOIT, B. & PAUQUET, J. *Propriétés thermoélectriques des systèmes à deux couches minces superposées. Application a la mesure des flux thermiques* . Revue de Physique Appliquée, 15, pp. 741-747, 1980.

XIV Brazilian Congress of Mechanical Engineering
Obeid Plaza Hotel Convention Center - Bauru - SP/Brazil
December 08-12th 1997

PAPER CODE: COB1233

COEFICIENTES HIDRODINÂMICOS EM SEÇÕES SEMI-CIRCULARES EM ESCOAMENTO TURBULENTO / *HYDRODYNAMIC COEFFICIENTS IN A SEMI-CIRCULAR DUCTS IN TURBULENT FLOW*

PHILEMON MELO CUNHA, FRANCISCO EDUARDO MOURÃO SABOYA
Dep. Eng. Mecânica CEFET-RJ, Dep. Eng. Mecânica UFF-RJ
CEP: 22 451-070 Rua Rubens Berardo 175/3/408 Rio de Janeiro - RJ

Abstract

Pressure drop coefficients have been experimentally determined for turbulent flow in smooth semi-circular ducts. The experiments were performed by measuring the pressure distribution along the flow. The flowing fluid was air and the pressure drop coefficients are presented as function of the flow Reynolds number. Results for circular ducts are also presented and compared with Blasius. The agreement was very good.

Keywords

Perda de Carga - Métodos Experimentais - Mecânica dos fluidos - Trocadores de Calor
Pressure Drop - Experimental Methods - Fluid Mechanics - Heat Transfer

INTRODUÇÃO

Nos escoamentos de fluidos cada dia mais se depara com limitações de espaço o que muitas vezes requer uma modificação da seção reta da tubulação que possibilite o transporte deste fluido com um desempenho, se não ideal, mas que satisfaça certos objetivos: transferência de calor e/ou simplesmente o transporte do fluido de um lugar a outro.

Para tubulações de seção circular (exemplos de bom comportamento para escoamento) quando colocadas em conjuntos adensados, o espaço externo tem forma de "cúspide" (em escoamento paralelo) o que requer um estudo particular, e um diâmetro hidráulico de difícil semelhança para comparações com outras seções. Muitos pesquisadores têm mostrado bons resultados para seções diferentes da circular.

Nieckele, A. O. (1981) analisou um escoamento em tubos concêntricos levantando dados experimentais para desenvolvimentos teóricos bastante estudados.

Braga, C. V. M. (1987) levantou uma grande quantidade de dados também para seções de tubos concêntricos quando colocadas aletas externas no tubo interno. Estas aletas tinham distribuição contínua e segmentada, para um aumento de superfície, objetivando um aumento da troca de calor. O mesmo verifica que existe um preço bastante alto a pagar que é a perda de carga. Existe então, para novas seções de escoamento e seus arranjos, um compromisso entre aumento de troca de calor e potência de bombeamento de fluidos. Este compromisso não pode se resumir em bom ou ruim, o que pouco contribuiria para pesquisas futuras em áreas semelhantes. É necessário quantificar estas relações em diversos arranjos geométricos e regimes de escoamento.

Braga, S. L. (1985) também gerou correlações para seções triangulares lisas e pinadas procurando aumentar a área de contato com diminuição do volume ocupado.

Bordalo, S. N. (1981) fez um trabalho bem cuidado para seções elípticas em diversos tipos de arranjos, o que possibilitou a determinação de correlações para perda de carga ao longo do escoamento.

Saboya, S. M. (1979) também estudou as seções elípticas aletadas com relação ao escoamento, assim como a troca de calor.

Metzger, D. E. (1982) analisou a performance de trocadores de calor com seção retangular quando colocados em arranjos diferentes e aletados.

Altemani, C. A. C. (1980) publicou um trabalho também para seções triangulares assimétricas em regime turbulento.

Carnavos, T. C. (1979) com um trabalho bastante voltado para trocadores de calor, estudou tubos de seção circular aletados internamente.

Cunha, P. M. (1987) estudou arranjos com a forma circular lisa e pinada deixando uma contribuição na área de fenômenos de transporte.

Saboya, F. E. M. (1986) reuniu trabalhos referentes a seções diferentes da circular e superfícies estendidas, estudando tanto a perda de carga como a transferência de calor.

Este trabalho procura complementar a pesquisa com seções semi-circulares, com escoamento interno, quando submetidos a escoamento turbulento.

Com o objetivo de fornecer dados referentes a novas opções de seção de escoamento para os projetistas que lidam com fenômenos de fluxo, foi montado um aparato experimental de tubulação única semi-circular, instrumentada para a medição de todos os parâmetros necessários (relativos ao escoamento).

Procurou-se determinar coeficientes, e correlações para seções semi-circulares dentro das faixas de utilização. As experiências foram realizadas em regime turbulento e os resultados são apresentados sob a forma de fator de fricção em função do número de Reynolds. Também foram confeccionados gráficos para melhor comparação com outras seções encontradas na literatura.

O método experimental foi acompanhado de uma análise de incertezas, e duplicidade de alguns medidores para melhor confiabilidade dos resultados. Verificou-se também o comportamento do escoamento na entrada da tubulação, para verificar os parâmetros da região (desenvolvimento do perfil de velocidade).

Os resultados poderão ser utilizados também na área de Transferência de Calor.

Este trabalho faz parte de um conjunto de seções analisadas para fenômenos de transporte ou termodinâmica, no que se relaciona a maior ou menor dissipação de energia, ou perda de disponibilidade.

METODOLOGIA

Foi montada uma seção de testes de mais ou menos 200 diâmetros de comprimento para escoamento interno. O escoamento aconteceu no regime turbulento numa faixa de Reynolds de 4×10^3 a 3×10^4.

O fluido de trabalho foi o ar atmosférico, o que demandou instrumentação de boa resolução (10^{-2} Pa) para medida das pressões diferenciais ao longo do escoamento.

O ar era captado de uma sala de 200 m^3 , com controle de pressão, temperatura e umidade relativa. O escoamento era considerado estável (ou permanente) depois de algumas horas de escoamento e verificação da instrumentação de apoio [Barômetro, Termômetro e Higrômetro].

Devido a grande sensibilidade do sensor/indicador de pressão foi também inserido um atenuador de flutuações, não perdendo no entanto a confiabilidade das medidas, e observadas a repetição dos valores em diversas corridas.

Foi utilizado *diâmetro hidráulico* para parâmetro comparativo com outras seções que tiveram definições semelhantes, ou tubos circulares e aletados internamente.

As tomadas de pressão tiveram uma distribuição adequada desde a região de entrada até 200 diâmetros. O desenvolvimento (do ponto de vista do perfil linear da perda de carga) ocorre entre 20 e 30 diâmetros. A definição do diâmetro hidráulico utilizada é a encontrada na literatura, para possibilitar comparações com outras seções que foram testadas, assim como com outros trabalhos na área.

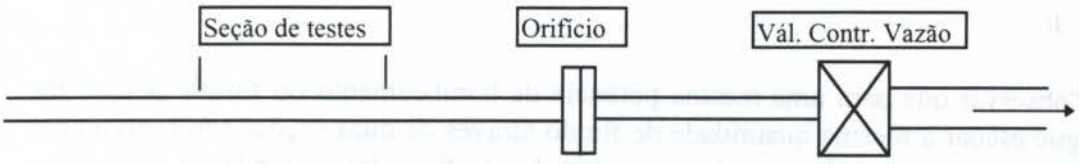

Figura 1: Esquema de montagem da seção de teste
Medidor de vazão [placa de Orifício] e válvula controladora de vazão

SEÇÃO DE TESTE

Foram construídas duas seções de testes semi-circulares para tomada dos resultados.

- Seção de teste A - foi conseguida pela usinagem de um tubo circular até sua metade (do diâmetro), então era colocada uma lâmina plana na superfície usinada de modo a se obter a seção desejada. Os resultados obtidos com esta montagem foram muito bons e dentro do esperado, porém causando dificuldade na variação de seção desta para uma seção circular que dirigia o escoamento para o Ventilador/Exaustor que propiciava o escoamento.
- Seção de teste B - foi conseguida a partir de um tubo circular de bom acabamento interno, onde foi introduzida uma lâmina (de pequena espessura) diametralmente e ao longo de toda a tubulação.
- A seção de teste C - foi utilizada no início das experiências primárias, como testes da instrumentação, assim como para a verificação das condições de acabamento interno do tubo que seria a matriz das seções A e B.

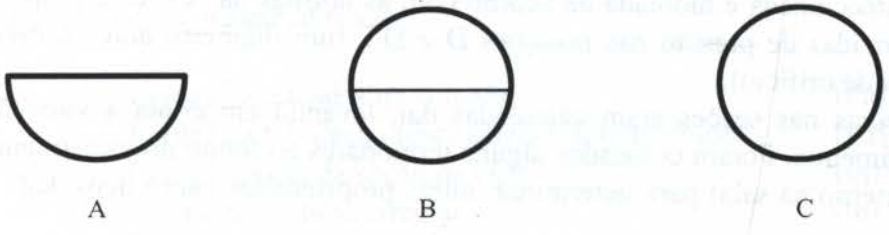

Figura 2: Seção reta da canaleta semi-circular em duas montagens e a circular

Para o diâmetro hidráulico nas seções semi-circulares foi utilizado a definição envolvendo área de escoamento e perímetro molhado conforme segue :

$$Dh = \frac{4Area}{Pw} \quad (1)$$

o que resulta em

$$Dh = \frac{\pi}{(\pi + 2)} D \quad (2)$$

e número de Reynolds

$$Re = \frac{\rho \, V \, Dh}{\mu} \quad (3)$$

Deve-se observar que para uma mesma potência de bombeamento do fluido de trabalho não se consegue escoar a mesma quantidade de fluido através de duas seções semi-circulares, o que se conseguiria com o tubo circular correspondente (fica claro quando se observa as seções A , B e C).

Para medida de pressões (ou diferenças de pressão) foram feitos pequenos orifícios na parede do tubo, e instaladas tomadas (parte de agulhas hipodérmicas). Estas tomadas eram ligadas a uma "chave seletora" que possibilitava a leitura de pressões diferenciais a cada escoamento. Os dois sensores de pressão diferencial eram do tipo capacitivo (marca Baratron) com 1 mmHg e 10mmHg (full scale).

O transdutor e leitor de sinal (eletro-eletrônico) possibilitava a introdução de atenuadores de flutuação (o que foi utilizado algumas vezes). As experiências eram realizadas à noite ou nos fins de semana por diversas razões: ruído do ventilador (3 HP) junto aos outros centros de estudo e pesquisas, e menor movimento próximo à sala de testes muito afetada por variações de pressão.

MEDIDAS DE VAZÃO (volumétrica)

Para medida da vazão foram utilizados dois instrumentos: um bocal de entrada e uma placa de orifício. O bocal de entrada foi utilizado durante uma parte do trabalho para uma menor perda na entrada e verificar a coerência com os valores obtidos na placa do orifício. A placa de orifício foi confeccionada e montada de acordo com as normas da ASME e a opção pela distribuição das tomadas de pressão nas posições D e D/2 (um diâmetro antes e meio diâmetro depois da placa de orifício).

As velocidades médias nas seções eram calculadas daí, levando em conta a variação (possível) de outros parâmetros. Foram colocados alguns termopares ao longo do escoamento (além do termômetro externo na sala) para determinar outras propriedades como densidade e viscosidade.

SISTEMA DE EXAUSTÃO

Utilizou-se um ventilador centrífugo com possibilidade de causar vazão suficiente e um ΔP equivalente a 6 kPa. A conecção foi feita na sucção do mesmo, para evitar perturbações indesejáveis no escoamento.

SISTEMA DE CONTROLE DE VAZÃO

A vazão era controlada por uma válvula (tipo "borboleta") colocada entre a tubulação e o ventilador, com possibilidade de pequenas variações de vazão.

EQUACIONAMENTO

Para a queda de pressão ao longo do escoamento temos duas regiões:

Na região de entrada a queda de pressão ΔPe

$$\Delta P_e = \rho K_e \frac{V^2}{2} \tag{4}$$

é uma região perturbada com um coeficiente de perdas em torno da unidade.

Na região desenvolvida do escoamento (após 40 diâmetros) a queda de pressão pode ser calculada por

$$\Delta P_l = \rho \frac{L}{Dh} \frac{V^2}{2} f \tag{5}$$

ou

$$f = \frac{\Delta P_l}{\rho} \frac{2Dh}{LV^2} \tag{6}$$

Como se sabe este coeficiente (ou fator de fricção) é função de outros parâmetros do escoamento e do regime. No caso de tubo liso temos

$$f = f(\mathrm{Re}) \tag{7}$$

Os parâmetros aqui apresentados são:

ΔPe	= Perdas localizadas na entrada	(Pa)
ΔP_l	= Perdas na tubulação (escoamento desenvolvido)	(Pa)
L	= Comprimento da seção de teste	(m)
D	= Diâmetro do tubo circular	(m)
Dh	= Diâmetro hidráulico da seção	(m)
A	= Área da seção de escoamento	(m^2)
V	= Velocidade média na seção	(m/s)
ρ	= Densidade absoluta do fluido	(kg/m^3)
μ	= Viscosidade absoluta	(Pa.s)
υ	= Viscosidade cinemática	(ms^2/s)
Re, Ke, f	= parâmetros adimensionais	

Com os gráficos procura-se mostrar algumas comparações de resultados.

Na curva referente ao tubo liso são os resultados de uma calibração dos diversos instrumentos com medidas primárias. No caso temos os pontos experimentais conseguidos na medição e uma curva para tubo liso da equação de Blasius.

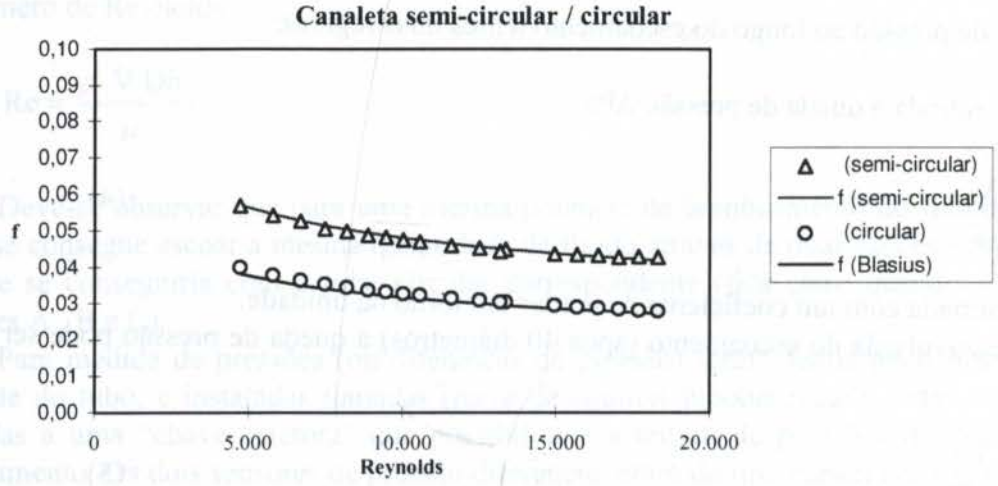

Figura 3: Gráfico (f x Re) para tubo circular liso e para canaleta semi-circular lisa pontos experimentais e curva ajustada.

RESULTADOS E COMPARAÇÕES

Para tubos circulares temos:

Correlação de Blasius

$$f = \frac{0{,}316}{\mathrm{Re}^{0{,}25}} \tag{8}$$

Correlação encontrada neste trabalho para Re (4.000 e 20.000)

$$f = \frac{0{,}367}{\mathrm{Re}^{0{,}265}} \tag{9}$$

No caso da canaleta semi-circular temos a equação (correlação) ajustada.

$$f = \frac{0{,}421}{\mathrm{Re}^{0{,}236}} \tag{10}$$

Cabe ressaltar ainda que a previsão era de uma perda de carga maior (quando comparado com tubo circular) devido ao diâmetro hidráulico em torno de 60% do diâmetro do tubo.

APLICAÇÕES / CONCLUSÕES

Como foi colocado na introdução, uma seção semi-circular pode se fazer necessária por um problema de configuração espacial; mas em aplicações simples parece ser mais indicada para coletores solares planos com convecção forçada.

Uma análise de incertezas dos resultados mostrou boa concordância com os valores experimentais. Quando comparados com os valores para tubo liso (correlação e gráfico) nota-se a semelhança do comportamento entre os casos.

Nenhuma variação brusca do fator de fricção ocorreu em toda a faixa de número de Reynolds, configurando não haver mudança de regime de escoamento -{turbulento}.

O escoamento se mostrou bem comportado, e motivou uma análise de transferência de calor, mostrando sua performance quando utilizado em trocadores de calor.

REFERÊNCIAS

ALTEMANI, C.A.C. and SPARROW, E.M. , "Turbulent Heat Transfer and Fluid Flow in an Unsymmetrically Heated Triangular Duct" Journal of Heat Transfer , Vol. 102 , November 1980, pp. 590-597 .

ASME (American Society of Mechanical Engineers), "Application of Fluid Meters" , Sixth Edition , USA , 1971 .

BORDALO, S.N., "Queda de Pressão em Permutadores de Calor de Tubos Elípticos e Circulares Aletados", Tese de Mestrado, Departamento de Engenharia Mecânica, PUC-Rio,1981.

BRAGA, C.V.M., "Análise Termohidráulica de Seções Anulares Lisas e Aletadas", Tese de Doutorado, Departamento de Engenharia Mecânica, PUC-Rio 1987.

BRAGA, S.L., "Coeficientes de Transportes em Dutos Triangulares Lisos e Pinados", Tese de Doutorado, Departamento de Engenharia Mecânica, PUC-Rio , 1985.

CARNAVOS, T.C. ," Cooling Air in Tubular Flow with Internally Finned Tubes" , Heat Transfer Engineering , Vol. 1 nº 2 , 1979 , pp. 41-46 .

CUNHA, P.M., "Características Termohidráulicas de Escoamentos Turbulentos em Configurações Circulares Lisas e Pinadas" Tese de Doutorado, Departamento de Engenharia Mecânica, PUC-Rio, 1987.

KLINE, S.J. and Mc CLINTOCK, F.A., "Describing Uncertainties in Single-Sample Experiments", Mechanical Engineering, January 1953, pp. 3-8.

METZGER, D.E., BERRY, R.A. and BRONSON, J.P., "Developing Heat Transfer in Retangular Ducts with Staggered Arrays of Short Fins", Journal of Heat Transfer, Vol. 104, November 1982, pp. 700-706 .

Com os gráficos procura-se mostrar algumas comparações de resultados.

Na curva referente ao tubo liso são os resultados de uma calibração dos diversos instrumentos com medidas primárias. No caso temos os pontos experimentais conseguidos na medição e uma curva para tubo liso da equação de Blasius.

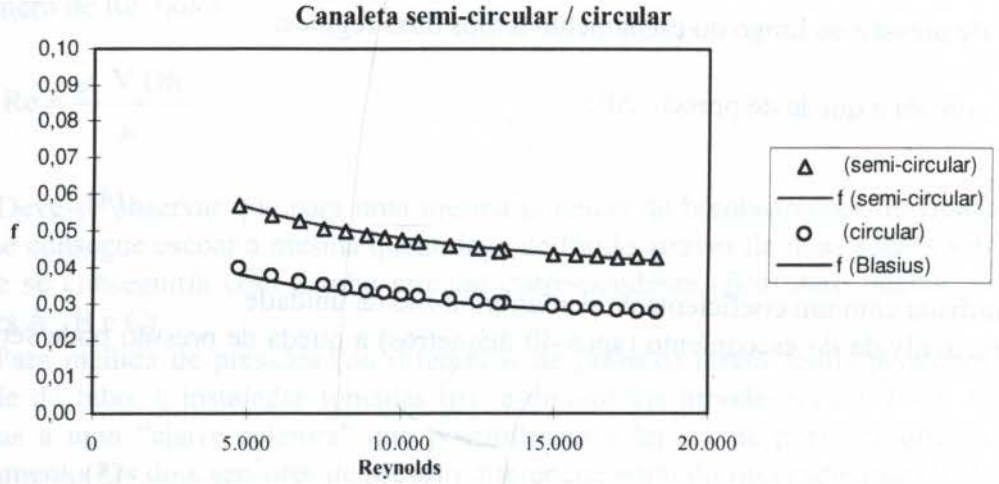

Figura 3: Gráfico (f x Re) para tubo circular liso e para canaleta semi-circular lisa pontos experimentais e curva ajustada.

RESULTADOS E COMPARAÇÕES

Para tubos circulares temos:

Correlação de Blasius

$$f = \frac{0{,}316}{\mathrm{Re}^{0.25}} \tag{8}$$

Correlação encontrada neste trabalho para Re (4.000 e 20.000)

$$f = \frac{0{,}367}{\mathrm{Re}^{0.265}} \tag{9}$$

No caso da canaleta semi-circular temos a equação (correlação) ajustada.

$$f = \frac{0{,}421}{\mathrm{Re}^{0.236}} \tag{10}$$

Cabe ressaltar ainda que a previsão era de uma perda de carga maior (quando comparado com tubo circular) devido ao diâmetro hidráulico em torno de 60% do diâmetro do tubo.

APLICAÇÕES / CONCLUSÕES

Como foi colocado na introdução, uma seção semi-circular pode se fazer necessária por um problema de configuração espacial; mas em aplicações simples parece ser mais indicada para coletores solares planos com convecção forçada.

Uma análise de incertezas dos resultados mostrou boa concordância com os valores experimentais. Quando comparados com os valores para tubo liso (correlação e gráfico) nota-se a semelhança do comportamento entre os casos.

Nenhuma variação brusca do fator de fricção ocorreu em toda a faixa de número de Reynolds, configurando não haver mudança de regime de escoamento -{turbulento}.

O escoamento se mostrou bem comportado, e motivou uma análise de transferência de calor, mostrando sua performance quando utilizado em trocadores de calor.

REFERÊNCIAS

ALTEMANI, C.A.C. and SPARROW, E.M. , "Turbulent Heat Transfer and Fluid Flow in an Unsymmetrically Heated Triangular Duct" Journal of Heat Transfer , Vol. 102 , November 1980, pp. 590-597 .

ASME (American Society of Mechanical Engineers), "Application of Fluid Meters" , Sixth Edition , USA , 1971 .

BORDALO, S.N., "Queda de Pressão em Permutadores de Calor de Tubos Elípticos e Circulares Aletados", Tese de Mestrado, Departamento de Engenharia Mecânica, PUC-Rio,1981.

BRAGA, C.V.M., "Análise Termohidráulica de Seções Anulares Lisas e Aletadas", Tese de Doutorado, Departamento de Engenharia Mecânica, PUC-Rio 1987.

BRAGA, S.L., "Coeficientes de Transportes em Dutos Triangulares Lisos e Pinados", Tese de Doutorado, Departamento de Engenharia Mecânica, PUC-Rio , 1985.

CARNAVOS, T.C. ," Cooling Air in Tubular Flow with Internally Finned Tubes" , Heat Transfer Engineering , Vol. 1 nº 2 , 1979 , pp. 41-46 .

CUNHA, P.M., "Características Termohidráulicas de Escoamentos Turbulentos em Configurações Circulares Lisas e Pinadas" Tese de Doutorado, Departamento de Engenharia Mecânica, PUC-Rio, 1987.

KLINE, S.J. and Mc CLINTOCK, F.A., "Describing Uncertainties in Single-Sample Experiments", Mechanical Engineering, January 1953, pp. 3-8.

METZGER, D.E., BERRY, R.A. and BRONSON, J.P., "Developing Heat Transfer in Retangular Ducts with Staggered Arrays of Short Fins", Journal of Heat Transfer, Vol. 104, November 1982, pp. 700-706 .

NIECKELE, A.O., "Determinação dos Coeficientes de Transporte em um Trocador Bi-Tubular Pinado", Tese de Mestrado, PUC-Rio, 1981.

SABOYA, F.E.M. and Braga, C.V.M. , "Turbulent Heat Transfer and Pressure Drop in Smooth and Finned Annular Ducts", Proceedings of the Eight International Heat Transfer Conference and Exhibition, San Francisco CA., August 1986, pp. 2831-2836.

SABOYA, S.M., "Coeficientes de Transportes em Trocadores de Tubos Elípticos Aletados", Tese de Mestrado, Divisão de Engenharia Mecânica Aeronáutica, ITA/SJC, 1979 .

XIV Brazilian Congress of Mechanical Engineering
Obeid Plaza Hotel Convention Center - Bauru - SP/Brazil
December 08-12th 1997

PAPER CODE: COB1273

DIESEL PARTICULATE MATTER EMISSIONS MEASUREMENT BY MEANS OF A PARTIAL DILUTION MINITUNNEL

Paper Code 1273

A. F. Romero López, D. E. Arroyo Amaro, H. Cabadas Estrella, J. A. Canuto Carranco, O. Hernández Romero, L. López Godínez, J. Saavedra Badillo, V.A. Trejo Chávez.
Departamento de Mecánica, Térmica y Fluidos, Instituto de Ingeniería, UNAM 04510 México,
D. F., Tel. (5) 622-8138 Fax (5) 622-8091 e-mail: afrl@servidor.unam.mx

ABSTRACT

A minitunnel is proposed in lieu of a full dilution tunnel, that will allow determination of carbon monoxide (CO, CO_2), unburned hydrocarbons (HC), oxides of nitrogen (NO_x)and particulate matter (PM). The design will permit independent evaluation of emissions from Diesel engines.

KEYWORDS

Sample, Control, Filters, Particulate Matter, Mesurement, Sign, Acquisition.

1.INTRODUCTION

The basic principle of the design of a dilution minitunnel, is taking exhaust gas samples and dilute them simultaneosly with filtered atmospheric air until reaching the minimum equilibrium temperature and in this way be able to carry out all of the corresponding measurements.

Through an extraction and pumping system the diluted sample is passed through two filters (primary and secondary) to collect particles. The corresponding measurements of the pollutants (HC, NO_x and CO) are performed by means of a batch process with plastic bags filled with diluted exhaust gases. The dilution is performed with the purpose of simulating the actual environmental conditions.

2.CONCEPTUAL DESIGN

The present work is based upon the Norm. EEC-R49 (European Economic Comunity), for the implementation of the minitunnel, to quantify motor emissions of Diesel engines in steady state. The process consists to take gas samples at the exit of the engine exhaust and to carry them to a dilution chamber to mix them with atmospheric air previously filtered at the inlet of the fan.

The air/gas ratio is 4:1, the mixture goes through a venturi, in order to achieve a homogeneous mixture. At the exit of the venturi there is a stabilizing flow chamber. Finally a quantification of the gases is acomplished. The norm recommends that particles colection be accomplished in 4.5 to and 6 minutes.

The fundamental objetive of the project is to measure and analyze the combustion gases of the engine. Another goal is to verify that the emission limits established for 1998 and beyond by the EPA (Environment al Protection Agency) of the USA and by the California Air Resources Board (CARB) and/or South California Air Quality Management District (SCAQMD) are met (Photograph 1).

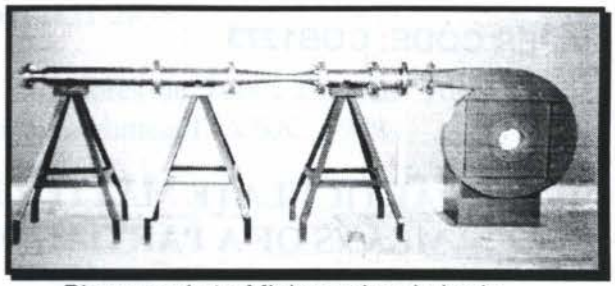

Photograph 1 : Minitunnel main body

It is important to quantify the constituents of the differents pollutants so that in the future better fuels are produced. (Figure 1) .

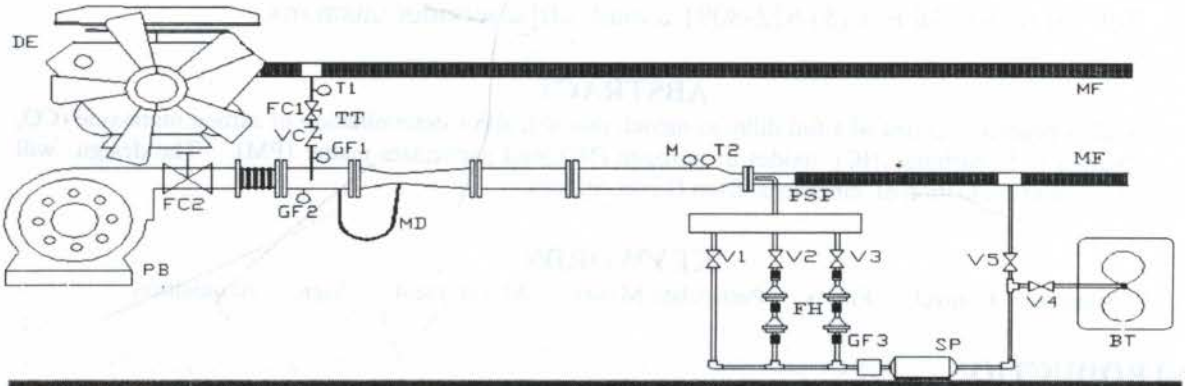

Symbol	description
PB	Dilution air fan
GF1,GF2,GF3	Flow meter
TT	Exhaust gas sampling line
PSP	Particulate matter collection pipe
FH	Primary and secondary filters
SP	Vacuum pump
FC1 , FC2	Flow controllers
T1 , T2	Thermometer
M	Pressure gauge
DE	Diesel engine
VC	Check valve
MD	Differential gauge
V1,V2,V3,V4, V5	Valves 1,2,3,4 and 5
BT	Teflon bag
MF	Flexible hose

Figure1. Minitunnel, engine and pipe schematic

3.THEORETICAL CONSIDERATIONS

According to the required design characteristics of the minitunnel, it was manufactured in stainless 40, type AISI SS-316, schedule 40 that has an excellent resistance to the corrosion, with a content of 12% Cr, so that when exposed to high-temperature oxygen will not permit the formation of iron oxides.

The union flanges between the elements of the minitunnel were manufactured with the same material. To avoid leaks between unions O-rings were used (neoprene), resistant at high temperatures with a range of -54 ºC to 150ºC with a hardness Shore A(70) ASM 3209.

DATA USED IN THE PARTICLE MEASUREMENTS

Mc = 0.62	Tc = 60	Pc = 15.7
Mg = 8.5	Tg = 300	Pg = 10
Ma = 34	Ta = 18 - 22	Pa = 1
Mt = 42.5	Tt < 56	P∞ = 0.05

EQUATION FOR THE PARTICLES MEASUREMENT

$$Wfs - Wf = Wp \qquad (1)$$

4.SYSTEMS OF PARTICLES AND GASES MEASUREMENT

- The systems that are used are those wich are established in the norm EPA and EEC, to accomplish the quantification of the different pollutants (HC, NOx, CO and **particles**):

A. Flame ionization detection (FID) : This method measures hydrocarbon emissions from the exhaust, uses a flame produced by the hydrogen and combustion air. When the gas contains hydrocarbons is premixed with the hydrogen, the ions concentration is increased in large proportions and the flame becoms conductive. The FID; only reacts to oxigenated compounds such as aldehydes, cetanes and alcohols, that result from the incomplete or partial combustion from hydrocarbons .

B. Non dispersive infrared detection (NDIRD): This method measures the carbon monoxide and dioxide emissions from the exhaust, uses an infrared beam directed through two parallel optical cells. The quantity of absorbed infrared radiation is proportional to the concentration of the gas.

C. Chemical luminiscence detection (CLD): This technique is used to determine the presence of nitrogen oxides (NO /NO_X) in a sample the measurement of the NO involve the following reaction:

$$NO + O_3 \longrightarrow NO_2 + O_2 \qquad \text{where} \qquad NO_2 \longrightarrow NO_2 + \text{red light}$$

D. **Solid particles** : The procedure to weigh and capture the solid particles in the exhaust gases, employs an analytical scale (with a resolution of .001 mg) and filters of 70 mm of diameter , with a size of 10 μm. The gases are forced through a series of filters (Figure 2), primary and secondary to collect the solid particles at the exhaust gases, once the particles are collected, the filters will be weighed in an analytical scale (Figure 3), to get the particulate matter concentration. Worth to mention is the fact that the filters are weighed and dehumidifyed to remove all the implicit moisture in them and to obtain a precise mesurement of the solid particles.

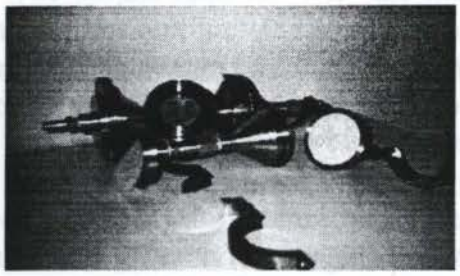

Figure 2 : Filter holders

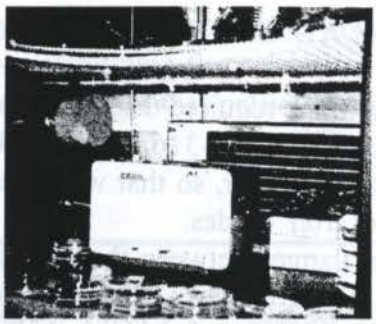

Figure 3 : Analytical scale

- Instrumentation System : Gravimetric flow meters, pressure gauges, thermometers and valves (solenoids and manual) are used, with the characteristic that they are electronic with an analogous or digital exit to avoid errors in the handling.
- Suction pump : Serves to operate the filtering process of particles in the elements made out of Micropore® of 70 mm of diameter (Figure 5) and to overcome the pressure drop in the primary and secondary filter holders, to collect the dilution gases sample tedlar bags are used (Figure 4), for a subsequent analysis.

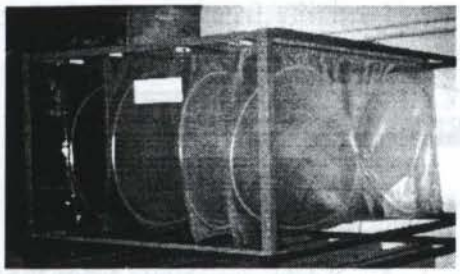

Figure 4 : Tedlar bags

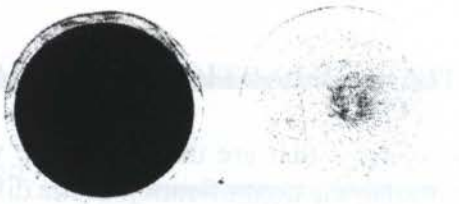

Figure 5 : Primary and secondary filters

REQUIREMENTS OF THE ANALYZERS

Requirements	*CO y CO_2*	*HC*	*O_2*	*NO_x*
Moisture & temperature control chamber	*0º - 40ºC (32º - 105ºF) less than 95%*	*0º - 40ºC (32º - 105ºF) less than 95%*	*0º - 40ºC (32º - 105ºF) less than 95%*	*5º - 35ºC (41º - 96ºF) less than 95%*
Eletrical Voltage Frec. And pot.	*115 VAC ±10% 60 Hz ±0.5 Hz 300 W*	*115 VAC ±10% 50/60 Hz 100 W*	*115 VAC 60 Hz ± 1% 100 W*	*115 VAC 50/60 Hz 800 w to the take-off*
Gas sample Pressure Temperature	*0.5 a 10 L/min (constant pressure) 2kg/cm² (25 psig)max 2 in. H_2O min (*) 0º - 40 ºC (32º - 105ºF)*	*3 - 5 L/min (6 - 10 SCFH) 0.4 kg/cm² (6 in.)*	*1.5± 0.5 L/min 0.2±0.5 kg/cm²*	*5 L/min (10.6 SCFH) 0.4 kg/cm² (6 in.)*
Base gas flow pressure Temperature	*nitrogen 10 ml/min (20 SCFH) 0.5 - 1.5 kg/cm² (7 - 21 psig)*	*oxygen or dry air (dewpoint -40 ºC) 10 ml/min 0.7 - 1 kg/cm² (10 - 14 psig)(**)*	*nitrogen 10 ml7min (20 SCFH) 0.5 - 1.5 kg/cm² (7 - 21 psig)*	*oxygen or dry air (dewpoint -40ºC) 10 ml/min 0.7 - 1 kg/cm² (10 - 14 psig)(**)*
Fuel flow pressure Temperature		*hydrogen / helium 120 ml/min 1 - 1.5 kg(cm² (14 - 21 psig)*		

(*)Vacuum operation is not recommended, (**)For the ozone generator

Note : All the analyzers should be free from vibrations

5.DESCRIPTION OF THE OPERATION OF A MINITUNNEL

A dilution minitunnel is used to simulate the quantities of pollutants that commonly are found in the atmosphere thrown by internal combustion engines emissions (Diesel). Its operation consists of taking a sample of exhaust gases and dilute them with filtered atmospheric air (in a ratio 4:1) until reaching the minimum equilibrium, below 52 °C, in order to accomplish the corresponding measurements (see Figure 6).

The dilution process of the emissions requires a system of measurement and electronic control for an adequate operation. The reason for this lies in the different variables that intervene in the process (temperature, pressure and flow).

The electronic regulation of the temperature is very important during a test with a minitunnel. The electronic controlling of the air-gas ratio in the dilution of the mixture and the monitoring in the variations of pressure and temperature of the emissions from the exhaust of the Diesel engine, are also very important.

Other of the tasks of the system of measurement is the measuring in parts per million (ppm) of the pollutants CO, HC and NOx, as well as the weight of the PM (solid particles). It's worth to mention that the analyzers NDIR, FID and DLQ, that will be used for the measurement of the pollutants have an analog exit of 0 to 5 V directly proportional to the ppm of each pollutant. Though the measurement devices will be acquired from a commercial supplier, the signals from the equipment were included in the design of the system of measurement and they are apart of the resolution of the analog/digital converter.

The implementation of the system will use a PC equipment with a data acquisition card connected to the bus of the PC, for this design a software for the system that will process the information acquired is necesary. Therefore the design of the system consist of several stages.

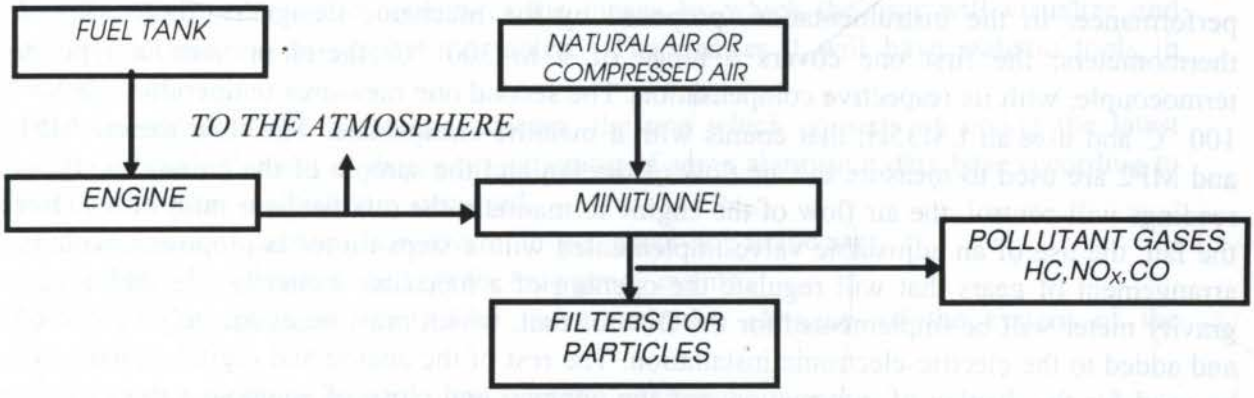

Figure 6. Block diagram of the minitunnel operation principle.

The stages of the design consist in the following points:

- Selection of the transducers and equipment of measurement for the instrumentation of the minitunnel.
- Conditioning and appropriateness of the signals from the transducers and equipment of measurement.
- Acquisition of the signals from the transducers and equipment of measurement, design of receptacles, shielding and protection of the signals and equipment of measurement for their reading through a data acquisition card connected to the PC bus.
- Elaboration of the control software and visualization of the acquired signals, as well as the hardware of the exit stage, that will get the control actions and managing of the minitunnel.

6.SELECTION OF TRANSDUCERS AND EQUIPMENT OF MEASUREMENT

- To simulate what happens in the environment an air to gas ratio of 4:1 will be used within the minitunnel.
- The variations of the minitunnel pressure will not exceed the ±250 Pa
- The maximum temperature of 52 °C will be reached at the end of the minitunnel in order to reach chemical equilibrium. A scale of 0 to 100 °C at the end of the pipe and 0 to 300 °C for the sampled gases with a resolution of 1 °C will be required. The air will have a temperature range of 25±5°C.
- The sampling of data will be from 4 to 6 minutes.
- The design norm for the implementation of the minitunnel is the CEE-R49 (European Economic Community).

The resolution of the analog-digital converter to use will be from 12 to 16 bits due to the procedures of construction of laboratory equipment. The measurements must be very reliable. Furthermore the instrumentation system will be able to sustain the appropriateness and the inclusion of equipment of high precision (v.g.measuring of NOx, CO, HC). The signals to condition must be as protected as possible from the noise produced by the environment, the supply sources, the Diesel engine and the minitunnel self. The data acquisition will be in real time with a sampling frequency of 30 kGHz using the Direct Memory Access (DMA). The DMA is the method that will allow free data movement from the data acquisition card toward the localities of the PC but without the intervention of the central processor unit (CPU). This is translated in a greater and fast transmission of data because it's accomplished directly toward the computer while the central processor accomplishes its tasks normally. Otherwise, the CPU will attend its tasks as well as the inlet demands of the card, reducing so much its performance. In the instrumentation, proposed by the mechanic designers, there exist 2 thermometers; the first one covers a range of 0 to 300 °C, therefore uses a type K termocouple, with its respective compensation. The second one measures temperatures below 100 °C and uses an LM35H, that counts with a metallic encapsulate. The flow meters MF1 and MF2 are used to measure the air flow of the fan and the sample of the emissions, these readings will control the air flow of the engine to maintain the mixture in a ratio of 4:1. For the fan, the use of an adjustable valve implemented with a steps-motor is proposed, with an arrangement of gears that will regulate the opening of a mechanic butterfly. In addition, a gravity meter will be implemented for the flow of fuel, which must be adequately calibrated and added to the electric-electronic installation. The rest of the analog and digital signals will be used for the display of information and the opening and close of solenoid valves of the system.

Finally, the control software will be accomplished taken into account the characteristics of the data acquisition card and making use of the tools of Visual Basic 3.0 and Delphi 2.0 languages. Though there exist new versions of the Visual Basic, the version 3.0 satisfies the needs of this project, since for example it offers visual environment for Windows which is very important in order to achieve a presentation agreeable and friendly to the user. These languages permit a practical programming and a relatively easy verification.

7.CONSTITUTIVE ELEMENTS OF THE SOFTWARE OF CONTROL

In the elaboration of the control software, the data acquisition card characteristics will be taken into account. The speed of transmission and the number of I/O channels will be the main to consider. DMA will be the main tool to facilitate the transmission of data between the

card and the computer. The DMA offers a data movement between a locality of memory and the external of the computer but without the intervention of the CPU. This will lead to the point in which the CPU will perform its operations as normal as possible while the card makes use of its resources independently. In this way the transmission of information is easier and therefore achieving the processing in real time as required.

Basically, the control software will be formed by three modules. To consider:

➤ Instrumentation System Initialization and Test of minitunnel module.
➤ Minitunnel Control module.
➤ Information System Processing module.

First module basically consists in a separate set of elements that constitute the instrumentation and control of the minitunel. In this point, it's worth to emphasize that the tests of each element can be controlled configuring the system either in manual or automatic operation.

Second module is the central one of the software. This module is responsible for controlling all physic variables in the system, for example temperatures and internal pressures as well as to control all valves and digital actuators and devices that constitute the control and instrumentation of the system. In the minitunel's control the different transducers will be widely considered, also interrupters and valves considering their operation ranges and their digital and analog characteristics are used.

Finally, the third module constitutes the means by which the user will visualize and manipulate information in graphs and tables. Thereinafter it will have statistic tools in addition to:

- Events recorded of the minitunnel system, the one which consists of saving the latest changes of each element or datum or activation of some alarm in a data base according to the date and hour in which they occurred.
- Implementation of passwords in several levels, according to the user.
- Alarms and/or automatic turned off for emergency events.
- Manual and/or automatic control of the constitutive elements of the system of the minitunel.
- Control and operation system simulation of the minitunel

8.CONCLUSIONS

The decision of designing a partial dilution tunnel of gases, is due to the fact that in the country there is not a developed form of measuring each one of the components of the exhaust gases of a Diesel engine.

The project represents an effort to limit as much as possible, damages to the human being, due to toxic or harmful substances inhalation present in the gases, therefore an additional effort is required in capital expenditures as well as in human resources training that are needed for the solution of the problem.

Accessories, electronic instruments and sensors are employed that permit to obtain electrical signals to control the necessary operating conditions of the different elements. Measurements are processed through a data base for their monitoring. Finally, it has the idea of heaving an independent laboratory that will permit comparable measurements to those of

Petróleos Mexicanos, Instituto Mexicano del Petróleo (PEMEX-IMP) Govemment monopoly on fuel production and research, and the engine manufacturers of Diesel engine and to confirm the international procedures and standars.

9. ACKNOWLEDGEMENTS

The authors are deeply indebted to the following organizations for their financial support of the project:
Consejo Nacional de Ciencia y Tecnología (CONACyT)
Dirección General de Asuntos del Personal Académico de Universidad Nacional Autónoma de México (DGAPA-UNAM)

10.REFERENCES

1. Anonymous., Automated Fractional Sampling of Particulate Emissions, catalogue; Sierra Instruments Inc. Monterrey California.
2. Anonymous., Diluted Particulate Measurement with Partial Flow Sampling (SPC 472) ., Smart Sampler AVL. Austria 1991
3. Anonymous., Engine Instrumentation, catalogue; AVL., Austria 1990
4. Anonymous., "Niveles de Emisión de Vehículos a Diesel con peso vehicular superior a 3857 KG", Social Development Secretary (SEDESOL), NOM-PA-CCAT-007-93, Published in the officiate Newspaper of the Mexican Government 23-06-93.
5. Anonymous., Partial Flow Dilution and Particulate Sampling System for Measuring Diesel Engine Emissions, catalogue. SPC 472 Smart Sampler. Austria. January 1991
6. Anonymous, Tunnel de Dilution Pour Banc D´essai Moteur Diesel Destine´au Controle D´Emissions de Particulatesá L´échappement, catalogue; Le Moteur Moderne., Societe D´Etudes et D´Applications en Mecanique Thermodinamique Et Dynamique des Fluides. Jun. 1987.
7. Anonymous. USER'S MANUAL OF THE PCL-812PG. Multi-Lab Card with Programmable Gain.
8. Maluf de Carvalho, J. E. "Microsoft Visual Basic 3.0". Mc Graw Hill. España. 1992.

11.NOMENCLATURE

Ma = air Flow	(m^3/h)	Wp = Particles weight	(mg)
Mt = total Flow of the diluted sample	(m^3 /h)	Wf = Clean filters weight	(mg)
Ta = Air temperature	(ºC)	Wfs = Loaded filters weight	(mg)
Tg = Exhaust temperature	(ºC)	Pc = Fuel pressure	(kg/cm^2)
Tc = Fuel temperature	(ºC)	P∞ = Pressure of the diluted	(kg/cm^2)
t_m = Diluted sample Temperature	(ºC)	Pg = Exhaust gases Pressure	
Mc = Fuel flow	(l/min)	the gases of comb.	(kg/cm^2)
Mg = Exhaust gases flow	(m^3 /h)	Pa = Atmospheric pressure	(kg/cm^2)

XIV Brazilian Congress of Mechanical Engineering
Obeid Plaza Hotel Convention Center - Bauru - SP/Brazil
December 08-12th 1997

PAPER CODE: COB1296

ANÁLISE EXPERIMENTAL DO AQUECIMENTO DE ÁGUA ATRAVÉS DE MICROONDAS / *EXPERIMENTAL ANALYSIS OF WATER HEATING BY MICROWAVE ENERGY*

MARIA HELENA FARIAS & CARLOS VALOIS MACIEL BRAGA
Departamento de Engenharia Mecânica - PUC-Rio
Rua Marquês de São Vicente, 225 - Gávea
CEP 22453-900 - Rio de Janeiro - RJ - Brasil - E-mail: mhfarias@mec.puc-rio.br
cvalois@rio.faperj.br

Abstract

In the present paper is showed an experimental study. The main object of this study is to improve the microwave power absorption by the water in a resonant cavity. This cavity has a cylindrical geometry and contains a glass (Pyrex) tube in its longitudinal position. Distilled water flows through this tube. The following parameters were varied: water flow mass, glass tubes diameters and the screws position (disturbances) inside the cavity. The results show a strong influence of those parameters about the absorbed power by the water. In this way, it is possible to obtain a situation for the maximum microwave power transferred to the water.

Keywords

Microwave, resonant cavity, water heating by microwave, thermal optimization: geometry.
Microondas, cavidade ressonante, aquecimento de água por microondas, otimização térmica: geometria.

1. INTRODUÇÃO

Os projetos de pesquisa na área de utilização da energia em microondas para aquecimento estão em desenvolvimento crescente. Inicialmente, as pesquisas neste campo estavam voltadas para o aquecimento de alimentos. Hoje, esta aplicação vai da indústria à área médica.

Microondas são utilizadas no processamento de materiais cerâmicos na produção de supercondutores, fabricação da parte cerâmica de fornos , boilers e isolantes. Esta forma de energia também é empregada em estudos ambientais (por exemplo, esterilização de dejetos hospitalares). Na área médica é utilizada para tratamento do câncer e diagnósticos. Encontram-se aplicações nas análises químicas tais como: preparação de amostras, extração de solventes para cromatografia de gases ou líquidos, dissolução de polímeros para determinação de viscosidade ou peso molecular, etc. Destaca-se ainda a utilização da energia em microondas na cura do concreto, esterilização de alimentos enlatados (evitar botulismo), além de muitas outras aplicações.

Algumas vantagens do emprego da energia em microondas para aquecer, com relação aos métodos convencionais, são, por exemplo, a diminuição do tempo de aquecimento, e em

consequência , melhoria na uniformidade do material e nas suas propriedades, levando assim a um menor custo até o produto final.

Por outro lado, cada tipo de aplicação de microondas necessita de um equipamento adequado, pois duas variáveis muito importantes para a construção de cavidades de aquecimento são a geometria e dimensões do produto que será aquecido. Isto às vezes dificulta o interesse pelo desenvolvimento da pesquisa, porque pelas equações de Maxwell (Rizzi, P.A., 1988) para radiação eletromagnética pode-se prever o campo eletromagnético dentro de um guia de ondas ou de uma cavidade vazia, ambos com geometria simples. Para a situação real onde, por exemplo, uma cavidade irá conter um material dielétrico (o produto a ser aquecido), o qual provocará perdas na potência que penetra na cavidade, devido ao fato desta e o dielétrico possuirem uma geometria complexa, pelos métodos analíticos não é mais possível resolver as equações acima citadas. O que se pode fazer então é, através de soluções numéricas, visualizar o campo eletromagnético dentro da cavidade sob condições aproximadas à situação real. Assim sendo, às vezes torna-se desanimadora a pesquisa no que se refere ao financiamento, porque além do investimento no desenvolvimento da solução numérica há sempre que se verificar a validade na situação real, pois energia em microondas é conhecida como *the black art.* Isto significa que ainda tem-se muito a conhecer sobre o emprego deste tipo de energia e, para o caso de aquecimento, a relação dielétrico/fonte/cavidade é complexa o suficiente, não sendo possível uma previsão real do seu comportamento.

Além disso, a indústria de equipamentos para a pesquisa nesta área ainda está mais voltada para o processamento de alimentos (em nível industrial e comercial), mas já tende a ampliar suas atenções.

1.1 Processo de aquecimento

O aquecimento por microondas se dá pela absorção direta da energia incidente sobre o material exposto à radiação, sem causar variação na sua estrutura molecular, sendo um processo irreversível, onde a energia eletromagnética se transforma em calor. Esta energia é radiação do tipo não ionizante, a qual causa movimentação molecular devido à migração dos íons e da rotação de dipolo.

Os materiais que são expostos à energia elétrica podem ser divididos em três categorias: condutores, isolantes (dielétricos) e semicondutores (que podem se comportar como condutores ou não).

Os dielétricos apresentam uma pequena condutividade (num dielétrico típico, a condutividade é 10^{20} vezes menor do que num bom condutor), o que é suficiente para dizer que os dielétricos são não condutores. Os dielétricos são materiais que podem ser polarizados pela ação de um campo elétrico. Nestes materiais, sob a influência de um campo elétrico, ocorre um pequeno deslocamento dos elétrons com relação à sua posição "normal".

Dentro de cada molécula este campo elétrico causará então uma separação entre as cargas negativas (elétrons) e as positivas (prótons no núcleo do átomo), isto é, o material se polariza (forma dipolo elétrico) . Estes são os dipolos induzidos (alguns dielétricos já possuem moléculas polares, ou seja, têm momentos de dipolo permanentes, como é o caso da água) . Os dipolos induzidos tendem a se alinhar na direção do campo elétrico incidente, enquanto que os permanentes tendem a se alinhar na direção oposta. Ambos os dipolos produzem um momento de dipolo, que reduz a potência do campo elétrico aplicado, porque sofrem um torque que tende a alinhá-los na direção do campo incidente.

Como as moléculas não estão completamente livres para girarem rapidamente, acompanhando a alternância do campo elétrico, esta "fricção" absorve parte da energia do

campo elétrico incidente, que é liberada como calor após decorrido um tempo τ, denominado tempo de relaxação. Este é o tempo que a molécula necessita para alcançar 63% da sua posição original de desordem. Esta energia térmica é então transferida à vizinhança por condução. A 2450 MHz o alinhamento das moléculas seguido pelo seu retorno à desordem ocorre 4,9 x 10^9 vezes por segundo, resultando num aquecimento muito rápido. Porém, o tempo característico de relaxação de cada material depende da sua viscosidade, que por sua vez depende da temperatura.

A capacidade de obstruir a energia eletromagnética (no caso, microondas) quando ela passa é medida pela **constante dielétrica** (ε) do material. O **fator de perda** quantifica a capacidade de dissipar esta energia, ou seja, transformá-la em calor. A constante dielétrica varia com a temperatura do material e com a frequência a que este estiver submetido. Quanto maior o fator de dissipação de um material, menor é a espessura de penetração da energia em microondas no mesmo. Nos materiais que são transparentes à microondas, por exemplo, vidro "Pyrex", considera-se penetração infinita, enquanto que nos materiais refletivos considera-se penetração zero (ex.: metais). Os materiais denominados absortivos possuem penetração finita.

1.2 Motivação

Como dito anteriormente, quando se deseja aquecer substâncias por microondas é necessário sempre um trabalho experimental, pois cada projeto tem particularidades que não se pode validar somente a partir de estudos teóricos.

As propriedades das diversas substâncias submetidas ao aquecimento por microondas são estudadas em laboratórios. Um dos aparatos utilizados para isso é a denominada cavidade ressonante. A cavidade ressonante pode ter formas geométricas diversas onde, num ou mais locais da sua superfície, conecta-se um(s) guia(s) de ondas. Através deste passa a energia em microondas, que será absorvida por uma amostra localizada dentro da cavidade. Esta amostra pode ser estática ou não.

Algumas destas cavidades já estão projetadas para trabalharem dentro de determinada faixa de frequências. Tendo isto em vista, optou-se por uma cavidade de seção cilíndrica, conectada a um guia de ondas de seção retangular, para a qual se pretende encontrar o diâmetro ótimo de uma carga concêntrica a esta cavidade. Assim, obtém-se o diâmetro que provê a maior absorção de potência, isto é, maior dissipação da energia em microondas no fluido. Este estudo foi feito tendo-se a água destilada como fluido de trabalho. Optou-se por trabalhar com este fluido porque, além de se conhecer sua constante dielétrica (que é bem alta comparada a outros dielétricos), sabe-se que a água está presente em muitos materiais que são aquecidos por RF (Rádio-Freqüência). Deste modo, o teor de água influencia diretamente fatores como a avaliação da umidade, o cozimento, etc.

A vantagem da cavidade ressonante é que a energia é concentrada em regiões específicas, dentro das quais as cargas são inseridas e o campo tem seu mais alto valor.

1.3 Revisão bibliográfica

A maioria das aplicações de aquecimento por microondas se faz através de aplicadores não ressonantes, com um único passe ou multi-passes pelo guia de ondas, e através de cavidades ressonantes com multi-modo.

Dois trabalhos de Metaxas (1974, 1976) são de relevante importância para a pesquisa que ora se apresenta. Num trabalho o autor apresentou um método teórico para a determinação do raio de uma cavidade cilíndrica, para o aquecimento de amostras com constantes dielétricas

conhecidas. Posteriormente, desenvolveu um trabalho onde, para uma cavidade semelhante à anterior, porém operando em outra freqüencia, verificou a performance com água destilada e fluidos alimentícios (leite, molho).

No presente trabalho (baseado nas referências citadas) utilizou-se uma cavidade semelhante e realizou-se um estudo da influência de "perturbações" dentro da mesma, visando a otimização do aquecimento nesta. As perturbações foram três parafusos posicionados radialmente à seção cilíndrica.

2. APARATO EXPERIMENTAL

Conforme mostra a Figura 1, acoplou-se a uma fonte de microondas (magnetron de um forno comercial com potência nominal em microondas de 700 watts) uma cavidade ressonante de forma cilíndrica (Fig. 2), através de um guia de ondas de latão, banhado a ouro, cuja seção reta é retangular, de dimensões 81 × 36mm e altura 93 mm.

A cavidade ressonante é de latão e banhada a ouro, com as seguintes dimensões:

- comprimento **L**: 120 mm
- diâmetro interno $\mathbf{d_i}$: 91 mm

Concentricamente à cavidade colocou-se um tubo de vidro "Pyrex". Os diâmetros externos dos tubos de vidro utilizados foram **5,10 , 9,00 , 12,00 e 15,05 mm**, cujos diâmetros internos são, respectivamente, **4,90 , 5,90 , 10,00 e 12,60 mm.**

Colocou-se na cavidade três parafusos de latão (cada um com diâmetro nominai de ¼") defasados de 120° entre si, localizados radialmente na posição $^{L}/_{2}$.

Para medir as temperaturas da água utilizou-se dois termopares do tipo K, um na entrada e outro na saída do tubo de vidro "Pyrex" da cavidade. Utilizou-se ainda uma balança eletrônica e um cronômetro para monitoração da vazão de água, que era variada por um registro localizado após a cavidade. O sistema de alimentação de água consistia de um reservatório mantido a nível constante.

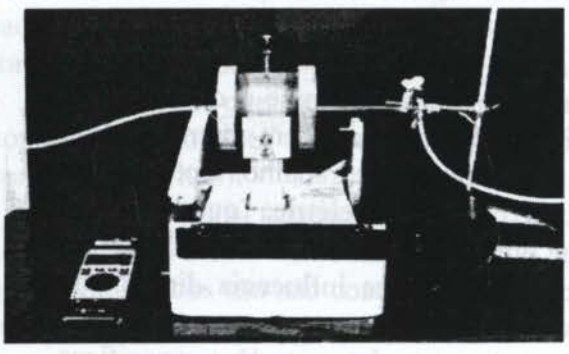

Figura 1- Cavidade cilíndrica acoplada à fonte de microondas

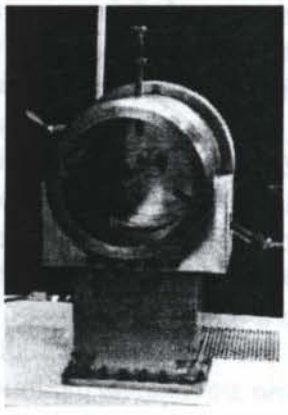

Figura 2 - Cavidade cilíndrica

2.1 Procedimento experimental

A água destilada, ao sair do reservatório principal sob a ação da gravidade, passa por uma tubulação para penetrar na cavidade ressonante. Dentro da cavidade o tubo é de vidro "Pyrex", pois este material é transparente e praticamente não absorve microondas, sendo sua constante dielétrica muito baixa ($\varepsilon \cong 4$, à temperatura ambiente de 20° C, 2450 MHz). A vazão do fluido é avaliada a partir de grandezas básicas: tempo de escoamento(**s**) e

massa (**kg**) coletada neste intervalo. Medem-se as temperaturas de saída e entrada (temperatura ambiente) do fluido na cavidade. Varia-se a vazão através de um registro localizado depois da saída do fluido da cavidade. O nível de fluido dentro do reservatório principal, de onde o fluido parte em direção à cavidade, é mantido constante.

Em cada tubo colocado dentro da cavidade, para todas as vazões consideradas, experimentou-se as mesmas variações de penetração dos parafusos (os três foram igualmente penetrados dentro da cavidade em cada medição) e nos seguintes módulos de penetração: zero fios (ou seja, sem penetração), 4 , 9, 14, 19, 24, 29 e 32 fios.

A máxima penetração dos parafusos foi de 32 fios, porém só se pôde experimentar com este módulo utilizando-se os tubos de diâmetros externos 5,10 e 9,00 mm. Para os tubos de diâmetros 12,00 e 15,05 mm, a máxima penetração permitida foi de 29 fios.

Outro fator que limitou a coleta de dados foi o surgimento de arcos voltaicos na região de contato entre a tampa da cavidade e a conexão dos tubos (bucha) . Embora tenha-se tomado o cuidado para melhorar o contato elétrico entre as conexões dos tubos com a tampa da cavidade, não foi possível anular completamente o surgimento das faíscas. Para isso seria necessário mudar o material das conexões, o que não estava no objetivo do projeto em estudo.

Assim sendo, nas medições com os tubos de diâmetros externos 12,00 mm e 15,05 mm houve uma limitação na vazão mínima permitida, pois a partir de uma determinada temperatura de saída do fluido os arcos voltaicos surgiam.

Todas as séries de medições foram feitas após o pré-aquecimento da cavidade durante uma hora, com água destilada escoando na vazão mínima permitida para cada tubo.

Isto foi feito porque no final de cada série de medições a temperatura da superfície externa da cavidade mantinha-se em torno daquela medida logo após decorrido o tempo de pré-aquecimento. A variação estava em torno de 3^0 C num intervalo de tempo de aproximadamente 6 horas. Baseando-se neste fato, desprezou-se a contribuição da convecção para o aquecimento do fluido.

3. REDUÇÃO DE DADOS

A partir dos dados coletados pôde-se então avaliar a capacidade de aquecimento do fluido pela cavidade através das equações:

$$\dot{m} = \frac{\Delta m}{\Delta t} \qquad (1)$$

onde

Δm é a massa coletada [kg]

Δt é o intervalo de tempo decorrido [s]

$\dot{m}$ é a vazão mássica de fluido [kg/s]

Sabe-se que, aplicando a equação da primeira lei da termodinâmica a um volume de controle, desprezando-se pequenas parcelas de energia, tais como variação de energia cinética, potencial, etc., chega-se à seguinte equação para o balanço térmico:

$$\dot{Q}_{abs} = \dot{m}\, c_p\, \Delta T \qquad (2)$$

onde:

ΔT é a variação de temperatura do fluido entre a entrada e a saída do tubo;

c_p é o calor sensível (específico) do fluido à pressão constante, e será considerado constante para a faixa de temperatura trabalhada, sendo seu valor conhecido da literatura;

$\dot{Q}_{abs}$ é a potência absorvida pelo fluido.

Com estes dados foi possível comparar, para uma determinada razão de diâmetros entre cavidade e tubo e várias vazões de fluido, as curvas que relacionam a temperatura média do fluido com a potência absorvida pelo mesmo, visualizadas através de um gráfico $\dot{Q}_{abs} \times \overline{T}$,

onde:

$$\overline{T} = \frac{T_{entrada} + T_{saida}}{2} \qquad (3)$$

Comparou-se também a potência absorvida para cada tubo, considerando-se uma mesma vazão. A análise dos dados foi feita sempre tendo como parâmetro de base a mesma penetração dos parafusos.

4. RESULTADOS

Vários gráficos foram feitos a partir dos dados coletados para os diferentes diâmetros de tubos e para cada penetração dos parafusos.

A Figura 3 mostra o aumento da temperatura do fluido ao passar pela cavidade, através da temperatura média (eq. 3) em função da vazão, para os tubos de diâmetros externos 9,00 e 12,00 mm, com os valores experimentais e a curva de ajuste do tipo ln. Gráficos similares foram feitos para os outros tubos, porém o que aqui se apresenta é o mais significativo.

A Figura 4 ilustra a absorção de potência para vários módulos de penetrações dos parafusos com os tubos de 5,10 e 12,00 mm de diâmetro externo, os quais proporcionaram a menor e a maior absorção de potência, respectivamente. Com os tubos de 9,00 e 15,05 mm de diâmetros externos a absorção de potência ficou em valores intermediários aos anteriores.

Através desta Figura 4 constata-se:

1) O tubo de diâmetro externo 5,10 mm propiciou uma absorção praticamente insignificante, independentemente da penetração dos parafusos;

2) Para o diâmetro de 12,00 mm verificou-se um patamar de potência absorvida significativamente mais elevada que em outros diâmetros.

Nestes gráficos fez-se um ajuste linear na relação entre potência absorvida e vazão.

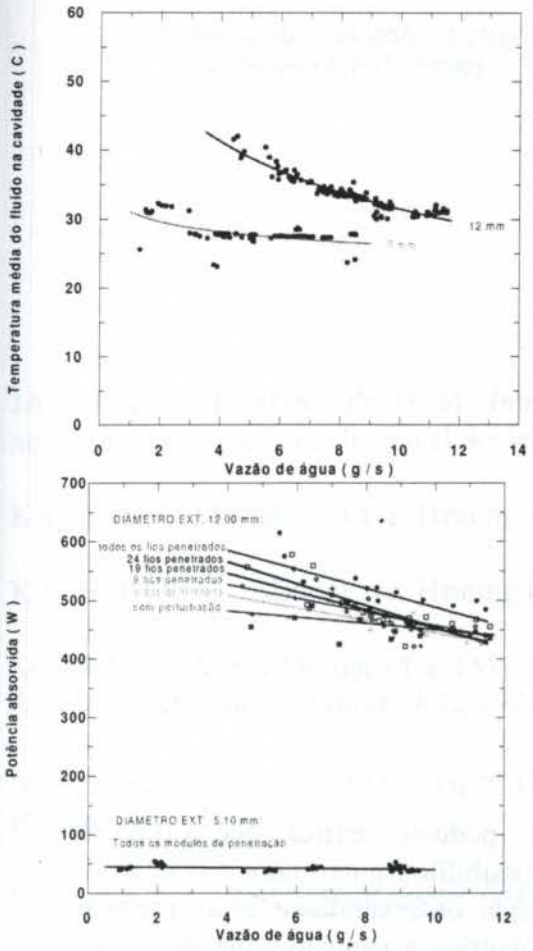

Figura 3 - Temperatura média do fluido na cavidade

Figura 4 - Influência da penetração dos parafusos na absorção de potência

A partir das equações das curvas de ajuste dos gráficos similares ao da Figura 4, pôde-se comparar os níveis de absorção de potência, sob condições de mesma vazão nos diferentes tubos , para vários módulos de penetração dos parafusos na cavidade. As Figuras 5, 6 e 7 mostram as diferenças de potências absorvidas, com as vazões 0,5, 4, 8 e 12 (**g / s**), para os quatro tubos de vidro utilizados, sob as condições de cavidade sem perturbação (sem penetração dos parafusos), com nove fios penetrados e com penetração total de 29 fios.

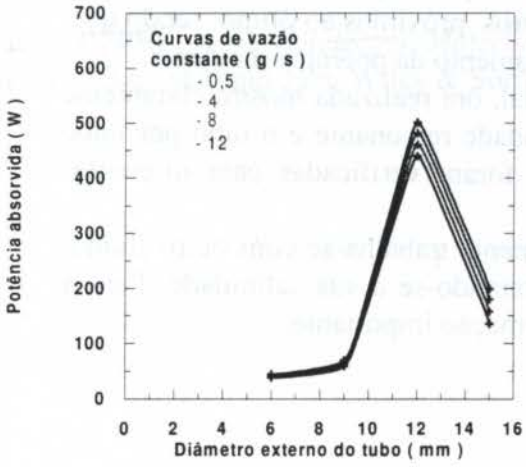

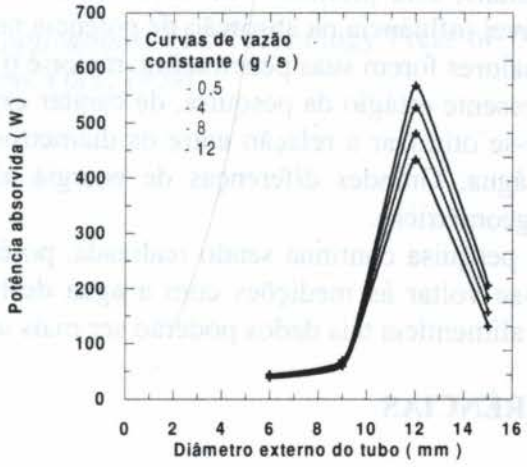

Figura 5 - Absorção de potência sem penetração dos parafusos

Figura 6 - Absorção de potência para 9 fios penetrados

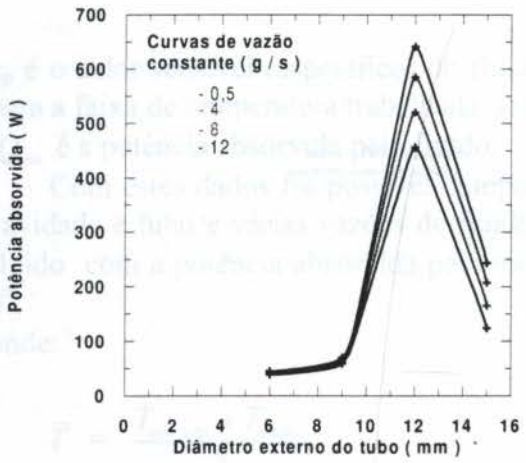

Figura 7 - Absorção de potência com penetração total dos parafusos

Analisando-se os dados obtidos nas Figuras 5, 6 e 7 , pode-se verificar que o tubo de vidro "Pyrex" de diâmetro externo 12,00 mm foi o que possibilitou uma maior absorção de microondas pela água destilada dentro da cavidade. Ainda observando-se estas mesmas figuras, percebe-se que há um diâmetro para o tubo concêntrico à cavidade que provê um maior aquecimento do fluido, sendo influenciado claramente pela "perturbação" imposta à cavidade.

5. CONCLUSÕES

Os resultados apresentados para o caso da água destilada permitem afirmar-se que existe um valor ótimo na relação de diâmetros entre tubo concêntrico e cavidade ressonante, para a qual se obtém maior absorção da potência. Para a cavidade ressonante cilíndrica utilizada, o diâmetro do tubo em que esta relação é máxima, conforme demonstram os resultados experimentais, está próximo de 12,00 mm. Além disso, a presença dos parafusos foi de considerável influência na absorção de potência nos diâmetros próximos ao ótimo, sendo que, quanto maiores forem suas penetrações, maior é o aproveitamento da potência incidente.

O presente estágio da pesquisa, de caráter experimental, ora realizada mostra claramente que deve-se otimizar a relação entre os diâmetros da cavidade ressonante e o tubo por onde escoa a água. Grandes diferenças de energia absorvida foram verificadas para diferentes relações geométricas.

Esta pesquisa continua sendo realizada, porém atualmente trabalha-se com outro fluido. Pretende-se voltar às medições com a água destilada, alterando-se a sua salinidade. Para a indústria alimentícia tais dados poderão ser mais uma informação importante.

6. REFERÊNCIAS

JASSIE, L. B., KINGSTON, H. M., *Introduction to Microwave Sample Preparation - Theory and Practice*, American Chemical Society Professional Reference Book, 1988.

KACHMAR, M., Microwave Heating Part I, *Microwaves & RF*, pp 41-49, september 1992.

KACHMAR, M., Microwave Heating Part II, *Microwaves & RF*, pp 39-46, october 1992.

METAXAS, A. C., Design of a TM_{010} Resonant Cavity as a Heating Device at 2.45 GHz, *Journal of Microwave Power*, 9(2), 1974.

METAXAS, A. C., Rapid Heating of Liquid Foodstuffs at 896 MHz, *Journal of Microwave Power*, 11(2), 1976.

OKRESS, E. C., *Microwave Power Engineering*, vol 2, Academic Press, Inc., 1968.

OSEPCHUK, J. M., A History of Microwave Heating Applications, *IEE Trans. on Microw. Th. and Tech.*, vol MTT-32, nº 9, pp. 1200-1224, 1984.

PLATTS, J., *Microwave Ovens*, IEE State of The Art Digest 4, Peter Peregrinus Ltda., London, 1991.

RIZZI, P. A., *Microwaves Engineering - Passive Circuits*, Prentice Hall, 1988.

SRIDHAR, S., Microwaves Technology and Materials Research, *Microwave Journal*, pp. 117-123, june 1987.

von HIPPEL, A. R., *Dielectric Materials and Applications*, The Technology Press of MIT, Cambridge, MA and John Wiley & Sons, Inc., New York, 1954.

XIV Brazilian Congress of Mechanical Engineering
Obeid Plaza Hotel Convention Center - Bauru - SP/Brazil
December 08-12th 1997

PAPER CODE: COB1419

A THEORETICAL AND EXPERIMENTAL STUDY OF THE VORTEX TUBE

LUIZ ALBERTO OLIVEIRA ROCHA[1], GEORGE STANESCU[2] & JOSE VIRIATO COELHO VARGAS[3]

[1]*Departamento de Fisica, Fundação Universidade do Rio Grande, 96201-900, Rio Grande, RS, E-mail: dfsrocha@super.furg.br*
[2]*Departamento de Matemática, Fundação Universidade do Rio Grande, 96201-900, Rio Grande, RS, E-mail: dmtgs@super.furg.br*
[3]*Departamento de Engenharia Mecanica, Universidade Federal do Parana, 81531-990, Curitiba, PR, E-mail: jvargas@demec.ufpr.br*

Abstract

This paper presents a theoretical and experimental study and introduces a mathematical model for a Vortex tube on steady state operation. The internal swirling flow is modeled by a set of ordinary differential equations that are integrated along the radial direction. Experimental temperature measurements from a Vortex tube built in the laboratory are compared to numerical results obtained with the theoretical model, with good qualitative agreement. The temperature variation with respect to the inlet fluid temperature along the radial direction is understood as a result of the distribution of the kinetic energy through the swirling flow, i.e., temperature increase in the periphery and decrease in the core. The theoretical estimation of the flow reversal at the Vortex tube axis agrees well with the internal swirling flow results of Armfield and Fletcher (1991).

Keywords

Refrigeration, swirling flow, irreversible model, experimental measurements

1. INTRODUCTION

The Vortex tube is an interesting device to produce the refrigerating effect when a limited amount of cooling is required in special circumstances: a reliable small size equipment and freedom from electrical supplies. It has been described first in 1933 and then patented in 1934 by Georges Ranque (1933, 1934), a French scientist. Later, in 1946, a larger interest in this non-conventional method for producing cooling has been generated by a widely read article of Rudolph Hilsch (1946).

Although it has been used industrially, the Vortex tube has remained partly misunderstood until now. A number of theories have been developed to understand and explain the physical phenomena inside the Vortex tube. The theory of D. C. Fulton (see the R433 Vortex Tube Refrigerator Technical Specification, P. A. Hilton Ltd., England, 1996.) relies on the conservation of angular momentum to explain the separation of the compressed gas entering the Vortex tube, into a cold gas stream and a hot one. Based on the First and Second Laws of Thermodynamics, Petrescu *et. al.* (1995) studied comparatively the

Hilsch-Ranque Vortex tube expansion processes and the adiabatic reversible expansion performances. A comprehensive study of various aspects of Vortex tubes' design has been presented by Radcenco (1990), through an exergetic analysis.

The objective of this paper is to present a theoretical and experimental study of a Vortex tube on steady state operation. First, we present the theoretical model, which captures the mechanisms of kinetic energy redistribution into the rotating mass of gas. Assuming the steady state operation, the internal swirling flow in the tube is modeled by a set of ordinary differential equations that are integrated along the radial direction. The controlled variables are the initial pressure of the compressed gas entering the Vortex tube, and the area of the larger pipe controlled by the outlet valve.

2. THEORY

Figure 1 shows the Vortex tube schematically. The control volume consists of the two cylindrical chambers within pipes, contained between the inlet ports into nozzles, and the outlet ports of pipes open to the atmosphere. The outlet area of the larger pipe (the "hot end") is controlled by a valve, while the smaller pipe outlet (the "cold end") is free.

A forced vortex is created when supplying compressed gas to the nozzles. Jets discharge into the chamber at a near sonic velocity and the vortex rotates at very high angular speed, approximately $5 \cdot 10^4\ s^{-1}$ when the pressure of the compressed air is P_0=7 bar (R433, 1996).

The internal swirling flow for the Vortex tube on steady state operation is studied by considering the rotation of the gas column within the larger cylindrical chamber. The gas column is divided into slices of arbitrary length z along axial direction of the pipes. Figure 2 shows an infinitesimal volume into one gas slice, filled by an ideal gas at local temperature T and local density ρ. Balancing forces acting along the radial direction on this infinitesimal volume, we write

$$Pr\,zd\theta + \omega^2 rdm = \left(P + \frac{dP}{dr}dr\right)(r + dr)zd\theta \qquad (1)$$

by assuming the variation of gas temperature and density only along radius. In Eq. (1) ω is the constant angular velocity of the vortex, and $\omega^2 rdm$ is the centrifugal force. Since the order of magnitude of angular velocity ω is $10^4\ s^{-1}$ and that of radius r is 10^{-2} m, the gravitation gdm represents $g/\omega^2 r \approx 2\%$ of the centrifugal force and may be neglected in Eq. (1).

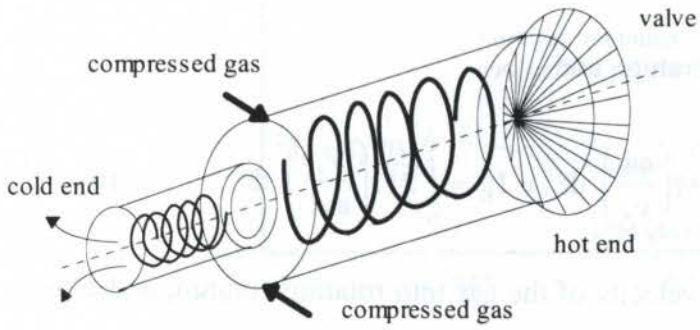

Figure 1: Schematic view of the Vortex Tube.

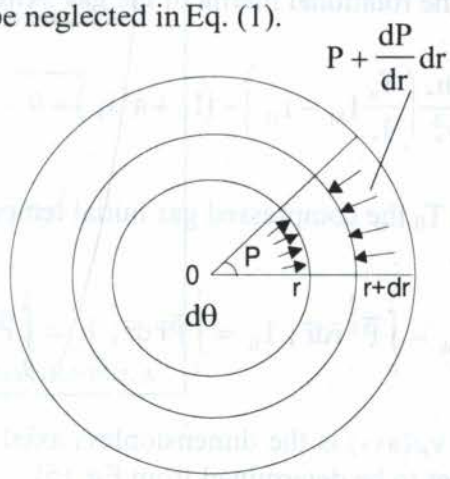

Figure 2: Infinitesimal volume.

Calculating the infinitesimal mass $dm = \rho rzd\theta dr$, where m is the mass of gas, and the local density $\rho = P / RT$ into the last equation, it is found, in terms of dimensioless radius $\bar{r} = r / r_0$ and dimensionless pressure $\bar{P} = P / P_*$

$$\frac{d\bar{P}}{d\bar{r}} = \frac{\bar{P}}{\bar{r}}\left[\left(\frac{\omega r}{v_*}\right)^2 \frac{v_*^2}{RT_*}\bar{P}^{\frac{1-k}{k}} - 1\right] \tag{2}$$

where r_0 is the larger pipe interior radius, and k is the isentropic expansion coefficient of the gas. By * we label the state of the gas leaving the nozzles. In writing Eq. (2) it is assumed that thermodynamic processes into the rotating gas column are isentropic, while the gas expansion into nozzles is considered an irreversible adiabatic process.

Based on the conservation of angular momentum, the angular momentum of a gas slice, $I = \int_0^1 r^2 \omega dm$, equals the angular momentum of exactly the same mass of gas when leaving the nozzles, $I_0 = I$. $I_o = \int_0^1 r_0^2 \omega dm$ is calculated by considering that the gas leaving the nozzles shapes a thin gas ring around the inner periphery of the pipe, and the angular momentum I is calculated for the disk-like gas slice. In dimensionless terms it is written

$$I_1 = I_0 - I = \int_0^1 \bar{P}^{\frac{1}{k}} \bar{r}\left[1 - \left(\frac{\omega r}{v_*}\right)\right] d\bar{r} = 0 \tag{3}$$

The law of energy conservation applied to a gas mass m, between the inlet ports into the Vortex tube and any cross-section along the chamber, states the equality

$$\int_0^m h_0 dm = \int_0^m h dm + \int_0^J \frac{\omega^2 dJ}{2} + \int_0^m \frac{v_z^2}{2} dm \tag{4}$$

where $h_0 = c_p T_0$ and $h = c_p T$ are the gas specific enthalpy before entering the Vortex tube, and the gas local specific enthalpy, respectively. The second and third therms in the right hand side represent the rotational and translational kinetic energy, respectively. In Eq. (4) $dJ = r^2 dm$ gives the rotational inertia of the gas .After some algebra, Eq. (4) yields

$$\frac{2h_*}{v_*^2}\left(\frac{T_0}{T_*} I_M - I_H\right) - \left(I_J + a^2 I_k\right) = 0 \tag{5}$$

with T_0 the compressed gas initial temperature, and

$$I_M = \int_0^1 \bar{P}^{\frac{1}{k}} \bar{r} d\bar{r}\,;\; I_H = \int_0^1 \bar{P}\bar{r}\, d\bar{r}\,;\; I_J = \int_0^1 \bar{P}^{\frac{1}{k}} \bar{r}\left(\frac{\omega r}{v_*}\right)^2 d\bar{r}\,,\; e\; I_K = \int_0^1 \bar{P}^{\frac{1}{k}} r\left(\frac{v_z}{a v_*}\right)^2 d\bar{r} \tag{6}$$

where $v_z/(av_*)$ is the dimensionless axial velocity of the gas into rotating column, and a is a constant to be determined from Eq. (5).

The system of differential and integral equations (2), (3),(5), (6) constitutes the mathematical model we employ to explain the energy redistribution between the cold and hot streams into the Vortex tube.

3. NUMERICAL RESULTS

To obtain numerical solutions for the integral-differential equations system (2), (3), (5), (6) we consider the derivatives of equations (3) and (6) instead, $\frac{dI_j}{d\bar{r}}$, j = I,..., M, such that the system becomes an ordinary differential equations (ODE) system. Once P_0 and T_0 are selected, v_* and T_* result from well known relations for isoentropic flow.

To complete the system, the dimensionless angular and axial velocities have been modeled by the analytical functions

$$\frac{\omega r}{v_*} = \frac{\mathrm{atn}(\bar{r})}{\mathrm{atn}(1)} \exp\left[\frac{1}{(\bar{r}-\bar{r}_\omega)^2+0.44} - \frac{1}{(1-\bar{r}_\omega)^2+0.44}\right] \tag{7}$$

$$\frac{v_z}{av_*} = \frac{\mathrm{atn}(\bar{r}-\bar{r}_\omega)}{\mathrm{atn}(1-\bar{r}_\omega)} \exp\left[\frac{1}{(\bar{r}-\bar{r}_\omega)^2+2} - \frac{1}{(1-\bar{r}_\omega)^2+2}\right] \tag{8}$$

according to the results of Armfield (1986) and Fletcher (1991) on axial and swirl velocities profiles for swirling diffuser flows, which have been adequately rearranged using the parameters herein presented. In these equations, $\bar{r}_\omega = \frac{r_\omega}{r_0}$ is the dimensionless orifice radius.

The ODE system is then integrated by using a fourth-order Runge-Kutta numerical scheme and the following initial conditions

$$\left[\bar{P} \quad I_I \quad I_M \quad I_H \quad I_J \quad I_K\right]^T = \left[1 \quad 0 \quad 0 \quad 0 \quad 0 \quad 0\right]^T \tag{9}$$

where initially $\bar{r}$ =1 and $\Delta\bar{r}$ =-0,005.

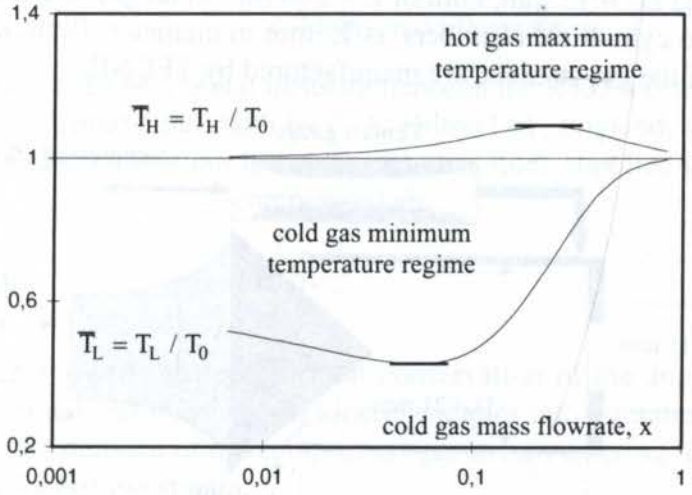

Figure 3: Dimensionless mean temperatures versus cold gas mass flowrate.

It is necessary to determine the pressure of the gas leaving the nozzles, P_*. This is done by an iterative process. Initially, we observe that $P_{atm} \le P_* \le P_0$, so we use a initial guess $P_* = P_{atm}$, for integrating the ODE system. Convergence to a solution is achieved when the integration is completed ($\bar{r} = 0$), if the integral I_1 is equal to zero, and the value of coefficient a in Eq. (5) is a real number, if not, an increment $\Delta P_* = 0.05$ bar is added to P_* and the integration is repeated, until this convergence criterion is satisfied.

Once the solution to the ODE system is available, the values of the dimensionless mean temperatures of the cold and hot streams are computed by the definitions

$$\overline{T}_L = \frac{T_L}{T_0} = \left(\int_0^{\bar{r}_\omega} h dm + \int_0^{\bar{r}_\omega} \frac{\omega^2 dJ}{2} + \int_0^{\bar{r}_\omega} \frac{v_z^2}{2} dm \right) \Bigg/ \int_0^{\bar{r}_\omega} h_0 \, dm \tag{10}$$

$$\overline{T}_H = \frac{T_H}{T_0} = \left(\int_{\bar{r}_\omega}^{1} h dm + \int_{\bar{r}_\omega}^{1} \frac{\omega^2 dJ}{2} + \int_{\bar{r}_\omega}^{1} \frac{v_z^2}{2} dm \right) \Bigg/ \int_{\bar{r}_\omega}^{1} h_0 \, dm \tag{11}$$

The cold gas mass flowrate is written as

$$x = \int_0^{\bar{r}_\omega} dm \Bigg/ \int_0^{1} dm \tag{12}$$

where the hot stream discharges from the larger tube passing through the circular cross-section between $\bar{r}_\omega$ and $\bar{r} = 1$.

Figure 3 shows the mean temperatures of the cold and hot gas streams against the cold gas mass flowrate, calculated for $P_* = 2.15$ bar (converged solution for $P_0 = 7$ bar).

4. EXPERIMENTAL STUDY

Figure 4 shows the main characteristics of the apparatus used in developing the experimental part of our study. The experimental Vortex tube is built by two PVC pipes of diameters $D_H = 21$ mm and $D_L = 15$ mm, both of $L = 200$ mm in length. The central orifice in the disk separating the two cylindrical chambers, is 13 mm in diameter. Both, the disk and the outlet valve which control the gas streams, are manufactured by TECNIL.

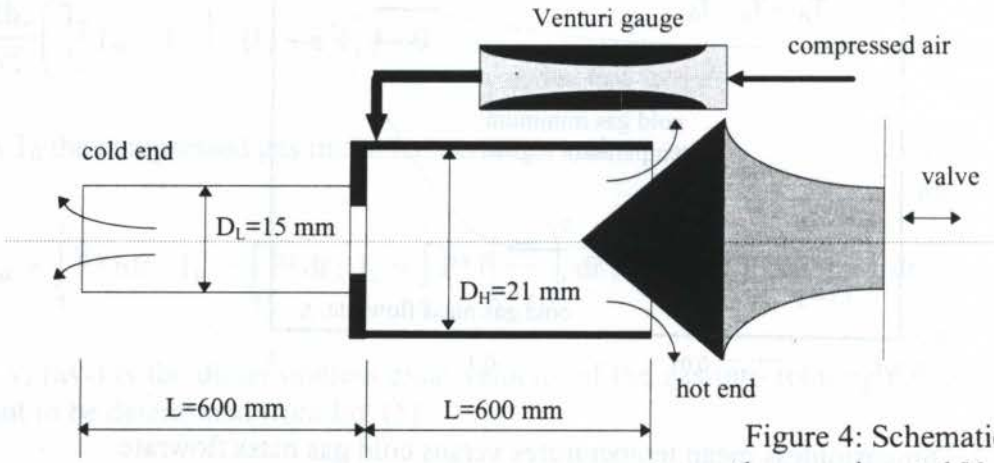

Figure 4: Schematic view of the experimental Vortex tube.

The compressed air is supplied to the experimental Vortex tube by a V2-20/250 SCHULZ compressor. The initial pressure of the gas entering the tube is kept constant by a NORGREN pneumatic industrial pressure regulator valve, ranging between 0 and 11 bar, which was controlled by a manometer.

We monitored the temperatures of the gas streams extracted from the cold and hot ends, T_L and T_H, and the temperature of the compressed gas entering the Vortex tube, T_0, for several fixed positions of the outlet valve fitted to the hot end. Temperatures were measured by using chrome-aluminum thermocouples, connected to a 486 IBM computer, by a NOVUS A/D 12 bits 10 Hz data aquisition system.

To determine the mass flowrate of the compressed gas supplied, and that of the cold gas stream, we used two Venturi gauges, one of them connected to the inlet port of the Vortex tube, and the other to the outlet port of the smaller pipe (cold end). The pressure drop ΔP is measured by using a U manometer, filled with a $\gamma = 859$ kgf/cm^3 oil.

Figure 5 depicts graphically the experimental set of data obtained from our experimental unit, showing the same trend as the R433 unit (1996), for different compressed gas pressures.

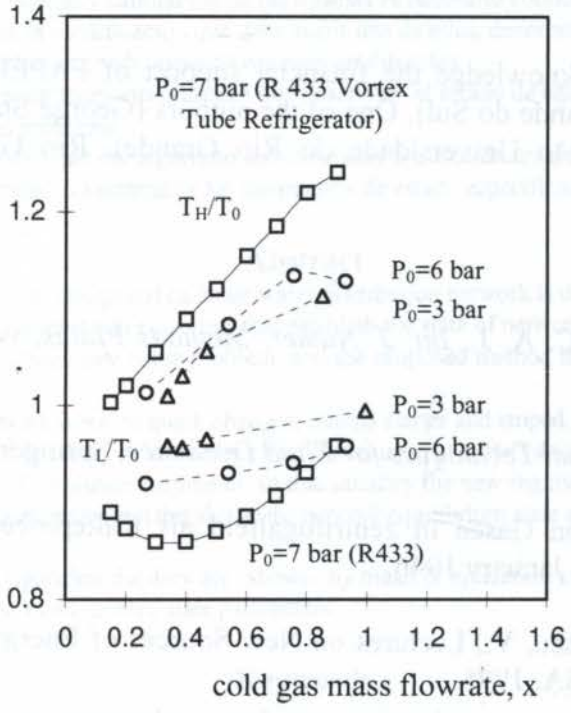

Figure 5: Experimental measurements on the R433 Vortex Refrigerator (plain line), built by P. A. Hilton Ltd., England, and the Vortex tube built in our laboratory (dashed line), supplied with compressed air.

5. CONCLUSIONS

In this paper, we showed theoretically that conservation of the angular momentum and redistribution of rotational and translational kinetic energies into a rotating gas column, could explain qualitatively the division of the compressed gas stream entering the Vortex tube into a cooled gas stream and a hot gas stream.

The internal swirling flow model captures the essential feature of the Vortex tube functioning, with a minimum cold stream temperature regime, and a maximum hot stream

temperature regime. Theoretical results of Fig. 3 compared to Fig. 5, qualitatively agree with experimental results for the R433 Vortex Tube Refrigerator, also showing the minimum T_L/T_0 and maximum T_H/T_0 regimes, observed experimentally.

Quantitative differences between theoretical estimation and experimental results suggest that a detailed analysis of the friction forces and viscosity, and a more accurate determination of the angular and axial velocity profiles, in the rotating gas column, should be done to improve the Vortex tube theoretical model. The present model does not account for the friction due to the relative motion between the layers of rotating gas, which otherwise would tend to heat both streams, i.e., that is why the theoretical maximum and minimum regimes are shifted and underestimate the hot temperature and lower the cold temperature, with respect to the experimental results.

Future developments will be focused on improving the theoretical model and on optimizing the design of the Vortex tube for some new applications, especially for the food industry.

6. ACKNOWLEDGMENTS

The authors gratefully acknowledge the financial support of FAPERGS (Fundação de Amparo a Pesquisa do Rio Grande do Sul). One of the authors (George Stanescu) would also like to thank FURG (Fundação Universidade do Rio Grande), Rio Grande, RS, for its hospitality.

7. REFERENCES

Armfield, S. W. & Fletcher, C. A. J., *Int. J. Numer. Methods Fluids*, vol. 6, pp. 541-556, 1986.

Fletcher, C. A. J., *Computational Techniques for Fluid Dynamics*, Springer-Verlag, 1991.

Hilsch, R.,"Die Expansion von Gasen in zentrifugalfeld als Kälteprocess". *Zeitschrift für Naturforschung*, Bd. 1, S. 208, January 1946.

Petrescu, S.,Zaiser, J. & Petrescu, V., Lectures on New Sources of Energy, Vol. 1, Bucknell University, Lewisburg, PA, USA, 1995.

R433 Vortex Tube Refrigerator Technical Specification, P. A. Hilton Ltd., England, 1996.

Radcenco, V., *Vortex tubes for producing cooling and heating effects*, Technical Publishing House, Bucharest, Romania, 1990.

Ranque, G. J., "Experiences sur la detente giratoire avec production simultanees d'un echappment d'air chaud et d'air froid", *Journal Physique et le Radium*, vol. 7, nº 4, pp. 112, 1933.

Ranque, G. J., "Method and apparatus for obtaining from fluid under pressure two currents of fluids at different temperatures", Patent USA No. 1,952,281/March 1934.

XIV Brazilian Congress of Mechanical Engineering
Obeid Plaza Hotel Convention Center - Bauru - SP/Brazil
December 08-12th 1997

PAPER CODE: COB1491

OPTIMIZACION EN EL DISEÑO Y CALIBRACION DE REDES DE DISTRIBUCION HIDRAULICA

*LISANDRO CURIA, *ALEJANDRA PERINI, **ARIEL MARCHEGIANI, *SERGIO CABEZAS, *GRISELDA ITOVICH

**Departamento de Matematica, Facultad de Economia, **Depto. de Mecanica Aplicada, Facultad de Ingenieria, UNIVERSIDAD NACIONAL DEL COMAHUE, Buenos Aires 1400 - (8300) Neuquen - ARGENTINA - E-mail: lcuria@uncoma.edu.ar*

Resumen

En este trabajo se desarrolla un algoritmo que permite diseñar y calibrar redes de distribución hidráulica en estado estacionario. La topología de la red se analiza mediante teoría de grafos. Las ecuaciones de conservación que establecen el estado de equilibrio de la red permiten formular el problema analíticamente como un problema con valores de contorno y el método propuesto puede aplicarse a redes cerradas, abiertas o combinadas.

Dado que en estado de regimen, una red está sometida a cambios bruscos: arranque y parada de bombas, variaciones en los caudales, etc, durante el diseño y calibración de las mismas es necesario conocer el efecto que produce sobre el conjunto de variables de campo, la modificación que debe sufrir una de ellas, denominada parámetro de resolución, de modo que la red satisfaga las nuevas condiciones de régimen establecidas.

La corrección del sistema de ecuaciones cuasilineales que describen el estado de equilibrio de la red permite obtener la solución analítica del nuevo problema.

El rango de operación y la ductilidad del algoritmo son ilustradas a través de un ejemplo de aplicación; La solución obtenida es optima ya que satisface exactamente los parámetros de estado especificados.

Abstract

In this Work an algorithm that allow design and calibrate water distribution network is developed. The network topology is analised by graph teory. The conservation equations that establish the state of network equilibrium allow the analytic formulation of the problem as boundary value problem, and the proposed method is applicable for open, closed and combinated networks.

Since that in regime state, a network is put to quick changes: pumps starter and stoped, flow rate variations, etc., during design and calibration of this is necesary to know the effect that caused over the variables group, the modification that try out one of this, denominated resolution parameter, so that satisficy the new regime conditions.

The correction of quasilineal equations system that shown the network equilibrium state allow obtain the analytic solution of new problem.

The operation range and the algorithm ductility are shown by mean of aplication example, the solution obtained is optimal since satify exactly the especificated state parameters.

Keywords

water distribution, calibration, networks analysis, graph teory, optimization.

1. INTRODUCCION

En los últimos años varios autores (Eiger 1994, Shamir 1979, Walters 1988, Ormsbee, 1986) han desarrollado algoritmos para calibrar y poner a punto redes de distribucion hidráulica. Estas técnicas se basan en el empleo de expresiones analíticas, simulación de modelos y técnicas de optimización .

En el caso de redes hidráulicas en estado estacionario el análisis consiste en estudiar el nivel de presiones y caudales circulantes cuando determinadas condiciones se especifican como condiciones de borde. Las leyes de Kircchoff describen el comportamiento de la red y pueden combinarse de distintas formas dando lugar a un sistema algebraico no lineal que debe ser resuelto

por métodos iterativos entre los cuales el de Newton Raphson (Martin, 1963) es el mas usual. Las características de convergencia del mismo estín asociadas al valor del radio de atracción, que se construye tomando como base el vector con el que se inicia el método iterativo (Marchegiani et. al. 1995).

Esta publicación presenta un enfoque particular del algoritmo de Boulos (Boulos 1991) y se basa en la construcción de pseudo circuitos que permiten incorporar las ecuaciones adicionales necesarias al sistema original de modo que se establezca un nuevo estado de equilibrio y la red satisfaga las nuevas condiciones especificadas.

2. DESCRIPCION TOPOLOGÍCA DE UNA RED DE DISTRIBUCIÓN

Una red de distribución puede ser considerada como un grafo lineal dirigido, compuesto de un número finito de arcos (secciones de tuberías, cada uno con su longitud, diámetro y rugosidad especificada) interconectados de acuerdo a una configuración específica. Las secciones de tuberías pueden contener bombas y otros accesorios como curvas o válvulas. Los puntos extremos (vértices) de los arcos, son identificados como nodos, dentro de los cuales se encuentran los nodos de unión y los nodos de grado fijo.

Sea G = (V , U) un grafo dado, donde V es el conjunto de vértices y U es el conjunto de aristas de G. Las siguientes definiciones son necesarias para adaptar la teoría de grafos al estudio de redes de distribución.

Definición 1: Se llama ***subgrafo de G*** a todo grafo G' donde G' = (V' , U') , V'$\subseteq$ V y U'$\subseteq$ U. (G' puede obtenerse a partir de G, eliminado los vértices de V - V' y las aristas que inciden en estos últimos).

Definición 2: Se llama ***nodo de unión de G*** al vértice donde dos o más aristas se unen. (Se puede considerar como el punto de consumo donde el flujo entra y sale del sistema de la red).

Definición 3: Se llama ***nodo de grado fijo de G*** a un punto de energía constante. (Por ejemplo: la conexión de un reservorio, elevación de un depósito o una región de presión constante)

Definición 4: Se llama ***grado de un nodo*** de G al número de aristas que inciden en el nodo.

Definición 5: Se llama ***grafo etiquetado*** a un grafo tal que a algunos de sus elementos (vértices o aristas) se les asigna etiquetas, es decir nombres, marcas, valores, símbolos, secuencia de símbolos, etc.

Definición 6: Se llama ***bucle de G*** a una arista de G en la que coinciden los extremos.

Definición 7: Se llama ***matriz de adyacencia (vértice - vértice) de G*** a la matriz A = (a_{ij}) donde a_{ij} = número de aristas de extremos i y j.

Definición 8: Se llama ***ciclo de G*** a un conjunto ordenado minimal u_1, u_2 ,...,u_n, u_1 donde u_i ϵ V y existen aristas en U que unen u_i, con u_{i+1} para todo i=1,2,....,n-1 y u_n con u_1.

3. ECUACIONES DE BALANCE EN LA RED

Las leyes que caracterizan la distribución del flujo estacionario en una red hidráulica o de gas son las leyes de Kirchoff , llamadas de energía y de continuidad. Éstas se vinculan a través de la relación entre pérdida de carga y caudal.

La Ley de continuidad dice que la suma algebraica de los caudales entrantes y salientes de un nodo de unión es nula, es decir:

$$\sum_{i=1}^{n} \alpha_i . Q_i + q_j = 0 \quad j=1,...,n \tag{1}$$

n = número de nodos
Q_i = caudal circulante en la tubería conectada al nodo i.
q_j= caudal externo entrante ó saliente del nodo j (suministros).
α_{jx}= {-1,0,1} dependiendo de la incidencia y la orientación de la tubería conectada al nodo i.

Por su parte la Ley de Conservación de la energía requiere que a lo largo de cada circuito, las pérdidas de energía acumulada (incluyendo pérdidas menores) menos cualquier energía entregada al fluído por las bombas debe ser 0 (cero).

(2)

donde:
t = número de circuitos fundamentales
e= número de turberías (aristas)
$\Delta H_x = H_i - H_j$, siendo H_i y H_j las presiones en los extremos de la tubería x conectada a los nodos i y j.
L_c = energía externa entregada en el loop **c.**
β = {-1,0,1} dependiendo de la pertenenecia y la orientación de la tubería x en el circuito **c.**

La pérdida de carga es una función no lineal del caudal Q_x (Bahve, 1991), que circula por la tubería x, es decir:

$$\Delta H_x = R_i . \tag{3}$$

donde:
R_i = constante de resistencia de la tubería i.
m = exponente que depende de la expresión del coeficiente de fricción utilizada.

Existen varias alternativas para analizar el estado estacionario de alturas y caudales en una red de distribución hidráulica, como ser, el método de los caudales, el de los nodos, etc., presentando el primero mejores características de convergencia (Marchegiani et al, 1995).

3.1. El método de los caudales

El método de los caudales tiene como incógnitas los caudales en las tuberías y consiste en la combinación de las ecuaciones anteriores de manera de obtener un sistema no lineal que puede escribirse como sigue:

$$\mathbf{F(Q_x) = 0}$$

donde
$\mathbf{F} = [F_1, F_2, ...F_e]^T$
$\mathbf{Q_x} = [Q_1, Q_2, ...Q_e]^T$ (4)

por métodos iterativos entre los cuales el de Newton Raphson (Martin, 1963) es el mas usual. Las características de convergencia del mismo estín asociadas al valor del radio de atracción, que se construye tomando como base el vector con el que se inicia el método iterativo (Marchegiani et. al. 1995).

Esta publicación presenta un enfoque particular del algoritmo de Boulos (Boulos 1991) y se basa en la construcción de pseudo circuitos que permiten incorporar las ecuaciones adicionales necesarias al sistema original de modo que se establezca un nuevo estado de equilibrio y la red satisfaga las nuevas condiciones especificadas.

2. DESCRIPCION TOPOLOGÍCA DE UNA RED DE DISTRIBUCIÓN

Una red de distribución puede ser considerada como un grafo lineal dirigido, compuesto de un número finito de arcos (secciones de tuberías, cada uno con su longitud, diámetro y rugosidad especificada) interconectados de acuerdo a una configuración específica. Las secciones de tuberías pueden contener bombas y otros accesorios como curvas o válvulas. Los puntos extremos (vértices) de los arcos, son identificados como nodos, dentro de los cuales se encuentran los nodos de unión y los nodos de grado fijo.

Sea G = (V , U) un grafo dado, donde V es el conjunto de vértices y U es el conjunto de aristas de G. Las siguientes definiciones son necesarias para adaptar la teoría de grafos al estudio de redes de distribución.

Definición 1: Se llama ***subgrafo de G*** a todo grafo G' donde G' = (V' , U') , V'⊆ V y U'⊆ U. (G' puede obtenerse a partir de G, eliminado los vértices de V - V' y las aristas que inciden en estos últimos).

Definición 2: Se llama ***nodo de unión de G*** al vértice donde dos o más aristas se unen. (Se puede considerar como el punto de consumo donde el flujo entra y sale del sistema de la red).

Definición 3: Se llama ***nodo de grado fijo de G*** a un punto de energía constante. (Por ejemplo: la conexión de un reservorio, elevación de un depósito o una región de presión constante)

Definición 4: Se llama ***grado de un nodo*** de G al número de aristas que inciden en el nodo.

Definición 5: Se llama ***grafo etiquetado*** a un grafo tal que a algunos de sus elementos (vértices o aristas) se les asigna etiquetas, es decir nombres, marcas, valores, símbolos, secuencia de símbolos, etc.

Definición 6: Se llama ***bucle de G*** a una arista de G en la que coinciden los extremos.

Definición 7: Se llama ***matriz de adyacencia (vértice - vértice) de G*** a la matriz A = (a_{ij}) donde a_{ij} = número de aristas de extremos i y j.

Definición 8: Se llama ***ciclo de G*** a un conjunto ordenado minimal $u_1, u_2, ..., u_n, u_1$ donde $u_i \in V$ y existen aristas en U que unen u_i, con u_{i+1} para todo i=1,2,....,n-1 y u_n con u_1.

3. ECUACIONES DE BALANCE EN LA RED

Las leyes que caracterizan la distribución del flujo estacionario en una red hidráulica o de gas son las leyes de Kirchoff , llamadas de energía y de continuidad. Éstas se vinculan a través de la relación entre pérdida de carga y caudal.

La Ley de continuidad dice que la suma algebraica de los caudales entrantes y salientes de un nodo de unión es nula, es decir:

$$\sum_{i=1}^{n} \alpha_i . Q_i + q_j = 0 \quad j=1,...,n \qquad (1)$$

n = número de nodos
Q_i = caudal circulante en la tubería conectada al nodo i.
q_j= caudal externo entrante ó saliente del nodo j (suministros).
α_{jx}= {-1,0,1} dependiendo de la incidencia y la orientación de la tubería conectada al nodo i.

Por su parte la Ley de Conservación de la energía requiere que a lo largo de cada circuito, las pérdidas de energía acumulada (incluyendo pérdidas menores) menos cualquier energía entregada al fluído por las bombas debe ser 0 (cero).

(2)

donde:
t = número de circuitos fundamentales
e= número de turberías (aristas)
$\Delta H_x = H_i - H_j$, siendo H_i y H_j las presiones en los extremos de la tubería x conectada a los nodos i y j.
L_c = energía externa entregada en el loop **c.**
β = {-1,0,1} dependiendo de la pertenenecia y la orientación de la tubería x en el circuito **c.**

La pérdida de carga es una función no lineal del caudal Q_x (Bahve, 1991), que circula por la tubería x, es decir:

$$\Delta H_x = R_i . \qquad (3)$$

donde:
R_i = constante de resistencia de la tubería i.
m = exponente que depende de la expresión del coeficiente de fricción utilizada.

Existen varias alternativas para analizar el estado estacionario de alturas y caudales en una red de distribución hidráulica, como ser, el método de los caudales, el de los nodos, etc., presentando el primero mejores características de convergencia (Marchegiani et al, 1995).

3.1. El método de los caudales

El método de los caudales tiene como incógnitas los caudales en las tuberías y consiste en la combinación de las ecuaciones anteriores de manera de obtener un sistema no lineal que puede escribirse como sigue:

$$\mathbf{F(Q_x) = 0}$$

donde
$\mathbf{F} = [F_1, F_2, ...F_e]^T$
$\mathbf{Q_x} = [Q_1, Q_2, ...Q_e]^T$ (4)

4. ALGORITMO DE DISEÑO Y OPTIMIZACION

El algoritmo que se propone permite optimizar el diseño de una red de distribución hidráulica. El problema consiste en deteminar componentes físicos característicos que deben satisfacer determinadas condiciones de funcionamiento como, por ejemplo, flujo en las aristas y presiones en los nodos de unión, las que se dan ,en general, dentro de un rango de operación establecido.

La aplicación de las leyes de continuidad y conservación de energía, permite obtener un sistema de ecuaciones no lineal que representa el estado de equilibrio de la red. El presente algoritmo permite aumentar el conjunto original de ecuaciones, para hacer frente a la aparicion de nuevas incognitas mediante la adicion de un numero determiando de ecuaciones extra, de acuerdo al siguiente criterio:

I) De continuidad: cuando se especifica el caudal en una arista particular, en tal caso la misma se denomina **arista crítica**. Esta nueva ecuación se escribe para un nodo de unión artificial que se conecta con la arista crítica.

II) De conservación de energía: cuando se especifica la presión en algún nodo de unión, al que se denomina **nodo crítico.** Esta nueva ecuación se escribe para un pseudocircuito construido entre el nodo crítico y el nodo dato del sistema que incorpora una variable adicional denominada **parámetro de resolución.**

Cada una de las restricciones impuestas, originadas al fijar una presión nodal o un caudal en una arista, conduce a la determinación de un parámetro adicional. Por ejemplo, tomando la red de la figura 1, compuesta por cinco aristas (tuberías T_1 ,...,T_5), cinco nodos de unión (U_2,...U_5), y dos nodos de grado fijo (F_1 y F_2), si se fija como nodo dato a F_1 un posible pseudocircuito puede formarse con los tramos T_1, T_3 y T_5. Si en el nodo U_2 se especifica una presión determinada H_{U2} este nodo actuará como nodo crítico. El otro pseudocircuito constituido por T_1 y T_2 aportará la ecuación adicional al sistema existente:

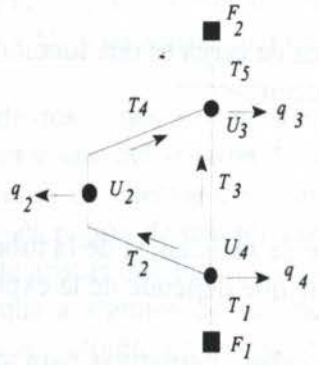

figura 1

$$R_1 (Q_1)^2 + R_2 (Q_2)^2 = H_{F1} - H_{U2}$$

donde H_{F1} es la presión en el nodo fijo F_1. Por otro lado el primer pseudocircuito aportará la ecuación:

$$R_1 (Q_1)^2 + R_3 (Q_3)^2 + R_5 (Q_5)^2 = H_{F1} - H_{U2}$$

Las dos últimas ecuaciones se suman al resto de las ecuaciones de balance.

El sistema ampliado de ecuaciones obtenido, representa el nuevo estado de equilibrio de la red bajo dichas restricciones. La condición suficiente para que el sistema tenga solucion está dada por la relación de Euler y la condición necesaria para que la solución sea unica por el teorema de

ensamblaje de matrices (Boulos, 1991).

Luego, el problema puede formularse como sigue:

$$\mathbf{F}(\mathbf{Q_x}, \mathbf{V}) = 0 \qquad (5)$$

donde
V es la variable de decisión adoptadas, $\mathbf{V} = [V_1, V_2, \ldots V_w]^T$
w es el número de variables de decisión elegidas.

Dado que el conjunto de ecuaciones (5) constituye un sistema no lineal se debe emplear en su resolución un procedimiento iterativo, el más utilizado es el de Newton-Raphson .

5. EJEMPLO DE APLICACION

La red de la figura 2 está compuesta por seis nodos: uno de grado fijo que está identificado como dato (correspondiente al nodo 1) y cinco nodos de unión. Aplicando las ecuaciones que gobiernan el flujo en la red se tiene:

Ecuaciones de continuidad:

nodo 2: $F_1 = Q_1 - Q_3 - q_2 = 0$

nodo 3: $F_2 = Q_3 + Q_4 - Q_6 - q_3 = 0$

nodo 4: $F_3 = Q_2 - Q_4 - Q_5 - q_4 = 0$

nodo 5: $F_4 = Q_5 - Q_7 - q_5 = 0$

nodo 6: $F_5 = Q_6 + Q_7 - q_6 = 0$

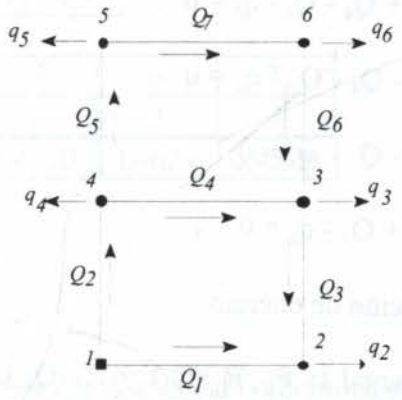

figura 2

y ecuaciones de conservación de energía:

circ.fundamental 1: $F_6 = R_1 (Q_1)^2 + R_3 (Q_3)^2 - R_4 (Q_4)^2 - R_2 (Q_2)^2 = 0$

circ.fundamental 2: $F_7 = R_6 (Q_6)^2 - R_7 (Q_7)^2 - R_5 (Q_5)^2 + R_4 (Q_4)^2 = 0$

Aplicando el método de los caudales (Bhave, 1991), se obtienen los valores dados en la tabla 1.

Tabla 1

nodo	1	2	3	4	5	6
q(l/s)	5	1,1	1,2	0,8	1	0,9
H(m)	100	91,0	88,87	91,50	88,12	87,69

arista	1	2	3	4	5	6	7
$R(s^2/m^5)$	2	1	2,5	4	2	3	4
Q(l/s)	2,0854	2,9146	0,9854	0,8149	1,2997	0,6003	0,2997

Eligiendo el árbol cubriente con raiz en el nodo 1 y formado por los aristas e_1, e_3, e_4, e_5, e_7, por las que se establecen los caudales Q_1 , Q_3 , Q_4 , Q_5 , Q_7 , respectivamente aplicaremos el algoritmo para analizar distintas situaciones.

Caso1: Se desea conocer el impacto que producesobre las variables un cambio de presión en el nodo 3 que se fija en 30m. De acuerdo a lo expuesto y si se considera a éste como un nodo crítico con una presión especificada H_3, de acuerdo al algoritmo de resolución debe agregarse una ecuación de energia adicional que se plantea para el pseudocircuito formado por las aristas e_1 . e_2 que unen el nodo dato con el crítico. Las ecuaciones que componen el sistema resultante son:

Ec. de continuidad:

nodo 2: $F_1 = Q_1 - Q_3 - q_2 = 0$

nodo 3: $F_2 = Q_3 + Q_4 - Q_6 - q_3 = 0$

nodo 4: $F_3 = Q_2 - Q_4 - Q_5 - q_4 = 0$

nodo 5: $F_4 = Q_5 - Q_7 - q_5 = 0$

nodo 6: $F_5 = Q_6 + Q_7 - q_6 = 0$

Ec. de conservación de energía

circuito fundamental 1: $F_6 = R_1 (Q_1)^2 + R_3 (Q_3)^2 - R_4 (Q_4)^2 - R_2 (Q_2)^2 = 0$

circuito fundamental 2: $F_7 = R_6 (Q_6)^2 - R_7 (Q_7)^2 - R_5 (Q_5)^2 + R_4 (Q_4)^2 = 0$

pseudocircuito: $F_8 = R_1 (Q_1)^2 + R_3 (Q_3)^2 = H_1 - H_3$

donde $\mathbf{R_3}$ es el **parámetro de resolusión** que se modifica y que se debe determinar junto con los caudales para satisfacer la restricción de presión impuesta de **90m**.

El nuevo estado de equilibrio de la red está representado a través de los valores que se muestran en la tabla 2.

Tabla 2

nodo	1	2	3	4	5	6
q(l/s)	5	1,1	1,2	0,8	1	0,9
H(m)	100	90,30	**90**	92,17	89,01	88,76

arista	1	2	3	4	5	6	7
R(s^2/m^5)	2	1	**0,25**	4	2	3	4
Q(l/s)	2,2024	2,7975	1,1024	0,7379	1,2575	0,6424	0,2576

La reducción en la resistencia de la tuberia correspondiente a la arista 3, puede obtenerse, por ejemplo, aumentando su diámetro : si se adopta una cañería de hierro de 60 m de longitud por la que circula agua; de la expresión de Darcy (Bahve, 1991), para un coeficiente de fricción de 0,02 resutará un diámetro de 0,052 m, comparado con el diámetro de 0,0346 obtenido para los datos de la tabla 1.

Caso 2: El caudal de suministro en el nodo 3 se modifica de 1,2 l/s a 1,5 l/s, el parémetro de resolución es la resistencia en la tuberia 3 y la presión disminuye a 85m en el nodo 3 (las demandas restantes se mantienen constantes de acuerdo con la tabla 1). Los valores resultantes se detallan en la tabla 3.

Tabla 3

nodo	1	2	3	4	5	6
q(l/s)	5	1,1	1,2	0,8	1	0,9
H(m)	100	91,74	**85**	89,32	85,19	84,35

arista	1	2	3	4	5	6	7
R(s^2/m^5)	2	1	**7,76**	4	2	3	4
Q(l/s)	2,0319	3,2680	0,9319	1,0309	1,4370	0,4629	0,4370

6. CONCLUSIONES

Dado que en las etapas de diseño y calibración de redes de distribución hidráulica es necesario repetir el procedimiento de resolución del sistema de ecuaciones resultantes varias veces, en esta publicación se presenta un algoritmo, descripto mediante teoria de grafos, que permite incorporar con claridad las ecuaciones de balance adicionales cuando uno o mas parámetros de la red sufren alguna modificación. Del análisis del impacto que provoquen las nuevas condiciones sobre el conjunto de variables de campo surgirán las características de diseño más eficiente de la red.

La técnica empleada, permite construir las ecuaciones suplementarias surgidas de las restricciones de funcionamiento impuestas, garantizando que la solución del sistema ampliado sea única. El procedimiento se empleó para el método de los caudales que presenta mejores características de convergencia que el metodo nodal, y la solución obtenida de ésta forma es óptima ya que satisface exactamente las condiciones de borde impuestas a la red .

La flexibilidad del algoritmo se pone de manifiesto a través de un ejemplo de aplicación donde se describen diferentes casos. Puede observarse claramente la gran cantidad de combinaciones que se presentan en la práctica y que pueden ser resueltos mediante el algoritmo propuesto.

7. REFERENCIAS

EIGER, G., SHAMIR, U., BEN-TAL, A., Optimal design and operation of water distribution systems, *Water Resour.Res.* Vol 30,Nro.9, pp. 2637-2646, 1994.

SHAMIR, U. Optimization in water distribution systems, *Math Programing*, 1979.

WALTERS, G.A., Optimal design of pipe networks: A review, *First International Conference on Computer Methods and Water Resources*. Vol. 2, Marrakesh, Morocco, 1988.

ORMSBEE, L.E. and WOOD, D.J., Hydraulic design algorithms for pipe networks, *J. Hydaul. Engn*, 1986.

MARTIN D. W., and PETERS, G., The application of Newton's method to network analysis by digital computers, *J. Inst. Water Engn. Sci.*, 17 (2), 115-129, 1963.

MARCHEGIANI, A. R., CURIA, L. y PERINI A., Formulación de un algoritmo en notación matricial para la resolución de redes de distribución hidráulica, *COBEM-CIDIM 95,* Belo Horizonte, Brasil, 1995.

BOULOS P.F., and ALTMAN T., A graph -teoretic approach to explicit nonlinear pipe network optimization, *Appl. Math Modelling,* vol. 15 , pp 459-466, 1991.

BHAVE, P.R., *Analysis of flow in water distribution networks,* Technomic Publishing Co. Inc., Lancaster, 1991.

UNESP
COBEM 97
XIV Brazilian Congress of Mechanical Engineering
Obeid Plaza Hotel Convention Center - Bauru - SP/Brazil
December 08-12th 1997

PAPER CODE: COB268

ANÁLISE DA PROPAGAÇÃO DE PERTURBAÇÕES NO CAMPO DE VELOCIDADES DO ESCOAMENTO EM BANCO DE TUBOS / *ANALYSIS ON THE PROPAGATION OF DISTURBANCES IN THE VELOCITY FIELD OF TUBE BANK FLOW*

LUIZ AUGUSTO MAGALHÃES ENDRES & SERGIO VIÇOSA MÖLLER
Programa de Pós-Graduação em Engenharia Mecânica, UFRGS
CEP 90.050 - 170 Porto Alegre, Brasil-E - mail: endres@if.ufrgs.br & svmoller@vortex.ufrgs.br

Abstract

This paper presents the experimental analysis of the propagation of a disturbance with a fixed frequency, generated, by means of an obstacle, in the incidence velocity of the cross flow through a tube bank and its influence on the pressure and velocity fluctuations inside the bank. The tube bank investigated had square arrangement and aspect ratio P/D = 1.60 and air was the working fluid. Measurements were performed with hot wires and pressure transducers. Behavior of fluctuating quantities is described by means of autospectral density functions and the propagation of the disturbance is discussed based on the analysis of cross-correlation functions. The results show that the frequency of the disturbance remains unchanged as it passes through the bank, in spite of the high turbulence intensities and of the fact that flow velocity inside the bank varies with the position. This fact may indicate that external excitations can be transferred to the solid boundaries of the bank.

Keywords

Banco de Tubos, Turbulência, Anemometria de Fio-Quente / Tube Bank, Turbulence, Hot-Wire Anemometry.

1. INTRODUÇÃO

No projeto de trocadores de calor adota-se como critério otimizar a transferência de calor e minimizar perdas de carga no escoamento do fluido refrigerante. No entanto, "falhas espetaculares" (expressão utilizada por Païdoussis, 1982) causadas por vibração induzida pelo escoamento elevaram, com o passar do tempo e com o exame dos relatórios dos acidentes, o nível de consideração deste fator nas diretrizes dos projetistas. Blevins (1990) comenta que a indução à vibração não é um fator prioritário em projetos de estruturas do tipo banco de tubos que buscam, primeiramente, a otimização da transferência de calor preterindo outros parâmetros, ao menos enquanto não ocorrerem falhas no sistema.

Em geral pode-se classificar os esforços a que um banco de tubos está submetido, quanto à sua origem, em estáticos e dinâmicos (Endres et al., 1995). Os primeiros são decorrentes da variação de pressão média no escoamento entre os tubos. Quanto aos processos dinâmicos, decorrentes das flutuações de pressão, serão caracterizados, principalmente, através da influência da geometria do arranjo sobre o escoamento (Endres & Möller, 1997). Estes processos manifestam-se através de fenômenos como o martelamento turbulento ("turbulent

buffeting"), o desprendimento de vórtices ("vortex shedding") ou, ainda, ressonância acústica decorrente do próprio escoamento turbulento.

Muitos estudos consideram estes processos, porém são poucos os que levam em conta a influência das condições de entrada do escoamento no canal. Fenômenos externos aos bancos de tubos como a separação da camada limite, ação das pás das bombas ou ação das chicanas ou elementos estruturais poderão influenciar ou participar do processo hidrodinâmico sobre os tubos.

O trabalho de Fitzpatrick et al. (1988) investigou auto-espectros de turbulência, a partir de medições de flutuações de velocidades, na região de passagem principal do escoamento ("through flow") de arranjos quadrangulares com razão de espaçamento de P/D = 1,73. O objetivo deste trabalho era de avaliar valores dos números de Strouhal em arranjos de tubos com um elevado número de linhas transversais ao escoamento. No trabalho destes autores são analisadas as periodicidades surgidas no interior do banco, devido aos efeitos de desprendimento de vórtices na esteira dos tubos e de martelamento ("buffeting") do escoamento gerado pela alternância periódica de passagens, ora mais estreitas, ora mais largas, entre os tubos, considerada a direção transversal ao escoamento de aproximação. Entretanto, conforme a descrição apresentada deste último fenômeno, com uma freqüência de pico bem caracterizada, não se trata do martelamento turbulento ("turbulent buffeting") referido por Grover e Weaver (1978) que tem origem na distribuição, em toda a faixa de freqüências do espectro, de uma significativa parcela de energia. Aqui, está sendo feita referência ao processo cuja ocorrência está vinculada à distância existente entre as sucessivas linhas de tubos e que tem picos estreitos na representação gráfica dos espectros devido ao efeito de amplificação passa-banda das passagens entre os tubos do arranjo.

Ainda segundo estes autores, nas primeiras linhas do arranjo predomina o efeito do desprendimento de vórtices resultando em valores mais elevados dos números de Strouhal para os picos de freqüência encontrados nos espectros. Estes valores vão reduzindo mais para o interior do banco de tubos onde predomina o efeito do martelamento aliado à redução nas velocidades convectivas locais, que induzirão a uma redução na razão com que o processo de desprendimento de vórtices ocorre. Assim, em função da posição no interior do banco de tubos (além da geometria do arranjo e valores do número de Reynolds do escoamento), foram obtidas diferentes freqüências características associadas ao processo de flutuação de velocidades que dão origem a flutuações de pressão na superfície dos tubos do arranjo, sem a característica de uma larga faixa de freqüências com energia considerável, porém, concentrada em uma faixa estreita.

Žukauskas et al. (1980) partem da hipótese de que as forças induzidas pelo escoamento sobre os tubos, e as vibrações geradas por estas forças, são controladas pelas estruturas do escoamento existentes a montante do arranjo e no espaço do casco do trocador de calor. Para o estudo destas relações foram empregados tubos com liberdade para vibrar e medidas das flutuações de pressão sobre os contornos dos tubos e amplitudes de vibração dos mesmos. Os autores apresentam comentários no sentido de que, devido à complexidade do escoamento que se estabelece no interior do arranjo, não existe uma relação única entre as vibrações dos tubos nas diferentes linhas, mas que existem, apenas, pequenas diferenças nas freqüências de vibração, situando-se, este parâmetro, muito próximo à freqüência natural de vibração destes tubos.

No presente trabalho, são comparadas as características do escoamento no interior de um banco de tubos com arranjo na geometria quadrangular e espaçamento relativo entre os tubos de P/D=1,60, com o de um canal livre em seu desenvolvimento, através de funções de densidade auto-espectral e de correlações cruzadas de flutuações de velocidade e de pressão medidas. Para este fim, analisou-se, também, o comportamento no interior de um banco de

tubos de uma periodicidade ou perturbação transportada, com sua origem a montante do banco, ainda na região de aproximação no modelo utilizado, representando o que seria a região do casco em um trocador de calor do tipo casco e tubo com escoamento na transversal.

2. SEÇÃO DE TESTES

O canal utilizado nos testes tem seção transversal com 146 mm de altura por 193 mm de largura, ajustável. Através deste canal, o ar é impulsionado por um ventilador centrífugo com vazão regulável. Após a válvula reguladora, o ar passa por uma câmara de tranqüilização, difusor, colméias e telas de malha fina para uniformização do perfil de velocidades.

No interior do canal foi instalado o banco de tubos com arranjo quadrangular de eixos orientados a 90° com o escoamento. O arranjo era constituído por cinco linhas de tubos, com um total de 20 tubos, sendo a razão de espaçamento dada por P/D=1,60, onde P é a distância entre os centros das seções transversais dos tubos e D seu diâmetro, igual a 32,1 mm.

Um dos tubos no interior do banco era instrumentado com uma tomada de pressão à meia altura, à qual foi conectado, através de uma pequena mangueira plástica, um transdutor de pressão piezo-resistivo ENDEVCO. Esta técnica de conexão da tomada ao transdutor mostrou-se adequada a investigações experimentais do tipo aqui realizado (Endres & Möller, 1994). As flutuações de velocidade no interior do banco de tubos e a montante deste, foram medidas com um sistema de anemometria a fio quente DANTEC, a temperatura constante, usando sondas com fios retos montados a 90 ° com o escoamento.

As aquisições de dados foram realizadas via conversão analógico-digital dos sinais elétricos produzidos pelos sensores e o processamento dos mesmos em micro computador PC. As amostras foram adquiridas a uma freqüência de 4 kHz e filtradas para passar entre 1 Hz e 2 kHz.

Representações esquemáticas do canal e do banco de tubos, assim como o posicionamento das sondas, serão apresentadas no item de resultados, referentes a cada etapa do trabalho.

3. RESULTADOS

3.1 Medidas Preliminares

Tanto na situação do canal livre, sem o banco de tubos, como na situação do canal com o banco de tubos, foram introduzidas perturbações no escoamento com características conhecidas visando a comparação do efeito do banco de tubos sobre a propagação desta perturbação, quando transportada pelo escoamento médio, na direção longitudinal do canal. As perturbações foram obtidas com o emprego de um obstáculo montado no canal, a jusante do qual formava-se uma trilha constituída por desprendimento de vórtices. Esquematicamente, os canais livre e com banco de tubos estão representados nas figuras 1 e 2, respectivamente.

As dimensões dos dois geradores de perturbações são diferentes para que resultem, estabelecidos os escoamentos, aproximadamente, a mesma freqüência de desprendimento de vórtices, necessária para a comparação entre os resultados. Este fato é devido à diferença de velocidades entre os escoamentos nos canais livre e com o banco de tubos, causada pela diferença na perda de carga entre os dois canais, uma vez que o conjunto motor ventilador trabalha com a mesma potência nos dois casos. As respostas em termos de freqüências dominantes (f_D), do desprendimento de vórtices de cada gerador, são 42 Hz e 45 Hz, respectivamente para o utilizado no canal livre e para o utilizado no canal com o banco de tubos. Para a situação do canal livre, além do pico na freqüência dominante de 42 Hz, aparece

um segundo pico, de menor intensidade, na freqüência de 84 Hz, correspondente à influência da recirculação periódica de fluido existente na esteira do gerador de vórtices. Este efeito aparecerá novamente em análises feitas no decorrer deste trabalho.

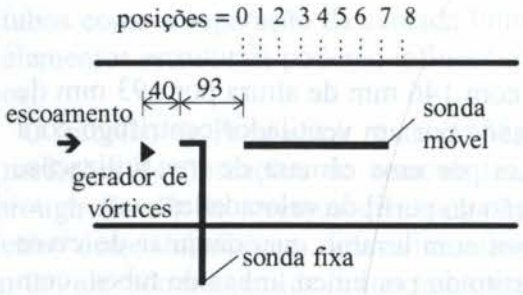

Figura 1: Representação esquemática do canal livre, sem banco de tubos (medidas em mm).

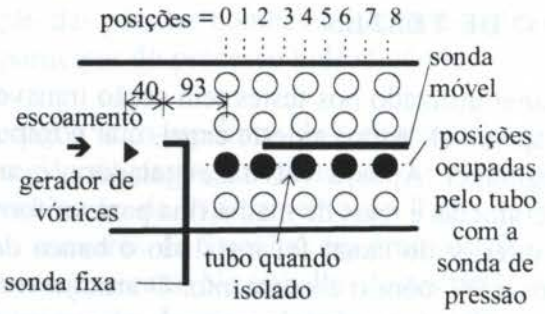

Figura 2: Representação esquemática do canal com banco de tubos (medidas em mm).

3.2 Canal Livre

Antes de ser instalado o banco de tubos, foram avaliadas as características do canal com o fluido escoando livre. Medições simultâneas de flutuações de velocidades em dois pontos na direção longitudinal do escoamento, sendo que um deles era móvel nesta mesma direção, permitiram avaliar a forma com que os vórtices eram transportados pelo escoamento principal, tanto no que diz respeito a uma possível perda na intensidade das flutuações na sonda móvel, como quanto aos valores de freqüência medidos nesta posição variável, na medida em que se afastava da origem de geração. Foram, também, realizadas medidas simultâneas de flutuações de velocidade na sonda fixa e de flutuações de pressão sobre a parede de um tubo isolado, rigidamente fixado ao canal na esteira do gerador de vórtices, para avaliar de que maneira o desprendimento de vórtices do gerador agia sobre os contornos sólidos do tubo. A figura 2 representa a montagem utilizada.

A partir das determinações de correlações cruzadas entre flutuações de velocidades medidas na sonda fixa e na sonda móvel, para suas diferentes posições, foram calculadas velocidades de transporte dos vórtices gerados, através da relação entre a defasagem de tempo para a máxima correlação e a distância entre as duas sondas. Os resultados revelaram um crescimento suave desde a posição 0 até a posição 7 (ver figura 2), situando-se entre 54% e 73% da velocidade de aproximação ao banco, igual a 9,70 m/s.

Além desses resultados, os espectros de densidade de potência das flutuações de velocidade nas posições assumidas pela sonda móvel assim como as correlações cruzadas entre flutuação de velocidade na sonda fixa e flutuação de pressão sobre o contorno do tubo isolado (estando o tubo instalado na posição 4 - ver figura 2), e ainda os espectros das flutuações de pressão com a tomada orientada a 0^{o} ou a 90^{o} com o escoamento, permitem observar que a perturbação provocada é transportada ao longo do canal, mantendo sua freqüência característica idêntica à original, podendo ser detectada com intensidades menores, porém significativas, não apenas no escoamento, em posições distantes da geração inicial, como também sobre os contornos sólidos das estruturas situadas a jusante. Para as posições mais afastadas da geração da perturbação, onde já existe uma maior uniformização do escoamento na seção transversal do canal, as velocidades de transporte da perturbação são crescentes, tendendo, provavelmente, ao valor da velocidade de aproximação.

3.3 Canal com Banco de Tubos

Após a montagem do banco de tubos no canal e a substituição do gerador de vórtices pelo de menores dimensões, um conjunto de medições semelhante ao anterior foi efetuado. Além disso, o tubo instrumentado com a tomada de pressão foi movimentado ao longo das linhas do arranjo de tubos, sempre na mesma coluna central, visando avaliar de que maneira o desprendimento de vórtices do gerador agia sobre os contornos sólidos do tubo instalado em diferentes posições no interior do banco.

A figura 2 esquematiza o posicionamento do gerador de vórtices, banco de tubos, e posições das sondas de velocidade e de pressão. Esta última, podia ser colocada tanto na posição orientada contra o escoamento (0^o) como na normal ao escoamento (90^o).

Os resultados de correlações cruzadas entre flutuações de velocidades medidas com a sonda fixa e com a sonda móvel, para suas diferentes posições, são apresentados na figura 3. As velocidades de transporte dos vórtices gerados, são obtidas através da relação entre a defasagem de tempo para a máxima correlação e a distância entre as duas sondas (tempo de trânsito), e revelam, novamente, um crescimento uniforme desde a posição 0 até a posição 7 (ver figura 2), porém, agora com o banco de tubos instalado no canal, seus valores variaram desde 75% até 177% da velocidade de aproximação ao banco, igual a 8,351 m/s.

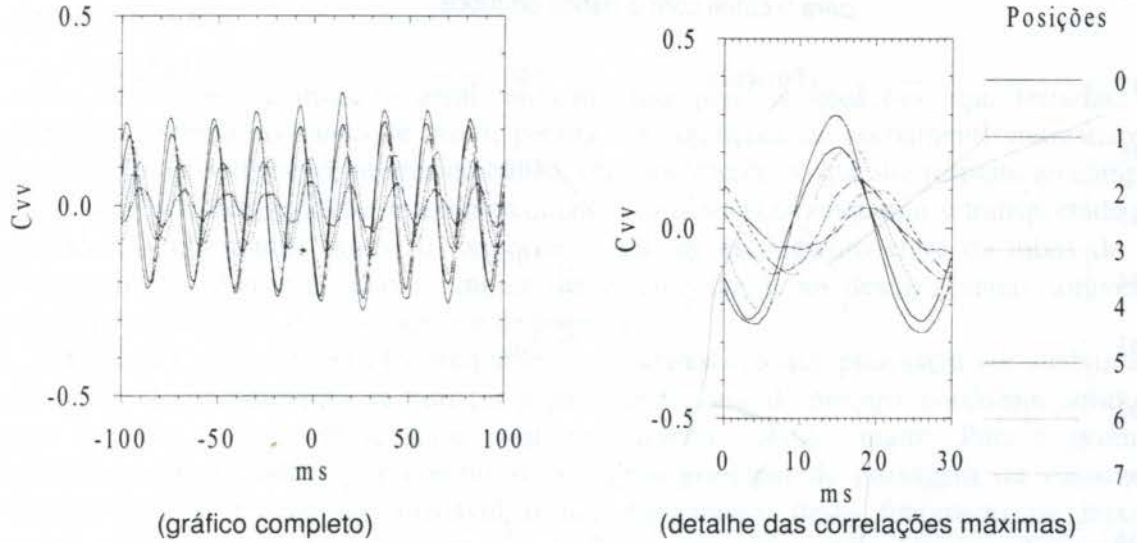

Figura 3: Correlações cruzadas entre sonda fixa e sonda móvel para o canal com banco de tubos (posições das sondas na figura 2).

O espectro de densidade de potência das flutuações de velocidade medidas na sonda fixa, os espectros de densidade de potência das flutuações de velocidade nas posições assumidas pela sonda móvel e o espectro de densidade de potência das flutuações de pressão, todos para a situação do canal com o banco de tubos, estão apresentados na figuras 4 e 5. A figura 5 mostra o detalhe dos picos a 45 Hz.

As medições relizadas neste trabalho, foram também empregadas para as seguintes determinações: correlações cruzadas entre flutuações de velocidade na sonda fixa e flutuações de pressão sobre os contornos do tubo instrumentado nas diferentes linhas do arranjo, considerada a tomada de pressão na posição de 0^o e na posição de 90^o; correlações cruzadas entre as flutuações de velocidade na sonda móvel e na tomada de pressão orientada a 90^o com o escoamento principal, estando o tubo instrumentado instalado na terceira linha (posição 4 na

um segundo pico, de menor intensidade, na freqüência de 84 Hz, correspondente à influência da recirculação periódica de fluido existente na esteira do gerador de vórtices. Este efeito aparecerá novamente em análises feitas no decorrer deste trabalho.

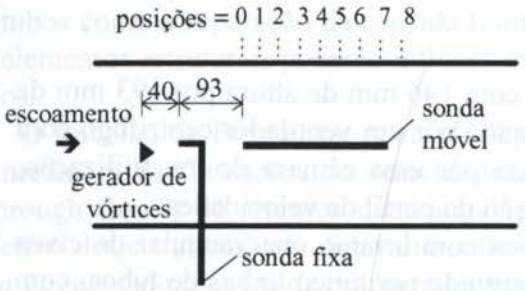

Figura 1: Representação esquemática do canal livre, sem banco de tubos (medidas em mm).

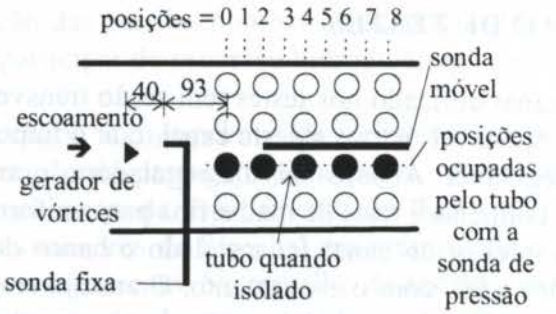

Figura 2: Representação esquemática do canal com banco de tubos (medidas em mm).

3.2 Canal Livre

Antes de ser instalado o banco de tubos, foram avaliadas as características do canal com o fluido escoando livre. Medições simultâneas de flutuações de velocidades em dois pontos na direção longitudinal do escoamento, sendo que um deles era móvel nesta mesma direção, permitiram avaliar a forma com que os vórtices eram transportados pelo escoamento principal, tanto no que diz respeito a uma possível perda na intensidade das flutuações na sonda móvel, como quanto aos valores de freqüência medidos nesta posição variável, na medida em que se afastava da origem de geração. Foram, também, realizadas medidas simultâneas de flutuações de velocidade na sonda fixa e de flutuações de pressão sobre a parede de um tubo isolado, rigidamente fixado ao canal na esteira do gerador de vórtices, para avaliar de que maneira o desprendimento de vórtices do gerador agia sobre os contornos sólidos do tubo. A figura 2 representa a montagem utilizada.

A partir das determinações de correlações cruzadas entre flutuações de velocidades medidas na sonda fixa e na sonda móvel, para suas diferentes posições, foram calculadas velocidades de transporte dos vórtices gerados, através da relação entre a defasagem de tempo para a máxima correlação e a distância entre as duas sondas. Os resultados revelaram um crescimento suave desde a posição 0 até a posição 7 (ver figura 2), situando-se entre 54% e 73% da velocidade de aproximação ao banco, igual a 9,70 m/s.

Além desses resultados, os espectros de densidade de potência das flutuações de velocidade nas posições assumidas pela sonda móvel assim como as correlações cruzadas entre flutuação de velocidade na sonda fixa e flutuação de pressão sobre o contorno do tubo isolado (estando o tubo instalado na posição 4 - ver figura 2), e ainda os espectros das flutuações de pressão com a tomada orientada a 0^{o} ou a 90^{o} com o escoamento, permitem observar que a perturbação provocada é transportada ao longo do canal, mantendo sua freqüência característica idêntica à original, podendo ser detectada com intensidades menores, porém significativas, não apenas no escoamento, em posições distantes da geração inicial, como também sobre os contornos sólidos das estruturas situadas a jusante. Para as posições mais afastadas da geração da perturbação, onde já existe uma maior uniformização do escoamento na seção transversal do canal, as velocidades de transporte da perturbação são crescentes, tendendo, provavelmente, ao valor da velocidade de aproximação.

figura 2); espectros das flutuações de pressão nas diferentes linhas do arranjo para as posições da tomada de pressão orientada a 0° e 90°.

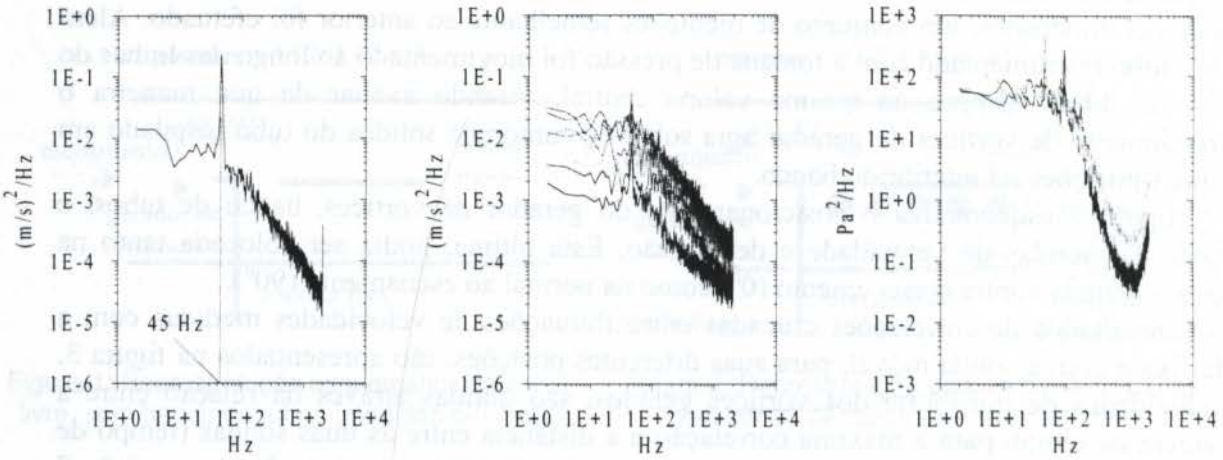

a) sonda de velocidade, fixa b) sonda de velocidade, móvel c) sonda de pressão, a 90°

Figura 4: Espectros de densidades de potência das flutuações de velocidade e pressão para o canal com o banco de tubos.

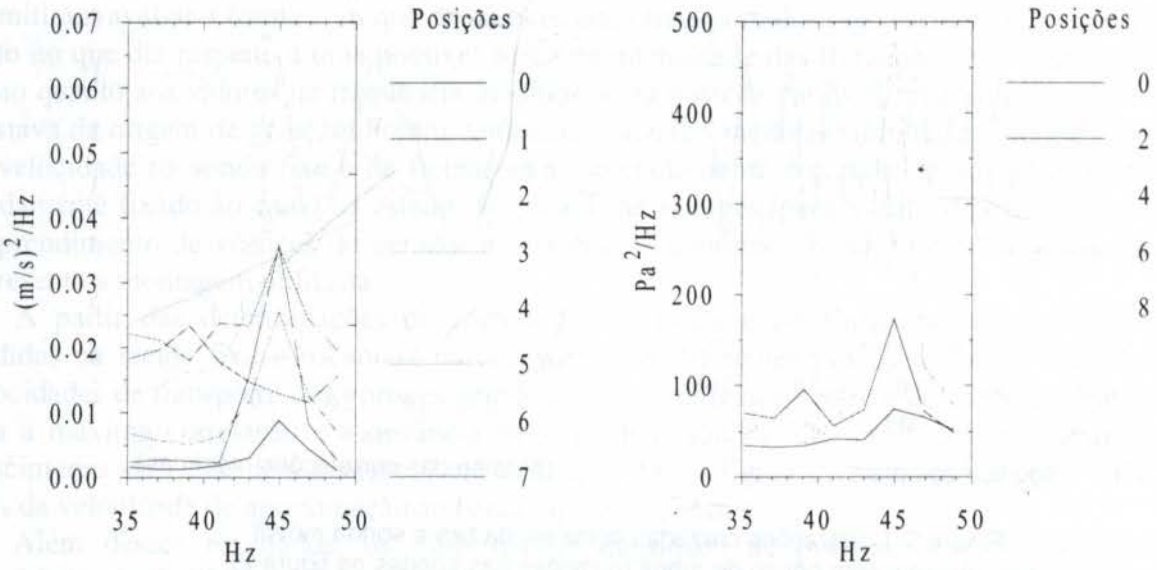

b) sonda de velocidade, móvel c) sonda de pressão, a 90°

Figura 5: Detalhes dos espectros de densidades de potência das flutuações de velocidade e pressão para o canal com o banco de tubos.

Do conjunto de resultados obtidos nas medições com banco de tubos (não apresentados por questões de limitação de espaço), observa-se que a perturbação provocada é transportada ao longo da passagem entre duas colunas de tubos (no sentido longitudinal do canal), mantendo sua freqüência característica idêntica à original (figuras 4 e 5), embora a velocidade de aproximação calculada seja, na maior parte dos casos, sensivelmente diferente, não só das velocidades de transporte calculadas, como também das velocidades médias, medidas com o sistema de anemometria a fio quente nas passagens entre os tubos.

Com relação aos espectros de flutuações de velocidades (figura 4), na faixa de baixas freqüências, pode-se observar menores intensidades nas passagens entre tubos das primeiras linhas e maiores, chegando a aumentar uma década, na passagem entre os tubos das últimas linhas. Quanto ao pico de energia espectral, na freqüência de geração dos vórtices (45 Hz), tem-se magnitudes crescentes da primeira linha de tubos (posição 0) até entre a terceira e quarta linha de tubos (posição 3). Deste ponto em diante, esta magnitude é reduzida, deixando mesmo de ser percebida na passagem entre os tubos após a quarta linha (posição 7).

As densidades espectrais das flutuações de pressão (figuras 4 e 5), por sua vez, apresentam uma maior uniformidade de valores, principalmente nas medidas em que a tomada de pressão esteve voltada para a passagem do escoamento (90°). Para esta posição da tomada de pressão, a freqüência original do desprendimento de vórtices tem sua magnitude com valores crescentes desde a primeira até a quarta linha de tubos (posição 6), reduzindo, posteriormente, seu valor junto à última linha (posição 8). Com a tomada de pressão na posição relativa a 0°, as intensidades da função de densidade espectral para a freqüência de 45 Hz são menores do que no caso anterior, provavelmente por basear-se em medida realizada na esteira dos tubos precedentes, tendo seu máximo junto à segunda linha de tubos (posição 2). No entanto, pode ser percebida, até mesmo, nos resultados correspondentes às posições ensaiadas mais afastadas.

4. CONCLUSÕES

Os resultados, de maneira geral, indicam que, para as situações aqui testadas, uma perturbação externa ao banco de tubos, gerada em condições do escoamento marcadamente diferentes das existentes no interior do banco, principalmente no que diz respeito ao campo de velocidades, permanece com a mesma freqüência característica enquanto é transportada. Este fato pôde ser constatado tanto ao longo da região de escoamento entre os tubos de duas colunas centrais adjacentes, como também nas esteiras dos tubos destas colunas, através das medições de flutuações de velocidade e de pressão.

Não foram, aqui, observadas freqüências características que pudessem ser atribuídas ao processo de desprendimento de vórtices a partir dos tubos do arranjo, conforme obtido por outros autores, embora em arranjos com espaçamento relativo maior. Para a geometria empregada neste trabalho, por possuir uma região principal de passagem do escoamento ("through flow"), parece ser razoável o não surgimento deste fenômeno na faixa de espaçamento relativo em que se encontra. Por outro lado, para arranjos de geometria triangular, em que a esteira de cada tubo obrigatoriamente pertence à região de escoamento principal, é de se esperar a presença de picos nos espectros de potência das flutuações medidas, associados ao processo de desprendimento de vórtices na esteira dos tubos situados no interior dos bancos (Fitzpatrick et al., 1988 e Endres & Möller, 1996).

As diferentes condições do campo de velocidades entre o exterior e o interior do banco de tubos aliadas à comprovada manutenção de freqüências características, indicam uma provável variação nos números de onda característicos, no sentido de aumento dos comprimentos de onda das perturbações, em decorrência do aumento verificado nas velocidades, no interior do banco.

Esta combinação de efeitos indica que exitações periódicas, geradas externamente, influenciam os contornos sólidos dos tubos de um banco, com suas freqüências externas características mantidas, aumentando suas amplitudes no interior do banco. Esta constatação é reforçada pelo fato de estar disponível uma maior energia cinética do escoamento, entre os tubos de um banco, para ser parcialmente convertida em energia de pressão, transferida às fronteiras sólidas dos tubos.

5. AGRADECIMENTOS

Este trabalho foi realizado com apoio do CNPq - Conselho Nacional de Desenvolvimento Científico e Tecnológico, processos 414216/90-3 e 400180/92-8.

6. REFERÊNCIAS

Blevins, R. D. *Flow-Induced Vibration*, Van Nostrand Reinhold, New York, 1990.

Endres, L. A. M. & Möller, S. V. Estudo Experimental da Influência de Conexões entre Tomadas e Transdutores de Pressão, *Anais do 8º Simpósio Brasileiro sobre Tubulações e Vasos de Pressão*, pp.416-424, Gramado, 1994.

Endres, L. A. M. & Möller, S. V. Flutuações de Pressão nas Paredes de um Banco de Tubos com Escoamento Turbulento, *Anais do VI Congresso Brasileiro de Engenharia e Ciências Térmicas*, pp.865-870, Florianópolis, 1996.

Endres, L. A. M. & Möller, S. V. Some Characteristics of the Fluctuating Wall Pressure Field in Tube Banks, *Transactions of SMiRT 14 - International Conference on Structural Mechanics in Reactor Technology*, a ser publicado, Lyon, 1997.

Endres, L. A. M., Silva, C. & Möller, S. V. Experimental Study of Static and Dynamic Fluid Flow Loads in Tube Banks, *Transactions of SMiRT 13 - International Conference on Structural Mechanics in Reactor Technology*, pp.451-456, Porto Alegre, 1995.

Fitzpatrick, J. A., Donaldson, I. S. & McKnight, W. Strouhal Numbers for Flows in Deep Tube Array Models, *Journal of Fluids and Structures*, vol.2, pp.145-160, 1988.

Grover, L. K.& Weaver, D. S. Cross-Flow Induced Vibrations in a Tube Bank - Vortex Shedding, *Journal of Sound and Vibration*, vol.59, pp.263-276, 1978.

Païdoussis, M. P. A Review of Flow-Induced Vibrations in Reactors and Reactor Components, *Nuclear Engineering and Design*, vol. 74, pp.31-60, 1982.

Žukauskas, A. A., Katinas, V. J., Perednis, E. E. & Sobolev, V. A. Viscous Flow over Inclined In-Line Tube Bundles, and Vibrations Induced in the Latter, *Fluid Mechanics - Soviet Research*, vol.9, pp.1-12, 1980.

XIV Brazilian Congress of Mechanical Engineering
Obeid Plaza Hotel Convention Center - Bauru - SP/Brazil
December 08-12th 1997

PAPER CODE: COB269

ESCOAMENTO TURBULENTO NA SAÍDA DE UM DUTO CURVO DE SEÇÃO RETANGULAR DIVERGENTE - ESTUDO EXPERIMENTAL / *TURBULENT FLOW AT OUTLET OF A CURVED RECTANGULAR DIVERGENT DUCT - EXPERIMENTAL STUDY*

MARIA LUIZA SPERB INDRUSIAK & SÉRGIO VIÇOSA MÖLLER
Programa de Pós Graduação em Engenharia Mecânica, Escola de Engenharia - UFRGS - Porto Alegre
CEP 90.050-170 R. Sarmento Leite, 425,Porto Alegre, RS - Brasil - E-mail: svmoller@vortex.ufrgs.br

Abstract

This paper presents the experimental study of the turbulent flow in a curved duct which simulates part of a thermal-electrical power plant. Ashes, carried in the power plant by the flow of gases from the furnace, impinge on the pipes of the heat exchanger, which pre-heat water prior of the steam generator, after passing a curved duct, and produce erosion of the pipes of the heat exchanger, leading to failures which stop plant operation. Flow distribution after the curve increase the erosion near the concave wall of the duct. Classical solutions for flow redistribution in curves, like vanes, are not applicable since they could increase operational risks due to the erosion of the vanes. This problem was investigated in a scale model of the curved duct, with, for simplicity, air as the working fluid. Flow visualizations with wool threads on the duct wall, Pitot tube and hot wire measurements were applied. Based on the results, modifications in the test section were made, using boundary-layer control techniques. The results show that flow redistribution after the curve was improved, and the modifications, when implemented in the plant, may lead to safer and economical operation conditions.

Keywords

Escoamento turbulento; Dutos retangulares curvos; Anemometria de fio quente; turbulent flow; curved rectangular ducts; hot wire anemometry

1. INTRODUÇÃO

Durante o ano de 1996, enquanto este trabalho era realizado, a usina termelétrica Presidente Médici, no município de Candiota - RS, composta de duas unidades de 160MW , deixou de gerar 126 GWh por indisponibilidade devido a furos nos tubos dos economizadores das duas caldeiras, além de 2710 horas indisponíveis para serviço de troca preventiva de tubos dos mesmos economizadores, conforme relatório INDIMAN/96 da CEEE.

Esta usina aproveita as jazidas carboníferas a céu aberto do extremo sul do país, de alto teor de cinzas. Suas caldeiras apresentam, desde o início da operação, acentuados problemas de erosão causada pelas cinzas que, conforme Andrade (1985), são de granulometria fina (50%<19μm), com densidade 2,1 g/cm^3 e compostas predominantemente de partículas vítreas arredondadas de composição sílico-aluminosa e outros elementos em menor proporção.

O economizador é um banco de tubos montado transversalmente ao duto retangular formado pela união de dois dutos curvos também de seção retangular, iguais. Os dutos curvos

são levemente divergentes (a seção inicial é de 4200 por 4320 mm e a final, de 6000 por 4320 mm) e apresentam raios de curvatura variando de 3000 a 8000 mm na parede externa e de 300 a 6000 mm na parede interna. A entrada dos dutos situa-se na parede lateral no topo da caldeira, logo após uma brusca inflexão de 90^0 no escoamento. A altura da caldeira, de 60 m, corresponde a aproximadamente seis diâmetros hidráulicos.

O desgaste dos tubos é bem mais acentuado naqueles situados mais próximos à parede côncava da curva, como pode ser visto na Figura 1. Como o economizador está logo abaixo da união dos dois dutos curvos, o gráfico mostra duas regiões com maior desgaste.

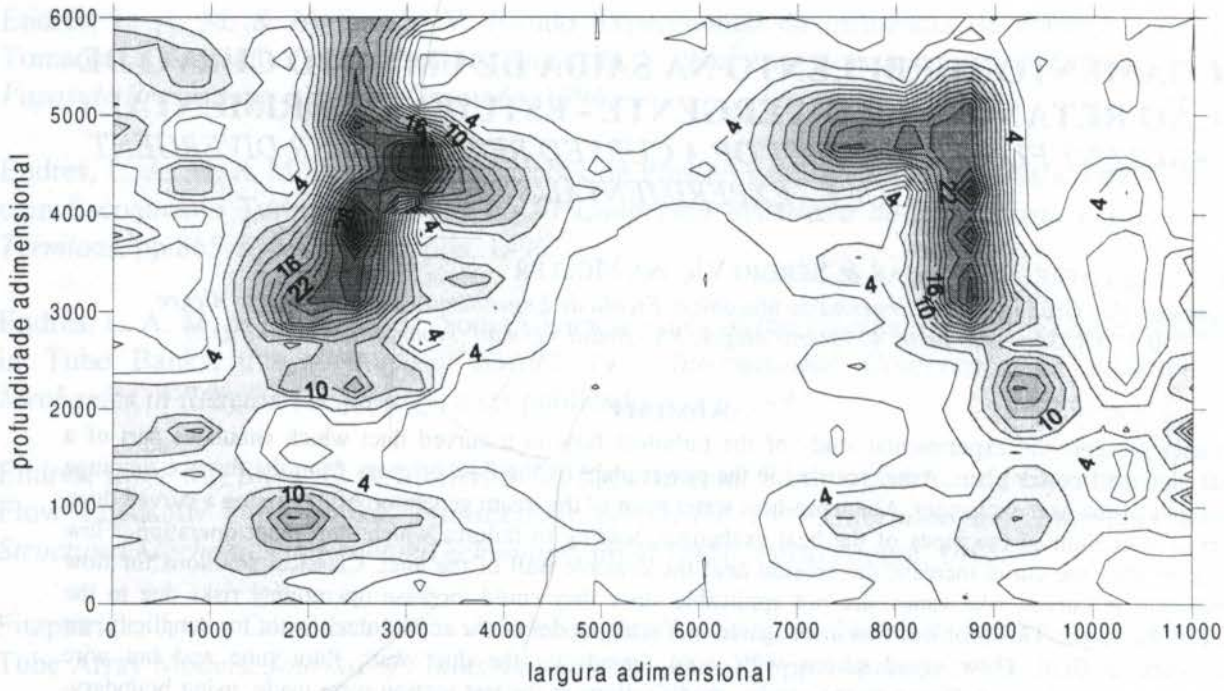

Figura 1: Gráfico de desgaste percentual dos tubos do economizador. A parte superior corresponde à região próxima à parede côncava das curvas.

A solução mais comum para escoamentos em dutos curvos é a colocação de várias chapas direcionadoras na região da curva, de modo a transformar o duto em vários dutos paralelos de menor seção. No caso que estamos estudando, a montagem destas chapas, com todos os suportes necessários, além de acrescentar um peso extra considerável à estrutura, seriam elas próprias um risco para a integridade do economizador, pois estariam sujeitas à erosão e situadas em uma região de difícil inspeção. Uma pequena parte desta estrutura, ao se desprender, causaria possivelmente grandes danos nos tubos logo abaixo.

Buscou-se então outra solução, e para isto foi montado um modelo em escala com paredes em acrílico transparente, conforme Figura 2. O número de Reynolds do escoamento nessa região da caldeira é 9.10^5. No modelo, pelas limitações do equipamento disponível, o número de Reynolds atingido é $1{,}8.10^5$.

Para este modelo foi estabelecida uma sistemática de ensaios e então testadas várias alternativas de solução. Os resultados foram comparados com os dados experimentais e numéricos de outros autores.

Em um duto curvo de seção retangular há escoamentos secundários de primeiro e segundo tipo, determinados respectivamente pela curvatura e pela forma retangular da seção.

Segundo Humphrey et al. (1981), o escoamento secundário de primeiro tipo é criado a partir do desequilíbrio entre a força centrífuga e o gradiente de pressão radial agindo sobre o fluido da camada limite das paredes laterais da curva, deslocando-o, ao longo destas paredes,

para a região interna da curva. A continuidade exige um movimento correspondente deslocando fluido, ao longo do plano de simetria, da região interna (parede convexa) para a externa (parede côncava) da curva, gerando-se assim os dois grandes vórtices em contra rotação característicos do escoamento em duto curvo.

O escoamento secundário de segundo tipo se dá ao longo da bissetriz em direção aos cantos, onde se bifurca e retorna em direções opostas (Schlichting, 1968). Este escoamento secundário é bem mais fraco que o de primeiro tipo e seu efeito se mostra pelo alongamento das isolinhas de velocidade em direção aos cantos.

Estes efeitos tornam-se mais importantes devido à presença das cinzas misturadas aos gases de combustão da caldeira, tornando o escoamento bifásico (sólido-gás). O comportamento das partículas sólidas em tubos horizontais foi estabelecido por Owen (1969), comparando o tempo de relaxação da partícula com a escala de tempo dos vórtices do escoamento.

Chow (1970) formula uma teoria macroscópica para fluido bifásico, aplicável quando o tamanho das partículas é muito menor que o comprimento característico do escoamento e quando não há troca de massa entre as fases. Ele propõe uma fórmula para a viscosidade efetiva em um escoamento incompressível, assumindo què não há velocidade relativa entre o fluido e as partículas.

Choi & Chung (1983), estudando escoamentos bifásicos em tubos, consideraram que o movimento das partículas suspensas, no conjunto, pode ser considerado como o de um escoamento secundário misturado ao escoamento primário. O trabalho conclui que, para um dado escoamento e uma dada concentração de partículas, a maior parte do atrito nas paredes é causado predominantemente pelas partículas menores.

À ação das paredes, neste problema, alia-se o fato das mesmas serem curvas, o que leva à ocorrência de separação da camada limite na parede convexa. Em um escoamento turbulento, porém, a possibilidade de separação da camada limite na presença de gradiente adverso de pressão é relativamente menor que no escoamento laminar. No entanto, as experiências de Nikuradse com canais divergentes, relatadas em Schlichting (1968) indicam separação a partir de 6 graus de divergência.

A separação da camada limite pode ser evitada de várias maneiras, tais como: a adoção de perfis adequados; a sucção do fluido na região de estagnação; a aceleração da camada limite pela injeção, na região de estagnação, de fluido com mais energia; o resfriamento da parede e a promoção de turbulência para antecipar a transição da camada limite.

O objetivo deste trabalho é, portanto, estudar o comportamento do escoamento em um duto curvo, reproduzindo em escala as condições da usina Presidente Médici e introduzindo simplificações que permitam a análise experimental em laboratório, investigando soluções exeqüíveis que possam reduzir os efeitos da erosão.

2. DESCRIÇÃO DA SEÇÃO DE ENSAIOS

A seção de ensaios, que pode ser vista nas fotografias da Figura 2, é um modelo com fator de escala 1:15,8. Esta escala foi escolhida a partir da seleção do material para o modelo do economizador, construído com varetas de solda, devido a suas características mecânicas adequadas e seu baixo preço. O modelo do tubo curvo que liga o topo da caldeira ao economizador possui um comprimento linear de 1120 mm e foi confeccionado em chapa acrílica de 10 mm e chapa de aço de 2 mm. Na entrada do duto foi montada uma seção convergente (não mostrada) para evitar os efeitos da entrada brusca.

Foram feitas algumas simplificações no modelo em relação à usina, como a montagem de apenas um duto curvo e metade do economizador. Também foram ignorados os contraventos ao longo de todo o duto e os tirantes de sustentação dos tubos do economizador.

O banco de tubos também foi simplificado, pois as varetas que simulam os tubos foram montadas de um extremo ao outro, ignorando a região de curvas de retorno existentes na extremidade. Além disso, no economizador temos 18 camadas de tubos enquanto no modelo foram montadas apenas 3. O banco de tubos tem dimensões 273 por 379 mm.

Para se medir o campo de velocidade incidente (normal) nos tubos do economizador, uma vareta foi substituída, nos pontos onde se fez medidas de pressão total, por uma agulha cirúrgica de mesmo diâmetro (2,4 mm) com uma agulha de 0,8 mm de diâmetro montada de modo a formar um tubo em L, tipo Pitot. Foram feitas seis tomadas para pressão estática ao longo da parede lateral, 5 mm acima do banco de tubos.

Ligando o banco de tubos à sucção do ventilador de 5 HP foi montada uma câmara plena com as dimensões de entrada iguais às do banco de tubos e 800 mm de altura. A vazão foi controlada por meio de um obturador de ajuste contínuo montado na descarga do ventilador. Entre o ventilador e o obturador foi montado um venturi com um manômetro de coluna d'água para a medição de vazão, a partir da qual foi calculada a velocidade média na seção de testes, usada como valor de referência para adimensionalizar todas as medidas de velocidade.

Foram feitas visualizações do escoamento por meio de fios de lã fixados ao longo de uma das paredes planas do duto curvo, como se pode ver na Figura 2. As fotos foram feitas utilizando-se filme de alta sensibilidade para permitir menores tempos de exposição.

As leituras de pressão estática, dinâmica e total foram feitas com um manômetro Mannesmann-Hartmann & Braun ARA200. Um anemômetro de fio quente a temperatura constante Dantec tipo 55M01 com sonda com fio inclinado a 45°, foi utilizado para as medidas de velocidade e ângulo de incidência do escoamento sobre os tubos. Usou-se uma placa conversora analógico/digital Keithley MetraByte/Asyst DAS-58, instalada em um computador pessoal, para a aquisição de dados. Para cada medida foram usados 10000 dados, com uma freqüência de aquisição de 500 Hz.

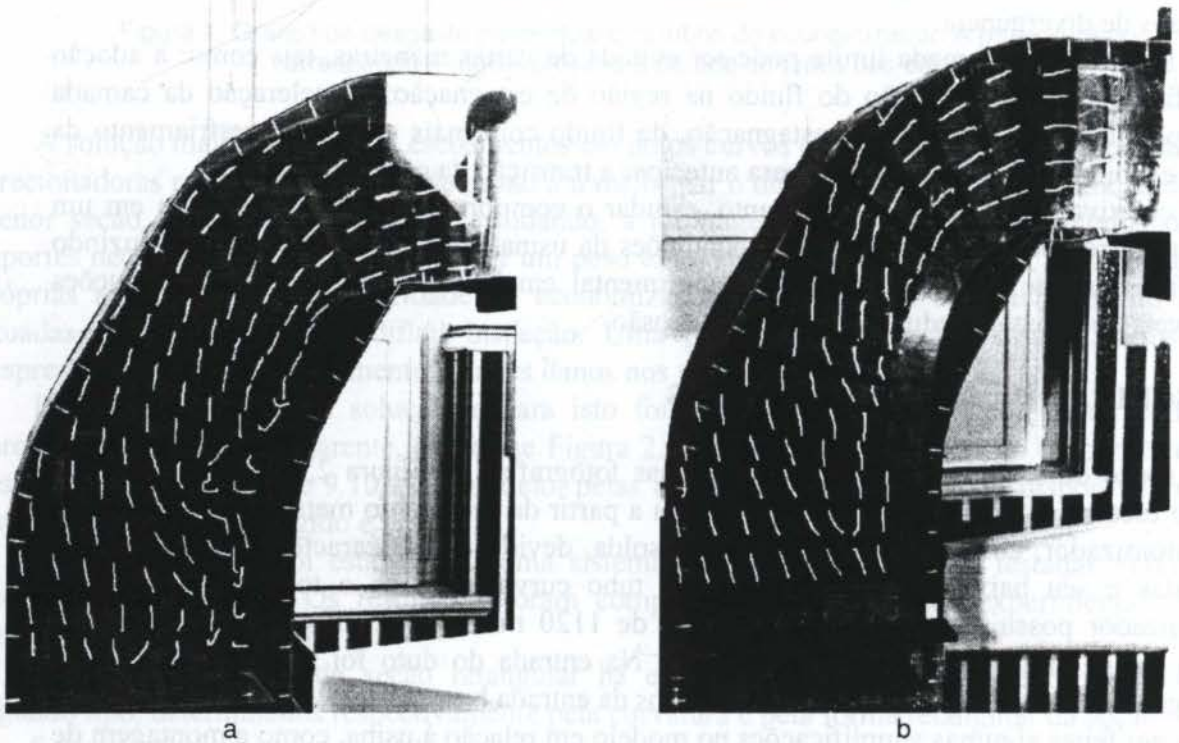

Figura 2: Vista da seção de ensaios: a) configuração original e b) modificação proposta. Visualização do escoamento com fios de lã.

3. ENSAIOS

A visualização do escoamento (Figura 2a) sugere a separação da camada limite logo após a primeira curva da parede interna do duto. Idelchik (1986) e Kim (1994) mostram que, na região de entrada na curva do escoamento, há um aumento de pressão na parede côncava do duto e uma diminuição na parede convexa. A passagem do escoamento da seção curva para a reta, por outro lado, é acompanhada pelo efeito inverso: diminuição de pressão na parede convexa e aumento na parede côncava. Isto cria as condições para a separação da camada limite e o efeito será tanto mais acentuado quanto mais aguda a curvatura da parede convexa. Idelchik sugere que o raio de curvatura deve ficar entre 1 e 2 vezes o diâmetro do duto. No presente caso o raio da primeira curvatura é de 0,05 vezes o diâmetro do duto. Fica bastante claro que há efetivamente separação da camada limite com a conseqüente redução da área útil do duto e o aumento das velocidades na área remanescente. Foram desenvolvidos estudos com técnicas de controle de camada limite, tais como a colocação dos "arames de tropeço" de Prandtl e de canais ao longo da parede interna da curva para injetar fluido com mais energia na camada limite separada, todos com resultados insatisfatórios.

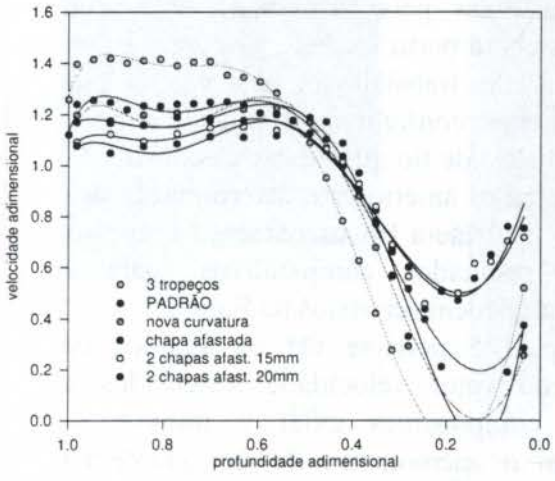

Figura 3: Comparação de perfis de velocidade na seção central do duto para as diversas configurações.

Experimentou-se então uma solução mista: instalou-se uma parede falsa refazendo a parede convexa e eliminando a inflexão abrupta existente. Acima desta parede foi colocada outra de modo a formar, com a primeira, um canal por onde o fluido com mais energia vai escoar até a região com tendência à separação, sendo então injetado na camada limite. A Figura 2b mostra a visualização do escoamento com as paredes instaladas.

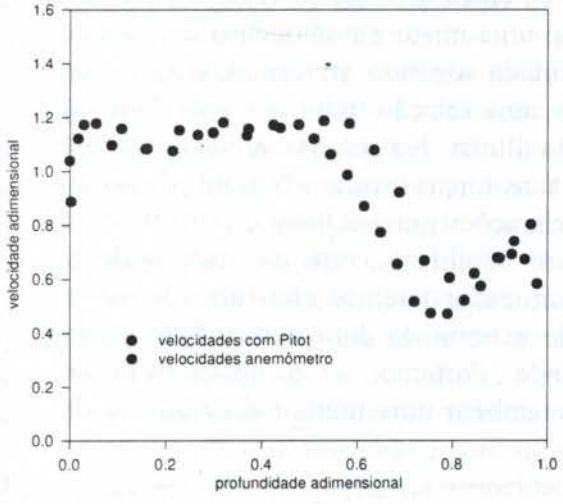

Figura 4: Comparação entre as leituras de velocidade feitas com Pitot e com anemômetro de fio quente.

Esta última solução mostrou-se a mais eficiente das investigadas, como pode ser visto na Figura 3, onde aparecem os perfis de velocidade ao longo da linha central do economizador, para as diversas alternativas testadas. Enquanto soluções como 3 tropeços aumentaram a velocidade justamente na região onde ocorrem os maiores desgastes, o que certamente iria aumentar este desgaste, a solução do canal na região da parede convexa do duto curvo, aumentando as velocidades nesta região, produziram o efeito de diminuí-la na região da parede côncava. Foram também testados vários raios de curvatura, além de uma distância maior entre as paredes do canal. O melhor desenho para as paredes propostas é o que aparece na Figura 2b, onde vemos a visualização do escoamento para esta situação. Observa-se que os sinais de separação da camada limite desapareceram, pois as posições dos fios de lã, sugerindo linhas de corrente, tornam-se regulares em toda a seção.

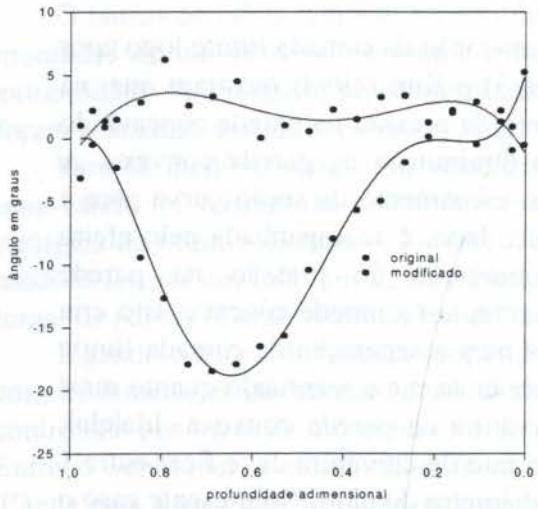

Figura 5: ângulos de incidência do vetor velocidade sobre os tubos do economizador, calculados a partir das leituras do AFQ.

Todos os ensaios foram feitos usando-se a sonda tipo Pitot para a medição das pressões totais e as tomadas de parede para as pressões estáticas. As velocidades foram adimensionalizadas pela velocidade média na seção, calculada a partir da leitura do venturi. A última etapa do trabalho foi a medição das velocidades, nas configurações inicial e final, com anemômetro de fio quente, para comparação com os resultados anteriores e determinação dos ângulos de incidência do escoamento sobre os tubos. Os resultados comparativos, para a situação final, podem ser vistos na Figura 4.

Na Figura 5 pode-se ver os ângulos de incidência do vetor velocidade, calculados a partir das componentes axial e transversal, obtidas com o anemômetro de fio quente na seção central do banco de tubos. Os ângulos correspondem à defasagem em relação à incidência ortogonal aos tubos, sendo positivo o sentido horário. Observa-se que, enquanto na situação original há ângulos de até 20 graus, com a modificação proposta a direção do escoamento incidente oscila entre 0 e 5 graus.

Quanto ao papel da cinza no mecanismo da erosão, foi usado um critério estabelecido por Owen (1969), que compara o tempo de relaxação das partículas com a escala de tempo dos vórtices do escoamento. Por este critério, as partículas de cinza acompanham os vórtices do escoamento e este poderia, então, ser considerado como uma mistura homogênea de gases e partículas de cinza. A viscosidade da mistura foi calculada segundo as fórmulas de vários autores, apresentadas no trabalho de Chow, resultando uma relação entre a viscosidade da mistura e a viscosidade do gás da ordem de 0,02% desta última. No entanto, ainda conforme critérios de Owen, para as densidades do nosso problema, as forças inerciais têm influência no escoamento e teremos que levar em consideração as acelerações gravitacional e centrífuga no comportamento das partículas. A partir da equação de equilíbrio entre as fases pode-se concluir que, para a geometria e velocidades do economizador teremos efetivamente maior concentração de partículas na região próxima à parede externa do duto curvo. Este efeito cresce quadraticamente com o aumento da velocidade. Portanto, se a distribuição de velocidades for melhorada ao longo do duto, teremos também uma melhor distribuição da concentração de partículas.

4. RESULTADOS

A distribuição de velocidades incidentes no banco de tubos pode ser vista na Figura 6, na configuração original e na configuração final (duto com as duas paredes propostas), junto com os resultados experimentais de Humphrey et al. (1981) para escoamento turbulento, desenvolvido, em duto com curvatura constante. Observa-se a região de estagnação na configuração original (abaixo na Figura 6a) e como esta região desaparece na configuração final. As isolinhas tomam um aspecto semelhante às do trabalho de Humphrey, com as diferenças sendo explicadas por ser o escoamento do presente trabalho não desenvolvido, com um maior gradiente de velocidade junto à parede e um patamar na direção da parede externa (acima na figura) ocupando mais da metade da seção transversal.

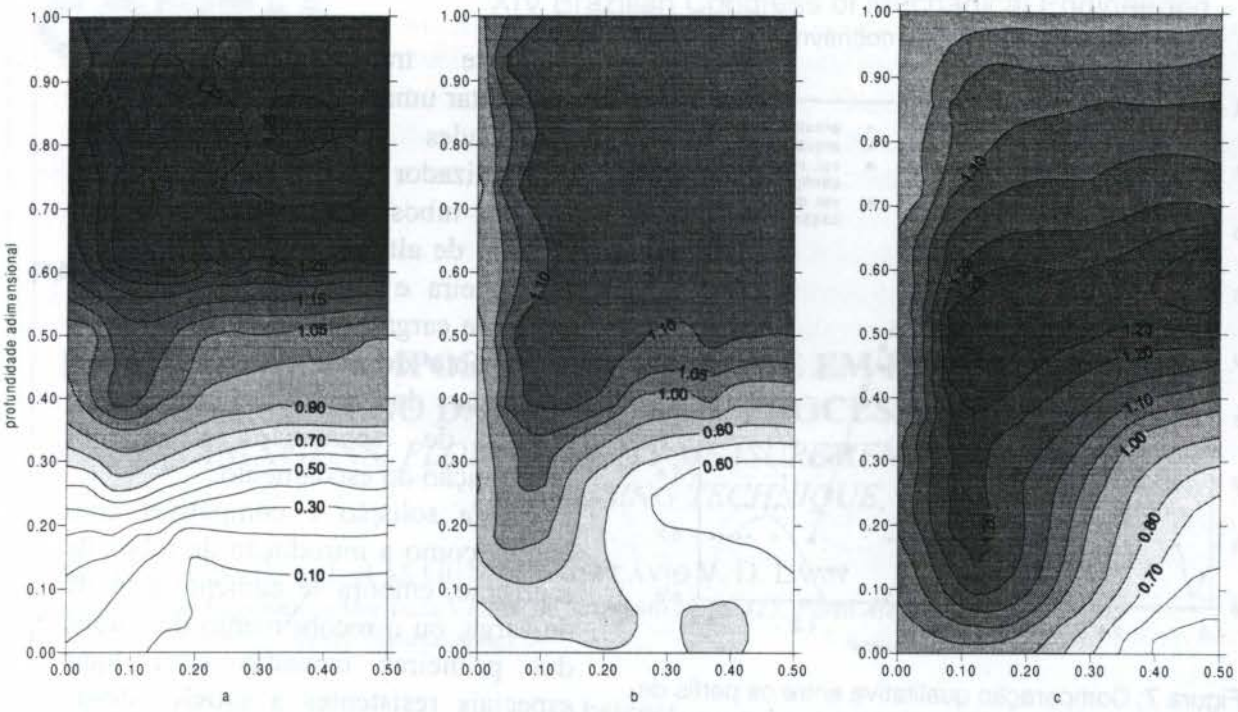

Figura 6: Comparação entre as isolinhas de velocidade axial adimensionalizadas pela velocidade média da seção para as configurações a)inicial, b)final e c)Humphrey.(1981).

Observando-se as Figuras 3 e 6 pode-se ver que as velocidades ficaram melhor distribuídas na seção do economizador na configuração final, tendo desaparecido a região de separação da camada limite. Embora o gradiente de velocidade ainda ocupe uma região bastante grande na parede convexa da curva, se compararmos com a lateral, isto pode ser atribuído ao duto curvo e não à separação, como se conclui comparando-se as Figuras 6b e 6c, pois no trabalho de Humphrey não há separação da camada limite. A visualização do escoamento, Figura 2b, também mostra linhas de corrente mais regulares, sem indício de separação. Como conseqüência do aumento da seção efetiva do duto, houve uma redução significativa das maiores velocidades antes verificadas na região de maior desgaste. A uniformização das velocidades (Figura 6b) deverá contribuir para o aumento do rendimento do economizador, pois o gradiente de temperaturas nas paredes dos tubos será mais uniforme em todo o economizador. Além disso, a perda de carga ao longo do duto curvo fica reduzida com a eliminação dos grandes vórtices na região de separação.

Na Figura 7 são mostrados, para uma seção transversal, na metade da largura total do banco, no modelo, os perfis de velocidade, antes e depois da alteração proposta por este trabalho. Também estão desenhados os perfis de erosão dos tubos do banco na mesma seção, para os dois dutos curvos, conforme os mesmos dados da Figura 1. A diferença entre o perfil conforme configuração atual da Figura 7 e o perfil padrão da Figura 3 deve-se ao fato de, na caldeira real, ter sido montado, há alguns anos, um defletor na parede côncava da curva, na tentativa infrutífera de desviar o escoamento da região de erosão crítica, cujo efeito foi diminuir a velocidade na região bem próxima da parede. O perfil de velocidade conforme configuração atual da Figura 7 foi feito com um defletor em escala montado no modelo. Nota-se que às regiões de maior erosão correspondem as de maior velocidade. Como a alteração proposta reduz as velocidades nesta região, isto irá determinar um menor índice de erosão dos tubos do economizador, pois a erosão é proporcional à energia cinética das partículas, que podem ser consideradas como tendo a mesma velocidade do escoamento, como já foi visto.

5. CONCLUSÃO

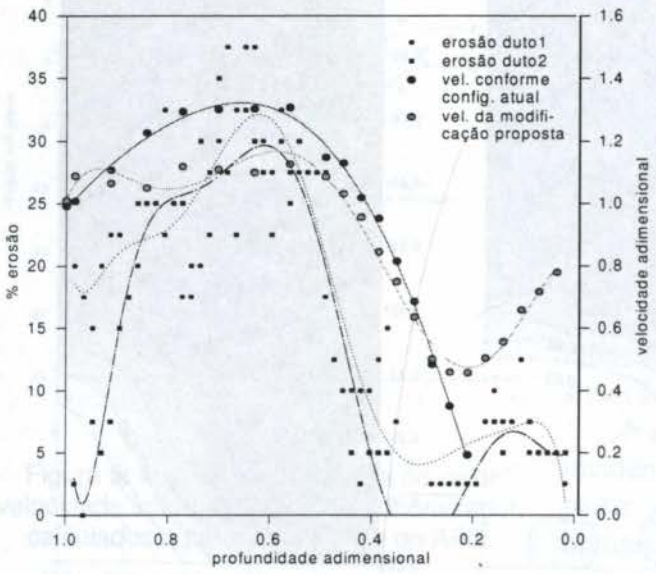

Figura 7: Comparação qualitativa entre os perfis de erosão dos tubos do economizador nas seções centrais dos dutos curvos e o perfil de velocidades na mesma região do modelo em escala.

Este trabalho propõe-se a apresentar uma solução para reduzir as velocidades incidentes no economizador e assim aumentar a vida útil dos tubos, o que foi feito com o mínimo de alterações na configuração da caldeira e ainda com redução da perda de carga e possível aumento do rendimento do economizador, com a supressão dos grandes vórtices da região de separação e melhor distribuição do escoamento.

Esta solução é compatível com outras, como a introdução de tubos de sacrifício, embora se aumente a perda de carga, ou o recobrimento dos tubos das primeiras camadas com ligas especiais resistentes à erosão, desde que não se altere significativamente o rendimento do trocador.

6. BIBLIOGRAFIA

Andrade, A., *A caracterização das cinzas volantes do carvão de Candiota*, Dissertação de Mestrado, PPGEMM/UFRGS,1985

Choi, Y. D. e Chung , M. K., Analysis of Turbulent Gas-Solid Suspension Flow in a Pipe, *J. of Fluids Engineering, Transactions of the ASME*, vol. 105, 1983

Chow, J. C. F., On a Macroscopic Theory of a Two-phase Fluid Flow and its Effective Viscosity, *First International Conference on the Hydraulic Transport of Solids in Pipes,* 1970

Hinze, J. O., *Turbulence*, McGraw-Hill Book Company, 1959

Humphrey, J. A. C., Whitelaw, J. H. e Yee, G., Turbulent flow in a square duct whit strong curvature, *Journal of Fluid Mechanics*, vol.103 ,pp 443-463, 1981

Idelchick, I. E., *Handbook of Hidraulic Resistance*, Hemisphere Publishing Corporation, pp. 265-328, 1986

Kim W. J., e Patel, V. C., Origin and Decay of Longitudinal Vortices in Developing Flow in a curved Rectangular Duct, *Journal of Fluids Engineering*, vol. 116 pp. 45-52, 1994

Owen, P. R. , Pneumatic Transport, *Journal of Fluid Mechanics*, vol. 39 pp. 407-432.1969

Schlichting, H., Boundary-Layer Theory, McGraw-Hill, New York (1968)

XIV Brazilian Congress of Mechanical Engineering
Obeid Plaza Hotel Convention Center - Bauru - SP/Brazil
December 08-12th 1997

PAPER CODE: COB276

MEDIÇÃO DE CAMPOS DE VELOCIDADE EM ESCOAMENTOS COM O EMPREGO DA TÉCNICA DE PROCESSAMENTO DE IMAGENS/ *FLOW VELOCITY MEASUREMENT USING IMAGE PROCESSING TECHNIQUE*

VILSON C. S. FERREIRA, LUCAS GUTKOSKI & FLÁVIO V. D. LAAN
Departamento de Engenharia Mecânica - UFRGS, Sarmento Leite, 425, Porto Alegre, RS CEP 90050-170, e-mail, vferreir@vortex.ufrgs.br

Abstract

One of the great problem for measuring flow field properties, such as velocity and vorticity, using an intrusive or nonintrusive techniques, is the time consuming. Hot-Wire (HW) and Laser Doppler Velocimetry (LDV), apart from their advantages and disadvantages, demand great effort and care for measuring extensive flow field. Highly unsteady flow is another type of problem not solved when using HW or LDV because both are local velocity techniques, that is, resolving the velocity field at each point at a time. Measuring flow properties having spatial and temporal information is now possible due to new techniques appearing since the great development achieved by the laser technology and the fast digital processors. Particle Image Velocimetry (PIV) is one emerging technology with the proposal of solving part of these measuring flow field problems. The paper describes two developing methodologies for measuring low and fast velocities inside an extensive field flow of a tundish model used in metallurgical process.

Palavras Chave

Processamento de Imagens, Video Velocimetria, Velocimetria por Processamento de Imagens.
Image Processing, Video Velocimety, Particle Image Velocimetry

1. INTRODUÇÃO

Técnicas não intrusivas para a medição de velocidades de fluidos tem tido grande desenvolvimento nos últimos anos. Suas vantagens, quando comparadas com técnicas tradicionais intrusivas, tais como tubos de pitot, anemômetro de fio quente etc.., são bastante óbvias. Nestas últimas, a calibração dos sensores, a não linearidade do sinal, além, da natural perturbação local do fluido exatamente no ponto de medida, são desvantagens significativas. O Laser Doppler Velocímetro LDV e o Doppler Acústico ADV foram as primeiras técnicas não intrusivas aplicadas a medição pontual de velocidade. O LDV utiliza as características da luz coerente e suas propriedades para medir diretamente a velocidade de partículas em deslocamento no fluido. Sob certas circunstâncias esta velocidade é considerada a própria velocidade do fluido. Além de ser uma técnica não intrusiva tem características "sui generis" pois apresenta uma resposta direta (não é necessário calibração), muito rápida e pode atingir pontos até então não acessíveis às técnicas convencionais. Sua incerteza de medição, sob condições controladas, é muito baixa. A caracterização de um campo de velocidade, no entanto, é feita como nas técnicas convencionais, ou seja, com a determinação da velocidade

em sucessivos pontos. Se o campo de velocidades a ser analisado tem dimensões reduzidas o LDV não oferece grandes inconvenientes pois, normalmente, a frequência de aquisição dos dados é muito alta. Porém, quando as geometrias em estudo são muito amplas o tempo de medida é longo e as condições de escoamento durante o teste podem facilmente se alterar. Este é um dos grandes inconvenientes da medição não simultânea de velocidades. Recentemente, há pouco mais de uma década conforme Lourenço (1996), com o avanço da tecnologia de microprocessadores dedicados ao processamento de imagens e o aprimoramento das fontes de laser de altas potências, foi possível desenvolver uma nova técnica para a medição de velocidade em amplos escoamentos, denominada de "Velocimetria por Processamento de Imagens de Partículas" (PIV - Particle Image Velocimetry). Esta técnica apresenta as vantagens do LDV (não intrusiva) aliada à simultaneidade de medição não existente nas anteriores.

O objetivo do presente trabalho é apresentar um sistema tipo PIV bidimensional para o levantamento dos campos de velocidade em áreas internas de um modelo físico a frio de um distribuidor de lingotamento contínuo empregado na produção de aços especiais. O sistema de medição de velocidade emprega uma fonte de laser, um conjunto de lentes para produzirem um plano iluminado onde imagens de partículas disseminadas no escoamento são registradas por meio de uma câmara de vídeo de alto desempenho. Dois algorítmos de processamento de imagens são apresentados, o primeiro para baixas velocidades e o segundo para altas velocidades.

2. DESCRIÇÃO DO SISTEMA

O sistema de medição de velocidade por processamento de imagens de partículas empregado no presente projeto é formado dos seguintes componentes básicos: "componentes ópticos", "componente de captura de imagens" e do "processador de sinal". Os testes de desempenho e validação do sistema de medição desenvolvido são aplicados no modelo físico do distribuidor de lingotamento contínuo representado esquematicamente na figura 1. Foi construído em acrílico transparente com forma geométrica definida pela indústria siderúrgica e com as suas dimensões em verdadeira grandeza para uma melhor similaridade com o processo real, conforme Szekely et al. (1988) empregando-se a água como fluido de circulação.

Os componentes ópticos são responsáveis pela geração do plano de iluminação. Uma fonte de laser modelo 2016 (Spectra Physics, 4w) do tipo íons de argônio, uma sonda composta por cabos de fibra óptica e lentes esféricas (Dantec série 60X) e uma lente cilíndrica produzem um intenso plano de laser com abertura de 40^0 e espessura de 5mm na região central do distribuidor, variando de ± 4 a $\pm 5{,}5$ mm ao longo de todo o plano.

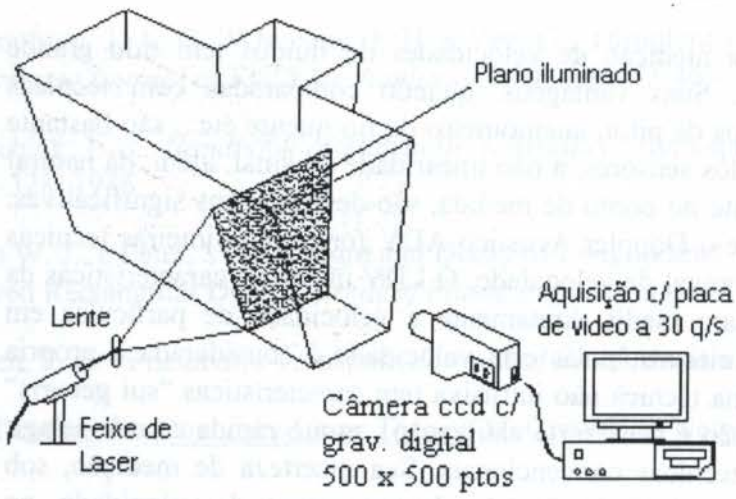

Figura 1 - Medição de Velocidade com Processamento de Imagens num distribuidor de Lingotamento Contínuo

A captura de imagens é feita por uma câmera de vídeo modelo VR-1000

(Sony), colorida (3xCCD) de 500 x 500 "pixels", com dezenove opções de velocidades de obturação (de 1/4 à 1/10000 segundos) e gravação digital em fita magnética tipo DV com resolução de 180.000 pontos na reprodução. Partículas de baixa granulometria (500μm máximo) e com densidade próxima da água (δ=1,03) foram empregadas para a geração de discretos pontos em movimento. Imagens foram também feitas sem a adição de partículas empregando-se somente água potável.

O processamento digital de sinais é feito por meio de um cartão de aquisição (TR 288) para trabalhos em velocidades de captura até 30 quadros por segundo e um cartão (EPIX 4MEGVÍDEO) para mais altas velocidades, até 9000 quadros por segundo, resolução de até 4000 "pixeis" por linha e de até 16000 linhas por quadro. As imagens gravadas são processadas num microcomputador (Pentium 200PRO) por meio de um algoritmo para a solução de imagens desenvolvido em linguagem C^{++}. No presente estágio de desenvolvimento o processamento é feito posteriormente com as imagems gravadas em fita DV, no entanto, o processamento em tempo real estará disponível num futuro próximo. Mesmo em tempo real, gravações em fita DV serão feitas a fim de que se disponha de dados para pós-processamento e permitir melhor análise de regiões de interesse.

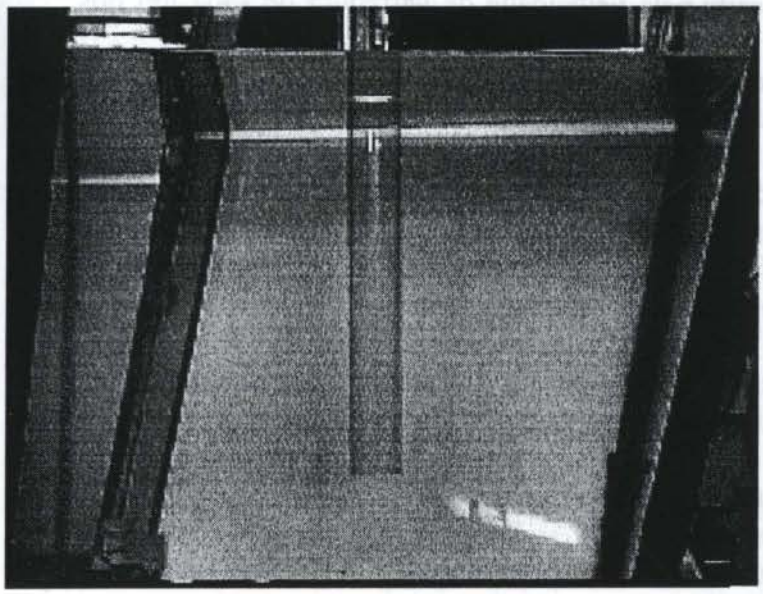

Figura 2 - Vista parcial do distribuidor na posição de entrada

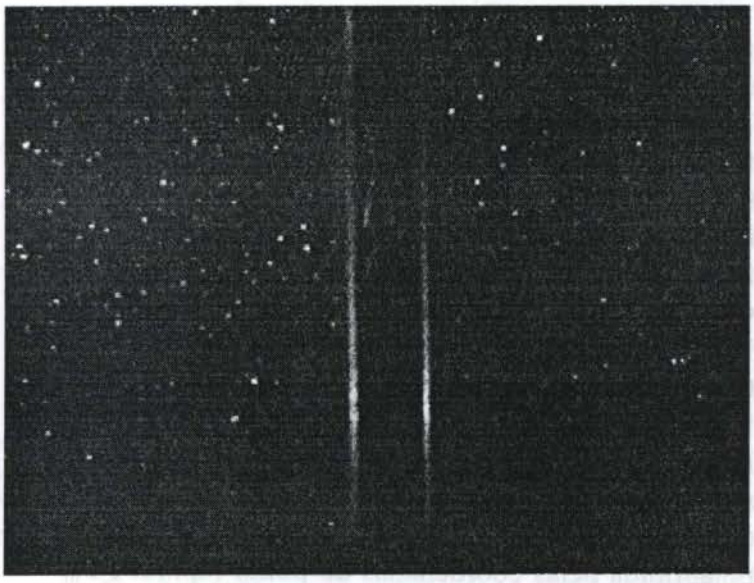

Figura 3 - Imagem adquirida pela câmara de video

3. GERAÇÃO E AQUISIÇÃO DE IMAGENS

A figura 2 apresenta uma vista parcial do distribuidor na posição de entrada do fluido. O conduto de alimentação descarrega água num jato vertical descendente que se mistura com o restante do fluido do distribuidor. O escoamento é do tipo jato do mesmo fluido promovendo uma intensa mistura e trocas de quantidade de movimento ("Free Shear Layer").

A figura 3, apresenta a mesma vista iluminada com um plano de laser e adquirida com auxílio da câmara de video. Esta imagem capturou partículas de "pliolite - S6H" em movimento no interior do distribuidor e que será processada

conforme procedimentos abaixo.

4. PROCESSAMENTO DAS IMAGENS

Duas técnicas de processamento de imagens estão em desenvolvimento. A primeira para velocidades baixas onde o acompanhamento das trajetórias das partículas é feito pela superposição de quadros utilizando-se como base de tempo a velocidade de obturação de ¼ até 1/30 segundos pois a câmera adotada possibilita reprodução das imagens nestas velocidades de gravação. A segunda para velocidades mais altas onde uma partícula é acompanhada na mesma imagem utilizando-se como base de tempo a velocidade de obturação (de 1/30 até 1/10000 segundos) multiplicada pela velocidade de varredura de cada um dos campos que compõe um quadro.

4.1 Processamento com a Superposição de Quadros

O processamento com superposição de quadros pode ser explicado com auxílio da figura 4. Consiste, em localizar uma mesma partícula numa sequência de quadros diferentes perseguindo-se o seu traçado e calculando suas componentes de velocidade em cada quadro. Na figura as duas imagens representam uma mesma partícula em dois instantes diferentes.

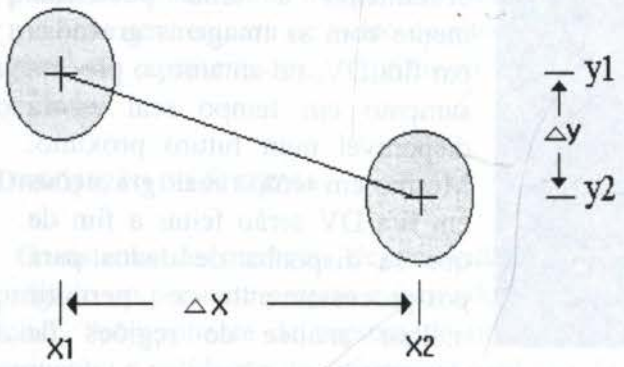

Figura 4. Processamento por superposição de quadros.

As componentes do vetor velocidade no plano (x e y) são calculadas conforme as Equações abaixo:

$$u = \lim_{t_2 \to t_1} \frac{x_2 - x_1}{t_2 - t_1} \quad \text{e} \quad v = \lim_{t_2 \to t_1} \frac{y_2 - y_1}{t_2 - t_1} \qquad (1)$$

Uma sequência de quadros como o da figura 3 é tomada na região de determinação dos campos de velocidades. Inicialmente as imagens são "filtradas" (limpas) identificando-se somente as partículas traçadoras no fluido. Para se fazer esta identificação foi desenvolvido um algoritmo para analisar o arquivo na forma hexadecimal da imagem. A matriz da imagem é processada de forma a inverter o fundo, identificar o tubo de entrada que servirá como padrão de referência espacial deste plano e dar um código de cor para cada quadro de forma a distinguí-lo de seus quadros subsequentes.

O código de cores (nível numérico) torna possível a identificação da direção da partícula eliminando-se assim a ambiguidade de sentido do vetor velocidade, problema existente na grande maioria dos sistema de processamento por imagens (Adrian, 1991).

Obtidas as imagens filtradas de cada quadro a posição de uma dada partícula ***i*** pertencente a um quadro ***n*** (nível de cor) é definida pelas coordenadas do ponto ("pixel", P_{in} $[x_i, y_i]$) no centro geométrico da partícula. Um ponto correspondente a uma mesma partícula tem, em quadros subsequentes, cor e coordenadas diferentes. Uma superimagem é montada com a superposição de um número de quadros escolhidos sequencialmente. Uma matriz

esparsa de posição (500 x 500) para a superimagem é gerada para a obtenção das velocidades instantâneas a cada quadro. Uma partícula é considerada a mesma em quadros subsequentes quando o ponto é unívoco num entorno e comparece em mais de dois quadros consecutivos. Caso contrário ela é descartada. A densidade de partículas capturadas pela câmera define o número de superposição de quadros. Quanto maior a densidade, menor deverá ser o número de quadros a serem superpostos e vice-versa. Neste tipo de processamento a densidade de partículas não deve ser muito alta pois um mínimo de dois quadros são necessários para o processamento.

Figura 5 - Imagem superposta com 14 quadros.

A figura 5 mostra uma superimagem com quatorze quadros onde o tempo de exposição de cada quadro é de 1/30 segundos e o tempo total de observação aproximadamente de ½ segundo. Nesta figura pode se notar que nem todas as partículas (pontos) comparecem nos quatorze quadros, porém diversas trajetórias de partículas podem ser facilmente visualizadas pela sequência de cores.

A figura seguinte (figura 6) mostra duas superimagens superpostas (azul e preta) após o seu processamento, com o vetor velocidade identificado em módulo, direção e sentido. Cada superimagem foi processada utilizando sete quadros na mesma base de tempo da figura anterior, 1/30 segundos por quadro.

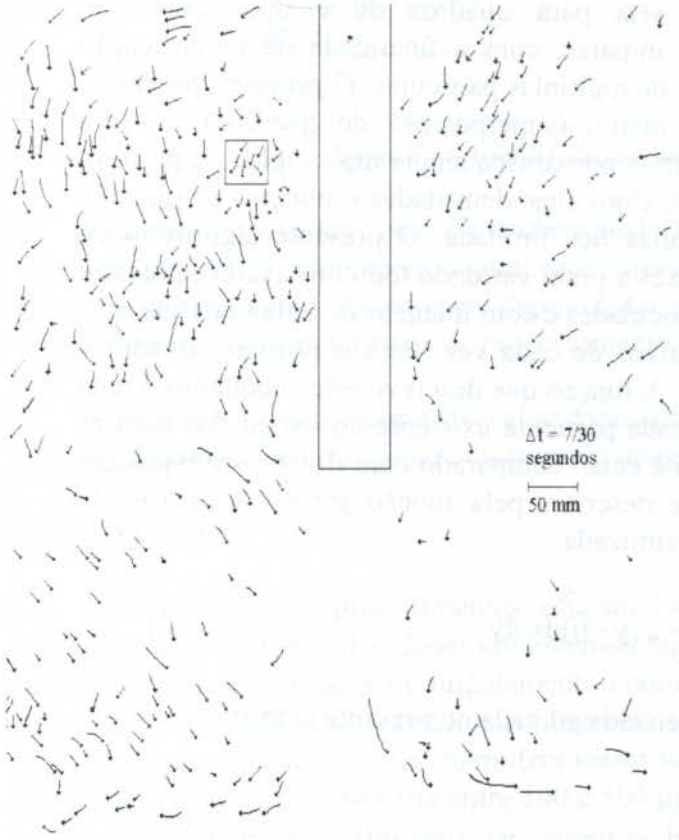

Figura 6 - Campo bidimensional da velocidade V

O campo total de velocidade será obtido pelo processamento de diversas superimagens onde a análise do escoamento médio será feita calculando-se a média das componentes de velocidades ($\overline{u}$ e $\overline{v}$) em cada ponto P_{in} e os parâmetros de turbulência ("skewness", "flatness", "turbulence intensity") em função das respectivas flutuações de velocidades.

4.2 Processamento na Velocidade de Varredura de Campo

Uma das grandes dificuldades da técnica PIV é a captura de imagens em altas velocidades. A utilização de câmeras de obturação rápida resolve parcialmente o problema pois quanto maior a velocidade de captura mais iluminada deve ser a imagem das partículas ou maior definição deve ter a câmera. No presente

caso a limitação de iluminação é de 4 lux com uma abertura focal de 1,6. Este processamento consiste em operar uma imagem capturada numa determinada velocidade de obturação e desmembrá-la em dois quadros formados pelos dois campos de linhas entrelaçadas, o campo de linhas ímpares (262 e ½ linhas) e o de linhas pares (262 e ½ linhas). Uma mesma partícula é capturada em diversas linhas porém o algorítmo caracteriza-a como um ponto ("pixel") no centro geométrico da imagem da partícula. Cada linha do campo par ou ímpar conterá somente um ponto identificando a mesma partícula. A subsequente superposição dos dois quadros de linhas pares e ímpares permite identificar uma mesma partícula deslocada na linha superposta.

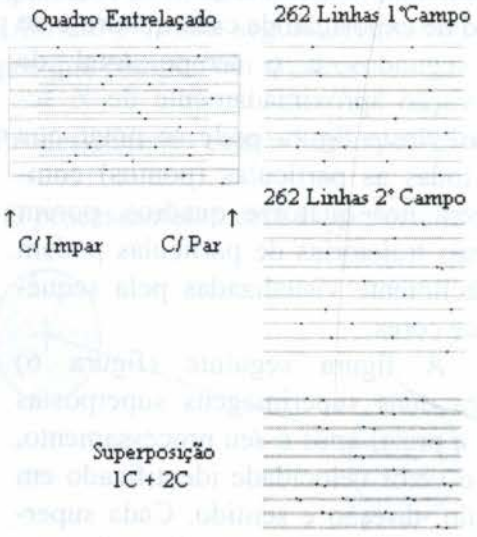

Figura 7 - Superposição de dois campos entrelaçados

A figura 7 mostra um quadro entrelaçado de 525 linhas, composto pelos dois campos, o par e o ímpar. Pode ser observado na mesma figura, na sua parte inferior, a superposição dos dois campos onde o deslocamento das partículas é visualizado na mesma linha superposta.

5. CORRELAÇÃO DE QUADROS SUBSEQUENTES

Para os dois processamentos anteriormente descritos é possível aplicar-se um algorítmo de correlação entre quadros consecutivos, seja para um quadro completo seja para quadros de .campos pares ou ímpares, com a finalidade de identificação de múltiplas partículas. O primeiro processamento (superposição de quadros) usa um número maior de quadros e uma técnica mais direta por consequência mais rápida. É próprio, no entanto, para baixas densidades de partículas. Com altas densidades o número de quadros deve ser reduzido e a identificação das partículas fica limitada. O presente algorítimo de correlação é mais lento pois a análise é feita pixel-a-pixel varrendo todo um quadro, porém é muito mais precisa principalmente para altas velocidades e com imagens de baixa qualidade.

O algoritmo analisa dois quadros consecutivos de cada vez. Para o primeiro quadro é escolhido um subquadro com x por y elementos. A função que descreve este subquadro é uma matriz f(x,y) que relaciona as coordenadas de cada partícula existente no subquadro com as coordenadas dos pixels do quadro. O subquadro é então comparado com diversos subquadros homólogos definidos no quadro subsequente e descritos pela função g(x,y). A função de correlação dada pela equação abaixo é então maximizada.

$$H(\zeta,\eta) = f(x,y) \otimes g(x,y) = \iint_{\lambda\lambda} f(x,y)\cdot g(x-\zeta, y-\eta)\,dx\,dy \qquad (2)$$

A equação seguinte apresenta a forma discretizada adotada no presente algoritmo:

$$H(\zeta,\eta) = \sum_{i=0}^{m-1}\sum_{j=0}^{n-1} f(x_i, y_j)\cdot g([x-\zeta]_i, [y-\eta]_j) \qquad (3)$$

A figura 8 auxilia o entendimento do algoritmo de identificação de partículas através da correlação entre dois quadros consecutivos. Um conjunto de partículas do primeiro subquadro é comparado, ao longo de todo o segundo quadro, com deslocamentos varrendo toda a imagem. Se o formato das partículas do primeiro subquadro diferir completamente do formato das partículas de todas as possibilidades no segundo quadro, diminui-se a velocidade de obturação de captura das imagens para que o deslocamento das partículas não se altere muito. A dimensão da matriz inicial pode também ser modificada com a finalidade de otimizar o algoritmo.

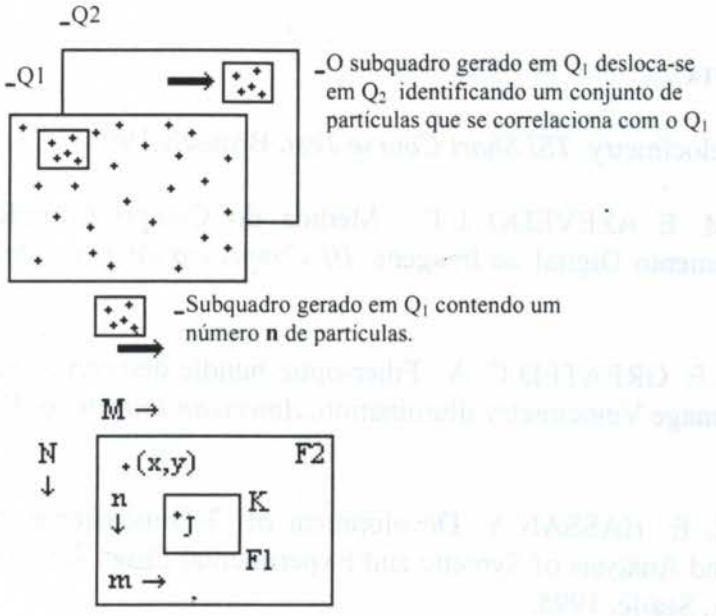

Figura 8 - Identificação das partículas por Correlação

Processo de "overlay" de telas também pode ser criado, mostrando-se simultaneamente a imagem gravada e a imagem digitalizada, possibilitando assim a comparação das duas imagens integralmente. As imagens digitalizadas são gravadas em formato "BMP" e "TIFF" para serem tratadas por técnicas de processamento de imagens desenvolvidas em linguagem C e C^{++}.

A medição de um campo de velocidades tridimensional também será possível com a utilização de mais de uma câmara capturando imagens, simultaneamente.

6- CONCLUSÕES

Embora os dois procedimentos estejam longe de estarem concluídos já é possível levantar-se campos de velocidades em extensas regiões de escoamento, como por exemplo no interior de um distribuidor de lingotamento contínuo. A validação dos dois processamentos está sendo feita com auxílio de LDV em regiões controladas e restritas do mesmo distribuidor.

As duas técnicas descritas permitem medir velocidades de partículas numa faixa de 0,01 até 1000 m/s com granulometria entre 100 e 500 μm. Para velocidades maiores ou a utilização de partículas menores (<100 μm), tais como as próprias impurezas existentes no fluido em escoamento, será necessário dispor-se de uma câmera mais sensível com velocidades de reprodução da ordem de 340 quadros por segundo.

Uma análise de incerteza de medição para o primeiro sistema de processamento de imagens, "processamento com superposição de quadros" está em andamento e seus resultados devem ser publicados oportunamente.

7- AGRADECIMENTOS

Os autores agradecem a FAPERGS e a Aços Finos Piratini pelo suporte financeiro dedicado ao projeto bem como aos participantes do LTMF-UFRGS pela colaboração no presente trabalho.

8 - REFERÊNCIAS E BIBLIOGRAFIA

ADRIAN R.J. Particle Image Velocimetry. *TSI Short Course Test.* Brussels,1991.

ALMEIDA J.A., CUNHA C.M. E AZEVEDO L.F. Medida do Campo Completo de Velocidade Através do Processamento Digital de Imagens. *III Congresso de Eng. Mecânica Norte-Nordeste* . Belem, 1994.

ANDERSON D.J., JONES J. D. E GREATED C. A. Fiber-optic-bundle delivery system for high peak power Laser Particle Image Velocimetry illumination. *American Intitute of Physics, Rev. Sci Instrum,* UK, 1996.

COSTES S. V., OKAMOTO K. E HASSAN Y. Development of 3-Dimensional Particle Image Velocimetry Algorithm and Analysis of Syntetic and Experimental Flow. *International Symposium on Flow Visulization*, Seatle, 1995.

GONZALES R. E WOODS R. *Digital Imaging processing.* Massachusetts. Addison Wesley, 1993.

LIM J.S. *Two-Dimensional Signal and Image Processing.* N.Y. Prentice Hall Inc., 1990.

LOURENÇO, L.M. Particle Image Velocimetry - Lecture Series 1996-03, von Karman Institute for Fluid Dynamics, Belgium, Jun/96.

MASTERS, T. *Signal and Image Processing with Neural Net and C^{++} Source Book.* N.Y. Willey, 1994.

OPPENHEIM A. V. *Aplication of Digital Signal Processing.* N.J Prentice Hall Inc., 1990

PERSON D. *Image Processing.* U.K. Mcgraw-Hill, 1991

RABINER L.R. E GOLD B. *Theory and Application of Digital Signal Processing.* N.J. Prentice Hall Inc., 1990.

SHALKOFF R.. *Digital Image and Computer Vision.* N.Y. John Wiley & Sons, 1989.

SHEPHERD I.C., LA FONTAINE R.F. E PERSON I.G. Measurement of Instantaneous Flows using Particle Image Velocimetry. *CSIRO Division Bilding*, Victoria, Autralia, 1991.

SZEKELY, A.& BRIMACOMBE, J.K. *The Mathematical and Physical Modeling of Primary Metals Processing Operations*, John Wiley and Sons, NY, 1988

WATKINSON J. *The guide to compression MPEG2*. Snell&Wilcox Inc. Sunnyvalley, 1996.

XIV Brazilian Congress of Mechanical Engineering
Obeid Plaza Hotel Convention Center - Bauru - SP/Brazil
December 08-12th 1997

PAPER CODE: COB497

DESIGN OF AN EIGHT-STAGES CASCADE IMPACTOR FOR THE CLASSIFICATION OF AIRBORNE PARTICLES

MARCOS SEBASTIÃO DE PAULA GOMES
Dept. de Eng. Mecânica, Pontifícia Universidade Católica do Rio de Janeiro, DEM/PUC-Rio
CEP 22453-900, Rio de Janeiro, RJ, Brasil - E-mail: mspgomes@mec.puc-rio.br

Abstract

The work describes the design of a prototype eight-stages cascade impactor, capable of classifying airborne particles with sizes in the range of aerodynamic diameters between 17 and 0.5 microns, while operating with a nominal flow rate of 30 liters/minute. A summary of the theory involved in the project of such devices is also presented. The collection surfaces accommodate 37 mm substrates which may be of different materials (e.g. filter media, aluminum foil), depending on the application of interest. The design is optimized for reducing inter-stage particulate losses, and the instrument may be used in the separation of inhalable PM10 particulate (Particulate Matter 10 microns cut off size). It is also flexible enough for permitting the operation with different sets of nozzle diameters, accepting a diverse selection of cut off sizes.

Keywords

Aerosol Technology, Instrumentation, Air Pollution, Atmospheric Aerosols, Environmental Assessment.
Tecnologia de Partículas, Instrumentação, Poluição do Ar, Aerossóis Atmosféricos, Avaliações Ambientais.

1. INTRODUCTION

Inertial impactors, also known as cascade impactors, are multiple stage devices with the ability of classifying suspended particles in particulate laden gases (aerosol systems). They have been employed for a long time in obtaining the mass-size distribution of airborne contaminants. Some of the applications of such instruments are in the areas of: (i) air pollution studies, (ii) in the evaluation of occupational hazards, and (iii) in bio-aerosols sampling (Cox and Wather, 1995).

Although several instruments have been constructed based in the above principle, since its introduction by May (1945), there is much space for development. Present research interests focus on the steepness of the collection efficiency curves for each stage, and on the minimization of entrance and inter-stage losses (Marple *et al.*, 1993).

2. IMPACTION THEORY

In cascade impactors, the size fractionation is achieved by drawing the particulate contaminated gas though the consecutive stages of the instrument. Generally speaking, each stage is composed by a "nozzle" (one or more orifices) and an "impaction plate" (where the material will collect) placed perpendicularly and just underneath the jet stream. The aerosol impinges against the collection plate and is forced to go around it, with increasing velocities

from one stage to the next. In each stage, the inertia force is responsible for causing a deviation in the trajectories of the large particles with respect to the gas streamlines, forcing them to impact on top of plate. The finer particulate proceed to the next stage. If no significant bouncing occurs, and if no deposit overload is observed in the collection surface, it is theoretically possible to assume a cut-off size for the retention of particles in every stage. Above this theoretical size limit, all particles will be collected in that stage. Therefore, one may obtain the mass-size distribution for a particular aerosol by weighing the collection plates, before and after sampling. The mass concentration may be calculated by taking into account the sampling time and flow rate.

However, the collection of particles in each stage follows an efficiency curve, mostly due to the positioning of the particles within the jet stream. This will cause particulate which is finer than the theoretical cut-off size to be collected, and some of the coarser particulate to follow with the gas for the next stage. General impactor theory was developed with the purpose of predicting the shape of the collection efficiency curves and a representative cut-off size for each stage. The particle cut-off diameter, which was naturally chosen to represent the performance for each impactor stage, corresponded to a collection efficiency of 50% (d_{50}).

In a moving particulate-gas stream, the ability of a particle to perfectly follow the fluid motion is translated by a dimensionless parameter denominated the Stokes number (Stk). It may be defined as the ratio between the particle relaxation time (τ) and a time scale for the flow. The greater the Stokes number, the slower will be the particle response with respect to changes in the flow configuration (the greater the particle inertia), which will cause the particles to have a different trajectory than the fluid elements. For the geometry of an impactor stage, and taking into account the cut-off diameter d_{50} , the Stokes number which corresponds to 50% particle collection efficiency (Stk_{50}) may be defined according to equation 1 (Hinds, 1982).

$$Stk_{50} = \frac{\rho_p \, V_o \, d_{50}^2 \, C}{9 \, \mu \, W} \qquad (1)$$

In the equation above, ρ_p is the particle density. If the definition of a particle aerodynamic diameter (the diameter of an equivalent sphere having unity density and the same settling velocity as the original particle) is used for d_{50} , ρ_p will assume the value of 1 g/cm^3. Regarding the other variables, V_o is the average velocity in the nozzle or jet throat, C is the Cunningham slip correction coefficient, μ is the absolute viscosity of the fluid, and W corresponds to the diameter of the jet orifices (for round nozzles) or the width of the jet (for rectangular nozzles).

Impactor model results, which represent the numerical solution of the fluid dynamic and particle trajectory equations for the jet-plate geometry, have been used as guidelines during the design process (Marple and Liu, 1974; Rader and Marple, 1985). The impactor performance is usually characterized by the specification of three dimensionless parameters: S/W, T/W and Re, where S is the jet-to plate distance, T is the jet throat length, and Re is the Reynolds number based in a characteristic dimension for the jet D_C (D_C=W for round jets, D_C=2W for rectangular jets).

According to these model calculations, the collection efficiency curves are steeper for large Re. The performance improves from Re=100 to Re=500, and a sharp cut-off is maintained up to Re=10,000, above which some deterioration starts to appear. For very low Re, below 100, impactors become inefficient, and the collection efficiency may never reach 100% (Hering, 1995). Marple and Liu (1974), plotted their results for the collection efficiency

against $Stk^{1/2}$ (the same as a dimensionless particle size), for different values of S/W, Re and T/W, varying one of the parameters at a time and keeping the others constant. It was concluded that: (i) the position of the efficiency curves was relatively independent of the ratio S/W, for S/W > 0.5 for round nozzles, and for S/W > 1 for rectangular nozzles; (ii) the position of the curves were also independent of Re for 500 < Re < 3,000, and (iii) the effect of T/W was negligible. It was also observed that for S/W larger than 5, and depending on Re, the cut-off sizes had a tendency to increase due to the expansion of the jet.

In summary, it is recommended that S/W should be around 1 to 3 for round nozzles, and at about 1.5 to 3 for rectangular nozzles. The recommended range for Re is 500 < Re < 3000, and for T/W is between 0.5 and 2. Another important conclusion from the theoretical analysis is that the value of Stk_{50} is almost constant for these range of recommended parameters. Recent studies suggested that Stk_{50} should be around 0.24 for round nozzles, and about 0.59 for rectangular nozzles (Hering, 1995).

3. IMPACTOR DESIGN

3.1 Important Considerations

The first step in the design procedure is to select the range of cut-off sizes, the number of stages, and the operating flow rate for the impactor. The size range depend on the design. Conventional cascade impactors usually collect particles in the range of aerodynamic diameters between 0.4 μm and 15 to 20 μm. The upper limit is a result of the poor penetration efficiency through the inlet of the instrument, for particles which are larger than that. The lower limit is a consequence of the manufacturing process, making it expensive to produce a large number of small diameter nozzles in the last stages. However, specially designed devices, such as the low-pressure and the micro-orifice impactors, are able to collect particles as small as 0.05 μm.

During the calculations, it is important to know the pressure in the impaction region. The necessity for knowing the pressure will obligate the design to start in the first stage, just below the inlet, and then proceed to next ones. Due to the inter-dependence between the pressure and some of the operating variables (ρ, C, and the sampling flow rate Q = mass flow rate/ρ), the solution of the problem must be obtained iteratively, stage by stage. Usually, the pressure at the exit of the nozzles is estimated by using Bernoulli's equation. Another important aspect in the design process is the necessity of adjusting the number of nozzles N to an appropriate integer, and matching the size of the nozzles W to available tool gauges. These factors may require the recalculation of d_{50} for each stage, which will correspond to the final feasible dimensions.

3.2 Prototype Design

It was decided to build a round nozzles cascade impactor with eight stages, for the range of aerodynamic diameter cut-off sizes between 0.5 μm and 16.5 μm, and operating with a flow rate Q of 30 liters per minute. It is common practice to select the cut-off sizes for the stages following a geometric distribution. For most aerosols, the mass-size relationship may usually be approximated by a log-normal distribution. The selection of cut-off sizes which follows a geometric ratio, will result in evenly spaced size ranges when plotting the mass concentration data for analysis. Table 1 indicates the tentative parameters for the design. It was assumed that the inlet was at atmospheric conditions, $\rho_{inlet} = 1.205 \times 10^{-3}$ g/cm^3, and $\mu = 1.81 \times 10^{-4}$ g/cm.s.

Table 1: Tentative Design for the Eight Stages Cascade Impactor (Q=30 lpm).

d_{50} (μm)	$d_{50} C^{1/2}$ (μm)	Re	W (cm)	V_o (cm/s)	P_{stg}/P_{inlet}	$N_{theoretical}$
16,5	16,58	3000	1,78	253	1,000	0,8
10,0	10,08	3000	1,08	416	1,000	1,3
6,1	6,18	3000	0,66	679	1,000	2,1
3,7	3,78	3000	0,41	1111	0,999	3,5
2,2	2,28	3000	0,24	1842	0,997	5,8
1,4	1,48	3000	0,16	2841	0,992	8,9
0,82	0,90	3000	0,10	4682	0,979	14,6
0,50	0,58	3000	0,06	7314	0,948	22,4

Next, it was necessary to adjust N and W and recalculate $d_{50}C^{1/2}$. The last step was to recalculate d_{50} and to verify the Reynolds number. Due to the dependence of the Cunningham slip correction coefficient on the size of the particle itself, this had to be accomplished through an iterative process. Table 2 shows the final values of the design parameters.

Table 2: Final Design for the Eight Stages Cascade Impactor (Q=30 lpm).

N	W (cm)	$d_{50} C^{1/2}$ (μm)	V_o (cm/s)	P_{stg}/P_{inlet}	Re	d_{50} (μm)
1	1,70	17,37	220	1,000	2493	17,3
3	0,85	10,64	294	1,000	1662	10,5
3	0,61	6,47	570	1,000	2316	6,4
5	0,37	3,94	930	0,999	2291	3,8
7	0,24	2,44	1580	0,998	2523	2,3
10	0,16	1,58	2492	0,994	2649	1,5
14	0,10	0,92	4575	0,982	3027	0,85
18	0,07	0,61	7353	0,950	3364	0,53

The prototype was built in aluminum, except for the base which was built from brass, for making it easy of manufacturing. Figure 1 shows the schematic drawings of the various parts of the instrument. All sections are presented in a top and a side view, except for the inlet, stage 1 and the base. The external diameter of the body is 54 mm. A multidirectional inlet was designed with the purpose of reducing penetration losses. All stages, but number 1, have a separate block for the nozzles, to simplify the selection of a different cut-off size for each one of the stages. The impaction plates hold 37 mm substrates, which may be of different material, depending on the application. The inlet may be positioned on top of any of the sections, so that a smaller number of stages may be used during sampling. The base receives all the stages, and serves as a holder for a 37 mm back-up filter. It also has a threaded hose fitting for connecting it to a vacuum pump. A critical orifice is used in the suction line for maintaining a known constant flow rate during sampling.

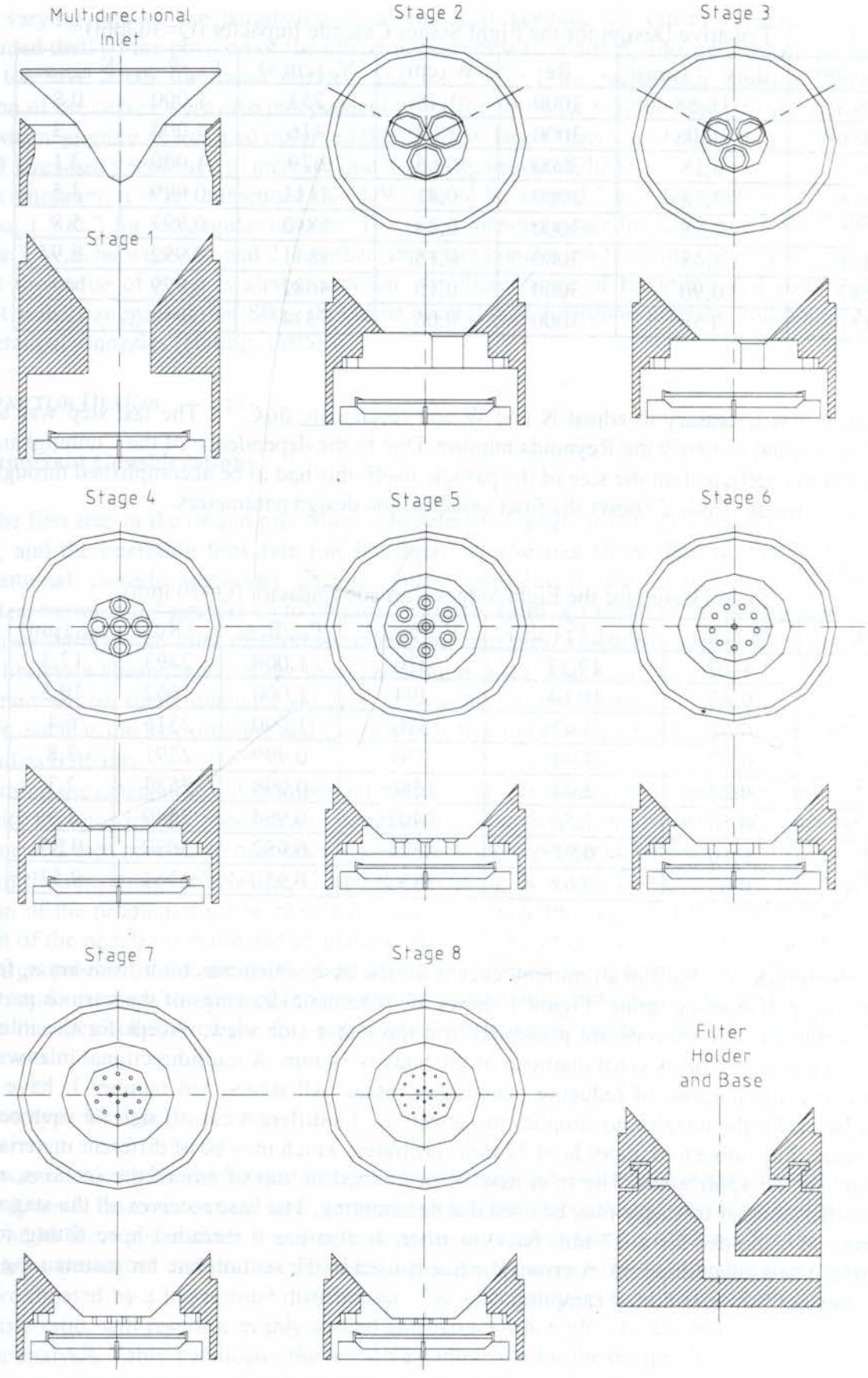

Figure 1: Schematic Drawings of the Prototype Eight Stages Cascade Impactor.

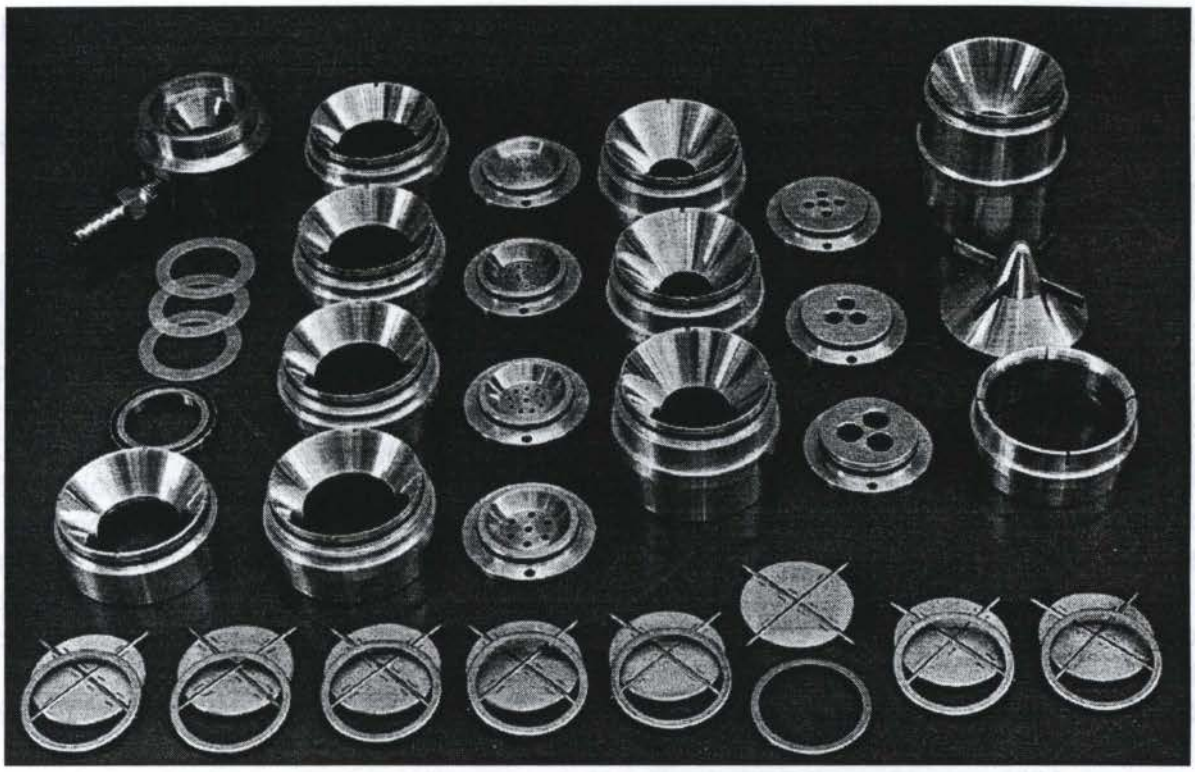

Figure 2: Eight Stages Cascade Impactor Disassembled.

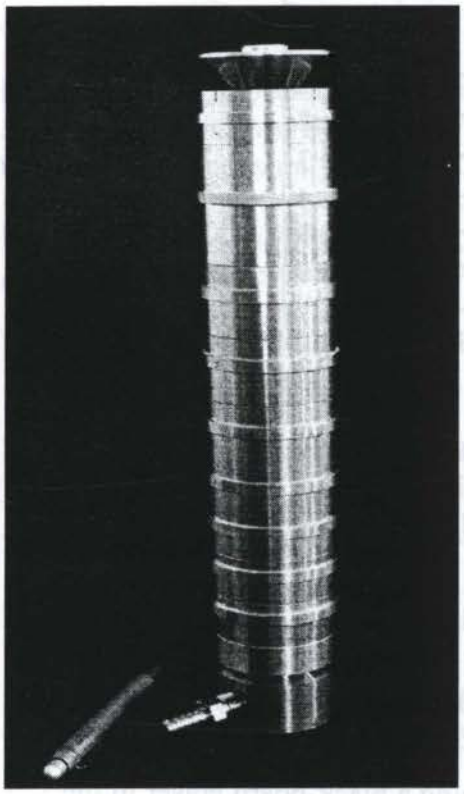

Figure 3: Assembled Impactor.

Figure 2 is a picture of the disassembled impactor. The impaction plates and respective caps, for holding the collection substrates, are arranged horizontally in the bottom of the picture. The following description is given in a top to bottom direction. In the far left column, it is possible to observe the bottom of the impactor base (male thread), Teflon washers for the base, and the top of the base (female thread). The washers are used for holding the back-up filter in place, and to guarantee an air-tight seal. In the next four columns to the right, stages from eight to two appear together with their respective orifice blocks. In the far right column, it is shown stage one, and the two parts which form the multidirectional inlet. O'rings were used in the coupling between the stages, and also in between the orifice blocks and the bodies of the stages. The whole design took into consideration the minimization of inter-stage losses. Obstructions and sudden changes in the flow direction were avoided to a maximum. Figure 3 shows the assembled impactor. The height of the instrument is about 40 cm.

4. IMPACTOR PERFORMANCE

According to Frank *et al.* (1996), the behavior of an impactor stage under flow rate conditions which are different from the one assumed in the design, may be estimated by employing an expression of the power-law type, consistent with equation 2.

$$d_{50} = a\, Q^{b} \qquad (2)$$

However, for satisfying equation 2, due to the dependence between the Cunningham slip correction coefficient and the particle size, and taking equation 1 into consideration, either the coefficient a or the exponent b will need to vary, mainly for small d_{50} . A more appropriate way of representing the relationship between d_{50} and Q is given by equation 3.

$$d_{50}\, C^{1/2} = \alpha\, Q^{\beta} \qquad (3)$$

According to equation 3, the coefficient α will assume a different constant value for each impactor stage. It may be estimated by using equation 1. The theoretical value for the exponent β will be 0.5. Figure 4 shows the theoretical performance of the eight impactor stages for flow rates between 20 and 60 liters per minute.

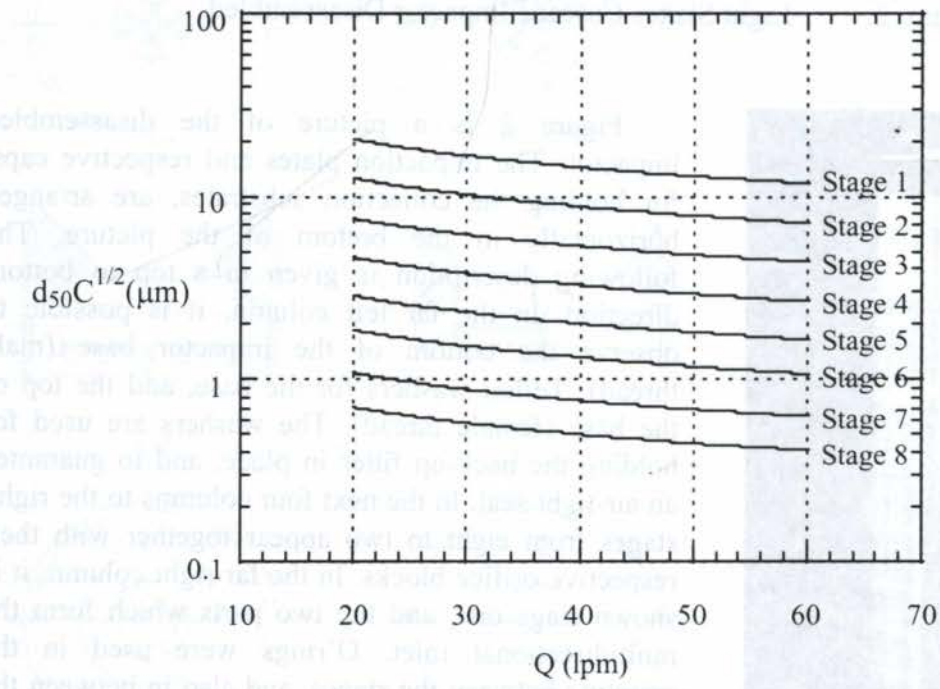

Figure 4: Stages cut-off aerodynamic diameters as a function of the flow rate.

Preliminary tests for investigating the inter-stage losses were conducted by aspirating large size polydispersed dusts (chalk particles produced by tapping a black-board eraser in the neighborhood of the instrument). They revealed no visible deposition of particles outside the impaction plates, what indicated small inter-stage losses. This is in agreement with the careful

design process, avoiding obstructions perpendicularly to the flow and reducing the possibility of recirculation zones.

5. CONCLUSION

It was described the design of an eight stages cascade impactor, for sampling aerosols with aerodynamic diameters in the range between 0.5 and 17 μm, while operating with a sampling flow rate of 30 liters per minute. As a guideline for future inquiries, a summary of the theory involved in the design process, as well as some of the most important design considerations were presented. The inter-dependence between the pressure in the impaction region and the gas density ρ, the Cunningham slip correction coefficient C, and the flow rate Q, will require an iterative process for obtaining the solution to the design problem. The theoretical response of the impactor, operating with sampling flow rates between 20 and 60 liters per minute, was also demonstrated. Preliminary qualitative tests indicated low inter-stage losses. The instrument is now ready for a broader evaluation, which should include the quantification of the inlet and inter-stage losses, and the estimation of the collection efficiency curves.

6. REFERENCES

COX, C. S., AND WATHER, C. M. *Bioaerosols Handbook,* CRC Press, Florida, 1995.

FRANK, G., KASHPAROV, V., PROTSAK, V., AND TSCHIERSCH, J. Comparison Measurements of a Russian STANDARD Aerosol Impactor with several Western Standard Aerosol Instruments. *Journal of Aerosol Science,* vol.27, pp.477-486, 1996.

HERING, S. V. Impactors, Cyclones and other Inertial and Gravitational Collectors, in *Air Sampling Instruments,* B. S. Cohen and S. V. Hering ed., 8th edition, American Conference of Governmental Industrial Hygienists, Ohio, 1995.

HINDS, W. C. *Aerosol Technology - Properties, Behavior, and Mesurement of Airborne Particles,* John Wiley and Sons, New York, 1982.

MARPLE, V. A., AND LIU, B. Y. H. Characteristics of Laminar Jet Impactors, *Environ. Sci. Technol.,* vol.8, pp.648-654, 1974.

MARPLE, V. A., RUBOW, K. L., AND OLSON, B. A. Inertial, Gravitational, Centrifugal, and Thermal Collection Techniques, in *Aerosol Measurement - Principles, Techniques, and Applications,* K. Willeke and P. A. Baron ed., Van Nostrand Reinhold, New York, 1993.

MAY, K. R. The Cascade Impactor. An Instrument for Sampling Coarse Aerosols, *J. Scient. Instrum.,* vol.22, pp.187-195, 1945.

RADER, D. J., AND MARPLE, V. A. Effect of Ultra-Stokesian Drag and Particle Interception on Impaction Characteristics, *Aerosol Science and Technology,* vol.4, pp.141-156, 1985.

XIV Brazilian Congress of Mechanical Engineering
Obeid Plaza Hotel Convention Center - Bauru - SP/Brazil
December 08-12th 1997

PAPER CODE: COB58

ANÁLISE EXPERIMENTAL DO ESCOAMENTO AO REDOR DE UM PERFIL DE BASE QUADRADA EM DOIS DIFERENTES ÂNGULOS DE ATAQUE / *EXPERIMENTAL ANALYSIS OF THE FLOW AROUND A SQUARE CYLINDER WITH TWO DIFFERENT INCIDENCE ANGLES*

CLÁUDIO LINDQUIST, EDSON DEL RIO VIEIRA & SÉRGIO SAID MANSUR
Departamento de Engenharia Mecânica, Faculdade de Engenharia - UNESP - Ilha Solteira
CEP 15.385-000 Ilha Solteira - SP, Brasil, E-mail: delrio@feis.unesp.br

Abstract

Flow visualization have been performed to study the flow along a square cylinder placed perpendicularly to the main flow. Two different attack angles have been considered ($\alpha = 0$ and $\alpha = 45$ degrees), for Reynolds numbers up to 300. The experimental facilities are composed by a water tunnel of low turbulence intensity and an apparatus for a flow visualization, image capture and processing. A direct dye injection visualization technique has been employed and the images have been captured on two different media, photo-sensible chemical film and video tape with the help of a modern three CCD video camera. Strouhal numbers have been determined by video tape image analysis by frames counting. A sequence of images is shown for $\alpha = 0$ from which the vortices formation and shedding can be seen.

Keywords

Square cylinder; Strouhal number; flow visualization; water tunnel; image processing; cilindro quadrado; número de Strouhal; visualização de escoamento; túnel hidrodinâmico; processamento de imagem.

1. INTRODUÇÃO

O escoamento ao redor de corpos não-aerodinâmicos – dentre os quais incluem-se os cilindros de base quadrada – encontra larga aplicação em diversos campos da engenharia. Edifícios, monumentos e construções civis em geral acham-se expostos à ação do vento natural, assim como cabos de sustentação, linhas e torres de transmissão de energia elétrica. Do mesmo modo, pilares de pontes e estruturas de plataformas de prospecção de petróleo estão submetidos aos efeitos de correntes fluviais ou marítimas. Escoamentos envolvendo a interação fluido-estrutura são, ainda, observados em trocadores de calor, componentes de turbomáquinas hidráulicas e inúmeros outros sistemas fluidomecânicos. Em todos estes casos, a identificação e análise das variáveis hidrodinâmicas características do escoamento apresenta enorme interesse prático.

O presente trabalho realiza um estudo experimental do escoamento ao redor de um cilindro de base quadrada, posicionado transversalmente ao fluxo livre não perturbado em dois diferentes ângulos de ataque – $\alpha = 0^\circ$ e $\alpha = 45^\circ$ – para valores do número de Reynolds inferiores a 300. Informações qualitativas e quantitativas acerca do escoamento em torno deste

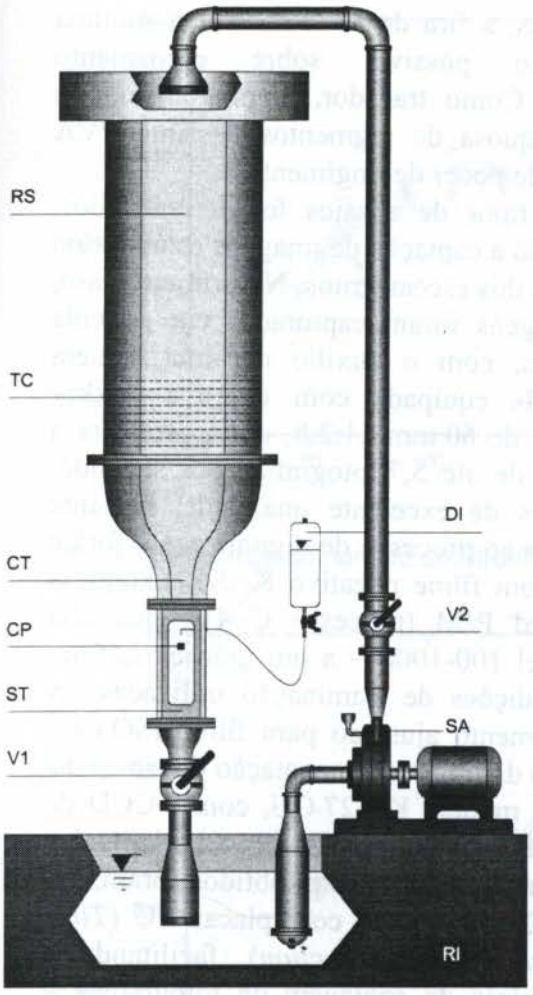

Figura 1: Túnel hidrodinâmico vertical em circuito aberto, operado pela ação da gravidade.

tipo de obstáculo são obtidas utilizando-se, exclusivamente, técnicas de visualização em meio líquido como ferramenta de análise.

2. Dispositivo e Técnica Experimental

Os ensaios experimentais foram conduzidos num túnel hidrodinâmico vertical em circuito aberto, cujos detalhes construtivos são apresentados no trabalho de Vieira (1997). Conforme mostra a Figura 1, este dispositivo compõe-se, fundamentalmente, de um reservatório superior (RS) de seção octogonal, munido de telas e colmeias (TC) em sua parte inferior, seguido de uma contração (CT) e de uma seção de testes (ST) medindo $146 \times 146 \times 500$ mm, dotada de janelas de observação confeccionadas em acrílico de boa qualidade óptica. Capaz de operar em modo contínuo ou intermitente (*blow-down*), sempre pela ação da gravidade, este túnel foi concebido para o desenvolvimento de pesquisas experimentais envolvendo a visualização de escoamentos.

Em modo de operação *blow-down* – condição em que foi realizada a presente campanha de ensaios – o reservatório superior é abastecido com água da rede urbana por intermédio de um conjunto moto-bomba (SA), até atingir o seu nível máximo. Em seguida a bomba é desligada, aguardando-se o tempo necessário para que a água no interior do túnel se tranqüilize. A válvula de controle de vazão (V1) é, então, ajustada para uma abertura previamente estabelecida, dando-se início ao ensaio propriamente dito. Evidentemente, devido à diminuição do nível da água do reservatório superior, a velocidade média do escoamento na seção de testes decresce continuamente durante a operação do túnel em modo *blow-down*. Em vista disso, durante a realização do ensaio, a abertura da válvula V1 deve ser ajustada com critério, a fim de produzir uma queda suficientemente lenta na velocidade média, capaz de ser encoberta pela magnitude das próprias flutuações turbulentas. Nas condições de abertura de válvula para as quais foram realizados os presentes testes experimentais, ensaios com duração de até 20 s puderam ser efetuados, sem introduzir erros significativos nos resultados. A Figura 2 comprova o que foi dito, apresentando a evolução temporal da velocidade num ponto sobre o eixo longitudinal da seção de ensaios, obtida com o auxílio de um anemômetro de fio quente Dantec Measurements 55M01, equipado de uma sonda 55R11, conectado a uma placa de aquisição de sinais National Instruments AT-MIO-16F-5.

O sistema de injeção de corantes líquidos (DI) é composto de uma garrafa pressurizada, ligada a uma longa agulha hipodérmica de 0,6 mm de diâmetro externo, dobrada em forma de cotovelo. A injeção é efetuada à montante do modelo (CP), com velocidade e pressão

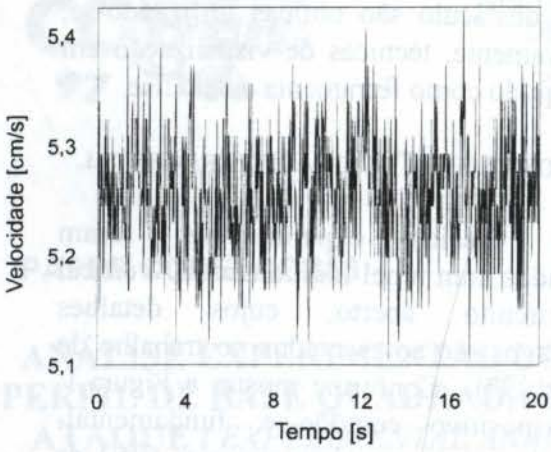

Figura 2: Sinal de velocidade colhido num ponto central da seção de testes, durante a realização de um ensaio em modo *blow-down*.

controladas, a fim de se introduzir a mínima perturbação possível sobre escoamento principal. Como traçador, empregou-se uma solução aquosa de pigmentos de tinta PVA com grande poder de tingimento.

Dois tipos de ensaios foram realizados, envolvendo a captação de imagens estáticas ou dinâmicas dos escoamentos. No primeiro caso, estas imagens foram capturadas em película fotográfica, com o auxílio de uma câmera Nikon F4s equipada com objetiva Nikkor micro AF de 60 mm/f.1:2.8, que possibilita a aquisição de até 5,7 fotografias por segundo. Resultados de excelente qualidade, bastante adequados ao processo de digitalização, foram obtidos com filme negativo Kodak Ektapress Multispeed PJM (processo C–41), que alia uma extraordinária latitude de exposição – ISO variável 100-1000 – a um grão extra-fino. Uma fase preliminar de testes mostrou que, nas condições de iluminação utilizadas, as melhores fotografias foram conseguidas com o equipamento ajustado para filme ISO 640, 1/125 s de velocidade de obturador e 1:22 de abertura do diafragma. Na captação das imagens dinâmicas, por sua vez, empregou-se uma câmera JVC modelo KY 27 CU, com 3 CCD de 2/3" e 410.000 pixel, capaz de adquirir imagens com 800 linhas de resolução horizontal e 63 dB de SNR (*Signal Noise Ratio*). Os registros em fita magnética assim obtidos foram, em seguida, analisados em um vídeo editor JVC BR-S822U, equipado com placas TC (*Time Code*), TBC (*Time Base Corrector*) e DNR (*Digital Noise Reduction*), facilitando a determinação do número de Strouhal a partir do princípio de contagem de fotogramas – Mansur *et al.* (1996) e Vieira *et al.* (1997). Com efeito, a presença da placa TC no vídeo editor permite associar um código magnético a cada fotograma, dispensando a gravação de qualquer código de identificação do tempo na própria imagem, como vinha sendo realizado anteriormente através da técnica SITC (*Superimposed Image Time Coding*), descrita por Vieira (1997).

3. Resultados e Discussão

As Figuras 3 e 4 apresentam a evolução do número de Strouhal em função do número de Reynolds para o escoamento ao redor do cilindro de base quadrada de aresta (L), em dois diferentes ângulos de ataque, $\alpha = 0^{\circ}$ e $\alpha = 45^{\circ}$, respectivamente. Para ângulo de ataque nulo, os dados experimentais do presente trabalho mostram-se em bom acordo com os resultados de Okajima (1982), obtidos em túnel de água, a partir da análise espectral do sinal de velocidade num ponto previamente estabelecido da esteira turbilhonária, colhido com o auxílio de uma sonda de fio quente. Uma análise comparativa entre os valores para $\alpha = 0$ e $\alpha = 45^{\circ}$ mostram que, no segundo caso, o número de Strouhal se estabiliza em valor significativamente menor que no primeiro. Para a faixa do número de Reynolds correspondente aos ensaios realizados, o número de Strouhal em $\alpha = 45^{\circ}$ atinge um valor assintótico da ordem de 0,125 e, para $\alpha = 0^{\circ}$, em torno de 0,145. A comparação destes resultados com aqueles obtidos por Vieira (1997) para cilindro circular – Sr = 0,19 – mostram que a presença de arestas vivas provoca uma diminuição na freqüência de emissão de vórtices para o mesmo número de Reynolds, que incide diretamente sobre os valores do número de Strouhal.

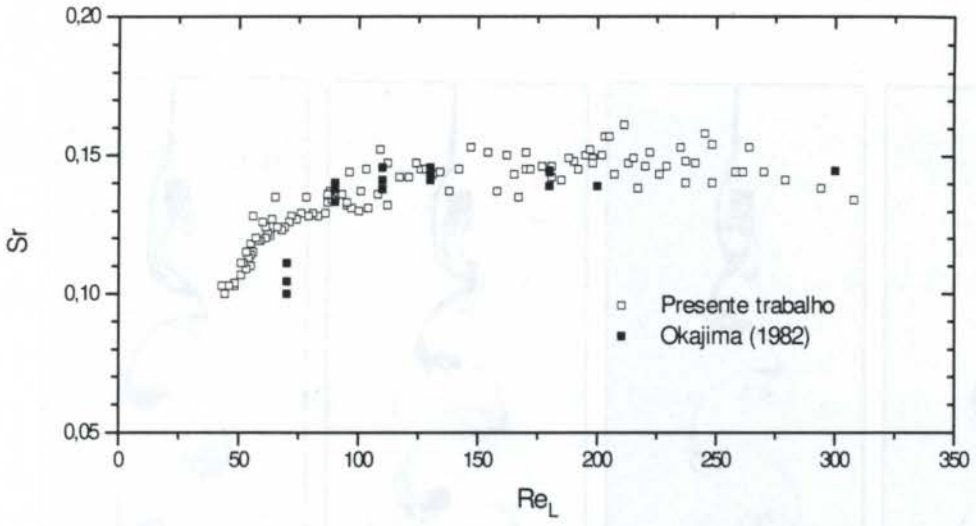

Figura 3: Evolução do número de Strouhal em função do número de Reynolds: $\alpha = 0^{\circ}$.

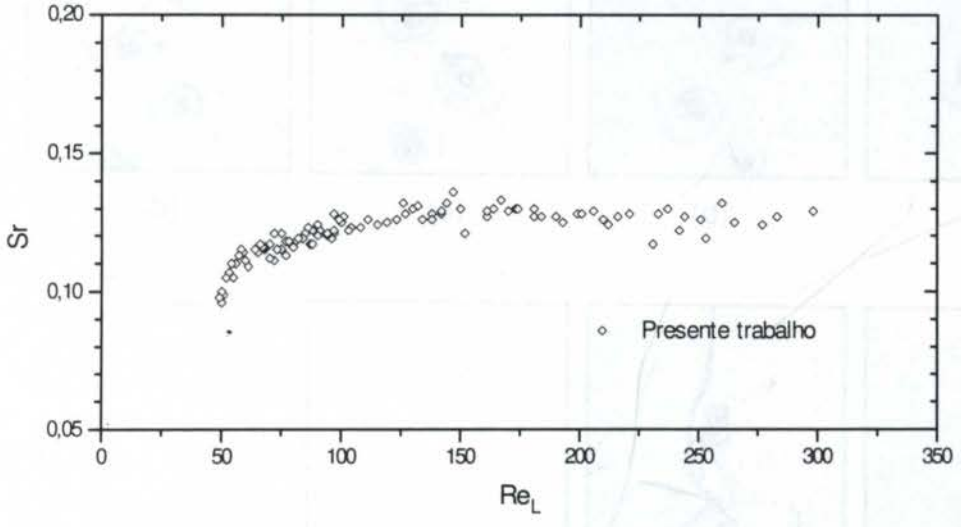

Figura 4: Evolução do número de Strouhal em função do número de Reynolds: $\alpha = 45^{\circ}$.

As imagens fotográficas obtidas através da visualização do escoamento ao redor do modelo com ângulo de ataque nulo, $\alpha = 0^{\circ}$, podem ser observadas na Figura 5, mostrando uma esteira de von Kármán já plenamente desenvolvida em Re = 100. É importante destacar que a presença de arestas vivas favorece o descolamento da camada limite, antecipando a formação dos vórtices em regimes mais brandos que aqueles verificados no caso dos cilindros circulares, como discutido no trabalho de Mansur *et al.* (1996).

4. CONCLUSÃO

A literatura mostra que, além de manter estrita dependência com o número de Reynolds, o número de Strouhal pode ser fortemente influenciado por outras variáveis, tais como: o nível de turbulência e a forma do perfil de velocidade da corrente livre – Vickery (1966) e Mukhopadhyay *et al.* (1992) – , a rugosidade superficial do modelo, e a razão de bloqueio. Os dados de Kawakita & Silvares (1993) correspondentes ao ensaio de um perfil quadrado, para Reynolds baseado na largura do perfil quadrado entre 6.10^3 e 6.10^4, apresentam um número de Strouhal em torno de 0,27 com uma razão de bloqueio superior a 39 %. Este valor mostra-se

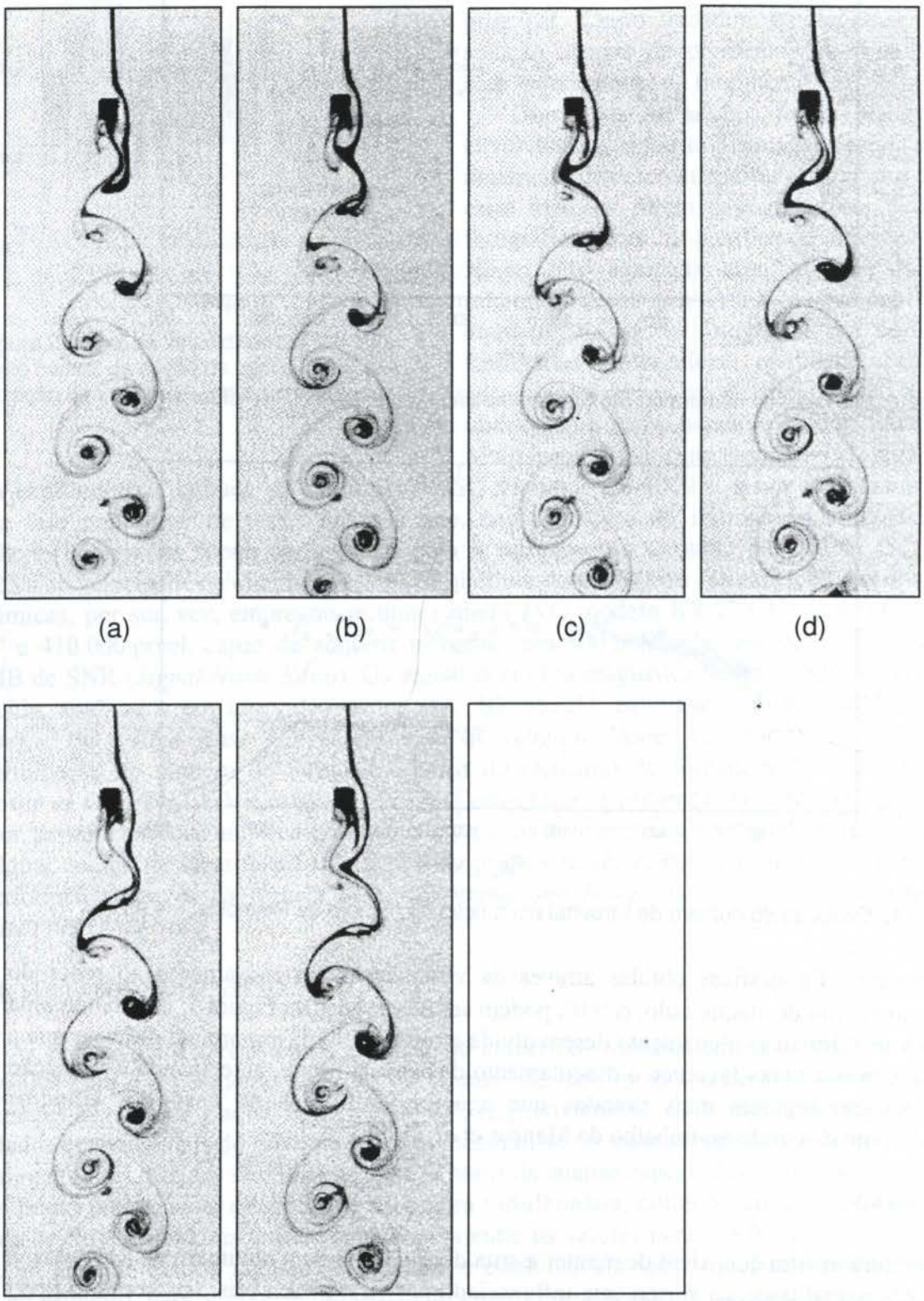

(a) (b) (c) (d)

ERROR: VMerror
OFFENDING COMMAND: image

STACK:

XIV Brazilian Congress of Mechanical Engineering
Obeid Plaza Hotel Convention Center - Bauru - SP/Brazil
December 08-12th 1997

PAPER CODE: COB59

VORTEX VELOCITY MEASUREMENT BY HYDRODYNAMIC FLOW VISUALIZATION

EDSON D. R. VIEIRA, CLÁUDIO LINDQUIST, EMANUEL R. WOISKI & SÉRGIO S. MANSUR
Departamento de Engenharia Mecânica, Faculdade de Engenharia - UNESP - Ilha Solteira
CEP 15.385-000 Ilha Solteira - SP, Brasil, E-mail: mansur@feis.unesp.br

Abstract

Since von Kármán's studies of vortex propagation, vortex streets in wakes of bluff bodies have become a subject of interest to engineers and scientists, producing a great number of experimental vortex velocity measurements. In this work, hydrodynamic flow visualization, by direct dye injection technique, has been employed in order to determine the frequency and propagation speed of vortices shed from circular cylinders in the Reynolds number range up to 600. The experimental procedure consisted on changing the Reynolds number of the flow and evaluating the distance between two vortices on a same row from static images captured on negative film by a SLR camera and determining the Strouhal number from images recorded with a 3 CCD video camera. From the distance and the corresponding Strouhal number, vortex velocity against Reynolds numbers have been calculated and depicted. Results regarding the Strouhal number obtained compared well with literature.

Keywords

Vortex speed; vortex shedding; flow visualization; Strouhal frequency; circular cylinder; velocidade de vórtices; emissão de vórtices; visualização de escoamentos; freqüência de Strouhal; cilindro circular.

1. INTRODUCTION

Laminar flow around bluff objects, such as cylinders, placed crosswise to a fluid flow, under certain conditions, can be disturbed to the point of vortex shedding regularly and alternately from the body sides. The cyclical nature of the phenomenon induces periodic forces on the cylinder, which tend to produce oscillations. Understanding the vortex-shedding phenomenon is vital to the design of elastic structures such as suspension bridges, electrical transmission lines and bundles of heat exchangers, because when they are exposed to the wind or water stream, failure may occur if the natural vibration frequency of these structures is close enough to the frequency of vortex formation.

Because of von Kármán's studies on the vortex patterns stability, they are generally known as *Kármán vortex trails*. Those trails consist on two parallel infinite rows of the same spacing a, but of opposite vorticities with intensities k and $-k$, so arranged that each vortex along each row stays aligned to the mid-point of the line joining two vortices of the other, as shown in Figure 1. Based on the potential flow theory, it was induced by him that a row of vortices travels with a velocity V_{VK} given by

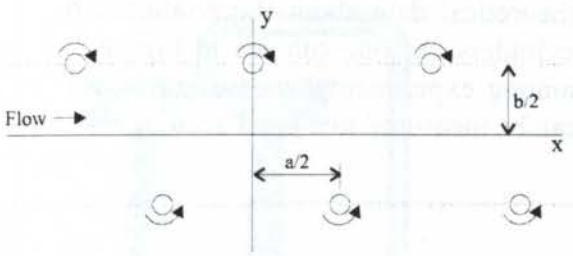

Figure 1: Scheme of the von Kármán's vortex street.

$$V_{VK} = \frac{k\pi}{a} tanh \frac{\pi b}{a} \qquad (1)$$

and from the vortex street stability condition, he also found that there should be a constant relationship between b and a, such that

$$\frac{b}{a} = 0.281 \qquad (2)$$

For a further discussion on the matter of potential flows, reference may be made to Lamb (1945) and Milne-Thomson (1938). Remarkably, the literature has found a persistent disagreement between the theoretical b/a relation and experimental or numerical data, see Vieira *et al.* (1996).

The wake of cylinders have been a subject of theoretical and experimental study for a great many years. In respect to numerical investigation, Eaton (1987) has analyzed the laminar vortex shedding in the wake of a circular cylinder by computer-aided flow visualization at a Reynolds number of 110, while Lin *et al.* (1976) have computed numerical solutions for separated flow around a circular cylinder at Reynolds numbers 40, 80 and 200.

Bloor & Gerrard (1966) have measured the vortex speed in the wake of a circular cylinder in a wind tunnel with hot wire anemometers over the range of Reynolds numbers from 10^3 to 4×10^4. Obasaju (1983) have studied the flow around a square section cylinder in a wind tunnel, measuring the shedding frequency and the longitudinal spacing a between vortices in a row, with pressure transducer and hot wire probe simultaneously.

Experimental flow visualization in towing tanks has also been reported. Taneda (1956) has studied the wake of circular cylinders for Reynolds numbers less than 120 by photographic investigation using aluminum dust visualization technique. Gerrard (1978), on his turn, has investigated the near wake of bluff cylinders of different cross sectional shapes by means of flow visualization, with dye washed from the rear of painted cylinders, at Reynold numbers less than 2000. In order to measure the speed of vortices or instability propagation in the wake, photographic exposures have been made at known time intervals.

The vortex emission frequency n is related with the free stream velocity V and the body's characteristic length D by the Strouhal number Sr, written as

$$Sr = \frac{n \, . D}{V} \qquad (3)$$

The nondimensional vortex velocity V^* based on the velocity of one vortex V_V and the free stream velocity V is given by

$$V^* = \frac{V_V}{V} = Sr \, . a^* \qquad (4)$$

Therefore, knowing the nondimensional vortex spacing $a^* = a/D$ and the Strouhal number Sr, it is immediate to determine the vortex velocity V^*. Vortex spacing a^* for circular cylinders has been evaluated with hot-wire anemometer by Zdero *et al.* (1995) for Re of 2000 and Griffin & Ramberg (1975), by forcing the circular cylinder to oscillate at a frequency close to that of the naturally shed vortices. Wille (1960) on his turn, has shown measurements of the lateral spacing $b^* = b/D$ of vortex rows from static photographic images of vortex trails visualized with direct injection of solid particles.

Several authors have reported experimental and theoretical data about the relationship between Strouhal and Reynolds numbers for circular cylinders. As one can see in Figure 2, there is a remarkable disparity on the order of 20% among experimental measurements of Strouhal frequency, even when the involved quantities can be measured to a good accuracy.

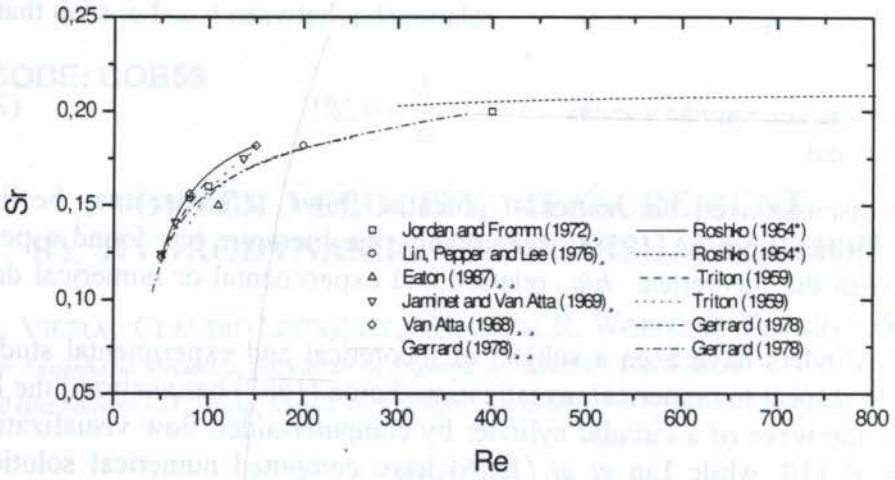

Figure 2: Strouhal - Reynolds number relation for circular cylinder: comparison of results.

The present work represents a contribution to Strouhal and vortex velocity evaluation for flow transversally a circular cylinder, using experimental hydrodynamic flow visualization. In the following sections, the steps involved in their determination, a mixture of video and photographic techniques, are described. Results from the flow visualization of a circular cylinder are presented and discussed.

2. EXPERIMENTAL APPARATUS AND PROCEDURE

2.1 Test Facility

All experiments have been carried out in a vertical open circuit water tunnel with a 146 × 146 × 500 mm square cross test section, shown in Figure 3. The water tunnel has a free stream velocity range of 30 to 300 mm/s with a turbulence intensity always less than 1%. All tests were run over the Reynolds number range, based on approach flow velocity V and cylinder diameter D, of $70 < Re < 600$.

The water tunnel is operated by gravitational action, and can be used in continuous or blow-down mode. Blow-down mode have been used in this work, due to its lower turbulence level, although in this mode, the free stream mean velocity decreases noticeably with the water level inside the upper reservoir. To account for that, it has been estimated that, for a period up to 15 seconds, the effects of decreasing free stream mean velocity are overshadowed by turbulence. The free flow velocity has been determined by measuring the mass flow during the experiments; the uncertainty in the free flow velocity determination is estimated in ±5%. For further information on the water tunnel characteristics, reference may be made to Vieira (1997), Vieira *et al.* (1996) e Mansur *et al.* (1996).

2.2 Test Model

Two circular cylinders - 4 and 6.5 mm outside diameters - have been machined out of a smooth brass rod, resulting in a blockage ratio of 3.2 and 5.3 %, and aspect ratio of 36.5 and

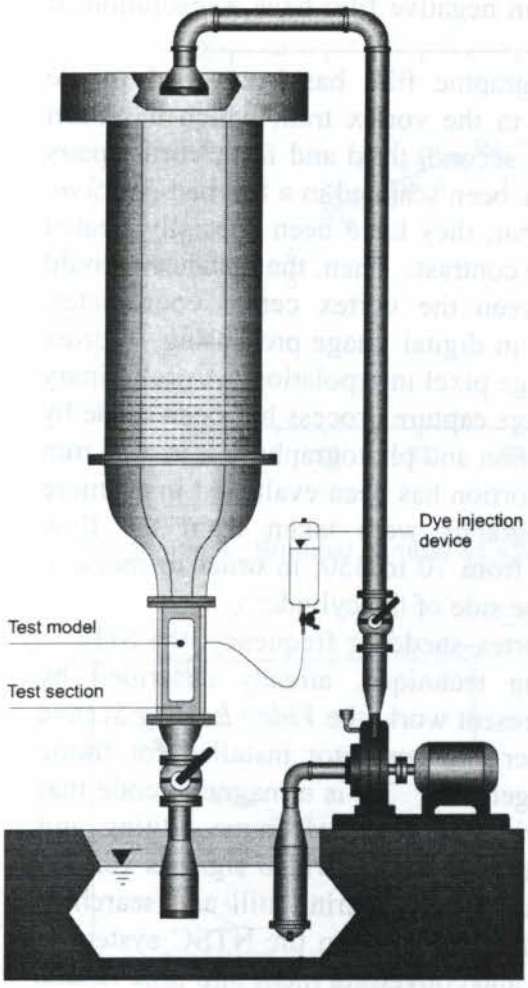

Figure 3: Water tunnel flow visualization facility.

22.5, respectively. Each one at a time, the cylinders have been placed crosswise to the main flow direction, and firmly attached to the test section. Both cylinders have a longitudinal small perforation, to be connected to the dye injection system. Dye has been introduced into the flow trough two very small holes on the upper face of the cylinder, both the holes performing an angle of 45 degrees with the free stream direction.

2.3 Flow Visualization

In order to understand the nature of vortex-shedding process and to collect quantitative data of it, liquid dye injection flow visualization technique have been employed, due to its simplicity and efficiency. The dye injection device consists on a pressurized reservoir containing a strong aqueous solution of black PVA dye, connected to the test model perforated end through a flexible tube, regulated by a needle valve.

Photographs from the flow have been taken with a *Nikon F4s* camera mounted on a tripod in front of the test section by looking through its transparent front wall towards a translucent sheet attached to the opposite wall. In order to improve the image quality, a proper illumination has been supplied by a set of *G.E. Photo-Flood* lights placed behind the test section, so that a suitable combination of diaphragm aperture and shutter speed could be selected, hence furnishing sharp pictures of the vortex street. The pictures have been taken at several Reynolds number with a *Nikkor 60mm f/1:2.8 AF* macro lens at 1/30s and f/1:16 on *Kodak Ultra ISO 400* film.

In order to investigate the behavior of the periodic vortex shedding phenomenon and to obtain the Strouhal number, several short videos have been made out of the flow patterns at several Reynolds numbers with a tripod-mounted *Panasonic NV-MS1PX* SVHS camcorder, at a frame rate of 30 frames per second. The images have been recorded by looking through the transparent front wall of the test section towards a white graduated sheet placed behind the opposite wall.

2.4 Image Processing

The video images have been recorded in a SVHS NTSC video tape recorder (VTR), with a resolution of 400 horizontal lines (while a low-end VHS video system has less than 240 lines). Determination of vortex spacing length *a* between two consecutive vortices directly from video tape images is very difficult because of its low resolution. On the other hand, commercial chemical photographic films have a resolution of more than a hundred lines per

millimeter in every direction, while a professional 35 mm negative film have a resolution of more than 3600 horizontal lines.

In this work, professional 35 mm negative photographic film has been used in the measurements of the spacing a^* between two vortices in the vortex trail, which has been determined by averaging over the distances between the second, third and forth vortex pairs respectively from each vortex row. The photographs have been scanned in a flat bed *HP Scan Jet 3C* scanner with 600 dpi optical resolution. After that, they have been specially treated with *Corel Photo Paint 5.0* software, in order to enhance contrast. Then, the distance a could be determined just by measuring the difference between the vortex center coordinates. Automatic object identification can be an arduous work in digital image processing. Vortex center, in this work, has been determinate by manual image pixel interpolation. A preliminary estimation of the errors due to optical distortion and image capture process has been made by inserting a 10 division per millimeter ruler in the test section and photographing it in a 35 mm negative film. This image has been scanned and the distortion has been evaluated in no more than 1 %. Proceeding as described, 30 static photographs were taken from the flow visualization at 11 different Reynolds numbers ranging from 70 to 350, in order to measure the distance a between two vortices generated at each one side of the cylinder.

As for Strouhal number, in order to measure the vortex-shedding frequency, the SITC – *Superimposed Image Time Coding* – frame counting technique, already described by Vieira (1997) could have been used. However, for the present work, the *Video Editing System JVC BR-S822U* with SA-R22U Time Code (TC) reader and generator installed for frame counting, replacing SITC with advantage, albeit at a larger cost. TC is a magnetic code that stores a time code data on the magnetic tape allowing for accurate frame editing and identification. Vertical interval TC addresses are recorded during the video signal's vertical blanking period by a rotated head; this permits accurate readout during still and search at speeds less than normal. As the actual number of fields per second in the NTSC system is 59.94, counting them at 60 fields (30 frames) per second and converting them into time results in time error accumulating with elapsed time of about 1.8 frames per minute.

3. RESULTS AND DISCUSSION

Figure 4 clearly shows the von Kármán vortex trails obtained from the visualization of flow over circular cylinder at a Reynolds number of 70. Notice that the picture is 90° counterclockwise rotated.

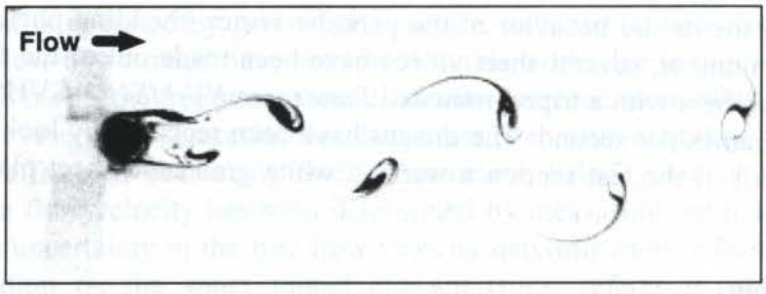

Figure 4: Photograph of the vortex street behind the circular cylinder at Re = 70.

From the flow visualization, 46 short videos at Reynolds numbers ranging from 70 to 600 have been recorded. By frame counting, the corresponding vortex frequencies have been computed and the values of Strouhal number obtained. Figure 5 shows the resulting Strouhal number Sr against the Reynolds number Re.

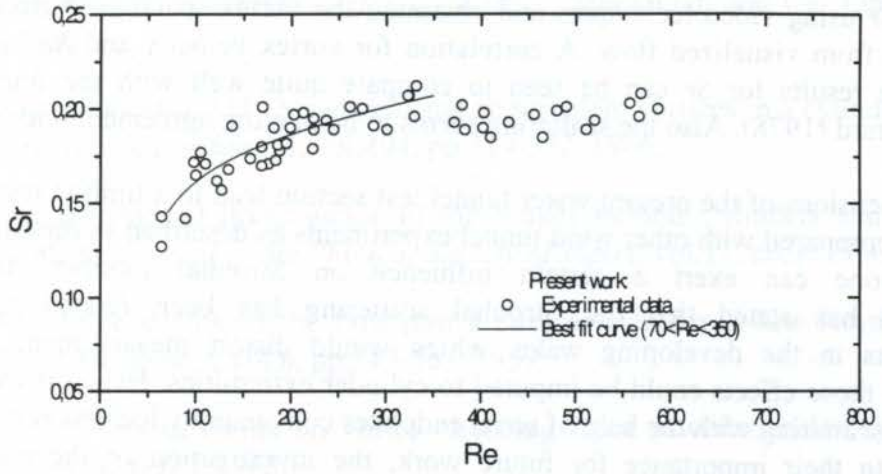

Figure 5: Strouhal number as a function of Reynolds number for circular cylinder.

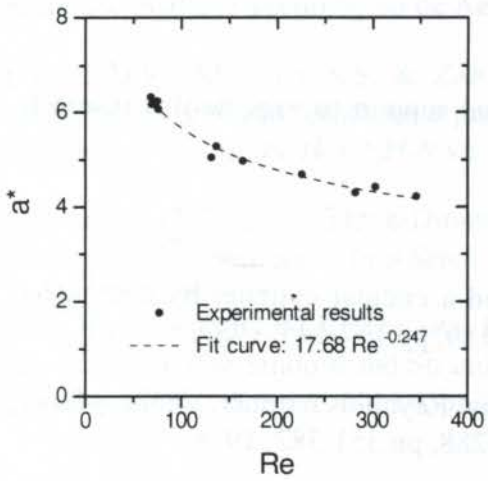

Figure 6: Plot of a^* as a function of *Re* for circular cylinder.

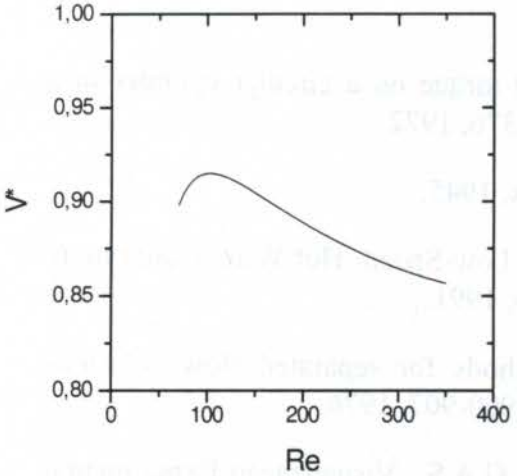

Figure 7: Vortex speed V^* as a function of *Re* for circular cylinder.

Figure 6 depicts the plotting of the nondimensional average distance a^* between two pairs of vortices as a function of the Reynolds number as well as the best fit found for the data, in the Reynolds range of 70 to 350.

A Strouhal-Reynolds correlation has been developed, equation 5, that fits quite well the experimental data for the Reynolds numbers ranging from 70 to 350:

$$Sr = \frac{-3.198}{Re} + 0.185 + 8.667 \times 10^{-5}\, Re \qquad (5)$$

Figure 7, on its turn, displays the vortex velocity V^* as a function of the Reynolds number, which has been determined by means of equation 4 and substituting for the corresponding values of Strouhal number *Sr* and a^*. Notice that the nondimensional velocity exhibits a maximum for a Reynolds number of about 100. Such behavior should be anticipated since Strouhal number increases asymptotically and a^* decreases monotonously with Reynolds number.

4. CONCLUSIONS

A methodology employing flow visualization for measuring the mean vortex speed V_V in the trail of bluff bodies has been presented. The mean vortex speed for a circular

cylinder for Reynolds numbers ranging from 70 to 350 has been evaluated, by determining the Strouhal number *Sr* using video techniques and obtaining the vortex spacing a^* from static photographs taken from visualized flow. A correlation for vortex velocity and *Re* has been developed and the results for *Sr* can be seen to compare quite well with the ones from literature as in Gerrard (1978). Also the scattering seems to be in close agreement with all data from the literature.

The small dimensions of the present water tunnel test section lead to a limited test model aspect ratio when compared with other wind tunnel experiments as described in the literature, and this fact alone can exert a certain influence on Strouhal number. In fact, Williamson (1996) has stated that the Strouhal scattering has been related to three dimensional effects in the developing wake, which would distort measurement results. According to him, those effects could be imputed to cylinder extremities. Hence it would be possible to reduce scattering with the help of some endplates conveniently located at each side of cylinder. Due to their importance for future work, the investigation of the effects of endplates on the wake behavior is under planning.

Finally, comparison between results coming from direct visualization and those obtained through hot wire measurements along the wake is also left to further exploration.

5. ACKNOWLEDGMENTS

Thanks are due to FAPESP for providing the financial support to execute this research (Grant n° 95/6833-4).

6. REFERENCES

EATON, B.E. Analysis of laminar vortex shedding behind a circular cylinder by computer-aided flow visualization, *Journal of Fluid Mechanics*, vol.180, pp.117-145, 1987.

GERRARD, J.H. The wakes of cylindrical bluff bodies at low Reynolds number, *Philosophical Transaction of the Royal Society of London - series A*, vol.288, pp.351-382, 1978.

GRIFFIN, O.M. & RAMBERG, S.E On Vortex Strength and Drag in Bluff-Body Wakes, *Journal of Fluid Mechanics*, vol.69, part 4, pp.721-728, 1975.

JAMINET, J.F., & VAN ATTA, C.W. Experiments on vortex shedding from rotating circular cylinders, *AIAA Journal*, vol.7, n.9, pp.1817-1819, 1969.

JORDAN, K.S. & FROMM, J.E. Oscillatory drag, lift, and torque on a circular cylinder in a uniform flow, *The Physics of Fluids*, vol.15, no.3, pp.371-376, 1972.

LAMB, H. *Hydrodynamics*, Dover Publications, New York, 1945.

LEE, T. & BUDWIG, R. Two Improved Methods for Low-Speed Hot-Wire Calibration, *Measurements and Science Technology*, vol.2, pp.643-646, 1991.

LIN, C.L., PEPPER, D.W., & LEE, S.C. Numerical methods for separated flow solutions around a circular cylinder, *AIAA Journal*, vol.14, no.7, pp.900-907, 1976.

MANSUR, S.S., VIEIRA, E.D.R., SAITO, M. & ESPERANÇA, G.A.S. Visualização Experimental do Escoamento ao Redor de Cilindros de Base Quadrada Posicionados Transversalmente ao Fluxo Livre, *Proc. of the VI ENCIT/LATCYN*, vol.2, pp.1103-1108, Florianópolis, 1996.

MILNE-THOMSON, L.M. *Theoretical Hydrodynamics*, MacMillan and Co. Limited, London, pp.336-344, 1938.

BLOOR, M.S. & GERRARD, J.H. Measurements on turbulent vortices in a cylinder wake, *Proc. of the Royal Society of London - A*, vol.294, pp.319-342, 1966.

TANEDA, S. Experimental Investigation of the Wakes Behind Cylinders and Plates at low Reynolds Numbers, *Journal of the Physical Society of Japan*, vol.11, no.3, 1956.

TRITTON, D.J. Experiments on the flow past a circular cylinder at low Reynolds numbers, *Journal of Fluid Mechanics*, vol.6, pp.547-567, 1959.

VAN ATTA, C.W. Experiments on vortex shedding from yawed circular cylinders, *AIAA Journal*, vol.6, pp.931-933, 1968.

VIEIRA, E.D.R. *Estudo Qualitativo e Quantitativo de Escoamentos ao Redor de Corpos Não-Aerodinâmicos Utilizando-se Técnicas de Visualização em Meio Hidrodinâmico*, Tese de Doutorado, Instituto Tecnológico de Aeronáutica, São José dos Campos, 1997.

VIEIRA, E.D.R., MANSUR, S.S. & ZAPAROLI, E.L. Visualização de escoamentos em meio hidrodinâmico: geração, captação e processamento digital de imagens através de sistema de baixo custo, *Proc. of the IV CEM-NNE/96*, vol.2, pp.839-844, Recife, 1996.

WILLIAMSON, C.H.K. Three-Dimensional Vortex Dynamics in Bluff Body Wakes, *Experimental Thermal and Fluid Science*, vol.12, pp.150-168, 1996.

ZDERO, R., TURAN, Ö.F. & HAVARD, D.G. Toward Understanding Galloping: Near-Wake Study of Oscillating Smooth and Stranded Circular Cylinders in Forced Motion, *Experimental Thermal and Fluid Science*, vol.10, pp.28-43, 1995.

XIV Brazilian Congress of Mechanical Engineering
Obeid Plaza Hotel Convention Center - Bauru - SP/Brazil
December 08-12th 1997

PAPER CODE: COB70

ANÁLISE EXPERIMENTAL DO PROCESSO DE ASPERSÃO DE GOTAS EM UM SISTEMA JATO-PLACA/ EXPERIMENTAL ANALISYS OF THE DROPS ASPERSION PROCES OVER A JET-PLATE SYSTEM

JORGE LUIZ Z. TARQUI, ARISTEU SILVEIRA-NETO & THOMAZ W. MENDOZA-HAREL
Departamento de Engenharia Mecânica, Centro de Ciências Exatas e Tecnologia - UFU
CEP 38400-206 Uberlândia - MG, Brasil - E-mail: aristeus@ufu.br

Abstract

This article presents the results obtained with the technique of high-speed photography used to freeze the high frequency dynamic phenomena involved in the problem of drop generation by means of a spray nozzle-plate system. The instabilities that characterize jet transition were initially analyzed to validate the method of experimentation. The physical nature of drop formation was also analyzed and the more important physical phenomena were pointed out: the dynamic instabilities over the liquid sheet; the holes formation and the mass accumulation belongs the borders of the holes and liquid sheet.

Keywords

Experimentation; turbulence; drops ; aspersion; transition.

1. INTRODUÇÃO

O processo de aspersão de um dado líquido em gotas é utilizado em muitas aplicações práticas, tais como em sistemas de irrigação agrícola, injeção de combustível em sistemas de combustão interna, processos químicos e sistemas de proteção contra incêndio. Uma quantidade importante de trabalhos têm sido desenvolvida neste tipo de problema. Uma revisão bibliográfica detalhada sobre processos de geração de gotas foi desenvolvida por Kolev (1993). Dombroski e Jones (1963) propuseram um modelo físico para a transformação de um lençol de fluido em gotas. Segundo o modelo proposto, as instabilidades que são geradas sobre o lençol dão origem a cilindros de fluido que se quebram em gotas. Será mostrado no presente trabalho que os fenômenos físicos que dão origem às gotas são bem mais complexos e diferenciados em relação ao que se propõe neste modelo. Um modelo similar foi proposto por Chin *et al.* (1991), utilizando-se do formalismo de máxima entropia. Spielbauer and Aidum (1994) propuseram que o processo de geração de gotas se deve às perfurações que aparecem sobre o lençol líquido, o que é confirmado no presente trabalho.

Um caso particular de sistema de aspersão é composto de um jato e uma placa aspersora. A colisão do jato contra a placa propicia a sua transformação em uma núvem de gotas, como se ilustra na Figura 1. Este tipo de aspersor é particularmente utilizado em sistemas de irrigação agrícola. O objetivo visado com o presente trabalho é adquirir uma melhor compreensão fundamental sobre o processo físico que caracteriza a aspersão de gotas num sistema tipo jato-placa. Esta compreensão é importante para se desenvolver experiências mais avançadas, bem como desenvolver teoria e modelagem matemática do problema.

Em termos práticos objetiva-se, com este projeto, a otimização de sistemas de irrigação, buscando-se minimizar o consumo de água e energia e também otimizar o processo produtivo. De fato, em processos de irrigação por aspersão, gotas muito pequenas são transportadas pelo vento e gotas muito grandes geram problemas de erosão do solo. Por outro lado, uma distribuição de diâmetros de gotas mais estreita e centrada sobre um valor médio ótimo propicia uma faixa de molhamento uniforme do solo (Mccreery and Stoots, 1996), contribuindo assim para uma melhor produtividade com menor consumo de água e de energia. No presente artigo apresenta-se resultados qualitativos que possibilitam compreender de forma global os fenômenos físicos envolvidos neste tipo de problema.

2. EQUIPAMENTO

O sistema de aspersão utilizado é composto de um bico de injeção e de uma placa aspersora cônica (NP), contra a qual o jato colide, após o que, é gerada um lençol líquido que se quebra em uma núvem de gotas, conforme se ilustra na Figura 1. Um reservatório coletor é equipado com três janelas de vidro transparente (W) que permitem o processo de visualização e a tomada de fotografias. Os demais equipamentos são ilustrados nesta figura: uma bomba de 3 HP (P); um reservatório de água (R); três rotâmetros (FM); tubos de PVC de 25 mm de diâmetro interno e um manômetro (M). Para todos os testes realizados, o escoamento antes do bico injetor encontrava-se em regime turbulento estatisticamente estabelecido.

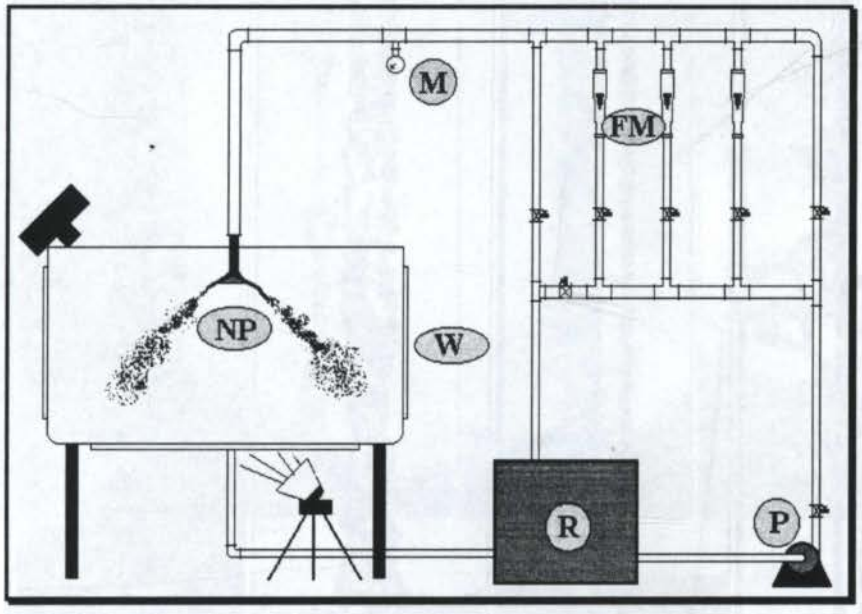

Figure 1 - Esquema da bancada experimental.

As fotografias foram obtidas com uma câmera de 35 mm e com uma lâmpada estroboscópica de alta frequência (1 MHz). Uma vez focalizada a imagem, as fontes de luz do laboratório eram desativadas. O diafrágma da máquina era aberto permanentemente, até que a lâmpada fosse disparada com um circuito eletrônico, o qual permitia a obtenção de um flash de 50 μs de duração. Este curto período e o uso de um filme preto e branco de alta sensibilidade (3200 ASA-ISO 400) possibilitaram o congelamento de fenômenos de altas frequências tais como: instabilidades, ondas, perfurações no lençol de líquido e o processo de acumulação de massa na borda do lençol de líquido, com a consequente formação de gotas.

Tarqui (1996) apresenta maiores detalhes sobre este trabalho.

3. RESULTADOS

Os resultados obtidos no presente trabalho são apresentados nesta seção em dois grupos: captura das instabilidades de um jato livre em transição à turbulência e análise do processo de aspersão em gotas de um lençol de líquido.

3.1. TRANSIÇÃO DE UM JATO LIVRE

Um jato livre vertical de água foi visualizado para vários números de Reynolds. Este parâmetro de contrôle é definido como $Re_d = Ud / \nu$, onde U é a velocidade média do jato, d é o diâmetro interno do bico injetor e ν é a viscosidade cinemática da água. Fotografias de alta velocidade foram obtidas pelo método já descrito.

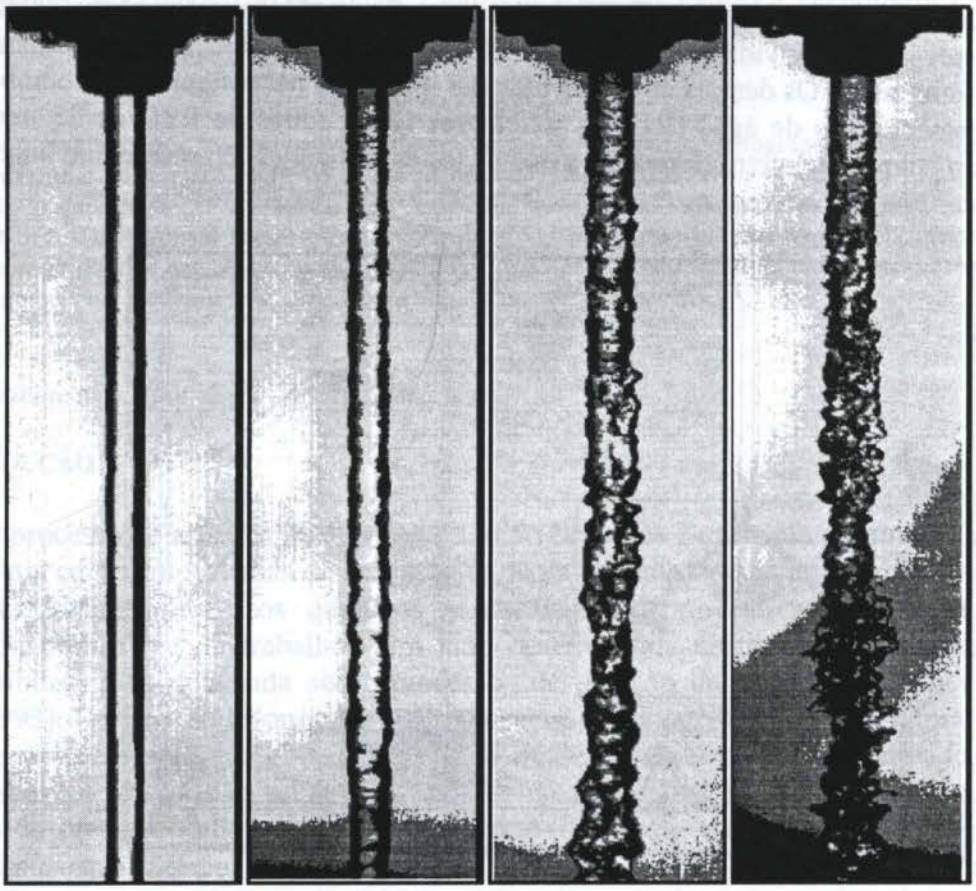

(a) (b) (c) (d)

Figura 2 - Visualização de jatos livres: Re_d=1.100; Re_d=33.000; Re_d=56.000; Re_d=122.000.

Na Figura 2 mostra-se quatro fotografias relativas a diferentes números de Reynolds, como indicado na legenda. Na Figura 2 (a) visualiza-se um jato livre, tipicamente laminar, sem nenhuma instabilidade na sua superfície. Para maiores números de Reynolds o escoamento torna-se irregular e apresenta-se com fortes instabilidades tridimensionais que caracterizam a transição do escoamento para o regime turbulento. Conjectura-se que estas instabilidades são o resultado da amplificação de perturbações injetadas pelo sistema de

bombeamento. Obviamente elas se amplificam espacialmente como ilustram as Figuras 3 (b)-(d). Para melhor visualizar esta transição, mostrar-se-á no parágrafo seguinte a evolução espacial dos jatos das Figuras 2 (a) e (d). Nas Figuras 3 (a) e (b) observa-se a instabilidades clássicas de Rayleigh que dão origem a gotas em regime laminar. Observa-se que sobre o filamento remanescente entre as gotas nascem os harmônicos de Rayleigh que dão origem a gotas de tamanhos menores. No caso das Figuras 3 (c) e (d) tem-se a transição para o regime turbulento com a formação de instabilidades tridimensionais altamente complexas. Este resultado é semelhante ao que foi obtido por Chigier (1991). Visualiza-se também a emisão de filamentos de fluido e de pequenas gotas (Figura 3 (d)). O ponto no qual este processo de emissão de gotas se inicia é definido como o ponto de "breakup" do jato (Wu *et al.*, 1995 e Faeth *et al.*, 1995). Maiores detalhes são apresentados por Tarqui *et al.* (1997).

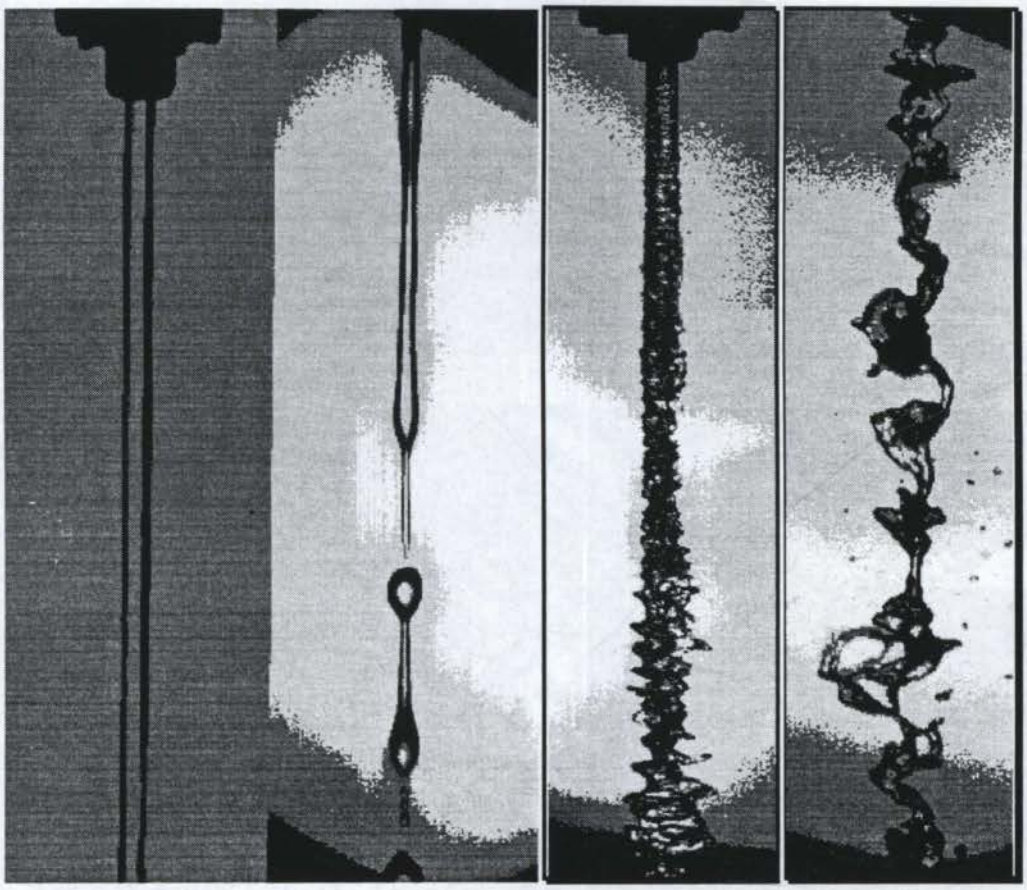

(a) (b) (c) (d)

Figura 3 - Transição do regime de escoamento de um jato livre vertical; (a) e (b) instabilidades de Rayleigh, Re_d=5.000, (b) é a sequência espacial de (a); (c) e (d) instabilidades tridimensionais, Re_d=122.000, (d) é a sequência espacial de (c).

3.2. ASPERSÃO DE GOTAS NO SISTEMA JATO-PLACA

O cenário da transição deste sistema de aspersão, desde um jato de água até a quebra em gotas, foi anteriormente descrito por Reis e Silveira-Neto (1993). Inicialmente tem-se as instabilidades formadas sobre o jato, antes da colisão contra a placa aspersora, como pode ser observado na Figura 3 (c), próximo do bico injetor; após a colisão, forma-se um lençol de fluido que deixa a placa com um ângulo aproximadamente igual ao ângulo da placa. As

instabilidades do jato são transportadas e amplificadas pelo lençol e outras instabilidades são também formadas devido ao cizalhamento aerodinâmico entre o lençol e o ar que a envolve. Na medida em que o fluido é transportado radialmente a espessura do lençol diminui e, com a amplificação das instabilidades, formam-se perfurações que também se amplificam e dão origem a um processo intermitente de formação de gotas nas suas bordas.

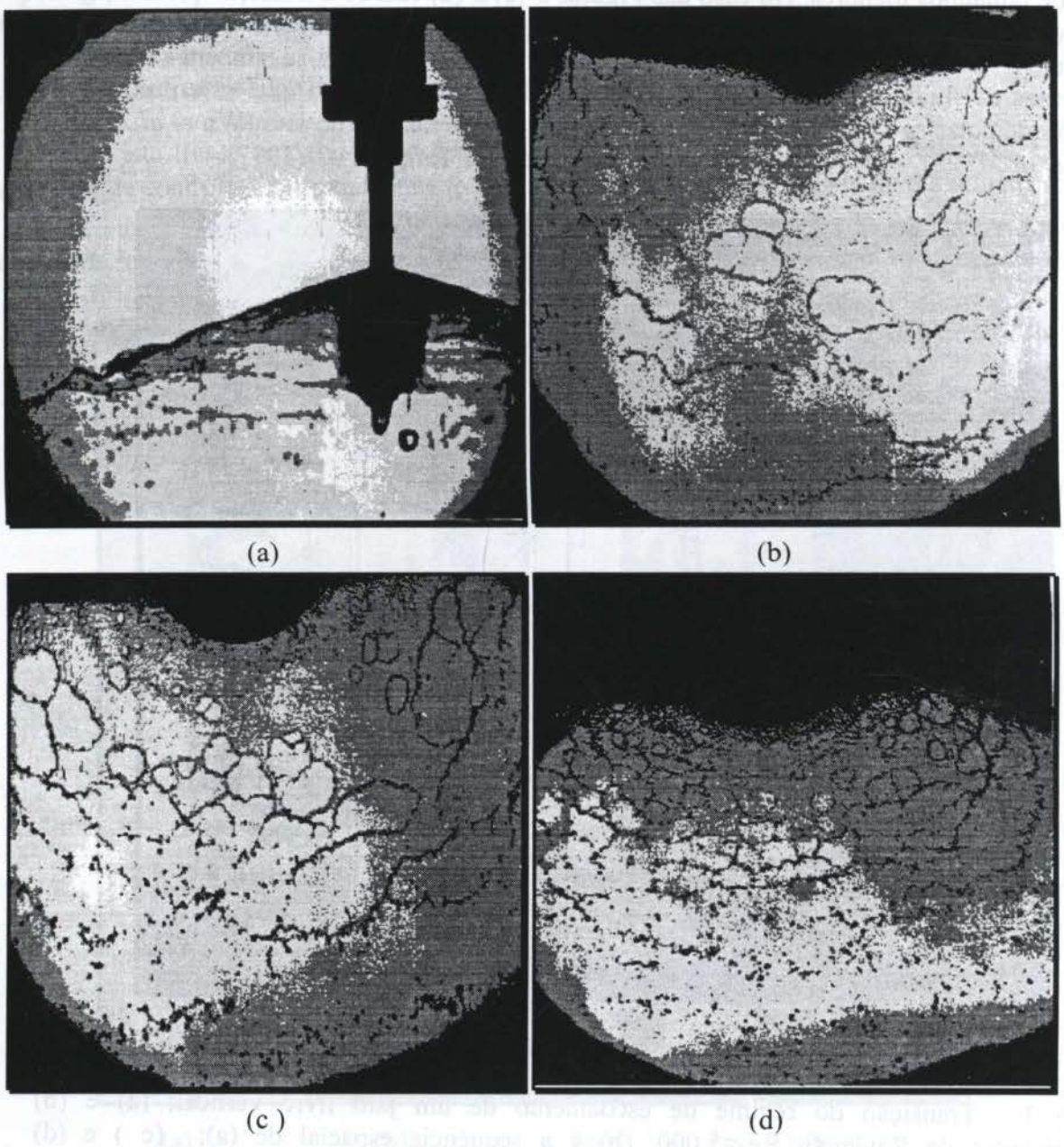

Figure 4 - Sistema de aspersão jato-placa; (a): vista lateral do sistema de aspersão de gotas; (b): vista superior do lençol de líquido, ilustrando as perfurações que caracterizam o processo de aspersão, Re_d= 32.000; (c): Re_d=36.000; (d): Re_d=50.000.

Na Figura 4 (a) mostra-se uma vista lateral do sistema de aspersão. Na parte superior visualiza-se o bico injetor, seguido do jato que colide contra uma placa cônica. O lençol de líquido deixa a placa com um ângulo inicialmente bem definido, após o que a mesma se coloca a oscilar como se visualiza à esquerda desta figura. A presença destas oscilações é muito importante para o processo de irrigação, uma vez que são elas que promovem um largo

leque de aspersão de gotas e em consequência uma maior faixa de molhamento do solo. O controle destas oscilações é, portanto, importante para a otimização do processo de aspersão e de irrigação.

Nas Figuras 4 (b)-(d) visualiza-se o lençol de fluido por uma vista superior do sistema. Estas três figuras são relativas a três valores do número de Reynolds indicados na legenda. Percebe-se o processo de formação, amplificação e transporte das lacunas. Observa-se ainda que, à medida que elas são transportadas, as gotas são formadas nas suas bordas por um processo de enrolamento e acumulação de massa que será descrito e visualizado a seguir. É interessante perceber que a frequência destas lacunas cresce com o número de Reynolds. Outro detalhe é que elas se formam mais cedo (mais próximo da placa aspersora) com o aumento do número de Reynolds.

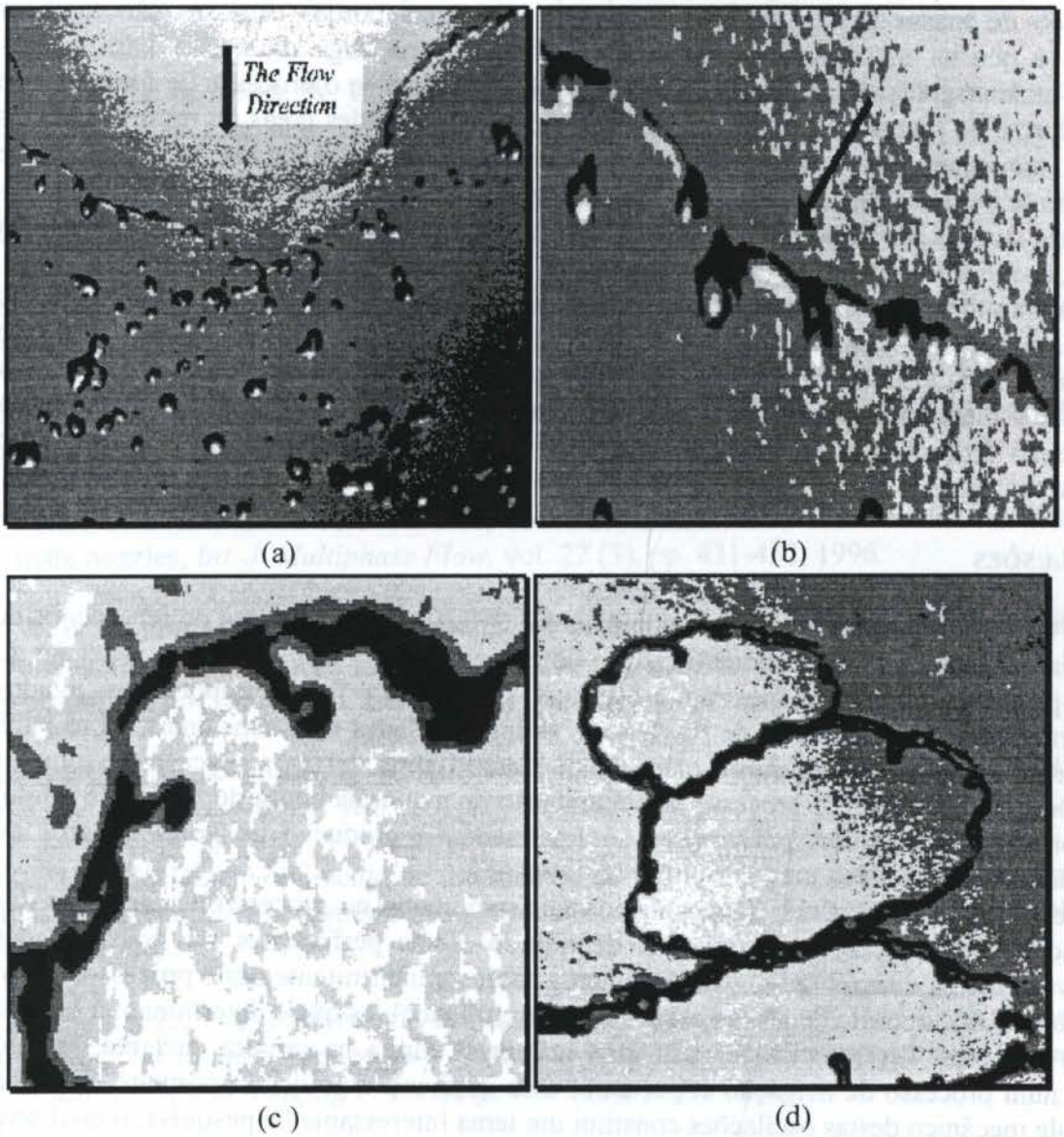

Figura 5 - Amplificação da Figura 4 (b).

A visualização ''a olho humano'' deste escoamento mostra uma nuvem contínua de gotas, o que não corresponde à realidade física. De fato, as Figuras 4 (a)-(d) mostram frentes discretas de gotas que são formadas em consequência da presença destas lacunas. Constata-se

pois que a frequência destas frentes depende do número de Reynolds. Não foi possível determinar, no entanto, qual a natureza desta dependência, se tem um comportamento linear ou assintótico. Esta informação também é muito importante do ponto de vista prático, uma vez que grandes números de Reynolds implicam também em grandes potências de bombeamento. Medidas quantitativas serão desenvolvidas visando a obtenção precisa deste tipo de informação.

Nas Figuras 5 (a)-(d) mostra-se os detalhes do processo de aspersão de gotas a partir das bordas das lacunas. Nestas figuras representa-se vistas amplificadas da Figura 4 (b). Na Figura 5 (a) tem-se um detalhe com a geração de gotas da borda do lençol de fluido. Para melhor compreender este processo, esta vista foi amplificada, a qual é visualizada na Figura 5 (b). Percebe-se que a espessura da borda é superior à espessura do lençol, mostrando que os efeitos da tensão superficial superaram os efeitos de inércia e inicia-se um curioso processo de acumulação de massa nestas bordas. Observa-se que estas bordas espessas são também instáveis, e que as instabilidades formadas promovem uma fuga de massa para pontos distintos, onde as gotas são formadas. Na Figura 5 (c) visualiza-se o processo de formação de gotas na forma de filamentos, os quais podem dar origem a grandes gotas ou mesmo a várias gotas de tamanhos menores. Finalmente, na Figura 5 (d) visualiza-se o processo de crescimento e de fusão das lacunas, bem como a formação de gotas nas suas bordas. Acredita-se que estas lacunas são importantes para se determinar o tamanho e a frequência de formacão das gotas, o que tem grandes implicações práticas.

Para a otimização do processo de irrigação é importante que a banda de diâmetros das gotas seja controlada, visando-se, de um lado, minimizar os efeitos nocivos da erosão do solo e, de outro lado, visando-se minimizar o processo de evaporação para a atmosfera. Na continuidade deste projeto objetiva-se uma vizualização mais acurada, assim como a quantificação do processo. Objetiva-se também o contrôle dos fenômenos identificados no presente trabalho.

4. Conclusões

A técnica de fotografia de alta velocidade foi utilizada para a captura de fenômenos de frequências elevadas que ocorrem na transição do escoamento em um sistema de aspersão do tipo jato-placa. As fotografias mostram a estrutura e fenômenos físicos importantes, ligados ao escoamento: as instabilidades de Rayleigh e as instabilidades tridimensionais sobre jatos livres verticais; as oscilações sobre o lençol de líquido após deixar a placa aspersora; as perfurações sobre o lençol; o processo de acumulação de massa na borda do lençol de fluido, assim como nas bordas das perfurações, e, finalmente, a produção de gotas a partir de instabilidades nestas bordas.

Pelo que foi constatado, o mecanismo mais importante no processo de formação das gotas, são as perfurações sobre o lençol de líquido. Estas perfurações são transportadas convectivamente na direção radial e determinam a natureza intermitente deste processo. Outro fenômeno também importante são as oscilações sobre o lençol, as quais determinam a largura da frente de gotas. Estas oscilações têm uma influência direta na largura da faixa de solo molhada num processo de irrigação e, portanto, uma implicação prática importante. A busca do controle mecânico destas oscilações constitui um tema interessante de pesquisa, o qual será desenvolvido na sequência deste trabalho. Informações qualitativas mais detalhadas, bem como informações quantitativas, via experimentação, assim como via simulação numérica, são necessárias para melhor compreender este complexo problema.

5. AGRADECIMENTOS

Os autores agradecem à Universidade Federal de Uberlândia, ao CNPq e à FAPEMIG pelo apoio concedido durante o desenvolvimento deste trabalho.

6. REFERÊNCIAS BIBLIOGRÁFICAS

CHIGIER, N. Optical imaging of sprays, *Prog. Energy Combust. Sci.*, vol. 17, pp. 211-262, 1991.

CHIN, L. P., LAROSE, P. G., TANKIN, R. S., JACKSON, T., STURND, J. & SWITZER, G. Droplet distributions from the breakup of a cylindrical liquid jet, *Physics of Fluids A*, vol. 3, pp. 1897-1906, 1991.

DOMBROVSKI, N. & JONES, W. R. The aerodynamic instability and disintegration of viscous liquid sheets, *Chem. Eng. Science*, vol. 18, pp. 203-214, 1993.

FAETH, G. M., HSIANG, L. P. & WU, P. K. Structure and brakup properties of sprays, *Int. J. Multiphase Flow,* vol. 21, pp. 99-127, 1995.

KOLEV, N. I. Fragmentation and coalescence dynamics in multiphase flows, *Experimental Thermal and Fluid Science*, vol. 6, pp. 211-251, 1993.

MANSOUR, A. & CHIGIER, N. Turbulence characteristics of cylindrical liquid jets, *Phys. Fluids*, vol. 6, pp. 3380-3391, 1994.

MCCREERY, G. E. AND ŠTOOTS, C. M. Drop formation mechanisms and size distributions for spray plate nozzles, *Int. J. Multiphase Flow,* vol. 22 (3), pp. 431-452, 1996.

REIS, W. & SILVEIRA-NETO, A. Comportamento dinâmico de um jato incidente sobre placas aspersoras-cenário da transição à turbulência, *Proceedings of the XII Brazilian Mech. Eng. Congress*, vol. 2, pp. 1033-1036, 1993.

SPIELBAUER, T. M. & AIDUN, C. K. The wave thining and breakup of liquid sheets, *ASME Journal of Fluids Engineering*, vol. 116, pp. 728-734, 1994.

TARQUI, J. L. Z. Desenvolvimento de um método de fotografia para o estudo de fenômenos de altas frequências em asperssores jato-placa, Mestrado, Universidade Federal de Uberlândia, 1996.

TARQUI, J. L. Z., SILVEIRA-NETO, A. & MENDOZA-HARRELL, T. M. Short Exposure Photographic Techinique Applied to Visualize a Free Liquid Jet, to appears at *Journal of Flow Visualization and Imaging Processing*, vol. 3 (3), 1997.

WU, P. K., MIRANDA, R. F. & FAETH, G. M. Effects of initial flow conditions on primary breakup of nonturbulent and turbulent liquid jets, *Atomization and Sprays,* vol. 5, pp. 175-195, 1995.

XIV Brazilian Congress of Mechanical Engineering
Obeid Plaza Hotel Convention Center - Bauru - SP/Brazil
December 08-12th 1997

PAPER CODE: COB702

UM ESTUDO EXPERIMENTAL DE VÓRTICES ANELARES VISCOSOS

MAURÍCIO DZIEDZIC
CEHPAR - Centro de Hidráulica e Hidrologia Prof. Parigot de Souza, UFPR/COPEL
C.P. 1309, Curitiba - PR - 80001-970 — E-mail: dziedzic@cch.copel.br

Abstract

Motivated by the role played by vortex rings in the turbulent mixing processes, the present work investigates the stability and evolution of a single vortex ring. A new classification is proposed for vortex rings, which is based on extensive hot-wire measurement of velocities in the vortex core and wake, and on flow visualization. Vortex rings may be classified as laminar, wavy, turbulence-producing, and turbulent.

Resumo

Com motivação no papel desempenhado pelos vórtices anelares nos processos turbulentos de mistura, o presente trabalho investiga a estabilidade e a evolução de um vórtice anelar. É proposta uma nova classificação para vórtices anelares, baseada em medições extensivas com anemômetro de fio quente das velocidades na estrutura do vórtice e em sua esteira, e na visualização do escoamento. Vórtices anelares podem ser classificados como laminar, ondulado, produtor de turbulência, e turbulento.

Kewywords Vórtice Anelar, Turbulência, Mecânica dos Fluidos, Experimental.

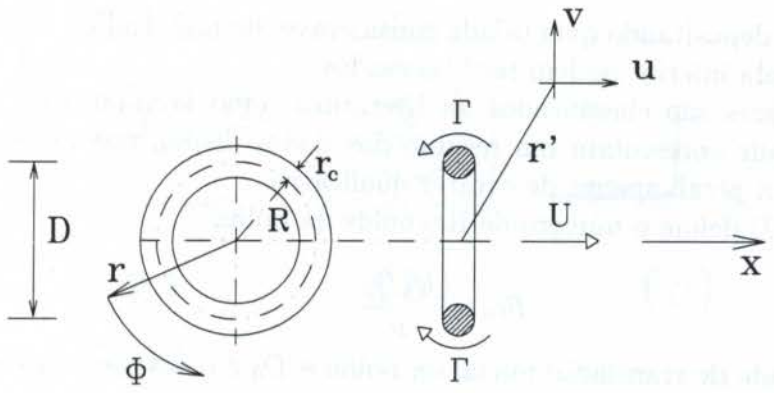

Figura 1: Vórtice anelar - características e terminologia.

1 Introdução

Dentre as muitas formas em que um vórtice pode ocorrer, a forma anelar se destaca. Uma vez criado, o vórtice é auto-contido, automotivo e duradouro. Devido a essas características, o vórtice anelar já foi utilizado como veículo de transporte de massa em engenharia ambiental. Em um nível mais fundamental, suspeita-se que a interação de vórtices anelares pode ser utilizada para a modelagem da turbulência.

Muito já foi estudado a respeito dessas interações, e muito mais ainda precisa ser desvendado. Logo, pontos básicos, como a classificação de um vórtice anelar, ainda precisam ser elucidados e são objetos do presente trabalho.

2 Revisão da Literatura

A figura 1 é uma representação esquemática de um vórtice anelar, definindo a principal terminologia empregada na seqüência. A circulação ao redor do toróide é Γ, a velocidade de propagação, auto-induzida, é U, o diâmetro do anel é D, seu raio é $R = D/2$, e o raio do toróide é r_c.

No caso mais comum, o vórtice anelar é formado pelo enrolamento de um vórtice em lâmina cilíndrica, criado pela ejeção impulsiva de fluido através de uma abertura de diâmetro D_{ori} (Lugt, 1983, lista vários exemplos que ilustram a diversidade de situações em que se pode encontrar vórtices anelares).

A visualização do escoamento de vórtices anelares de intensidades variadas, ou seja, circulação, identifica os modos em que estes podem ocorrer. No limite inferior dessas intensidades iniciais, os vórtices anelares possuem uma superfície toroidal lisa. À medida que a intensidade inicial aumenta, ondas azimutais de pequena amplitude podem ser observadas ao redor do toróide. Aumento adicional da circulação traduz-se na deposição de material no fluido ambiente, formando uma esteira, cuja extensão aumenta com o aumento da circulação inicial. No limite superior de intensidades iniciais, já não se obversa uma forma toroidal bem definida após a formação do vórtice. Ao invés disso, uma massa de

fluido se movimenta depositando quantidade considerável de material no fluido ambiente, onde vórtices de escala inferior podem ser observados.

Os vórtices anelares são classificados na literatura como laminares ou turbulentos. Os parágrafos a seguir apresentam um resumo dos dados disponíveis antes do presente trabalho, que são, em geral, apenas de caráter qualitativo.

Maxworthy (1972) define o número de Reynolds da bolha[1]

$$Re_0 = \frac{U_0 D_0}{\nu} \tag{1}$$

onde U_0 é a velocidade de translação inicial da bolha e D_0 é o diâmetro inicial da bolha.

Ele constatou experimentalmente que:

- para $Re_0 < 600$ os anéis são estáveis (laminares);
- para $Re_0 > 600$ os anéis apresentam ondas azimutais;
- para $Re_0 > 1000$ após a formação do anel, o escoamento se degenera em movimento turbulento (ou seja, apenas uma bolha pode ser vista), do qual um vórtice anelar depois emerge.

Sallet & Widmayer (1974) mostraram que sinais de velocidade obtidos por anemômetro de fio quente de vórtices anelares laminares são contínuos ("lisos"), enquanto que aqueles de vórtices anelares turbulentos mostram a mesma forma básica mas com superposição de ruído de alta freqüência e pequena amplitude. As posições nas quais tais sinais foram obtidos não é especificada. Entretanto, evidência obtida no presente trabalho indica que tais sinais devam ter sido obtidos fora do toróide.

O comportamento do anel parece depender da geometria do gerador.

Auerbach (1988) constatou que vórtices anelares ejetados de um orifício absorvem menos fluido ambiente que aqueles ejetados de um tubo, e que os primeiros também se deslocam com maior velocidade. Ele menciona que uma possível explicação para esse fato é o aumento da separação de vórtices secundários da parede externa para o caso do orifício, e conseqüente diminuição da circulação. Ele também observou que a velocidade de propagação de um vórtice anelar laminar bem definido diminui gradativamente, que a troca de material com o fluido ambiente é mínima, e que o vórtice apresenta velocidades axial e radial negligenciáveis. Finalmente, ele conclui que vórtices anelares geralmente passam por quatro fases durante sua evolução: geração, laminar, ondulado e turbulento.

O presente trabalho se concentra na elucidação das seguintes questões:

- Qual é o significado exato dos adjetivos "laminar" e "turbulento" quando aplicados a vórtices anelares ?

[1] Alguns autores utilizam o termo "bolha" com base no conceito de que a forma da massa fluida que se desloca é de uma bolha, ao invés de um anel.

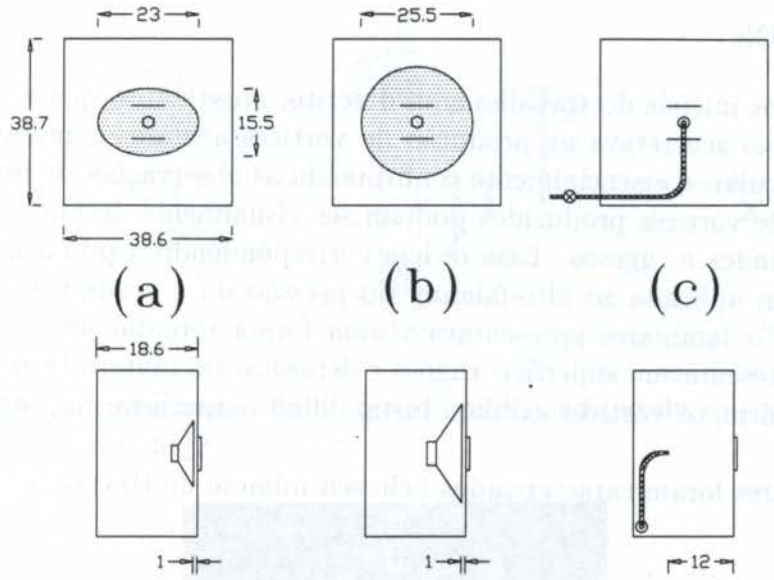

Figura 2: Vista frontal e lateral dos três tipos de gerador utilizados: (a) pistão = alto-falante pequeno; (b) pistão = alto-falante grande; (c) ar comprimido ejetado por válvula solenóide. Dimensões em centímetros, e $D_{ori} = 2$cm.

- Vórtices anelares gerados por diferentes métodos apresentam instabilidade nos mesmos números de Reynolds (definido em termos da velocidade e do diâmetro do anel) ?

O trabalho experimental (Dziedzic, 1994) foi conduzido no laboratório de mecânica dos fluidos do Departamento de Engenharia Mecânica da Universidade de Toronto.

3 Equipamento experimental

Os vórtices anelares estudados foram gerados em ar, dentro de uma câmara cúbica de 2,40 m de lado, que minimiza a influência de correntes de ar ambiente. O gerador de vórtices, ou canhão de vórtices, consiste basicamente de um recipiente e um pistão. O recipiente é uma caixa de acrílico, e o pistão um alto-falante ou ar comprimido ejetado através de uma válvula solenóide de ação rápida. A figura 2 mostra os três tipos de geradores empregados ($D_{ori} = 2$ cm).

A amplitude de movimento dos alto-falantes pode ser controlada eletronicamente, possibilitando a geração de vórtices de intensidades iniciais variadas. O mesmo efeito pode ser obtido variando-se a pressão do ar ejetado pela válvula solenóide.

O esoamento foi visualizado com névoa de óleo de parafina, e gravado em vídeo e fotografado. Anemômetros de fio quente também foram empregados para medições instantâneas de velocidade do fluido.

4 Resultados

Já durante os estágios iniciais do trabalho aqui descrito, observou-se que a variação dos parâmetros de geração acarretava na produção de vórtices anelares com características diferentes. Em particular, e essencialmente confirmando as observações de investigadores anteriores, os tipos de vórtices produzidos podiam ser visualmente divididos em três categorias: lisos, ondulados e rugosos. Essa ordem correspondendo a potências crescentes do gerador (voltagem aplicada ao alto-falante, ou pressão do ar comprimido). Os que aparentavam ser anéis laminares apresentavam uma forma toroidal lisa, enquanto que anéis turbulentos apresentavam superfície rugosa e depositavam material em uma esteira. No estado intermediário, os vórtices exibiam instabilidade superficial na forma de ondas azimutais.

Os vórtices anelares foram caracterizados pelo seu número de Reynolds

$$Re = \frac{UD}{\nu} \tag{2}$$

A seguir apresenta-se um resumo das características observadas para cada gerador:

- Alto-falante pequeno: o número de Reynolds variou de 400 a 5350, com ondas azimutais sendo inicialmente detectadas para $Re = 800$, e rugosidade superficial para $Re = 1900$.
- Alto-falante grande: o número de Reynolds variou de 850 a 2950, com ondas azimutais sendo inicialmente detectadas para $Re = 1050$, e rugosidade superficial para $Re = 1250$.
- Ar comprimido ejetado por válvula solenóide: o número de Reynolds variou de 800 a 1850, com ondas azimutais sendo inicialmente detectadas para $Re = 1300$, e rugosidade superficial para $Re = 1500$.

Medições de velocidade no toróide e no eixo do anel foram efetuadas com anemômetro de fio quente, e a figura 3 ilustra essas posições.

As figuras 4 a 8 mostram vários vórtices anelares analisados. As velocidades correspondentes, medidas durante os testes de laboratório são apresentadas em Dziedzic (1994).

Com base na evidência coletada, é possível propor a seguinte classificação para vórtices anelares:

- Vórtices anelares laminares são aqueles com superfície lisa, toróide laminar e esteira laminar.
- Vórtices anelares ondulados são aqueles com ondas azimutais, toróide laminar e esteira laminar.
- Vórtices anelares produtores de turbulência são aqueles com superfície rugosa, toróide laminar e esteira turbulenta.
- Vórtices anelares turbulentos são aqueles com aparência de "bolha", toróide turbulento e esteira turbulenta.

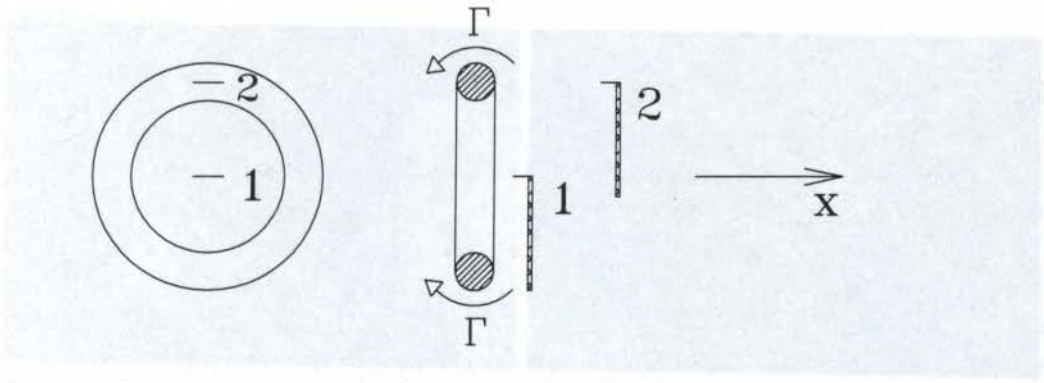

Figura 3: Posição do anemômetro de fio quente para medição de velocidade no eixo do anel (1) e no eixo do toróide (2).

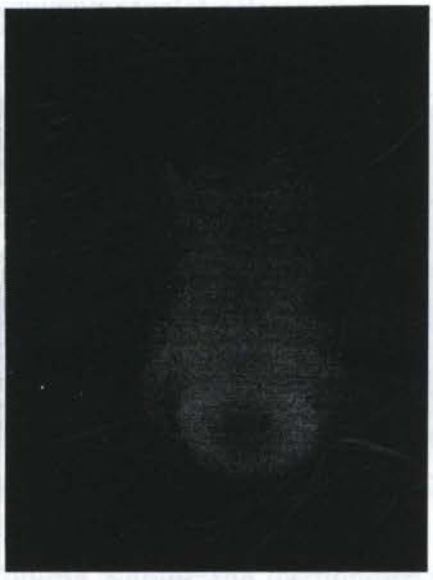

Figura 4: Vórtice anelar gerado com alto-falante pequeno, com $Re = 400$

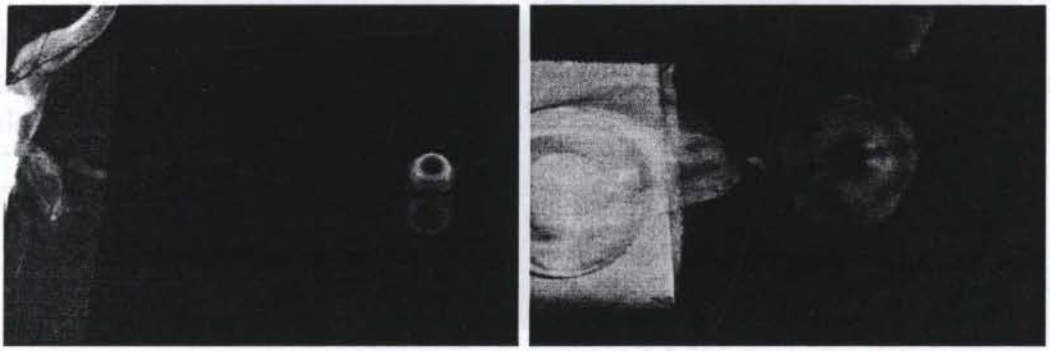

Figura 5: Vórtice anelar gerado com alto-falante pequeno, com $Re = 1300$

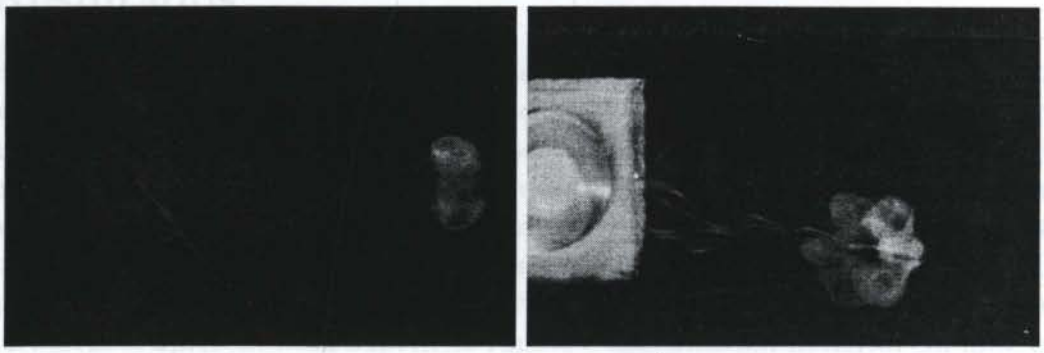

Figura 6: Vórtice anelar gerado com alto-falante pequeno, com $Re = 1650$

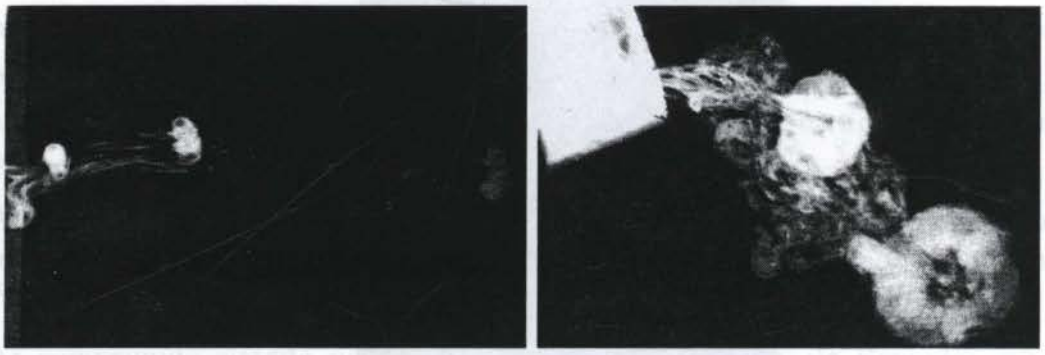

Figura 7: Vórtice anelar gerado com alto-falante grande, com $Re = 2900$

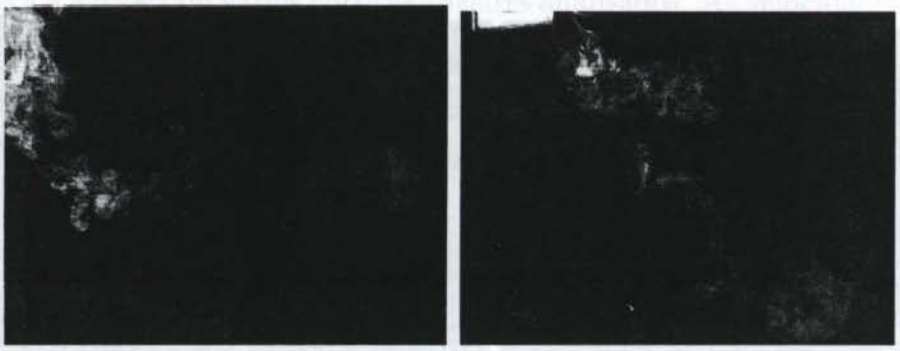

Figura 8: Vórtice anelar gerado com ar comprimido, com $Re = 1850$

5 Conclusões

A previsão de instabilidade em um vórtice anelar em função do seu número de Reynolds parece possível, considerando-se os dados obtidos (Dziedzic, 1994; Dziedzic & Leutheusser, 1996). A superfície ondulada foi inicialmente detectada para números de Reynolds de 800, 1050 e 1300, respectivamente para vórtices anelares gerados com um alto-falante pequeno, alto-falante grande, e ar comprimido. A turbulência, seja no toróide ou na esteira, foi detectada para números de Reynolds de 2300, 2500 e 1650, respectivamente. Considerando-se o grau de incerteza associado aos números de Reynolds críticos de outros tipos de escoamento, parece razoável concluir que ondulações ocorrem, aproximadamente, para $Re \simeq 1000$, e turbulência ocorre, aproximadamente, para $Re \simeq 2000$.

O trabalho aqui descrito foi possível devido ao apoio financeiro do "Natural Sciences and Engineering Research Council of Canada". Agradecimentos especiais são dirigidos à CAPES pela concessão de bolsa de estudos ao autor.

Referências

AUERBACH, D. 1988 Some Open Questions on the Flow of Circular Vortex Rings. *Proc. IUTAM Symp. Fundamental Aspects of Vortex Motion* , held in Tokyo, Japan, Aug. 31 - Sep. 4/87. *Fluid Dynamics Research* **3**, pp. 209–213.

DZIEDZIC, M. 1994 An experimental study of viscous vortex rings. PhD thesis, University of Toronto, Toronto, Canada.

DZIEDZIC, M. & LEUTHEUSSER, H.J. 1996 An Experimental Study of Viscous Vortex Rings *Experiments in Fluids* **21**, pp. 315–324.

LUGT, H. J. 1983 *Vortex Flow in Nature and Technology.* John Wiley & Sons - Interscience.

MAXWORTHY, T. 1972 The Structure and Stability of Vortex Rings. *J. Fluid Mech.* **51** (1), pp. 15–32.

SALLET, D.W. & WIDMAYER, R.S. 1974 An Experimental Investigation of Laminar and Turbulent Vortex Rings in Air. Zeitschrift für *Flugwissenschaften* **22** (6), pp. 207–215.

XIV Brazilian Congress of Mechanical Engineering
Obeid Plaza Hotel Convention Center - Bauru - SP/Brazil
December 08-12th 1997

PAPER CODE: COB753

Experimental Determination of Thruster Plume Heat Loads on SAC-C

753

Abstract

In this paper, a theoretical and experimental study of the impact of the exhausted gas produced by a 2N hydrazine thruster is presented, simulating the thermal conditions attained in space during the operation of a spacecraft propulsion system used for orbit control. For this purpose, two different configurations were examined, either in continuous and pulsed firing regimes. The first configuration consisted of a set of small aluminum plates placed perpendicular to the plume flow field, in order to have a direct measurement of the heat load on a surface whose normal is aligned with the incident molecular flow field. The second configuration consisted in a fiberglass-epoxy boom placed near the thruster and parallel to its axis, representing a possible configuration for SAC-C (Satélite Argentino de Aplicaciones Científicas). The boom, when deployed, extends into the area of the flow field of the thrusters used for orbit control and may be subjected to high heat loads during the firing.

Keywords
Plume Impingement, Heat Estimations

1. INTRODUCTION

In spacecraft design, the effect of heating due to the impingement of a rocket plume on external surfaces is one of the main thermal concerns. The formulation of a theoretical model to determine the heat load is a complex task, since it is based upon many uncertainties. As a result, any analysis based only on theoretical calculations is not satisfactory, being necessary to perform tests in order to guarantee the predictions.

In this paper, an experimental study of the impact of the exhausted gas produced by a 2N hydrazine thruster is presented, consisting in the measurement of the heating load over two different test configurations, either in continuous or pulsed firing regimes. The first configuration consisted of a set of small aluminum plates placed perpendicular to the plume flow field where the heat flux was determined from the plates temperature evolution during the thruster firing. The second configuration consisted of a fiberglass-epoxy boom test section placed near the thruster and parallel to its axis. In this case, in order to correlate the measured temperatures with heat fluxes, a first order model was proposed based upon the estimation of the heat transfer between a single-node boom element and its environment.

2. THRUSTER AND EXHAUST GAS CHARACTERISTICS

The characteristics of the propulsion system used in the tests are listed subsequently: thrust 2N, fuel hydrazine, throat radius 0.5 mm; exit radius 5.7 mm; exit angle 15 degrees; ratio

between exit and throat area 50. The tests were performed with the following characteristics: pressure in the hydrazine tank 22 bar; pressure in the thruster combustion chamber 14 bar; pressure at the exit 0.01 bar; mass flow rate 0.9 g/s; maximum velocity in fully expanded gas 2200 m/s; gas specific heat ratio 1.28. See Hinckel, J. (1990).

3. ALUMINUM PLATES CONFIGURATION

3.1. Experimental Arrangement

Figure 1 presents the sketch of the sensor used in this configuration. It was an aluminum plate (25mm x 25mm x 1.4 mm) oriented perpendicularly to the gas flow field and fixed to the support by two Teflon rods having a diameter of 3 mm and a length of 20 mm. A thermocouple was put at the center of the plate and fixed by aluminum tape. In addition, another aluminum tape was put at the front side of the plate to take advantage of its low and known IR emittance. Four sensors were placed at the same radial distance from the thruster axis (90mm) and at different longitudinal positions (51, 189, 337 and 486 mm), as shown in Figure 2 .

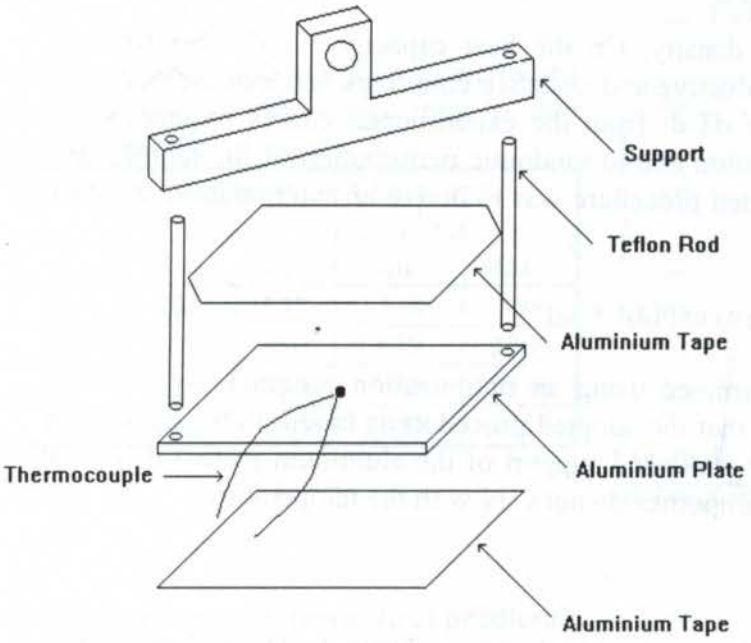

Figure 1 - Exploded View of the Sensor

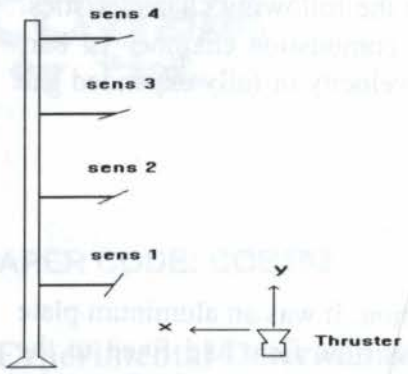

Figure 2 - Position of the Sensors, Related to the Thruster

3.2. Methodology for Absorbed Heat Flux Calculation.

The thermal equilibrium of an isothermal plate of temperature T in a vacuum environment, receiving a heat flux q" which varies as a function of time, can be formulated as follows:

$$q" = V \rho Cp \, dT/dt + C (T-T_o) + R (T^4 - T_o^4) \quad (1)$$

Where V is the plate volume, ρ the density, Cp the heat capacity, T_o the environment temperature, while C and R are the conductive and radiative couplings between the plate and the environment. The determination of dT/dt from the experimental curves requires some treatment in order to avoid large oscillation due to randomic perturbation of the temperature measurement. For this reason, the adopted procedure was to derive an interpolation equation of the following type:

$$T = a_1 + a_2 \exp(a_3 t + a_4) \quad ; \quad dT/dt = a_2 a_3 \exp(a_3 t + a_4) \quad (2)$$

The parameters a_1, a_2, a_3, a_4 are determined using an optimization program, by the least squares method. It is important to note that the adopted procedure is based on the hypothesis that the environment (vacuum chamber walls and support of the aluminum plates) is kept at constant temperature, and the material properties do not vary with the temperature.

3.3. Tests

Each test was as sequence of five firing cycles as shown in Table 1. The pulsed regime consisted in an alternation of 400 milliseconds ON and 600 milliseconds OFF. The test chamber pressure was kept between $3.6\ 10^{-1}$ tor and $4.4\ 10^{-1}$ tor for continuous firing and between $1.9\ 10^{-1}$ tor and $2.2\ 10^{-1}$ tor for pulsed firing. The methodology was applied on the temperature versus time experimental curves and the absorbed heat flux was calculated for each sensor and each firing. The condensed results are presented in Table 2.

Table 1 - Sequence of firing in each test.

Firing (phase)	type of firing	period of firing (s)
phase 1	cont.	200
phase 2	pulsed	500

Table 2 - Thermal flux determined for each sensor and for continuous and pulsed firing.

Sensor	Cont. Firing (W/m2)		Pulsed Firing (W/m2)	
	Min.	Max.	Min.	Max.
1	104	535	151	239
2	100	550	223	906

phase 3	pulsed	500
phase 4	pulsed	500
phase 5	cont.	200

3	225	796	309	1028
4	303	1509	595	1461

From the obtained results, the following observations can be established: a) the absorbed heat fluxes vary in a large range from test to test, and also during the firing time and b) the absorbed heat flux is larger in the pulsed firing than in continuous firing, although the thruster is turned on only 40% of the time in the pulsed firing.The probable reason for this behavior is that the pressure in the chamber affects the boundary and characteristics of the plume, as mentioned by Madox,A.R.(1968). The higher chamber pressure during the continuous firing in comparison with the pulsed regime ($4\ 10^{-1}$ versus $2\ 10^{-1}$ tor), results in less expansion of the plume in the first case. The consequence is a smaller gas density (and heat flux) in the continuous firing than in pulsed firing. With this in mind, the absorbed heat flux for continuous firing supposing a chamber pressure of $2\ 10^{-1}$ tor can be calculated taking the results for pulsed firing (in Table 2) and dividing them by 0.4 (in pulsed firing the thruster is exhausting gas only during 40% the time). Such results are presented in Table 3 and Figure 4.

Table 5 - Thermal flux (in W/m^2) determined for each sensor for continuous firing for two levels of chamber pressure

Sensor	Cham.pres.: 4.10^{-1} tor		Cham. pres.: 2.10^{-1} tor	
	Min.	Max.	Min.	Max.
1	104	535	378	598
2	100	550	558	2265
3	225	796	773	2570
4	303	1509	1488	3653

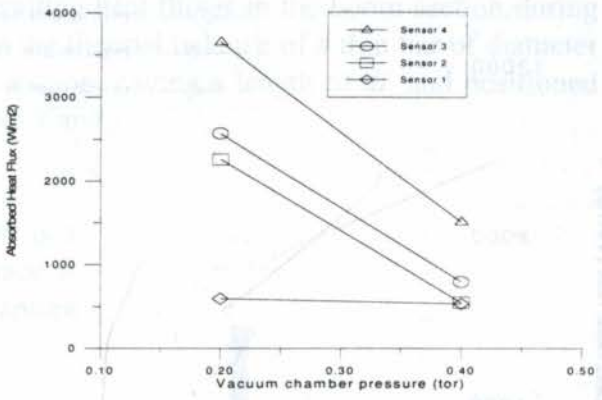

Figure 4 - Maximum Heat Flux in Function of Test Chamber Pressure

3.4. Comparison with theoretical prediction

The theoretical prediction is based on the formulation of Mayer,E. (1987). However, to adapt the conditions of the test to those of this reference, some parameters had to be calculated. These parameters are related to the sensor position (h, θ and δ) as presented in Figure 5, while Table 6 presents the results of the calculation. The obtained heat fluxes are then compared to those obtained by the formulation presented by Mayer,E. (1987) and summarized in Figure 6, showing that the theoretical prediction presents higher values of heat flux for sensors 1, 2 and 3 while exhibits a compatible value for sensor 4.

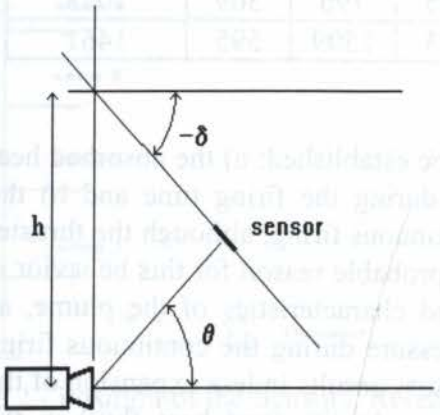

Figure 5 - Geometrical Parameters

Table 4 Geometrical parameters h, θ and δ, for each sensor.

Sensor	θ (deg.)	δ (deg.)	h (mm)	Heat flux (W/m2)
1	60.5	29.5	119	3562
2	25.5	64.5	486	9632
3	15.0	75.0	1343	5891
4	10.5	79.5	2710	3759

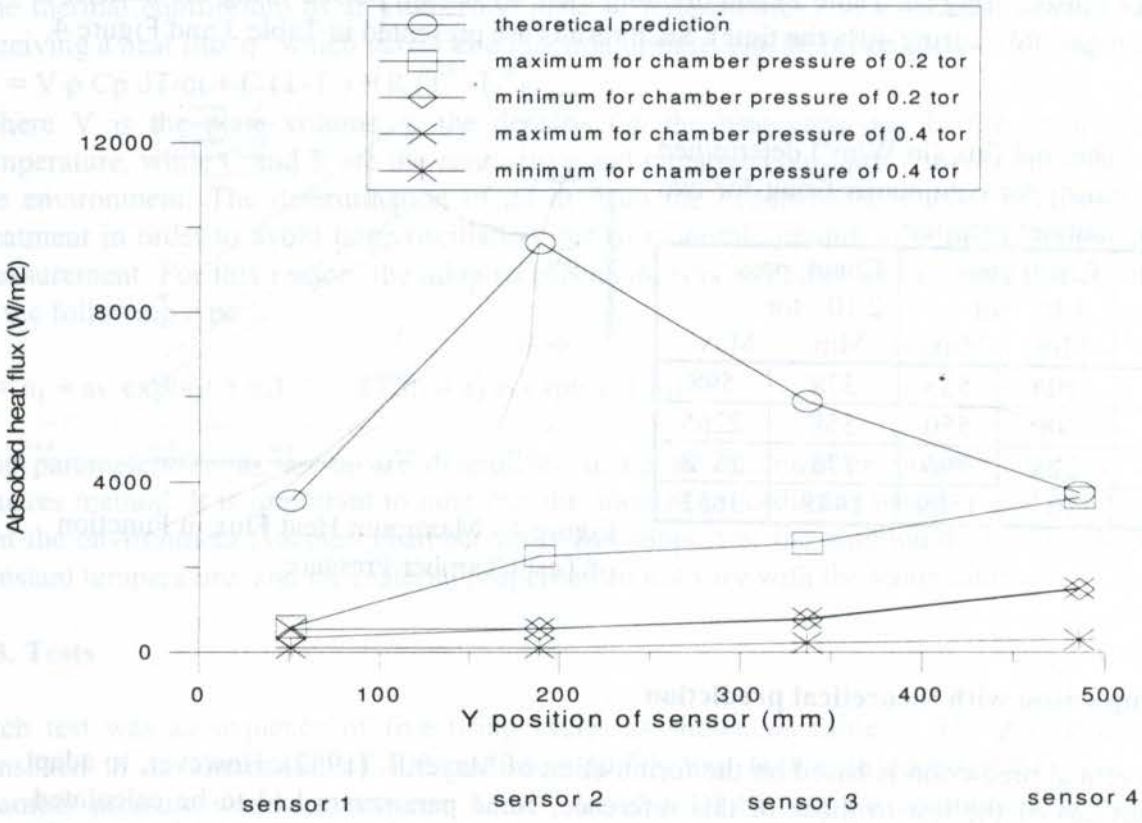

Figure 6 - Comparison of theoretical and experimental absorbed heat flux, for each sensor

4. BOOM CONFIGURATION.

4.1. Experimental Arrangement

In this case the experimental study was performed with a flight-like boom test section (with a length of 1 m and a weight of 60gr), made of three glass/epoxy longherons with a cross section of 2x2.1 mm; a set of 2mm thick polycarbonate spacers and seven 0.36mm core stainless cross wires. The boom was mounted in the vacuum chamber parallel to the thruster axis. A total of six Copper-Constantan thermocouples covered with 1/10 width aluminum tape were used. The performed tests are summarized in Table 5:

Table 5. Summary of Performed Tests

Test #	Firing	Time [sec]	Hydrazine Pressure [bar]	Initial C. Pres. [torr]	Final C. Pres. [torr]
1	Continuous	100	22	N/A	N/A
2	Continuous	100	22	10^{-3}	3.4×10^{-1}
3	Pulsed 50%ON	100	22	10^{-3}	1.8×10^{-1}
4	Pulsed 20%ON	100	22	10^{-3}	7.7×10^{-2}
5	Pulsed 10%ON	100	22	10^{-3}	6×10^{-2}
6	Continuous	100	11	10^{-3}	2.4×10^{-1}
7	Continuous	100	15	10^{-3}	2.55×10^{-1}
8	Continuous	100	21.5	10^{-3}	4×10^{-1}

4.2. Methodology for Absorbed Heat Flux Calculation

In order to have a numerical approach to the resulting heat fluxes in the boom section during the test, a first order model is proposed based in the thermal balance of a thin bar of diameter D, corresponding to a portion of the boom test section, having a length of dL and positioned with respect to the thruster through its coordinates x and y.

Under the assumption that the gas-flow regime is a free molecule flow, which means that the surface is far enough from the thruster, the effective capture area dA^* is calculated in the following way:

$$dA^* = dA\, x/(x^2 + y^2)^{1/2} = D\, dl\, x/(x^2 + y^2)^{1/2} \qquad (3)$$

The hypothesis of an interaction "far enough from the source", is acceptable if the distance between the thruster and the test element is at least in the order of ten nozzle diameters, which is satisfied in the test conditions. The thermal balance is then given by the following equation:

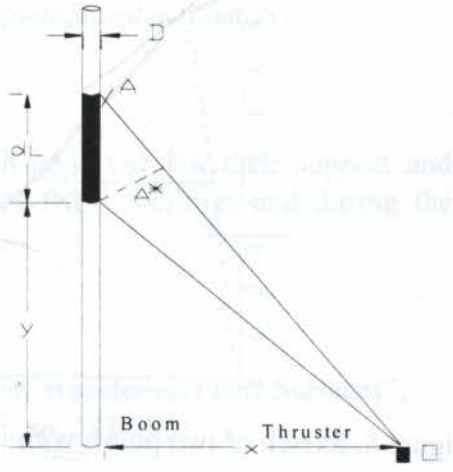

Figure7.Boom-Thruster Conf

$$\rho\, Cp\, \pi/4\, D^2\, dL\, (dT/dt) = q''\, Ddl\, x/(x^2 + y^2)^{1/2} - \pi\, DdL\, \varepsilon\, \sigma\, (T^4 - T_o^4) + \pi/4\, D^2 dL\, k\, (d^2T/dx^2) \qquad (4)$$

Where ρ, Cp, k, ε are average properties like density, thermal capacity, conductivity and emisivity, q'' is the absorbed energy flux per unit area and unit time, T is the resulting temperature of the node and T_o is a reference temperature. This equation can be greatly simplified if the conduction term is considered negligible, an approach that is acceptable in this case since the thermal conductivity of the fiber glass is small and since the temperature along the bar increases monotonously with respect to the height. Therefore, the net power stored in differential element can be considered as negligible in comparison with other sources (absorbed flux and radiation exchange). Moreover, there are other negligible effects that have

not been considered as the increase of chamber pressure during the firing which provides some additional heat exchange. For this reason, a more general expression of the equation can be written in the following way:

$$dT/dt = q''[x/(x^2 + y^2)^{1/2}]/[\rho\, Cp\, D\, \pi/4] - f(T) \quad (5)$$

Where $f(T)$ takes into account all the thermal losses (i.e. radiation and conduction) under the assumption that those losses are a function only of temperature. According to Figure 8, this hypothesis means that the rate of heat loss $f(T)$ in point 1 is equal to the rate of heat loss in point 2. Therefore, if $(dT/dt)_1$ is the first derivative in point 1 while $(dT/dt)_2$ is the derivative corresponding to point 2, an equivalence statement can be written which provides a direct way to obtain the resulting heat flux q'' as a function of x, y and the parameters ρCpD:

$$(dT/dt)_1 - (dT/dt)_2 = q''[x/(x^2 + y^2)^{1/2}]/[\rho\, Cp\, D\, \pi/4] \quad (6)$$

4.3. Comparison With Theoretical Predictions

The applicable theoretical model for this phenomena is the method derived by Genovese,J.E (1978). An application of this model for the conditions of the test is presented in Table 6, where E is the incident energy per unit time and unit area, E_A is the fraction that is finally absorbed by a normal surface while q'' is the heat flux derived from the tests for this conditions.

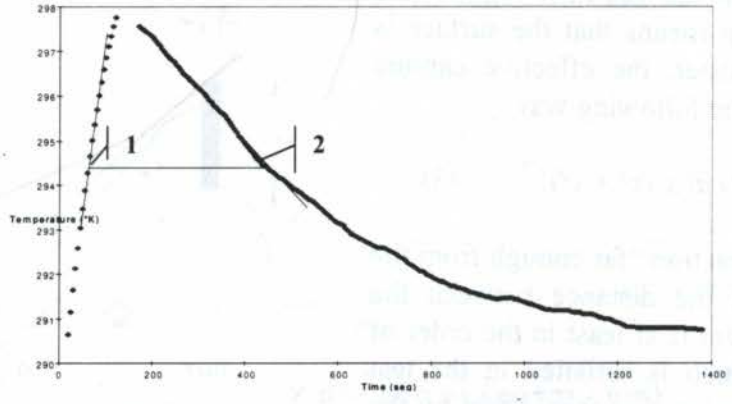

Figure 8. Sketch of two points with identical temperature and therefore with the same $f(T)$

Table 6. Comparison of predicted and measured values of heat flux

Channel #	x (cm)	y (cm)	$E_A=E/2$ (W/m²)	q'' (W/m²)	q''/E (%)
3A	15.0	17.0	3003	329	5.4
5A	15.0	34.0	3903	715	9.1
1A	15.0	51.0	2581	1479	28.6
2A	15.0	9.0	848	505	29.5
4A	15.0	25.0	4207	1585	18.8
6A	15.0	42.0	3258	2491	38.2

As Table 6 shows, the predicted heat fluxes are higher than the measured values. This discrepancy can be interpreted through two opposed points of view: a) the test is not

conservative due to the poor vacuum during the firing and therefore the measured fluxes are lower than those really attained in space conditions or b) the experimental results are close to space conditions and the discrepancy is maybe due to the fact that the gas-surface interface might be absorbing less energy than predicted (according to Table 6 less than 50%).

5. Conclusions

In the first part of the analysis, heat fluxes from plume impingement on aluminum plates were determined experimentally. The results show that the absorbed heat fluxes vary in a wide range as function of the test parameters. One remark is that although the gas mass flow is lower in pulsed firing than in continuos firing, the heat flux is greater in the first case. The probable reason is the effect of the chamber pressure (lower in pulsed firing) that changes the shape and characteristics of the plume. The same behavior was also observed during the tests on the SAC-C boom test section, where pulsed firings were performed with 50%, 20% and 10% cycled regimes, resulting in chamber pressures of $1.8\ 10^{-1}$, $7.7\ 10^{-2}$ and $6.0\ 10^{-2}$ tor respectively. The determined heat fluxes, considering the fraction of the time that the thruster is turned on, are higher as lower is the chamber pressure.Comparing the experimental results with theoretical predictions by Mayer,E. (1987) and Genovese J.E. (1978), a difference was observed in the distribution of heat flux along the plume flow field axis. As it is shown in Figure 6, in the theoretical calculation the maximum heat flux occurs in a middle position (sensor 2) while in the experimental determination the highest value was detected in the extreme (sensor 4). The same experimental profile was obtained with the boom test section. Moreover, even considering the tendency for lower chamber pressure, the profiles do not seem to become close. Further investigation should be done to explain this discrepancy.

6. Acknowledgments

Mr C.Barrientos and Mrs. A.Bartoli wish to thank Dr.Nivaldo et.al. for their support and worthwhile cooperation in performing the tests at the LIT-INPE facilities and during the discussion of the results.

7. Reference

Mayer, E. and Prickett, R., "Rocket Plume Impingement Heat Transfer on Plane Surfaces", *Journal of Spacecraft and Rockets*, Vol. 24, Jul. -Aug. 1987, pp. 291-295.

Madox, A.R., "Impingement of Underexpanded Plumes on Adjacent Surfaces", *Journal of Spacecraft and Rockets*, Vol. 5, June1968, pp. 718-724.

J.E. Genovese. "Rapid Estimation Of Hydrazine Exhaust Plume Interaction". No. 78-1091. AIAA/SAE 14th Joint Propulsion Conference. Las Vegas,Nev/ July 25-27,1978.

J.N.Hinckel, V.J.Trava Airoldi, E.J.Corat, I.E. de Oliveira Jr, C.Bressan. "Desenvolvimento De Propulsor Catalítico A Hidrazina Com 2n De Empuxo." III ENCIT - Itapema, SC (December1990).

XIV Brazilian Congress of Mechanical Engineering
Obeid Plaza Hotel Convention Center - Bauru - SP/Brazil
December 08-12th 1997

PAPER CODE: COB778

LIQUID FILM THICKNESS MEASUREMENT BY ULTRASONIC TRANSMISSION TECHNIQUE

MARCELO L. MORANDIM[1], MARCELO ALBUQUERQUE L. GONÇALVES[2], FERNANDO A. FRANÇA[1], GERALDO S. RIBEIRO[2] & EUGENIO S. ROSA[1]

1- Depto. de Energia, Fac. de Eng. Mecânica - UNICAMP - CEP 13081-970 - Campinas, SP - BRASIL (morandim@fem.unicamp.br , ffranca@fem.unicamp.br e erosa@fem.unicamp.br)
2- PETROBRAS - CENPES - DIPLOT - Ilha do Fundão - 21949-900 - Rio de Janeiro, RJ - BRASIL (marcelog@cenpes.petrobras.com.br e spin@cenpes.petrobras.com.br)

Abstract

In this paper is proposed and tested the use of a non-intrusive ultrasonic transmission technique for the measurement of the thickness of a liquid film flowing along a solid wall. The physical principles, as well as the experimental procedures for the method are presented. The tests were performed measuring film thickness inside a cylindrical chamber in which a liquid was tangentially injected, causing a film of liquid containing certain quantities of dissolved gas bubbles to rotate along the wall. The technique was tested using water, and the results were compared with values measured with an electric impedance sensor. In general, there was a good agreement between the values obtained from both methods, though there is a systematic difference due to the fact that the electric sensor is able to measure film thickness almost locally, while the ultrasonic technique averages the values over a larger region. The ultrasonic technique was also tested with a higher viscosity liquid, obtained by adding corn syrup to the water, for which the electric sensor was unable to measure. In this case, the results were compared to an analytical model, which was verified for the previous measurements with water. The results also showed good agreement.

Keywords

Liquid films, ultrasonic sensors, measurement techniques

1. INTRODUCTION

Liquid films flowing over solid walls are found very frequently in process equipment. Particularly, in gas-liquid cyclonic separators a liquid film is formed, rotating along the walls. To verify the flow models used in the development of design codes for these equipment, very often a reliable measurement of the thickness of the liquid films involved in the process is needed.

This paper presents and tests a method for liquid film thickness measurement using an ultrasonic technique. Tests were performed in a cylindrical chamber with a tangential inlet, through which a gas-liquid mixture is injected. This generated a rotating liquid film along the chamber's wall. With this arrangement, the flow at the entrance region of a cyclonic gas-liquid separator was simulated, and the results could be compared with the analytical model for laminar and turbulent flow developed by Rosa *et al.* (1996).

Tests were performed injecting water and a high viscosity liquid. The results obtained by the ultrasonic technique with water were compared with values measured by an electrical impedance probe, working under the conductance principle. A small but systematic difference was found between the two methods, and both results were compatible with the analytical model. For the tests with the high viscosity fluid, the ultrasonic was the only suitable technique for the measurements. As the viscosity of the liquid increases, also increases the time it takes to dry the tip of the conductance probe, distorting the phase density function, the primary data measured by the probe. Nevertheless, the results were again compatible with those given by the analytical model.

2. LIQUID FILM THICKNESS MEASUREMENT

2.1 Ultrasonic Method

The ultrasonic technique is based on the principle of the propagation of a sonic pulse through a non-homogeneous medium. Its application to the measurement of the thickness of a liquid film was first suggested (but not tried) by Chang *et al.* (1982). As far as mentioned in the relevant literature, there were no attempts to implement this method. In a related area, Tsouris & Tavlarides (1993) used ultra-sound for the measurement of the water content in a two-phase oil-water current.

The ultrasonic signal is emitted by a transducer and reflected at the gas-liquid interface. The measured transit time between the emitted and received signals is proportional to the film thickness, and the proportionality constant is the sonic velocity in the liquid medium, which can be easily determined. Figure 1 shows the measuring process and the resulting plot in the equipment screen.

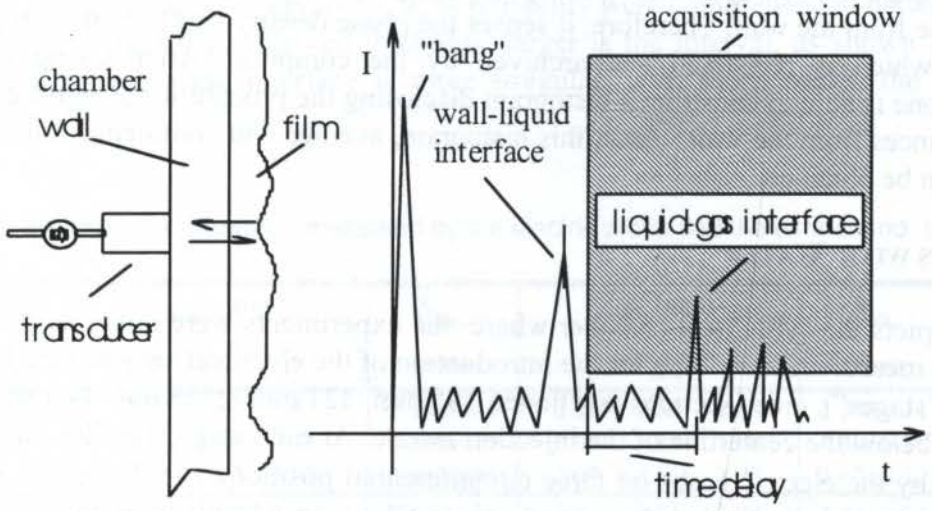

Figure 1 - Film thickness measurement and the resulting plot.

On the ultrasonic meter screen there are two "static" peaks, which do not move with time. The first one is the emitted pulse ("bang"), the second corresponds to the wall-liquid interface. The peak corresponding to the liquid-gas interface appears moving on the screen, because the ultrasonic signal is emitted several times per second (200 Hz, in this case) and the film thickness is not constant in time. Actually, there are several moving peaks showing up on the

screen, corresponding to the various reflections of the sonic pulse at the liquid-gas interface. However, the significant "moving peak" is registered as the first which occurs inside the acquisition window. The ultrasonic device has an analog output proportional to the time delay inside the window. The analog signal has a square wave profile, which must be integrated to calculate the average time delay value. Once the average time delay is determined and given the sonic velocity, it is possible to determine the thickness of the film.

2.1.1 Procedure for Film Thickness Measurement using Ultra-Sound

The ultrasonic device used was a *Epoch II* model, manufactured by *Panametrics,* for applications on non-destructive testing of materials. It was connected to a 486 PC microcomputer equipped with a *National Instruments*® A/D bus board and *LabWindows*® software.

The first step is to determine the medium sonic velocity, by taking a fluid sample in a beaker. The sensor is installed outside the glass wall, and the emitted pulse will reflect on the inner walls of the beaker. The sonic speed is the quotient between the signal path (which is the beaker diameter) and the analog value obtained for the transit time to the opposite wall reflection.

The following step is the measurement itself. The sensor shall be placed on the measurement spot. Then the signal of the first echo, corresponding to the wall-liquid interface, must be located. By setting the acquisition window after the first echo signal, the transit time (corresponding to the "moving peak") can be obtained through the analog signal (Figure 1).

2.2 Electric Sensor

The impedance sensor (Rosa *et al.*, 1996) is a needle probe that detects the phase occurring on its edge. Driven by a micrometer positioning device, the probe edge is located at a known distance from the wall. Therefore, it senses the phase density function of each phase, liquid or gas, which is registered and archived by the computer. After taking several measurements, one is able to construct a histogram disclosing the probability of finding liquid at different distances from the wall. From this histogram, average and confidence interval for the thickness can be obtained.

3. EXPERIMENTS WITH WATER

Figure 2 depicts the cylindrical chamber where the experiments were done, marking the positions of the measurements. Taps for the introduction of the electrical sensor were located at three levels ("stages"), cross sections positioned 185 mm, 327 mm e 515 mm (stages 1, 2 e 3, respectively) below the centerline of the injection nozzle. At each stage, the film thickness, δ, is measured by the electric probe on three circunferential positions (A, B and C), and on six positions (A through F) by the ultra-sound sensor. Here, an advantage of the ultrasonic technique becomes evident: by being an non-intrusive method, it allows much greater flexibility regarding the choice of the measurement position.

Three flow rates were tested with water: 2.30 kg/s, 3.00 kg/s e 3.77 kg/s. Table 1 shows the results obtained by both methods for positions A, B and C, on all stages.

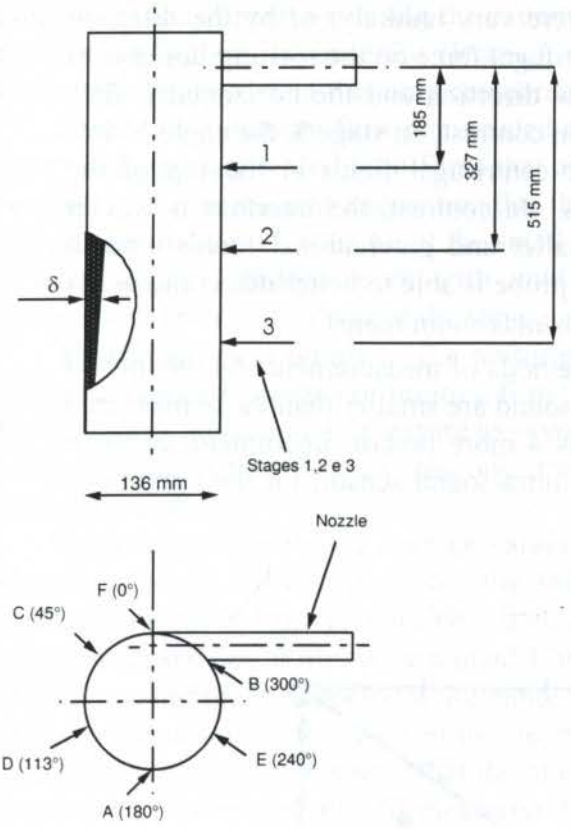

Figure 2 - Experimental setup

Film thickness measured by the ultra-sound were systematically smaller than the values measured by the conductance probe. The conductance probe, because of its small dimensions, provides an almost local measurement, while the ultra-sound averages the film thickness on a larger measurement volume. In fact, the sonic beam was emitted with a divergence angle of 5° and had around 7 mm diameter on its base (the diameter of the piezoelectric element). When it gets to the interface, the measuring volume is large. In contrast, the conductance probe detects the film within a circular region of around 1 mm diameter. Consequently, if the interfacial structure is smooth or presents smooth waviness, the values obtained by both methods must be very close. However, on a sharp wavy interface, the ultra-sound will attenuate the average value, because peaks will not be detected. Given the dimension of the sonic beam at the interface, the reflections on the flat surface region will overcome those from the peaks.

The analysis of confidence intervals for the ultrasonic measurements reinforces this explanation. The confidence intervals for 95% reliability were comprehended between 0.2 and 0.4 mm, and the larger the measured thickness, larger is the interval, as shown in Table 1. This means that where the interface is more irregular, with sharp peaks, the confidence intervals are wider.

Table 1: Film thickness for the water measured by the electric probe and the ultra-sound sensor

Flow Rate (kg/s)	Stage	$\delta_{elec.}$ (mm) A	B	C	$\bar{\delta}_{elec.}$ (mm)	$\delta_{ult.}$ (mm) A	B	C	$\bar{\delta}_{ult.}$ (mm)	$\frac{\bar{\delta}_{elec.}}{\bar{\delta}_{ult.}}$
2.30	1	2.48	2.89	2.35	2.58±0.41	2.29	2.65	1.88	2.27±0.34	1.14
	2	2.57	2.38	3.16	2.70±0.45	2.05	2.18	2.68	2.30±0.28	1.16
	3	2.72	2.67	3.08	2.82±0.75	2.07	2.12	2.03	2.07±0.32	1.36
3.00	1	2.78	3.49	2.57	2.95±0.43	2.34	3.13	2.08	2.85±0.24	1.04
	2	2.90	2.64	3.91	3.15±0.48	2.40	2.53	3.23	2.72±0.27	1.16
	3	3.77	3.07	3.18	3.34±0.57	2.97	2.57	2.48	2.67±0.30	1.25
3.77	1	2.48	3.68	2.79	2.98±0.43	2.24	3.80	2.34	2.79±0.24	1.07
	2	3.40	2.71	4.59	3.57±0.50	2.75	2.78	3.63	3.05±0.29	1.17
	3	5.17	3.43	3.47	4.02±0.70	4.45	2.92	2.93	3.43±0.39	1.17

The last column of Table 1 shows the ratio between the values measured by both techniques for each liquid flow rate tested at all stages. From stage 1 to stage 3, as the flow descended in the chamber, this ratio always increased, for all flow rates. This increase may be

explained either by small positioning errors (which were very unlikely) or by the different interface structures on each stage. On stage 1, the centrifugal force on the rotating liquid is of a considerable magnitude. The angle between the flow direction and the horizontal is 25°, which indicates a high tangential velocity component. In contrast, on stage 3, the angle is 44°, indicating a smaller tangential velocity. The higher centrifugal fields at the top of the chamber causes a smooth film interface in this region. In contrast, the interface is wavier down the chamber, where the centrifugal field is smaller and gravitational forces tend to disturb the smoothness of the flat surface. The electric probe is able to better detect the peaks in this region, and this explains why the ratio $\bar{\delta}_{elec.}/\bar{\delta}_{ult.}$ is maximum there.

Figure 3 shows the correlation between the two methods of measurement. As mentioned before, it is clear that the values measured by the ultra-sound are smaller than those measured by the electric probe. Assuming the electric probe is a more precise instrument, one can easily draw from this graph a calibration curve for the ultra-sound sensor, for the conditions tested.

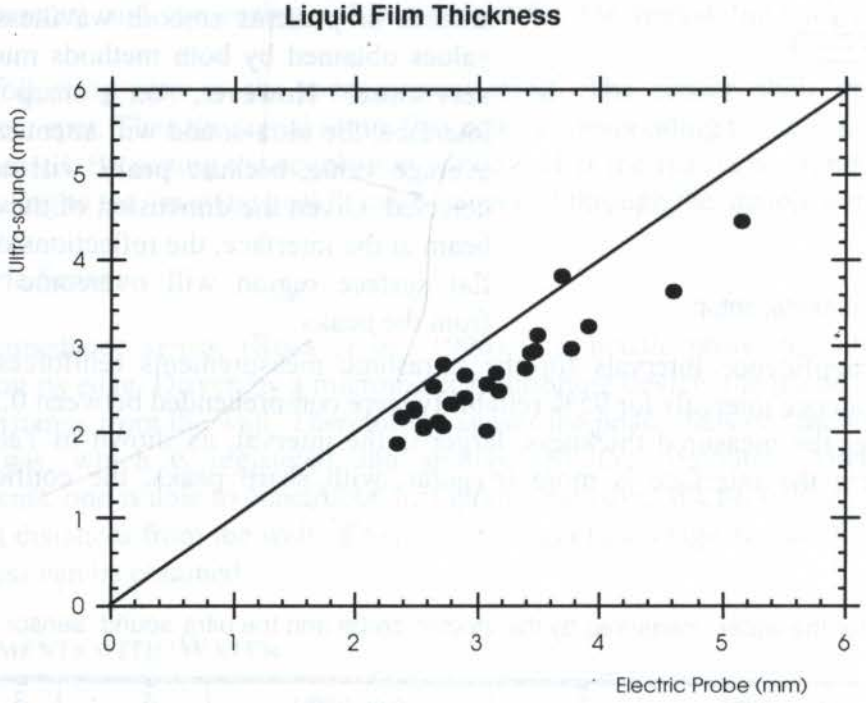

Figure 3 - Film thickness measured by the electric probe and the ultra-sound.

An analytical model for turbulent and laminar film flow is given by Rosa *et al.* (1996). The authors provide a comparison between the values furnished by the model and measured by the electric probe for the same flows tested in the present work, finding a good agreement between them. Adding the ultrasonic data to those, one can say that their analytical model was validated by two different experimental methods.

4. EXPERIMENTS WITH HIGH VISCOSITY LIQUID

The ultrasonic technique for film thickness measurement was also tested with a high viscosity fluid. The working fluid was a mixture of water and corn syrup (*Buffalo* 500-viscosity 40 cP, density 1.285 g/cm^3, at 35 °C). A heat exchanger provided control for

constant fluid temperature during the experiments. Only the ultrasonic technique was suitable for this application, because the electrical probe does not work with non-conductive fluids. Hence, the obtained data was only compared with the analytical model of Rosa *et al.* (1996).

There is a minimum flow rate needed to assure the axi-symmetric flow. However, high flow rates generate wide liquid films that are difficult to measure with the ultrasonic sensor, because of the increase of attenuation due the distance the signal has to travel. In the case of a viscous aerated liquid, because of the small gas bubbles carried in the film, signal attenuation is even higher. Indeed, even with void fractions as low as 1% there was significant attenuation. Thus, only a part of the sonic pulses was able to reach back the receptor probe.

To deal with this problem, the sensor gain was set as high as possible and a compromise had to be reached in terms of limiting film thickness, reducing the flow rate to 2.6 kg/s. This flow rate was high enough to ensure axi-symmetric flow and a reasonable film thickness. Due to the fact that there was a low response frequency, data acquisition occurred at rates ranging from 50 to 200 Hz.

Table 2 summarizes the average values for film thickness measured at each stage by the ultrasonic probe. Also shown, for the sake of comparison, are the values given by the analytical model of Rosa *et al.* (1996), both for the laminar and turbulent cases. The Reynolds numbers for the liquid film were around 1700. According to Levich (1962) the transition from laminar to turbulent happens at Reynolds 1500. Due to the proximity of transition, both laminar and turbulent flows given by the model were considered for comparison. From the data shown in Table 2, it seems that the model fits the experimental data. In addition, it was verified that the model also fit measured data of the film angle with the horizontal the and tangential and axial film velocities.

Table 2: Film thickness for the high viscosity liquid (flow rate 2.6 kg/s): measured by the ultra-sound probe and calculated by the model of Rosa *et al.* (1996)- laminar and turbulent cases.

Stages	Model - Laminar $\overline{\delta}$ (mm)	Model - Turbulent $\overline{\delta}$ (mm)	Ultrasonic data $\overline{\delta}$ (mm)
1	3.2	3.2	3.2 ± 0.4
2	3.4	2.9	3.4 ± 0.4
3	3.4	2.8	3.4 ± 0.4

It is important to note that the uncertainty for the measurements with the high viscosity liquid is greater than in the case of water. Low frequencies of data acquisition may be the reason for this higher uncertainty.

5. CONCLUSION

The tests showed that the ultrasonic technique is a viable method for liquid film thickness measurement. The experimental results indicate that the values measured by the ultrasonic sensor are compatible (within a systematic difference intrinsic to the technique) with those obtained with an conductance probe, a more precise method.

Though the ultrasonic method is not as precise as the electric probe, its use may present some advantages, in many cases. First of all, it is a flexible method: one can install the sensor anywhere over the surface where the film flows, without the need for special taps required by the electric probes. Furthermore, the ultra-sound sensor is non-intrusive, it does not influence significantly the flow field which is being measured. Plus, it is suitable for use with high

viscosity fluids or non-conductive fluids, in contrast with the electric probe. However, the ultra-sound technique also has its limitations because of signal attenuation, in the cases of thick films, or films aerated or with solids in suspension.

Additionally, it appears that the ultra-sound technique can also be used to measure film thickness in situations other than the tested (rotating film on a cyclone walls), such as in annular gas-liquid or liquid-liquid flows, and around gas bubbles in slug flows. Further studies on these applications are recommended.

6. ACKNOWLEDGMENTS

The authors thank the Engineers Ricardo O. Carneval and Cláudio S. Camerini (PETROBRAS/CENPES/DIPLOT), for lending the ultrasonic equipment and for the advises on its operation.

7. REFERENCES

CHANG, J.S., ICHIKAWA, Y. & IRONS, G.A. Flow regime characterization and liquid film thickness measurement in horizontal gas-liquid two-phase flow by an ultrasonic method, in *Measurements in poliphase flows*, ASME, 1982.

LEVICH, V.G. *Physicochemical hydrodynamics*, Prentice Hall, Englewood Cliffs, NJ, 1962.

ROSA, E.S., MORANDIN, M.L., DIAS, S.G. & FRANÇA, F.A. Liquid film motion under the action of gravitational and centrifugal fields, *Anais do VI Congresso Brasileiro de Engenharia e Ciências Térmicas (ENCIT 96)*, pp. 1127-1131, Florianopolis, SC, 1996.

TSOURIS, C. & TAVLARIDES, L.L. Volume fraction measurements of water in oil by an ultrasonic technique, *Ind. Eng. Chem. Res.*, vol. 32, pp. 998-1002, 1993.

XIV Brazilian Congress of Mechanical Engineering
Obeid Plaza Hotel Convention Center - Bauru - SP/Brazil
December 08-12th 1997

PAPER CODE: COB799

DETERMINAÇÃO DO COEFICIENTE GLOBAL DE TRANSFERÊNCIA DE CALOR EM RODAS FERROVIÁRIAS / *DETERMINATION OF THE OVERALL HEAT TRANSFER COEFFICIENT IN RAILROAD WHEELS.*

AUTELIANO ANTUNES DOS SANTOS JÚNIOR & FAUSTO RODRIGUES FILHO
Laboratório Ferroviário - Departamento de Projeto Mecânico
Faculdade de Engenharia Mecânica - UNICAMP
CEP. 13100-970 - Campinas (SP) - Brasil - E.mail: aute@fem.unicamp.br

Abstract

The objective of this work is to present a determination of a value for the overall heat transfer coefficient to be able to simulate the heating during the braking process in 33 inch (838 mm) railroad wheels. To achieve this objective it was necessary to design and construct a full scale dynamometer to reproduce the most commom braking conditions found in railway operation. The variations in brake power and temperature were measured during standardized tests and were compared to the results obtained from a finite element numerical simulation. Many trial simulations were realized in orde to achieve better agreement betwen the numerical predictions and the experimental results. A value of 25 W/m^2 °C was found for the overall heat transfer coefficient when used with 80% of the total generated friction power. The results of this work are important to determine the thermal stresses in railway wheels during braking and this represents the major aim of the Railway Laboratory of the State University of Campinas.

Keywords

Railroad wheels, railroad braking, wheels failures, brake heating, frenagem ferroviária

1. INTRODUÇÃO

O processo de frenagem ferroviária em vagões de carga consiste na aplicação de uma sapata sobre a superfície de rolamento da roda, visando retardar o movimento do veículo (figura 1). Como em todas as frenagens por atrito, a energia potencial ou cinética subtraída do sistema é transformada em calor. Na frenagens em rampas com velocidade constante, é usual aplicar uma força normal fixa e corrigí-la com novas aplicações ou alívios conforme haja variação na velocidade inicial. Pode-se também fixar a força de aplicação da sapata de forma a iniciar a descida de uma rampa com velocidade baixa e chegar ao final com uma velocidade maior, porém dentro da faixa segura para as características do transporte. Este último procedimento pode ser visto na Estrada de Ferro Carajás da Companhia Vale do Rio Doce (MA), onde a composição inicia a descida com velocidade de 25 km/h e, cerca de 25 minutos depois, a conclui a 80 km/h (Santos; 1995).

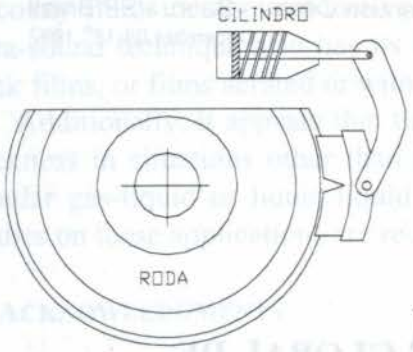

Figura 1. Esquema simplificado de aplicação da força de frenagem

O calor gerado na interface sapata-roda durante o processo de frenagem flui para a roda, para a sapata e perde-se para o meio sob outras formas de energia. A parte do calor que entra na roda aquece a superfície imediatamente sob a área de contato com a sapata e o calor flui por condução para o seu interior. Devido a resistência térmica do material da roda, as regiões próximas à fonte de calor aquecem-se mais do que as demais partes. Quanto mais distante a região, ou seja, mais próxima do centro da roda, maior é a diferença de temperatura em relação à superfície de rolamento. Esse gradiente térmico causa expansão diferenciada das diversas regiões da roda: o aro (aquecido) tende a aumentar suas dimensões enquanto o disco e o cubo (mais frios) restringem sua expansão. O formato característico das rodas atualmente utilizadas ("Deep Dish") facilita o surgimento de tensões de tração radiais no disco e de compressão circunferenciais (tangenciais) no aro. Parte das tensões de tração são devidas ao deslocamento axial do aro em relação ao cubo, causando flexão na concordância aro-cubo durante a expansão do primeiro, e parte são devidas diretamente à expansão do aro aquecido, que tende a alongar o disco.

Os principais problemas relacionados à este aquecimento e que surgem durante a operação são: escamação superficial ("thermal shelling"), cavitação superficial("spalling") e trincas. A escamação é um fenômeno típico do contato durante o rolamento entre superfícies metálicas (ex. mancais de rolamento) e que consiste no surgimento de pequenas trincas superficiais que se propagam na direção da tensão máxima de cisalhamento. Após suficiente propagação, o próprio movimento do veículo causa o arrancamento das escamas, formando pequenas crateras (Wetenkamp; 1992). Esse tipo de dano é muito comum em veículos de elevada carga e tem causados a perda significativa de recursos por parte das ferrovias nacionais (CVRD, 1988). A cavitação superficial surge devido à mudança estrutural que ocorre em regiões localizadas da superfície de rolamento durante a frenagem com travamento da roda. Nessas ocasiões, a superfície em contato com o trilho aquece-se a temperaturas elevadas (acima de 700 ^{o}C) e, quando o veículo para, permanece em contato com o trilho frio. Isso permite que haja um rápido resfriamento, o que causa a formação de estruturas diferentes das que originalmente formam a roda. A estrutura passa de perlita fina para bainita ou martensita. Como são estruturas diferentes em contato, surgem trincas na interface entre elas, as quais se propagam rapidamente. Da mesma forma que na escamação, o próprio movimento se encarrega de retirar a estrutura diferente do meio original. As crateras causadas por este tipo de dano são maiores do que as causadas por escamação e são localizadas, enquanto que na escamação são uniformemente distribuídas ao longo de toda a superfície de rolamento. O terceiro tipo de problema, trincas, não ocorre necessariamente na superfície de rolamento e tem como principal característica poder levar a danos catastróficos, tais como descarrilhamentos, quebras de suspensão, etc...

O processo de fabricação de rodas leva ao surgimento de tensões residuais de compressão circunferenciais no aro (Wandrisco, 1960). Durante a operação, frenagens severas causam a alteração do padrão inicial de distribuição de tensões para tração. Trincas que eventualmente surjam e que jamais se propagariam, têm assim a condição necessária para seu desenvolvimento. Essa mudança no padrão residual acontece porque há escoamento à compressão no aro durante a frenagem. Quando a roda esfria, as partes vizinhas da região sob escoamento e que se deformaram apenas elasticamente aliviam a pressão que causavam sobre

a parte que deformou-se plasticamente e essa pode voltar a ocupar o volume inicial. Como houve escoamento à quente, a porção do material não mais tende a ocupar todo o volume inicial e, ao ser forçada a isso pelas partes frias, passa a ser solicitada à tração.

Para modelar o efeito de frenagens severas sobre a distribuição de tensões em rodas ferroviárias utilizando métodos numéricos é necessário conhecer as condições de contorno do problema e as propriedades dos materiais. Para obter a distribuição de tensões é preciso conhecer primeiro a distribuição de temperaturas. A Associação Americana de Ferrovias - A.A.R. (A.A.R.; 1985) recomenda o uso dos programas Ansys e Batelle para o cálculo da distribuição de tensões e temperaturas na avaliação do efeito de frenagens severas sobre as rodas e lista valores de referência para as condições de contorno e propriedades dos materiais que devem ser usados. As propriedades térmicas do aço utilizado em rodas são bem conhecidas e não é esperado um erro significativo quando da utilização dos valores citados. No entanto, as condições de contorno do problema dependem de uma série de fatores. Em especial, o coeficiente global de transferência de calor (radiação e convecção) pode variar com a velocidade, emissividade, condições ambientais, etc. Além disso, os valores de temperatura medidas por pesquisadores ligados à área ferroviária (Novac *et al*, 1975; Novac *et al*, 1977; Johnson *et al*, 1977) não concordam suficientemente com os valores calculados.

Este trabalho tem como objetivo apresentar em linhas gerais o desenvolvimento e os resultados de um trabalho de doutoramento visando determinar um valor do coeficiente global de transferência de calor que possa ser usado para simular numericamente a distribuição de temperaturas em rodas ferroviárias visando o estudo dos problemas causados pelo aquecimento na frenagem.

2. MATERIAIS E MÉTODOS

Para determinar o valor do coeficiente que seja representativo do processo de transferência de calor ao meio foi feita a comparação entre os valores calculados e medidos da temperatura superficial durante frenagens conhecidas. A medição foi feita na Máquina de Ensaio de Sapatas, dinamômetro construído como resultado de convênios com ferrovias nacionais e posto em operação como resultado deste trabalho.

A Máquina de Ensaio de Sapatas é um dinamômetro capaz de ensaiar rodas e sapatas ferroviárias em escala real. É formado por um motor Garret C.C. (134 CV, 1800 rpm) com conversor de potência, torquímetro, redutor Sauer (5:1), eixo de rodas e cilindro de freios, conforme mostrado na figura 2. A instrumentação acoplada é composta de medidor de pressão pneumática, temperatura e velocidade, além do torquímetro. Todos os ensaios são feitos utilizando um sistema de aquisição e controle de dados baseado em um equipamento HP 3852 A e controlado por um programa desenvolvido no próprio Laboratório Ferroviário (Resende, 1996). A força normal aplicada à sapata é controlada por uma válvula pneumática proporcional. A calibração desta força em função da excitação da válvula foi feita utilizando uma célula de carga com valores rastreáveis da relação entre a força e a tensão elétrica de saída. A calibração do torquímetro foi feita da mesma forma. A calibração dos termopares foi feita no laboratório de instrumentação e medidas do Depto. de Energia Térmica e Fluídos da FEM\UNICAMP. A velocidade foi medida por um tacômetro acoplado ao eixo do motor, o qual é a referência para o conversor de velocidades.

O método dos elementos finitos (programa Ansys v. 5.0) foi utilizado para o cálculo da distribuição de temperaturas. O problema foi modelado como axissimétrico em relação ao eixo central da máquina. Um estudo foi feito para verificar a validade desta hipótese.

A roda ensaiada foi do tipo utilizado na Estrada de Ferro Vitória-Minas (Companhia Vale do Rio Doce), fundida e com 838 mm de diâmetro externo (33 pol.).

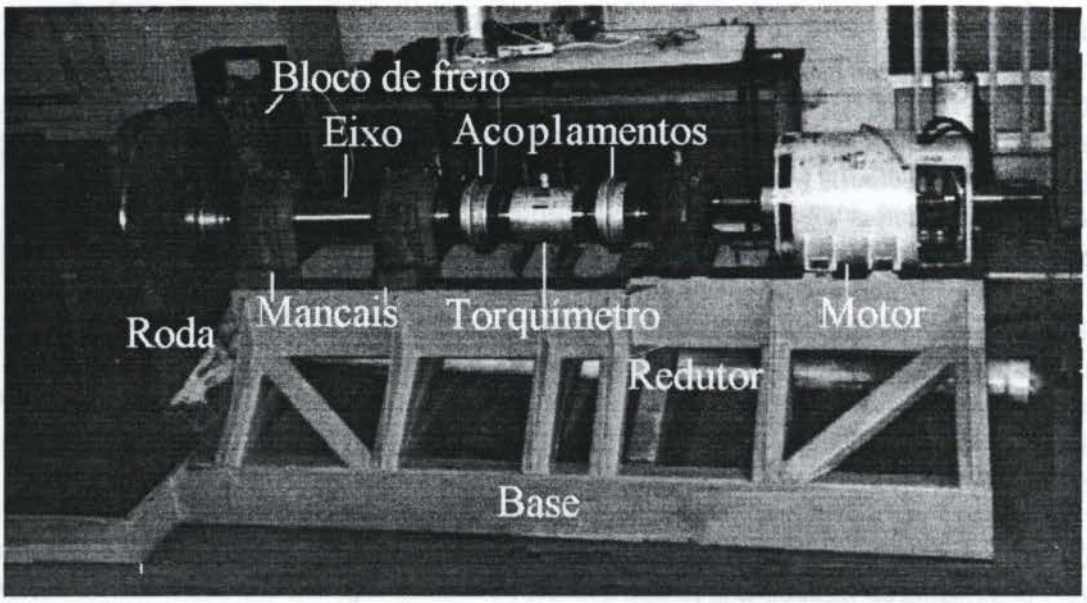

Figura 2. Máquina de Ensaio de Sapatas (M.E.S.) - Laboratório Ferroviário\DPM\FEM

3. METODOLOGIA

Devido à grande variação existente nas frenagens em operação foi necessário definir parâmetros que fossem representativos das condições reais de trabalho. É consenso atualmente no Brasil utilizar a norma M-926, da Associação Americana de Ferrovias (A.A.R., 1992), para ensaios de sapatas de freio, já que as características de carga, velocidade e tipo de veículo são muito semelhantes. Este ensaio consiste em dois módulos: um para frenagem constante, simulando descida em rampas, e outro para frenagens de parada, simulando tanto frenagens comuns como de emergência. Devido às características da M.E.S., até o momento sem inércias mecânicas ou eletrônicas, e também devido a instabilidade no comportamento do coeficiente de atrito durante a frenagem, além do pouco tempo até a parada, optou-se por utilizar apenas o primeiro módulo. Embora ciente de que o valor obtido seria, à princípio, válido apenas para a velocidade do ensaio tratava-se do primeiro passo na obtenção do coeficiente procurado. Um outro fator a ser considerado é a velocidade transversal do ar em relação à roda durante as frenagens em operação real. Algumas simulações foram feitas levando com ventiladores, mas os resultados ainda não são conclusivos. Estudos levando em conta a variação dos parâmetros serão feitos posteriormente.

3.1 Características dos Experimentos

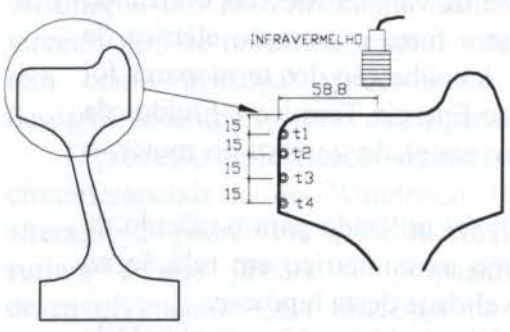

Figura 3. Posição de medida das temperaturas t1,t2, t3 e t4

Quatro termopares tipo K foram presos por resina epóxi, previamente testada, à pontos localizados na superfície da roda e que serviram para comparação com a distribuição calculada. A figura 3 mostra a localização desses pontos. Um aparelho Omega OS-42 KC foi utilizado para amplificar o sinal dos termopares antes que esses passassem através da escova coletora de sinais presa à ponta do eixo.

A velocidade do Ensaio de Frenagem Constante (EFC) é de 32,5 km/h, que pode ser

considerada a velocidade média em frenagens no país. A força normal aplicada à sapata tem dois níveis: 4120,0 e 6376,5 N (420 e 650 kgf). Para este trabalho foi utilizada o valor de 6376,5 N. A taxa de aquisição utilizada foi de 10 Hz para todos os sinais e a duração da frenagem de 45 min.

3.2 Simulação Numérica

As propriedades utilizadas para o material da roda são (A.A.R., 1985):

Condutividade Térmica:	$k = 48{,}27 - 0{,}0187 * T(^{o}C)$	$[W/m.^{o}C]$
Calor Específico:	$c = 434{,}00 + 39{,}10\ e\text{-}2 * T(^{o}C)$	$[J/kg.^{o}C]$
Densidade:	$dens = 7833{,}40$	$[kg/m^3]$

Os valores de potência de frenagem foram calculados a partir do torque de atrito medido e da velocidade de rotação. A simulação foi feita com valores da potência de frenagem real medida em cada ensaio. Foram utilizados seguimentos de reta para descreverem a variação do coeficiente de atrito durante o ensaio. Essas retas descrevem o comportamento com diferenças máximas de 3% em relação aos valores medidos durante cada ensaio. A entrada de calor consistiu em uma região com largura equivalente à da sapata ferroviária (70 mm) localizada na região central da superfície de rolamento, com a face externa posicionada no ponto de tangência entre o raio de concordância aro-superfície de rolamento e essa última. Os elementos utilizados foram o Plane77 (8 nós, axissimétrico, opção para cálculo de temperatura) para o material da roda e Surf19 (3 nós, axissimétrico, para convecção), elemento superficial que permite o cálculo da quantidade total de calor gerada em regime transiente e onde são aplicadas as condições de contorno. A seção radial da roda foi dividida em cinco áreas e o tamanho dos elementos variou de 8 a 20 mm, partindo da região próxima à superfície de rolamento em direção ao eixo de simetria (cubo).

3.3 Comparação Teórico-experimental

Foram realizados cerca de cem ensaios, quarenta dos quais considerados válidos, e as temperaturas medidas sempre se comportaram de forma coerente com o valor do coeficiente de atrito, aumentando conforme aumentava a potência de frenagem.

Inicialmente as simulações foram feitas considerando os valores de literatura para o valor do coeficiente global de transferência de calor h_t . Esse variam de 19,9 W / m^2 °C (Larson *et al.*, 1978) a 22,7 W / m^2 °C (A.A.R., 1985). Os resultados calculados apresentavam diferenças significativas em relação aos medidos. A seguir optou-se por utilizar as equações clássicas para a determinação do coeficiente médio de convecção h_c em discos girantes (eq. 1) (Cobb e Sauders in Kreith, 1977) e em cilindros (eq.2) (Kays in Kreith, 1977). Novamente os resultados calculados mostravam valores de temperatura maiores do que os medidos.

$$Nu = h_c \,.\, D / k = 0{,}11 \,.\, [(0{,}5.\, R_{ew}{}^2 + Gr_D) \,.\, Pr\,]^{0{,}35} \qquad (1)$$

$$Nu = h_c \,.\, D / k = 0{,}35 \,.\, (w.r_o{}^2 / \mu)^{0{,}5} \qquad (2)$$

Diversas simulações foram feitas e verificou-se que os valores de h_c coerentes sempre levavam a temperaturas mais elevadas, significando que as perdas de potência para a sapata ou para o meio não são desprezíveis, ou seja, um valor de potência de frenagem menor deveria estar aquecendo a roda. Wetemkamp (1992), ciente desse fato, utilizou considera que apenas

2/3 da potência total gerada aquece a roda. Simulações com esse valor levaram a temperaturas calculadas mais baixas que as medidas.

Buscando determinar se a quantidade de calor que flui para a sapata é significativa, mediu-se as temperaturas superficiais desta durante um ensaio e determinou-se que não mais que 5% do valor total aquece a sapata. Além disso, a avaliação da transferência de calor por radiação no intervalo de temperaturas atingido durante o ensaio (25 a 400 °C) mostra que a troca de calor por radiação chega a apenas 3% da potência de frenagem na superfície sob a sapata, mas pode chegar até a cerca de 15 % nas demais superfícies. Com base nesses valores optou-se por reduzir a potência total que aquece a roda na simulação numérica. Como a análise de incertezas na instrumentação mostra um desvio de até 3% no valor da potência de atrito, optou-se por variar esse valor em intervalos de 5% (0,7 ; 0,75 ; 0,8 ; 0,85 e 0,9 da potência gerada), considerando o coeficiente global de transferência de calor entre os valores obtidos em literatura para disco girantes sob convecção (~ 20 W / m^2 °C) e para cilindros rotativos longos (~ 70 W / m^2 °C).

4. RESULTADOS

As diferenças entre os valores calculados e medidos para os pontos selecionados foram traçadas graficamente em relação ao tempo de ensaio. A melhor concordância foi atingida quando considerado que somente 80% da potência de atrito gerada aquece a roda a partir da superfície de rolamento, aliado a um coeficiente global de transferência de calor de 25 W/m^2.°C para toda a roda. A figura 4 mostra a diferença percentual para o ensaio para o ensaio E96143. Embora a diferença possa chegar a 20 % para as temperaturas mais distantes da superfície de rolamento, os valores absolutos dessas temperaturas nesse momento são baixos, o que não implica em maiores problemas em termos de falhas em rodas. Conforme pode ser visto na figura 5, no momento em que as diferenças percentuais são mais significativas as temperaturas diferem de apenas 10 °C, chegando a um máximo de 20 ° C durante todo o ensaio. Esse comportamento se repetiu em todos os demais ensaios realizados, inclusive quando, ao invés de frear durante 45 minutos, optou-se por frear 30 minutos e deixar o freio aliviado durante os 15 minutos restantes do ensaio. Nesse caso, a concordância entre os valores no resfriamento foi ainda maior.

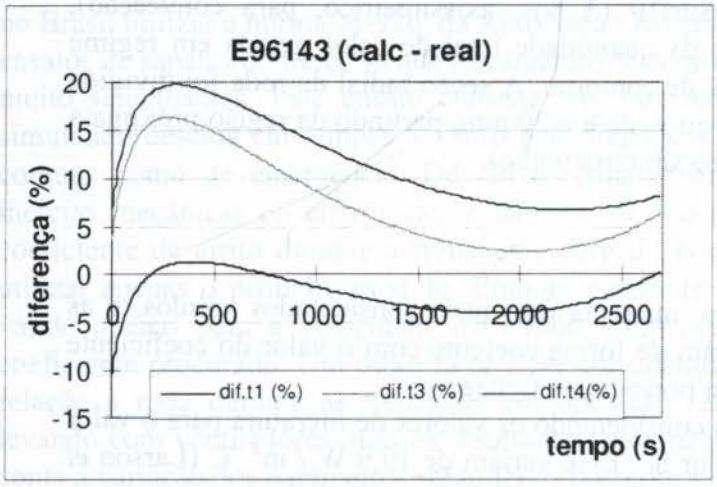

Figura 4. Diferença percentual entre as temperaturas calculadas e medidas - Ensaio E96143

Na análise das diferenças entre os valores obtidos foi estudada também a influência da radiação durante todo o processo de aquecimento. Com base em valores estimados de emissividade, obtidos em literatura (Kreith, 1977), foram calculadas perdas por radiação de até 13 % do calor gerado. Certamente esta variação pode explicar parte da diferença de temperaturas encontrada, mesmo considerando que essa porcentagem limite não representa o valor da perda a todo instante durante os ensaios.

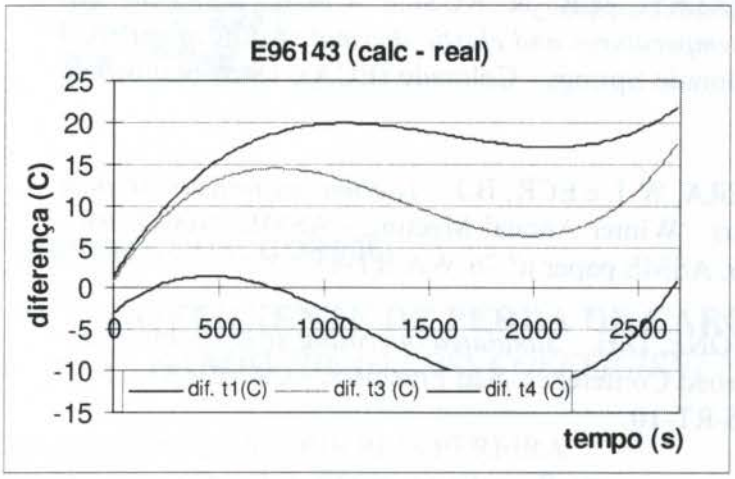

Figura 5. Diferença entre as temperaturas calculadas e medidas - Ensaio E96143

5. CONCLUSÕES

Este trabalho mostra os resultados de uma tese de doutoramento visando determinar experimentalmente um valor do coeficiente global de transferência de calor que possa ser utilizado na simulação numérica do aquecimento em rodas ferroviárias durante a frenagem, com o qual espera-se calcular a distribuição de tensões térmicas a fim de analisar problemas de falhas em serviço. Através de comparação teórico-experimental determinou-se que nem toda a potência gerada é utilizada no aquecimento das rodas. Na realidade, cerca de 20 % do total gerado aquece a sapata (condução) ou é transferido quase que imediatamente por radiação e convecção na superfície de rolamento. Essa observações condizem com o fato de que a parcela devida a radiação superficial aumenta com a temperatura, chegando a até 15%; que o coeficiente de transferência de calor por convecção na superfície cilíndrica pode ser até três vezes maior do que o valor para as laterais, consideradas como discos girantes, e que a sapata pode absorver até 5% do calor total gerado. Assim, um modelo que use um valor apenas para o coeficiente em questão deve necessariamente incluir uma redução na potência total gerada, que é aplicada à parte cilíndrica, para compensar a maior perda de calor nessa região. O valor do coeficiente global de transferência de calor que resultou na melhor concordância entre os valores calculados e medidos é 25 W / m^2 °C. Este valor, como esperado, se aproxima muito do valor para discos girantes, já que as diferenças para a parte cilíndrica foram consideradas na redução da potência total.

Novos ensaios estão sendo feitos a fim de verificar a influência da velocidade tangencial e da força normal.

6. REFERÊNCIA BIBLIOGRÁFICAS

A.A.R., Association of American Railroads. *Wheel and axle manual: manual of standards and recommended practices.* Washington, A.A.R., agosto de 1985.

A.A.R., Association of American Railroads. *Brake shoes: high friction composition type - M-926.* Washington, 1992.

JOHNSON, M.R.; WELCH, R.E. & YEUNG, K.S. *Analysis of thermal stresses and residual stress changes in railroad wheels caused by severe drag braking.* Transactions of ASME. Fevereiro de 1977. p. 18-23.

KREITH, F. *Princípios da transmissão de calor.* 3 ed. Ed. Edgard-Blucher, São Paulo (SP), 1977. 552 p.

LARSON, H.R.; COUGHLIN, J.M.; HALEY, M.R. & RUSIN, T.M. *Experimental verifications of computer predicted temperatures and elastic thermal strains in railroad wheels*. Int. Wheelset Congress. Colorado Springs - Colorado (EUA), 18 de outubro de 1978. p. 4-1-1 a 4-1-21.

NOVAK, G.E.; DAHLMAN, G.E.; KUCERA, W.J. e ECK, B.J. *Thermal patterns in 36 inch fright car wheels during service tests.* Winter Annual Meeting - ASME. New York - N.Y. (EUA), 5 de dezembro de 1976. ASME paper nº 76-WA/RT-11.

NOVAK, G.E.; GREENFIELD, L.P. e STONE, D.H. *Simulated operating stresses in 28-in.-Dia wheels*. ASME-IEEE Joint Railroad Conference. São Francisco - CA (EUA), 15-17 de abril de 1975. ASME paper nº 75-RT-10.

RESENDE, W.A.A.M.C. *Aquisição de dados e controle automático de ensaios de frenagem.* Dissertação de Mestrado, FEM\UNICAMP. Campinas, 9 de agosto de 1996.

SANTOS, A.A. e RODRIGUES Fº, F. *Aquecimento em rodas ferroviárias durante e após frenagens contínuas prolongadas*. XIV Congresso Brasileiro de Engenharia Mecânica - COBEM. Belo Horizonte, dezembro de 1995.

SANTOS, A.A. Jr. *Problemas causados pelo aquecimento em rodas ferroviárias - o ensaio krauss.* Dissertação de Mestrado, FEM\UNICAMP. Campinas (SP), 31 de março de 1992. 168 p.

SANTOS, A.A. Jr. *Determinação do coeficiente global de transferência de calor em rodas ferroviárias.* Tese de Doutorado, FEM\UNICAMP. Campinas (SP), 17 de outubro de 1996. 124 p.

WANDRISCO, J.M. e DEWEZ, Jr. *Study of the defects that originate and develop in the treads of railroad wheels during service.* ASME-IEEE Railroad Conference. Pittsburg - PA (EUA), 20-21 de abril de 1960. ASME paper nº 60-RR-1.

WETENKAMP, H.R. *et al.* ***Increase loading of 36 inch wheels - thermal and mechanical considerations***. Car Department Officer Association Annual Meeting. Chicago - IL (EUA), 17 de setembro de 1992.

XIV Brazilian Congress of Mechanical Engineering
Obeid Plaza Hotel Convention Center - Bauru - SP/Brazil
December 08-12th 1997

PAPER CODE: COB906

COEFICIENTE DE PERDA DE CARGA (f) EM TUBOS DE BAMBU/*HEAD LOSS COEFFICIENT (f) IN BAMBOO TUBES*

MARCO ANTONIO DOS REIS PEREIRA
Departamento de Engenharia Mecânica - Unesp - Bauru
Cep. 17033-360 Bauru - S.P. - Brazil E-mail pereira@bauru.unesp.br
Hans George Arens
Departamento de Hidráulica - USP - São Carlos

Abstract

The giant bamboo species seem to be suitable to be used as a water conductor, concerning to its good agronomycal, silvicultural, physical and mechanical characteristics and also due the culm dimensions showed by this species. Nevertheless, few information is available concerning its hidraulics characteristics. In this paper, the giant bamboo (*Dendrocalamus giganteus*) was tested as water conductor when submitted a pressurized flow, verifying some hidraulic characteristics to be used in the irrigation practice as the **f** factor (Darcy-Weisbach). The bamboo tubes had its diaphragm removed by two different tools, a hand working impact tool that produces a bad quality of remotion and an electrical working rotate tool that produces a good quality of remotion. The **f** factor was obtained applying the Blasius equation to bamboo tubes or, **f** as a function of Reynolds number. The results showed that the quality of the diaphragm remotion is important concerning to a head loss observed. The research showed that the rotate tool produces better results than the impact tool as can be observed through of the f coefficient obtained. The expressions resulted for fhe f factor were $\mathbf{f = 0.3459\ Re^{-0.117}}$ and $\mathbf{f = 0.1107\ Re^{-0.097}}$ for bad and good quality of remotion, respectively.

Keywords

Bambu - tubo - hidráulica - coeficientes Bamboo - conduct - hidraulic - coefficients

1. Introdução

O bambu é uma planta predominamtemente tropical, de rápido crescimento e grande produtividade, sendo ainda um material auto-renovável e com características físicas e mecânicas tais, que o habilitam a possuir milhares de aplicações nos mais diversos campos, entre eles, como condutor de água para a irrigação (Pereira, 1992). É um material barato que pode ser facilmente trabalhado com ferramentas simples e de baixo custo, acessíveis ao agricultor, bastando possuir uma moita de bambu para se ter acesso a uma pequena "fábrica" de tubos na própria propriedade.

Segundo alguns autores Farrely (1984), Liese (1985), Hsiung (1988), o bambu existe e vem sendo utilizado à séculos na vida diária das pessoas de muitos países tropicais, especialmente da Ásia, devido principalmente, as suas excelentes características físicas e mecânicas de retidão, leveza, força, dureza, conteúdo de fibras, flexibilidade e facilidade de trabalho, as quais são ideais para os diferentes propósitos tecnológicos. Acrescentam que atualmente, o bambu tem despertado uma crescente curiosidade em função dos seus múltiplos usos e por ser ainda um material renovável, no entanto, seu conhecimento é ainda incompleto e os relatos sujeitos a controvérsias.

Dentre as mais de mil espécies de bambu existentes, as gigantes parecem ser as mais adequadas para utilização em irrigação, devido ao fato de produzirem colmos com dimensões e características compatíveis para este fim. Dentre as espécies gigantes, optou-se inicialmente pela espécie *Dendrocalamus giganteus* (bambu gigante ou bambu balde) por ser uma espécie relativamente comum no Brasil. No entanto, apesar de conhecido e comum, o bambu é muito pouco utilizado, seja devido à falta de pesquisas ou seja devido a falta de conhecimento e divulgação das diversas espécies, suas principais características e diferentes aplicações.

Sabe-se, por outro lado, que a técnica de irrigação embora seja muito útil para o aumento da produtividade agrícola, é pouco utilizada,. seja em decorrência do custo da irrigação, da falta de informação e/ou do baixo poder aquisitivo de nossos agricultores, especialmente os pequenos.

São escassas as informações existentes, relativas às características hidráulicas de tubos de bambu, notadamente à perda de carga e aos coeficientes das principais equações utilizadas para seu cálculo. Quando existentes, estes dados referem-se normalmente ao bambu em geral, havendo ainda significativa diferença entre os valores encontrados, bem como na metodologia utilizada. Este trabalho objetivou contribuir para o desenvolvimento do bambu como condutor de água para fins de irrigação de pequeno porte, através da determinação do fator de perda de carga f da equação de Darcy-Weisbach.

2. Material e métodos

2.1 Colmos de bambu utilizados

2.1.1 - Corte e dimensões dos colmos

Os colmos inteiros de comprimentos entre 25 a 30 m, foram subdivididos em 3 partes sucessivas, a partir da base e com cerca de 4 m cada com diâmetro interno de aproximadamente 4 polegadas (0,1 m), que é a dimensão mais comum à esta espécie de bambu, e que se ajustava melhor à ferramenta para usinagem interna.

2.1.2 - Usinagem dos diafragmas internos

Os colmos foram usinados internamente para retirada dos diafragmas através de 2 ferramentas construídas para tal fim, uma por impacto de acionamento manual e outra giratória com acionamento elétrico, promovendo cada uma delas, diferentes qualidades de remoção.

2.1.2.1 - Ferramenta de impacto manual

Baseada em ferramenta similar, mostrada em PEREIRA (1992), consiste de uma ferramenta simples, composta por um pedaço de cano de ferro de 2 1/2" (0,064 m) de diâmetro e 0,30 m de comprimento, afiado em suas duas extremidades. Nesta ferramenta foi soldado um cano com 2 m de comprimento e 1" (0,0254 m) de diâmetro, que serve como cabo da ferramenta. A usinagem foi feita pelo vai e vem da ferramenta manual dentro do bambu, que era girado regularmente para a usinagem de todo o diâmetro.

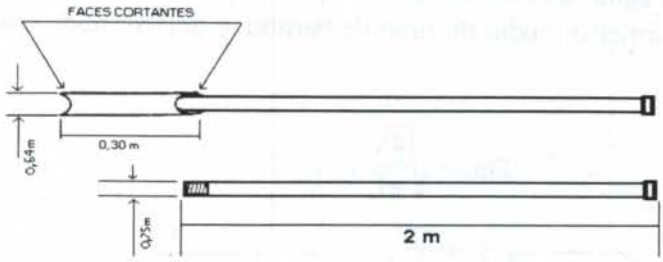

Figura 1 - Ferramenta de impacto - acionamento manual.

2.1.2.2 - Ferramenta giratória - elétrica

Baseada em ferramenta mostrada em ALMEIDA NETO (1992), foi construída uma ferramenta giratória com acionamento por motor elétrico.A peça giratória mecânica consiste de 3 ferramentas de corte montadas simetricamente em um núcleo cilíndrico de alumínio, que apoia-se internamente no bambu através de cilindros ocos acionados por molas, o que permite que exista alguma variação no diâmetro interno do bambu. O núcleo cilíndrico tinha aproximadamente 0,12 m de comprimento e 0,08 m de diâmetro, de onde saíam as ferramentas cortantes. A peça foi ligada a um tubo de aço galvanizado que servia de eixo transmissor de torque, sendo o conjunto acionado por um motor de 3/4 HP de potência acoplado a um redutor de velocidade (15:1). A Figura 2 mostra a ferramenta giratória mecânica de acionamento elétrico.

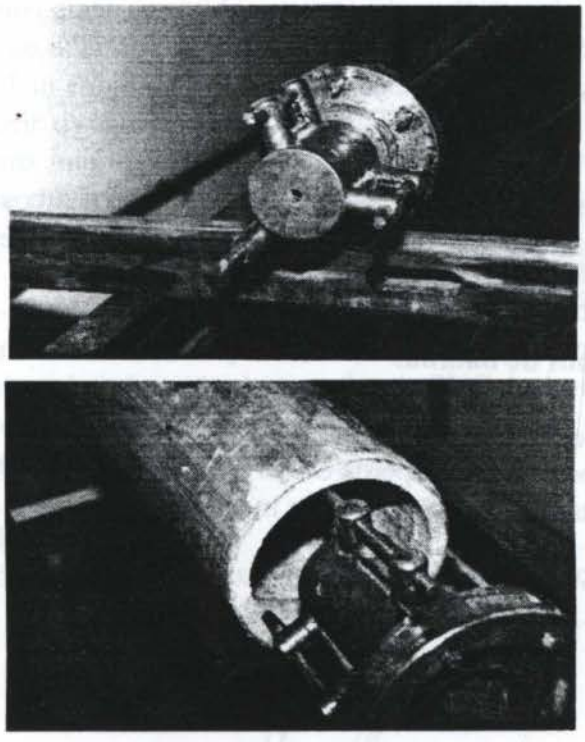

Figura 2 - Ferramenta giratória mecânica - acionamento elétrico.

2.2 - Determinações experimentais

2.2.1. - Diâmetro

Os diâmetros dos tubos de bambu foram determinados através da medida do volume interno do tubo, que é o volume de um cilindro, de comprimento (L) e diâmetro (D). O

volume interno (V) foi determinado através do enchimento total do tubo de bambu, colocado na posição vertical, com água, através de um recipiente previamente calibrado. O diâmetro assim obtido, chamado diâmetro médio do tubo de bambu, é determinado como segue:

$$Dm = \sqrt{\frac{4V}{\pi L}} \qquad (1)$$

onde:

Dm = Diâmetro interno médio do tubo de bambu [m]
V = Volume interno do tubo de bambu [m^3]
L = Comprimento do tubo de bambu [m]

2.2.2 - Vazão , velocidade e pressão estática

Para a determinação da vazão Q (m^3/s), foi construído um medidor de placa-orifício, tipo diafragma, com uma relação de áreas, Área do Orifício (Ao) / Área do conduto (A1), ou seja A0/A1 = 0,6. O medidor de orifício foi previamente calibrado resultando a seguinte equação de calibração, em função do desnível manométrico H (m) obtido :

$$\mathbf{Q = 0{,}01668\ H^{0{,}51922}} \qquad (2)$$

A velocidade média de escoamento dentro do tubo de bambu(Vm - m/s), foi determinada através da vazão (Q) obtida com o medidor de orifício, do diâmetro médio do tubo de bambu (Dm) e da equação da continuidade como segue:

$$Vm = \frac{4Q}{\pi Dm^2} \qquad (3)$$

Foram construídos e instalados 4 anéis piezométricos sobre os tubos de PVC de 4" (0,1 m) para a determinação das pressões estáticas. Estes anéis piezométricos receberam a identificação de h_1, h_2, h_3, h_4.

2.3 - Perda de carga nos tubos de bambu.

2.3.1 - Bancada de ensaios

Para a determinação experimental da perda de carga nos tubos de bambu e verificação do sistema de medidas, foi montado o banco de ensaios mostrado na Figura 3.

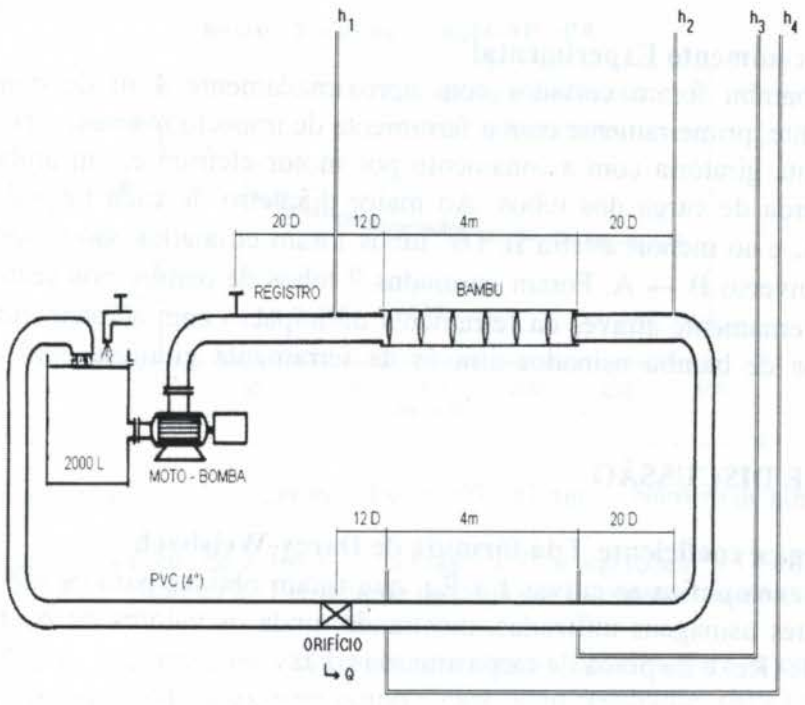

Figura 3 - Bancada de ensaios.

A bancada de ensaios era constituída por uma caixa d'água de 2.000 litros mantida com nível constante através de uma alimentação contínua por uma torneira, e uma saída de igual vazão por um vertedor. Um conjunto moto-bomba estava fixado e ligado ao banco de ensaios e à caixa d'água. A partir da moto-bomba foi instalada uma linha de tubulação de PVC de parede grossa e diâmetro interno de 4" (0,1 m) com cerca de 20 m de comprimento que retornava à caixa d'água, mantendo o sistema fechado.

Na linha principal, foram instalados os anéis piezométricos h_1, h_2, h_3, e h_4, uma seção com cerca de 4 m para os testes com os tubos de bambu e o medidor de vazão tipo orifício, todos ligados através de mangueiras transparentes e com parede grossa, a um quadro piezométrico para leitura das alturas ou pressões estáticas respectivas. A bancada de ensaios foi previamente calibrada pela colocação de um tubo de PVC de 4 m de comprimento, 4" (0,1 m) de diâmetro e parede grossa, na seção destinada aos tubos de bambu, de modo a reproduzir os resultados clássicos da literatura (Equação de Blasius), com erro inferior a 5%.

2.3.2 - Fórmula utilizada

Dentre as várias fórmulas práticas existentes para a determinação da perda de carga em tubulações foi utilizada a fórmula de Darcy-Weisbach

$$hf_{bambu} = f \frac{L}{D_m} \frac{Vm^2}{2g} \qquad (4)$$

onde:

hf_{bambu} = Perda de carga nos tubos de bambu (m)

L = Comprimento dos tubos de bambu (m)

f =.Coeficiente ou fator de perda de carga.

g = 9,81 (m/s^2)

2.3.3 - Procedimento Experimental

Os tubos de bambu foram cortados com aproximadamente 4 m de comprimento e usinados internamente, primeiramente com a ferramenta de impacto manual, e posteriormente através da ferramenta giratória com acionamento por motor elétrico e, em ambos os casos, determinou-se a perda de carga dos tubos. Ao maior diâmetro de cada tubo de bambu foi designado a letra A, e ao menor, a letra B. Os tubos foram ensaiados no sentido A → B e depois no sentido inverso B → A. Foram ensaiados 9 tubos de bambu nos sentidos A→B e B→A, usinados internamente através da ferramenta de impacto com acionamento manual, e igualmente, 6 tubos de bambu usinados através de ferramenta giratória com acionamento elétrico.

3.RESULTADOS E DISCUSSÃO

3.1 - Perda de Carga e coeficiente f da fórmula de Darcy-Weisbach

A Figura 4 exemplifica as curvas f × Re, que foram obtidas para os tubos de bambu através das diferentes usinagens utilizadas, mostrando ainda os valores do coeficiente f, do número de Reynolds (Re) e da perda de carga unitária (J).

J (m/m)	Re	f
0,1110	281024	0,0406
0,0935	259581	0,0401
0,0814	241746	0,0403
0,0676	218367	0,0410
0,0513	191075	0,0406
0,0446	175925	0,0417
0,0366	158446	0,0422
0,0310	145686	0,0422
0,0239	128001	0,0421
0,0170	92887	0,0444
0,0133	67964	0,0454
0,0073	48949	0,0498

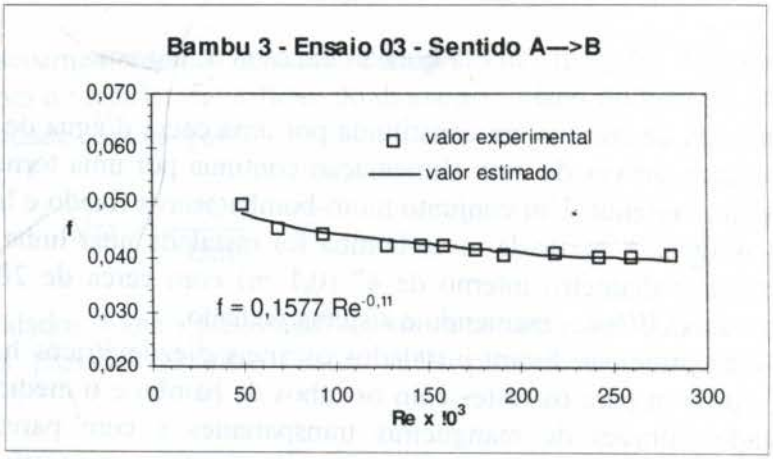

J (m/m)	Re	f
0,1114	280227	0,0410
0,0930	258938	0,0401
0,0803	238988	0,0406
0,0680	217780	0,0415
0,0568	198613	0,0416
0,0480	182660	0,0416
0,0403	166269	0,0421
0,0341	151663	0,0429
0,0269	135488	0,0423
0,0204	116689	0,0433
0,0153	99679	0,0444
0,0105	81524	0,0457
0,0070	64940	0,0480

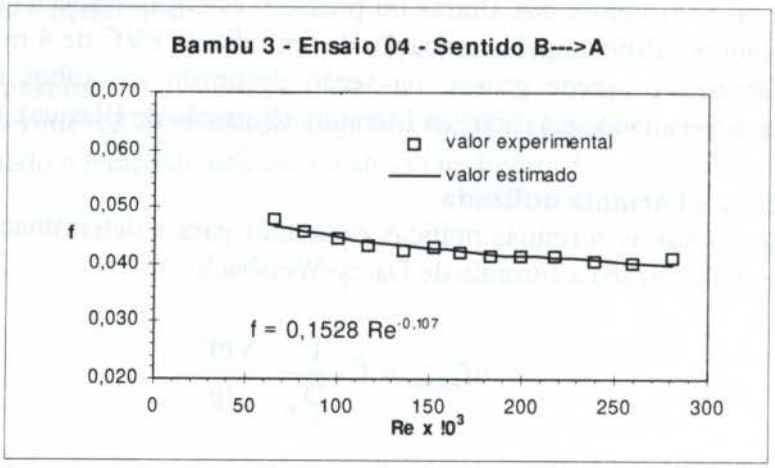

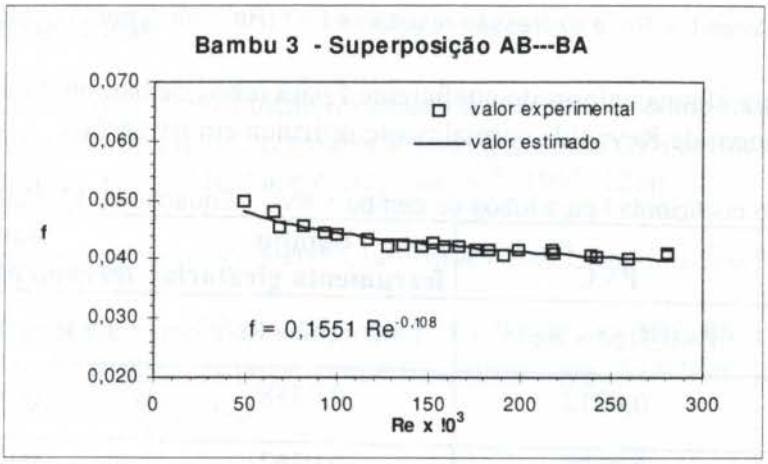

Dados do bambu 3 : L = 3,94 m - Dm = 107,987 mm - Número de nós = 9

Figura 4- Valores de J, Re, f . Curvas f x Re e equações f = f (Re)
Bambu 3 - Ferramenta giratória com acionamento elétrico

As Figuras 5 e 6 mostram os valores experimentais obtidos para o coeficiente f em função do número de Reynolds (Re), bem como a expressão resultante para f = f (Re) obtida pela superposição de todos os ensaios, respectivamente para as usinagens por impacto e giratória.

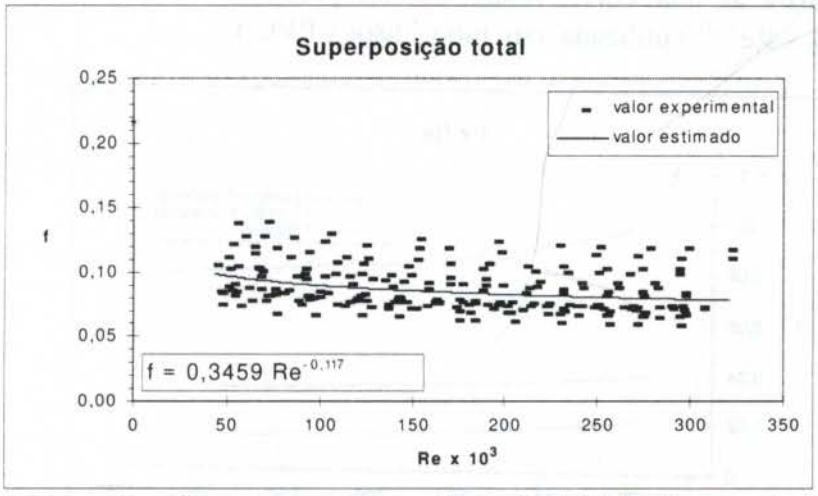

Figura 5 - Valores f × Re, e expressão resultante f = f (Re) - ferramenta de impacto

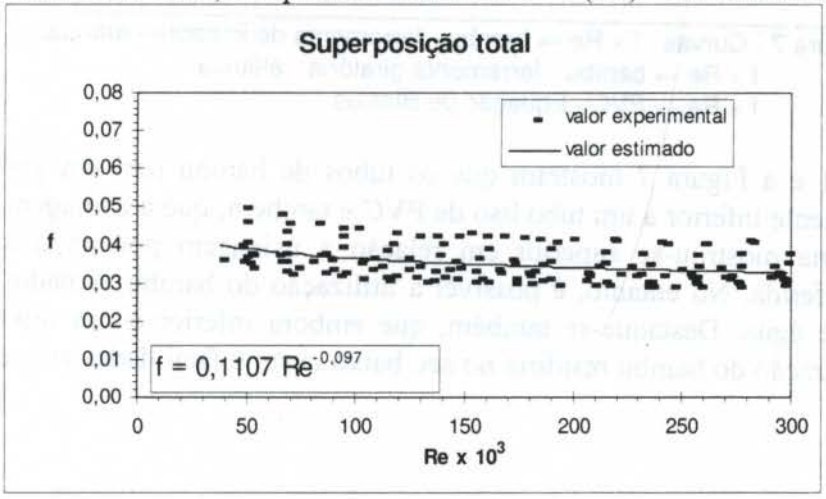

Figura 6 - Valores f × Re, e expressão resultante f = f (Re) - ferramenta giratória.

O Quadro 1 mostra alguns valores do coeficiente f para tubos de bambu e tubos de PVC, dentro da faixa de número de Reynolds normalmente utilizada em irrigação.

QUADRO 1 - Valores do coeficiente f para tubos de bambu e PVC (Equação de Blasius)

Re	PVC	bambu ferramenta giratória	bambu ferramenta impacto
$\times 10^3$	$f = 0{,}3164 \times Re^{-0.25}$	$f = 0{,}1107 \times Re^{-0.097}$	$f = 0{,}3459 \times Re^{-0.117}$
50	0,0212	0,0388	0,0975
100	0,0178	0,0362	0,0899
150	0,0161	0,0348	0,0858
200	0,0149	0,0339	0,0829
250	0,0141	0,0331	0,0808
300	0,0135	0,0326	0,0791

A Figura 7 mostra as duas curvas finais obtidas para os tubos de bambue a equação de Blasius ($f = 0{,}3164 \times Re^{-0,25}$) utilizada em tubos lisos (PVC).

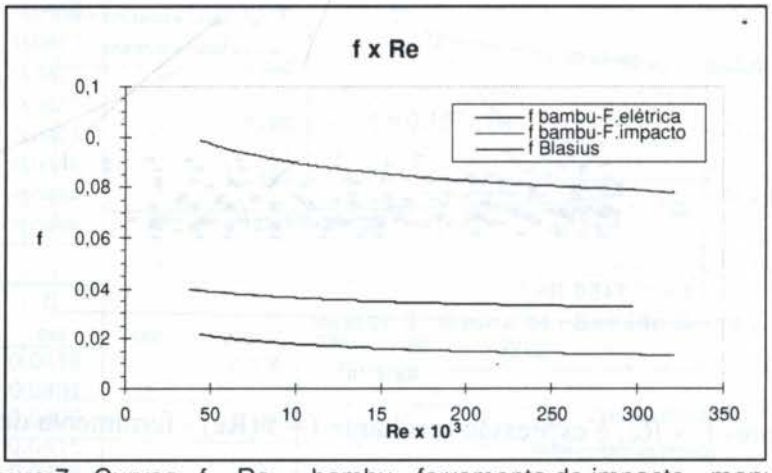

Figura 7 - Curvas f × Re → bambu - ferramenta de impacto - manual
f × Re → bambu - ferramenta giratória - elétrica
f × Re → PVC - Equação de Blasius

O Quadro1 e a Figura 7 mostram que os tubos de bambu tem um comportamento hidráulico nitidamente inferior a um tubo liso de PVC e também, que a usinagem interna com ferramenta giratória mostrou-se superior em relação a usinagem por impacto, devendo portanto ser a preferida. No entanto, é possível a utilização do bambu usinado por impacto como condutor de água. Destaque-se também, que embora inferior a um tubo de PVC, a vantagem da utilização do bambu residiria no seu baixo custo e facilidades em ser trabalhado e utilizado.

4.Referências bibliográficas

ALMEIDA NETO, J.A. de . Contribuição ao estudo do bambu : o comportamento hidráulico de tubos de bambu bambu gigante (*Dendrocalamus giganteus*). Dissertação (Mestrado em Engenharia Agrícola). Feagri/Unicamp.Campinas, S.P. 1992. 126p.

FARRELY, D. The book of bamboo. Sierra Club Books. San Francisco, EUA.1984, 340p.il.

HSIUNG, W. Prospects for bamboo development in the world. In : **IBC 88**, 1988, Prafrance.

LIESE, W. Bamboos - Biology, silvies, properties, utilization. Eschborn, dt.Ges.fur.Techn. Zusammnarbeit (GTZ),1985, 132p.

PEREIRA, M. A. dos R. P. Viabilidade da utilização do bambu para fins de irrigação-aspectos técnicos. Dissertação (Mestrado em Agronomia) - Faculdade de Ciências Agronômicas FCA, UNESP, Botucatu,S.P.,1992, 103p.

Tema 41

Mecânica do Contínuo

XIV Brazilian Congress of Mechanical Engineering
Obeid Plaza Hotel Convention Center - Bauru - SP/Brazil
December 08-12th 1997

PAPER CODE: COB449

DESCRIPTION OF THE SHAPE MEMORY EFFECT IN THE SETTING OF STANDARD GENERALIZED MATERIALS : A THREE-DIMENSIONAL MODEL

ANGELA C. DE SOUZA†, NESTOR ZOUAIN† & EDGAR MAMIYA‡
† *Programa de Engenharia Mecânica, Universidade Federal do Rio de Janeiro 21945-970 Rio de Janeiro, RJ - E-mail: nestor@serv.com.ufrj.br*
‡ *Departamento de Engenharia Mecânica, FT - Universidade de Brasília 70910-900 Brasília, DF - E-mail: mamiya@enm.unb.br*

Abstract

A phenomenological model describing the mechanical behavior of solids undergoing stress-induced phase transformations is presented in the setting of three-dimensional media. Pseudoelasticity as well as shape memory effect can be described by the model at hand. Numerical results are presented so as to illustrate the capabilities of the three-dimensional constitutive model.

Keywords

Plasticity, pseudoelasticity, shape memory effect, martensitic transformation, constitutive model.

1 INTRODUCTION

Pseudoelastic materials can be seen as apparently elastic materials for which stress-strain curves define path dependent hysteresis loops. Shape memory alloys, by their turn, are materials with apparently plastic behavior which can recover its original shape under a heating process. Both mechanical behaviors are associated with stress-induced phase transformation from austenite (or twinned martensite) to detwinned martensite and vice-versa, rather then with motion of dislocations. Figure 1.a illustrates the hysteretic behavior of the pseudoelastic material subject to loading followed by unloading in a traction tensile test performed at a given temperature. At a lower temperature, transformation strain can be observed under a stress-free state, as show in Figure 1.b. Rise of temperature leads to upward translation of the hysteresis loop, so that strain free configuration is recovered, characterizing this way the shape memory effect.

Studies on the subject include Abeyaratne and Knowles (1988), Gurtin (1983) and Müller and Xu (1991), amongst others. Until recently, constitutive models have been conceived within the context of one-dimensional media. In the setting three-dimensional

media, models for shape memory alloys include those proposed in Leclercq and Lexcellent (1996), Boyd and Lagoudas (1996) or Sun and Hwang (1994), for instance.

In the present work, we propose a new model which can describe essential mechanical features of such classes of materials, in the setting of three-dimensional media. It is conceived within the framework of Generalized Standard Materials, where internal variables are defined so as to describe the phase transformation processes. As a consequence, the model at hand can be shown to present thermodynamically consistent behavior in the sense that eventual energy dissipation is necessarily positive. The resulting model is qualitatively consistent with the phenomenological features of polycristaline materials presenting pseudoelastic and shape memory behaviors. It is relatively simple and very well suited for finite element implementations.

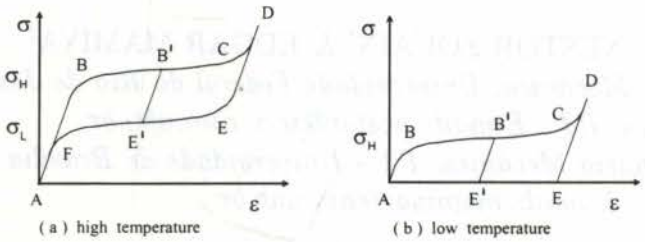

Figure 1 - (a) Pseudoelasticity (b) Shape memory effect

2 THE THREE-DIMENSIONAL MODEL

For the sake of simplicity, small deformations are assumed throughout this work, and only quasi-static motions are considered. Let the classical **linear strain tensor** be denoted by ε. Stress induced phase transformation involves detwinning and, from the kinematical point of view, can be viewed as a shear deformation process. In the present study, the detwinning process is described by a symmetric and deviatoric **transformation strain** tensor subject to the constraint:

$$||\mathbf{e}_T|| \leq \xi_0 \tag{1}$$

where ξ_0 is a material parameter which characterizes the complete phase transformation to detwinned martensite and the norm is considered in this work in the sense of Frobenius. The parent phase is associated with $||\mathbf{e}_T|| = 0$, while the product one is related to $||\mathbf{e}_T|| = \xi_0$. In what follows, the three-dimensional model is presented within the context of Generalized Standard Materials, which ensures thermodynamic consistency in the sense that the Clausius-Duhen inequality is automatically satisfied.

Let us consider the trace of the total strain ε, the deviatoric part $\mathbf{e}$ of the total strain ε, the transformation strain $\mathbf{e}_T$ and the temperature θ as state variables. We define the following **potential of free energy**:

$$\psi(tr\,\varepsilon, \mathbf{e}, \mathbf{e}_T, \theta) := \left(\frac{\lambda}{2} + \frac{\mu}{3}\right)(tr\,\varepsilon)^2 + \mu\,||\mathbf{e}-\mathbf{e}_T||^2 + \sigma_M(\theta)\,||\mathbf{e}_T|| + I_{\xi_0}(\mathbf{e}_T) + \frac{h}{2}||\mathbf{e}_T||^2 \tag{2}$$

where λ and μ are the Lamé constants of the material, h is a scalar parameter related to the slope of the kinematic hardening and $I_{\xi_0}(\mathbf{e}_T)$ is the indicator function of the transformation strain $\mathbf{e}_T$ such that:

$$I_{\xi_0}(\mathbf{e}_T) := \begin{cases} 0 & \text{if } ||\mathbf{e}_T|| \leq \xi_0 \\ +\infty & \text{otherwise} \end{cases} \tag{3}$$

The quantity $\sigma_M(\theta)$ is the so called Maxwell stress . We consider the form $\sigma_M(\theta) :=< \alpha\,\theta + \sigma_{M_0} >$, where $< \bullet >$ accounts for the positive part of $(\bullet)$, while α and σ_{M_0} are positive material parameters.

Since the convex functional $\psi(tr\,\varepsilon, \mathbf{e}, \mathbf{e}_T, \theta)$ is not a differentiable function of $\mathbf{e}_T$ neither of θ, we make use of the concept of subdifferentials when writing the following constitutive equations:

$$T_m := \frac{\partial \psi}{\partial (tr\,\varepsilon)}\,(tr\,\varepsilon, \mathbf{e}, \mathbf{e}_T, \theta) = \left(\lambda + \frac{2\mu}{3}\right)\,tr\,\varepsilon \tag{4}$$

$$\mathbf{S} := \frac{\partial \psi}{\partial \mathbf{e}}\,(tr\,\varepsilon, \mathbf{e}, \mathbf{e}_T, \theta) = 2\mu\,(\mathbf{e} - \mathbf{e}_T) \tag{5}$$

$$\mathbf{X} \in -\partial_{\mathbf{e}_T}\,\psi(tr\,\varepsilon, \mathbf{e}, \mathbf{e}_T, \theta) = \mathbf{S} - \sigma_M(\theta)\,\partial\,||\mathbf{e}_T|| - \partial I_{\xi_0}(\mathbf{e}_T) - h\,\mathbf{e}_T \tag{6}$$

$$\eta \in -\partial_\theta\,\psi\,(tr\,\varepsilon, \mathbf{e}, \mathbf{e}_T, \theta) = -\partial_\theta\,\sigma_M(\theta)\,||\mathbf{e}_T|| \tag{7}$$

where $T_m\,\mathbf{I}$ and $\mathbf{S}$ are respectively the spherical and the deviatoric part of the Cauchy stress tensor $\mathbf{T}$, $\mathbf{X}$ is the thermodynamic force corresponding to the transformation strain $\mathbf{e}_T$, while η is the entropy. Since the subdifferential is considered in the setting of symmetric deviatoric tensors, it follows that $\mathbf{X}$ is also symmetric and deviatoric.

In the sequence, an evolution law for the transformation strain $\mathbf{e}_T$ has to be conceived. In this sence, let us define the **potential of dissipation** given by:

$$\phi(\dot{\mathbf{e}_T}) := R\,||\dot{\mathbf{e}_T}|| \tag{8}$$

where R is a positive material parameter.It can be shown that convexity and positiveness of $\phi(\dot{\mathbf{e}_T})$, thogether with the fact that this potential is null at the origin, ensure thermodynamic consistency of the proposed model. The following constitutive relation is associated with the functional (8):

$$\mathbf{X} \in\, \partial\phi(\dot{\mathbf{e}_T}) = R\,\partial\,||\dot{\mathbf{e}_T}|| \tag{9}$$

A more convenient way to express the relation between $\mathbf{X}$ and $\dot{\mathbf{e}_T}$ can be obtained from the **complementary potential of dissipation**:

$$\phi^*(\mathbf{X}) = I_R(\mathbf{X}) := \begin{cases} 0 & \text{if } ||\mathbf{X}|| \leq R \\ +\infty & \text{otherwise} \end{cases} \tag{10}$$

From (10), the following flow rule can be written:

$$\dot{\mathbf{e}_T} \in\, \partial\,\phi^*(\mathbf{X}) = \partial\,I_R(\mathbf{X}) \tag{11}$$

An equivalent statement of the flow rule (11), better suited to numerical implementations, is given by:

$$\begin{aligned} &\dot{\mathbf{e}}_T = \dot{\zeta}\,\frac{\mathbf{X}}{||\mathbf{X}||} && (a)\\ &\dot{\zeta} \geq 0 && (b)\\ &f(\mathbf{X}) := ||\mathbf{X}|| - R \leq 0 && (c)\\ &\dot{\zeta}\, f(\mathbf{X}) = 0 && (d) \end{aligned} \tag{12}$$

The thermodynamic force $\mathbf{X}$ must necessarilly remain within a closed ball of radius R. The complementarity condition (12.d) states that, for $||\mathbf{X}|| < R$, the multiplier $\dot{\zeta}$ has to be equal to zero, which is equivalent to say that we must not have changes in the transformation strain $\mathbf{e}_T$. On the other hand, $||\mathbf{X}|| = R$ is a necessary condition for the occurence of a flow $\dot{\mathbf{e}}_T \neq 0$.

The constitutive relation (6) has to be analysed for the following three distinct cases:

1) If $\mathbf{e}_T = 0$: Only the parent phase is present in the material and we have:

$$\mathbf{S} - \mathbf{X} = \sigma_M(\theta)\,\mathbf{H} \in \overline{Sym^3};\ ||\mathbf{H}|| \leq 1 \tag{13}$$

where $\mathbf{H}$ is a symmetric deviatoric tensor.

2) If $0 < ||\mathbf{e}_T|| < \xi_0$: Here we have a mixture of phases and:

$$\mathbf{S} - \mathbf{X} = \sigma_M(\theta)\,\frac{\mathbf{e}_T}{||\mathbf{e}_T||} + h\,\mathbf{e}_T \tag{14}$$

3) If $||\mathbf{e}_T|| = \xi_0$: This equality characterizes the fact that all the parent phase has been completely transformed into the product phase. Here we have:

$$\mathbf{S} - \mathbf{X} = (\sigma_M(\theta) + \gamma)\,\frac{\mathbf{e}_T}{||\mathbf{e}_T||} + h\,\mathbf{e}_T, \quad \gamma \geq 0 \tag{15}$$

When $\mathbf{e}_T = \mathbf{0}$, the relations (12.c) and (13) involving the thermodynamic force $\mathbf{X}$ are not sufficient for its determination. As a consequence, difficulties arise when using (12) to determine whether nucleation of the product phase should take place or not. The proposition below gives us the answer.

Proposition 1: If $\mathbf{e}_T = \mathbf{0}$, then phase transformation takes place only if $||\mathbf{S}|| = \sigma_M(\theta) + R$. Moreover, when the product phase nucleates, the thermodynamic force $\mathbf{X}$ is given by:

$$\mathbf{X} = R\,\frac{\mathbf{S}}{||\mathbf{S}||} \tag{16}$$

3 NUMERICAL ASPECTS

A backward Euler scheme was adopted for the integration of the mechanical model under consideration. Consequently, expressions (5) and (6) for the constitutive relations, together with the flow rule (12), become:

$$(T_m)_{n+1} = \left(\lambda + \frac{2\mu}{3}\right)\, tr\, \varepsilon_{n+1}$$

$$\mathbf{S}_{n+1} = 2\,\mu\,(\mathbf{e}_{n+1} - \mathbf{e}_{Tn+1})$$

$$\mathbf{S}_{n+1} - \mathbf{X}_{n+1} = \begin{cases} \sigma_M(\theta)\,\mathbf{H}_{n+1}, \quad ||\mathbf{H}_{n+1}|| \leq 1, & \text{if } \mathbf{e}_{Tn+1} = \mathbf{0} \\ \sigma_M(\theta)\,\dfrac{\mathbf{e}_{Tn+1}}{||\mathbf{e}_{Tn+1}||} + h\,\mathbf{e}_{Tn+1}, & \text{if } 0 < ||\mathbf{e}_{Tn+1}|| < \xi_0 \\ (\sigma_M(\theta) + \gamma_{n+1})\,\dfrac{\mathbf{e}_{Tn+1}}{||\mathbf{e}_{Tn+1}||} + h\,\mathbf{e}_{Tn+1}, & \text{if } ||\mathbf{e}_{Tn+1}|| = \xi_0 \\ \gamma_{n+1} \geq 0, \end{cases} \tag{17}$$

$$\mathbf{e}_{Tn+1} = \mathbf{e}_{Tn} + \Delta\zeta\,\mathbf{X}_{n+1}$$

$$\Delta\zeta \geq 0$$

$$f(\mathbf{X}_{n+1}) := ||\mathbf{X}_{n+1}|| - R \leq 0$$

$$\Delta\zeta\, f(\mathbf{X}_{n+1}) = 0$$

where subscripts n and $n+1$ refer respectively to time instants t_n and t_{n+1}, while $\Delta\zeta := \dot{\zeta}\,\Delta t$.

In the present study, we consider a Return Mapping Algorithm for the integration of expressions (17), inspired on developments presented by Simo and Taylor (1986), within the context of infinitesimal plasticity. Basically, the algorithm consists in: (i) computing a trial state under the assumption that the material behaves elastically, (ii) determining whether the computed trial state is actually elastic and (iii) projecting the state variables so as to verify all the constraints imposed by the problem, if the trial state is not elastic.

We consider here that the mechanical loading upon the material is imposed through a prescribed strain ε_{n+1}. The resulting algorithm is given by:

ALGORITHM:

Initializations: $t_n = 0$, $\varepsilon_n = 0$, $\mathbf{e}_{Tn} = 0$;

For each time step:

$t_{n+1} = t_n + \Delta t$;

$\varepsilon_{n+1} = \varepsilon_n + \Delta\varepsilon_{n+1}$;

$\mathbf{e}_{Tn+1}^{trial} = \mathbf{e}_{Tn}$;

$\mathbf{S}_{n+1}^{trial} = 2\,\mu\,\left(\mathbf{e}_{n+1} - \mathbf{e}_{Tn+1}^{trial}\right)$;

If $\mathbf{e}_{Tn} = \mathbf{0}$ and $||\mathbf{S}_{n+1}^{trial}|| \leq \sigma_M(\theta) + R$ or

if $0 < ||\mathbf{e}_{Tn}|| < \xi_0$ and

$$||\mathbf{X}_{n+1}^{trial}|| := \left|\left|\mathbf{S}_{n+1}^{trial} - \sigma_M(\theta)\,\frac{\mathbf{e}_{Tn+1}^{trial}}{||\mathbf{e}_{Tn+1}^{trial}||} - h\,\mathbf{e}_{Tn+1}^{trial}\right|\right| \leq R \quad \text{or}$$

if $||\mathbf{e}_{Tn}|| = \xi_0$ and

$$\exists \gamma \geq 0; \quad ||\mathbf{X}_{n+1}^{trial}|| := \left\| \mathbf{S}_{n+1}^{trial} - (\sigma_M(\theta) + \gamma) \frac{\mathbf{e}_{T\,n+1}^{trial}}{||\mathbf{e}_{T\,n+1}^{trial}||} - h\,\mathbf{e}_{T\,n+1}^{trial} \right\| \leq R$$

then the step is **elastic** and thus:

$$\mathbf{e}_{Tn+1} = \mathbf{e}_{T\,n+1}^{trial};$$

else **phase transformation** takes place:

Find the solution $\mathbf{e}_{Tn+1}$ of the set of nonlinear equations:

$$R \frac{\mathbf{e}_{Tn+1} - \mathbf{e}_{Tn}}{||\mathbf{e}_{Tn+1} - \mathbf{e}_{Tn}||} - 2\mu\,(\mathbf{e}_{n+1} - \mathbf{e}_{Tn+1}) + \sigma_M(\theta) \frac{\mathbf{e}_{Tn+1}}{||\mathbf{e}_{Tn+1}||} + h\,\mathbf{e}_{Tn+1} = \mathbf{0}$$

If $||\mathbf{e}_{Tn+1}|| > \xi_0$, then find the solution $(\mathbf{e}_{Tn+1}, \gamma_{n+1})$ of the expanded set of nonlinear equations:

$$R \frac{\mathbf{e}_{Tn+1} - \mathbf{e}_{Tn}}{||\mathbf{e}_{Tn+1} - \mathbf{e}_{Tn}||} - 2\mu\,(\mathbf{e}_{n+1} - \mathbf{e}_{Tn+1}) + (\sigma_M(\theta) + \gamma_{n+1}) \frac{\mathbf{e}_{Tn+1}}{||\mathbf{e}_{Tn+1}||} + h\,\mathbf{e}_{Tn+1} = \mathbf{0}$$

$$||\mathbf{e}_{Tn+1}|| - \xi_0 = 0$$

4 NUMERICAL RESULTS

The numerical results presented here illustrate the capabilities of the proposed model. We consider two distinct situations, where proportional and nonproportional loadings are imposed under prescription of stress.

Figure 2 shows the classical curves: isothermal mechanical load cycling by the application of a prescribed uniaxial stress. For these numerical simulations, we consider the following material paramenters: Young's modulus $E = 70$ GPa, Poisson's ratio $\nu = 0.33$, Maxwell stress $\sigma_{M_0} = 150$ MPa at 0°C, radius of the elastic domain $R = 45$ MPa, coefficient associating the Maxwell stress to the temperature $\alpha = 7.5$ MPa °C^{-1}, amplitude of the transformation strain corresponding to the product phase $\xi_0 = 0.03$ and hardening parameter $h = 500$ MPa. The tensile tests are performed at temperatures $\theta = -20$°C, -4°C and 12°C.

The numerical results associated with the nonproportional case are qualitatively compared with experimental curves obtained by Sittner et al. (1995) for tension-torsion tensile tests. The following material parameters were obtained by data fitting, as showed in Figure 3: $E = 30.7$ GPa, $\nu = 0.36$, $\sigma_M = 131$ MPa , $R = 73.4$ MPa and $h = 9.23$ GPa. The stress history imposed during the tensile test in space $T_{11} \times T_{12}$ is shown in Figure 4. The results obtained from the model for these stress paths is showed in Figures 5, 6 and 7.

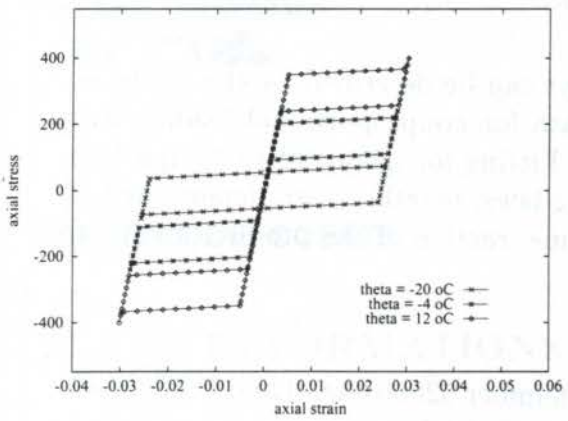

Figure 2: Cyclic response for varying temperature

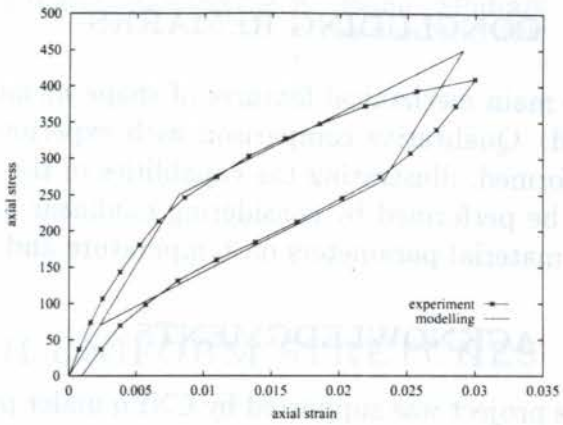

Figure 3: Tension-strain curve

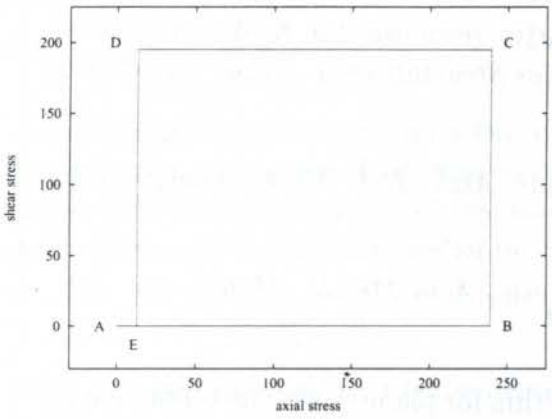

Figure 4: Path followed by stress

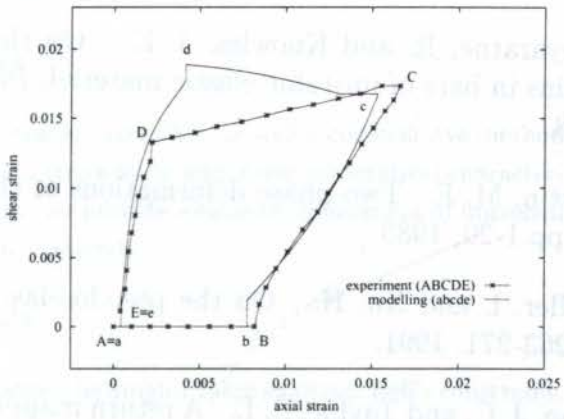

Figure 5: Path followed by strain

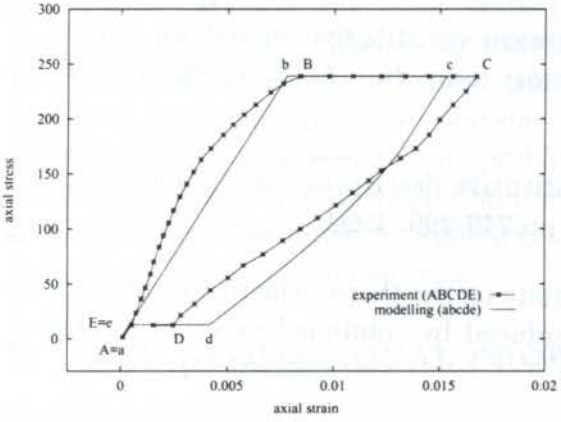

Figure 6: Axial stress strain curve

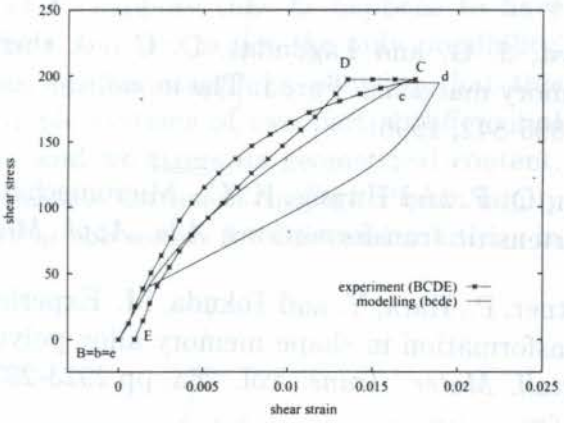

Figure 7: Shear stress strain curve

5 CONCLUDING REMARKS

The main mechanical features of shape memory alloys can be described by the model at hand. Qualitative comparison with experimental data for nonproportional loading was performed, illustrating the capablities of the model. Fitting for quantitative comparison can be performed by considering nonlinear hardening laws, together with dependence of the material parameters on temperature and or volume fraction of the product phase.

6 ACKNOWLEDGMENTS

This project was supported by CNPq under projects number 520564/96-0 and 523386/96-6, and by CAPES. These supports are gratefully acknowledged.

7 REFERENCES

Abeyaratne, R. and Knowles, J. K. On the dissipative response due to discontinuous strains in bars of unstable elastic material, *Int. J. Solids Structures* vol. 24,pp.1021-1044, 1988.

Gurtin, M. E. Two-phase deformations of elastic solids, *Arch. Rat. Mech. Analysis* vol. 84, pp.1-29, 1983.

Müller, I. and Xu, H. On the pseudo-elastic hysteresis, *Acta Metall. Mater.*, vol. 39, pp.263-271, 1991.

Simo, J. C. and Taylor, R. L. A return mapping algorithm for plane stress elastoplasticity, *Int. J. Numer. Meth. Engng.*, vol. 22, pp.649-670, 1986.

Leclercq, S. and Lexcellent, C. A general macroscopic description of the thermomecanical behavior of shape memory alloys, *J. Mech. Phys. Solids*, vol. 44, pp.953-980, 1996.

Boyd, J. G. and Lagoudas, D. C. A thermodynamical constitutive model for shape memory materials. Part I. The monolithic shape memory alloy, *Int. J. Plasticity*, vol. 12, pp.805-842, 1996.

Sun, Q. P. and Hwang, K. C. Micromechanics constitutive description of thermoelastic martensitic transformations, *Adv. Appl. Mech.*, **31**, pp.249-299, 1994.

Sittner, P., Hara, Y. and Tokuda, M. Experimental study on the thermoelastic martensitic transformation in shape memory alloy polycrystal induced by combined external forces, *Metall. Mater. Trans.*, vol. 26a, pp.2923-2935, 1995.

XIV Brazilian Congress of Mechanical Engineering
Obeid Plaza Hotel Convention Center - Bauru - SP/Brazil
December 08-12th 1997

PAPER CODE: COB676

PLANE DEFORMATIONS WITH UNIFORM STRETCHES

FERNANDO P. DUDA & LUIZ C. MARTINS
Programa de Engenharia Mecânica, Universidade Federal do Rio de Janeiro
21945-970 Rio de Janeiro, RJ - E-mail: duda@serv.com.ufrj.br

Abstract

A complete characterization of plane deformations with constant stretches, as well a constructive method to obtain them, is presented. With these results at hand we arrive at an important kinematical characterization of the Singh-Pipkin family of deformations. Finally, we provide a complet treatement of universal deformations with constant stretches for the Bell's elastic materials.

Keywords

Deformations with constant stretches, universal deformations, the Singh-Pipkin solution, Bell's constraint.

1 INTRODUCTION

Consider a smooth, invertible, mapping ϕ from $\mathbb{R}^2$ into $\mathbb{R}^2$ and let $\mathbf{F}$ be its derivative. Writing $\mathbf{F} = \mathbf{RU}$ for the polar decomposition of $\mathbf{F}$, suppose that $\mathbf{U}$ happens to have constant eigenvalues. This is the case if ϕ is affine, but this is not the only possibility. In this paper we characterize the family of such special mappings, showing that this family is generated from the solutions of two simple systems of two partial differential equations. Our approach to this problem is new and we stress its geometrical content. With the results at hand, we give an important characterization of the Sigh-Pipkin family of deformatios. We finish by applying the results in the search for universal solutions in the case of Bell's elastic material.

2 THE GEOMETRICAL PROBLEM

Let (X_1, X_2) be the cartesian coordinates of a plane region. A deformation $\phi : \mathbb{R}^2 \to \mathbb{R}^2$ is a smooth one to one mapping such that $\det\nabla\phi > 0$, and is expressed in cartesian coordinates as

$$\begin{aligned} x_1 &= \phi_1(X_1, X_2), \\ x_2 &= \phi_2(X_1, X_2). \end{aligned}$$

By the polar decomposition theorem, $\nabla\phi = \mathbf{F} = \mathbf{RU}$, where $\mathbf{R}$ is a field of rotations in the plane and $\mathbf{U}$ is a symmetric positive definite plane tensor field. The rotation $\mathbf{R}$ can be written as $\mathbf{R}(\alpha) = \cos\alpha\mathbf{I} + \sin\alpha\mathbf{W}$, where α is the angle of rotation, $\mathbf{I}$ is the identity and $\mathbf{W}$ is the rotation of $\frac{\pi}{2}$. It can be shown(Duda and Martins (1995)) that α and $\mathbf{U}$ are related by the equation

$$\nabla\alpha = \frac{\mathbf{U}}{\det\mathbf{U}}\mathrm{div}\mathbf{U}\mathbf{W}. \tag{1}$$

Observe that (1) express locally the necessary and sufficient condition on $\mathbf{U}$ for $\mathbf{R}(\alpha)\mathbf{U}$ to be a gradient field.

Now, suppose ϕ with corresponding constant and distinct stretches, i.e, $\mathbf{U} = \lambda_1\mathbf{e}\otimes\mathbf{e} + \lambda_2\mathbf{f}\otimes\mathbf{f}$ with constant eigenvalues. We can characterize the moving frame $\{\mathbf{e},\mathbf{f}\}$ by defining the field of rotations $\mathbf{R}(\beta)$ mapping the standard basis $\{\mathbf{e_1},\mathbf{e_2}\}$ of $\mathbb{R}^2$ into the frame $\{\mathbf{e},\mathbf{f}\}$. In this case, by decomposing $\mathbf{U}$ in its spherical and traceless components, (1) is equivalent to

$$\nabla\gamma = \mathbf{R_e}\nabla\beta, \tag{2}$$

where $\gamma = \frac{(m^2-n^2)\alpha-2n^2\beta}{2mn}$, $2m = \lambda_1+\lambda_2$, $2n = \lambda_1-\lambda_2$ and $\mathbf{R_e} = \mathbf{e}\otimes\mathbf{e} - \mathbf{f}\otimes\mathbf{f}$ is a field of reflections in the plane characterized by the field of angles β. Observe that (2) will have a solution iff

$$\mathrm{div}\mathbf{W}\mathbf{R_e}\nabla\beta = 0. \tag{3}$$

Thus, if a field of reflections $\mathbf{R_e}$ satisfies (3), we can find a solution γ for (2) and over this field to construct a family of deformations ϕ with constant stretches by choosing m and n, and from this choice determining the correponding field $\mathbf{R}(\alpha)$ and, finally, integrating $\mathbf{R}(\alpha)\mathbf{U}$.

At this point we remark the analogy between the present problem and the slip line field theory in plasticity(see, e.g., Hill (1950)). In the plane $\mathbb{R}^2$ let $\mathbf{T}$ be a symmetric tensor field. Write $\mathbf{T} = \frac{\mathrm{tr}\mathbf{T}}{2}\mathbf{I} + (\mathbf{T} - \frac{\mathrm{tr}\mathbf{T}}{2}\mathbf{I}) = -p\mathbf{I} + \mathbf{T}_\mathrm{d}$. Thus, $\mathbf{T} = -p\mathbf{I} + q\hat{\mathbf{R}}$, where $\hat{\mathbf{R}}$ is a reflection in the plane, with $\hat{\beta}$ giving its attitude. We want to solve the problem

$$\mathrm{div}\mathbf{T} = \mathbf{0}, \tag{4}$$

with $q = k$, a positive constant. Observe that $\|\mathbf{T}_\mathrm{d}\| = \sqrt{2}q$. As $\mathrm{div}\mathbf{T} = -\nabla p + 2q\mathbf{W}\hat{\mathbf{R}}\nabla\hat{\beta}$, if we define $\mathbf{R_e} = \mathbf{W}\hat{\mathbf{R}}$, then $\beta = \hat{\beta} + \frac{\pi}{4}$ is the angle defining the unit vector $\mathbf{e}$ and our problem is to find p such that $\nabla\left(\frac{p}{2q}\right) = \mathbf{R_e}\nabla\beta$, which is exactly the equation (2) with $\gamma = \frac{p}{2k}$.

Observe that (2) is equivalent to the system

$$\begin{aligned}\nabla(\gamma-\beta)\cdot\mathbf{e} &= 0,\\ \nabla(\gamma+\beta)\cdot\mathbf{f} &= 0.\end{aligned} \tag{5}$$

Now we recall that for any smooth fields of directions $\{\mathbf{e},\mathbf{f}\}$ corresponds a parametrization $(X_1,X_2) = \Psi(u,v)$ for which $\frac{\partial\Psi}{\partial u}$ and $\frac{\partial\Psi}{\partial v}$ are paralell to $\mathbf{e}$ and $\mathbf{f}$, respectively. From (5), γ and β, as functions of the parameters (u,v), satisfy

$$\begin{aligned}\gamma-\beta &= 2g(v),\\ \gamma+\beta &= 2f(u),\end{aligned} \tag{6}$$

for smooth functions f and g. Thus the fields γ and β are given by

$$\begin{aligned} \gamma &= f(u) + g(v), \\ \beta &= f(u) - g(v). \end{aligned} \tag{7}$$

Because $\frac{\partial \Psi}{\partial u} \cdot \frac{\partial \Psi}{\partial v} = 0$, the derivative $\bar{\mathbf{F}}$of Ψ has polar decomposition $\bar{\mathbf{F}} = \bar{\mathbf{R}}\bar{\mathbf{U}}$ where the rotation angle of $\bar{\mathbf{R}}$ equals to $\beta(X_1, X_2)$ at the corresponding point and $\bar{\mathbf{U}}$ is diagonal for the basis $\{\mathbf{e_1}, \mathbf{e_2}\}$. We write $\bar{\mathbf{U}} = \Lambda(u, v)\mathbf{e_1} \otimes \mathbf{e_1} + \Omega(u, v)\mathbf{e_2} \otimes \mathbf{e_2}$. So, as β is known in the (u, v) plane and $\bar{\mathbf{U}}$ admits the above representation, we can determine Ψ, and the problem is solved. Taking into account the local character of our analysis, we limit ourselves to considering the cases:

Case 1. $f'g' \neq 0$;

Case 2. $f' \neq 0$, $g' \equiv 0$ or $g' \neq 0$, $f' \equiv 0$;

Case 3. $f' \equiv g' \equiv 0$;

The above conditions on the derivatives of f and g must be understood as valid on a region. Fields for which the Case 3 holds correspond to γ and β both constant and ϕ is an homogeneous deformation. Thus, we will investigate the Cases 1 and 2.

In the first case, we introduce a new tranformation $(X_1, X_2) = \tilde{\Psi}(\xi, \eta)$ defined by

$$\tilde{\Psi}(\xi, \eta) = \Psi(f^{-1}(\xi), g^{-1}(\eta)). \tag{8}$$

Observe now that $\gamma = \xi + \eta$ and $\beta = \xi - \eta$. Also, $\nabla\tilde{\Psi} = \tilde{\mathbf{F}} = \tilde{\mathbf{R}}(\beta)\tilde{\mathbf{U}}$, and $\tilde{\mathbf{U}} = A\mathbf{e}_1 \otimes \mathbf{e}_1 + B\mathbf{e}_2 \otimes \mathbf{e}_2$. Then (2) is equivalent to

$$\begin{aligned} A_\eta + B &= 0, \\ B_\xi + A &= 0. \end{aligned} \tag{9}$$

From (9) we obtain

$$\begin{aligned} A_{\xi\eta} - A &= 0, \\ B_{\xi\eta} - B &= 0, \end{aligned} \tag{10}$$

and A and B satisfy the telegraph equation.

Now, let's consider the second case. Firstly, we will consider the case where $f' \neq 0$ and $g' \equiv 0$. Now, we introduce a new tranformation $(X_1, X_2) = \tilde{\Psi}(\xi, \eta)$ defined by

$$\tilde{\Psi}(\xi, \eta) = \Psi(f^{-1}(\xi), \eta). \tag{11}$$

In this case $\gamma = \xi + c$, and $\beta = \xi - c$.Also, $\nabla\tilde{\Psi} = \tilde{\mathbf{R}}(\beta)\tilde{\mathbf{U}}$ where $\tilde{\mathbf{U}}$ admits the the representation $\tilde{\mathbf{U}} = A\mathbf{e}_1 \otimes \mathbf{e}_1 + B\mathbf{e}_2 \otimes \mathbf{e}_2$. Then, (2) can be written as

$$\begin{aligned} A_\eta + B &= 0, \\ B_\xi &= 0. \end{aligned} \tag{12}$$

The above system implies that $A_{\xi\eta} = 0$. Thus,

$$\begin{aligned} A &= h_1(\xi) + h_2(\eta), \\ B &= -h_2'(\eta), \end{aligned} \tag{13}$$

where h_1 and h_2 are smooth functions of each variable. The situation where $f' \equiv 0$ and $g' \neq 0$ is treated in similar lines(see Duda (1996)).

3 CONSTRUCTING PLANE DEFORMATION

From the knowledge of A and B, $AB \neq 0$, satisfying either (9) or (13), we must proceed as follows to obtain the corresponding plane deformation with constant stretch:

1) Integrate

$$\tilde{\mathbf{F}} = \tilde{\mathbf{R}}(\beta)(A\mathbf{e}_1 \otimes \mathbf{e}_1 + B\mathbf{e}_2 \otimes \mathbf{e}_2) \tag{14}$$

to obtain $(X_1, X_2) = \tilde{\Psi}(\xi, \eta)$.

2) Find $(\xi, \eta) = \tilde{\Psi}^{-1}(X_1, X_2)$ in order to obtain the fields $\beta(X_1, X_2)$ and $\gamma(X_1, X_2)$[1].

3) Choose m and n, where $2m = \lambda_1 + \lambda_2$ and $2n = \lambda_1 - \lambda_2$ such that λ_1 and λ_2 are greater than zero, to find α by

$$\alpha = \frac{2mn\gamma + 2n^2\beta}{m^2 - n^2} \tag{15}$$

or by direct integration of (1)[2].

4) Finally, integrate $\mathbf{F} = \mathbf{R}(\alpha)\mathbf{U}$, where $\mathbf{U} = m\mathbf{I} + n\mathbf{R}_{\mathbf{e}}$, to get the corresponding deformation field.

3.1 EXAMPLES

We will consider two examples, which will be useful later. More examples can be found in Duda (1996).

EXAMPLE 1

Let $A = De^{-\frac{1}{c}\xi - c\eta}$, with $c \neq 0$ and D constants. It's easy to see that A satisfy the telegraph equation. By (9_1), $B = cDe^{-\frac{1}{c}\xi - c\eta}$. Thus, by integration we conclude that

$$\begin{aligned} X_1 &= \frac{cD}{\sqrt{1+c^2}} e^{-\frac{1}{c}\xi - c\eta} \cos(\beta + \mu), \\ X_2 &= \frac{cD}{\sqrt{1+c^2}} e^{-\frac{1}{c}\xi - c\eta} \sin(\beta + \mu). \end{aligned}$$

where $\mu = \arctan c$. Using polar coordinates (R, Θ), the above equations can be written as

$$\begin{aligned} R &= \frac{c}{\sqrt{1+c^2}} e^{-\frac{1}{c}\xi - c\eta}, \\ \Theta &= \beta + \mu. \end{aligned}$$

[1] In most examples this step can be omitted because we can find β and γ directly.

[2] In order to find α by (1) we just need β. So by the expression for α we can find γ. This gives a hint to a possible tranformation of variables that can be used in plasticity.

Hence, $\beta = \Theta + \beta_0$, where $\beta_0 = -\mu$. The integral lines of the fields $\{\mathbf{e}, \mathbf{f}\}$ form two families of logarithmic spirals. To obtain the corresponding deformation we determine α directly by equation (1) to find

$$\alpha = K_1\Theta + K_2 \log R, \tag{16}$$

where where $K_1 = \frac{2n(n-m\cos 2\beta_0)}{m^2-n^2}$ and $K_2 = \frac{2mn\sin 2\beta_0}{m^2-n^2}$. The corresponding deformation, parametrized by m, n, and β_0 is given in polar coordinates by

$$\begin{aligned} r &= \sqrt{\tfrac{m^2-n^2}{K_1+1}}R, \\ \theta &= (K_1+1)\Theta + K_2 \log R. \end{aligned} \tag{17}$$

EXAMPLE 2

Put $B = h(\eta)$, $B = -h'(\eta)$ and $\beta = \xi$. Then

$$\begin{aligned} X_1 &= h(\eta)\cos(\xi + \frac{\pi}{2}), \\ X_2 &= h(\eta)\sin(\xi + \frac{\pi}{2}). \end{aligned}$$

Thus $\beta = \gamma = \xi = \Theta - \frac{\pi}{2}$. Following the steps 3 and 4 we arrive at

$$\begin{aligned} r &= (m-n)R, \\ \theta &= \frac{m+n}{m-n}\Theta. \end{aligned}$$

Observe that the above deformation can obtained from that of Example 1 doing $\beta_0 = -\frac{\pi}{2}$.

3.2 GEOMETRY OF THE SINGH-PIPKIN SOLUTION

Now, we will give an important geometric characterization of the Singh-Pipkin solution[3].

Remember that (2) will have a solution iff the equation (3) holds. Let β be a solution of the equation (3). We want to find those β such that $\hat{\beta} = \beta + \beta_0$, for any $\beta_0 \in \mathbb{R}$, is also a solution.

These solutions are characterized by following property: Property 1. Let β be a non-constant solution of (3) and γ the corresponding field given by (2). Then, the following conditions are equivalents:

(i) $\hat{\beta} = \beta + \beta_0$ is also a solution of (3), for an arbitrary constant β_0.

(ii) $\triangle\gamma = 0$.

When the Property 1 holds, we have necessarily that $\triangle\beta = 0$, as a corollary of the following lemma :

Lemma 1. Let $\varphi = a\gamma + b\beta$, with a, b constants, such that $a^2 - b^2 \neq 0$. If $\triangle\varphi = 0$, then $\left(\frac{B}{A}\right)_\xi = \left(\frac{A}{B}\right)_\eta = 0$ in Case 1 and $\left(\frac{B}{A}\right)_\xi = 0$ or $\left(\frac{A}{B}\right)_\eta = 0$ in Case 2. In particular $\triangle\varphi = 0$ implies $\triangle\gamma = \triangle\beta = 0$.

Corollary. If $\triangle\gamma = 0$, then $\triangle\beta = 0$.

[3]By reasons of space, we will omit all proofs in this section. Such proofs are given in Duda (1996)

Under the conditions of Lemma 1 we have in the Case 1, $\frac{B}{A} = c$, where $c \neq 0$ is an arbritray constant, implying that $A = De^{-\frac{1}{c}\xi - c\eta}$ and $B = cDA$, which is the content of the Example 1. In the Case 2, $\left(\frac{B}{A}\right)_\xi = 0$ or $\left(\frac{A}{B}\right)_\eta = 0$, and we have that $A = A(\eta)$ and $B = -A'(\eta)$, which is the content of the Example 2 or $B = B(\xi)$ and $A = -B'(\xi)$.

Deformation fields corresponding to the Case 2 can be obtained through the solution of Case 1 by letting $\beta_0 = 0$ or $\beta_0 = \pm\frac{\pi}{2}$. So, the solutions corresponding to both cases can be put together. This solution is known as the Singh-Pipkin solution, in the context of the Ericksen's problem in elasticity, and is given by (17).

4 APPLICATIONS

Let's superpose to the deformation ϕ an uniform transverse stretch $x_3 = \lambda X_3$, with $\lambda > 0$. To such generalized plane deformation, the plane part of the first Piola-Kirchhoff stress tensor for a Bell's constrained elastic material[4] is given by

$$\mathbf{S} = (f_1 + p)\mathbf{R} + f_0\mathbf{F}^*, \tag{18}$$

where p is an arbitrary function, f_0 and f_1 are constitutive functions depending on the eigenvalues of $\mathbf{U}$ and λ, $\mathbf{F} = \mathbf{RU}$ is the plane part of $\nabla\phi$, and $\mathbf{F}^* = \det\mathbf{F}\mathbf{F}^{-\mathbf{T}}$.

In this case, the equilibrium equation $\mathrm{div}\mathbf{S} = 0$ is conveniently written as

$$\nabla p = -(f_1 + p)\mathbf{W}\nabla\alpha, \tag{19}$$

where α is the angle of rotation corresponding to $\mathbf{R}$. The above system will have a solution p iff

$$(f_1 + p)\triangle\alpha = 0. \tag{20}$$

In fact $p = -f_1$ is always a solution of (19). On the other hand, $\triangle\alpha = 0$ is the sufficient condition of the Frobenius' Theorem, and p can be chosen arbitrary at a point. In particular, we see that all generalized plane deformation whose stretches are constants, are universal solutions for a Bell constrained elastic material.

As $\alpha = \frac{2n}{m^2-n^2}(m\gamma + n\beta)$ with $m^2 - n^2 > 0$ and $n > 0$[5], then it follows from Lemma 1 that $\triangle\alpha = 0$ implies $\triangle\gamma = \triangle\beta = 0$. Then, the corresponding solutions are given by the Singh-Pipkin family. In fact, this result is valid to more general constraints.

In this section, we arrived at the following results:

i) Any generalized plane deformation (compatible with the constraint) with constant stretches is an universal solution for Bell's materials;

ii) If ϕ is a Singh-Pipkin solution, p can be arbitrarily chosen at point. Othewise p is constant.

Both results are new in the literature.

[4] A Bell's constrained elastic material is an elastic, homogeneous, isotropic material with the constraint $\lambda_1 + \lambda_2 + \lambda = 3$. Bell (1985) has observed that this constraint closely describes experimental data for plastic deformation of metals.

[5] The condition $m^2 - n^2 > 0$ means that ϕ preserves orientation whereas $n > 0$ prevents that $\mathbf{U}$ is not a multiple of the identity, which would imply that ϕ would be a homogeneous deformation.

5 REFERENCES

Bell, J. F., "Contemporary perspectives in finite strain plasticity",*Int. J. Plasticity*, **1**, 3-27, 1985.

Duda, F. P. and Martins,L. C., "Compatibility conditions for the Cauchy-Green strain fields: solutions for the plane case", *J. Elasticity*, **39**, 247-264, 1995.

Duda, F. P., "Corpos Elásticos com Vinculo Interno e Soluções Universais na Classe de Deformações Planas com Estiramento Constante", Tese de Doutorado, Coppe/UFRJ, dezembro, 1996.

Hill, R., "The Mathematical Theory of Plasticity", Oxford Press, 1950.

XIV Brazilian Congress of Mechanical Engineering
Obeid Plaza Hotel Convention Center - Bauru - SP/Brazil
December 08-12th 1997

PAPER CODE: COB96

UMA TEORIA SIMPLES PARA O CÁLCULO DE TENSÕES EM VIGAS INELÁSTICAS SUBMETIDAS A CARREGAMENTOS COMPLEXOS / *A SIMPLE THEORY TO PERFORM AN APPROXIMATE COMPUTATION OF THE STRESSES IN SLENDER INELASTIC MEMBERS SUBJECTED TO VARIABLE TRANSVERSE AND AXIAL LOADING*

Marcio Assimos de almeida, Heraldo S. Costtos e Marcelo Magalhães Valente
PGMEC - Depto. de Engenharia Mecânica - Universidade Federal Fluminense
Rua Passo da Pátria, 156 - Niterói/RJ CEP:24210-240

Abstract

The present paper presents a simple theory to perform an approximate computation of the stresses in slender elasto-plastic and elasto-viscoplastic members subjected to variable transverse and axial loading. Theories for inelastic beams found in the literature are restricted to very simple hardening rules (generally a perfectly plastic behavior) which are not adequate to model cyclic loadings. Although the proposed theory is adequate for any kind of elasto-plastic and elasto-viscoplastic constitutive equations with internal variables , a particular set of constitutive equations which accounts for the isotropic and kinematic hardening induced by plastic deformations is considered in the presentation. No matter the non-linearity of the evolution laws adopted for the kinematic and isotropic hardening variables, simple expressions are obtained connecting the stress components with the bending moment, the shear force, the normal force and the plastic strains. The theory allows a low cost analysis of the stresses and strains in many structural elements used in industrial applications. The usefulness of the proposed theory is checked through the simulation of a combination of axial and transversal loading in 316 L stainless steel bars at $600^{\circ}\ C$.

Keywords

Theory of beams, Plasticity, Viscoplasticity, Internal Variables/Teoria de vigas, Plasticidade, Viscoplasticidade, Variáveis internas.

1. INTRODUÇÃO

O estudo do comportamento de componentes mecânicos metálicos, que operam além do limite elástico tem grande importância industrial. Problemas de grande interesse ocorrem, por exemplo, nas indústrias petroquímica, nuclear e aeroespacial. O desenvolvimento de equações constitutivas mais realísticas para este tipo de comportamento vem tomando um grande impulso nas duas últimas décadas. Diversos trabalhos vêm sendo desenvolvidos procurando modelar adequadamente os fenômenos de plasticidade, fluência, dano, relaxação, além do endurecimento causado pela plastificação, por exemplo, Costa Mattos (1988), Lemaitre e Chaboche (1990). Uma modelagem mais sofisticada desses mecanismos físicos dissipativos não lineares é fundamental para se obter uma previsão confiável das tensões e deformações, as quais são necessárias em qualquer critério de avaliação da integridade estrutural. Por exemplo, ao contrário da teoria da elasticidade, a ordem de aplicação dos carregamentos

influi diretamente no campo de tensões resultante. No entanto, de uma forma contraditória, a grande sofisticação mecânica dessas equações constitutivas tem sido um empecilho para sua popularização entre projetistas e engenheiros.

Surge então a questão que motiva este trabalho - desenvolver uma 'Resistência dos Materiais Inelásticos'. Isto é, usar certas hipóteses simplificadoras de carater cinemático no estudo de alguns problemas inelásticos visando obter soluções aproximadas de forma rápida e a baixo custo, mesmo se leis de comportamento mais complexas forem consideradas. Estas hipóteses simplificadoras são tradicionalmente usadas no estudo de vigas elásticas. Este trabalho apresenta uma teoria para o estudo da flexão de vigas elasto-plásticas e elasto-viscoplásticas, válida para qualquer tipo de lei de comportamento com variáveis internas. Teorias para vigas inelásticas encontradas na literatura (Crandall et al, 1978 e Moura Branco, 1985, por exemplo) se restringem a leis de comportamento muito simples que não levam em conta o endurecimento causado por uma história complexa de plastificação.

2. TEORIA DE VIGAS INELÁTICAS

O objetivo desta seção é usar as hipóteses simplificadoras de Kirchhoff-Love sobre a deformação da seção transversal de vigas de forma a obter um método simples para a aproximação da tensão e da deformação numa viga inelástica.

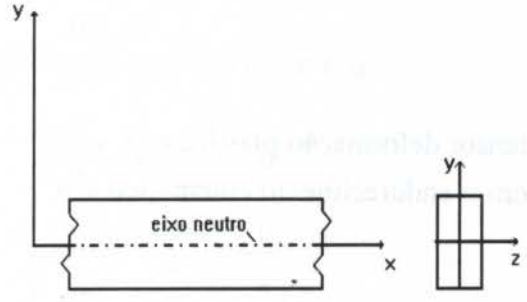

fig.1 - Sistema de eixos

Diversos trabalhos foram propostos na literatura visando a modelagem do fenômeno de fluência e de plastificação em vigas usando a hipótese de Kirchhoff-Love. No entanto, as leis de comportamento consideradas são muito simples e, portanto, não são realísticas no ponto de vista físico.

Conhecem-se diversas aplicações de materiais submetidos a carregamentos inelásticos cíclicos. Como exemplo, é possível citar as turbinas a vapor e a gás, fornos, equipamentos da indústria química e nuclear, componentes de motores, estrutura de avião, etc. Estas aplicações e sua importância justificam a realização deste trabalho. Apesar da teoria poder ser desenvolvida dentro de um contexto bastante geral, a apresentação se restringirá no estudo da flexão plana de vigas retas, homogêneas e de seção transversal constante. Ao longo deste trabalho, o sistema de eixo será adotado como o da figura 1. Observações: A seção transversal será considerada simétrica em relação aos eixos y e z e o eixo neutro é a reta formada pelo centro geométrico de cada seção transversal.

2.1. Equações Constitutivas Abstratas

As equações apresentadas a seguir, propostas por Lemaitre e Chaboche(1990), descrevem adequadamente o comportamento de alguns metais e ligas em temperatura elevadas e à temperatura ambiente. Ao logo deste trabalho, grandezas tensoriais serão notadas por letras sublinhadas por um número de traços igual a sua ordem :

$$\underline{\underline{\sigma}} = 2\mu(\underline{\underline{\varepsilon}} - \underline{\underline{\varepsilon}}^{p}) + \lambda\ tr(\underline{\underline{\varepsilon}} - \underline{\underline{\varepsilon}}^{p})\underline{\underline{1}} \tag{1}$$

$$\dot{\underline{\underline{\varepsilon}}}^{p} = \frac{3}{2}\, \dot{p}\, \frac{(\underline{\underline{\sigma}} - \underline{\underline{X}})_{dev}}{J(\underline{\underline{\sigma}} - \underline{\underline{X}})} \qquad \underline{\underline{\varepsilon}}^{p}(t=0) = \underline{\underline{0}} \tag{2}$$

$$\dot{\underline{\underline{X}}}=\frac{2}{3}a\dot{\underline{\underline{\varepsilon}}}^{p}-b\underline{\underline{X}}\dot{p} \qquad \underline{\underline{X}}(t=0)=\underline{\underline{0}} \tag{3}$$

$$\dot{Y}=v_1(v_2+\sigma_y-Y)\dot{p}; \qquad Y(t=0)=\sigma_y \tag{4}$$

plasticidade: $p\geq 0,\ F(\underline{\underline{\sigma}},\underline{\underline{X}},Y)\leq 0,\ pF=0$ (5)

viscoplasticidade: $\dot{p}=\left\langle\frac{F}{K}\right\rangle^{n}$ (6)

Onde <A>=MAX{0,A} e $\underline{\underline{\sigma}}$ é o tensor tensão, $\underline{\underline{\varepsilon}}^{p}$ é o tensor deformação plástica e $\underline{\underline{X}}$ e Y são variáveis auxiliares associadas, respectivamente, com o endurecimento cinemático e o endurecimento isotrópico causado pela plastificação.

$$F=J(\underline{\underline{\sigma}}-\underline{\underline{X}})-Y \tag{7}$$

$$J(\underline{\underline{\sigma}}-\underline{\underline{X}})=\left[\frac{3}{2}(\underline{\underline{\sigma}}-\underline{\underline{X}})_{dev}\cdot(\underline{\underline{\sigma}}-\underline{\underline{X}})_{dev}\right]^{\frac{1}{2}} \tag{8}$$

$(\underline{\underline{\sigma}}-\underline{\underline{X}})_{dev}$ é a parte desviadora de $(\underline{\underline{\sigma}}-\underline{\underline{X}}),\mu,\lambda,k,a,b,v_1,v_2,\sigma_y,n$ são constantes do material. $J(\underline{\underline{\sigma}}-\underline{\underline{X}})$ é chamado de tensão equivalente de Von-Mises.

Neste trabalho, para simplificar a apresentação da teoria de vigas, as equações constitutivas são apresentadas sem comentários sobre suas principais características e sobre o papel das variáveis auxiliares $\underline{\underline{X}}$, Y, $\underline{\underline{\varepsilon}}^{p}$, p. Uma análise detalhada pode ser encontrada em Lemaitre e Chaboche (1990). Entretanto é importante notar que em todas as referências pesquisadas, teorias de vigas inelásticas foram desenvolvidas usando-se um caso particular das equações (1) a (4) onde se considera as constantes a,b,v_1,v_2,σ_y iguais a zero. Este modelo simplificado é inadequado para descrever os fenômenos de endurecimento associados a deformação plástica.

2.2. Hipóteses Básicas

Supondo que a viga é muito esbelta e que uma das dimensões é predominante (pelo menos dez vezes maior do que as outras) considera-se que

HIPÓTESE 1 - O tensor das tensões é da forma,

$$\underline{\underline{\sigma}} = \begin{bmatrix} \sigma_{xx} & \sigma_{xy} & 0 \\ \sigma_{yx} & 0 & 0 \\ 0 & 0 & 0 \end{bmatrix} \tag{9}$$

Introduzindo esta hipótese nas equações (1) a (4) é possível concluir que:

$$\begin{aligned} \sigma_{xx} &= E(\varepsilon_{xx} - \varepsilon^p_{xx}) \\ \sigma_{xy} &= G(\varepsilon_{xy} - \varepsilon^p_{xy}) \\ (\varepsilon_{zz} - \varepsilon^p_{zz}) &= (\varepsilon_{yy} - \varepsilon^p_{yy}) = (\varepsilon_{xx} - \varepsilon^p_{xx}) \end{aligned} \tag{10}$$

com:

$$E = \mu\left[\frac{3\lambda + 2\mu}{\lambda + \mu}\right] \quad ; \quad G = \frac{E}{2(1+\nu)} \quad ; \quad \nu = \frac{\lambda}{2(\lambda+\mu)}$$

Além disso é possível mostrar que

$$\underline{\underline{\sigma}}_{dev} = \begin{bmatrix} \frac{2\sigma_{xx}}{3} & \sigma_{xy} & 0 \\ \sigma_{yx} & \frac{-\sigma_{xx}}{3} & 0 \\ 0 & 0 & \frac{-\sigma_{xx}}{3} \end{bmatrix} \tag{11}$$

e que $\underline{\underline{\varepsilon}}^p$ e $\underline{\underline{X}}$ têm a seguinte forma

$$\underline{\underline{\varepsilon}}^p = \begin{bmatrix} \varepsilon^p_{xx} & \varepsilon^p_{xy} & 0 \\ \varepsilon^p_{yx} & \frac{-\varepsilon^p_{xx}}{2} & 0 \\ 0 & 0 & \frac{\varepsilon^p_{xx}}{2} \end{bmatrix} \qquad \underline{\underline{X}} = \begin{bmatrix} X_{xx} & X_{xy} & 0 \\ X_{xy} & X_{xy} & 0 \\ 0 & 0 & X_{xy} \end{bmatrix} \tag{12}$$

Usando-se a notação $X_{xx} = \frac{2X}{3}$, obtém-se de (8) que:

$$J(\underline{\underline{\sigma}} - \underline{\underline{X}}) = \left[(\sigma_{xx} - X_{xx})^2 + 3(\sigma_{xy} - X_{xy})^2\right]^{\frac{1}{2}} \tag{13}$$

Portanto as equações (1) - (4) se reduzem a:

$$\sigma_{xx} = E(\varepsilon_{xx} - \varepsilon^p_{xx}); \qquad \sigma_{xy} = G(\varepsilon_{xy} - \varepsilon^p_{xy}); \tag{14}$$

$$\dot{\varepsilon}^p_{xx} = \dot{p}\,\frac{(\sigma_{xx} - x_{xx})}{J}; \qquad \varepsilon^p_{xx}(t=0) = 0; \tag{15}$$

$$\dot{\varepsilon}^{p}_{xy} = \frac{3}{2}\ \dot{p}\ (\sigma_{xy} - x_{xy}); \qquad \varepsilon^{p}_{xy}(t=0) = 0; \tag{16}$$

$$\dot{X} = a\dot{\varepsilon}^{p}_{xx} - bx\dot{p}; \qquad X(t=0) = 0; \tag{17}$$

$$\dot{X}_{xy} = \frac{2}{3}a\dot{\varepsilon}^{p}_{xy} - bx_{xy}\dot{p}; \qquad X_{xy}(t=0) = 0; \tag{18}$$

$$\dot{Y} = v_1(v_2 + \sigma_y - Y)\dot{p}; \qquad Y(t=0) = 0. \tag{19}$$

O valor de $\dot{p}$, F e J são os mesmos mencionados nas fórmulas (6), (7) e (8).

Além da hipótese anterior, considera-se que as seções ortogonais ao eixo neutro permanecem planas após a deformação.

HIPÓTESE 2- O deslocamento $\underline{u}$ têm a seguinte forma

$$\underline{u} = [u(x) - \phi(x)y]\,\underline{i} + w(x)\underline{j} \tag{20}$$

onde: $\phi(x)$ é o ângulo de rotação da seção ortogonal no ponto x

w(x) é o deslocamento do eixo neutro na direção de $\underline{j}$.

A deformação $\varepsilon = \frac{1}{2}(\nabla\underline{u} + \nabla\underline{u}^{T})$ associada ao deslocamento $\underline{u}$ é dada por:

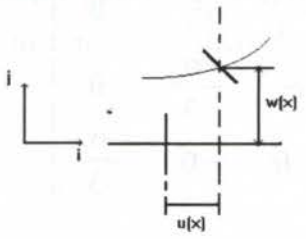

Fig. 2 - Deformação hipotética de uma seção

$$\underline{\underline{\varepsilon}} = \begin{bmatrix} [u'(x) - \phi'(x)y] & [w'(x) - \phi(x)]/2 & 0 \\ [w(x) - \phi(x)]/2 & 0 & 0 \\ 0 & 0 & 0 \end{bmatrix} \tag{21}$$

Portanto usando (10) e (21) obtém-se:

$$\sigma_{xx} = E[u'(x) - \phi'(x)y] - E\varepsilon^{p}_{xx}(x,y), \quad \sigma_{xy} = G\left[\frac{w'(x) - \phi(x)}{2}\right] - G\varepsilon^{p}_{xy}(x,y) \tag{22}$$

Os esforços normal, cortante e momento fletor atuando numa seção fixa (x) da viga são definidos da seguinte maneira:

$$N(x) = \int_A \sigma_{xx}\,dA = EAu(x) - E\int_A \varepsilon^{p}_{xx}\,dA \tag{23}$$

$$Q(x) = \int_A \sigma_{xy} dA = GA\left[\frac{w(x) - \phi(x)}{2}\right] - G\int_A \varepsilon_{xy}^{p} dA \tag{24}$$

$$M(x) = -\int_A \sigma_{xx}\, y\, dA = EI\phi(x) + E\int_A \varepsilon_{xx}^{p}\, y\, dA \tag{25}$$

Com as equações (22),(23) e (25) obtém-se:

$$\sigma_{xx}(x,y) = \frac{-y}{I}\left[M(x) - E\int_A \varepsilon_{xx}^{p}\, y\, dA\right] + \frac{1}{A}\left[N(x) + E\int_A \varepsilon_{xx}^{p}\, dA\right] - E\,\varepsilon_{xx}^{p}(x,y). \tag{26}$$

De (22) e (24) segue que

$$\sigma_{xy}(x,y) = \frac{1}{A}\left[Q(x) + G\int_A \varepsilon_{xy}^{p}\, dA\right] - G\,\varepsilon_{xy}^{p}(x,y). \tag{27}$$

Se $\varepsilon_{xx}^{p} = \varepsilon_{xy}^{p} = 0$, de (27) e (25) obtém-se:

$$\sigma_{xx} = \frac{-M(x)\, y}{I} + \frac{N(x)}{A} \tag{28}$$

$$\sigma_{xy} = \frac{Q(x)}{A} \tag{29}$$

que são as relações clássicas da teoria de vigas elásticas.

Portanto, (26) e (27) serão as relações básicas para a obtenção das tensões numa viga inelástica. A equação (29) fornece um valor médio da componente cizalhante da tensão ao longo da seção. Obviamente, esta forma aproximada da componente σ_{xy} não satisfaz as condições de contorno do problema. No entanto, para vigas esbeltas (L é pelo menos dez vezes maior do que as outras dimensões), o máximo valor calculado de σ_{xy} numa seção é sempre muito menor do que o máximo valor da componente axial σ_{xx}. Além disso, devido às condições de contorno, $|\sigma_{xy}|$ é nulo quando $|\sigma_{xx}|$ for máximo e vice-versa. Portanto, para o cálculo da tensão equivalente de Von Mises, ver equação (8), é possível desprezar σ_{xy}, o que é equivalente a desprezar a distorção ε_{xy}. Do ponto de vista cinemático isto é equivalente a considerar que as seções transversais além de planas permanecem perpendiculares a linha neutra após a deformação.

3.EXEMPLOS

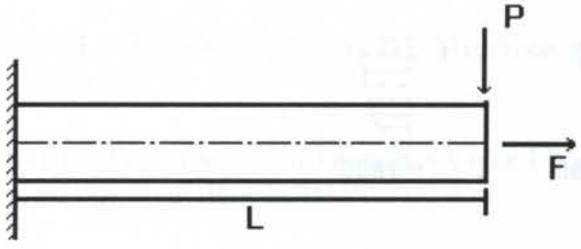

Fig.3 -Barra engastada

Considera-se uma viga reta, homogênea e de seção reta constante à uma temperatura de $600^{\circ}C$, engastada em uma das extremidades e submetida a duas forças F e P, que varia no tempo conforme a figura 3. Devido a não linearidade das equações, a ordem do carregamento influi na distribuição das tensões.

Foi considerada nestes cálculos uma barra de seção reta quadrada de altura H=35mm e comprimento L=500mm, para a velocidade de carregamento $\alpha = 1.33N/s$. Os coeficientes do material para uso das equações elasto-viscoplásticas são: k=150 Mpa.s, n=12, a=24800 Mpa, b=300, v_1=10, v_2=80 Mpa e $\sigma_y = 6$ Mpa. O método numérico utilizado (Runge-Kutta de quarta ordem) está discutido em Valente (1993).

Dois tipos de carregamentos serão considerados:

3.1 Flexão Seguida de Tração

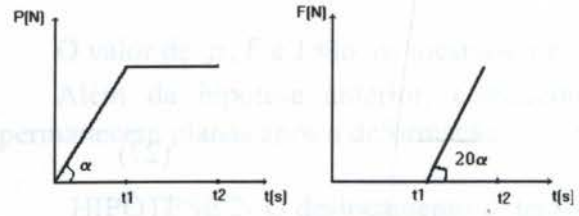

Fig.4 - Flexão seguido de tração

Neste caso P evolui linearmente no tempo t até atingir o intante t_1=900s. A partir deste instante P passa a ser constante e F evolui linearmente até atingir o instante t_2=1800s como pode ser visto na figura 4.

A distribuição da componente σ_{xx} da tensão na seção x = 0 é mostrada na figura 6.

3.2 Tração Seguida de Flexão

Neste caso F evolui linearmente no tempo t até atingir o instante t_1. A partir desse instante F passa a ser constante e P evolui linearmente até atingir o instante t_2 como mostrado na figura 5.

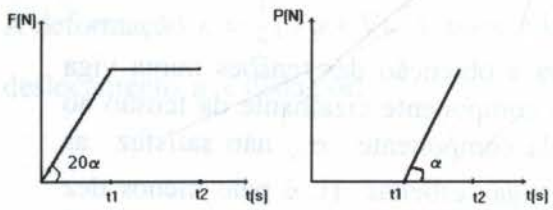

Fig.5 - Tração seguido de flexão

A distribuição da componente σ_{xx} da tensão na seção x = 0 é mostrada na figura 7. Como se pode verificar, a distribuição de tensões é completamente diferente em cada caso, apesar do valor final dos carregamentos serem os mesmos.

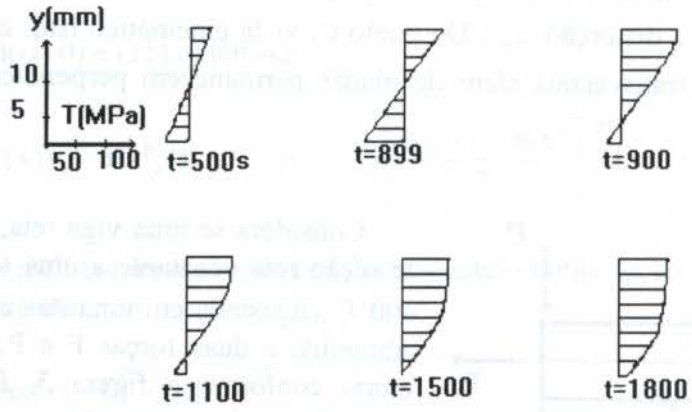

Fig.6 - Distribuição de tensão flexão + tração

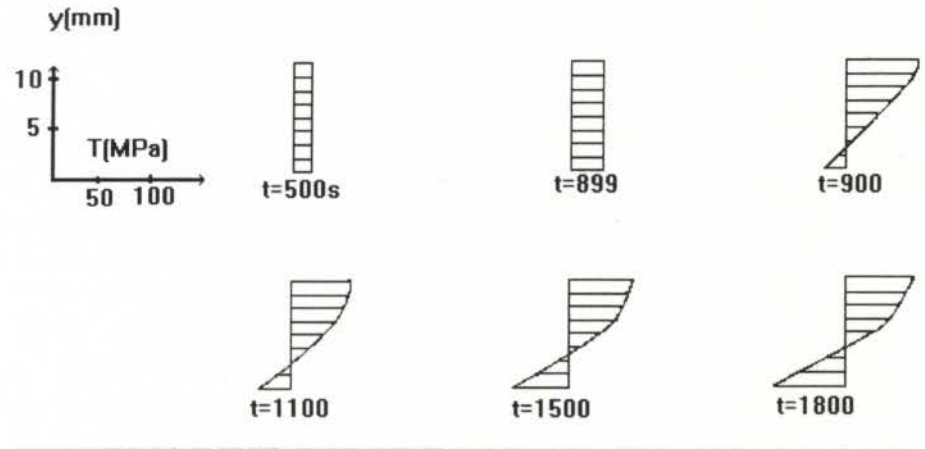

fig.7 - Distribuição de tensão tração + flexão

4.CONCLUSÕES

Os resultados mostram como a ordem de aplicação dos carregamentos pode alterar completamente a distribuição final das tensões. Modelos usando uma relação tensão - deformação elástica não linear são incapazes de descrever este efeito. Modelos que consideram um comportamento elastico-perfeitamente plástico não descrevem de forma fisicamente realista o endurecimento causado pela plastificação. O trabalho apresentado é um primeiro passo no desenvolvimento de procedimentos simplificados de cálculo para vigas inelásticas submetidas à carregamentos complexos. Ele permite levar em conta a ordem e a velocidade dos carregamentos na resposta da estrutura, bem como descrever fenômenos como o endurecimento cíclico ou amolecimento cíclico induzidos pela plastificação. No entanto, para uma validação adequada, está sendo feita uma comparação sistemática dos resultados obtidos através desta 'Resistência dos Materiais Inelásticos' com simulações feitas por elementos finitos (sem hipóteses simplificadoras de caráter cinemático) para tentar quantificar o erro na aproximação obtida e os fatores de segurança adequados a serem utilizados.

5.REFERÊNCIAS

COSTA MATTOS, H. Uma Contribuição `a Formulação Termodinâmica da Elasto-plasticidade e da Elasto-viscoplasticidade". Tese de doutorado, Departamento de Engenharia Mecânica da PUC-Rio, 1988.

CRANDALL, S.H., DAHL, N. C., LARDNER, T., An Introduction to the Mechanics of Solids, McGraw-Hill International Editions, 1978.

LEMAITRE, J. e CHABOCHE J.L. Mechanic of Solids Materials, Cambridge University Press, London, 1990.

MOURA BRANCO, C. A. G., Mecânica dos Materiais, Fundação Calouste Goulbenkian, Porto, 1985.

VALENTE, M.M. Uma Teoria de Vigas Elasto-plastico com Endurecimento, Dissertação de Mestrado, PUC-Rio,1993.

Tema 42

Método de Elementos Finitos

XIV Brazilian Congress of Mechanical Engineering
Obeid Plaza Hotel Convention Center - Bauru - SP/Brazil
December 08-12th 1997

PAPER CODE: COB103

STRESS PREDICTIONS FOR SHORT FLAT BARS WITH PROJECTIONS SUBJECTED TO SHEAR LOADING

M. K. PIPELZADEH & S. J. HARDY
Department of Mechanical Engineering, University of Wales, Swansea, SA2 8PP, U. K.

Abstract

The finite element method has been used to obtain stress concentration factor data for flat ' T' shaped components subjected to shear loading with local restraints being applied. This paper presents and describes the stress contours developed as a result of the shear load for a typical geometry. In addition, the stress concentration factor (SCF) data are used to obtain prediction equations using a multiple linear regression model. These equations provide guidelines for the assessment of the SCF by designers. The contours show the localised and large stress gradients in the vicinity of the fillet region. The ratio of the length to depth (or slenderness ratio) of the shank region is generally less than 3:1. For these short components particularly under shear (or bending) loads, primary bending stresses are no longer dominant and the transverse shear becomes an important secondary effect.

Keywords

Shear loading, stress concentration factor, finite element analysis, flat bars with projections.

1. INTRODUCTION

It is very rare that machine components have a uniform cross-section. Often there are abrupt changes in the cross-section and other geometric discontinuities (e.g. fillets, holes, grooves, projections etc.). These are termed 'notches' in the configuration of components and are the locations for stress and strain concentrations. The resulting distribution of stress over a cross-section containing a notch can be highly non-uniform. Maximum values occur at the bottom of the notch and the stress is lower over the remaining part of the cross-section. The effect of these stress raisers must be taken into account in the design assessment of such components and any inadequacy at the design stage may result in mechanical failure.

The elastic stress concentration factor (SCF) associated with notched components relates the maximum localised stress to the nominal stress away from the discontinuity. The SCF is generally geometry and loading dependent. The significance of the stress concentration factor depends, to an extent, on the ductility of the component material. For ductile materials, local regions of high stress are relieved as yielding occurs. For less ductile materials, brittle and fatigue failures predominate and stress concentration factors are used in order to predict the peak stress.

The flat 'T' shaped components with projections, the subject of this investigation, have wide applications throughout the field of engineering and are extensively used to transmit axial, bending and shear loads between two or more parts. Typical

applications include turbine blade roots, lifting lugs, connecting collars, shouldered plates and anchorage points for machinery parts.

This geometry has been studied by many investigators under a variety of loading and reaction conditions (e.g. axial, bending, torsion). These include the experimental work of Timoshenko and Dietz (1925) and Kumagai and Shimada (1968) on components subjected to tensile load, the photoelastic tension and bending results of Weibel (1934) and the photoelastic bending results of Hartman and Leven (1951). A substantial collection of design data is presented by Peterson (1974). More recently, Hardy and Malik (1992) have presented a compilation of post-Peterson stress concentration factor data, including data for flat plates, bars and strips with similar stress raising features.

SCF data for remote loading and reaction conditions is readily available, however there is far less data for the same component features when local loading or reactions are applied. For the case of shear loading, little information is available on stress effects. For components with a short length:span (known as slenderness ratio) subjected to shear loading, the resulting primary bending stresses are not the dominant factor and other important secondary effects have to be included because the plane-sections-remain-plane criteria (the fundamental assumption of classical bending theory) is violated. These secondary effects have been highlighted by Hardy and Pipelzadeh (1991), which include transverse shear, non-classical axial stresses and normal strain effects.

In this paper, the finite element method has been used to predict the elastic SCF data for short flat plates with projections. The results are complementary to previously published data by Hardy and Pipelzadeh (1994). The SCF data are used to obtain prediction equations using a multi-linear regression model. These equations provide guidelines for the assessment of the SCF data for the designers.
The results have been normalized with respect to material properties so that they can be applied to all geometrically similar components made from other materials which may be represented by the same material models.

1.1 NOTATION

d	Shank depth
t	Component thickness
D	Head depth
E	Young's modulus
H	Head length
I_m	Meridional stress index
$\bar{I}_m$	Maximum meridional stress index
L	Shank length
R	Fillet radius
δ	Applied lateral displacement
σ_b	Maximum bending stress based on strain energy theory
σ_m	Meridional stress

2. GEOMETRIES, LOADING AND BOUNDARY CONDITIONS

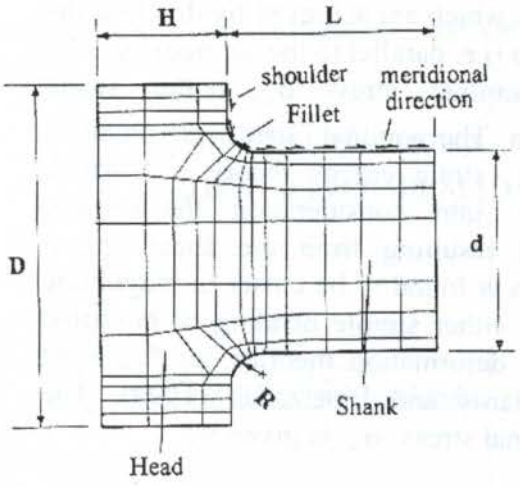

Figure 1- Component geometry and finite element mesh.

Figure 1 shows a typical finite element model of the component which can be divided into the following regions, these include, uniform shank, fillet, shoulder and head regions. Five dimensions are used to define a geometry. They are shank length, L; shank depth, d; head length, H; head depth, D and fillet radius, R (90 degree circular arc fillet), from which four non-dimensional geometric parameters are achieved by normalizing with respect to the shank depth, d. The range of normalized geometries considered in the analysis are as follows:

$2.0 \geq L/d \geq 0.5, 0\ 1.5 \geq H/d \geq 0.4$
$2.9 \geq D/d \geq 1.5, 0.15 \geq R/d \geq 0.05$

Figure 2 shows the loading and boundary conditions applied to the component. The shear load is applied as a prescribed displacement of a magnitude 'δ' across the shank end and reacted by local restraints at the shoulder in the vicinity of the fillet region. Also, the top and bottom surfaces of the head region are restrained in the direction of the applied load.

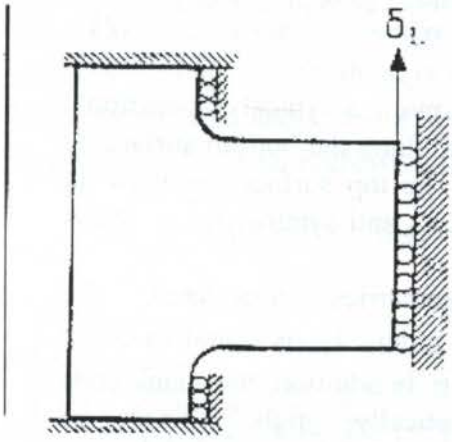

Figure 2- Loading and boundary conditions.

3. FINITE ELEMENT ANALYSIS

The finite element predictions have been obtained using the standard elastic facilities of the PAFEC suite of programs (1991).

Eight-noded plane stress isoparametric elements are used as shown in Figure 1 for a typical geometry. A plane stress (i.e. thin plate) assumption is used because in practice, the thickness is likely to be much smaller when compared to the component length or depth, Chow *et al.*(1952). Predictions for a plane strain assumption (i.e. thick plate) have shown that the resulting displacement and stress distributions were very similar. The discontinuities in stress at inter-elemental boundaries for the chosen degree of mesh refinement in the region of high stress gradient were found to be within an acceptable level and therefore the mesh was considered to be satisfactory for this investigation. Values for Young's modulus and Poisson's ratio of 209 GPa and 0.3 respectively were used throughout the analysis.

The results have been normalized with respect to the material properties so that they can be applied to all geometrically similar components made from other materials which can be represented by the same material models.

4. RESULTS

Results are presented in the form of stress indices which are achieved by dividing the nodal stress component in the meridional direction (i.e. parallel to the surface) by the nominal stress, σ_b, in the shank region. The nominal stress is obtained using strain energy theory (which takes into consideration the warping effect resulting from the shear stress) which is found to be closer in magnitude than either simple bending or modified shear deformation theories, as discussed by Hardy and Pipelzadeh (1994). The nominal stress, σ_b, is given by:

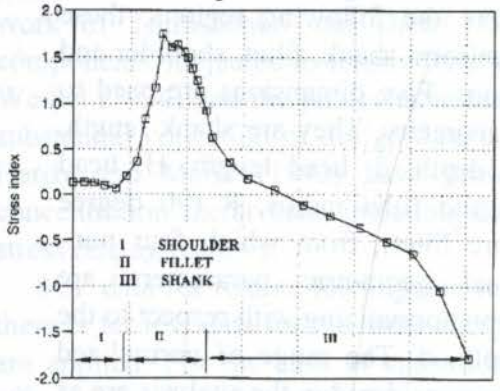

Figure 3 - The distribution of I_m along the bottom surface of the component under shear loading (L/d =1.0, H/d = 0.6, D/d =1.7 & R/d = 0.15).

$$\sigma_b = 3E\,\delta/\{\, d((L/d)^2 + 3.12\} \qquad (1)$$

where δ is the applied transverse displacement. Hence, the meridional stress index becomes,

$$I_m = \sigma_m / \sigma_b \qquad (2)$$

Figure 3 shows a typiçal meridional stress distribution along the bottom surface of the component. The top surface develops an identical, but anti-symmetric, stress distribution.

For all geometries considered, the maximum stress index, $\bar{I}_m$, is found to occur in the fillet region. In addition, the shank ends exhibit unrealistically high values of meridional stresses. These overestimates are mainly caused by the singularity effect due to the nature of the applied load as discussed by Hardy and Pipelzadeh (1991, 1994). The remainder of the shank region experiences an approximately linear variation.

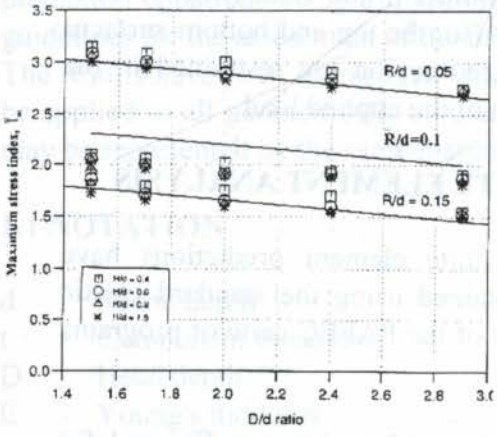

Figure 4 - The variation of $\bar{I}_m$ with H/d and for L/d=1.0, including the results from equation 4 for the range of R/d considered

Figure 4 shows the variation of $\bar{I}_m$ with D/d for the range of H/d and R/d values and L/d=1, including the results from equation 4, derived below. $\bar{I}_m$ is found to vary approximately linearly with D/d and R/d and is virtually independent of H/d. This is because the flexibility of the head of the component is restricted. Also, there is a reduction in stress index with the increase in R/d, as would be expected due to the reduction in stress concentration effect with the reduction in the severity of the geometric discontinuity.

Correlation between $\bar{I}_m$ and R/d, H/d and D/d, based on a multi-linear regression model, has been investigated and can be expressed by the following equation for L/d=1,

$$\bar{I}_m = 3.98 - 12.54\ R/d - (0.089 + 1.2R/d)H/d + \{ (0.13\ R/d - 0.24) + (0.006 + 0.134\ R/d)H/d \}D/d \quad (3)$$

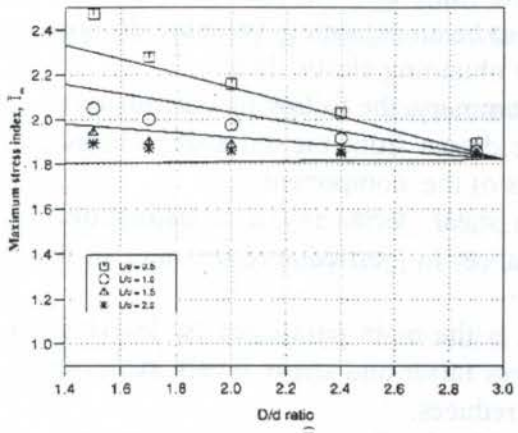

Figure 5 - The variation of $\bar{I}_m$ with D/d and for H/d=0.6 and R/d=0.1, including results from equation 5 for the range of L/d considered.

The above equation can be simplified further since $\bar{I}_m$ is virtually independent of H/d. For L/d = 1.0,

$$\bar{I}_m = 3.98 - 12.54R/d + (0.13R/d - 0.24)D/d \quad (4)$$

Similar equations can be derived for other values of L/d. Figure 5 shows thevariations of $\bar{I}_m$ with D/d for various L/d (H/d=0&6, R/d= 0.1) including the results from Equation 5, derived below. Again, the relationship is approximately linear. For the range of L/d and D/d considered, a relatively small change in $\bar{I}_m$ is observed particularly for L/d $\geq$ 1. The relationship between $\bar{I}_m$, D/d and L/d (for R/d=0.1) can be expressed by the following equation using the multi-linear regression model:

$$\bar{I}_m = (0.22\ L/d - 0.43)\ D/d + (3.11 - 0.66\ L/d) \quad (5)$$

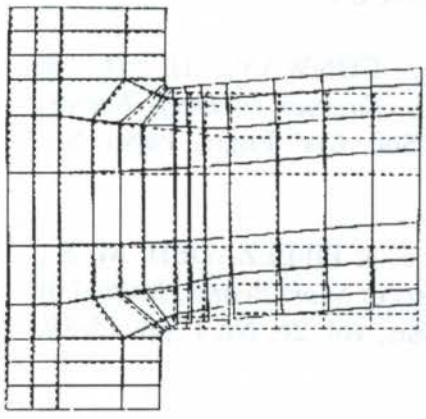

Figure 6 - Exaggerated displaced shape for shear loading

Similar equation can be obtained for other values of R/d. Figure 6 shows a typical exaggerated deformed shape of the component super-imposed on the undeformed shape.

The distortion is clearly visible along the shank region. However, there is greater localised deformation in the fillet region. This results in warping deformation in the head particularly around the fillet region. The degree of deformation in the critical sections is reflected in the corresponding stress contour plots shown in Figure 7 for local, shear and principal stresses.

The contours in the shank region are similar to those previously obtained for the corresponding sinking beam with local restraints by Hardy and Pipelzadeh (1991).

5. CONCLUSIONS

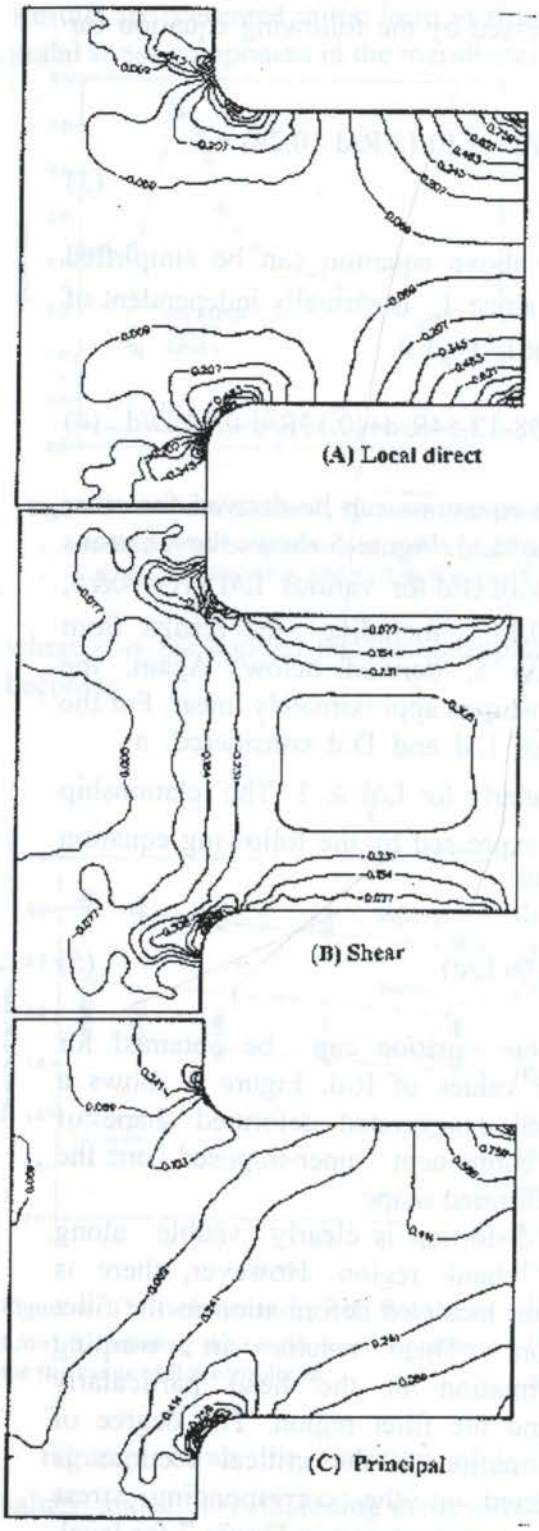

Figure 7 - Normalized stress contours for shear loading.
(L/d =1.0, H/d = 0.6, D/d = 1.7 & R/d = 0. 15)

The results in this paper have provided useful information about the elastic behaviour of these two dimensional components with projections subjected to shear loading. Such information is not readily available in the open literature. Also, the finite element method has been shown to be an extremely valuable design tool for obtaining elastic data.

In summary, the following conclusions may be drawn from the extensive elastic analysis of the component :

i) the shear term is of considerable importance in particular for small L/d ratios,

ii) R/d is the main parameter to describe the stress raiser and stress levels increase as R/d reduces.

The simple linear equations derived from the finite element results, using the multi-linear regression model, were found to be of reasonable accuracy with an estimated discrepancy of upto 10 percent and therefore provide a useful aid to designers in assessing the integrity of these components under shear loading.

6. REFERENCES

CHOW, L., CONWAY, H. D. & WINTER, G., *Stresses in Deep Beams*, Trans. Am. Soc. Civ. Engrs, Paper No. 2557, 1952.

HARDY, S. J. & PIPELZADEH, M. K., *Static Analysis of Short Beams*, Journal of Strain Analysis, vol. 26, No 1, pp. 15-29, 1991.

HARDY, S. J. & PIPELZADEH, M. K. *Stress Concentration Factors for Axial and Shear loading Applied to Short Flat Bars with Projections*, Journal of Strain Analysis, vol. 29, No 2, pp. 93-100, 1994.

HARDY, S. J. & MALIK, N. H., *A Survey of post-Peterson Stress Concentration Factor Data*, Int. Journal of Fatigue, vol. 14, pp. 147-153, 1992.

HARTMAN, J. B. & LEVEN, M. M., *Factors of Stress Concentration for Flat Bars with Centrally Enlarged Section*, Proc. Soc. Exper. Anal., vol. 9, No 1, p. 53, 1951.

KUMAGAI, K. & SHIMADA, H., *The Stress Concentration Factor Produced by a Projection under Tensile Load*, Bull. Japan Soc. Mech Eng., vol. 11, p.739, 1968.

PAFEC, Level 7, *Data Preparation Manual*, PAFEC Limited, Nottingham, 1991.

PETERSON, R. E., *Stress Concentration Design Factors*, 2nd Edn., John Wiley & Sons, N. Y., 1974.

TIMOSHENKO, S. & DIETZ, W., *Stress Concentration Produced by Holes and Fillets*, Trans. ASME, vol. 47, p. 199, 1925.

WEIBEL, E. E., *Studies in Photoelastic Stress Determination*, Trans. ASME, vol. 56, p. 637, 1934.

XIV Brazilian Congress of Mechanical Engineering
Obeid Plaza Hotel Convention Center - Bauru - SP/Brazil
December 08-12th 1997

PAPER CODE: COB109

ELASTIC CONTACT WITH FRICTION AS A CONDITIONAL MINIMIZATION PROBLEM / *CONTATO ELÁSTICO COM ATRITO COMO UM PROBLEMA DE MINIMIZAÇÃO CONDICIONAL*

ALBERTO LUIZ SERPA[1,2] & FERNANDO IGUTI[2]
1. Eaton Limited - Transmissions Division, Rua Clark, 2061 - Valinhos - SP, C.P. 304, 13279-400, Brazil - E-mail: albertolserpa@eaton.com
2. Department of Computational Mechanics, Faculty of Mechanical Engineering, Unicamp, C.P. 6122, Campinas - SP, 13083-970, Brazil - E-mail: serpa@fem.unicamp.br

Abstract

This work presents a study of contact with friction between elastic bodies under the assumptions of infinitesimal elasticity. This is a non-linear problem due to the unilateral constraints (interpenetration of bodies) and friction. The solution can be found using optimization concepts, modelling the problem as a constrained minimization problem. The Finite Element Method is used to model the equations of elasticity. The minimization problem has the total potential energy of the elastic bodies as the objective function, the non-interpenetration conditions are represented by inequality constraints, and equality constraints are used to deal with the friction. Due to stick and slip conditions, equality constraints are present or not according to the current condition. Since the Coulomb friction condition depends on the normal and tangential contact stresses related to the constraints of the problem, it is devised an approach called here as a conditional dependent constrained minimization problem. An Augmented Lagrangian Method is used. This method, when applied to a contact problem, presents Lagrange Multipliers which have the physical meaning of contact forces. This fact allows to check the friction condition at each iteration.

Keywords

Finite Element, Contact Problem, Mathematical Programming, Augmented Lagrangian / Elementos Finitos, Problema de Contato, Programação Matemática, Lagrangiano Aumentado.

1. INTRODUCTION

The main difficulties of contact problems are: analytical solutions are not available, except for particular geometries; how to deal with unknown boundary conditions (contact region and contact forces); and the friction effect. A comprehensive list of references about the contact problem can be found in Serpa (1996).

The contact problem between elastic bodies, including friction, is formulated as a *generalized minimization problem.* It is called here a *conditional constrained minimization problem.* The Coulomb law of friction is employed, and it is assumed small displacements and linear elastic materials.

This minimization problem presents inequality constraints which represent the non-interpenetration of the bodies, and equality constraints are used to represent the friction. There are two friction conditions, adhesion and sliding, depending on the contact forces. The presence of the equality constraints depends on the adesion condition. These conditions are tested even when the constraints are not satisfied. The satisfaction of the correct friction condition is achieved simultaneously with the progress through the iterations.

An Augmented Lagrangian Method is employed to solve this minimization problem. This method is used to solve the constrained minimization problem through successive unconstrained minimizations. The Lagrange multipliers have the physical meaning of the contact forces, allowing the verification of the friction conditions.

Some previous works based on the Augmented Lagrangian approach for contact problems can be found in Simo and Laursen (1992, 1993). In these works an incremental process was used.

The elasticity equations were dealt with using the Finite Element Method.

2. CONTACT AS A MINIMIZATION PROBLEM

The total potential energy of a discretized elastic system formed by the bodies A and B in quasi-static conditions can be written in the form

$$\Pi(\boldsymbol{u}) = \Pi_A(\boldsymbol{u}) + \Pi_B(\boldsymbol{u}) = \frac{1}{2} \left\{ \begin{array}{c} \boldsymbol{u_A} \\ \boldsymbol{u_B} \end{array} \right\}^t \left[\begin{array}{cc} \boldsymbol{K_A} & 0 \\ 0 & \boldsymbol{K_B} \end{array} \right] \left\{ \begin{array}{c} \boldsymbol{u_A} \\ \boldsymbol{u_B} \end{array} \right\} - \left\{ \begin{array}{c} \boldsymbol{f_A} \\ \boldsymbol{f_B} \end{array} \right\}^t \left\{ \begin{array}{c} \boldsymbol{u_A} \\ \boldsymbol{u_B} \end{array} \right\}, \quad (1)$$

where $\boldsymbol{u}$ is the displacement vector, $\boldsymbol{K}$ is the stiffness matrix and $\boldsymbol{f}$ is the equivalent load vector. In order to simplify the notation the sub-indexes A and B are omitted.

Representing the non-interpenetration condition by $h_j(\boldsymbol{u}) \leq 0$ and the adhesion condition as $c_i(\boldsymbol{u}) = 0$ one can write a generalized minimization problem in the form

$$(P_1) \left\{ \begin{array}{lll} \textit{minimize} & \Pi(\boldsymbol{u}) & \\ \textit{subjected to} & h_j(\boldsymbol{u}) \leq 0 & j = 1, ..., m \\ & \textit{if} \ \ ||\boldsymbol{t}_i|| \leq \mu_e ||\boldsymbol{n}_i|| \Rightarrow c_i(\boldsymbol{u}) = 0, & i = 1, ..., l \\ & \textit{if} \ \ ||\boldsymbol{t}_i|| > \mu_e ||\boldsymbol{n}_i|| \Rightarrow \boldsymbol{t}_i = -\mu_d ||\boldsymbol{n}_i|| \frac{\boldsymbol{u_t}}{||\boldsymbol{u_t}||} & i = 1, ..., l, \end{array} \right. \quad (2)$$

where $\boldsymbol{n}$ and $\boldsymbol{t}$ are the normal and tangential forces, $\frac{\boldsymbol{u_t}}{||\boldsymbol{u_t}||}$ is a relative tangential displacement unit vector, μ_e and μ_d are the static and dynamic friction coefficients.

The constraint $c_i(\boldsymbol{u}) = 0$ is a function of the friction condition in terms of the normal and the tangential forces $\boldsymbol{n}_i$ and $\boldsymbol{t}_i$. In the case of adhesion, $c_i(\boldsymbol{u}) = 0$ must be present, which ensures no relative displacement in the considered point. The sliding condition occurs when the adhesion capacity is overcome. In this case, the constraint $c_i(\boldsymbol{u}) = 0$ does not appear, and the corresponding tangential sliding friction force is applied.

3. AUGMENTED LAGRANGIAN AND CONTACT

Consider the minimization problem (P_2):

$$(P_2) \left\{ \begin{array}{lll} \textit{minimize} & \Pi(\boldsymbol{u}) & \\ \textit{subjected to} & c_i(\boldsymbol{u}) = 0 & i = 1, ..., l \\ & h_j(\boldsymbol{u}) \leq 0 & j = 1, ..., m. \end{array} \right. \quad (3)$$

The Augmented Lagrangian function (see Luenberger, 1984) can be defined as

$$\Phi(\boldsymbol{u},\boldsymbol{\nu},\boldsymbol{\lambda},r)=\Pi(\boldsymbol{u})+\sum_{i=1}^{l}\nu_i c_i(\boldsymbol{u})+\sum_{i=1}^{l}\frac{r_i}{2}(c_i(\boldsymbol{u}))^2+\sum_{j=1}^{m}\frac{r_j}{2}[h_j(\boldsymbol{u})+\frac{\lambda_j}{r_j}]_+^2-\sum_{j=1}^{m}\frac{\lambda_j^2}{2r_j}, \quad (4)$$

where $[a]_+ = max[0,a]$; ν_i, λ_j are the Lagrange Multipliers (vectors $\boldsymbol{\nu}$ and $\boldsymbol{\lambda}$); r_i and r_j are the penalty parameters.

The null gradient of the Augmented Lagrangian function related to $\boldsymbol{u}$ is

$$\boldsymbol{\nabla}\Pi(\boldsymbol{u})+\sum_{i=1}^{l}(\nu_i+r_i c_i(\boldsymbol{u}))\boldsymbol{\nabla}c_i(\boldsymbol{u})+\sum_{j=1}^{m}r_j[h_j(\boldsymbol{u})+\frac{\lambda_j}{r_j}]_+\boldsymbol{\nabla}h_j(\boldsymbol{u})=\boldsymbol{0}. \quad (5)$$

To satisfy the Kuhn-Tucker condition (Luenberger, 1984) the multipliers can be:

$$\bar{\nu_i}=\nu_i+r_i c_i(\boldsymbol{u}) \;\; and \;\; \bar{\lambda_j}=r_j[h_j(\boldsymbol{u})+\frac{\lambda_j}{r_j}]_+. \quad (6)$$

Eq. (6) suggests the following Lagrange multipliers update scheme:

$$\nu_i^{k+1}=\nu_i^k+r_i c_i(\boldsymbol{u}^k) \;\; and \;\; \lambda_j^{k+1}=[\lambda_j^k+r_j h_j(\boldsymbol{u}^k)]_+. \quad (7)$$

With these concepts in mind, it is possible to formulate an Augmented Lagrangian algorithm based on the unconstrained minimization of $\Phi(\boldsymbol{u},\boldsymbol{\nu}^k,\boldsymbol{\lambda}^k,r^k)$, and on updating the multipliers according to eq. (7). This scheme is repeated until convergence.

In the specific case of the contact problem one has that

$$\boldsymbol{\nabla}\Pi(\boldsymbol{u})=\boldsymbol{K}\boldsymbol{u}-\boldsymbol{f}. \quad (8)$$

Vectors $\boldsymbol{h}(\boldsymbol{u})=[h_1(\boldsymbol{u})\; h_2(\boldsymbol{u})\; ...\; h_m(\boldsymbol{u})]^t$ and $\boldsymbol{c}(\boldsymbol{u})=[c_1(\boldsymbol{u})\; c_2(\boldsymbol{u})\; .:.\; c_l(\boldsymbol{u})]^t$ are usual.

A particular situation occurs when the constraints are linear, i.e.,

$$\boldsymbol{h}(\boldsymbol{u})\leq\boldsymbol{0}\Rightarrow\boldsymbol{A}\boldsymbol{u}+\boldsymbol{\alpha}\leq\boldsymbol{0}, \;\; and \;\; \boldsymbol{c}(\boldsymbol{u})=\boldsymbol{0}\Rightarrow\boldsymbol{B}\boldsymbol{u}+\boldsymbol{\beta}=\boldsymbol{0}, \quad (9)$$

where $\boldsymbol{A}$ is a matrix $m\times ndof$, $\boldsymbol{\alpha}$ is a vector $m\times 1$, $\boldsymbol{B}$ is a matrix $l\times ndof$, $\boldsymbol{\beta}$ is a vector $l\times 1$, and $ndof$ is the number of degrees of freedom (number of optimization variables).

The Augmented Lagrangian function, when eq. (9) and $\boldsymbol{R_i}$ and $\boldsymbol{R_j}$ (diagonal matrices of r_i and r_j) are used, becomes

$$\begin{aligned}\Phi(\boldsymbol{u},\boldsymbol{\lambda},\boldsymbol{\nu},r) \;=\; & \frac{1}{2}\boldsymbol{u}^t\boldsymbol{K}\boldsymbol{u}-\boldsymbol{f}^t\boldsymbol{u}+\frac{1}{2}[\boldsymbol{u}^t\boldsymbol{A}^t\boldsymbol{R_j}\boldsymbol{A}\boldsymbol{u}+2\boldsymbol{\alpha}^t\boldsymbol{R_j}\boldsymbol{A}\boldsymbol{u}+\\ & +\boldsymbol{\lambda}^t(\boldsymbol{A}\boldsymbol{u}+\boldsymbol{\alpha})+\boldsymbol{\lambda}^t\boldsymbol{R_j}^{-1}\boldsymbol{\lambda}]_+ +\frac{1}{2}\boldsymbol{\lambda}^t\boldsymbol{R_j}^{-1}\boldsymbol{\lambda}+\\ & +\frac{1}{2}(\boldsymbol{u}^t\boldsymbol{B}^t\boldsymbol{R_i}\boldsymbol{B}\boldsymbol{u}+2\boldsymbol{\beta}^t\boldsymbol{R_i}\boldsymbol{B}\boldsymbol{u}+\boldsymbol{\beta}^t\boldsymbol{R_i}\boldsymbol{\beta})+\boldsymbol{\nu}^t(\boldsymbol{B}\boldsymbol{u}+\boldsymbol{\beta}). \quad (10)\end{aligned}$$

Consequently the gradient and the Hessian of eq. (10) are

$$\boldsymbol{\nabla}\Phi=\boldsymbol{K}\boldsymbol{u}-\boldsymbol{f}+[\boldsymbol{A}^t\boldsymbol{R_j}\boldsymbol{A}\boldsymbol{u}+\boldsymbol{A}^t\boldsymbol{R_j}\boldsymbol{\alpha}+\boldsymbol{A}^t\boldsymbol{\lambda}]_*+\boldsymbol{B}^t\boldsymbol{R_i}\boldsymbol{B}\boldsymbol{u}+\boldsymbol{B}^t\boldsymbol{R_i}\boldsymbol{\beta}+\boldsymbol{B}^t\boldsymbol{\nu}, \quad (11)$$

$$\boldsymbol{H}=\boldsymbol{K}+[\boldsymbol{A}^t\boldsymbol{R_j}\boldsymbol{A}]_*+\boldsymbol{B}^t\boldsymbol{R_i}\boldsymbol{B}, \quad (12)$$

where $[\;]_*$ denotes the presence of the term inside the brackets according to the value of the term $[\;]_+$ in the Augmented Lagrangian function (10).

It is convenient to denote the contact terms as

$$\boldsymbol{f_c}(\boldsymbol{u})=[\boldsymbol{A}^t\boldsymbol{R_j}\boldsymbol{A}\boldsymbol{u}+\boldsymbol{A}^t\boldsymbol{R_j}\boldsymbol{\alpha}+\boldsymbol{A}^t\boldsymbol{\lambda}]_*+\boldsymbol{B}^t\boldsymbol{R_i}\boldsymbol{B}\boldsymbol{u}+\boldsymbol{B}^t\boldsymbol{R_i}\boldsymbol{\beta}+\boldsymbol{B}^t\boldsymbol{\nu}. \quad (13)$$

4. CONSTRAINT FORMULATION

In the case of a 2D discretization problem using linear 4-node isoparametric finite elements, the side of the element is a line segment and the displacement field is a linear one.

Figure 1 shows the definition of the local coordinate system $(\bar{x}_1, \bar{x}_2)$ and the global coordinate system (x_1, x_2). The nodes i, j and k are used to establish the constraints; $\bar{x}_1$ is oriented in the jk direction, and $\bar{x}_2$ is oriented in the jk segment normal direction.

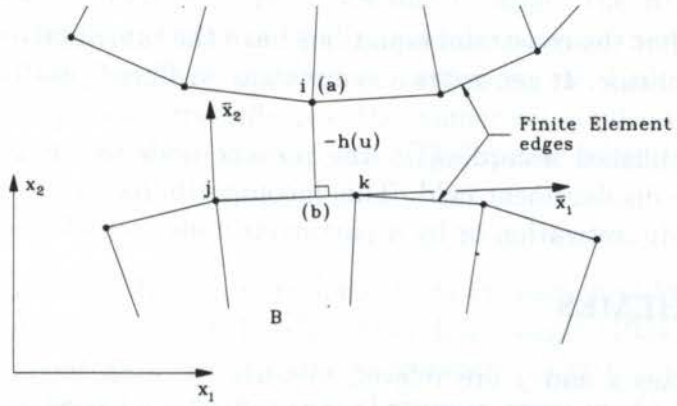

Figure 1: $h(\boldsymbol{u})$ constraint representation and notation for a discretized problem.

Considering nodes i, j and k and their related degrees of freedom $\bar{u}_1^i$, $\bar{u}_2^i$, $\bar{u}_1^j$, $\bar{u}_2^j$, $\bar{u}_1^k$, $\bar{u}_2^k$ (local coordinate system), and according to figure 1 it is possible to write

$$a = \frac{\bar{x}_1^i - \bar{x}_1^j}{\bar{x}_1^k - \bar{x}_1^j} \quad and \quad h_j(\bar{\boldsymbol{u}}) = -\bar{u}_2^i + (1-a)\bar{u}_2^j + a\bar{u}_2^k - \bar{x}_2^i. \tag{14}$$

The terms that appear in (11), for a typical inequality constraint, are:

$$\bar{\boldsymbol{A}}^t \boldsymbol{R}_j \bar{\boldsymbol{A}} = r_j \begin{bmatrix} 0 & 0 & 0 & 0 & 0 & 0 \\ 0 & 1 & 0 & a-1 & 0 & -a \\ 0 & 0 & 0 & 0 & 0 & 0 \\ 0 & a-1 & 0 & (1-a)^2 & 0 & a(1-a) \\ 0 & 0 & 0 & 0 & 0 & 0 \\ 0 & -a & 0 & a(1-a) & 0 & a^2 \end{bmatrix}, \tag{15}$$

$$\bar{\boldsymbol{A}}^t \boldsymbol{R}_j \bar{\boldsymbol{\alpha}} = r_j(-\bar{x}_2^i) \begin{Bmatrix} 0 \\ -1 \\ 0 \\ 1-a \\ 0 \\ a \end{Bmatrix} \quad and \quad \bar{\boldsymbol{A}}^t \boldsymbol{\lambda} = \lambda_j \begin{Bmatrix} 0 \\ -1 \\ 0 \\ 1-a \\ 0 \\ a \end{Bmatrix}. \tag{16}$$

Similarly it is possible to define an equality constraint

$$c_i(\bar{\boldsymbol{u}}) = -\bar{u}_1^i + (1-a)\bar{u}_1^j + a\bar{u}_1^k. \tag{17}$$

The other terms in eq. (11), related to an equality constraint, i.e., $\bar{\boldsymbol{B}}^t \boldsymbol{R}_i \bar{\boldsymbol{B}}$, $\bar{\boldsymbol{B}}^t \boldsymbol{R}_i \bar{\boldsymbol{\beta}}$ and $\bar{\boldsymbol{B}}^t \boldsymbol{\nu}$, can be similarly obtained. The sign of these constraints can be used to determine the relative tangential displacement direction in the contact region.

The terms previously mentioned were formulated in the local coordinate system and they can be rewritten in the global coordinate system by means of a usual transformation of coordinates defined by the rotation matrix $\boldsymbol{T}$, i.e., $\bar{\boldsymbol{u}}=\boldsymbol{T}\,\boldsymbol{u}$.

Thus, these terms in the global coordinate system are:

$$\boldsymbol{A}^t\boldsymbol{R}_j\boldsymbol{A}=\boldsymbol{T}^t(\bar{\boldsymbol{A}}^t\boldsymbol{R}_j\bar{\boldsymbol{A}})\boldsymbol{T};\;\; \boldsymbol{A}^t\boldsymbol{R}_j\boldsymbol{\alpha}=\boldsymbol{T}^t(\bar{\boldsymbol{A}}^t\boldsymbol{R}_j\bar{\boldsymbol{\alpha}})\boldsymbol{T};\;\; \textit{and}\;\; \boldsymbol{A}^t\boldsymbol{\lambda}=\boldsymbol{T}^t(\bar{\boldsymbol{A}}^t\boldsymbol{\lambda}); \tag{18}$$

$$\boldsymbol{B}^t\boldsymbol{R}_i\boldsymbol{B}=\boldsymbol{T}^t(\bar{\boldsymbol{B}}^t\boldsymbol{R}_i\bar{\boldsymbol{B}})\boldsymbol{T};\;\; \textit{and}\;\; \boldsymbol{B}^t\boldsymbol{\nu}=\boldsymbol{T}^t(\bar{\boldsymbol{B}}^t\boldsymbol{\nu}). \tag{19}$$

It is possible to see that the constraint equations have the same matrix structure of a standard finite element scheme. It generates a symmetric "stiffness" matrix and a "load" vector.

The constraints established according to the present node-to-segment scheme can generate an incompatible displacement field. This incompatibility can be reduced by the means of a more refined discretization or by a particular node-to-node mesh scheme.

5. NUMERICAL SCHEMES

The constraint indexes i and j are related because for each inequality constraint equation there is a corresponding equality. Thus, the following algorithm is proposed:

1. Initial definitions: friction coefficients μ_e and μ_d; starting point $\boldsymbol{u}^0=\boldsymbol{0}$ (in general); Lagrange multipliers $(\boldsymbol{\lambda}^0,\,\boldsymbol{\nu}^0)$; and penalty parameters $(r_i^0,\,r_j^0)$.
2. $k=0$ (iteration counter).
3. While the convergence criteria is not satisfied, repeat item 3.1 to 3.6:

   3.1) Contact forces definition (through the Lagrange multipliers):

   $$\boldsymbol{n}=\boldsymbol{\lambda}^k \text{ (normal forces) and } \boldsymbol{t}=\boldsymbol{\nu}^k \text{ (tangential forces).}$$

   3.2) Verify the friction conditions for each inequality and equality couple:

   - if $\lambda_i^k+r_i^k h_i(\boldsymbol{u})\le 0 \Rightarrow [\lambda_i^k+r_i^k h_i(\boldsymbol{u})]_+=0$ (no contact term) $\Rightarrow \boldsymbol{f}_{c,i}=\boldsymbol{0}$.
   - if $\lambda_i^k+r_i^k h_i(\boldsymbol{u})>0 \Rightarrow [\lambda_i^k+r_i^k h_i(\boldsymbol{u})]_+=\lambda_i^k+r_i^k h_i(\boldsymbol{u})$, and $||\boldsymbol{t}_i||\le\mu_e||\boldsymbol{n}_i||$, (terms related to $h_i(\boldsymbol{u})$ and $c_i(\boldsymbol{u})$ - adhesion), then:

   $$\boldsymbol{f}_{c,i}=(\lambda_i^k+r_i^k h_i(\boldsymbol{u}))\boldsymbol{\nabla}h_i(\boldsymbol{u})+(\nu_i^k+r_i^k c_i(\boldsymbol{u}))\boldsymbol{\nabla}c_i(\boldsymbol{u}).$$

   - if $\lambda_i^k+r_i^k h_i(\boldsymbol{u})>0 \Rightarrow [\lambda_i^k+r_i^k h_i(\boldsymbol{u})]_+=\lambda_i^k+r_i^k h_i(\boldsymbol{u})$, and $||\boldsymbol{t}_i||>\mu_e||\boldsymbol{n}_i||$, (terms related to $h_i(\boldsymbol{u})$ and sliding), then:

   $$\boldsymbol{t}_i=-\mu_d||\boldsymbol{n}_i||\frac{\boldsymbol{u_t}}{||\boldsymbol{u_t}||}\;\; \textit{and}\;\; \boldsymbol{f}_{c,i}=(\lambda_i^k+r_i^k h_i(\boldsymbol{u}))\boldsymbol{\nabla}h_i(\boldsymbol{u})+\boldsymbol{t}_i.$$

   3.3) Determine $\boldsymbol{f_c}(\boldsymbol{u})=\sum_{i=1}^m \boldsymbol{f}_{c,i}$ (assembly).

   3.4) Solve eq. (11), i.e., $\boldsymbol{K}\boldsymbol{u}-\boldsymbol{f}+\boldsymbol{f_c}(\boldsymbol{u})=\boldsymbol{0}$, obtaining $\boldsymbol{u}^{k+1}$.

   3.5) Update Lagrange multipliers and penalty parameters.

   3.6) $k=k+1$.
4. $\boldsymbol{u}^*=\boldsymbol{u}^{k+1}$ is the obtained solution. End.

In the case of linear constraints the non-linearity of this problem is due to $[\ ]_+$ term and due to changes in the equality constraint set due to the friction condition test. If the active constraint set does not change during the iterative procedure a particular situation of a linear system of equations appears. If the active constraint set changes it is used a line search procedure to enlarge the convergence region.

Static condensation, Guyan (1965), is very suitable in this case because terms $[\boldsymbol{A}^t \boldsymbol{R}_j \boldsymbol{A}]_*$ and $\boldsymbol{B}^t \boldsymbol{R}_i \boldsymbol{B}$ affect only the degrees of freedom related to the contact region. So, the equation system to be solved at each iteration has the same order of the partition matrix of the contact degrees of freedom. It is possible to apply the routines of the Gauss elimination shown in Hughes (1984) using the "skyline" storage, Serpa (1996).

The Lagrange Multipliers are updated according to the Kuhn-Tucker conditions, eq. (7). The penalty parameters influence the numerical conditioning of the Hessian matrix, and affect the multipliers variation rate. The update scheme used in this work is

$$r^{k+1} = r^k t + r_0, \quad t \geq 1, \tag{20}$$

where t e r_0 are determined by computational tests for each problem. A bad choice of parameters can cause divergence of the algorithm, Luenberger (1984) and Serpa (1996).

Some schemes to control the penalty parameters variation were employed, i.e., Lagrange multipliers variation control using the limits given by $\delta\lambda$ and $\delta\nu$, and matrix condition number control. In this work, the system of equations condition number was estimated using the estimator of Gill, Murray and Wright (1981).

6. EXAMPLE AND NUMERICAL RESULTS

The convergence criteria used in this work are based in a feasible point and in a maximum point variation, i.e.,

$$h_i(\boldsymbol{u}^{k+1}) < \epsilon; \quad -\epsilon < c_i(\boldsymbol{u}^{k+1}) < \epsilon; \quad and \quad max|\boldsymbol{u}^{k+1} - \boldsymbol{u}^k| < \epsilon. \tag{21}$$

The unbalanced nodal forces $\boldsymbol{f_d}$, see Irons and Ahmad (1981), are also employed to check the convergence through the comparison with the external applied forces.

The example consists of a dovetail of two elastic bodies, figure 2. The Young modulus is $240.0 N/mm^2$, the Poisson's ratio is 0.38, the thickness is 6.4mm, and $q_v = 0.0265625 N/mm^2$ (a total of 17.0 N). It is assumed a plane stress situation, and $\mu_e = \mu_d = 0.2$.

The displacements and forces in the contact region are shown in table 1, where $u_{n,A}$ is the normal displacement of the body A, $u_{t,A}$ is the tangential displacement of the body A. Similarly it is defined $u_{n,B}$ and $u_{t,B}$. The obtained results are very similar to the ones presented by Fancello (1989) and Raous, Chabrand and Lebon (1988).

In can be noted in table 1 a separation region corresponding to nodes 1 and 2, and a sliding region corresponding to nodes 3 to 17. The contact nodes are numbered from the left to the right in the contact region.

Table 2 shows the effect of the penalty parameters in the convergence properties.

7. COMMENTS AND CONCLUSIONS

The contact with friction was modeled as a minimization problem. The total potential energy of the bodies is the objective function, the interpenetration of the bodies are considered as inequality constraints, and the friction is considered through adhesion and

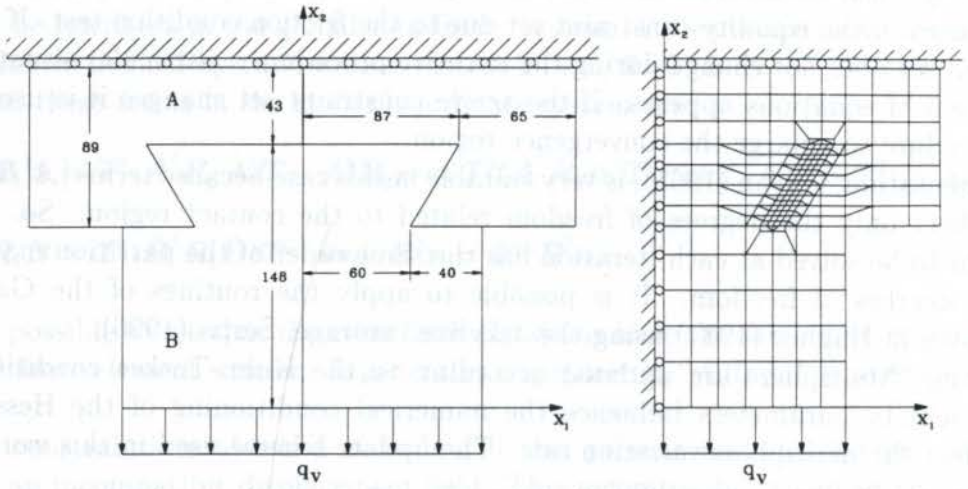

Figure 2: Dovetail (in mm), Finite Element Mesh ($ndof$ =507, 17 couple of constraints).

Table 1: Displacements and contact forces ($r_0 = 1.0$, $t = 1.0$, $\delta\lambda = \delta\nu = 0.1$, $\epsilon = 1e-8$).

Node	$u_{n,A}$	$u_{t,A}$	$u_{n,B}$	$u_{t,B}$	$\|\|\boldsymbol{n}\|\|$	$\|\|\boldsymbol{t}\|\|$
1	-.16215	-.26787	-.16369	-.03028	0.00000	0.00000
2	-.15641	-.26161	-.15730	-.03028	0.00000	0.00000
3	-.15098	-.25698	-.15098	-.03023	0.11831	0.02366
4	-.14506	-.25327	-.14506	-.03011	0.75628	0.15126
5	-.13917	-.24979	-.13917	-.02991	1.37918	0.27584
6	-.13296	-.24640	-.13296	-.02959	1.54526	0.30905
7	-.12678	-.24361	-.12678	-.02913	1.84810	0.36962
8	-.12048	-.24061	-.12048	-.02859	2.12218	0.42444
9	-.11397	-.23724	-.11397	-.02793	2.45878	0.49176
10	-.10677	-.23515	-.10677	-.02713	2.11765	0.42353
11	-.09958	-.23261	-.09958	-.02610	2.29183	0.45836
12	-.09200	-.23000	-.09200	-.02492	2.30529	0.46106
13	-.08385	-.22754	-.08385	-.02349	2.20177	0.44035
14	-.07495	-.22516	-.07495	-.02169	2.01331	0.40266
15	-.06500	-.22293	-.06500	-.01919	1.72176	0.34435
16	-.05355	-.22076	-.05355	-.01511	0.99099	0.19820
17	-.03817	-.21971	-.03817	-.00867	1.20017	0.24003

sliding using suitable equality constraints. The global problem can not be viewed as a convex one due to the constraint equation set nature.

Using an Augmented Lagrangian Method the constrained minimization problem is solved through successive unconstrained minimizations of the Augmented Lagrangian function. This method when applied to the contact problem allows the employment of the Lagrange multipliers as the contact forces. This physical interpetration allows to test the friction condition, defining the presence or not of a specific set of equality constraints in the iteration.

The constraint equations have a similar matrix structure to the one in the Finite Element Method. It gives way to a symmetric stiffness matrix and a load vector.

Table 2: Penalty parameters effect ($\epsilon = 1e-8$, $\delta\lambda = \delta\nu = 1.0$).

r_0	t	condition number	iterations	time (s)	$max\|\boldsymbol{f_d}\|$
0.1	1.0	243.64	707	1541	1.74×10^{-2}
1.0	1.0	128.41	258	585	1.60×10^{-2}
10.0	1.0	94.38	109	268	2.44×10^{-2}
100.0	1.0	83.87	31	99	9.18×10^{-2}
1000.0	1.0	177.35	15	55	1.29×10^{-1}
10000.0	1.0	1249.42	16	54	1.49×10^{-1}
100000.0	1.0	10998.13	14	50	1.41×10^{-1}

It can be noted that the penalty parameters influence directly the numerical conditioning of the system of equations. Some schemes to control the penalty parameters increasing rate were used, looking for a better convergence behavior of the algorithm.

In order to improve the proposed algorithm the development of some optimized criteria to update penalty parameters without user's interference, and the use of some adaptive mesh scheme to reduce the incompatibility of the displacement fields in the contact region (h or p refinement) are some aspects that should be considered.

8. REFERENCES

FANCELLO E. A., *"Variational Formulation for the Contact Problem with Friction; Resolution by Regularization"*, Master Thesis, COPPE - UFRJ - Rio de Janeiro Federal University, Rio de Janeiro - RJ, Brazil, 1989, (in Portuguese).

GILL P.E., MURRAY W. & WRIGHT M.H., *"Practical Optimization"*, Academic Press, 1981

GUYAN R.J., "Reduction of Stiffness and Mass Matrices", *AIAA Journal*, Vol. 3, No. 2, 380, 1965.

HUGHES T. J. R., *"The Finite Element Method - Linear Static and Dynamic Finite Element Analysis"*, Prentice-Hall, Inc., 1987.

IRONS B. & AHMAD S., *"Techniques of Finite Elements"*, E. Horwood & J. Willey, 1980.

LAURSEN T. A. & SIMO J. C., "Algorithmic Symmetrization of Coulomb Frictional Problems Using Augmented Lagrangians", *Comp. Meth. Appl. Mech. Engng.*, Vol. 108, 133-146, 1993.

LUENBERGER D. G., *"Linear and Non Linear Programming"*, Addison-Wesley Publishing Company, Inc., 1984.

RAOUS M., CHABRAND P. & LEBON F., "Numerical Methods for Frictional Contact Problems and Applications", *J. Méc. Théor. Appl.*, Special Issue, Supplement No. 1, Vol. 7, 111-128, 1988.

SERPA A. L., *"Contact Problem with friction using the Augmented Lagrangian Method"*, Doctorate Thesis, Faculty of Mechanical Engineering, Unicamp - Campinas State University, Campinas - SP, Brazil, 1996, (in Portuguese).

SIMO J. C. & LAURSEN T. A., "An Augmented Lagrangian Treatment of Contact Problems Involving Friction", *Comput. Struct.*, Vol. 42, No. 1, 97-116, 1992.

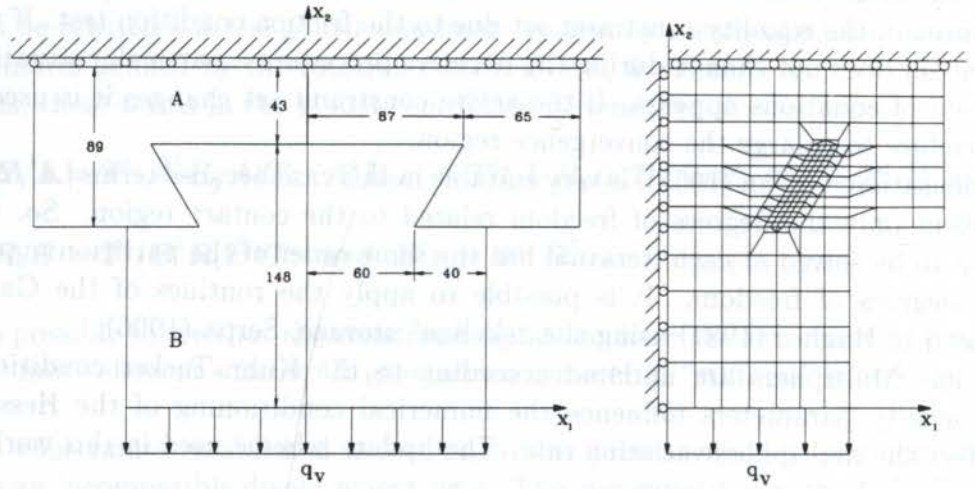

Figure 2: Dovetail (in mm), Finite Element Mesh ($ndof$ =507, 17 couple of constraints).

Table 1: Displacements and contact forces ($r_0 = 1.0$, $t = 1.0$, $\delta\lambda = \delta\nu = 0.1$, $\epsilon = 1e-8$).

Node	$u_{n,A}$	$u_{t,A}$	$u_{n,B}$	$u_{t,B}$	$\|\|\boldsymbol{n}\|\|$	$\|\|\boldsymbol{t}\|\|$
1	-.16215	-.26787	-.16369	-.03028	0.00000	0.00000
2	-.15641	-.26161	-.15730	-.03028	0.00000	0.00000
3	-.15098	-.25698	-.15098	-.03023	0.11831	0.02366
4	-.14506	-.25327	-.14506	-.03011	0.75628	0.15126
5	-.13917	-.24979	-.13917	-.02991	1.37918	0.27584
6	-.13296	-.24640	-.13296	-.02959	1.54526	0.30905
7	-.12678	-.24361	-.12678	-.02913	1.84810	0.36962
8	-.12048	-.24061	-.12048	-.02859	2.12218	0.42444
9	-.11397	-.23724	-.11397	-.02793	2.45878	0.49176
10	-.10677	-.23515	-.10677	-.02713	2.11765	0.42353
11	-.09958	-.23261	-.09958	-.02610	2.29183	0.45836
12	-.09200	-.23000	-.09200	-.02492	2.30529	0.46106
13	-.08385	-.22754	-.08385	-.02349	2.20177	0.44035
14	-.07495	-.22516	-.07495	-.02169	2.01331	0.40266
15	-.06500	-.22293	-.06500	-.01919	1.72176	0.34435
16	-.05355	-.22076	-.05355	-.01511	0.99099	0.19820
17	-.03817	-.21971	-.03817	-.00867	1.20017	0.24003

sliding using suitable equality constraints. The global problem can not be viewed as a convex one due to the constraint equation set nature.

Using an Augmented Lagrangian Method the constrained minimization problem is solved through successive unconstrained minimizations of the Augmented Lagrangian function. This method when applied to the contact problem allows the employment of the Lagrange multipliers as the contact forces. This physical interpetration allows to test the friction condition, defining the presence or not of a specific set of equality constraints in the iteration.

The constraint equations have a similar matrix structure to the one in the Finite Element Method. It gives way to a symmetric stiffness matrix and a load vector.

Table 2: Penalty parameters effect ($\epsilon = 1e-8$, $\delta\lambda = \delta\nu = 1.0$).

r_0	t	condition number	iterations	time (s)	$max\|\boldsymbol{f_d}\|$
0.1	1.0	243.64	707	1541	1.74×10^{-2}
1.0	1.0	128.41	258	585	1.60×10^{-2}
10.0	1.0	94.38	109	268	2.44×10^{-2}
100.0	1.0	83.87	31	99	9.18×10^{-2}
1000.0	1.0	177.35	15	55	1.29×10^{-1}
10000.0	1.0	1249.42	16	54	1.49×10^{-1}
100000.0	1.0	10998.13	14	50	1.41×10^{-1}

It can be noted that the penalty parameters influence directly the numerical conditioning of the system of equations. Some schemes to control the penalty parameters increasing rate were used, looking for a better convergence behavior of the algorithm.

In order to improve the proposed algorithm the development of some optimized criteria to update penalty parameters without user's interference, and the use of some adaptive mesh scheme to reduce the incompatibility of the displacement fields in the contact region (h or p refinement) are some aspects that should be considered.

8. REFERENCES

FANCELLO E. A., *"Variational Formulation for the Contact Problem with Friction; Resolution by Regularization"*, Master Thesis, COPPE - UFRJ - Rio de Janeiro Federal University, Rio de Janeiro - RJ, Brazil, 1989, (in Portuguese).

GILL P.E., MURRAY W. & WRIGHT M.H., *"Practical Optimization"*, Academic Press, 1981

GUYAN R.J., "Reduction of Stiffness and Mass Matrices", *AIAA Journal*, Vol. 3, No. 2, 380, 1965.

HUGHES T. J. R., *"The Finite Element Method - Linear Static and Dynamic Finite Element Analysis"*, Prentice-Hall, Inc., 1987.

IRONS B. & AHMAD S., *"Techniques of Finite Elements"*, E. Horwood & J. Willey, 1980.

LAURSEN T. A. & SIMO J. C., "Algorithmic Symmetrization of Coulomb Frictional Problems Using Augmented Lagrangians", *Comp. Meth. Appl. Mech. Engng.*, Vol. 108, 133-146, 1993.

LUENBERGER D. G., *"Linear and Non Linear Programming"*, Addison-Wesley Publishing Company, Inc., 1984.

RAOUS M., CHABRAND P. & LEBON F., "Numerical Methods for Frictional Contact Problems and Applications", *J. Méc. Théor. Appl.*, Special Issue, Supplement No. 1, Vol. 7, 111-128, 1988.

SERPA A. L., *"Contact Problem with friction using the Augmented Lagrangian Method"*, Doctorate Thesis, Faculty of Mechanical Engineering, Unicamp - Campinas State University, Campinas - SP, Brazil, 1996, (in Portuguese).

SIMO J. C. & LAURSEN T. A., "An Augmented Lagrangian Treatment of Contact Problems Involving Friction", *Comput. Struct.*, Vol. 42, No. 1, 97-116, 1992.

XIV Brazilian Congress of Mechanical Engineering
Obeid Plaza Hotel Convention Center - Bauru - SP/Brazil
December 08-12th 1997

PAPER CODE: COB1160

A DIRECTIONAL ERROR ESTIMATOR FOR ADAPTIVE LIMIT ANALYSIS

LAVINIA BORGES[1], RAÚL FEIJÓO[2] & NESTOR ZOUAIN[1]

[1] *Programa e Departamento de Engenharia Mecânica, COPPE/EE- UFRJ - Cx. Postal 68503 - Ilha do Fundão, Rio de janeiro,RJ - Brasil - CEP:21945-970. E-mail: lavinia@serv.com.ufrj.br*

[2] *Laboratório Nacional de Computação Científica Rua Lauro Müller, 455 - Botafogo, Rio de janeiro, RJ - Brasil CEP:22290-160. E-mail:feij@alpha.lncc.br*

Abstract

We present some results on finite element adaptive mesh-refinement strategies for limit analysis, using *a posteriori* error estimator based on local directional interpolation error and recovering of the second derivatives of the finite element solution. The abstract framework of the adopted error estimation techniques is discussed. Some possibilities of derivatives recovery are considered, including the proposal of a directional error estimator. We apply the above abstract formulation to finite element models of limit analysis.

Keywords

Finite elements, limit analysis, error estimator, adaptive mesh, elementos finitos análise limite, estimativa de erro, malhas adaptadas.

1. INTRODUCTION

This paper presents results on finite element adaptive strategies for limit analysis, using *a posteriori* error estimator based on local directional interpolation error and recovering of the second derivatives of the finite element solution.

The limit analysis deal with the direct computation of the load producing plastic collapse of a body - a phenomenon where, under constant stresses, kinematically admissible plastic strain rates take place. In most collapse situations there is the development of localized plastic deformations or slip bands (Borges *et al.*,1996 and papers therein). The accuracy in the numerical solution of limit analysis is seriously affected by local singularities arising from these localized plastic deformations.

One possibility to overcome this problem is to add more grid-points where the solution presents those singularities. So, it is necessary not only to identify these regions, but also to obtain a good equilibrium between the refined and un-refined regions, such that the overall accuracy is optimal (Verfüth, 1995). In limit analysis, an *a priori* error estimates, as provided by the standard error analysis of finite element, is often insufficient to assure reliable estimates of the computed numerical solution accuracy. This is due to the fact that they only yield information on the asymptotic error behaviour and require regularity

conditions of the solution, which are not satisfied in the presence of the singularities as described above. Those facts show us the need for an estimator which can *a posterori* be exctracted from the computed numerical solution and the given data of the problem.

The advantages of adapting meshes are well known, but we place particular emphasis on the anisotropic mesh adaptation process, generated by a directional error estimator based on the recovering of the second derivatives of the finite element solution. The goal of this approach is to achieve a mesh-adaptive strategy that allows to refine the mesh, stretch and orient the elements in such a way that, along the adaptation process, the mesh turns aligned with the discontinuities. This mesh adaptation process gives improved results in localizing regions of rapid or abrupt variations of the variables, whose location is not known *a priori* (Peiró, 1989,Dompierre *et al.* ,1995, Buscaglia *et al.* , 1996 and Feijoó *et al.* , 1997).

Firstly, it is discussed the abstract framework of the adopted error estimation techniques, considering the derivatives recovery and the proposal of a directional error estimator. In the light of the abstract theory, by applications in some classical examples, it is presented an adaptive mesh-refinement process for limit analysis.

2. ERROR ESTIMATION AND ADAPTIVE MESH-REFINEMENT

Following, it is described the abstract framework of the adopted error estimation techniques and the sketch of the adaptive mesh-refinement strategy.

2.1 The interpolation error as an error indicator of the approximate solution

Let u be the exact solution of the variational problem associated to the problem at hand. Then, at the point x_0, the Taylor expansion gives

$$u(x) = u(x_0) + \nabla u(x_0) \cdot (x - x_0) + \tfrac{1}{2}\mathbf{H}(u(x_0))(x - x_0)(x - x_0) + \cdots \tag{1}$$

If the piecewise finite element solution u_h , defined by $u(x_0) + \nabla u(x_0) \cdot (x - x_0)$, is a good approximation of the constant and the linear part of the expansion, the interpolation error is dominated by the quadratic term

$$\|u - u_h\| \simeq \tfrac{1}{2}\|\mathbf{H}(u(x_0))(x - x_0) \cdot (x - x_0)\| \tag{2}$$

Hence, the interpolation error at x_0 is governed by the Hessian matrix $\mathbf{H}(u(x_0))$, i.e., by the second partial derivatives of the solution at that point. The interpolation error is not isotropic but depend on the direction defined by $x - x_0$ and the local values of the Hessian matrix at x_0 point. The above result suggests the use of expression (2) as a *directional* error estimator in the terminology used by Peiró(1989). Since the Hessian matrix is not positive definite it can not be taken as a metric tensor. Then, Peiró introduce the metric tensor

$$\mathbf{G} = \mathbf{Q}\Lambda\mathbf{Q}^T \tag{3}$$

where $\mathbf{Q}$ is the matrix of eigenvectors of the Hessian matrix, $\Lambda = diag\{|\lambda_1|, |\lambda_2|\}$ and $|\lambda_i|, i = 1,2$, are the absolute value of the associated eigenvalues ($|\lambda_1| \leq |\lambda_2|$). According to this definition, the metric tensor field $\mathbf{G}$ is at least positive semi-definite. In particular, a zero eigenvalue poses no difficulty since it leads to infinite mesh sizes that are inhibited by the limitation in the element size or by the finiteness of the computational domain.

Following the above ideas, Dompierre *et al.* (1995), introduce an error estimator associated with the size of the element edges and Buscaglia *et al.*,1996 use (3) in a quality mesh indicator. The error estimator introduced herein is a variation of first one. Instead of considering an estimator error associated with the element edge, it is proposed another one

that provide a measure of the second derivative contribuition in each element. Basically, given a finite element mesh $\mathcal{T}$ of the domain Ω, the error estimator at element level $T \in \mathcal{T}$, is defined by the expression:

$$\eta_T = \{\int_{\Omega_T} (\mathbf{G}(u_h(x_0))(x - x_0) \cdot (x - x_0))^2 d\Omega\}^{\frac{1}{2}} \tag{4}$$

and the global error estimator η is given by:

$$\eta = (\sum_{T \in \mathcal{T}} \eta_T^2)^{\frac{1}{2}} \tag{5}$$

where Ω_T is the area of the element T, x_0 is the *center* of this element.

Therefore, to obtain the *error estimator*, it is necessary to *recover* the Hessian matrix from the information given by the finite element solution u_h (Zienkiewicz and Zhu, 1992). It is well known that the derivatives of the u_h function is superconvergent in some interior points of the mesh elements. Taking advantage of superconvergence results, the central idea of the proposed estimator is to recover the Hessian with a higher order of accuracy than that naturally obtained from the finite element approximation. The algorithms used to recover the Hessian matrix need first derivatives information.

2.2 First and second derivatives recuperation

In the context of the Finite Element Method, different approaches were proposed to recover first derivative. Among them it is mentioned (Zienkiewicz *et al.* ,1987,1993): *Least Square Root Technique*, *Patch Recovering* and *Wheighted Average*.

The analysis made here is restricted to the last approach quoted – *Wheighted Average*. The technique consists on turning the inter-elements discontinuous field ∇u_h into the continuous field $\nabla_R u_h$. This is made by employing the own element basis functions to compute ∇u_h, and adopting for the value of the gradient in node with coordinate x_N, that is, $\nabla_R u_h(x_N)$, a wheighted average of the ∇u_h of the elements adjoinig to the node N. It was used as ponderation factor, the inverse of distance between the node N and the point of superconvergence of the gradient (for linear triangle the center of the element).

Second derivatives can also be recovered by using the same approaches used for the first derivative recuperation. In fact, taking $\nabla_R u_h$ as a new field, we can reapply the algorithm in order to find $\nabla_R(\nabla_R u_h)$. Its symmetric part is adopted, in order to ensure the symmetry of Hessian matrix (Zienkiewicz and Taylor,1991).

2.2 Adaptive procedure

As mentioned before, it is taken as a *local error indicator* at element level, η_T, the value expressed by equation (4). Denoting η the *global error indicator* in the triangulation $\mathcal{T}_k$, given by equation (5), the main idea to adapt the mesh, according to this error indicator, is to find a new mesh $\mathcal{T}_{k+1}$, with a given number of elements *Nel*. The new finite element mesh is generated trying to produce a uniform distribution of the local error estimator over all elements (Zienkiewicz and Zhu, 1987).

In the following, for simplicity, it is used the argument N to indicate the value of a function estimated in the node with coordinate x_N.

In order to do this, our remeshing algorithm is based on the *advancing front technique* (Peiró,1989, Oliveira, M. *et al.*, 1995 and papers therein). In this technique, the mesh generator tries to build equilateral triangles in the metric defined by the variable metric tensor $\mathbf{S}$ which, at node N of the actual mesh, takes the value:

$$\mathbf{S}(N) = \frac{1}{s*h(N)} \mathbf{e}_1(N) \otimes \mathbf{e}_1(N) + \frac{1}{h(N)} \mathbf{e}_2(N) \otimes \mathbf{e}_2(N) \tag{6}$$

where $\mathbf{e}_i(N)$, $(i = 1,2)$ are the eigenvectors of the Hessian matrix $\mathbf{H}(u_h(N))$, $h(N)$ is the *size*

in the $\mathbf{e}_2$ direction and $s \geq 1$ is the stretching in the $\mathbf{e}_1$ direction of an element generated at node N. To evaluate this two parameters we proceed as follows(see Feijóo *et al.*, 1997, for more details).

1 - For each element comput the local error η_T and the global error η.

2 - Given a number of elements Nel in the new adapted mesh, the expected local error indicator, equally distributed on all elements in the triangulation $\mathcal{T}_{k+1}$, is given by

$$\eta^* = \frac{\eta}{\sqrt{Nel}} \tag{7}$$

3 - The decreasing or increasing rate of the element size is estimated by $\beta_T = (\eta^*/\eta_T))^{\frac{1}{3}}$. From the rate β_T, computed at elementwise, different approaches can be selected to find the distribution at nodal level. Those approaches can be the same used to performe the derivatives. This rate at nodal level is noted $\beta(N)$.

4 - The size of the new element, to be generated at node N, is defined by

$$h_{k+1}(N) = \beta(N) h_k(N) \tag{8}$$

In the computational implementation of the present method, two threshold values for the computed new element size are used $\underline{\alpha} * h_k \leq h_{k+1} \leq \overline{\alpha} * h_k \leq L$. This two parameters are used in order to ensure a progressively mesh adaptation to the solution. Moreover, L represents the characteristic length of the domain Ω.

5 - The stretching factor s at node N is defined by

$$s(N_k) = \sqrt{|\lambda_2|/|\lambda_1|} \tag{9}$$

where $|\lambda_1| \leq |\lambda_2|$ are the absolute eigenvalue of the Hessian matrix $\mathbf{H}(u_h(N))$. This stretching factor must bounded in order to ensure that the length of the element in the direction $\mathbf{e}_1$, $s h_{k+1}$, must be no greater than the characteristic length L of the domain Ω, i.e., $s \leq L/h_{k+1}$.

6 - h_{k+1}-*scaling*. Due to the limitation on the values of h and s, the number of elements in the new adapted mesh may be different from the expected Nel. To force the equallity between these two numbers, the elements size h at nodal level, must be scaled. In particular, the number of elements in the new finite element mesh is given by

$$Nel_{new} = \frac{4}{\sqrt{3}} \int_\Omega \frac{2}{s h^2} \, d\Omega \tag{10}$$

Then, the scaled value for the element size is given by

$$h_{k+1} \leftarrow \sqrt{\frac{Nel_{new}}{Nel}} \times h_{k+1} \tag{11}$$

The adaptive strategy described is repeated until the error estimator in the mesh $\mathcal{T}_k$, relative to the solution of the problem analysed, becomes lower than a given admissible relative error $\overline{\gamma}$, that is, $\frac{\eta_k}{\{\|u_h\|_{L_2(\Omega)} + \eta_k\}^{\frac{1}{2}}} \leq \overline{\gamma}$

3. LIMIT ANALYSIS

Under the assumption of proportional loading, the limit analysis problem consists in finding a load factor α such that the body undergoes plastic collapse when subject to the reference loads F uniformly amplified by α. In turn, a system of loads produces plastic collapse if there exists a stress field in equilibrium with these loads, which is plastically admissible and related, by the constitutive equations, to a plastic strain rate field being kinematically admissible. Thus, the limit analysis problem consists in finding $\alpha \in \mathbb{R}$, a stress field $T \in W'$, a plastic strain rate field $D^p \in W$ and a velocity field $v \in V$ such that

$$D^p = \mathcal{D}v, \qquad v \in V \tag{12}$$

$$\int_{\mathcal{B}} T \cdot \mathcal{D}v \; d\mathcal{B} = \alpha \left(\int_{\mathcal{B}} b \cdot v \, d\mathcal{B} + \int_{\Gamma_\tau} \tau \cdot v \, d\Gamma \right) \quad \forall v \in V \tag{13}$$

$$T \in \mathbf{P} = \{T \in W' \mid f(T) \leq 0 \quad in \; \mathcal{B}\} \tag{14}$$

$$D^p = \nabla f(T) \, \dot{\lambda} \tag{15}$$

$$f \cdot \dot{\lambda} = 0 \qquad \dot{\lambda} \geq 0 \quad f \leq 0 \tag{16}$$

We explain, in what follows, the meaning of these relations and the used notation . Equation (12) imposes that the collapse plastic strain rate is related to a kinematically admissible velocity field v by means of the tangent deformation operator $\mathcal{D}$. In (13) is expressed the Principle of Virtual Power, imposing the equilibrium of the stress fields with a given body loads αb and surface loads $\alpha\tau$ prescribed in region Γ_τ of the body.

For elastic ideally-plastic materials the plastic admissibility of stress fields is defined by the set P, as in (14). The admissibility function f is a $m-$vector field, comprising in each component a plastic mode. The inequality in (14) is understood as imposing that each one of those components f_k (a regular convex function) is non-positive. The constitutive relation is expressed by the normality rule (15) and complementarity condition (16). In (15), $\nabla f(T)$ denotes the gradient of f, and $\dot{\lambda}$ is the $m-$vector field of plastic multipliers. Also, in (16) the inequalities hold componentwise.

The discretized version of the limit analysis formulation leads to a finite dimensional problem that can be seen as a discret version of the system (12-16). A Newton-like strategy for solving this discrete problem is describe in (Borges *at al.*, 1996).

In equation (16), can be observed that the plastic multipliers $\dot{\lambda}_k$ are no zero only when the function f_k is zero, that is when the stress is in the yield surface. So, the plastic multipliers field is suitable to indicate if , in some point of the body, there are plastic deformations. For this reason, the mesh–adaptive strategy, based on error estimation techniques suggested in section 2, is applied under this field. The sketch of the adaptive process is summarized in following.

Repeat

(1)Apply the Newton-like strategy for solving the discrete limit analysis

- comput $\dot{\lambda}$ in elementwise.
- Using the same strategy of recovering derivative,to estimate $\dot{\lambda}$ at nodal level.

(2)Compute the local estimator error η_T and the global error η.

(3)For a given Nel for each node of the mesh $\mathcal{T}_k$ estimate η^*, h_{k+1} and s_{k+1}.

(4)Scaling h_{k+1}.

(5)Generate a new mesh $\mathcal{T}_{k+1}$.

Until $\{\eta_k \leq \overline{\gamma}\{\|u_h\|_{L_2(\Omega)} + \eta_k\}^{\frac{1}{2}}\}$

4. APPLICATIONS

In this section, two examples of limit analysis are presented, applying the finite element adaptive strategy previously outlined. The kinematic principle for limit analysis was dicretized by using a three-node interpolation finite element basis for the velocity field. In this model the approximate collapse factor α is greater than or equal to the true $\hat{\alpha}$, defined by the continuum model(Borges *et al*,1996). In both, it was adopted the Von Mises criterion for plastic admissibility.

4.1 - Square slab with symmetrical internal slit.

A square slab with a symmetrical internal slit subjected to traction, presents localized

deformation in the form of slip bands emanating from the roots of the crack. This collapse mechanism, obtained by the numerical solution, is shown in figure 1.

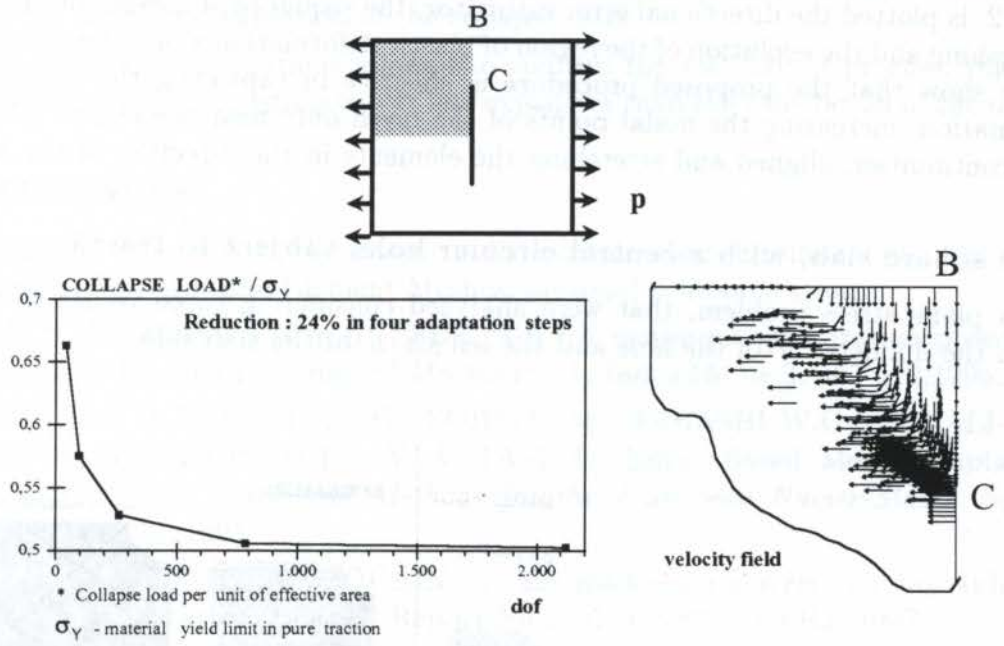

Figura 1: Slab with an internal slit – Collapse load evolution and velocities field.

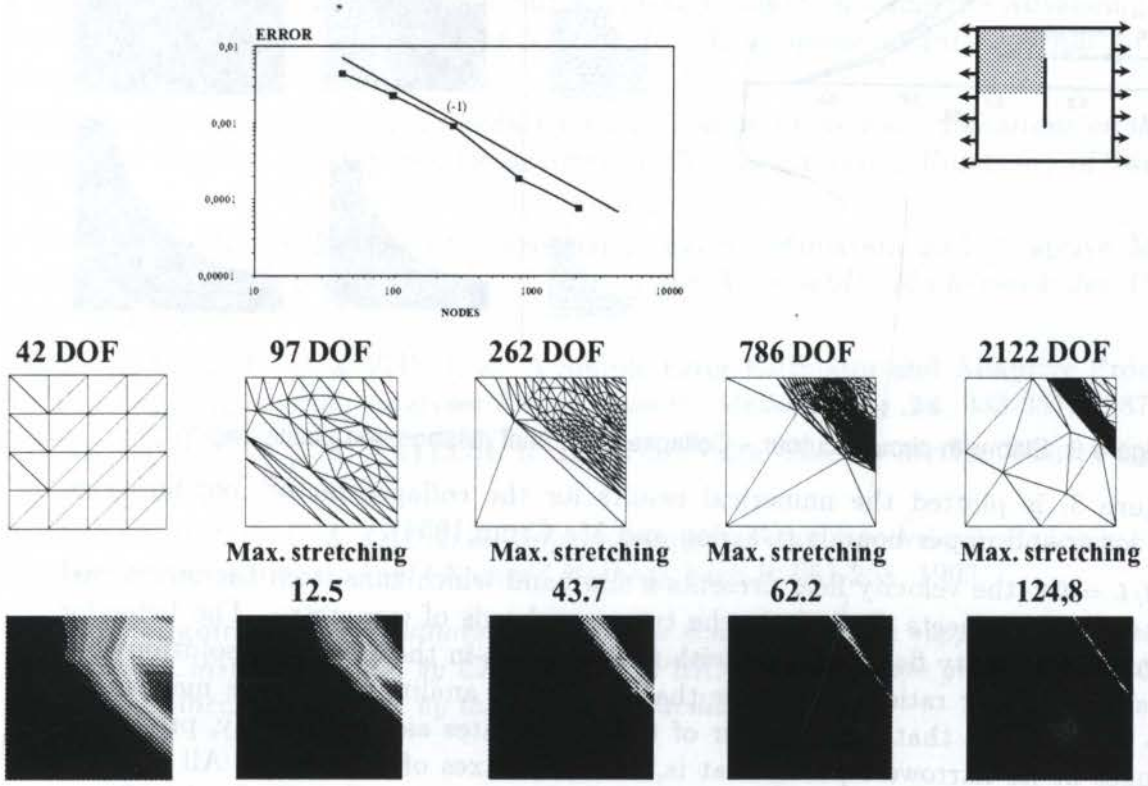

Figura 2: Slab with an internal slit – Erro, mesh and plastic deformation evolution.

In four adaptation steps, we obtain a reduction of 24% in the collapse load (figure 1). It is worth noting that the kinematical principle adopted, yield to a upper bound to the exact collapse load, so this reduction during the adaptive process is presumed.

In figure 2, is plotted the directional error estimator, the sequence of meshes obtained with the remeshing and the evolution of the region of plastic deformation along the process. Those results show that the proposed procedure is effective in capturing the localized plastic deformation, increasing the nodal points of the mesh only near the region where there are discontinuities, aligned and stretching the elements in the direction of the slip bands.

4.2 - A thin square slab, with a central circular hole, subject to traction.

This is a plane stress problem, that were analyzed considering three values of the ratio between the diameter d of the hole and the length L of the slab side.

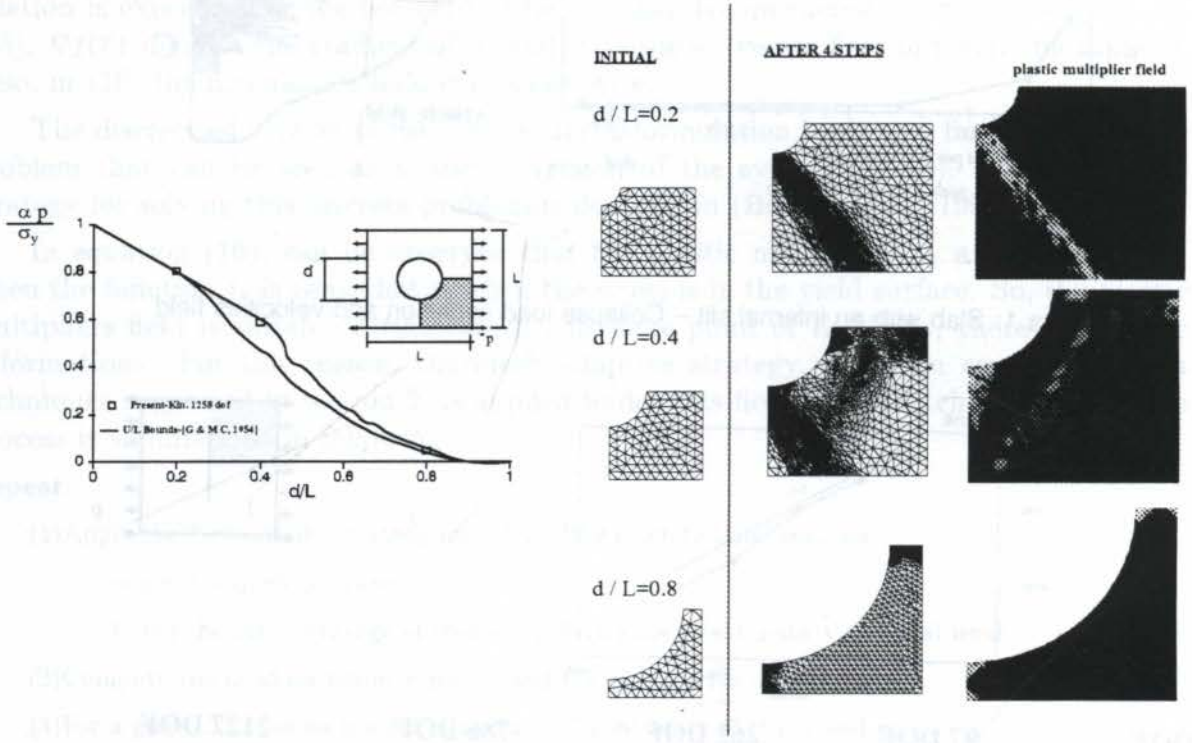

Figura 3: Slab with circular cutout – Collapse load, final meshes and plastic region.

In figure 3, is plotted the numerical results for the collapse factor, compared to analytical lower and upper bounds (Gaydon and Mc Crum,1954).

For $d/L = 0.2$ the velocity field presents a slip band which runs from the unstressed edge of the slab and meets the hole in the transversal axis of symmetry. The behavior of this numerical velocity field complies with that foreseen in the analytical solution that identifies slip bands for ratios d/L lower than 0.4. The analitycal collapse mechanism for $d/L > 0.6$ imposes that each quarter of the slab rotates as a rigid body, producing plastic hinges at its narrowest parts, that is, along the axes of symmetry. All of those kind of mechanisms are detected in the numerical solution, as can be observed in figure 3, where plastic region is the clearest one.

5. CONCLUSION

The adaptive technique proposed shows to be appropriated to capture discontinuities arising from the localized plastic deformations during plastic collapse, and as consequence, improve the numerical valuation of the collapse load.

The numerical applications allowed to confirm the viability of process, that is, the computation of the error estimate was less expensive than the calculation of the numerical solution

6. REFERENCES

BUSCAGLIA, G.C., DARI, A; Adaptive Anisotropic Mesh Optimization: Construction of Solution Adapted Finite Element Meshes, personal communication.

BORGES, L.A., ZOUAIN,N. e HUESPE, A.E.; A nonlinear optimization procedure for limit analysis , *European Journal of Mechanics A/Solids*,**15**, no 3, 487-512,1996.

DOMPPIERRE, J.,VALLET, M. G., FORTIN, M., HABASHI W.G., AÏT-ALI-YAHIA, D., BOIVIN, S., BOURGAULT, Y. & TAM A.; Edge -Based Mesh Adaptation for CFD, *Conference on Numerical Methods for the Euler and Navier-Stokes Equations*, Montreal,p.265-299, 1995.

FEIJÓO, R.A., BORGES, L., ZOUAIN, N.; Estimadores *a posteriori* y sus Aplicaciones en el Análisis Adaptativo. Internal Report N0 1/97- COPPE/UFRJ, 1997.

GAYDON F. A., McCRUM A. W.,A Theoretical Investigation of the Yield Point Loading of a Square Plate with a Central Circular Hole, *J. Mech. and Phys. Solids*, **2**, 156-169,1954.

OLIVEIRA, M., GUIMARÃES, A.C.S., FEIJÓO, R.A, VÉNERE, M.J., DARI, E.; An Object Oriented Tool for Automatic Surface Mesh Generation Using the Advancing Front Technique,*Report of P&D, LNCC/CNPq N⁰ 18/95, to appear in Int. Journal for Latin America Applied Research*, 1995.

PEIRÓ, J.; *A Finite Element Procedure for the Solution of the Euler Equations on the Unstructured Meshes.* Ph.D. these, Department of Civil Engineering, University of Swansea, UK, 1989.

VERFÜRTH, R.; A Review of a Posterriori Error Estimation and Adaptive Mesh - Refinement Techniques,*Publication of Institut für Angewandte Mathematik der Universität Zürich*,1995.

ZIENKIEWICZ, O. C. & ZHU,J. Z.; A Simple Error Estimator and Adaptive Procedure for Practical Engineering Analyses,*Int. J. Numer. Methods Eng.*,**24**, 333-357, 1987.

ZIENKIEWICZ, O. C. & TAYLOR, R. L. ; *The Finite Element Method*, Fourth Edition, McGraw Hill Int. Ed., 1991.

ZIENKIEWICZ, O. C. & ZHU,J. Z.; Superconvergent Patch Recovery Techniques – Some Further Tests,*Commun. Appl. Numer. Methods*, texb 9, 251-258, 1993.

Acknowledgement: *The authors would like to acknowledge the support of this research by their own institutions and by CNPq and FAPERJ. Also they are grateful to TACSOM group (www.lncc.br/ tacsom) by the softwares facilities offered.*

XIV Brazilian Congress of Mechanical Engineering
Obeid Plaza Hotel Convention Center - Bauru - SP/Brazil
December 08-12th 1997

PAPER CODE: COB1266

MODELO CONSTITUTIVO PARA DANO EM MATERIAIS FRÁGEIS / *CONSTITUTIVE MODEL FOR DAMAGE IN BRITTLE MATERIALS*

ROQUE LUIZ PITANGUEIRA[1] E RAUL ROSAS E SILVA[2]
[1] *Departamento de Engenharia de Estruturas - UFMG - Av. do Contorno, 842 - 2o. andar CEP 30110-060, Belo Horizonte, Brasil - E-mail:roque@dees.ufmg.br*
[2] *Departamento de Engenharia Civil - PUC-Rio - Rua Marquês de São Vicente, 225 CEP 22453-900, Rio de Janeiro, Brasil - E-mail:raul@civ.puc-rio.br*

Abstract

A simple constitutive model which includes heterogeneity and size effects is presented. Distributed and discrete approaches for modeling of damage in brittle materials are discussed. Different implementations of the distributed approach are established, according to the choice of the initial compliance matrix, the treatment of the damage direction variation during the analysis, the approximation of the tangent constitutive relation, and the local damage evolution laws in tension and compression. The implications of the different approximations of constitutive tensors in a tangent formulation are adressed in a numerical example.

Keywords

Constitutive, Damage, Fracture, Localization, Size effect, Dano, Fratura, Localização, Efeito de Tamanho

1. INTRODUÇÃO

Na análise do comportamento de estruturas feitas de materiais frágeis, estes são normalmente considerados como inicialmente homogêneos, elásticos e isotrópicos. Admite-se que, com a aplicação de cargas e conseqüentes deformações, os materiais deixam de ser elásticos e isotrópicos e tornam-se heterogêneos, pela ocorrência de dano em tração e compressão nas regiões mais solicitadas. O fenômeno ocorre de tal maneira que, durante o processo de deterioração da estrutura, alguns pontos do domínio apresentam características mecânicas distintas dos demais, observando-se que esta combinação de materiais com características muito diversas (algumas regiões danificadas junto a outras com as características do material homogêneo inicial) causa efeitos não-lineares pronunciados na resposta da estrutura.

Em um meio contínuo e homogêneo, todos os pontos do domínio têm as mesmas propriedades e, portanto, reagem da mesma maneira às ações externas. Assim, a relação entre tensões e deformações é única e não depende da geometria da amostra. Esta única relação tensão-deformação é dita uma propriedade do material, sua lei constitutiva. Esta é a idéia da análise usual, por elementos finitos, que considera o meio contínuo, o material inicialmente homogêneo e a lei tensão-deformação conhecida a priori. Entretanto, a idealização de um meio contínuo homogêneo só é válida se as tensões e deformações são tomadas em um volume representativo que deve ser, portanto, algumas vezes superior ao tamanho das não-

homogeneidades existentes no material ou nele introduzidas pelo processo de carregamento da estrutura. Esta limitação impede que sejam considerados os fenômenos, presentes em materiais frágeis, ligados à localização de deformações.

A consideração destes fenômenos é importante na verificação de que a forma da resposta carga-deslocamento da estrutura depende de seu tamanho, fazendo com que a lei constitutiva seja, não somente uma propriedade do material mas, também, uma propriedade estrutural (Van Mier, 1984). Também é importante ressaltar que a resposta constitutiva está relacionada com a natureza heterogênea do material e que esta deve ser evidenciada na análise por elementos finitos.

Assim, se as hipóteses do modelo constitutivo só são válidas localmente, este deve ser o mais simples possível já que a resposta constitutiva global deve considerar o efeito conjunto do comportamento constitutivo local, da heterogeneidade do material e do efeito de tamanho.

No que se segue, os modelos clássicos para tratamento da fissuração em materiais frágeis são revisados (seção 2). O enfoque de fissuras distribuídas é generalizado para considerar também a ocorrência de dano em compressão (seção 3). As possibilidades do modelo no que diz respeito à escolha da matriz de compliância inicial (seção 3.1), às leis locais de evolução do dano (seção 3.2) e às aproximações do tensor constitutivo tangente (seção 3.3) são então discutidas.

2. MODELOS PARA FISSURAÇÃO

Ainda que considerando o material como inicialmente homogêneo, com a aplicação de cargas e conseqüentes deformações o material se torna heterogêneo, pela ocorrência de dano em tração e compressão nas regiões mais solicitadas. Tal processo leva eventualmente à formação de descontinuidades geométricas denominadas fissuras ou trincas.

Diferentes modelos têm sido propostos para representação deste fenômeno, podendo-se dividi-los em dois grupos: o modelo de fissuras discretas e o modelo de fissuras distribuídas.

A formulação discreta, modela a fissura como descontinuidade geométrica. Neste enfoque imagina-se a separação entre os lados dos elementos adjacentes à fissura formada. Isto implica em mudança da conectividade nodal na progressão da fissura e na restrição da localização da fissura ao longo dos lados dos elementos finitos.

No caso do modelo de fissuras distribuídas, a região danificada é imaginada como um meio contínuo formado por um número infinito de pequenas fissuras paralelas.

Este modelo considera que o material torna-se ortotrópico na região fissurada, modificando-se sua relação constitutiva no sistema local, posicionado no plano de fissuração. Tem a vantagem da geração automática das fissuras sem redefinição da topologia da malha e da generalidade em relação à orientação dos planos de fissuras. Uma outra vantagem do modelo distribuído é que, devido ao fato de considerar a deterioração da rigidez a partir de uma modificação da relação constitutiva local, este pode ser generalizado para considerar também regiões com dano em compressão.

Os trabalhos iniciais com o modelo de fissuras distribuídas consideravam nulos o módulo de elasticidade na direção perpendicular ao plano de fissura e o módulo de elasticidade transversal. O uso do modelo assim concebido, resultou em dificuldades numéricas e, em alguns casos, em distorções na configuração de fissuras da discretização por elementos finitos.

3. MODELO DE DANO DISTRIBUÍDO

A evolução do modelo distribuído para representação de fissuras requer uma reformulação do mesmo para considerar a degradação gradativa da rigidez em lugar da redução brusca dos modelos iniciais, a possibilidade de ocorrência de dano em compressão e o

acoplamento entre as deformações direta e indireta devido ao efeito de Poisson. Este refinamento do modelo leva ao uso da chamada Teoria de Dano.

Desconsiderando os mecanismos microscópicos associados ao fenômeno da ruptura, a idealização de um meio contínuo e homogêneo com o comportamento ortotrópico sugerido para regiões com ocorrencia de dano distribuído, só é válida se as tesões e deformações são tomadas em um volume representativo que deve ser, portanto, algumas vezes superior ao tamanho das não-homogeneidades existentes no material.

Com esta limitação, o modelo de dano escalar supõe a validade de uma relação de compliância entre deformações e tensões num sistema local, posicionado nas direções principais de ortotropia, dada por

$$\varepsilon_{12} = \mathbf{C}\, \sigma_{12} \tag{1}$$

onde σ_{12}, ε_{12} e $\mathbf{C}$ são, respectivamente, os vetores de tensão e deformação referidos ao sistema local de coordenadas e a matriz de compliância. Em (1) $\mathbf{C}$ pode ser obtida a partir de hipóteses para a relação de ortotropia nas direções principais. A inversão de (1) permite obter a relação constitutiva secante local para o modelo de dano distribuído na forma

$$\sigma_{12} = {}^{s}\mathbf{D}_{12}\, \varepsilon_{12}, \tag{2}$$

onde, ${}^{s}\mathbf{D}_{12} = \mathbf{C}^{-1}$ é o tensor constitutivo secante, referido ao sistema local.

Formada a relação constitutiva secante no sistema local (1-2) é necessário transformá-la para o sistema global (X-Y). Equacionada a energia de deformação virtual complementar para os dois sistemas de coordenadas, obtém-se

$$\sigma_{XY} = \mathbf{T}_{\varepsilon}^{T}\, {}^{s}\mathbf{D}_{12}\, \mathbf{T}_{\varepsilon}\, \varepsilon_{XY}, \tag{3}$$

onde $\mathbf{T}_{\varepsilon}$ é a matriz de transformação de deformações entre os sistemas.

A obtenção de trajetórias de equilíbrio no espaço parâmetro de carga-deslocamentos envolve um processo iterativo-incremental. Se tal processo só utiliza relações secantes de equilíbrio, as equações (2) e (3) são suficientes. Se, entretanto, o processo requer o cálculo de rigidez tangente, uma relação incremental entre tensões e deformações precisa ser obtida.

Diferenciando (3) em relação a ε_{XY}, obtém-se

$$\mathbf{d}\sigma_{XY} = (\mathbf{T}_{\varepsilon}^{T}\, {}^{t}\mathbf{D}_{12}\, \mathbf{T}_{\varepsilon} + \frac{\partial \mathbf{T}_{\varepsilon}^{T}}{\partial \varepsilon_{XY}} \sigma_{12})\, \mathbf{d}\varepsilon_{XY}, \tag{4}$$

onde ${}^{t}\mathbf{D}_{12} = \dfrac{\partial \sigma_{12}}{\partial \varepsilon_{12}}$ exprime o tensor constitutivo tangente referido ao sistema local de coordenadas e $\dfrac{\partial \mathbf{T}_{\varepsilon}^{T}}{\partial \varepsilon_{XY}} \sigma_{12}$ exprime a influência de possíveis mudanças na matriz de transformação durante o processo iterativo-incremental de obtenção das trajetórias de equilíbrio. Para obter a equação (4) consistentemente com a equação (3) deve-se tomar o diferencial total das tensões locais a partir da relação dada pela equação (2) e, portanto, entender o significado do tensor tangente local (${}^{t}\mathbf{D}_{12}$). Assim, derivando-se (2), tem-se

$$ {}^{t}\mathbf{D}_{12} = \frac{\partial \sigma_{12}}{\partial \varepsilon_{12}} = \frac{\partial}{\partial \varepsilon_{12}}({}^{s}\mathbf{D}_{12}\varepsilon_{12}) = {}^{s}\mathbf{D}_{12} + \frac{\partial {}^{s}\mathbf{D}_{12}}{\partial \varepsilon_{12}}\varepsilon_{12}. \qquad (5) $$

O termo ${}^{s}\mathbf{D}_{12}$ é simétrico já que é o próprio tensor constitutivo secante local, mas a parcela $\frac{\partial {}^{s}\mathbf{D}_{12}}{\partial \varepsilon_{12}}\varepsilon_{12}$ é, em geral, não simétrica. Dentre as possibilidades para sua simetrização, a que toma a média da matriz e sua transposta, parece oferecer melhores resultados, quanto à estabilidade numérica.

Com relação à parcela dependente da variação da matriz $\mathbf{T}_{\varepsilon}$ com as deformações, para o caso bidimensional, esta é expressa por uma única variável escalar (θ). Assim, o segundo termo à direita da equação (4) pode ser reescrito como

$$ \frac{\partial \mathbf{T}_{\varepsilon}^{T}}{\partial \varepsilon_{XY}}\sigma_{12} = \frac{\partial \mathbf{T}_{\varepsilon}^{T}}{\partial \theta}\sigma_{12}\left(\frac{\partial \theta}{\partial \varepsilon_{XY}}\right)^{T}. \qquad (6) $$

Esta expressão é simétrica desde que se garanta que o sistema local é sempre principal durante o processo incremental de análise.

Substituindo-se as parcelas simétricas dadas pelas equações (5) e (6) em (4), obtém-se o tensor constitutivo tangente consistente, referido ao sistema global de coordenadas.

O modelo acima descrito permite a tratamento do processo de dano do material, seja em tração ou em compressão, partindo-se de uma relação constitutiva secante referida ao sistema local de coordenadas. Adotando as direções principais de deformação como as direções de ortotropia do modelo, algumas possibilidades para o mesmo devem ser investigadas.

A hipótese a ser adotada para obtenção de uma matriz de compliância simétrica (matrizes **C** em (1)) define o tensor constitutivo secante local do modelo. As variações dos módulos de elasticidade secantes de forma gradual (valores de $\mathbf{E}_1$, $\mathbf{E}_2$ e $\mathbf{G}_{12}$ no tensor constitutivo secante local em (2)), dependendo do sinal e do valor da deformação ocorrida em cada direção do sistema local, definem as leis de evolução do dano. A forma do tensor constitutivo tangente local (${}^{t}\mathbf{D}_{12}$ em (5)) e a variação da direção do sistema local, influenciando a obtenção do tensor constitutivo tangente referido ao sistema global (equação (6)), definem a aproximação a ser usada para o referido tensor. Nas seções que se seguem, estas possibilidades serão analisadas.

3.1 Matrizes de Compliância

Para que a matriz de compliância resulte simétrica, uma hipótese para o acoplamento devido ao efeito de Poisson deve ser adotada.

A hipótese mais usada é que este acoplamento é comandado pelo módulo de elasticidade inicial do material, antes de sofrer dano ($\mathbf{E}_0$) e por um único valor de coeficiente de Poisson (ν), válido para qualquer direção. Assim, para estado plano de tensões, tem-se

$$ {}^{s}\mathbf{D}_{12} = \frac{1}{1-\frac{\mathbf{E}_1\mathbf{E}_2}{\mathbf{E}_0^2}\nu^2}\begin{bmatrix} \mathbf{E}_1 & \frac{\nu\mathbf{E}_1\mathbf{E}_2}{\mathbf{E}_0} & 0 \\ \frac{\nu\mathbf{E}_1\mathbf{E}_2}{\mathbf{E}_0} & \mathbf{E}_2 & 0 \\ 0 & 0 & (1-\frac{\mathbf{E}_1\mathbf{E}_2}{\mathbf{E}_0^2}\nu^2)\mathbf{G}_{12} \end{bmatrix}. \qquad (7) $$

acoplamento entre as deformações direta e indireta devido ao efeito de Poisson. Este refinamento do modelo leva ao uso da chamada Teoria de Dano.

Desconsiderando os mecanismos microscópicos associados ao fenômeno da ruptura, a idealização de um meio contínuo e homogêneo com o comportamento ortotrópico sugerido para regiões com ocorrencia de dano distribuído, só é válida se as tesões e deformações são tomadas em um volume representativo que deve ser, portanto, algumas vezes superior ao tamanho das não-homogeneidades existentes no material.

Com esta limitação, o modelo de dano escalar supõe a validade de uma relação de compliância entre deformações e tensões num sistema local, posicionado nas direções principais de ortotropia, dada por

$$\varepsilon_{12} = \mathbf{C}\ \sigma_{12} \tag{1}$$

onde σ_{12}, ε_{12} e $\mathbf{C}$ são, respectivamente, os vetores de tensão e deformação referidos ao sistema local de coordenadas e a matriz de compliância. Em (1) $\mathbf{C}$ pode ser obtida a partir de hipóteses para a relação de ortotropia nas direções principais. A inversão de (1) permite obter a relação constitutiva secante local para o modelo de dano distribuído na forma

$$\sigma_{12} = {}^{s}\mathbf{D}_{12}\ \varepsilon_{12}, \tag{2}$$

onde, ${}^{s}\mathbf{D}_{12} = \mathbf{C}^{-1}$ é o tensor constitutivo secante, referido ao sistema local.

Formada a relação constitutiva secante no sistema local (1-2) é necessário transformá-la para o sistema global (X-Y). Equacionada a energia de deformação virtual complementar para os dois sistemas de coordenadas, obtém-se

$$\sigma_{XY} = \mathbf{T}_{\varepsilon}^{T}\ {}^{s}\mathbf{D}_{12}\ \mathbf{T}_{\varepsilon}\ \varepsilon_{XY}, \tag{3}$$

onde $\mathbf{T}_{\varepsilon}$ é a matriz de transformação de deformações entre os sistemas.

A obtenção de trajetórias de equilíbrio no espaço parâmetro de carga-deslocamentos envolve um processo iterativo-incremental. Se tal processo só utiliza relações secantes de equilíbrio, as equações (2) e (3) são suficientes. Se, entretanto, o processo requer o cálculo de rigidez tangente, uma relação incremental entre tensões e deformações precisa ser obtida.

Diferenciando (3) em relação a ε_{XY}, obtém-se

$$\mathbf{d}\sigma_{XY} = (\mathbf{T}_{\varepsilon}^{T}\ {}^{t}\mathbf{D}_{12}\ \mathbf{T}_{\varepsilon} + \frac{\partial \mathbf{T}_{\varepsilon}^{T}}{\partial \varepsilon_{XY}}\sigma_{12})\,\mathbf{d}\varepsilon_{XY}, \tag{4}$$

onde ${}^{t}\mathbf{D}_{12} = \frac{\partial \sigma_{12}}{\partial \varepsilon_{12}}$ exprime o tensor constitutivo tangente referido ao sistema local de coordenadas e $\frac{\partial \mathbf{T}_{\varepsilon}^{T}}{\partial \varepsilon_{XY}}\sigma_{12}$ exprime a influência de possíveis mudanças na matriz de transformação durante o processo iterativo-incremental de obtenção das trajetórias de equilíbrio. Para obter a equação (4) consistentemente com a equação (3) deve-se tomar o diferencial total das tensões locais a partir da relação dada pela equação (2) e, portanto, entender o significado do tensor tangente local (${}^{t}\mathbf{D}_{12}$). Assim, derivando-se (2), tem-se

onde $\mathbf{E_1}$ e $\mathbf{E_2}$ são os módulos de elasticidade secantes no sistema local, função das deformações neste sistema. O módulo de elasticidade transversal dada em (7), para considerar a rugosidade da fissura e o engrenamento dos agregados, deve ser limitado por $\mathbf{G_{21} \geq \beta G_0}$, onde $\mathbf{G_0}$ é o módulo transversal do material intacto e β, um escalar ($0 < \beta < 1.0$) normalmente chamado de fator de retenção em cisalhamento.

Esta hipótese para simetrização da matriz de compliância, foi a adotada por Bazant e Oh (1983) que, também, consideraram a evolução do dano somente numa direção. Outras hipóteses para o acoplamento devido ao efeito de Poisson podem ser adotadas, resultando em matrizes de compliância simétricas.

3.2 Leis de Dano

O enfoque de dano distribuído permite que o comportamento constitutivo do material seja modelado em termos de uma relação tensão-deformação. Com o processo de deterioração do material, suas propriedades elásticas iniciais são modificadas, a partir de uma função de dano. Tal função caracteriza o dano do material a partir das deformações ocorridas no sistema local, modificando-se suas propriedades elásticas por meio da relação

$$\mathbf{E_i = E_0 \times \Phi(\varepsilon_i)}, \tag{8}$$

onde $\Phi(\varepsilon_i)$ é uma função de dano escalar, dependente somente da deformação ocorrida numa direção. Com a ocorrência de diminuição de deformações, adotando-se a hipótese de dano irreversível, o descarregamento se dará na direção secante.

Várias formas podem ser adotadas para descrever a evolução do dano, tanto em tração como em compressão, tais como linear, bi-linear, exponencial e não-linear.

Adotando um comportamento linear com "softening" exponencial (Boone e Ingraffea, 1987) para regiões de tração, a função de dano fica

$$\Phi(\varepsilon) = \begin{cases} \mathbf{1.0} & \textbf{para} \quad \varepsilon < \varepsilon_t \\ \dfrac{\mathbf{f_t}}{\mathbf{E_0}\varepsilon} \mathbf{e}^{-\mathbf{k}(\varepsilon - \mathbf{f_t}/\mathbf{E_0})} & \textbf{para} \quad \varepsilon > \varepsilon_t \end{cases} \tag{9}$$

com k dado em função de parâmetros de Mecânica da Fratura por $\mathbf{k = \dfrac{h f_t}{G_f}}$ e onde $\mathbf{f_t}$ é a resistência a tração uniaxial, $\mathbf{E_0}$ é o módulo de elasticidade inicial, $\mathbf{G_f}$ é a energia de fratura e **h** é o tamanho característico do material que serve como limitador da região de validade da relação constitutiva local.

Para regiões de compressão, admite-se a evolução do dano baseada na curva não-linear proposta por Carreira e Chu (1985) para modelar concreto em regiões de compressão, de modo que a função de dano fica

$$\Phi(\varepsilon) = \left[1 + \left(\frac{\varepsilon}{\varepsilon_c} \right)^{k} \cdot \left(\frac{\mathbf{E_0 \varepsilon_c}}{\mathbf{f_c}} - 1 \right) \right]^{-1}, \tag{10}$$

com $\mathbf{k} = \left[1 - \left(\mathbf{f_c} / \varepsilon_c \cdot \mathbf{E_0} \right) \right]^{-1}$ e onde, $\mathbf{f_c}$ é a resistência limite à compressão, ε_c é a deformação correspondente ao limite de compressão e $\mathbf{E_0}$ é o módulo de elasticidade inicial.

3.3 Tensores Constitutivos

As equações (5) e (6) mostram que a aproximação usada para o tensor constitutivo tangente local e a variação da direção do sistema local, influenciam a obtenção do tensor constitutivo tangente referido ao sistema global, necessário ao processo iterativo-incremental de análise.

Dentre as aproximações possíveis para a obtenção do tensor constitutivo do modelo adotado, pode-se citar as seguintes, agrupadas em quatro modelos. Em todos os modelos as tensões totais, dadas as deformações totais, são obtidas a partir da equação (3), podendo a direção local ser fixa ou variável. Com relação ao tensor constitutivo tangente, entretanto, cada modelo tem sua particularidade.

MODELO 1: *direção de dano fixa e equilíbrio secante.* Adota o tensor constitutivo secante local como uma aproximação para o tensor tangente local e despreza a parcela referente as derivadas do tensor secante local (equação (5)) além de considerar a direção de ocorrência de dano constante durante toda análise.

MODELO 2: *direção de dano fixa e equilíbrio tangente.* Adota as duas parcelas da equação (5), devidamente simetrizadas, para obter o tensor tangente, mas considera a direção de ocorrência de dano constante durante toda análise.

MODELO 3: *direção de dano variável e equilíbrio secante.* Adota o tensor constitutivo secante local como uma aproximação para o tensor tangente local desprezando a parcela referente as derivadas do tensor secante local (equação (5)). Considera que a direção de ocorrência de dano pode variar em cada passo da análise, mas despreza a parcela relativa às derivadas da matriz de transformação de deformações (equação (6)), o que permite o uso deste modelo para obtenção de equações totais de equilíbrio bem como para aproximação de equações incrementais de equilíbrio.

MODELO 4: *direção de dano variável e equilíbrio tangente.* Considera que a direção de ocorrência de dano pode variar durante a análise e adota todas as parcelas (dadas nas equações (5) e (6)) da equação incremental de equilíbrio.

Foi feita a implementação computacional de todas estas possibilidades para aproximações do tensor constitutivo, com as leis de evolução do dano local e as hipóteses para a compliância inicial adotadas. As implicações numéricas são ilustradas no exemplo, a seguir.

4. EXEMPLO

Um ensaio uniaxial é utilizado para mostrar os resultados das várias aproximações do modelo constitutivo.

Um único elemento finito em estado plano de tensões com quatro nós e espessura unitária é adotado para o problema usando-se integração 2x2, como mostra a Figura 1. Os parâmetros do material, usados no exemplo são f_c=20MPa, f_t=2MPa, E_0=2.0e4MPa, ε_c=0.002, G_f=2.0e-2kN/m, h=0.05m, β=0.05 e coeficiente de Poisson ν= 0.2.

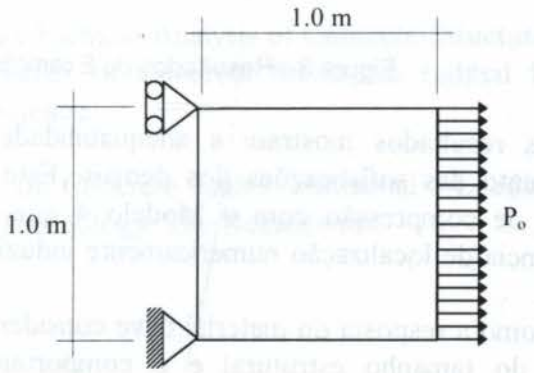

Figura 1 - Discretização do Exemplo

Utilizou-se o método de controle de deslocamentos generalizados (Yang e Shieh, 1989) para obtenção das trajetórias de equilíbrio, adotando-se uma carga de referência P_0=2MN/m, para tração, e P_0=-20MN/m, para compressão, e uma tolerância para a convergência de 10^{-4}.

Os gráficos da Figura 2, mostram as trajetórias de equilíbrio relativas ao deslocamento horizontal da extremidade livre do elemento finito, para os quatro modelos citados no item 3.3, no ensaio de tração. Para o ensaio de compressão os resultados estão na Figura 3.

Figura 2 - Resultados do Exemplo para o ensaio de tração

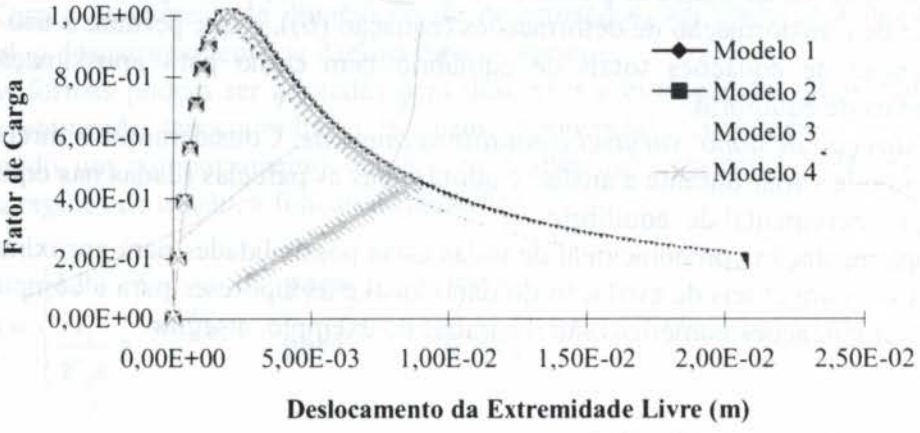

Figura 3 - Resultados do Exemplo para o ensaio de compressão

Os resultados mostram a adequabilidade do modelo mais simples (Modelo 1) em detrimento das sofisticações dos demais. Este aspecto fica mais evidente no resultado do ensaio de compressão com o Modelo 4 que, apesar da sofisticação matemática, levou à ocorrência de localização numericamente induzida, forçando o descarregamento mostrado na figura.

Como a resposta do material deve considerar conjuntamente sua natureza heterogênea, o efeito do tamanho estrutural e o comportamento constitutivo, é válido esperar que o funcionamento mecânico local (válido apenas para pequenos volumes representativos das não homogeneidades existentes) seja representado da forma mais simples possível.

5. CONCLUSÕES

Apresentou-se uma revisão dos modelos normalmente usados para representação de fissuras no método dos elementos finitos. Como uma generalização do modelo de fissuras

distribuídas, mostrou-se um modelo constitutivo e investigaram-se as várias possibilidades para sua implementação computacional: hipótese de simetria para a relação de compliância definindo o tensor constitutivo secante local, leis de evolução do dano local em tração e em compressão e aproximações do tensor constitutivo tangente global. Com a obtenção de trajetórias de equilíbrio semelhantes tanto para os modelos mais simples como para os mais sofisticados, ressaltou-se a adequabilidade do uso dos modelos mais simples em conjunto com os outros aspectos influenciadores da resposta constitutiva global: natureza heterogênea dos materiais frágeis, efeito do tamanho estrutural e comportamento constitutivo local.

AGRADECIMENTOS

Os autores agradecem o apoio recebido do CNPq para a tese na PUC-Rio, na forma de bolsas, respectivamente, de doutorado e de pesquisa e ao Departamento de Engenharia de Estruturas da UFMG, pelo apoio ao desenvolvimento do trabalho.

REFERÊNCIAS

Bazant, Z. P. e Oh, B. H. (1983) - "Crack Band Theory for Fracture of Concrete", Materials and Structures, RILEM, 93(16), pp. 155-177.

Boone, T. J. e Ingraffea, A. R. (1987)- "Simulation of the Fracture Process at Rock Interfaces", Proceedings of the Fourth International Conference held in San Antonio, Texas.

Carreira, D. J. and Chu, K. (1985) - "Stress-Strain Relationship for Plain Concrete in Compression", ACI Journal, nov-dec, pp. 797-804.

Frydman, M. (1990) - "Fissuração, Esmagamento e Fluido Penetrante em Materiais Frágeis", Dissertação de Mestrado, Departamento de Engenharia Civil, PUC-Rio, Rio de Janeiro.

Yang, Y. B. e Shieh, M. S. (1990) - "Solution Method for Nonlinear Problems with Multiple Critical Points", AIAA Journal, vol. 28, No. 12, pp. 2110-2116.

Pitangueira, R. L. (1991) - "Modelo Numérico para Concreto Heterogêneo", Dissertação de Mestrado, Departamento de Engenharia Civil , PUC/RJ.

Rosas e Silva, R. e Pitangueira, R. L. (1992) - "Finite Element Analysis of Concrete Structures with Smeared Heterogeneity", In Fracture Mechanics of Concrete Structures (edited by Zdenec P. Bazant), pp. 385-388, Elsevier Applied Science.

Van Mier, J. G. M. (1984) - "Strain-softening of Concrete under Multiaxial Loading Conditions", PhD Thesis, Eindhoven University ot Thecnology, The Netherlands.

XIV Brazilian Congress of Mechanical Engineering
Obeid Plaza Hotel Convention Center - Bauru - SP/Brazil
December 08-12th 1997

PAPER CODE: COB155

ANALYSIS OF COLD ROLL FORMING OF THIN SHEET METAL FOR SOME ROLL-STANDS

SYLVIE IDRISSI-RONEL, THEOPHILE MEHINTO & GERARD CHALANT
Laboratoire 'Mécanique, Matériaux, Environnement' (L.M.M.E.) , Faculté de Technologie
Avenue d'Estrée-BP 792-97337 CAYENNE -France E-mail: 105606.3500@compuserve.com

Abstract

The cold-roll-forming of thin sheets is a forming process where initialy flat sheet is drawn along through roll stands which may have a complex form. The cold-roll-forming is a three dimensionnal problem with large transformations, elasto-plastic behaviour with contact and friction . The objectif of the model is to have a better knowledge of sheet strains, in order to obtain a product with optimised mecanical and geometrical qualities. The proposed method simulates the cold-roll-forming process by a two dimensionnal analysis on the sheet cross section resolved by linear finite elements, coupled with a three dimensionnal analysis of the sheet between adjacent roll stands. Complex profiles were modeled with this method.

Keywords

Finite Element, Large Deformations, elastoplastic behaviour, Contact, Cold-Roll-Forming.

1 INTRODUCTION

Our Study is about cold-roll forming process where a sheet metal is continously and progressively formed into a serie of roll-stands arranged in tandem. The basis governing equations are given by the Principle of Virtual Work with updated Lagrangian description. The equilibrium state of the discretized global finite elements system is calculated by Newton's iterative method. The integration of the elasto-plastic relations is done with a rotating frame formalism with control of the numerical unloading. The sheet is successively deformed by contact with the rigid surface representing the tools, which is also being deformed continously. In the incremental approach of the updated Lagrangian description, we integrate the contact with friction by exterior penalization. This software has been installed in industry in order to be validated and is now used for profiles with more complexity as those simulated in this study. The strains results show an excellent comparison between numerical and experimental study. The displacements results present more differences on ribs than on flat parts, where as well as the global form as the amplitude are correct. If the roll stands are correctly positionned, the sheet will have a global equilibrium and also musn't be subjected, during the forming process, to lengthening or rotation interference (Ronel et al., Marocco 1995). This paper propose a general numerical method for arbitrary cross section where any complex profiles may be treated.

2 Cross-section analysis

The basic governing equations are given by the principle of virtual work at time **t + Δ t** referred to the current configuration at time t which can be written in following way :

$$\int_V [\Delta S:\delta\varepsilon + (\sigma + \Delta S):(\nabla\Delta u.\delta u\nabla)]dV = R + \int_{St} \Delta t.\delta u.ds_t + \int_{Sc} \Delta f.\delta u.ds_c \qquad (1)$$

where σ is the Cauchy stress tensor and ΔS the convected increment of Kirchhoff stress.

This permits us to calculate a certain state of equilibrium based on the knowledge of previous equilibrium state together with the actual increment in the external loads on St or the prescribed displacements and contact force on Sc.

To avoid error accumulation and to permit unloading the new equilibrium state is calculate by an iterative Newton's method where the term :

$$R = \int_t t.\delta u.ds_t + \int_c f.\delta u.ds_c - \int \sigma:\delta\varepsilon.dV \qquad (2)$$

is often called the residual which is expected to vanish in the increment.

The finite element discretisation has been made on plane strain shell element of Reissner-Mindlin type. Since independant rotational degrees of freedom are used only Co continuity is required and this by-passes the difficulties caused by the C1 requirement of the classic Kirchhoff theory. With these assumptions using linear shape functions and considering generalised plane strain conditions we derived a finite element with two nodes and, one rotational and two translational degrees of freedom at each nodes.

The element which allows for combined in-plane and bending behaviour is divided into a number of layers in order to capture the spread of plasticity over the thickness. For integration over the sheet thickness five layers are used although the number of layers can be extended up to 10 in particular for element on small tolls radii.

Since moderately thick sheets will be analysis the usual assumption of plane stress state in the thickness direction can be justified here. Then the thinning effect due to large plastic strain is taken into account by an update procedure assuming plastic incompressibility in every time step.

It is well known that the so-called Reissner Mindlin thick element family in direct application to thin plate situations can induce locking. In the thin plate limit Kirchoff's assumptions of vanishing transverse shear strain must be satisfied. A procedure is to impose a shear strain field which satisfies the limit thin plate condition. For our two nodes element this is achieved by evaluating the shear strain γ at the element mid-point.

3 Bounding conditions

In the present formulation of sheet-metal forming process it is assumed that the tool parts are completely rigid bodies whose relative movements are forced on a deformable elasto-plastic solid. It is worth noting that the moving tools not only translate as rigid bodies but can change their shapes continuously with time for roll-forming process . Then we can use parametric functions of space and coordonnates varying with time to describe the rigid moving surfaces :

$$X(t) = \sum_{k=1}^{n} N_k(\xi).x_k(t) \qquad (3)$$

$$Z(t) = \sum_{k=1}^{n} N_k(\xi).z_k(t) \qquad (4)$$

where n=2 or 3

In an incremental approach of time step dt we determine an appropriate prescribed displacement where the non-penetration inequality is used to just bring a or some material points to be in contact with the rigid surface :

$$du_n - dg_n + d_n \leq 0 \qquad \text{on Sc} \qquad (5)$$

where du_n is the increment of the normal displacement constrained by the given rigid surface motion dg_n . To resolve this boundary constraint we apply the exterior penalty method :

$$df_n = -k_n(du_n - dg_n) \qquad \text{on Sc} \qquad (6)$$

with a large penalty parameter $k_n \rangle 0$. The point will stay in contact as long as the resultant contact pressure f_n update by its material increment df_n remains negative. We assume that there exists a Coulomb friction law so that no relative motion is observed if :

$$|f_t| \langle \mu |f_n| \qquad (7)$$

Thus an same relation that (6) holds between the tangential increment of the friction force and the tangential tangential of the displacement :

$$df_t = -k_t(du_t - dg_t) \qquad \text{on Sc} \qquad (8)$$

When the state of stress of a contact point is such that :

$$|f_t| = \mu |f_n| \quad \text{and} \quad |df_t| = \mu |df_n| \qquad (9)$$

the point is said to be sliding and (8) gives the consistent tangential penalty parameter as :

$$k_t = \mu |df_n| / |du_t - dg_t| \qquad (10)$$

The contact condition and the Coulomb's friction law are statisfied in a integrated sense over each individual contact element side (upper and lower surface) consistent with the level of finite element shape functions used . The friction forces can then be determined using the quantities available in the course of the iteration process and contribute via the penalty parameters to the applied loads and to the stiffness matrix of the system (Brunet et al., 1993).

4 Solution

Our method to analyse the roll-cold forming is to have a bimensional resolution in cross section coupled with a tridimensional resolution in the surface between two roll-stands (Ronel et al., Giens 1995). The curved surface is discretised with 4 nodes quadrilateral Mindlin element shell and 5 liberty degrees. Therefore the same family of element is used in cross section analysis with 2 nodes and 3 liberty degrees. The longitudinal strains calculed in

surface are reintroducted in the cross section calcul. The Boundery conditions imposed incrementally to the surface are the cross-sectional deformed on the two roll-stands between this surface.This model is based on the plane stress hypothesis and the thickness variations negliged. In forming problems where large membrane strain are present , thickness variation has to be take account by the constitutive equations. The extension to the complete large strain cases requires an objective formulation of classical small strain constitutive relations . This simply achieve by using an rotating frame formalism where the stress and strain state variables tensors are replaced by their rotated tensors by un objective rotation R :

$$\overline{\sigma} = R^T.\sigma.R \quad \text{and} \quad \overline{\varepsilon} = R^T.\varepsilon.R \tag{11}$$

In order to integrate the elastoplastic relations the rotating frame formalism simply requires following the rotation R for all elements and making the appropiate rotation but taken in the state at the middle of the total displacement icrement to evaluate the rotated tensors of strain and stress (Brunet et al., U.K. 1994). We use the elastic predictor-radial corrector implicit algorithm in the rotating frame to integrate the constitutive relations and many authors have demonstrated the overall superiority of this method over others algorithms.

5 Numerical examples

We tested this method with several complex cross-sectional design, and these presented on figure 1 and 2 are industrial ones.

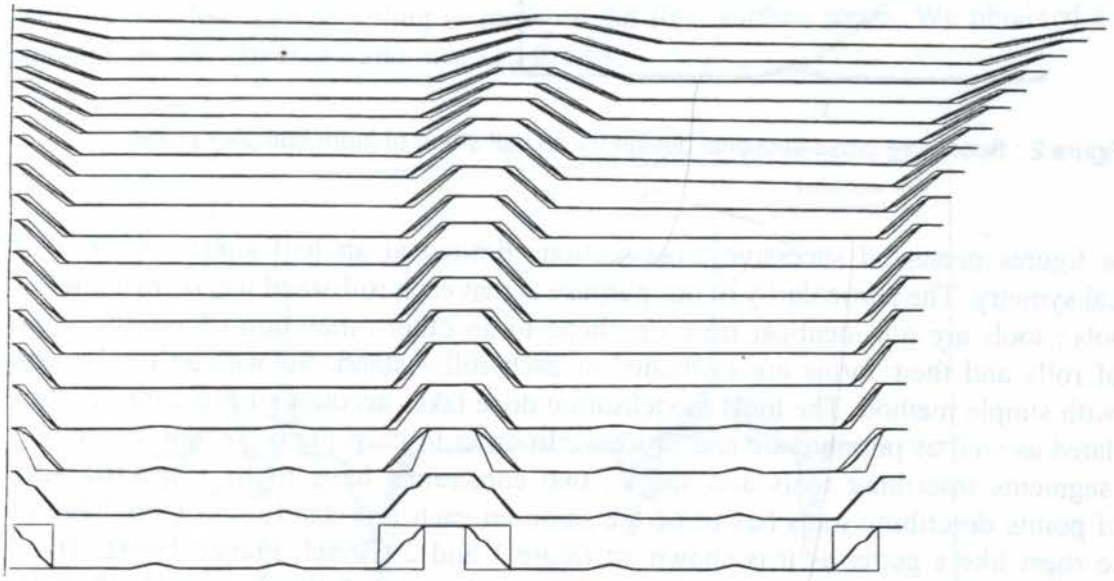

Figure 1 : Succesive cross-sectional design for an half sheet of industrial profil

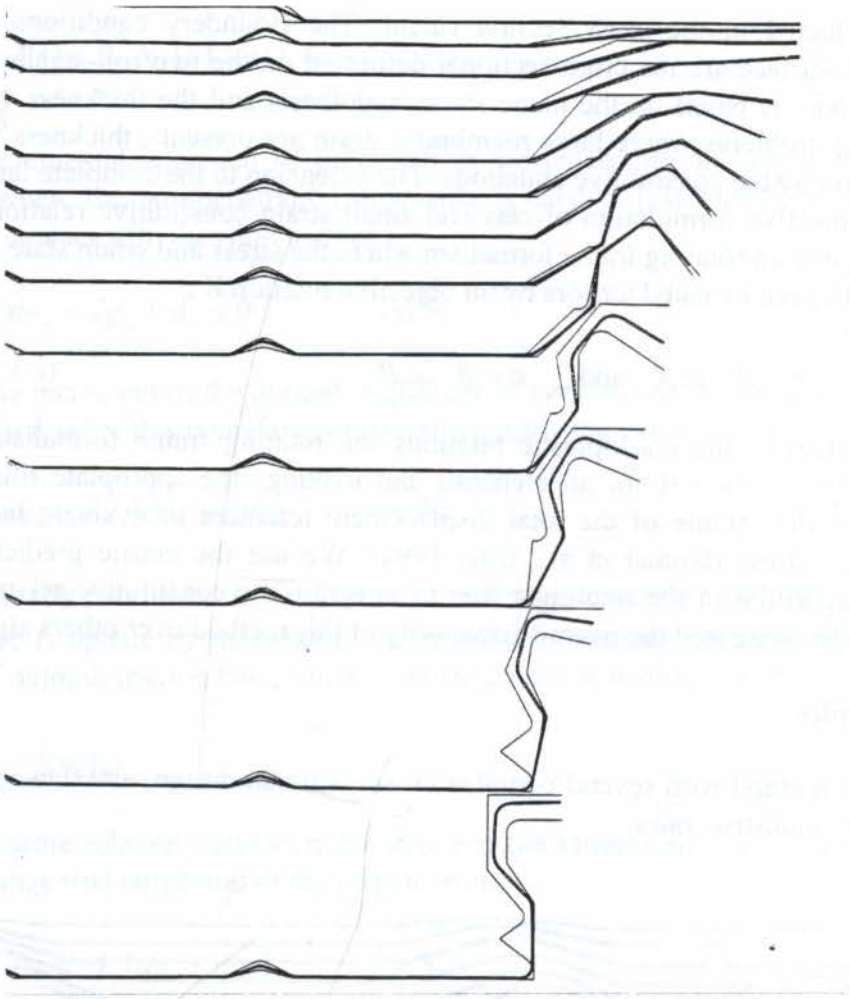

Figure 2 : Succesive cross-sectional design for an half sheet of more complex profile

This figures presented sucessive cross-sections limited at an half sheet because of geometrical symetry. The particularity of our purpuse is that each roll-stand has is own kind of rolling tools ; tools are not identical from one head to an other : they don't have the same number of rolls and their forms are evoluated at each roll - stand. So we can't solve the problem with simple method. The tools modelisation done takes account all this caracteristics and simulated as well as possible the real process . In order to keep the projection continuity between segments inscribing tools and sheet , two constraints have to be respected : the number of points describing tools has to be the same on each roll-stand , and tools have to follow the sheet like a gutter as it is shown on figure 1 and 2 (Ronel, France 1994). Tools description of a head has to take account heads before and prepare following heads : the roll-stand segments discretisation has to be finest on the non linear section because this is the zones where the contact and the forming will be. If we want to have the same number of description points , every rounds have to be declared at each head with a fine description.

The passage from a cross-section to the next one is done with an incremental polynomial interpolation of every intermediary successive points.

By the above mentioned method of 2D and 3D, numerical calculations were made about forming process on a half-wave of profil shown figure 1 :

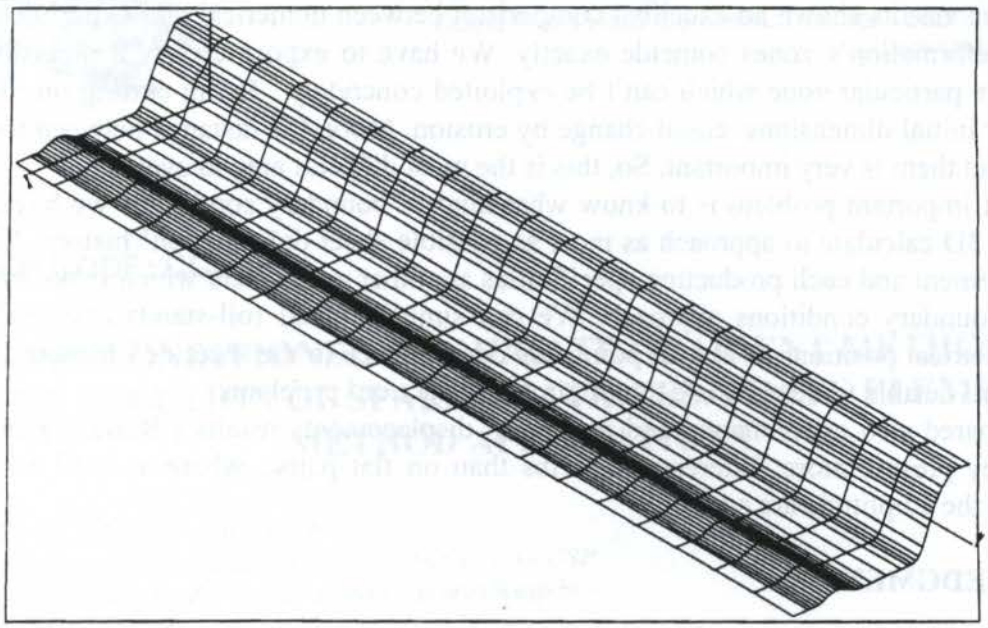

Figure 3 - Deformed meshes 3D of an half-wave of the profil figure 1

Figure 4 shows the calculated and experimental measure cross-section bottom strains on the final form profile (half-wave) shown in figure 1. Experimentaly, a square grid has been deposed on the sheet before rolling to measure the final surface strain. We obtained a good agreement between calculated and measure strains.

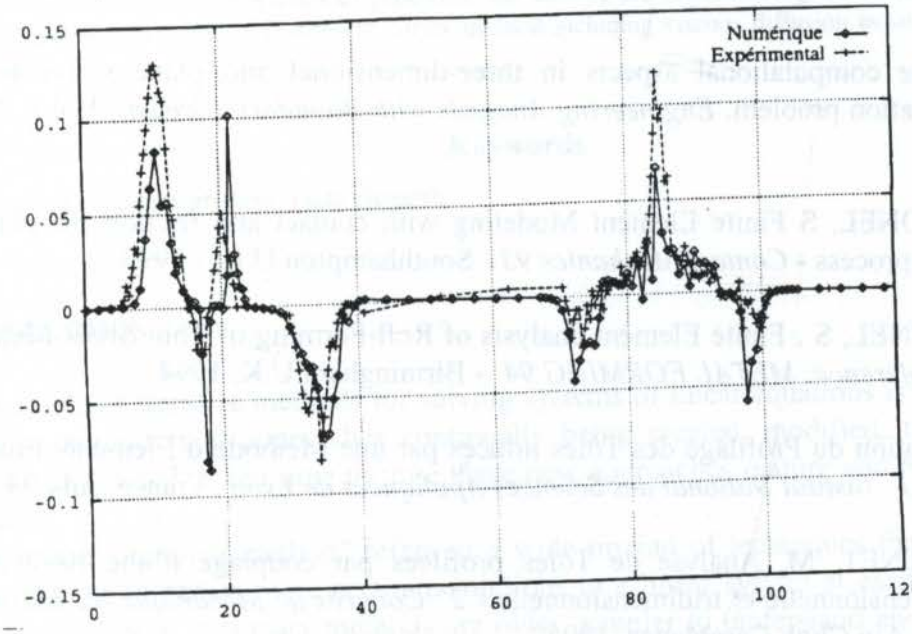

Figure 4 -Final cross-section bottom strain

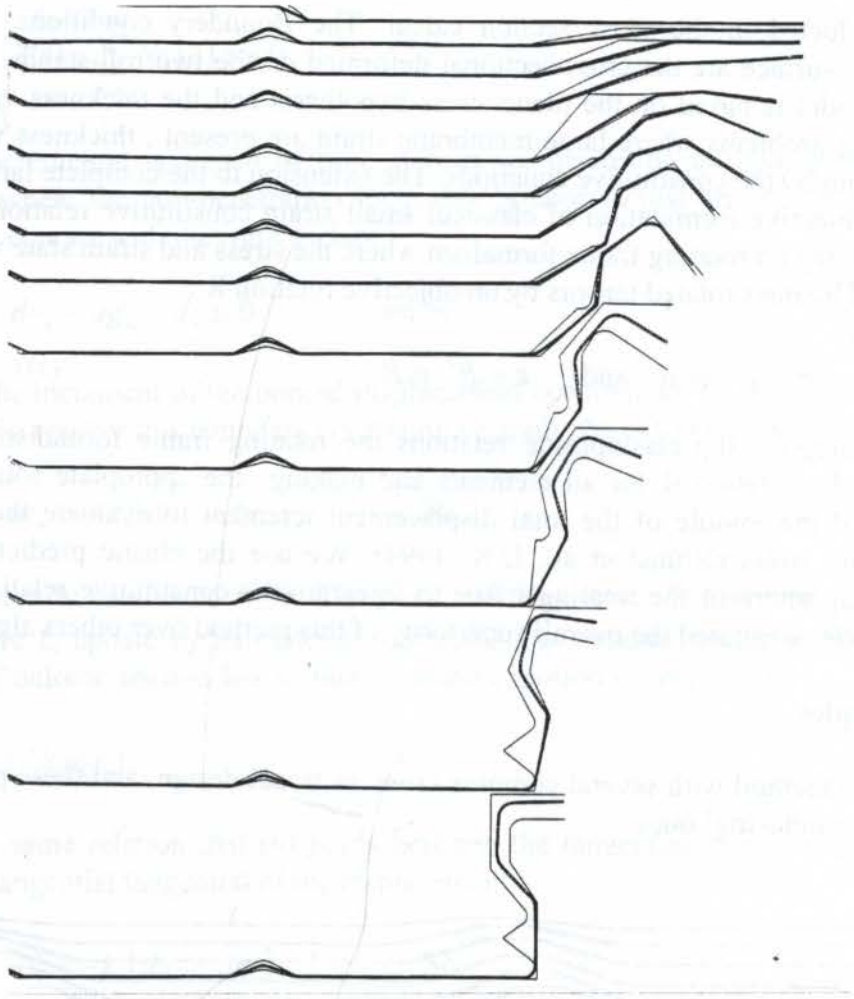

Figure 2 : Succesive cross-sectional design for an half sheet of more complex profile

This figures presented sucessive cross-sections limited at an half sheet because of geometrical symetry. The particularity of our purpuse is that each roll-stand has is own kind of rolling tools ; tools are not identical from one head to an other : they don't have the same number of rolls and their forms are evoluated at each roll - stand. So we can't solve the problem with simple method. The tools modelisation done takes account all this caracteristics and simulated as well as possible the real process . In order to keep the projection continuity between segments inscribing tools and sheet , two constraints have to be respected : the number of points describing tools has to be the same on each roll-stand , and tools have to follow the sheet like a gutter as it is shown on figure 1 and 2 (Ronel, France 1994). Tools description of a head has to take account heads before and prepare following heads : the roll-stand segments discretisation has to be finest on the non linear section because this is the zones where the contact and the forming will be. If we want to have the same number of description points , every rounds have to be declared at each head with a fine description.

The passage from a cross-section to the next one is done with an incremental polynomial interpolation of every intermediary successive points.

By the above mentioned method of 2D and 3D, numerical calculations were made about forming process on a half-wave of profil shown figure 1 :

The strains results shown an excellent comparison between numerical and experimental study. Large deformation's zones coincide exactly. We have to expose clearly a precision : ribs constitute a particular zone which can't be exploited concretely . Being cutting on tools geometry, their initial dimensions could change by erosion. More, the distance between tools and sheet around them is very important. So, this is the most difficult area to evaluate.

The most important problem is to know what kind of boundary conditions we have to declare for the 3D calculate to approach as most as possible sheet deformation' history. Real machine' ajustement and each production specificities are other parameters which make more difficult this boundary conditions approach. We can simulate ideal roll-stands and see by changing geometrical positions of certain points the consequence in the sheet deformation. By this way, we will be able to determinate the origin of production' problems.

We compared also experimental and numerical displacements results (Ronel , France 1994) and they present more differences on ribs than on flat parts , where as well as the global form as the amplitude are correct.

6 ACKNOWLEDGMENT

This work was realised in close collaboration with the 'Laboratoire de Mécanique des Solides ' de l'Institut National des Sciences Appliquées de Lyon, more precisely Pr M. BRUNET.

This work was realised thanks to the 'Institut Universitaire de Formation des Maîtres' des Antilles et de la Guyane which financed our travels to go in our French Laboratory .

7 REFERENCES

BRUNET, M A finite element method for unilateral contact and friction problem involving finite strain and large displacment. *Journal of Theoretical and Applied Mech.* Vol 7 209-220, 1988.

BRUNET, M Some computational aspects in three-dimensional and plane stress finite elastoplastic deformation problem. *Engineering Analysis with Boundary Element*, Vol 6, N°2 78-83, 1989

BRUNET, M & RONEL, S Finite Element Modeling with contact and friction for planes strain sheet forming process - *Contact Mechanics 93* - Southhampton U.K. - 1993

BRUNET, M & RONEL, S . Finite Element analysis of Roll-Forming of Thin Sheet Metal - *5° international Conference 'METAL FORMING 94'* - Birmingham U.K. 1994

RONEL, S Modélisation du Profilage des Tôles minces par une Méthode d'Elements Finis - *Thèse de doctorat Sci : Institut National des Sciences Appliquées de Lyon* , France, July 94

RONEL, S & BRUNET, M. Analyse de Tôles profilées par couplage d'une résolution éléments finis bidimensionnelle et tridimensionnelle - *2° Congrés de Mécanique du Maroc* - Faculté des Sciences Ain Chok Casablanca ,1995

RONEL, S & BRUNET, M . Etude tridimensionnelle du Processus de mise en forme par Profilage - *2° Colloque National en Calcul de Structures* - Giens - France - 1995

XIV Brazilian Congress of Mechanical Engineering
Obeid Plaza Hotel Convention Center - Bauru - SP/Brazil
December 08-12th 1997

PAPER CODE: COB182

THE PRECONDITIONED CONJUGATE GRADIENT METHOD FOR THE SOLUTION OF SPARSE MATRICES: FINITE ELEMENT METHOD APPLICATIONS

CESAREO DE LA ROSA SIQUEIRA
Naval Engineering Department, University of São Paulo - USP
CEP: 05508-900 São Paulo, Brazil - E-mail: cesareo@usp.br
JULIO R. MENEGHINI
Mechanical Engineering Department, University of São Paulo -USP
CEP: 05508-900 São Paulo, Brazil - E-mail: jmeneg@usp.br

Abstract

This paper presents the Preconditioned Conjugate Gradient Method (PCG) for the solution of sparse matrices and its application in the Finite Element Method. The Preconditioned Conjugate Gradient Method was implemented for the solution of a heat transfer problem in an unstructured mesh. The stiffness matrix generated by the Finite Element Method is sparse and banded. The results obtained for a conduction problem were in very good agreement with the analytical results. The performance of PCG is also compared with the unpreconditioned version of the algorithm in terms of CPU time for different computer platforms. This result is of practical importance when dealing with transient problems where saving time is essential as so many iterations are involved. As an example of this class of problems, the authors are implementing the method to study vortex shedding phenomenon using a 2D discrete vortex method including viscous diffusion in an unstructured finite element mesh.

Keywords

Preconditioned conjugate gradient, finite elements.

1. INTRODUCTION

The field of iterative methods for solving systems of linear equations is in constant flux, with new methods and approaches continually being created, modified, tuned, and some eventually discarded. From time to time these new approaches mature and become the state-of-the-art.

The term "iterative method" refers to a wide myriad of techniques that use successive approximations to obtain more accurate solutions to a linear system at each step. Following Barrett *et al.*(1992), stationary methods are older, simpler to understand and implement, but usually not as effective. Nonstationary methods are a recent development; their analysis is usually harder to understand, but they can be highly effective. They differ from stationary methods in a way that the computations involve information that changes at each iteration. Typically, constants are computed by taking inner products of residuals, or other vectors

arising from the iterative method. An example of this class of iterative methods is the Preconditioned Conjugate Gradient method, which is, generally speaking, based on the idea of constructing sequences of orthogonal vectors.

The rate at which an iterative method converges depends greatly on the spectrum of the coefficient matrix. Therefore, iterative methods usually involve a second matrix that transforms the coefficient matrix into one with a more favourable spectrum. This transformation matrix is called a *preconditioner*. The use of a good preconditioner improves the convergence of the iterative method, sufficiently to overcome the extra cost of constructing and applying the preconditioner. Regarding efficiency purposes, a particular point should be stressed here: without a preconditioner the iterative method may even fail to converge.

In this work a preconditioned version of the Conjugate Gradient Method was employed for a solution of a sparse system of linear equations and applied to a heat transfer problem with Finite Element Method formulation. It is well known that the coefficient stiffness matrix generated by the Finite Element Method is sparse and banded, becoming an excellent test case for proving the algorithm efficiency.

2. THE PRECONDITIONED CONJUGATE GRADIENT METHOD

A system of linear equations is called sparse if only a relatively small number of its matrix elements are nonzero. So far, it is wasteful to use general methods of linear algebra on such problems, because most of the $O(N^3)$ arithmetic operations devoted to solving the set of equations or inverting the matrix involve zero operands. Furthermore, it will be interesting to work problems so large as to tax the available memory space, and it does not seem convenient to reserve storage for unfruitful zero elements. Note that are two distinct (and not always compatible) goals for any sparse matrix method: saving time and/or saving space.

The **Conjugate Gradient Method (CG)** provides a quite general means for solving the N x N linear system

$$\mathbf{A} \cdot \mathbf{x} = \mathbf{b} . \qquad (1)$$

As can be seen in Press *et al.*(1992), the attractiveness of this method for large sparse systems is that they reference **A** only through its multiplication of a vector, or the multiplication of its transpose and a vector. These operations can be very efficient for a properly stored sparse matrix. Consequentially, storing only the upper or lower part of the coefficient matrix (only nonzero elements) is the most interesting way to face up such task.

Following Golub and Loan(1989), a difficulty associated with other numerical methods like SOR (successive over relaxation), Chebyshev semi-iterative, and related methods is that they depend upon parameters that are sometimes hard to choose properly. For instance, for Chebyshev method to be successful one needs good estimates of the largest and smallest eigenvalue of the underlying iteration matrix $\mathbf{M}^{-1}\ \mathbf{N}$. Unless this matrix is sufficiently structured, this may be analytically impossible and/or computationally expensive.

The conjugate gradient method is an effective method for symmetric positive definite systems and guarantees a solution in at most n iterations (with 'exact' arithmetic). The method proceeds by generating vector sequences of iterates, i.e. successive approximations to the solution, residuals corresponding to the iterates, and search directions used in updating the iterates and residuals. Although the length of these sequences can become large, only a small number of vectors needs to be kept in memory. In every iteration of the method, two inner products are performed in order to compute update scalars that are defined to make the

sequences satisfy certain orthogonality conditions. On a symmetric positive definite linear system these conditions imply that the distance to the true solution is minimized in some norm.

Following Barrett *et al.*(1992), the iterates $x^{(i)}$ are updated in each iteration by a multiple (α_i) of the search direction $p^{(i)}$:

$$x^{(i)} = x^{(i-1)} + \alpha_i p^{(i)} . \quad (2)$$

Correspondingly the residuals $r^{(i)} = b - A x^{(i)}$ are updated as

$$r^{(i)} = r^{(i-1)} - \alpha q^{(i)} , \quad (3)$$

where $q^{(i)} = A p^{(i)}$. (4)

The choice $\alpha = \alpha_i = r^{(i)T} r^{(i)} / p^{(i)T} A p^{(i)}$ minimizes $r^{(i)^T} = A^{-1} r^{(i)}$ over all possible choices for α in equation (3).

The search directions are updated using the residuals

$$p^{(i)} = r^{(i)} + \beta_{i-1} p^{(i-1)}, \quad (5)$$

where the choice $\beta_i = r^{(i)^T} r^{(i)} / r^{(i-1)^T} r^{(i-1)}$ ensures that $p^{(i)}$ and $A p^{(i-1)}$ - or equivalently - $r^{(i)}$ and - $r^{(i-1)}$ - are orthogonal. It can be demonstrated that this choice of β_i makes $p^{(i)}$ and $r^{(i)}$ orthogonal to all previous $A p^{(j)}$ and $r^{(j)}$ respectively.

The pseudocode for the **Preconditioned Conjugate Gradient Method (PCG)** is given in figure 1. It uses a preconditioner **M**; for **M** = **I** one obtains the unpreconditioned version of the Conjugate Gradient Method Algorithm. In that case the algorithm may be further simplified by skipping the "solve line", and replacing $z^{(i-1)}$ by $r^{(i-1)}$ (and $z^{(0)}$ by $r^{(0)}$). In the Conjugate Gradient method two coupled two-term recurrences are used; one that updates residuals using a search direction vector, and one updating the search direction with a newly computed residual. This makes the CG method quite attractive computationally. Details can be found in Barret *et al.*,(1992).

The preconditioned version of the method uses a different subspace for constructing the iterates when compared to the unpreconditioned method. Nevertheless, it satisfies the same minimization property. It also requires that the preconditioner **M** is symmetric and positive definite. As can be found in Golub and Van Loan(1989), the conjugate gradient method works well on matrices that are either well conditioned or have just a few distinct eigenvalues (the case when **A** is a low rank perturbation of matrix identity).

In devising a preconditioner, one is faced with a choice between finding a matrix **M** that approximates **A**, and for which solving a system is easier than solving one with **A**, or finding a matrix **M** that approximates $\mathbf{A}^{-1}$, so that only multiplication by **M** is needed. The majority of preconditioners falls in the first category.

In this paper the **Diagonal Scalling** was employed, which improved convergence rates dramatically. This was suggested by Arkell(1997) in a private communication and consists of taking as preconditioner the diagonal of the coefficient matrix **A**.

Compute $r^{(0)} = b - A x^{(0)}$ for some initial guess $x^{(0)}$

for $i = 1, 2, ...$

solve $M z^{(i-1)} = r^{(i-1)}$

$\rho_{i-1} = r^{(i-1)^T} z^{(i-1)}$ (inner product)

if $i = 1$

$p^{(i)} = z^{(0)}$

else

$\beta_{i-1} = \rho_{i-1} / \rho_{i-2}$

$p^{(i)} = z^{(i-1)} + \beta_{i-1} p^{(i-1)}$

endif

$q^{(i)} = A p^{(i)}$ (matrix-vector product)

$\alpha_i = \rho_{i-1} / \left(p^{(i)^T} q^{(i)} \right)$ (inner product)

$x^{(i)} = x^{(i-1)} + \alpha_i p^{(i)}$

$r^{(i)} = r^{(i-1)} - \alpha\ q^{(i)}$

check convergence; continue if necessary

end

Figure 1. The Preconditioned Conjugate Gradient Method (Barrett *et al.*, 1992).

3. FINITE ELEMENT METHOD APPLICATION

In order to apply the Preconditioned Conjugate Gradient Method, a particular two-dimensional problem is chosen using Finite Element Method formulation. The problem to be considered is that of solving the now familiar equation for the steady-state heat conduction in two dimensions,

$$\frac{\partial}{\partial x}\left(k\frac{\partial \phi}{\partial x}\right) + \frac{\partial}{\partial y}\left(k\frac{\partial \phi}{\partial y}\right) + Q = 0 \quad \text{in}\,\Omega, \tag{6}$$

with standard boundary conditions

$$\begin{aligned} \phi &= \bar{\phi} \quad \text{in}\,\Gamma_\phi \\ k\frac{\partial \phi}{\partial n} &= -\bar{q}\ \text{in}\,\Gamma_q \end{aligned} \tag{7}$$

where $\Gamma_\phi + \Gamma_q = \Gamma$.

The Finite Element Method formulation for this kind of problem will be presented considering that triangles are used for the domain discretisation. Indeed, the triangle is a particularly useful shape for any two-dimensional analysis, as assemblies of triangles can easily be used to represent accurately regions enclosed by boundaries of quite complex shape.

For a typical triangular element e, with nodes numbered anticlockwise as i, j, k, and placed at the vertices of the triangle, the linear form of the shape function N_i^e is given by

$$N_i^e = \alpha_i^e + \beta_i^e x + \gamma_i^e y. \tag{8}$$

The constants in this expression are determined by making $N_i^e(x_i, y_i) = 1$ e $N_i^e(x_j, y_j) = N_i^e(x_k, y_k) = 0$, where the nodal coordinates are specified by positioning of the nodes in the domain subdivision process. So far, we have

$$\alpha_i^e = \frac{x_j y_k - x_k y_j}{2\Delta^e}, \quad \beta_i^e = \frac{y_j - y_k}{2\Delta^e}, \quad \gamma_i^e = \frac{x_k - x_j}{2\Delta^e}, \tag{9}$$

where Δ^e is the area of element e.

Following Zienkiewicz and Morgan(1983), the unknown function ϕ (in this case, the temperature) in the usual element form is given by

$$\phi \cong \hat{\phi} = \sum_{m=1}^{M} \phi_m N_m . \tag{10}$$

It can be seen that the boundary condition on Γ_ϕ can be satisfied immediately at the nodes which lie on Γ_ϕ by specification of the appropriate nodal values ϕ_m.

The weak form of the weighted residual statement, using the trial functions themselves as weighting functions (The Galerkin Method), is given by

$$\int_\Omega \left(\frac{\partial N_l}{\partial x} k \frac{\partial \hat{\phi}}{\partial x} + \frac{\partial N_l}{\partial y} k \frac{\partial \hat{\phi}}{\partial y} \right) dx\, dy = \int_\Omega Q N_l \, dx\, dy - \int_{\Gamma_q} \bar{q} N_l \, d\Gamma , \quad l = 1, 2, 3, \ldots M. \tag{11}$$

Inserting the approximation of equation (10) leads to the standard equation system, where the Preconditioned Conjugate Gradient is employed

$$\mathbf{K}\phi = \mathbf{f}, \tag{12}$$

in which the components of the matrices **K** and **f** are determined by summing the individual element contributions

$$K_{lm}^e = \int_{\Omega^e} \left(\frac{\partial N_l^e}{\partial x} k \frac{\partial N_m^e}{\partial x} + \frac{\partial N_l^e}{\partial y} k \frac{\partial N_m^e}{\partial y} \right) dx\, dy , \tag{13}$$

$$f_l^e = \int_{\Omega^e} Q N_l^e dx\, dy - \int_{\Gamma_q^e} N_l \bar{q} \, d\Gamma . \tag{14}$$

In the equations above Ω^e is the area of element e and Γ_q^e is that portion of the element boundary which lies on, or approximates to, a portion of Γ_q.

3.1 Test case

The test case to be considered is that of solving the steady-state heat conduction in a rectangular plate with prescribed temperatures at the boundary nodes (Dirichlet boundary condition type). Furthermore, neither heat flux is present at the boundaries nor heat generation inside the domain ($Q = \overline{q} = 0$ in equation 14). In the upper side of the plate the nodal temperature distribution is given by a function with position dependence

$$T = T_m \operatorname{sen}\left(\frac{\pi x}{W}\right) + T_1 \tag{15}$$

where T_m = 150 °C , T_1 = 30 °C, W=1.0 (side plate length). The remaining three sides have a nodal temperature of T_1.

The domain was divided in 3526 triangles (1842 nodes) through an unstructured mesh generator developed by Auada(1997) based on the Advance Front Method. Figure 2 shows the domain discretisation.

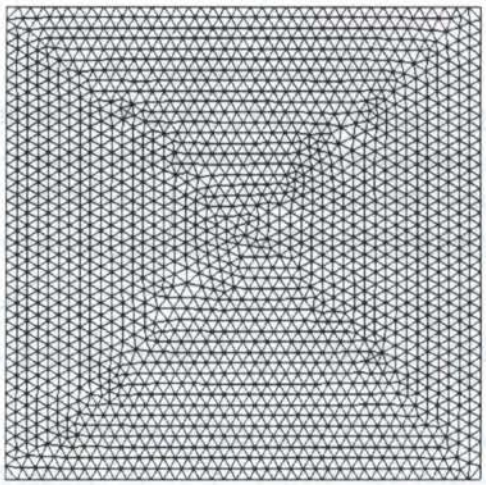

Figure 2. Domain discretisation for the heat conduction problem in a rectangular plate through the Advancing Front Method (Auada, 1997).

The number of unknowns in this problem (1686) corresponds to the internal nodes temperatures risen from the assembly process of matrix **K** in equation (12). The matrix **K** is sparse and banded, a major characteristic of the matrices found in the Finite Element Method. The Preconditioned Conjugate Gradient Method was applied to solve this linear system of equations and the results are given next.

Holman(1983) gives the nodal temperature distribution (analytical results) for the case considered here through Fourier analysis. For a rectangular plate with same specified boundary conditions, the temperature distribution is

$$T = T_m \frac{\operatorname{senh}(\pi\, y / W)}{\operatorname{senh}(\pi\, H / W)} \operatorname{sen}\left(\frac{\pi\, x}{W}\right) + T_1 \tag{16}$$

where x and y are the nodal coordinates.

3.2 Results and concluding remarks

In this section the results of the heat conduction problem are given with the conditions discussed previously. Figure 3 shows the temperature distribution obtained by solving the linear system through the Preconditioned Conjugate Gradient method with Diagonal Scalling.

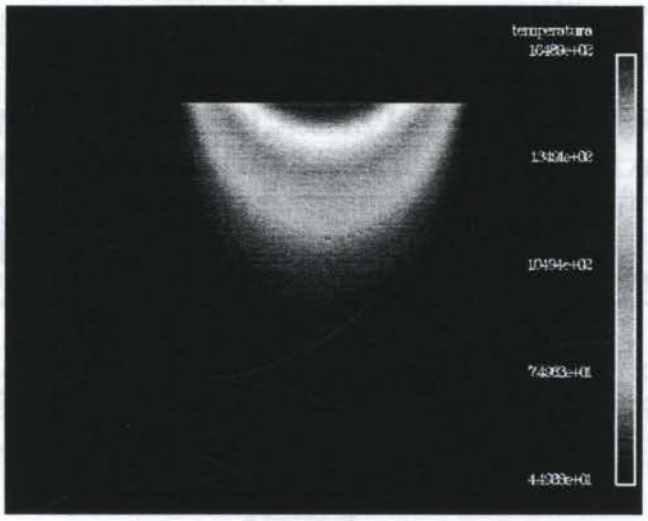

Figure 3. Temperature distribution for the heat conduction problem employing the Preconditioned Conjugate Gradient Method in an unstructured Finite Element mesh.

The numerical results are in very good agreement with those obtained by the analytical method given by Holman(1983). The comparison was performed at each node of the domain and the maximum error between the numerical and the analytical result was 0.0954%. This number was obtained at node number 123, located near the upper side of the plate.

Another interesting point that is treated in this paper is the Preconditioned Conjugate Gradient method efficiency regarding convergence achievement. In this way, a comparison between an unpreconditioned version of the method and the preconditioned one is performed in order to obtain the CPU time spent when solving the linear system assembled in the heat transfer analysis. For this task, two different workstations were used. The first one is a SparcStation 20 with 80MB memory and the other a Dec Alpha Station 600 5/266 with 128MB of memory. It can be seen analysing the figure 4 which contains the performance comparison how fast is the Preconditioned Conjugate Gradient method to converge the solution when compared to the unpreconditioned version. The difference is specially considerable (about 10 times faster) when running the program in a SparcStation 20. This result is of practical importance when dealing with transient problems where saving time is essential as so many iterations are involved. As an example, the authors are implementing the method to study vortex shedding phenomenon using a 2D discrete vortex method including viscous diffusion in an unstructured finite element mesh. In this method the solution of the stream function and the diffusion equation of vorticity are modelled with the Finite Element method similarly to the one presented in this paper.

Following Arkell(1997), even the cheap, simple preconditioner of Diagonal Scaling improves convergence rates dramatically and the greater the difference in mesh sizes (locally) the greater the influence of the preconditioner. Although, the diagonal scaling preconditioner has no effect on the convergence rate of a problem consisting of regular, same size elements.

Another type of preconditioner that can be used is the ICCG - incomplete Cholesky factorisation which is often a popular choice, but it is not as simple as the Diagonal Scalling regarding implementation procedures. Details can be found in Barret *et al.*(1992).

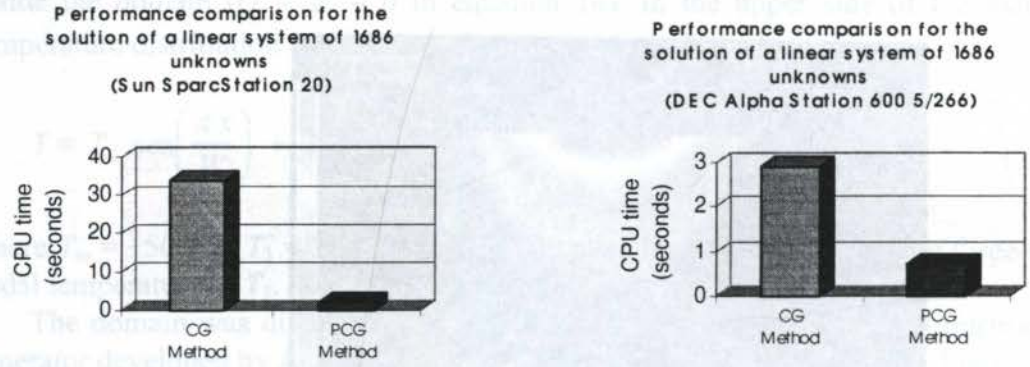

Figure 4. Performance comparison regarding convergence achievement for the heat conduction problem in a rectangular plate.

4. ACKNOWLEDGEMENTS

The authors are grateful to FAPESP (grant 94/3057-0 and 94/3528-3) and PETROBRAS (Brazilian Oil Company) for providing them a Research Grant for this project.

5. REFERENCES

Arkell, Richard H., private communication, 1997.

Arkell, Richard H., *Wake dynamics of cylinders encountering free surface gravity waves,* PhD Thesis, Imperial College of Science, Technology and Medicine, Department of Aeronautics, London, UK, 1995.

Auada, R. B., *Utilização de malhas não-estruturadas em dinâmica dos fluidos computacional.* Master thesis, Escola Politécnica, University of São Paulo, 1997.

Barrett, Richard *et al.*, *Templates for the solution of linear systems: building blocks for iterative methods*, 1992.

Golub, G. H., and Van Loan, C. F., *Matrix Computations*, 2nd ed. Baltimore: Johns Hopkins University Press, chapter 10, 1989.

Holman, J. P. *Transferência de Calor*, Editora McGraw-Hill do Brasil, 1983.

Press, William H., Flannery, Brian P., Teukosky, Saul A . Vetterling, William T., *Numerical Recipes*, Cambridge Press, 1992.

Zienkiewicz O. C. and Morgan K., *Finite Elements and Approximation*, University of Wales, United Kingdom, John Wiley & Sons, 1983.

XIV Brazilian Congress of Mechanical Engineering
Obeid Plaza Hotel Convention Center - Bauru - SP/Brazil
December 08-12th 1997

PAPER CODE: COB194

ANÁLISE DINÂMICA DE PLACAS E CASCAS ATRAVÉS DE ELEMENTOS FINITOS QUADRILATERAIS QUADRÁTICOS COM INTEGRAÇÃO NUMÉRICA CONSISTENTE / *DYNAMIC ANALYSIS OF PLATES AND SHELLS THROUGH QUADRILATERAL QUADRATIC FINITE ELEMENTS WITH CONSISTENT NUMERICAL INTEGRATION*

AMARILDO TABONE PASCHOALINI, LOIR AFONSO MOREIRA & FERNANDO IGUTI
Departamento de Engenharia Mecânica, Faculdade de Engenharia - UNESP/FEIS
CEP 15.385-000 Ilha Solteira, Brasil - E-mail: tabone@feis.unesp.br

Abstract

The purpose of this work is a comparative performance study of plates and shells dynamic analysis, considering *consistent numerical integration*, of the Serendipity and Lagrangean isoparametric quadrilateral quadratic finite element families, obtained both from the *Ahmad*'s formulation; one intends to establish, between both elements, which is the most adequate to start the development of a *subparametric hierarchical element*, based on the *p* mesh refinement concept, intending to remove the excessive rigidity characteristic of the *Ahmad*'s element for thin plates and shells problems. One could notice from the obtained results that the Lagrangean family element has a consistently better performance than the Serendipity family element, particularly for thin plates and shells problems.

Keywords

Finite Elements Method, Numerical Integration, Structural Analysis, Shell, Plate.
Método dos elementos finitos, Integração numérica, Análise estrutural, Casca, Placa.

1. INTRODUÇÃO

Ahmad et al. (1970) apresentaram uma formulação para a análise de placas e cascas baseada na degeneração de um elemento sólido tridimensional através da redução de sua dimensão na direção da espessura. O campo de deslocamento era, então, interpolado a partir das funções de forma da família Serendipity e, para a obtenção das características do elemento, utilizava-se *integração numérica consistente*. Os resultados obtidos por este elemento foram excelentes para situações de placas e cascas moderadamente espessas, atendendo, portanto, à teoria de *Mindlin-Reissner*; contudo, com a redução da espessura, o elemento tornava-se excessivamente rígido e os resultados não tendiam àqueles da teoria clássica de *Kirchhoff* para placas e cascas finas. A partir de então, um grande número de autores tem estudado este elemento e feito suas propostas para melhorar seu comportamento. Com a introdução da *Técnica de Integração Reduzida*, proposta por *Zienkiewicz et al.* (1971), conseguiu-se uma melhora considerável no desempenho do elemento para as aplicações de placas e cascas finas. Neste caso, para a obtenção da matriz de rigidez, ao invés de (3×3), utilizam-se (2×2) pontos de integração na superfície média, caracterizando, desta forma, o que se convencionou chamar de *integração reduzida*. A utilização da integração reduzida mostrou

resultados notáveis para as situações de placas e cascas finas. Para o elemento de *Zienkiewicz*, consideram-se, também, as funções de forma da família Serendipity com 8 nós na superfície média, conforme mostra a Figura 1-a.

O objetivo deste trabalho é o estudo comparativo, na análise dinâmica de placas e cascas, entre o desempenho, utilizando-se *integração numérica consistente*, do elemento finito isoparamétrico quadrilateral quadrático da família Serendipity e o elemento finito isoparamétrico quadrilateral quadrático da família Lagrangiana, obtido, também, da degeneração do elemento sólido tridimensional (formulação de *Ahmad*), mas que considera 9 nós na superfície média, como mostra a Figura 1-b.

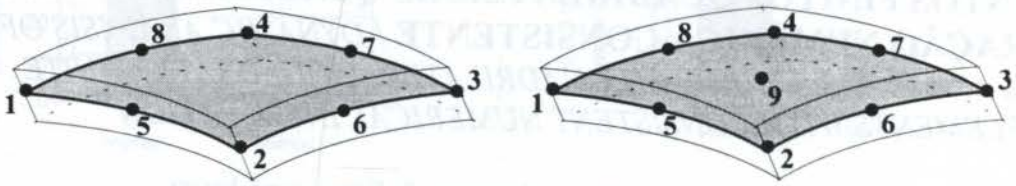

Figura 1 - Elementos de casca das famílias Serendipity (a) e Lagrangiana (b).

Embora o elemento da família Lagrangiana tenha um número maior de graus de liberdade, a Figura 2 mostra que a expansão polinomial correspondente a este elemento também gera um polinômio completo de segundo grau (Fig. 2-b) da mesma forma que o elemento da família Serendipity (Fig. 2-a). O elemento da família Lagrangiana tem, entretanto, mais termos parasíticos do que o elemento da família Serendipity. Pretende-se, ainda, com este trabalho, verificar a influência dos termos parasíticos na taxa de convergência dos dois elementos.

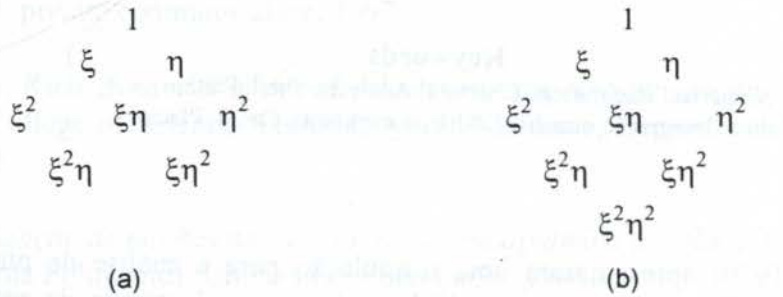

Figura 2 - Expansões polinomiais obtidas a partir dos elementos finitos quadrilaterais quadráticos das famílias Serendipity (a) e Lagrangiana (b).

2. CAMPO DE DESLOCAMENTO

De acordo com *Ahmad et al.* (1970), o campo de deslocamento do elemento de casca é interpolado a partir das funções de forma $N_i(\xi,\eta)$ quadráticas da família Serendipity e é dado por:

$$\vec{\Delta}(\xi,\eta,\zeta) = \sum_{i=1}^{8} N_i(\xi,\eta)\,\vec{\delta}_i + \zeta \cdot \sum_{i=1}^{8} N_i(\xi,\eta) \cdot \frac{t_i}{2}\,\vec{v}_{1i} \cdot \alpha_i - \zeta \cdot \sum_{i=1}^{8} N_i(\xi,\eta) \cdot \frac{t_i}{2}\,\vec{v}_{2i} \cdot \beta_i \qquad (1)$$

Quando se consideram as funções de forma $N_i(\xi,\eta)$ quadráticas da família Lagrangiana, o campo de deslocamento é dado por:

$$\vec{\Delta}(\xi,\eta,\zeta)=\sum_{i=1}^{9}N_i(\xi,\eta)\,\vec{\delta}_i+\zeta\cdot\sum_{i=1}^{9}N_i(\xi,\eta)\cdot\frac{t_i}{2}\vec{v}_{1i}\cdot\alpha_i-\zeta\cdot\sum_{i=1}^{9}N_i(\xi,\eta)\cdot\frac{t_i}{2}\vec{v}_{2i}\cdot\beta_i \tag{2}$$

Se u, v e w são, respectivamente, as componentes do deslocamento $\vec{\Delta}(\xi,\eta,\zeta)$ nas direções X, Y e Z de um sistema de referência global associado ao elemento de casca e, da mesma maneira, u_i, v_i e w_i, as componentes do deslocamento $\vec{\delta}_i$, v_{11i}, v_{12i} e v_{13i}, as componentes do vetor $\vec{v}_{1i}$ e v_{21i}, v_{22i} e v_{23i}, as componentes do vetor $\vec{v}_{2i}$, as equações anteriores podem ser reescritas na seguinte forma matricial:

$$\{u\}=[N]\cdot\{a\} \tag{3}$$

onde, $\{u\}$ é uma matriz coluna (3×1), constituída dos deslocamentos $u(\xi,\eta,\zeta), v(\xi,\eta,\zeta)$ e $w(\xi,\eta,\zeta)$, $[N]$ é uma matriz (3×40), para o elemento da família Serendipity e (3×45), para o elemento da família Lagrangiana, constituída das funções de forma $N_i(\xi,\eta)$ e $\{a\}$ é uma matriz coluna (40×1), para o elemento da família Serendipity e (45×1), para o elemento da família Lagrangiana, constituída dos deslocamentos nodais: u_i, v_i, w_i, α_i e β_i.

3. DETERMINAÇÃO DAS MATRIZES DE RIGIDEZ E DE MASSA DO ELEMENTO

De acordo com as hipóteses básicas da teoria de placa e casca (*Timoshenko et al.* ,1959) e em função da solicitação do elemento, um seu ponto genérico vai apresentar, segundo o sistema de referência local (x', y', z'), a ele associado, o seguinte estado de deformação específica:

$$\begin{Bmatrix}\varepsilon_{x'}\\ \varepsilon_{y'}\\ \gamma_{x'y'}\\ \gamma_{y'z'}\\ \gamma_{x'z'}\end{Bmatrix}=\begin{bmatrix}\frac{\partial}{\partial x'} & 0 & 0\\ 0 & \frac{\partial}{\partial y'} & 0\\ \frac{\partial}{\partial y'} & \frac{\partial}{\partial x'} & 0\\ 0 & \frac{\partial}{\partial z'} & \frac{\partial}{\partial y'}\\ \frac{\partial}{\partial z'} & 0 & \frac{\partial}{\partial x'}\end{bmatrix}\cdot\begin{Bmatrix}u'\\ v'\\ w'\end{Bmatrix} \tag{4}$$

ou ainda,

$$\{\varepsilon'\}=[L]\cdot\{u'\} \tag{5}$$

onde $\{u'\}$ corresponde aos deslocamentos segundo o sistema de referência local e $[L]$ é um operador diferencial linear. Os deslocamentos $\{u'\}$ podem ser dados em função dos deslocamentos globais $\{u\}$ de acordo com a seguinte expressão:

$$\{u'\}=[\theta]^T\cdot\{u\} \tag{6}$$

sendo que $[\theta]$ é uma matriz (3×3) constituída dos cossenos diretores do sistema de referência local com relação ao sistema de referência global. Desta forma, pode-se escrever que:

$$\{\varepsilon'\}=[L]\cdot[\theta]^T\cdot\{u\}=[L]\cdot[\theta]^T\cdot[N]\cdot\{a\} \tag{7}$$

Chamando-se de $[B]$ a matriz que relaciona as deformações específicas com os deslocamentos e as rotações nodais, tem-se que:

$$[B] = [L] \cdot [\theta]^T \cdot [N] \tag{8}$$

Aplicando-se, agora, o "Princípio dos Trabalhos Virtuais" e o "Princípio de D'Alembert" determinam-se as matrizes de rigidez e de massa do elemento:

$$[K^e] = \int_{-1}^{1}\int_{-1}^{1}\int_{-1}^{1} [B]^T \cdot [D'] \cdot [B] \cdot |J(\xi,\eta)| \cdot d\xi\, d\eta\, d\zeta \tag{9}$$

$$[M^e] = \rho \cdot \int_{-1}^{1}\int_{-1}^{1}\int_{-1}^{1} [N]^T \cdot [N] \cdot |J(\xi,\eta)| \cdot d\xi \cdot d\eta \cdot d\zeta \tag{10}$$

onde $[K^e]$ e $[M^e]$ são matrizes quadradas, simétricas, de ordem (40×40), para o elemento da família Serendipity e (45×45), para o elemento da família Lagrangiana; $[D']$ é uma matriz quadrada (5×5), simétrica, constituída das constantes elásticas do material e $|J(\xi,\eta)|$, o jacobiano da transformação de coordenadas global-local.

5. EXEMPLOS DE APLICAÇÃO

Apresentam-se, a seguir, os resultados obtidos a partir dos elementos isoparamétricos quadrilaterais quadráticos das famílias Serendipity e Lagrangiana com *integração numérica consistente*. Os resultados se referem à análise dinâmica de placas e cascas, utilizando-se diversas configurações de condições de contorno, relações *t/a* (entre espessura e dimensão característica) e malhas de discretização regular (Fig. 3) e distorcida (Fig. 4).

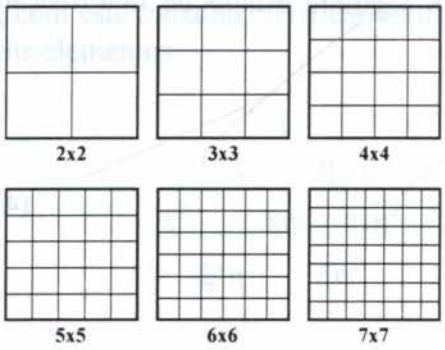

Figura 3 - Malha regular.

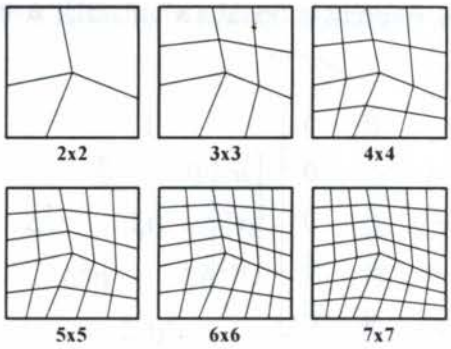

Figura 4 - Malha distorcida.

Estes resultados são comparados com aqueles obtidos através de outras formulações disponíveis na literatura, como também, com resultados obtidos a partir de soluções analíticas.

Ainda, com o intuito de se estudar a sensibilidade dos elementos quanto à distorção de malha, foram utilizadas malhas de discretização regulares (SER3x3 e LAG3x3) e, também, malhas de discretização distorcidas (SER3x3D e LAG3x3D).

As malhas distorcidas empregadas foram adaptadas com base naquelas propostas por *MacNeal* e *Harder* (1985).

5.1. Placa Quadrada SESL

Uma placa quadrada com as condições de contorno SESL (simplesmente apoiada, engastada, simplesmente apoiada e livre) foi analisada. Em função da geometria e para se obter as curvas de convergência (Fig. 5 e Fig. 6), a placa foi modelada com malhas de

discretização regulares e distorcidas de 2x2, 3x3, 4x4, 5x5, 6x6 e 7x7 elementos. Foram calculadas as seis primeiras freqüências naturais para os dois elementos em análise e esses resultados comparados com os obtidos analiticamente por *Dawe* e *Roufaeil* (1979) para t/a=0,01 (placa fina) e t/a=0,1 (placa moderadamente espessa). Foram obtidos também os seis primeiros modos de vibrar e apresentados na Figura 7.

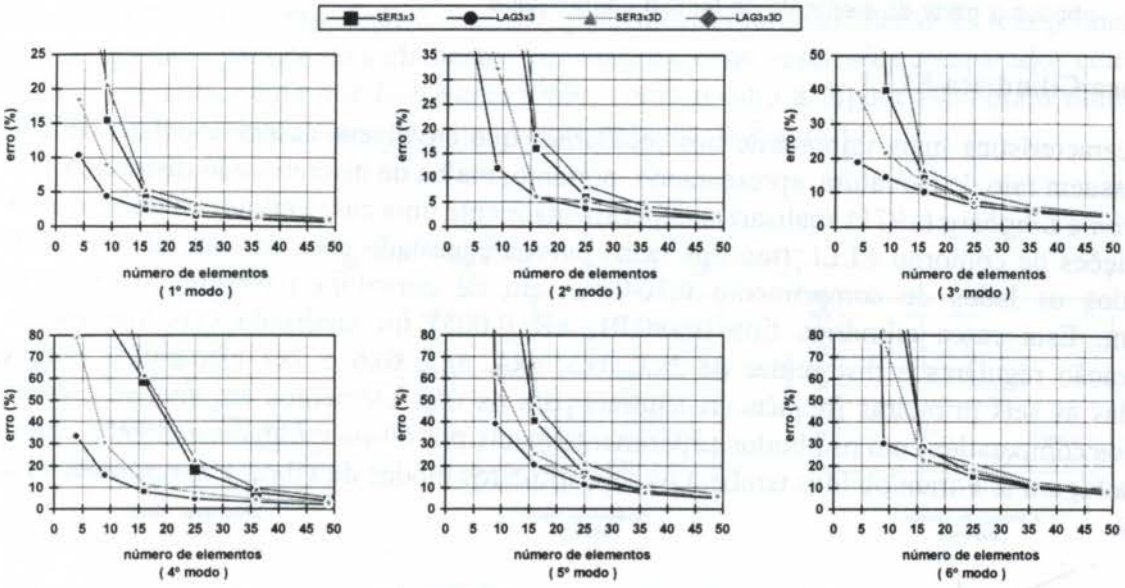

Figura 5 - Curvas de convergência para os elementos em análise utilizando malhas regulares (SER3x3 e LAG3x3) e distorcidas (SER3x3D e LAG3x3D) para placa quadrada SESL com t/a=0,01.

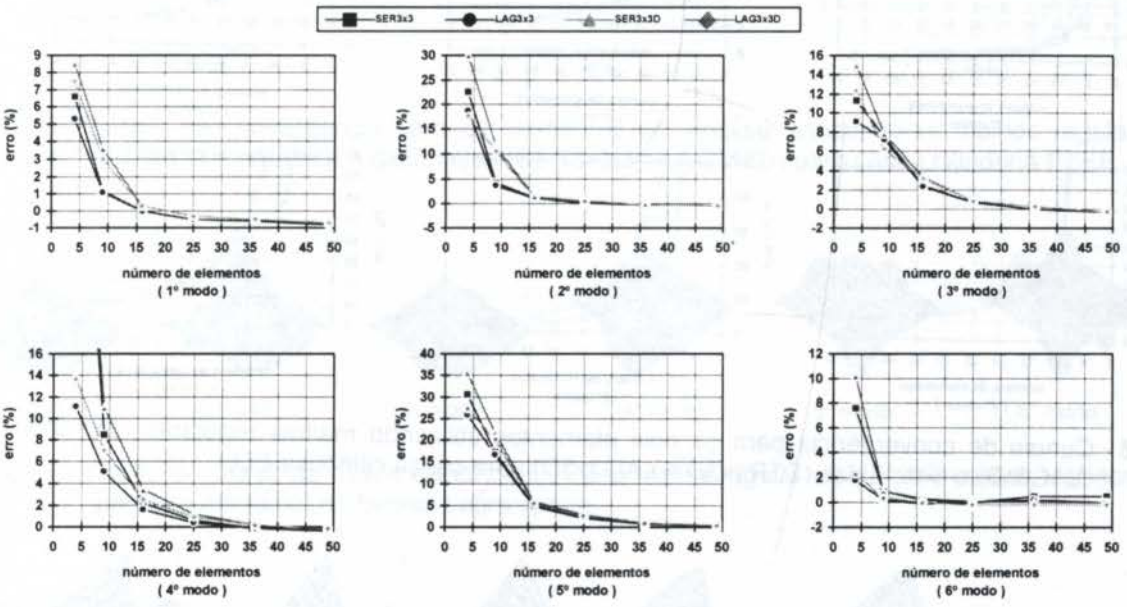

Figura 6 - Curvas de convergência para os elementos em análise utilizando malhas regulares (SER3x3 e LAG3x3) e distorcidas (SER3x3D e LAG3x3D) para placa quadrada SESL com t/a=0,1.

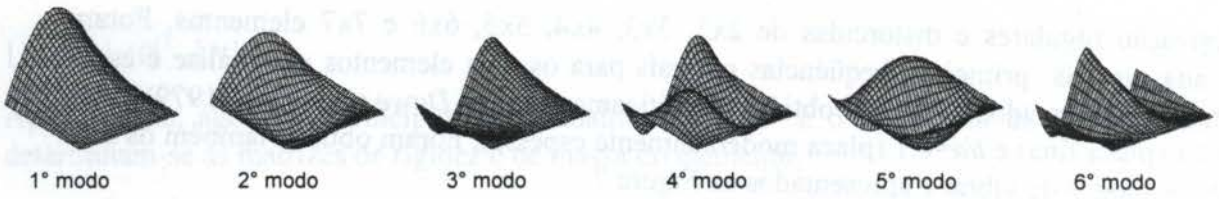

Figura 7 - Modos de vibrar da placa quadrada SESL com *t*/*a*=0,01 e malha regular de 7x7 elementos, obtidos a partir do elemento da família Lagrangiana.

5.2. Casca Cilíndrica ELLL

A característica mais importante nos problemas que envolvem cascas é o fato de que estas possuem raio de curvatura, apresentando, portanto, malha de discretização distorcida.

Olson e *Lingberg* (1971) analisaram experimentalmente uma casca cilíndrica de aço, com as condições de contorno ELLL (um dos lados curvos engastado e os demais lados livres), com todos os lados de comprimento 0,3048m, raio de curvatura 0,6096m e espessura 3,048mm. Esta casca cilíndrica fina (*t*/a=0,01, *t*/R=0,005) foi analisada com malhas de discretização regulares e distorcidas de 2x2, 3x3, 4x4, 5x5, 6x6 e 7x7 elementos. Foram calculadas as seis primeiras freqüências naturais para os dois elementos em análise e esses resultados comparados com os obtidos experimentalmente por *Olson* e *Lingberg* (1971), como mostra a Figura 8. Foram obtidos também os seis primeiros modos de vibrar e apresentados na Figura 9.

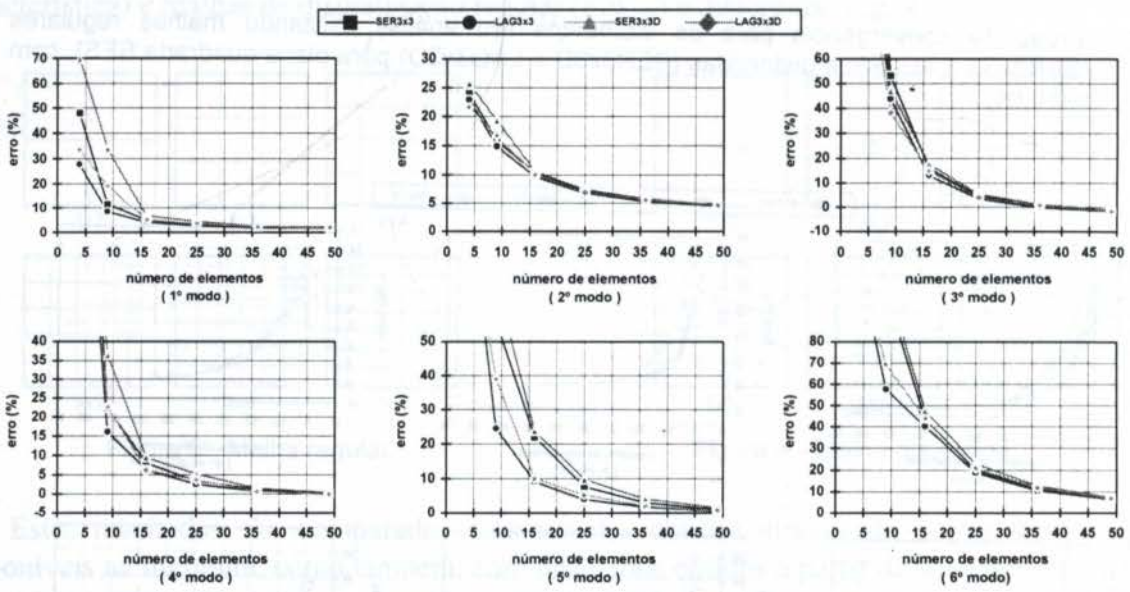

Figura 8 - Curvas de convergência para os dois elementos utilizando malhas regulares (SER3x3 e LAG3x3) e distorcidas (SER3x3D e LAG3x3D) para casca cilíndrica ELLL.

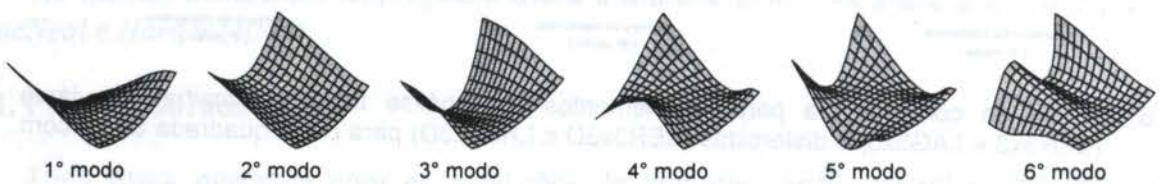

Figura 9 - Modos de vibrar da casca cilíndrica ELLL, malha regular de 7x7 elementos, obtidos a partir do elemento da família Lagrangiana.

5.3 Casca Cilíndrica EEEE

Deb Nath (1969) analisou experimentalmente uma casca cilíndrica com as condições de contorno EEEE (todos lados engastados), com os lados curvos iguais a 101,6mm e os demais lados 76,2mm, raio de curvatura 762,0mm, espessura 0,33mm, módulo de elasticidade $6{,}89 \times 10^{10}$ N/m^2, densidade $2{,}66 \times 10^3$ Kg/m^3 e coeficiente de Poisson 0,33. Esta casca cilíndrica fina (t/a=0,003, t/R=0,0004) foi analisada com malhas de discretização regulares e distorcidas de 2x2, 3x3, 4x4, 5x5, 6x6 e 7x7 elementos. Foram calculadas as seis primeiras freqüências naturais para os dois elementos em análise e esses resultados comparados com os obtidos experimentalmente por *Deb Nath* (1969), como mostra a Figura 10. Foram obtidos, também, os seis primeiros modos de vibrar e apresentados na Figura 11.

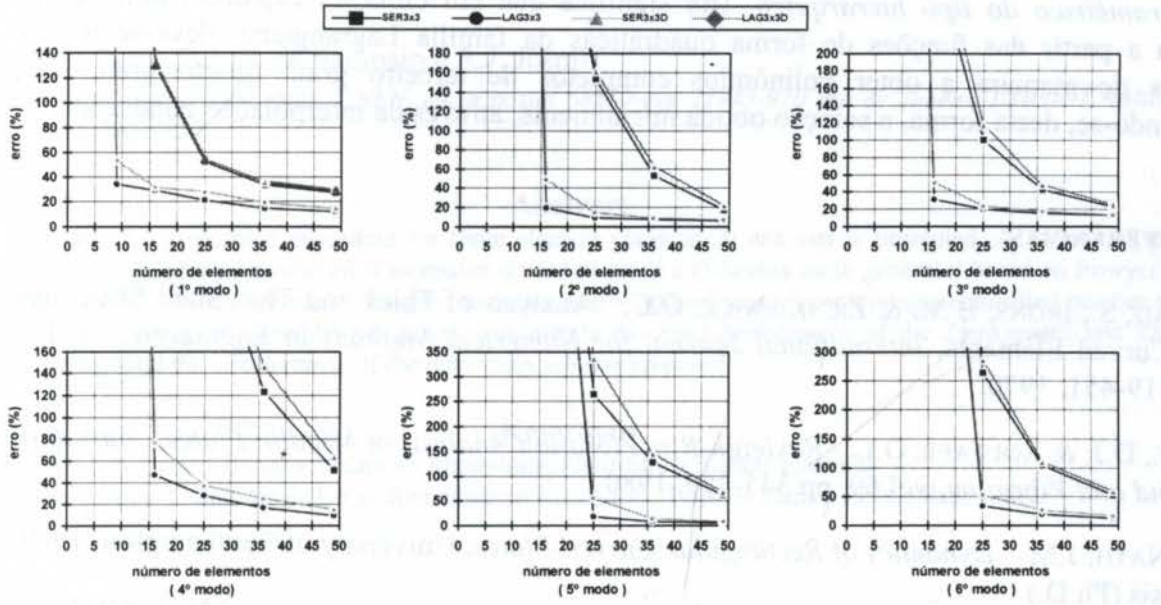

Figura 10 - Curvas de convergência para os elementos em análise, utilizando-se malhas regulares (SER3x3 e LAG3x3) e distorcidas (SER3x3D e LAG3x3D) para casca cilíndrica EEEE.

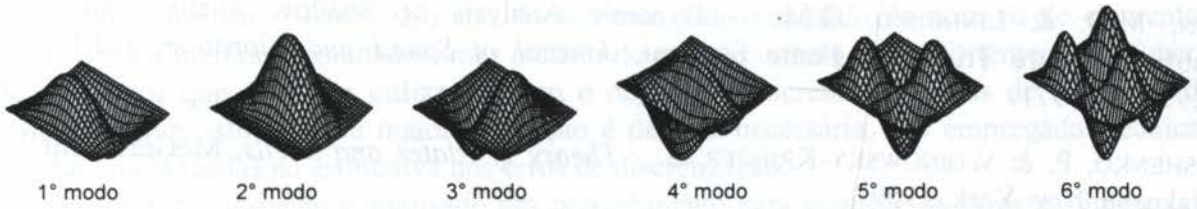

Figura 11 - Modos de vibrar da casca cilíndrica EEEE e malha regular de 7x7 elementos, obtidos a partir do elemento da família Lagrangiana.

6. CONCLUSÕES

Verifica-se a partir dos resultados obtidos nos exemplos anteriores, que o *elemento da família Lagrangiana* apresentou um desempenho consistentemente melhor que o *elemento da família Serendipity*, principalmente, para situações de placas e cascas finas, considerando-se tanto malhas de discretização regulares como distorcidas. Constatou-se, também, que, quanto

mais severas as condições de contorno impostas (por exemplo, todos os lados engastados), a convergência se torna mais lenta, mas sempre, obtendo-se melhores resultados para o *elemento da família Lagrangiana*, em comparação com os obtidos para o *elemento da família Serendipity*. Nota-se, ainda, que mesmo tendo a expansão polinomial correspondente ao elemento da família Lagrangiana um maior número de termos parasíticos a sua taxa de convergência é melhor.

Pode-se verificar, também, que os resultados obtidos pelos elementos em análise para situações de placas moderadamente espessas são excelentes (convergência rápida) e com a redução da espessura, situações de placa fina, a convergência se torna mais lenta em função do elemento apresentar um aumento excessivo de sua rigidez (*Zienkiewicz et al.*, 1971). Desta forma, com o objetivo de retirar essa característica de rigidez excessiva do elemento de *Ahmad*, para situações de placas e cascas finas, pode-se estabelecer que o *elemento da família Lagrangiana* é o mais apropriado para iniciar o desenvolvimento de um *elemento finito subparamétrico do tipo hierárquico*. Isto significa que em cima da expansão polinomial, obtida a partir das funções de forma quadráticas da família Lagrangiana, deve-se inserir termos de maneira a obter polinômios completos de terceiro grau, quarto grau, etc., refinando-se, desta forma, a solução obtida inicialmente, através da interpolação quadrática.

7. REFERÊNCIAS

AHMAD, S., IRONS, B.M. & ZIENKIEWICZ, O.C. Analysis of Thick and Thin Shell Structures by Curved Elements, *International Journal for Numerical Methods in Engineering,* vol.3, pp.419-451, 1970.

DAWE, D.J. & ROUFAEIL O.L. *Rayleigh-Ritz Vibration Analysis of Mindlin Plates*, *Journal of Sound and Vibration,* vol.69, pp.345-359, 1980.

DEB NATH, J.M. *Dynamics of Rectangular Curved Plates*. University of Southampton, 1969, Thesis (Ph.D.).

MACNEAL, H. & HARDER, R. L., A Proposed Standard Set of Problems to Test Finite Element Accuracy, *Finite Elements in Analysis and Design*, vol.1, pp.3-20, 1985.

OLSON, M.D. & LINDBERG, G.M. Dynamic Analysis of Shallow Shells with a Doubly-Curvature Triangular Finite Element, *Journal of Sound and Vibration*, vol.19, pp.299-318, 1971.

TIMOSHENKO, P. & WOINOWSKY-KRIEGER, S. *Theory of Plates and Shells*, McGraw-Hill Kogakusha, New York, 1959.

ZIENKIEWICZ, O.C., TOO, J. &. TAYLOR, R.L. Reduced Integration Technique in General Analysis of Plates and Shells, *International Journal for Numerical Methods in Engineering,* vol.3, pp.375-390, 1971.

XIV Brazilian Congress of Mechanical Engineering
Obeid Plaza Hotel Convention Center - Bauru - SP/Brazil
December 08-12th 1997

PAPER CODE: COB358

MALHAS ADAPTATIVAS DE ELEMENTOS FINITOS: APLICAÇÃO À ANÁLISE DE TENSÕES EM ELASTICIDADE BIDIMENSIONAL / *ADAPTIVE FINITE ELEMENT MESHES: APPLICATION TO STRESS ANALYSIS IN TWO-DIMENSIONAL ELASTICITY*

D.E.de Sá Nery, P.A.B. de Sampaio e R.J. Jospin
Instituto de Engenharia Nuclear /CNEN, caixa postal 68550 cep 21945-970 Rio de Janeiro-Brasil-E-mail: reinaldo@cnen.gov.br

Abstract

An adaptive remeshing procedure for finite element plane stress analysis is presented. A variant of the Zienkiewicz and Zhu *a posteriori* error estimator is used to guide a Delaunay mesh generator based on Bowyer's algorithm. The remeshing scheme is designed to create nearly optimal meshes containing a controlled number of elements. The numerical examples presented demonstrate the good performance of the Zienkiewicz and Zhu error estimator and the effectiveness of the remeshing scheme proposed.

Keywords

Finite Elements, Error Estimator, Adaptive Remeshing, Plane Stress, Linear Elasticity
Elementos Finitos, Estimador de Erros, Remalhagem Adaptativa, Tensões Planas, Elasticidade Linear

1. INTRODUÇÃO

A aplicação do método dos elementos finitos ao caso de tensões planas pode conduzir a previsões pouco realistas para as tensões quando a malha utilizada não acompanha de forma adequada o problema físico analisado. O aumento indiscriminado do número de elementos finitos leva a melhores resultados, mas o custo do processamento limita fortemente o número de elementos que pode ser utilizado. Com o objetivo de acrescentar graus de liberdade de forma seletiva, isto é, onde maior resolução é de fato necessária, são empregadas técnicas adaptativas baseadas na estimativa dos erros de discretização.

No presente trabalho é analisado um procedimento para controle de erros e aumento de precisão na avaliação de tensões planas usando-se o estimador de erros *a posteriori*, desenvolvido por Zienkiewicz e Zhu (Zienkiewicz et al., 1987). É utilizado um gerador de malhas do tipo Delaunay-Bowyer (Bowyer, 1981), que acoplado ao estimador de erros, permite criar as malhas refinadas.

2. TENSÕES PLANAS-ESTIMATIVA DO ERRO DAS TENSÕES

Na formulação variacional clássica de elementos finitos, quando são utilizados elementos triangulares lineares com continuidade C^0, as tensões discretizadas $\hat{\mathbf{T}}$ obtidas são constantes no interior dos elementos apresentando descontinuidades entre elementos finitos adjacentes.

Genericamente o erro associado à discretização pode ser escrito $\mathbf{E} = \mathbf{T}^{ex} - \hat{\mathbf{T}}$, onde $\mathbf{T}^{ex}$ é o tensor das tensões exatas e $\hat{\mathbf{T}}$ (constante no interior de cada elemento) é o tensor das tensões obtidas da análise elástica discretizada. O erro irá variar ao longo do domínio, sendo maior nos locais onde a malha usada não permite uma boa descrição do campo de tensões que está sendo aproximado.

O número de elementos finitos em uma análise é necessariamente limitado. Assim, dada uma certa quantidade de elementos, deseja-se reduzir os erros por meio de uma remalhagem na qual a malha resultante acompanhe melhor o campo de tensões. Considera-se aqui como malha ótima aquela na qual os erros se distribuem uniformemente sobre todo o domínio.

Para estimar o erro não é necessário o conhecimento da tensão exata, mas será suficiente que se tenha uma estimativa dela, baseada em uma aproximação melhor do que $\hat{\mathbf{T}}$.

Seja $\mathbf{T}^*$ o tensor correspondente a uma melhor aproximação das tensões exatas do que a representada por $\hat{\mathbf{T}}$. Esta melhor aproximação $\mathbf{T}^*$ pode ser obtida, se o campo de tensões for interpolado com as mesmas funções de interpolação usadas para os deslocamentos e determinando-se os valores nodais das tensões por um ajuste de mínimos quadrados de $\mathbf{T}^*$ a $\hat{\mathbf{T}}$ (Zienkiewicz et al., 1987). Para a estimativa dos erros é necessário quantificar $\mathbf{T}^*$ e $\hat{\mathbf{T}}$. Em geral o erro será: $\mathbf{E}^* = \mathbf{T}^* - \hat{\mathbf{T}}$. O erro $\mathbf{E}^*$ será representado daqui por diante, simplesmente por $\mathbf{E}$. Por conveniência, propõe-se neste trabalho utilizar um indicador de erro baseado numa medida escalar para as tensões, E

$$E^2 = tr\,\mathbf{E}\mathbf{E}^{\mathrm{T}} = E_{xx}^2 + E_{yy}^2 + 2E_{xy}^2 \tag{1}$$

onde tr representa o traço. As componentes cartesianas de $\mathbf{E}$ são:

$$E_{xx} = T_{xx}^* - \hat{T}_{xx}\,,\quad E_{yy} = T_{yy}^* - \hat{T}_{yy} \qquad \text{e} \qquad E_{xy} = T_{xy}^* - \hat{T}_{xy} \tag{2}$$

O erro no domínio Ω do problema será

$$\|e\|_{\Omega}^2 = \int_{\Omega} E^2 d\Omega \tag{3}$$

e no sub domínio Ω_i de um elemento i, genérico,

$$\|e\|_{\Omega_i}^2 = \int_{\Omega_i} E^2 d\Omega_i \tag{4}$$

Considerando uma triangulação usual de elementos finitos tem-se que $\bigcup_i \overline{\Omega}_i = \overline{\Omega}$, (i=1,...,m) e $\Omega_i \bigcap \Omega_j = \phi$, para $i \neq j$, de modo que o erro no domínio relaciona-se com os erros nos elementos de acordo com a equação 5, onde m é o número de elementos finitos.

$$\|e\|_{\Omega}^2 = \sum_{i=1}^{m} \|e\|_{\Omega_i}^2 \tag{5}$$

A partir desta equação, o erro médio por elemento $\overline{e}_m$ pode ser definido:

$$\bar{e}_m = \frac{\|e\|_\Omega}{\sqrt{m}} \tag{6}$$

Pode-se também definir o erro relativo η pela equação 7. A qualidade da solução será: $Q = 1 - \eta$.

$$\eta = \left(\frac{\|e\|_\Omega^2}{\|\hat{t}\|_\Omega^2 + \|e\|_\Omega^2} \right)^{\frac{1}{2}} \tag{7}$$

onde:

$$\|\hat{t}\|_\Omega^2 = \int_\Omega \left(\hat{T}_{xx}^2 + \hat{T}_{yy}^2 + 2\,\hat{T}_{xy}^2 \right) d\Omega \tag{8}$$

3. REFINAMENTO ADAPTATIVO

O esquema de refinamento é baseado na idéia de gerar uma nova malha de tal modo que o erro se distribua uniformemente entre os novos elementos. Isto exige a definição de um erro visado por elemento e leva a estratégias alternativas de refinamento. No trabalho de Zienkiewicz et al. (1987), o erro visado por elemento é definido em função da fixação pelo usuário do erro relativo $\overline{\eta}$ que representa a qualidade desejada para a análise. Este enfoque mantém o nível de erro aproximadamente constante em toda a malha não havendo entretanto controle do número de elementos gerados, número este que pode ser excessivo em alguns casos. Será usada aqui uma estratégia diferente, proposta por De Sampaio et al. (1996), na qual é permitido ao nível de erro se ajustar durante a análise em função do número máximo de elementos determinado pelo usuário.

Suponha que começando um esquema de remalhagem com uma malha grosseira com m elementos, possa ser obtida uma malha refinada com m_1 elementos, tal que $m_1 > m$. Suponha ainda que a malha refinada seja ótima no sentido que os erros se distribuam igualmente entre os m_1 elementos. Então, usando a equação 6, a relação entre os erros médios por elemento medidos nas duas malhas será:

$$\frac{\bar{e}_{m_1}}{\bar{e}_m} = \frac{\sqrt{m}\|e_1\|_\Omega}{\sqrt{m_1}\|e\|_\Omega} \tag{9}$$

Notando-se que o erro do domínio na malha ótima refinada $\|e_1\|_\Omega$ é menor do que na malha grosseira, $\|e\|_\Omega$, conclui-se que:

$$\frac{\bar{e}_{m_1}}{\bar{e}_m} = \frac{\sqrt{m}}{\sqrt{m_2}} \qquad \text{para algum } m_2 > m_1 \tag{10}$$

Assim, o seguinte erro visado por elemento será escolhido para a remalhagem

$$\bar{e}_t = \sqrt{\frac{m}{m_2}}\,\bar{e}_m \qquad (11)$$

onde m_2 é o número máximo de elementos prescrito pelo usuário, m é o número de elementos na malha atual e $\bar{e}_m$ é o erro médio por elemento medido na malha atual.

Para o elemento linear usado aqui será assumido que os erros individuais dos elementos são proporcionais aos tamanhos dos elementos. Como tamanho típico de um elemento é usada aqui a altura de um triângulo equilátero de mesma área. Pode-se então definir a nova distribuição de tamanhos de elemento necessária para se atingir um erro visado $\bar{e}_t$ em cada elemento da nova malha.

A nova distribuição de tamanhos pode ser expressa em termos dos tamanhos e dos erros dos elementos da malha atual e do erro visado uniforme para a nova malha, como:

$$h_i^{k+1} = h_i^k \frac{\bar{e}_t}{\|e\|_{\Omega_i}} \qquad \text{para } i = 1,\ldots,m \qquad (12)$$

onde k+1 e k denotam a malha nova e atual respectivamante.

A equação 12 fornece uma distribuição descontínua de tamanhos de elementos para a nova malha, que é contudo definida na malha atual. O gerador de malhas utilizado neste trabalho exige que a distribuição de tamanhos dos elementos seja contínua e definida nos nós de uma malha de base. Assim tal como foi feito para as tensões, pode-se interpolar os tamanhos usando-se as mesmas funções de interpolação dos deslocamentos procedendo-se então a um ajuste de mínimos quadrados dos tamanhos nos nós, aos tamanhos constantes nos elementos à semelhança do que foi feito para as tensões.

4. EXPERIMENTO NUMÉRICO 1: PLACA INFINITA COM UM FURO CIRCULAR NO CENTRO

Para uma avaliação do indicador de erros é necessária uma comparação do mesmo com o erro real . O erro real só pode ser computado quando a solução analítica exata é conhecida.

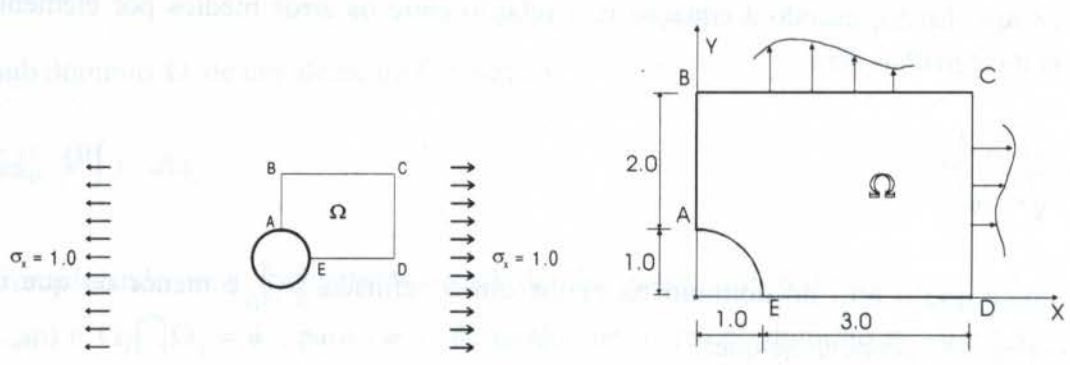

Figura 1 - Placa infinita com furo.

Essa situação se apresenta no caso de uma placa infinita com um furo circular de raio a=1.0 em seu centro, sujeita a tração uniforme uni direcional (figura 1). Para resolver o problema em um domínio finito, isola-se uma porção finita retangular ABCDE em torno do furo, porção esta que se constituirá no domínio Ω da análise. Nos lados BC e CD a placa é sujeita a

trações $\bar{\mathbf{t}}$. Nos lados AB e DE são prescritas as condições de contorno (no caso, condições de simetria com o lado AB sem deslocamentos no sentido x e o lado DE sem deslocamentos no sentido y). As componentes do tensor tensão em cada ponto da placa infinita são conhecidas analiticamente (Timoshenko et al., 1970). O tensor das tensões exatas é $\mathbf{T}^{ex}$ e sendo $\mathbf{n}$ a normal exterior de uma face, (BC ou CD), a tração nesta face devida ao estado de tensões na placa infinita é $\bar{\mathbf{t}} = \mathbf{T}^{ex} \cdot \mathbf{n}$.
O erro no elemento finito i será dado pela diferença entre a tensão exata e a tensão da análise.

$$\left\| e^{ex} \right\|_{\Omega_i}^2 = \int_{\Omega_i} \left(T_{xx}^{ex} - \hat{T}_{xx} \right)^2 d\Omega_i + \int_{\Omega_i} \left(T_{yy}^{ex} - \hat{T}_{yy} \right)^2 d\Omega_i + 2 \int_{\Omega_i} \left(T_{xy}^{ex} - \hat{T}_{xy} \right)^2 d\Omega_i \qquad (13)$$

enquanto que o erro relativo à solução analítica em todo o domínio é:

$$\eta^{ex} = \left(\frac{\left\| e^{ex} \right\|_{\Omega}^2}{\left\| \hat{t} \right\|_{\Omega}^2 + \left\| e^{ex} \right\|_{\Omega}^2} \right)^{\frac{1}{2}} \qquad (14)$$

Para a solução numérica foi usada uma malha inicial mostrada na figura 2 com 640 elementos e 672 graus de liberdade e refinamentos sucessivos foram feitos. A opção por esta estratégia de refinamento onde a malha de base é a malha imediatamente anterior foi feita para que a geometria do círculo pudesse ser aproximada simultaneamente com a solução, usando-se elementos lineares. Foram pedidos ao gerador de malhas sucessivamente 1280, 2560, 5120, 10240 e 17000 elementos, tendo sido gerados 1408, 2729, 5304, 10452 e 19486 elementos, correspondendo a 1473, 2805, 5421, 10592 e 19697 graus de liberdade, respectivamente.

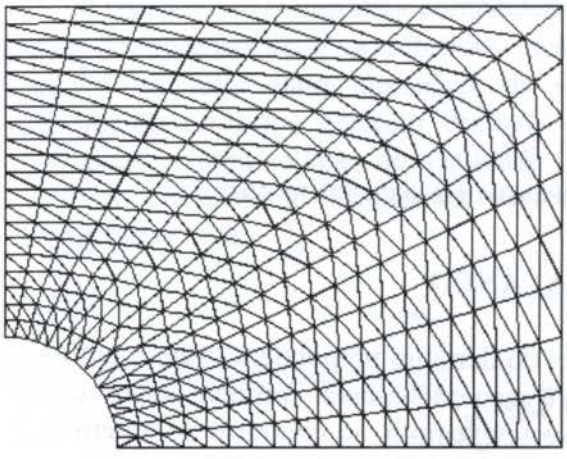

Figura 2 - Malha inicial

Nota-se que o número de elementos gerados é ligeiramente superior ao número de elementos pedido, o que contraria as conclusões da seção 3. Deve-se contudo levar em conta que em cada etapa é resolvido um problema diferente, no qual o círculo é aproximado por um polígono com cada vez mais lados. Logo, a área do domínio varia, violando uma das hipóteses implícitas na argumentação da seção 3. O fato do gerador de malhas ter de atender a muitos requisitos, nem sempre compatíveis, tais como: acomodar a malha à geometria do domínio, efetuar a transição entre tamanhos muito diferentes, não gerar elementos muito distorcidos, etc. faz com que a malha gerada não seja de fato ótima, mas quase ótima, violando também uma das hipóteses assumidas na seção 3. Ainda assim o número de elementos permaneceu controlado, bastante próximo ao número pedido ao gerador de malhas.

A figura 3 mostra a malha com 2805 graus de liberdade, obtida do refinamento adaptativo e a distribuição de tensões de Von Mises correspondente. Na figura 4 mostra-se a evolução dos erros relativos estimados e exatos durante uma seqüência de refinamentos. Observa-se que o erro relativo estimado converge para o erro relativo exato.

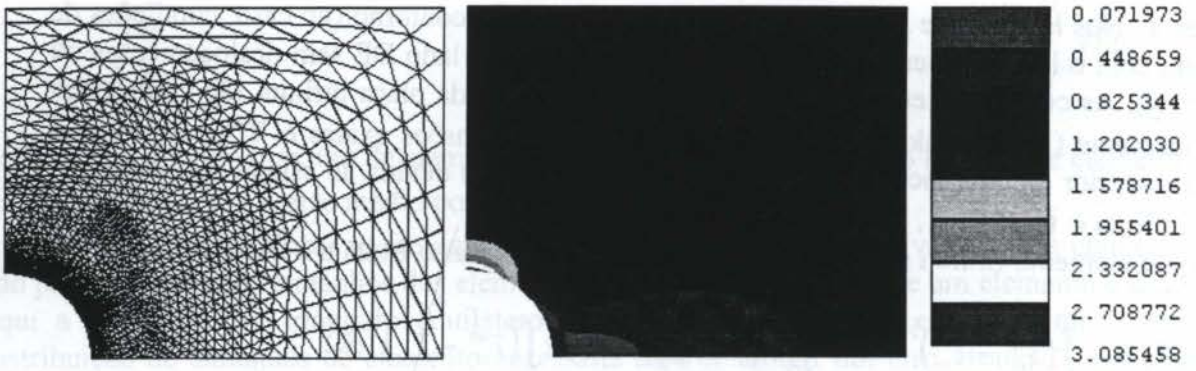

Figura 3 - Malha e tensões com 2805 graus de liberdade.

E interessante notar que mesmo a primeira estimativa de erros da seqüência mostrada já é uma boa aproximação do erro relativo exato da análise.

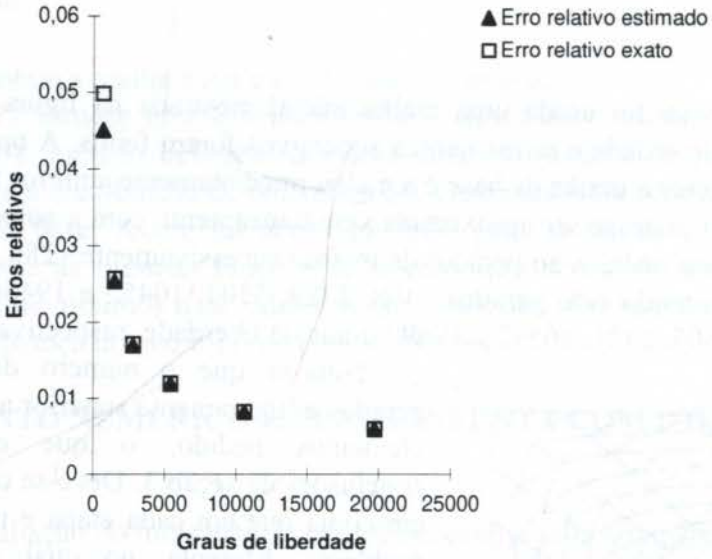

Figura 4 Comparação entre erros relativos estimados e exatos das tensões

5. EXPERIMENTO NUMÉRICO 2 - VIGA EM BALANÇO

Analisa-se aqui o caso em que uma das dimensões do domínio prepondera sobre a outra, como é o caso da viga em balanço da figura 5. Para este caso é feita uma comparação entre o refinamento adaptativo e um refinamento uniforme. Neste exemplo, ao contrário do anterior, todos os refinamentos são feitos a partir da malha inicial.

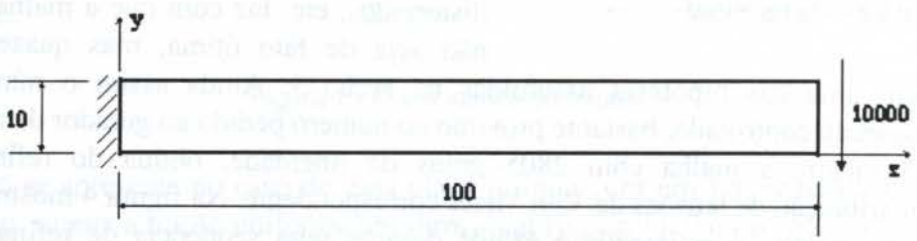

Figura 5 - Viga em balanço

No refinamento adaptativo foram feitas remalhagens partindo-se de uma malha de base de 160 elementos. Foram pedidos ao gerador de malhas 250, 420, 760, 1800, 3200, 7800 e 13000 elementos tendo sido gerados 298, 380, 830, 1438, 3432, 6312 e 13968 elementos, respectivamente. Também aqui, em virtude da malha gerada não ser exatamente ótima, são gerados em alguns casos mais elementos do que o número pedido. Ainda assim o número de elementos gerados permanece próximo ao solicitado.

O custo de processamento da solução do sistema de equações lineares, obtida aqui pelo método dos gradientes conjugados, pode ser estimado como sendo proporcional à potência 1.25 do número de graus de liberdade (Claes Johnson , 1990).

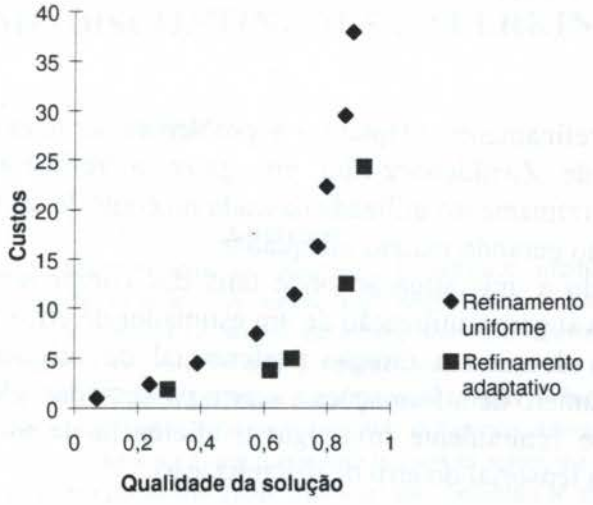

Figura 6 - Comparação de custos entre refinamentos uniformes e adaptativos

A figura 6 apresenta uma comparação de custos entre os dois tipos de refinamento. Os custos de processamento são referidos ao da malha uniforme com 80 elementos. Nota-se que à medida que uma maior qualidade da solução é exigida, os custos computacionais do refinamento uniforme crescem dramaticamente. Para erros relativos da ordem de 15%, equivalente a uma solução de qualidade 0.85, muito ruim, eles já são cerca de 2.6 vezes o custo do refinamento adaptativo, crescendo ainda mais para qualidades das soluções consideradas boas.

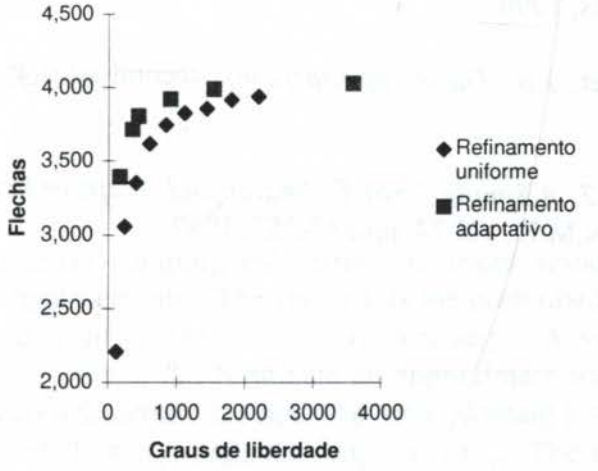

Figura 7 - Flechas na extremidade do balanço

A figura 7 mostra que o valor da flecha na extremidade do balanço converge muito mais rapidamente no caso do refinamento adaptativo, o que é um resultado esperado. Contudo, foi observado que as malhas geradas tendem a se distribuir de forma mais ou menos uniforme tanto na direção x quanto na y, nas regiões onde o erro indica refinamento. Isto ocorre porque o indicador de erros utiliza como medida do erro das tensões um invariante escalar. Assim, são introduzidos graus de liberdade em número aproximadamente igual nas duas direções, apesar da nítida preponderância da componente E_{xx}. É de se esperar que a velocidade de convergência aumente em casos como o da viga, se for usado um estimador de erros que trate o erro $\mathbf{E} = \mathbf{T}^* - \hat{\mathbf{T}}$ como um campo tensorial.

6. CONCLUSÃO

A aplicação feita de refinamento adaptativo a problemas de tensões planas mostrou a eficiência do estimador de Zienkiewicz-Zhu em guiar o refinamento nos problemas analisados. A estratégia de refinamento utilizada baseada no controle do número de elementos apresentou bom desempenho gerando malhas adequadas.

A aplicação do método a uma situação onde uma das componentes do tensor tensão prepondere sobre as demais sugere a utilização de um estimador de erros tensorial que permita captar em cada ponto do domínio a direção preferencial de refinamento. Contudo este procedimento aumenta o número de informações a serem processadas, elevando assim o custo computacional. Pretende-se futuramente investigar a eficiência de um gerador de malhas baseado em uma estimativa tensorial do erro de discretização.

7. REFERÊNCIAS

Bowyer, A. *Computing Dirichlet Tesselations*, The Computer Journal, vol 24, pp 162-166, 1981.

De Sampaio, P.A.B., Coutinho, A.L.G.A. *Simulation of Cross Flow Past a Tube Bank Employing an Adaptive Parallel/Vector Finite Element Procedure*, Anais do VI Encontro Nacional de Ciências Térmicas - ENCIT, Florianópolis, Brasil, 1996.

Johnson, C. *Numerical Solutions of Partial Differential Equations by Finite Element Method*, Cambridge University Press, 1990

Timoshenko, S.P., Goodier, J.N. *Theory of Elasticity* second edition McGraw-Hill Book Company Inc., 1970.

Zienkiewicz, O.C., Zhu, J.Z. *A Simple Error Estimator and Adaptive Procedure for Practical Engineering Analysis*, I.J.N.M.E., vol.24, pp.337-357, 1987.

XIV Brazilian Congress of Mechanical Engineering
Obeid Plaza Hotel Convention Center - Bauru - SP/Brazil
December 08-12th 1997

PAPER CODE: COB403

STRUCTURAL DYNAMIC ANALYSIS OF NONLINEAR MULTIBODY SYSTEMS BY A TIME-DISCONTINUOUS GALERKIN FORMULATION

J. G. DAMILANO & J. A. A. DUARTE
Instituto de Aeronáutica e Espaço - CTA/IAE/ASE-E
CEP 12228-904 S. J. Campos, SP, Brazil

Abstract

This work presents a study for structural dynamic analyses of nonlinear multibody systems, by a time-discontinuous Galerkin finite element method. A single-field formulation is used with the displacements approximated as a parabolic function continuous within each time slab, but discontinuous across time levels. Since the resulting system of equations is prone to high frequency oscillations the algorithm presented is well suited for the solution of such problems as it provides unconditional stability, third order accuracy and high frequency numerical damping. For conservative systems the relative difference in total energy at each time step is used as error indicator and an adaptive time stepping procedure is used to select the proper time step size. The solution for a linear oscillator gives access to the applicability of the algorithm to more complex problems and then the scheme is applied to a strongly nonlinear oscillator whose results are in excellent agreement with their analytical counterparts. The scheme allows the freedom to choose whatever initial time step size, since it searches for the best time step size that will provide the desired accuracy.

Key Words

Structural Dynamics; Adaptive Time Integration; Discontinuous Galerkin.

1. INTRODUCTION

The ordinary differential equations associated with the semidiscrete form of linear elastodynamics are written as:

$$\begin{aligned} M\underline{\ddot{u}} + C\underline{\dot{u}} + K\underline{u} &= \underline{F} \\ \underline{\dot{u}}_0 &= \underline{v}_0 \\ \underline{u}_0 &= \underline{d}_0 \end{aligned} \qquad (1)$$

where M, C and K are the mass, damping and stiffness matrices, respectively; $\underline{u} = \underline{u}(t)$ is the vector of unknown nodal displacements. The vector $\underline{F}$ is the prescribed load vector, $\underline{v}_0$ and $\underline{d}_0$ are the initial velocity and displacement vectors, respectively. A superposed dot denotes differentiation with respect to time. To formulate an approximate solution to (1) using the single-field time-discontinuous Galerkin method, the time domain $I =]0,T[$ is partitioned as $0 = t_0 < t_1 < ... < t_n = T$, and $I_n =]t_{n-1}, t_n[$, with $\Delta t_n = t_n - t_{n-1}$. The resulting finite element interpolation functions for the trial displacements and displacements weighting functions are:

$$\underline{S}^h = \left\{ \underline{u}^h \in \bigcup_{n=1}^{N} \left(P^2(I_n) \right)^{n_{eq}} \right\} \tag{2}$$

$$\underline{W}^h = \left\{ \underline{w}^h \in \bigcup_{n=1}^{N} \left(P^2(I_n) \right)^{n_{eq}} \right\} \tag{3}$$

where, by construction, the interpolation functions are continuous within each time slab and may be discontinuous across the time intervals; P^2 means second-order polynomial implying that each member of $\underline{S}^h$ and $\underline{W}^h$ is a vector of n_{eq} quadratic functions on each time step I_n. To account for the discontinuity across time intervals a *temporal jump operator* is defined (Hulbert, 1989) by:

$$\left[\underline{w}(t_n) \right] = \underline{w}(t_n^+) - \underline{w}(t_n^-) \tag{4}$$

where

$$\underline{w}(t_n^{\pm}) = \lim_{\varepsilon \to 0^{\mp}} \underline{w}(t_n + \varepsilon). \tag{5}$$

2. THE TIME-DISCONTINUOUS GALERKIN FINITE ELEMENT METHOD

The time-discontinuous Galerkin method was originally developed for first-order hyperbolic equations and successfully applied to incompressible and compressible fluid dynamics and heat conduction (see Hulbert (1989) and Damilano (1993), for a list of references on the subject). The method leads to stable, high-order accurate finite element formulations. The method in its fundamental form, which is herein used, only requires a jump operator to enforce continuity at time boundaries.

To formulate an approximate solution for the ordinary differential equations associated with the semidiscrete form of linear elastodynamics the method, by construction, requires that the interpolation functions for the trial displacements and displacement weighting functions be continuous within each time slab and may be discontinuous across time intervals.

The statement of the time-discontinuous Galerkin method for the single-field formulation, applied to the ordinary differential equations associated with the semidiscrete form of linear elastodynamics is:

Find $\underline{u}^h \in S^h$ such that for all $\underline{w}^h \in W^h$

$$\begin{aligned} &\int_{t_{n-1}^+}^{t_n^-} \left[\dot{\underline{w}}^h \cdot \left(M\ddot{\underline{u}}^h + C\dot{\underline{u}}^h + K\underline{u}^h - \underline{F} \right) \right] dt + \\ &\underline{w}^h(t_{n-1}^+) \cdot M \left[\dot{\underline{u}}^h(t_{n-1}^+) - \dot{\underline{u}}^h(t_{n-1}^-) \right] + \\ &\underline{w}^h(t_{n-1}^+) \cdot K \left[\underline{u}^h(t_{n-1}^+) - \underline{u}^h(t_{n-1}^-) \right] = 0, \qquad n = 1,2,\ldots,N. \end{aligned} \tag{6}$$

where $\underline{u}^h$ and $\underline{w}^h$ are, respectively, the displacement and weighting functions; $\dot{\underline{u}}^h$ and $\ddot{\underline{u}}^h$ are, respectively, the velocities and accelerations. The last two terms on the left-hand side in equation (6) weakly enforce the initial conditions for each time interval. These jump terms are stabilizing operators that have the effect of "up-winding" information with respect to time (Hulbert, 1989). Linear interpolations in time, for a single-field formulation, render first-order

accuracy, whereas quadratic interpolations yield third-order accuracy (Hulbert, 1989) directly implying in less damping in the low frequency range. Since first order accurate schemes are too dissipative in the low frequency range, they are inappropriate for solving structural dynamic problems. The formulation given by equation (6) leads to systems of coupled equations that are larger than those emanating from commonly used semidiscrete methods. In fact, they yield systems with "(p n) x (p n)" equations, where "p = s + 1", with "s" being the order of the interpolation functions used, and "n" is the dimension of the system given by (1).

Hulbert (1989) studies the algorithm stability and accuracy characteristics, showing that the scheme is unconditionally stable, possess high frequency numerical damping, and presents an error of the order of $O(\Delta t^3)$ with a coefficient equals to 1/72.

3. THE ADAPTIVE TIME-STEPPING PROCEDURE

It is very convenient, in modern structural dynamic analysis, that an integration scheme allows automatic time step size control. It will reduce computational effort while a desired accuracy in the solution is maintained.

Li and Wiberg (1996) applied an adaptive time-stepping algorithm on linear structural dynamic problems, based on the two-field formulation of the time-discontinuous Galerkin method. Their scheme uses piece wise linear interpolation functions for both, displacements and velocities.

In this work we are concerned with the solution of highly nonlinear structural dynamic problems and, based on the single-field formulation employing quadratic interpolation functions for displacements, we use the adaptive time-stepping algorithm discussed as follows.

If we require a certain error tolerance ε^{tol}, throughout the entire time integration process, and for a given Δt_n we obtain a corresponding error ε_n, which does not satisfy the requirement

$$\varepsilon_n \leq \varepsilon^{tol}, \tag{7}$$

given that the convergence rate for the algorithm is $O(\Delta t^3)$, the new step size that will satisfy the tolerance required may be calculated as

$$\Delta t_n^{tol} = \left(\frac{\varepsilon^{tol}}{\varepsilon_n} \right)^{1/3} \Delta t_n \,. \tag{8}$$

On the other hand, if the calculated error is smaller than the tolerance ε^{tol}, the solution is accepted but the time step size may be increased according to equation (8) when equation (7) is satisfied for K_{nt} successive time steps. The error ε_n used herein is, for the time being, the relative error in total energy of the system at two consecutive time steps.

4. NUMERICAL EXAMPLES

The numerical results show the applicability and performance of the algorithm. First, a single-DOF linear oscillator is studied. Next, the response is computed for a highly nonlinear oscillator. The results are compared with their analytical counterparts. The solutions are obtained using the standard semidiscrete algorithm, and $K_{nt} = 5$ is used for all cases.

4.1 Linear Oscillator

The equation of motion for the undamped free vibration of a single-DOF linear oscillator is

$$\begin{aligned} m\,\ddot{u} + k\,u &= 0 \\ u(0) &= u_0 \\ \dot{u}(0) &= v_0 \end{aligned} \qquad (9)$$

where unit values are used for m and k, and $u_0 = 0.0$ and $v_0 = 1.0$ are considered. An initial time step size $\Delta t = 1.0$ s is used on the computation of the response for 30.0 s.

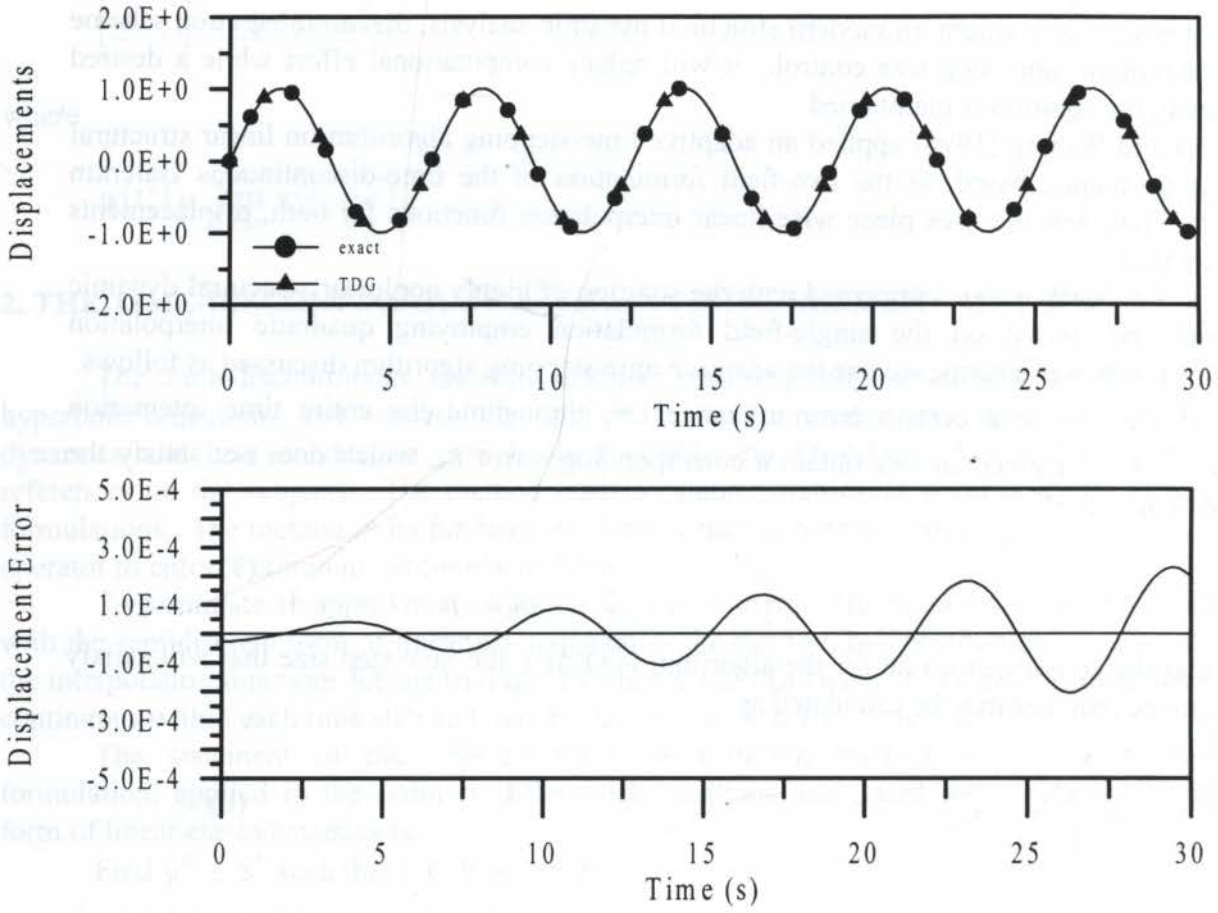

Figure 1. Response and Absolute Error distribution for displacements.

Numerical and analytical solutions are in good agreement. Figure 1 shows results for displacements and displacements absolute errors. After 30.0 seconds of integration such an error remains at the order of 2.0E-04, which is due to the high order of accuracy of the time-discontinuous Galerkin algorithm. Results for velocities and velocities errors behave exactly in the same way and are omitted here. Accelerations, which usually show how good a scheme is in terms of accuracy, presented a very interesting error distribution. Based on the results shown previously, one would expect the accelerations error distribution to behave just like those for displacements and velocities did. However, it was said that the interpolation function

used is quadratic for displacements, consequently rendering velocities and accelerations, respectively, linear and constant within each time step. The constant acceleration in each time step results in an error distribution of the order of ±3.0E-02 oscillating with the fundamental frequency of the system $\omega = 1$ rad/s, as shown in Figure 2. It is also seen that the error values increase as accelerations get close to zero, and decrease the other way around. A relative error analysis would show a flat curve with values at the order of $O(10^{-02})$, but with large peaks at instants in which accelerations are close to zero.

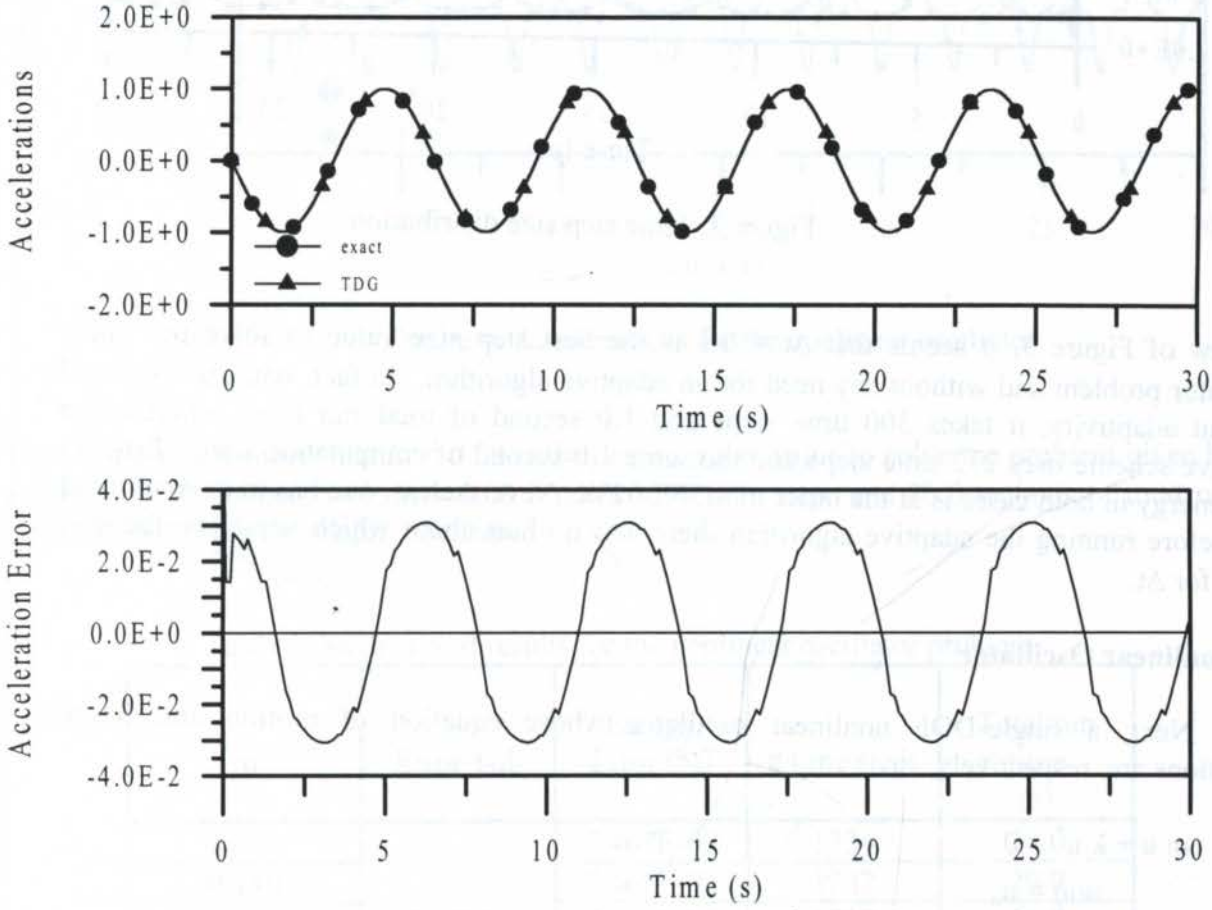

Figure 2. Response and Absolute Error distribution for accelerations.

In a second run, a time step size $\Delta t = 0.005$ s is used and the algorithm shows the same performance, i.e., it required the same number of time steps to obtain the same results with the same accuracy. Figure 3 brings the time step size distribution. After several runs with different initial time step size it was verified that no matter which initial time step is used, the scheme will always use the best time step size to carry out the calculations and keep the error within the required accuracy. The scheme will use small enough a time step to take the results to the desired accuracy, but in order to save computer time such a time step will be the largest one allowed by accuracy requirements. In other words, there is a time step size that is best for a certain required accuracy. The algorithm increases the time step size in order to improve computer run time. However, if the results obtained with such a step size do not satisfy the error tolerance, then the step size goes down to a smaller enough value in order to have the solutions satisfying the error tolerance.

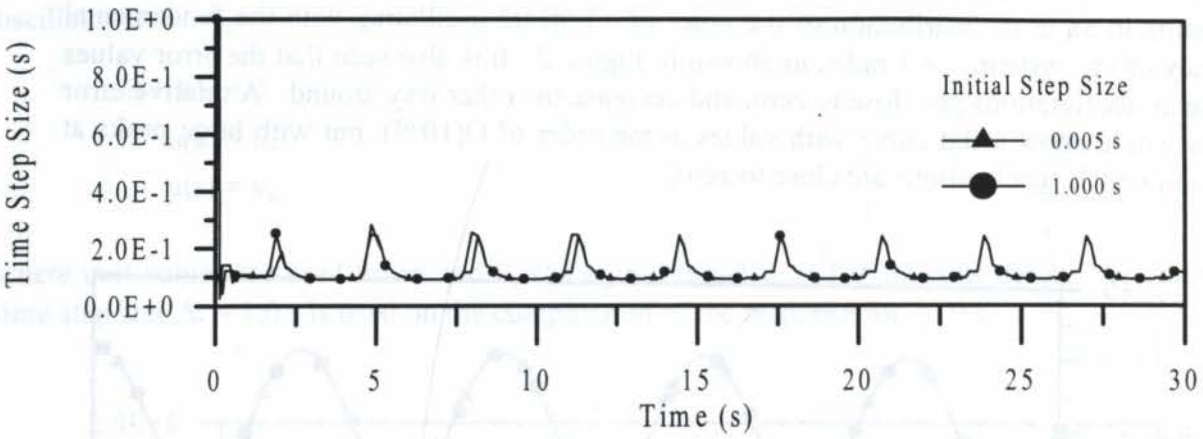

Figure 3. Time step size distribution.

In view of Figure 3, it seems that $\Delta t = 0.1$ is the best step size value to solve the linear oscillator problem and without any need for an adaptive algorithm. In fact, with $\Delta t = 0.1$ and without adaptivity, it takes 300 time steps and 1.0 second of total run time, whereas the adaptive scheme uses 272 time steps and the same 1.0 second of computation time. Error in total energy in both cases is at the order of 4.30E-02%. Nevertheless, one has to keep in mind that before running the adaptive algorithm there was no hint about which would be the best value for Δt.

4.2 Nonlinear Oscillator

Next, a single-DOF nonlinear oscillator whose equation of motion and initial conditions are, respectively,

$$\begin{aligned} m\,\ddot{u} + k\,u^3 &= 0 \\ u(0) &= u_0 \\ \dot{u}(0) &= v_0 \end{aligned} \qquad (10)$$

is studied. Mass and stiffness are equal to 1.0 and 25.0, respectively. Initial conditions are set $u_0 = 0.0$ and $v_0 = -1.5$. An initial time step size $\Delta t \doteq 1.0\text{E-}03$ s is used on the computation of the response for 30.0 s, without using the adaptive algorithm. The total energy is E = 1.125, preserved to the accuracy of $O(10^{-12})$ throughout the time integration process, and the total run time is 337 seconds. Applying the adaptive scheme to the same initial conditions reduces the total run time to 20 seconds with 1234 time steps, which brings the total computation time to less than 10% of the case without adaptivity. Total energy at the last time step is E = 1.12416 and the error tolerance in total energy used is $\varepsilon^{tol} = 1.0\text{E-}06$. The total energy is preserved throughout the time integration period to the accuracy of $O(10^{-07})$. The results for these analyses can be better seen in Table 1 from which we conclude that the error tolerance, and not the initial time step size, governs the total run time and number of time steps. Results for accelerations, in excellent agreement with the exact solution, are shown in Figure 4. Displacements and velocities also show solutions on the top of their analytical counterparts. Figure 5 shows the time step size distribution for the nonlinear oscillator problem. After

computing the solution with several different initial time step sizes it was observed that, exactly as for the linear problem, the algorithm searches for the best Δt size that makes the solution satisfy accuracy requirements.

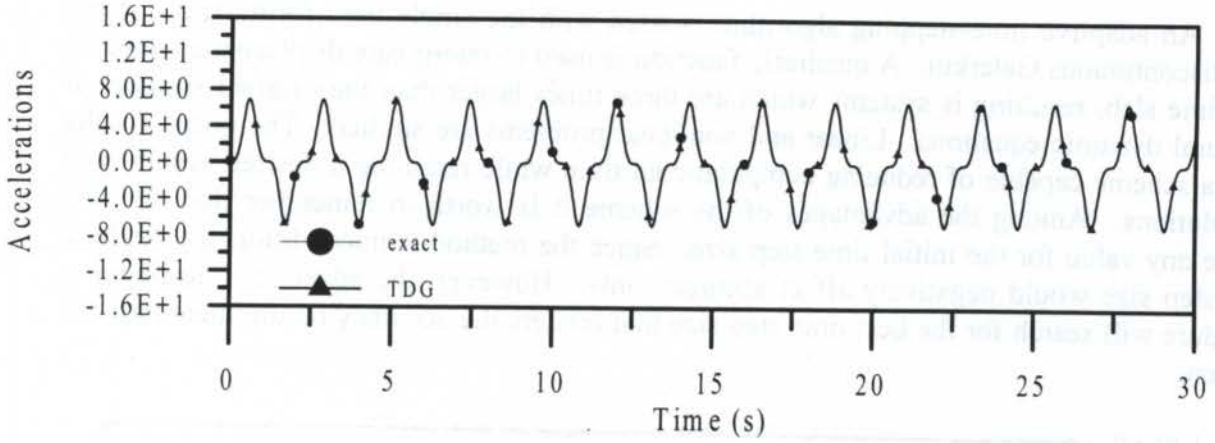

Figure 4. Accelerations for the nonlinear oscillator.

From Figure 5, it seems that $\Delta t = 0.02$ is the best step size value to solve the problem given by equation (10). Indeed, with $\Delta t = 0.02$ it takes 1500 time steps and 20.0 seconds of total run time without using the adaptive scheme.

Table 1. Summary of results for the nonlinear oscillator problem.

Δt	Error Tol.	Energy Error (%)	# time steps	Total run time (s)
0.001	1.0E-06	7.467E-02	1234	20.0
0.010		7.467E-02	1232	20.0
0.100		7.467E-02	1212	20.0
0.500		7.467E-02	1239	20.0
1.000		7.556E-02	1209	20.0
0.005	2.0E-06	1.236E-01	1041	18.0
1.000		1.236E-01	1049	18.0
0.001 (not adaptive)	–	–	30,000	337.0

Adaptivity brings the number of time steps down to about 1200 and uses the same 20.0 seconds of total run time. Total energy, for both cases, is preserved to a high level of accuracy. Again, the same observation made for the linear case is valid, i.e., one has to keep in mind that before running the adaptive algorithm there was no hint about which would be the best value for Δt. Therefore, with the adaptive scheme it is possible to start up the time integration

process without worrying about an initial value for the time step, and with the confidence that the solution will be given to the order of accuracy requested.

5. CONCLUSIONS

An adaptive time-stepping algorithm is used with the single-field formulation of the time-discontinuous Galerkin. A quadratic function is used to interpolate displacements within each time slab, resulting is systems which are three times larger than the original systems of structural dynamic equations. Linear and nonlinear problems are studied. The initial results show a scheme capable of reducing computational time while retaining a desired accuracy in the solutions. Among the advantages of the scheme it is worth to remember that one can choose any value for the initial time step size. Since the method is unconditionally stable, a large step size would negatively affect accuracy only. However, the adaptive time-stepping procedure will search for the best time step size that renders the accuracy requirements for the solution.

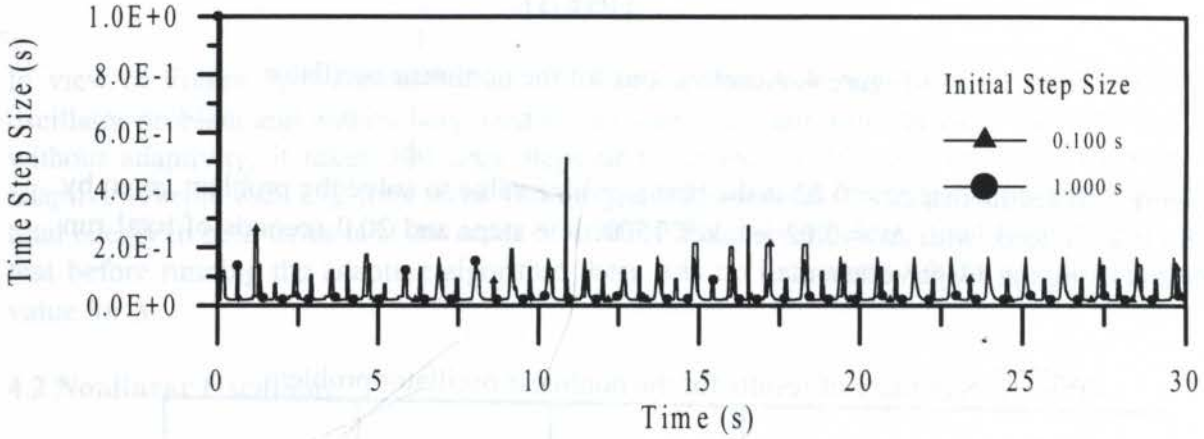

Figure 5. Time step size distribution for the nonlinear oscillator.

In a future work we will study improvements on the adaptive procedure itself and the scheme will be applied to problems with constraints in their formulations. It is known (Damilano, 1993) that special care must be taken on applying the time-discontinuous Galerkin method to such problems, due to the fact that the resulting algebraic-differential equations render responses with high level of high frequencies content that unable standard direct time integration schemes to perform well on their solutions.

6. REFERENCES

Damilano, J.G., *Finite Element Method for Nonlinear Elastic Constrained Multibody Systems*, Ph.D. Thesis, Department of Mechanical Engineering, Aeronautical Engineering and Mechanics, Rensselaer Polytechnic Institute, Troy, NY, USA 1993.

Hulbert, G.M., *Space-Time Finite Element Methods for Second Order Hyperbolic Equations*, Ph.D. Thesis, Department of Mechanical Engineering, Stanford University, Stanford, CA, USA, 1989.

Li, X.D. and Wiberg, N.-E., *Structural Dynamic Analysis by a Time-Discontinuous Galerkin Finite Element Method*, Int. J. Num. Meth. Eng, Vol. 39, pp. 2131-2152, 1996.

XIV Brazilian Congress of Mechanical Engineering
Obeid Plaza Hotel Convention Center - Bauru - SP/Brazil
December 08-12th 1997

PAPER CODE: COB41

NUMERICAL SIMULATION OF FLUID FLOW BY THE CONTROL VOLUME-FINITE ELEMENT METHOD

J.B. CAMPOS SILVA(*) & L. F. M. MOURA(**)

(*) Departamento de Engenharia Mecânica, Faculdade de Engenharia - UNESP - Ilha Solteira
CEP 15.385-000 Ilha Solteira - SP, Brasil - E-mail: jbcampos@feis.unesp.br
(**) Departamento de Engenharia Térmica e de Fluidos - FEM/UNICAMP - Campinas
CEP 13.081-970 Barão Geraldo/Campinas -SP, Brasil - E-mail: felipe@fem.unicamp.br

Abstract

A control volume-finite element method (CVFEM) to simulate unsteady, incompressible and viscous fluid flows using nine-noded quadrilateral elements is presented. The mathematical modeling of flows is the Navier-Stokes equations in primitive variables u-v-p. The set of non-linear partial differential equations was integrated and after using interpolation functions and the time discretization, the algebraic system of equations was solved by using the frontal method of solution. The obtained results of some benchmark problems compared favorable with available results from the literature.

Keywords

Finite Element, Control Volume, Navier-Stokes Equations, Primitive Variables, Computational Fluid Dynamics.

1. INTRODUCTION

The numerical computation of fluid flows is of interest in several applications of the engineering. It requires the solution of a set of non-linear partial differential equations of convection-diffusive type. The Finite Difference Method (FDM), the Finite-Volume Method (FVM) and/or the Finite Element Method (FEM) are the most used methods for solution of such problems as can be found in specialized literature. This area of Computational Fluid Dynamic (CFD) has presented a large development with the increase of processing of the computers and more realistic problems can be solved. It can be demonstrated by the large number of papers published in the open literature. The goal of the present work is to implement a control volume-finite element method (CVFEM) by using a quadratic, quadrilateral nine-noded element to simulate unsteady, incompressible and viscous fluid flows. The CVFEM was firstly presented by Baliga and Patankar (1980) and later by Raw and Schneider (1986). They used triangular and linear quadrilateral elements, respectively. The CVFEM has been enhanced by several authors since that time till nowadays. To the authors knowledge, the nine-noded element based on control volume formulation has not been applied to simulate fluid flows. Raw et al. (1985) applied this type of element to solve heat conduction problems.

The CVFEM combines the flexibility of the finite element methods to meshing complex geometry and the conservative formulation of the finite volume methods where the variables have an easy physical interpretation in terms of fluxes and forces. Saabas and Baliga (1994) presented a list of some works in FVMs and CVFEMs. As pointed out by these authors, the formulation of CVFEMs involves five basic steps: (1) discretization of the domain of interest into elements; (2) further discretization of the domain into control volumes that surround the nodes in the finite element mesh, Figure 1; (3) definition of element-based interpolation functions for variables and physical properties of the fluid; (4) derivation of algebraic equations by using the sub-domain weighted residual method; and (5) choice of a procedure to solve the system of algebraic equations. In this work, these basic steps were applied to an isoparametric quadrilateral nine-noded element for velocity field and four-noded for pressure field (it is known as unequal-order) in structured meshes. The quadrilateral element used can be deformed to fit irregular contours of the domain. Each element of the physical domain is mapped into one element of reference, the master element, defined on a local system of coordinates as can be seen in Figure 2.

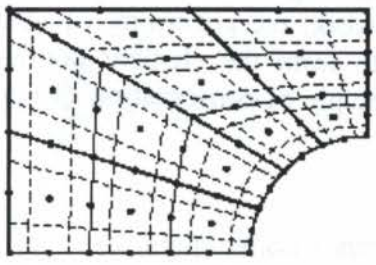

Figure 1. Finite element and control volume meshes

The method utilized in the present work has been codified to solve, in its first version, some 2D, laminar fluid flows. However, an extension to simulate turbulent fluid flows using the Reynolds average equations has been also developed, including turbulence models. The results obtained with the first version show that the physics of the problems considered has been correctly simulated.

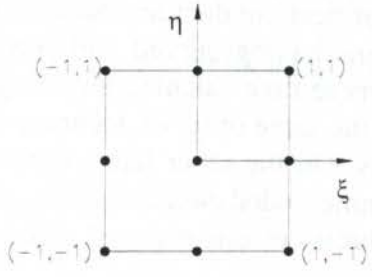

Figure 2.(a) Element in local coordinates

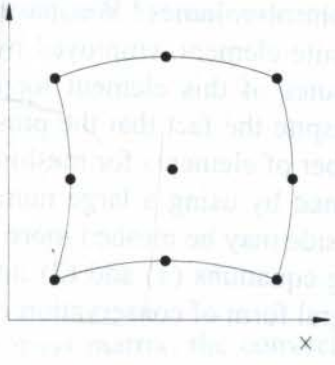

Figure 2.(b) Element in global coordinates

2. ANALYSIS

2.1 Governing Equations

The unsteady, incompressible viscous flows of Newtonian fluids are governed by the transport of momentum and continuity equations that can be cast in the following general tensorial form:

$$\frac{\partial(\rho u_i)}{\partial t} + \frac{\partial(\rho u_j u_i)}{\partial x_j} - \frac{\partial}{\partial x_j}\left[\mu\left(\frac{\partial u_i}{\partial x_j} + \frac{\partial u_j}{\partial x_i}\right)\right] = S_i - \frac{\partial p}{\partial x_i} \qquad (1)$$

$$\frac{\partial u_i}{\partial x_i} = 0 \tag{2}$$

The transport of any scalar variable can be written as

$$\frac{\partial(\rho\phi)}{\partial t} + \frac{\partial(\rho u_j \phi)}{\partial x_j} - \frac{\partial}{\partial x_j}\left(\Gamma \frac{\partial \phi}{\partial x_j}\right) = S_\phi \tag{3}$$

The above equations are in conservative form used in the FVMs and CVFEMs. These equations must be integrated into each control volume surrounding each node. This is the procedure frequently adopted in the literature. In the present work, the governing equations are integrated in each sub-control volume within elements to form the element matrices. When the assembly of the global matrix is performed, the principle of conservation of mass, momentum and energy is satisfied.

2.2 Finite Element Mesh

Preliminary, two-dimensional domains were meshed by nine-noded quadrilateral elements. However, the structure of the computational program permits the easy usage of any other type of element. After discretising the domain, each quadrilateral element is subdivided in nine sub-control-volumes. We have choose the nine-noded, isoparametric, quadratic, quadrilateral finite element, employed by Raw et al. (1985) for heat conduction; because the desirable attributes of this element for modeling both domains having curved and straight boundaries. Despite the fact that the present element involve more time calculation, one may use a less number of elements for meshing a domain to obtain the same order of accuracy that could be obtained by using a large number of linear elements. On the other hand, domains having curved side may be meshed more accurately, using the nine-noded elements.

Integrating equations (1) and (2) into the sub-control volumes of one element gives the following integral form of conservation equations:

$$\int_V \frac{\partial(\rho u_i)}{\partial t} dV + \int_{\delta S} \rho u_j u_i n_j ds - \int_{\delta S} \mu \frac{\partial u_i}{\partial x_j} n_j ds = \int_V \left(S_i - \frac{\partial p}{\partial x_i}\right) dV + \int_{\delta S} \mu \frac{\partial u_j}{\partial x_i} n_j ds \tag{4}$$

$$\int_V \frac{\partial u_i}{\partial x_i} dV = 0 \tag{5}$$

where δs is the surface area (contour in 2D) of the control volume, and n_j is the component of a unit outward normal vector to the differential surface area δs in the direction j.

The volume integral of the pressure term in equation (4) and of the continuity, equation (5), were not transformed to surface integrals, because calculation tests showed better results with the volume integrals.

2.3 Interpolation Functions

The integral equations were transformed to one system of algebraic equations, by using of interpolation functions for approximation of variables in each element. The interpolation functions employed were obtained from Dhatt & Touzot (1984). No upwind was considered. In the domain of one element, variables and coordinates were approximated as

$$u_i = \sum_{\alpha=1}^{nnep} N_\alpha U_{i\alpha} \tag{6}$$

$$p = \sum_{\alpha=1}^{nnel} N_\alpha P_\alpha \tag{7}$$

$$x_i = \sum_{\alpha=1}^{nnep} N_\alpha X_{i\alpha} \tag{8}$$

where N_α are interpolation functions; $U_{i\alpha}$ the velocity components; P_α the pressure and $X_{i\alpha}$ components of the coordinate system at nodes α of one element; nnep and nnel are numbers of nodes of quadratic (parabolic) and linear elements respectively.

The variables defined by equations (6), (7) and the coordinates obtained by equation (8) were substituted in the equations (4) and (5). The following matrix system was obtained:

$$M_{\alpha\beta}\dot{U}_{i\beta} + C_{\alpha\beta}(U_{i\beta})U_{i\beta} - S_{i\alpha\beta}U_{i\beta} + H_{i\alpha\beta}P_\beta = F_{i\alpha} \tag{9}$$

$$D_{i\alpha\beta}U_{i\beta} = 0 \tag{10}$$

where $M_{\alpha\beta}$, $C_{\alpha\beta}$, $S_{i\alpha\beta}$, $H_{i\alpha\beta}$, $D_{i\alpha\beta}$ and $F_{i\beta}$ are the mass matrix, the convection matrix, the diffusive matrix, the pressure term matrix, the continuity matrix and the source term vector respectively into the element. These matrices will be presented in the doctorate thesis of the first author.

2.4 Time Discretization

The equations (9) and (10) discretized in time have the following form:

$$\frac{M_{\alpha\beta}}{\Delta t}U_{i\beta}^{n+1} + \theta(C_{\alpha\beta}^{n+1} - S_{i\alpha\beta})U_{i\beta}^{n+1} + \theta H_{i\alpha\beta}P_\beta^{n+1} = F_{i\alpha}^{n} \tag{11}$$

$$D_{i\alpha\beta} U_{i\beta}^{n+1} = 0 \tag{12}$$

where

$$F_{i\alpha}^{n} = \frac{M_{\alpha\beta}}{\Delta t} U_{i\beta}^{n} - (1-\theta)(C_{\alpha\beta}^{n} - S_{i\alpha\beta}) U_{i\beta}^{n} - (1-\theta) H_{i\alpha\beta} P_{\beta}^{n} \tag{13}$$

and $0 \le \theta \le 1$. An implicit scheme has been employed, therefore θ =1, which eliminates the needing of any initial condition for the pressure field.

We can linearize the inertial terms by computing the matrix $C_{\alpha\beta}$ on the step n instead of updating it on each iteration at the time n+1. The updating of the convection matrix may compute more accurate results, however, it is very time consuming for large problems.

2.5 Solution Procedures

The algebraic system of equations must be assembled element by element to form the global system of equations that can be solved by some methods of solution. Depending on the number of degrees of freedom of the problem, the global matrix could become very large and it requires a large capacity of storage. The frontal method of solution has been applied. This method solves the global matrix by blocks of specified front size as explained in the book of Taylor & Hughes (1981). Some computational subroutines from Taylor & Hughes (1981) developed for eight-noded elements were also used and modified to solve the algebraic systems of equations. Starting from a specified field of velocity and pressure, the variables u-v-p may be calculated at any other specified time. The size of the front can be found by trial and error. If the front size is too small, the program sends a message to the user. The smaller the front the faster the calculation of the variables at each time step. However, this method of solution requires a temporary memory space in hard disc to storage data during the calculation. The larger the front size the higher the space on hard disc.

3. RESULTS

The performance of the numerical method was tested by solving some benchmark problems found in the literature. The first of them is the lid driven cavity that has been used by most of the researchers to validate numerical methods. The second is the flow over a backward-facing step.

3.1 Lid Driven Cavity

The flow induced in square cavity by moving the upper plate is considered. For a lid driven square cavity, the velocity profile normalized to the lid velocity are shown in Figure 3, for a non-uniform grid of 12x12 elements. Velocity profiles u(x=0.5,y) and v(x,y=0.5) for Reynolds numbers equal to 400 are presented at some time steps. The pressure was set to zero at the center of the cavity. The initial condition was set to zero for the velocity field in the whole domain except on the upper limit. A comparison between the results of the present work with the results from Kettleborough et al. (1989) is showed in Figure 4. The agreement of results is quite good. The mesh employed correspond to 25 grid points along the coordinates.

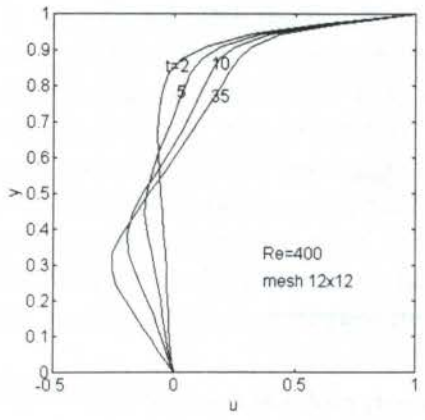

Figure 3 - (a) Variation of u along vertical centerline of the cavity

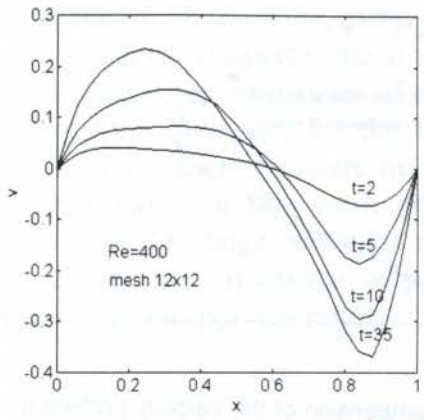

(b) Variation of v along horizontal centerline of the cavity

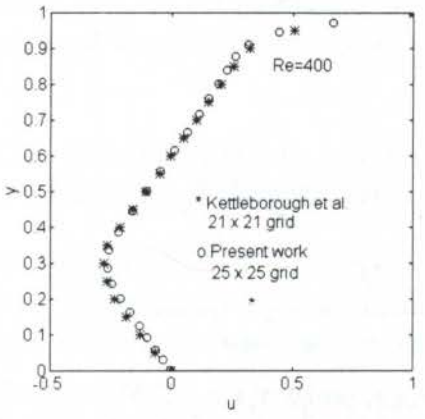

Figure 4 - Comparison of the velocity profiles at x = 0.5 for steady flow

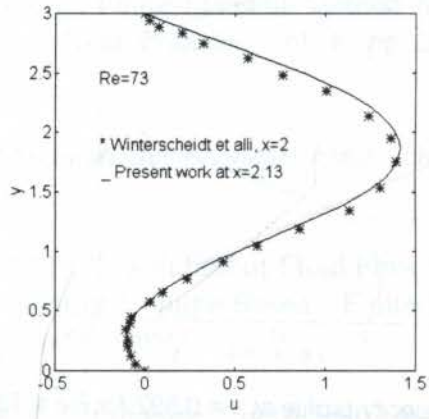

Figure 5 - Comparison of the velocity profiles at x = 2 for steady flow

3.2 Flow Over a Backward-Facing Step

The next example considered was the flow over a backward-facing step. A fluid enters a two-dimensional channel of width 2h with a parabolic velocity profile. Some distance down the channel (1.5h) there is a one-sided step increase in width to 3h. A re-circulation is set up behind the step. The longitudinal extent of re-circulation is marked by the point of reattachment or the point at which unidirectional flow is re-established across the entire width of the channel. Prediction of the point of reattachment was calculated for a Reynolds number of 73. The comparisons of the calculated velocity profiles and velocity profiles of Winterscheidt & Surana (1994) are showed in Figure 5 and Figure 6. The agreement between the results is also quit good. The developing of the velocity profiles for t=50 at various axial x positions along the channel is shown from Figure 7 to Figure 10. Figure 11 shows the variation of u along the re-circulation zone at y = 0.0343 and that the value of the point of reattachment is approximately at x = 4.9. The re-circulation zone length predicted by Winterscheidt and Surana (1994) was 5.3 and the experimental result presented by them was approximately 4.0.

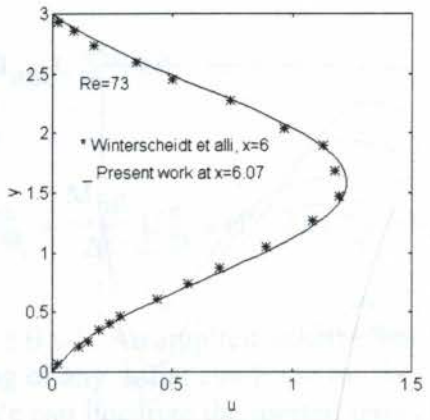

Figure 6 - Comparison of the velocity profiles at x = 6 for steady flow

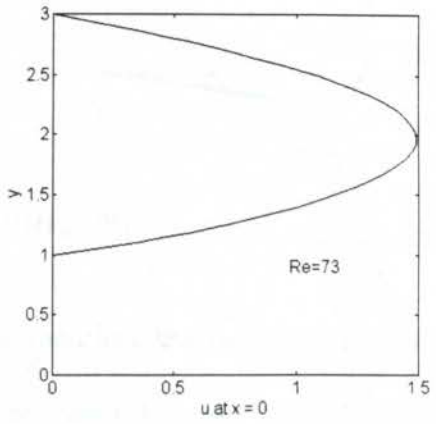

Figure 7 - Velocity profile at x = 0 for Re = 73 and t =50.

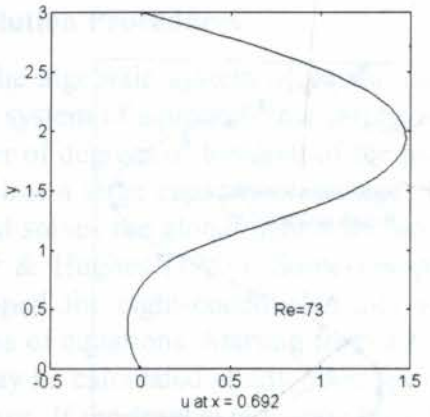

Figure 8 - Velocity profile at x = 0.692 for Re = 73 and t = 50.

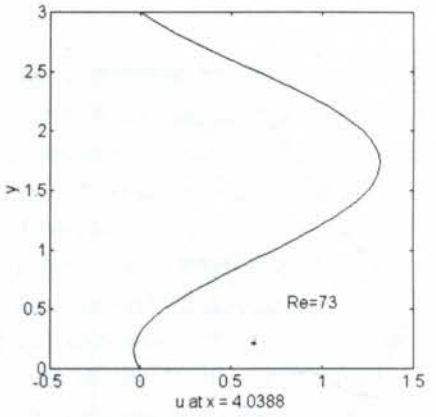

Figure 9 - Velocity profile at x = 4.0388 for Re =73 and t = 50

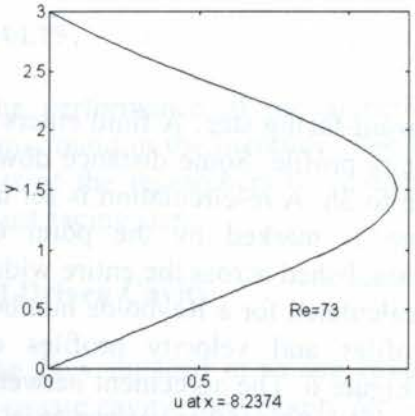

Figure 10 - Velocity profile at x = 8.2374 for Re=73 and t = 50

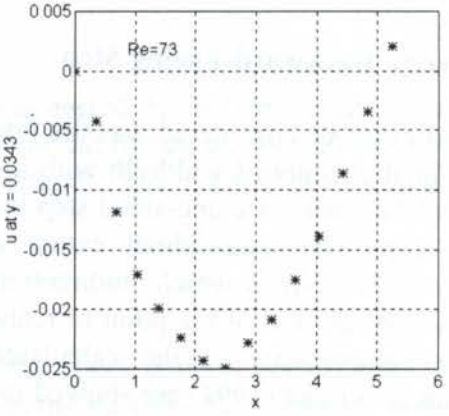

Figure 11 - Variation of u along of the re-circulation zone for Re = 73 and t = 50.

4. CONCLUSIONS

In the present work the results of a CVFEM implementation for unsteady, incompressible and viscous fluid flow using nide-noded elements were obtained. However, the structure of the numerical code permits the easy extension of the calculation for other types of elements. The comparisons of the present results and results from the literature, for the Reynolds numbers specified, show good agreement. The results from the literature were obtained by other CVFEMs or other numerical methods or experimentally. In this work no special interpolation function have been used in concern of upwind. For large Reynolds numbers, modification of the interpolation functions may be need for the calculation of physically realistic results if no refinement of the grid can be doing to prevent spurious results.

5. REFERENCES

BALIGA, B.R. & PATANKAR, S.V. A New Finite-Element Formulation for Convection-Diffusion Problems. *Numerical Heat Transfer,* vol. 3., pp. 393-409, 1980.

BALIGA, B.R. & PATANKAR, S.V. A Control Volume Finite-Element Method for Two-Dimensional Fluid-Flow and Heat Transfer. *Numerical Heat Transfer,* vol. 6, pp. 245-261, 1983.

DHATT, G. & TOUZOT, G. *Une Presentation de la Méthode des Éléments Finis*, Deuxieme Édition, Maloine S.A. Éditeur, Paris, 1984.

KETTLEBOROUGH, C.F., HUSAIN, S.R. & PRAKASH, C. Solution of Fluid Flow with the Vorticity-Streamfunction Formulation and the Control-Volume-Based Finite-Element Method, *Numerical Heat Transfer,* Part B, vol. 16, pp.31-58, 1989.

RAW, M.J & SCHNEIDER, G.E. A Skewed, Positive Influence Coefficient Up-winding Procedure for Control-Volume-Based Finite-Element Convection-Diffusion Computation. *Numerical Heat Transfer,* vol. 9, pp. 1-26, 1986.

RAW, M.J., SCHNEIDER, G.E. & HASSANI, V. A Nine-Noded Quadratic Control-Volume-Based Finite Element for Heat Conduction, *J. Spacecraft*, vol. 22, No. 5, pp.523-529, 1985

SAABAS, H.J. & BALIGA, B.R. Co-Located Equal-Order Control-Volume Finite-Element Method for Multidimensional, Incompressible, Fluid Flow - Part I: Formulation, *Numerical Heat Transfer,* Part B, vol. 26, pp.381-407, 1994.

SAABAS, H.J. & BALIGA, B.R. Co-Located Equal-Order Control-Volume Finite-Element Method for Multidimensional, Incompressible, Fluid Flow - Part II: Verification, *Numerical Heat Transfer,* Part B, vol. 26, pp.409-424, 1994.

TAYLOR, C. & HUGHES, T.G. *Finite Element Programming of the Navier-Stokes Equations*, Pineridge Press Ltd, Swansea, U.K., 1981.

WINTERSCHEIDT, D. & SURANA, K.S., p-Version Least Squares Finite Element Formulation for Two-Dimensional, Incompressible Fluid Flow, *Int. J. Numer. Methods Fluids*, vol. 18, pp.43-69, 1994.

XIV Brazilian Congress of Mechanical Engineering
Obeid Plaza Hotel Convention Center - Bauru - SP/Brazil
December 08-12th 1997

PAPER CODE: COB420

CONTACT PROBLEMS IN PLATES UNDERGOING LARGE DEFLECTIONS, USING A HIGHER ORDER PLATE THEORY

JACKSON LUÍS BARP
Departamento de Engenharia Mecânica - Centro de Ciências Tecnológicas -UNISINOS
CEP 93.022-000 São Leopoldo, RS, Brasil - E-mail: jbarp@stihl.com.br

MARCO ANTÔNIO LUERSEN
Departamento de Mecânica
NuPES - Núcleo de Pesquisa em Engenharia Simultânea - CEFET-PR
CEP 80.230-901 Curitiba, PR, Brasil - E-mail: luersen@nupes.cefetpr.br

CARLOS ALBERTO DE CAMPOS SELKE
GRANTE - Grupo de Análise de Tensões - Departamento de Engenharia Mecânica - UFSC
CEP 88.040-900, Florianópolis, SC, Brasil - Email: selke@grante.ufsc.br

Abstract

This work presents an incremental finite element formulation for contact problems of plates undergoing large deflections, with unilateral constraints, such as rigid foundations. A nine node lagrangian type isoparametric finite element, based on the Lo, Christensen and Wu higher order plate theory, is obtained using this formulation. The penalty method is used to solve the variational inequality that usually arises in contact problems, and the solution depends on the penalty parameter. Using the finite element obtained, bending problems of beams and plates, with their lateral displacements constrained by walls, are numerically solved, and the results are compared with solutions available in the literature.

Keywords

Contact, plate theories, finite elements.

1. INTRODUCTION

The application of the classical plate theory to solve contact problems in plates presents some inherent physical inconsistencies such as the discontinuity of the resultant shear stresses at the boundary of the contact region, and the failure of predicting the correct force field transmitted by the constraining surface to the deformed plate (Essenburg, 1962). Trying to remove these inconsistencies, the use of the plate theories that take into account the influence of the transverse shear deformation, like Mindlin-Reissner theory, has been made (Luersen, Barp & Selke, 1995), even though some limitations can still stand, such as an incorrect prediction of the tractions at the periphery of the contact region, and the failure to predict the regions of separation, after correctly predicting the increase in the contact region for a monotonically increasing load (Essenburg, 1962).

Another way of removing the above listed inconsistencies is to use higher order plate theories, where the effect of the transverse normal strain is taking into account, together with the effect of the transverse shear deformation (Reissner, 1981). This approach was used when a higher order beam theory was introduced for solving contact problems in beam bending (Essenburg, 1975), and it has been used since in the numerical analysis of buckling and bending of beams (Selke & Kikuchi, 1987).

This work presents a numerical study of unilateral contact problems in plates, using a nine node lagrangian isoparametric finite element. This element is obtained from an incremental updated lagrangian formulation of the bending problem of plates, undergoing large deflections, subjected to frictionless local unilateral contact conditions. The formulation used is based on the Lo, Christensen and Wu higher order plate theory (Lo, Christensen & Wu, 1977), and the variational inequality is solved using the penalty method.

2. THE INCREMENTAL FORMULATION OF THE CONTACT PROBLEM IN THICK PLATES

The incremental representation of the deformation problem of an elastic body Ω, caused by the action of body forces and forces applied at the boundary Γ_F, whose displacements are constrained by a rigid surface, which coincides with the surface Γ_C of this body, can be done by writing the principle of virtual work, using a general incremental lagrangian formulation, as (Luersen, Barp & Selke, 1995)

$$\int_{\Omega_R}\left(\Delta S_{ij}\delta E_{ij} + S_{ij}\Delta u_{k,i}\delta u_{k,j}\right)d\Omega = \int_{\Omega_R}\Delta b_{R_i}\delta u_i\, d\Omega + \int_{\Gamma_{F_R}}\Delta t^F_{R_i}\delta u_i\, d\Gamma + \\ + \int_{\Gamma_{C_R}}\Delta t^C_{R_i}\delta u_i\, d\Gamma + R \quad \forall\, \delta u_i \mid \delta u_i = 0 \ \text{ on } \ \Gamma_{D_R}, \tag{1}$$

where

$$R = -\int_{\Omega_R} S_{ij}\delta E_{ij}\, d\Omega + \int_{\Omega_R} b_{R_i}\delta u_i d\Omega + \int_{\Gamma_{F_R}} t^F_{R_i}\delta u_i d\Gamma + \int_{\Gamma_{C_R}} t^C_{R_i}\delta u_i d\Gamma, \tag{2}$$

with Ω_R being the reference configuration, $t^F_{R_i}$ the traction components on the boundary Γ_{F_R}, $t^C_{R_i}$ the traction components on the contact surface Γ_{C_R}, not known a priori, b_i the components of the body force vector, S_{ij} the components of the 2nd Piola-Kirchhoff stress tensor, ΔS_{ij} the components of its increment, Δu_i the components of the incremental displacement vector, δE_{ij} the components of virtual Green strain tensor, and with the index R indicating that all the quantities are being used in the reference configuration.

Let $x_3 = \phi(x_1, x_2)$ and $x_3 = \psi(x_1, x_2)$ the boundaries of the body Ω and of the rigid foundation, respectively, and $\boldsymbol{N}$ the unit normal vector to the rigid foundation, given by (Kikuchi & Oden, 1984)

$$\boldsymbol{N} = N_i\,\boldsymbol{e}_i = \frac{1}{\sqrt{1+\left(\frac{\partial\psi}{\partial x_1}\right)^2+\left(\frac{\partial\psi}{\partial x_2}\right)^2}}\left(\frac{\partial\psi}{\partial x_1}\boldsymbol{e}_1 + \frac{\partial\psi}{\partial x_2}\boldsymbol{e}_2 - \boldsymbol{e}_3\right). \tag{3}$$

The impenetrability condition, which is also known as the Signorini's boundary condition (Duvaut & Lions, 1976), can be written, in its incremental form, as

$$\Delta u_N - \Delta g_N \leq 0 \quad on \quad \Gamma_C \tag{4}$$

where

$$\Delta u_N = N_i \Delta u_i \quad \text{and} \quad \Delta g_N = \frac{\psi(X_1, X_2) - \phi(X_1, X_2)}{\sqrt{1 + \left(\frac{\partial \psi}{\partial X_1}\right)^2 + \left(\frac{\partial \psi}{\partial X_2}\right)^2}} \tag{5}$$

The equations presented above represent the contact conditions in terms of displacements, which have correspondent conditions in terms of stresses, given by (Luersen & Selke, 1993)

$$\begin{aligned} t_N(\boldsymbol{X} + \Delta \boldsymbol{u}) &= 0 \quad if \quad \Delta u_N - \Delta g_N < 0 \\ t_N(\boldsymbol{X} + \Delta \boldsymbol{u}) &< 0 \quad if \quad \Delta u_N - \Delta g_N = 0 \end{aligned} \tag{6}$$

where t_N is the normal component of the Cauchy traction vector on the contact surface Γ_C.

All the contact conditions obtained are referred to the deformed configuration. In order to insert them into the incremental principle of virtual work, one needs to rewrite them in the reference configuration. When this is done, and using a procedure similar to the one used by Kikuchi and Oden (1984), one can obtain a variational inequality (Selke, 1986). This inequality can be solved using the penalty method, which transforms it into an equality, by including the contact conditions, with the incremental contact pressure given as

$$\Delta t_N = -\frac{1}{\varepsilon}\left(\Delta u_N - \Delta g_N\right), \tag{7}$$

where ε is the penalty parameter and $\left(\Delta u_N - \Delta g_N\right)$ represents the incremental contact constraint. Therefore, after using the penalty method, the incremental principle of virtual work becomes (Luersen and Selke, 1994)

$$\begin{aligned} &\int_{\Omega_R} \left(\Delta S_{ij}\, \delta E_{ij} + S_{ij}\, \Delta u_{k,i}\, \delta u_{k,j}\right) d\Omega + \frac{1}{\varepsilon} \int_{\Gamma_{C_R}} J\, F_{ij}^{-1} n_{R_j} n_k\, \Delta u_k \delta u_i d\Gamma - \\ &- \int_{\Gamma_{C_R}} J\, \Delta F_{ij}^{-1} n_{R_j} t_N^C\, \delta u_i\, d\Gamma - \int_{\Gamma_{C_R}} \Delta J\, F_{ij}^{-1} n_{R_j} t_N^C\, \delta u_i\, d\Gamma = \\ &= \int_{\Omega_R} \Delta b_{R_i}\, \delta u_i\, d\Omega + \int_{\Gamma_{F_R}} \Delta t_{R_i}^F\, \delta u_i\, d\Gamma + \frac{1}{\varepsilon} \int_{\Gamma_{C_R}} J\, F_{ij}^{-1} n_{R_j}\, \Delta g_N\, \delta u_i\, d\Gamma + R. \end{aligned} \tag{8}$$

where

$$R = -\int_{\Omega_R} S_{ij}\, \delta E_{ij}\, d\Omega + \int_{\Omega_R} b_{R_i}\, \delta u_i\, d\Omega + \int_{\Gamma_{F_R}} t_{R_i}^F\, \delta u_i\, d\Gamma + \int_{\Gamma_{C_R}} t_{R_i}^C\, \delta u_i\, d\Gamma. \tag{9}$$

Considering the reference state placed on the deformed configuration, one has the updated lagrangian formulation, where the following approximations are valid:

$$J \cong 1,\ S_{ij} \cong \sigma_{ij},\ F_{ij}^{-1} \cong \delta_{ij} \quad \text{and} \quad \delta E_{ij} \cong \delta \varepsilon_{ij}\ , \tag{10}$$

where ε_{ij}^* is the infinitesimal version of the Green strain tensor (Washizu, 1982), and σ_{ij} is the Cauchy stress tensor. The incremental principle of virtual work, in its updated lagrangian form, becomes (Luersen, Barp & Selke, 1995)

$$\int_{\Omega}\left(\Delta S_{ij}\,\delta\varepsilon^{*}_{ij}+\sigma_{ij}\,\Delta u_{k,i}\,\delta u_{k,j}\right)d\Omega+\frac{1}{\varepsilon}\int_{\Gamma_C} n_i\,n_k\,\Delta u_k\,\delta u_i\,d\Gamma=$$
$$=\int_{\Omega}\Delta b_i\,\delta u_i\,d\Omega+\int_{\Gamma_F}\Delta t_i^{F}\,\delta u_i\,d\Gamma+\frac{1}{\varepsilon}\int_{\Gamma_C} n_i\,\Delta g_N\,\delta u_i\,d\Gamma+R \tag{11}$$

where

$$R=-\int_{\Omega}\sigma_{ij}\,\delta\varepsilon^{*}_{ij}\,d\Omega+\int_{\Omega} b_i\,\delta u_i\,d\Omega+\int_{\Gamma_F} t_i^{F}\,\delta u_i\,d\Gamma+\int_{\Gamma_C} t_N^{C}\,\delta u_i\,d\Gamma. \tag{12}$$

As the main interest in this work is the study of contact problems in thick plates, one must insert, into the incremental principle of virtual work, the displacement field for the Lo, Christensen and Wu higher order plate theory, given by (Lo, Christensen & Wu, 1977)

$$\begin{aligned}\Delta u_x(x,y,z)&\cong\Delta u+z\Delta\theta_x+z^2\Delta\xi_x+z^3\Delta\phi_x\\ \Delta u_y(x,y,z)&\cong\Delta v+z\Delta\theta_y+z^2\Delta\xi_y+z^3\Delta\phi_y\\ \Delta u_z(x,y,z)&\cong\Delta w+z\Delta\theta_z+z^2\Delta\xi_z\end{aligned} \tag{13}$$

where Δu and Δv are the incremental in-plane displacements in the reference surface of the plate, Δw is the incremental transversal displacement of a point on the reference surface, $\Delta\theta_x$ and $\Delta\theta_y$ are the normal incremental rotations of the reference surface, in *xz* and *yz* planes, respectively, $\Delta\theta_z$ and $\Delta\xi_z$ are the degrees of freedom related to the normal transversal strains, $\Delta\xi_x$, $\Delta\xi_y$, $\Delta\phi_x$ and $\Delta\phi_y$ are the degrees of freedom related to the warping of the cross section, all of them depending upon the in-plane coordinates x and y.

The discretization procedure of the incremental principle of virtual work, with the interpolation of the incremental and the virtual displacements, in terms of the incremental and virtual nodal displacements, using the shape functions for a nine node lagrangian isoparametric finite element, leads to the following system of equations, for each element,

$$\left(\left[K_0^{E}\right]+\left[K_\sigma^{E}\right]+\left[K_p^{E}\right]\right)\left\{\Delta u^{E}\right\}=\left(\left\{\Delta F^{E}\right\}+\left\{\Delta F_p^{E}\right\}+\left\{R^{E}\right\}\right) \tag{14}$$

where K_0^E is the elemental linear incremental stiffness matrix, K_σ^E is the elemental geometric stiffness matrix, K_p^E is the elemental penalty stiffness matrix, ΔF^E is the elemental incremental load vector, ΔF_p^E is the elemental incremental contact load vector and R^E is the residual vector. The global finite element equation of the whole structure is obtained after the superposition process of the elemental stiffness matrices and loads vectors of all plate elements.

3. NUMERICAL RESULTS AND DISCUSSION

In order to show the capabilities of the formulation presented and to test the finite element obtained, two problems are numerical solved. The first problem to be analyzed is a simply supported beam subjected to a couple on its ends, with an unilateral constraint, placed at a distance *d* below the beam. The second problem is a clamped square plate, subjected to an uniformly distributed transversal load, with an unilateral constraint, also placed at a distance *d* below the plate.

3.1 Beam Bending Against a Rigid Surface

The problem of a simply supported beam, showed on Figure 1, loaded by a couple applied on its ends, and with the transversal displacements constrained unilaterally by a rigid surface, placed at a distance $d = 0.08\ cm$ below, is numerically solved. The beam has the following properties: Young's Modulus $E = 2.1 \times 10^4\ KN/cm^2$, Poisson ratio $\nu = 0.29$, length $2L = 2\ cm$, height $h = 0.2\ cm$, and thickness $b = 0.2\ cm$.

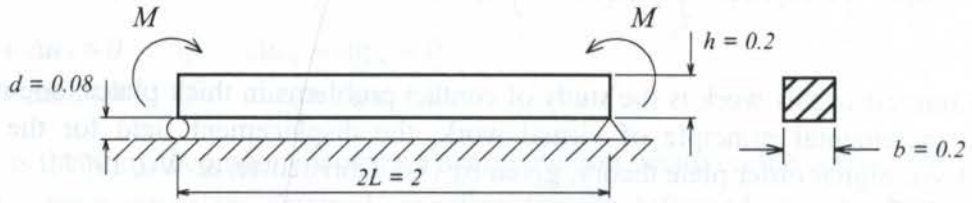

Figure 1 - Bending of a simply supported beam.

The beam is discretized using a mesh with 13 finite elements (13 x 1), and the penalty parameter used is $10^{-1}/E$. The transversal displacements of the central point of the beam and the correspondent moment values are presented in Table 1. This table also presents the numeric results obtained by Selke and Kikuchi (1987), using the classic beam theory (Euler-Bernoulli theory) and the Essenburg higher beam theory, and the numeric results obtained by Luersen and Selke (1994), using the Mindlin-Reissner first order shear plate theory.

Table 1: Transversal displacements of the central point of the beam [cm]

Moment M [KN.cm]	Present work (Lo, Christensen and Wu plate theory)	Mindlin-Reissner plate theory (Luersen & Selke, 1994)	Classical beam theory (Selke & Kikuchi, 1987)	Essenburg beam theory (Selke & Kikuchi, 1987)
0.4	0.07073	0.07160	0.0715	0.0706
0.4475	0.07909	0.08008	0.0799	0.0790
0.4485	0.08003	0.08008	0.0800	0.0792
0.4495	0.08003	0.08008	0.0800	0.0800
0.5	0.08001	0.08008	0.0800	0.0800
2.5	0.08001	0.08063	0.0800	0.0800
3.0	0.08000	0.08008	0.0800	0.0800
3.5	0.08000	0.08008	0.0800	0.0799*
5.0	0.07997*	0.07999	0.0800	0.0771
5.18	0.07991	0.08000	0.0800	0.0769
7.5	0.07989	0.08000	0.0800	0.0735
10.0	0.07988	0.08000	0.0800	0.0703

(*) indicates loss of contact

Figure 2 shows the normalized contact pressure along the beam, and the correspondent normalized moments, with respect to the moment when the contact starts (M). The origin of coordinate system is the central point of the beam. In Figure 2, HOST represents the *Higher Order Shear Plate Theory* used in the present formulation, and FOST represents the *First Order Shear Plate Theory*, or the Mindlin-Reissner first order plate theory. Figure 3 shows the analytical pressure distribution obtained by Naghdi and Rubin (1989), with respect to the same moment values of the Figure 2. There, T represents the Timoshenko beam theory, in which only the transversal shear deformation is taken into account, N represents a beam theory where only the normal transversal strain is taken into account, and the transversal shear

strain is not considered, and G represents the general theory, which takes into account both, the normal transversal strain, and the transversal shear strain.

The loss of contact is adequately represented but, after its occurrence, the transversal displacements do not exhibit the same degree of accuracy obtained for the contact pressures. This accuracy can be verified by the comparison between Figures 2 and 3.

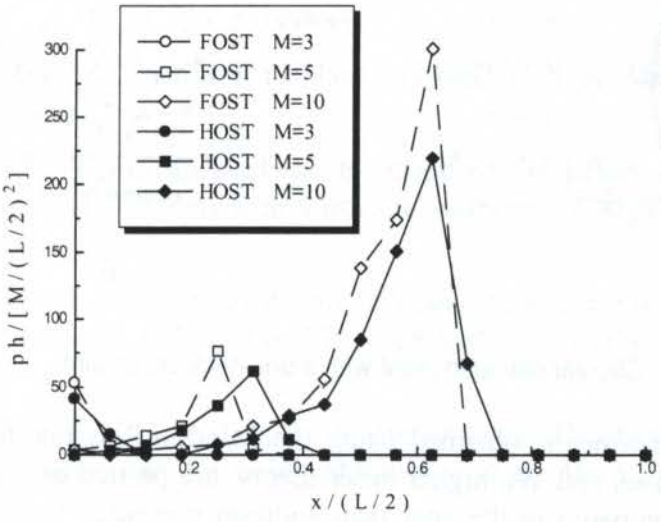

Figure 2 - Contact pressure distribution along the beam.

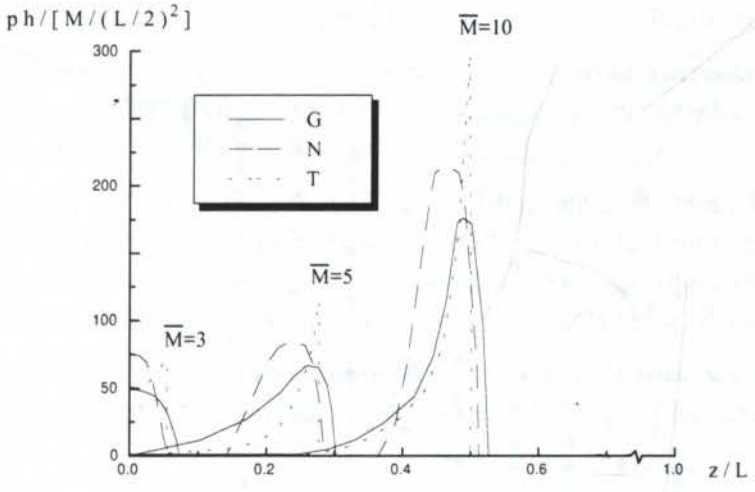

Figure 3 - Contact pressure distribution along the beam, from Naghdi and Rubin (1989).

3.2 Bending of a Circular Clamped Plate with an Unilateral Constraint

The problem of a circular clamped plate, showed in Figure 4 (a), subjected to an uniformly distributed transversal load, and with the transversal displacements constrained unilaterally by a rigid surface, placed at a distance *d* below, is numerically solved. Considering the symmetries of the problem, the plate of the Figure 4(a) is discretized using a mesh of 16 finite elements, as shown in Figure 4(b).

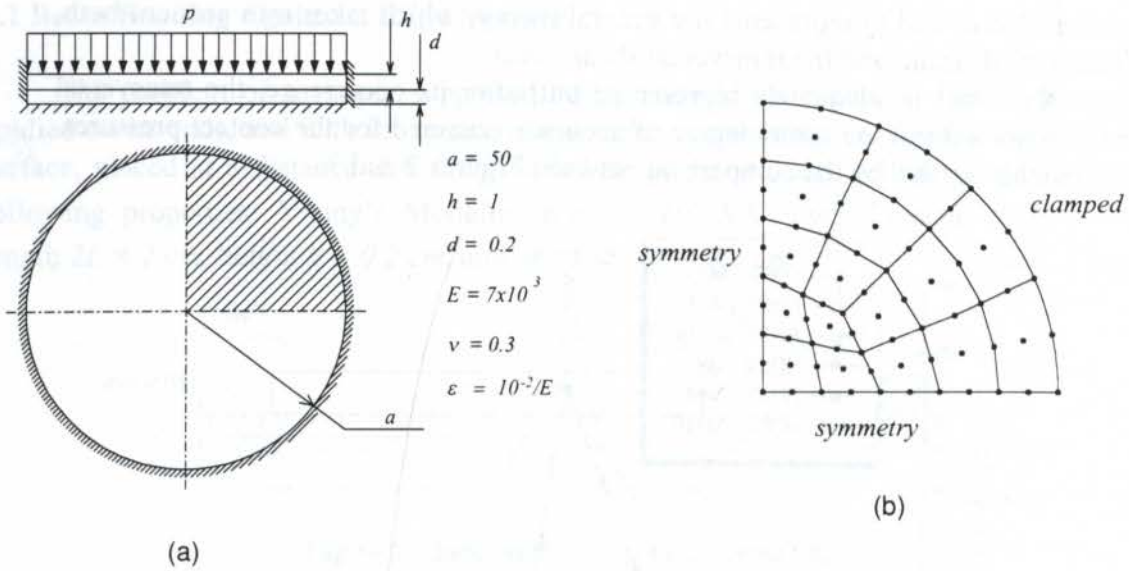

Figure 4 - Circular clamped plate with a unilateral constraint.

The transversal displacements, obtained using the Mindlin-Reissner first order shear theory and the Lo, Christensen and Wu higher order theory, are plotted in Figure 5, for four load steps, and they are compared to the analytical solution presented by Timoshenko and Woinowsky-Krieger (1959), using the classical thin plate theory. As can be seen, the obtained numerical results present a good degree of similarity between themselves, and with the analytical solution.

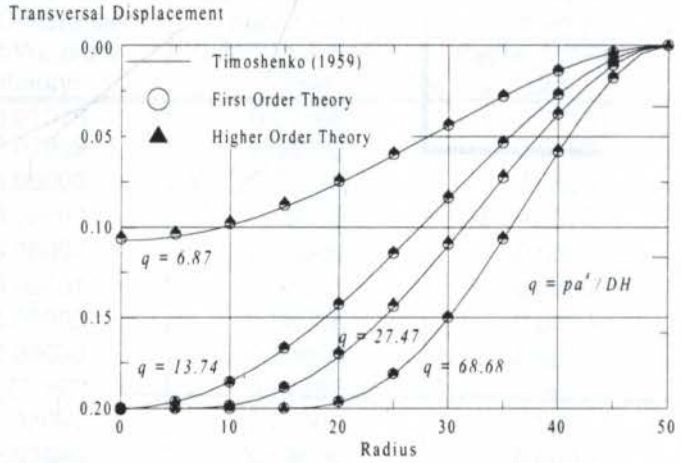

Figure 5 - Deflection of the circular clamped plate.

4. CONCLUSIONS

The formulation presented has shown to be effective in solving unilateral contact problems in plates undergoing large deflections, even adequately simulating the loss of contact. The contact pressures obtained using this formulation also presented a very good degree of accuracy.

5. ACKNOWLEDGMENTS

The authors would like to express their sincere thanks to the Brazilian funding agencies CNPq and CAPES, and to the RHAE Program of CNPq, for supporting this research.

6. REFERENCES

BARP, J.L., *Local Unilateral Contact Problems in Thick Plates Undergoing Large Deflections, Using a Higher Order Theory*, M.Sc. Dissertation, CPGEM/UFSC, Florianópolis, SC, Brazil, 1996 (in Portuguese).

DUVAUT, G. & LIONS, J.L., *Inequalities in Mechanics and Physics*, Springer-Verlag, Berlin, 1976.

ESSENBURG, F., On Surface Constraints in Plate Problems, *J. Appl. Mech.*, Trans. ASME, Nº 29, pp. 342-344, 1962.

ESSENBURG, F., On the Significance of the Inclusion of the Effect of Transverse Normal Strains in Problems Involving Beams with Surface Constraints, *J. Appl. Mech.*, Vol. 42, Nº 1, pp. 127-132, 1975.

KIKUCHI, N. & ODEN, J.T., Contact Problems in Elastostatics, in *Finite Elements - Special Problems in Solid Mechanics*, vol. V, Ed. J.T. Oden and G.H. Carey, Cap. 4, Prentice Hall, New Jersey, 1984.

LO, K.H., CHRISTENSEN, R.M. & WU, E.M., A Higher Order Theory of Plate Deformation - Part 1: Homogeneous Plates; Part 2: Laminated Plates, *J. Appl. Mech.*, Vol. 44, Nº 4, pp. 663-668 and 669-676, 1977.

LUERSEN, M.A. & SELKE, C.A.C., Unilateral Contact Problems in Plates Using a Thick Plate Finite Element, *XIV CILAMCE - Ibero Latin American Congress on Computational Methods in Engineering*, São Paulo, Brazil, Vol. I, pp. 212-221, 1993 (in Portuguese).

LUERSEN, M.A. & SELKE, C.A.C., A Finite Element Incremental Formulation for Unilateral Contact Problems in Thick Plates, *VI Chilean Congress on Mechanical Engineering*, Santiago, Chile, pp. 205-210, 1994 (in Portuguese).

LUERSEN, M.A., BARP, J.L. & SELKE, C.A.C. - Local Unilateral Contact Problems in Plates Undergoing Large Deflections, Using a First Order Thick Plate Finite Element, *COBEM-CIDIM/95 - XIII Brazilian Congress on Mechanical Engineering, and II Ibero Latin American Congress on Mechanical Engineering*, Belo Horizonte, MG, Brasil, 1995.

NAGHDI, P.M. & RUBIN, M.B. - On the Significance of Normal Cross-Sectional Extension in Beam Theory with Aplication to Contact Problems, *Int. J. Solids Structures*, vol. 25, 3:129-265, 1989.

REISSNER, E. A Note on Bending of Plates Including the Effects of Transverse Shearing and Normal Strains, *ZAMP*, Nº 32, pp. 764-767, 1981.

SELKE, C.A.C. & KIKUCHI, N., Local Unilateral Contact Problems in Beams Using a Higher Order Theory, *COBEM 87 - 9th Brazilian Congress on Mechanical Engineering*, Florianópolis, SC, Brazil, Vol. II, pp. 551-554, 1987.

SELKE, C.A.C., *Local Unilateral Contact Problems of Beams and Plates Undergoing Large Deflections*, Ph.D. Thesis, The University of Michigan, Ann Arbor, U.S.A., 1986.

TIMOSHENKO, S.P. & WOINOWSKY-KRIEGER, S., *Theory of Plates and Shells*, 2nd Edition, McGraw-Hill, New York, U.S.A., 1959.

WASHIZU, K., *Variational Methods in Elasticity and Plasticity*, 3rd Edition, Pergamon Press, Oxford, 1982.

XIV Brazilian Congress of Mechanical Engineering
Obeid Plaza Hotel Convention Center - Bauru - SP/Brazil
December 08-12th 1997

PAPER CODE: COB504

DINÂMICA DE CASCAS CILÍNDRICAS CONTENDO FLUIDO EM FLUXO CIRCULAR: SOLUÇÃO DO PROBLEMA EM REGIME PERMANENTE / *DYNAMIC OF THE CYLINDRICAL SHELL CONTAINE FLUID AT CIRCULAR FLUX: SOLUTION OF THE PROBLEM AT STEADY STATE*

D.S.Aguiar e J.C. Menezes
CTA - ITA - IEM – Departamento de Projetos. CEP: 12228-904 – São José dos Campos – S.P
EMAIL: menezes@mec.ita.cta.br

Abstract

This work present the solution and numerical results of the governing equations of a viscous fluid in steady state circunferencial motion. To describe the motion of the fluid, *Navier-Stokes* and *Continuit* equations are used (Panton,R.L.1984). The numerical solution is basead on the studies of Taylor e Hughes (Taylor e Hughes,1981), who employed the Finite Element Method for the two-dimension solution of the flow. Three velocity components are considered in a cylindrical coordinate system. To validate the results, the problem of a concentric journal bearing is solved , which shows a predictable press and velocities profile.

Keywords

Fluxo circular, regime permanente, método dos elementos finitos, dinâmica dos fluido/ circular flow, steady state, finite element method, fluid dynamic.

1.0 INTRODUÇÃO

O estudo da interação estrutura fluido é de importância em muitos campos os quais incluem a indústria aeroespacial, geração/ transmissão de energia, engenharia civil e tecnologia submarina (Chen,S.S. 1987). A configuração cilíndrica é extensamente encontrada e usada como vasos de pressão, tubulações, feixes de fibras, reservatórios, barris, e membros estruturais. Em muitas aplicações, em que essas estruturas são empregadas, o meio de operação do ambiente é um fluido. A presença do fluido tem uma significante influência na dinâmica da estrutura e resulta em um complexo problema a ser resolvido (Brown,S.J.1982). Portanto é necessário descrever com rigor o comportamento do fluido para possibilitar a determinação das freqüências naturais de vibração do sistema com maior precisão.

Muitos dos problemas de fluxo rotativo aplicados em engenharia sofrem simplificações, considerando apenas a componente tangencial de velocidade. Assim é possível determinar-se uma solução analítica para descrever o movimento do fluido. No entanto o surgimento de instabilidades tais como as células de Taylor (D.J.Tritton,1985), levam a necessidade de se resolver equações mais complexas para descrever o movimento do fluido. As equações de Navier-Stokes juntamente com a equação da Continuidade são geralmente empregadas para descrever a maioria dos problemas de escoamento, porém a presença de termos não lineares dificultam a solução analítica, o que leva a necessidade de se utilizar uma solução numérica iterativa.

O método de elementos finitos consiste hoje em uma poderosa ferramenta numérica que aliado a grande evolução dos computadores inclusive os de uso pessoal, é empregado para resolver diversos problemas de engenharia. Taylor e Huges (Taylor e Huges,1981) desenvolveram um estudo para resolver as equações de Navier-stokes empregando o método de elementos finitos, e muito das hipóteses empregadas neste trabalho para resolver o fluxo circular estão de acordo com esses estudos.

2.0 - DESENVOLVIMENTO TEÓRICO

2.1 - Equações de Elementos Finitos

Quando consideramos o fluido contido interno ao reservatório, certas adoções físicas e geométricas são feitas para resolver as equações do fluido: a) o domínio do fluido é axisimétrico e suas equações podem ser expressas em coordenadas cilíndricas, b) não existem mudanças de temperatura no fluido nem transferência de calor entre o fluido e o ambiente externo, c) o fluido é viscoso , incompressível e newtoniano, d) o fluxo está em movimento circular em regime permanente, e) a massa do sistema é mantida constante. As relações diferenciais entre as componentes de velocidade e gradientes de pressão em um certo ponto do domínio, que asseguram as adoções estabelecida em (a) , (b) , (c) e (d) são dadas pelas equações de Navier- Stokes como:

$$\rho\left(v_r \frac{\partial v_r}{\partial r} + \frac{v_\theta}{r}\frac{\partial v_r}{\partial \theta} - \frac{v_\theta^{\,2}}{r} + v_z \frac{\partial v_r}{\partial t}\right) =$$
$$\mu\left[\frac{\partial}{\partial r}\left(\frac{1}{r}\frac{\partial}{\partial r}(r v_r)\right) + \frac{1}{r^2}\frac{\partial^2 v_r}{\partial \theta^2} - \frac{2}{r}\frac{\partial v_\theta}{\partial \theta} + \frac{\partial^2 v_r}{\partial z^2}\right] - \frac{\partial p}{\partial r} + \rho g_\theta \qquad (1)$$

$$\rho\left(v_r \frac{\partial v_\theta}{\partial r} + \frac{v_\theta}{r}\frac{\partial v_\theta}{\partial \theta} + \frac{v_r v_\theta}{r} + v_z \frac{\partial v_\theta}{\partial z}\right) =$$
$$\mu\left[\frac{\partial}{\partial r}\left(\frac{1}{r}\frac{\partial}{\partial r}(r v_\theta)\right) + \frac{1}{r^2}\frac{\partial^2 v_\theta}{\partial \theta^2} + \frac{\partial^2 v_\theta}{\partial z^2} + \frac{2}{r^2}\frac{\partial v_r}{\partial \theta}\right] - \frac{1}{r}\frac{\partial p}{\partial \theta} + \rho g_\theta \qquad (2)$$

$$\rho\left(v_r \frac{\partial v_z}{\partial r} + \frac{v_\theta}{r}\frac{\partial v_z}{\partial \theta} + v_z \frac{\partial v_z}{\partial z}\right) =$$
$$\mu\left[\frac{1}{r}\frac{\partial}{\partial r}\left(r\frac{\partial v_z}{\partial r}\right) + \frac{1}{r^2}\frac{\partial^2 v_z}{\partial \theta^2} + \frac{\partial^2 v_z}{\partial z^2}\right] - \frac{\partial p}{\partial z} + \rho g_z \qquad (3)$$

onde as equações (1), (2) e (3)correspondem às componentes r, θ e z respectivamente. Para assegurar a hipótese (e), a equação da Continuidade tem que ser considerada no sistema de equações , como :

$$\frac{\partial v_r}{\partial r} + \frac{v_r}{r} + \frac{1}{r}\frac{\partial v_\theta}{\partial \theta} + \frac{\partial v_z}{\partial z} = 0 \qquad (4)$$

identificando-se as seguintes variáveis das equações anteriores: r, θ, z - coordenadas cilíndricas; v_r, v_θ, v_z - componentes de velocidade do fluido; ρ- densidade do fluido; μ - viscosidade dinâmica; g_r, g_θ, g_z - componentes de aceleração gravitacional.

Os gradientes de pressão podem ser escritos como :

$$\left(\frac{\partial p}{\partial r}=\frac{\partial p_e}{\partial r}+\frac{\partial p_d}{\partial r}\right),\left[\frac{\partial p}{\partial \theta}=\frac{1}{r}\left(\frac{\partial p_e}{\partial \theta}+\frac{\partial p_d}{\partial \theta}\right)\right],\left(\frac{\partial p}{\partial z}=\frac{\partial p_e}{\partial z}+\frac{\partial p_d}{\partial z}\right) \qquad (5)$$

onde p_e = pressão estática do fluido, p_d = pressão dinâmica do fluido.

Considerando-se elementos finitos quadriláteros de oito e quatro pontos nodais; pode-se expressar as variáveis como :

$$v_r=\sum_{j=1}^{8} N_j v_{rj}\,,\quad v_\theta=\sum_{j=1}^{8} N_j v_{\theta j}\,,\quad v_z=\sum_{j=1}^{8} N_j v_{zj} \quad \text{e} \quad P=\sum_{k=1}^{4} M_k p_k \qquad (6)$$

Substituindo (5) e (6) e aplicando-se o método de Galerkin às equações (1) ,(2) ,(3) e (4) :

$$\sum_{i=1}^{8} N_i \int_v (\text{equação j})\, dv = 0 \quad \text{onde j= 1,2,3} \qquad (7)$$

$$\sum_{i=1}^{4} M_i \int_v (\text{equação 4})\, dv = 0 \qquad (8)$$

Assumindo-se que $dv = r\,dr\,d\theta\,dz$, as equações (7) e (8) podem ser integradas analiticamente na direção circunferencial. Sendo v_r , v_θ , v_z e p supostamente constantes para uma variação de θ antes das equações serem integradas, alguns termos das equações (1) à (4) tornam-se nulos. Sabendo-se que o termo $(\partial p_e / \partial r)$ é igual a zero, e que $(\partial \dot{p}_e / \partial z)$ tenha mais influência sobre as tensões causadas na parede do reservatório, este termo é desconsiderado. Empregando-se o teorema de *Green*, sobre à componentes r , os termos de segunda ordem podem ser reduzidos da seguinte forma :

$$\int_A N_i\left(\sum_{j=1}^{8}\frac{\partial^2 N_j}{\partial r^2}v_{rj}+\sum_{j=1}^{8}\frac{\partial^2 N_j}{\partial z^2}v_{rj}\right)r\,dr\,dz = -\int_A\left(\frac{\partial N_i}{\partial r}\sum_{j=1}^{8}\frac{\partial N_j}{\partial r}v_{rj}+\frac{\partial Ni}{\partial z}\sum_{j=1}^{8}\frac{\partial N_j}{\partial z}v_{rj}\right)r\,dr\,dz$$

$$-\int_A\left(+\frac{1}{r}Ni\sum_{j=1}^{8}\frac{\partial N_j}{\partial r}v_{rj}\right)r\,dr\,dz \quad +\int_S Ni\,\frac{\partial v_r}{\partial n}\,ds \qquad (9)$$

o que é também válido para os termos de segunda ordem das componentes θ e z. Quando os termos $(\partial v_r / \partial n)ds$, $(\partial v_\theta / \partial n)ds$ e $(\partial v_z / \partial n)ds$ são somados na adjacências S dos elementos a contribuição final torna-se nula. Por simplicidade tais termos poderão ser retirados das equações. Dessa forma as equações de *Navier- Stokes* e da *Continuidade,* são apresentadas como:

$$\sum_{i=1}^{8} N_i \int_A \rho\left(\sum_{i=1}^{8} N_j v_{rj}\sum_{j=1}^{8}\frac{\partial N_j}{\partial r}v_{rj}\right)r\,dr\,dz - \sum_{i=1}^{8} N_i \int_A \rho\left[\frac{1}{r}\left(\sum_{i=1}^{8} N_j v_{\theta j}\right)^2\right]r\,dr\,dz +$$

$$\sum_{i=1}^{8} N_i \int_A \rho\left(\sum_{i=1}^{8} N_j v_{zj}\sum_{j=1}^{8}\frac{\partial N_j}{\partial z}v_{rj}\right)r\,dr\,dz + \sum_{i=1}^{8} N_i \int_A\left(\sum_{k=1}^{4}\frac{\partial M_k}{\partial r}p_k\right)r\,dr\,dz -$$

$$\mu\sum_{i=1}^{8}N_i\int_A\left(\frac{1}{r^2}\sum_{i=1}^{8}N_jv_{rj}\right)r\,dr\,dz+\mu\sum_{i=1}^{8}\int_A\left(\frac{\partial N_i}{\partial r}\sum_{j=1}^{8}\frac{\partial N_j}{\partial r}v_{rj}\right)rdrdz+$$

$$\mu\sum_{i=1}^{8}\int_A\left(\frac{\partial N_i}{\partial z}\sum_{j=1}^{8}\frac{\partial N_j}{\partial z}v_{rj}\right)rdrdz-\mu\sum_{i=1}^{8}\int_S N_i\frac{\partial v_r}{\partial n}ds-\sum_{i=1}^{8}N_i\int_A(\rho g_r)\,r\,dr\,dz=0 \quad (10)$$

$$\sum_{i=1}^{8}N_i\int_A\rho\left(\sum_{j=1}^{8}N_jv_{rj}\sum_{j=1}^{8}\frac{\partial N_j}{\partial r}v_{\theta j}\right)r\,dr\,dz+\sum_{i=1}^{8}N_i\int_A\rho\left(\frac{1}{r}\sum_{j=1}^{8}N_jv_{rj}\sum_{j=1}^{8}N_jv_{\theta j}\right)r\,dr\,dz+$$

$$\sum_{i=1}^{8}N_i\int_A\rho\left(\sum_{j=1}^{8}N_jv_{zj}\sum_{j=1}^{8}\frac{\partial N_j}{\partial z}v_{\theta j}\right)r\,dr\,dz+\mu\sum_{i=1}^{8}\int_A\left(\frac{\partial N_i}{\partial r}\sum_{j=1}^{8}\frac{\partial N_j}{\partial r}v_{\theta j}\right)rdrdz+$$

$$\mu\sum_{i=1}^{8}\int_A\left(\frac{\partial N_i}{\partial z}\sum_{j=1}^{8}\frac{\partial N_j}{\partial z}v_{\theta j}\right)rdrdz+\sum_{i=1}^{8}N_i\int_A\mu\left(\frac{1}{r^2}\sum_{j=1}^{8}N_jv_{\theta j}\right)rdrdz+$$

$$\mu\sum_{i=1}^{8}N_i\frac{\partial v_\theta}{\partial n}ds-\sum_{i=1}^{8}N_i\int_A(\rho g_\theta)\,r\,dr\,dz=0 \quad (11)$$

$$\sum_{i=1}^{8}N_i\int_A\rho\left(\sum_{j=1}^{8}N_jv_{rj}\sum_{j=1}^{8}\frac{\partial N_j}{\partial r}v_{zj}\right)r\,dr\,dz+\sum_{i=1}^{8}N_i\int_A\rho\left(\sum_{j=1}^{8}N_jv_{zj}\sum_{j=1}^{8}\frac{\partial N_j}{\partial z}v_{zj}\right)r\,dr\,dz+$$

$$\sum_{i=1}^{8}N_i\int_A\left(\sum_{k=1}^{4}\frac{\partial M_k}{\partial z}p_k\right)r\,dr\,dz+\mu\sum_{i=1}^{8}\int_A\left(\frac{\partial N_i}{\partial r}\sum_{j=1}^{8}\frac{\partial N_j}{\partial r}v_{zj}\right)rdrdz+$$

$$\mu\sum_{i=1}^{8}\int_A\left(\frac{\partial N_i}{\partial z}\sum_{j=1}^{8}\frac{\partial N_j}{\partial z}v_{zj}\right)rdrdz-\mu\sum_{i=1}^{8}\int_S N_i\frac{\partial v_z}{\partial n}ds+$$

$$\sum_{i=1}^{8}N_i\int_A(\rho g_\theta)\,r\,dr\,dz=0 \quad (12)$$

onde as equações (10), (11) e (12) correspondem às direções r, θ e z, e a equação da continuidade:

$$\sum_{i=1}^{4}\int_A M_i\left(\sum_{j=1}^{8}\frac{\partial N_j}{\partial r}v_{rj}+\frac{1}{r}\sum_{j=1}^{8}N_jv_{rj}+\sum_{j=1}^{8}\frac{\partial N_j}{\partial z}v_{zj}\right)r\,dr\,dz \quad (13)$$

2.2 Elementos Finitos

Foram empregados elementos finitos isoparamétricos retangulares de oito pontos nodais para descrever as equações de *Navier-Stokes,* figura (1), e de quatro pontos nodais para a equação da Continuidade. Para o elemento de oito pontos as funções de interpolação são:

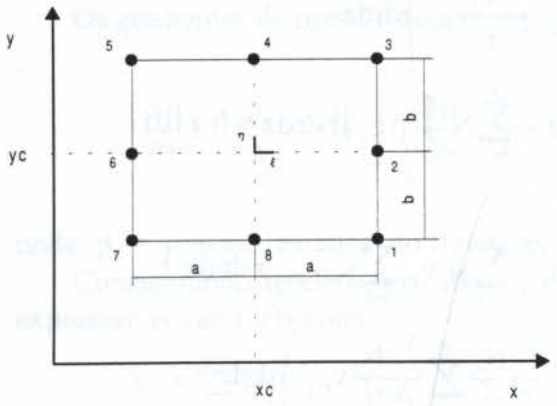

Figura 1: Elemento de oito pontos nodais

Função de interpolação para os nós extremos

$$N_i = \frac{1}{4}(1+\xi_i\xi)(1+\eta\eta_i)(\xi_i\xi+\eta\eta_i-1) \quad (14)$$

e funções de interpolação para os nós intermediários

$$N_i = \frac{1}{2}(1-\xi^2)(1-\eta\eta_i) \text{ para } \xi_i = 0 \quad (15)$$

$$N_i = \frac{1}{2}(1-\eta^2)(1+\xi\xi_i) \text{ para } \eta_i = 0 \quad (16)$$

Para o elemento de quatro pontos nodais é considerado apenas os nós da extremidades e as funções de interpolação são :

$$N_i = \frac{1}{4}(1+\xi_i\,\xi)(1+\eta_i\,\eta) \quad (17)$$

3.0 - SIMULAÇÃO

Esta etapa do trabalho procura estabelecer a validade das equações (10), (11), (12) e (13). Para este fim foi estudado um sistema fisico na condição de fluxo de interesse, comparando-se o comportamento conhecido das variáveis do sistema com os valores calculados pelas equações. A figura (2), mostra um mancal hidráulico rotativo com os perfis de pressão e velocidade periférica, que servirão de parâmetro comparativo.

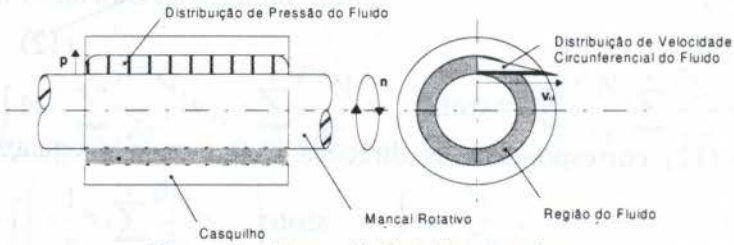

Figura 2: Mancal hidráulico rotativo

O modelo de elementos finitos da figura (3), procura estabelecer a condição do domínio do fluido de acordo com o exemplo empregado. As condições de contorno invariantes no tempo são: a) na lateral direita as velocidades v_r , v_θ e v_z são zero; b) na lateral esquerda a velocidade v_θ é prescrita e v_r e v_z zero, c) no topo e na base da malha as pressões são zero.

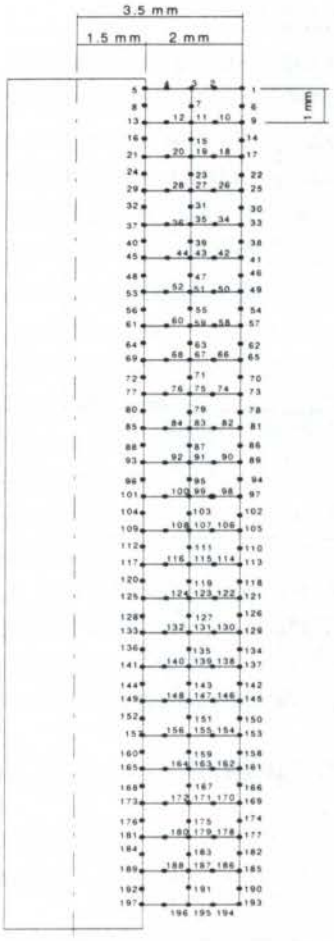

Figura 3: Modelo de elementos finitos com 48 elementos

4.0 - RESULTADOS GRÁFICOS

As figuras (4, 5, 6 e 7), referem-se ao perfil de distribuição de pressão na lateral direita do modelo. As figuras (8, 9, 10 e 11) apresentam a distribuição radial das velocidades tangenciais em quatro diferentes níveis a partir do topo, , com cinco nós cada um.

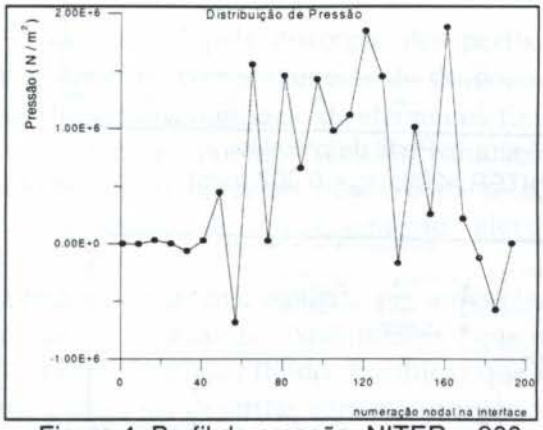

Figura 4: Perfil de pressão, NITER = 200
v_θ = 2,0 (m/s)

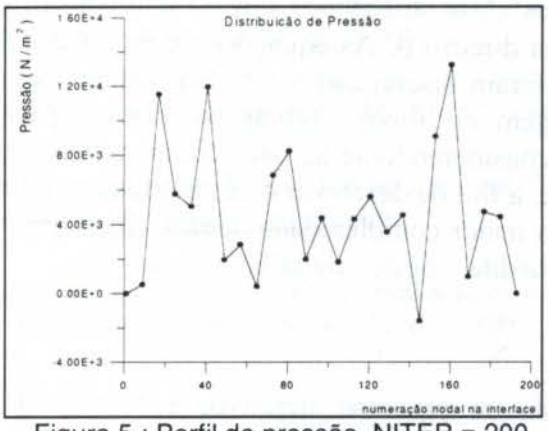

Figura 5 : Perfil de pressão, NITER = 200
v_θ = 0,2 (m/s)

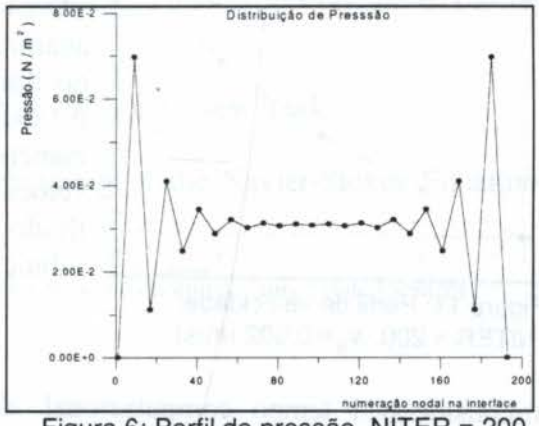

Figura 6: Perfil de pressão, NITER = 200
v_θ = 0,02 (m/s)

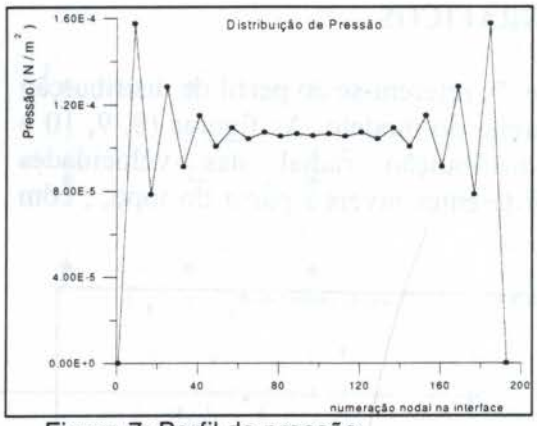

Figura 7: Perfil de pressão, NITER =200, v_θ= 0,002 (m/s)

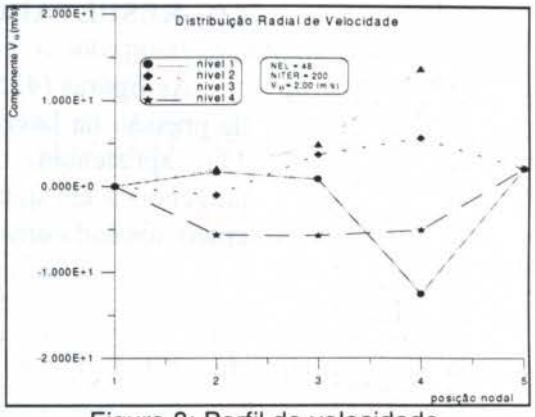

Figura 8: Perfil de velocidade, NITER = 200, v_θ= 2,0 (m/s)

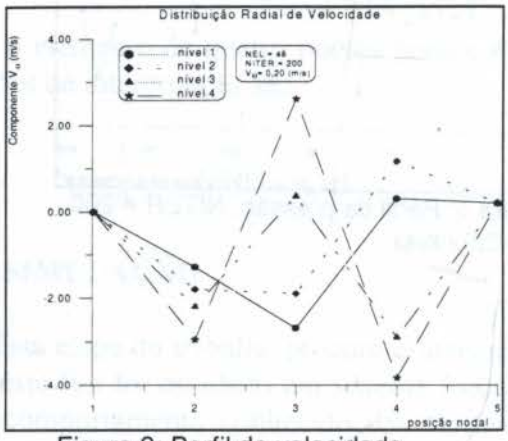

Figura 9: Perfil de velocidade, NITER = 200, v_θ= 0,2 (m/s)

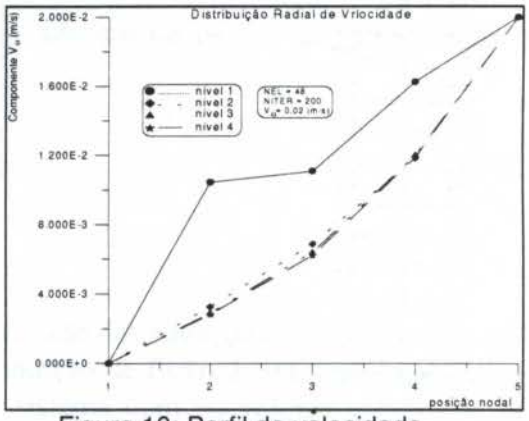

Figura 10: Perfil de velocidade, NITER = 200, v_θ= 0,02 (m/s)

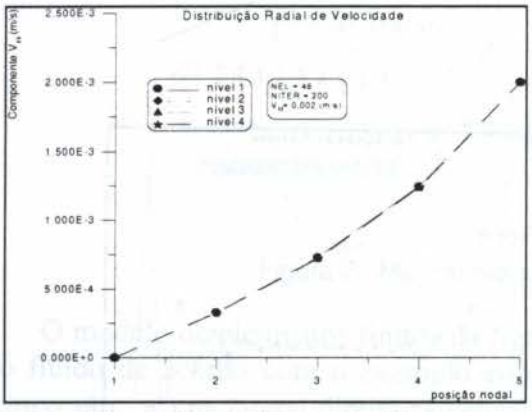

Figura 11: Perfil de velocidade, NITER = 200, v_θ= 0,002 (m/s)

5.0 – COMENTÁRIOS

A configuração geométrica cilíndrica, facilitou a solução dos casos analisados devido à integração analítica na direção θ. As equações de movimento do fluido foram discretizadas em duas dimensões. A abordagem do fluxo circular em regime permanente, considerando-se as três componentes de velocidade, a fim de descrever o comportamento do fluido com maior complexidade, caracteriza a contribuição inédita deste trabalho. Apesar de consumirconsiderável tempo computacional, devido ao processo iterativo, a técnica de solução empregando o método de elementos finitos desenvolvidas por Taylor e Hughes , constitui um procedimento de tratamento do problema.

6.0 - CONCLUSÕES

Quanto à solução numérica das equações de movimento na condição de fluxo circular em regime permanente, pode-se chegar às seguintes conclusões, visto os resultados apresentados:

- os perfis de pressão e velocidade encontrados aproximam-se do comportamento esperado quando as velocidades periféricas são impostas com valores menor ou igual à ordem de grandeza de $10^{-2}\,(m/s)$. Portanto o modelo de elementos finitos é mais aceitável para níveis de velocidades baixas. Velocidades superiores provavelmente forçam o fluido a entrar na condição de regime turbulento.
- a presença da componente z de velocidade é responsável pela distorção dos perfis de pressão e velocidade que são geradoras de instabilidades no comportamento do fluido.
- de acordo com as conclusões anteriores, pode-se afirmar que o modelo de elementos finitos apresentou resultados qualitativos aceitáveis. Deve-se, porém, realizar simulações empregando malhas mais refinadas, observando-se que o processo iterativo da solução numérica torna-se um fator limitador, pois o tempo de processamento eleva-se consideravelmente.

A solução do problema de fluxo circular em regime permanente ganha a sua importância na análise de fluxo rotativo devido à possibilidade de se analisar as instabilidades , que não são consideradas em modelos mais simplificados. Assim, as forças fluido-dinâmicas que são desenvolvidas pelas pressões provocadas pelo fluido podem ser descritas com maior rigor.

REFERÊNCIAS BIBLIOGRÁFICAS

Brown, S.J.,"A Survey of Studies Into the Hydrodynamic Response of Fluid Coupled Circular Cylinders", Transactions of the ASME, J. Pressure Vessel Technology, Vol.104, pp.2 - 19, 1982.

Chen,S.S. "Flow Induced Vibration of Circular Cylindrical Structures", Hemisphere Publishing Corporation, USA, 1987

D.J.Tritton, "Physical Fluid Dynamics", 1985.

Mistry J.and Menezes J.C.. "Vibration of Cylinders Partially-Filled with Liquids ".J. of Sound and Vibration, Vol.117, N° 2 ,pp.87- 93

Panton,R.L.,1984, "Incompressible Flow", John Wiley & Sone , New York.

Taylor,C.and Huges,T.G., "Finite Element Programming of the Navier-Stokes Equations", Pinerideg Press Limited, U.K.,1981.

Taylor,C. and Hood, P. 1973, "A Numerical Solution of Navier-Stokes Equations Using Finite Element Technique", Computers & Fluids, Vol.1 , pp. 73-100.

XIV Brazilian Congress of Mechanical Engineering
Obeid Plaza Hotel Convention Center - Bauru - SP/Brazil
December 08-12th 1997

PAPER CODE: COB76

OBTENCIÓN DE LA MATRIZ DE RIGIDEZ SECANTE EN MECÁNICA NO LINEAL DEL SÓLIDO

DERIVATION OF THE SECANT STIFFNESS MATRIX FOR NON LINEAL FINITE ELEMENT ANALYSIS OF SOLIDS

WILLIAM MATIAS & EUGENIO OÑATE †
Departamento de Engenharia Civil, Universidade de Brasília - ENC/UnB
CEP 70910-900 Brasília, Brasil - E-mail: taylor@guarany.cpd.unb.br

Abstract

In this paper the general non symmetric parametric form of the secant stiffness matrix for non linear analysis of solids using finite element method is derived. A convenient symmetric expression for a particular value of the parameters is obtained. The geometrically non linear formulation is based on a Generalized Lagragian approach. Detailed expressions of all the relevant matrices involved in the analysis of 3D solids are obtained. The potential of using the secant stiffness matrix for developing new solution algorithms for non linear structural problem is also discussed. Examples of application are given for the non linear analysis of pin joined frames and 2D solids.

Keywords

geometric nonlinear analysis, secant stiffness matrix, Generalized Lagragian description

1. INTRODUCCIÓN

La utilización de manera general del concepto de la matriz de rigidez secante en el contexto de la mecánica no lineal del sólido ha recibido poca atención por parte de la comunidad científica de la mecánica computacional. Una excepción la constituye el empleo de métodos basados en una expresión aproximada de la matriz secante en la resolución del sistema de ecuaciones no lineales como los métodos cuasi-Newton y secante-Newton. En estos métodos se deduce una expresión númerica de la matriz secante utilizando algoritmos de Broyden y los derivados del BFGS. Se trata de métodos potentes para la solución de ecuaciones no lineales. En este artículo se propone un algoritmo incremental-iterativo con control de la respuesta basado en la matrices de rigidez tangente y secante "exacta".

Recientemente, varios investigadores (BADAWI & CUSENS [1992], CARRERA [1992], FELIPPA *et al* [1994] y OÑATE [1995]) han reconocido las posibilidades de aplicación de la forma "exacta" de la matriz de rigidez secante en el análisis no lineal de sistemas estructurales. Se pueden encontrar en la literatura técnica en el área de mecánica no lineal trabajos que han desarrollado el concepto de la matriz secante aplicada a distintos

† *International Center for Numerical Methods in Engineering - UPC Barcelona, Spain*

campos como, por ejemplo, en la deducción de distintos algoritmos para la solución de sistemas de ecuaciones no lineales; en la predicción del grado de inestabilidad de sistemas estructurales en análisis estático y dinámico; en la predicción y localización de puntos límite y de bifurcación; en el análisis postcrítico através de la formulación de algoritmos de búsqueda de ramas secundarias de equilibrio.

Las ideas presentadas en este artículo constituyen un breve resumen de los trabajos desarrollados por los autores sobre las posibilidades de aplicación de la matriz secante en la mecánica no lineal del sólido (OÑATE & MATIAS [1995,96], MATIAS [1996]).

2. OBTENCIÓN DE LA MATRIZ DE RIGIDEZ SECANTE

Para obtener la matriz de rigidez secante se parte de la expresión incremental del *Principio de los Trabajos Virtuales* (*PTV*) en su forma completa, es decir, manteniendo todos los términos que son función no lineal del gradiente de desplazamientos. Recientemente, OÑATE [1995] ha desarrollado una metodología general para obtener una expresión paramétrica de la matriz de rigidez secante en el análisis de no linealidad geométrica de sólidos. Para ello, ha utilizado una formulación *Lagrangiana Generalizada* (*LG*). Dicha metodología es la que se adopta en este trabajo y sus hipótesis básicas serán desarrolladas a continuación, de manera sucinta.

2.1 Descripción incremental de la cinemática

Considérese un cuerpo 3D con volumen inicial ${}^0V$ en una configuración de equilibrio conocida ${}^tV$ sometida a la acción de fuerzas de volumen ${}^t\mathbf{b}$, fuerzas de superficie ${}^t\mathbf{t}$ y fuerzas puntuales ${}^t\mathbf{p}$. En problemas cuasi-estáticos t indica el paso de carga en un proceso incremental. Al incrementar las fuerzas externas, el cuerpo cambia su configuración de ${}^tV$ a ${}^{t+\Delta t}V$. Las coordenadas del cuerpo en cada configuración están referidas al sistema global cartesiano (x_1, x_2, x_3). El vector de desplazamientos en $t+\Delta t$ se expresa como ${}^{t+\Delta t}\mathbf{u} = {}^t\mathbf{u} + \Delta\mathbf{u}$, donde ${}^t\mathbf{u}$ son los desplazamientos en t y $\Delta\mathbf{u}$ son los incrementos de desplazamientos del cuerpo de ${}^tV$ a ${}^{t+\Delta t}V$.

En la descripción *LG*, los tensores de deformación, de tensión y constitutivo se escriben respecto a una configuración de referencia intermediaria cualquiera ${}^rV$.

El tensor de deformación en $t+\Delta t$ referido a ${}^rV$ viene dado por

$$ {}^{t+\Delta t}_{r}\boldsymbol{\varepsilon}_{ij} = \frac{1}{2}({}^{t+\Delta t}_{r}u_{i,j} + {}^{t+\Delta t}_{r}u_{j,i} + {}^{t+\Delta t}_{r}u_{k,i}\,{}^{t+\Delta t}_{r}u_{k,j}) \tag{1a} $$

donde

$$ {}^{t+\Delta t}_{r}u_{i,j} = \frac{\partial\,{}^{t+\Delta t}u_i}{\partial\,{}^{r}x_j} \qquad i,j = 1,2,3 \tag{1b} $$

Nótese que para ${}^rV = {}^0V$ la ecuación (1a) se convierte precisamente en la conocida expresión del tensor de deformación de Green-Lagrange utilizada en la formulación *Lagrangiana Total (LT)*. Si ${}^rV = {}^tV$, se obtiene la descripción *Lagrangiana Actualizada (LA)*.

Los incrementos de deformación se escriben como

$$ {}_{r}\Delta\varepsilon_{ij} = {}^{t+\Delta t}_{r}\varepsilon_{ij} - {}^{t}_{r}\varepsilon_{ij} \;=\; {}_{r}e_{ij} + {}_{r}\eta_{ij} \tag{2} $$

donde ${}_re_{ij}$ y ${}_r\eta_{ij}$ son los incrementos de deformación de primer y segundo orden, respectivamente. En forma matricial se expresan como

$$ {}_r\mathbf{e} = \left[\mathbf{L}_0 + {}^t_r\mathbf{L}_1({}^t_r\mathbf{g})\right] {}_r\mathbf{g} \tag{3a} $$

$$ {}_r\boldsymbol{\eta} = \frac{1}{2}\, {}_r\mathbf{L}_1({}_r\mathbf{g})\, {}_r\mathbf{g} \tag{3b} $$

donde ${}^t_r\mathbf{g}$ y ${}_r\mathbf{g}$ son los gradientes de los desplazamientos y de los incrementos de desplazamientos, respectivamente. $\mathbf{L}_0$ es una matriz rectangular con unidades y ceros. ${}^t_r\mathbf{L}_1$ y ${}_r\mathbf{L}_1$ son matrices función de los gradientes de los desplazamientos y de los incrementos de desplazamientos, respectivamente (Cuadro 1).

Se supone ahora una variación virtual en el campo de desplazamientos en la configuración ${}^{t+\Delta t}V$ considerándose la configuración ${}^tV$ fija, es decir, $\delta^t u_i = 0$. De esta manera, puede expresarse la variación virtual de las ecuaciones (3) como

$$ \delta_r\mathbf{e} = \left(\mathbf{L}_0 + {}^t_r\mathbf{L}_1\right) \delta_r\mathbf{g} \tag{4a} $$

$$ \delta_r\boldsymbol{\eta} = {}_r\mathbf{L}_1\, \delta_r\mathbf{g} \tag{4b} $$

$$ \mathbf{L}_0 = \begin{bmatrix} 100 & 000 & 000 \\ 000 & 010 & 000 \\ 000 & 000 & 001 \\ 010 & 100 & 000 \\ 001 & 000 & 100 \\ 000 & 001 & 010 \end{bmatrix} $$

$$ {}^t_r\mathbf{L}_1 = \begin{bmatrix} {}^t_r\mathbf{g}^T\ \mathbf{H}_1 \\ {}^t_r\mathbf{g}^T\ \mathbf{H}_2 \\ \vdots \\ {}^t_r\mathbf{g}^T\ \mathbf{H}_6 \end{bmatrix} \quad ; \quad {}^t_r\mathbf{g} = \begin{Bmatrix} {}^t_r\mathbf{g}_1 \\ {}^t_r\mathbf{g}_2 \\ {}^t_r\mathbf{g}_3 \end{Bmatrix} \quad ; \quad {}^t_r\mathbf{g}_i = \frac{\partial\, {}^t\mathbf{u}}{\partial\, {}^r x_i} = \begin{Bmatrix} \frac{\partial\, {}^t u_1}{\partial\, {}^r x_i} \\ \frac{\partial\, {}^t u_2}{\partial\, {}^r x_i} \\ \frac{\partial\, {}^t u_3}{\partial\, {}^r x_i} \end{Bmatrix}. $$

$$ {}_r\mathbf{L}_1 = \begin{bmatrix} {}_r\mathbf{g}^T\ \mathbf{H}_1 \\ {}_r\mathbf{g}^T\ \mathbf{H}_2 \\ \vdots \\ {}_r\mathbf{g}^T\ \mathbf{H}_6 \end{bmatrix} \quad ; \quad {}_r\mathbf{g} = \begin{Bmatrix} {}_r\mathbf{g}_1 \\ {}_r\mathbf{g}_2 \\ {}_r\mathbf{g}_3 \end{Bmatrix} \quad ; \quad {}_r\mathbf{g}_i = \frac{\partial(\Delta\mathbf{u})}{\partial\, {}^r x_i} = \begin{Bmatrix} \frac{\partial(\Delta u_1)}{\partial\, {}^r x_i} \\ \frac{\partial(\Delta u_2)}{\partial\, {}^r x_i} \\ \frac{\partial(\Delta u_3)}{\partial\, {}^r x_i} \end{Bmatrix} $$

$$ \mathbf{H}_1 = \begin{bmatrix} \mathbf{I}_3 & \mathbf{0} & \mathbf{0} \\ \mathbf{0} & \mathbf{0} & \mathbf{0} \\ \mathbf{0} & \mathbf{0} & \mathbf{0} \end{bmatrix}; \quad \mathbf{H}_2 = \begin{bmatrix} \mathbf{0} & \mathbf{0} & \mathbf{0} \\ \mathbf{0} & \mathbf{I}_3 & \mathbf{0} \\ \mathbf{0} & \mathbf{0} & \mathbf{0} \end{bmatrix}; \quad \mathbf{H}_3 = \begin{bmatrix} \mathbf{0} & \mathbf{0} & \mathbf{0} \\ \mathbf{0} & \mathbf{0} & \mathbf{0} \\ \mathbf{0} & \mathbf{0} & \mathbf{I}_3 \end{bmatrix} $$

$$ \mathbf{H}_4 = \begin{bmatrix} \mathbf{0} & \mathbf{I}_3 & \mathbf{0} \\ \mathbf{I}_3 & \mathbf{0} & \mathbf{0} \\ \mathbf{0} & \mathbf{0} & \mathbf{0} \end{bmatrix}; \quad \mathbf{H}_5 = \begin{bmatrix} \mathbf{0} & \mathbf{0} & \mathbf{I}_3 \\ \mathbf{0} & \mathbf{0} & \mathbf{0} \\ \mathbf{I}_3 & \mathbf{0} & \mathbf{0} \end{bmatrix}; \quad \mathbf{H}_6 = \begin{bmatrix} \mathbf{0} & \mathbf{0} & \mathbf{0} \\ \mathbf{0} & \mathbf{0} & \mathbf{I}_3 \\ \mathbf{0} & \mathbf{I}_3 & \mathbf{0} \end{bmatrix} $$

$$ \mathbf{I}_3 = \begin{bmatrix} 1 & 0 & 0 \\ 0 & 1 & 0 \\ 0 & 0 & 1 \end{bmatrix}; \quad \mathbf{0} = \begin{bmatrix} 0 & 0 & 0 \\ 0 & 0 & 0 \\ 0 & 0 & 0 \end{bmatrix} $$

Cuadro 1. Forma matricial de las relaciones cinemáticas para sólidos 3D

Se supone que las relaciones constitutivas relacionan los incrementos del segundo tensor de tensión de Piola-Kirchhoff con los incrementos del tensor de deformación de Green-Lagrange, así

$$ {}_r\Delta\mathbf{S} = {}_r\mathbf{D}\ {}_r\Delta\boldsymbol{\varepsilon} = {}_r\mathbf{D}\ ({}_r\mathbf{e} + {}_r\boldsymbol{\eta}) \tag{5} $$

donde ${}_r\mathbf{D}$ es la matriz constitutiva definida en la configuración ${}^rV$. Las tensiones en $t + \Delta t$ se obtienen según la expresión

$$ {}^{t+\Delta t}_r\mathbf{S} = {}^t_r\mathbf{S} + {}_r\Delta\mathbf{S} \tag{6} $$

Por último, considerando las ecuaciones (3), (4), (5), y (6), la expresión del PTV en ${}^{t+\Delta t}V$ se escribe en forma matricial del modo siguiente

$$\int_{{}_rV} \Big[\delta_r\mathbf{e}^T \, {}^t_r\mathbf{D} \, {}_r\mathbf{e} + \overbrace{\underbrace{(\delta_r\mathbf{e}^T \, {}_r\mathbf{D} \, {}_r\boldsymbol{\eta} + \delta_r\boldsymbol{\eta}^T \, {}_r\mathbf{D} \, {}_r\mathbf{e})}_{\text{términos no lineales en } {}_r\mathbf{g}} + \delta_r\boldsymbol{\eta}^T \, {}_r\mathbf{D} \, {}_r\boldsymbol{\eta}}^{=f({}_r\mathbf{g}^3)} + \delta_r\boldsymbol{\eta}^T \, {}^t_r\mathbf{S} \Big] dV = \overbrace{\qquad\qquad}^{=f({}_r\mathbf{g}^2)}$$

$$= \int_{{}_rV} \delta(\Delta\mathbf{u})^T \, {}^{t+\Delta t}\mathbf{b} \; dV - \int_{{}_rV} \delta_r\mathbf{e}^T \, {}^t_r\mathbf{S} \; dV \tag{7}$$

En la ecuación (7) se expresa la *forma incremental completa* del PTV. Esta ecuación es la base para la obtención de las ecuaciones de equilibrio incrementales al discretizarla por el método de los elementos finitos. Nótese que el segundo miembro de (7) es independiente del gradiente del incremento de desplazamientos ${}_r\mathbf{g}$ y expresa las fuerzas residuales o en desequilibrio después de la discretización por elementos finitos. Por otro lado, en el primer miembro de (7) todos los términos son dependientes del gradiente del incremento de desplazamientos ${}_r\mathbf{g}$. En particular, los términos subrayados son funciones cuadráticas y cúbicas en ${}_r\mathbf{g}$. La consideración de los términos no lineales en ${}_r\mathbf{g}$ es básica para la obtención de la matriz de rigidez secante. En la linealización de la ecuación (7) se desprecian estos términos, lo que conduce a la obtención de la expresión de la matriz de rigidez tangente. En el próximo apartado se obtendrán estas matrices para problemas de elasticidad lineal.

3. DISCRETIZACIÓN POR ELEMENTOS FINITOS. OBTENCIÓN DE LAS MATRICES DE RIGIDEZ SECANTE Y TANGENTE

Considérese una discretización estándar en elementos finitos isoparamétricos con continuidad C^0 de sólidos 3D, con n nodos y funciones de forma $N^k(\xi,\eta,\zeta)$ definidas en coordenadas naturales (ξ,η,ζ). Los campos de desplazamientos y de incremento de desplazamientos de cada elemento se definen por funciones de interpolación estándar, BATHE [1996].

Una vez discretizado el sólido, pueden reescribirse las ecuaciones (3), (4) y (5) en función de los incrementos de los desplazamientos nodales por

$$\begin{aligned} {}_r\mathbf{e} &= {}^t_r\mathbf{B}_L \; \Delta\mathbf{a} \quad , \quad \delta_r\mathbf{e} = {}^t_r\mathbf{B}_L \; \delta(\Delta\mathbf{a}) \\ {}_r\boldsymbol{\eta} &= \frac{1}{2} \, {}_r\mathbf{B}_1 \; \Delta\mathbf{a} \quad , \quad \delta_r\boldsymbol{\eta} = {}_r\mathbf{B}_1 \; \delta(\Delta\mathbf{a}) \end{aligned} \tag{8}$$

$${}_r\Delta\mathbf{S} = {}_r\mathbf{D} \left[{}^t_r\mathbf{B}_L + \frac{1}{2} \, {}_r\mathbf{B}_1 \right] \Delta\mathbf{a} \tag{9}$$

La forma de las matrices en (8) y (9) queda detallada en el Cuadro 2.

Sustituyendo las ecuaciones (8) y (9) en la expresión del PTV (7) se obtiene una relación entre los incrementos de las fuerzas externas nodales y los incrementos de los desplazamientos nodales para cada elemento

$${}^t_r\mathbf{K}_S({}^t\mathbf{a}, \Delta\mathbf{a}) \; \Delta\mathbf{a} = - \, {}^{t+\Delta t}_r\mathbf{r} \tag{10}$$

donde ${}^{t+\Delta t}_r\mathbf{r}$ es el vector de fuerzas residuales y ${}^t_r\mathbf{K}_S$ es la *matriz de rigidez secante incremental* que se escribe como

$$\boxed{{}^t_r\mathbf{K}_S({}^t\mathbf{a}, \Delta\mathbf{a}) = {}^t_r\mathbf{K}_L({}^t\mathbf{a}, {}^t\mathbf{a}^2) \; + \; {}^t_r\mathbf{K}_M({}^t\mathbf{a}, \Delta\mathbf{a}) \; + \; {}^t_r\mathbf{K}_N(\Delta\mathbf{a}^2) \; + \; {}^t_r\mathbf{K}_\sigma} \tag{11}$$

donde para cada elemento

$$ {}_r\mathbf{g} = {}_r\mathbf{G}\ \Delta\mathbf{a} \quad ; \quad {}_r\mathbf{G}^k = \begin{bmatrix} \dfrac{\partial N^k}{\partial\, {}_r x_1}\ \mathbf{I}_3 \\ \dfrac{\partial N^k}{\partial\, {}_r x_2}\ \mathbf{I}_3 \\ \dfrac{\partial N^k}{\partial\, {}_r x_3}\ \mathbf{I}_3 \end{bmatrix} $$

$$ {}_r\mathbf{e} = {}^t_r\mathbf{B}_L\ \Delta\mathbf{a} \quad ; \quad {}_r\boldsymbol{\eta} = \frac{1}{2}\ {}_r\mathbf{B}_1\ \Delta\mathbf{a} $$

$$ {}^t_r\mathbf{B}_L({}^t\mathbf{a}) = {}_r\mathbf{B}_{L_0} + {}^t_r\mathbf{B}_{L_1}({}^t\mathbf{a}) $$

$$ {}_r\mathbf{B}^k_{L_0} = \mathbf{L}_0\ {}_r\mathbf{G}^k \quad ; \quad {}^t_r\mathbf{B}^k_{L_1}({}^t\mathbf{a}) = {}^t_r\mathbf{L}_1({}^t\mathbf{a})\ {}_r\mathbf{G}^k \quad ; \quad {}_r\mathbf{B}^k_1(\Delta\mathbf{a}) = {}_r\mathbf{L}_1(\Delta\mathbf{a})\ {}_r\mathbf{G}^k $$

$$ {}_r\mathbf{E} = \begin{bmatrix} a\ \mathbf{I}_3 & d\ \mathbf{I}_3 & e\ \mathbf{I}_3 \\ & b\ \mathbf{I}_3 & f\ \mathbf{I}_3 \\ \text{sym.} & & c\ \mathbf{I}_3 \end{bmatrix} ; \quad [\,a,\ b,\ c,\ d,\ e,\ f\,]^T = {}_r\mathbf{D}\ {}_r\mathbf{e} $$

$$ {}^t_r\hat{\mathbf{S}} = \begin{bmatrix} {}^t_r S_{11}\ \mathbf{I}_3 & {}^t_r S_{12}\ \mathbf{I}_3 & {}^t_r S_{13}\ \mathbf{I}_3 \\ & {}^t_r S_{22}\ \mathbf{I}_3 & {}^t_r S_{23}\ \mathbf{I}_3 \\ \text{sym.} & & {}^t_r S_{33}\ \mathbf{I}_3 \end{bmatrix} $$

$$ {}_r\mathbf{H} = \sum_{i=1}^{6}\sum_{j=1}^{6} {}_r d_{ij}\ {}_r\eta_j\ \mathbf{H}_i \quad ; \quad {}_r\eta_j = {}_r\mathbf{g}^T\mathbf{H}_j\ {}_r\mathbf{g} $$

${}_r d_{ij}$: elemento ij de la matriz constitutiva ${}_r\mathbf{D}$

Cuadro 2. Matrices relevantes para sólidos elásticos 3D

$$ {}^t_r\mathbf{K}_L({}^t\mathbf{a}, {}^t\mathbf{a}^2) = \int_{{}_rV^{(e)}} {}^t_r\mathbf{B}_L^T\ {}_r\mathbf{D}\ {}^t_r\mathbf{B}_L\ dV \tag{12a} $$

$$ {}^t_r\mathbf{K}_M({}^t\mathbf{a}, \Delta\mathbf{a}) = \int_{{}_rV^{(e)}} \left[\frac{1}{2}\ {}^t_r\mathbf{B}_L^T\ {}_r\mathbf{D}\ {}_r\mathbf{B}_1 \ + \ \alpha\ {}_r\mathbf{B}_1^T\ {}_r\mathbf{D}\ {}^t_r\mathbf{B}_L \ + \right. $$

$$ \left. + \ (1-\alpha)\ {}_r\mathbf{G}^T\ {}_r\mathbf{E}\ {}_r\mathbf{G} \right] dV \tag{12b} $$

$$ {}^t_r\mathbf{K}_N(\Delta\mathbf{a}^2) = \int_{{}_rV^{(e)}} \left[\frac{1}{4}(2-\beta)\ {}_r\mathbf{B}_1^T\ {}_r\mathbf{D}\ {}_r\mathbf{B}_1 + \frac{\beta}{4}\ {}_r\mathbf{G}^T\ {}_r\mathbf{H}\ {}_r\mathbf{G} \right] dV \tag{12c} $$

$$ {}^t_r\mathbf{K}_\sigma = \int_{{}_rV^{(e)}} {}_r\mathbf{G}^T\ {}^t_r\hat{\mathbf{S}}\ {}_r\mathbf{G}\ dV \tag{12d} $$

Para obtener la matriz de rigidez secante y el vector de fuerzas globales del sólido discretizado se ensambla la contribución de cada elemento de manera estándar. Las matrices que aparecen en (12) quedan detalladas en el Cuadro 2.

Nótese que la expresión de ${}^t_r\mathbf{K}_S$ es no simétrica para valores de $\alpha \neq 1/2$. Una infinidad de formas simétricas pueden ser obtenidas para $\alpha = 1/2$ y valores arbitrarios de β. Una expresión paramétrica similar a la ecuación (12) ha sido obtenida por FELIPPA *et al* [1994] usando una descripción *LT*. La expresión de la matriz de rigidez tangente puede obtenerse haciendo tender a cero en el límite el incremento de desplazamiento en la expresión de la matriz de rigidez secante. De esta manera, a partir de la ecuación (11) se puede escribir

$$ \boxed{ {}^t_r\mathbf{K}_T = \lim_{\Delta\mathbf{a}\to 0} {}^t_r\mathbf{K}_S = {}^t_r\mathbf{K}_L \ + \ {}^t_r\mathbf{K}_\sigma } \tag{13} $$

4. EJEMPLOS NUMÉRICOS

En este apartado se utiliza el concepto de la matriz secante en un algoritmo incremental-iterativo para la obtención de la curva de equilibrio no lineal. Se puede utilizar con idénticos resultados en el equema predictor-corrector de dicho algoritmo las matrices tangente o secante. Se utiliza el método de longitud de arco (CRISFIELD [1992]) conjuntamente con dicho algoritmo en los ejemplos presentados a continuación.

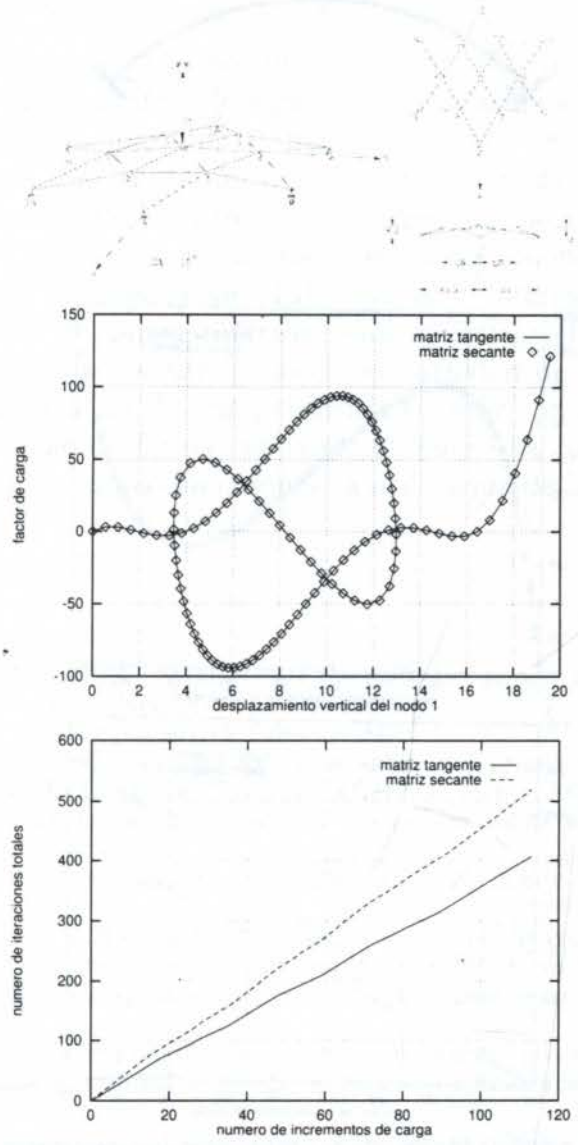

Figura 1. Estructura articulada espacial en forma de estrella. Características geométricas y propiedades mecánicas. a) Trayectoria fundamental de equilibrio no lineal. b) Número de total de iteraciones a lo largo de la respuesta

Se analiza como primer ejemplo una estructura articulada espacial en forma de estrella. Sus características geométricas y propiedades mecánicas se muestran en la Figura 1. La estructura está cargada con una fuerza puntual en el nodo central, (PAPADRAKAKIS [1987] y ROTHERT *et al* [1981]). Su comportamiento postcrítico es fuertemente no lineal conforme se observa en la Figura 1.a. Para trazar la trayectoria fundamental de equilibrio de dicha estructura se ha utilizado el método de control de la respuesta con las siguientes características; ecuación de coacción: cilíndrica; longitud

de arco constante: 0.55; tolerancia para la convergencia: 10^{-10}; esquema predictor-corrector: Newton Raphson (${}_0^t\mathbf{K}_T$) y Secante incremental (${}_0^t\mathbf{K}_S$); número total de incrementos: 113; número total de iteraciones: 407 utilizando la matriz tangente y 520 con la matriz secante; promedio de iteraciones por incremento: 3.6 con ${}_0^t\mathbf{K}_T$ y 4.6 con ${}_0^t\mathbf{K}_S$.

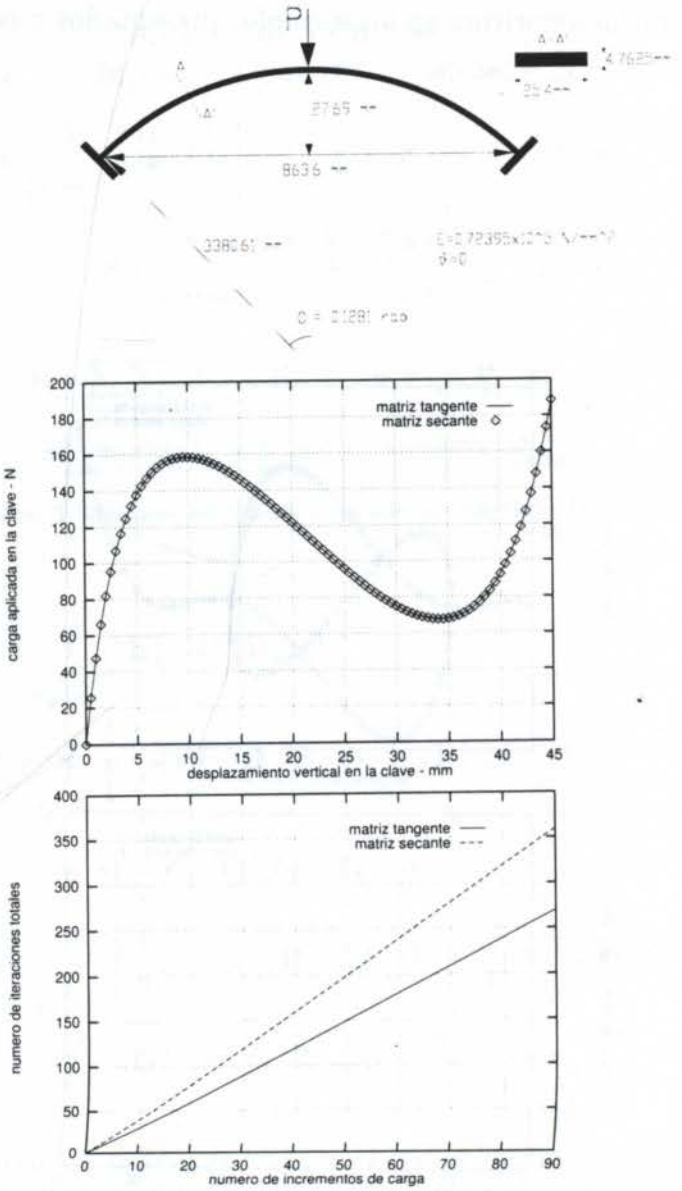

Figura 2. Arco circular rebajado biempotrado. Características geométricas y propiedades mecánicas. a) Trayectoria de equilibrio primária no lineal. b) Número de total de iteraciones a lo largo de la respuesta

En el segundo ejemplo se considera un arco rebajado de directriz circular, con ambos extremos empotrados, sometido a la acción de una carga vertical en la clave, (DAWE [1971] OLIVER [1982]). Las características geométricas y propiedades mecánicas del arco se describen en la Figura 2. El arco ha sido discretizado en 20 elementos isoparamétricos de 8 nodos con cuadratura de Gauss 2×2. Presenta una situación de inestabilidad representada por *el cambio de forma hacia delante (snap-trough)* que puede observarse en la Figura 2.a. Para trazar la trayectoria fundamental de equilibrio en este caso se ha utilizado el método de control de la respuesta con las siguientes

características; ecuación de coacción: control de desplazamiento (se ha controlado la componente vertical del desplazamiento de la clave); longitud de arco constante: -0.5; tolerancia para la convergencia: 10^{-5}; esquema predictor-corrector: Newton Raphson (${}^t_0\mathbf{K}_T$) y Secante incremental (${}^t_0\mathbf{K}_S$); número total de incrementos: 90; número total de iteraciones: 270 utilizando la matriz tangente y 360 con la matriz secante; promedio de iteraciones por incremento: 3 con ${}^t_0\mathbf{K}_T$ y 4 con ${}^t_0\mathbf{K}_S$.

5. CONCLUSIONES

El algoritmo propuesto para la resolución de sistemas de ecuaciones no lineales utilizando el concepto de la matriz de rigidez secante incremental obtiene resultados coincidentes con los obtidos aplicando la matriz tangente. Se trata de un algoritmo distinto a los basados en una expresión numérica aproximada de la matriz de rigidez secante, como los métodos cuasi-Newton, secante-Newton, de Broyden y los derivados del BFGS. La facilidad con que se puede pasar de la expresión de la matriz secante a la de la matriz tangente, ver la ecuación (13), es de gran interés práctico, pues permite hacer uso de las ventajas de ambas matrices para optimizar el proceso de resolución. Así, sería de gran interés aprovechar la mayor versatilidad de la matriz secante para garantizar su definición positiva, lo que permitiría superar con mayor facilidad puntos de inestabilidad por cambio de forma, así como obtener una convergencia más rápida en puntos próximos a la carga máxima, donde la utilización de la matriz tangente suele ser desfavorable.

6. REFERENCIAS

BADAWI, M. & CUSENS, A.R. [1992], Symmetry of the stiffness matrices for geometrically non linear analysis, *Communications in Appl. Num. Meth.*, Vol.**8**, 135–40.

BATHE, K.J. [1996], *Finite element procedures*, Prentice Hall.

CARRERA, E. [1992], Sull' uso dell' operatore secante in analisi non lineare di strutture multistrato con il metodo degli elementi finiti, XI Congresso Nazionale AIMETA, Trento, 28 September–2 October.

CRISFIELD, M.A. [1991], *Non-Linear finite element analysis of solids and structures, Volumen 1: Essentials*, John Wiley & Sons

DAWE, D.J. [1971], Finite deflection analysis of shallow arches by discrete element method, J. Num. Meth. Engng., Vol. 3, nº 4.

FELIPPA, C. CRIVELLI, L.A. & HAUGEN, B. [1994], A survey of the core–congruential formulation for geometrically nonlinear TL finite elements, *Archives of Comp. Meth. in Engrg.*, Vol. **1**, 1, 1–48.

MATIAS, W. [1996], El método de desplazamiento crítico en el análisis de inestabilidad estructural, Tesis Doctoral, UPC, Barcelona.

OLIVER, J. [1982], Una formulación cuasi-intrínseca para el estudio, por el método de los elementos finitos, de vigas, arcos, placas y láminas, sometidas a grandes corrimientos en régimen elastoplástico. Tesis Doctoral, UPC, Barcelona.

OÑATE, E. [1995], On the derivation and possibilities of the secant stiffness matrix for non linear finite element analysis, *Computational Mechanics*, Vol. 15, 572–593.

OÑATE, E. & MATIAS, W. [1995], Enhanced prediction of structural instability points using a critical displacement method. Published on *Advances in Finite Element Technology*, Nils-Erik Wiberg (Ed.), CIMNE, pp. 63-89.

OÑATE, E. & MATIAS, W. [1996], A critical displacement approach for predicting structural instability, *Comp. Meth. Appl. Mech. Engng.* 134, pp. 135-161.

PAPADRAKAKIS, M. [1987], Analysis methods for spatial structures, in: G. De Roeck, A. Quiroga, M. van Laethem and E. Backx, eds., *Shell and Spatial Structures: Computational Aspects*, Springer, Berlin, 121–148.

ROTHERT, H.; DICKEL, T. & RENNER, D. [1981], Snap–through buckling of reticulated space trusses, *ASCE J. Struct. Div.*, Vol. **107**, 129–143.

XIV Brazilian Congress of Mechanical Engineering
Obeid Plaza Hotel Convention Center - Bauru - SP/Brazil
December 08-12th 1997

PAPER CODE: COB79

A SIMPLE LOCKING-FREE THREE-NODE SHELL FINITE ELEMENT

R.J. Marczak[1] and A.M. Awruch[2]

[1]Departamento de Eng. Mecânica - Universidade Federal do Rio Grande do Sul
Rua Sarmento Leite, 425, 90050-170, Porto Alegre-RS, Brazil - E-mail: rato@vortex.ufrgs.br
[2]Departamento de Eng. Civil - Universidade Federal do Rio Grande do Sul
Av. Osvaldo Aranha, 99, 3º andar, 90035-190, Porto Alegre-RS, Brazil

Abstract

A simple triangular shell finite element with fifteen degrees of freedom for the analysis of general shell structures is presented in this work. The element uses a substitute transverse shear strain field to avoid locking, and is formulated on the basis of RSDS-element (Resultant Stress Degenerated Shell Element) approach, which leads to very simple strain-displacement expressions. The substitute shear strain field is derived assuming constant shear strains along the sides of the element, similar to the MITC (Mixed Interpolation in Tensorial Componentes) procedure. All integrations can be performed using only one point Gaussian rule, leaving the element with one non-comunicable zero energy mode, which does not affect the results. This procedure allows the use of symbolic engines to derive analytic expressions for stiffness matrices, reducing computational cost of the analysis by a significative amount.

Keywords

Finite element method, plates and shells, shear locking.

1. INTRODUCTION

The study and development of shell finite elements has been under intense development during the last three decades. Still today this is a very fruitful research area, with several related subjects yet to be explored.

The reason why there are so many formulations for shell finite element analysis is intrinsically related to the complex nature of shell equations, arguably the most challenging among the usual structural theories. The difficulty (or the impossibility) of finding analytical solutions for practical cases of geometry, material and loading, even with the aid of modern symbolic algebra programs, leaves the use of computer based discrete solutions as the natural trend. In addition, practical needs as negative gaussian curvature, the influence of shear strains and the extensibility of thickness fibers, among other things, bring the governing equations to an even higher degree of complexity.

Moreover, the accurate solution of practical cases requires the use of adequate meshes that can be obtained only with intensive use of mesh generators. In spite of the the quality

which can be achieved by modern mesh generators, the intervention of the user is still necessary for practical cases. Stress concentration points and rapidly varying geometry areas always need semi-automatic mesh adaption, and this can be very cumbersome when using high order elements. These are among the main reasons why low order elements have been prefered in many situations. In addition, the code for a low order element (like three-node or four-node element) can be easily vectorized, which enable the use of supercomputers and huge meshes.

In spite of the large number of shell elements formulations already published, several of them lack one or more features which would be necessary to allow their general use in complex engineering problems commonly found in industry. A short list of requirements that would be present in any general shell formulation is (we restrict ourself to some arguments valid for low order shell elements in linear elastic analysis): (a) The element has to pass in the patch test for constant membrane, constant bending and constant shear. (b) If possible, the element should have only its middle surface nodes coordinates as input data. (c) The stiffness matrix of the element should achieve the correct rank, specially for triangular elements, which usually presents severe shear locking and can not be solved only with reduced integration. (d) If reduced integration is to be used, all the resulting spurious zero energy deformation modes should be controlled. (e) The numerical efficiency of the element can be much improved by the use of an analytical or semi-analytical integration of the stiffness matrix. (f) The shear and bending energy norms of the element should be bounded, specially for very thin shells.

An attempt to incorporated partially the requirements listed above in a general three-node shell element is the main goal of this work. The element is formulated on a basis similar to the MITC (Mixed Interpolation in Tensorial Components) family.

2. GENERAL FORMULATION OF AN ELEMENT BASED ON THE DEGENERATED SHELL CONCEPT

This section discusses some general characteristics of a three node shell element based on Ahmad's kinematics (Ahmad *et alli*, 1970). In the context of a displacement based formulation, the degenerated element concept leads to a very simple and robust way to formulate elements with any number of nodes. In this section, we follow very closely the approach proposed by Liu *et alli* (Liu *et alli*, 1986) for the kinematic description of the element, particularized for the case of a three node element.

The element has three nodes, each one associated with a thickness h_i. The coordinates of the nodes in the global coordinate system are denoted $\mathbf{x}_i = \{\ x_i \quad y_i \quad z_i\ \}^T$. The thickness are measured over an normal vector $\mathbf{p}_i = \{\ p_{1_i} \quad p_{2_i} \quad p_{3_i}\ \}$. The purpose of fiber vector is merely to define an axis along which the zero normal stress hypotesis will be invoked. Thus, in the case of an element with variable fiber vector one can expect a behavior more sensitive to curvature changes.

The element will be mapped to a normalized domain (ξ_1, ξ_2, ξ_3) to allow the use of standard linear shape functions: $\{N_1, N_2, N_3\} = \{1 - \xi_1 - \xi_2,\ \xi_1,\ \xi_2\}$, in such a way that the position vector of a point on the middle surface of the element in a given time t is interpolated in the usual way: $\mathbf{x}\,(\xi_1, \xi_2, t) = N_i\,(\xi_1, \xi_2)\ \mathbf{x}_i\,(t)$. Inside an element, the fiber vector is interpolated in the same way (Liu *et alli*, 1986):

$$\mathbf{p}\,(\xi_1, \xi_2, \xi_3, t) = \sum_{i=1}^{3} N_i\,(\xi_1, \xi_2)\,\frac{h_i}{2}\,\xi_3\,\mathbf{p}_i\,(t) \qquad \text{(no sum on } i\text{)} \quad ,$$

as well as the thickness: $h\,(\xi_1, \xi_2, t) = N_i\,(\xi_1, \xi_2)\ h_i\,(t)$. Then, the fiber vector accounts

for the position of a general point not belonging to the middle surface of the element, which allows one to write the position vector of a general point as

$$\mathbf{X}(\xi_1, \xi_2, \xi_3, t) = \mathbf{x}(\xi_1, \xi_2, t) + \mathbf{p}(\xi_1, \xi_2, \xi_3, t) \quad .$$

In addition to the usual global coordinate system, most shell formulations employ several coordinate systems attached to the element (Hughes, 1987):

- Global coordinate system (GCS): The GCS is simply a non-inertial coordinate system defined by a canonical base.
- Normalized coordinate system (NCS): The NCS stands for the base vectors of the normalized domain used for interpolation and integration of the variables. In this system ξ_1,$\xi_2 = [0, 1]$, while $\xi_3 = [-1, 1]$.
- Lamina coordinate system (LCS): The LCS is the system used to employ the kinematic description of the Mindlin-Reissner plate/shell models. The element stiffness matrix will be defined first in this system, and then rotated to appropriate systems. The transformation of a tensor $\mathbf{V}^l$ in the LCS to the GCS is accomplished by the following operator:

  $$\mathbf{R} : \mathbf{V}^l \rightarrow \mathbf{V} \quad \text{where} \quad R_{ij} = \mathbf{e}_i \cdot \mathbf{e}_j^l \quad .$$

  The LCS is obviously constant for three-node flat elements, but in the case of higher order elements the LCS vectors are interpolated by the standard shape functions: $\mathbf{e}_j^l(\xi_1, \xi_2, t) = N_i(\xi_1, \xi_2)\, \mathbf{e}_{j_i}^l$.
- Fiber coordinate system (FCS): The FCS is used to define the rotational degrees of freedom of the element. It is choosen in such a way that $\mathbf{e}_{3_i}^f \equiv \mathbf{p}_i$ at each node i. Several diferent conventions can be used to generate the FCS. In general, it is defined as a system *following* the shell middle surface. In this work, we used the algorithm proposed by Liu *et alli* (Liu *et alli*, 1986). Inside the element, the FCS vectors are interpolated in the standard way: $\mathbf{e}_j^f(\xi_1, \xi_2, t) = N_i(\xi_1, \xi_2)\, \mathbf{e}_{j_i}^f$.

The transformation from FCS to the GCS is given by the linear transformation $\mathbf{S}$, given by:

$$\mathbf{S} : \mathbf{V}^f \rightarrow \mathbf{V} \quad \text{where} \quad S_{ij} = \mathbf{e}_i \cdot \mathbf{e}_j^f \quad .$$

It is worth to note that $\mathbf{e}_3^l \neq \mathbf{e}_3^f$, in general. This algorithm generates an orthogonal FCS uniquely defined at each node and always ensures one of the axis ($\mathbf{e}_1^f$ or $\mathbf{e}_2^f$) to be tangent to a continuous boundary of the shell, which makes the imposition of the boundary conditions an easy task. By other hand, it can turn difficult to the user to visualize which FCS axes is tangent to a given boundary, specially for complex geometries. Because the stiffness matrix will be derived in the LCS, but the rotational degrees of freedom will stay attached to the FCS, the following relation is useful in order to perform the transformations from one system to the other:

$$\mathbf{Q} : \mathbf{V}^l \rightarrow \mathbf{V}^f \quad \text{where} \quad \mathbf{Q} = \mathbf{S}^T \mathbf{R} \quad .$$

The strain-displacement matrix considered in RSDS elements are obtained directly from the Ahmad's kinematic relations for shells, for linear static analysis. In view of

the absence of transverse normal stresses, the 6×6 constitutive matrix can be contracted to a 5×5 form. In addition, we are not considering drilling degrees of freedom. From these assumptions, and making use of the Green strain tensor definition for infinitesimal displacements, the strain vector can be approximated by the following relation:

$$\boldsymbol{\varepsilon}^l = \mathbf{B}_i^l \mathbf{d}_i^l \quad ,$$

with

$$\mathbf{B}_i^l = \begin{bmatrix} \frac{\partial N_i}{\partial x_1^l} & 0 & 0 & \xi_3 \frac{h_i}{2} \frac{\partial N_i}{\partial x_1^l} & 0 & 0 \\ 0 & \frac{\partial N_i}{\partial x_2^l} & 0 & 0 & \xi_3 \frac{h_i}{2} \frac{\partial N_i}{\partial x_2^l} & 0 \\ \frac{\partial N_i}{\partial x_2^l} & \frac{\partial N_i}{\partial x_1^l} & 0 & \xi_3 \frac{h_i}{2} \frac{\partial N_i}{\partial x_2^l} & \xi_3 \frac{h_i}{2} \frac{\partial N_i}{\partial x_1^l} & 0 \\ 0 & 0 & \frac{\partial N_i}{\partial x_2^l} & 0 & \frac{N_i h_i}{h^l} & 0 \\ 0 & 0 & \frac{\partial N_i}{\partial x_1^l} & \frac{N_i h_i}{h^l} & 0 & 0 \end{bmatrix} \quad , \tag{1}$$

or

$$\mathbf{B}_i^l = \begin{bmatrix} \mathbf{B}_{m_i}^l & \mathbf{B}_{b_i}^l \\ 0 & \mathbf{B}_{s_i}^l \end{bmatrix} \quad , \tag{2}$$

Note that the last row of $\mathbf{B}_i^l$ resulted in zero entries because it refers to the drilling rotation stiffness, not considered here. The associated jacobian is written as:

$$J = \frac{1}{2} h^l \begin{vmatrix} \frac{\partial x_1^l}{\partial \xi_1} & \frac{\partial x_2^l}{\partial \xi_1} \\ \frac{\partial x_1^l}{\partial \xi_2} & \frac{\partial x_2^l}{\partial \xi_2} \end{vmatrix} = \frac{1}{2} h^l A^l \quad . \tag{3}$$

The stiffness matrix block relating the nodes i and j now can be evaluated by integration over the thickness and over the area of the element:

$$\bar{\mathbf{K}}_{ij}^l = \int \left(\int_h \mathbf{B}_i^{l^T} \mathbf{D}^l \mathbf{B}_j^l \, dh \right) dA \quad . \tag{4}$$

In order to transform $\bar{\mathbf{K}}_{ij}^l$ to the GCS, the following transformation is performed:

$$\mathbf{K}_{ij} = \mathbf{Q} \bar{\mathbf{K}}_{ij}^l \mathbf{Q}^T \quad . \tag{5}$$

3. A SIMPLE SOLUTION FOR SHEAR LOCKING

The main problem of standard isoparametric three or four node plate and shell elements with full integration is their inability to predict correct values for shear deflection. The use of reduced or selective integration alliviates the problem for quadrilateral elements, although leading to the possible manifestation of hourglass modes, which necessarily have to be controlled for a reliable analysis. In the case of triangular elements, even the use of reduced integration may not solve this problem. Several remedies other than reduced integration has been proposed in the literature to solve the shear locking problem. Particularly in the case of a three or four node plate and shell elements, some solutions are equivalent from the variational point of view, others are purely tentative. But in any case, the main purpose of the corrections is to improve the ability of the element to reproduce constant shear situations and still pass in the patch test.

Among the usual solutions for the shear locking in low order plate/shell elements we have: (a) $\bar{\mathbf{B}}$ **methods**: these methods are based in the substitution of the shear strain-displacement matrix $\mathbf{B}_s$ with a substitute matrix $\bar{\mathbf{B}}_s$ able to adequately represent shear

strains. (b) **Bubble functions**: this method consists in the addition of some high order terms in the interpolation function to allow an enriched displacement representation. (c) **EAS methods**: The enhanced assumed strain methods are based on the Hu-Washizu principle. The key point of the method lies in the use of a strain field composed of a compatible strain field and an enhanced strain field. (d) **Mixed methods**: Are based on hybrid models derived from the Hellinger-Reissner principle with displacement and stress assumptions. (e) **Energy correction**: An energy correction is accomplished by adding a complementary energy term which *neutralizes* the locking effect.

The most successful approaches to achieve correct rank in a locking-free element have the same key point: to evaluate the shear strains at each node using the mean value of the shear strains evaluated along the sides adjacent to the node (whoose values are considered constants). The nodal values of the shear strains are interpolated using the same shape functions used for the displacements, thus ensuring a consistent formulation. In this section we will develop the same ideas in a slighly different way, in order to demonstrate that in fact these methods are only based in the use of substitute shape functions for the shear strains, and investigate if these shape functions hold the necessary conditions for a consistent interpolation. We used an approach similar of the work of Aalto (Aalto, 1988). It is worth to point out that we have deriving a new shear stiffness matrix to replace $\mathbf{B}^l_{s_i}$ in eq.(2), using the LCS as reference. Because of the close resemblance with the approach used to derive the MITC plate/shell element family (Bathe and Dvorkin, 1986), we called the present element MITC3.

Considering the LCS arbitrarily oriented in the plane of the element, the shear strain components simply read (the index l will be supressed for clarity purposes):

$$2\varepsilon_{i3} = \frac{\partial u_3}{\partial x_i} + \theta_i \quad . \tag{6}$$

Now define an orthogonal coordinate system (t^i, n^i) aligned to the side i of the element. For convenience, let's call

$$2\varepsilon_{i3} = \gamma_{i3} = \gamma_i \mathbf{e}^l_i \qquad \text{(no sum on } i\text{)} \quad .$$

At each nodal point i, define a *shear vector* given by:

$$\boldsymbol{\gamma}_i = \gamma_{j_i} \mathbf{e}^l_j \quad .$$

Using the same nodal convention $j(i=1)=2$, $j(i=2)=3$, $j(i=3)=1$ one can write, for each side

$$\gamma_i = \boldsymbol{\gamma}_i \cdot \mathbf{t}_i \tag{7}$$

$$\gamma_j = \boldsymbol{\gamma}_i \cdot \mathbf{t}_j \quad . \tag{8}$$

Noting that, in the LCS

$$\mathbf{t}_i = \frac{x_{ki}}{l_i}\mathbf{e}^l_1 + \frac{y_{ki}}{l_i}\mathbf{e}^l_2$$

where $x_{ki} = x^l_k - x^l_i$, $y_{ki} = y^l_k - y^l_i$ and l_i is the length of the side i, eqs.(7-8) can be inverted in the following form:

$$\boldsymbol{\gamma}_1 = \mathbf{T}_1 \left\{ \begin{array}{c} \gamma_1 \\ \gamma_3 \end{array} \right\} \qquad \text{for side 1,}$$

$$\boldsymbol{\gamma}_2 = \mathbf{T}_2 \left\{ \begin{array}{c} \gamma_2 \\ \gamma_1 \end{array} \right\} \qquad \text{for side 2,}$$

$$\boldsymbol{\gamma}_3 = \mathbf{T}_3 \left\{ \begin{array}{c} \gamma_3 \\ \gamma_2 \end{array} \right\} \qquad \text{for side 3.}$$

Grouping the variables in an element-wise vector results:

$$\boldsymbol{\gamma}^e = \mathbf{P}\boldsymbol{\gamma} \quad ,$$

where

$$\begin{aligned} \boldsymbol{\gamma}^e &= \left\{ \begin{array}{cccccc} \gamma_{1_1} & \gamma_{2_1} & \gamma_{1_2} & \gamma_{2_2} & \gamma_{1_3} & \gamma_{2_3} \end{array} \right\}^T = \left\{ \begin{array}{ccc} \boldsymbol{\gamma}_1 & \boldsymbol{\gamma}_2 & \boldsymbol{\gamma}_3 \end{array} \right\}^T \\ \boldsymbol{\gamma} &= \left\{ \begin{array}{ccc} \gamma_1 & \gamma_2 & \gamma_3 \end{array} \right\}^T \end{aligned}$$

and

$$\mathbf{P} = \frac{1}{A^l} \begin{bmatrix} y_{31}l_1 & 0 & -y_{21}l_3 \\ -x_{31}l_1 & 0 & x_{21}l_3 \\ -y_{32}l_1 & y_{21}l_2 & 0 \\ x_{32}l_1 & -x_{21}l_2 & 0 \\ 0 & -y_{13}l_2 & y_{32}l_3 \\ 0 & x_{13}l_2 & -x_{32}l_3 \end{bmatrix} ,$$

where A^l is given by eq.(3).

Now it is possible to interpolate $\boldsymbol{\gamma}_i$ using the linear shape functions:

$$\left\{ \begin{array}{c} 2\varepsilon^l_{13} \\ 2\varepsilon^l_{23} \end{array} \right\} = N_i \boldsymbol{\gamma}_i \quad , \tag{9}$$

or

$$\left\{ \begin{array}{c} 2\varepsilon^l_{13} \\ 2\varepsilon^l_{23} \end{array} \right\} = \mathbf{N}\,\mathbf{P}\,\boldsymbol{\gamma} = \bar{\mathbf{N}}\,\boldsymbol{\gamma} \quad , \tag{10}$$

with

$$\bar{\mathbf{N}} = \begin{bmatrix} N_1 & 0 & N_2 & 0 & N_3 & 0 \\ 0 & N_1 & 0 & N_2 & 0 & N_3 \end{bmatrix} \mathbf{P} = \mathbf{N}\,\mathbf{P} \quad , \tag{11}$$

where $\bar{\mathbf{N}}$ is the substitute shape functions used for the shear strain components. In a mixed finite element formulation, eq.(9) plays the role of a constraint equation for the shear strains with respect to the parameters $\boldsymbol{\gamma}_i$.

Finally, it is necessary to relate the mid-edge shear strain $\boldsymbol{\gamma}_i$ with the element nodal displacements. Recalling eq.(6), it is clear that, for each side i, the following relations hold:

$$\gamma_i = \frac{\partial u_{3_i}}{\partial l} + \bar{\theta} \quad , \tag{12}$$

where:

$$\frac{\partial u_{3_i}}{\partial l} = \frac{u_{3_k} - u_{3_i}}{l_i} \qquad \text{and} \qquad \bar{\theta} = \frac{\theta_{n_i} + \theta_{n_k}}{2}$$

The shear constraint then can be written as

$$\gamma_i = \frac{u^l_{3_j} - u^l_{3_i}}{l_i} + \frac{\mathbf{n}_i \cdot \left(\boldsymbol{\theta}^l_j + \boldsymbol{\theta}^l_i \right)}{2} \quad , \tag{13}$$

where $\mathbf{n}_i$ is the vector normal to the side i. Recovering eq.(13) for all nodes in matrix form results:

$$\boldsymbol{\gamma} = \mathbf{A}\,\mathbf{d}_b \quad ,$$

where $\mathbf{d}_b^e$ stands for the bending/shear nodal displacements only, in such a way that:

$$\begin{aligned}
\mathbf{d} &= \{\ \mathbf{d}_m \ \ \mathbf{d}_b\ \}^T = \{\ u_{1_1} \ \ u_{2_1} \ \ u_{3_1} \ \ \theta_{1_1} \ \ \theta_{2_1} \ \ \cdots \ \ \theta_{2_3}\ \}^T \\
\mathbf{d}_m &= \{\ u_{1_1} \ \ u_{2_1} \ \ \cdots \ \ u_{2_3}\ \}^T \\
\mathbf{d}_b &= \{\ u_{3_1} \ \ \theta_{1_1} \ \ \theta_{2_1} \ \ \cdots \ \ \theta_{2_3}\ \}^T \quad .
\end{aligned}$$

and

$$\mathbf{A} = \begin{bmatrix}
-1/l_1 & n_{1_1}/2 & n_{2_1}/2 & 1/l_2 & n_{1_1}/2 & n_{2_1}/2 & 0 & 0 & 0 \\
0 & 0 & 0 & -1/l_2 & n_{1_2}/2 & n_{2_2}/2 & 1/l_2 & n_{1_2}/2 & n_{2_2}/2 \\
1/l_3 & n_{1_3}/2 & n_{2_3}/2 & 0 & 0 & 0 & -1/l_3 & n_{1_3}/2 & n_{2_3}/2
\end{bmatrix} \tag{14}$$

Rewriting eq.(10) using $\mathbf{A}$ and remembering that we are using the LCS leads to:

$$\begin{Bmatrix} 2\varepsilon_{13}^l \\ 2\varepsilon_{23}^l \end{Bmatrix} = \mathbf{N}\,\mathbf{P}\,\mathbf{A}\,\mathbf{d}_b^l = \bar{\mathbf{B}}_s^l \mathbf{d}_b^l = \begin{bmatrix} \bar{\mathbf{B}}_{s_1}^l & \bar{\mathbf{B}}_{s_2}^l & \bar{\mathbf{B}}_{s_3}^l \end{bmatrix} \mathbf{d}_b^l \quad .$$

The matrix $\bar{\mathbf{B}}_{s_i}^l$ replaces $\mathbf{B}_{s_i}^l$ in eq.(2). If we write

$$\bar{\mathbf{B}}_{s_i}^l = \begin{bmatrix} N_{w_x}^i & M_{\theta_1}^i & M_{\theta_2}^i \\ N_{w_y}^i & L_{\theta_1}^i & L_{\theta_2}^i \end{bmatrix}$$

it becomes clear that

$$\begin{aligned}
2\varepsilon_{13}^l &= N_{w_x}^i u_{3_i} + M_{\theta_1}^i \theta_{1_i} + M_{\theta_2}^i \theta_{2_i} \\
2\varepsilon_{23}^l &= N_{w_y}^i u_{3_i} + L_{\theta_1}^i \theta_{1_i} + L_{\theta_2}^i \theta_{2_i} \quad .
\end{aligned}$$

At this point it is interesting to note that the following relations can be easily verified:

$$\begin{aligned}
\sum_{i=1}^{3} M_{\theta_1}^i &= 1 \\
\sum_{i=1}^{3} M_{\theta_2}^i &= 0 \\
\sum_{i=1}^{3} L_{\theta_1}^i &= 0 \\
\sum_{i=1}^{3} L_{\theta_2}^i &= 1 \quad ,
\end{aligned}$$

and so the fundamental constant strain criterion is guaranteed (Donea and Lamain, 1987).

The development of the equations presented above is merely a formalization of the idea of considering a shear deformable beam attached to each side of the element. A more rigorous way to derive the substitute shear strain field was presented by Boisse et alli (Boisse et alli [1992]), using the Green-Lagrange strain definitions written in a covariant base along the sides of the element.

4. REMARKS ABOUT THE MITC3 ELEMENT

The present MITC3 element represents merely the three-node counterpart of the MITC4 element presented by Bathe & Dvorkin (1986). The shear constrained elements proposed by Oñate et alli (1992) also uses similar ideas, but in their approach the shear strains are additional degrees of freedom which have to be condensed before the stiffness matrix assembly phase, what usually requires matrix inversions.

The present approach generates a stiffness matrix with the correct rank when integrated by three Gauss stations, as the element shows the optimum constraint ratio. A very attractive explicit computer code can be generated using only one centroidal Gauss station, but in this case the element has one in-plane torsional non-comunicable spurious mode, which cannot manifest in an assembly of two or more elements.

Some further improvements on the behavior of the element can be achieved by means of the residual bending flexibility but, as proved by Prathap (1995), this is an extravariational trick, and should not be included in the element formulation without a strong mathematical basis. Finally, it is interesting to say that whichever the approach used to constrain the shear strains, the same procedure should be followed to derive the consistent mass matrix and the geometrical stiffness matrix. This is sometimes overlooked when extending the application range of an element to dynamic as well as to non-linear analysis.

5. REFERENCES

J. Aalto: *From Kirchhoff to Mindlin Plate Elements*, *Comm.Appl.Num.Meth.*, **4**, pp. 231-241, 1988.

S. Ahmad, B.M. Irons and O.C. Zienkiewicz: *Analysis of Thick and Thin Shell Structures by Curved Finite Elements*, *Int.J.Num.Meth.Engng.*, **2**, pp. 419-451, 1970.

K.-J. Bathe and E.N. Dvorkin: *A Formulation of General Shell Elements - The Use of Mixed Interpolation of Tensorial Components*, *Int.J.Num.Meth.Engng.*, **22**, pp. 697-722, 1986.

P. Boisse, J.L. Daniel and J.C. Gelin: *A Simple Isoparametric Three-Node Shell Finite Element*, *Computers & Structures*, 44 **(6)**, pp. 1263-1273, 1992.

J. Donea and L.G. Lamain: *A Modified Representation of Transverse Shear in C^o Quadrilateral Plate Elements*, *Comp.Meth.Appl.Mech.Engng.*, **67**, pp. 183-207, 1987.

T.J.R. Hughes: *The Finite Element Method - Linear Static and Dynamic Analysis*, Prentice-Hall, 1987.

W.K. Liu, E.S. Law, D. Lam and T. Belytschko: *Resultant-Stress Degenerated-Shell Element*, *Comp. Meth. Appl. Mech. Engng.*, 55, pp. 259-300, 1986.

R.H. MacNeal: *The Evolution of Lower Order Plate and Shell Elements in MSC/Nastran*, *Finite Elements in Analysis and Design*, **5**, pp. 197-222, 1989.

E. Oñate, O.C. Zienkiewicz, B. Suarez and R.L. Taylor: *A General Methodology fro Deriving Shear Constrained Reissner-Mindlin Plate Elements*, *Int.J.Num.Meth.Engng.*, **33**, pp. 345-367, 1992.

G. Prathap: *The Variationally Correct Rate of Convergence for a Two-Noded Beam Element, or Why Residual Bending Flexibility Correction is an Extra Variational Trick*, *Comm.Num.Meth.Engng.*, **11**, pp. 403-407, 1995.

XIV Brazilian Congress of Mechanical Engineering
Obeid Plaza Hotel Convention Center - Bauru - SP/Brazil
December 08-12th 1997

PAPER CODE: COB855

APLICAÇÃO DO MÉTODO DE ELEMENTOS FINITOS COM O AUXÍLIO DE SISTEMA ESPECIALISTA / *APPLICATION OF FINITE ELEMENT METHOD AIDDED BY EXPERT SYSTEMS*

MICHAEL J. FERNANDES, LAURO F. S. IGNÁCIO JR. & EDISON DA ROSA
Departamento de Engenharia Mecânica - Universidade Federal de Santa Catarina - UFSC
CP. 476 - Campus Universitário, Florianópolis, SC, Brasil - CEP 88040-900
E-mail: michael@grante.ufsc.br, lf@grante.ufsc.br, darosa@emc.ufsc.br

Abstract

This paper presents an expert system to help the tasks of modelling physical problems through the finite element method. The construction of the modelling system is associated with two modules. The first one is an expert system that helps in the numerical model building , and the other one is a model manager that controls the whole process remaining, i. e., the model manager gets the geometry from a CAD modeller, based on ACIS standard, and perform a mesh generation. The user, following the advices received from the expert system, applies the loads and boundary conditions. After that, a finite element package reads this data, and solve the problem using adaptive methods to take accurate results.

Keywords

Expert Systems, Knowledge Based Systems, Structural Analysis, Finite Element Method, Preprocessor, Modelling / Sistemas especialistas, Sistemas baseados em Conhecimento, Análise Estrutural, Método de Elementos Finitos, Pré-processador, Modelagem.

1. INTRODUÇÃO

Problemas físicos, em análises de engenharia, necessitam de uma série de simplificações por apresentarem infinitos graus de liberdade e muitos detalhes. Estas simplificações são vinculadas ao comportamento do material, geometria, carregamento e condições de contorno e traduzem-se na geração do modelo de referência, sendo este portanto uma idealização do sistema real. Este procedimento deve ser cuidadoso e seguir uma metodologia específica. Como proposta para a abordagem de solução de problemas estruturais, sugere-se iniciar o processo investigando os modos de falha a serem tratados na análise. Entretanto, para que se possa avaliá-los, faz-se necessário definir os reais objetivos da análise. Para alcançar tais objetivos algumas exigências devem ser atendidas as quais orientam a criação do modelo matemático.

Como não se conhece uma solução analítica para a maioria dos problemas reais de engenharia, recorre-se aos métodos numéricos, dentre os quais destaca-se o método de elementos finitos em função de sua versatilidade. Porém, por ser este um método de aproximação, deve-se tomar extremo cuidado com as simplificações impostas ao modelo, para não comprometer a análise. Além disso, pode-se destacar o uso indevido da ferramenta por engenheiros que não têm efetivo domínio sobre a técnica envolvida.

Para minimizar problemas como estes é conveniente que o processo seja sistematizado, pois desta forma pode-se admitir um certo grau de confiança no modelo e, conseqüentemente, nos resultados deste. Neste caso, o uso de sistemas especialistas para auxiliar a modelagem de sistemas físicos constitui-se em uma alternativa interessante para engenheiros inexperientes ou em fase de treinamento. Assim sendo, apresenta-se o emprego de sistema especialista para o auxílio à tarefa de modelagem de problemas estruturais lineares através do método de elementos finitos.

Uma representação esquemática das várias fases do processo de modelagem pode ser visualizada na figura 1, onde destaca-se a área de atuação do sistema especialista.

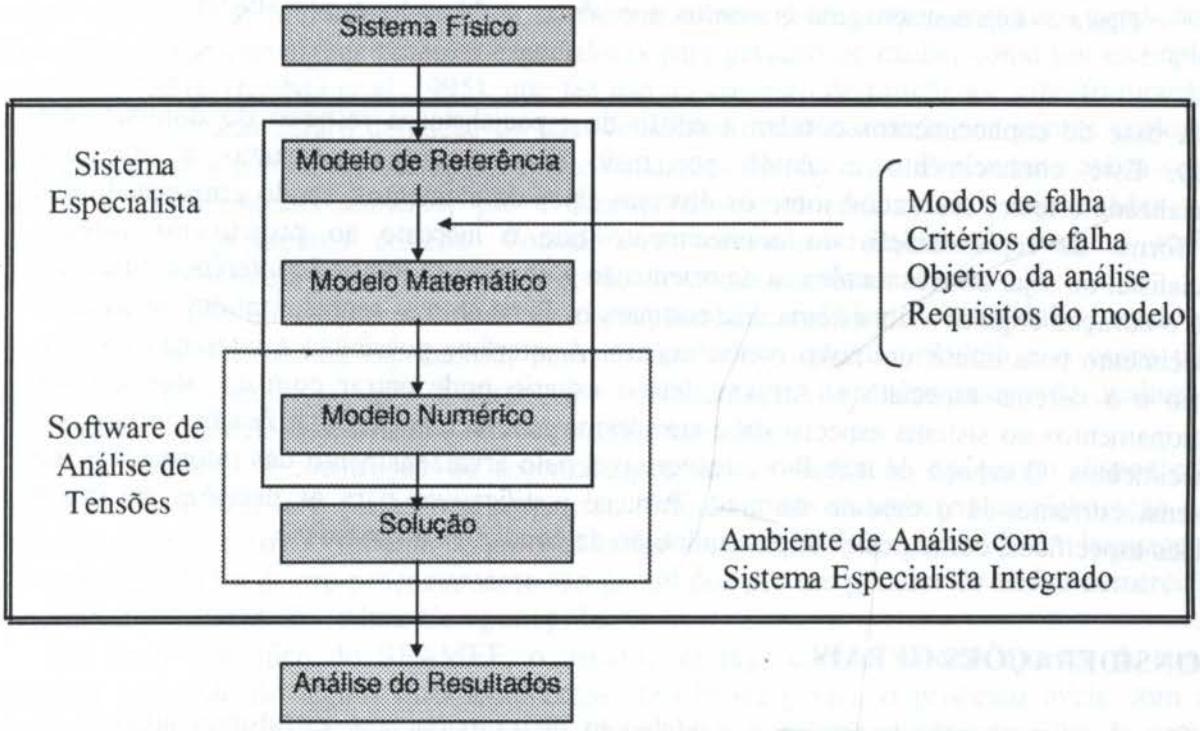

Figura 1 - Representação das fases do processo de modelagem

Sistemas especialistas são programas particulares que armazenam fatos, experiências, conhecimento diversos e simulam o processo de raciocínio para reagir com perícia na solução de tarefas relativamente difíceis. O conhecimento usado pelos sistemas especialistas é montado com base em regras e experiências associadas ao comportamento das partes integrantes de um domínio particular. As principais características que os diferenciam dos programas convencionais são a separação da base de conhecimento do controle procedural, a transparência de diálogo, a capacidade de atualização da base de conhecimento, o uso de procedimentos que imitam o raciocínio humano e a manipulação de símbolos ao invés de dados, (BASRI et al., 1995).

O Sistema Especialista de Apoio à Modelagem por Elementos Finitos, SEAMEF, pode ser esquematizado, com o auxílio da figura 2, onde são destacadas suas partes principais.

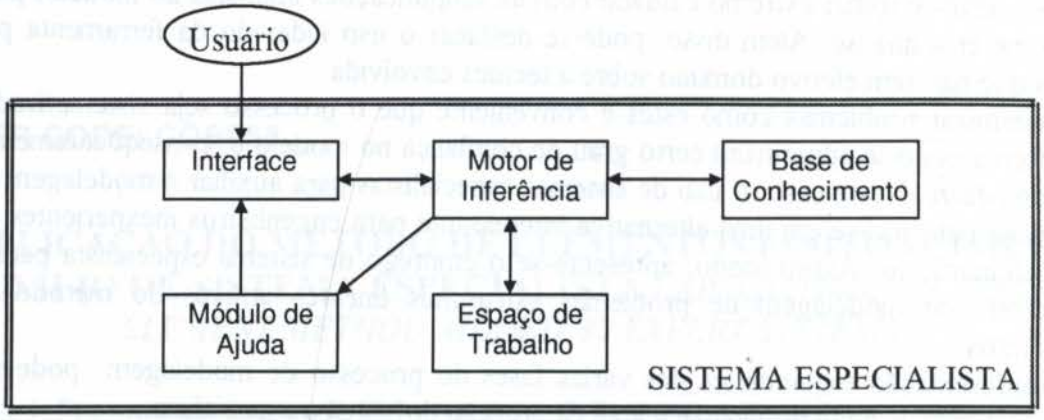

Figura 2 - Representação geral de sistemas especialistas, também adotada pelo SEAMEF.

A base de conhecimentos contém a noção de especialistas a respeito do domínio sob estudo. Este conhecimento é obtido por meio de entrevistas, consultas a literatura especializada e testes realizados sobre os diversos tipos de elementos, sendo armazenado em uma forma de representação do conhecimento que é inerente ao projeto do sistema especialista, ou seja, através da técnica de orientação a objetos. O motor de inferência funciona como o coração cognitivo do sistema. Ele compara os fatos com as regras contidas na base de conhecimento para inferir um novo conhecimento. A interface possibilita a interação entre o usuário e o sistema especialista. Através dela o usuário pode entrar com os fatos e fazer questionamentos ao sistema especialista e até mesmo acrescentar regras e funções à base de conhecimentos. O espaço de trabalho é responsável pelo armazenamento das informações do problema corrente. Já o módulo de ajuda fornece justificativas para as decisões e explica detalhes específicos, como por exemplo, aplicação de condições de contorno.

2. CONSIDERAÇÕES GERAIS

O sistema proposto destina-se à modelagem de componentes estruturais através do método de elementos finitos. Para tanto acompanha o processo desde a elaboração do modelo de referência até a solução do problema. Portanto, faz-se necessário tomar por base a geometria, os carregamentos, as condições de contorno, informações sobre o material e o objetivo da análise. Em outras palavras, o sistema atua diretamente sobre o modelo de referência, que representa o fenômeno físico e leva em consideração as informações anteriormente destacadas para construir de forma adequada o modelo matemático, que é a parte mais importante da análise, por causa da complexidade das análises de engenharia e da incerteza das informações disponíveis, (BABUŠKA et al.,1990).

Definido o modelo matemático parte-se em busca do modelo numérico que exige uma discretização do domínio, através da criação de uma malha de análise. A discretização do problema depende, na maioria dos casos, do bom senso do analista e da experiência adquirida na solução de outros problemas. Por outro lado pode-se praticamente renunciar a estes atributos, no que se refere à qualidade da discretização, com o uso de estratégias adaptativas.

Entretanto, a qualidade da malha inicial necessariamente influencia no processo de adaptação de malha. Portanto, gerar malhas iniciais de boa qualidade é uma questão importante até mesmo no processo de geração de malha adaptativa, (YAGAWA et al., 1992). Assim sendo, tem-se como meta alcançar uma malha relativamente boa para reduzir o tempo de processamento de modelos numéricos destinados à análise em um software comercial de elementos finitos, onde encontram-se disponíveis os métodos de refino h- e p-adaptativos. Para executar esta tarefa o domínio é subdividido em regiões e assim pode-se efetuar o processo de refino adaptativo somente nas regiões consideradas críticas, diminuindo então o custo computacional, com o uso inteligente do recurso. Por outro lado, a ausência de métodos adaptativos não inviabiliza o sistema. A estratégia utilizada é, neste caso, a de determinar um refino seletivo de malha nas regiões críticas, por meio da definição de uma densidade nodal apropriada, tomando por base a experiência dos especialistas e resultados de modelos de elementos finitos de peças simples.

Boa parte dos sistemas especialistas de auxílio à geração de malha já desenvolvidos (YAGAWA et al., 1992), (POURAZADY et al., 1991), (LO, 1989), (BACHMANN et al., 1989), utilizam somente detalhes geométricos para definir regiões onde deve-se efetuar um refino. Considera-se importante verificar também a influência dos carregamentos e condições de contorno. Existem alguns sistemas especialistas para geração de malha, como por exemplo o INTELMESH, (KANG et al.,1995), que faz uso do conceito de primitivas, subestruturação e de outras técnicas para a definição de uma densidade nodal associada aos pontos críticos, para considerar a geometria, carregamentos e condições de contorno. Porém este aplica-se a domínios bidimensionais somente, provavelmente devido às dificuldades encontradas na determinação dos pontos críticos. Considera-se adequado trabalhar de maneira mais abrangente, admitindo a possibilidade de se construir modelos tridimensionais.

A construção do sistema de modelagem está fundamentada em dois módulos, sendo o primeiro deles um sistema especialista, para auxiliar construção do modelo e o outro um gerenciador de modelo, o qual é responsável pela geração da malha inicial de análise e elaboração do modelo de elementos finitos propriamente dito.

Para viabilizar a construção do sistema especialista, em função do tempo disponível, optou-se por utilizar uma plataforma comercial, focando todos os esforços na elaboração da base de conhecimentos. O módulo de gerenciamento do modelo, é desenvolvido em linguagem C++ e as atividades de pré-processamento são garantidos por um gerador de malha comercial, denominado HyperMesh, (Altair Computing, Inc.).

No caso específico do SEAMEF, o usuário interage com o sistema através de uma interface respondendo alguns questionamentos. Em linhas gerais, o processo inicia com o sistema especialista argüindo o usuário para identificar a topologia, modos de falha da peça, características materiais, carregamentos e vinculação.

Para analisar o problema, de acordo com as informações associadas à topologia, o sistema classifica as peças como sendo prismática, tipo casca, de revolução ou irregular. Em se tratando de peças prismáticas, identifica-se as três medidas básicas da peça, comprimento, largura e profundidade ou espessura e, conforme os valores dos quocientes entre elas, aproxima-se o problema para espaços uni, bi ou tridimensionais. O tratamento dado às peças de revolução é semelhante ao atribuído a domínios bidimensionais, com pequenas alterações no que se refere aos carregamentos. É importante lembrar que a escolha de elementos axissimétricos está voltada a problemas onde existe axissimetria geométrica, de carga e de condições de contorno. No caso da geometria ser uma superfície desenvolvida no espaço, segue-se uma série de regras heurísticas associadas aos elementos de placa e casca. Considerando agora a possibilidade do componente em análise não se encaixar em nenhuma das classificações anteriores, resta-lhe somente ser configurado como uma peça irregular, a

qual pode ser reduzida ao domínio 2 D quando houver a possibilidade de efetuar a representação com base na sua seção transversal ou ao longo do plano longitudinal. Em outro caso, gera-se um modelo 3 D.

Definida a dimensionalidade do problema, ou seja, o número de dimensões da idealização geométrica, segue-se à observação dos objetivos da análise. Estes objetivos constituem-se nos valores ou quantidades que realmente se deseja obter do modelo, com base nos modos de falha. A falha por início de escoamento, por exemplo, requer a determinação do campo de tensões no ponto crítico. Sendo este portanto, em última análise, o objetivo do modelo. Com base nestas informações chega-se à dimensionalidade do modelo.

Na seqüência, o usuário indica os tipos de cargas envolvidas considerando a natureza, e suas direções, sendo que podem ser avaliadas tanto no domínio global quanto local. O sistema apresenta então uma série de informações para o usuário, as quais devem ser consideradas no momento da aplicação das cargas e condições de contorno.

O chamado gerenciador de modelo captura informações geométricas junto a um software de CAD, no padrão ACIS, e efetua a geração de malha, tomando por base as informações adquiridas junto ao sistema especialista. O usuário por sua vez aplica as condições de contorno e carregamentos, sobre a malha gerada, seguindo as orientações previamente destacadas. Desta forma, explora-se ao máximo os recursos do gerador de malha, fazendo com que este trabalhe como pré-processador.

Em paralelo é construído um arquivo ASCII que contém informações de propriedades materiais e propriedades geométricas, assim como, dados sobre o erro associado à solução aceitável. Este arquivo controla todo o fluxo de operações da geração do modelo de elementos finitos e culmina com a apresentação, em tela, das "quantidades", ou pelo menos parte delas, necessárias para a verificação dos critérios de falha.

A figura 3 apresenta o esquema de integração dos diferentes módulos. Note que o usuário, respondendo às questões sugeridas pelo sistema especialista, abastece o espaço de trabalho do mesmo com informações do problema. O motor de inferência as utiliza efetuando comparações com a base de conhecimento e posteriormente cede uma série de informações ao usuário e ao gerenciador de modelo. O usuário analisa estas informações e constrói o modelo geométrico no CAD. O gerenciador de modelo, por sua vez, toma por base as informações cedidas pelo SEAMEF para coordenar as atividades a serem desenvolvidas pelo gerador de malha. Uma vez gerada a malha, o usuário efetua a aplicação das condições de contorno e o gerenciador de modelo une todos os dados para criar um arquivo de entrada para o pacote de análise.

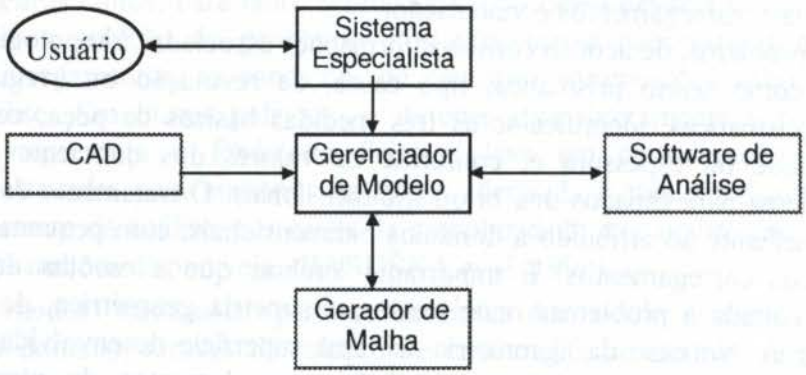

Figura 3 - Esquema de integração do sistema de modelagem

3. APLICAÇÕES

Como exemplo da potencialidade do sistema apresenta-se a análise efetuada em um vaso de pressão. O objetivo desta análise é verificar o campo de tensões nos pontos críticos para atender ao modo de falha de início de escoamento. Criou-se então um modelo global para determinar os pontos mais solicitados na análise. Posteriormente, partiu-se à geração dos modelos de detalhe para possibilitar a avaliação das tensões de forma mais precisa. A figura 4 apresenta o modelo global e as figuras 5 e 6 demonstram os modelos de detalhe nas regiões onde há um elevado gradiente de tensões.

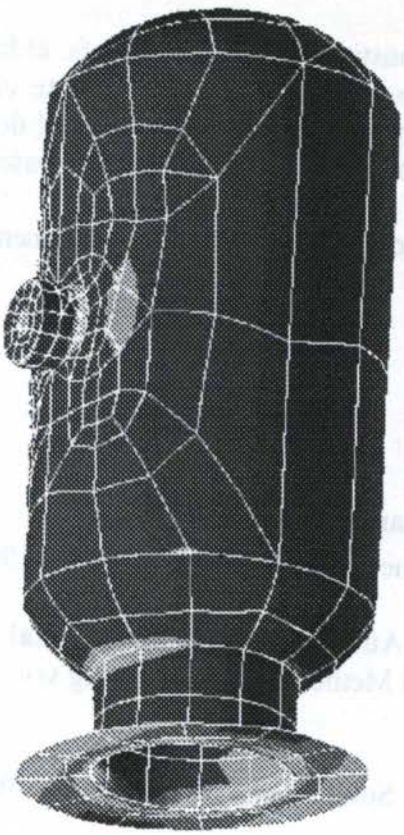

Figura 4 - Modelo global

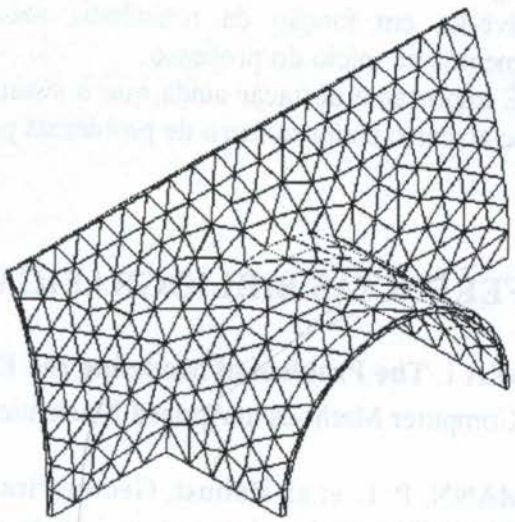

Figura 5 - Modelo de detalhe

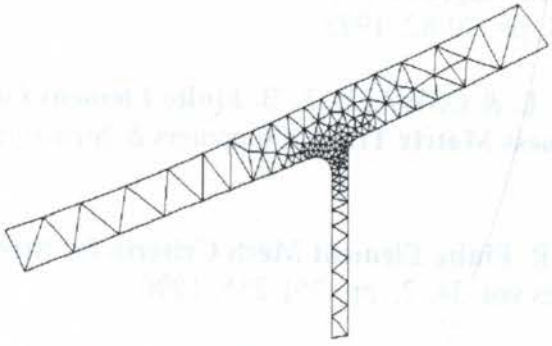

Figura 6 - Modelo de detalhe

4. CONCLUSÕES

O uso integrado de pacotes computacionais de CAD, análise estrutural, geração de malha e sistemas especialistas, apresenta-se como uma alternativa bastante válida para considerar as simplificações envolvidas na redução de um sistema físico a um modelo numérico de forma consistente.

O emprego de ferramentas de inteligência artificial, como por exemplo sistemas especialistas, no processo de análise estrutural via método de elementos finitos, deve ser mais explorado para que este conhecimento, até hoje tão restrito, seja disseminado nos ambientes acadêmico e industrial.

O desenvolvimento de um sistema especialista constitui-se em uma tarefa árdua e consome bastante tempo, principalmente para montar a base de dados. É interessante então que o engenheiro do conhecimento tenha um envolvimento prévio com a área na qual deseja desenvolvê-lo, em função da resistência natural dos especialistas em suprir a base de conhecimentos no início do processo.

É importante destacar ainda que o sistema discutido ainda está em desenvolvimento e espera-se atacar o maior número de problemas possíveis.

5. REFERÊNCIAS BIBLIOGRÁFICAS

BABUŠKA I. **The Problem of Modeling the Elastomechanics in Engineering .** Computer Methods in Applied Mechanics and Engineering vol. 82, pp.155-182, 1990

BACHMANN, P. L. et all **Robust, Geometrically Based, Automatic Two-dimensional Mesh Generation.** International Journal Numerical Methodos in Engineering vol. 24, pp. 1043-1078, 1987

BASRI, H. B. & STENTIFORD, E. I. **Expert Systems in Solid Waste Management.** Waste Management & Research vol. 13, pp. 67-89, 1995

HyperMesh Manual – Altair Computing Inc., 1757 Maplelawn Drive, Troy, MI, USA, 1997

KANG, E. & HAGHIGHI, K. **Intelligent Finite Element Mesh Generation.** Engineering with Computers vol. 11, pp. 70-82, 1995

KITTUR, M. G., HUSTON R. L. & OSWALD, F. B. **Finite Element Grid Improvement by Minimization of Stiffness Matrix Trace.** Computers & Structures vol. 31, pp. 891-896, 1989

KITTUR, M. G. & HUSTON R. **Finite Element Mesh Criteria for Stress Analysis.** Computers & Structures vol. 34, 2, pp. 251-255, 1990

LO, S. H. **Delaunay Triangulation of Non-convex Planar Domains** International Journal Numerical Methodos in Engineering vol. 28, pp. 2695-2707, 1989

POURAZADY, M. & RADHAKRISHNAN, M. **Optimization of a Triangular Mesh.** Computer & Structures vol.40, 3, pp. 795-804 1991

YAGAWA, G., YOSHIMURA, S., SONEDA, N. & NAKAO, K. **Automatic Two- and Three-dimensional Mesh Generation Based on Fuzzy Knowledge Processing.** Computational Mechanics vol. 9, pp 333-346, 1992

XIV Brazilian Congress of Mechanical Engineering
Obeid Plaza Hotel Convention Center - Bauru - SP/Brazil
December 08-12th 1997

PAPER CODE: COB988

MODELAGEM DA INTERAÇÃO QUASI-ESTÁTICA ENVOLVENDO SÓLIDOS ELÁSTICOS E RÍGIDO-PLÁSTICOS COM ÊNFASE NO FENÔMENO DE CONTATO / *QUASISTATIC INTERACTION OF ELASTIC AND RIGID PLASTIC SOLIDS WITH EMPHASIS ON CONTACT PHENOMENA*

REYNALDO TAYLOR-DE-LIMA & WLADMIR SYBINE
Departamento de Engenharia Civil - Pontifícia Universidade Católica do Rio de Janeiro
Rua Marques de São Vicente, 225. CEP 22.453-900 Rio de Janeiro, RJ - Brasil
e-mail: taylor@civ.puc-rio.br / sybine@civ.puc-rio.br

Abstract

Interaction and contact between solids are relevant phenomena in the context of structural engineering. In this field, loads are transmited by contact to structures which, in their turn, transmit loads to foundations by contact between bodies. In metal forming computations, such phenomena also play a major role. A good description of the interaction between workpiece and tools is of fundamental importance for a realistic simulation of fabrication processes. Actualy, contact mechanics have many applications in structural and mechanical engineering and contact models can be generated by the variational principles of solid mechanics. The present work describes a finite element model, based on a treatment of boundary conditions by penalty functions, developed in order to analyse the quasi-static interaction between a rigid solid and a deformable solid. The model is verified in its simpler version through the analysis of the Signorini's problem without friction. It is extended, in order to take into account the inelastic behavior of the deformable solid in the domain of finite strains, through rigid-plastic constitutive equations. In the extended version the model is verified by the analysis of a metal forming process.

Keywords

contact mechanics / finite elements / metal forming computation
mecânica de contato / elementos finitos / conformação mecânica computacional

1. INTRODUÇÃO

As metodologias utilizadas na análise de problemas de contato têm sua origem na teoria dos "Hydrocodes" da década de 60. Estes eram sistemas que utilizavam o método das diferenças finitas e a teoria hidrodinâmica dos sólidos na modelagem de problemas de contato com impacto oriundos da indústria bélica. Nesses problemas, um dos aspectos mais importantes é o da propagação de ondas elasto-plásticas e de choque e a sua modelagem numérica, assunto que foi extensivamente discutido em Taylor-de-Lima (1988). Contudo outros aspectos importantes são também abordados na literatura. J. O. Hallquist foi um dos autores que deram valiosas contribuições ao estudo de problemas de contato com impacto. Seu código DYNA2D de 1978, é muitíssimo utilizado até os dias atuais. O DYNA2D incorpora os avanços e vantagens dos "Hydrocodes" ao método dos elementos finitos e adota um algoritmo explícito para a evolução no tempo. Com relação ao tratamento das condições de contato, a metodologia de Hallquist está sintetizada em Hallquist et al.(1985) (1992).

Com base nos trabalhos de Hallquist, Doltsinis et al.(1989) (1990) desenvolveram um modelo simples e eficiente para tratamento automático de condições de contato e atrito, em simulações de processos tridimensionais de conformação mecânica. Mais recentemente, os problemas de contato vêm sendo tratados como problemas variacionais com restrições de desigualdade, como discutido por Bathe (1996).

Neste trabalho, seguindo-se a formulação variacional, tratam-se as metodologias de Hallquist e Doltsinis et ali, interpretando-as e desenvolvendo-as como formas eficientes de tratar as restrições de desigualdade na forma como estas se apresentam. Um problema aqui estudado inicialmente é o do equilíbrio de sólidos considerados linearmente elásticos, em contato com uma fundação rígida e com condições de contato unilateral, que foi estudado por Signorini em 1933 e em 1959. Outro problema estudado é o da conformação mecânica de sólidos, idealizada a partir do modelo rígido-plástico.

2. O MODELO RÍGIDO PLÁSTICO PARA SÓLIDOS CONFORMADOS

Quando corpos sólidos experimentam grandes deformações, observa-se que as componentes inelásticas são predominantes, uma vez que as deformações elásticas são infinitesimais. Nestes casos, uma boa aproximação para descrever o comportamento do sólido é o modelo rígido plástico, que, desprezando a componente elástica da deformação, modela o processo de deformação como um escoamento de estokesiano de um fluido não-newtoniano. Como deformações plásticas se dão a volume constante, o escoamento é modelado como incompressível. Consequentemente a formulação forte (S) do problema pode ser escrita como se segue. Sejam $\Omega \subset \Re^3$ e Γ, respectivamente, o domínio onde se define o problema de escoamento e seu contorno. Dados $b_i : \Omega \to \Re$ (i = 1, 2, 3 = x, y, z), componentes cartesianas das forças de corpo; $\bar{v}_i : \Gamma_v \to \Re$ e $\bar{t}_i : \Gamma_t \to \Re$, com Γ_v e Γ_t representando, as porções do contorno onde tem-se, respectivamente, velocidades e tensões prescritas; encontrar o campo vetorial $\mathbf{v}$ das velocidades, de componentes cartesianas $v_i : \overline{\Omega} \to \Re$ ($\overline{\Omega} = \Omega \cup \Gamma$) tal que:

$$(S)\begin{cases} \sigma_{ij,j} + b_i = 0, & \text{em } \Omega \\ v_i = \bar{v}_i, & \text{em } \Gamma_{V_i} \\ \sigma_{ij} n_j = \bar{t}_i, & \text{em } \Gamma_{V_i} \\ v_{i,i} = 0, & \text{em } \Omega \end{cases} \tag{1}$$

onde σ_{ij} representa as componentes do tensor das tensões de Cauchy e n_j representa a componente normal externa do contorno Γ.

A restrição de incompressibilidade $v_{i,i} = 0$ é tratada de forma aproximada neste modelo através de uma função de penalidade. Para tanto, faz-se a decomposição do tensor das taxas de deformação $\dot{\varepsilon}_{ij}$, nas suas componentes volumétrica $\dot{\varepsilon}_v$ e desviadora $\dot{\varepsilon}_{D_{ij}}$. Calcula-se o estado de tensões pelas seguintes equações constitutivas:

$$p = -k\, v_{i,i} = -k\, \dot{\varepsilon}_v \quad \text{e} \quad \sigma_{D_{ij}} = 2\mu \dot{\varepsilon}_{D_{ij}} \tag{2}$$

onde p e $\sigma_{D_{i,j}}$ representam a pressão e a componente desviadora de σ_{ij}, enquanto k é a função de penalidade, que deve assumir valores muito grandes para garantir que $\dot{\varepsilon}_v = v_{i,i}$ tenda para zero.

O comportamento plástico do material é, por sua vez, simulado através de uma viscosidade $\mu = \mu(\sigma_{ij})$, dependente do nível de tensões atuantes, da seguinte forma: Sejam

$$\bar{\sigma} = \sqrt{(3/2)\sigma_{D_{ij}}\sigma_{D_{ij}}} \quad \text{e} \quad \dot{\bar{\varepsilon}} = \sqrt{(3/2)\varepsilon_{D_{ij}}\varepsilon_{D_{ij}}} \tag{3}$$

respectivamente, a tensão e a taxa de deformação equivalentes. Pré multiplicando-se (2.b) por $3/2\,\sigma_{D_{ij}}$ obtem-se:

$$\bar{\sigma} = 3\mu\dot{\bar{\varepsilon}} \quad \text{e} \quad \mu = \bar{\sigma}/(3\dot{\bar{\varepsilon}}) \tag{4}$$

onde $\mu = \mu(\sigma_{ij})$ pode ser obtido substituindo-se $\bar{\sigma}$ em (4.b), pela expressão analítica $\bar{\sigma} = f(\bar{\varepsilon}, \dot{\bar{\varepsilon}})$, obtida com base no ensaio de tração ou compressão uniaxial.

Em seguida, aplicando-se o principio das potências virtuais sobre as forças que atuam num elemento infinitesimal de volume e usando as eqs. (2) para computar p e $\sigma_{D_{i,j}}$, chega-se à forma fraca (W) do escoamento de Stokes, formulado anteriormente em (S):

$$\int_\Omega \delta\dot{\varepsilon}_{D_{ij}}\sigma_{D_{ij}}\,d\Omega - \int_\Omega \delta\dot{\varepsilon}_v\,d\Omega = \int_\Omega \delta v_i\, b_i\,d\Omega + \sum_{i=1}^{3}\int_{\Gamma_{t_i}} \delta v_i\,\bar{t}_i\,d\Gamma \tag{5}$$

3. FORMULAÇÃO VARIACIONAL DO PROBLEMA DE CONTATO

Como já foi discutido em Sybine et al.(1997), os problemas de contato são tratados aqui considerando-se a interação quasi-estática entre dois sólidos, sendo um deles deformável, chamado na literatura de "contactante" (Bathe, 1996) e correspondendo a uma peça sendo fabricada por um processo de conformação mecânica, enquanto o outro sólido, chamado na literatura de "alvo", é considerado rígido e representa uma das ferramentas que dão forma à peça no processo de fabricação.

Considere-se, portanto, a interação com o corpo contactante representado por um domínio $\Omega_1 \subset \Re^3$, de contorno Γ^1, enquanto um domínio $\Omega_2 \subset \Re^3$, de contorno Γ^2, representa o corpo alvo. A dedução a seguir pode ser automaticamente estendida para o caso de vários corpos alvo, ou seja, para o caso de múltiplas ferramentas, como é comum se encontrar na prática.

Usando-se, como na seção 2, o principio das potências virtuais, aplicado aqui novamente para o caso da interação quasi-estática entre dois sólidos, considerando-se ainda Γ_c^1 e Γ_c^2 como as partes dos contornos Γ^1 e Γ^2 que entram em contato uma com a outra, escreve-se a forma fraca

$$\int_{\Omega_1\cup\Omega_2} \delta\bar{\varepsilon}_{ij}\sigma_{ij}\,d\Omega = \int_{\Omega_1\cup\Omega_2} \delta v_{ij}\, b_i\,d\Omega + \sum_{i=1}^{3}\int_{\Gamma_{t_i}} \delta v_i\,\bar{t}_i\,d\Gamma + \sum_{i=1}^{3}\int_{\Gamma_c} \delta v_i^{12}\, t_i^c\,d\Gamma \tag{6}$$

para o problema de contato, na qual δv_i^{12} representa a velocidade virtual relativa de um ponto de Γ_c^1 em relação ao seu correspondente em Γ_c^2 ($\delta v_i^{12} = \delta v_i^1 - \delta v_i^2$), quando os dois estão em contato. A ocorrência ou não do último termo da eq. (6) e a determinação da superfície Γ_c dependem da satisfação de condições de desigualdade (Bathe, 1996), que são tratadas aqui de acordo com o modelo simplificado que será discutido na seção 5.

Nas eqs. (6), o tensor das tensões σ_{ij}, ao longo do domínio Ω_1, pode ser obtido, para o caso da elasticidade infinitesimal, de forma incremental, de acordo com a expressão $\sigma_{ij}^{n+1} = \sigma_{ij}^n + E_{ijkl}\dot{\varepsilon}_{kl}^{n+1}\Delta t$, onde E_{ijkl} representa as componentes cartesianas do tensor de elastisticidade material e Δt representa o incremento de tempo. No caso de se considerar o modelo rígido-plástico para o sólido deformável, σ_{ij} é calculado de acordo com $\sigma_{ij} = \sigma_{D_{ij}} - p$, onde p e $\sigma_{D_{ij}}$ são obtidos através das eqs. (2).

4. DISCRETIZAÇÃO POR ELEMENTOS FINITOS

Admita-se que o campo de velocidades **v** seja aproximado no interior de um elemento de acordo com Bathe (1996), pela expressão $\mathbf{v}_e = \mathbf{N}\mathbf{V}_e$, onde **N** contém as funções de forma para $\mathbf{v}_e$ e $\mathbf{V}_e$ representa o vetor das velocidades nodais do elemento *e*. Considerem-se $\dot{\varepsilon}$ e σ como sendo, respectivamente, os vetores das taxas de deformação e das tensões, com seis componentes cada um. O vetor $\dot{\varepsilon}$ é obtido a partir do vetor de velocidades nodais $\mathbf{V}_e$ por meio das relações taxa-de-deformação x velocidade $\dot{\varepsilon} = (\partial\mathbf{N})\,\mathbf{V}_e = \mathbf{B}\,\mathbf{V}_e$. Apartir de $\dot{\varepsilon}$, o vetor das tensões σ é determinado de acordo com o modelo constitutivo adotado, que pode ser o da elasticidade infinitesimal ou o rígido-plástico baseado no escoamento de Stokes.

Introduzindo-se, portanto, na forma fraca do problema de contato da eq. (6) a aproximação de elementos finitos descrita acima, chega-se às equações:

$$\mathbf{F}(\mathbf{V}) = \sum_{i=1}^{2} \left(\underbrace{\int_{\Omega_i} \mathbf{B}^t \sigma \, d\Omega}_{\mathbf{S}_i} - \underbrace{\int_{\Omega_i} \mathbf{N}^t \mathbf{b} \, d\Omega}_{\mathbf{R}_i^{\Omega}} - \underbrace{\int_{\Gamma_t^i} \mathbf{N}^t \bar{\mathbf{t}} \, d\Gamma}_{\mathbf{R}_i^{\Gamma}} - \underbrace{\int_{\Gamma_c^i} \mathbf{N}^t \mathbf{t}^c \, d\Gamma}_{\mathbf{R}_i^{\Gamma}} \right) = \mathbf{0} \qquad (7)$$

que traduzem o equilíbrio dos dois corpos em contato. Como o domínio Ω_2 é considerado rígido, tem-se que o vetor das forças internas $\mathbf{S}_2$ é nulo. Sua condição de equilíbrio é descrita, por tanto, pela equação $\mathbf{R}_2^{\Omega} + \mathbf{R}_2^{\Gamma} + \mathbf{R}_2^{C} = \mathbf{0}$, que não necessita ser resolvida para obtenção do campo de velocidades uma vez que, como o domínio Ω_2 representa uma ferramenta, possui um movimento de corpo rígido cuja cinemática é conhecida a priori. Desta forma a simplificação da eq. (7) fornece o seguinte sistema de equações algébricas não lineares

$$\mathbf{F}(\mathbf{V}) = \mathbf{R}_1^{\Omega} + \mathbf{R}_1^{\Gamma} + \mathbf{R}_1^{C} - \mathbf{S}_1(\mathbf{V}) = \mathbf{0} \qquad (8)$$

que é resolvido iterativamente para o vetor das velocidades nodais **V**, de acordo com o esquema apresentado em Taylor-de-Lima (1994). O movimento durante o processo de deformação é acompanhado através das coordenadas atualizadas dos pontos nodais da malha de elementos finitos, que são obtidas pela integração do vetor de velocidades nodais **V**.

5. MODELO SIMPLIFICADO PARA CONTATO

Como já foi mencionado, este trabalho toma por base as contribuições de Hallquist et al.(1985) e (1992) e Doltsinis et al.(1989) e (1990). Uma descrição mais abrangente da metodologia aqui utilizada pode ser encontrada em Sybine (1997). Aqui são apresentados apenas os aspectos principais do algoritmo.

A descrição da superfície de contato Γ_c se dá via discretização do contorno do sólido indeformável, por elementos finitos. Por conveniência utilizam-se elementos com normal única em cada face. O teste de ocorrência de contato requer uma comparação da configuração atual do contorno Γ_c^1 com a posição da sua respectiva superfície alvo, aqui representada por Γ_c^2. De acordo com a Figura (1), o ponto nodal $\underline{m}$, pertencente à superfície contactante do sólido deformável discretizado, é suposto estar a ponto de entrar em contato com a superfície alvo.

Define-se que num dado sólido indeformável, o "master point" de $\underline{m}$, é o ponto nodal $k \in \Gamma_c^2$, que possui a menor distância euclidiana a $m \in \Gamma_c^1$. Esta definição pode ser traduzida pelas expressões:

$$\mathbf{x}_{km} = \mathbf{x}_m - \mathbf{x}_k \quad \text{e} \quad \mathbf{x}_{km}^t \mathbf{x}_{km} = \min\left(\mathbf{x}_{jm}^t \mathbf{x}_{jm}\right),\ j = 1,\ldots,n_c \tag{9}$$

onde n_c denota o número de nós da superfície alvo Γ_c^2.

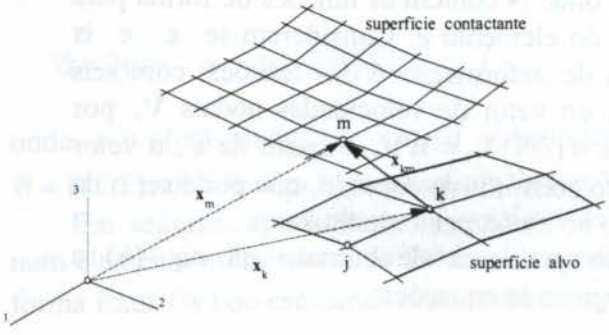

Figura 1: Ponto nodal $m \in \Gamma_c^1$ ***associado a "master point"*** $k \in \Gamma_c^2$

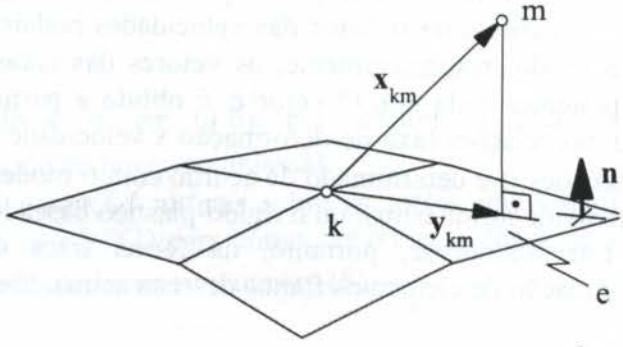

Figura 2: Identificação do elemento e de Γ_c^2

Conhecido o "master point" k, sabe-se que o ponto onde provavelmente se dará o contato ou a penetração de m é interior a um dado elemento *e* de Γ_c^2, que contém esse "master point". Este dado elemento *e* é especificado como sendo aquele que contém a projeção $\mathbf{y}_{km}$ do vetor distância $\mathbf{x}_{km}$ (Figura 2). Com isso a posição do ponto $m \in \Gamma_c^1$ em relação a Γ_c^2 é indicada pela distância normal ao plano do elemento *e*, de acordo com $d_n = \mathbf{n}_e^t \mathbf{x}_{km}$, onde $\mathbf{n}_e$ denota a normal externa da face do elemento *e*. Quando d_n=0, verifica-se que se deu o contato entre as malhas. Nesta situação, o movimento na direção normal à superfície alvo Γ_c^2 deve ser impedido. Quando $d_n < 0$, verifica-se que ocorreu a penetração da superfície alvo. Induz-se a expulsão do nó que viola o limite definido pela superfície alvo. Prescreve-se para este nó uma velocidade normal à face perfurada, de modo a conduzi-lo de volta à superfície.

Seja $\mathbf{v}^m$ a velocidade do ponto nodal m, num dado instante, e seja $\mathbf{v}^e$ a velocidade do ponto de contato, de Γ_c^2, obtido por meio de interpolação. Devido à restrição de contato, tem-se a seguinte condição de contorno:

$$v_n^m - v_n^e = \mathbf{n}_e^t\left[\mathbf{v}^m - \mathbf{v}^e\right] = 0, \ \text{em} \ \Gamma^c \tag{10}$$

que deve ser satisfeita em Γ_c, enquanto a reação $\mathbf{F}_n$ no ponto de contato for de compressão ($\mathbf{n}_e^t \mathbf{F}_n \geq 0$). Como alternativa, introduzem-se essas condições através de um método de penalidades. Para tanto, a eq. (10) é substituída por:

$$\mathbf{v}_n^m - \mathbf{v}_n^e = -\frac{1}{k_n} F_n \to 0 \tag{11}$$

onde $F_n = \mathbf{n}_e^t \mathbf{F}_m \in \Re$ representa a intensidade da reação normal no ponto m, enquanto k_n é o parâmetro de penalidade que segue a condição: $k_n \to \infty$. Como $\mathbf{n}_e^t \mathbf{F}_n \geq 0$, tem-se que:

$$\mathbf{F}_n = -k_n\left[\mathbf{v}_n^m - \mathbf{v}_n^e\right] \tag{12}$$

enquanto $\mathbf{n}_e^t\left[\mathbf{v}_n^m - \mathbf{v}_n^e\right] \leq 0$, condição esta que equivale a $\mathbf{n}_e^t \mathbf{F}_n \geq 0$.

$\mathbf{F}_n$ é tratada, através da eq. (12), da mesma forma como as forças nodais resultantes das tensões. Portanto, quando se dá o contato, em lugar de se introduzir uma restrição ao

deslocamento como na eq. (10), o coeficiente k_n é somado como uma contribuição direta para a matriz de rigidez, sem que a estrutura de montagem desta seja alterada. Desta maneira, vínculos não precisam ser impostos de forma explícita e a estrutura da matriz de rigidez permanece inalterada. Tal fato simplifica o procedimento de imposição de contato a cada passo da análise.

6- APLICAÇÕES

6.1- Placa Espessa Apoiada por Sobre Fundação Rígida

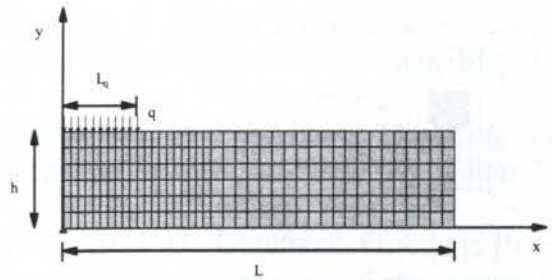

- comprimento da placa — L = 0.40 m;
- extensão da placa onde é aplicada carregada — L_q = 0.075 m;
- espessura da placa — h = 0.10 m
- carga uniformemente distribuída na extensão L_q — q = 400.0 MPa;
- módulo de elasticidade da placa — E = 10^7 MPa;
- coeficiente de Poison — ν = 0.30;
- coeficiente de atrito na interface fundação/placa — μ= 0

Figura 3: Proporções da placa analisada e primeira discretização.

É considerada uma placa espessa e longa de seção retangular constante, simplesmente apoiada sobre fundação rígida. A placa é submetida a um carregamento vertical, uniformemente distribuído, em região próxima à sua extremidade esquerda, conforme ilustra a Figura (3). Despreza-se o atrito entre a fundação e a placa, leva-se em consideração a interação de contato entre os sólidos envolvidos e modela-se o problema como um caso de estado plano de deformações, no domínio da elasticidade infinitesimal. As dimensões da placa e as características do material de que é constituída são extraídas de Mamiya et al.(1988), e aparecem indicadas na Figura (3).

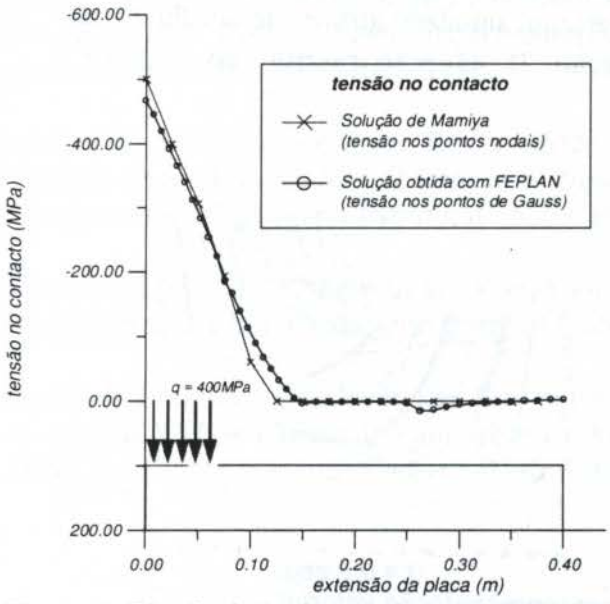

Figura 4: Distribuição de tensões ao longo da superfície de contato.

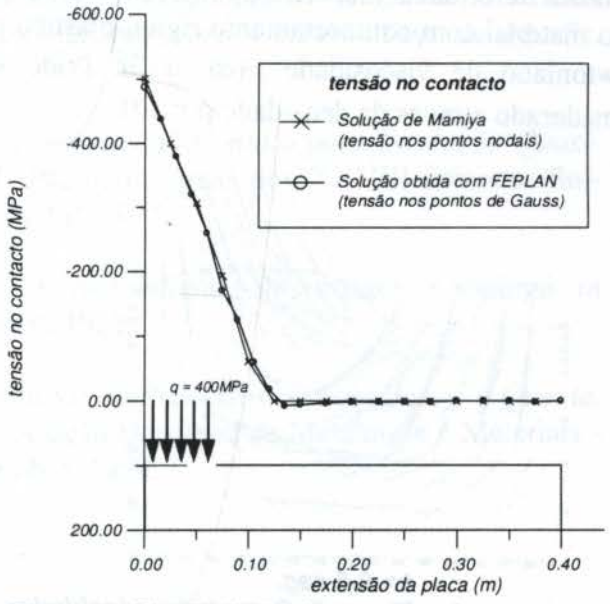

Figura 5: Distribuição de tensões de contato, sem a consideração da tolerância.

A discretização da placa, também mostrada na Figura (3), é feita com uma malha de elementos finitos com 240 elementos bi-lineares Q4 e 287 pontos nodais, na qual adota-se uma maior densidade de elementos nas imediações da região L_q, onde a carga **q** é aplicada.

Na análise, com o carregamento considerado progressivo, dividido em 10 passos, obtem-se a distribuição de tensões na face inferior da placa ilustrada na Figura (4). Uma discussão aprofundada destes resultados pode ser encontrada em Sybine (1997). Realizando mais uma vez a análise, desconsiderando a tolerância para esforços trativos em Γ^c e considerando uma malha com apenas 80 elementos Q4, obtem-se a distribuição de tensões ilustrada na Figura (5).

Por outro lado na Figura (6), ilustra-se a deformada da placa quando submetida ao carregamento total. Esta deformada é apresentada multiplicada por um fator de escala de 10^4, para deformações, e revela um descolamento da placa na região em que não se verifica compressão sobre a fundação.

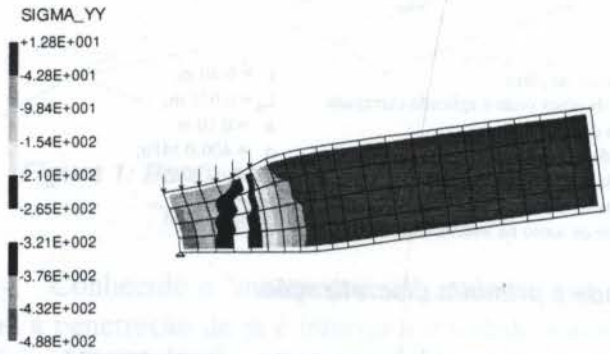

Figura 6: Distribuição de tensões na placa.

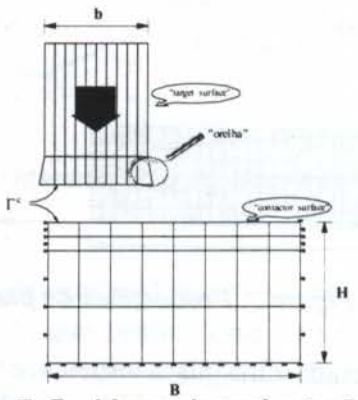

Figura. 7: Problema de endentação rígida.

6.2- Endentação Rígida

Este exemplo consiste na modelagem de um processo de conformação mecânica, ilustrado na Figura (7). O processo de deformação de uma peça metálica, se dá pela descida de uma ferramenta rígida (superfície alvo) com velocidade constante de 0.01 mm/s sobre a peça metálica deformável (superfície contactante a ser conformada), que é modelada considerando-se o material com comportamento rígido-plástico perfeito, simulado através de um fluído não-newtoniano de viscosidade $\mu(\sigma) = 1/3\dot{\bar{\varepsilon}}$ (vide seção 2). O peso próprio do material é considerado através da densidade $\rho = 1.0$.

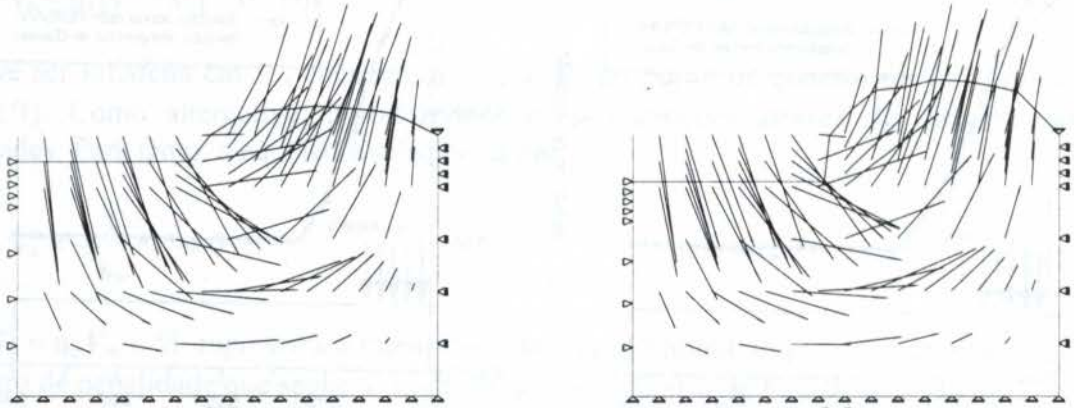

t = 0.5 seg. ***t = 0.9 seg.***

Figura 8: Campo de velocidades em representação vetorial.

A malha de elementos finitos para a análise deste exemplo, ilustrada na Figura (7), é constituída por 32 elementos Q8 de interpolação quadrática e 121 pontos nodais. As proporções da peça são dadas por H/b=2.70 e B/b = 1.70.

A geometria atualizada é obtida através da integração do campo de velocidades, realizada por meio de um esquema de Euler explícito, onde cada incremento de tempo é de 0.1 seg. A solução das equações não lineares é obtida em média após dez iterações de Newton-Raphson, para uma tolerância da ordem de 10^{-10}. Os resultados da análise vêm apresentados nas Figura (8) para os instantes t = 0.5 seg e t = 0.9 seg.

7. REFERÊNCIAS

Bathe, K.-J.: *Finite Element Procedures*. pp. 622-629 Prentice-Hall, Inc. NJ, 1996.

Doltsinis, I. St. and Luginsland, J.: *Computer Aided modelling of Metal Forming Processes*. Proc. Materials'88 Conf., London, May 9-13, 1988. The Institute of metals, London, 1989.

Doltsinis, I. St.: *Aspects of Modelling and Computation in the Analysis of Metal Forming*. Engeneering Computations, vol. 7, num. 1, march, 1990.

Hallquist, J. O.; Goudreau, G. L. and Benson, D. J.: *Sliding Interfaces with Contact-Impact in Large-Scale Lagrangian Computations*. Computer Methods in Applied Mechanics and Engeneering 51, pp. 107-137, 1985.

Hallquist, J. O.; Schweizerhof, K. and Stillman, D.: *Efficiency of Contact Strategies and Algorithms in Explicit FE Programming*. Proceedings of the Conference on Computational Plasticity, Barcelona, Pineridge Press, 1992.

Mamiya, E. N.; Mattos, H. S. da Costa; Raous, M. and Sampaio, R: *Solução Numérica de Problema de Contato Unilateral com Atrito - Aplição a uma Placa Apoiada sobre Solo Rígido*. Revista Brasileira de Ciências Mecânicas, vol. X, nº 1, pp. 45-69, 1988.

Sybine, W.: *Uma Modelagem de Fenômenos de Contato com Impacto Utilizando o Método dos Elementos Finitos Numa Implementação Orientada para Objetos*. Tese de M. Sc. apresentada ao DEC/PUC-RIO, 1997.

Sybine, W and Taylor-de-Lima, R: *Um Modelo Numérico de Contato para Interação Quasi-Estática Envolvendo Sólidos Elásticos e Rígido-Plásticos*, Anais dos XXVIII Jornadas Sul-Americanas de Engenharia Estrutural - São Carlos, SP, 1997.

Taylor-de-Lima, R.: *Numerische Verfahren zur Behandlung Stossartiger Vorgänge in Festkörpern*. Dr.-Ing. thesis, University of Stuttgart, 1988.

Taylor-de-Lima, R.: *Simulação por Elementos Finitos de Processos de Laminação a Quente*. Anais do XXXI Seminário de Laminação da Associação Brasileira de Metalurgia e Materiais - ABM, pp. 125-137, Juiz de Fora, 23-25 de novembro, 1994.

XIV Brazilian Congress of Mechanical Engineering
Obeid Plaza Hotel Convention Center - Bauru - SP/Brazil
December 08-12th 1997

PAPER CODE: COB995

A-POSTERIORI ERROR ESTIMATORS FOR STRONGLY NONLINEAR PROBLEMS

FELIX CHRISTIAN GUIMARÃES SANTOS
Departamento de Engenharia Mecânica - Universidade Federal de Pernambuco
CEP 50740-530 Recife, Brasil - e-mail: fcgs@dmat.ufpe.br

Abstract

The use of auxiliary linear problems in order to estimate the approximation error of finite element discrete solutions to nonlinear elliptic problems has been one of the most reliable and robust way of assessing the accuracy of a discrete model. There has been an understanding that if an implicit estimator is asymptotically exact for linear problems, then it will be so when being used for nonlinear problems through a suitable auxiliary problem. In this work we prove that statement for a wide class of implicit estimators.

Keywords

Finite element method, Nonlinear PDE's, A-posteriori estimators.

1 INTRODUCTION

This work deals with the relationship between the approximation error of finite element solutions to strongly nonlinear elliptic partial differential equations in some norms with the error estimators computed for some suitably defined linear elliptic partial differential equations. It will be proved in what follows that, provided the problem data are smooth, it is possible to build linear elliptic problems such that its finite element error is asymptotically equal to the finite element error for the nonlinear problem, and, provided the estimator being used is asymptotically exact for smooth linear problems, then, it will also be asymptotically exact for that auxiliary linear problem and, consequently for the original nonlinear problem. The estimators considered are in a very large class, including virtually all implicit estimators, i.e., those estimators computed through the solution of a local elliptic problem (either patchwise or elementwise). This is important in the sense that one may use estimators for nonlinear problems in the same fashion as it is done for linear problems, and with the understanding that the same advantages and disadvantages of any particular estimator originally developed for linear problems will occur when it is used for nonlinear problems.

Let $F : W_0^{1,p_1} \times \mathcal{R}^m \rightarrow W^{-1,p_2'}$ be given and consider the following problem

Pr.1 : Find $(u_0, \lambda_0) \in (W_0^{1,p_1} \times \mathcal{R}^m)$ such that

$$F(u_0, \lambda_0) = 0 \quad \text{on } \Omega$$

where $\Omega \subset \mathcal{R}^2$ is open and bounded. Here

$$F(u,\lambda) = -\nabla \cdot [\mathbf{a}(\nabla u, u, \lambda, x)] + \mathbf{b}(\nabla u, u, \lambda, x) + \mathbf{c}(u, \lambda, x) - \mathbf{f}(\lambda, x);$$

with $u : \Omega \to \mathcal{R}$; $\mathbf{a} : \mathcal{R}^2 \times \mathcal{R} \times \mathcal{R}^m \times \mathcal{R}^2 \to \mathcal{R}^2$; $\mathbf{b} : \mathcal{R}^2 \times \mathcal{R} \times \mathcal{R}^m \times \mathcal{R}^2 \to \mathcal{R}$; $\mathbf{c} : \mathcal{R} \times \mathcal{R}^m \times \mathcal{R}^2 \to \mathcal{R}$; $\mathbf{f} : \mathcal{R}^m \times \mathcal{R}^2 \to \mathcal{R}$ are given smooth enough functions.

■

In this work we are interested in the a-posteriori numerical analysis, so we are going to assume that the following hypothesis holds

Hyp. 1.1 : *There exists a nonempty set $\Lambda \subset \mathcal{R}^m$ such that, for all $\lambda_0 \in \Lambda$, Pr.1 has at least one solution point $u_0(\lambda_0)$ in some given admissible closed convex set $\mathcal{K} \subset W_0^{1,p_1}$.*

■

The discrete problem is set as

DPr.1 : Find $(u_h, \lambda_h) \in (S^h(\tau_h, p, \Omega) \cap \mathcal{K}) \times \mathcal{R}^m$ such that

$$< F(u_h, \lambda_h), v_h >= 0, \quad \text{for all } v_h \in S^h(\tau_h, p, \Omega) \cap W_d^{1,p_2}$$

■

The main issue now is to establish some restrictions on the differential equations we are going to deal with. Actually there are further issues which will not be covered here, but the reader will find them in (Babuska *et al.*, to appear-III), where a more complete description of the hypothesis will be found. For a more detailed analysis on the differentiability structure required in the hypothesis stated below see (Babuska *et al.*, to appear-I); and for the existence and convergence results we refer to (Babuska *et al.*, to appear-II).

Let us be specific and assume that $F : W_0^{1,p_1} \times \mathcal{R}^m \to W^{-1,p_2'}$, $1 < p_1 < \infty$, $1 < p_2$, is defined by

$$F(u,\lambda) = Q(u,\lambda) - R(u,\lambda) - f(\lambda) \tag{1}$$

Here $Q(.,\lambda) : W_0^{1,p_1} \to W^{-1,p_2'}$ is an isomorphism and a strongly nonlinear operator for all $\lambda \in \mathcal{R}^m$; $R : W_0^{1,p_1} \times \mathcal{R}^m \to W^{-1,p_2'}$ is a compact and smooth nonlinear operator, and $f(\lambda) \in W^{-1,p_2'}$.

Also, assume

Hyp. 1.2 *$F : W_0^{1,p_1} \times \mathcal{R}^m \to W^{-1,p_2'}$ satisfies the following properties:*

i) F is a Θ-Fredholm operator of index $i(F) = m$ from $\Theta = (W_0^{1,p_1}, H_0^1, W_0^{1,\infty})$ into $\Theta^* = (W^{-1,p_2'}, H^{-1}, W^{-1,\infty})$.

ii) The extension

$$D_u Q_H(w,\lambda) : H_0^1 \to H^{-1}$$

is a coercive and bounded linear operator for all $w \in W^{1,\infty}$ and $\lambda \in \mathcal{R}^m$, with the constants of boundedness and coercivity being bounded uniformly away from ∞ and 0, respectively, in bounded sets of $(w,\lambda) \in W^{1,\infty} \times \mathcal{R}^m$. Furthermore, its coefficients are in L^∞.

iii) For all $u_1, u_2 \in W_0^{1,\infty}$ and $\lambda \in \mathcal{R}^m$, there exists $C = C(\|u_1\|_{W^{1,\infty}}, \|u_2\|_{W^{1,\infty}}, |\lambda|)$, such that

$$\|D_u Q_H(u_1,\lambda) - D_u Q_H(u_2,\lambda)\|_{\mathcal{L}(H_0^1, H^{-1})} \leq C \|u_1 - u_2\|_{W^{1,\infty}}$$

and

$$\|D_u R(u_1,\lambda) - D_u R(u_2,\lambda)\|_{\mathcal{L}(H_0^1,H^{-1})} \leq C\|u_1 - u_2\|_{W^{1,\infty}}.$$

Furthermore, all the coefficients of $D_u F(u_0,\lambda_0)$ *are as smooth as the gradient of* u_0.

iv) For all $(u,\lambda) \in W_0^{1,\infty} \times \mathcal{R}^m$, *all the existent derivatives of* F *with respect to the function and the parameter at* (u,λ) *are Hölder-continuous with respect to* λ. *Moreover, the existing derivatives of* F *with respect to the parameter are in* $W^{-1,p}$, *for all needed values of* p, *and are Hölder-continuous with respect to the function.*

v) For all $(u,\lambda) \in W_0^{1,\infty} \times \mathcal{R}^m$, *the linear operator* $D_u R(u,\lambda) : W_0^{1,p} \to W^{-1,r'}$ *is a compact operator for all* p, $r' \leq p \leq r$, *with* $r > 2$ *as large as needed.*

■

2 A-POSTERIORI ESTIMATORS

In this section we develop a procedure for relating computable a-posteriori error estimators for a suitably defined auxiliary linear problem with the exact error (in the norm of $W^{1,s}$, $s \in [r',r]$, $r \geq 2$) for the nonlinear problem (between a given solution to Pr.1 and the corresponding discrete solution to DPr.1). A large class of estimators will be considered, namely, implicit estimators, obtained through a solution of a suitably defined local problem and defined either elementwise or patchwise. In order to make the procedures clear, we will consider only strong regular solution points. The procedures regarding simple turning points will be presented in later works.

A first linear auxiliary problem will be defined by a bilinear form $B_1 : H_0^1 \times H_0^1 \to \mathcal{R}$ and a right-hand side f_1. Similarly, a second linear auxiliary problem will be defined by $B_0 : H_0^1 \times H_0^1 \to \mathcal{R}$ and f_0. For the exact, discrete and error equations of both problems we refer to LP.0, DLP.0 and Er.0 below, respectively.

In what follows, the expression $\omega \cap T \neq \emptyset$ will mean that the interior of the region defined by ω has an empty intersection with the region defined by T.

Def. 2.1 : *Let a mesh* τ_h *be given. Suppose that a way of building a set of patches* ω *by making union of adjacent elements* $T \in \tau_h$, *such that the union of all patches covers* Ω, *is given. Let* $\mathcal{V}_h$ *be that set. Define*

a) the trial space

$$W_\omega = span\{\psi_j^\omega\}_{j=1}^{j=k(\omega)}$$

and the test space

$$V_\omega = span\{\phi_j^\omega\}_{j=1}^{j=k(\omega)}$$

defined over each correspondent patch $\omega \in \mathcal{V}_h$.

b) the spaces (defined elementwise), for each $T \in \tau_h$,

$$Y_T = span\ \{\psi_j^\omega|_T, \quad j = 1,..,k(\omega),\ for\ all\ \omega,\ such\ that\ \omega \cap T \neq \emptyset\ \}$$

$$Z_T = span\ \{\phi_j^\omega|_T, \quad j = 1,..,k(\omega),\ for\ all\ \omega,\ such\ that\ \omega \cap T \neq \emptyset\ \}$$

■

It is clearly seen that there exist a decomposition $w_h^T = \sum_{\omega \cap T \neq \emptyset}[w_h^\omega]$, for all $w_h^T \in Y_T$, where $w_h^\omega \in W_\omega$ with $\omega \cap T \neq \emptyset$. Similarly, there exists a decomposition $v_h^T = \sum_{\omega \cap T \neq \emptyset}[v_h^\omega]$, for all $v_h^T \in Z_T$, where $w_h^\omega \in W_\omega$.

Hyp. 2.1 : *Let a bilinear form* $B(..,.) : W_0^{1,s} \times W^{1,s'} \longrightarrow \mathcal{R}$ *be given, for all* $s \in [r', r]$, *where* $r \in [2, \infty)$ *is given. Let a mesh* τ_h *and the set of patches* $\mathcal{V}_h$ *be given as defined above. Then,*

a) there exists a real number $\gamma > 0$, *such that, for each* $T \in \tau_h$, *and for all* $w_h \in Y_T$,

$$\gamma \|w_h\|_{W^{1,s}(T)} \leq \sup_{v_h^T \in Z_T} \{ \sum_{\omega \cap T \neq \emptyset} [\frac{B_\omega(w_h^\omega, v_h^\omega)}{\|v_h^\omega\|_{W^{1,s'}(\omega)}}] \}$$

where $\gamma \neq \gamma(h)$ *does not depend neither on* $T \in \tau_h$, *nor on* $\mathcal{V}_h$. $B_\omega(..,.)$ *means the restriction of* B *to the patch* ω. *Note that we are using the decomposition of* $v_h^T \in Z_T$ *described just above.*

b) Let $R \in W^{-1,r}$ *be given, and consider* $R|_\omega$ *as being a suitably defined restriction of* R *to* ω, *for all* $\omega \in \mathcal{V}_h$. *Then, there exist positive constants* C_1 *and* C_2, *not depending neither on the* τ_h *nor on* $\mathcal{V}_h$, *such that*

$$C_1 \|R\|_{W^{-1,s}(\Omega)} \leq [\sum_{T \in \tau_h} (\sum_{\omega \cap T \neq \emptyset} \|R|_\omega\|_{W^{-1,s}(\omega)})]^{\frac{1}{s}} \leq C_2 \|R\|_{W^{-1,s}(\Omega)}.$$

■

Remark : Hypothesis 2.1 means that the given bilinear form B is patchwise elliptic and the patches do not overlap too much, destroying the stability of the sum of quantities defined patchwise.

■

We, then, define two basic types of a-posteriori estimators:

Def. 2.2 (Implicit Estimators) *Let a mesh* τ_h *and a set of patches* $\mathcal{V}_h$ *be given. Let a bilinear form* $B(....)$ *be given, which satisfies the inf-sup comdition, and Hypothesis 2.1 for some* $r \in [2, \infty)$ *and spaces* $\{V_\omega\}_{\omega \in \mathcal{V}_h}$ *and* $\{W_\omega\}_{\omega \in \mathcal{V}_h}$. *Let* $f \in W^{-1,r}$ *be given, and define* $w_0 \in W_0^{1,r}$, $w_h \in S^h(\tau_h)$ *and* $e \in W_0^{1,r}$ *to be the solutions of LP.0, DLP.0 and Er.0, respectively. For each* $T \in \tau_h$, *define* $\xi_T(x) \in Y_T$ *as* $\xi_T(x) = \sum_{\omega \cap T \neq \emptyset} [\sum_{j=1,...,k(\omega)} C_j^\omega \psi_j^\omega(x)]$, *for* $x \in T$, *where* $\{\{C_j^\omega\}_{j=1}^{j=k(\omega)}\}_{\omega \cap T \neq \emptyset}$ *are constants, which are obtained by finding* $\xi^\omega \in W_\omega$, *such that*

$$B_\omega(\xi^\omega, \phi_j^\omega) = < R_{h\omega}, \phi_j^\omega > \quad j = 1, ..., k(\omega), \quad \text{for all } \omega \in \mathcal{V}_h$$

where $R_{h\omega} = R_h|_\omega$ *is the restriction of the residual* $R_h \in W^{-1,r}$ *to the patch* $\omega \in \mathcal{V}_h$. *Thus,* $\xi_T(x)$ *is computed by*

$$\xi_T(x) = \sum_{\omega \cap T \neq \emptyset} [\xi^\omega(x)]$$

for all $x \in T$. *The restricted residual* R_ω, *the trial and the test spaces should be such that the above problem has a unique solution.*

For some given $s \geq 1$, *set*

$$\eta_T(s) = \|\xi_T\|_{W^{1,s}(T)}$$

and

$$\eta(s) = \{ \sum_{T \in \tau_h} \eta_T^s \}^{\frac{1}{s}}$$

The value η_T *is called the elemental estimator for* $T \in \tau_h$ *(indicator) and* η *is the (global) estimator.*

■

LP.0 : Find $w \in W_0^{1,s}$, such that

$$B(w,v) =< f, v >, \quad \text{for all } v \in W_0^{1,s'}$$

■

DLP.0 : Find $w_h \in S^h$, such that

$$B(w_h, v_h) =< f, v_h >, \quad \text{for all } v_h \in S^h$$

■

where $f \in W^{-1,s'}$. Defining the error by $e = w - w_h$, the error equations for the above problems are given by

Er.0 : Find $e \in W_0^{1,s}$, such that

$$B(e,v) =< R_h, v >= B(w_h, v) - < f, v >, \quad \text{for all } v \in W_0^{1,s'}$$

■

The following result shows that the implicit estimators change at most linearly with perturbations in the coefficients of the operators and in the right-hand side.

Theorem. 2.1 : *Let the bilinear forms $B_0(..,.) : H_0^1 \times H_0^1 \longrightarrow \mathcal{R}$ and $B_1(..,.) : H_0^1 \times H_0^1 \longrightarrow \mathcal{R}$ be given. Let both bilinear forms satisfy the inf-sup condition and Hypothesis 2.1 for some $r \in [2, \infty)$ and spaces $\{W_\omega\}_{\omega \in \mathcal{V}_h}$ and $\{V_\omega\}_{\omega \in \mathcal{V}_h}$. Let f_0, $f_1 \in W^{-1,r}$ be given to be right-hand sides for B_0 and B_1, respectively. Let w_0 and $w_1 \in W_0^{1,r}$ be solutions of LP.0, w_{0h}, $w_{1h} \in S^h$ solutions of DLP.0 and R_{0h}, $R_{1h} \in W^{-1,r}$ the residuals, all related to B_0 and B_1, respectively. If η_0 and η_1 are implicit estimators related to B_0, f_0 and B_1, f_1, respectively, then, there exists a constant C, which depends only on the $L^\infty(\Omega)$-norm of the coefficients of both bilinear forms,such that, for each $s \in [r', r]$,*

$$|\eta_0(s) - \eta_1(s)| \leq C[\|\Delta B\|_{L^\infty} \eta_0 + \|\Delta R_h\|_{W^{-1,s}(\Omega)}].$$

For the above, $\|\Delta B\|_{L^\infty}$ means the $L^\infty(\Omega)$-norm of the difference between the respective coefficients of B_0 and B_1; and ΔR_h is the difference between the residuals R_{0h} and R_{1h}.

Proof : See (Babuska *et al.*, to appear-III).

■

Now, let us be specific and introduce our two auxiliary linear problems, the first for the actual computation of the error estimator and the second for theoretical purposes only. As before, and for the rest of this paper, (u_0, λ_0) and (u_h, λ_0) will be the solution to Pr.1 and the solution to DPr.1, respectively. Next, let $F : W_0^{1,p_1} \to W^{-1,p_2'}$ be given. For any fixed $r \in [2, \infty)$, as close to 2 as needed, we take $s \in [r', r]$ and set K_0, $K_h : W^{1,s} \to W^{-1,s}$; and B_0, $B_1 : W_0^{1,s} \times W_0^{1,s'} \to \mathcal{R}$ as

$$K_0 = D_u F(u_0, \lambda_0) \tag{2}$$

$$K_h = D_u F(u_h, \lambda_0) \tag{3}$$

$$B_0(u,v) = < K_0 u, v >, \quad \text{for all } u \in W_0^{1,s} \text{ and } v \in W_0^{1,s'} \tag{4}$$

$$B_1(u,v) = < K_h u, v >, \quad \text{for all } u \in W_0^{1,s} \text{ and } v \in W_0^{1,s'} \tag{5}$$

Furthermore, set

$$e_h = u_0 - u_h \tag{6}$$

$$b_0 = K_0 u_0 \tag{7}$$

The two auxiliary problems will be defined by the bilinear form B_1 (computable) and B_0 (abstract), together with the right-hand sides

$$f_1 = -F(u_h, \lambda_0) \tag{8}$$

$$f_0 = b_0, \tag{9}$$

respectively. Let $w_0^h \in W_0^{1,s}$ and $w_{0h}^h \in S^h$ solve LP.0 and DLP.0 with $B \equiv B_1$ and $f \equiv f_1$, that is,

$$B_1(w_0^h, v) =< -F(u_h, \lambda_0), v > \quad \text{for all } v \in W_0^{1,s'} \tag{10}$$

$$B_1(w_{0h}^h, v_h) =< -F(u_h, \lambda_0), v_h > \quad \text{for all } v_h \in S^h. \tag{11}$$

Since by definition, u_0 solves LP.0 with $B \equiv B_0$ and $f \equiv f_0$, let $u_{0h} \in S^h$ solve the corresponding discrete problem (DLP.0), i.e.,

$$B_0(u_{0h}, v_h) =< b_0, v_h > \quad \text{for all } v_h \in S^h \tag{12}$$

Next, let us define the error expressions

$$e_{0h} = u_0 - u_{0h}$$

$$e_{wh} = w_{0h} - w_{0h}^h$$

which are solutions to Er.0 for the abstract and computable auxiliary problems, respectively.

Now, define $\eta_0(s)$ and $\eta_1(s)$ as being the same a-posteriori estimator (with respect to the norm of $W_0^{1,s}$, $s \in [r', r]$) appllied for estimating the errors $e_{0h} = u_0 - u_{0h}$ and $e_{wh} = w_{0h} - w_{0h}^h = w_{0h}$, respectively.

Lemma. 2.2 : *Let $F : W_0^{1,p_1} \times \mathcal{R}^m \longrightarrow W^{-1,p_2'}$ satisfies Hypothesis (1.2). Let $\Omega \in \mathcal{D}^t$, for some $t > 2$. Let (u_0, λ_0) be a strong regular solution point to Pr.1, such that $u_0 \in W_0^{1,p_1} \cap W^{1+\xi,p}$, with $\xi > \frac{n}{\min\{p,r\}}$. Then, if $\eta_0(s)$, $s \in [r', r]$, is asymptotically exact, so will be $\eta_1(s)$, i.e., if there exists a constant $C \neq C(h)$ and $\varepsilon_0 > 0$, such that, for all small enough $h > 0$,*

$$|\eta_0(s) - \|e_{0h}\|_{W^{1,s}}| \leq Ch^{\varepsilon_0}\|e_{0h}\|_{W^{1,s}}$$

then, the same is true for $\eta_1(s)$, that is, there exists a constant $C \neq C(h)$, and $\varepsilon > 0$, such that

$$|\eta_1(s) - \|e_{wh}\|_{W^{1,s}}| \leq Ch^{\varepsilon}\|e_{wh}\|_{W^{1,s}}$$

Proof: See (Babuska *et al.*, to appear-III). ∎

Lemma. 2.3 : *Let the hypothesis of Lemma 2.2 be satisfied for given implicit estimators $\eta_0(s)$ and $\eta_1(s)$, $s \in [r', r]$. Then, for all $h > 0$ small enough, the estimator $\eta_1(s)$ is asymptotically equal to $\|e_h\|_{W^{1,s}}$, for all $s \in [r', r]$. That is, there exists $\varepsilon > 0$ and a constant $C \neq C(h)$, such that*

$$|\eta_1(s) - \|e_h\|_{W^{1,s}}| \leq Ch^{\varepsilon}\|e_h\|_{W^{1,s}}$$

for all $s \in [r', r]$.

Proof: See (Babuska *et al.*, to appear-III).

■

Remark : The definition of asymptotic exactness given in the statement of Lemma 2.3 may be weakened by supposing that there exists a function $\mathcal{Q}(h)$, with $\mathcal{Q}(h) \to 0$ as $h \to 0$, and such that

$$|\eta_1(s) - \|e_h\|_{W^{1,s}}| \leq \mathcal{Q}(h)\|e_h\|_{W^{1,s}}$$

for all $s \in [r', r]$.

■

As an example, in order to ilustrate the procedures described in this section, we analyse the following partial differential equation, $F : W_0^{1,p_1} \times \mathcal{R} \to W^{-1,p_1'}$, $\frac{1}{p_1} + \frac{1}{p_1'} = 1$,

$$F(u, \lambda) = -\nabla \cdot [(1 + |\nabla u|^2)^{\frac{p_1-2}{2}} \nabla u] + \lambda u - f$$

Here we will assume that $p_1 > 1$ and that the domain $\Omega \subset \mathcal{R}^n$ is as smooth as we wish. The above definition implies that $Q(u, \lambda) = -\nabla \cdot [(1 + |\nabla u|^2)^{\frac{p-2}{2}} \nabla u]$, $R(u, \lambda) = -\lambda u$ and $f(\lambda) = f$. It is observed that when $\lambda > 0$, then $Q - R$ is a uniformly coercive monotone operator and, then, Pr.1 has a unique solution for each such λ. Also, provided u_0 is smooth enough it is not a difficult task to show that Hypothesis 1.2 is satisfied. The smoothness of u_0 depends on the smoothness of $\partial\Omega$ and of f, which are assumed to be as smooth as needed.

Now, we observe that, for all $\psi \in H_0^1$,

$$K_0\psi = D_u F(u_0, \lambda_0)\psi = -\nabla \cdot [A(x) \cdot \nabla\psi] + \lambda_0\psi$$

where A is the matrix

$$A(x) = (1 + |\nabla u_0|^2)^{\frac{p_1-4}{2}}[(p_1 - 2)\nabla u_0 \nabla u_0 + (1 + |\nabla u_0|^2)I]$$

It is easily seen that, for all $\xi \in \mathcal{R}^n$,

$$(A \cdot \xi) \cdot \xi \geq \left\{ \begin{array}{cc} |\xi|^2[1 + (p_1 - 1)|\nabla u_0|^2] & 1 < p_1 \leq 2 \\ |\xi|^2(1 + |\nabla u_0|^2) & p_1 > 2 \end{array} \right\}$$

Then, for all $\lambda_0 > 0$, $D_u F(u_0, \lambda_0) : H_0^1 \to H^{-1}$ is a uniformly coercive elliptic linear operator with smooth coefficients. let (u_h, λ_0) be the finite element solution to $DPr.1$, which does exists and which converges following (Babuska *et al.*, to appear-II), with rate $\min\{q, \xi - \frac{n}{r}\}$, in the $W^{1,\infty}$-norm, where $q \geq 1$ is the polynomial order of approximation of the shape functions in each element. It is assumed that $u_0 \in W^{1+\xi,p}$, $\xi > \frac{n}{p}$.

In a similar fashion as we did for K_0, we obtain that, for all $\psi \in H_0^1$

$$K_h\psi = D_u F(u_h, \lambda_0)\psi = -\nabla.[A_h(x).\nabla\psi] + \lambda_0\psi$$

where A_h is the matrix

$$A_h(x) = (1 + |\nabla u_h|^2)^{\frac{p_1-4}{2}}[(p_1 - 2)\nabla u_h \nabla u_h + (1 + |\nabla u_h|^2)I]$$

It is easily seen that, for all $\xi \in \mathcal{R}^n$,

$$(A_h \cdot \xi) \cdot \xi \geq \left\{ \begin{array}{cc} |\xi|^2[1 + (p_1 - 1)|\nabla u_h|^2] & 1 < p_1 \leq 2 \\ |\xi|^2(1 + |\nabla u_h|^2) & p_1 > 2 \end{array} \right\}$$

and thus, $K_h : H_0^1 \to H^{-1}$ is a uniformly coercive linear elliptic operator.

Now, the strategy to obtain $\eta_1(s)$, $s \in [r', r]$ is to estimate e_{wh}, considering the following error equation

$$B_1(e_{wh}, v) =< -F(u_h, \lambda_0), v > \qquad \text{for all } v \in W^{1,s'}$$

Recall that $B_1(.,..) =< K_h(.),(..) >$. There are several options for computing the implicit estimator η_1. The best choices will be among those which may be asymptotically exact, provided some smoothness requirements are satisfied. Particularly, if those requirements are met by our abstract and smooth linear problem defined by the bilinear form B_0 and the right-hand side f_0. Hence, by Lemma 2.3, $\eta_1(s)$, computed by such a method, will be asymptotically exact with respect to the error $e_h = u_0 - u_h$ in the $W_0^{1,s}$-norm.

3 REFERENCES

Babuška, I., Rheinboldt, W. C., *Computational Error Estimates and Adaptive Processes for Some Nonlinear Structural Problems*, Comp. Meth. in Appl. Mech. and Eng. 34, 1982, pp. 895-937.

Babuška, I., Santos, F. C. G., *Numerical Analysis of Finite Element Solutions of Nonlinear Partial Differential Equations: Part I - On the Regularity of Linearized Operators*, To Appear.

Babuška, I., Santos, F. C. G., *Numerical Analysis of Finite Element Solutions of Nonlinear Partial Differential Equations: Part II - A-Priori Analysis*, To Appear.

Babuška, I., Santos, F. C. G., *Numerical Analysis of Finite Element Solutions of Nonlinear Partial Differential Equations: Part III - A-Posteriori Analysis*, To Appear.

Babuška, I., Santos, F. C. G., *Numerical Analysis of Finite Element Solutions of Nonlinear Partial Differential Equations: Part IV - Numerical Experiments with NFEARS - Nonlinear Finite Element Analysis Research Solver*, To Appear.

Tsuchiya, T., *A-priori and A-posteriori Error Estimates of Finite Element Solutions of Parameterized Nonlinear Equations*, Ph.D. Thesis, University of Maryland, 1990.

Verfürth, R., *A Review of A-posteriori Error Estimation and Adaptive Mesh Refinement* , Tech. Rep., Institute Für Angewandte Mathematik, Universität Zürich, 1993.

Tema 43

Método de Elementos de Contorno

UNESP COBEM 97

XIV Brazilian Congress of Mechanical Engineering
Obeid Plaza Hotel Convention Center - Bauru - SP/Brazil
December 08-12th 1997

PAPER CODE: COB839

Simulações Computacionais do Comportamento Dinâmico de Barras de Seção Linearmente Variável Através do Método dos Elementos de Contorno /*Computational Simulations of Dynamic Behavior of Linear Tapered Rods Using Boundary Element Method*

Carlos Friedrich Loeffler & André Bulcão
Departamento de Entgenharia Mecânica, Universidade Federal do Espírito Santo - UFES
Av. Fernando Ferrari s/nº Vitória, E.S., Brasil - Email: bulcao@npd.ufes.br

Abstract

This job presents the Dual Reciprocity Boundary Element formulation applied to dynamic analysis of tapered rods with linear variation in its transverse section. Some features of Boundary Element discretization in this case are discoursed in this work: the influence of area's radio; level of refination; opening angle of rod and internal póles. The performance of numerical displacements are compared with analytical response. Only constant element are used in this analysis carried out here. Houbolt's time stepping is employed to advance the solution.

Keywords

Boundary Elements; Numerical Methods, Dynamics of Structures, Dynamic Response of Tapered Rods
Elementos de Contorno, Métodos Numéricos, Dinâmica de Estruturas, Resposta Dinâmica em Barras de Seção Variável, Propagação de Ondas.

1. INTRODUÇÃO

O desenvolvimento industrial acelerado e sofisticado dos tempos atuais tem resultado em problemas físicos cujos modelos matemáticos representativos possuem alto nível de dificuldade. O atendimento a este elevado padrão de exigência demanda muita criatividade da engenharia atual, mas também subordina-se à existência de técnicas e recursos que viabilizem sua solução em termos de engenharia. O advento do computador e o surgimento de métodos aproximados de resolução são os principais instrumentos que tornaram acessíveis a abordagem de problemas arrojados, de modo cada vez mais fácil e pouco custoso.

Um exemplo da capacidade operacional dos métodos computacionais consiste na solução dos modelos da área de dinâmica estrutural. Neta os tratamentos analíticos são sabidamente limitados pela enorme dificuldade matemática, enquanto as técnicas experimentais são muito caras.

Embora sejam elementos estruturais geometricamente muito simples, a obtenção da resposta ao impacto em barras de seção reta variável é um desses casos cujo nível de complexidade torna qualquer abordagem não computacional muito difícil. Tais problemas são encontrados freqüentemente na prática, envolvendo isolamento de vibrações em estruturas, equipamentos acústicos e carcaças de exaustores e caldeiras especiais.

Este trabalho apresenta a formulação e solução deste problema através do Métodos dos Elementos de Contorno (MEC). São simulados diversos casos, com diferentes relações entre as áreas inicial e final, arrolando malhas de diversos níveis de refinamento.

2. EQUACIONAMENTO BÁSICO

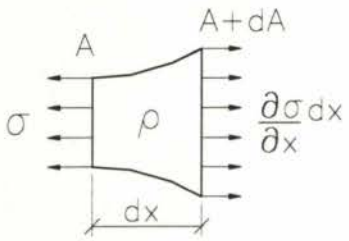

Fig. 1 - Tensões normais σ numa fatia elementar da barra

Em termos práticos, a equação diferencial do movimento para o caso de barras axialmente solicitadas de seção reta variável é obtida desprezando-se efeitos tridimensionais e admitindo-se exclusivamente a propagação de ondas longitudinais. Isto implica na consideração de uma estado uniaxial de tensões, que não se afasta significativamente do que ocorre nos problemas reais quando a variação de seção reta é suave. Assim, a partir do equilíbrio dinâmico numa fatia elementar da barra, mostrada na figura 1, considerando-se pequenas deformações e um material elástico Hookiano, chega-se a seguinte equação de governo:

$$\frac{\partial^2 u(x,t)}{\partial x^2}+\frac{1}{A(x)}\frac{dA(x)}{dx}\frac{\partial u(x,t)}{\partial x}=\frac{1}{K^2}\frac{\partial^2 u(x,t)}{\partial t^2} \qquad (1)$$

Na equação (1), A é a área da seção transversal, u é o deslocamento longitudinal e t é o tempo. K é a velocidade de propagação de onda:

$$K=\sqrt{\frac{E}{\rho}} \qquad (2)$$

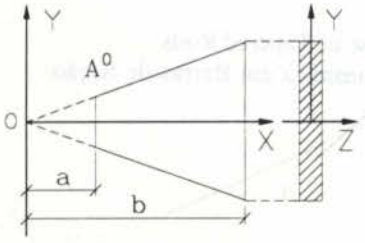

Fig. 2 - Barra com variação linear da seção reta

onde: ρ é a massa específica por unidade de comprimento e E é o módulo de Young.

No caso da variação linear da seção reta, adotando-se um sistema de referência conveniente, como mostrada na figura (2), pode-se escrever que:

$$A(x)=\frac{A_0 x}{a} \quad ; \qquad x \geq a \qquad (3)$$

Nessa situação, a equação (1) particulariza-se de modo a expressar-se por:

$$\frac{\partial^2 u(x,t)}{\partial x^2}+\frac{1}{x}\frac{\partial u(x,t)}{\partial x}=\frac{1}{K^2}\frac{\partial^2 u(x,t)}{\partial t^2} \qquad (4)$$

3. APLICAÇÃO DO MÉTODO DOS ELEMENTOS DE CONTORNO

Embora seja uma equação espacialmente unidimensional, sua solução, mesmo discreta, é difícil, tanto pelos aspectos anômalos da resposta dinâmica (que, naturalmente, também dependem do tipo de excitação imposta), quanto por características do próprio modelo matemático. No caso da abordagem via MEC, que se baseia na obtenção da forma integral inversa da equação diferencial de governo (equação 4), não se pode empregá-la nesse caso sem alguma estratégia ou aproximação especial.

Nesse sentido, identifica-se uma estrutura similar entre a equação do problema em questão e a equação de governo de um problema espacialmente bidimensional com simetria circunferencial que, ao ser expresso num sistema de referência polar, independe da

coordenada θ. Assim, fisicamente, o movimento de uma membrana plana circular, com carregamento circunferencialmente simétrico, é similar ao caso da barra de seção reta linearmente variável. De modo a aproveitar as características escalares do problema no modelo numérico do MEC, doravante o problema em questão é tratado como um problema polar simplificado, utilizando-se uma discretização espacial em duas dimensões.

Com base na tática descrita, a equação do problema escreve-se como:

$$\nabla^2 u(r,t) = \frac{1}{K^2}\frac{\partial^2 u(r,t)}{\partial t^2} \tag{5}$$

onde $\nabla^2(\ )$ é o operador Laplaciano em coordenadas polares. O procedimento primordial do MEC consiste no estabelecimento de uma sentença integral equivalente à equação (5), na forma:

$$\int_\Omega \nabla^2 u(r,t)\, u^*(\xi,r)\, d\Omega(r,\theta) = \frac{1}{K^2}\int_\Omega \frac{\partial^2 u(r,t)}{\partial t^2}\, u^*(\xi,r)\, d\Omega(r,\theta) \tag{6}$$

Na expressão precedente, $\Omega(r,\theta)$ é o domínio espacial do sistema e a função $u^*(\xi,r)$ é a solução fundamental estática, característica da formulação do MEC com Dupla Reciprocidade, aqui utilizada. Mediante integração por partes e utilização do teorema de Green, o lado esquerdo da equação (6) pode ser escrito exclusivamente em termos de integrais de contorno. A expressão resultante fica:

$$\begin{aligned} &c(\xi)u(\xi,t) + \int_\Gamma u(r,t)\, q^*(\xi,r)\, d\Gamma(r,\theta) - \int_\Gamma q(r,t)\, u^*(\xi,r)\, d\Gamma(r,\theta) = \\ &= \frac{1}{K^2}\int_\Omega \frac{\partial^2 u(r,t)}{\partial t^2}\, u^*(\xi,r)\, d\Omega(r,\theta) \end{aligned} \tag{7}$$

A Dupla Reciprocidade impõe um tratamento particular ao lado direito da equação integral (7), em que a aceleração ü(r,t) é substituída por uma soma finita de funções na forma:

$$\frac{\partial^2 u(r,t)}{\partial t^2} = \frac{\partial^2 \alpha^j(t)}{\partial t^2} F^j(r) \qquad , j = 1, 2, \cdots M \tag{8}$$

A expressão (8) permite transformar a integral de domínio existente em uma integral de contorno, desde que introduzam-se novas funções ψ e η tais que:

$$\frac{\partial^2 \psi^j(r)}{\partial r^2} + \frac{1}{r}\frac{\partial \psi^j(r)}{\partial r} = F^j(r) \tag{9}$$

$$\eta^j(r) = \frac{\partial \psi^j(r)}{n(r,\theta)} \tag{10}$$

Assim, substituindo-se a equação (9) na expressão (8) pode-se, de modo análogo ao efetuado anteriormente, empregar novamente o teorema de Green e obter-se:

$$c(\xi)u(\xi,t)+\int_{\Gamma} u(r,t)\, q^{*}(\xi,r)\, d\Gamma(r,\theta)-\int_{\Gamma} q(r,t)\, u^{*}(\xi,r)\, d\Gamma(r,\theta)=$$

$$=\frac{1}{K^{2}}\frac{\partial^{2}\alpha^{j}(t)}{\partial t^{2}}\left\{c(\xi)\psi^{j}(\xi)+\int_{\Gamma}\psi^{j}(r)q^{*}(\xi,r)\, d\Gamma(r,\theta)-\int_{\Gamma}\eta^{j}(r)u^{*}(\xi,r)\, d\Gamma(r,\theta)\right\} \qquad (11)$$

As funções F^{j} podem ser arbitradas. Para domínios fechados são introduzidas apenas como o intuito de permitir a transformação que resulta na formulação integral somente em termos de valores de contorno. Deve-se ter cautela unicamente para não se introduzir funções intrincadas e custosas. Uma opção bastante comum, simples e razoavelmente eficiente consiste da distância euclidiana entre dois pontos (Loeffler & Mansur, 1990 e Patridge, 1996).

Determinando-se as funções $\psi^{j}(r)$ e $\eta^{j}(r)$ e discretizando-se o contorno $\Gamma(r,\theta)$ em elementos distintos, segundo o procedimento tradicional do MEC, gera-se um conjunto de equações que pode ser matricialmente exposto na forma:

$$\underset{\sim}{H}\,\underset{\sim}{u} - \underset{\sim}{G}\,\underset{\sim}{q}=\frac{1}{K^{2}}\left\{\underset{\sim}{H}\,\underset{\sim}{\psi} - \underset{\sim}{G}\,\underset{\sim}{\eta}\right\}\underset{\sim}{\ddot{\alpha}} \qquad (12)$$

Escolhendo-se a quantidade de funções $F^{j}(r)$ igual ao número de pontos nodais da discretização, pode-se reescrever a equação anterior em termos da aceleração $\ddot{u}$, interpolados de acordo com a expressão (8). Definindo-se:

$$\underset{\sim}{M}=\frac{1}{K^{2}}\left\{\underset{\sim}{G}\,\underset{\sim}{\eta} - \underset{\sim}{H}\,\underset{\sim}{\psi}\right\}\underset{\sim}{F}^{-1} \qquad (13)$$

chega-se a expressão matricial definitiva:

$$\underset{\sim}{M}\,\underset{\sim}{\ddot{u}} + \underset{\sim}{H}\,\underset{\sim}{u} = \underset{\sim}{G}\,\underset{\sim}{q} \qquad (14)$$

Para o avanço da solução no tempo recomenda-se o esquema de integração incremental Houbolt (Loeffler & Mansur, 1987).

4. EXEMPLO DE APLICAÇÃO

A dificuldade numérica de um problema desta natureza depende de varios fatores ligados à geometria e ao carregamento. Com relação a este último, sabe-se que solicitações impulsivas súbitas são as mais difíceis de simular numericamente. Por esta razão, apenas este tipo de excitação será aqui considerado.

Relativamente à geometria, é possível estabelecer algumas comparações interessantes. Um caso extremo do problema em questão consiste na barra de seção constante, já estudado e simulado através da mesma formulação do MEC, em outros trabalhos já referenciados (Loeffler & Mansur, 1990 e 1987). Esta conformação geométrica apresenta uma resposta em deslocamento, para carga súbita, com comportamento bem característico, na forma de um dente de serra. Na figura 3, é mostrada a solução analítica juntamente com a resposta numérica via MEC, usando elementos constantes e esquema Houbolt para avanço da solução no tempo.

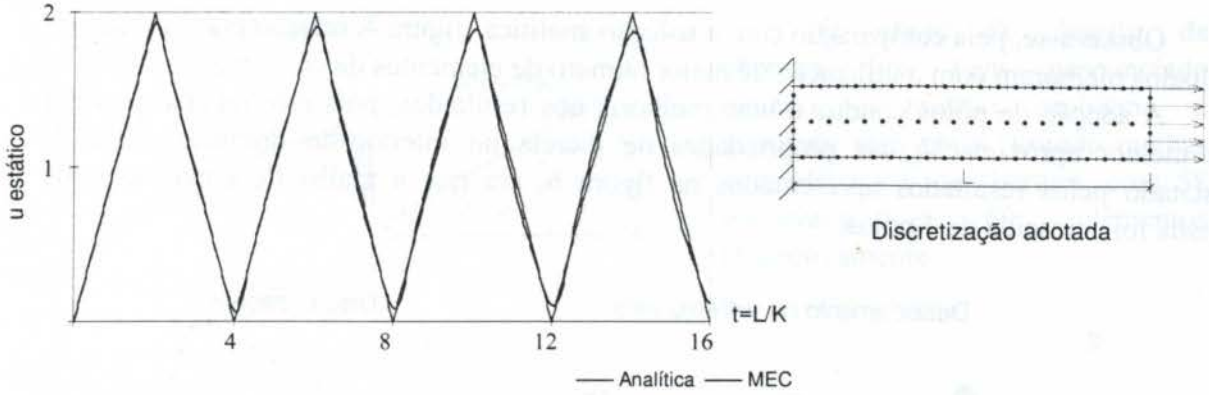

Figura 3 - Deslocamento do extremo livre

À medida que se aumenta as relações b/a (vide figura 2) percebe-se um agravamento do comportamento aperiódico e anômalo da resposta. A figura (4) apresenta a solução analítica em dois casos distintos da relação b/a (Silva, 1995).

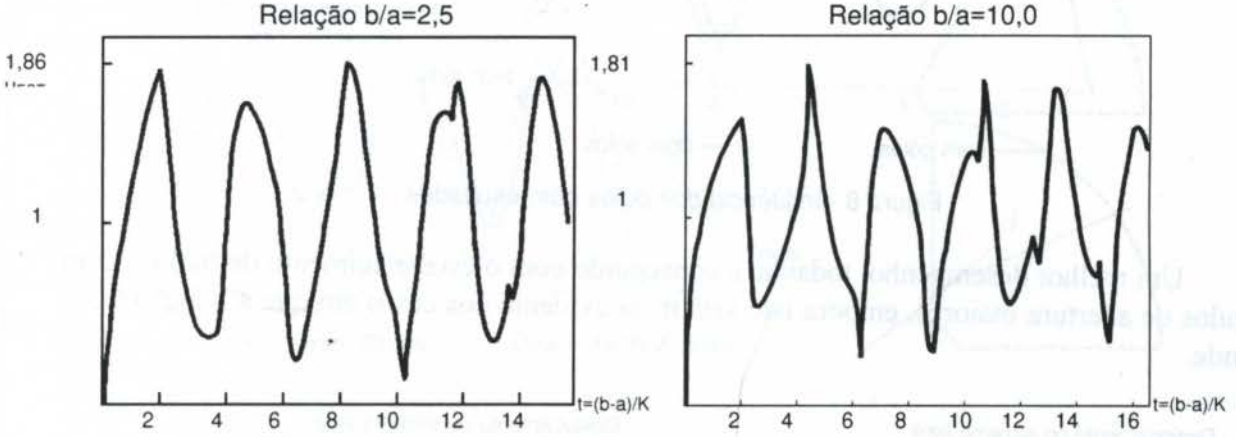

Figura 4 - Solução Analítica

Nota-se que a resposta para relações b/a elevadas são mais complexas. Logo, as comparações e testes numéricos principiarão pelos casos de configurações geométricas mais favoráveis, ou seja, relações b/a pequenas.

Assim, primeiramente são mostradas as respostas para deslocamentos das extremidades numa barra com relação b/a igual a 2,5 enfocando a influência da malha de contorno.

São comparadas duas malhas, expostas na figura 5, com 10 e 19 elementos de contorno, sem pólos, igualmente espaçados no contorno e com ângulo de abertura de 30^0.

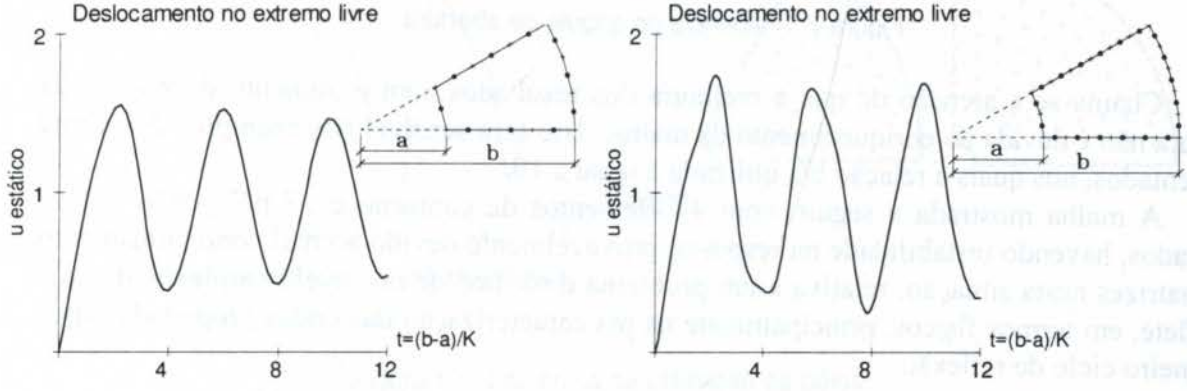

Figura 5 - Influência do refinamento da malha de contorno

Observa-se, pela comparação com a solução analítica (figura 4, relação b/a=2,5) que os resultados melhoram com a utilização de maior número de elementos de contorno.

A adoção de pólos conduz a uma melhoria nos resultados, pois este recurso permite uma melhor aproximação das propriedades de inércia no interior do domínio. Isto é, constatado pelos resultados apresentados na figura 6, em que a malha de contorno mais refinada foi acrescida de 4 pólos.

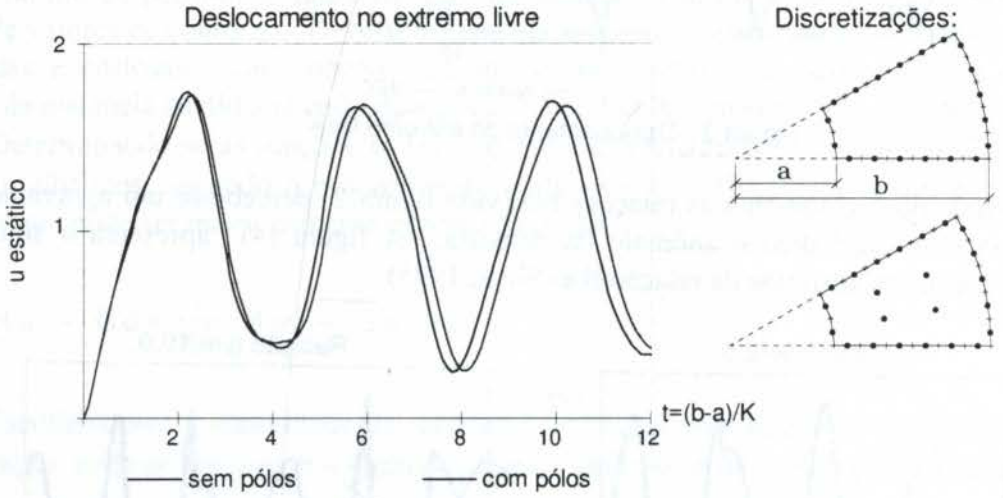

Figura 6 - Influência dos pólos nos resultados

Um melhor desempenho, todavia, é conseguido com o estabelecimento de malhas com ângulos de abertura maiores, embora isto seja mais evidente nos casos em que a relação b/a é grande.

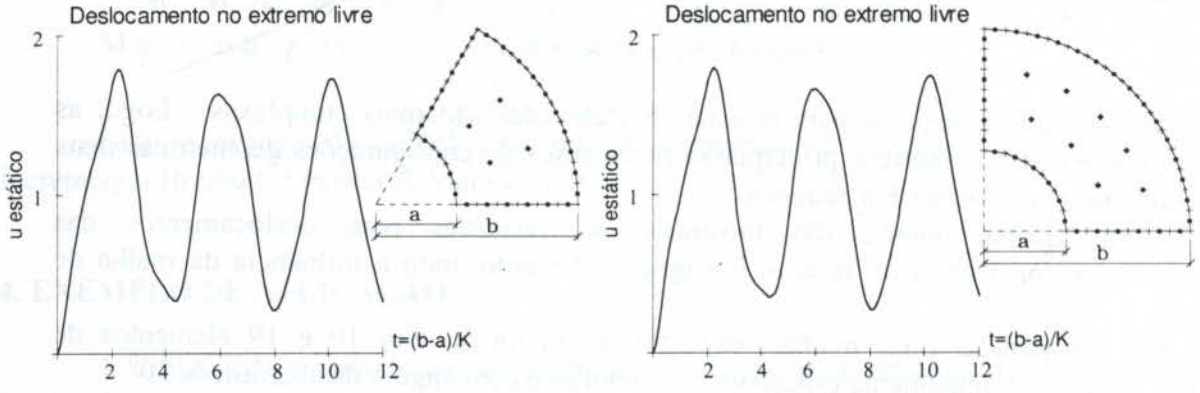

Figura 7 - Influência do ângulo de abertura

Chama-se a atenção de que a melhoria dos resultados com o aumento do ângulo de abertura não é devida ao enriquecimento da malha. Isto será sensível nos exemplos doravante apresentados, nos quais a relação b/a utilizada é igual a 10.

A malha mostrada a seguir, com 47 elementos de contorno e 17 pólos não obteve resultados, havendo instabilidade na resposta, provavelmente devido ao mal condicionamento das matrizes nesta situação, relativa a um problema dinâmico de razoável complexidade, que se reflete, em termos físicos, principalmente na má caracterização das ondas propagadas após o primeiro ciclo de reflexão.

Observa-se, pela comparação com a solução analítica (figura 4, relação b/a=2,5) que os resultados melhoram com a utilização de maior número de elementos de contorno.

A adoção de pólos conduz a uma melhoria nos resultados, pois este recurso permite uma melhor aproximação das propriedades de inércia no interior do domínio. Isto é, constatado pelos resultados apresentados na figura 6, em que a malha de contorno mais refinada foi acrescida de 4 pólos.

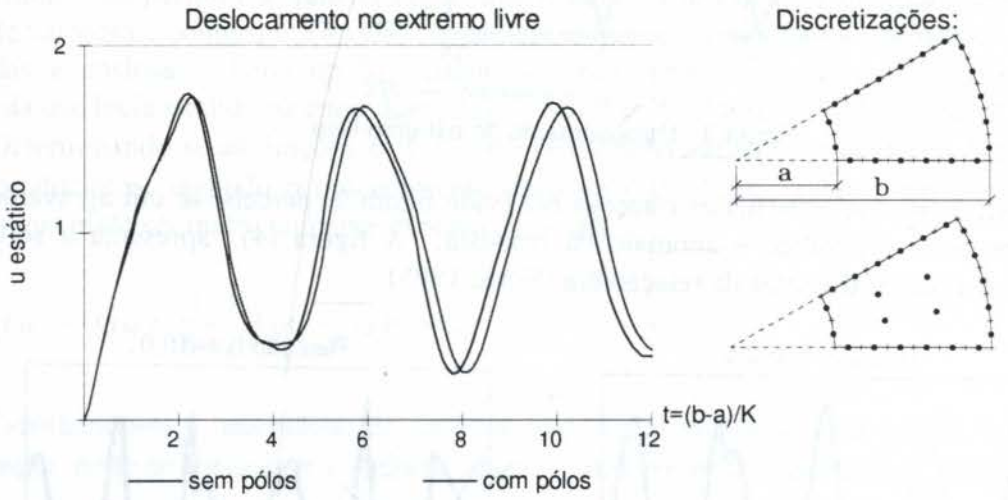

Figura 6 - Influência dos pólos nos resultados

Um melhor desempenho, todavia, é conseguido com o estabelecimento de malhas com ângulos de abertura maiores, embora isto seja mais evidente nos casos em que a relação b/a é grande.

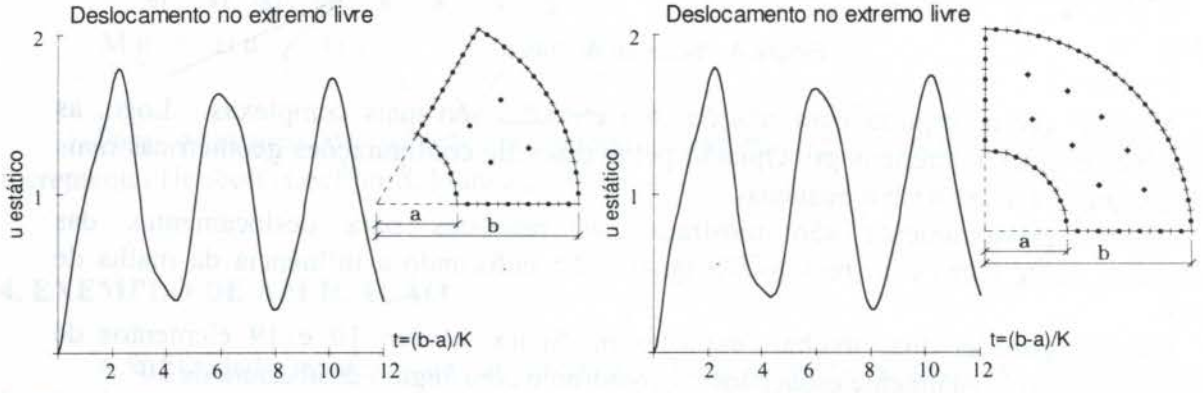

Figura 7 - Influência do ângulo de abertura

Chama-se a atenção de que a melhoria dos resultados com o aumento do ângulo de abertura não é devida ao enriquecimento da malha. Isto será sensível nos exemplos doravante apresentados, nos quais a relação b/a utilizada é igual a 10.

A malha mostrada a seguir, com 47 elementos de contorno e 17 pólos não obteve resultados, havendo instabilidade na resposta, provavelmente devido ao mal condicionamento das matrizes nesta situação, relativa a um problema dinâmico de razoável complexidade, que se reflete, em termos físicos, principalmente na má caracterização das ondas propagadas após o primeiro ciclo de reflexão.

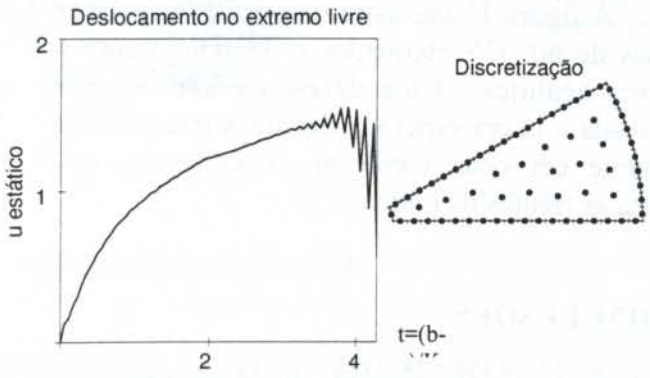

Figura 8 - Influência da malha

O efeito do ângulo de abertura fica bem pronunciado quando o mesmo problema é simulado sem pólos, usando malhas com 60^0 e 90^0 de abertura, com 58 elementos e 69 elementos respectivamente.

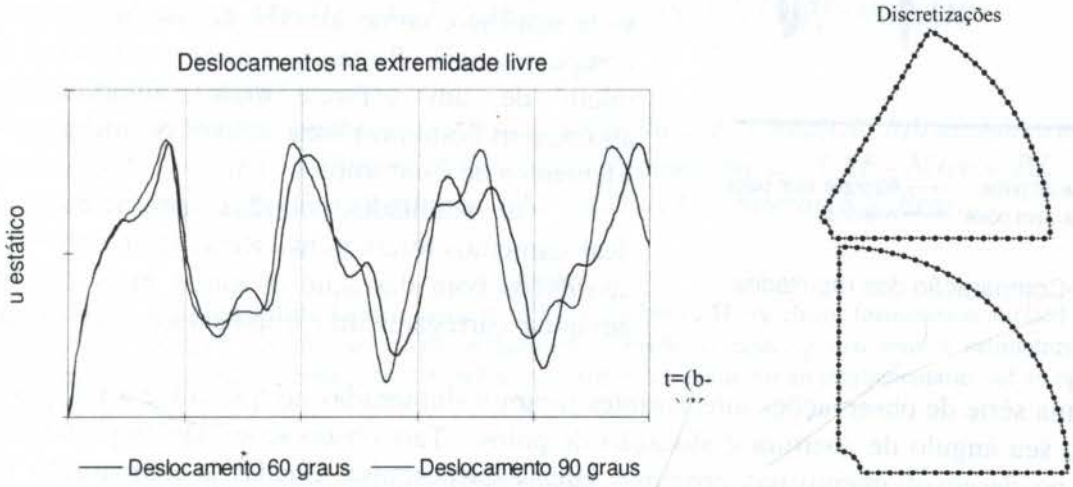

Figura 9 - Influência do ângulo de abertura, com b/a=10.

Os resultados com 90^0 são mais próximos da solução analítica.

Introduzindo-se pólos em ambas as configurações de elementos de contorno anteriores, verifica-se uma melhoria dos resultados. As curvas com 60^0 e 90^0 praticamente coincidem, como mostrado na figura 10.

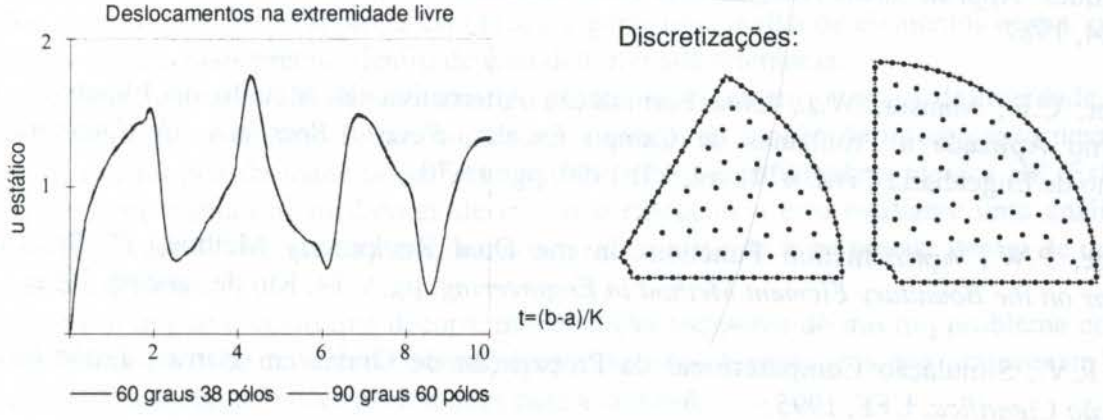

Figura 10 - Influência da utilização de pólos

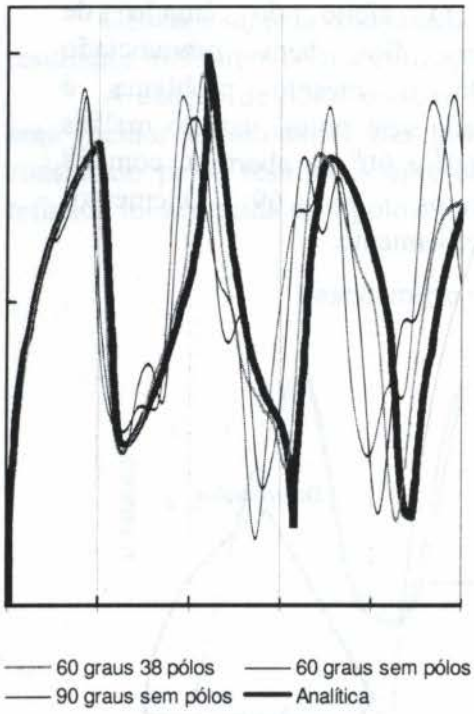

Figura 11 -Comparação dos resultados

A figura 11 compara os resultados para as malhas de 60^0 (58 elementos e 38 pólos) com a resposta analítica. Uma defasagem no tempo é observada e já era esperada devido à interpolação constante em cada elemento de contorno, que adianta as frentes de onda.

5. CONCLUSÕES

Na literatura especializada, o problema de dinâmica de barras de seção variável não é abordado com o devido relevo, seja sob o ponto de vista analítico, como através do uso de métodos computacionais. Portanto, o presente trabalho é o inicio de um esforço mais importante na abordagem deste problema através do método dos Elementos de Contorno.

Os resultados obtidos em termos de deslocamentos foram bons. Ressalta-se que foram abordados com destaque os casos mais críticos, em que o carregamento é impulsivo e a relação b/a é elevada.

Uma série de observações interessantes foram vislumbradas no que tange a relação da malha, do seu ângulo de abertura e alocação de pólos. Tais observações são importantes e auxiliam no desenvolvimento das próximas etapas da pesquisa, ligadas a comparação das respostas em termos de tensões e ao uso de elementos de contorno de ordem superior. Este último fator, com certeza, fará com que os resultados desta formulação do MEC sejam grandemente melhorados.

6. REFERÊNCIAS BIBLIOGRÁFICAS

Loeffler, C.F.; Mansur, W.J., Analysis of Time Integrations Schemes for Boundary Elements Techniques: Appl in Stress Analysis and Heat Transfer, *Computacional Mechanics Pub*, pg. 105-124, 1987.

Loeffler, C.F.; Mansur, W.J., Uma Formulação Alternativa do Método de Elementos de Contorno Aplicada a Problemas de Campo Escalar, *Revista Brasileira de Engenharia*, Caderno de Engenharia Civil, nº 1, vol. VII 1990, pg. 43-70.

Patridge, P.W., Aproximation Functions in the Dual Reciprocity Method, *1st Brasilian Seminar on the Boundary Element Method in Engineering*, pg. 9-14, Rio de Janeiro, 1996.

Silva, R.V., Simulação Computacional da Propagação de Ondas em Barras, *Trabalho de Iniciação Cientifica*, UFF, 1995.

XIV Brazilian Congress of Mechanical Engineering
Obeid Plaza Hotel Convention Center - Bauru - SP/Brazil
December 08-12th 1997

PAPER CODE: COB441

FORMULAÇÃO H-HIERÁRQUICA ADAPTATIVA PARA O MÉTODO DOS ELEMENTOS DE CONTORNO EM ELASTICIDADE / *ADAPTIVE H-HIERARCHICAL BOUNDARY FORMULATION FOR THE BOUNDARY ELEMENT METHOD APPLIED TO ELASTICITY PROBLEMS*

RAUL BERNARDO VIDAL PESSOLANI
Pesquisador da FAPERJ - Fundação de Amparo à Pesquisa do Estado do Rio de Janeiro
Departamento de Engenharia Mecânica, Faculdade de Engenharia - UFF - Niteroi, RJ.
Rua Passos da Pátria, 156 - São Domingos, CEP 24210-240 - Niterói, R J, Brasil

Abstract

The present paper is concerned with the development of the H-Adaptive Hierarchical formulation applied to the Boundary Element Method. An analysis of the refinement is made, comparing two error's estimators. The convergence tax is also tested and commented. Finally, suggestions are made for an implementation of an optimal adaptive strategy.

Keywords

Numerical Methods, Boundary Elements Method, Adaptive Procedures.

1. INTRODUÇÃO

Os programas auto-adaptativos têm sido objeto crescente de interesse entre os pesquisadores do MEC. Essas técnicas podem ser vistas como formas de automatização de procedimentos de cálculo, com vistas à minimização do erro. Para tal, o projetista fornece ao programa adaptativo as informações mínimas necessárias para se definir a geometria e as condições de carregamento e apoio, e este procura gerar uma malha de elementos ótima, que possibilite o cálculo mais preciso dentro de uma determinada tolerância.

As técnicas adaptativas podem ser do tipo H, que acrescentam os graus de liberdade às regiões mais críticas, e do tipo P, que aumentam a ordem da função de interpolação nessas regiões. Há ainda a possibilidade de se combinarem ambas, constituindo a técnica HP. Estas técnicas possuem embutidos medidores de erro que calculam o erro mediante uma análise preliminar e, através de sucessivas iterações, conduzem à resposta mais precisa dentro de uma determinada tolerância.

Para se minimizar o custo que decorre da resolução sucessiva do mesmo problema com diferentes malhas, tem-se procurado desenvolver programas hierárquicos que armazenam as informações obtidas das soluções precedentes para a corrente.

Este trabalho visa à análise da formulação H Hierárquica e Adaptativa, com o acoplamento de dois medidores de erro que terão seus desempenhos comparados.

2 - FORMULAÇÃO CONVENCIONAL DO MEC

A formulação direta do Método dos Elementos de Contorno é dada por:

$$C_{ij}(\xi)U_i(\xi) + \int_{\Gamma} T_{ij}^{*}(\xi,\chi).U_j(\chi).d\sigma(\chi) = \int_{\Gamma} U_{ij}^{*}(\xi,\chi).T_j(\chi).d\sigma(\chi) \qquad (1)$$

com as condições de contorno $U_j = \overline{u}_j$, em Γ_u e $T_j = \overline{t}_j$, em Γ_t

A solução numérica do sistema é obtida à partir da divisão do contorno Γ em N_e elementos.

Usualmente, no interior do elemento as variáveis são interpoladas segundo funções como as de Lagrange. Aplicando as condições de contorno, $u_j = \overline{u}$ em Γ_u e $t_j = \overline{t}_i$ em Γ_t, e reordenando a equação, monta-se o sistema $2N_e x 2N_e$,

$$\mathbf{Ax=b} \qquad (2)$$

Resolve-se o sistema por eliminação de Gauss ou por meio de solver's iterativos, especialmente quando há um maior número de graus de liberdade (cfr. Pessolani, 1995).

3 - FORMULAÇÃO H-HIERÁRQUICA

Utilizando-se as funções de interpolação de Lagrange, qualquer subdivisão de elemento ou acréscimo de algum ponto de colocação provoca a remontagem do sistema com o recalculo de todos os coeficientes da matriz **A** e do vetor **b**. Quando o processo é adaptativo, várias discretizações são necessárias até se encontrar a resposta correta. Sendo assim, o método convencional mostra-se pouco apropriado para o procedimento adaptativo, pois cada nova iteração requer um novo cálculo dos componentes da matriz do sistema (2).

Uma alternativa introduzida em 1976 no Método dos Elementos Finitos por Peano é a utilização de famílias de interpolação ditas hierárquicas. Essas funções possuem a característica de serem acumulativas, ou seja, as funções de ordens superiores são geradas sem alterações dos elementos de ordem mais baixa. Numa rediscretização, o novo sistema (2) então é montado, mantendo-se o sistema anterior inalterado e acrescentando-se as submatrizes A_{12}, A_{12}, A_{22} e o vetor b_2., correspondentes aos novos pontos de colocação.

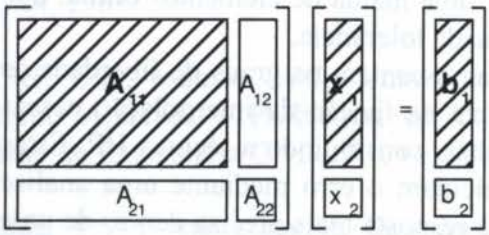

(3)

No Método dos Elementos de Contorno, a formulação hierárquica foi aplicada por Charafi, Neves e Wrobel (1995), e por Parreira (1992). A idéia é se incluir pontos de colocação intermediários ao elemento com funções de interpolação da mesma ordem das funções precedentes, que podem ser as Langrangeanas convencionais.

Para uma interpolação parabólica define-se:

$$N_{2,kl} = \begin{cases} 0 & \text{se } |\eta - \eta_{2l}| \geq D_\eta / k \\ 1 - \dfrac{(\eta - \eta_{2l})^2}{\left(D_\eta / k\right)^2} & \text{se } |\eta - \eta_{2l}| \leq D_\eta / k \end{cases} \quad (4)$$

onde D_η é a metade do comprimento do elemento a ser refinado em coordenadas naturais, k o número de divisões requeridas, η_{1l} é a coordenada natural dos nós usados na interpolação linear e η_{2l} é a coordenada natural dos nós usados na interpolação quadrática.

Graficamente representam-se as funções quadráticas conforme a figura 1:

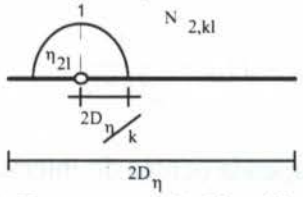

Figura 1. Função quadrática hierárquica

Nesse caso, as funções hierárquicas são chamadas de *Buble Functions* e são expressas por:

$$N_n = \begin{cases} 1 - \eta^2 & \text{para } \eta \in [a,b]_{\lambda,n} \\ 0 & \text{para o restante} \end{cases} \quad (5)$$

sendo λ o grau de hierarquização, n o ponto de colocação associado à *Bolha*, η a coordenada natural remapeada no intervalo [a,b].

Para cada grau λ são geradas $2^{\lambda-1}$ Bolhas com os correspondentes pontos de colocação dispostos simetricamente ao longo do elemento. A titulo de exemplo, para o segundo nível de hierarquização serão incluidos 4 pontos de colocação conforme a figura 2.

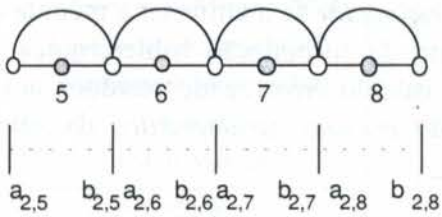

Figura 2 - Segundo nível de discretização hierárquica

A aproximação sobre o elemento também é em função dos novos valores em $\hat{\varphi}_3$ e $\hat{\varphi}_4$, valendo:

$$\hat{\varphi} = \sum_{c=0}^{2} N_c(\xi)\hat{\varphi}_c + \sum_{c=3}^{8} N_c(\xi)\hat{\varphi}_c \quad (6)$$

Genéricamente, seja a iteração λ, Λ o número de níveis hierárquicos e Π_λ a lista de inteiros indicando quais pares de funções hierárquicas Π que estão sendo aplicadas na malha corrente (para cada nível λ existem $2^{\lambda-1}$ pares). A solução aproximada é dada por:

$$\hat{\varphi}(\eta) = \sum_{c=0}^{2} N_c(\eta)\hat{\varphi}_c + \sum_{\lambda=1}^{\Lambda} \sum_{k \in \Pi_\lambda} \left[N_{\lambda,2k-1}(\eta)\hat{\varphi}_{\lambda,2k-1} + N_{\lambda,2k}(\eta)\hat{\varphi}_{\lambda,2k} \right] \tag{7}$$

Onde na iteração λ, tem-se:

$$N_{\lambda,n} = \begin{cases} \mathrm{N}_{\lambda,2}(\mathrm{t}_{\lambda,\mathrm{n}}(\eta)) & \text{para } \eta \in [a,b]_{\lambda,n} \\ 0 & \text{para o restante} \end{cases} \tag{8}$$

Onde :

$$a_{\lambda,n} = -1 + (n-1)\frac{1}{2^{(\lambda-1)}} \quad \text{e} \quad b_{\lambda,n} = a_{\lambda,n} + \frac{1}{2^{(\lambda-1)}} \tag{9}$$

Sendo $t_{\lambda,n}$ a coordenada natural mapeada dentro do intervalo $[a_{\lambda,n}, b_{\lambda,n}]$, definida por:

$$t_{\lambda,n}(\eta) = 2^{\lambda}(\eta + 1) - 2n + 1 \tag{10}$$

Existem inúmeros relatos na literatura informando que um excessivo número de refinamentos na formulação H-Hierarquica leva a problemas de convergência devido ao mau condicionamento do sistema de equações. Em vista disso, conclui-se que é bastante conveniente que o ponto de partida do esquema adaptativo seja um refinamento que leve em conta os pontos de singularidade do problema, ou as regiões onde deverá haver uma maior discretização.

4. ESTIMATIVA DO ERRO

A chave do processo adaptativo é o medidor de erro que fornece um conhecimento aproximado a respeito do tamanho e da distribuição do erro. Esse conhecimento do erro chama-se *indicador* se for local, e *estimador* se manifestar a medida de erro global.

Recentemente, com o advento da formulação h-hierárquica, Parreira e Dong (1992) desenvolveram procedimentos de cálculo envolvendo resíduos adimensionais. Esse cálculo baseia-se na obtenção do chamado *resíduo característico* da solução, e interpolando este resíduo através da expressão:

$$r^k = \sum_{i=0}^{m} N_k r_i^k \tag{11}$$

onde N_K são funções de interpolação Lagrangeanas associados aos **m+1** nós dentro do elemento k. Pelo Método da Colocação no MEC, sabe-se que para uma aproximação de grau **n**, o resíduo é nulo nos **n+1** pontos de colocação. Calcula-se, portanto, os resíduos nos pontos de colocação acrescentados:

$$r^k = \sum_{i=n+1}^{m} N_i r_i^k \tag{12}$$

As funções de grau entre N_{N+1} e N_M são as acrescentadas no processo hierárquico. Calcula-se o resíduo em cada nó hierárquico, utilizando-se os termos adicionais da matriz **A** e do vetor **b**:

$$r_i^k = A_{21}\bar{x}_1 - b_2 = \sum_{l=1}^{N_e} A_{il}\bar{x}_l - b_i \tag{13}$$

sendo $\bar{x}_l$ a solução atual..

Uma vez calculados os valores de r_i^k, os indicadores são calculados a partir da expressão:

$$\left(\lambda_i^k\right)^2 = \sum_{l,m} C_{lm} r_i^l r_k^m \tag{14}$$

onde na norma L_2.

$$C_{lm} = L_k \int_{-1}^{1} N_l N_m d\eta \tag{15}$$

Analisando-se esta estratégia, nota-se que esta formulação utiliza os próprios coeficientes calculados no processo hierárquico, agilizando o processo. Há porém críticas quanto à definição do resíduo característico, necessário para tornar o medidor adimensional.

Numa outra linha, Charafi, Neves e Wrobel (1995), implementaram uma técnica chamada de Reanálise Local cujo algoritmo é mostrado na figura 3.

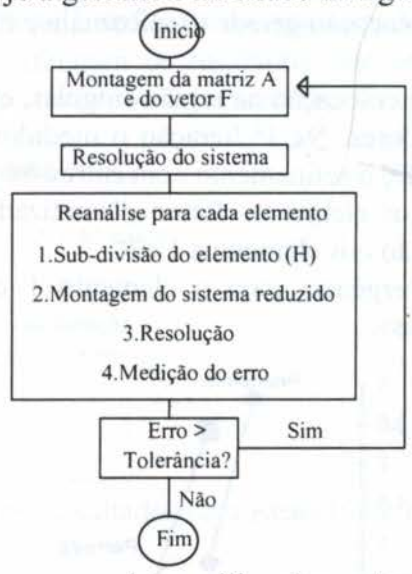

Figura 3. Fluxograma da reanálise elemento por elemento.

Esta técnica mede o grau de alteração da solução no elemento. Para tal, discretiza-se somente o elemento que esta sob análise e monta-se um sistema admitindo somente como incógnitas os valores nesse elemento. Verifica-se assim, o grau de alteração da solução que o elemento terá, avaliando-se em função disso o erro. Uma crítica que de antemão pode ser feita, é que este procedimento torna-se demasiado lento quando o número de elementos cresce exageradamente. Na figura 3, indica-se o fluxograma baseado nesse procedimento.

5. EXEMPLOS

Seja uma placa uniformemente tracionada. Levando em conta que a velocidade de convergência do programa adaptativo depende da malha inicial adotada, procurou-se concentrar mais elementos nas regiões onde a geometria ou a solução do problema era mais complicada.

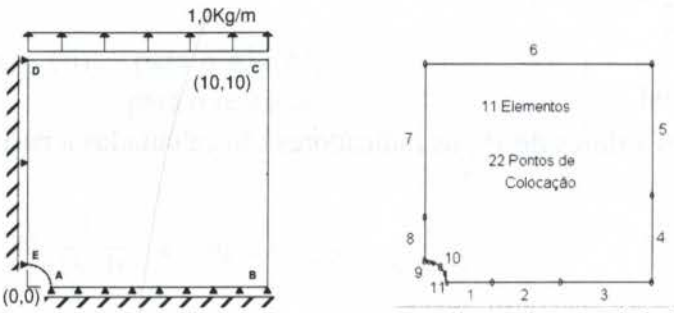

Figura 4 - Condições de contorno e discretização inicial

O refinamento final utilizando os estimadores da Reanálise Local ou dos resíduos é indicado na figura 5.

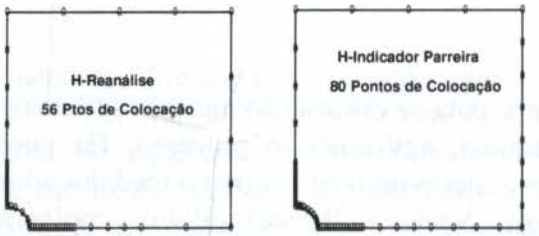

(a) (b)

Figura 5. Pontos de Colocação gerados. (a)Reanálise e (b) Parreira

Nota-se o acúmulo de pontos de colocação na região singular, exprimindo a sensibilidade e o bom funcionamento dos indicadores. Na 1ª Iteração o medidor da Reanálise refinou os elementos 1, 2, 6, 7 e 8. A partir da 2ª, o refinamento concentrou-se nos elementos 1 e 8. Para o medidor de Parreira, na 1ª todos os elementos foram discretizados. Porém a partir da 2ª, notou-se igualmente uma concentração nos elementos 1 e 8.

Na figura 6, indica-se a convergência para o elemento 1 que possui uma resposta singular. Nota-se a exatidão do processo.

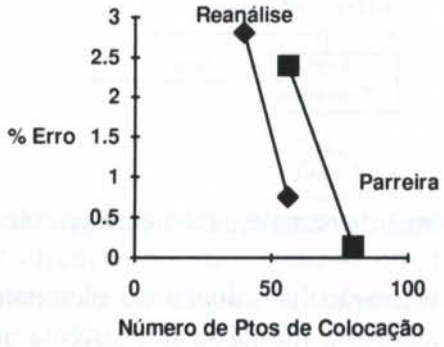

Figura 6. Convergência no elemento 1

Na figura 7 mostra-se a convergência para o elemento 7 que possui uma solução suave. Nota-se como a percentagem de erro permanece inalterada mesmo em face de novas

discretizações. A explicação para este comportamento é o de que nessas regiões seria necessária a adoção de funções de interpolações de grau superior.

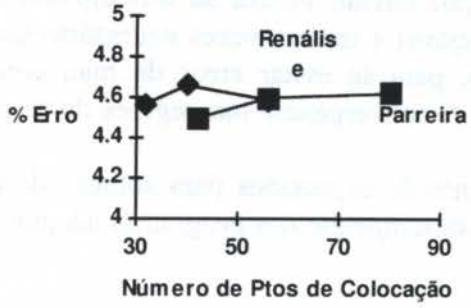

Figura 7- convergência no elemento 7

Como segundo exemplo, tomou-se a placa com um canto singular.

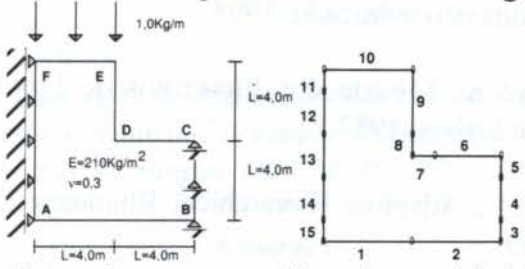

Figura 8 - Condições de contorno e discretização inicial do exemplo 2

Na figura 9 mostram-se os resultados para as várias iterações e pode-se observar a convergência para a solução real. Utilizando o indicador da Reanálise, na última iteração houve problemas de mau condicionamento do sistema ocasionados talvez por surgimento de integrais quase-singulares que afetaram os resultados dos elementos 13, 14 e 15. Com o indicador de Parreira não houve o mau condicionamento.

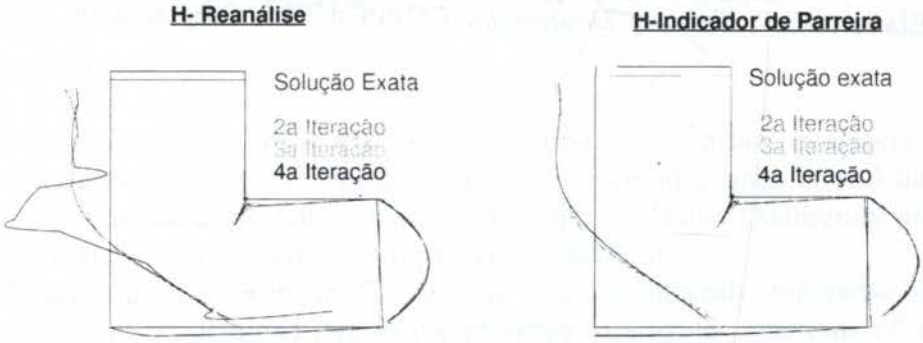

Figura 9. Resultados para Reanálise e Parreira

6. CONCLUSÕES

A formulação H-Hierárquica com a utilização de elementos quadráticos mostra-se bastante eficaz, convergindo rapidamente em regiões singulares. Com relação as regiões com solução mais suave, a convergência é mais lenta e tende a estacionar em um erro médio de 4%. Seria desejável nessas regiões aplicar a técnica P. Nota-se também que os resultados estão excessivamente dependentes de uma correta distribuição da malha inicial, em razão dos pontos de colocação serem gerados uniformemente ao longo do elemento. Seria desejável que os pontos de colocação acompanhassem a distribuição do erro dentro do elemento. Por

exemplo, no caso do erro estar concentrado na extremidade, somente essa região seria subdivida. Isto aceleraria em muito a velocidade de convergência e deixaria a formulação menos dependente da discretização inicial. Porém há dificuldades de implementação desse algoritmo. Por outro lado, é desejável e muitas vezes necessário que o projetista efetue um controle do processo adaptativo, para se evitar erros de mau condicionamento e para se acelerar a taxa de convergência. A convergência nas regiões de resposta suave é igualmente rápida.

Por último, o desenvolvimento de expressões para solução de integrais semi-singulares parece ser necessário para o bom desempenho dos programas adaptativos.

7. REFERÊNCIAS

CHARAFI A.; NEVES, A.C.; WROBEL L.C "H-Hierarchical Adaptive Boundary Element Method using Local Reanalysis: I-Quadratic Shape Functions", *International Journal for Num. Meth. in Engng*, artigo submetido e ainda não publicado, 1995.

PARREIRA, P.G., Análise do erro no Método dos Elementos de Fronteira em Elasticidade, *Master Thesis*, Univ. Técnica de Lisboa, 1987.

PARREIRA P.; DONG Y.F (1992) , Adaptive Hierarchical Boundary Elements, *Advances in Engng. Software*, pags 249 a 259.

PEANO, A.G, Hierarchics of Conforming Finite Elements for Plane Elasticity and Plate Bending, *Comput. and Maths. with Appl.*, 2, No. 3-4, 1976.

PESSOLANI, R.B.V., Formulação H auto-adaptativa de Elementos de Contorno para Problemas de Potencial e Elasticidade, *Tese de Mestrado*, PUC-RJ, 1989.

PESSOLANI, R.B.V.; Formulação H-P auto-adaptativa de Elementos de Contorno para Problemas de Elasticidade", *Tese de Doutorado*, COPPE-UFRJ, Programa de Engenharia Civil, 1995.

XIV Brazilian Congress of Mechanical Engineering
Obeid Plaza Hotel Convention Center - Bauru - SP/Brazil
December 08-12th 1997

PAPER CODE: COB442

SEMI-ANALYTICAL SINGULAR INTEGRATION FOR THE BOUNDARY ELEMENT METHOD IN ELASTICITY

RAUL BERNARDO VIDAL PESSOLANI
Pesquisador da FAPERJ - Fundação de Amparo à Pesquisa do Estado do Rio de Janeiro
Departamento de Engenharia Mecânica, Faculdade de Engenharia - UFF - Niteroi, RJ.
Rua Passos da Pátria, 156 - São Domingos, CEP 24210-240 - Niterói, R J, Brasil

Abstract

This paper shows an alternative formulation to compute the value of the singular integral elements in the Boundary Element Method for Elasticity Problems, employing a process called semi-analytical. The expressions to be implemented are discussed and the precision obtained is illustrated with a numerical example.

Keywords

Numerical Methods, Boundary Element Method, Adaptive Procedures

Palavras-Chave

Métodos Numéricos, Método dos Elementos de Contorno, Procedimentos Adaptativos.

1. INTRODUCTION

Since its first steps the BEM has been submitted to a constant evolution, developing mainly the process of numerical integration, mostly concerning singular and quasi-singular integrals. These must be evaluated numerically through the Gauss Quadrature process, since analytical expressions only exist in certain particular situations.

Special care must be taken, in the case of singular integrals, otherwise imprecise or incorrect results will be obtained due to the presence of singular functions of 1/r and ln(r) order. For the terms containing 1/r, integration in the sense of finite part of integral can be employed, making use of Kutt's points or computing these parts by rigid body movements. In the hierarchical adaptive formulation, the computation through rigid body motion is not possible because the variables are not traction or displacements anymore, but are derived from them. The terms which contain ln(r) are integrated with an excessive number of Gauss points and making use of Telles transformation of third order, that rearranges the Gauss points inside the element.

For adaptive procedures which uses hierarchical schemes, the computation of this numerical integrals is necessary, due to the fact of the generation of new collocation points inside the elements (Guiggiani (1992) and Pessolani (1995)).

Alternatives to estimate the singular integrals have been looked for to improve computational efficiency and the precision of BEM. Efficient and conceptually consistent procedures have been proposed by Guigianni e Casalini (1987) and Dumont e Souza (1992), which employed the Hadamard's (1923) concept, to compute these singular integrals.

The present paper introduces an alternative procedure for the computation of integrals containing singularities of 1/r and Ln(r) type, employing a process called semi-analytical. With this method, undeterminations are evaluated with the Hadamard Finite Part Integral concept. The expressions are discussed and the precision obtained is illustrated with numerical examples. The coordinate transformation suggested by Telles(1987) is used both in conventional and semi-analytical formulations to compute quasi-singular integrals as well as the ones containing singularity of the 1/r type.

2. THE SINGULARITY IN THE BEM

The BEM for bidimensional elasticity consists in the solution of the boundary integral equation:

$$C_{ij}(\xi)U_i(\xi) + \int_\Gamma T_{ij}^*(\xi,\chi).U_j(\chi).d\sigma(\chi) = \int_\Gamma U_{ij}^*(\xi,\chi).T_j(\chi).d\sigma(\chi) \qquad (1)$$

The fundamental solutions T* and U* have the singularity of Ln(r) and (1/r) (Brebbia (1978)).

The terms of the integral equation are calculated and stored in matrixes. Applying the boundary conditions, we can find the final system form, which can be solved by the Gauss Elimination process or through iterative algorithms proposed by Shakib et alii (1987).

The computation of [H] diagonal sub-matrices (2x2), involve the total sum of two parcels: one corresponding to the first integral (1) and the other corresponding to the C_{ij} (j=i) term, as follows:

$$H_{ii} = \hat{H}_{ii} + C_{ii} \qquad (2)$$

The C_{ii} coefficient depends on the boundary geometry in ξ and the Poisson ν. (Pessolani (1995) and Hartmann (1987)).

The $\hat{H}_{ii}$ term is the integration's result when the source point coincides with the field point ($r \to 0$), and requires special considerations. The terms that presented a smooth behavior become singulars of 1/r and ln(r) order. These singularities may turn numerical computation of these integrals into these elements a highly imprecise one. Ln(r) singularity can be numerically integrated by Gauss, but it demands a great number of points and the use of Telles'(1987) transformation to remaping the integration points. On the other hand, singularities of 1/r order require the integration in the sense of Cauchy's Principal Value. The usually adopted solution in Elasticity consists in the computation of these terms by rigid body displacements. However, these singular integrals may be directly estimated.

The exact computation of the integrals indicated in expression (1) can be done by analytical procedures. However, expressions may become too complex in curve elements. So, the semi-analytical integration discussed below is recommended.

3. FORMULATION FOR THE 1/R TERM

The defined integral in a surface with the limits Γ_i and Γ_f, is defined in figure 1.

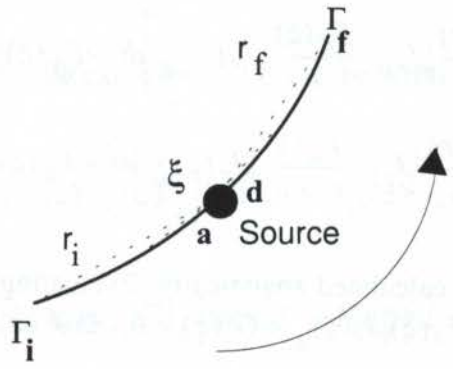

Figure 1 - Integration on singular element.

Where **a** and **d** are the adjacent points before and after the field point. The vector **r** assume a null value about the point ξ. So the integral (3) is improper and divergent.

$$I = \int_{\Gamma_i}^{\Gamma_f} \frac{F(\Gamma)}{r} d\Gamma \tag{3}$$

The BEM requires the computation of the Cauchy Principal value of integral. So, the expression (3) become:

$$I_H = VP \int_{\Gamma_i}^{\Gamma_f} \frac{F(\Gamma)}{r} d\Gamma = \lim_{\varepsilon \to 0} \left\{ \int_{\Gamma_i}^{\Gamma_\xi - \varepsilon} \frac{F(\Gamma)}{r} d\Gamma + \int_{\Gamma_\xi + \varepsilon}^{\Gamma_f} \frac{F(\Gamma)}{r} d\Gamma \right\} \tag{4}$$

Changing to a generical variable θ and expanding in series the integration limits, the expression (4) in terms of θ coordinates is (Pessolani (1995)):

$$I = \lim_{\varepsilon \to 0} \left\{ \int_{\theta_i}^{\theta_\xi - \left(1/J_a\right)\varepsilon} \frac{F(\Gamma(\theta))}{r} J_\theta d\theta + \int_{\theta_\xi + \left(1/J_d\right)\varepsilon}^{\theta_f} \frac{F(\Gamma(\theta))}{r} J_\theta d\theta \right\} \tag{5}$$

where $|J_a|$ e $|J_d|$ are Jacobean computed relative to the points **a** and **d** as can be seen in figure 3.

Making θ=r, which is the vector position of the field point, related to the source point, the expression (5) is now given by:

$$I = \lim_{\varepsilon \to 0} \left\{ \int_{\varepsilon}^{\Gamma_i} \frac{F(\Gamma)}{r} |J_r| d\Gamma + \int_{\varepsilon}^{\Gamma_f} \frac{F(\Gamma)}{r} |J_r| d\Gamma \right\} \tag{6}$$

Hadamard(1923) shows a methodology for treating this problem, which, if applied to the present study, induces to write expression (6) as follows:

$$I_H = \lim_{\varepsilon\to 0}\left\{\begin{array}{l}\displaystyle\int_{\varepsilon}^{r_f}\left[\frac{F_d(r)}{r}|J_r| - \frac{F_d(\xi)}{r}|J_r(\xi)|_d\right]dr + F_d(\xi)|J_r(\xi)|_d\int_{\varepsilon}^{r_f}\frac{1}{r}dr \\ \displaystyle+\int_{\varepsilon}^{r_i}\left[\frac{F_a(r)}{r}|J_r| - \frac{F_a(\xi)}{r}|J_r(\xi)|_a\right]dr + F_a(\xi)|J_r(\xi)|_a\int_{\varepsilon}^{r_i}\frac{1}{r}dr\end{array}\right\} \tag{7}$$

The integral 1/r can be calculated analytically. Evaluating this integration and defining: $G(r) = F(r)|J_r|$, e $G_d(\xi) = F_d(\xi)|J_r(\xi)|_d$ e $G_a(\xi) = F_a(\xi)|J_r(\xi)|_a$, this leads to::

$$I_H = \lim_{\varepsilon\to 0}\left\{\begin{array}{l}\displaystyle\int_{\varepsilon}^{\Gamma_a}\frac{G_a(r)-G_a(\xi)}{r}dr + G_a(\xi)\ln(r_a) - G_a(\xi)\ln(\varepsilon) \\ \displaystyle+\int_{\varepsilon}^{\Gamma_d}\frac{G_d(r)-G_d(\xi)}{r}dr + G_d(\xi)\ln(r_d) - G_d(\xi)\ln(\varepsilon)\end{array}\right\} \tag{8}$$

I_H exist only if $G_a(\xi) = -G_d(\xi)$, which is real for Elasticity. Consequently, the expression (8) becomes:

$$I_H = \int_0^{r_f}\frac{G_d(r)-G_d(\xi)}{r}dr + G_d(\xi)\ln(r_f) + \int_0^{r_i}\frac{G_a(r)-G_a(\xi)}{r}dr + G_a(\xi)\ln(r_i) \tag{9}$$

Doing a coordinate change, **r** for Γ:

$$I = \int_{\Gamma(\xi)}^{\Gamma_f}\frac{G_d(r)-G_d(\xi)}{r}\left|\frac{dr}{d\Gamma}\right|d\Gamma + G_d(\xi)\ln(r_f) + \int_{\Gamma_a}^{\Gamma(\xi)}\frac{G_a(r)-G_a(\xi)}{r}\left|\frac{dr}{d\Gamma}\right|d\Gamma + G_a(\xi)\ln(r_i) \tag{10}$$

The procedure described that results in the expression (10), must be applied only for the parcel of T_{ij}^* that is not multiplied by $\partial r/\partial n$, since $\lim_{r\to 0}\frac{1}{r}\frac{\partial r}{\partial n}$ is equal to $1/2\,\rho$ (Mansur *et al.*(1992)). Consequently these procedures are not necessary in Potential Problems.

4. FORMULATION FOR THE LN(R) TERM

The term U_{ij}^* is a sum of two parcels: one regular and the other having a logarithm representation singularity, that can be smoothed by procedures such as expression (10). In this case, an equivalent expression of equation (4) is:

$$I_G = VP\int_{\Gamma_i}^{\Gamma_f} F'(\Gamma)\ln(r)d\Gamma = \lim_{\varepsilon\to 0}\left\{\int_{\Gamma_i}^{\Gamma_\xi-\varepsilon} F'(\Gamma)\ln(r)d\Gamma + \int_{\Gamma_\xi+\varepsilon}^{\Gamma_f} F'(\Gamma)\ln(r)d\Gamma\right\} \tag{11}$$

Doing the same transformations, the expression (11) can be written:

$$I_G = \lim_{\varepsilon\to 0}\left\{\begin{array}{l}\displaystyle\int_{\varepsilon}^{r_f}\left[F'(r)|J_r| - F'_d(\xi)|J_r(\xi)|_d\right]\ln(r)dr + F'_d(\xi)|J_r(\xi)|_d\int_{\varepsilon}^{r_f}\ln(r)dr \\ \displaystyle+\int_{\varepsilon}^{r_i}\left[F'(r)|J_r| - F'_a(\xi)|J_r(\xi)|_a\right]\ln(r)dr + F'_a(\xi)|J_r(\xi)|_a\int_{\varepsilon}^{r_i}\ln(r)dr\end{array}\right\} \tag{12}$$

Or:

$$I_G = \lim_{\varepsilon\to 0}\left\{\begin{array}{l}\displaystyle\int_{\varepsilon}^{r_f}\left[G'(r) - G'_d(\xi)\right]\ln(r)dr + G'_d(\xi)\Big[r\ln(r) - r\Big]_{\varepsilon}^{r_f} \\ \displaystyle+\int_{\varepsilon}^{r_i}\left[G'(r) - G'_a(\xi)\right]\ln(r)dr + G'_a(\xi)\Big[r\ln(r) - r\Big]_{\varepsilon}^{r_i}\end{array}\right\} \tag{13}$$

Considering that $\lim_{r\to 0} r\ln(r) = 0$ and returning to Γ:

$$I_G = \left\{\begin{array}{l}\displaystyle\int_{\Gamma(\xi)}^{\Gamma_f}\left[G'(\Gamma) - G'_d(\xi)\right]\ln(r)\left|\frac{dr}{d\Gamma}\right|d\Gamma + G'_d(\xi)\Big[r_f\ln(r_f) - r_f\Big] \\ \displaystyle+\int_{\Gamma(\xi)}^{\Gamma_i}\left[G'(r) - G'_a(\xi)\right]\ln(r)\left|\frac{dr}{d\Gamma}\right|d\Gamma + G'_a(\xi)\Big[r_i\ln(r_i) - r_i\Big]\end{array}\right\} \tag{14}$$

The function G(r) (or G(Γ)) that arises in expressions (8), (9) and (10) is the result of the multiplication of F(r) by $\left|d\Gamma/dr\right|$. When $x \neq \xi$, the possibility exists of **r** be perpendicular to **t** (Tangent vector) in x, that implied $\left|d\Gamma/dr\right| \to \infty$. However, a more careful analysis of the expression (10), show that the Jacobian singularity doesn't require special considerations, since $G(\Gamma)$ is multiplied by $\left|d\Gamma/dr\right|$:

$$G(\Gamma)\left|\frac{\partial r}{\partial\Gamma}\right| = F(\Gamma)\left|\frac{\partial\Gamma}{\partial r}\right|\left|\frac{\partial r}{\partial\Gamma}\right| = F(\Gamma) \tag{15}$$

That is, the function 1/r is the unit singularity. These commentaries are also applied to expression (14).

5. TESTS

To test the efficiency of the formulation discussed here, a program with iso-parametrical quadratic continuous and discontinuous elements has been elaborated. In all the analysis the singular integrations have been estimated by the coordinates transformation developed by Telles (1987). The number of integration's points was 12 per element. When the element is divided by two, as it occurs when the collocation point is in the central node and the discussed scheme here is adopted, 6 points of integration have been used for each sector. This procedure has also been adopted to discontinuous elements. In this case the most efficient procedure would have been the one in which the number of integration points is divided proportionally to the length of each sector .

With the purpose of testing the efficiency of the formulation discussed here, the following analysis, that differ only in the way of calculating the singular integrals, have been effected:

1.MEC1 - H calculated by rigid body displacements and G by the third order transformation, with 6 points of integration per sector when the collocation point is situated inside the element.

2.MEC2 - H and G calculated according the procedures described here without the third order transformation

3.MEC3 - H and G calculated according the procedures described here using the third order transformation.

CIRCULAR DOMAIN

To test the efficiency for problems in curved boundaries, the problem illustrated in figure 3 was tested.

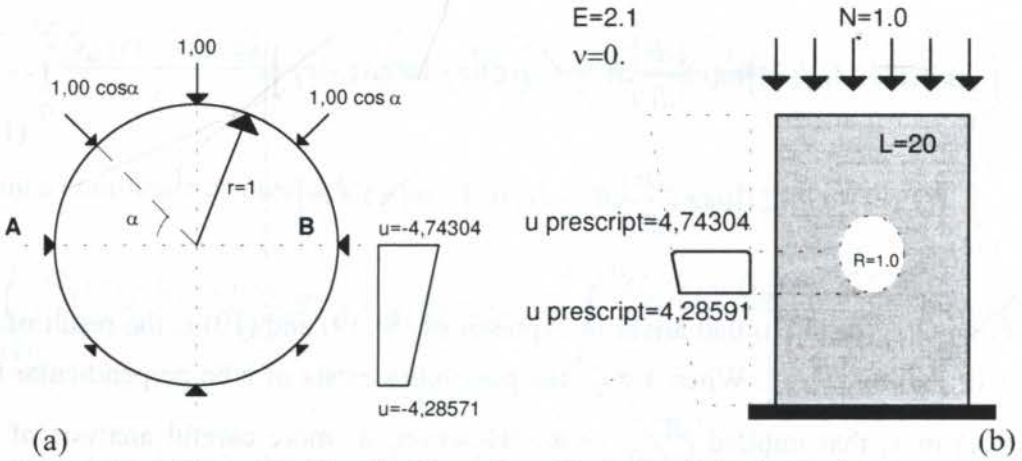

Figure 3 - Circular Domain with the analytical solution

CONTINUOS ELEMENT

The adopted discretization contains 16 quadratics continuos elements uniformly distributed around the boundary.

Table 5 - Traction

	Analytical	MEC 1	MEC 2	MEC 3

(-1.,0.)	0.	,0009678	,0009541	,00095165
(-,9239,-,3827)	-,38268343	-,3826696	-,3826899	-,3826894
(-,707,-,707)	-,7071067812	-,707094603	-,70713544	-,70713500
(-,3827,-,9239)	-,92387953	-,92386852	-,92392119	-,92390945
(0,1.)	-1,0000000	-,99998911	-1,00004592	-1,00004561

Table 6 - Displacements

Joints coord	Analytical	MEC 1	MEC 2	MEC 3
(0,9239, 0,3827)	4,94413497	4,9441224	4,9441212	4,94412126
(0,707, 0,707)	5,09862228	5,0986045	5,09860309	5,09860306
(0,3827, 0,9239)	5,201847397	5,2018300	5,2018285	5,2018285
(0, 1)	5,238095238	5,23807223	5,23807069	5,23807067

DISCONTINUOUS ELEMENT

The adopted mesh is similar having 16 discontinuous quadratical elements.

Table 7 - Traction

Joint Coordinates	Analytical	MEC 1	MEC 2	MEC 3
(-,981,-,195)	-,1950903	-,1950519	-,19505406	-,19504756
(-,908,-,419)	-,418969	-,4191579	-,4190377	-,41915202
(-,7345,-,6785)	-,6785074	-,6783882	-,67846987	-,678380
(-,5556,-,8315)	-,8314696	-,83144172	-,83143964	-,8314339
(-,3458,-,9383)	-,9382759	-,93839165	-,938355238	-,938382426

Table 8 - Displacements

Joints Coordinates	Analytical	MEC 1	MEC 2	MEC 3
(0,9808, 0,1951)	4,854809524	4,854778	4,854778	4,8547779
(0,908, 0,419)	4,96141380	4,9614314	4,961436	4,96143147
(0,735, 0,6785)	5,0850033	5,0850165	5,0850141	5,08501722
(0,556, 0,831)	5,15761904	5,1578033	5,157805	5,15780448
(0,346, 0,938)	5,23087023	5,208696	5,2086997	5,208697
(0,004, 0,99917)	5,237747	5,2376700	5,2376700	5,2376718

6. CONCLUSIONS

The procedure discussed here refers to the singular integrals computation in the Boundary Elements Method, when curve elements are used (iso-parametrical quadratic elements in this paper).

Initially the paper refers to basic conceptual aspects not always familiar to researches that study this method. From this initial discussion, an alternative procedure to estimate singular integrals in 2D analysis has been proposed .

The example shows that the proposed scheme improves the integration performance, although integration errors are smaller than the ones of modeling (hypothesis and interpolation).

As a future research, the extension of the method to quasi-singular integrals can be suggested.

7. REFERENCES

BREBBIA, C.A., The Boundary Element Method for Engineers, *Pentech Press*, London, 1978

DUMONT, N.A.; SOUZA, R.M. de, A Simple, Unified Technique for the Evaluation of Quasi-Singular, Singular and Strongly Singular Integrals, *Boundary Elements XIV*, 619- 632, 1992.

GUIGGIANI, M.; CASALINI, P., Direct Computation of Cauchy Principal Value Integrals in Advanced Boundary Elements, *Int. Journal for Num. Meth. in Engng*, vol 24, 1711-1720, 1987.

GUIGGIANI M.; LOMBARDI F, Self-Adaptive Boundary Elements with h-Hierarchical Shape Functions, *Advances in Engng. Software*, pags 269 a 278, 1992.

HADAMARD, J., Lectures on Cauchy's Problem in Linear Partial Differential Equations, *Yale University Press*, 1923.

HARTMANN, F., Computing the C-matrix in nom-smooth Boundary Points, *New Developments in Boundary Element Methods*, C.A. Brebbia (ed), Butterwords, 1987

PESSOLANI, R.B.V., Formulação HP-hierárquica Adaptativa para Elasticidade com o Método dos Elementos de Contorno, *D.Sc. Thesis*, COPPE - Programa de Engª Civil, Univ. Federal do Rio de Janeiro, 1995

MANSUR, W.J.; TELLES, J.C.F.; PRODANOFF, J.H.A.; FRAUCHES, E., On BEM Singular Integrals for Two-Dimensional Potential Applications, *Engng Analysis with Boundary Elements*, vol. 9, pp. 185-187, 1992.

SHAKIB, F, HAKIB, F, HUGHES, J.R., JOHAN, A Multi-Element Group Preconditioned GMRES Algorithm for Nonsymmetric Systems Arising in Finite Element Analysis, *Comp. Meth. in Appl Mech and Engng*, 75, 415-456, 1989.

TELLES, J.C.F., A Self-Adaptive Co-ordinate Transformation for Efficient Numerical Evaluation of General Boundary Element Integrals, *in Int Journal for Num. Meth. in Engng*, vol 24, 952-973, 1987.

XIV Brazilian Congress of Mechanical Engineering
Obeid Plaza Hotel Convention Center - Bauru - SP/Brazil
December 08-12th 1997

PAPER CODE: COB1222

ALGORÍTMO PARA INTEGRAÇÃO FRACA PRESENTE NO MEC APLICADO A PROPAGAÇÃO DE ONDAS / *NEARLY SINGULAR INTEGRAL ALGORITHM IN BEM APPLIED TO WAVE PROPAGATION*

Mauro G. J. Veloso[1] & Webe J. Mansur[2]
[1] *Departamento de Engenharia Mecânica, Centro Tecnológico - UFPA - Belém (Pa) CEP 66.000-000, e-mail: lme@amazon.com.br*
[2] *Programa de Engenharia Civil, COPPE, UFRJ, Rio de Janeriro, Cx. Postal : 68506 CEP 21945-970 e-mail: webe@coc.ufrj.br*

Abstract

Nearly singular integrals arise in boundary element formulation applied to elastodynamics problems. In this paper is proposed an algorithm to integrate this nearly singular integrals. The method is formulated on subtract the nearly singular parcel from the nearly integration expression, and integrate this expression by numerical approach them the nearly singular parcel is algebraically integrated.

Keywords

Método dos elementos de çontorno aplicado a elastodinâmica, Integral fracamente singular, Métodos de integração numérica, Propagação de ondas no contínuo, BEM Applied to Elastodynamics, Nearly Singular Integral, Numerical Integration, Wave Propagation.

1. INTRODUÇÃO

A propagação de ondas no meio contínuo é representada matematicamente pela equação de Navier, a qual consiste em uma equação diferencial parcial. Em problemas que apresentam geometria complexas, a resolução somente é possível por métodos numéricos. Dentre os vários métodos conhecidos, o método dos elementos de contorno é uma alternativa de abordagem para estes problemas, principalmente quando o meio contínuo é infinito ou semi-infinito.

Na aplicação deste método a problemas da elastodinâmica no domínio da freqüência, estão presentes expressões a integrar de comportamento quase singular, um método clássico atualmente disponível é aplicar a integração Gaussiana com pesos logarítmicos. Neste trabalho será apresentado uma técnica que consiste em separar a parcela fracamente singular e integrá-la analiticamente, uma vez que o comportamento assintótico da solução fundamental para elastodinâmica no domínio da freqüência tende para solução fundamental da elasticidade.

2. MÉTODO DOS ELEMENTOS DE CONTORNO APLICADO À ELASTODINÂMICA

A equação integral do método dos elementos de contorno formulada para problemas da elastodinâmica no domínio da freqüência é dado pela expressão a seguir:

$$C_{ij}(\xi)U_j(\xi,\omega)+VP\int_\Gamma T_{ij}^d(x,\xi,\omega).U_j(x,\omega)d\Gamma=\int_\Gamma U_{ij}^d(x,\xi,\omega)T_j(x,\omega)d\Gamma+$$
$$\int_\Omega U_{ij}^d(y,\xi,\omega)\cdot B_j(y,\omega)d\Omega;\ \forall\, y\in\Omega\ ,\ x\in\Omega\ \wedge\ \omega\neq 0 \qquad (1)$$

sendo que as soluções fundamentais são escritas sob a forma:

$$U_{ji}^d=\frac{1}{2\pi\rho c_s^2}\left[\Psi\delta_{ij}-Xr_{,i}r_{,j}\right] \qquad (2)$$

$$T_{ji}^d=\frac{1}{2\pi r}\left[\left(r\frac{d\Psi}{dr}-X\right)\left(\delta_{ij}\frac{\partial r}{\partial n}+r_{,i}n_j\right)-2X\left(n_ir_{,j}-2r_{,i}r_{,j}\frac{\partial r}{\partial n}\right)-\right.$$
$$\left.2r\frac{dX}{dr}\frac{\partial r}{\partial n}r_{,i}r_{,j}+\left(\frac{c_d^2}{c_s^2}-2\right)\left(r\frac{d\Psi}{dr}-r\frac{dX}{dr}-X\right)r_{,j}n_i\right] \qquad (3)$$

com:

$$X=K_2(k_sr)-\frac{C_s^2}{C_d^2}K_2(k_dr) \qquad (4)$$

$$\Psi=K_0(k_sr)+\frac{1}{k_sr}\left[K_1(k_sr)-\frac{C_s^2}{C_d^2}K_1(k_dr)\right] \qquad (5)$$

As constantes C_d e C_s são as velocidades de propagação das ondas de dilatação e ondas de cisalhamento, $K_0(kr), K_1(kr)$ e $K_2(kr)$ são funções modificadas de Bessel de segunda espécie de ordem zero, um e dois (Dominguez et alli, 1984), de argumento kr, sendo k expresso pelas seguintes equações, com $i=\sqrt{-1}$:

$$k_d=\frac{i\omega}{C_d} \qquad (6)$$

$$k_s=\frac{i\omega}{C_s} \qquad (7)$$

a matriz **C**(ξ) (Brebbia et alli, 1989; Guiggiani, 1987, 1990) é escrita em função do perfil da geometria do contorno Γ em torno do ponto fonte 'ξ', cujo valor é dado por:

$$\mathbf{C}(\xi)=\begin{cases}-\dfrac{1}{8\pi(1-\nu)}\begin{bmatrix}C_{11} & C_{12}\\ C_{21} & C_{22}\end{bmatrix}\text{; quando }\Gamma\text{ não é suave em }\xi\\ \begin{bmatrix}0{,}5 & 0\\ 0 & 0{,}5\end{bmatrix}\text{; quando }\Gamma\text{ é suave em }\xi\end{cases} \qquad (8)$$

$$\begin{cases} C_{11} = 4(1-\nu)(\pi+\theta_2-\theta_1)+\text{sen}(2\theta_1)-\text{sen}(2\theta_2) \\ C_{12} = C_{21} = \cos(2\theta_2)-\cos(2\theta_1) \\ C_{22} = 4(1-\nu)(\pi+\theta_2-\theta_1)+\text{sen}(2\theta_2)-\text{sen}(2\theta_1) \end{cases} \quad (9)$$

3. FORMULAÇÃO PARA INTEGRAÇÃO DAS EXPRESSÕES FRACAMENTE SINGULARES

Com o objetivo de subsidiar a formulação, vale lembrar que a solução fundamental da elastodinâmica para o deslocamento U_{ij}^d, tende para solução fundamental da elastostática U_{ij}^s acrescida de constantes, (Lacerda, 1993). Porém para $\omega \to 0$, U_{ij}^d apresenta uma singularidade em 'ω', restrição esta que não será analisada neste trabalho.

Observa-se que em U_{ij}^s a singularidade fraca está presente apenas quando i=j, uma vez que para valores de i≠j, o termo delta de Kronecker, δ_{ij}, é nulo, como pode-se atestar pela expressão abaixo:

$$U_{ij}^s(\omega,\xi,\mathbf{x}) = \frac{(3-4\nu)}{8\pi(1-\nu)\mu}\left[\ln\left(\frac{1}{r}\right)\delta_{ij}\right] = C\left[\ln\left(\frac{1}{r}\right)\delta_{ij}\right] = f_{ij}\ln(r)$$
$$C = \frac{(3-4\nu)}{8\pi(1-\nu)\mu} \quad (10)$$

A figura 1, mostra o contorno Γ dividido em duas partes, tal que o ponto singular ξ, ponto fonte, pertence a interseção entre esses dois pedaços, $\Gamma_a \cap \Gamma_d$. Seja um círculo de raio ε, centrado no ponto singular, ξ, do conceito de parte finita (Kutt, 1975), a equação (2) pode ser escrita sob a forma seguinte, após a mudança de variável de integração, Γ, por θ, (Veloso, 1995):

$$\lim_{\varepsilon\to 0}\left\{\int_{\varepsilon}^{r_a} U_{ij}^d(\omega,\xi,\mathbf{x})\left|J_r\right|_a T_j(\omega,\mathbf{x})dr + \int_{\varepsilon}^{r_d} U_{ij}^d(\omega,\xi,\mathbf{x})\left|J_r\right|_d T_j(\omega,\mathbf{x})dr\right\} \quad (11)$$

Subtraindo e somando a parcela singular (10) de (11) e simplificando resulta a equação:

$$\lim_{\varepsilon\to 0}\left\{\int_{\varepsilon}^{r_a}\left[U_{ij}^d(\omega,\xi,\mathbf{x})\left|J_r\right|_a T_j(\omega,\mathbf{x}) - f_{ij}\ln(r)\left|J_\xi\right|_a T_j(\omega,\xi)\right]dr + \int_{\varepsilon}^{r_a} f_{ij}\ln(r)\left|J_\xi\right|_a T(\omega,\xi)dr\right.$$
$$\left.\int_{\varepsilon}^{r_d}\left[U_{ij}^d(\omega,\xi,\mathbf{x})\left|J_r\right|_d T_j(\omega,\mathbf{x}) - f_{ij}\ln(r)\left|J_\xi\right|_d T_j(\omega,\xi)\right]dr + \int_{\varepsilon}^{r_d} f_{ij}\ln(r)\left|J_\xi\right|_d T_j(\omega,\xi)dr\right\} \quad (12)$$
$$\forall\,\xi \in (\Gamma_a \cap \Gamma_d) \wedge \mathbf{x} \in \Gamma_s;\ \omega \neq 0$$

sendo Γ_s a parcela do contorno que contém a singularidade. As duas primeiras parcelas de (12) são expressões regulares que podem ser integradas pelos métodos numéricos clássicos, e a terceira e quarta parcela serão integradas analiticamente. O valor $T_j(\omega,\xi)$ é independente de x, este vetor que atua sobre o contorno pode ser retirado do sinal de integração, resultando a expressão:

$$\lim_{\varepsilon\to 0}\left[f_{ij}T_j(\omega,\xi)_a\left|J_\xi\right|\int_\varepsilon^{r_a}\ln(r)dr + f_{ij}T_j(\omega,\xi)_d\left|J_\xi\right|_d\int_\varepsilon^{r_d}\ln(r)dr\right],\ \forall\,\xi\wedge\mathbf{x}\in\Gamma_s \qquad (13)$$

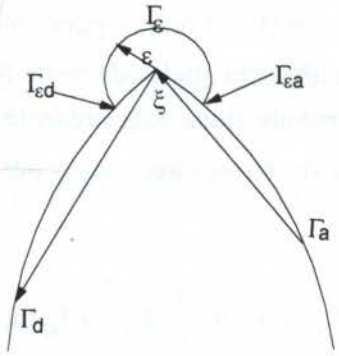

Figura 1: Contorno Γ com ponto fonte em ξ
envolvido pelo arco de círculo de raio ε.

Calculando a integral (13) e avaliando o limite, resulta a expressão:

$$-CT_j(\omega,\xi)_a\left|J_\xi\right|_d r_d\left[\ln(r_d)-1\right]\delta_{ij} - CT_j(\omega,\xi)_a\left|J_\xi\right|_a r_a\left[\ln(r_a)-1\right]\delta_{ij} \qquad (14)$$

Substituindo (14) em (12) resulta a expressão abaixo para a integração fracamente singular, expressão esta que será integrada numericamente através da quadratura de Gauss, sendo portanto, desnecessário o processo de integração numérica com pesos logarítmicos, para o cálculo da expressão da integral com singularidade fraca presente na equação integral (1) (Veloso, 1995):

$$\begin{aligned}
&\int_0^{r_a}\left[U_{ij}^d(\omega,\xi,\mathbf{x})T_j(\omega,\mathbf{x})\left|J_r\right|_a - f_{ij}\ln(r)T_j(\omega,\xi)\right]dr + \\
&\int_0^{r_d}\left[U_{ij}^d(\omega,\xi,\mathbf{x})T_j(\omega,\mathbf{x})\left|J_r\right|_d - f_{ij}\ln(r)T_j(\omega,\xi)\right]dr \qquad (15)\\
&-CT_j(\omega,\xi)r_d\left[\ln(r_d)-1\right]\delta_{ij} - CT_j(\omega,\xi)r_a\left[\ln(r_a)-1\right]\delta_{ij}\Big\} \\
&\qquad ;\ \forall\,\xi\in(\Gamma_i\cap\Gamma_f)\wedge\mathbf{x}\in\Gamma_s;\ \omega\neq 0
\end{aligned}$$

Observando que:

$$\left|J_r\right|\left|\frac{dr}{d\Gamma}\right| = 1 \tag{16}$$

$$\left|J_\xi\right|_a = \left|J_\xi\right|_d = 1 \tag{17}$$

A equação (15) toma a forma final:

$$\begin{aligned}
&\int_{\Gamma_\xi}^{\Gamma_a}\left[U_{ij}^d(\omega,\xi,\mathbf{x})T_j(\omega,\mathbf{x}) - f_{ij}\ln(r)T_j(\omega,\xi)\left|\frac{dr}{d\Gamma}\right|\right]d\Gamma + \\
&\int_{\Gamma_\xi}^{\Gamma_d}\left[U_{ij}^d(\omega,\xi,\mathbf{x})T_j(\omega,\mathbf{x}) - f_{ij}\ln(r)T_j(\omega,\xi)\left|\frac{dr}{d\Gamma}\right|\right]d\Gamma \\
&- CT_j(\omega,\xi)_d\, r_d\left[\ln(r_d)-1\right]\delta_{ij} - CT_j(\omega,\xi)_a\, r_a\left[\ln(r_a)-1\right]\delta_{ij}\Big\} \\
&\qquad ;\ \forall\,\xi \in (\Gamma_i \cap \Gamma_f) \wedge\ \mathbf{x} \in \Gamma_s;\ \omega \neq 0
\end{aligned} \tag{18}$$

As equações integrais resultantes são portanto válidas quando o ponte fonte pertence a parcela do contorno sobre o qual realiza-se a integração, observa-se a presença de expressões do tipo , rln (r), como resultado das integrações analíticas, este processo torna o comportamento da integral da função $U_{ij}^d(\omega,\xi,\mathbf{x})T_j(\omega,\mathbf{x})$ mais suave para integração numérica (Veloso, 1995).

4. EXEMPLO NUMÉRICO

Como exemplo de aplicação do método seja o problema da barragem de terra de dimensões 900 ft de base por 300 ft de altura com as seguintes características físicas: $\mu = 4{,}037\ 10^6\ \text{lbf}/\text{ft}^2$, $\nu = 0{,}45$ e massa específica $\rho = 4{,}037\ \text{lbf}/\text{ft}^3$.,sujeita a uma força distribuída linearmente q=1.000 lbf/ft e freqüência de 5,0 hz sobre as bordas BC e CA (figura 2). A malha foi discretizada de tal forma que os elementos que contém os pontos de canto são menores que os demais.

As figuras (3) e (4) mostram o comportamento das amplitudes de deslocamento na direção x para os pontos nodais pertencentes a borda BC com diferentes números de elementos na malha, observa-se que para elementos lineares mesmo para um reduzido número de elementos na malha os resultados apresentam boa aproximação.

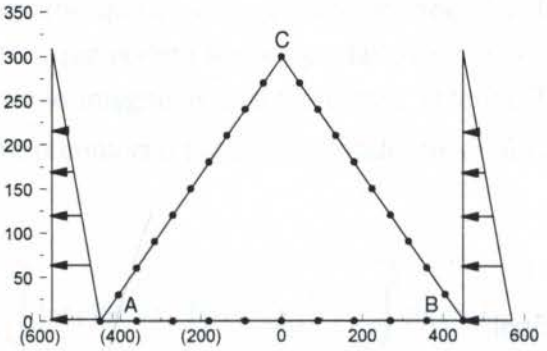

Figura 2: Barragem de terra sujeita a uma solicitação harmônica de 1,0 E+03 N a freqüência de 5,0 Hz.

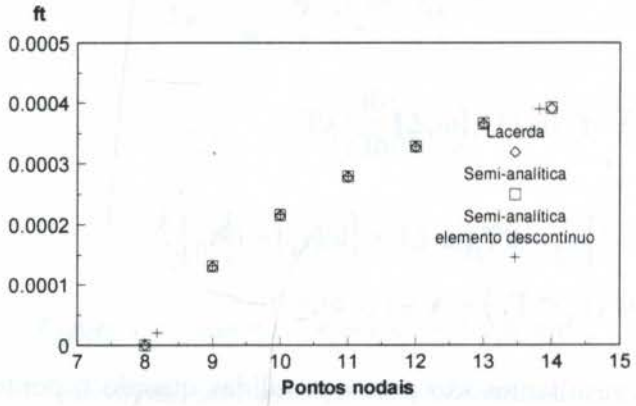

Figura 3: Amplitude de deslocamento na direção x dos pontos nodais da borda AB, malha com 14 elementos.

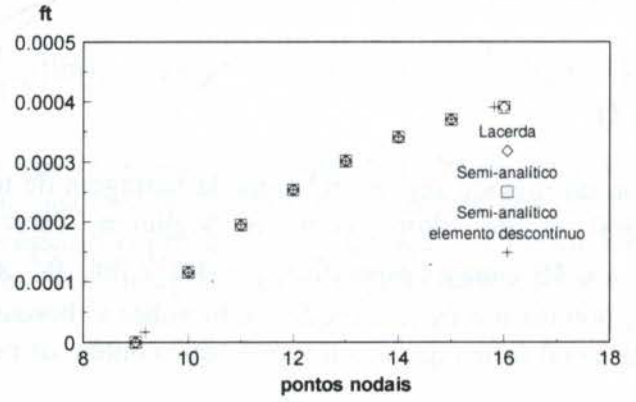

Figura 4:Amplitude de deslocamento na direção y dos pontos nodais da borda BC, malha com 21 elementos.

5. CONCLUSÃO

Neste artigo, um método para cálculo da integração quase singular presente no Método dos Elementos de Contorno para Elastodinâmica bidimensional foi apresentado. Esse método pode ser aplicado a problemas da elastodinâmica vetorial e também em problemas escalares, como propagação de ondas acústicas. Esta metodologia simplifica a integração a uma soma de integrais regulares e a utilização de reduzido número de elementos na malha.

6. REFERÊNCIAS

BREBBIA, C. A. E DOMINGUEZ, J., "Boundary Element Method - An Introdutory Course", McGraw Hill Book Co., (1989).

DOMINGUEZ, J. E ABASCAL, R., "On Fundamental Solutions for The Boundary Integral Equations Method in Static and Dynamic Elasticity", Engg. Analysis with Boundary Elements 1, 3, 128-134, (1984).

GUIGGIANI, M, E CASALINI, PAOLO, "Direct Computation of Cauchy Principal Value Integrals in Advanced Boundary Elements", Int. J. Num. Meths. in Engg., 24, 1711-1720, (1987)

GUIGGIANI, M, E GIGANTE, A., "A General Algorithm for Multidimensional Cauchy Principal Value Integrals in Boundary Element Method", Trans. ASME, J. Appl. Mech., 57, 906-915, (1990).

KUTT, H. R., "On the Numerical Evaluation of Finite Part Integrals Involving an Algebraic Singularity", The National Research Institute for Mathematical Sciences,Report Wisk 179, Pretória, (1975).

LACERDA, A., O., "O Método dos Elementos de Contorno para Elastodinâmica Bi-dimensional no Domínio da Freqüência com Emprego de Elementos Quadráticos", Dissertação de M. Sc., COPPE-UFRJ, (1993).

MANOLIS, G. D. E BESKOS, D. E., "Boundary Element Methods in Elastodynamics", Unwin Hyman, London, (1988)

VELOSO, M. J. G, "Um Algoritmo para Integração Singular e Quase-singular no Metódo dos Elementos de Contorno aplicado à Elastodinâmica Bidimensional no Domínio da Freqüência", Dissertação de M.Sc., COPPE-UFRJ, (1995)

XIV Brazilian Congress of Mechanical Engineering
Obeid Plaza Hotel Convention Center - Bauru - SP/Brazil
December 08-12th 1997

PAPER CODE: COB1224

UM ALGORÍTMO PARA INTEGRAÇÃO DA SINGULARIDADE NO MEC APLICADO A PROPAGAÇÃO DE ONDAS / *AN ALGORITHM FOR SINGULAR INTEGRATION IN BEM APLLIED TO WAVE PROPAGATION*

Mauro G. J. Veloso[1] & Webe J. Mansur[2]
[1] *Departamento de Engenharia Mecânica, Centro Tecnológico - UFPA - Belém (Pa) CEP 66.000-000, e-mail: lme@amazon.com.br*
[2] *Programa de Engenharia Civil, COPPE, UFRJ, Rio de Janeriro, Cx. Postal : 68506 CEP 21945-970 e-mail: webe@coc.ufrj.br*

Abstract

This work concern on the development of a scheme to integrate the singular expression, present at the boundary element method, applied to elastodynamics problems in frequency domain. The mathematical formulation of the problem is discussed as well as some examples are presented and compared with the other methods implemented to show the method accuracy.

Keywords

Método dos elementos de contorno aplicado a elastodinâmica, Integração singular, Métodos de integração numérica, Propagação de ondas no contínuo, Boundary Elements in Elastodynamics, Singular Integration, Wave Propagation in continuum.

1. INTRODUÇÃO

Grande parte dos fenômenos fisicos podem ser modelados por equações diferenciais parciais. Quando estas equações diferenciais são simples, problemas onde a geometria do domínio e do contorno não são complicados, são possíveis as soluções analíticas. Entretanto, para problemas com geometria irregular e problemas não lineares, tais soluções não estão disponíveis ou são difíceis de serem determinadas. Para transpor tal dificuldade vários métodos numéricos são propostos e estão em desenvolvimento. Dentre esses métodos, o Método dos Elementos de Contorno tem sido largamente empregado na abordagem de problemas da engenharia.

Em particular, nas aplicações do Método dos Elementos de Contorno à Elastodinâmica bidimensional, são deparadas integrais que envolvem produtos entre o jacobiano, as funções de forma e as soluções fundamentais, esta última escrita na forma de funções de Bessel e suas derivadas. Para funções de forma constantes, essas integrais podem ser avaliadas analiticamente (Lacerda, 1993), caso sejam funções lineares ou quadráticas, sua avaliação analítica é complexa e se faz necessário o emprego de técnicas numéricas.

Nesse trabalho é desenvolvida uma metodologia numérica para integração das expressões singulares presentes na formulação do Método dos Elementos de Contorno aplicado à elastodinâmica bidimensional linear, homogênea e isotrópica no domínio da freqüência.

2. ELEMENTOS DE CONTORNO PARA ELASTODINÂMICA NO DOMÍNIO DA FREQÜÊNCIA

Como ponto de partida à formulação do método será utilizada a equação dos Elementos de contorno no domínio da freqüência obtida a partir do teorema da reciprocidade de Betti (Dominguez, 1984; Lacerda 1993):

$$C_{ij}(\xi)U_j(\xi,\omega) + VP\int_\Gamma T_{ij}^d(x,\xi,\omega).U_j(x,\omega)d\Gamma = \int_\Gamma U_{ij}^d(x,\xi,\omega)T_j(x,\omega)d\Gamma + \int_\Omega U_{ij}^d(y,\xi,\omega)\cdot B_j(y,\omega)d\Omega;\ \forall\, y\in\Omega\,,\ x\in\Omega\ \wedge\ \omega\neq 0 \tag{1}$$

Sendo $\mathbf{T}=T_{ij}^d(x,\xi,\omega)$ e $\mathbf{U}=U_{ij}^d(x,\xi,\omega)$ soluções fundamentais obtidas e discutidas em Dominguez e Lacerda (Dominguez, 1984; Lacerda, 1993), e escritas nas seguintes formas:

$$U_{ji}^d = \frac{1}{2\pi\rho c_s^2}\left[\Psi\delta_{ij} - Xr_{,i}r_{,j}\right] \tag{2}$$

$$T_{ji}^d = \frac{1}{2\pi r}\left[\left(r\frac{d\Psi}{dr} - X\right)\left(\delta_{ij}\frac{\partial r}{\partial n} + r_{,i}n_j\right) - 2X\left(n_i r_{,j} - 2r_{,i}r_{,j}\frac{\partial r}{\partial n}\right) - 2r\frac{dX}{dr}\frac{\partial r}{\partial n}r_{,i}r_{,j} + \left(\frac{c_d^2}{c_s^2} - 2\right)\left(r\frac{d\Psi}{dr} - r\frac{dX}{dr} - X\right)r_{,j}n_i\right] \tag{3}$$

sendo:

$$X = K_2(k_s r) - \frac{C_s^2}{C_d^2}K_2(k_d r) \tag{4}$$

$$\Psi = K_0(k_s r) + \frac{1}{k_s r}\left[K_1(k_s r) - \frac{C_s^2}{C_d^2}K_1(k_d r)\right] \tag{5}$$

Onde C_d e C_s são as velocidades de propagação das ondas de dilatação e ondas de c2isalhamento $K_0(kr), K_1(kr)$ e $K_2(kr)$ são funções modificadas de Bessel de segunda espécie de ordem zero, um e dois (Dominguez et alli, 1984), de argumento kr, onde k_s e k_d são expressos pelas seguintes equações, com $i = \sqrt{-1}$:

$$k_d = \frac{i\omega}{C_d} \tag{6}$$

$$k_s = \frac{i\omega}{C_s} \tag{7}$$

a matriz $\mathbf{C}(\xi)$ (Brebbia et alli, 1989; Guiggiani, 1987, 1990) é escrita em função do perfil da geometria do contorno Γ em torno do ponto fonte 'ξ'.

3. ALGORÍTMO PARA INTEGRAÇÃO NUMÉRICA DAS EXPRESSÕES SINGULARES

Ao discretizar a equação integral (1), utilizando elementos constantes, são obtidas expressões que podem ser avaliadas analiticamente (Lacerda, 1993), no entanto quando discretizado por elementos lineares ou quadráticos as equações resultantes são difíceis ou impossíveis de serem avaliadas analiticamente, face a presença do produto, polinômio de interpolação de Lagrange, linear ou quadrático, com as soluções fundamentais e o Jacobiano. O primeiro processo, com a finalidade de resolver o problema da singularidade, foi introduzido por Lachat e Watson, restrito à elastostática e estendido para os problemas de potencial. Neste esquema as integrais no sentido do valor principal de Cauchy não são avaliadas diretamente. Este esquema de integração, foi estendido com algumas modificações para elastodinâmica (Ahmad et alli, 1987), uma vez que na dinâmica a singularidade, tem o mesmo comportamento assintótico que o apresentado pela elastostática (Ahmad et alli, 1987; Guiggiani, 1991; Manolis, 1988).

Para auxiliar na formulação do processo que será introduzido, o contorno Γ dividido em duas partes, de tal forma que o ponto singular ξ, ponto fonte, pertença a interseção entre esses dois pedaços, $\Gamma_a \cap \Gamma_d$ (figura 1). Considerando um círculo de raio ε, centrado no ponto singular ξ (figura 1), entre duas partes do contornos, Γ_a e Γ_d, utilizando o conceito de Parte Finita (Kutt, 1975), a segunda parcela da equação (1) pode ser escrita com a forma seguinte.

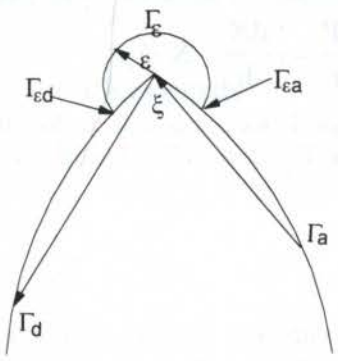

Figura 1: Ilustração do processo limite usual ponto singular em ξ envolvido pelo arco de círculo de raio ε.

$$VP\int_{\Gamma_s} T_{ij}^{d}(\omega,\xi,\mathbf{x})U_j(\omega,\mathbf{x})d\Gamma = \lim_{\varepsilon\to 0}\left[\int_{\Gamma_a}^{\Gamma_\xi-\varepsilon} T_{ij}^{d}(\omega,\xi,\mathbf{x})U_j(\omega,\mathbf{x})d\Gamma + \int_{\Gamma_\xi+\varepsilon}^{\Gamma_d} T_{ij}^{d}(\omega,\xi,\mathbf{x})U_j(\omega,\mathbf{x})d\Gamma\right] \quad ,\forall\ \mathbf{x}\wedge\xi\in\Gamma_s,\ \omega\neq 0 \tag{8}$$

Aproximando a expressão do contorno $\Gamma(r)$ por sua expansão em série Taylor em torno do ponto singular ξ (Aliabadi et alli, 1985), resulta:

$$\Gamma_\varepsilon - \Gamma_\xi = \left.\frac{d\Gamma}{d\theta}\right|_{\theta_\xi} \left(\theta_\varepsilon - \theta_\xi\right) + O^2(\theta) \tag{9}$$

$$\varepsilon = \left.\frac{d\Gamma}{d\theta}\right|_{\theta_\xi} \Delta\theta \tag{10}$$

$$J_\xi = \left.\frac{d\Gamma}{d\theta}\right|_{\theta_\xi} \tag{11}$$

$$\theta_\varepsilon - \theta_\xi = \frac{\varepsilon}{J_\xi} \tag{12}$$

Substituindo as equações (12) em (8), é obtida a expressão a seguir:

$$\lim_{\varepsilon\to 0}\left\{\int_{\theta_a}^{\theta_\xi - \varepsilon(1/J_\xi)_a} \mathbf{T}^d(\omega,\xi,\mathbf{x})\left(J_\xi\right)_a \mathbf{U}\, d\theta + \int_{\theta_\xi + \varepsilon(1/J_\xi)_d}^{\theta_d} \mathbf{T}^d(\omega,\xi,\mathbf{x})\left(J_\xi\right)_d \mathbf{U}\, d\theta\right\} \tag{13}$$

Observando que θ é uma variável genérica, então θ pode ser substituído por r, portanto a expressão (13) assume a forma:

$$\lim_{\varepsilon\to 0}\left\{\int_{\varepsilon}^{r_a} \mathbf{T}^d(\omega,\xi,\mathbf{x})\left(J_\xi\right)_a \mathbf{U}\, dr + \int_{\varepsilon}^{r_d} \mathbf{T}^d(\omega,\xi,\mathbf{x})\left(J_\xi\right)_d \mathbf{U}\, dr\right\} \tag{14}$$

O comportamento assintótico das soluções fundamentais U_{ij}^d e T_{ij}^d quando $r \to 0$, é discutido em Dominguez (Dominguez, 1984 e Lacerda, 1993). Neste trabalho será reapresentado apenas o resultado abaixo:

$$\lim_{r\to 0} T_{ij}^d = \frac{(1-2\nu)}{[8\pi(1-\nu)]}\left(r_{,i}n_j - r_{,j}n_i\right) = f_{ij}(\xi) \tag{15}$$

Subtraindo e somando a parcela singular (15) à equação integral (14) escrita para a vizinhança do ponto singular ξ, e considerando que na a vizinhança ao ponto singular 'ξ', $J_\xi = \left.\frac{d\Gamma}{dr}\right|_\xi = 1$, resulta:

$$\lim_{\varepsilon\to 0}\left\{\int_{\varepsilon}^{r_a}\left[T_{ij}^d(\omega,\xi,\mathbf{x})\left|J_r\right|U_j(\omega,\mathbf{x}) - \frac{f_{ij}(\xi)_a}{r}\left|J_\xi\right|_a U_j(\omega,\xi)\right]dr +\right.$$

$$\int_{\varepsilon}^{r_d}\left[T_{ij}^{d}(\omega,\xi,\mathbf{x})|J_r|U_j(\omega,\mathbf{x})-\frac{f_{ij}(\xi)_d}{r}|J_\xi|_d\,U_j(\omega,\xi)\right]dr+$$

$$f_{ij}(\xi)_a|J_\xi|U_j(\omega,\xi)\int_{\varepsilon}^{r_a}\frac{1}{r}dr+f_{ij}(\xi)_d|J_\xi|U_j(\omega,\xi)\int_{\varepsilon}^{r_d}\frac{1}{r}dr\Bigg\} \qquad (16)$$

A expressão (16) pode ser avaliada segundo o senso clássico do cálculo diferencial e integral. Observando que o comportamento de $f_{ij}(\xi)$ antes e após o ponto fonte ξ (Veloso, 1995) são iguais a menos do sinal. Restabelecendo as integrais para a variável Γ e lembrando que $|J_r\|dr/d\Gamma|=1$, resulta a forma final para o cálculo do valor principal de Cauchy:

$$VP\int_{\Gamma_s}T_{ij}^{d}(\omega,\xi,x)U_j(\omega,x)d\Gamma=\int_{\Gamma_a}^{\Gamma_\xi}\left[T_{ij}^{d}(\omega,\xi,x)U_j(\omega,x)-\frac{1}{r}f_{ij}(\xi)_a\left|\frac{dr}{d\Gamma}\right|U_j(\omega,\xi)\right]d\Gamma+$$

$$\int_{\Gamma_\xi}^{\Gamma_b}\left[T_{ij}^{d}(\omega,\xi,x)U_j(\omega,x)-\frac{1}{r}f_{ij}(\xi)_d\left|\frac{dr}{d\Gamma}\right|U_j(\omega,\xi)\right]d\Gamma+f_{ij}(\xi)_a\log(r_a)U_j(\omega,\xi)+$$

$$f_{ij}(\xi)_d\,U_j(\omega,\xi)\log(r_d) \qquad ,\forall\, x\wedge\xi\in\Gamma_s=(\Gamma_a\cup\Gamma_d)\,,\ \omega\neq 0 \qquad (17)$$

Esta formulação permite o cálculo das integrais nos pontos onde aparece a singularidade e somente será válida se $f_{ij}(\xi_a)=-f_{ij}(\xi_d)$, caso esta condição não seja satisfeita, surge uma indeterminação decorrente de $\lim_{\varepsilon\to 0}[\ln(\varepsilon)]$(Veloso, 1995). Deve-se observar que, o valor do termo $\left(r_{,i}n_j-r_{,j}n_i\right)$ é possível ser interpretado como o valor escalar do produto vetorial $\mathbf{r}_u\times\mathbf{n}$, em torno do ponto nodal 'ξ'. Observa-se também que a expressão resultante (17) permite a avaliação do VPC bastando que esta expressão seja integrada numericamente. Os termos fora do sinal de integração são valores obtidos pela integração de $\frac{dr}{r}$, e $\mathbf{r}_a$ e $\mathbf{r}_d$ são as distâncias do ponto 'ξ' ao ponto extremo dos elementos Γ_a , Γ_d.

4. EXEMPLOS NUMÉRICOS

Nesta seção serão apresentados alguns exemplos numéricos aplicados à elastodinâmica bi-dimensional no domínio da freqüência, nos quais poderá ser verificada a eficácia da metodologia proposta.

Na implementação do programa os pontos de canto foram abordados como nós duplos ou com elementos descontínuos.

A expressão com singularidade fraca foi avaliada numericamente com a quadratura Guassiana com pesos logarítmicos. A integração numérica da parcela regularizada foi avaliada segundo a quadratura Gaussiana. A ordem de integração e o número de subdivisões do elemento vizinho ao ponto fonte foram estabelecidas segundo o critério de Lachat e Watson,

onde a ordem de integração e o número de subdivisões são obtidos automaticamente, através da relação entre a distância do ponto fonte ao ponto campo e o tamanho do elemento.

Placa quadrada sujeita a uma força harmônica

Neste exemplo foi resolvido o problema da placa quadrada de dimensões 0,3 m x 0,3 m de lado sujeita a uma força de $9{,}0\text{x}10^4$ na freqüência de 1.400 hz e com as seguintes características, constantes de Lamé: $\mu = 8{,}575\ 10^{10}\,\text{N}/\text{m}^2$, $\nu = 0{,}2$ e massa específica $\rho = 7{,}85\ 10^3\ \text{kg}/\text{m}^3$. Face à simetria do problema discretizou-se apenas 1/4 do domínio original da placa (figura 2) onde estão representadas as condições de contorno. A malha foi discretizada de tal forma que os elementos que contêm os pontos de canto são menores que os demais.

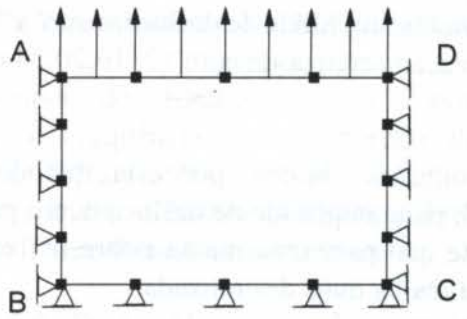

Figura 2 : ¼ da placa sujeita a um tensão de 9,0E04 sobre a borda AD na freqüência de 1,4 Khz.

A figura 3 mostra o comportamento da amplitude de deslocamento na direção 'y' da borda AB, com malhas de 12 e 24 elementos, para o esquema analítico proposto e implementado com elementos lineares e lineares descontínuos. Observa-se que para uma malha de 12 elementos os resultados estão muito próximo do método indireto (Lacerda, 1993).

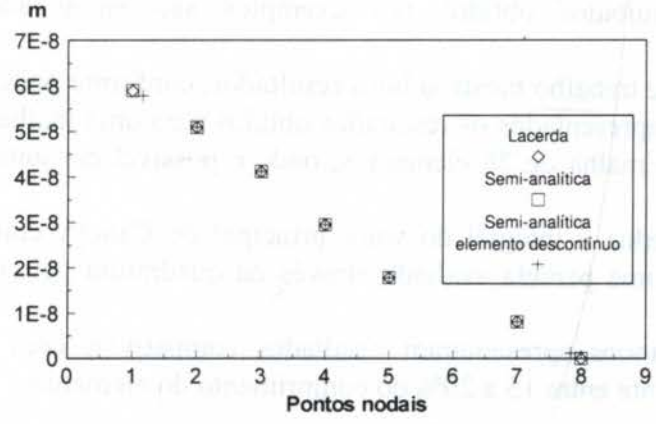

Figura 3: Amplitude de vibração na direção y na borda AB, placa discretizada com 24 elementos

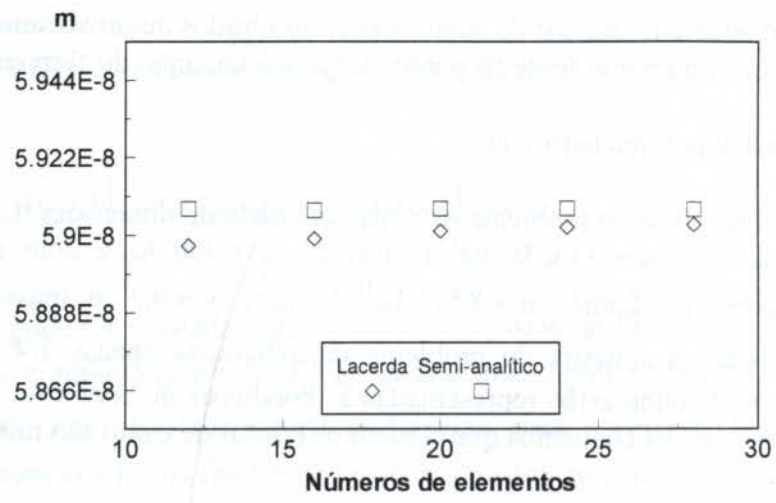

Figura 4: Comportamento da amplitude de deslocamento"y" com o grau de refinamento da malha, placadiscretiza-da com 12, 16,20,24 e 28 elementos.

A figura 4, mostra os resultados obtidos, por esta metodologia e a metodologia implementada por Lacerda, 1993, para amplitude de deslocamento para uma malha com 12 a 28 elementos lineares. Observa-se que para uma malha pobre os resultados não apresentam diferenças significativas para uma malha mais discretizada.

5. CONCLUSÃO

Neste trabalho, foi aplicado uma metodologia semi-analítica de integração singular, para análises de problemas de vibrações forçadas com o método dos elementos de contorno.

O desenvolvimento da metodologia que é apresentado para a formulação bi-dimensional, está fundamentada na avaliação analítica da parcela singular, e de uma parcela regular, calculada numericamente através da quadratura de Gauss. Este processo diferencia-se da metodologia até então utilizada, (veja por exemplo Lacerda, 1993) conhecida na literatura como metodologia indireta (Manolis, 1988).

Examinando os resultados obtidos nos exemplos são enumerados as seguintes proposições:

- O método utilizado neste trabalho mostrou bons resultados, conforme pode ser atestado pela figura 3. Na figura 4 são apresentados os resultados obtidos para uma malha de 12 elementos e os resultados para uma malha de 28 elementos, onde é possível constatar a convergência entre os dois métodos.
- O esquema proposto reduz a integral do valor principal de Cauchy como uma soma de termos regulares, sendo uma parcela avaliada através da quadratura gaussiana e a segunda integrada analiticamente.
- Os Elementos descontínuos apresentaram resultados compatíveis com o esperado para deslocamento do ponto fonte entre 15 a 20% do comprimento do elemento.

6. REFERÊNCIAS

AHMAD, S. E MANOLIS, G. D., "Dynamic Analysis of 3-D structures by a Transformed Boundary Element Method", Comput. Mech., 2, 185-196, (1987).

ALIABADI, M. H., HALL, W. S. E PHEMISTER, W. S.,"Taylor Expansions for Singular Kernels in Boundary Element Methods", Int. J. Num. Meth. Engg., 21, 2221-2236, (1985)

BREBBIA, C. A. E DOMINGUEZ, J., "Boundary Element Method - An Introdutory Course", McGraw Hill Book Co., (1989).

DOMINGUEZ, J. E ABASCAL, R., "On Fundamental Solutions for The Boundary Integral Equations Method in Static and Dynamic Elasticity", Engg. Analysis with Boundary Elements 1, 3, 128-134, (1984).

GUIGGIANI, M, E CASALINI, PAOLO, "Direct Computation of Cauchy Principal Value Integrals in Advanced Boundary Elements", Int. J. Num. Meths. in Engg., 24, 1711-1720, (1987)

GUIGGIANI, M, E GIGANTE, A., "A General Algorithm for Multidimensional Cauchy Principal Value Integrals in Boundary Element Method", Trans. ASME, J. Appl. Mech., 57, 906-915, (1990).

KUTT, H. R., "On the Numerical Evaluation of Finite Part Integrals Involving an Algebraic Singularity", The National Research Institute for Mathematical Sciences,Report Wisk 179, Pretória, (1975).

LACERDA, A., O., "O Método dos Elementos de Contorno para Elastodinâmica Bi-dimensional no Domínio da Freqüência com Emprego de Elementos Quadráticos", Dissertação de M. Sc., COPPE-UFRJ, (1993).

LACHAT, J. C. E WATSON, J. O., "Effective Numerical Treatment of Boundary Integral Equations : A Formulation for Three-dimensional Elastostatics", Int. J. Num. Meth. Engg., 10, 991-1005, (1976).

MANOLIS, G. D. E BESKOS, D. E., "Boundary Element Methods in Elastodynamics", Unwin Hyman, London, (1988)

VELOSO, M. J. G, "Um Algoritmo para Integração Singular e Quase-singular no Metódo dos Elementos de Contornó aplicado à Elastodinâmica Bidimensional no Domínio da Freqüência", Dissertação de M.Sc., COPPE-UFRJ, (1995)

Tema 44

Método de Diferenças Finitas

XIV Brazilian Congress of Mechanical Engineering
Obeid Plaza Hotel Convention Center - Bauru - SP/Brazil
December 08-12th 1997

PAPER CODE: COB1018

ANÁLISE DO DESEMPENHO DE DIFERENTES MÉTODOS PARA CALCULAR GRADIENTES EM MALHAS NÃO ESTRUTURADAS DE VORONOI / *ANALYSIS OF PERFORMANCE OF DIFFERENTS METHODS TO CALCULATE GRADIENTS IN VORONOI UNSTRUCTURED MESH*

VIVIANA COCCO MARIANI & SÉRGIO PETERS
Departamento de Informática e Estatistica, Universidade Federal de Santa Catarina - UFSC - Florianópolis
CEP 88040-900 Florianópolis, Brasil - E-mail: viviana@inf.ufsc.br, peters@inf.ufsc.br

Abstract

This paper presents an investigation on the solution of the linear systems arising from the numerical discretization of the Navier-Stokes equations through Voronoi grids. Three techniques are utilized and compared for evaluation of the pressure gradients: the minimum squared residue, the weighted mean between the projected normal gradients (MPGNP) and the modified weighted mean between the projected normal gradients, through a modification of the MPGNP. They are validated, adoting for the case of the incompressible flow in square cavity with sliding upper wall (driven cavity) with slide upper wall. All numerical results are obtained in distinct geometrical grids.

Keywords

Navier-Stokes, Voronoi grids, pressure gradients / Navier-Stokes, diagramas de Voronoi, gradientes de pressão.

1. INTRODUÇÃO

Os Diagramas de Voronoi (DV) vem se destacando em simulações numéricas de fenômenos físicos, dadas as suas características de construção, permitindo que fluxos sejam facilmente aproximados nas fronteiras dos volumes de controle. Além de permitir refinamentos localizados em regiões de interesse. O uso do método dos volumes finitos (MVF) em malhas estruturadas é tradicional na mecânica dos fluidos (Patankar, 1980), enquanto o uso em malhas não-estruturadas é mais recente (Taniguchi *et al.*, 1991; Marcondes *et al.*, 1995; Cardoso, 1997; Mariani & Peters, 1997).

Presentemente propõe-se a solução numérica das equações de Navier-Stokes para escoamento de fluidos pelo MVF, utilizando-se malhas não-estruturadas geradas por DV. As malhas não-estruturadas geradas por DV, dão origem a volumes de controle cujas faces são sempre ortogonais aos segmentos de ligação entre o ponto nodal gerador de cada volume de controle, e os pontos nodais dos volumes vizinhos. Esta característica, por sua vez, simplifica as aproximações numéricas existentes, facilitando a realização dos balanços conservativos sobre cada volume.

Na discretização dos termos fontes, das equações de Navier-Stokes, são necessárias avaliações dos gradientes de pressão nos pontos nodais centrais de cada volume de controle. Presentemente são analisadas três formas distintas de cálculo: o mínimo resíduo quadrático (MRQ) proposto por Taniguchi *et al.* (1991), a média ponderada entre os gradientes normais projetados (MPGNP) proposta por Cardoso (1997) e a média ponderada modificada entre os

gradientes normais projetados (MPMGNP), proposta neste trabalho, efetuando-se uma mudança no MPGNP.

Para validação dos esquemas numéricos promove-se a simulação, em diferentes formatos de malha, do escoamento laminar incompressível em uma cavidade quadrada de profundidade infinita, sujeita a uma parede superior deslizante (Ghia *et al.*, 1982). Os resultados são coletados em malhas de volumes retangulares, hexagonais e aleatórios com diferentes níveis de refino, usando diferentes combinações do número de iterações internas na resolução do sistema de correção da pressão. Para a resolução dos sistemas de equações discretizadas utilizou-se o método iterativo Gradiente Conjugado.

2. DISCRETIZAÇÃO

No presente trabalho as equações da conservação da massa e de conservação da quantidade de movimento são escritas em termos da variável genérica ϕ, onde ϕ assume os valores 1, u e v, sendo u e v as componentes horizontal e vertical da velocidade, conforme a equação (1). A aplicação do MVF à equação (1) é mais simples quando se trabalha com a forma divergente do fluxo advectivo e difusivo associados ($\vec{J}$). Integrando-se a equação (1) no volume de controle definido pelo DV da figura 1, onde $\mathbf{V}$ é o volume de integração para cada volume de controle, tem-se:

$$\underbrace{\int_V \frac{\partial(\rho\phi)}{\partial t}\, d\mathbf{V}}_{(a)} + \underbrace{\int_V \left(\vec{\nabla}.\vec{J}\right) d\mathbf{V}}_{(b)} = \underbrace{\int_V S^{\phi} d\mathbf{V}}_{(c)} \qquad (1)$$

$$\vec{J} = \rho\vec{V}\phi - \Gamma^{\phi}\vec{\nabla}\phi \qquad (2)$$

onde ρ é a massa específica do fluído, S indica um termo fonte por unidade de volume, $\vec{J}$ é o fluxo total de ϕ e $\vec{V}$ é o vetor velocidade.

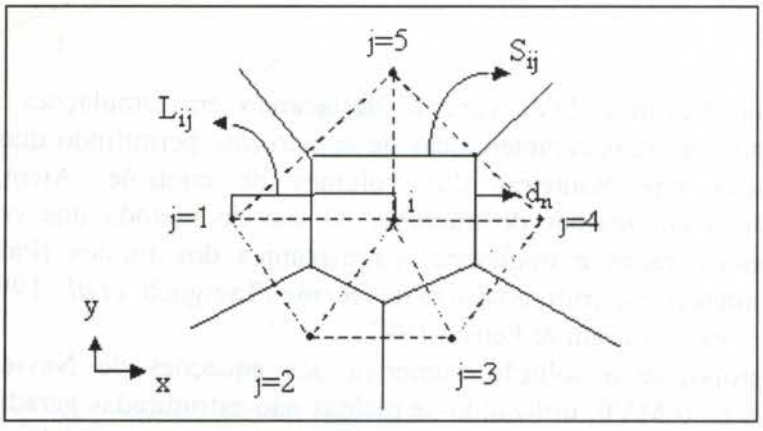

Figura 1: Volume de controle elementar para o diagrama de Voronoi.

Na figura 1 a triangulação, identificada pelas linhas pontilhadas, representam o dual do DV, conhecida como Triangulação de Delaunay. O procedimento de integração numérica da equação (1) pode ser encontrado em Cardoso (1997), e é realizado genericamente no volume de controle do DV, segundo princípios do MVF. Trata-se de uma integração análoga àquela implementada para malha estruturada com variáveis colocalizadas, adotando o esquema lei da Potência (Patankar, 1980) de interpolação das variáveis nas faces.

Na integração do termo fonte S^{ϕ} surge a necessidade de avaliação do gradiente da pressão no centro do volume de controle i para as equações de conservação da quantidade de movimento, que será descrito a seguir.

3. AVALIAÇÃO DOS GRADIENTES DE PRESSÃO

O vetor gradiente de pressão ($\vec{\nabla} p_i$) deve ser avaliado sobre cada ponto nodal central do domínio, através de suas componentes ∇p_x e ∇p_y ,

$$\vec{\nabla} p_i = \nabla p_x \hat{i} + \nabla p_y \hat{j} \tag{3}$$

Estão disponíveis apenas as componentes do gradiente nas direções normais $(\nabla p)_{ij}$ a cada face, dos volumes de controle avaliadas sobre estas faces e não no ponto central do volume de controle ($\vec{\nabla} p_i$).

$$(\nabla p)_{ij} = \frac{p_j - p_i}{L_{ij}} \tag{4}$$

onde p_i é a pressão avaliada no ponto central i e p_j é a pressão avaliada nos pontos j vizinhos de i. No presente trabalho experimentou-se três formas diferenciadas para o cálculo dos gradientes de pressão na direção x e y.

3.1 Mínimo resíduo quadrático

Existe uma diferença $(\delta p)_{ij}$ entre a avaliação do gradiente de pressão normal sobre cada interface ij e a projeção do gradiente na direção normal $\hat{n}_{ij}$, avaliado sobre o ponto nodal central. Esta diferença é dada por:

$$(\delta p)_{ij} = (\nabla p)_{ij} - (\vec{\nabla} p_i).\hat{n}_{ij} \tag{5}$$

Conforme Taniguchi *et al.*(1991), é proposta uma função global ψ_i de minimização das diferenças δp_{ij}, entre todos os vizinhos j,

$$\Psi_i = \sum_{j=1}^{NV} (g_{ij} \delta p_{ij} \delta p_{ij}) \tag{6}$$

onde g_{ij} é um fator peso de ponderação da influência de cada face sobre o gradiente normal. Neste caso, adota-se g_{ij} como sendo proporcional ao ângulo de visão de cada face *ij* em relação ao ponto central *i*. Este valor é equivalente a razão entre a área de passagem S_{ij} e a distância L_{ij},

$$g_{ij} = \frac{S_{ij}}{L_{ij}} \tag{7}$$

Substituindo a equação (3), (4) e (5) na equação (6), obtém-se

$$\Psi_i = \sum_{j=1}^{nv} \left\{ g_{ij} \left[(\nabla p)_{ij} - \left(\nabla p_x \hat{i} + \nabla p_y \hat{j} \right) \hat{n}_{ij} \right]^2 \right\} \tag{8}$$

como

$$\hat{n}_{ij} = e_{x_{ij}} \hat{i} + e_{y_{ij}} \hat{j} \tag{9}$$

tem-se,

$$\Psi_i = \sum_{j=1}^{NV} \left\{ g_{ij} \left[(\nabla p)_{ij} - \left(\nabla p_x e_{x_{ij}} + \nabla p_y e_{y_{ij}} \right) \right]^2 \right\} \tag{10}$$

Fazendo-se uma minimização de Ψ_i em função de cada componente do vetor gradiente de pressão, $\left(\vec{\nabla} p_x\right)_i$ e $\left(\vec{\nabla} p_y\right)_i$, obtém-se duas equações lineares para duas variáveis. Resolvendo-se o sistema, para estas duas variáveis tem-se:

$$\nabla p_x = \frac{\left[\sum_{j=1}^{NV} \left[g_{ij} \nabla p_{ij} e_{x_{ij}} \right] \right] \left[\sum_{j=1}^{NV} g_{ij} \left(e_{y_{ij}} \right)^2 \right] - \left[\sum_{j=1}^{NV} g_{ij} \left(e_{y_{ij}} e_{x_{ij}} \right) \right] \left[\sum_{j=1}^{NV} \left[g_{ij} \nabla p_{ij} e_{y_{ij}} \right] \right]}{\left[\sum_{j=1}^{NV} g_{ij} (e_{x_{ij}})^2 \right] \left[\sum_{j=1}^{NV} g_{ij} \left(e_{y_{ij}} \right)^2 \right] - \left[\sum_{j=1}^{NV} g_{ij} (e_{x_{ij}} e_{y_{ij}}) \right]^2} \tag{11}$$

$$\nabla p_y = \frac{\left[\sum_{j=1}^{NV} \left[g_{ij} \nabla p_{ij} e_{y_{ij}} \right] \right] \left[\sum_{j=1}^{NV} g_{ij} \left(e_{x_{ij}} \right)^2 \right] - \left[\sum_{j=1}^{NV} g_{ij} \left(e_{x_{ij}} e_{y_{ij}} \right) \right] \left[\sum_{j=1}^{NV} \left[g_{ij} \nabla p_{ij} e_{x_{ij}} \right] \right]}{\left[\sum_{j=1}^{NV} g_{ij} (e_{x_{ij}})^2 \right] \left[\sum_{j=1}^{NV} g_{ij} \left(e_{y_{ij}} \right)^2 \right] - \left[\sum_{j=1}^{NV} g_{ij} (e_{x_{ij}} e_{y_{ij}}) \right]^2} \tag{12}$$

Nesta avaliação foram consideradas apenas as contribuições das pressões internas ao domínio geométrico, sem considerar o campo de pressão sobre o contorno geométrico, que nesta formulação do MVF é avaliado através de extrapolação dos pontos internos.

3.2 Média ponderada entre os gradientes normais projetados

Uma das idéias mais simples para avaliação do gradiente de pressão é considerar as contribuições de cada componente normal nas faces, desta forma, o gradiente de pressão pode ser obtido por médias ponderadas de seus componentes sobre cada face. Assim,

$$\nabla p_x = \frac{\sum_{j=1}^{NV} \left[\left(\vec{\nabla} p_{ij} . \hat{i} \right) L_{ij} \right]}{\sum_{j=1}^{NV} L_{ij}} \quad \text{e} \quad \nabla p_y = \frac{\sum_{j=1}^{NV} \left[\left(\vec{\nabla} p_{ij} . \hat{j} \right) L_{ij} \right]}{\sum_{j=1}^{NV} L_{ij}} \tag{13}$$

onde $\vec{\nabla} p_{ij}$ é o vetor gradiente de pressão normal à interface *ij*, calculado por:

$$\vec{\nabla} p_{ij} = \left(\frac{p_j - p_i}{L_{ij}} \right) . \hat{n}_{ij} = \left(\frac{p_j - p_i}{L_{ij}} \right) . \left(e_{x_{ij}} \hat{i} + e_{y_{ij}} \hat{j} \right) \tag{14}$$

A equação (13) é uma proposta da primeira versão do livro de Maliska (1995), o qual verificou posteriormente que esta proposta não era genérica, sugerindo uma forma de avaliação mais eficiente. Contudo, esta expressão permitiu que Cardoso (1997) fizesse uma reflexão sobre as mesmas, propondo, que se considerassem apenas as influências das distâncias L_{ij} projetadas nas

direções das componentes avaliando o gradiente de pressão. Verifica-se que as projeções de L_{ij} em y nada acrescentam ao cálculo do gradiente de pressão na direção x. Propôs-se, então, que para o cálculo do gradiente de pressão na direção x fosse considerado apenas as distâncias L_{ij} projetadas em x e de forma análoga para o gradiente de pressão y, conforme segue:

$$\nabla p_x = \frac{\sum_{j=1}^{NV}\left[\left(\vec{\nabla} p_{ij}.\hat{i}\right)L_{ij}\right]}{\sum_{j=1}^{NV}\left(L_{ij}\left|e_{x_{ij}}\right|\right)} \quad \text{e} \quad \nabla p_y = \frac{\sum_{j=1}^{NV}\left[\left(\vec{\nabla} p_{ij}.\hat{j}\right)L_{ij}\right]}{\sum_{j=1}^{NV}\left(L_{ij}\left|e_{y_{ij}}\right|\right)} \tag{15}$$

Este cálculo do gradiente de pressão é denominado média ponderada entre os gradientes normais projetados (MPGNP). Tratamento especial foi dispensado aos pontos nodais ligados às fronteiras do domínio, considerando-se apenas as contribuições do campo de pressão interno, pois as pressões sobre as fronteiras não apresentam informações novas ao gradiente do ponto nodal.

3.3 Média ponderada modificada entre os gradientes normais projetados

Neste trabalho propõe-se uma modificação no gradiente de pressão apresentado por Cardoso (1997). O método denominado média ponderada modificada entre os gradientes normais projetados (MPMGNP), utiliza o mesmo fator peso apresentado por Taniguchi (1991), na equação (16), como fator de ponderação da influência de cada gradiente normal $\vec{\nabla} p_{ij}$, conforme as equações,

$$\nabla p_x = \frac{\sum_{j=1}^{NV}\left[\left(\vec{\nabla} p_{ij}.\hat{i}\right)g_{ij}\right]}{\sum_{j=1}^{NV}\left(g_{ij}\left|e_{x_{ij}}\right|\right)} \quad \text{e} \quad \nabla p_y = \frac{\sum_{j=1}^{NV}\left[\left(\vec{\nabla} p_{ij}.\hat{j}\right)g_{ij}\right]}{\sum_{j=1}^{NV}\left(g_{ij}\left|e_{y_{ij}}\right|\right)} \tag{16}$$

No presente trabalho objetiva-se avaliar esta nova proposta, analisando a sua performance frente aos métodos anteriormente apresentados. Obtidas numericamente as duas componentes do gradiente de pressão, por algum método, pode-se avaliar as componentes de velocidade u e v a partir de um campo inicial u^*, v^* e p^*.

4. ACOPLAMENTO PRESSÃO-VELOCIDADES

Os sistemas resultantes da discretização das equações de Navier-Stokes, são apresentados nas equações que seguem,

$$AP_i u_i = \sum_{j=1}^{NV}\left(A_{ij}u_j\right) + b_i^u - \Delta \boldsymbol{V}_i.\nabla p_x \tag{17}$$

$$AP_i v_i = \sum_{j=1}^{NV}\left(A_{ij}v_j\right) + b_i^v - \Delta \boldsymbol{V}_i.\nabla p_y \tag{18}$$

$$AP_i p_i' = \sum_{j=1}^{NV} A_{ij}p_j' - \sum_{j=1}^{NV}\rho_{ij}w_{ij}^* S_{ij} \tag{19}$$

onde $p_i = p_i^* + p_i'$

Tais sistemas sistemas para o cálculo das velocidades u, v e correção da pressão são resolvidas de maneira segregada para cada uma das variáveis. Para avaliar o campo de pressão, p, adota-se um acoplamento entre pressão e velocidades, presentemente é usado o esquema SIMPLEC, isto é, o SIMPLE consistente, modificado para malhas co-localizadas. A idéia principal do método é encontrar um campo de pressão que satisfaça a equação da conservação da massa. Maiores detalhes sobre a discretização numérica podem ser encontrados em Maliska (1995), Peters (1996) e Cardoso (1997).

5. RESULTADOS E DISCUSSÕES

Para avaliar os métodos de cálculo propostos para os gradientes de pressão é utilizado o escoamento bidimensional em uma cavidade de seção quadrada, sujeita a uma parede superior deslizante, semelhante a uma esteira. A especificação da cavidade quadrada, juntamente com as condições de contorno são apresentadas na figura 2.

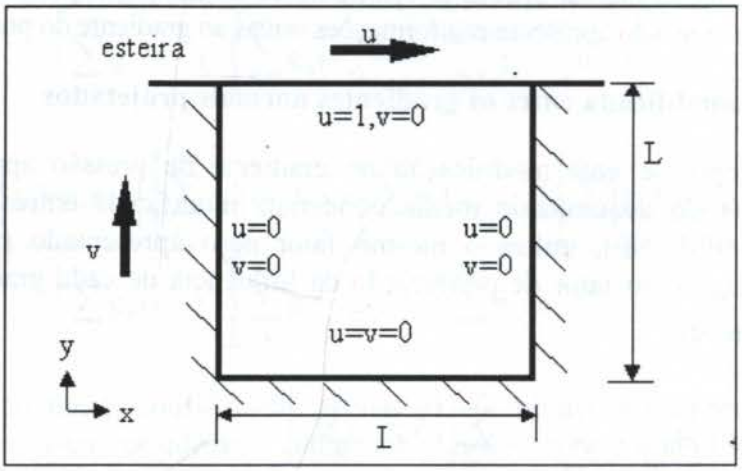

Figura 2: Cavidade quadrada com parede superior deslizante e condições de contorno.

As malhas utilizadas são formadas por 50x49 e 80x80 pontos com disposição hexagonal, 37x37 pontos com disposição retangular e a malha aleatória formada por 530 volumes de controle, conforme apresentado na figura 3.

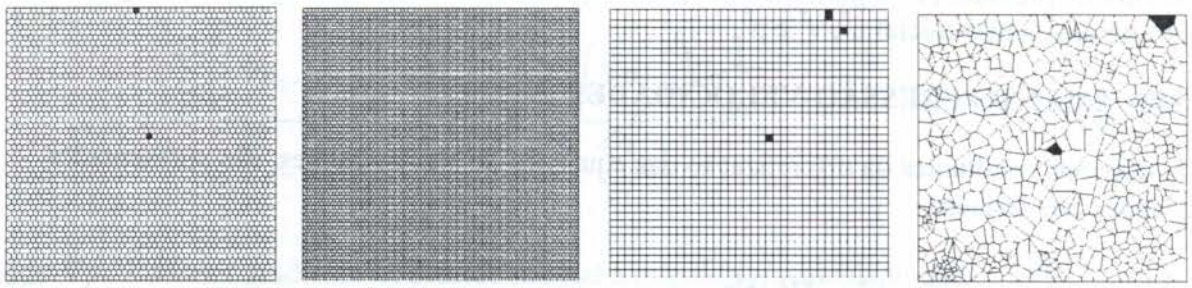

Figura 3: Malhas geradas por Diagramas de Voronoi.

A velocidade de convergência, do método Gradiente Conjugado (GC) (Hestenes & Stiefel, 1952) utilizado para a resolução dos sistemas, está relacionada ao fator de relaxação ω empregado e, ao número de vezes em que cada uma das variáveis são resolvidas durante cada iteração. O fator de subrelaxação ω é necessário no processo iterativo de resolução dos sistemas para u e v, devido às linearizações efetuadas nas equações de conservação da quantidade de movimento. O fator utilizado neste trabalho é ω=0,5.

A tabela 1 apresenta os resultados obtidos utilizando o GC, avaliados com Reynolds 100, cujos gradientes de pressão são calculados com MRQ, MPGNP e MPMGNP. Os sistemas são resolvidos por um laço iterativo interno, formado por duas iterações para as variáveis u e v e três iterações para a correção da pressão. A convergência é estabelecida pela equação (20),

$$\text{erro} = |F_{ij}| < \xi \qquad (20)$$

sendo $\xi = 10^{-4}$, e F_{ij} é o resíduo da conservação da massa. Os resultados deste trabalho foram obtidos no "sp2", disponível no Núcleo de Processamento de Dados da UFSC.

Tabela 1: Desempenho do GC utilizando o MRQ, MPGNP e MPMGNP (tempo = minutos).

Malhas / dimensões	MRQ		MPGNP		MPMGNP	
	iterações	tempo	iterações	tempo	iterações	tempo
hexagonal (50x49)	614	19,35	515	20,12	402	21,36
hexagonal (80x80)	1137	23,28	nc	-	1408	32,57
retangular (37x37)	352	8,32	340	9,27	334	9,32
aleatória (530 pts.)	1497	32,41	nc	-	3538	65,47

Com os resultados da tabela 1 nota-se que o MRQ apesar de algumas vezes necessitar de maior número de iterações para convergir apresenta o menor tempo de processamento em todas as malhas adotadas, o MPGNP e MPMGNP possuem resultados semelhantes quanto a tempo de processamento e número de iterações necessárias para alcançar a convergência. Na malha aleatória o MPGNP não convergiu e o MRQ e MPMGNP necessitaram maior tempo de processamento e número de iterações para convergir.

Na tabela 2 apresenta-se os valores obtidos utilizando as diferentes formas de avaliação do gradiente, para os volumes identificados nas malhas da figura 3. Escolheu-se dois pontos nodais um localizado na região central da cavidade quadrada e outro em um ponto localizado próximo ao contorno da parede deslizante.

Tabela 2: Avaliação das componentes dos gradientes de pressão na direção x e y.

Malhas/ Gradientes de Pressão		MRQ	MPGNP	MPMGNP
retangular (37x37)	∇Px_{725}	0,002906	0,002476	0,002914
	∇Py_{725}	-0,016825	-0,015636	-0,016243
	∇Px_{1362}	0.080579	0.080116	0,080379
	∇Py_{1362}	0,003113	0,003161	0,003123
hexagonal (50x49)	∇Px_{1314}	0,003364	-0,015103	0,002787
	∇Py_{1314}	-0,012030	-0,01300	-0,013937
	∇Px_{2450}	-0.010256	-0,009673	-0,011828
	∇Py_{2450}	0,006295	0,006532	0,006510
aleatória (530 pts.)	∇Px_{511}	0.008548	-	0.011881
	∇Py_{511}	-0.002521	-	-0.003132
	∇Px_{238}	0,037540	-	0,039696
	∇Py_{238}	-0,015307	-	-0,019583

Na tabela 2 observa-se que os valores encontrados com o MPMGNP são semelhantes aos valores obtidos com o MRQ, enquanto o MPGNP apresenta valores sensivelmente diferentes.

6. CONCLUSÕES

O presente trabalho apresentou e analisou algumas expressões usadas no cálculo dos gradientes de pressão. Entre estas expressões, propôs-se a MPMGNP, visando avaliar adequadamente os gradientes nos pontos nodais centrais. A MPMGNP utiliza a influência entre os gradientes normais de cada face, calculada pela ponderação com o ângulo de visão de cada face, traduzida pela razão entre a superfície de contato e a distância entre cada ponto nodal e seu vizinho, tal ponderação parece fisicamente mais consistente. Contudo, não pretendeu-se com isto cobrir todas as alternativas de avaliações dos gradientes de pressão, encontrados na literatura, nem mesmo dar uma comparação que permita a escolha da melhor avaliação, mas o que objetivou-se foi expor algumas alternativas de tal forma que o leitor possa escolher o caminho que pretende seguir, a fim de solucionar os seus problemas de interesse. Os resultados encontrados, até o momento, não evidenciam a preferência por um ou outro tipo de avaliação dos gradientes de pressão, apenas indicam alguns tipos que podem ser utilizados.

7. REFERÊNCIAS

Aurenhammer, F. Voronoi Diagrams - A Survey of a Fundamental Geometric Data Structure, *ACM Computing Surveys*, vol.23, no.3, 1991.

Cardoso, F.C. Algoritmo para Simulação Numérica das Equações do Movimento pelo Método dos Volumes Finitos usando Diagramas de Voronoi, Dissertação de Mestrado, Universidade Federal de Santa Catarina, Florianópolis, 1997.

Ghia, U., Ghia, K.N. & Shin, C.T. High-Re Solutions for Incompressible Flow Using the Navier-Stokes Equations and Multigrid Method, *Journal of Computational Physics*, vol.48, pp.387-411, 1982.

Hestenes, M.R. & Stiefel, E. Methods of Conjugate Gradients for Solving Linear Systems, *J. Res. Natn. Bur. Standards* 49, pp.409-436, 1952.

Maliska, C.R. *Transferência de Calor e Mecânica dos Fluidos Computacional*, Livros Técnicos e Científicos Editora, Rio de Janeiro, 1995.

Marcondes, F., Zambaldi, M.C. & Maliska, C.R. Comparação de Métodos Iterativos Não Estacionários em Malhas Não Estruturadas na Solução de Problemas de Petróleo, *COBEM-CIDIM*, 1995.

Mariani, V.C. & Peters, S. Analysis of Performance of Iterative Methods for Solution of the Heat Conduction Problem in Voronoi Unstructured Mesh, *III International Congress on Information Engineering*, pp.476-485, Buenos Aires, 1997.

Mariani, V.C., Resolução de Sistemas Lineares Gerados na discretização das Equações de Navier-Stokes em Malhas de Voronoi, Dissertação de Mestrado, Universidade Federal de Santa Catarina, Florianópolis, 1997.

Patankar, S.V. *Numerical Heat Transfer and Fluid Flow*, McGraw-Hill, 1980.

Taniguchi, N., Arakawa, C. & Kobayashi, T., Construction of a Flow-Simulating Method with Finite Volume Based on a Voronoi Diagram, *JSME International Journal*, vol.34, pp.18-23, 1991.

Tanyi, B.A. & Thatcher, R.W. Iterative Solution of the Incompressible Navier-Stokes Equations on the Meiko Computing Surface, *International Journal for Numerical Methods in Fluids*, vol.22, pp.225-240, 1996.

XIV Brazilian Congress of Mechanical Engineering
Obeid Plaza Hotel Convention Center - Bauru - SP/Brazil
December 08-12th 1997

PAPER CODE: COB298

FORMULAÇÃO BIDIMENSIONAL GERAL PARA PROBLEMAS INVERSOS DE CONDUÇÃO DE CALOR / A GENERAL TWO-DIMENSIONAL FORMULATION FOR INVERSE HEAT CONDUCTION PROBLEMS

J. P. Alencar Jr. and H. R. B. Orlande
DEM/PEM-EE/COPPE - UFRJ
Cid. Universitária, Cx. Postal: 68503
Rio de Janeiro, RJ, 21945-970, Brasil

M. N. Ozisik
Dept. of Mechanical Engineering. - NCSU
PO. Box: 7910
Raleigh, NC 27695-7910, USA

Abstract

In this paper we present a general solution for two-dimensional boundary inverse heat conduction problems, by using the *conjugate gradient method of minimization* together with an *elliptic scheme of numerical grid generation*. The direct problem, as well as other auxiliary problems, are formulated in terms of generalized coordinates in a computational domain, where they are solved by finite-differences over a rectangular region. Simulated measurements are used to illustrate the application of the present approach with a practical inverse problem of engineering interest.

Keywords

Boundary Inverse Problem, Conjugate Gradient Method, Function Estimation, Numerical Grid Generation, Generalized Coordinates.

1. INTRODUCTION

A Direct Heat Conduction Problem involves the determination of the temperature field of a body when the physical properties, boundary and initial conditions, heat-source terms, and the body geometry are all accurately known. An *Inverse Heat Conduction Problem*, on the other hand, is concerned with the estimation of at least one of the quantities listed above, by using temperature and/or heat flux measurements taken at appropriate locations of the body.

The *Conjugate Gradient Method* is a powerful technique based on the iterative regularization approach, which can be applied to the solution of linear and nonlinear inverse problems, as well as to the estimation of parameters or functions. It has been successfully applied in the recent past to the solution of various inverse heat transfer problems (Alifanov, 1994, Jarny et al, 1991, Bokar and Ozisik, 1995, Orlande and Ozisik, 1993, Dantas and Orlande, 1996, Machado and Orlande, 1997).

Generally, the solution of an inverse heat transfer problem requires the solution of the associated direct problem. The recent development of numerical grid generation has provided finite-difference methods with the geometrical capabilities of treating irregular geometries of

the finite-element method, while maintaining their intrinsic simplicity of discretization (Thompson et al, 1985, Ozisik, 1994, Maliska, 1995).

In this paper, we solve the inverse problem of estimating the timewise variation of the heat flux applied on part of the boundary of a general irregular two-dimensional region, by using the *conjugate gradient method with adjoint equation*. The irregular two dimensional region in the physical domain is transformed into a rectangle in the computational domain, by using an elliptic scheme of numerical grid generation (Thompson et al, 1985, Ozisik, 1994, Maliska, 1995). The present formulation is sufficiently general and can be applied for the estimation of the heat flux on part of the irregular boundary of any two-dimensional region that can be transformed into a rectangle, as described next.

2. DIRECT PROBLEM

The physical problem considered here involves the linear heat conduction in a two-dimensional general region, in the Cartesian coordinates system (x,y). The initial temperature distribution in the region is F(x,y). For times t>0, the boundary of the region is subjected to a second kind boundary condition. The mathematical formulation of this problem, in terms of the generalized coordinates (ξ,η) in the computational domain, is given as (Thompson et al, 1985, Ozisik, 1994, Maliska, 1995):

$$\frac{1}{\alpha_t}\frac{\partial}{\partial t}T(\xi,\eta,t)=\frac{1}{J^2}\left(\alpha T_{\xi\xi}-2\beta T_{\eta\xi}+\gamma T_{\eta\eta}\right)+\left(PT_{\xi}+QT_{\eta}\right)$$

$$\text{in } 1<\xi<M,\ 1<\eta<N \quad \text{, for } t>0 \tag{1.a}$$

$$\frac{k_t}{J\sqrt{\alpha}}\left(\beta T_{\eta}-\alpha T_{\xi}\right)=q_1(t) \qquad \text{at } \xi=1 \ ,\ 1<\eta<\mathrm{N} \quad \text{, for } t>0 \tag{1.b}$$

$$\frac{k_t}{J\sqrt{\gamma}}\left(\beta T_{\xi}-\gamma T_{\eta}\right)=q_2(t) \qquad \text{at } \eta=1 \ ,\ 1<\xi<\mathrm{M} \quad \text{, for } t>0 \tag{1.c}$$

$$\frac{k_t}{J\sqrt{\alpha}}\left(\alpha T_{\xi}-\beta T_{\eta}\right)=q_3(t) \qquad \text{at } \xi=M \ ,\ 1<\eta<N \quad \text{, for } t>0 \tag{1.d}$$

$$\frac{k_t}{J\sqrt{\gamma}}\left(\gamma T_{\eta}-\beta T_{\xi}\right)=q_4(t) \qquad \text{at } \eta=N \ ,\ 1<\xi<M \quad \text{, for } t>0 \tag{1.e}$$

$$T(\xi,\eta,0)=F^{*}(\xi,\eta) \qquad \text{for } t=0 \quad \text{, in } 1<\xi<M,\ 1<\eta<N \tag{1.f}$$

where α_t and k_t are the thermal diffusivity and conductivity, respectively, and the subscripts ξ and η above denote partial derivatives. The functions $P(\xi,\eta)$ and $Q(\xi,\eta)$ can be used to control the grid spacing. The coefficients α, β, γ and the Jacobian J are defined as

$$\alpha=x_{\eta}^2+y_{\eta}^2 \ , \ \beta=x_{\xi}x_{\eta}+y_{\xi}y_{\eta} \ , \ \gamma=x_{\xi}^2+y_{\xi}^2 \ , \ J=x_{\xi}y_{\eta}-y_{\xi}x_{\eta} \tag{2.a-d}$$

The irregular region in the physical domain (x,y) is transformed into a rectangle in the computational domain (ξ,η), as shown in Fig. 1, by using Thompson's scheme of numerical grid generation(Thompson et al, 1985, Ozisik, 1994, Maliska, 1995).

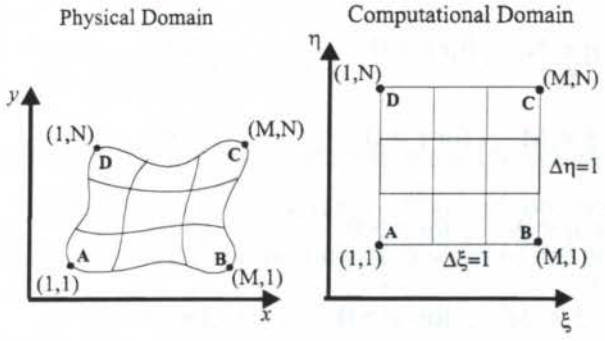

Fig. 1: Physical and computational domains

For the *Direct Problem,* the thermophysical properties α_t and k_t , the initial condition $F^*(\xi,\eta)$, the heat fluxes $q_1(t)$, $q_2(t)$, $q_3(t)$ and $q_4(t)$ applied on the boundary of the region, as well as the transformation from the physical domain into the computational domain, defined by α, β, γ, J, $P(\xi,\eta)$ and $Q(\xi,\eta)$, are considered known. The direct problem is concerned with the determination of the temperature field $T(\xi,\eta,t)$ in the region.

3. INVERSE PROBLEM

For the inverse problem considered here, the heat flux $q_3(t)$ at the boundary ξ=M is regarded as unknown, while all the other quantities appearing in Eqs.(1) are assumed to be known with sufficient degree of accuracy. The heat flux $q_3(t)$ is to be estimated by using the transient readings of S temperature sensors located at the positions (ξ_s,η_s), s=1,...,S, during the time interval $0 < t < t_f$. The present inverse problem is solved as a function estimation approach, that is, no information regarding the functional form of the unknown is considered available for the inverse analysis, except that it belongs to the Hilbert space L_2 in $0 < t < t_f$ (Alifanov, 1994). The ill-posed inverse problem stated above is re-formulated as a well-posed minimization problem. Hence, an estimation for the function $q_3(t)$ is obtained by minimizing the following functional

$$L[q_3(t)] = \frac{1}{2}\int_{t=0}^{t_f} \sum_{s=1}^{S} \left[T(\xi_s,\eta_s,t;q_3) - Y_s(t)\right]^2 dt \qquad (3)$$

where $Y_s(t)$ and $T(\xi_s,\eta_s,t;q_3)$ are the measured and estimated temperatures at the measurement positions (ξ_s,η_s), s=1,...,S. The estimated temperatures are obtained from the solution of the direct problem (1) by using an estimate for the heat flux $q_3(t)$.

In order to apply the conjugate gradient method of minimization, we need to develop two auxiliary problems known as the *sensitivity* and *adjoint problems*, as described next.

4. SENSITIVITY PROBLEM

In order to develop the sensitivity problem, we assume that the temperature $T(\xi,\eta,t)$ undergoes a variation $\Delta T(\xi,\eta,t)$, when the unknown boundary heat flux $q_3(t)$ undergoes a variation $\Delta q_3(t)$. By substituting into the direct problem given by Eqs. (1), $T(\xi,\eta,t)$ by $[T(\xi,\eta,t)+\Delta T(\xi,\eta,t)]$ and $q_3(t)$ by $[q_3(t)+\Delta q_3(t)]$, and subtracting from the resulting expressions the original direct problem, we obtain the following *sensitivity problem* for the determination of the *sensitivity function* $\Delta T(\xi,\eta,t)$:

$$\frac{1}{\alpha_t}\frac{\partial}{\partial t}\Delta T(\xi,\eta,t) = \frac{1}{J^2}\left(\alpha\Delta T_{\xi\xi} - 2\beta\Delta T_{\eta\xi} + \gamma\Delta T_{\eta\eta}\right) + \left(P\Delta T_{\xi} + Q\Delta T_{\eta}\right)$$

$$\text{in } 1 < \xi < M,\ 1 < \eta < N \quad \text{, for } t > 0 \qquad (4.a)$$

$$\frac{k_t}{J\sqrt{\alpha}}\left(\beta\Delta T_\eta - \alpha\Delta T_\xi\right) = 0 \qquad \text{at } \xi = 1\ ,\ 1 < \eta < \mathrm{N}\ ,\ \text{for } t > 0 \qquad (4.b)$$

$$\frac{k_t}{J\sqrt{\gamma}}\left(\beta\Delta T_\xi - \gamma\Delta T_\eta\right) = 0 \qquad \text{at } \eta = 1\ ,\ 1 < \xi < \mathrm{M}\ ,\ \text{for } t > 0 \qquad (4.c)$$

$$\frac{k_t}{J\sqrt{\alpha}}\left(\alpha\Delta T_\xi - \beta\Delta T_\eta\right) = \Delta q_3(t) \qquad \text{at } \xi = M\ ,\ 1 < \eta < N\ ,\ \text{for } t > 0 \qquad (4.d)$$

$$\frac{k_t}{J\sqrt{\gamma}}\left(\gamma\Delta T_\eta - \beta\Delta T_\xi\right) = 0 \qquad \text{at } \eta = N\ ,\ 1 < \xi < M\ ,\ \text{for } t > 0 \qquad (4.e)$$

$$\Delta T(\xi,\eta,0) = 0 \qquad \text{for } t = 0\ ,\ \text{in } 1 < \xi < M,\ 1 < \eta < N \qquad (4.f)$$

5. ADJOINT PROBLEM AND GRADIENT EQUATION

In order to develop the adjoint problem, we multiply the differential equation (1.a) of the direct problem by the Lagrange multiplier $\lambda(\xi,\eta,t)$, integrate over the time and space domains and add the resulting expression to the functional (3). We then assume that such extended functional is perturbed by $\Delta L[q_3(t)]$ when the boundary heat flux $q_3(t)$ undergoes a variation $\Delta q_3(t)$. After some lengthy but straightforward algebraic manipulations (Alencar Jr., 1996), the following *adjoint problem* for the determination of the Lagrange multiplier $\lambda(\xi,\eta,t)$ is obtained:

$$-\frac{J}{\alpha_t}\frac{\partial\lambda(\xi,\eta,t)}{\partial t} - \left(\frac{\alpha\lambda}{J}\right)_{\xi\xi} + 2\left(\frac{\beta\lambda}{J}\right)_{\eta\xi} - \left(\frac{\gamma\lambda}{J}\right)_{\eta\eta} + (PJ\lambda)_\xi + (QJ\lambda)_\eta + \sum_{s=1}^{S}\left[T(\xi,\eta,t;q_3) - Y_s(t)\right]\delta(\eta-\eta_s)\delta(\xi-\xi_s) = 0$$

$$\text{in } 1 < \xi < M,\ 1 < \eta < N\ ,\ \text{for } t > 0 \qquad (5.a)$$

$$\frac{1}{J\sqrt{\alpha}}\left(\beta\lambda_\eta - \alpha\lambda_\xi\right) = 0 \qquad \text{at } \xi = 1\ ,\ 1 < \eta < \mathrm{N}\ ,\ \text{for } t > 0 \qquad (5.b)$$

$$\frac{1}{J\sqrt{\gamma}}\left(\beta\lambda_\xi - \gamma\lambda_\eta\right) = 0 \qquad \text{at } \eta = 1\ ,\ 1 < \xi < \mathrm{M}\ ,\ \text{for } t > 0 \qquad (5.c)$$

$$\frac{1}{J\sqrt{\alpha}}\left(\alpha\lambda_\xi - \beta\lambda_\eta\right) = 0 \qquad \text{at } \xi = M\ ,\ 1 < \eta < N\ ,\ \text{for } t > 0 \qquad (5.d)$$

$$\frac{1}{J\sqrt{\gamma}}\left(\gamma\lambda_\eta - \beta\lambda_\xi\right) = 0 \qquad \text{at } \eta = N\ ,\ 1 < \xi < M\ ,\ \text{for } t > 0 \qquad (5.e)$$

$$\lambda(\xi,\eta,t_f) = 0 \qquad \text{for } t = t_f\ ,\ \text{in } 1 < \xi < M,\ 1 < \eta < N \qquad (5.f)$$

In the process of obtaining the adjoint problem, we also obtain the *gradient equation* for the functional as:

$$L'[q_3(t)] = \int_{\eta=1}^{N} -\frac{\lambda(\xi,\eta,t)\sqrt{\alpha}}{k_t}\bigg|_{\xi=M} d\eta \qquad (6)$$

6. CONJUGATE GRADIENT METHOD OF MINIMIZATION

The iterative procedure of the conjugate gradient method, as applied to the estimation of the heat flux $q_3(t)$, can be written as (Alifanov, 1994, Jarny et al, 1991):

$$q_3^{k+1}(t) = q_3^k(t) - \beta^k d^k(t) \tag{7.a}$$

where β^k is the search step-size used to advance the estimation from iteration k to k+1.

The direction of descent $d^k(t)$ is obtained as a conjugation of the gradient direction $L'[q_3^k(t)]$ and the direction of descent of the previous iteration. It is given by:

$$d^k(t) = L'[q_3^k(t)] + \gamma^k d^{k-1}(t) \tag{7.b}$$

The conjugation coefficient γ^k is obtained from the Polak-Ribiere expression as:

$$\gamma^k = \frac{\int_{t=0}^{t_f} \left\{ L'\left[q_3^k(t)\right] - L'\left[q_3^{k-1}(t)\right] \right\} L'\left[q_3^k(t)\right] dt}{\int_{t=0}^{t_f} \left\{ L'\left[q_3^{k-1}(t)\right] \right\}^2 dt} \quad \text{for k=1,2,... with } \gamma^0 = 0 \tag{7.c}$$

The search step size β^k is obtained by minimizing the functional given by Eq. (3) with respect to β^k. We obtain:

$$\beta^k = \frac{\int_{t=0}^{t_f} \sum_{s=1}^{S} \left[T(\xi_s, \eta_s, t; q_3^k) - Y_s(t) \right] \Delta T(\xi_s, \eta_s, t; d^k)\, dt}{\int_{t=0}^{t_f} \sum_{s=1}^{S} \left[\Delta T(\xi_s, \eta_s, t; d^k) \right]^2 dt} \tag{7.d}$$

where $\Delta T(\xi_s, \eta_s, t; d^k)$ is the solution of the sensitivity problem given by Eqs. (4), obtained by setting $\Delta q_3^k(t) = d^k(t)$.

7. STOPPING CRITERION

We stop the iterative procedure of the conjugate gradient method when the functional given by equation (3) becomes sufficiently small, that is,

$$L\left[q_3^k(t)\right] < \varepsilon \tag{8}$$

If the measurements are assumed to be free of experimental errors, we can specify ε as a relative small number. However, actual measured data contain experimental errors, which will introduce oscillations in the inverse problem solution as the estimated temperatures approach those measured. Such difficulty can be alleviated by assuming that the inverse problem solution is sufficiently accurate when the difference between estimated and measured temperatures is less than the standard deviation (σ) of the measurements. Thus, the value of the tolerance ε is obtained from equation (3) as

$$\varepsilon = \frac{1}{2} S \sigma^2 t_f \tag{9}$$

8. COMPUTATIONAL ALGORITHM

We suppose available an estimate $q_3^k(t)$ for the unknown heat flux $q_3(t)$ at iteration k. Thus:

STEP 1: Solve the direct problem given by equations (1) to obtain $T(\xi,\eta,t)$;
STEP 2: Check the stopping criterion given by equation (8). Continue if not satisfied;
STEP 3: Solve the adjoint problem given by equations (5) to obtain $\lambda(\xi,\eta,t)$;
STEP 4: Compute $L'\left[q_3^k(t)\right]$ from equation (6);
STEP 5: Compute γ^k from equation (7.c) and then $d^k(t)$ from equation (7.b);
STEP 6: Solve the sensitivity problem given by equations (4) to obtain $\Delta T(\xi,\eta,t)$, by setting $\Delta q_3^k(t) = d^k(t)$;
STEP 7: Compute β^k from equation (7.d);
STEP 8: Compute the new estimate $q_3^{k+1}(t)$ from equation (7.a) and go to step 1.

9. RESULTS AND DISCUSSION

We illustrate below the present approach for solving inverse problems based on generalized coordinates, with an example involving the cooling of an electronic component. Figure 2 shows a module used for the cooling of thyristors (Cavalcanti et al, 1989). In such a module, a fluid in convective boiling is forced through channels to remove the heat released by the thyristor. The heat flux to the boiling fluid may vary depending on the two-phase flow regime and is to be estimated by using transient temperature measurements taken at appropriate locations inside the module.

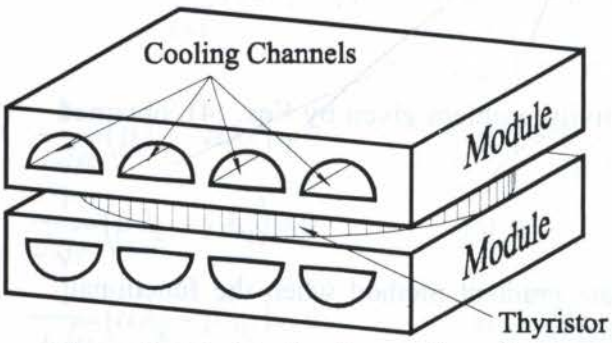

Figure 2: Module for the cooling of thyristors.

We consider for the analysis a single central channel with a half-circle cross section and take into account its symmetry. The transformation of the irregular region in the physical domain into a rectangle in the computational domain is presented in Fig. 3. We note in this figure that the channel surface (E-F-G), with unknown boundary heat flux, is mapped into the boundary ξ=M in the computational domain.

For simplicity in the analysis, we solve the present inverse problem in dimensionless form (Alencar Jr., 1996). The final dimensionless time was taken as 5.6. During this time interval, 50 measurements per sensor were considered available for the inverse analysis. The direct, sensitivity and adjoint problems were solved with finite-differences by using the Alternating-Direction-Implicit (ADI) method (Anderson et al, 1984). The resultant tri-diagonal systems were solved with a vector version of Thomas algorithm (Alencar Jr., 1996), in order to take advantage of the vector capabilities of the Cray J-90 used for the computations. The speedup of our code over its non-vector version was 7.9. The domain shown in Fig. 3 was discretized with M=30 and N=100 points in the ξ and η directions, respectively. The time step was taken as 3.33×10^{-4}. Such time step and number of points were chosen based on a grid convergence analysis.

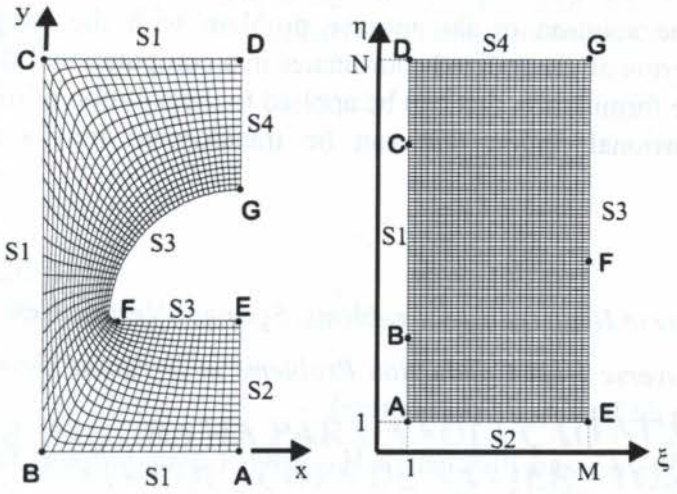

Figure 3. Transformation from the physical domain into the computational domain

We present in Figs. 4.a,b the results obtained with simulated measurements for a triangular and step variations for the heat flux, respectively, and for two different levels of measurement errors, $\sigma=0$ and $\sigma=0.01T_{max}$, where T_{max} is the maximum measured temperature. Such results were obtained with the measurements of a single sensor located at the position A, as shown in Fig. 3. The agreement between exact and estimated functions, obtained with both levels of measurement errors, is excellent for the functional forms tested. Basically no smoothness is noticed in the corners of Fig. 4.a and very little oscillations are observed in the neighborhood of the discontinuities in Fig. 4.b.

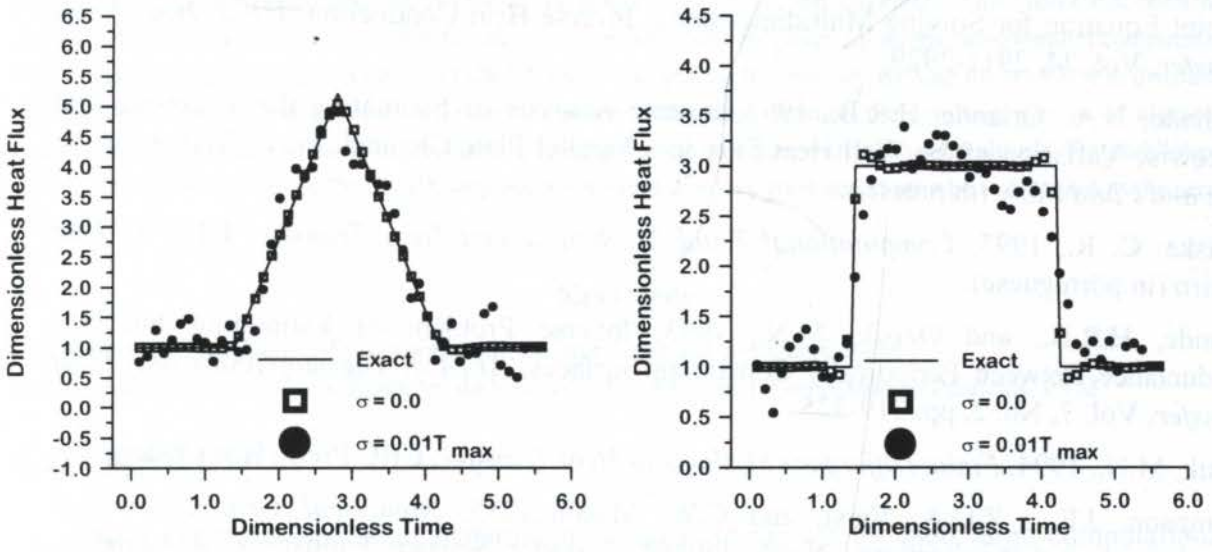

Figure 4. Inverse problem solutions for a triangular (a) and step (b) variations for $q_3(t)$

10. CONCLUSIONS

The boundary inverse heat conduction problem involving two-dimensional geometries was solved by using the conjugate gradient method with adjoint equation. The direct, sensitivity and adjoint problems, as well as the gradient equation and other additional

quantities required for the solution of the inverse problem with the conjugate gradient method, were derived in terms of generalized coordinates in a computational domain. Such an approach provides a single formulation that can be applied to the solution of inverse problems involving any two-dimensional region that can be transformed into a rectangle in a computational domain.

11. REFERENCES

Alifanov, O.M., 1994, *Inverse Heat Transfer Problems*, Springer-Verlag, New York.

Alencar Jr., J. P., 1996, *Inverse Heat Conduction Problems in Irregular Geometries*, Master Thesis, PEM-COPPE, Rio de Janeiro (in portuguese).

Anderson, D.A., Tannehill, J.C. and Pletcher, R.H., 1984, *Computational Fluid Mechanics and Heat Transfer*, Hemisphere, New York.

Bokar, J.C. and Özisik, M.N., 1995, An Inverse Problem for the Estimation of Radiation Temperature Source Term in a Sphere, *Inverse Problems in Engineering*, Vol. 1, 191-205.

Cavalcanti, E.S.C., Cruz, F.R.L., Orlande, H.R.B., 1989, A Forced Convective Boiling Module for the Cooling of Thyristors, *X Brazilian Congress of Mechanical Engineering*, Rio de Janeiro, pp. 375-378.

Dantas, L.B. and Orlande, H.R.B., 1996, A Function Estimation Approach for Determining Temperature-Dependent Thermophysical Properties, *Inverse Problems in Engineering*. Vol.3, pp.261-279

Jarny, Y., Ozisik, M. N. and Bardon, J. P., 1991, A General Optimization Method using Adjoint Equation for Solving Multidimensional Inverse Heat Conduction, *Int. J. Heat Mass Transfer*, Vol. 34, 2911-2929.

Machado, H.A., Orlande, H.R.B., 1997, Inverse Analysis of Estimating the Timewise and Spacewise Variation of the Wall Heat Flux in a Parallel Plate Channel, *Int. J. Numer. Meth. Heat and Fluid Flow* (in press).

Maliska, C. R., 1995, *Computational Fluid Mechanics and Heat Transfer*, LTC, Rio de Janeiro (in portuguese).

Orlande, H.R.B., and Özisik, M.N., 1993, Inverse Problem of Estimating Interface Conductance Between Periodically Contacting Surfaces, *AIAA J. Thermophysics and Heat Transfer*, Vol. 7, No. 2, pp. 319-325.

Özisik, M.N., 1994, *Finite Difference Methods in Heat Transfer*, CRC Press, Boca Raton.

Thompson, J.F., Z.U.A. Varsi, and C.W. Mastin.,1985, *Numerical Grid Generation Foundations and Applications*, North-Holland, Elsevier Science Publishers, Amsterdam, Netherlands.

12. ACKNOWLEDGEMENTS

The support provided by CAPES and CNPq for the visits of Prof. Orlande to NCSU and of Prof. Ozisik to COPPE/UFRJ are greatly appreciated. The CPU time for this work was provided by NACAD/COPPE/UFRJ.

XIV Brazilian Congress of Mechanical Engineering
Obeid Plaza Hotel Convention Center - Bauru - SP/Brazil
December 08-12th 1997

PAPER CODE: COB319

SCYL: UM PROGRAMA PARA A SOLUÇÃO NUMÉRICA EM PARALELO DAS EQUAÇÕES DE NAVIER-STOKES / *SCYL: A PROGRAM FOR THE NUMERICAL SOLUTION IN PARALLEL OF THE NAVIER-STOKES EQUATIONS*

Armando de Oliveira Fortuna
Departamento de Ciências de Computação e Estatística - ICMSC - USP
Av. Dr. Carlos Botelho, 1465-CP 668-CEP 13560-970-São Carlos, SP, Brasil-Email: fortuna@icmsc.sc.usp.br

Abstract

The use of parallel computing in Computational Fluid Dynamics problems has greatly increased over the past few years, placing an important and useful tool in the hands of scientists and engineers. This works discusses the implementation of a solution algorithm for the incompressible Navier-Stokes equations using parallel computation techniques. Program SCYL is written in FORTRAN 77 and utilizes the message passing library PVM to distribute and control computations between different computers. After discretization the resulting system of algebraic equations is solved using an iterative procedure. Convergence is accelerated with the use of multigrid. The parallelized code running on a cluster of Pentium™ processor machines displays good speed-up when compared to the serial version.

Keywords

Incompressible flow, Navier-Stokes equations, multigrid, parallel computers, PVM
Escoamentos incompressíveis, Equações de Navier-Stokes, Multigrid, Computadores Paralelos, PVM

1. INTRODUCTION

Many computational fluid dynamics problems are known for their large computational requirements. This usually means that they are executed in fast (and usually expensive) computers. An alternative to this situation is to have a *cluster* of high-end personal computers (such as those based on the Intel Pentium™ processor) and to use them, in parallel, to solve the fluid flow problem. Such a cluster offers a number of advantages, such as low cost, ease of upgrading and fault-tolerance. Besides, many university departments already have personal computers or workstations but do not have a dedicated parallel computer. Those available personal computers can be used to simulate a bigger, more powerful (parallel) computer.

This paper describes the implementation of the SCYL code on one such cluster of personal computers, the SPP2 multicomputer. The code, written in FORTRAN 77, solves the incompressible, laminar and isothermal Navier-Stokes equations in cylindrical coordinates with axial symmetry. The flow solution is obtained in terms of primitive variables using an iterative

procedure. The equations are discretized on staggered grids to prevent the appearance of the well known even-odd pressure coupling. The convergence rate of the iterative solution method is increased by the use of the multigrid technique.

Parallelization is achieved by dividing the physical domain between different computers. Each computer works only on the part of the domain it has been assigned to, reducing communication costs. This follows the SPMD (Single Program, Multiple Data) paradigm, by which the same program (the iterative solver) runs with different data (the flow variables allocated to each computer). Data exchange between computers is required only for nodes close to the boundaries dividing the domain. PVM, a message passing library, controls data exchange and synchronization between computers. From the user's point of view, this library allows different computers to behave as a single, *parallel machine*.

The rest of this paper is divided as follows. Section 2. describes the SPP2 multicomputer. Section 3. briefly introduces the PVM library. The numerical algorithm is shown in Section 4. Section 5. describes the multigrid technique. Section 6. presents the parallelization of the code. Communication between nodes is discussed in Section 7. Code performance and factors affecting it are shown in Section 8. Conclusions are presented in Section 9.

2. THE SPP2 MULTICOMPUTER

The SPP2 multicomputer (Trindade *et al.*, 1995) is composed of eight standard Pentium™ processor motherboards running at 133 MHz (the *computing nodes*), and one machine running at 120 MHz (the *front-end*), complete with disks, video adapter, etc. Each node has 16 MBytes of memory, no disks and the only I/O card present is an ethernet adapter.

The operating system is Linux 2.0.27, a freely available UNIX-like operating system for personal computers. The front-end has 32 MBytes of memory and also runs Linux. The whole system is interconnected via a 10 MBit/s ethernet. To avoid external network traffic between the nodes and the front-end, they are connected to their own subnet. All nodes boot from the front end, from where they also mount their file system.

Compilers for FORTRAN 77 and C/C++ are available, as well as debuggers and the XWindows system.

3. THE PVM MESSAGE PASSING LIBRARY

The PVM (Parallel Virtual Machine) library is used in this work to coordinate and control processes running on different computers, so that they can cooperate on the solution of a computational problem (Geist *et al.*, 1994). PVM provides a uniform framework within which parallel programs can be developed using existing hardware such as workstations. PVM enables a group of (potentially heterogeneous) computers to be viewed as a single parallel machine. In particular, PVM runs under Linux on IBM-PCs with 386 or higher processors. The programming interface is simple: PVM's functions are accessed through subroutine calls from the user's application. PVM has libraries for programs written in C, C++ and FORTRAN 77.

The user writes his application as a collection of cooperating tasks. Each of those tasks can be executed on a different computer, and they exchange data whenever necessary through

messages, blocks of data sent across the network. Each message can contain, among other data types, floating point, integers and complex numbers. Double precision is supported.

4. DESCRIPTION OF THE NUMERICAL ALGORITHM

Program SCYL solves the incompressible Navier-Stokes equations in cylindrical coordinates with axial symmetry. The axial and radial momentum equations, together with the continuity equation are, respectively:

$$\frac{\partial u^2}{\partial x}+\frac{1}{r}\frac{\partial (ruv)}{\partial r}=-\frac{1}{\rho}\frac{\partial p}{\partial x}+\nu\left(\frac{\partial^2 u}{\partial x^2}+\frac{\partial^2 u}{\partial r^2}+\frac{1}{r}\frac{\partial u}{\partial r}\right) \tag{1}$$

$$\frac{1}{r}\frac{\partial (rv^2)}{\partial r}+\frac{\partial (uv)}{\partial x}=-\frac{1}{\rho}\frac{\partial p}{\partial r}+\nu\left(\frac{\partial^2 v}{\partial x^2}+\frac{\partial^2 v}{\partial r^2}+\frac{1}{r}\frac{\partial v}{\partial r}-\frac{v}{r^2}\right) \tag{2}$$

$$\frac{\partial u}{\partial x}+\frac{1}{r}\frac{\partial (rv)}{\partial r}=0 \tag{3}$$

where u,v are the velocity components in the x (axial) and r (radial) directions, respectively. The radius is r, and p, ρ and ν are the pressure, density and kinematic viscosity, respectively.

These equations were discretized using finite differences and staggered grids, where the velocities u and v are defined in the cell faces and the pressure p is located in the cell center (see Figure 1). The non-linear convective terms are discretized using central differences if the Peclet number (e.g. defined as $|u|\Delta x/\nu$ in the x-direction) is less than 2, or upwind differences otherwise. Derivatives of the viscous terms are discretized using standard second order differences. When close to a solid boundary, derivatives are discretized using appropriate non-centered formulas.

After discretizing the momentum equations, one obtains a system of coupled non-linear equations having the form:

$$A^u u_{j+1/2,k}=B^u u_{j+3/2,k}+C^u u_{j-1/2,k}+D^u u_{j+1/2,k+1}+E^u u_{j+1/2,k-1}+\frac{1}{\rho}\frac{p_{j,k}-p_{j+1,k}}{\Delta x} \tag{4}$$

$$A^v v_{j,k+1/2}=B^v v_{j,k+3/2}+C^v v_{j,k-1/2}+D^v v_{j+1,k+1/2}+E^v v_{j-1,k+1/2}+\frac{1}{\rho}\frac{p_{j,k}-p_{j,k+1}}{\Delta r} \tag{5}$$

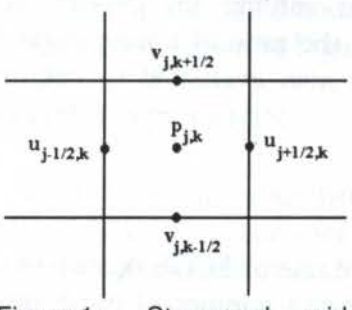

Figure 1 - Staggered grid, showing the locations of the u, v velocities and pressure p.

where are A^u, A^v, B^u, B^v,etc., are coefficients obtained during the discretization process. The continuity equation is discretized as:

$$\frac{\partial u}{\partial x}+\frac{1}{r}\frac{\partial (rv)}{\partial r}=\frac{u_{j+1/2,k}-u_{j-1/2,k}}{\Delta x}+\frac{A^c v_{j,k+1/2}-B^c v_{j,k-1/2}}{\Delta r} \tag{6}$$

Equations (4)-(6) are solved using the iterative procedure *Symmetric-Coupled Gauss-Seidel* (SCGS) (Vanka 1986). Given the finite difference cell of Figure 1, one can write the momentum equations for the variables located on its four sides:

$$A^u_{j-1/2,k}u_{j-1/2,k} = F^u_{j-1/2,k},\quad A^u_{j+1/2,k}u_{j+1/2,k} = F^u_{j+1/2,k}$$
$$A^v_{j,k-1/2}v_{j,k-1/2} = F^v_{j,k-1/2},\quad A^v_{j,k+1/2}v_{j,k+1/2} = F^v_{j,k+1/2} \tag{7}$$

where F^u and F^v are given by the right hand side of the discretized momentum equations (4)-(5). SCGS works by assuming a correction δ to the unknowns $u_{j\pm1/2,k}, v_{j,k\pm1/2}, p_{j,k}$, so that the momentum and continuity equations are *simultaneously satisfied* at the end of the procedure. For instance, by adding the corrections to the momentum equation for $u_{j+1/2,k}$, one has:

$$A^u_{j+1/2,k}\delta u_{j+1/2,k} - \frac{\delta p_{j,k}}{\rho\Delta x} = R^u_{j+1/2,k} = F^u_{j+1/2,k} - A^u_{j+1/2,k}u_{j+1/2,k} \tag{8}$$

Analogous expressions are obtained from the other three momentum equations. Adding the corrections to the continuity equation gives

$$\frac{\delta u_{j+1/2,k} - \delta u_{j-1/2,k}}{\Delta x} + \frac{A^c_{j,k}\delta v_{j,k+1/2} - B^c_{j,k}\delta v_{j,k-1/2}}{\Delta r} = R^c_{j,k} = -CEQ_{j,k} \tag{9}$$

where $CEQ_{j,k}$ is the numerical value of the continuity equation (6) evaluated at the center of the cell. The continuity equation is being used here to correct the pressure of the cell based on the net mass flow into the cell. The four correcting momentum equations and the correcting continuity equation (9) can be written in matrix form:

$$\begin{bmatrix} A^u_{j-1/2,k} & 0 & 0 & 0 & 1/\rho\Delta x \\ 0 & A^u_{j+1/2,k} & 0 & 0 & -1/\rho\Delta x \\ 0 & 0 & A^v_{j,k-1/2} & 0 & 1/\rho\Delta r \\ 0 & 0 & 0 & A^v_{j,k+1/2} & -1/\rho\Delta r \\ -1/\Delta x & 1/\Delta x & -B^c_{j,k}/\Delta r & A^c_{j,k}/\Delta r & 0 \end{bmatrix} \times \begin{bmatrix} \delta u_{j-1/2,k} \\ \delta u_{j+1/2,k} \\ \delta v_{j,k-1/2} \\ \delta v_{j,k+1/2} \\ \delta p_{j,k} \end{bmatrix} = \begin{bmatrix} R^u_{j-1/2,k} \\ R^u_{j+1/2,k} \\ R^v_{j,k-1/2} \\ R^v_{j,k+1/2} \\ R^c_{j,k} \end{bmatrix} \tag{10}$$

where the R's are the residuals. The main diagonal elements of the coefficient matrix are over-relaxed by dividing them by ω ($\omega \le 1.0$). The above matrix can be written in partitioned form and inverted using explicit formulas (Wesseling 1992).

The iterative procedure is terminated after the euclidean norm of the residuals of the momentum equations are reduced below 10^{-3}. Since when solving the Navier-Stokes incompressible equations one is interested in *conserving mass*, the ratio of excess mass flux inside the domain to the total mass flux into the domain is also evaluated to determine convergence. Again, it should be smaller than 10^{-3}.

5. MULTIGRID ACCELERATION

As with other iterative solution procedures, the convergence rate of SCGS decreases with each iteration and with decreasing mesh spacing and/or increasing number of mesh points. Iterative procedures eliminate the high frequency components of the error (i.e. the difference between the guessed and actual solution) in a few iterations, but require many iterations to

eliminate the low frequency, long wavelength components of the error. However, low frequency components of the error on the original, fine grid, become high frequency components on a coarser grid, and can be efficiently eliminated using the *same iterative procedure* employed on the original, finer grid. This procedure can be applied recursively, using a series of coarse grids to eliminate high frequency components, and the results interpolated back to the finest grid, where the solution is sought.

Since the Navier-Stokes equations are non-linear, this work adopted the *Full Approximation Storage* (FAS) multigrid technique (Wesseling 1992), using *F* and *W multigrid cycles* to move data between four grids.

6. PARALLELIZATION OF THE CODE

There were two possible ways to parallelize the code: a division based on control or based on data. The former requires the individual parallelization of the main routines in the code, while the latter divides the computational domain among all computers making up the parallel computer. In the first approach (*control parallelism*), different parts of the program require data to be located on different computers, potentially increasing communication costs. It also makes it difficult to *balance the load* between computers, so that no computer is idle while others are busy with computations. Therefore, the second approach (*data parallelism*) was adopted. It is well suited to this kind of problem, where the same operation (SCGS iterative procedure) is performed on large data sets (the fluid flow unknowns).

Figure 2 shows a block diagram of the code. The "Parallel Region" encompasses practically all of the heavy computational work of the code (evaluation of the momentum equations, relaxation of all cells in the domain, multigrid acceleration). Within this region, the code in the hatched area (convergence check) is performed by a single processing node, based on information (*e.g.* residuals) sent to it by all other nodes.

The computational domain, a pipe with an orifice plate inside, is shown in Figure 3. Due to the assumed axial symmetry of the domain, only two directions were involved in the simulation: axial and radial.

By dividing the domain as evenly as possible, load balance among the SPP2 nodes is naturally enforced. This division is shown in Figure 4.

7. COMMUNICATION

While communication between processing nodes is unavoidable, its occurrence and length in the code should be minimized to avoid loss in performance.

When evaluating the discretized momentum equations at the boundary between sub-domains, data

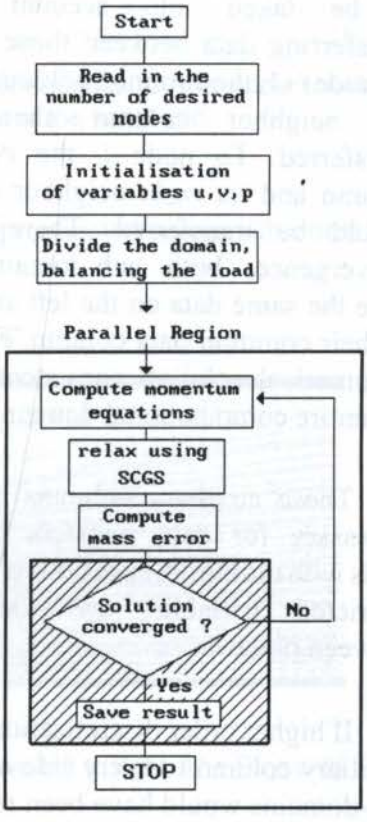

Figure 2 - Block diagram of program SCYL.

points which lie outside the node's sub-domain become necessary. To see why, consider Figure 5, which shows the stencil of the discretization employed. The evaluation of the momentum equation at point (×) requires information from points (•) belonging to the adjacent computing node. While such information could be *requested on demand* by node i from node i+1, it would considerably increase the program's complexity.

Instead, internal domains (those which contain neither the inflow nor the outflow) are flanked by two "ghost" columns of cells (shown in gray in Figure 6), one on each side, containing all data required for the evaluation of the momentum equation at their "real" boundaries. Now each domain can evaluate the momentum equations independently from each other, without having to request data from adjacent processing nodes. These "ghost" columns are updated *at the end of every iteration*, by having adjacent processors transfer data between themselves. In Figure 6, the thick vertical line represents columns of data which are common to two adjacent nodes. This has to be taken into account when transferring data between those nodes. To node i+1, the common column and its *left* neighbor column should be transferred. To node i, the common column and its *right* neighbor column should be transferred. Therefore, at convergence, both sub-domains will have the same data on the left and right of their common data column, ensuring a numerical solution consistent across the entire computational domain.

These auxiliary columns are also necessary for data transfers between grids with multigrid, as residuals of some restricted variables are transferred between nodes.

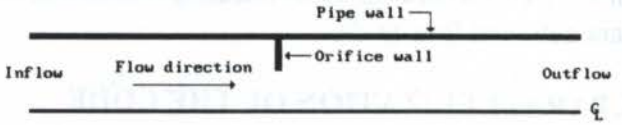

Figure 3 - Computational domain. The axis of the pipe (center line) is assumed to be a "slip" boundary, while all other solid boundaries are assumed to be "no-slip".

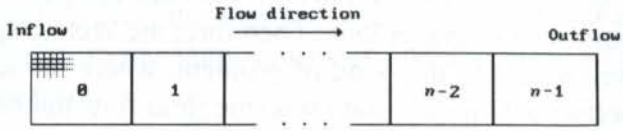

Figure 4 - Computational domain evenly divided among n computing nodes.

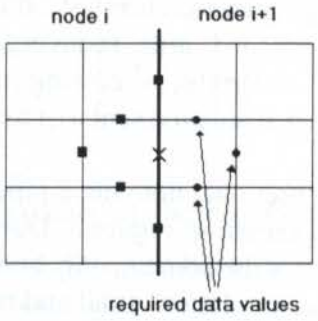

Figure 5 - Stencil of the discretization close to the boundary between two sub-domains. To evaluate the momentum equation at position marked with ×, data points (shown as •) from the adjacent sub-domain are required.

If higher order discretizations had been used, it would have been necessary to add a second auxiliary column to every side of adjacent sub-domains, as more data points from neighboring sub-domains would have been required at the boundary.

8. CODE PERFORMANCE

Results are shown below for a sample problem (flow past an orifice plate at Reynolds number 40) with three fine grid sizes: 401 × 34, 801 × 34 and 1601 × 34 (see Figure 8).

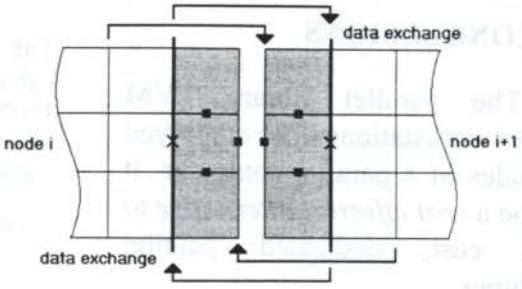

Figure 6 - Data exchange between sub-domains. Auxiliary ("ghost") data columns are shown in gray.

Shown in Figure 7 is the measured speedup plotted against the number of processing nodes. The greater the number of mesh points on the finest grid, the better the scalability of the computation. This is to be expected from multigrid. Under multigrid, most of the work is performed on the coarser grids (see Table 1). Because on coarser grids there are less mesh points (than on finer grids), a greater proportion of time is spent exchanging information between nodes than in computations. If the finest grid is "small", then there is not enough work on the coarser grids to allow good scalability of the computation. This can be clearly seen on the 401 × 34 grid, where the speedup actually dropped when moving from four to eight processing nodes. The "optimum" value of the relaxation parameter ω also influences the performance of the code. It changes for different grid sizes and for different number of domain partitions (*i.e.* number of computing nodes), reflecting the way boundary conditions are propagated across sub-domains.

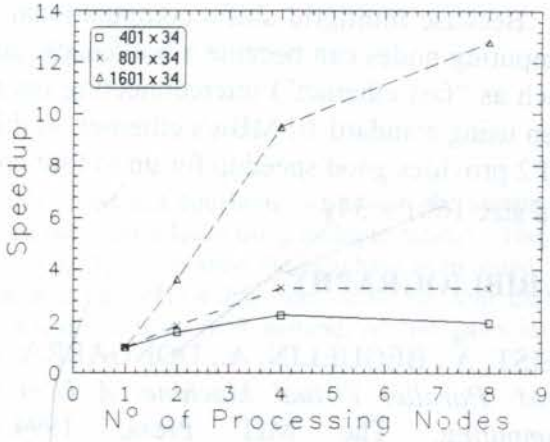

Figure 7 - Performance of the code for three different sizes of the finest grid.

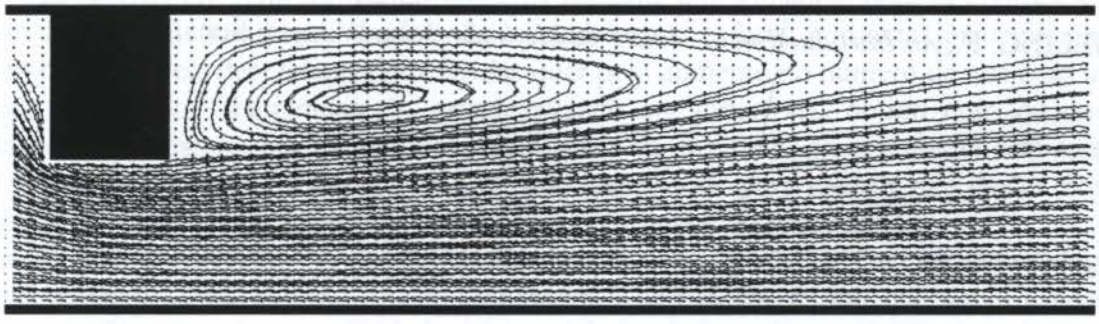

Figure 8 - Streamlines of flow across an orifice plate. Flow is from left to right. The Reynolds number is 40.

9. CONCLUSIONS

The parallel library PVM allows workstations to be employed as nodes of a parallel computer. It can be a *cost effective alternative* to high cost, dedicated parallel machines.

Equally dividing the computational domain between processing nodes is a natural way to parallelize the code.

Table 1 - Total number of sweeps through the grid four various sizes of the finest grid. Each coarser grid has 1/4th the number of mesh points as the previous grid.

grid number/size	401× 34	801× 34	1601 × 34
grid 1 (finest)	36	36	60
grid 2	90	90	135
grid 3	160	160	250
grid 4 (coarsest)	665	788	1494

Because multigrid shifts computational work to coarser grids, communication between computing nodes can became a bottleneck, suggesting the usefulness of having a fast network (such as "fast ethernet") interconnecting the nodes, reducing communication costs. However, even using standard 10 MBit/s ethernet, in this Computational Fluid Dynamics application the SPP2 provides good speedup for up to four computing nodes (eight in case of the problem with grid size 1601 × 34).

10. BIBLIOGRAPHY

GEIST, A., BEGUELIN, A., DONGARRA, J., JIAN, W., MANCHEK, Ŕ., SUNDERAN, V., *PVM: Parallel Virtual Machine. A User's Guide and Tutorial for Networked Parallel Computing*. The MIT Press, 1994. Available in Postscript format from http://www.netlib.org/pvm3/book/pvm-book.html.

TRINDADE, O., MARQUES, E., JEUKENS, I., *A Parallel Architecture based on Personal Computers - Requirements and Definitions.* In Simpósio Nipo-Brasileiro de Ciência e Tecnologia, p.203-212, August 1995.

VANKA, S.P., *Block-Implicit Multigrid Solution of Navier-Stokes Equations in Primitive Variables*. Journal of Computational Physics 65, 138-158, 1986.

WESSELING, P., *An Introduction to Multigrid Methods*. John Wiley & Sons, 1992.

XIV Brazilian Congress of Mechanical Engineering
Obeid Plaza Hotel Convention Center - Bauru - SP/Brazil
December 08-12th 1997

PAPER CODE: COB347

APLICAÇÃO DE TÉCNICAS MULTIGRID EM PROBLEMAS DE DINÂMICA DOS FLUIDOS/*APPLICATIONS OF MULTIGRID METHODS TO FLUID DYNAMICS PROBLEMS*

RIVÂNIA H. PAULINO & WASHINGTON BRAGA
Departamento de Engenharia Mecânica, PUC-Rio
R. Marquês de São Vicente, 225
CEP: 22453-900, Rio de Janeiro, RJ, email: wbraga@mec.puc-rio.br

Abstract

The present work deals with the numerical solution of the Navier-Stokes equations, written in the stream function-vorticity form, by the finite difference method and acceleration techniques using multiple meshes. The classical method (storage of the correction) and the method FAS (Full Approximation Storage) have been tested. The results obtained clearly show that a very efficient computational scheme has been achieved with the multigrid method. For example, when comparing this method with the basic SOR method, relative gains in processing time in the order of 80% have been obtained.

Keywords

Solução Numérica, Navier-Stokes, Multigrid, Full Approximation Storage/
Numerical Solution, Navier-Stokes, Multigrid, Full Approximation Storage.

1. INTRODUÇÃO

A solução numérica de problemas de valor inicial ou de contorno é indispensável em muitos campos da matemática, da física e da engenharia. A simulação destes problemas que no passado recente era feita utilizando modelos bastante aproximados, hoje já começa a ser feita em forma mais complexa, traduzindo-se num maior esforço computacional quer pelo aumento das variáveis dependentes envolvidas quer pelo aumento no número de nós para uma adequada simulação. Felizmente, o grande avanço computacional obtido com os novos processadores e mesmo com as máquinas paralelas têm auxiliado enormemente esta tarefa. Ainda assim, novas técnicas numéricas têm sido necessárias para melhor uso destes novos recursos, possibilitando que problemas ainda mais complexos sejam estudados.

Este trabalho apresenta os resultados obtidos na investigação do uso de metodologias multigrid aplicadas à formulação função de corrente - vorticidade de um problema típico de Dinâmica de Fluidos. Entretanto, todo o material estudado e desenvolvido se aplica com mínimas variações às demais formulações, como a que usa variáveis primitivas ou ainda à formulação vorticidade-potencial de velocidade.

2. DESCRIÇÃO

A base de qualquer simulação numérica é a substituição das equações diferenciais que descrevem o fenômeno físico por uma sequência de equações algébricas equivalentes, resultando num grande sistema de equações lineares ou linearizadas, cuja solução deve ser obtida por métodos diretos ou iterativos.

Por muitos anos, os métodos de Jacobi e de Gauss-Seidel (métodos de relaxação) foram as únicas ferramentas para a obtenção de solução de problemas por métodos iterativos, fazendo com que as suas propriedades de convergência e estabilidade sejam hoje bastante entendidas. De forma semelhante, os métodos de direções alternadas (ADI) também têm sido utilizados com os mesmos propósitos.

Observando a taxa de convergência destes métodos iterativos, percebe-se claramente que ela decresce rapidamente após algumas iterações. Em consequência, o esforço computacional aumenta de forma significante, tornando tais métodos pouco eficientes após algumas iterações. Isto levou ao aparecimento dos chamados métodos multigrid que, após um determinado número de iterações com a malha inicial, propõem a troca para uma malha mais grosseira, isto é, com menor número de pontos nodais. A sequência destas trocas e a posterior recuperação das informações necessárias às malhas mais refinadas constituem a essência desta classe de métodos. O atrativo maior deles é a possibilidade de se resolver problemas com N incógnitas com um número ótimo de operações e armazenagem que é de O(N), como sabido.

3. DESENVOLVIMENTOS HISTÓRICOS

Os métodos multigrid foram desenvolvidos no começo dos anos sessenta. Entretanto, só após a metade dos anos setenta eles passaram a ser reconhecidos como realmente eficientes computacionalmente para uma ampla área de aplicações. Apesar de alguns outros trabalhos anteriores, foi Brandt quem, em 1970, apresentou inúmeras contribuições aos métodos, entre eles seu desenvolvimento para sistemas não lineares (Full Approximation Storage - FAS), discussão de domínios gerais e refinamentos locais de malhas entre outros (Brandt, 1984). Hackbush (1976-1978) desenvolveu os elementos fundamentais dos métodos multigrid e seus primeiros artigos contêm investigações teóricas e práticas de vários autores.

Desde 1980, os métodos multigrid vem sendo usados de forma mais intensa. Além de suas aplicações às equações diferenciais parciais, por exemplo, por Napolitano e Catalano (1991) que resolveu as equações de Navier-Stokes, outros autores os têm empregado na solução de problemas de turbulência (Ruttmann e Solchembach, 1984). Mais recentemente, Tralles (1995) e Paulino (1997) apresentaram desenvolvimentos sobre o assunto.

4. FORMULAÇÃO

Este trabalho pretende discutir alguns detalhes da implementação numérica da metodologia multigrid. Embora outras equações e metodologias tenham sido testadas (Paulino, 1997), apenas os resultados para um problema típico de Dinâmica dos Fluidos serão mostrados. O problema escolhido é o clássico escoamento de fluido Newtoniano, em regime permanente e incompressível dentro de uma cavidade quadrada com tampa superior móvel, supondo-se propriedades constantes e ausência de forças de empuxo. O estudo foi feito em um domínio bidimensional, em regime permanente e é descrito pelas equações de Navier Stokes, no presente caso, escritas na formulação função de corrente-vorticidade, mostradas abaixo:

$$\mathrm{Re}\left(\frac{\partial\psi}{\partial y}\frac{\partial\omega}{\partial x}-\frac{\partial\psi}{\partial x}\frac{\partial\omega}{\partial y}\right)=\frac{\partial^2\omega}{\partial x^2}+\frac{\partial^2\omega}{\partial y^2} \tag{1}$$

$$\frac{\partial^2\psi}{\partial x^2}+\frac{\partial^2\psi}{\partial y^2}=-\omega \tag{2}$$

junto com as seguintes condições de contorno:

$$\psi=0,\ \frac{\partial\psi}{\partial x}=0,\ \text{em}\ \partial\Omega_1\ \text{e}\ \partial\Omega_2 \tag{3 a}$$

$$\psi=0,\ \frac{\partial\psi}{\partial x}=0,\ \text{em}\ \partial\Omega_3 \tag{3 b}$$

$$\psi=0,\ \frac{\partial\psi}{\partial x}=-1,\ \text{em}\ \partial\Omega_4 \tag{3 c}$$

Utilizando uma técnica de discretização como diferenças finitas ou volumes finitos, estas equações são substituídas por um conjunto de equações algébricas (utilizando diferenças centrais para os termos de difusão e upwind para os termos de inércia) que serão representadas genéricamente pela equação:

$$A\Phi(x)=f(x)\ \text{em}\ \Omega \tag{4}$$

onde Φ é a variável dependente discretizada, x indica a posição, A é um operador e f é uma função de x. Naturalmente, a questão a ser tratada aqui é a obtenção de Φ com um menor custo operacional. Ω indica o domínio de cálculo no plano físico, Ω_h indica o domínio discreto onde o subscrito h indica a malha utilizada na simulação. Em face aos objetivos do presente trabalho, a discussão, embora pertinente, sobre a capacidade da malha utilizada descrever adequadamente o fenômeno físico de interesse não será conduzida, ou seja, erros de modelagem ou de discretização não são pertinentes ao presente estudo.

5. MÉTODO NUMÉRICO

Antes de se dar prosseguimento, faz-se necessário algumas considerações sobre a notação utilizada. Φ é a solução exata do sistema definido por (4) e u é o valor aproximado para a solução, valor este gerado por algum método iterativo. Neste contexto, o termo erro refere-se à diferença entre a solução exata da equação (4) e uma solução aproximada obtida após algumas iterações, ou seja, antes da convergência. Assim, $e=\Phi-u$, é o erro que, como Φ e u, é um vetor que pode ser medido por qualquer norma. Uma outra medida numérica de quanto u se aproxima de Φ é denominada resíduo da equação que pode ser escrito como:

$$r=f-Au \tag{5}$$

e é simplesmente a quantidade pela qual a aproximação u falha em satisfazer o problema original definido por (4). Pode-se facilmente encontrar uma relação importante entre o resíduo e o erro, isto é, mostra-se facilmente que:

$$Ae=r \tag{6}$$

Esta equação, chamada de equação residual, indica que o erro satisfaz o mesmo conjunto de equações algébricas definidas por (4) se Φ e f são respectivamente trocados pelo erro e e pelo resíduo r. Supondo-se que uma aproximação u foi encontrada por algum método, pode-se calcular o resíduo utilizando a equação (5) acima. Para melhorar o valor aproximado u, pode-se resolver a equação residual para e e então calcular uma aproximação usando a definição do erro:

$$u = \Phi + e \tag{7}$$

Como mencionado por Briggs (1987), a equação do resíduo e a idéia de correção residual podem ser utilizadas com grandes vantagens nos métodos multigrid. Um procedimento comum no método multigrid é chamado de interpolação ou prolongamento. Normalmente, usa-se apenas a interpolação linear, de símbolo I_{2h}^{h} onde h é o espaçamento da malha. Os vetores a serem interpolados na malha grosseira para gerar os vetores na malha refinada são dados por:

$$I_{2h}^{h} e^{2h} = e^{h} \tag{8}$$

que se traduz em:

$$e_{2j}^{h} = e_{j}^{2h} \tag{9}$$

$$e_{2j+1}^{h} = \frac{1}{2} * \left(e_{j}^{2h} + e_{j+1}^{2h} \right) \tag{10}$$

onde a ordenação dos pontos é tal que $0 \le j \le \left(\frac{N}{2} - 1 \right)$. Com isto, nos pontos de numeração par da malha refinada, os valores do vetor erro são transferidos diretamente de Ω_{2h} para Ω_{h} [vide equação (9)]. Nos pontos ímpares da malha refinada (que não existem na malha grosseira), o valor de e_h é a média dos valores dos pontos vizinhos da malha grosseira, [vide equação (10)], definindo assim um operador de prolongamento linear, por simplicidade.

Uma segunda classe de transferências intermalhas constitui-se em um procedimento inverso, transferindo os vetores de uma malha refinada Ω_h para uma malha grosseira Ω_{2h}. Estes são genericamente chamados de operadores de restrição e são descritos por I_{h}^{2h} da forma:

$$I_{h}^{2h} e_{h} = e_{2h} \tag{11}$$

onde $e_{j}^{2h} = e_{2j}^{h}$, isto é, os vetores na malha grosseira simplesmente recebem os valores diretamente do correspondente na malha refinada. A extensão para situações bi ou mesmo tridimensionais é imediata (e.g. Paulino, 1997). Se a transferência for feita de uma malha muito grosseira para descrever o fenômeno físico, o erro poderá ser muito grande, provocando oscilações. Em casos semelhantes, melhores resultados foram obtidos utilizando-se um interpolante mais sofisticado, envolvendo um número maior de pontos, infelizmente à custa de um aumento no esforço computacional. Este procedimento é, entretanto, sugerido pois os custos do amortecimento de uma solução numericamente oscilatória pode ser grande.

Embora neste trabalho a ênfase tenha sido na implementação do método FAS (Full Approximation Storage) na solução das equações de Navier-Stokes, antes da sua

apresentação, os métodos 2-Grid e o Multigrid básico serão brevemente comentados, para a devida apreciação das vantagens do método FAS.

5.1 Método 2-Grid

Como o nome indica, este método utiliza apenas duas malhas de espaçamentos h e 2h. O processo é simples: começando, por exemplo, na malha mais fina, faz-se algumas etapas do processo de relaxção básico (neste trabalho, utilizou-se o método SOR), utilizando uma aproximação inicial u_h, numa etapa chamada de pré-suavização. Ao final destas poucas iterações (obviamente, antes da convergência), obtém-se uma estimativa $\overline{u}_h$, que espera-se seja melhor que a inicial. Interrompe-se o processo iterativo e calcula-se o resíduo, que será dado por

$$r_h = f_h - A_h \overline{u}_h \tag{12}$$

Para transferir os valores do resíduo calculado na malha fina para a malha grosseira, utiliza-se o operador de restrição, apresentado na equação (11). Da mesma forma, a matriz dos coeficientes (que dependem de h) é igualmente transferida. Neste ponto, a equação (6), equação residual, é resolvida sobre a malha grosseira:

$$A_{2h} e_{2h} = r_{2h} \tag{13}$$

O erro encontrado na malha mais grosseira, Ω_{2h}, é transferido para a malha refinada Ω_h através do operador de prolongamento, definido pela equação (8). Finalmente, para o refinamento da solução anteriormente encontrada, $\overline{u}_h$, utiliza-se a equação (7), escrita aqui novamente para facilidade de entendimento:

$$\tilde{u}_h = \overline{u}_h + e_h \tag{14}$$

Em seguida, o processo iterativo básico é retomado, para o início de um novo ciclo, utilizando agora a aproximação melhorada no processo.

5.2 Método Multigrid

A passagem do método 2-Grid para o Multigrid pode ser feita utilizando-se a equação residual (14). Vamos supor três malhas: Ω_h, Ω_{2h} e Ω_{4h}. Ao invés de se obter a solução exata, isto é, convergida para e_{2h} na equação (13), faz-se apenas algumas iterações de relaxação naquela equação. Em seguida, pode-se aplicar novamente o método 2-Grid entre Ω_{2h} e Ω_{4h}, procurando agora obter um refinamento para $\overline{e}_{2h}$. A extensão para 4 ou mais malhas é agora imediata.

5.3 Método FAS (Full Approximation Storage)

O método multigrid descrito acima é referido como de armazenamento da correção, pois é é o erro (também chamado de correção) refinado que é armazenado entre as malhas. Este método é dito ser adequado para problemas lineares. Como o presente interesse é a obtenção

de soluções para equações fortemente não-lineares, aplicou-se o método FAS que pretende armazenar a variável dependente u (na verdade, o incremento δ entre a solução aproximada antes e depois do refinamento) ao invés do erro e.

O incremento δ é definido como a diferença entre os valores de duas iterações, ou no caso, como a diferença entre o valor obtido antes e depois do uso do método multigrid, de refinamento da solução. Por exemplo:

$$\tilde{u}_h = u_h + \delta_h \tag{15}$$

A primeira etapa do método consiste na obtenção de $\bar{u}_h$, a aproximação corrente na malha mais fina e, utilizando a equação (10), o resíduo r_h. Utilizando os operadores de restrição, as aproximações u_{2h} e r_{2h} são obtidas. Na malha mais grossa, o problema a ser resolvido é:

$$A_{2h}\Phi_{2h} = f_{2h} \tag{16}$$

onde a aproximação inicial de Φ_{2h} é u_{2h}, já determinado. Portanto, f_{2h} pode ser definido de outra maneira:

$$f_{2h} = A_{2h}u_{2h} + r_{2h} \tag{17}$$

Com isto, a equação (16) passa a ser escrita:

$$A_{2h}\Phi_{2h} = A_{2h}u_{2h} + r_{2h} \tag{18}$$

que pode ser escrita como $A_{2h}\delta_{2h} = r_{2h}$. A solução desta equação será δ_{2h} que será transferida para a malha mais fina, gerando δ_h que, através da equação (15), irá determinar a nova aproximação $\tilde{u}_h$. Após isto, efetuam-se alguns passos de relaxação para que um novo ciclo multigrid seja iniciado.

5.4 Esquemas Cíclicos

O conceito básico dos ciclos é a execução de um certo número de passos de relaxação, σ_k, em cada malha para a suavização eficiente da solução. Embora existam outras possibilidades (Paulino, 1997), o ciclo multigrid associado ao método FAS consiste em se fazer σ_1 passos de relaxação na malha mais fina, Ω_h, trocando-se, em seguida, para uma malha mais grosseira, digamos Ω_{2h}, onde σ_2 passos são executados. Ao final destes, volta-se à malha mais fina para outros σ_1 passos. A etapa seguinte, se for o caso, é trocar o nível uma vez mais para uma terceira malha, Ω_{4h}, onde σ_3 passos são realizados. Como pode ser esperado, os passos σ_1, σ_2, σ_3.... não são deixados livres. Duas aproximações existem: esquema fixo ou esquema acomodativo. No primeiro caso, estes parâmetros são escolhidos a priori e permanecem fixos em todo a simulação, com a escolha podendo ser feita com base em experimentos anteriores ou alguma análise. Utilizando o esquema fixo (McCormick, 1987), os números σ_k devem ser tais que $\sigma_2 + \sigma_3 = \sigma_1 > 1$. Os valores de $\sigma_2 + \sigma_3$ são tipicamente pequenos (2 ou 3), com $\sigma_2 > \sigma_3$ e seguramente, $\sigma_2 + \sigma_3 < 4$.

Na segunda estratégia, os resíduos são calculados depois de sucessivos passos de relaxação. Quando $\|r^{novo}\| > \eta \|r^{velho}\|$, onde η é um parâmetro especificado (Briggs, 1987), a etapa de relaxação nesta malha é declarada não efetiva e é feita uma transferência para a próxima malha. O parâmetro η pode ser determinado para um certo modelo de problema. Para uma equação de Poisson bidimensional, utiliza-se η = 0,6 que é tido como um bom valor.

6. RESULTADOS

Como se pretendeu a implementação do método multigrid ao problema do escoamento no interior de uma cavidade com tampa móvel, escolheu-se os resultados mostrados no trabalho de Gupta e Manohar (1979) para orientação. A metodologia utilizada foi simples. Dois códigos numéricos foram utilizados, ambos com os mesmos tipos de tratamento de condições de contorno proposto por Gupta, por exemplo. A diferença entre eles foi a implementação do método FAS. Desta forma, o parâmetro de avaliação de desempenho foi o tempo de processamento, uma vez que os resultados deveriam ser bastante próximos (ao nível da tolerância, naturalmente). Embora óbvio, deve ser frisado que os métodos multigrid são "apenas" métodos de aceleração, não funcionando para se obter refinamentos de solução.

A Tabela 1, apresentada abaixo, mostra alguns dos resultados obtidos. Observando-se os resultados, percebe-se que o método FAS com 3 níveis apresentou desempenho ligeiramente melhor (isto é, resultados obtidos mais rapidamente) que o método FAS com 2 níveis. É provável que para situações mais complexas que necessitem malhas mais finas que 21x21, a diferença aumente. Os resultados indicados na coluna "Referência", referem-se àqueles obtidos pelo método S. O. R. com malha 21x21, isto é, sem o uso de aceleração multigrid,

Tabela 1: Tempos de Processamento (seg) para Método FAS malhas utilizadas 21x21, 11x11,6x6

Re	Referência	FAS: 2 níveis		FAS: 3 níveis	
	CPU	CPU	Ganho %	CPU	Ganho %
1	5,9	0,43	92,7	0,39	93,4
50	6,3	0,45	92,8	0,41	93,5
100	6,4	0,47	92,6	0,43	93,2
500	6,8	1,45	78,6	1,39	79,5

Como pode ser visto na Tabela 2, os resultados para uma malha mais fina são igualmente interessantes.

Tabela 2: Tempos de Processamento (seg) para Método FAS malhas utilizadas 33x33, 17x17 e 9x9

Re	Referência	FAS: 2 níveis		FAS: 3 níveis	
	CPU	CPU	Ganho %	CPU	Ganho %
1	33,4	1,2	96,5	1,2	96,7
50	41	1,3	97	1,3	97,3
100	41	1,4	96,8	1,3	97,1
500	41,7	2,7	93,9	2,8	96,9

7. CONCLUSÕES

Os resultados aqui mostrados indicam o potencial dos métodos multigrid, na formulação Full Approximation Storage, FAS, para acelerar a convergência dos problemas em Dinâmica dos Fluidos Computacional. Com base nos resultados mostrados, pretende-se utilizar o método para a obtenção de solução em situações que necessitem de coordenadas generalizadas adaptativas (Krieger, 1991).

8. REFERÊNCIAS

Brandt A, Multigrid Techniques: Guide with Applications to Fluid Dynamics, *GMD-Studien* no. 85, Maio 1984.

Briggs W.L., A Multigrid Tutorial, *Society for Industrial and Applied Mathematics*, 1987.

Gupta M.N. & Manohar R.P., Boundary Approximation and Accuracy in Viscous Flow Computations, *J. Computational Physics*, vol. 31, pp. 265-288, 1979.

Hackbush W., On the Convergence of a Multigrid Interaction Applied to Finite Element Equations, *Universitat Koln*, relatório 76-12, 1976.

Hackbush W., On Multigrid Methods Applied to a Difference Equations, *Computing* 20, pp. 291-306, 1978.

Krieger, G.C., Aplicação de Métodos de Malhas Auto-Adaptativas a Problemas em Dinâmica dos Fluidos - Um Estudo Comparativo, Dissertação de Mestrado, *Departamento de Engenharia Mecânica, PUC-Rio*, 1991.

McCormick S.F. , Multigrid Methods, Frontiers in Applied Mathematics (3), *Society for Industrial and Applied Mathematics*, Philadelphia, Pennsylvania, 1987.

Napolitano M. & Catalano L.A, A Multigrid Solver for the Vorticity-Velocity Navier-Stokes Equations, *International Journal for Numerical Methods in Fluids*, vol. 13, pp. 49-59, 1991.

Paulino, R.H., Aplicação de Técnicas Multigrid em Problemas de Dinâmica dos Fluidos, Dissertação de Mestrado, *Departamento de Engenharia Mecânica, PUC-Rio*, 1997.

Ruttmann B. & Solchembach K., A multigrid solver for the Cylinder Turbulent flows in engines, Proc. *GAMM-Seminar*, Kiel, 1984.

Trales P.R., Resolução das Equações de Navier-Stokes pelo Método das Projeções Via Elementos Finitos com Aceleração pelas Técnicas Multigrid, Tese de Doutorado, *Departamento de Informática, PUC-Rio*, 1995.

XIV Brazilian Congress of Mechanical Engineering
Obeid Plaza Hotel Convention Center - Bauru - SP/Brazil
December 08-12th 1997

PAPER CODE: COB755

APPLICATION OF THE UNIFIED FINITE APPROACH EXPONENTIAL SCHEME TO THE CAVITY PROBLEM

Dr. José Ricardo Figueiredo
State University at Campinas, FEM, DE
13083-970, Campinas, São Paulo, Brazil

Abstract

This paper presents the application of a new discretization scheme for convective-diffusive fluid transport equations to the Navier-Stokes equations. The scheme is a conservative-form discretization constructed within the control-volume approach employing an exponential interpolating curve obtained as the exact solution of an approximated equation that admits a source term, which is computed by incorporating Allen's finite difference approach into the finite volume method. It has been called the Unified Finite Approach Exponential Scheme, UNIFAES. A simple one-dimensional test case shows the scheme's ability to cope with irregular grids The main test problem considered is the recirculating flow in a cavity due to a moving wall, where UNIFAES demonstrates accuracy superior to the conservative form schemes central differencing and simple exponential scheme.

Keywords

CFD, Finite Volume, Finite Difference, UNIFAES, cavity problem

1. INTRODUCTION

The Unified Finite Approach Exponential Scheme for convective-diffusive fluid transport equations, UNIFAES, is applied to the Navier-Stokes equations, employing the classic test problem of the two-dimensional recirculating flow within a square cavity driven by a moving wall. This test is preceded by a simple linear one-dimensional test case regarding irregular grid.

The derivation of the scheme was described in details by Figueiredo (1997), that also presented an extensive comparison of the scheme with the central differencing, the simple exponential scheme and the Locally Analytic Differencing Scheme, LOADS, on several two-dimensional solutions of the transport equation upon a uniform velocity field, where it has shown systematically better accuracy than the other schemes. The derivation here presented is shorter, but more general with respect to the cell geometry.

The conservative-form transport equation with constant thermophysical properties can be written in non-dimensional terms:

$$\frac{\partial \phi}{\partial t} + \frac{\partial (Pu\phi)}{\partial x} + \frac{\partial (Pv\phi)}{\partial y} - \frac{\partial^2 \phi}{\partial x^2} - \frac{\partial^2 \phi}{\partial y^2} = S \qquad (1)$$

where ϕ is an intensive property such as temperature, concentration, a velocity component or vorticity. Spatial coordinates x and y are normalized by a characteristic dimension L and the respective velocity components u and v by a characteristic velocity V, t is the non dimensional time given by the dimensional time multiplied by $\Gamma/(\rho c L^2)$, S stands for a physical source term multiplied by L^2/Γ and $P = \rho VLc/\Gamma$ is the global Peclet number. Here ρ is the fluid density. In the thermal case c is the specific heat and Γ is the conductivity; in the case of species transport c is to be interpreted as unity and Γ as diffusivity and in the momentum equations case c turns into unity and Γ into dynamic viscosity.

Integrating equation (1) on the cell area (Fig. 1) and employing the divergence theorem, according to the control volume methodology, one obtains:

$$\delta x \delta y \frac{\partial \phi}{\partial t} + \left(J_e - J_w\right)\delta y + \left(J_n - J_s\right)\delta x = S\delta x \delta y \tag{2}$$

where J_e is the combined convective and diffusive flux at cell boundary e:

$$J_e = Pu\phi_e - \left.\frac{\partial \phi}{\partial x}\right|_e \tag{3}$$

and so on for the other cell boundaries.

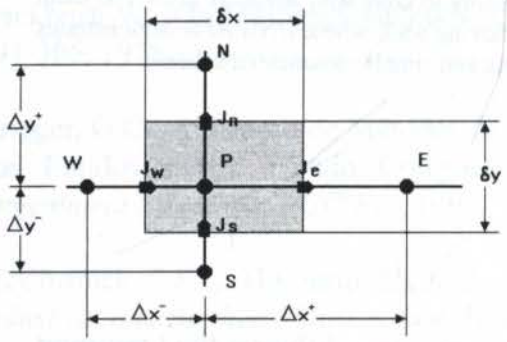

Fig. 1) Sketch of elementary control volume.

In UNIFAES, as well as in the other exponential-based schemes LOADS (Wong and Raithby, 1979) and Flux-Spline (Karki et al, 1989), the interpolating curve is obtained as the exact solution of the ordinary equation:

$$Pu\frac{d\phi}{dx} - \frac{d^2\phi}{dx^2} = K_x \tag{4}$$

which approximates partial equation (1) by assuming u to be locally constant, as well as the source term K_x, that represents all the terms of equation (1) not included in (4).

The general solution to equation (4) is:

$$\phi = C_1 + C_2 x + C_3 \exp(Pux) \tag{5}$$

where

$$C_2 = \frac{K_x}{Pu} \tag{6}$$

At the cell boundary e located between nodes P and E (figure 2), the interpolating curve (5) produces the combined convective-diffusive flux in the form:

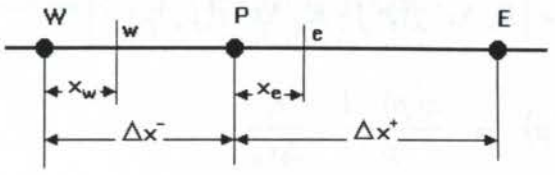

Fig. 2) One-dimensional sketch.

$$J_e = P u C_1 + C_2\left(P u x_e - 1\right) \qquad (7)$$

Adjusting the interpolating profile (5) to the nodes P and E one obtains:

$$C_1 = \phi_P - \frac{\phi_E - \phi_P}{\exp(P u_e \Delta x^+) - 1} + \frac{C_2 \Delta x^+}{\exp(P u_e \Delta x^+) - 1} \qquad (8)$$

Substituting (8) into (7), then employing (6), the flux at cell boundary e becomes:

$$\begin{aligned} J_e \;=\; & P u_e \phi_P \;+\; \frac{\phi_P - \phi_E}{\Delta x^+} \frac{P u_e \Delta x^+}{\exp(P u_e \Delta x^+) - 1} \;+ \\ & +\; K_e \Delta x^+ \left[\frac{1}{\exp(P u_e \Delta x^+) - 1} - \frac{1}{P u_e \Delta x^+} + \frac{x_e}{\Delta x^+} \right] \end{aligned} \qquad (9)$$

The above equation is substituted, together with its analogues for the other cell boundaries, into equation (2). Considering also the incompressible continuity equation in the discretized form:

$$\left(u_e - u_w\right)\delta y + \left(v_n - v_s\right)\delta x = 0 \qquad (10)$$

the resulting difference equation is:

$$\begin{aligned} & \delta x \delta y \frac{\partial \phi}{\partial t} \;+\; \left(\phi_P - \phi_E\right)\pi\left(p_e\right)\frac{\delta y}{\Delta x^+} \;+\; \left(\phi_P - \phi_W\right)\pi\left(-p_w\right)\frac{\delta y}{\Delta x^-} \;+ \\ & \left(\phi_P - \phi_N\right)\pi\left(p_n\right)\frac{\delta x}{\Delta y^+} \;+\; \left(\phi_P - \phi_S\right)\pi\left(-p_s\right)\frac{\delta x}{\Delta y^-} \;=\; S \delta x \delta y \;-\; \Psi \end{aligned} \qquad (11)$$

where

$$p_{e/w} \;=\; P u_{e/w} \Delta x^{+/-} \qquad (12)$$

$$p_{n/s} \;=\; P v_{n/s} \Delta y^{+/-} \qquad (13)$$

$$\pi(p) \;=\; \frac{p}{\exp(p) - 1} \qquad (14)$$

$$\Psi = \left[K_e \Delta x^+ \chi(p_e) - K_w \Delta x^- \chi(p_w)\right]\delta y + \left[K_n \Delta y^+ \chi(p_n) - K_s \Delta y^- \chi(p_s)\right]\delta x \tag{15}$$

$$\chi(p) = \frac{\pi(p)-1}{p} + \frac{x_b}{\Delta x_B} \tag{16}$$

In Eq. (16) x_b stands for x_e, x_w, y_n or y_s and Δx_B respectively for Δx_E, Δx_W, Δy_N or Δy_S.

Above developments are common to all exponential based exponential schemes. The simple exponential assumes null generating equation's source terms *K*. LOADS and Flux-Spline compute them by specific means. In the next section the procedure for computing them in UNIFAES is described.

2- UNIFIED FINITE APPROACH EXPONENTIAL SCHEME

The extension of the Allen and Southwell (1955) scheme to irregular grids will be presented first, followed by its application in the control volume method.

By adjusting the interpolating curve (5) to the nodes W , P and E one forms a three equations system that can be solved for C_2. Then employing equation (6) one obtains:

$$Pu_P \frac{\partial \phi}{\partial x} - \frac{\partial^2 \phi}{\partial x^2} = K_x = (\phi_P - \phi_E)\Pi^+ + (\phi_P - \phi_W)\Pi^- \tag{17}$$

where

$$\Pi^+ = \frac{Pu_P\left[1-\exp(-Pu_P \Delta x^-)\right]}{\Delta x^+\left[\exp(-Pu_P \Delta x^-)-1\right] + \Delta x^-\left[\exp(Pu_P \Delta x^+)-1\right]} \tag{18}$$

$$\Pi^- = \frac{Pu_P\left[\exp(Pu_P \Delta x^+)-1\right]}{\Delta x^+\left[\exp(-Pu_P \Delta x^-)-1\right] + \Delta x^-\left[\exp(Pu_P \Delta x^+)-1\right]} \tag{19}$$

In the uniform grid case ($\Delta x^+ = \Delta x^- = \Delta x$) these expressions reduce to Allen and Southwell's scheme, where:

$$\Pi^\pm = \frac{\pm Pu_P \Delta x}{\Delta x^2\left[\exp(\pm Pu_P \Delta x)-1\right]} \tag{20}$$

As expressed in the first equality of (17), Allen's finite difference analogue of the convective and diffusive terms is equal to the generating equation's source term K_x at each node. In UNIFAES the source term K_e is generally determined as a mean value between the estimates of K_x on nodes *(i,j)* and *(i+1,j)*:

$$K_e^{i,j} = 0.5\left(K_x^{i,j} + K_x^{i+1,j}\right) \tag{21}$$

and so on for the other cell boundary source terms. At cell boundaries neighbour to the domain boundaries the source term is linearly extrapolated from the internal nodes.

Above procedure guarantees conservation since $K_e^{i,j} = K_w^{i+1,j}$, so that $J_e^{i,j} = J_w^{i+1,j}$.

3. RESULTS

3.1 One Dimensional Test Case

A simple investigation concerning irregular grids is performed with the linear equation (4), whose exact solution is given at (5) and (6), with $K_x = S$. Computations employ the central differencing, the simple exponential scheme, UNIFAES and LOADS.

All the finite volume exponential-type schemes are computed according to expressions (11) to (16) taking a unit-size δy. Terms K_x are suppressed for the simple exponential scheme. Since in this case $K_x = S$, the souce terms can be included explicitly for LOADS. In UNIFAES the source terms are computed according to equations (17) to (19), demanding an iterative process.

Figure (3) shows the results for the case P=10 and S=5 with boundary conditions $\phi(0) = 0$ and $\phi(1) = 1$. The node positions are defined as $x_i = (1 - r^i)/(1 - r^n)$, where r=0.5 is the ratio between successive spacings and i is the node index varying from 0 to n=10.

The numerical solutions with UNIFAES and LOADS are absolutely coincident with the exact solution, but the simple exponential shows errors much greater than those of central differencing, which is not fitted to an exponential solution. The importance of taking the source term of the generating equation into account is clear.

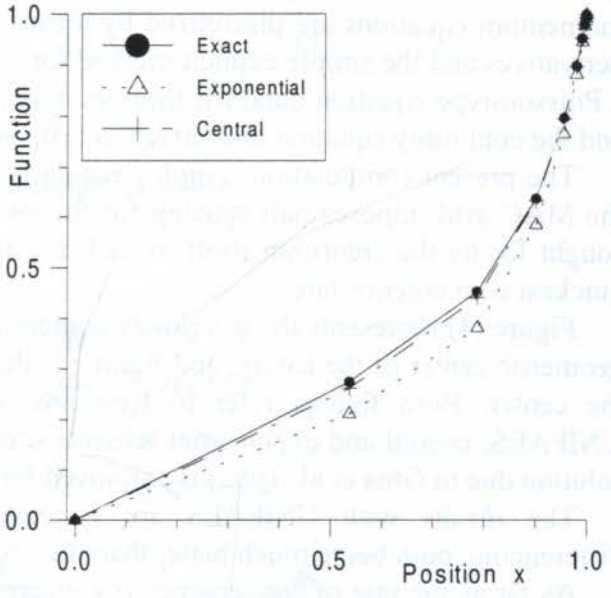

Fig. 3) One-dimensional test case for irregular grid.

3.2 Driven Cavity Test Case

The present scheme is compared to the central differencing and the simple exponential scheme in the test case of the recirculating flow in a square cavity driven by a moving wall.

The problem is governed by the continuity equation for incompressible flow:

$$\frac{\partial u}{\partial x}+\frac{\partial v}{\partial y}=0 \tag{22}$$

together with the Navier-Stokes equations for incompressible newtonian fluid, written here in conservative form analogous to equation (1):

$$\frac{\partial u}{\partial t}+\frac{\partial (R\,u u)}{\partial x}+\frac{\partial (R\,v u)}{\partial y}-\frac{\partial^2 u}{\partial x^2}-\frac{\partial^2 u}{\partial y^2}=-\frac{\partial p}{\partial x} \tag{23}$$

$$\frac{\partial v}{\partial t}+\frac{\partial (R\,u v)}{\partial x}+\frac{\partial (R\,v v)}{\partial y}-\frac{\partial^2 v}{\partial x^2}-\frac{\partial^2 v}{\partial y^2}=-\frac{\partial p}{\partial y} \tag{24}$$

where $R=\rho VL/\Gamma$ is the Reynolds number, and p stands for the pressure normalized by twice the specific kinetic energy. The no-slip condition is imposed at all walls.

The Navier-Stokes solver emploied is a primitive-variable transient-like algorithm similar to SOLA (Hirt at al, 1975), that uses the MAC staggered grid (Harlow and Welch, 1965). The momentum equations are discretized by means of the three different schemes for the spatial derivatives and the simple explicit method for time integration. The pressure is determined by a Poisson-type equation obtained from the momentum equations discretized as just described and the continuity equation discretized as (10), and it is solved via steady-state ADI.

The present computations employ regularly spaced grid, except close to the walls where the MAC grid imposes half spacing for the tangential velocity component. The time step is sought for by the algorithm itself in such a way as to avoid divergence and to establish the quickest convergence rate.

Figure (4) represents the u velocity component along the vertical line passing through the geometric center of the cavity, and figure (5) the v velocity along the horizontal line through the center. Both figures refer to Reynolds number equal to 1,000 and the results for UNIFAES, central and exponential schemes were obtained with 42X42 grid. The benchmark solution due to Ghia et al (1982) is employed for comparison.

The results with UNIFAES are systematically better than those with the central differencing, both being much better than the results with the simple exponential scheme.

As far as the rate of convergence is concerned, the simple exponential scheme demanded 1389 time steps, UNIFAES took 2586 steps and central differencing 5200 steps.

4. CONCLUSIONS

The Unified Finite Approach Exponential Scheme, UNIFAES, has been presented as a conservative-form discretization for convective-diffusive fluid transport equations constructed in the finite-volume approach, that employes Allen's finite difference method in a complementary fashion.

Through a simple one-dimensional test case the scheme has been shown to adequately cope with irregular grids. In the classic problem of the wall driven recirculating flow in a cavity the scheme has demonstrated accuracy superior to the central differencing and to the simple exponential scheme, showing convergence rate significantly greater than central differencing.

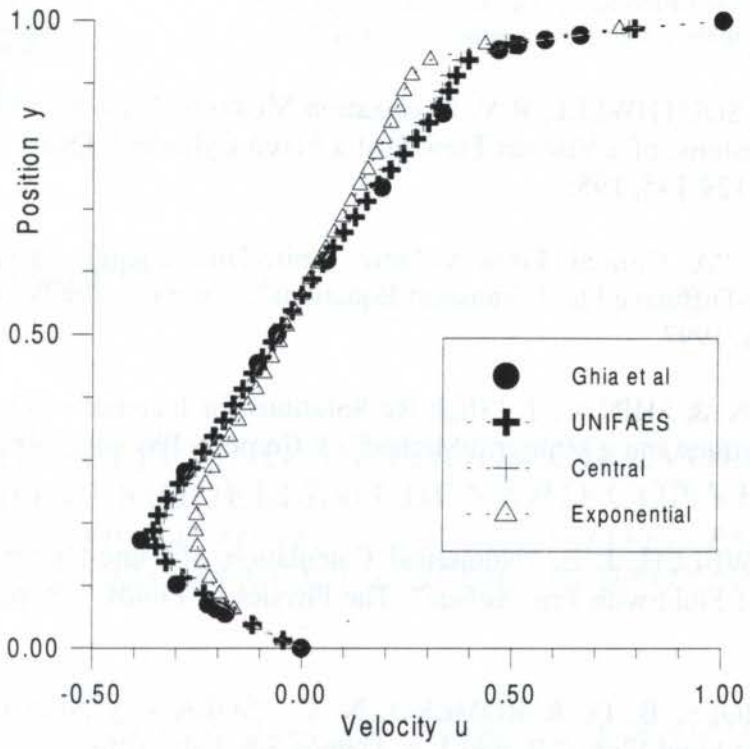

Fig. 4) u--velocity component along vertical line through the center.

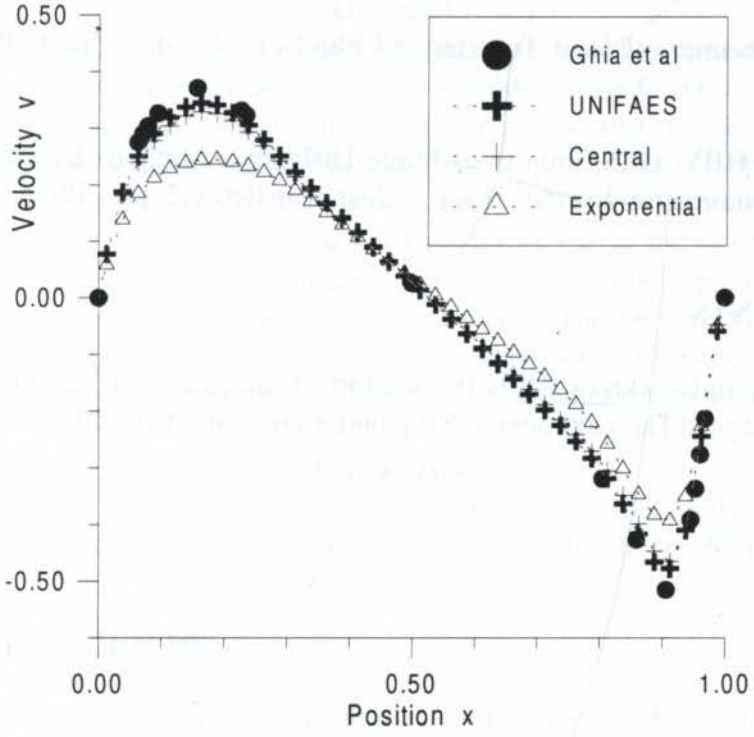

Fig. 5) v–velocity component along horizontal line through the center.

5. REFERENCES

ALLEN, D.N.de G. & SOUTHWELL, R.V. "Relaxation Methods Applied to Determine the Motion, in Two Dimensions, of a Viscous Flow Past a Fixed Cylinder"; Quart. J. Mech. and Applied Math.,v.8, pp. 129-145, 1955.

FIGUEIREDO, J. R. "A Unified Finite-Volume Finite-Differencing Exponential-Type Scheme for Convective-Diffusive Fluid Transport Equations", Journal of the Brazilian Society of Mechanical Sciences, 1997.

GHIA, U. ; GHIA, K. N. & SHIN. C. T. "High-Re Solutions for Incompressible Flow Using the Navier-Stokes Equations and a Multigrid Method", J. Comput. Physics, v.48, pp. 387-411, 1982.

HARLOW, F. H. & WELCH, J. E. "Numerical Calculation of Time-Dependent Viscous Incompressible Flow of Fluid with Free Suface", The Physics of Fluids, v.8, pp. 2182-2189, 1965.

HIRT, C. W. ; NICHOLS, B. D. & ROMERO, N. C. "SOLA - A Numerical Solution Algorithm for Transient Fluid Flows" Report Los Alamos Sci. Lab., University of California, 1975.

KARKI, K. C.; PATANKAR, S. V. & MONGIA, M. C. "Solution of Three-Dimensional Flow Problem Using a Flux-Spline Method", AIAA-89-0687, 1989.

PATANKAR, S. V. "Numerical Heat Transfer and Fluid Flow", Mc-Graw-Hill, New York, 1980.

WONG, H.H. & RAITHBY, G.D. "Improved Finite-Difference Methods Based on a Critical Evaluation of the Approximation Errors", Numer. Heat Transfer, v.2, pp.139-163, 1979.

ACKNOWLEDGMENTS

The author gratefully acknowledges the support of the Brazilian National Council for Scientific and Technological Development, CNPq, under grant number 350776/94.8

XIV Brazilian Congress of Mechanical Engineering
Obeid Plaza Hotel Convention Center - Bauru - SP/Brazil
December 08-12th 1997

PAPER CODE: COB764

A TIME SPLITTING METHOD FOR EVOLUTION EQUATIONS MODELLING BENARD CONVECTION/

UM MÉTODO DE SEPARAÇÃO TEMPORAL DE VARIÁVEIS PARA EQUAÇÕES DE EVOLUÇÃO UTILIZADAS NA MODELAGEM DE CONVECÇÃO DE BENARD

J. Pontes
PEMM/COPPE/UFRJ
PO Box 68505, 21945-970 Rio de Janeiro, R. J. Brazil *jopontes@metalmat.ufrj.br*

C. I. Christov
National Intitute of Meteorology and Hydrology
66 Tsarigradsko Chaussee, Sofia 1784, Bulgaria *christov@meteo.bg*

Abstract

Pattern formation in a thin layer of fluid heated by below is often studied by numerical integration of nonlinear parabolic equations, containing fourth-order space-derivatives in the x and the y directions. A finite-difference semi-implicit coordinate-splitting scheme of first order in time and of second order in space is developed and applied to solving two such equations in finite geometries, namely the Swift-Hohenberg and the Knobloch equations. The construction of the scheme is accomplished by assigning terms to the implicit and to the explicit parts, and by replacing the spatial and time operators by discrete representations. The stability properties of the algorithm are defined at this stage. The scheme is splitted in two equivalent equations, to reduce the storage requirements. The resulting algebraic linear system displays a left hand side operator with a pentadiagonal structure and is solved by gaussian elimination with pivoting. Some results and a criteria to characterize the asymptotic state are presented.

Keywords

Nonlinear Systems, Bénard Convection, Implicit Methods, Finite Difference Methods
Sistemas não-lineares, Convecção de Bénard, Métodos Implícitos, Método de diferenças finitas

1 INTRODUCTION

We present a finite-difference semi-implicit coordinate-splitting scheme of first order in time and of second order in space developed to numerically solving time-evolution parabolic equations with fourth-order space derivatives. The scheme is applied to integrating two evolution equations used in the study of pattern formation in a thin layer of fluid with large Prandtl number, heated from below. The first equation was derived by Swift & Hohenberg (1977) and describes Rayleigh-Bénard convective patterns in layers confined between horizontally good-conducting boundaries. The second one was derived

by Knobloch (1990) and describes pattern formation in layers confined between horizontally poor-conducting boundaries, induced by buoyancy or by surface-tension instabilities.

In fluids with large Prandtl number, the response of the velocity field to changes in the system state is much faster than the response of the temperature field. The velocity field is *slave* of the temperature field. In consequence, the system evolution can be described in terms of a two-dimensional (x and y) function representing the average vertical deviation of the local temperature from the conductive state. The single dependent variable in the Swift-hohenberg and in the Knobloch equations represents that average deviation.

2 POSING THE PROBLEM

The condition of stability of explicit numerical schemes imposes, as a rule, very restrictive limitations on the time increment used in the numerical integration of evolution equations. It is much more true when the equations contain fourth-order derivatives, where $\tau \leq (\Delta x)^4/4$. Implicit schemes are not subjected to that limitation but the straightforward implementation in more than one spatial dimension results into very large linear systems. An effective way to combine the stability properties of implicit schemes and the storage-efficiency of the explicit ones is to use the so-called coordinate splitting. The time step is implemented through several *half-time steps* in which only one of the operators is implemented implicitly. The notion of splitting (Peaceman & Rachford, 1955, Douglas & Rachford, 1956) was introduced for the second-order parabolic equation (heat equation) and proved very fruitful (see Yanenko (1971), for a review of the earlier results).

To the best of our knowledge, coordinate splitting methods had not been applied to parabolic equations with higher-order diffusion operators (see also Christov *et al.*, 1997, Pontes *et al.*, 1996). In the present work we corroborate the technique of splitting with application to the Swift-Hohenberg and Knobloch equations. These equations are, respectively,

$$\tau_0 \frac{\partial u}{\partial t} = \varepsilon u - g u^3 - \xi^4 \left(\nabla^2 + \kappa_0^2\right)^2 u, \tag{1}$$

$$\tau_0 \frac{\partial u}{\partial t} = \alpha u - \mu \nabla^2 u - \nabla^4 u + \kappa \nabla \cdot |\nabla u|^2 \nabla u + \beta \nabla \cdot \nabla^2 u \nabla u - \gamma \nabla \cdot u \nabla u + \delta \nabla^2 |\nabla u|^2. \tag{2}$$

Here, $u(x, y, t)$ is the horizontal planform of the temperature deviation from the conductive profile. The parameter κ_0 in Eq. (1) is the critical wavenumber of the structure. The coefficient μ in Eq. (2) is the scaled bifurcation parameter, and α represents the effect finite thermal conductivity of the horizontal boundaries, or finite Biot number. The coefficients β, δ and γ are present when the boundary conditions at top and bottom are not identical ($\beta \neq 0, \delta \neq 0$) or when non-Boussinesq effects are taken into account ($\gamma \neq 0$). The coefficient κ can always be scalled to ± 1 (Knobloch, 1990).

We rescale the space coordinates x and y as well as κ_0 in the Swift-Hohenberg equation by introducing the new variables $x^* = x/\xi$, $y^* = y/\xi$ and $\kappa^* = \kappa_0/\xi$. The time is also rescaled according to $\tau = t/\tau_0$. However we shall write the new variables without the asterisk in order to simplify the notation.

Boundary conditions are set to $u = \partial u/\partial n = 0$ at the sidewalls, where n is the direction of the unitary vector pependicular to the walls.

3 THE SPLITTING

First we show the desired form of the first-order in time implicit scheme for Eqs. (1, 2) in full time steps. According to the role of the different terms they are taken either on the "new" time step, $n+1$, or on the "old" one, n. Then, the implicit scheme reads:

$$\frac{u^{n+1}-u^n}{\tau} = \left(\Lambda_x^n + \Lambda_y^n\right) u^{n+1} + f^n, \tag{3}$$

whose equivalent form is as follows:

$$\left(I - \tau\,\Lambda_x^n + \Lambda_y^n\right) u^{n+1} = u^n + \tau\, f^n. \tag{4}$$

The main idea is to invert on the "new" time stage $n+1$ the negative definite operators in order to avoid the limitations on the time increment of the type $\tau \sim \mathcal{O}(\Delta x^4)$ while the non-definite lower-order operators are kept on the "old" time stage n. The operators Λ_x^n, Λ_y^n and the function f^n are defined by:

$$\Lambda_x^n = \frac{\partial^4}{\partial x^4} - \left(\frac{\kappa_0^4}{2} + \frac{3}{2}(u^n)^2\right), \tag{5}$$

$$\Lambda_y^n = \frac{\partial^4}{\partial y^4} - \left(\frac{\kappa_0^4}{2} + \frac{3}{2}(u^n)^2\right), \tag{6}$$

$$f^n = \varepsilon\, u^n + 2(u^n)^3 - 2\frac{\partial^4 u^n}{\partial x^2 \partial y^2} - 2\kappa_0^2\left(\frac{\partial^2}{\partial x^2} + \frac{\partial^2}{\partial y^2}\right) u^n, \tag{7}$$

in the case of the Swift-Hohenberg equation. The nonlinear term, gu^3, is evaluated in the "new" time stage $n+1$ according to $g(u^3)^{n+1} \approx 3(u^2)^n\, u^{n+1} - 2(u^3)^n$.

In the case of the Knobloch equation, Λ_x^n, Λ_y^n and f^n are defined by:

$$\Lambda_x^n = \frac{\alpha}{2} - \frac{\partial^4}{\partial x^4} + \kappa\frac{\partial}{\partial x}\left(|\nabla u^n|^2\,\frac{\partial}{\partial x}\right), \tag{8}$$

$$\Lambda_y^n = \frac{\alpha}{2} - \frac{\partial^4}{\partial y^4} + \kappa\frac{\partial}{\partial y}\left(|\nabla u^n|^2\,\frac{\partial}{\partial y}\right), \tag{9}$$

$$f^n = -2\frac{\partial^4 u^n}{\partial x^2 \partial y^2} - \mu\nabla^2 u^n + \beta\nabla\cdot\nabla^2 u^n \nabla u^n - \gamma\nabla\cdot u^n \nabla u^n + \delta\nabla^2|\nabla u^n|^2. \tag{10}$$

For the boundary conditions considered here, the mixed fourth derivative is an oblique operator and does not affect the stability, but is taken on the "new" time stage since it spoils the structures of the matrices to be inverted when the splitting is effected. For this reason it is left on the "old" time stage. Equation (4) results in a three-dimensional matrix of "stereo-five diagonal" structure. The inversion of this kind of matrix is an expensive procedure even though it is sparse. The most acceptable way to avoid this problem is to use coordinate splitting.

The first thing one can do here is to generalize the so-called *Alternating Directions Implicit (ADI)* scheme (Douglas & Rachford, 1956). However, ADI is at its stability margin and the inclusion of nonlinear terms could bring into play considerable limitations on the time increment. That is why we prefer the scheme of *Stabilizing Correction*, also called *Second Douglas Scheme* (Yanenko, 1971), which is more robust for nonlinear problems than ADI. Besides, Stabilizing Correction is stable in 3D while ADI is not even for linear problems. The only disadvantage is that the Second Douglas Scheme is first order in time. In terms of the notation of the present work, we have the following:

$$\frac{\tilde{u} - u^n}{\tau} = \Lambda_x^n \tilde{u} + \Lambda_y^n u^n + f^n, \tag{11}$$

$$\frac{u^{n+1} - \tilde{u}}{\tau} = \Lambda_y^n (u^{n+1} - u^n). \tag{12}$$

In order to show that the splitting scheme approximates the original implicit scheme we rewrite eqs. (11, 12) as follows:

$$(I - \tau \Lambda_x^n)\, \tilde{u} = \left(I + \tau \Lambda_y^n\right) u^n + \tau f^n, \tag{13}$$

$$\left(I - \tau \Lambda_y^n\right) u^{n+1} = \tilde{u} - \tau \Lambda_y^n u^n. \tag{14}$$

In order to exclude the intermediate variable $\tilde{u}$ we apply the operator $(I - \tau \Lambda_x^n)$ to Eq. (14) and add the result to Eq. (13), namely

$$(I - \tau \Lambda_x^n)(I - \tau \Lambda_y^n) u^{n+1} = (I + \tau \Lambda_y^n) u^n - \tau (I - \tau \Lambda_x^n) \Lambda_y^n u^n + \tau f^n, \tag{15}$$

or else,

$$\left(I - (\tau)^2 \Lambda_x^n \Lambda_y^n)\right) \frac{u^{n+1} - u^n}{\tau} = (\Lambda_x^n + \Lambda_y^n) u^{n+1} + f^n. \tag{16}$$

The latter is in fact Eq. (3) save the operator $B \equiv I + \tau^2 \Lambda_x^n \Lambda_y^n = I + \mathcal{O}(\tau^2)$, acting upon the time difference $(u^{n+1} - u^n)/\tau$. One sees that the time splitting scheme approximates the original scheme within the order $\mathcal{O}(\tau^2)$, which is better than the order of approximation of the latter. In other words, the splitting scheme coincides with the original scheme within the order of approximation of the latter.

When the norm of the operator B is greater than unit the splitting scheme is even more stable than the original one. In fact, the scheme proved to be stable for all time steps used in the tests performed with the Swift-Hohenberg code. In the case of Eq. (2), the operator acting on the unknowns is not always negative definite, so a limit for the time step used in the numerical simulations exists in certain regions of the parameters domain of that equation.

The implementation of the semi-implict scheme consists in defining a rectangular grid of points over the system and in solving Eqs. (13, 14) in the points of the grid, using the system state at each step n as the initial condition to evaluate u in the time $n + 1$. A random initial condition was assigned as the system state in $t = 0$.

Eq. (13) is decoupled from Eq. (14), being solved first in each time step n. Furthermore, the former contains space derivatives in x direction only. In consequence, the equation associated to each particular point of the grid is coupled to the equation of neighbour points in the same line, but not to equations associated to points of other lines. Eq. (11) is then solved line by line, reducing the storage requirements of the numerical code. A system of algebraic linear equations is obtaining for each line, where the operator acting in the vector of unknows diplays a penta-diagonal structure. First, all operators are evaluated and then, the linear system associated to each line is solved by gaussian elimination with pivoting.

Upon solving Eq. (13) we store the results concerning the operator $(I + \tau \Lambda_y^n)$ and $\tau \Lambda_y^n u^n$, which will be used to solve Eq. (14). So, at the end of the first "half-step", when Eq. (13) has been solved in all lines, all operators and known variables appearing in Eq. (14) have already been evaluated. The second "half-step" reduces to merely solving Eq. (14) column by column.

4 ASYMPTOTIC STATES

When performing the numerical simulations we faced the problem of distinguishing time-dependent and time-independent asymptotic states. In the latter case we needed a criteria to ascertaining when a pattern still evolved, and further qualitative changes were likely to occur, or rather, when we could, with reasonable confidence, expect that only minor adjustments would possibly occur, not justifying to proceed with the computational effort. In the case of the Swift-hohenberg equation the patterns always evolve towards time-independent asymptotic states, since that equation admits a Lyapunov potential in the form

$$\Psi = \tau_0 \int_D \left[-\frac{\varepsilon}{2} u^2 + \frac{g}{4} u^4 + \frac{\xi^4}{2} \left((\nabla^2 + \kappa_0^2) u \right)^2 \right] dx\, dy, \tag{17}$$

$$\frac{\partial \Psi}{\partial t} = -\tau_0 \int_D \left(\frac{\partial u}{\partial t} \right)^2 dx\, dy < 0. \tag{18}$$

The existence of a Lyapunov potential rules out possible time-dependent behavior in the long times. In the case of the Knobloch equation no such potential exits, opening to the possibility of existence of time-dependent asymptotic states. We found both time-dependent and time-indepent asymptotic patterns in our simulations of Eq. (2).

We followed the time evolution of patterns by monitoring a figure that measures the rate of change of the *distance* between two successive states of the system, and is sensitive to the evolution of both the *amplitude* and the *phase*. This figure is defined by (Christov *et. al.*, 1997), (Pontes *et. al.*, 1996):

$$L_1 = \frac{1}{\tau} \frac{\sum_{i,j} |u_{i,j}^{n+1} - u_{i,j}^{n}|}{\sum_{i,j} |u^{n+1}|}, \tag{19}$$

where the summs are made over the i and j points of the spatial grid. In the case of patterns that evolve towards an asymptotic steady state three different stages of evolution can be distinguished : In the first one, the velocity of evolution rapidly decays from a very high value. This is the stage in which the pattern forms, grows and the *amplitude* of the structure saturates under the action of the nonlinearities of the problem. However the pattern displays a high density of defects. In the second phase L_1 presents an irregular behaviour, but clearly non-decaying. Defects are eliminated, dislocations "climb" or "glide", the number of "grains" diminishes and the whole pattern moves. This is the stage in which the *phase* evolves. In the third stage no further qualitative changes are observed and the velocity of evolution L_1 exponentially decays. We suspended the numerical simulations after observing a sustained exponential decay of L_1.

In cases in which the system evolves towards a time-dependent pattern, L_1 initially decays, when the structure forms. Then it displays an irregular non-decaying behaviour at a level much higher than the one seen in patterns that evolve to a stady state.

5 NUMERICAL RESULTS

In this section we present some results obtained with two numerical codes based on the semi-implicit scheme above described. Fig. 1 shows a sequence of images obtained by integration of Eq. (1) and the associated $L_1 \times t$ curve. The bifurcation parameter ε varies linearly along the x direction from 0 to 0.2. A numerical grid containing 82×202

points was used, leading to a mesh of aproximately eight points per wavelength of the structure. The time-step used in the simulation was $\Delta t = 0.0085$, so approximately 10^6 time steps were accomplished in the simulation. The first image shows the random initial condition, and the following ones show an unstable focus, the colapse of the focus and the asymptotic time-independent pattern. The $L_1 \times t$ curve captures the acceleration of the dynamics when the focus colapses, and the decay of the rate of evolution, as the pattern approaches a steady state.

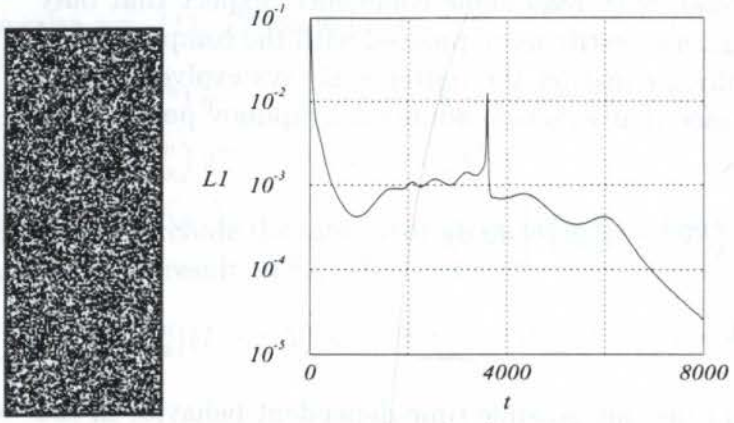

$t = 0$

$t = 500$ $t = 3580$ $t = 3604$ $t = 8000$

Figure 1: Evolution of a Bénard pattern obtained by integration of Eq. (1) with $\tau_0 = 0.0509$, $g = 1.29$, $\xi^4 = 0.015$, $\kappa_0 = 3.1172$ and ε linearly varying along x, from 0 to 0.2. The $L_1 \times t$ displays a sharp peak around $t = 3600$, when the focus appearing in $t = 500$ colapses. After that no further qualitative changes occur.

Figs. 2–4 show the results from integration of Eq. (2). The selected type of tesselation depends on the coefficients of the quadratic terms, β, γ and δ. Stable patterns include squares, hexagons, rolls and the coexistence of these motifs (Knobloch, 1990, Shtilman & Sivashinsky, 1991, Pontes *et. al.*, 1996) . Besides, this equation holds a non-variational structure, opening to the possibility of existence of time-dependent asymptotic patterns. Fig. 2 shows an evolution from the random initial condition to a time-independent tesselation of squares. A time step $\Delta t = 0.1$ was used in this simulation, so 2×10^6 of time-steps were accomplished. A numerical grid containing 402×402 points was used, leading to a mesh of aproximately 16 points per wavelenght of the pattern. All defects disappear before $t = 30000$, then the pattern slowly moves to align with the sidewalls.

Fig. 4 shows a time-dependent pattern, aperiodic in space and time. The numerical grid contains 202×202 points and a time-step $\Delta t = 5 \times 10^{-3}$ was used in this simulation.

6 CONCLUSIONS

The results presented in this work show that coordinate splitting schemes can be successefully implementeded to numerically solving parabolic equations containing fourth-order space-derivatives. These schemes are not subjected to the severe limitations on the time

XIV Brazilian Congress of Mechanical Engineering
Obeid Plaza Hotel Convention Center - Bauru - SP/Brazil
December 08-12th 1997

PAPER CODE: COB786

COMPARAÇÃO ENTRE VÁRIOS ALGORITMOS DE FATORAÇÃO APROXIMADA NA SOLUÇÃO DAS EQUAÇÕES DE NAVIER-STOKES

/ COMPARISON OF SOME APPROXIMATE FACTORIZATION ALGORITHMS IN THE SOLUTION OF THE NAVIER-STOKES EQUATIONS

EDISSON S. G. MACIEL[1] & JOÃO L. F. AZEVEDO[2]
[1] *Instituto Tecnológico de Aeronáutica, Centro Técnico Aerospacial - CTA/ITA - mesg@aer.ita.cta.br*
[2] *Instituto de Aeronáutica e Espaço, Centro Técnico Aerospacial - CTA/IAE - azevedo@ase2.iae.cta.br*
12228-904 - São José dos Campos - SP - Brasil

Abstract

The Navier-Stokes equations, written in conservative form, are applied to simulate the flowfield in a two-dimensional convergent-divergent transonic nozzle. A finite difference formulation is used to perform the spatial discretization in a generalized coordinate system. The march in pseudo-time is performed by the implicit Euler method to obtain steady state solutions. Three implicit, approximately factored, difference schemes are described and tested in the present work. These include the standard Beam and Warming algorithm, Chaussee and Pulliam's diagonal version of it, and the Steger and Warming flux vector splitting scheme. Several options for spatial discretization of the split fluxes are studied in connection with the Steger and Warming scheme. The main objectives of the present work are to perform a comparative study of the different algorithms and to assess their cost/accuracy performance characteristics.

Keywords

Equações de Navier-Stokes, Escoamento em Bocal, Esquemas Implícitos, Esquemas de Diferenças Centradas, Separação de Vetores de Fluxo / Navier-Stokes Equations, Nozzle Flow, Implicit Schemes, Central Difference Schemes, Flux Vector Splitting.

1. INTRODUÇÃO

Na indústria aeroespacial, a análise dos escoamentos em bocais transônicos assume caráter importante na determinação de desempenho e otimização do sistema de propulsão de aeronaves, bem como na previsão de possíveis influências no comportamento aerodinâmico externo dos veículos. Além da importância destes dispositivos para a indústria, eles representam bons testes para o desenvolvimento de códigos de simulação de escoamento devido a simplicidade da geometria. Estudos de escoamentos em bocais baseados em métodos computacionais já são amplamente detalhados na literatura (Azevedo, 1990, Azevedo, 1992 e Azevedo *et al.*, 1992). A utilização de uma formulação de diferenças finitas, fazendo uso de esquemas implícitos de fatoração aproximada, como o de Beam e Warming (1978), para resolução das equações resultantes do processo de discretização espacial e temporal, é um procedimento já clássico na área de CFD (do inglês: "Computational Fluid Dynamics"). Além disso, este procedimento é caracterizado por produzir resultados confiáveis a um custo

aceitável. Levando em consideração as vantagens conceituais e computacionais que outros algoritmos também clássicos na área de CFD apresentam e baseado na larga experiência que o grupo de trabalho dos presentes autores já possui na utilização do esquema padrão de Beam e Warming (1978), foi decidido que seria importante comparar as características relativas deste esquema implícito de fatoração aproximada com as características dos esquemas de Chaussee e Pulliam simplificado e completo (1981), e Steger e Warming (1981), em três variações de discretização, a fim de avaliá-los na qualidade da solução e no desempenho computacional.

2. EQUAÇÕES DE NAVIER-STOKES

As equações de Navier-Stokes em forma conservativa diferencial no sistema de coordenadas curvilíneo geral (ξ,η), são:

$$\frac{\partial \overline{Q}}{\partial \tau} + \frac{\partial (\overline{E}_e - \overline{E}_v)}{\partial \xi} + \frac{\partial (\overline{F}_e - \overline{F}_v)}{\partial \eta} = 0 \ , \tag{1}$$

onde: $\overline{Q}$ é o vetor de variáveis conservadas; $\overline{E}_e$ e $\overline{F}_e$ são os vetores de fluxo de Euler nas direções ξ e η, respectivamente; e $\overline{E}_v$ e $\overline{F}_v$ são os vetores de fluxo viscoso nas direções ξ e η, respectivamente. A adimensionalização adotada no presente trabalho segue a referenciada por MacComack (1985). As grandezas presentes na Eq. (1) podem ser definidas conforme abaixo:

$$\overline{Q} = J^{-1}\begin{Bmatrix} \rho \\ \rho u \\ \rho v \\ e \end{Bmatrix}, \quad \overline{E}_e = J^{-1}\begin{Bmatrix} \rho U \\ \rho u U + p\xi_x \\ \rho v U + p\xi_y \\ (e+p)U - p\xi_t \end{Bmatrix}, \quad \overline{F}_e = J^{-1}\begin{Bmatrix} \rho V \\ \rho u V + p\eta_x \\ \rho v V + p\eta_y \\ (e+p)V - p\eta_t \end{Bmatrix}, \tag{2}$$

$$\overline{E}_v = J^{-1}\frac{1}{Re}\begin{Bmatrix} 0 \\ \tau_{xx}\xi_x + \tau_{xy}\xi_y \\ \tau_{xy}\xi_x + \tau_{yy}\xi_y \\ \beta_x\xi_x + \beta_y\xi_y \end{Bmatrix} \quad \text{e} \quad \overline{F}_v = J^{-1}\frac{1}{Re}\begin{Bmatrix} 0 \\ \tau_{xx}\eta_x + \tau_{xy}\eta_y \\ \tau_{xy}\eta_x + \tau_{yy}\eta_y \\ \beta_x\eta_x + \beta_y\eta_y \end{Bmatrix}, \tag{3}$$

sendo que:

$$\tau_{xx} = 2\mu\frac{\partial u}{\partial x} - \frac{2}{3}\mu\left(\frac{\partial u}{\partial x} + \frac{\partial v}{\partial y}\right), \tau_{xy} = \mu\left(\frac{\partial u}{\partial y} + \frac{\partial v}{\partial x}\right), \tau_{yy} = 2\mu\frac{\partial v}{\partial y} - \frac{2}{3}\mu\left(\frac{\partial u}{\partial x} + \frac{\partial v}{\partial y}\right), \tag{4}$$

$$\beta_x = \tau_{xx}u + \tau_{xy}v + \frac{\gamma\mu}{Pr}\frac{\partial e_i}{\partial x}, \beta_y = \tau_{xy}u + \tau_{yy}v + \frac{\gamma\mu}{Pr}\frac{\partial e_i}{\partial y}, \tag{5}$$

$$u_x = u_\xi\xi_x + u_\eta\eta_x, u_y = u_\xi\xi_y + u_\eta\eta_y, v_x = v_\xi\xi_x + v_\eta\eta_x, v_y = v_\xi\xi_y + v_\eta\eta_y, \tag{6}$$

$$(e_i)_x = \left[\frac{e}{\rho} - \frac{u^2+v^2}{2}\right]_\xi \xi_x + \left[\frac{e}{\rho} - \frac{u^2+v^2}{2}\right]_\eta \eta_x, \ (e_i)_y = \left[\frac{e}{\rho} - \frac{u^2+v^2}{2}\right]_\xi \xi_y + \left[\frac{e}{\rho} - \frac{u^2+v^2}{2}\right]_\eta \eta_y, \tag{7}$$

com ρ sendo a densidade do meio; u e v os componentes cartesianos de velocidade; U e V os componentes contravariantes de velocidade; p a pressão estática do meio; $\underline{e}$ a energia total por unidade de volume; e_i a energia interna do meio, Pr o número de Prandtl, μ a viscosidade dinâmica do fluido e Re o número de Reynolds. O jacobiano da transformação de coordenadas e os termos de métrica possuem expressões definidas em Azevedo *et al.* (1995). A equação de

estado dos gases perfeitos é utilizada para fechar o sistema matricial da Eq. (1).

3. ALGORITMO DE BEAM E WARMING

O algoritmo implícito de fatoração aproximada de Beam e Warming (1978) é obtido pela discretização das equações de Navier-Stokes em um contexto de diferenças finitas. É utilizado o método de Euler implícito para marcha no tempo e, após uma linearização local por expansão em série de Taylor, as equações resultantes são fatoradas por um processo tipo ADI. Derivadas espaciais são discretizadas por operadores centrados. As instabilidades não lineares do método número devido ao cascateamento de frequências do espectro de erro não são naturalmente amortecidas devido à discretização espacial centrada. Assim, o esquema requer a introdução de termos de dissipação artificial para manter a estabilidade durante a convergência. O sistema de equações de diferenças finitas pode ser escrito como (Pulliam e Steger, 1980):

$$L_\eta L_\xi \Delta_t \overline{Q}^n = R_\eta + R_\xi \ , \tag{8}$$

em que:

$$L_\xi = I + \Delta t_{i,j}\delta_\xi \hat{A}^n_{i,j} - D_{\xi_i} \ ; \quad L_\eta = I + \Delta t_{i,j}\delta_\eta \hat{B}^n_{i,j} - D_{\eta_i} \ ; \quad R_\xi = -\Delta t_{i,j}\delta_\xi \overline{E}^{\,n}_{ei,j} + \Delta t_{i,j}\delta_\xi \overline{E}^{\,n}_{vi,j} + D_\xi \ ;$$
$$R_\eta = -\Delta t_{i,j}\delta_\eta \overline{F}^{\,n}_{ei,j} + \Delta t_{i,j}\delta_\eta \overline{F}^{\,n}_{vi,j} + D_\eta \quad \text{e} \quad \Delta_t \overline{Q}^n = \overline{Q}^{n+1} - \overline{Q}^n , \tag{9}$$

sendo $\Delta t_{i,j}$ o passo no tempo; δ_ξ e δ_η operadores centrados padrões com segunda ordem de precisão espacial; $\hat{A}^n_{i,j}$ e $\hat{B}^n_{i,j}$ as matrizes jacobianas não viscosas (detalhes em Pulliam e Steger, 1980); e os operadores D_{ξ_i} e D_{η_i} no lado esquerdo e D_ξ e D_η no lado direito da Eq. (9) são os termos de dissipação artificial que no presente trabalho seguiram o modelo não linear isotrópico proposto por Pulliam (1986) (detalhes também em Azevedo *et al.*, 1995).

4. ALGORITMO DE CHAUSSEE E PULLIAM

O algoritmo diagonal de Chaussee e Pulliam (1981) foi desenvolvido visando a redução de custo do algoritmo de Beam e Warming (1978) pela substituição da resolução de um sistema tridiagonal de blocos cheios pela resolução de um sistema pentadiagonal de blocos diagonais, e o aumento de razão de convergência provido por uma melhor consistência na linearização do esquema resultante através da utilização de operadores de dissipação artificial de mesma ordem em ambos os lados do algoritmo. É recomendado, então, a utilização de um operador de diferenças quarta a fim de evitar a competição entre a dissipação natural do modelo físico e a própria dissipação artificial. O algoritmo diagonal de Chaussee e Pulliam (1981) é obtido escrevendo a Eq. (8) como (ver Ferrari, 1996, para detalhes):

$$(T_\xi)^n_{i,j}\left(I + \Delta t \delta_\xi \lambda_\xi\right)^n_{i,j} (\hat{N})_{i,j} \left(I + \Delta t \delta_\eta \lambda_\eta\right)^n_{i,j} (T_\eta^{-1})^n_{i,j} \Delta_t \overline{Q}^n = (R_\eta + R_\xi)^n_{i,j} \ , \tag{10}$$

em que T_ξ, T_ξ^{-1}, T_η, T_η^{-1}, e $\hat{N}$ possuem expressões analíticas definidas em Chaussee e Pulliam (1981) e λ_ξ e λ_η são as matrizes diagonais de autovalores do sistema de equações de Euler nas direções ξ e η, respectivamente.

A Eq. (10), com a introdução de termos de dissipação artificial de diferenças quartas no lado esquerdo, constitui o algoritmo diagonal padrão de Chaussee e Pulliam (1981); enquanto

que, a introdução de termos de dissipação artificial apenas de diferenças segundas constitui o que está sendo denominado neste trabalho do algoritmo de Chaussee e Pulliam simplificado.

5. ALGORITMO DE STEGER E WARMING

O algoritmo proposto por Steger e Warming (1981) é obtido pela separação dos vetores de fluxo não viscoso em contribuições associadas exclusivamente aos autovalores positivos e negativos das matrizes jacobianas de fluxo não viscosas. Estes autovalores determinam direções características de propagação de informações. No algoritmo de Steger e Warming (1981), existe a proposta de separação da discretização espacial com operadores avançados e recuados, segundo uma análise de estabilidade linear, de primeira ou segunda ordem de precisão, para beneficiar tais direções de propagação de informações (esquema "upwind").

Os vetores de fluxo $\overline{E}_e$ e $\overline{F}_e$ da Eq. (1) podem ser separados, respectivamente, em E_e^+ e E_e^- e F_e^+ e F_e^-, comportando exclusivamente as contribuições dos autovalores positivos ou negativos das matrizes jacobianas não viscosas. Expressões analíticas para os vetores de fluxo separados podem ser encontradas no trabalho de Steger e Warming (1981). Similarmente, as matrizes jacobianas não viscosas são aproximadas pelas matrizes jacobianas "reconstruídas":

$$\overline{A}^+ = T_\xi \lambda_\xi^+ T_\xi^{-1}, \qquad \overline{A}^- = T_\xi \lambda_\xi^- T_\xi^{-1}, \qquad \overline{B}^+ = T_\eta \lambda_\eta^+ T_\eta^{-1} \qquad \text{e} \qquad \overline{B}^- = T_\eta \lambda_\eta^- T_\eta^{-1}. \tag{11}$$

Por uma análise de estabilidade de von Neumann, os vetores de fluxo positivos devem ser discretizados com operadores recuados enquanto os vetores de fluxo negativos por operadores avançados. O algoritmo de Steger e Warming (1981) resultante para resolução da Eq. (1), com primeira ordem de precisão espacial, em sua forma padrão, é:

$$\left\{I + \Delta t_{i,j}\left[\nabla_\xi(\overline{A}^+) + \nabla_\eta(\overline{B}^+) + \Delta_\eta(\overline{B}^-)\right]_{i,j}^n\right\}\left\{I + \Delta t_{i,j}\left[\Delta_\xi(\overline{A}^-)\right]_{i,j}^n\right\}\Delta\overline{Q}_{i,j}^n = RHS_{i,j}^n \tag{12}$$

$$RHS_{i,j}^n = -\Delta t_{i,j}\left(\nabla_\xi E_e^+ + \Delta_\xi E_e^- + \nabla_\eta F_e^+ + \Delta_\eta F_e^-\right)_{i,j}^n + \Delta t_{i,j}\left(\delta_\xi E_v + \delta_\eta F_v\right)_{i,j}^n, \tag{13}$$

em que Δ_ξ e Δ_η são operadores avançados padrões e ∇_ξ e ∇_η são operadores recuados padrões, nas direções ξ e η, respectivamente. Para segunda ordem de precisão, os operadores de primeira ordem são substituídos por operadores como, por exemplo, os descritos abaixo:

$$\delta_\xi^r(\cdot)_{i,j} = \frac{1}{2}\left[3(\cdot)_{i,j} - 4(\cdot)_{i-1,j} + (\cdot)_{i-2,j}\right] \quad \text{e} \quad \delta_\xi^a(\cdot)_{i,j} = \frac{1}{2}\left[-3(\cdot)_{i,j} + 4(\cdot)_{i+1,j} - (\cdot)_{i+2,j}\right]. \tag{14}$$

6. CONDIÇÃO INICIAL E CONDIÇÕES DE CONTORNO

A condição inicial adotada no presente trabalho é a de estagnação para todo o domínio de cálculo, com a excessão da saída aonde existirá uma redução no valor da pressão e da densidade para inicializar o escoamento. As condições de contorno implementadas são:

a) Condição de parede: Condição de não deslizamento e de impermeabilidade (vetor velocidade igual ao vetor nulo). O gradiente de pressão normal à parede é igual a zero bem como o gradiente de temperatura, o que corresponde à condição de parede adiabática.

b) Condição de simetria: É imposta admitindo que o vetor de variáveis conservadas na linha computacional j = JMAX seja igual ao da linha j = JMAX-2 com a excessão do termo ρv, que deve ter o sinal oposto a fim de garantir o fluxo nulo através da linha de centro do bocal.

c) Condições de entrada e saída: A implementação das condições de contorno na entrada e saída do bocal seguiu o conceito de relações características unidimensionais com operação

em x (ver detalhes em Azevedo, 1992 e Azevedo *et al.*, 1992).

7. PROBLEMA FÍSICO DE INTERESSE

O exemplo de simulação estudado foi o escoamento ao longo de um bocal transônico convergente-divergente, simétrico e bidimensional. A garganta do bocal está localizada equidistantemente entre a entrada e a saída. O comprimento total do bocal é 0,380 ft (0,116 m) e a meia altura da garganta vale 0,045 ft (0,014 m). O ângulo de convergência do bocal vale 22,33° e o de divergência vale 1,21°. As condições de estagnação na entrada do bocal são: temperatura igual a 531,2° R (294,8 °C) e pressão igual a 2117,0 lb/ft^2 (1,0136×10^5 N/m^2).

A malha utilizada no presente problema foi gerada algebricamente e é exibida na Fig. 1. Devido à simetria do escoamento, apenas metade do bocal é discretizado, com uma linha computacional a mais acima da linha de centro a fim de facilitar a implementação da condição de contorno. A malha apresenta estiramento exponencial em ambas as direções coordenadas.

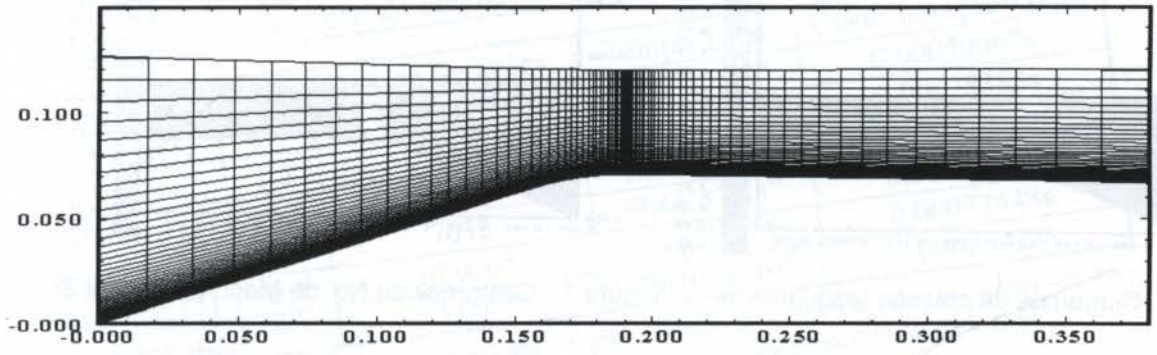

Figura 1 - Malha computacional 81x60 gerada algebricamente (10% de estiramento)

8. RESULTADOS E ANÁLISES

Para realizar os estudos comparativos foi estruturado um código com seis opções de esquemas: algoritmo de Beam e Warming padrão (esquema 1); algoritmo de Chaussee e Pulliam simplificado (esquema 2); algoritmo de Chaussee e Pulliam completo (esquema 3); algoritmo de Steger e Warming conforme a Eq. (12) (esquema 4); algoritmo de Steger e Warming com lado esquerdo conforme a Eq. (12) e lado direito com segunda ordem de precisão (esquema 5); e algoritmo de Steger e Warming com discretização de segunda ordem de precisão (esquema 6). O número de Reynolds utilizado foi 1,0x10^6 e o número de Prandtl foi 0,72. No presente trabalho não foi implementado nenhum modelo de turbulência.

8.1 Algoritmo de Beam e Warming As Figs. 2 e 3 exibem as curvas de contorno de pressão e de no. de Mach obtidas pelo esquema de Beam e Warming (1978).

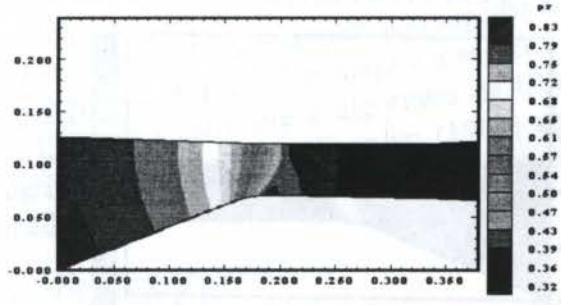

Figura 2 - Contornos de pressão (esquema 1).

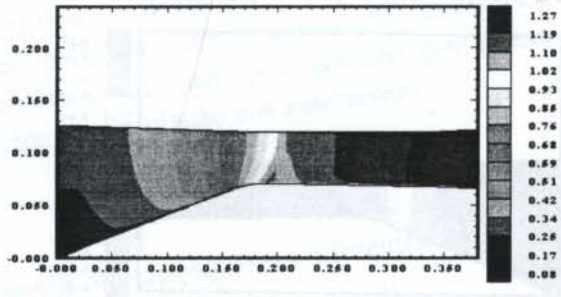

Figura 3 - Contornos de No. de Mach (esquema 1).

8.2 Algoritmo de Chaussee e Pulliam As Figs. 4 até 7 exibem as curvas de contorno de pressão e de no. de Mach para as versões do algoritmo de Chaussee e Pulliam (1981). As Figs. 4 e 5 exibem os resultados do algoritmo simplificado e as Figs. 6 e 7 do algoritmo completo.

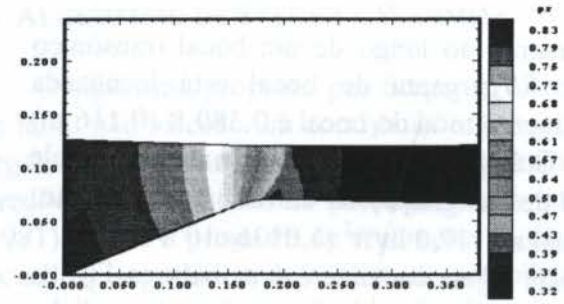

Figura 4 - Contornos de pressão (esquema 2).

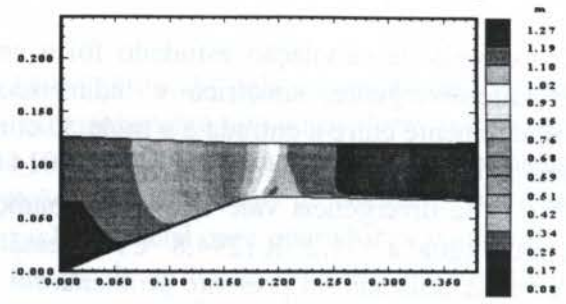

Figura 5 - Contornos de No. de Mach (esquema 2).

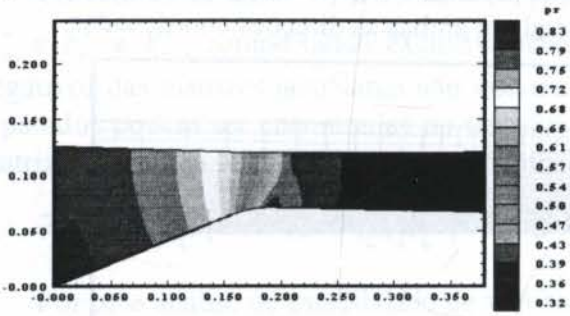

Figura 6 - Contornos de pressão (esquema 3).

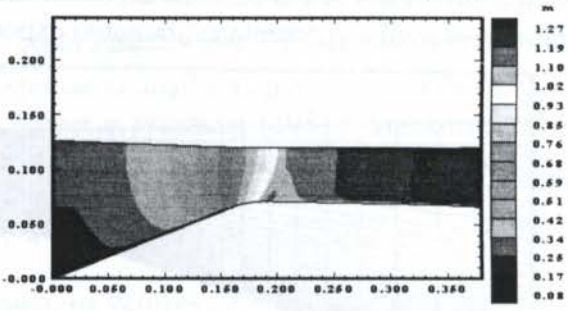

Figura 7 - Contornos de No. de Mach (esquema 3).

8.3 Algoritmo de Steger e Warming As Figs. 8 até 13 exibem as curvas de contorno de pressão e de no. de Mach para as versões do algoritmo de Steger e Warming (1981). As Figs. 8 e 9 exibem os resultados para o algoritmo de Steger e Warming (1981) com discretização de primeira ordem. As Figs. 10 e 11 exibem os resultados para este algoritmo com discretização de primeira ordem no lado esquerdo e de segunda ordem no lado direito. Por fim, as Figs. 12 e 13 exibem os resultados para uma discretização de segunda ordem deste esquema.

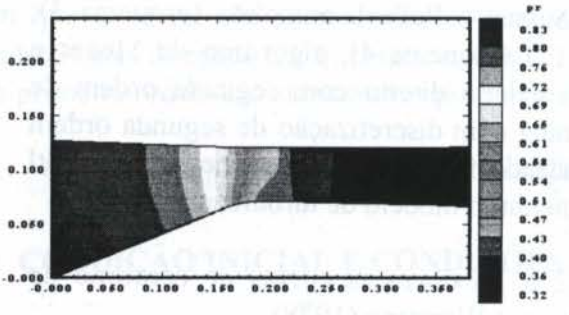

Figura 8 - Contornos de pressão (esquema 4).

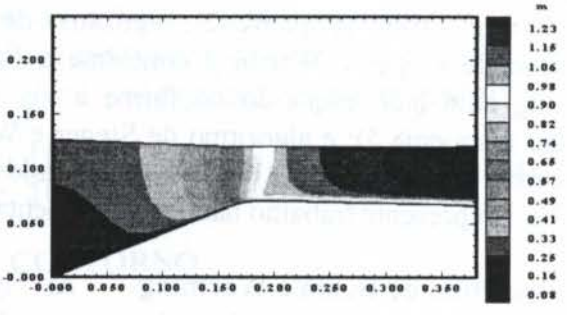

Figura 9 - Contornos de No. de Mach (esquema 4).

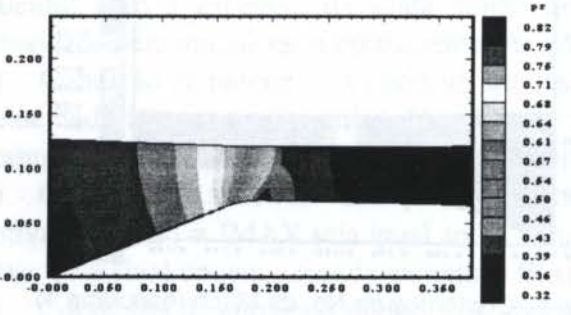

Figura 10 - Contornos de pressão (esquema 5).

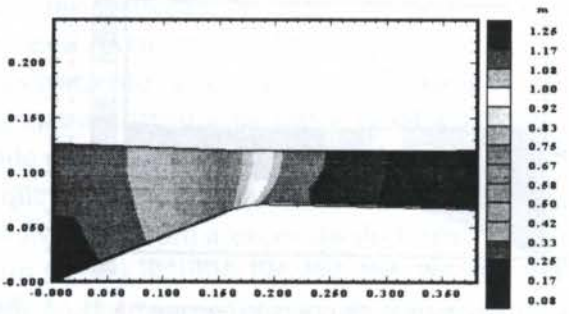

Figura 11 - Contornos de No. de Mach (esquema 5).

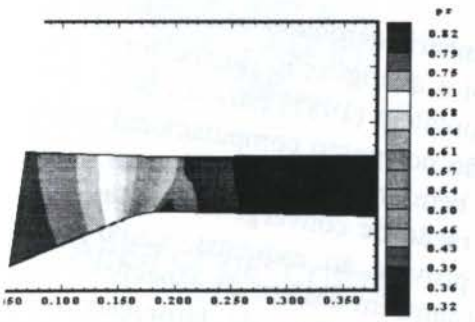

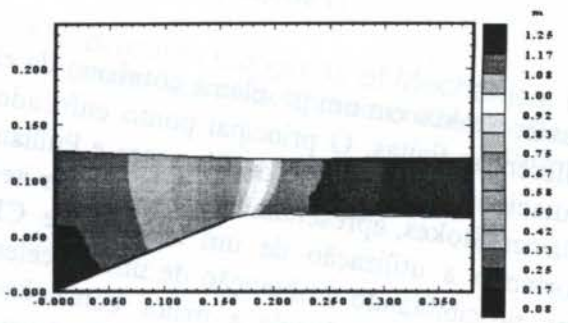

- Contornos de pressão (esquema 6). Figura 13 - Contornos de No. de Mach (esquema 6).

mparação de Desempenho entre os Algoritmos Implementados

1: Desempenho Computacional dos Algoritmos de Beam e Warming (1981), Pulliam e ee simplificado e completo (1981) e Steger e Warming (1981) (Máquina: IBM 6091-19).

lha : 81 x 60 Número Total de Pontos : 4860 Critério de Convergência: 10^{-10}

Esquema:	CFL	No. de Iterações	Tempo Total	Custo/Iteração/Ponto
am e Warming (1)	1,7	4947	2h40'33,08"	0,00040067s
aussee e Pulliam (2)	1,5	5362	2h03'16,39"	0,00028383s
aussee e Pulliam (3)	35,0	3068	1h20'26,20"	0,00032368s
eger e Warming (4)	0,7	7032	6h44'57,43"	0,00071096s
teger e Warming (5)	0,3	10.000*	9h46'49,73"	0,00072448s
teger e Warming (6)	0,3	15.000*	17h30'06,01"	0,00086428s

execução dos esquemas foi interrompida em 10.000 e 15.000 iterações, respectivamente, pela demora de convergência observada. Estes uemas tiveram seus processos de convergência interrompidos quando o máximo resíduo no domínio de cálculo era da ordem de 10^{-9}.

Do exposto na tabela 1, os menores custos por iteração por ponto da malha estão sociados aos algoritmos diagonais de Chaussee e Pulliam simplificado e completo (1981), o e era esperado pois consistem em soluções de sistemas de matrizes diagonais. Os esquemas ais caros são os derivados do algoritmo de separação de vetores de fluxo de Steger e arming (1981), devido principalmente ao cálculo das matrizes "reconstruídas" e à resolução sistemas tridiagonais e pentadiagonais de blocos cheios em alguns casos. O melhor sempenho coube ao algoritmo de Chaussee e Pulliam completo (1981) com um custo por ração por ponto da malha pequeno (cerca de 14,04% mais caro que o algoritmo de aussee e Pulliam simplificado e 19,22% mais barato que o algoritmo de Beam e Warming) e m uma razão de convergência excelente (cerca de 37,98% menos iterações são requeridas ra atingir a convergência em comparação com Beam e Warming). Assim, para o caso das uações de Navier-Stokes, o algoritmo de Chaussee e Pulliam completo (1981) foi o que resentou o melhor desempenho entre os esquemas testados. Próximo a ele está o algoritmo Chaussee e Pulliam simplificado (apenas 8,39% mais iterações são requeridas em relação ao goritmo de Beam e Warming) e a seguir o algoritmo de Beam e Warming (1978) (cerca de ,17% mais caro que o algoritmo de Chaussee e Pulliam simplificado). As derivações do goritmo de Steger e Warming (1981) apresentaram um custo por iteração por ponto da alha elevado e por isso ficaram sem competitividade em relação aos anteriores.

CONCLUSÕES

O trabalho descreve a implementação numérica de seis esquemas diferentes para resolução

das equações de Navier-Stokes em um problema cotidiano da engenharia aeronáutica, usando a formulação de diferenças finitas. O principal ponto enfocado foi a averigüação do melhor desempenho computacional do algoritmo de Chaussee e Pulliam completo (1981) para o caso das equações de Navier-Stokes, apresentando um custo por iteração por ponto computacional pequeno e comportando a utilização de um número de CFL bem maior que os demais algoritmos testados, possibilitando a obtenção de uma excelente razão de convergência. Esta característica de convergência é devida a maior consistência provida ao esquema, como preconizado por Chaussee e Pulliam (1981). O trabalho procurou também discutir os aspectos teóricos básicos envolvidos na implementação computacional de algoritmos de fatoração aproximada clássicos da literatura e ressaltar suas vantagens e desvantagens práticas.

10. AGRADECIMENTOS

Este trabalho faz parte de um projeto de pesquisa financiado em parte pela Fundação de Amparo à Pesquisa do Estado de São Paulo (FAPESP), através de uma bolsa de Doutorado, nível I, sob o Processo Nº 96/02601-4. Os autores também agradecem o suporte parcial do Conselho Nacional de Desenvolvimento Científico e Tecnológico, CNPq, através do Projeto Integrado de Pesquisa associado ao Processo Nº 522413/96-0.

11. REFERÊNCIAS BIBLIOGRÁFICAS

AZEVEDO, J. L. F., Euler Solutions of Transonic Nozzle Flows, *Anais do III Encontro Nacional de Ciências Térmicas (III ENCIT)*, Vol. I, pp. 243-48, Itapema, SC, Brazil,1990.

AZEVEDO, J. L. F., A Finite Difference Method Applied to Internal Axisymmetric Flows, *Boletim da Sociedade Brasileira de Matemática Aplicada e Computacional*, Vol. 3, No. 1, Série II, pp. 1-20, 1992.

AZEVEDO, J. L. F., FICO, N. G. C. R., JR. & ORTEGA, M. A., Two-Dimensional and Axisymmetric Nozzle Flow Computations Using the Euler Equations, *Revista Brasileira de Ciências Mecânicas*, Vol. XVII, No. 2, pp. 147-170, 1995.

AZEVEDO, J. L. F., FICO, N. G. C. R., JR., ORTEGA, M. A., & LUNA, G. C., Nozzle Flow Computations Using the Euler Equations, Paper ICAS No. 92-4.1.2, *Proceedings of the 18th Congress of the International Council of the Aeronautical Sciences*, pp. 97-107, Beijing, P. R. China, 1992.

BEAM, R. M., & WARMING, R. F., An Implicit Factored Scheme for the Compressible Navier-Stokes equations, *AIAA Journal*, Vol. 16, No. 4, pp. 393-402, 1978.

CHAUSSEE, D. S. & PULLIAM, T. H., Two-Dimensional Inlet Simulation Using a Diagonal Implicit Algorithm, *AIAA Journal*, Vol. 19, No. 2, pp. 153-159, 1981.

FERRARI, M. A. S., Aceleração de Convergência de um Método Numérico Implícito para Escoamentos em Qualquer Regime de Velocidade, *Tese de Mestrado*, ITA, São José dos Campos, SP, 1996.

MACCORMACK, R. W., Current Status of Numerical Solutions of the Navier-Stokes Equations, AIAA Paper 85-0032, *AIAA 23rd Aerospace Sciences Meeting*, Reno, Nevada, EUA, 1985.

PULLIAM, T. H., Artificial Dissipation Models for the Euler Equations, *AIAA Journal*, Vol. 24, No. 12, pp. 1931-1940, 1986.

PULLIAM, T. H., & STEGER, J. L., Implicit Finite-Difference Simulations of Three-Dimensional Compressible Flow", *AIAA Journal*, Vol. 18, No. 2, pp. 159-67, 1980.

STEGER, J. L., & WARMING, R. F., Flux Vector Splitting of the Inviscid Gasdynamic Equations with Application to Finite-Difference Methods, *Journal of Computational Physics*, Vol. 40, pp. 263-293, 1981.

XIV Brazilian Congress of Mechanical Engineering
Obeid Plaza Hotel Convention Center - Bauru - SP/Brazil
December 08-12th 1997

PAPER CODE: COB794

ANÁLISE DO ESFORÇO COMPUTACIONAL DE SOLUÇÕES MULTIGRID DE PROBLEMA CONDUTIVO-CONVECTIVO / *COMPUTATIONAL EFFORT ANALYSIS OF MULTIGRID SOLUTIONS OF CONDUCTIVE-CONVECTIVE PROBLEM*

JOSÉ ANTONIO RABI & MARCELO JOSÉ SANTOS DE LEMOS
Depto. Engenharia Mecânica-Aeronáutica, Instituto Tecnológico de Aeronáutica - ITA / CTA
12.228-901 S.J.Campos SP Brasil - E-mails: jrabi@mec.ita.cta.br, lemos@mec.ita.cta.br

Abstract

Multigrid methods have been used for predicting flows achieving considerable computational time savings. In the present paper, a multigrid method has been applied to a finite-volume numerical solution of a 2-D conductive-convective problem. Structured and regular grids of different sizes were employed. Internodal interpolation has been achieved through the *Weighted Upstream Differencing Scheme*, which depends upon the computational Peclet number Pe. A study on the effect of the number of distinct grids on the overall algorithm performance is presented. Also reported is a comparative study of the computational effort as a function of Pe.

Keywords

Multigrid	Laminar flow	Convergence acceleration	Finite-volume
Malhas múltiplas	Escoamento laminar	Aceleração da convergência	Volumes finitos

1. INTRODUÇÃO

O avanço experimentado pela dinâmica dos fluidos computacional está relacionado ao uso de métodos numéricos rápidos e precisos aliado à crescente disponibilidade computacional. Problemas envolvendo escoamento em geometrias e condições de contorno complexas já podem ser resolvidos, para os quais o tempo computacional era proibitivo anos atrás. Porém, para que certos detalhes do escoamento possam ser analisados, muitas vezes é necessário se lançar mão de malhas computacionais refinadas, acarretando em grandes esforços computacionais. Por isso, técnicas para acelerar a convergência de métodos numéricos têm sido intensivamente pesquisadas e desenvolvidas.

A técnica de *multigrid* utiliza uma seqüência de malhas cada vez menos refinadas, a fim de relaxar a solução numérica de modo eficiente (Hackbuch, 1985). A aplicação desta técnica proporciona um aumento aproximadamente linear do tempo de computação com o número de pontos nodais, enquanto que, com malha única, o mesmo tempo computacional aumenta quadraticamente com o refinamento da malha (Hortmann & Peric & Scheuerer, 1990).

Com tal motivação, o presente trabalho aplica o método *multigrid* na solução numérica de um problema condutivo-convectivo 2-D. As equações aproximadas são obtidas segundo uma discretização em volumes finitos, usando o esquema de interpolação *Weighted Upstream Differencing Scheme* - WUDS, cujos coeficientes de ponderação dependem do número de Peclet Pe para cada direção coordenada. Compara-se o esforço computacional para a solução

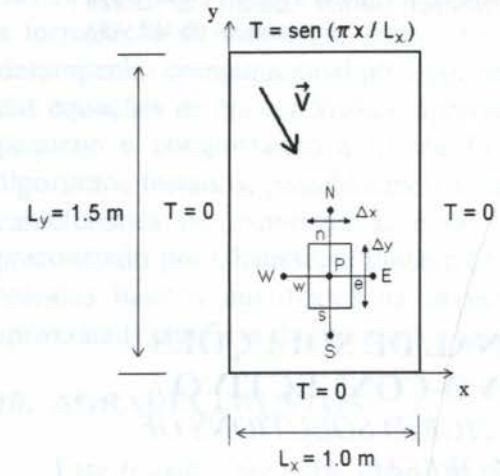

Fig. 1 Esquema do problema físico e do volume elementar para discretização.

do problema para diferentes valores de *Pe* e discute-se a influência deste parâmetro no uso da técnica de *multigrid*. Apresenta-se também a solução do problema de condução pura, cuja comparação com a solução analítica visa validar o método numérico empregado.

2. MODELO MATEMÁTICO

O presente trabalho aborda um problema condutivo-convectivo 2-D em um domínio retangular com temperatura prescrita em suas fronteiras. O regime é permanente, não há fontes internas de calor e o campo de velocidades no interior do domínio é conhecido e constante, conforme esquema da Fig. 1. Este problema é útil para a análise de funções de interpolação e sua dependência com *Pe*, sendo aqui também utilizado para aplicação da técnica de *multigrid*.

A equação diferencial que descreve o problema é

$$\frac{\partial}{\partial x}(\rho u T)+\frac{\partial}{\partial y}(\rho v T)=\frac{\partial}{\partial x}\left(\frac{K}{C_P}\frac{\partial T}{\partial x}\right)+\frac{\partial}{\partial y}\left(\frac{K}{C_P}\frac{\partial T}{\partial y}\right) \quad . \tag{1}$$

sendo ρ a densidade, u e v os componentes de $\vec{V}$, T a temperatura, K a condutividade térmica e C_P o calor específico. Para as constantes físicas foram adotados $K / C_P = 1$ kg/m.s e $\rho = 1$ kg/m^3 e para as velocidades u e v foram utilizadas combinações entre os valores 0, 1, 10 e 100 m/s. Para o problema puramente condutivo ($u = v = 0$) a solução analítica para as condições de contorno da Fig. 1 é dada por

$$T(x,y)=\frac{\operatorname{senh}(\pi\, y/L_x)}{\operatorname{senh}(\pi\, L_y/L_x)}\operatorname{sen}\left(\frac{\pi\, x}{L_x}\right) \quad . \tag{2}$$

3. DESCRIÇÃO DO MÉTODO NUMÉRICO

3.1 Formulação em Volumes Finitos

O domínio de interesse é discretizado através de uma malha estruturada, ortogonal e regular, segundo um esquema *cell-centered*. As equações algébricas são obtidas integrando-se a Eq. (1) sobre um volume elementar mostrado na Fig. 1, resultando em

$$\dot{M}_e T_e - \dot{M}_w T_w + \dot{M}_n T_n - \dot{M}_s T_s = D_e \left.\frac{\partial T}{\partial x}\right|_e - D_w \left.\frac{\partial T}{\partial x}\right|_w + D_n \left.\frac{\partial T}{\partial y}\right|_n - D_s \left.\frac{\partial T}{\partial y}\right|_s \quad , \tag{3}$$

onde

$$\dot{M}_e = \rho u \Delta y\big|_e \qquad \dot{M}_w = \rho u \Delta y\big|_w \qquad \dot{M}_n = \rho v \Delta x\big|_n \qquad \dot{M}_s = \rho v \Delta x\big|_s$$
$$D_e = \frac{K}{C_P}\Delta y\Big|_e \qquad D_w = \frac{K}{C_P}\Delta y\Big|_w \qquad D_n = \frac{K}{C_P}\Delta x\Big|_n \qquad D_s = \frac{K}{C_P}\Delta x\Big|_s \quad . \tag{4}$$

Para a função de interpolação da temperatura e suas derivadas nas interfaces do volume de controle utiliza-se o esquema WUDS (Raithby, 1974), o qual faz uso de dois coeficientes α e β que ponderam os processos de convecção e difusão. Para a face leste, por exemplo, o valor da temperatura e de sua derivada são aproximados por

$$T_e = \left(\frac{1}{2} + \alpha_e\right)T_P + \left(\frac{1}{2} - \alpha_e\right)T_E \qquad \text{e} \qquad \left.\frac{\partial T}{\partial x}\right|_e = \beta_e\left(\frac{T_E - T_P}{\Delta x}\right) \tag{5}$$

com os coeficientes sendo expressos por

$$\alpha_e = \frac{1}{2} - \frac{\exp\left(\mathrm{Pe}_{\Delta x}/2\right) - 1}{\exp\left(\mathrm{Pe}_{\Delta x}\right) - 1} \qquad \text{e} \qquad \beta_e = \mathrm{Pe}_{\Delta x}\frac{\exp\left(\mathrm{Pe}_{\Delta x}/2\right)}{\exp\left(\mathrm{Pe}_{\Delta x}\right) - 1} \quad . \tag{6}$$

O parâmetro $\mathrm{Pe}_{\Delta x}$ é o *número de Peclet* computacional (baseado em Δx) e é dado por

$$\mathrm{Pe}_{\Delta x} = \frac{\rho u \Delta x}{K/C_P} \quad . \tag{7}$$

Contudo, as expressões para α e β na forma dada pelas Eq. (6) acarretam dificuldades relacionadas com o tempo de computação para avaliar as exponenciais. Para contorná-las, Raithby (1976) propõe as seguintes aproximações, também adotadas no presente trabalho:

$$\alpha_e = \frac{\mathrm{Pe}_{\Delta x}^2}{10 + 2\,\mathrm{Pe}_{\Delta x}^2} \qquad \text{e} \qquad \beta_e = \frac{1 + 0.005\,\mathrm{Pe}_{\Delta x}^2}{1 + 0.05\,\mathrm{Pe}_{\Delta x}^2} \tag{8}$$

Substituindo as expressões para T_e e sua derivada na face e, Eq. (5), assim como equações similares para as demais faces w, n e s na Eq. (3), obtém-se

$$A_P T_P = A_e T_E + A_w T_W + A_n T_N + A_s T_S \quad . \tag{9}$$

Os coeficientes A_P, A_e, A_w, A_n e A_s são definidos em (Maliska, 1995), sendo, por exemplo,

$$A_e = -\dot{M}_e\left(\frac{1}{2} - \alpha_e\right) + \left.\frac{D\beta}{\Delta x}\right|_e \quad . \tag{10}$$

3.2 O Método Multigrid

A taxa de convergência da solução numérica é máxima no início dos cálculos, decaindo sensivelmente à medida que o processo iterativo evolui. Tal efeito é tanto mais pronunciado quanto mais refinada for a malha computacional. O motivo é que o método iterativo utilizado

é capaz de remover de modo eficiente somente aquelas componentes de Fourier do erro cujos comprimentos de onda são menores que ou comparáveis com o espaçamento da malha.

O método *multigrid* procura cobrir um espectro maior de comprimento de onda através da iteração em mais de uma malha. Comprimentos de onda do erro que são grandes em malhas finas são transformados em comprimentos de onda menores em malhas grossas, onde então podem ser suavizados. Assim em cada malha visitada, as componentes do erro ali correspondentes são eficientemente relaxadas, acelerando o processo de convergência.

O sistema linear de equações algébricas definido pela Eq. (9) escrita para cada volume de controle pode ser colocado na forma

$$\mathbf{L}_k \mathbf{T}_k = \mathbf{f}_k \tag{11}$$

onde $\mathbf{L}_k$ é a chamada *matriz dos coeficientes*, $\mathbf{T}_k$ é o *vetor das incógnitas* e $\mathbf{f}_k$ é o vetor que acomoda os demais termos da equação. O subscrito k refere-se a uma dada malha computacional, sendo $k = 1$ referente à malha mais grossa.

Um pequeno número de iterações (suavizações) resulta em um valor intermediário $\overline{\mathbf{T}}_k$, acompanhado da respectiva *correção* $\mathbf{t}_k = \overline{\mathbf{T}}_k - \mathbf{T}_k$. Introduzindo $\overline{\mathbf{T}}_k$ na Eq. (11), obtém-se para um problema linear o *resíduo*

$$\mathbf{d}_k = \mathbf{L}_k \overline{\mathbf{T}}_k - \mathbf{f}_k \tag{12}$$

Hackbuch (1985) mostra que a *correção exata* $\mathbf{t}_k$ é a solução de

$$\mathbf{L}_k \mathbf{t}_k = \mathbf{d}_k \tag{13}$$

a qual tem a mesma forma que a Eq. (11). A solução *exata* da Eq. (13) é tão difícil quanto a da Eq. (11). Contudo, $\mathbf{t}_k$ pode ser melhor *aproximada* que $\mathbf{T}_k$ (Hackbuch, 1985). Tal aproximação é realizada em malhas mais grossas

$$\mathbf{L}_{k-1} \mathbf{t}_{k-1} = \mathbf{d}_{k-1} \tag{14}$$

onde $\mathbf{d}_{k-1}$ é obtido segundo

$$\mathbf{d}_{k-1} = I_k^{k-1} \mathbf{d}_k \tag{15}$$

O operador I_k^{k-1}, denominado *restrição*, leva valores da malha k para a malha $k-1$.

Em situações ideais, recomenda-se (Hackbuch, 1985) que a Eq. (14) na malha mais grossa ($k = 1$) seja resolvida exatamente, o que nem sempre é possível. Todavia, por envolver um número expressivamente menor de volumes elementares, pode-se, pelo menos, realizar um número bem maior de iterações nesta malha sem comprometer muito o esforço computacional.

Uma vez obtida, a aproximação da correção $\tilde{\mathbf{t}}_{k-1}$ (ou a solução exata $\mathbf{t}_{k-1}$) em malha grossa é levada de volta para malhas mais finas através do operador *prolongamento* I_{k-1}^k

$$\tilde{\mathbf{t}}_k = I_{k-1}^k \tilde{\mathbf{t}}_{k-1} \tag{16}$$

de forma a refinar a aproximação $\overline{\mathbf{T}}_k$

$$\mathbf{T}_k^{new} = \overline{\mathbf{T}}_k - \tilde{\mathbf{t}}_k \tag{17}$$

O procedimento que vai de $\overline{\mathbf{T}}_k$ a $\mathbf{T}_k^{new}$ é conhecido como *coarse-grid correction* e pode ser resumido segundo

$$\mathbf{T}_k^{new} = \overline{\mathbf{T}}_k - I_{k-1}^{k}\, \mathbf{L}_{k-1}^{-1}\, I_{k}^{k-1}\left(\mathbf{L}_k \overline{\mathbf{T}}_k - \mathbf{f}_k\right) \tag{18}$$

A ordem como os procedimentos (18) são concatenados entre valores consecutivos de k é o que caracteriza os chamados *ciclo-V* e *ciclo-W*. A Fig. 2 mostra a seqüência de operações em

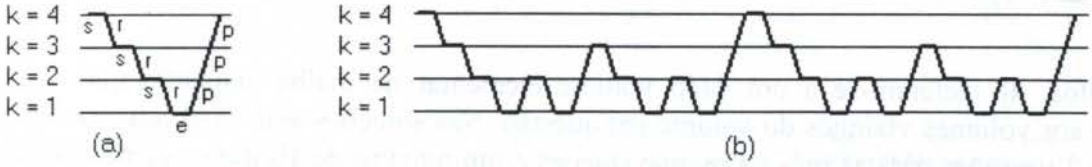

Fig. 2 Seqüência de operações para uma iteração *multigrid* completa com 4 malhas: (a) ciclo-V ; (b) ciclo-W (s = pré-suavização ; r = restrição ; e = solução exata ; p = prolongamento).

cada ciclo durante uma iteração *multigrid* completa.

4. RESULTADOS E DISCUSSÃO

A Fig. 3 mostra como o refinamento da malha computacional influi na qualidade da solução obtida para o problema de condução pura, onde o perfil de temperatura exibido corresponde à posição $x = L_x / 2$. Para comparação, a solução exata dada pela Eq. (2) para a mesma posição $x = L_x / 2$ também é mostrada. Para os casos apresentados, uma única malha foi utilizada e o algoritmo de solução aplicado foi o TDMA - *TriDiagonal Matrix Algorithm* (Pantankar, 1980), (Maliska, 1995). Vê-se que a partir de uma malha 16 x 16 a solução numérica pouco difere da solução analítica.

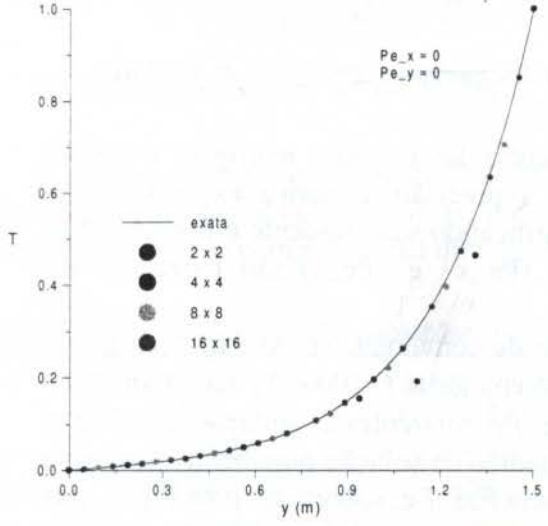

Fig. 3 Influência da malha na solução

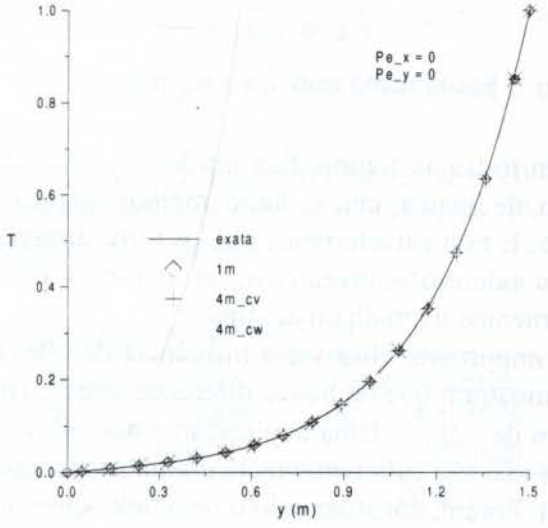

Fig. 4 Consistência dos métodos numéricos.

A Fig. 4 compara a consistência dos métodos numéricos utilizados, ainda para o problema de condução pura, em malha 16 x 16 . O algoritmo TDMA é novamente utilizado tanto para a solução em malha única como para as soluções *multigrid*, nestas últimas para realizar as pré- e pós-suavizações e as iterações na malha mais grossa. Em ambas soluções, ciclo-V ou ciclo-W, são usadas 4 malhas computacionais, sendo a mais fina também 16 x 16 . Observa-se, para todos os casos analisados, a concordância com a solução exata.

As figuras seguintes comparam o esforço computacional (redução do resíduo em função do tempo de cpu) em cada tipo de solução. Tanto em malha única (1m) como em *multigrid* com 3, 4, 5 ou 6 malhas, ciclo-V ou ciclo-W (3m_cv, 4m_cv, etc.), a malha mais fina contém N x N volumes elementares, $N = 128$. Os ensaios foram realizados em computador IBM-PC com processador Intel, pentium, de 166 MHz. O resíduo é normalizado e calculado segundo

$$R = \sqrt{\sum_{ij}\left(R_{ij}^2\right)\Big/N^2} \qquad \text{onde} \qquad R_{ij} = A_P T_P - \left(\sum_{vz} A_{vz} T_{vz}\right) \quad . \tag{19}$$

Os subscritos ij referem-se a um dado volume elementar da malha enquanto que vz referem-se aos volumes vizinhos do volume em questão. Nas soluções *multigrid* fixou-se um número de 2 iterações para as pré- e pós-suavizações e um número de 10 iterações na malha mais grossa (na qual recomenda-se obter uma solução exata do sistema algébrico).

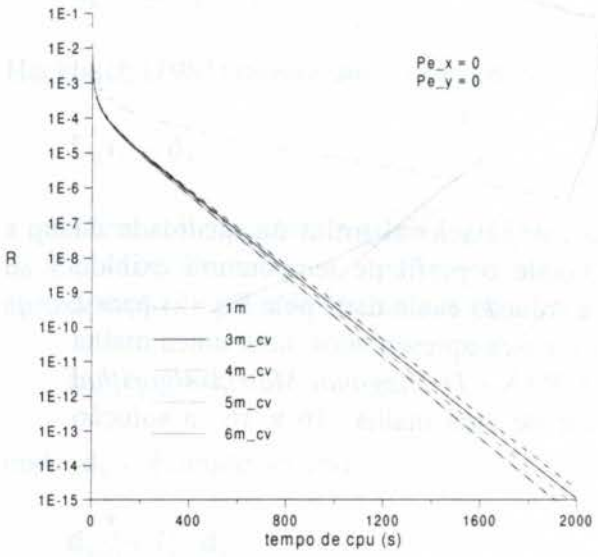

Fig. 5 Escoamento com $u = v = 0$ m/s .

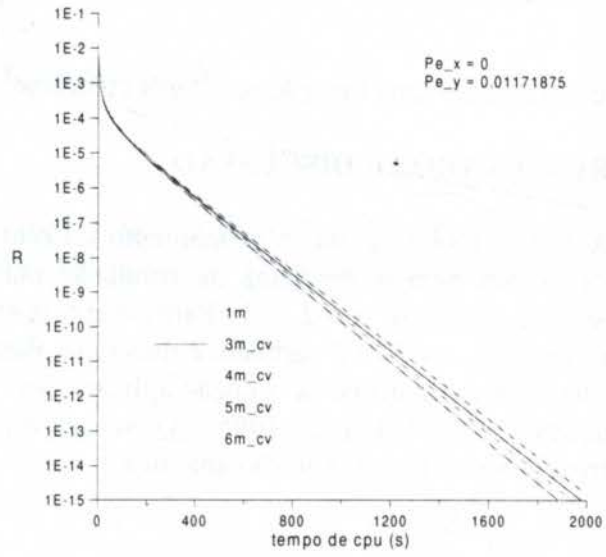

Fig. 6 Escoamento com $u = 0$ e $v = 1$ m/s .

Em todas as figuras fica nítido o melhor desempenho dos métodos *multigrid* frente ao método de malha única; tanto melhor quanto maior a precisão numérica exigida para a solução. É esta característica que os torna atraentes, justificando sua crescente utilização. Nos casos condutivos-convectivos, os números de Peclet (Pe_x e Pe_y) são baseados nos espaçamentos da malha mais fina.

É importante observar a influência de Pe na taxa de convergência. As Fig. 5, Fig. 6 e Fig. 8 mostram que há pouca diferença entre o tempo de cpu gasto (~2000 s) para a reduzir R a ordem de 10^{-15} . Uma explicação é que os valores de Pe referentes às situações das Fig. 6 e Fig. 8 não são suficientemente grandes para alterar o padrão da solução puramente condutiva (Fig. 5). Porém, considerando o resultado apresentado pela Fig. 7 e, sobretudo, pela Fig. 9, nas quais Pe assume valores maiores, nota-se uma acentuada redução do tempo de cpu. Tal

efeito deve-se ao fato das condições de contorno serem mais rapidamente "varridas" para o interior do domínio pelo mecanismo de convecção devido, em última análise, a um aumento dos coeficientes a jusante na Eq. (9).

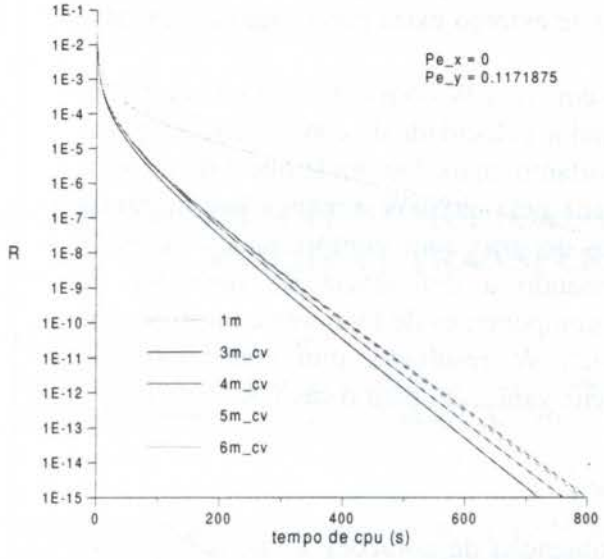

Fig. 7 Escoamento com $u = 0$ e $v = 10$ m/s .

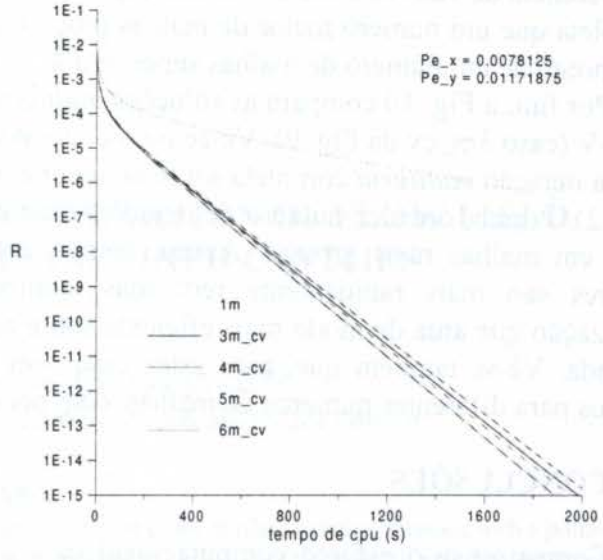

Fig. 8 Escoamento com $u = v = 1$ m/s .

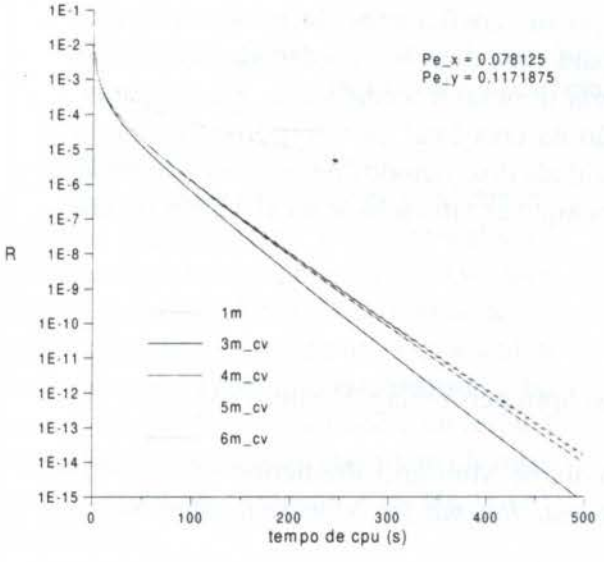

Fig. 9 Escoamento com $u = v = 10$ m/s .

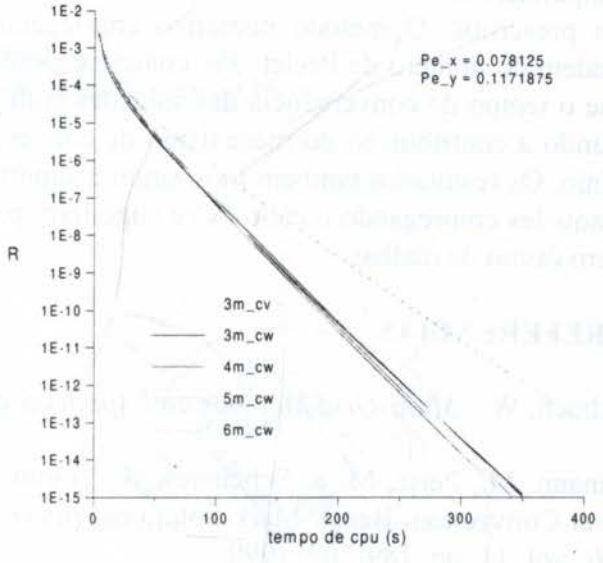

Fig. 10 Escoamento com $u = v = 10$ m/s .

A Tab. 1 compara o tempo de cpu (em segundos) necessário para atingir-se $R = 10^{-15}$ nas soluções *multigrid* com 4 malhas, em ciclo-V e ciclo-W, para valores distintos de Pe . Vê-se que o esforço computacional diminui à medida que Pe aumenta.

Tab. 1 Esforço computacional de soluções *multigrid* em 4 malhas para diferentes Pe .

	Pe_x = 0 Pe_y = 0 ($u = v = 0$)	Pe_x = 0.0078125 Pe_y = 0.01171875 ($u = v = 1$ m/s)	Pe_x = 0.078125 Pe_y = 0.1171875 ($u = v = 10$ m/s)	Pe_x = 0.78125 Pe_y = 1.171875 ($u = v = 100$ m/s)
ciclo-V	1910.4	1890.3	550.6	20.9
ciclo-W	899.0	892.6	338.8	28.4

Para os métodos *multigrid*, as figuras também sugerem a existência de um número ótimo de malhas (3 ou 4). As soluções em 5 ou 6 malhas possuem menor velocidade de convergência possivelmente porque consomem um esforço computacional adicional para a transferência de valores entre as malhas. Apesar do melhor desempenho por iteração *multigrid* completa que um número maior de malhas propicia, este esforço extra parece não compensar o emprego de um número de malhas superior a 4.

Por fim, a Fig. 10 compara as soluções *multigrid* em ciclo-W com o melhor resultado em ciclo-V (caso 3m_cv da Fig. 9). Vê-se ter o ciclo-W maior velocidade de convergência, apesar de sua iteração *multigrid* completa ser bem maior e, portanto, mais demorada que a do ciclo-V (Fig. 2). Porém, o maior número de iterações acarretado pelo ciclo-W é realizado em grande parte em malhas mais grossas. Assim, componentes do erro com comprimentos de onda maiores são mais rapidamente reduzidas, compensando a deficiência do operador de suavização que atua de modo mais eficiente sobre as componentes de menores comprimentos de onda. Vê-se também que, para estes casos em ciclo-W, resultados muito próximos são obtidos para diferentes números de malhas, com pequena vantagem para o caso de 4 malhas.

5. CONCLUSÕES

Comparou-se o esforço computacional para a obtenção de soluções numéricas de um problema condutivo-convectivo 2-D em malha única e pelo método *multigrid*. A distribuição de temperatura nas fronteiras do domínio de solução e o campo de velocidades em seu interior foram prescritos. O método numérico empregado possui coeficientes de ponderação que dependem do número de Peclet *Pe* computacional para cada direção coordenada. Verificou-se que o tempo de convergência das soluções *multigrid* diminui à medida que *Pe* aumenta, refletindo a contribuição do mecanismo de convecção na taxa total de transporte através do domínio. Os resultados também mostraram a superioridade dos métodos *multigrid* (sobretudo para aqueles empregando o ciclo-W) e sugeriram para aqueles em ciclo-V a existência de um número ótimo de malhas.

6. REFERÊNCIAS

Hackbuch, W. *Multi-Grid Methods and Applications*, Springer-Verlag, Berlin, 1985.

Hortmann, M., Peric, M. & Scheuerer, G. Finite Volume Multigrid Prediction of Laminar Natural Convection: Bench-Mark Solutions, *International Journal for Numerical Methods in Fluids*, vol. 11, pp. 189-207, 1990.

Maliska, C.R. *Transferência de Calor e Mecânica dos Fluidos Computacional*, Livros Técnicos e Científicos Editora, Rio de Janeiro, 1995.

Patankar, S.V. *Numerical Heat Transfer and Fluid Flow*, Hemisphere Publishing Corporation, 1980.

Raithby, G.D. & Torrance, K.E. Upstream-Weighted Differencing Schemes and Their Application to Elliptic Problems Involving Fluid Flow, *Computers & Fluids*, vol. 2, pp. 191-206, 1974.

Raithby, G.D. Prediction of Dispersion by Surface Discharge, *Basin Investigation and Modelling Section - Canada Centre for Inland Waters*, Canada, 1976.

CELL-IMPLICIT NUMERICAL COMPUTATION OF FLOW FIELD AND HEAT TRANSFER IN INCLINED CAVITIES

MARCELO J.S. DE LEMOS
Departamento de Energia, Instituto Tecnológico de Aeronáutica-CTA
12228-900 - São José dos Campos, SP, Brasil - E-mail: mlemos@tecsat.com.br

Abstract

This paper reports numerical results for incompressible thermally-driven flows in tilted cavities obtained with a point-wise solution scheme. The discretized momentum equations are applied to each computational cell and then, together with the mass-continuity and energy equations, are solved directly for each grid node. The effect of cavity inclination on the thermal field is discussed upon. Flow pattern and mass residual behavior are also reported.

Keywords

Tilted Cavities, CFD, Numerical Methods, Laminar Flow

1. INTRODUCTION

The problem of heat transfer enhancement through gaps between walls in cavities finds many applications in science and engineering. When the system is closed and subjected to a temperature gradient, a recirculating flow field is established. If the cavity itself is further inclined with respect to the vertical direction, important changes occur in the heat transfer strength across the domain.

For two-dimensional cases, in addition to having gravity directly affecting both coordinates, the numerical solution of such flows imposes additional difficulties due to the intricate coupling between *temperature* and *cross-flow* fields. Yet, it is known that the rate of convergence of any algorithm is essentially dictated by the degree in which physical coupling is mimicked by the method in question.

Motivated by the foregoing, de Lemos

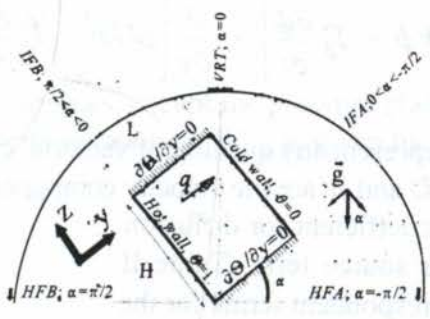

a) Geometry and boundary conditions

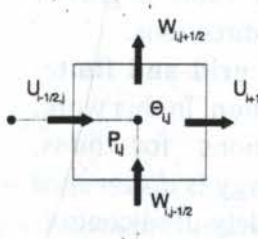

b) Control-volume notation

Fig. 1 Geometry and general notation.

(1988), based on the work of Vanka (1986a,1986b), simulated lid-driven cavity fluid motion using a block-implicit numerical scheme. Later, the technique was extended to flow through a cylindrical tank (de Lemos, 1990), to buoyancy-driven streams (de Lemos, 1992a), to calculation of swirling flows in combustors (de Lemos, 1992b) and to heated vertical chambers (de Lemos, 1996). In those papers qualitative and quantitative results were reported. The objective of this work is to present numerical results extending the developed formulation to incompressible laminar heated flows in an enclosure *tilted* with respect to the horizontal direction.

2. ANALYSIS AND NUMERICS

Geometry. The geometry here considered along with the boundary conditions used is schematically shown in Figure 1. An enclosure of height H and length L has a non-dimensional temperature Θ=1 imposed over its left wall, whereas at right, Θ is given a null value. Both top and bottom walls are kept insulated. Depending upon the value of tilt angle α, several cases can be identified as in Table 1 and referred to in Figure 1.

Table I - Cases investigated.

Case	Angle α	Description
HFB	$\pi/2$	Horizontal , heated from below
IFB	$\pi/2<\alpha<0$	Inclined, heated from below
VRT	$\alpha=0$	Vertical, heated from left
IFA	$0<\alpha<-\pi/2$	Inclined, heated from above
HFA	$-\pi/2$	Horizontal, heated from above

Compact notation. The conservation equations for mass, momentum and energy can be written in a compact form if it is observed the existing analogies among the processes of accumulation, transport, convection and generation/destruction of those quantities. This generic equation can be written in its conservative two-dimensional laminar form as:

$$\frac{\partial}{\partial z}\left[\rho W\phi - \Gamma_\phi \frac{\partial \phi}{\partial z}\right] + \frac{\partial}{\partial y}\left[\rho U\phi - \Gamma_\phi \frac{\partial \phi}{\partial y}\right] = S_\phi \qquad (1)$$

In (1) ϕ can represent any quantity of vectorial or scalar nature (velocity or temperature), ρ is the fluid density, U and W are the velocity components in the y- and z-directions, respectively, Γ_ϕ is the transport coefficient for diffusion and S_ϕ is the source term. Table II identifies correspondent terms for the different equations represented by (1). In equation (1) and Table II gravity acts in both y and z directions.

Table II - Terms in the transport equation.

	ϕ	Γ_ϕ	S_ϕ
Continuity	1	0	0
z-momentum	W	μ	$-\frac{\partial P}{\partial z} - \cos\alpha\, \rho_0 g\beta(T-T_0)$
y-momentum	U	μ	$-\frac{\partial P}{\partial y} - \sin\alpha\, \rho_0 g\beta(T-T_0)$
Energy	T	μ/Pr	0

Computational grid and finite-difference formulation. In this work, the set of equations for mass, momentum and energy is *differenced* by means of the widely-used control-volume approach of Patankar (1980). In that method, the computational domain is divided into finite non-

overlapping regions containing each a computational node. Figure 1 illustrates a control volume with relevant notation. The differential equations are then integrated over each volume yielding a set of algebraic equations for each dependable variable. Internodal variation for the dependent variables can be of different kind corresponding to different *Finite-Difference* Formulation. In the present work, for simplicity, the *Upwind Differencing Scheme* is used to model convective fluxes across volume faces.

Discretized Equations. The block-implicit arrangement below for the flow and continuity equations, as mentioned, was first presented by Vanka (1986a, 1986b). For the sake of completeness, the flow equations are here also included. Integrating then the continuity equation around point (*ij*) (see notation in Figure 1) one has (Patankar, 1988):

$$F_i^1 U_{i+1/2,j} - F_i^2 U_{i-1/2,j} + F_j^1 U_{i,j+1/2} - F_j^2 U_{i,j-1/2} = 0 \tag{2}$$

where the geometric coefficients F's can be interpreted as (area of flow)/(volume of computational node). For the horizontal momentum equation the final form for the $U_{i-½,j}$ component is:

$$U_{i-1/2,j} = \hat{U}_{i-1/2,j} + \hat{d}_{i-1/2}\left[P_{i-1,j} - P_{i,j}\right] + \hat{g}_{i-1/2}\Theta_{i,j} \tag{3}$$

where

$$\hat{U}_{i-1/2,j} = \left(\sum_{nb=1}^{4} a_{nb}^{u} U_{nb} + f_{1-1/2,j}^{u}\right) \Big/ a_{i-1/2,j}^{u} \tag{4}$$

$$\hat{d}_{i-1/2} = S_{i-1/2}^{u} / a_{i-1/2,j}^{u}; \quad \hat{g}_{i-1/2} = \rho_0 \sin\alpha g\beta(T_1 - T_0)/(2\, a_{i-1}^{u} \tag{5}$$

being *nb* referent to neighbor nodal points and f to all sources, except the pressure gradient and buoyancy term. A similar equation for the axial velocity component $W_{i,j-½}$ is given by:

$$W_{i,j-1/2} = \hat{W}_{i,j-1/2} + \hat{d}_{j-1/2}\left[P_{i,j-1} - P_{i,j}\right] + \hat{g}_{j-1/2}\Theta_{i,j} \tag{6}$$

where

$$\hat{W}_{i,j-1/2} = \left(\sum_{nb=1}^{4} a_{nb}^{w} W_{nb} + f_{1-1/2,j}^{w}\right) \Big/ a_{i,j-1/2}^{w} \tag{7}$$

$$\hat{d}_{j-1/2} = S_{j-1/2}^{w} / a_{i,j-1/2}^{w}; \quad \hat{g}_{j-1/2} = \rho_0 \cos\alpha g\beta(T_1 - T_0) / (2\, a_{i,j-1/2}^{w} \tag{8}$$

It is important to notice that the source term in (3) and (6) explicitly shows the contribution due to buoyancy. For the coupled treatment here presented, this arrangement is necessary as will be seen below. The non-dimensional temperature $\Theta = (T-T_0)/(T_1-T_0)$ is based on the maximum temperature drop in the computational domain $\Delta T = (T_1 - T_0)$. Following then a similar procedure

for the energy equation, final finite-difference equation can be assembled such that,

$$\Theta_{i,j} = \hat{\Theta}_{i,j} = \left\{ b^{\Theta}_{i,j}\,\Theta_{i+1,j} + c^{\Theta}_{i,j}\,\Theta_{i-1,j} + d^{\Theta}_{i,j}\,\Theta_{i,j+1} + e^{\Theta}_{i,j}\,\Theta_{i,j-1} \right\} \Big/ a^{\Theta}_{i,j} \tag{9}$$

Coupled strategy. In order to smooth out errors due to initial guessed fields, *corrections* are defined as differences between *exact* and *not-yet-converged* variables. Residuals for momentum transport at each control volume face, continuity of mass and Φ equations are obtained by applying the just defined *approximate* values into (3)-(6)-(9). After some manipulation (details are in de Lemos 1992a, 1992b, 1996), a system connecting the residuals and corrections can be written into matrix form as shown in Eqn. (10), where the subscripts identifies locations in the grid, the superscript ' distinguishes corrections and the l.h.s. residue vector corresponds to the one at previous iteration. In (10) the influence of Θ on the flow field is directly accounted for by the g-terms. The reverse effect, or say the cross-flow influence on the Θ, is here not treated implicitly. The solution of system (10) is then easily obtained by finding first corrections for Θ calculating later the pressure P and velocity components U and W. Essentially, the method consists of finding the corrective values for U, W,P and T, such that the balance equations are correctly satisfied.

$$\begin{bmatrix} 1 & 0 & 0 & 0 & +\hat{d}_{i-1/2,j} & \hat{g}_{i-1/2} \\ 0 & 1 & 0 & 0 & -\hat{d}_{i+1/2,j} & \hat{g}_{i+1/2} \\ 0 & 0 & 1 & 0 & +\hat{d}_{i,j-1/2} & \hat{g}_{j-1/2} \\ 0 & 0 & 0 & 1 & -\hat{d}_{i,j+1/2} & \hat{g}_{j+1/2} \\ -F^1_i & +F^2_i & -F^1_j & +F^2_j & 0 & 0 \\ 0 & 0 & 0 & 0 & 0 & 1 \end{bmatrix} \begin{bmatrix} U'_{i-1/2,j} \\ U'_{i+1/2,j} \\ W'_{i,j-1/2} \\ W'_{i,j+1/2} \\ P'_{i,j} \\ \Theta'_{i,j} \end{bmatrix} = \begin{bmatrix} R_{i-1/2,j} \\ R_{i+1/2,j} \\ R_{i,j-1/2} \\ R_{i,j+1/2} \\ R_{i,j} \\ R^{\Theta}_{i,j} \end{bmatrix} \tag{10}$$

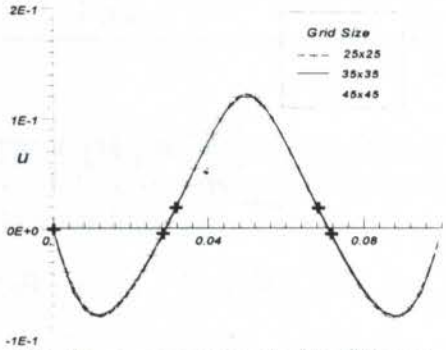

Fig. 2 - u- component with different grids

Segregated treatment. The algebraic equations for the velocity field were solved, in addition to the fully-coupled scheme here described, by performing outer iterations for the components Θ while keeping U-W-P from the previous iteration. A *line-by-line* smoothing operator, fully described elsewhere (e.g. Patankar, 1980), was used to relax Θ being the secondary flow field (U,W) calculated by the locally-coupled method seen above. This *segregated* solution was set in such a way that the same number of sweeps per outer iteration, throughout the scalar and cross-flow fields (U,W,P), was obtained in both the coupled and segregated methods. This procedure was found to be a reasonable way to fairly compare the two methods.

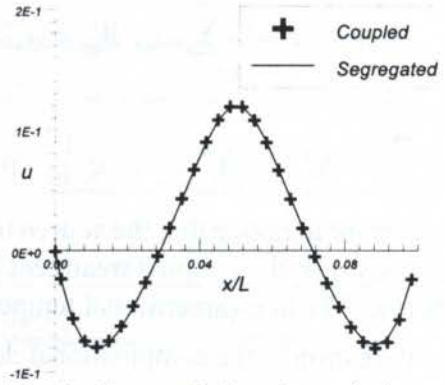

Fig. 3 -Segregated and coupled results

Boundary conditions and computational details. All velocity components were of null value at all boundaries. Interior velocities were also set to zero at start. For

temperature, Fig. 1 illustrates that both left and right walls were assigned the non-dimensional temperature of +1 and 0, respectively. At the upper and bottom plates the isolation condition $\partial\Theta/\partial z=0$ was applied. A **single** grid of several sizes and equally distributed in the domain was used. The same relaxation parameters (α=0.40 for P,T and α=0.6 for U,W) were used in all calculations. The Rayleigh number $Ra = (\rho^2 L^3 g\beta\Delta TPr)/\mu^2$, appearing after non-dimensionalizing the buoyancy term, was kept equal to $4.x10^4$ in all cases run.

3. RESULTS AND DISCUSSION

Preliminary results. Although this work has not been mainly concerned with the accuracy of the solution (absolute value), but rather the algorithm to achieve it, a few results on the velocity and temperature fields are here presented for completeness. Before this, a short discussion on the program validation seems timely.

Grid independence studies were conducted in order to determine a suitable grid size for the calculations. For inclined cavities, computations with different grids are presented in Fig. 2. The figure shows results for the u-velocity at the chamber mid-plane for the HFB case ($y=L/2$, $\alpha=\pi/2$, see Fig. 1 and Table I). One can see that for meshes larger than 30x30 the solution is nearly grid independent. Figure 3 presents again the u-component for the same case and position as the previous figure, but now comparing the results calculated by the *segregated* and *coupled* approaches. Inspecting the figure one can conclude that, independently of the smoothing technique used, final converged solutions, as expected, are essentially equal. The computational effort to achieve them, however, seems to be different, as it is discussed below.

Isotherms as a function of the tilt angle are shown in Figure 4. For the HFB case (upper left corner) one can clearly see the bulging of the isolines deeply penetrating into the flow core. The circulatory motion provoking that, known to exist for the range $1708 \le Ra \le 50000$, is illustrated in Fig. 5 and is called *Bénard Cells*. Also interesting to note is the small recirculating bubble at the bottom sides of the cavity in Fig. 5. Back to figure 4, one can also see temperature fields for the tilt angle α spanning from an unconditionally unstable situation (HFB, α=90°) to stable no-flow distribution (HFA, α=-90°). These results are in agreement with pertinent literature and indicate the correctness of the computer program developed.

Residues. Normalized residue was defined as the norm of the cell mass residue as,

$$R_{abs} = \left\{ \frac{\sum_{ij} R_{i,j}^2}{N \cdot M} \right\}^{1/2} \tag{11}$$

where N and M are the number of cells in the y- and z-directions, respectively, and $R_{i,j}$ can be seen as the difference, for every cell, between the cell outgoing mass flux, F_{out}, and the incoming mass flux, F_{in}. A *relative* mass residue can then be defined as,

$$R_{rel} = \left\{ \frac{\sum_{ij} \left(\frac{F_{out} - F_{in}}{F_{out} + F_{in}} \right)^2}{N \cdot M} \right\}^{1/2} \tag{12}$$

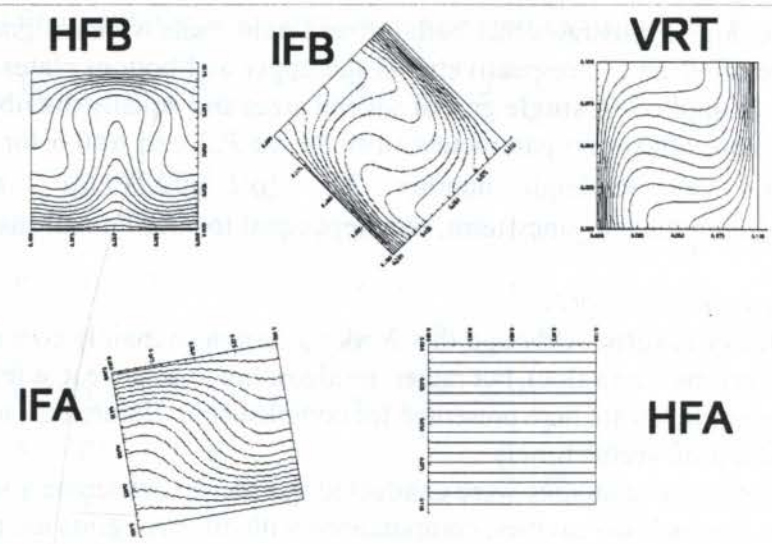

Figure 4 - Isotherms for different cavity inclinations: HFB, α=90°; IFB, α=45°; VRT, α=0°; IFA, α=-85°; HFA, α=-90°.

A discussion on the advantages in simultaneously monitoring R_{rel} in addition to R_{abs} is presented in de Lemos (1992b, 1996) and it is based on the small range of the former (0,+1).

Mass residues for the HFB case, calculated by equations (11) and (12), are presented in Figure 6. The iteration counter refers to the total number of sweeps over the domain, that is, the product of the **outer** counter times the number of **inner** sweeps. The relatively large number of necessary iterations could be associated with the use of a single grid, the tightness of the relaxation parameters and the strong coupling among all variables involved.

Figure 6 indicates that, after an initial period of about 1000 overall iterations, a better convergency rate is obtained with the coupled scheme in either residue form. For equation (9), the residue R_θ is presented in Figure 7, here also comparing the performance of both relaxation procedures. After the initial period mentioned before, low frequency errors are more efficiently swept off by the use of the coupled solver. Interesting to note is that, for the case analyzed in Fig. 7, no convergency was obtained with the segregated strategy, whereas with the coupled scheme, the close interaction between the temperature and flow fields was correctly simulated bringing down R_θ to the preselected error tolerance.

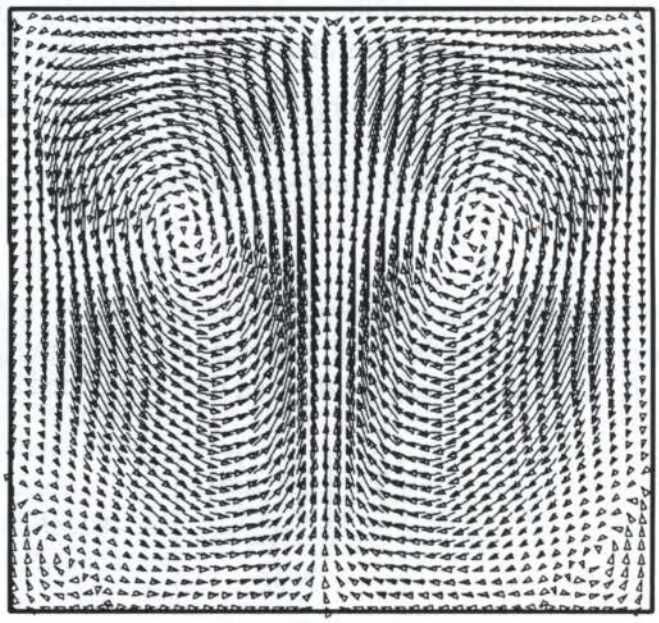

Figure 5 - Vector plot for HFBcase, α=90°.

4. CONCLUDING REMARKS

This paper detailed a fully-coupled technique for numerical prediction of flows in inclined cavities. Governing equations were written in terms of primitive variables and are recast into a general form. The discretization relation is obtained by integrating the differential equation over a finite control-volume. The discretized momentum equations are applied to each cell face and then, together with the mass-continuity and energy equations, are solved

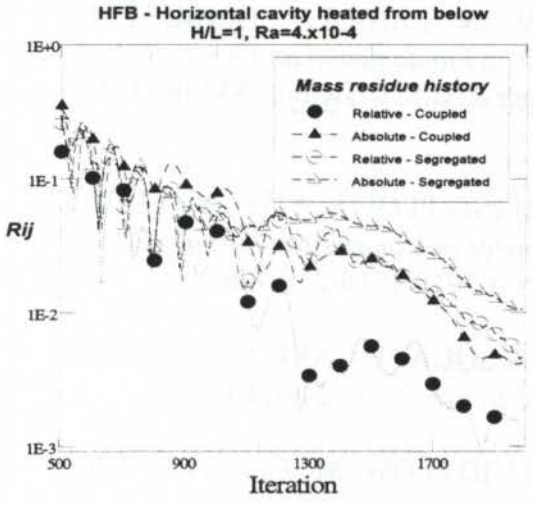

Figure 6 - Mass residue history for HFB case.

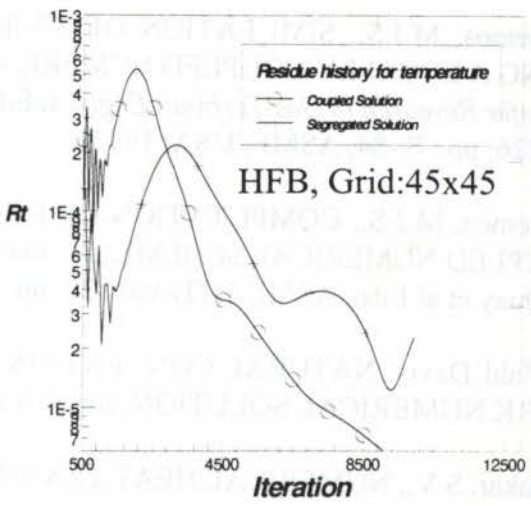

Figure 7 Residue history for temperature

simultaneously by means of a direct method in each computational cell. The error smoothing operator employed is based on An Alternating Symmetrical Coupled Gauss-Seidel procedure developed. Results are obtained with a Personal Computer under reasonable computing time. Flow patterns, mass residual behavior and indirect computing time (through iterations) were reported. The effect of the angle of inclination on temperature distribution was considered. The approach herein is promising regarding numerical stability of the entire equation set since inherent coupling among the variables is handled implicitly. Further, it is also expected that more advanced computer architectures can benefit from the point-wise error smoothing operator here described.

5. ACKNOWLEDGMENTS

The author is thankful to CNPq, Brazil, for financial support during the preparation of this work.

6. References

de Lemos, M.J.S., AN ALTERNATING SYMMETRICAL COUPLED GAUSS-SEIDEL PROCEDURE FOR TWO- AND THREE-DIMENSIONAL RECIRCULATING FLOWS, *ASME Winter Meeting*, Chicago, USA, 1988.

de Lemos, M.J.S., COMPUTATION OF LAMINAR AXI-SYMMETRIC RECIRCULATING FLOWS USING PRIMITIVE VARIABLES AND A BLOCK-IMPLICIT SCHEME, *Proc. 3rd Braz. Therm. Sci. Meeting*, vol. 1, pp. 375-380, Itapema, Brazil, 1990.

de Lemos, M.J.S., COMPUTATION OF BUOYANCY-DRIVEN FLOWS USING A BLOCK-IMPLICIT NUMERICAL SCHEME, in *Modern Developments in Numerical Simulation of Flow and Heat Transfer*, Eds. J.L.S. Chen & K. Vafai, ASME-HTD-vol.194, pp. 83-89, ASME, USA, 1992a.

de Lemos, M.J.S., SIMULATION OF SWIRLING FLOW IN A MODEL COMBUSTOR USING A LOCALLY-COUPLED NUMERICAL METHOD, in *Fundamental and Applied Heat Transfer Research in Gas Turbines Engines*, Eds. D.E. Metzger & M.E. Crawford, ASME-HTD-vol.226, pp. 79-84, ASME, USA, 1992b.

de Lemos, M.J.S., COMPUTATION OF HEATED SWIRLING FLOWS WITH A FULLY-COUPLED NUMERICAL SCHEME, in *Comput. Heat Transfer in Combustion Systems*, M.Q. McQuay et al Eds., ASME-HTD-vol.328, pp. 139-45, ISBN 0-7918-1510-2, 1996.

de Vahl Davis, NATURAL CONVENTION OF AIR IN A SQUARE CAVITY: A BENCH MARK NUMERICAL SOLUTION, *Int. J. Num. Meth. Fluids*, vol. 3, pp. 249-264, 1983.

Patankar, S.V., NUMERICAL HEAT TRANSFER AND FLUID FLOW, Mc-Graw Hill, 1980.

Patankar, S.V., PARABOLIC SYSTEMS, cap. 2 of HANDBOOK OF NUMERICAL HEAT TRANSFER, Minkowycs ed., John Wiley & Sons, New York, 1988.

Vanka, S.P., BLOCK-IMPLICIT MULTIGRID SOLUTION OF NAVIER-STOKES EQUATIONS IN PRIMITIVE VARIABLES, *J. Comp. Phys.*, vol. 65, pp. 138-158, 1986a.

Vanka, S.P., A CALCULATION PROCEDURE FOR THREE-DIMENSIONAL STEADY RECIRCULATING FLOWS USING MULTIGRID METHODS, *Comp. Meth. App. Mech. Eng.*, vol. 55, pp. 321-338, 1986b.

Tema 45

Métodos Estocásticos e Estatísticos

XIV Brazilian Congress of Mechanical Engineering
Obeid Plaza Hotel Convention Center - Bauru - SP/Brazil
December 08-12th 1997

PAPER CODE: COB1191

FLUXO DE ENERGIA VIBRATÓRIA ENTRE CHAPAS REFORÇADAS POR VIGAS / *POWER FLOW BETWEEN BEAM-REINFORCED PLATES*

ACIR EDVAM OZELAME[1], ARCANJO LENZI[1] e AYRES ELIAS SADA[2]
1 - Laboratório de Vibrações e Acústica (LVA) Depto de Engenharia Mecânica, UFSC
cp. 476 - CEP 88040-900 -tel. 048 234 0689 - fax 048-234 1519 - Florianópolis - SC
email: arcanjo@emc.ufsc.br
2 - CENPES - PETROBRÁS - Ilha do Fundão, Rio de Janeiro, RJ

Abstract

This work deals with modal density and coupling loss factors analysis of beam reinforced plates, by Finite Elements. The reinforcing beams were placed paralel and orthogonal direction with respect to the junction line. Experimental results showed good agreement with numerical predictions.

Keywords

Análise Estatistica Energética, Fator de Acoplamento, Placa Reforçada por Vigas, Fluxo de Energia
Statistical Energy Analisys, Coupling Loss Factor, Beam Reinforced Plates, Power Flow

1. INTRODUÇÃO

Estruturas compostas por chapas reforçadas por vigas são amplamente utilizadas principalmente nas indústrias naval e aeroespacial. Um bom exemplo desta utilização é o caso de plataformas offshore de prospecção e de produção de petróleo. Estas estruturas servem de apoio para um grande número de máquinas e equipamentos pesados que geram níveis elevados de vibrações. A energia vibratória propaga-se através da estrutura e atinge áreas sensíveis, tais como alojamentos, refeitórios e salas de controle e de estar, diminuindo o conforto e aumentando a fadiga dos ocupantes.

A faixa de freqüência de interesse nas análises do ruído que se propaga estruturalmente estende-se até freqüências acima de 1 kHz, pelo menos. A alta densidade modal destas estruturas, compostas por chapas reforçadas, inviabiliza o uso dos métodos que se baseiam na análise modal, como por exemplo, Elementos Finitos. A Análise Estatística Energética (SEA) tem se mostrado bastante útil nestas aplicações. Entretanto, deve-se determinar com precisão os parâmetros relacionados a esta metodologia de análise, que são densidade modal, fatores de acoplamento e resposta em freqüência, entre outros.

Este trabalho tem como objetivo determinar a densidade modal e os fatores de acoplamento de chapas reforçadas por vigas, conforme usadas em estruturas offshore, usando um software comercial (ANSYS 5.1) de Elementos Finitos. Os resultados numéricos obtidos são comparados aos experimentais.

2. EXPRESSÕES BÁSICAS

2.1 Densidade Modal

A densidade modal, n(f), é definida como a razão entre o número de modos contidos em uma faixa de freqüência de análise, e a largura desta faixa. É comumente expressa em modos/Hz. Para componentes estruturais de geometria simples, como vigas de seção constante e placas, de espessura constante e material homogêneo, pode-se determinar a densidade modal através de expressões simples. Por exemplo, para uma placa lisa (Lyon, 1973)

$$n(f) = \frac{\sqrt{3}S}{hc_l} \tag{1}$$

onde S representa a área da placa; h, a espessura e c_l , a velocidade das ondas longitudinais. Esta expressão considera a placa como sendo simplesmente apoiada nas bordas. Para componentes de geometria complexa ou construídas com materiais não-homogêneos, pode-se determinar (numérica ou experimentalmente) a densidade modal através da expressão (Clarkson, 1981)

$$n(f) = 4M\langle Re\{Y\}\rangle \tag{2}$$

onde M representa a massa do componente e $\langle Re\{Y\}\rangle$, a média espacial e na faixa de freqüência de análise, da parte real da mobilidade (relativa a uma força concentrada).

2.2 Fator de Acoplamento

O fator de acoplamento, η_{ij} possui significado físico análogo ao fator de perda (amortecimento estrutural). Representa a parcela de potência (ou de energia) que um componente "perde" para outro componente, através da união física entre eles. É expresso por

$$W_{ij} = \omega\eta_{ij}E_i \tag{3}$$

onde W_{ij} representa a potência transferida do i-ésimo para o j-ésimo componente; E_i, a energia vibratória do i-ésimo componente e ω (=2πf), a freqüência, em radianos por segundo.

A energia vibratória, E, de um componente é comumente obtida em função da velocidade RMS quadrada, média espacial (< >), calculada a partir dos valores de velocidade em N pontos distribuídos ao longo do componente. O valor RMS é também representado pelo símbolo $\bar{(\ )}$ sobre a variável.

$$E = M < \bar{V}^2 >; \qquad < \bar{V}^2 >= \frac{1}{N}\sum_{i=1}^{N} V_{RMS}^2 \tag{4}$$

Conhecidas as energias vibratórias, os amortecimentos e as densidades modais dos dois componentes, pode-se determinar o fator de acoplamento η_{21} através da expressão (Lyon, 1973 e Cremer e Heckel, 1973)

$$\frac{E_2}{E_1} = \frac{n_2}{n_1}\frac{\eta_{21}}{\eta_2 + \eta_{21}} \tag{5}$$

sendo η_2 , o fator de perda do subsistema 2. Uma vez determinada a potência líquida transferida (W_{ij}) em uma faixa de freqüência(Δf), através da união, pode-se também determinar os fatores de acoplamento usando as expressões:

$$W_{12} = \omega[\eta_{12}E_1 - \eta_{21}E_2]; \qquad n_1 \cdot \eta_{12} = n_2 \cdot \eta_{21} \tag{6}$$

3. DENSIDADE MODAL

Foi calculada a densidade modal de uma chapa de aço de 1,0m x 0,80m x 2mm, apoiada nas quatro bordas por um perfil L, de aço, com dimensões conforme indicadas na Figura 1. A placa é ainda reforçada por três vigas L, cujas dimensões estão também indicadas na mesma figura.

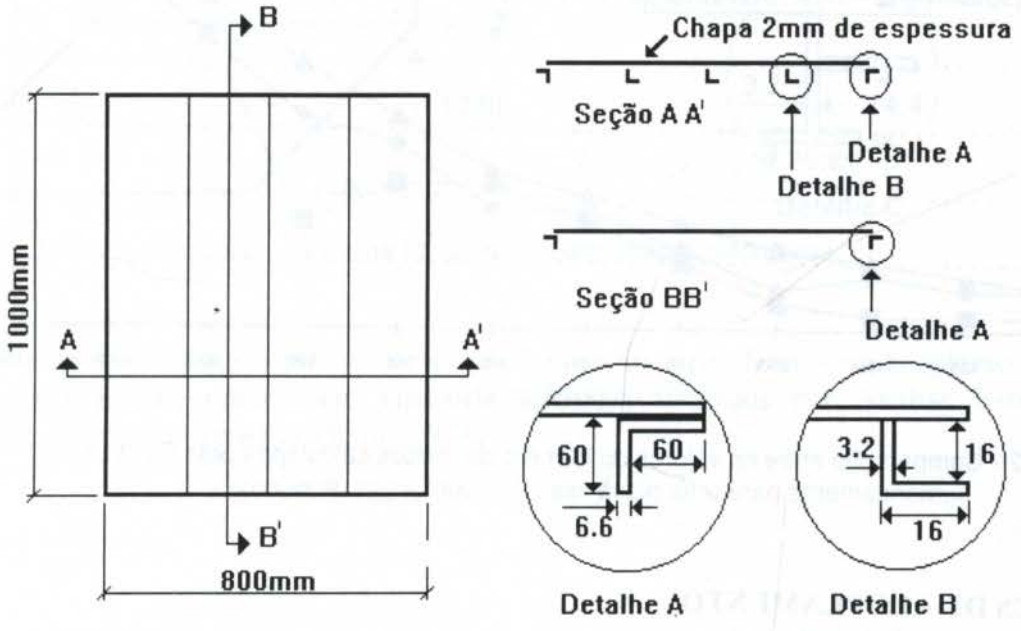

Figura 1- Dimensões (em mm)da chapa plana reforçada usada na determinação da densidade modal.

A densidade modal foi determinada numericamente usando a Equação 2, sendo que a mobilidade Y, referente à resposta a uma força concentrada, foi aplicada em vários pontos distribuídos aleatoriamente. Clarkson concluiu que para chapas sem descontinuidades do tipo vigas, de três a cinco pontos de excitação são suficientes para determinação da média espacial, e na faixa de freqüência (Δf), da parte real da mobilidade. Os resultados na forma de números de modos $N = n(f) \cdot \Delta f$, estão mostrados na Figura 2, sendo calculadas para faixas de 1/3 oitava. Foram usados cinco pontos para o cálculo da média da mobilidade.

Os valores teóricos referentes a uma placa lisa, de mesmas dimensões, estão também mostrados na Figura 2. Observa-se a pequena redução dos valores calculados numericamente, para o caso sem vigas de reforço, em relação ao teórico. Esta pequena diferença pode ser atribuída aos efeitos das vigas que servem de apoio nas bordas e que tendem a aumentar as

freqüências de ressonância da placa, deslocando toda a curva do número de modos em direção às altas freqüências. Mesmo assim, a diferença observada é da ordem de 0,5dB, apenas.

Os resultados obtidos para a chapa com três vigas (internas) de reforço, usando dezoito pontos para o cálculo da média espacial da mobilidade, aproximam-se bastante dos obtidos sem as vigas de reforço, exceto em duas faixas de freqüência. Sabe-se que as ressonâncias de chapas reforçadas, por serem estruturas periódicas (ou quase periódicas), tendem a apresentar grupos de freqüências de ressonância com pequenas lacunas, no espectro, entre elas (Cuschieri, 19957). Isto explica a divergência observada na Figura 2, nas faixas de 630 Hz e de 1250 Hz.

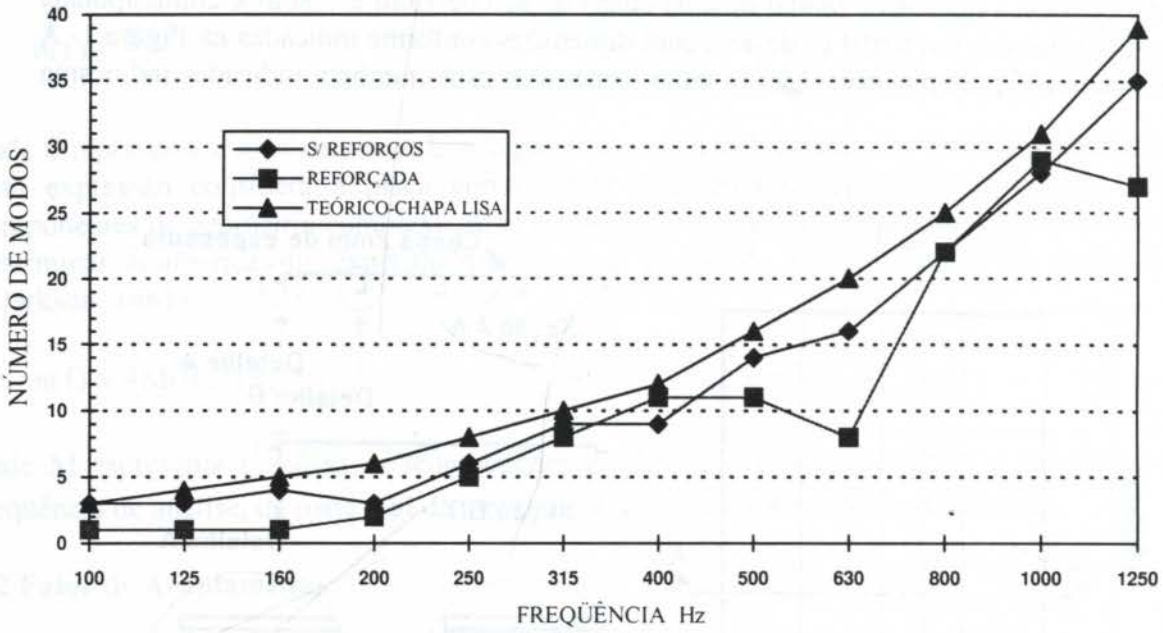

Figura 2 - Comparação entre os valores do número de modos calculados pela Eq. 1 (Δ), e numericamente para uma placa lisa (◊), e com vigas de reforço ( ).

4. FATORES DE ACOPLAMENTO

Os fatores de acoplamento estruturais entre duas placas reforçadas por vigas foram analisados numérica e experimentalmente. As dimensões das placas estão indicadas na Figura 3, e simulam as configurações (escala reduzida) de aplicações típicas em plataformas offshore.

Observa-se a presença de uma viga de reforço existente, também, na linha de união entre as placas, mostrada no Detalhe C. Outras configurações de disposição das vigas de reforço foram também analisadas.

Os fatores de acoplamento de duas placas reforçadas foram determinados através do uso da Equação 5, sendo as energias vibratórias das duas placas calculadas pelo Método de Elementos Finitos. Para tal, foi usado o software comercial ANSYS 5.1. As placas foram modeladas pelo elemento de casca SHELL 63, de 16 mm de lado. As vigas foram modeladas pelo elemento de viga BEAM 4, tendo também 16mm de extensão. A excitação foi aplicada através de forças concentradas em dezoitos pontos, na placa 1 (0,80 m^2). O amortecimento da placa e das vigas foi considerado igual a 0,01. As energias vibratórias, E1 e E2, foram calculadas a partir dos dados de velocidade dos elementos fornecidos pelo software. Os fatores de acoplamento foram determinados através da Equação 5. Os resultados para as

placas tendo vigas de reforço dispostas em ambas as placas na direção perpendicular à união, estão mostrados na Figura 5.

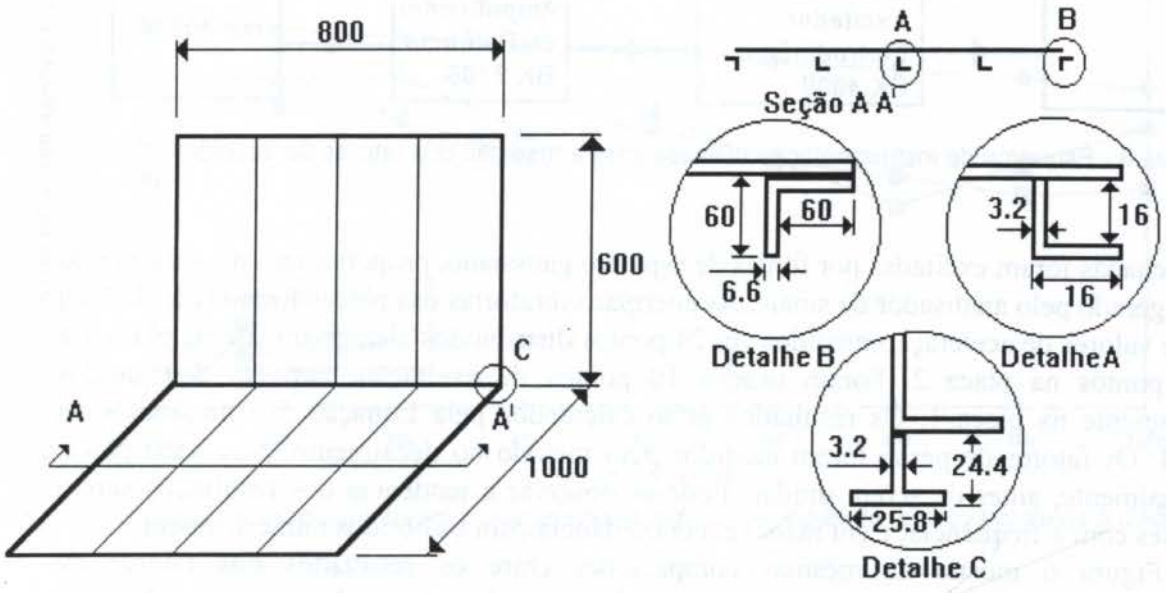

Figura 3 - Esquema da geometria das chapas reforçadas.

Para efeitos de comparação, esta mesma figura mostra os fatores de acoplamento das mesmas duas placas, porém sem vigas de reforço, calculados por Análise Estatística Energética, através da expressão (Lyon, 1973)

$$\eta_{12} = \frac{c_{g_1} L}{\pi \omega A_1} \bar{\tau}_{12} \qquad (7)$$

sendo A_1, a área e, c_{g1} a velocidade de grupo das ondas de flexão na placa 1; L, a extensão da união das duas placas, e, $\bar{\tau}_{12}$ o coeficiente de transmissão de energia médio com ângulo de incidência em relação a união. Este coeficiente pode ser expresso em relação a τ (θ=0°), para incidência normal, pela expressão (Cremer e Heckl, 1973), $\bar{\tau}_{12} = (2/3)\tau_{12}(\theta = 0^o)$.

Esta comparação indica as diferenças de variação de valores com a freqüência. Enquanto que os valores teóricos, para chapas não reforçadas, decrescem com a freqüência, aqueles para chapas reforçadas tendem para um valor constante e independente da freqüência, sendo esta observação válida até 1000 Hz. Não foram realizadas análises numéricas e experimentais para freqüências mais altas.

4. 1 Determinação Experimental dos Fatores de Acoplamento

Um experimento foi realizado com o objetivo de comparar os resultados àqueles obtidos numericamente. Um esquema da instrumentação utilizada está mostrado na Figura 4.

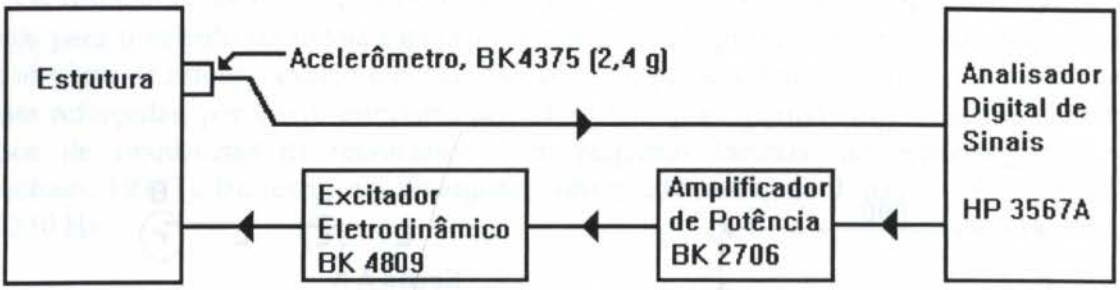

Figura 4 - Esquema de instrumentação utilizada para a medição dos fatores de acoplamento.

As chapas foram excitadas por forças de espectro gaussiano, proporcionais ao sinal (ruído branco) gerado pelo analisador de sinais. As energias vibratórias das placas foram calculadas a partir de valores de aceleração medidos em 24 pontos distribuídos aleatoriamente na placa 1 e em 20 pontos na placa 2. Foram usados 10 pontos de excitação, também distribuídos aleatoriamente na placa 1. Os resultados estão calculados pela Equação 5 e mostrados na Figura 4. Os fatores de perda foram medidos pelo método do decaimento, para cada placa, individualmente, antes de serem unidas. Pode-se observar a tendência dos resultados serem constantes com a freqüência, e em razoável concordância com os obtidos numericamente.

A Figura 6 mostra as mesmas comparações entre os resultados dos fatores de acoplamento, porém, desta vez para placas tendo vigas de reforço dispostas em direções paralelas à linha de união, em ambas as placas.

A Figura 7 mostra uma comparação semelhante considerando, entretanto, vigas dispostas perpendicularmente à união na placa 1 e paralelas à união na placa 2. De uma forma geral, observa-se a tendência de os fatores de acoplamento serem pouco dependentes com a freqüência. A concordância entre os resultados numéricos e experimentais é considerada razoavelmente boa, tendo em vista as dificuldades que são encontradas na determinação experimental destes parâmetros.

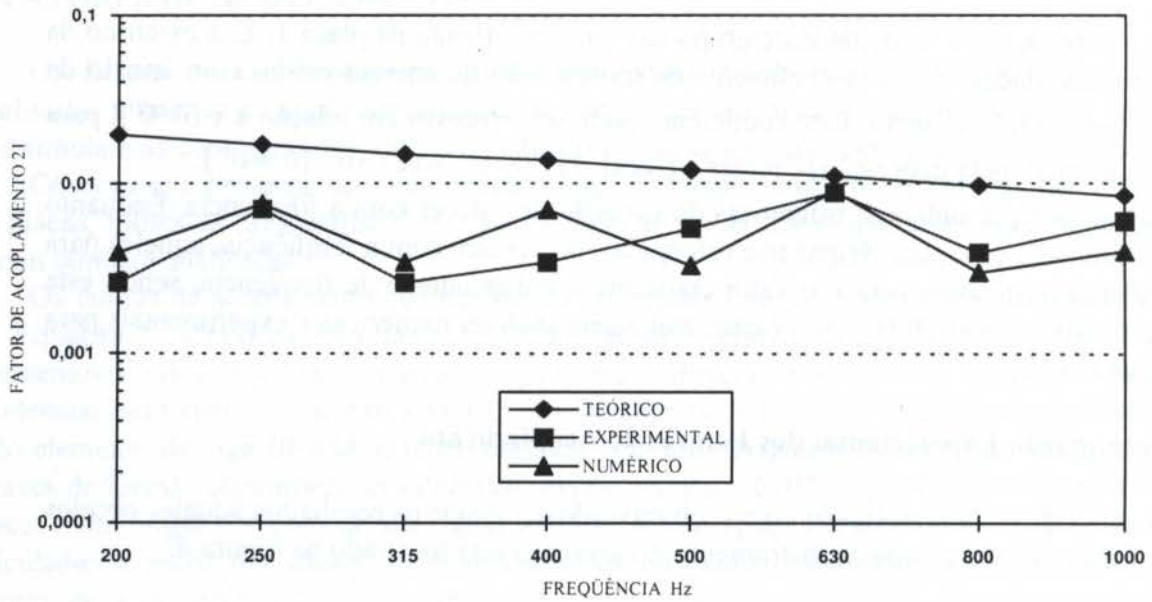

Figura 5 - Fatores de acoplamento η_{21} para placas unidas em L, tendo em vigas de reforço dispostas perpendicularmente à linha de união das placas. Comparação entre valores numéricos e experimentais, e valores teóricos para placas não reforçadas.

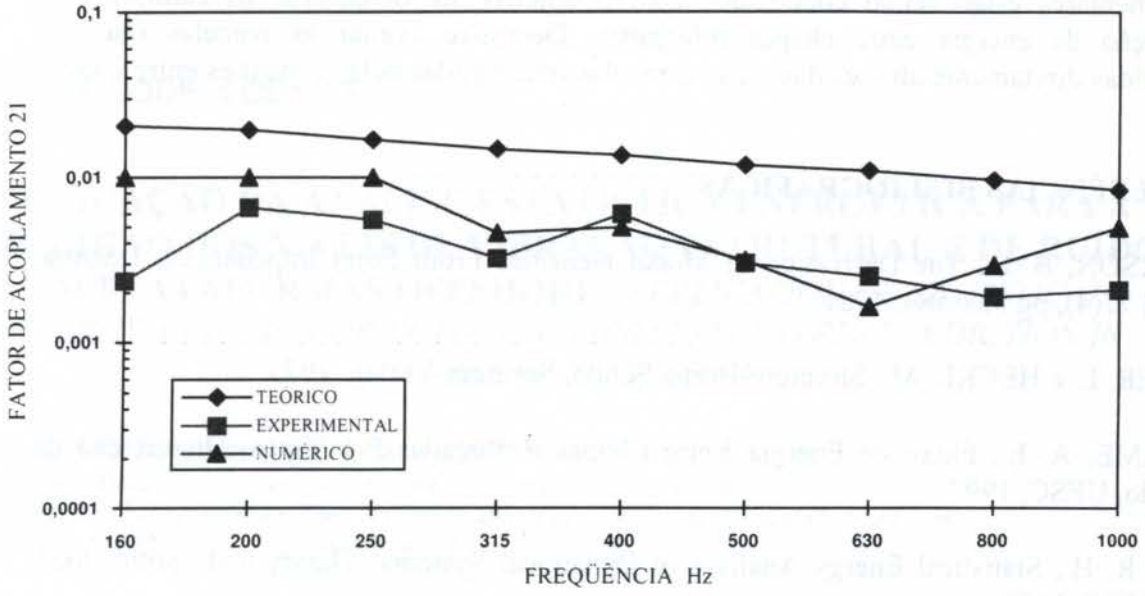

Figura 6 - Fatores de acoplamento entre placas unidas em L, com vigas de reforço paralelas à união.

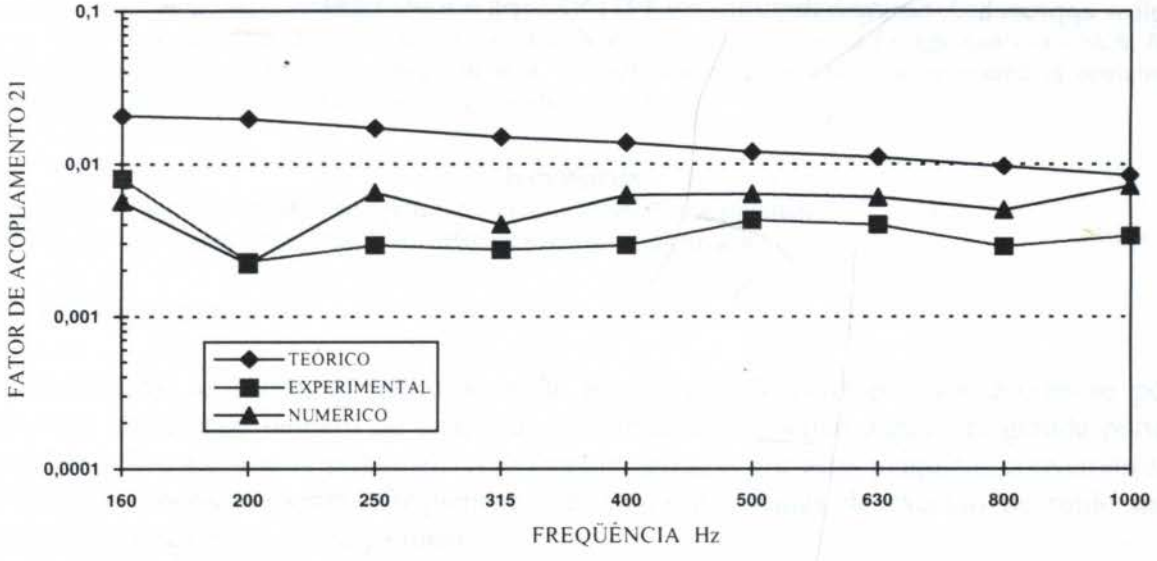

Figura 7 - Fatores de acoplamento η_{21} para placas tendo vigas de reforço perpendiculares à união na placa 1, e paralelas à união na placa 2. Valores teóricos para chapas não reforçadas.

5. CONCLUSÕES

A densidade modal de placas reforçadas é pouco influenciada pela presença das vigas de reforço. Tendo em vista as dificuldades de cálculo da resposta em freqüência destes tipos de estruturas, pode-se estimar a densidade modal, com pequeno erro, considerando as placas como não reforçadas.

Observou-se durante as análises que a energia vibratória está quase que totalmente contida nas chapas, apesar de terem pequena massa em relação às vigas, porém maior velocidade transversal.

Os valores dos fatores de acoplamento tendem a ser constantes com a freqüência. Estudos complementares estão sendo conduzidos com o objetivo de determinar os caminhos de propagação de energia entre chapas reforçadas. Deseja-se avaliar as parcelas que são transmitidas diretamente através das vigas e aquelas transmitidas pelas conexões entre chapas e vigas.

6. REFERÊNCIAS BIBLIOGRÁFICAS

CLARKSON, B. L., The Derivation of Modal Densities From Point Impedances, J Sound Vib, vol 77(4), pg 583-584, 1981.

CREMER, L. e HECKL, M., Structure-Borne Sound, Springer-Verlag, 1973.

OZELAME, A. E., Fluxo de Energia Entre Chapas Reforçadas Por Vigas, Dissertação de Mestrado, UFSC, 1997.

LYON, R. H., Statistical Energy Analisys of Dynamical Systems: Theory and applications, MIT PRESS, 1973.

CUSCHIERI, J. M., Vibration Transmition through periodic Structures using a mobility power glow approach, J. Sound Vibration, vol 143, N° 1, pg 65-74, 1990.

XIV Brazilian Congress of Mechanical Engineering
Obeid Plaza Hotel Convention Center - Bauru - SP/Brazil
December 08-12th 1997

PAPER CODE: COB1195

APLICAÇÃO DA ANÁLISE ESTATÍSTICA ENERGÉTICA PARA A PREDIÇÃO DOS NÍVEIS DE VIBRAÇÃO ESTRUTURAL E DE RUÍDO EM PLATAFORMAS OFFSHORE / *APPLICATION OF STATISTICAL ENERGY ANALYSIS FOR NOISE AND VIBRATION LEVELS PREDICTION IN OFFSHORE PLATFORMS*

L. C. de Souza, A. Lenzi e E. L. Sztajnbok
Depto. Eng. Mecânica, Universidade Federal de Santa Catarina - UFSC
CEP 88010-970 Florianópolis, Santa Catarina, Brasil - E-mail: lucianosouza@hotmail.com
Fone 048 - 234 0689 Fax 048 - 234 1519

Abstract

High Noise and Vibration levels usually existent in offshore platforms can cause severe discomfort and stress problems to their occupants. The vibrations of large machines and equipaments transfere large amounts of vibratory energy to the main structure which is propagated throughout the platform generating unpleasant noise levels. This work describes the characteristics of a software, based on Statistical Energy Analysis - SEA, for predicting noise levels at the accommodation area. Results are compared to those measured in operating platforms. An anlysis of some related parameters is also presented.

Keywords

vibração, ruído, análise estatística energética, plataforma offshore, microstation
vibration, noise, statistical energy analysis, offshore plataform, microstation

1. INTRODUÇÃO

Plataformas offshore de produção e de prospecção de petróleo caracterizam-se por possuírem um grande número de máquinas e equipamentos, sendo alguns de grande porte, instalados sobre a estrutura principal. As vibrações geradas por estas máquinas convertem-se em energia sonora, causando, freqüentemente, sérios problemas de excesso de ruído nas regiões dos alojamentos, principalmente.

Devido à alta densidade modal dos vários componentes estruturais, torna-se inviável a análise do ruído gerado através de métodos baseados na análise modal, como Elementos Finitos, por exemplo, pois torna-se totalmente inviável analisar em regiões do espectro localizadas acima de uma centena de modos, aproximadamente. Por este motivo optou-se pela Análise Estatística Energética - SEA, largamente utilizada em problemas dinâmicos que envolvem componentes com alta densidade modal.

Torna-se importante dispor de uma metodologia de análise, durante a fase de projeto destas estruturas, que permita orientar na localização das máquinas e prever as formas de controle das vibrações e do ruído gerado pela propagação estrutural.

Um software específico baseado na Análise Estatística Energética foi desenvolvido, tendo como objetivo final predizer o ruído nos alojamentos, avaliar os caminhos de

transmissão de vibrações, a contribuição de cada máquina para o nível de ruído global e os efeitos da alteração de parâmetros, como o amortecimento estrutural, por exemplo. Este trabalho apresenta as características principais do software e uma comparação com resultados de medições em plataformas.

2. MODELO DE CÁLCULO POR SEA

Um sistema acústico/estrutural ao ser modelado por SEA é decomposto em subsistemas. Os subsistemas são especificados em conformidade com as características geométricas do componente estrutural e da cavidade acústica, e com o tipo de onda que transmite energia vibratória. Por exemplo, um componente estrutural tipo viga poderá ser representado, num modelo por SEA, por três subsistemas, considerando as energias vibratórias por ondas de flexão, de torção e longitudinais.

Para cada subsistema é montada uma equação de equilíbrio de taxa de variação da energia vibratória.

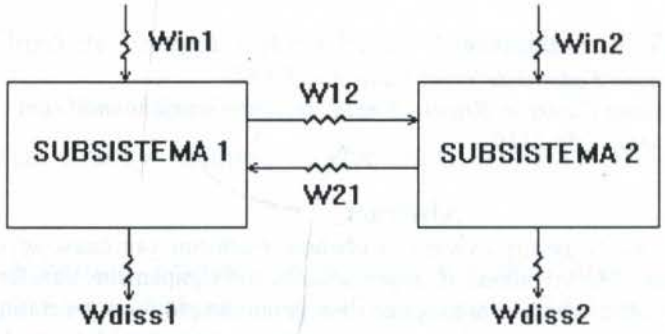

Figura 1 - Exemplo de dois subsistemas

Considerando-se apenas dois subsistemas acoplados e ambos excitados por fontes externas, conforme mostrados na Figura 1, pode-se escrever as seguintes equações:

SUBSISTEMA 1: $\quad Win_1 - Wdiss_1 - W_{12} + W_{21} = 0$

SUBSISTEMA 2 : $\quad Win_2 - Wdiss_2 - W_{21} + W_{12} = 0$

sendo $\quad Wdiss_i = \eta_i \, \omega \, E_i$

$\quad W_{ij} = \eta_{ij} \, \omega \, E_i$

η_i é o fator de perda do i-ésimo subsistema e η_{ij} o fator de acoplamento indicando o fluxo de energia do i-ésimo para o j-ésimo subsistema. E_i é a energia vibratória do i-ésimo subsistema. Em forma matricial, as equações acima podem ser representadas na forma

$$\begin{bmatrix} \eta_1 + \eta_{12} & -\eta_{21} \\ -\eta_{12} & \eta_2 + \eta_{21} \end{bmatrix} \cdot \begin{bmatrix} E_1 \\ E_2 \end{bmatrix} = \frac{1}{\omega} \begin{bmatrix} W_{in1} \\ W_{in2} \end{bmatrix}$$

Um sistema composto por N subsistemas, é representado através do sistemas de N equações, representadas por [Lyon, Lenzi]

$$[\eta] \{E\} = 1/\omega \ \{Win\}$$

sendo [η] a matriz de coeficientes; {E} o vetor das energias vibratórias e {Win} o vetor das potências externas aplicadas. Ao resolver o sistema acima, são determinadas as energias de cada subsistema, e com elas, são determinadas as respostas médias espaciais. Não são obtidos valores de resposta em pontos específicos, pois a análise não é determinística.

3. MODELOS DE SUBSISTEMAS

Os subsistemas podem ser representados por elementos de viga (vibrando em modos de flexão, de torção e longitudinais), de placa (vibrando em modos de flexão e longitudinais) e cavidades acústicas (Figura 2) usadas para o cálculo do nível de pressão sonora em ambientes. Os alojamentos são representados por elementos especialmente criados, para que fossem considerados os efeitos de atenuação do ruído no seu interior através da perda de transmissão do som das paredes e do teto, construídas rente à estrutura da plataforma e através do isolamento das vibrações do piso. A Figura 3 mostra um esquema do modelo de cálculo de um alojamento.

Os elementos tipo vigas e placas podem ser excitados por forças e momentos conhecidos. Pode-se também determinar a potência transferida a estes elementos estruturais através de dados de vibração, simulando, por exemplo, as vibrações nos pontos de fixação de uma máquina à estrutura.

As cavidades acústiças podem ser diretamente excitadas por fontes sonoras de potência conhecida.

Os elementos estruturais consideram também a possibilidade de existirem massas concentradas adicionadas (em relação ao peso próprio destes elementos) as quais simulam os efeitos de máquinas instaladas.

Figura 2 - Esquema de uma cavidade indicando as contribuições das superfícies adjacentes para o ruído gerado

Figura 3 - Esquema de um alojamento indicando as contribuições das paredes, piso e teto, na geração do ruído no seu interior.

4. O SOFTWARE

O software foi desenvolvido na linguagem MDL (MicroStation Development Language) e na linguagem C, sendo executado no MicroStation. Essa linguagem foi escolhida pelas facilidades que oferece na programação com relação a parte gráfica 3D, importantes na visualização do modelo físico sendo analisado.

A Figura 4 mostra um exemplo de modelo de uma plataforma em duas vistas, de topo e isométrica. A Figura 5 mostra os diversos "pulldowns" criados especificamente para este software.

O software possui uma implementação matemática com o que é capaz de resolver desde o problema da conectividade dos elementos, até o cálculo de velocidades (energias e deslocamentos, por exemplo) de cada elemento da plataforma.

Além disso, possui muitas ferramentas úteis na modelagem de plataformas, incluindo tabelas, cálculo automático de parâmetros e proteção contra erros do usuário. Procurou-se torna-lo o mais "amigável" possível com o usuário. A Figura 6 mostra um exemplo de uma das "Dialog Boxes" desenvolvidas. Neste caso, trata-se da implementação de um subsistema tipo placa plana retangular. Pode-se observar os dados de geometria, de material, de amortecimento e de carregamento que são solicitados pelo software.

O software permite, também, a manipulação dos resultados obtidos, através de gráficos, tabelas, arquivos em winchester e impressão em papel.

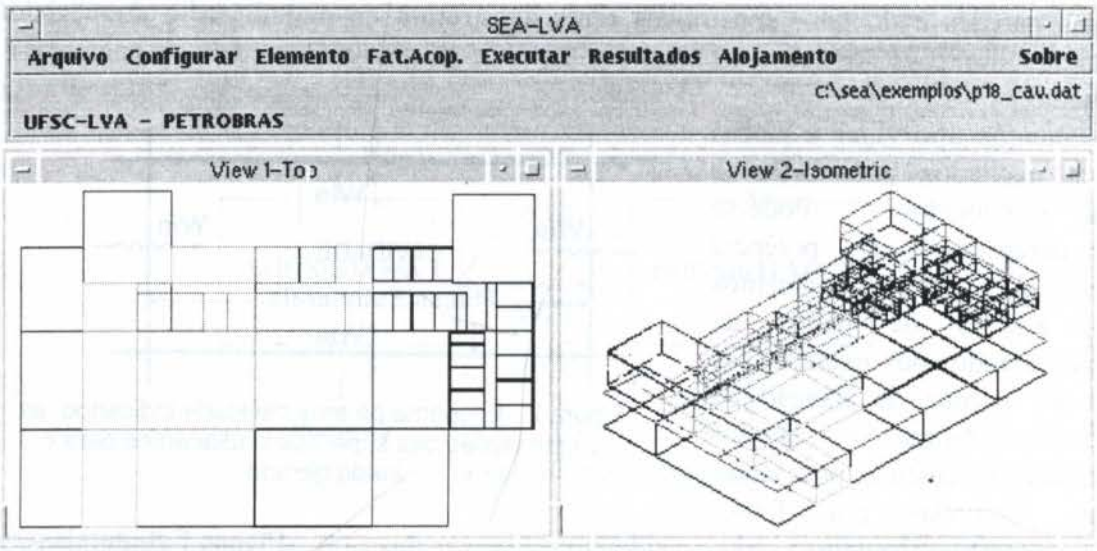

Figura 4 - Software SEA-LVA

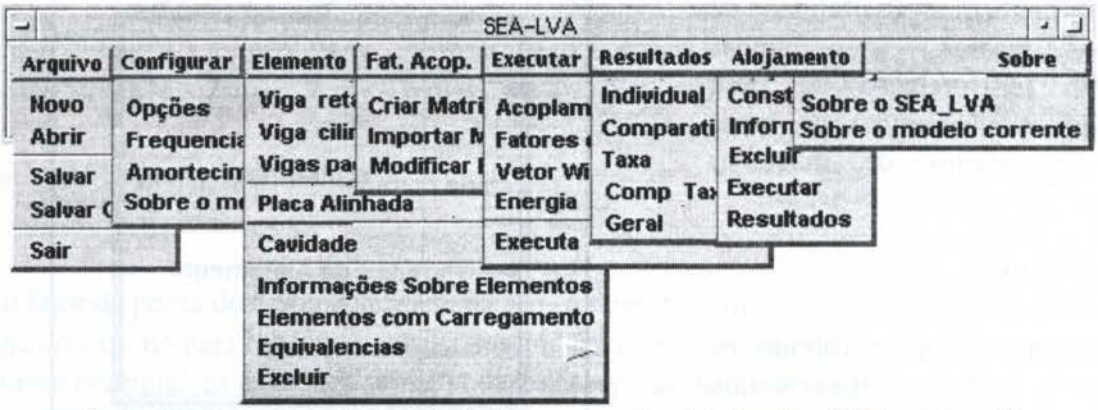

Figura 5 - Comandos diretos do Software que vão abrir janelas ("Dialog Boxes")

O usuário modela a plataforma observando-a tomar forma na tela, através de vistas isométricas, de topo e laterais. Com isso, erros de coordenadas ou de geometria podem ser facilmente detectados, até mesmo visualmente.

Tentou-se otimizar a entrada de dados, para que não se torne excessivamente moroso o trabalho de modelamento da estrutura. Pode-se assim, em cerca de um dia de trabalho, para um usuário com experiência na utilização do software, modelar uma plataforma completa (com as devidas simplificações).

Para tornar mais fácil a utilização do software, foi desenvolvido um algoritmo que, a partir do desenho da plataforma, determina automaticamente os acoplamentos entre os elementos. O usuário necessita fornecer apenas as informações geométricas, tais como dimensões de cada componente e sua localização no espaço.

Depois de modelada a plataforma, o software oferece a vantagem de permitir a análise da melhor forma construtiva para que os níveis limites de ruído e de vibração sejam obedecidos nos locais desejados.

A tabela abaixo mostra o tempo de processamento em função do número de subsistemas. Uma plataforma pode ser modelada com cerca de 300 subsistemas. Alguns problemas específicos podem ser analisados através de modelos contendo de 100 a 200 subsistemas.

Subsistemas	Processamento(minutos)
160	10
218	26
326	86

Máquina usada: Micro PC 486 DX2-66, 8Mb RAM, velocidade do winchester 1Mb/s

O software possui um módulo de saída de resultados, através do qual pode-se analisar a resposta dos subsistemas através de gráficos e tabelas, como os mostrados na Figura 8 e 9.

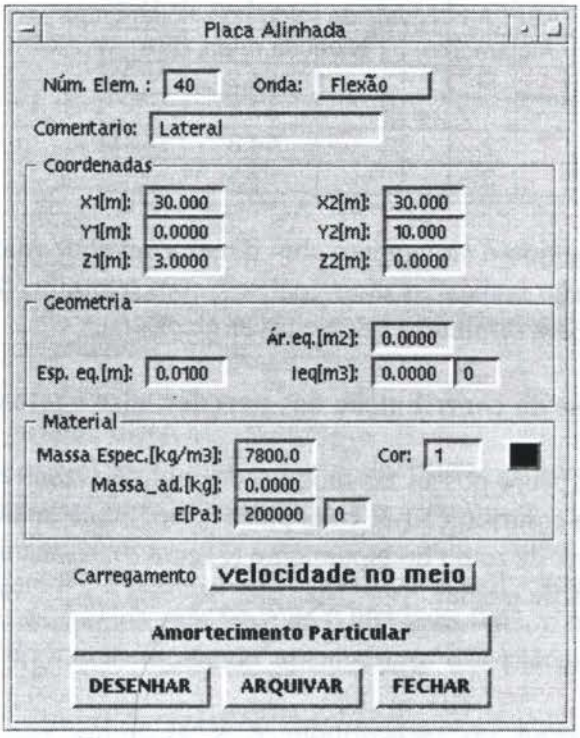

Figura 6 - Entrada de dados para placa

5. EXEMPLO DE APLICAÇÃO DO SOFTWARE SEA-LVA-UFSC

Para ilustrar a aplicação do software foi modelada uma parte de uma plataforma (hipotética), com 40 subsistemas (placas com ondas de flexão) e 4 alojamentos, conforme Figura 7.

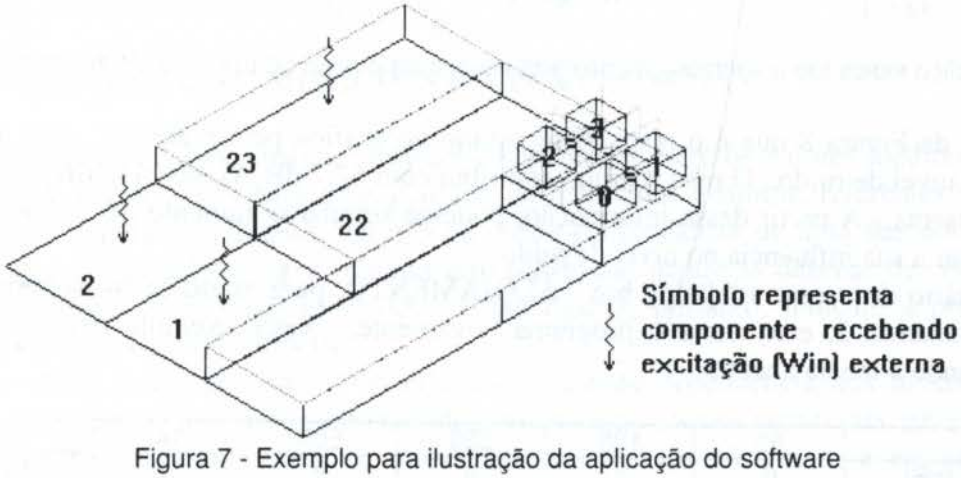

Figura 7 - Exemplo para ilustração da aplicação do software

A plataforma modelada contém dois pisos. Os alojamentos estão no piso superior, numerados de 0 a 3. Para excitar a plataforma, foram aplicados carregamentos em três placas, 1, 2 e 23, conforme mostradas na Figura 7. Esses carregamentos representam a vibração causada por máquinas instaladas nessas placas. Utilizaram-se valores das vibrações de bombas de injeção de água para as placas 1 e 2, e de um turbo-compressor para a placa 23.

Após a execução do software, os níveis globais de ruído, em dB(A), para cada alojamento, estão na tabela abaixo.

TABELA I - Níveis de ruído nos alojamentos

Alojamento	Nível de ruído, dBA
0	64.2
1	57.5
2	64.3
3	63.5

Conhecido o alojamento com o maior nível de ruído, nesse caso o de número 2, com 64.3 dB(A), serão realizadas duas análises, com o auxílio do software, com o propósito de propor soluções para diminuição desse nível.

5.1 Análise da contribuição das paredes, piso e teto do alojamento para o nível de ruído

O software possui no módulo de saída de resultados, uma opção que permite o usuário verificar a contribuição de cada placa (piso, teto e laterais) individualmente, em forma gráfica, para o nível de ruído do alojamento (Figura 8). Estes dados também encontram-se disponíveis em formas de tabelas.

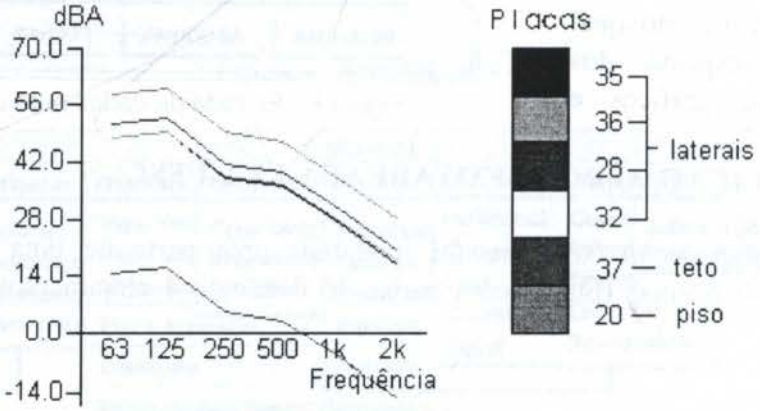

Figura 8 - Gráfico indicando a contribuição de cada placa para o nível de ruído no alojamento 2

Observa-se da Figura 8 que é o piso, representado no gráfico pela placa 20 , que mais contribui para o nível de ruído. O piso sozinho contribui com 62.7 dB(A), dos 64.3dBA que o alojamento apresenta. A partir dessa informação, pode-se simular o aumento de isolamento no piso e verificar a sua influência no nível de ruído.

Para isso, o usuário deve usar a "dialog box" ALOJAMENTO, para modificar o isolamento do piso do alojamento 2, e executar o programa novamente. Neste exemplo mudou-se o isolamento segundo a tabela abaixo.

Frequência (Hz)	63	125	250	500	1k	2k
Isolamento Antes (dB)	0	3	6	9	12	15
Isolamento Depois(dB)	10	13	16	19	22	25

Com essa modificação, o nível global de ruído caiu de 64.3 dB(A) para 59.8dB(A), isto é, quase 5 dBA.

Os novos valores da contribuição das placas para o nível de ruídos, são mostrados na Figura 9.

Observa-se que o piso deixou de ser a placa dominante na contribuição para o nível global de ruído.

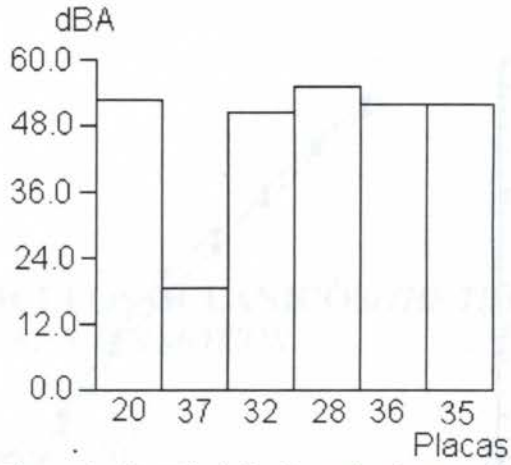

Figura 9 - Contribuição de cada placa, após aumento do isolamento do piso (nível global).

5.2 Análise da contribuição das máquinas para o nível de ruído

O software possui um recurso, que permite ao usuário, simular o desligamento de máquinas, com o propósito de se avaliar a contribuição de cada máquina no nível de ruído dos alojamentos.

Desligando-se o turbo-compressor, da placa 23, o nível de ruído do alojamento 2 reduz-se para 52 dB(A).

Conclui-se ser o turbo-compressor, o responsável pela maior fonte de ruído gerado no alojamento. Em seguida, o usuário pode simular soluções que reduzam esse ruído. Uma delas é agir no caminho da propagação das vibrações geradas pelo turbo-compressor. Um caminho importante, passa pela placa 22 (Figura 7), e pode-se então, verificar a influência de um aumento do fator de perda dessa placa. Aumentando este fator de 0.005 para 0.01, o nível de ruído do alojamento 2 cai para 63.6dB(A). Isso mudando apenas uma das placas do caminho de propagação.

Outra alteração importante que pode ser simulada, é a modificação do local do alojamento. Colocando-se o alojamento 2 no primeiro piso, logo abaixo de sua posição original, e executando o modelo, o novo nível de ruído é de 53 dB(A). Consegue-se uma redução de mais de 10 dB(A) sem nenhum investimento direto no controle de ruído, apenas escolhendo-se um local mais apropriado para sua localização.

Estas análises, são apenas exemplos das muitas possíveis que o software permite fazer, e demostram a grande potencialidade para a otimização de projetos de plataformas no que se referem aos níveis de vibrações e de ruído.

6. COMPARAÇÕES COM MEDIÇÕES EM PLATAFORMAS

As Figuras 10a e 10b, abaixo, mostram comparações entre os valores medidos (Lenzi e Reinas, 1995) e calculados para duas paredes, de ambientes distintos, referentes a uma das plataformas avaliadas. A Figura 10a mostra ótima concordância de uma das comparações, enquanto que a Figura 10b indica o maior erro observado dentre as dezenas de comparações feitas com valores obtidos de medições. Estas figuras, portanto, indicam a precisão das estimativas realizadas pelo software.

Após vários casos analisados, observou-se a grande dependência dos níveis de ruído preditos em relação ao amortecimento real dos vários componentes estruturais, principalmente aqueles situados na "linha direta"de transmissão da energia vibratória, e em relação aos fatores de acoplamento entre componentes tipo chapas contendo vigas nas uniões. Estudos

adicionais estão sendo conduzidos para aprimorar a precisão destes parâmetros, que servem como dados de entrada, com o objetivo de aprimorar a precisão das estimativas feitas pelo software.

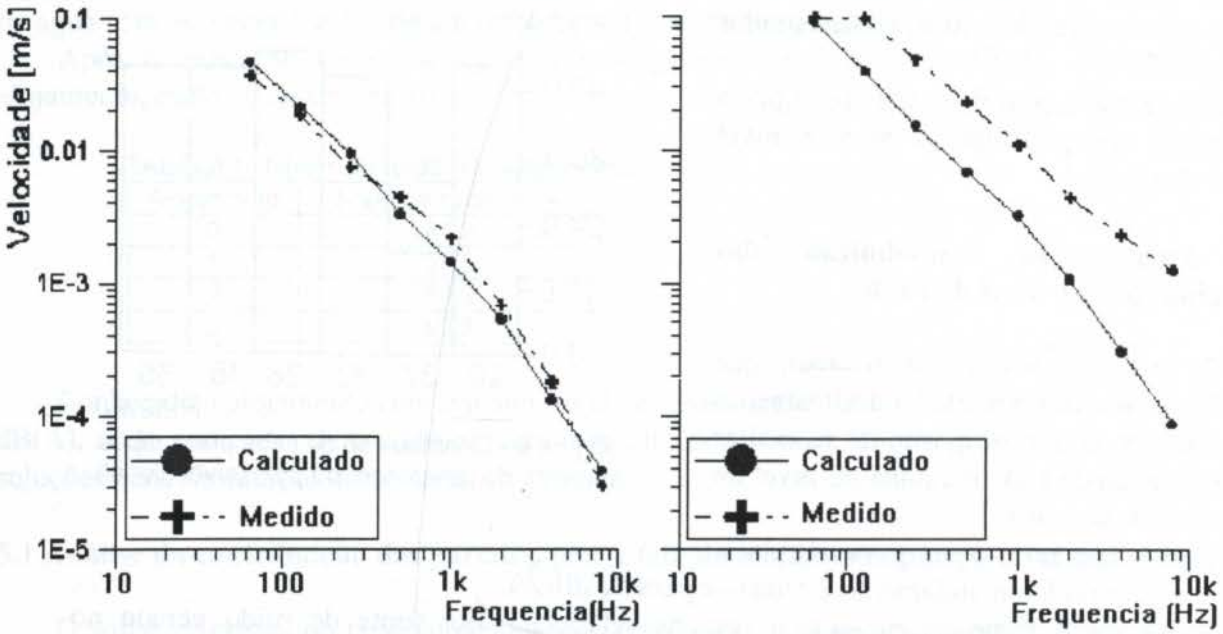

(a) (b)

Figura 10 - Comparação entre resultados calculados pelo software SEA-LVA-UFSC com valores de medições em plataformas em operação.

7. CONCLUSÕES

Inicialmente deve-se destacar o baixo tempo de processamento dispendido pelo software para cálculo de um modelo relativamente complexo, envolvendo mais de 200 subsistemas.

O software mostrou-se extremamente útil para análise do ruído formado nos alojamentos, permitindo identificar e quantificar o ruído transmitido individualmente para todas as paredes, piso e teto que o envolvem.

É possível avaliar os efeitos das várias "fontes" (máquinas e/ou equipamentos) individualmente, ou em grupos, bem como as reduções nos níveis de ruído em um determinado alojamento, caso algumas dessas "fontes" recebam tratamento de isolamento das vibrações transmitidas à estrutura.

Os caminhos de propagação de energia podem ser avaliados usando as funções implementadas de comparação entre fluxos líquidos de potência.

8. REFERÊNCIAS BIBLIOGRÁFICAS

LENZI, A., Análise Estatística Energética - Notas de aula, curso de Pós-Graduação em Engenharia Mecânica, UFSC, 1992.

LENZI, A., REINAS, J., Medições dos níveis de vibração e de ruído nas áreas de operação e de alojamentos da Plataforma SS-44 (Marlim). Relatório Interno, contrato FEESC(UFSC) / PETROBRAS, 1995.

LYON, R. H., Statistical Energy Analysis of Dynamical Systems: Theory and Applications, MIT Press, 1973.

XIV Brazilian Congress of Mechanical Engineering
Obeid Plaza Hotel Convention Center - Bauru - SP/Brazil
December 08-12th 1997

PAPER CODE: COB802

PREDIÇÃO DE MOVIMENTO DE VEÍCULOS OCEÂNICOS/*THE TIME PREDICTION OF OCEAN VEHICLES MOTION*

Helio Mitio Morishita
Departamento de Engenharia Naval e Oceânica, Escola Politécnica, USP
Av. Prof. Mello Moraes, 2231 CEP 05508-900, São Paulo, Brasil - E-mail: hmmorish@usp.br

Abstract

The study of the time prediction of ocean vehicle motions has always attracted the attention of naval architects due to its potential application to improve the performance of control systems of certain marine operations. The motion of an ocean vehicle is due to random action of wave and wind and it is influenced by its speed and load. Therefore, the vessel dynamics can be adequately modelled as a time variant stochastic system and an attempt to predict its motions can be based on adaptive approach developed to stochastic systems. In this paper the prediction of a ship roll motion based on an ARMA model is analysed. The coefficients of the model are estimated using the recursive prediction error method. The study is carried out using data collected during sea trial of a ship and a potential application is shown in the landing of a helicopter on the vessel.

Keyword

estimação recursiva, predição adaptativo, movimento de navios, recursive estimation, adaptive prediction, ship motion

1. INTRODUÇÃO

Um dos estudos que tem sido realizado na área de engenharia naval e oceânica é a predição dos movimentos de unidades flutuantes, com o objetivo de aperfeiçoar o desempenho de algum sistema de controle ou de alguma operação. Por exemplo, a predição de alguns movimentos pode tornar mais segura a aterrissagem de aeronaves em navios ou melhorar o sistema de controle de lançamento de projéteis. Na engenharia oceânica a predição dos movimentos pode ser útil na operação do sino de mergulho, ou ainda, na operação de embarcações de apoio como as barcaças com guindastes. Ainda nesta área, alguns sistemas de posicionamento dinâmico são dotados de preditores para preverem o deslocamento do veículo na eventualidade de falha de todos os sensores de posição.

No caso de aterrissagem de aeronaves em navios, os últimos segundos são os mais importantes, e a determinação do instante de contacto de modo seguro não é um problema fácil. Isto porque tanto a aeronave, devido ao vento, como o navio, devido ao vento e a onda, sofrem perturbações de natureza estocástica. Atualmente, a aterrissagem de helicópteros nos conveses de embarcações do porte das fragatas e corvetas, nos momentos finais, é comandada exclusivamente pelo piloto, sendo que o sucesso da operação depende, essencialmente, da sua perícia. A segurança desta operação, no entanto, poderia ser aumentada se fosse predito o

movimento do navio de no mínimo 5s a 10 ou 15 s adiante. Com 5 s haveria tempo de abortar a aterrissagem e, conhecendo-se a predição com horizonte de 10 a 15s, o início da operação poderia ser decidido com maior segurança.

O estudo de predição dos movimentos de navios tem sido realizado sob diversos enfoques. Por exemplo, O'Relly (1987) baseia sua análise no RAO (Response Amplitude Operator) e define um índice de energia para estabelecer o grau de segurança para a aterrissagem do navio. Este método requer a determinação do RAO para cada navio, além de sensores a bordo para determinar o índice de energia, uma vez que ele é baseado na velocidade e posição de um determinado ponto do navio. Predição baseado em filtro de Kalman tem sido usado por Sidar e Doolin (1983) e Chung, Bien e Kim (1990). No entanto a utilização do filtro de Kalman pressupõe o conhecimento de alguns parâmetros, que nem sempre é o caso, e a utilização do filtro extendido de Kalman pode levar a problemas de divergência numérica.

Uma alternativa atraente para a predição do movimento do navio é o método adaptativo na medida em que os coeficientes do modelo são estimados a cada momento, incorporando as alterações que ocorrem no ambiente marítimo, e não se exige praticamente nenhum conhecimento prévio do sistema, além da sua ordem. Nesta abordagem o sinal do movimento do navio é considerado como uma série temporal e tem sido utilizado por Jeffery e Samra (1985), Lin (1987), Broome e Pittaras (1990) e Pittaras (1992). Para utilizar esta abordagem são necessários desenvolver algoritmos para a estimação recursiva de parâmetros e também para a predição.

Neste trabalho é abordada, em particular, a predição do jogo do navio, utilizando o método adaptativo aplicado ao modelo ARMA. A motivação para este tipo de abordagem é a própria natureza do movimento do navio, que por ser excitado aleatoriamente, tanto pela onda do mar como pelo vento, pode ser considerado como um processo estocástico.

2. MODELO MATEMÁTICO E ESTIMAÇÃO DE PARÂMETROS

Para efetuar a predição de modo adaptativa é necessário adotar, inicialmente, uma estrutura matemática para a dinâmica do sistema e, posteriormente, estimar os valores dos seus coeficientes. Para processos estocásticos estacionários com média nula e densidade espectral de energia racional em $\cos\omega$ a estrutura conveniente é a conhecida como ARMA(Auto Regressive Moving Average):

$$A(q^{-1})y(t) = C(q^{-1})e(t) \tag{1}$$

onde: $A(q^{-1}) = 1 + a_1 q^{-1} + .. + a_{na} q^{-na}$; $C(q^{-1}) = 1 + c_1 q^{-1} + .. + c_{nc} q^{-nc}$; y é a saída do sistema; e é um ruído branco; t é o tempo discreto; na e nc são, respectivamente, as ordens dos polinômio $A(q^{-1})$ e $C(q^{-1})$ e q^{-1} é o operador de atraso, isto é, $q^{-1}y(t) = y(t-1)$

Se houver uma perturbação constante a equação (1) pode ser generalizada para:

$$A(q^{-1})y(t) = C(q^{-1})e(t) + d \tag{2}$$

onde d é uma constante. Um caso particular do modelo ARMA é o AR (Auto Regressive) que ocorre quando $C(q^{-1}) = 1$.

A estimativa dos coeficientes dos polinômios $A(q^{-1})$ e $C(q^{-1})$ e da constante d pode ser efetuada utilizando-se o método de estimação do erro previsto (Ljung e Soderstrom, 1985) que é obtida minimizando-se uma função de custo expressa por:

$$V(\theta) = E[\frac{1}{2}\varepsilon^T(t,\theta)\varepsilon(t,\theta] \tag{3}$$

onde $\theta = (-a_1 - a_2 .. - a_{na}\ c_1\ c_2\ ..c_{nc}\ d)$ e $\varepsilon(t) = y(t) - \hat{y}(t)$.

Pode-se mostrar que, a partir da equação (3), a estimação recursiva dos parâmetros do vetor θ, $\hat{\theta}$, é dada por:

$$\varepsilon(t) = y(t) - \hat{y}(t) \tag{4a}$$

$$R(t) = R(t-1) + \gamma(t)\left[\psi(t)\psi^T(t) - R(t-1)\right] \tag{4b}$$

$$\hat{\theta}(t) = \hat{\theta}(t-1) + \gamma(t)R^{-1}(t)\psi(t)\varepsilon(t) \tag{4c}$$

$$\varphi^T(t+1) = (-y(t) ..- y(t-na+1) \quad \varepsilon(t) ... \varepsilon(t-nc+1)\ 1) \tag{4d}$$

$$\hat{y}(t+1) = \hat{\theta}^T(t)\varphi(t+1) \tag{4e}$$

O vetor $\psi(t+1)$ é composto por:

$$\psi(t+1) = (-\tilde{y}(t) ..- \tilde{y}(t-na+1) \quad \tilde{\varepsilon}(t) ... \tilde{\varepsilon}(t-nc+1)\ \tilde{d}) \tag{4f}$$

onde: $\tilde{y}(t) = y(t) - c_1\tilde{y}(t-1) - ..- c_{nc}\tilde{y}(t-nc)$ (4g)

$$\tilde{\varepsilon}(t) = \varepsilon(t) - c_1\tilde{\varepsilon}(t-1) - ..c_{nc}\tilde{\varepsilon}(t-nc) \tag{4h}$$

$$\tilde{d}(t) = 1 - c_1\tilde{d}(t-1) - ..- c_{nc}\tilde{d}(t-nc) \tag{4i}$$

A implementação deste algorítimo, por ser um método numérico, comporta uma série de alternativas. A seguir são destacados alguns aspectos computacionais que merecem ser observados na utilização deste método.

a) Inversão da matriz $R(t)$

No algorítimo (4) comparece a inversão da matriz $R(t)$. A maneira simples de efetuar esta operação é aplicando o lema da inversão das matrizes. No entanto, este procedimento pode, potencialmente, levar a um mal condicionamento numérico. Para evitar este problema, neste trabalho foi utilizado a inversão de matriz baseado na fatoração U-D de Bierman;

b)Atualização com o resíduo

No desenvolvimento teórico do algorítmo comparece naturalmente o erro de predição que é dado por:

$$\varepsilon(t) = y(t) - \hat{y}(t) = y(t) - \hat{\theta}(t-1)\varphi(t)$$

No entanto, o desempenho do algoritmo (4) pode ser melhorado se o erro de predição for substituído pelo resíduo, isto é,

$$\bar{\varepsilon}(t) = y(t) - \hat{\theta}(t)\varphi(t)$$

Para considerar o resíduo no algoritmo recursivo desenvolvido para o modelo ARMA basta substituir $\varepsilon(t)$ por $\bar{\varepsilon}(t)$ nas equações (4d) e (4h).

c) Verificação da estabilidade

Pode-se mostrar que o critério de estimação de parâmetros adotado requer que as raízes de $C(q^{-1})$ estejam no interior do círculo unitário. Para garantir esta condição, a cada instante, o módulo das raízes do polinômio $\hat{C}(q^{-1})$ são comparados com a unidade e, se algum deles for maior, os valores do vetor $\hat{\theta}(t)$ são recalculados com um ganho menor.

d) Fator de esquecimento

O ganho $\gamma(t)$ é associado ao fator de esquecimento λ para ponderar com maior ênfase as últimas observações. Este fator, na sua forma variável, é dado por:

$$\lambda(t) = \lambda_0\,\lambda(t-1) + (1-\lambda_0)$$

3. PREDIÇÃO

A predição de um processo estocástico estacionário $y(t)$ é a "melhor" estimativa possível do seu valor no instante $t+k$, $k>0$ tendo observado os seus $n+1$ valores passados, isto é, $y(t), y(t-1), ..y(t-n)$. É natural supor que a predição de $y(t+k)$ dependa dos seus valores passados, e desta forma a sua estimativa, denotada por $\hat{y}(t+k|t)$, seja dada por:

$$\hat{y}(t+k|t) = f[y(t), y(t-1), .., y(t-n)] \tag{5}$$

Para determinar a função f o critério normalmente utilizado é minimizar o erro quadrático médio da predição, isto é,:

$$V(k) = E\{[y(t+k) - \hat{y}(t+k|t)]^2\} \tag{6}$$

Aplicando a equação (6) para o processo estocástico descrito pela equação (2) obtém-se que a predição é obtida por:

$$C(q^{-1})\hat{y}(t+k|t) = G(q^{-1})y(t) + F(1)d \tag{7}$$

onde

$$F(q^{-1}) = 1 + f_1 q^{-1} + .. + f_{k-1} q^{1-k}$$

$$G(q^{-1}) = g_0 + g_1 q^{-1} + .. + g_{ng} q^{-ng}, \text{ com } ng = \max(na,\ nc-k+1,\ 1) - 1$$

e os coeficientes dos polinômios $F(q^{-1})$ e $G(q^{-1})$ podem ser obtidos a partir da seguinte identidade:

$$C(q^{-1}) = A(q^{-1})F(q^{-1}) + q^{-k}G(q^{-1})$$

4. PREDIÇÃO DO JOGO DO NAVIO

Antes de efetuar a predição do jogo do navio é interessante discutir a consistência do modelo ARMA para representar a sua dinâmica. Para isto serão admitidas as seguintes hipóteses: a) o movimento do jogo do navio é desacoplado dos demais movimentos; b) a única ação ambiental que provoca o movimento do jogo do navio é a onda do mar; c) os movimentos angulares são de pequena magnitude; d) a elevação da superfície do mar é um processo ergódico, gaussiano e média nula. Com estas hipóteses, o movimento do jogo do navio pode ser descrito por:

$$\ddot{\Phi} + 2\varsigma\omega_n\dot{\Phi} + \omega_n^2\Phi = \frac{1}{I_x}K_o \tag{8}$$

onde: Φ é o ângulo do jogo; I_x é o momento de inércia virtual para o jogo do navio; ς é o fator de amortecimento; ω_n é a frequência natural não amortecida; K_o é o momento externo sobre o navio; o ponto sobre a variável significa derivada em relação ao tempo.

A equação (8) é caso de um sistema linear alimentado por um processo estocástico. Sendo assim, pode-se calcular a relação entre a densidade espectral de energia entre o sinal de saída e de entrada, que para uma onda de través, é dada por:

$$\mathbf{S}_{\Phi\Phi}(\omega) = |G_\Phi(j\omega)|^2\, \mathbf{S}_{KK}(\omega) \tag{9}$$

onde ω é a frequência; $j = \sqrt{-1}$; $\mathbf{S}_{\Phi\Phi}$ é a densidade espectral de energia do sinal do jogo do navio; $\mathbf{S}_{KK}$ é a densidade espectral de energia do esforço, e

$$G_\Phi(s) = \frac{\Phi(s)}{K_o(s)} = \frac{1}{I_x'(s^2 + 2\varsigma\omega_n s + \omega_n^2)} \tag{10}$$

Neste trabalho será admitido que o esforço pode ser calculado linearmente a partir da altura da onda, isto é, existe uma função de transferência $G_K(s)$ tal que:

$$\mathbf{S}_{KK}(\omega) = |G_K(j\omega)|^2\, \mathbf{S}_{\zeta\zeta}(\omega) \tag{11}$$

onde $\mathbf{S}_{\zeta\zeta}$ é o espectro da onda. Em princípio, os parâmetros desta função de transferência, para um determinado casco, deve depender da velocidade do navio e do ângulo de incidência da onda. Substituindo a equação (11) em (9) tem-se:

$$\mathbf{S}_{\Phi\Phi}(\omega) = \left|G_{\Phi}(j\omega)G_{K}(j\omega)\right|^{2}\mathbf{S}_{\zeta\zeta}(\omega) \tag{12}$$

A equação (12) mostra que o ângulo jogo do navio pode ser obtido filtrando a altura da onda através da função de transferência $G_{\Phi}(j\omega)G_{K}(j\omega)$. A altura da onda, por sua vez, pode ser gerada alimentando um filtro com ruído branco, isto é através de uma função de transferência $G_{o}(s)$ tal que

$$\mathbf{S}_{\zeta\zeta}(\omega) = \left|G_{o}(j\omega)\right|^{2} \tag{13}$$

Substituindo a equação (13) em (12) e transformando a função de transferência contínua em discreta tem-se a estrutura ARMA para o movimento do jogo do navio. Portanto, mediante as simplificações efetuadas, é possível adotar este modelo para o movimento do navio em questão. Até o presente momento considerou-se a onda de través. Para os demais casos de ângulo de incidência de onda, o navio responde `a frequência de encontro das ondas.

O estudo de predição foi realizado baseando-se nos dados experimentais obtidos a bordo de uma fragata durante a sua prova de mar e cedidas pela University College London. Foram efetuadas uma série de registros para diferentes manobras variando-se a velocidade e o seu aproamento e também para diferentes estados de mar e direção e velocidade do vento bem como com os estabilizadores ativados e desativados. Uma análise detalhada destes dados são mostrados em Morishita(1996).

O primeiro passo para a estimação dos parâmetros é a determinação da ordem do modelo. Neste trabalho ela foi selecionado analisando-se o índice FPE (Final Prediction Error) e também procurando minimizar o erro de predição quadrático acumulado definido como:

$$V(N) = \sum_{t=1}^{N}[y(t+1) - \hat{y}(t+1|t)]^{2} \tag{14}$$

Após exaustivos testes verificou-se que o melhor modelo é o AR de ordem 18. Esta magnitude é compatível com os resultados de outros trabalhos tais como de Broome e Pitaras(1990) e Pittaras(1992) que sugerem, respectivamente, 20 e 14 para a ordem do modelo AR para o estudo de predição do jogo do navio. É interessante observar que esta ordem é satisfatória independente do ângulo de incidência da onda sobre o navio desde que não haja a atuação dos estabilizadores.

Na Fig. 1 são mostrados os resultados de predição para os horizontes de 5, 10 e 15 s que correspondem, aproximadamente, de 0,5 a 1,5 vezes o período típico do movimento do jogo do navio, que é da ordem de 10 s. Uma análise visual permite perceber que há uma deterioração na qualidade da predição na medida em que o horizonte de predição aumenta e uma análise sistematizada destes erros são apresentados em Morishita (1996).

5. ATERRISSAGEM DE AERONAVES

A operação de aterrissagem é, obviamente, regulamentada por normas de segurança e, no caso de helicópteros, um dos itens estabelece o ângulo máximo de jogo permissível para a operação. Este ângulo máximo depende do tipo de navio e da aeronave, do ponto de aterrissagem ao longo do convés, e também das condições de visibilidade. Um valor típico de ângulo máximo é 4 graus.

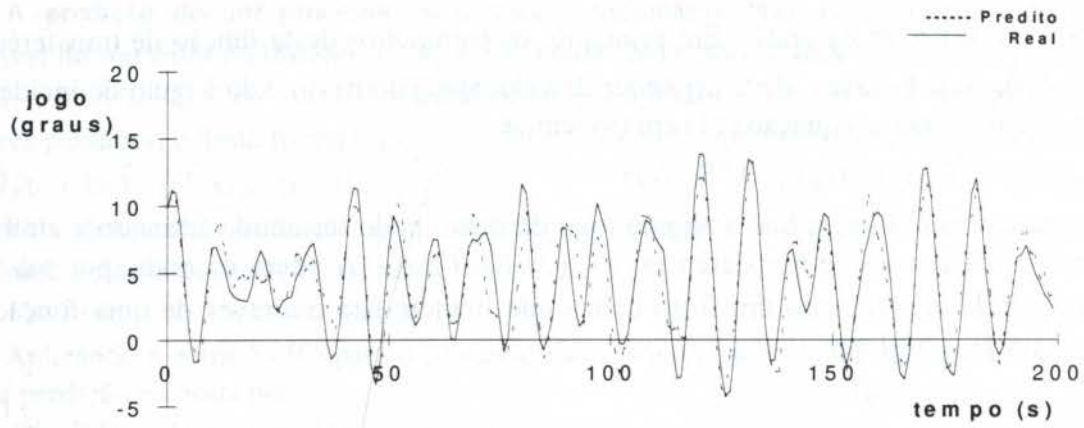

Figura 1a Predição de 5 segundos para o ângulo de jogo do navio

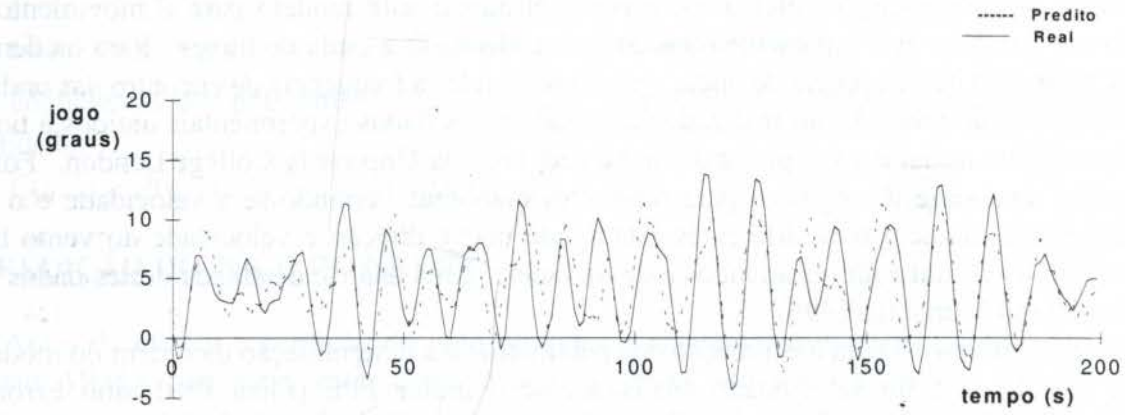

Figura 1b Predição de 10 segundos para o ângulo de jogo do navio

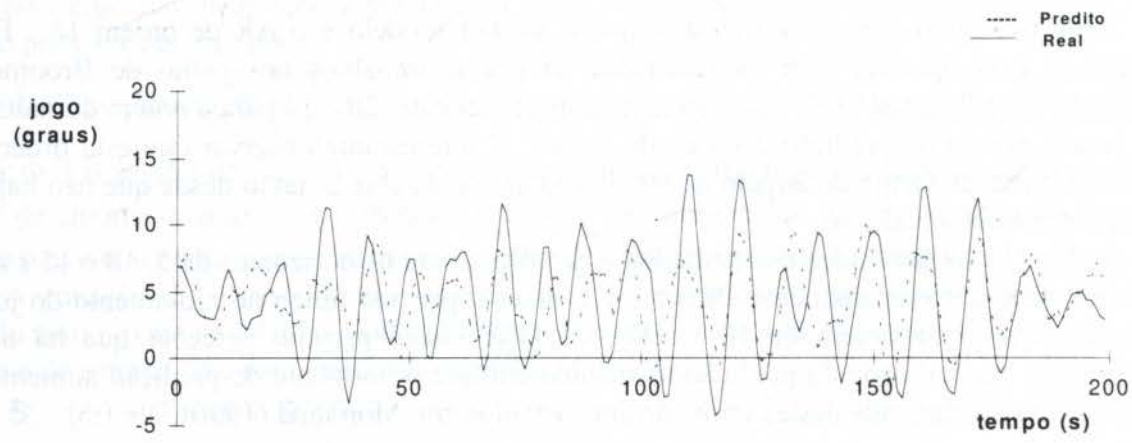

Figura 1c Predição de 15 segundos para o ângulo do jogo do navio

A segurança da operação de aterrissagem poderia ser aumentada se fosse predito a possibilidade de ocorrência destes valores limites dentro de um determinado intervalo de tempo Δt. Isso pode ser efetuado calculando-se a predição, em cada instante, para o intervalo $t+1 \leq t+\Delta t \leq t+k$, e comparando-os com os valores limites (Broome, 1994). Obviamente pode-se tomar uma decisão equivocada baseando-se nesta comparação, pois sempre há o erro de predição. Para analisar as consequências que poderiam advir desta comparação é

interessante admitir, hipoteticamente, que seja conhecido o valor real do ângulo do jogo durante o intervalo de predição. Com esta hipótese verifica-se que podem ocorrer quatro situações ao efetuar a predição:

a) os valores real e previsto são menores que os limites;
b) o valor real é menor que o valor limite, porém a predição indica que ela é maior;
c) o valor real é maior que o limite, porém a predição indica que é menor;
d) os valores real e preditos são maiores que o limite máximo;

Os casos a) e d) são, logicamente, as situações desejadas, pois não se incorre em nenhum tipo de erro. O caso b), embora indesejável, na medida que significa perda de oportunidade de realizar a operação de aterrissagem, está a favor da segurança. Já o caso c) é a situação indesejável, pois é uma indicação falsa que aumenta o risco da operação de aterrissagem. Para se avaliar o número de ocorrência de cada um dos casos acima, foi efetuada uma simulação com os dados de uma das manobras, considerando-se o horizonte de predição de 5, 10 e 15 s e o valor limite de 4^{o}. Os resultados, mostrados na Tab.1, indicam que nos 3 horizontes de predição considerados, os casos desejados, isto é, a soma de a) e d) ocorrem com maior frequência, e que o caso b), que seria a perda de oportunidade, não se apresenta com grande índice de ocorrência. Já no caso indesejado c), para os horizontes de 5, 10 e 15 s, as frequências de ocorrência são, respectivamente, de 9%, 18% e 23%. A primeira vista, parecem ser índices elevados. No entanto, os resultados obtidos com o procedimento utilizado neste trabalho devem ser confrontados com os obtidos a partir de outros critérios para averiguar a sua real validade. Além disso, qualquer que seja o procedimento de predição, os seus resultados devem ser integrados com outras informações para se ter uma operação segura de aterrisagem de aeronaves em embarcações marítimas.

Tab. 1 Frequência de ocorrência dos casos de comparação

	horizonte de predição		
casos de comparação	5 s	10 s	15 s
a) real menor e prev. menor que limite	28%	19%	14%
b) real menor e prev. maior que limite	06%	04%	03%
c) real maior e prev. menor que limite	09%	18%	23%
d) real maior e prev. maior que limite	57%	59%	60%

6. CONCLUSÕES

Neste trabalho foi apresentada a predição do movimento do jogo do navio considerando o registro do ângulo como sendo uma série temporal. O modelo utilizado para a identificação da dinâmica bem como a sua predição foi um modelo AR e os resultados de predição foram utilizados para prever os valores limites de ângulo de jogo recomendado para aterrissagem de helicópteros em navios, e os resultados mostraram que para predição de 10 s a 15 s, o erro que pode incorrer em acidentes é da ordem de 20%. No entanto, novos estudos devem ser realizados para verificar o quão útil é o resultado obtido neste trabalho, uma vez que, atualmente, a aterrissagem é efetuada sem nenhuma predição.

7. REFERÊNCIA BIBLIOGRÁFICA

Box, G. e Jenkins, G. (1976). *Time Series Analysis: forecasting and control*, San Francisco, Holden Day.

Broome, D. (1994) Further Analysis of Ship Motion Prediction, Automatic Control Group, University College London.

Broome, D. & Pittaras, A. (1990). The Time Prediction of Ship Motions at Sea, *Offshore Technology Conference, Proceedings*, vol1, 199-206.

Chung, C.;Bien, Z.e Kim, Y(1990). A Note on Ship-motion Prediction based on Wave-excitation Input Estimation. *IEEE Journal of Oceanic Engineering*, vol. 15 n.3, 244-250.

Jefferys, E. R. e Samra, B. S. (1985) Adaptive Prediction of the Motion of Marine Vehicles. *Transactions of the ASME, Journal of Energy Resources*, Vol 107, 450-454

Lin, N. . (1987). Real Time Estimation of Ship Motion Using Arma Filtering Techniques. *Proceedings OMAE.*

Ljung, L. e Soderstrom, T. (1985). *Theory and Practive of Recursive Identification*, Cambridge: The MIT Press.

Morishita, H. M. (1996) Controle e Predição Aplicados a Veículos Oceânicos, Tese de Livre-Docência apresentada a Escola Politécnica da USP.

O'Relly, P. (1987). Aircraft/Deck Interface Dynamics for Destroyers. *Marine Technology*, Vol. 24 n.1, 15-25.

Pittaras, A. (1992) Adaptive Signal Prediction with Application to Ship Motions, London, University College London. Tese (Doutorado).

Price, W. e Bishop, R. (1974). *Probabilistic Theory of Ship Dynamics*. London: Chapman and Hall.

Sidar, M.e Doolin, B. (1983). On the feasibility of real-time predction of aircraft carrier motion at sea. *IEEE Transactions on Automatic Control*, AC-28 n.3, 350-355.

Wellstead, P.e Zarrop, M. (1991). *Self Tuning Systems: Control and Signal Processing*. Chichester: John Wiley & Sons.

Agradecimentos

O autor agradece a University College London por ter cedido os dados para a elaboração deste trabalho.